18TH INTERNATIONAL CONFERENCE OF YOUNG SCIENTISTS ON ENERGY AND NATURAL SCIENCES ISSUES

CYSENI 2022

24-27TH MAY, 2022
KAUNAS, LITHUANIA

WWW.CYSENI.COM

ORGANIZED BY

Chair of the Scientific Committee   Dr. Sigitas Rimkevičius

Chair of the Organizing Committee   Simona Breidokaitė

IN COOPERATION WITH

INTERNATIONAL SCIENTIFIC COMMITTEE

Dr. Robertas Alzbutas	Lithuania	Dr. Artjoms Obushevs	Switzerland
Dr. Kristina Amalevičiūtė-Volungė	Lithuania	Habil. Dr. Florentin Paladi	Moldova
Dr. Karolina Barčauskaitė	Lithuania	Prof. Panos M. Pardalos	USA
Prof. Sten Bergstrom	Sweden	Dr. Bernhard Peters	Luxemburg
Prof. Dr. Habil. Ralf Ebinghaus	Germany	Dr. Alessandro Petruzzi	Italy
Prof. Bjørn C. Hauback	Norway	Dr. Virginijus Radziukynas	Lithuania
Dr. Luis E. Herranz	Spain	Prof. Finn Ravndal	Norway
Dr. Girmantė Jurkšienė	Lithuania	Dr. Sigitas Rimkevičius	Lithuania
Dr. Inga Konstantinavičiūtė	Lithuania	Prof. Andres Siirde	Estonia
Prof. Pierre-Etienne Labeau	Belgium	Dr. Nerijus Striūgas	Lithuania
Prof. Myriam Lazard	France	Dr. Vita Tilvikienė	Lithuania
Dr. Aleksandrs Ļvovs	Latvia	Dr. Monika Vilkienė	Lithuania
Prof. Dr. Habil. Vytautas Martinaitis	Lithuania	Dr. Akvilė Viršilė	Lithuania
Dr. Darius Milčius	Lithuania	Dr. Victor A. Zhovtyansky	Ukraine
Dr. Anna Mutule	Latvia		

Dear Colleagues,

The International Conference of Young Scientists on Energy and Natural Sciences Issues (CYSENI 2022) has been organized already for the 18th time since 2004, which became an annual tradition. We are very proud to bring together talented young scientists to participate in the 18th CYSENI conference. We expect that this will contribute to exchange of ideas, improved knowledge of young researchers, development of their acquired abilities and contribute to increasing level of exercised research activities. The initiative for such an event came from young and enthusiastic researchers of Lithuanian Energy Institute (LEI). They realised that there are a lot of young, smart and science-oriented young people and they do need a place to share their views, generated ideas and present the latest research results.

This year, Lithuanian Energy Institute with partners from the Lithuanian Research Centre for Agriculture and Forestry, the Center for Physical Sciences and Technology as well as RTO Lithuania continued a partnership in co-organizing the CYSENI 2022 conference. This partnership allowed us to expand the topics of the conference and maintain a high number of participants – more than 150 from around 20 countries.

The conference once again has brought together young researchers and scientists to discuss recent trends in energy and natural sciences sectors worldwide. We are pleased that young scientists further found the conference valuable to present their up to date research results and share scientific experience.

We thank all the contributors who made this conference possible. This includes all people from scientific and organising committees. We would like to thank all participants for their contributions to the Conference and submission of their research papers. Moreover, special thanks to Keynote speakers – Olga Sumińska-Ebersoldt, Marcos António Nogueira, Shulan Zhang, Viktorija Vaštakaitė-Kairienė, Gintaras Valušis, Wojciech Królas and Darius Milčius.

Sincerely,

Conference Organizers

CONTENTS

PLENARY SPEAKERS

- **SPEAKER | Olga Sumińska-Ebersoldt**
Project Manager at Karlsruhe Institute of Technology (KIT), Germany:
STORIES – ENERGY STORAGE ECO-SYSTEM FOR INNOVATION

- **SPEAKER | Marcos António Nogueira**
H2020-AURORAL Project Coordinator, Belgium:
SMART COMMUNITIES AND EUROPEAN GOVERNANCE

- **SPEAKER | Shulan Zhang**
Professor at Northwest A & F University, China:
ATTAINABLE WATER USE EFFICIENCY AND MANAGEMENT
STRATEGIES OF DRY LAND WHEAT/MAIZE IN THE CHINA LOESS
PLATEAU

- **SPEAKER | Viktorija Vaštakaitė-Kairienė**
Senior Researcher at Lithuanian Research Centre for Agriculture and Forestry,
Lithuania:
LIGHTING STRATEGIES FOR IMPROVED QUALITY OF LEAFY GREENS
INDOORS

- **SPEAKER | Gintaras Valušis**
Director at the Center for Physical Sciences and Technology (FTMC), Lithuania:
SEMICONDUCTORS CHIPS AND THEIR EMPLOYMENT FOR "COLOUR"
PHOTOS IN INVISIBLE LIGHT

- **SPEAKER | Wojciech Królas**
Professor at the Institute of Nuclear Physics of the Polish Academy of Sciences in
Kraków, Poland:
IFMIF-DONES: AN ACCELERATOR BASED FUSION-LIKE NEUTRON
SOURCE

- **SPEAKER | Darius Milčius**
Head of Center for Hydrogen Energy Technologies, Lithuanian Energy Institute,
Lithuania:
HYDROGEN TECHNOLOGIES AT LITHUANIAN ENERGY INSTITUTE

OLGA SUMIŃSKA-EBERSOLDT
Project Manager at Karlsruhe Institute of Technology (KIT), Germany

STORIES – ENERGY STORAGE ECO-SYSTEM FOR INNOVATION

The recent geopolitical developments show that Europe must become independent in terms of energy supply, which can only be achieved through intensive use of renewable energies. This process will help to speed up the reduction of greenhouse gas emissions and increase local added value if carried out efficiently.

There are studies indicating the potential of renewables in Europe to be sufficient to supply enough energy for European countries (EWG-LUT_Full-Study_Energy-Transition-Europe.pdf (energywatchgroup.org). Renewable energy can also be generated outside and transported to the EU. However, adequate infrastructure (including energy storage) to meet the needs of all sectors, including heat and electricity for industry, households, and transport exclusively with renewables is not yet in place.

To reach the goal of the European Clean Energy transition, the energy storage in Europe has to be widened and modernized to enable flexible and cost-effective usage of the renewables.

The H2020 project StoRIES addresses these issues by creating a Pan-European eco-system for energy storage providing:

• free-of-charge access to 64 most advanced research infrastructures working in energy storage (electrochemical, chemical, mechanical, thermal, superconducting-magnetic, cross-cutting) and linked topics

• schooling and training possibilities on the topics regarding the energy system technologies, their combinations at different levels (hybrid energy storage), their integration in the energy system and the resulting sustainability aspects

• cooperation and knowledge exchange on the barriers and gaps in the energy storage and overall energy system

• new approach focusing on the applications and solutions and braking the technology silos

StoRIES wants to build up a long-lasting eco-system and this is not possible without young scientists being active in gathering and sharing the knowledge, the skills and the understanding of the global energy and climate problems.

MARCOS ANTÓNIO NOGUEIRA
H2020-AURORAL Project Coordinator, Belgium

SMART COMMUNITIES AND EUROPEAN GOVERNANCE

Our Smart Community approach is not only technical, it is a European governance matter, which needs to be addressed. We are approaching a triple transformation, digital, ecological and social. And we need new ways to organize ourselves. We need to make Europe stronger, we need to co-develop in all three dimensions. Smart Communities are our response and solution to take care of our people and nature. We also need a public digital environment, where they can be placed, to co-develop solutions and to interact, and a freedom of entrepreneuring. With this framework, we can start to close digital divides, using the amazing part of digital proximity. For this we need skills and resources, like the AURORAL middleware, to become digital prosumers and to adapt our system. We also need investment, to balance and ensure that our solutions are not fractioned, but interoperable. Europe's digital sovereignty and security is of high importance. To ensure those, we need to helps rural ecosystems and use territorial intelligence. Europe needs to be a common economic space, a freedom of cooperation, and needs a reform of governance. The problem we face is the vast fractioning of our funding opportunities, the lack of opportunities for common and joint projects, the missing saleability of solutions. We need more room for regions to act and interact, a freedom of action and a new treaty. We have free movement in Europe, but not for the digital sector. We face many blockages yet to fully persuade the digital, ecological and social transition we need.

The H2020-AURORAL project addresses these challenges and makes small solutions big. The reference architecture enables free movement and interoperability, the investment platform and interest group of Smart Tomorrow brand enables regions to joint and cooperate. European policies need to do better in the aspect of digitalisation. And services need to be accessible for the communities, no matter where they are located, not only in the cities where the access is much better that in the rural areas. Because for the establishment of digitalised, better and smarter communities, the regions should be the scale, not the member states.

We need a common standard for the governance of the regions, because the national scale it so big to address and consider out challenges. Regions have to be autonomous on the digital side. Therefore, we need to come together, to work together and to co-design our solutions. This is what the SmarTomorrow European Interest Group does to rebuilt European Governance and to reform it.

Because we all have the common dream of **a free, united and independent Europe**.

SHULAN ZHANG
Professor at Northwest A & F University, China

ATTAINABLE WATER USE EFFICIENCY AND MANAGEMENT STRATEGIES OF DRY LAND WHEAT/MAIZE IN THE CHINA LOESS PLATEAU

Due to the pressure of water scarcity and population growth in arid and semi-arid regions, improving crop yield and water use efficiency (WUE) is critical. Here we discuss the attainable WUE of dryland wheat and maize and management strategies in the China Loess Plateau. Under different management practices wheat yield was between 818 and 7900 kg/ha, the WUE was between 3.4 and 23.4 kg/(ha *mm), and the attainable WUE was 26 kg /(ha *mm),. The yield of maize varied from 1.12 to14.6 Mg/ha, the WUE varied from 2.8 to 39.0 kg/(ha *mm), and the attainable WUE was 45 kg /(ha *mm),. The yield and WUE were the highest under plastic film mulching, and the lowest yield and WUE under no-till or conventional tillage conditions. Nevertheless, regional meta-analysis found that partial-film mulching and full-film mulching had similar yields and WUE. Besides crop variety, soil fertility and nutrient management also impacted crop yield and WUE. For both wheat and maize, the changes in yield and WUE were mainly related to the changes in the proportion of soil evaporation to total evapotranspiration (ET) and changes in the proportion of ET before and after anthesis. In conclusion, closing the yield and WUE gaps of the dryland wheat/maize on the Loess Plateau requires the integrated management practices, including variety, soil fertility, nutrient management, reasonable mulching measures (e. g. tillage) etc.

VIKTORIJA VAŠTAKAITĖ-KAIRIENĖ
Senior Researcher at Lithuanian Research Centre for Agriculture and Forestry, Lithuania

LIGHTING STRATEGIES FOR IMPROVED QUALITY OF LEAFY GREENS INDOORS

Global climate change intensifies droughts, rainfall variability, and extreme frost or heat waves. The unpredictable weather conditions lead to uncertain crop yield and economic losses. To obtain fresh and high-quality vegetable production and have economic benefits, more leafy greens are produced in vertical farming systems. In the climate-controlled environment, the natural sunlight and soil are not required, and the high quality of crops can be achieved by controlling carbon dioxide concentration, temperature, air velocity and moisture content, parameters of artificial lighting and composition of a nutrient solution, and refusing the use of chemical plant protection products. The electric lighting sources are used to illuminate the plants indoors. The environmentally-friendly technology of light-emitting diodes (LEDs) has recently gained popularity due to the indisputable advantages over fluorescent and high-intensity discharge lamps. Light parameters can be selected to stimulate plant photoreceptor activity, ensure healthy growth, enhance desired nutritional attributes, and maintain the quality during storage. In the world, and Lithuania, the most of the studies were conducted to evaluate the effects of the LED lighting spectrum, intensity and photoperiod on the development or growth characteristics or accumulation of nutrients, having health-promoting properties for humans, in leafy vegetables (microgreens, lettuces, spinach and basil plants etc.).

GINTARAS VALUŠIS

Director at the Center for Physical Sciences and Technology (FTMC), Lithuania

SEMICONDUCTORS CHIPS AND THEIR EMPLOYMENT FOR "COLOUR" PHOTOS IN INVISIBLE LIGHT

Semiconductor chips are essential components of all smart electronic devices. Operational principles will be discussed and main parameters will be considered. The particular focus will be dedicated to chips employment for terahertz (THz) imaging aims, when, under special design and excitation conditions, the operation range can exceed the cut-off frequency. Obtained images and applications will be presented.

WOJCIECH KRÓLAS

Professor at the Institute of Nuclear Physics of the Polish Academy of Sciences in Kraków, Poland

IFMIF-DONES: AN ACCELERATOR BASED FUSION-LIKE NEUTRON SOURCE

An ambitious Research Roadmap to the Realisation of Fusion Energy is being pursued in Europe. Its final aim is to provide the basis for an electricity-generating fusion power plant. In the short to medium term, the key research infrastructure is the ITER project, a worldwide endeavour, which will demonstrate the scientific and technological feasibility of fusion on Earth. It is closely followed by a demonstration fusion power plant DEMO (under design), which will be the first reactor producing electricity from fusion to the grid.

The International Fusion Materials Irradiation Facility – DEMO Oriented Neutron Source (IFMIF-DONES) is a research infrastructure for testing, validation and qualification of the materials to be used in DEMO and successive fusion power plants. It is based on a unique neutron source with energy spectrum and flux similar to those expected on the first wall of a D+T fusion reactor. It will also develop a high-current high duty-cycle accelerator technology and liquid metal target technology. I will discuss the need for studies and validation of materials subjected to the harsh radiation environment of fusion devices and present the conceptual design of IFMIF-DONES. Last but not least, I will also describe the research opportunities in other scientific areas, such nuclear physics, medical applications, basic physics studies and industrial application of neutrons offered at IFMIF-DONES beyond its standard program of material studies.

WWW.CYSENI.COM

DARIUS MILČIUS

Head of Center for Hydrogen Energy Technologies,
Lithuanian Energy Institute, Lithuania

HYDROGEN TECHNOLOGIES AT LITHUANIAN ENERGY INSTITUTE

Hydrogen fuel cells are widely considered as a promising power system for stationary and mobile applications in recent years. Hydrogen fuel cells have the potential to a future sustainable energy system and could contribute to the total decrease of CO_2 emission. Though, hydrogen has a high calorific value and its reaction by-product is water, expensive and complex technological methods for hydrogen production and storage must be included. Hydrogen can be extracted by means of various methods including biological process, photo-electrochemical methods, coal gasification, water electrolysis and hydrolysis. The main emphasis in the presentation will be focused on R&D activities at Lithuanian Energy Institute, presenting the latest activities and results on hydrogen production using direct reactions between plasma modified aluminum and water, development of metal hydrides for hydrogen storage and applications in biogas enhancement.

I. ENERGY SCIENCES

I.1. Renewable energy sources

DETECTION OF MECHANICAL DEFECTS IN WIND TURBINES BY VIBRATION ANALYSIS

I. Harida, A. Bouras, R. Boudiaf
Electromechanical Systems Laboratory, Department of Electromechanical Badji Mokhtar University
Annaba – Algeria
00213561518902
karim.bouras@hotmail.com

EXTENDED ABSTRACT

OVERVIEW

Wind energy has many advantages, including, for example, being a 100% natural, renewable and sustainable energy, the optimization of their maintenance process is essential, for this, several research projects have been developed aimed at detecting and diagnosing faults in wind systems. These new diagnostic techniques impress with their online functionalities, speed and precision. Our objective is to contribute to the diagnosis and predictive detection of mechanical faults affecting these wind systems based on electrical generators widely used for the production of electrical energy. For this, a laboratory investigation has been carried out by means of an experimental setup for the study of these faults, taking into account the diagnostic information required by the vibration analysis technique and the different signal processing methods, the number and importance of the faults that can be detected and the degree of certainty in the final diagnosis. Experience has shown that vibration analysis is a reliable tool for detecting and diagnosing wind turbine faults. This technique has high speed and precision to anticipate the fault, in this way, it can be included in a maintenance program using automation and artificial intelligence.

METHODS

This experimental research work has been particularly directed to the vibration signature analysis [1] in order to contribute to extract correctly and reliably the information relating to the failure of degradation caused by combined mechanical defects. For this, we experimentally and volitionally created two mechanical defects on a generator and collected a database of the vibration signal.

The consecutive application of the Fast Fourier transform (FFT) along with the discrete wavelet transform (DWT) [2] has the essential objective of reconciling the advantages of spectral and temporal signatures in favour of predictive detection and exact reading of the mechanical defects affecting the wind systems for different speeds [3].

The unbalance will induce, in a radial plane, a vibration whose spectrum has a component whose base frequency corresponds to the frequency of rotation f_r. It then represents the highest peak with lower amplitude peaks on the harmonics of f_r, this is determined by the following equation:

$$f_{unbalance} = 1 \times f_r. \qquad\qquad (1)$$

Poor tightening of the machine structure generates vibrations and some noise. The typical spectrum measured on a machine in which there is a game contains a large number of peaks at frequencies that are multiples of the rotational frequency. It is also sometimes possible to find peaks at the ½ harmonic (1/2 x the rotational frequency of the shaft) and its multiples.

$$f_{loosening} = 1/2 \times f_r. \qquad\qquad (2)$$

The wavelet transform is an advanced technique allowing the predictive detection of anomalies altering an electrical machine in stationary and variable mode through the signal processing of the supply current (generator). It makes it possible to make a significant improvement in the early diagnosis of degradations of an electric machine under stationary and variable conditions [4]. The wavelet theory indicates that each signal S (s_1, s_2... s_n) can be approximated by the sum of an approximation signal and with some signals detail d_j according to the following formula.

$$s(t) = \sum_i \alpha_i^n \psi_i^n(t) + \sum_{j=1}^n \sum_i \beta_i^j \psi_i^j(t) = a_n + d_n + \cdots + d_1, \qquad (3)$$

where:
α, β are the scales and coefficients of the wavelet.
ψ_n ,ψ_j are respectively the decomposed function at level n and the wavelet function at level j.
n is the level of decomposition, a_n is the approximation signal at level n, d_j is the signal detail at the level n.

RESULTS

Fig. 1 represents respectively the spectra of the generator vibration in the healthy state and in the presence of combined faults: unbalance fault in the shaft and a loosening fault.

It can be seen that the frequencies characterizing the repetitive shocks due to faults stand out clearly (signal in red) at the frequency of 20 Hz and 40 Hz, corresponding to the fault frequencies validated by the application of theoretical equations 1 and 2 when the speed of the generator is 2400 RPM.

The presence of other peaks is only linked to problems of anchoring, assembly, machining, etc.
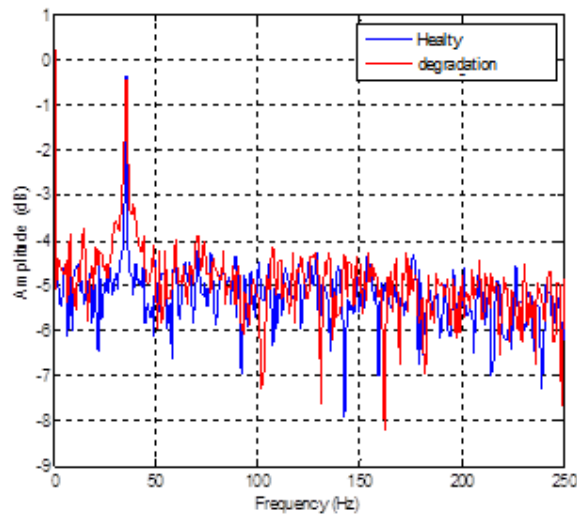
Fig. 1. FFT vibration of healthy and degraded generator for 2400 RPM

The DWT is applied to the experimental signals, Fig. 2 shows the healthy signal associated with the 6-level DWT. It should be noted that the signals of levels (details) show no significant variation apart from the initial oscillations corresponding to the healthy state.
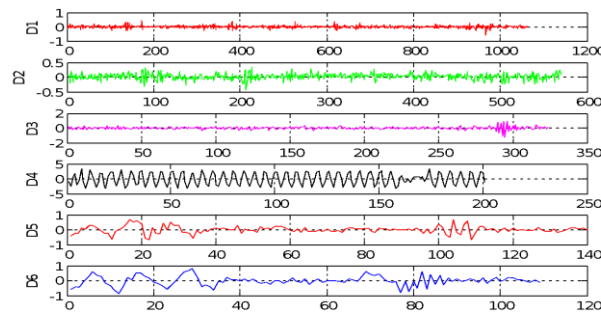
Fig. 2. DWT approaches for healthy generator
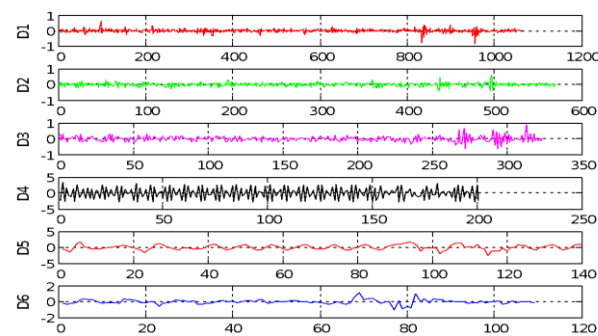
Fig. 3. DWT approaches for degraded generator

The DWT of the generator vibration in the degradation case carried out intentionally is represented in Fig. 3. A significant increase over the healthy state occurs in the energy of the higher level signals of the d3 details and d4 for the lower speed than 2400 RPM. The respective oscillations of these signals are different as soon as the state of the generator goes from the healthy to the degraded state.

CONCLUSIONS

This article focused on an experimental study conducted on the detection of mechanical degradation in order to reliably and quickly determine the faults shown in Figs 1, 2 and 3, for that FFT and DWT were applied simultaneously for analysis of vibration processing.

The experimental results obtained on a test bench may contribute to the reflection of an automated system that would be able to ensure a reliable diagnosis and predictive detection of anomalies affecting the elements of the wind power plant at variable speeds.

Keywords: Wind power plant, vibration analysis, diagnosis, data acquisition

REFERENCES

1. CRAZWFORD, A.R.; CRAWFORD, S. The simplified handbook of Vibration Analysis, Vol. 1: Introduction to Vibration Analysis Fundamentals. In: *Computational Systems Incorporated*, 1992.

2. SESHADRINATH, J.; SINGH, B.; PANIGRAHI, B.K. Investigation of vibration signatures for multiple fault diagnosis in variable frequency drives using complex wavelets, *IEEE Transactions Power Electronics*, 2014, Vol. 29, p. 936-945.

3. BOURAS, A.; BOURAS, S.; ROUABHIA, C.E.; CALLEJO, H.L.; HAOUAM, N.E. Experimental investigation of an alternative wind energy generator, particularly designed, *Revista Facultad De Ingeniería Universidad De Antioquia*, 2020, Vol. 101, p. 100-107.

4. GHODS, A.; LEE, H.H. A frequency-based approach to detect bearing faults in induction motors using discrete wavelet transform. In: *the IEEE International Conference on Industrial Technology*. Busan: South Korea. 2014 February 26 – March 1.

ESTIMATION OF UNCERTAINTIES IN THE PROJECTIONS OF LITHUANIAN RIVERS HYDRO-ENERGY RESOURCES

G. Adžgauskas
Lithuanian Energy Institute
Breslaujos g. 3, LT-44403 Kaunas – Lithuania
+370 682 51125
gintaras.adzgauskas@lei.lt

D. Jakimavičius
Lithuanian Energy Institute
Breslaujos g. 3, LT-44403 Kaunas – Lithuania
+370 37401965
darius.jakimavicius@lei.lt

EXTENDED ABSTRACT

OVERVIEW

As society moves towards a more sustainable world, using only renewable energy sources becomes important. The hydro-energy is one of the renewable energy sources, and it is divided into kinetic and potential resources. Hydrokinetic energy is extracted from running water without creating dams in rivers. Hydro potential energy is absorbed by the construction of dams in the river beds. The kinetic resources of Lithuanian rivers are about 40 kW from 1 km of the river [1]. However, they are not currently in use, but we have about 100 hydropower plants with a total capacity of 130 MW [2]. It is important to know how these resources will change in the future. Using various climate models and emission scenarios, hydrological modelling is applied to determine these changes. It is also important to assess the uncertainties of the projections. Uncertainties can arise for various reasons, such as the accuracy of the initial data, the assessment methodology used, and the choice of climate model and scenarios. The aim of this study is to assess the uncertainties in projections of the kinetic and potential hydro resources of rivers in Lithuania. The studied uncertainty sources are related to the choice of climate models and scenarios.

METHODS

According to the river runoff regime, Lithuania is divided into three hydrological regions: Western Lithuania, Central Lithuania, and South-Eastern Lithuania [3]. The river runoff is the main characteristic that is necessary to assess the uncertainties of hydro-energy resources. It is appropriate to select different rivers from each region for this study. Therefore, from each hydrological region, we selected three rivers that had hydrological measurements (Bartuva, Jūra and Minija from Western Lithuania, Venta, Dubysa and Mūša from Central Lithuania, and Šventoji, Žeimena and Merkys from the hydrological region of South-Eastern Lithuania). Five hydropower plants (Skuodas HPP, Balskai HPP, Kuodžiai

HPP, Dvariukai HPP and Kavarskas HPP) were selected for the uncertainty analysis of potential resources.

The main steps of this research methodology are presented in Fig. 1. In the first step, the climate model data under optimistic (RCP2.6) and pessimistic (RCP8.5) scenarios were adapted for the Lithuanian territory by applying the quantile mapping method. For this purpose, three climate models were developed by leading climate research centers in Europe (ICHEC-EC-EARTH – Ireland; MOHC-HadGEM2-ES – United Kingdom; MPI-M-M-MPI-ESM-LR – Germany) were selected. In the second step, the HBV model developed at the Swedish Meteorological and Hydrological Institute [4] was applied to model river runoff in the near (2021–2040) and far future (2081–2100). In the third step, the projection of kinetic [5] and potential [6] riverine energy was made according to the empirical equations:

$$K = \eta \frac{\rho}{2} v^3 A_D \frac{BL}{20h^2}; \qquad (1)$$

$$v = 0.43 \underline{Q}^{0.25} k^{0.53} I^{0.4}; \qquad (2)$$

$$B = 8 \underline{Q}^{0.30} k^{0.08} I^{-0.2}; \qquad (3)$$

$$h = 0.29 \underline{Q}^{0.45} k^{0.39} I^{-0.2}; \qquad (4)$$

$$P = 7 \Delta H Q, \qquad (5)$$

where K is the hydrokinetic capacity, W, η is the device power coefficient, ρ is the fluid density, kg m^{-3}, v is the average flow velocity, m s^{-1}, A_D is the device swept area, m^2, B is the average river bed width, L is the segment length, m, h is the average bed depth, m, $\underline{Q}$ is the average annual discharge, m^3 s^{-1}, k is the modular discharge coefficient, I is the bed slope, P is the hydro potential capacity, kW, EP is the potential generation, kWh, ΔH is the height of the HPP dam head, m, Q is the monthly discharge (m^3 s^{-1}).

In this study, the uncertainties of hydro-energy projections arise from the selection of climate models and RCP scenarios. All possible combinations of uncertainty sources were made to identify two main sources of uncertainty. Uncertainty was assessed in three steps: 1) the kinetic and potential energies for each model and RCP scenario were calculated; 2) the difference between the lowest and highest result was estimated; 3) using the ratio method, the contribution of each model and scenario to the final result was evaluated. More information on the application of the HBV model to project Lithuanian river runoff [7] and the methodology of estimation of hydro-energy resources is presented in our previous research [8–9].
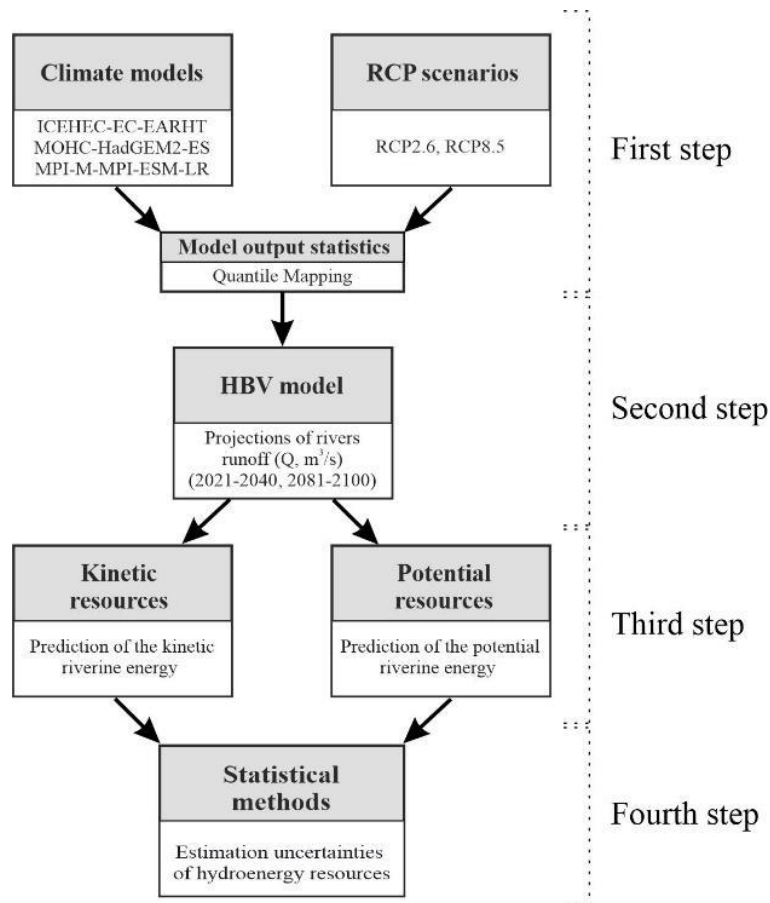
Fig. 1. The main scheme of the research

RESULTS

Before estimating the uncertainties of hydropower projections, an analysis of the runoff projections under different climate models and scenarios was performed. For this purpose, runoff projections for one of the investigated rivers are presented. The runoff projections of the Merkys River are very different (Fig. 1). The largest deviations from the historical period are expected according to MOHC-HadGEM2-ES, smaller according to ICHEC-EC-EARTH and the smallest by MPI-M-M-MPI-ESM-LR. Assessing the deviations by scenario, it was found that smaller differences were obtained under the RCP2.6 and larger under the RCP8.5 scenario.
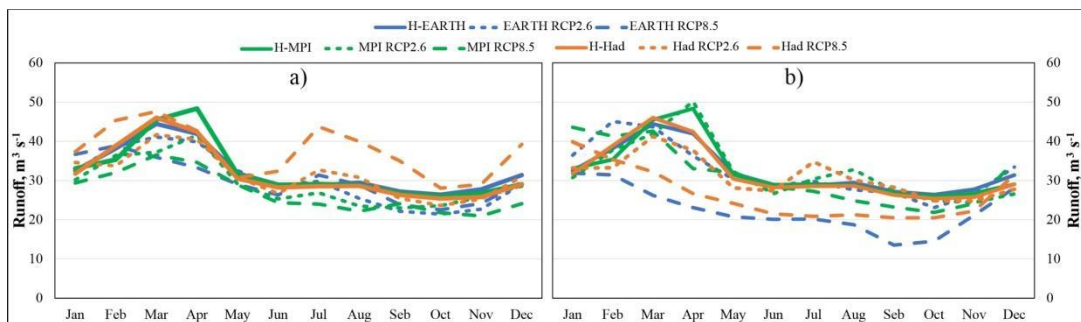
Fig. 2 Runoff projections of the Merkys River in the near (a) and far (b) future according to different climate models and scenarios.

Using calculated projections of river runoff, the hydro-energy resources were evaluated according to formulas (1 – 5). Then the impact of climate models and RCP scenarios on hydro resource projections in the different hydrological regions was determined. The analysis demonstrated that the uncertainty in river kinetic resource projections for the Western Lithuanian hydrological region was mainly caused by the choice of the climate model (70% of the uncertainty in the near future and 82% in the far future) (Fig. 2a). Meanwhile, the lowest spread of results was for the RCP scenarios (30% in the near future and 18% in the far future). In Central Lithuania, the influence of climate models drops to 64% in the near future and 68% in the far future. By contrast, the impact of RCP scenarios was 36% in the near future and 32% in the far future. In the South-eastern hydrological region, the influence of climate models was 62% in the near future, and 54% in the far future, and the influence of the RCP scenario was 38% and 46%, respectively.
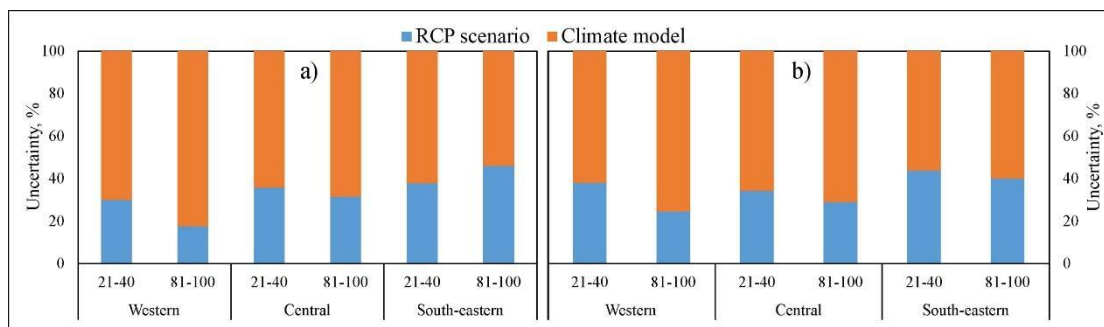
Fig. 3. Uncertainties in hydrokinetic (a) and hydro potential (b) resources projections in the near and far future.

The uncertainty in the prediction of hydro potential resources in the Western Lithuanian hydrological region significantly depended on climate models, ranging from 62% in the near future to 75% in the far future (Fig. 2b). The impact of RCP scenarios on the uncertainty was almost twice as small as that of climate models, at 38% in the near future and further reduced to 25% in the distant future (Fig. 2b).

In the Central Lithuanian hydrological region, the influence of climate models on the projection of hydro potential resources was 66% in the near future and 71% in the far future. The other part of the uncertainty was due to the scenarios. The smallest influence of climate models was in the South-Eastern hydrological region, 56% in the near future and 60% in the far future. The impact of the scenarios became the highest of all the hydrological regions, with 44% and 40%, respectively.

We estimated that the influence of climate models on the uncertainty of kinetic and potential resource projections is highest in the hydrological region of Western Lithuania, slightly lower in the hydrological region of Central Lithuania, and the lowest in the hydrological region of South-Eastern Lithuania. The reason for these tendencies is the different conditions of runoff formation in three hydrological regions. In the rivers of Western Lithuania, the runoff formation is significantly influenced by rain, which contributes to up to 62% of the runoff; and groundwater feeding is a minor contributor. In the South-Eastern hydrological region, the influence of rain on runoff formation decreases, and the contribution of groundwater feeding increases to 55%. Therefore, the prediction of river kinetic and potential resources in the Western Lithuanian hydrological region is more sensitive to the precipitation provided by the climate models as compared to the other two hydrological regions.

CONCLUSIONS

1. In the uncertainties in hydrokinetic and hydro potential resource projections, the impact of climate models in the near and far future was up to 70% and 82%, respectively, whereas in the case of RCP scenarios, up to 30% and 18%, respectively.

2. The greatest influence of climate models was in the hydrological region of Western Lithuania and the smallest – in South-Eastern Lithuania. This was due to different runoff formation conditions: a higher proportion of runoff being formed by rain in the Western Lithuanian hydrological region and predominant groundwater feeding in South-Eastern Lithuania.

Keywords: uncertainty, hydro-energy, RCP scenarios, climate models.

REFERENCES

1. JAKIMAVIČIUS, D.; GAILIUŠIS, B.; ŠARAUSKIENĖ, D.; JURGELĖNAITĖ, A.; MEILUTYTĖ-LUKAUSKIENĖ, D. Assessment of the riverine hydrokinetic energy resources in Lithuania. *Baltica*, 2014, Vol. 27, No. 2., p. 141–150. <https://doi.org/10.5200/baltica.2014.27.23>.

2. KASIULIS, E.; PUNYS, P.; KVARACIEJUS, A.; DUMBRAUSKAS, A.; JUREVIČIUS, L. Small Hydropower in the Baltic States—Current Status and Potential for Future Development. *Energies,* 2020, Vol. 13, No. 24, p. 6731. <https://doi.org/10.3390/en13246731>.

3. AKSTINAS, V.; ŠARAUSKIENĖ, D.; KRIAUČIŪNIENĖ, J.; NAZARENKO, S.; JAKIMAVIČIUS, D. Spatial and Temporal Changes in Hydrological Regionalization of Lowland Rivers. *International Journal of Environmental Research*, 2022, Vol. 16, No. 1, p. 1-14. <https://doi.org/10.1007/s41742-021-00380-8>.

4. KRIAUČIŪNIENĖ J.; JAKIMAVIČIUS, D.; ŠARAUSKIENĖ, D.; KALIATKA, T. Estimation of uncertainty sources in the projections of Lithuanian river runoff. *Stochastic Environmental Research and Risk Assessment*, 2013, Vol. 27, No. 4, p. 769–784. <https://doi.org/10.1007/S00477-012-0608-7>.

5. GAILIUŠIS, B. *River run-off management in the Lithuanian SSR*. Vilnius, Lithuania. 1986, 156 p. (In Russian)

6. PUNYS, P.; KVARACIEJUS, A.; DUMBRAUSKAS, A.; ŠILINIS, L.; POPA, B. An assessment of micro-hydropower potential at historic watermill, weir, and non-powered dam sites in selected EU countries. *Renewable Energy*, 2019, Vol. 133, p. 1108–1123. <https://doi.org/10.1016/j.renene.2018.10.086>.

7. AKSTINAS, V.; JAKIMAVIČIUS, D.; MEILUTYTĖ-LUKAUSKIENĖ, D.; KRIAUČIŪNIENĖ, J.; ŠARAUSKIENĖ, D. Uncertainty of annual runoff projections in Lithuanian rivers under a future climate. *Hydrology Research*, 2020, Vol. 51, No. 2, p. 257-271. <https://doi.org/10.2166/nh.2019.004>.

8. GAILIUŠIS, B.; JAKIMAVIČIUS, D.; ŠARAUSKIENĖ, D.; JURGELĖNAITĖ, A. Assessment of hydrokinetic resources of small and medium-size rivers: the Lithuanian

case. *Baltica*, 2017, Vol. 30, No. 1, p. 23-30 <http://dx.doi.org/10.5200/baltica.2017.30.03>.

9. JAKIMAVIČIUS, D.; ADŽGAUSKAS, G.; ŠARAUSKIENĖ, D.; KRIAUČIŪNIENĖ, J. Climate Change Impact on Hydropower Resources in Gauged and Ungauged Lithuanian River Catchments. *Water*, 2020, Vol. 12, No. 11, p. 3265. <https://doi.org/10.3390/w12113265>.

PROJECTED WIND ENERGY MAXIMUM POTENTIAL IN LITHUANIA

J. Jankevičienė
Lithuanian Energy Institute
Breslaujos str. 3, LT-44403 Kaunas – Lithuania
juste.jankeviciene@lei.lt

A. Kanapickas
Lithuanian Energy Institute,
Breslaujos str. 3, LT-44403 Kaunas – Lithuania
Vytautas Magnus University
K. Donelaičio str. 58, LT-44248 Kaunas – Lithuania
arvydas.kanapickas@vdu.lt

EXTENDED ABSTRACT

OVERVIEW

Climate change is encouraging countries to consider alternatives to fossil fuels [1]. One such alternative is wind power. Currently, Lithuania generates about 14 % of its annual demand using wind energy. However, this is too low to meet the European Union's target of at least 32 % renewable energy by 2030 [2], [3]. To estimate how much energy could be generated to the maximum possible extent, the Intergovernmental Panel on Climate Change (IPCC) reports need to be taken into account, as well as the projected future wind change and the locations where wind energy development is possible.

The following objectives are intended to be addressed by this study. First and foremost, a suitable location for wind farm development must be identified. Second, using the SSP2-4.5 climate change projection, analyse the impact of climate change on energy output throughout the next 40 years (2021–2060). Finally, consider how much electricity might be generated if wind turbines were installed in all permissible places in Lithuania, as well as if this would assist Europe to reach its renewable energy targets.

METHODS

Lithuania has a legal regulation in place that sets out where wind energy development is allowed. Based on the regulations, it has been calculated that the area with no restrictions covers 23 949 km^2. For this study, a wind turbine manufactured by ENERCON E-101 has been selected with the following parameters: height of 99 m, swept area of 8012 m^2, and cut-in and cut-out wind speed of 3 m/s and 25 m/s, respectively [4].

The study was carried out using one out of 5 Shared-Socioeconomic Pathways (SSP) scenarios. This scenario is SSP2-4.5. The name of the scenario indicates that the radiative forcing will reach 4.5 W/m^2 by the end of the century [5]. For this scenario, three models have been selected for use: MPI-ESM-LR (Max Planck Institute for Meteorology Earth

System, MPI), HadGem2-ES (the Hadley Centre Global Environmental Model, HAD) and IPSL-CM5A-MR (Institute Pierre Simon Laplace, IPSL).

The wind speed in the forecast models is given at the height of 10 m, so in order to calculate the maximum potential energy, this speed had to be converted to the wind speed at the height of the selected turbine. The potential of wind energy in the country was calculated using this equation [6], [7]:

$$P = \frac{1}{2}C_p\rho A \left(V_0 \cdot \left(\frac{h}{h_0}\right)^\alpha\right)^3 \qquad (1)$$

where: P – wind power, W, C_p – power coefficient of a turbine (dimensionless), ρ – air density (1.225 kg/m^3 is the standard value and is assumed in this study [6]), A – rotor swept area, m^2, V_0 – near-surface wind speed, m/s, h – specified height, m, h_0 – near-surface height, m, α – wind shear exponent, 1/7 in this study [7].

Enevoldsen et al. suggested a method to calculate the number of turbines that could possibly be installed in a selected region [8]:

$$N = \frac{A}{s^2 \cdot d^2} \qquad (2)$$

Where N – number of turbines, A – available area, m^2, s – mean wind turbine spacing density in Europe (4.4 in this study, dimensionless), d – rotor diameter, m.

RESULTS

The analysis of available space shows that Lithuania could accommodate up to 12 023 wind turbines of the size described. This would allow the country to produce up to four times more energy than it consumes.

Over the next 40 years, electricity production in wind farms in Lithuania is expected to change similarly for each one of the models. According to the MPI model, the following decade should be the most energy-efficient. Both the HAD and MPI models project similarly unfavourable outcomes. The IPSL and MPI models expect a drop in energy generation between 2031 and 2040. However, the HAD model predicts a minor gain at that time.

The analysis shows that MPI is the most favourable model among other models for wind energy over the next 40 years. In this model, the coastal region will account for the largest share of wind power (up to 55 GWh in the 2021-2030 decade), while the south-eastern part of the country will account for the least. Here, the lowest production will be recorded between 2031 and 2040 and could reach up to 20 GWh per decade with the wind turbine described earlier.

The most unfavourable model for wind energy is the IPSL. A case study of this model showed that wind energy production could not exceed 25 GWh in any given decade. It would also produce the lowest amount of energy in the north-eastern part of the country, around 12 GWh per decade, compared to the other models.

CONCLUSIONS

The new projections for wind power generation in Lithuania have been investigated. Two out of the three scenarios suggest a reduction in future energy production. This indicates that energy output will be lower than anticipated throughout the wind power plant's development.

WWW.CYSENI.COM

The maximum number of wind farms in Lithuania demonstrates the potential for the significant improvement of the country's power output from renewable energy sources in the future.

Keywords: Climate change, wind energy, projections, renewables, shared-socioeconomic pathways.

REFERENCES

1. INTERNATIONAL PANEL ON CLIMATE CHANGE. Technical Summary on Climate Change 2013. *The Physical Science Basis*, Cambridge University Press, 2014, pp. 31–116.

2. DIRECTIVES DIRECTIVE (EU) 2018/2001 OF THE EUROPEAN PARLIAMENT AND OF THE COUNCIL of 11 December 2018 on the promotion of the use of energy from renewable sources (recast) (Text with EEA relevance).

3. *Statistika | Lietuvos Respublikos energetikos ministerija*. [Referred on the Jan. 02, 2022]. Link to the internet <https://enmin.lrv.lt/lt/veiklos-sritys-3/atsinaujinantys-energijos-istekliai/statistika>.

4. *ENERCON product overview*. [Referred on the Jan. 05, 2022]. Link to the internet <: https://www.enercon.de/fileadmin/Redakteur/Medien Portal/broschueren/pdf/en/ENERCON_Produkt_en_06_2015.pdf>.

5. MEINSHAUSEN, M., *et al.* The shared socio-economic pathway (SSP) greenhouse gas concentrations and their extensions to 2500, *Geoscientific Model Development*, 2020, vol. 13, p. 3571–3605, doi: 10.5194/gmd-13-3571-2020.

6. CARVALHO, D.; ROCHA, A.; GÓMEZ-GESTEIRA, M.; SILVA SANTOS, C. Potential impacts of climate change on European wind energy resource under the CMIP5 future climate projections, *Renewable Energy*, 2017, vol. 101, no. 2017, p. 29–40, doi: 10.1016/j.renene.2016.08.036.

7. GAO, Y.; MA, S.; WANG, T. The impact of climate change on wind power abundance and variability in China, *Energy*, 2019, vol. 189, p. 116215, doi: 10.1016/j.energy.2019.116215.

8. ENEVOLDSEN, P. *et al.* How much wind power potential does Europe have? Examining European wind power potential with an enhanced socio-technical atlas, *Energy Policy*, 2019, vol. 132, no. 7, p. 1092–1100, doi: 10.1016/j.enpol.2019.06.064.

DAILY GLOBAL SOLAR IRRADIANCE FORECASTING USING LSTM AND ARIMA

E. A. ERFAN

Department of Electrical Electronic Engineering, Adana Çukurova University
Balcalı, Çukurova Üniversitesi Rektörlüğü, 01330 Sarıçam/Adana – Turkey
+905525952089
eman7arman@gmail.com

Abstract

Nature suffers from the dangerous effects and lack of fossil energy resources such as oil, coal, and natural gas. Thus, the reason why sustainable renewable energy generation gained significant consideration. To replace harmful fossil fuel resources with clean, safe, and sustainable energy, the photovoltaic market has had a rapid development in the last decades. The high accuracy of the daily solar global horizontal irradiance (GHI) forecasting model is an essential tool for the operation, maintenance, and optimization of photovoltaic systems, that is why designing an intelligent and robust (GHI) prediction model has become one of the most attractive topics for researchers in the last few years. In this paper, daily GHI data of Adana, Turkey, between the years 2017 and 2021 has been acquired from ERA5 to form a raw data set, then two effective time-series forecasting models, i.e. long short term memory (LSTM) and autoregressive integrated moving average (ARIMA), are applied on the cleansed and pre-processed data set for a day-ahead solar GHI prediction in Adana, Turkey. Consequently, the results of the prediction are evaluated using several performance metrics such as mean squared error (MSE), mean absolute percentage error (MAPE), and coefficient of discrimination (R^2). It has been observed that the LSTM model is outperforming the ARIMA model as it gives better results and correlation.

Keywords: Renewable Energy, Global Horizontal Irradiance, Artificial Neural Networks, Machine Learning, LSTM, ARIMA.

INTRODUCTION

Due to the rapid increase in energy demand on the earth, while harmful effects of the fossil energy resources such as oil, coal, and natural gas are inadequate to meet the world's energy needs, global potential trends toward renewable energy to provide clean, safe, and sustainable kinds of energy such as solar energy.

Solar irradiance forecasting is an essential tool in the process of planning stable and reliable energy photovoltaic system, but due to the nonlinearity of the solar irradiance, statistical and machine learning algorithms are employed by literature to forecast it accurately as it depends on using historical records of solar irradiance and other meteorological data such as temperature, relative humidity, and pressure to build forecasting models.

Boubaker et al. [1] proved that the LSTM model is the most investigated Deep Neural Networks type compared to a gated recurrent unit (GRU), bidirectional long short term memory (BiLSTM), bidirectional gated recurrent unit (BiGRU), convolutional neural network (CNN), CNN-LSTM, CNN-BiLSTM models for Predicting Solar Radiation at Hail Region, Saudi Arabia. Wang et al. [2] forecasted A day-ahead PV power using a recurrent renewal network (RNN) based on the LSTM-RNN model and time correlation modification under a partial daily pattern prediction framework. Brahma et al. [3] developed a comparison of the deep neural nets (DNN) models based on multiple horizons was also conducted. The results showed that forecasting tasks of shorter horizons show better accuracy while longer horizons require more complex models. H. Zhou et al. [4] evaluated the LSTM model, which effectively forecasts PV power in all four seasons, and the forecasting curves of the LSTM model are very close to the actual curves in all different time intervals. Husein et al. [5] presented a deep learning approach for day-ahead solar irradiance forecasting for micro grids using LSTM and feedforward neural network (FFNN) models in four different countries (Germany, USA, Switzerland, and South Korea). Alsharif et al. [6] performed time series ARIMA model for the prediction of daily and monthly average global solar radiation by Korea meteorological administration (KMA) and global solar radiation (GSR) data in Seoul, South Korea. Sharadga et al. [7] enhanced that Artificial neural networks learn the complexity of time series data better than seasonal autoregressive integrated moving average (SARIMA) models. Thus, NNs are better than the suggested statistical models for PV power time series prediction. Yu et al. [8] presented a comparison of deep learning methods (LSTM, ARIMA, support vector regression (SVR), backward propagation neural network (BPNN), CNN, RNN), which approved the LSTM Short-Term Solar Irradiance Forecasting Under Complicated Weather Conditions. Ghimire et al. [9]) evaluated predictions of half-hourly, daily, and monthly solar radiations whose input elements are defined by antecedent lagged GSR data. Essentially, for enhanced accuracy, the proposed model employs CNN to extract GSR data features and LSTM to encapsulate the features to generate a low latency-based time series GSR prediction. Qing et al. [10] enhanced Hourly day-ahead solar irradiance prediction using weather forecasts by LSTM. For a case using 10 years of historical data to predict 1 year of irradiance data, the prediction RMSE using the proposed LSTM algorithm decreases by 42.9% against BPNN. Gairaa et al. [11] combined linear autoregressive moving average (ARMA) and nonlinear artificial neural network (ANN) models to estimate the daily global solar radiation in Algeria.

In this paper, a day-ahead global horizontal irradiance forecasting model was implemented using an intelligent statistical algorithm, autoregressive integrated moving average (ARIMA), and deep algorithm long short term memory (LSTM) to predict daily solar irradiance in Adana, Turkey. The data set is acquired from ERA5 between 2017 and 2021

and concatenated with some calendar variables such as year, month, and day of the year to form a raw data set that is processed by some normalizing and cleaning functions to be predictable by the proposed models.

MATERIALS AND METHODS

MATERIALS

The material of this paper is a daily resolution data set between 1 January 2017 and 31 December 2021. The data set belongs to Adana; a Turkish city located on the north-eastern coast of the Mediterranean Sea with Coordinates: 37°0′N 35°19.28′E as shown in Fig. 1. Meteorological variables are acquired from European Centre for Medium-Range Weather Forecasts (ECMWF) Reanalysis 5th Generation (ERA5) [12]. The raw data set is normalized by Min-Max and transformed to [0, 1], outliers and erroneous data are removed from the data set, and then the linear interpolation method is applied to calculate the missing values in the data set. To evaluate the forecasting model, the solar global horizontal irradiance (GHI) data set is split into training data set (70%) and testing data set (30%), as illustrated in Fig. 3.

Fig. 1. Location of Adana, Turkey
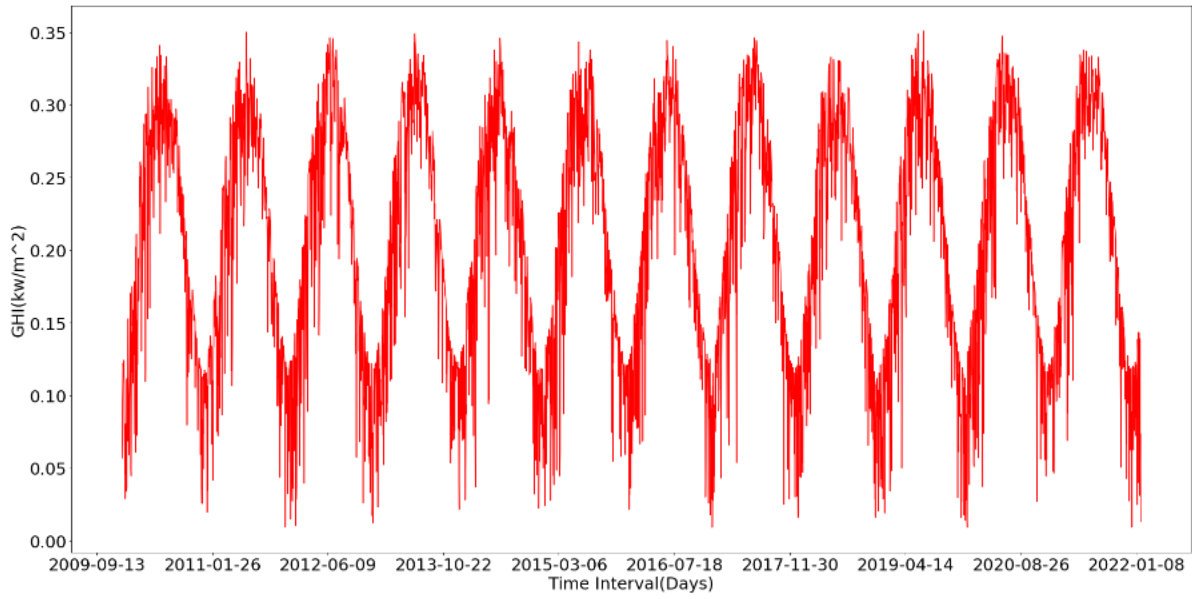
Fig. 2. A demonstration of global horizontal irradiance (GHI)
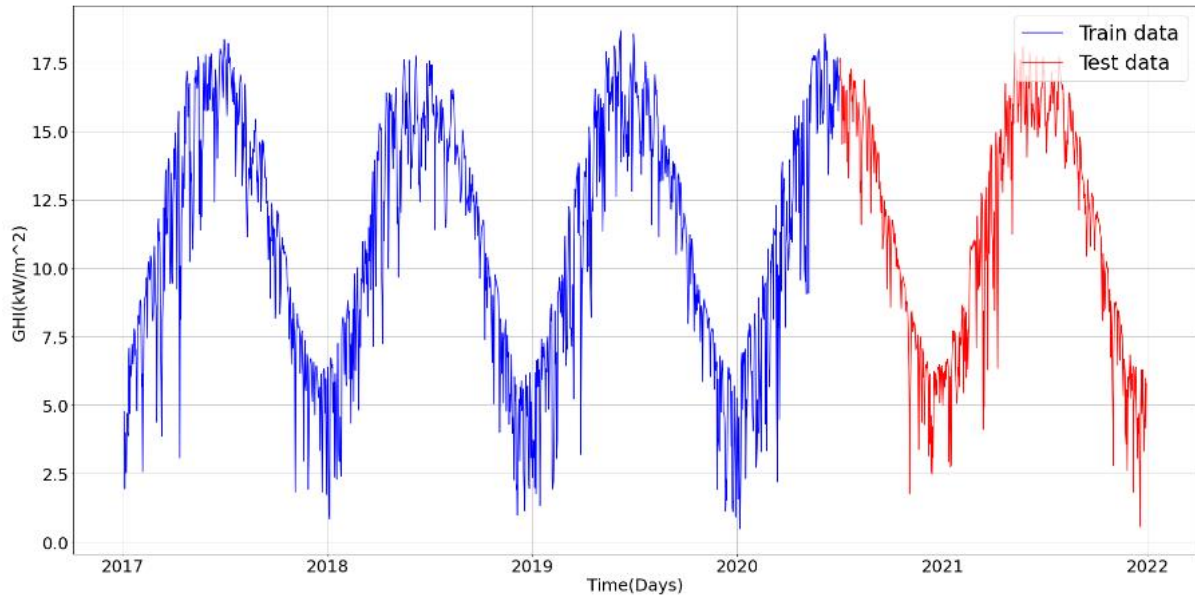
Fig. 3. A demonstration of training and testing data set

METHODS

In this paper, LSTM and ARIMA are employed as forecasting methods.

LONG SHORT-TERM MEMORY (LSTM)

Long Short-term Memory Neural Network is an improved version of recurrent neural networks that was proposed by (Hochreiter and Schmidhuber [13]) to overcome the vanishing and exploding gradient problems of traditional RNN that are generated during updating weights and biases. LSTM divides the hidden state of RNN into two parts, long-term memory cells c_t and short-term memory h_t, which are used as the output of the current state and input of the next state as h_{t-1} with its current input x_t that are controlled by gates: forget, input, and output as shown in Fig. 4 and expressed in the following equations.

$$f_t = \sigma\big(\omega_f \times [h_{t-1}, x_t] + b_f\big)$$

$$i_t = \sigma\big(\omega_i \times [h_{t-1}, x_t] + b_i\big)$$

$$\tilde{c}_t = \tanh\big(\omega_c \times [h_{t-1}, x_t] + b_c\big)$$

$$c_t = f_t \times c_{t-1} + i_t \times \tilde{c}_t$$

$$o_t = \sigma\big(\omega_o \times [h_{t-1}, x_t] + b_o\big)$$

$$h_t = o_t \times \tanh(c_t),$$

where w_f, w_i, w_c and w_o are weight matrices. b_f, b_i, b_c and b_o are bias vectors. $\tilde{c}_t$ is a new candidate state, and $\sigma()$ is the Sigmoid activation function that generates values between 0 and 1 to decide which information is important and which can be discarded.

The current input x_t and the previous state h_{t-1} are processed by the input gate (i_t) that decides the portion to be added in the long-term state C_t. The forget gate (f_t) that is responsible for deciding the portion of C_{t-1} is to be ignored, discarding the unnecessary parts. The output gate (O_t) decides the portion of C_t to be read and written as output.

In this paper, the LSTM is chosen as a forecasting method because it overcomes the problem of vanishing gradients and captures long-term dependencies between the variables in the time series even if the large gap distance between them Yu et al. [8].
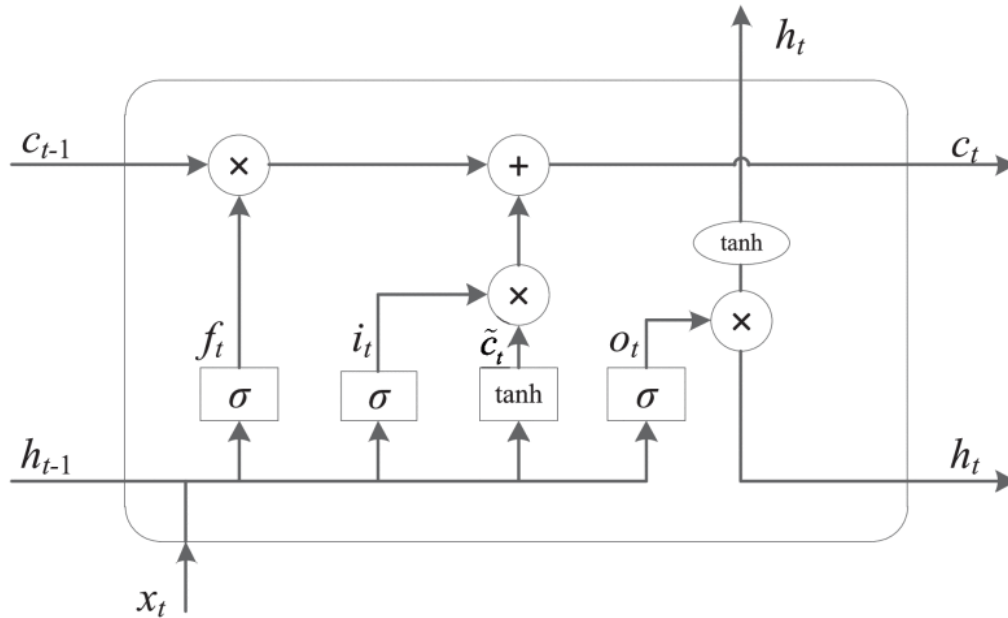

Fig. 4. Construction of LSTM unit

AUTOREGRESSIVE INTEGRATED MOVING AVERAGE (ARIMA)

Autoregressive Integrated Moving Average (ARIMA) was proposed in 1976 by Box and Jenkin [14]. ARIMA is a statistical analysis model that is widely used in time series forecasting and future trends prediction based on the assumption that any value in the time

series affects the past values that can be determined as regressive relation. ARIMA (p,d,q) consists of three parts: Autoregression (AR) which shows a changing variable that regresses on its values by the number of regression terms p, Integrated (I) represents the (d) differencing times of the data observations and its previous values, Moving average (MA) the moving average window with size (q) that specifies dependency between an observation and a residual error of the lagged observations. The general ARIMA (p, d, q) is briefly expressed as the following equation (Younes 2014[15]):

$$\Phi p(B)Wt = \theta q(B)et,$$

where *Φp(B)* is an auto-regressive operator of order *p, θq(B)* is a moving average operator of order *q* and *Wt = ΔdXt*.

In this paper, the ARIMA method is chosen as a forecasting method because it depends only on the time series data of the target, avoiding the problems that occur due to using some multivariate models.

RESULTS AND DISCUSSION

All computations in this paper were implemented with a personal laptop with OS version Windows 7 Ultimate, a processor of 2.1GHz (Intel(R)Core™), and a memory size of 2 GB by using the Kaggle platform [16], and scripts written by python language.

ARIMA model is tuned to fit the optimal model by calculating Akaike's Information Criterion (AIC) for a combination of p,d, and q parameters ranges between 0 and 10, the less AIC value indicates the better-fit model.

In LSTM, the search for the optimal number of hidden layer neurons is covered from 2 to 20 neurons. Hyperbolic tangent (tanh) and rectified linear unit (ReLU) activation functions are used respectively for the hidden layer and output layer.

In this study, two different methods are employed to predict day-ahead GHI. In Fig.5, the original values are compared to those computed by the ARIMA and the LSTM prediction models.
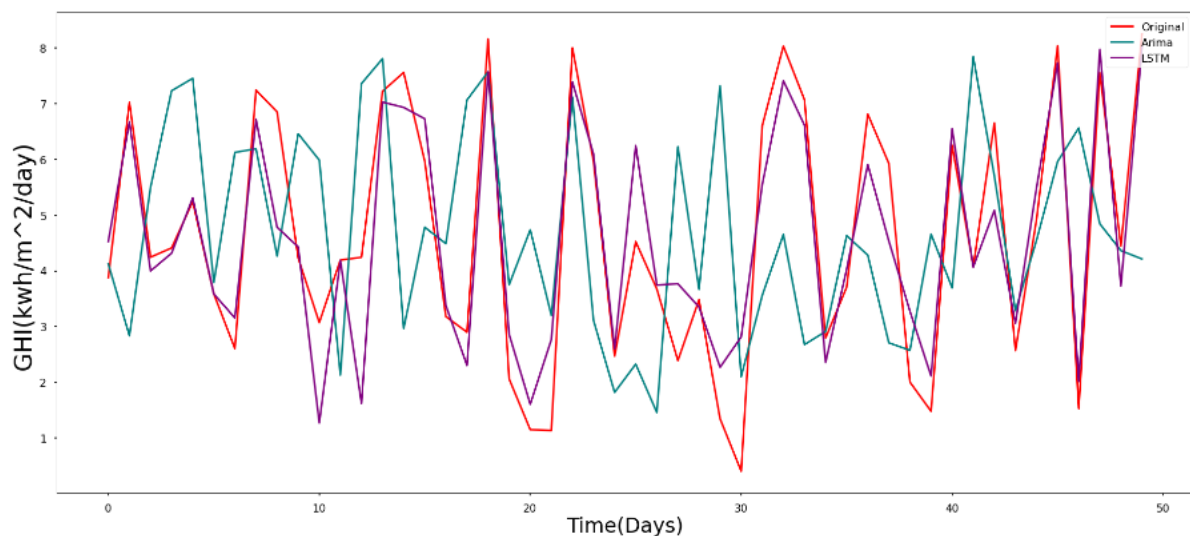

Fig. 5. Actual and predicted values comparison plot

Several evaluation metrics such as mean absolute percentage error (MAPE), coefficient of determination (R^2), and mean squared error (MSE) is applied to compare the performance of both models. In both LSTM and ARIMA models, the data splitting function was applied such that 70% and 30% of the whole data set were constructed for training and testing sets, respectively, as shown in Fig.3.

Table 1. Applied methods performances for all utilized metrics

Method	R2 (%)	MAPE (%)	MSE (kWh/m^2/Day)
LSTM	86.03	17.71	0.67
ARIMA	81.81	22.42	0.74

According to the results obtained from the comparison between MAPE, MSE, and R^2 as shown in Table 1, the LSTM model has better performance with lower error and higher correlation than the ARIMA model.

CONCLUSIONS

In this paper, a day-ahead global horizontal irradiance forecasting model was implemented using an intelligent statistical algorithm; autoregressive integrated moving average (ARIMA), and a deep algorithm; long short term memory (LSTM) to predict daily solar irradiance in Adana, Turkey. The data set is acquired from ERA5 between 2017 and 2022. The results of the prediction are evaluated using several performance metrics such as MSE, MAPE, and R2. It has been observed that the LSTM model is outperforming the ARIMA model as it gives better results and correlation.

REFERENCES

1. BOUBAKER, S.; BENGHANEM, M.; MELLIT, A.; LEFZA, A.; KAHOULI, O.; KOLSI, L. Deep Neural Networks for Predicting Solar Radiation at Hail Region, Saudi Arabia. *IEEE Access*, 2021, Vol. 9, p. 36719–36729.

2. WANG, F.; XUAN, Z.; ZHEN, Z.; LI, K.; WANG, T.; SHI, M. A day-ahead PV power forecasting method based on LSTM-RNN model and time correlation modification under partial daily pattern prediction framework. *Energy Conversion and Management*, 2020, Vol. 212, p. 112766.

3. BRAHMA, B.; WADHVANI, R. Solar Irradiance Forecasting Based on Deep Learning Methodologies and Multi-Site Data. *Symmetry*, 2020, Vol. 12, No. 11, p. 1830.

4. ZHOU, H.; ZHANG, Y.; YANG, L.; LIU, Q.; YAN, K.; DU, Y. Short-Term Photovoltaic Power Forecasting Based on Long Short Term Memory Neural Network and Attention Mechanism. *IEEE Access*, 2019, Vol. 7, p. 78063-78074.

5. HUSEIN, M.; Chung, I. Day-Ahead Solar Irradiance Forecasting for Microgrids Using a Long Short-Term Memory Recurrent Neural Network: A Deep Learning Approach. *Energies*, 2019, Vol. 12, No. 10, p. 1856.

6. ALSHARIF, M.H.; YOUNES, M.K.; KIM, J. Time Series ARIMA Model for Prediction of Daily and Monthly Average Global Solar Radiation: The Case Study of Seoul, South Korea. *Symmetry*, 2019, Vol. 11, p. 240.

7. SHARADGA, H.; HAJIMIRZA, S.; BALOG, R. S. Time series forecasting of solar power generation for large-scale photovoltaic plants. *Renewable Energy*, 2019, Vol. 10, p. 1016.

8. YU, Y.; CAO, J.; ZHU, J. An LSTM Short-Term Solar Irradiance Forecasting Under Complicated Weather Conditions. *IEEE Access*, (2019), Vol. 7, p. 145651–145666.

9. GHIMIRE, S.; DEO, R. C.; RAJ, N.; MI, J. Deep solar radiation forecasting with convolutional neural network and long short-term memory network algorithms. *Applied Energy*, 2019, Vol. 253, p. 113541.

10. QING, X.; NIU, Y. Hourly day-ahead solar irradiance prediction using weather forecasts by LSTM. *Energy*, 2018, Vol. 148, p. 461–468.

11. GAIRAA, K.; KHELLAF, A.; MESSLEM, Y.; CHELLALI, F. Estimation of the daily global solar radiation based on Box–Jenkins and ANN models: A combined approach. *Renewable and Sustainable Energy Reviews*, 2016, Vol. 57, p. 238–249.

12. Fifth generation of ECMWF atmospheric reanalyses Copernicus Climate Change Service Climate DataStore (CDS) of the global climate, 2017- [referred on the 3th of January in 2022 y.]. Link to the internet <https://doi.org/10.24381/cds.adbb2d47>.

13. GREFF, A.; SRIVASTAVA, R.K.; KOUTNÍK, J.; STEUNEBRINK ,B.R.; SCHM-IDHUBER, J. LSTM: A Search Space Odyssey. *IEEE Transactions on Neural Networks and Learning Systems*, 2017, Vol. 28, No. 3, p. 2222–2232.

14. KHASHEI, M.; BIJARI, M. A novel hybridization of artificial neural networks and ARIMA models for time series forecasting. *Applied Soft Computing*, 2011, Vol. 11, p.2664–2675.

15. YOUNES, M.K.; NOPIAH, Z.M.; BASRI, N.E.A.; BASRI, H. Medium term municipal solid waste generation prediction by autoregressive integrated moving average. SORIC 2013. Stat. Oper. Res. Int. Conf. 2014.

16. Kaggle online community, 2010- [referred on the 3th of January in 2022 y.]. Link to the internet <https://www.kaggle.com>.

PERFORMANCE ANALYSIS OF HYBRID PV AND PEMFC ENERGY SOURCES UNDER PARTIAL SHADING IN GRID-OFF APPLICATION

M. Büyük
Adıyaman University, Department of Electrical and Electronics Engineering, 02040, Adıyaman, Türkiye
+905074661167
mbuyuk@adiyaman.edu.tr

ABSTRACT

Renewable energy sources (RES) have gained more concern in recent years due to their environmental friendly structure and low-cost operation capability. Photovoltaic (PV) panels are more in the foreground compared with other RESs. However, the operation characteristic of PV sources is variable under partial shading circumstances. Thus, an additional power source is required with PV panels in off-grid connection in order to ensure continuous energy supply to the consumer. Otherwise, the PV source cannot provide the required power, and it loses its connection to the load. Batteries are commonly applied as extra sources with PV systems. But, it is energized from the PV system as well and may not ensure the required power under partial shading case in terms of low battery SOC. In this term, a hybrid PV panel with a proton exchange membrane fuel cell (PEMFC) source is proposed in this study to satisfy the energy sustainability once the radiation on PV panels reduces. The proposed system includes PV and FC sources. The sources are connected to the DC link bus via step-up converters to supply the consumer with DC loads. To verify the proposed system topology, a hybrid supplier model with a 3.4 kW DC load is constructed in a simulation environment. The proposed configuration is examined under various radiation values to show the performance of the developed structure under partial shading states. It is observed that the supplied power via PV panels decreases when the radiation lowers. In this case, the FC source supports the PV panels to provide energy for the load. As a result, a continuous energy supply to the load is fulfilled under the partial shading condition of the PV source.

Keywords: PV Source, PEMFC, Hybrid Energy, Partial Shading, Grid-off connection

INTRODUCTION

The applications of renewable energy sources (RESs) have been rising in recent years owing to rapid reduction and increased unit prices of fossil fuels and environmental pollution [1, 2]. Renewable energy technologies such as solar, fuel cell and wind energy systems have come into prominence that has a considerable impact on the energy sector. In addition, the usage of RESs in various areas has been widely a concern due to the development of society and the economy [3].

Photovoltaic (PV) panels are one of the most widespread applied RESs since they have low implementation costs and simple installation [4]. In addition, the usage of PV panels is more attractive in urban areas as a grid-off connection [5]. However, the generated power from PV panels reduces under partial shading situations [6, 7]. Fluctuations in radiation and temperature affect the PV arrays' open circuit voltage and power, respectively [8]. Thus, the required power cannot be provided from the PV sources under partial shading [9]. This condition may endanger the safe operation of the PV system if it exceeds its maximum power rating [10]. It is important to take into consideration this case in the control algorithm [11].

The performance of PV energy panel under partial shading case is determined via an analytical model in [12]. In [13], a control algorithm for hybrid PV and battery systems is offered in a stand-alone system. However, the system turns off the load energy under a zero radiation state. A multi-loop controller is suggested for the hybrid PV + battery model to manage power flow under low radiation conditions [14]. On the other hand, an energy management method without sensor requirement is proposed for off-grid connected PV with battery energy storage to solve the problem of PV systems under partial shading [15]. It is obvious that the standalone PV panels need an additional power source to ensure a sustainable energy supply. Nevertheless, the PV source with battery storage cannot satisfy continuous power to the consumer in case of a low battery state of charge (SOC) [16]. Thus, an alternative energy source is necessary with a PV system to provide energy continuity even under partial shading. There are several studies in the literature about hybrid PV and fuel cell (FC) sources in grid-connected applications. In [17], a grid-connected hybrid source system is studied for a VSC topology. On the other hand, the power control of hybrid PV+FC source in the grid-connected system is investigated in [18]. However, the partial shading of the PV source is not taken into account in this paper.

In this context, a hybrid PV with FC source system is proposed in this study to overcome the possible system faulty and de-energizing of the load. Proton-exchange membrane FC (PEMFC) is preferred as an additional RES to supply the load with a PV source. A DC load type is considered an energy consumer in the current study. By this means, a hybrid PV+FC source with a 3.2 kW DC load is designed and implemented in a simulation environment to investigate the response of the proposed system under partial shading of the PV panels. In order to analyse the system operation, the irradiance of the PV system is changed as a partial shading condition. The irradiance is reduced to 700 W/m^2 from 1000 W/m^2 for a second in the simulation. As a result of the irradiance drop, the power of the PV source is also dropped. The required power is supported by the FC system once partial shading occurs in PV panels. Thus, the safety operation of the PV system and continuous load supply is maintained with the proposed system configuration.

HYBRID ENERGY SYSTEM STRUCTURE

The single-line diagram of the proposed hybrid system structure for supplying a DC load is demonstrated in Fig. 1. The proposed system has two RESs, including PV and FC sources, to supply the DC load. Both energy sources and DC load are connected to a common DC bus. The PV and FC sources generate a variable DC voltage under different power conditions. Therefore, DC-DC converters are used to interface the PV and FC sources with the DC bus.
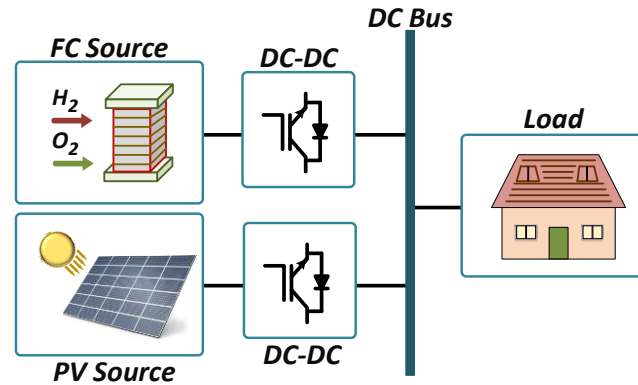
Fig. 1. Single-line diagram of the proposed hybrid system structure with FC and PV sources

The detailed circuit scheme of the proposed system model is illustrated in Fig. 2. Boost converters are applied between both PV-FC sources and DC buses. Each boost converter consists of an inductance, an electronic switch and a diode. The electronic switches are applied to control the DC bus voltage and injected power amount. To manage the control of the DC voltage and power level, the currents and voltages of PV and FC sources are firstly measured and evaluated in the controller. These parameters are adjusted by curbing the duty cycle value of the PWM signal applied to the electronic switches.
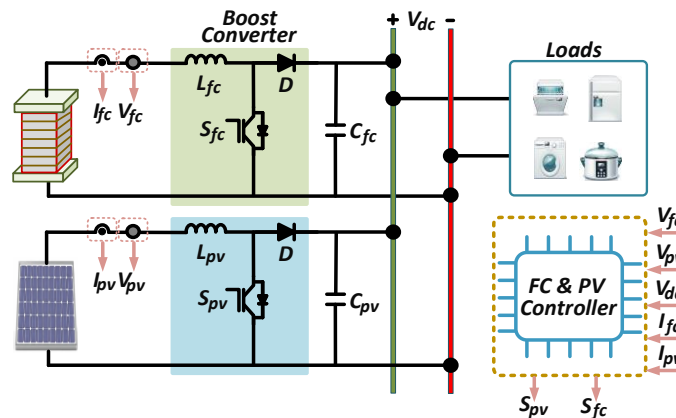
Fig. 2. Detailed representation of the proposed hybrid system

The power equations of the proposed system are given in (1-3). The relationship of the power between the PV, FC and load is defined by (1). The total load power is equal to the summation of the generated powers by PV and FC sources. The generated PV and FC powers are obtained by (2) and (3).

$$P_{load} = P_{PV} + P_{FC} ; \tag{1}$$

$$P_{PV} = V_{PV} I_{PV} ; \tag{2}$$

$$P_{FC} = V_{FC} I_{FC} , \tag{3}$$

where, P_{load}, P_{PV} and P_{FC} determine consumed power by load and generated power by PV and FC system, respectively. V_{DC}, V_{PV} and V_{FC} are the DC bus voltage, PV panel voltage and FC voltage, respectively. I_{PV} and I_{FC} are currents of PV and FC systems successively.

The boost converters operate according to the duty cycle value of the switching signals, which is defined by the source voltages and DC bus voltage. The relationship between the source voltages and DC bus voltage with respect to the duty cycles is given in equations (4) and (5).

$$V_{DC} = \frac{V_{PV}}{1 - D_{PV}} ; \tag{4}$$

$$V_{DC} = \frac{V_{FC}}{1 - D_{FC}} , \tag{5}$$

where D_{PV} and D_{FC} define the duty cycles of PWM signals applied to the PV and FC converters, respectively.

PERFORMANCE RESULTS

The proposed hybrid sources system is constructed in a simulation environment to examine the performance of the system. The PV and FC sources are designed to energize a 3.2 kW DC load at a 400V DC bus. The parameter values for the proposed hybrid PV+FC system are given in Table 1. The constructed system is tested under partial shading of the PV system. Fig. 3 demonstrates the temperature and the variation of the irradiance over the PV panels in the case of partial shading. The temperature is chosen as constant at 25 ^{0}C during the partial shading. The irradiance is variated between 1s and 2s time intervals. It drops to 700 W/m^2 from 1000 W/m^2.

Table 1. System parameters of the hybrid PV+FC energy sources in grid-off connection

Parameter	Value	Unit
$P_{FC(max)} - P_{PV(max)}$	2.4 - 2.7	kW
$V_{FC(nom)} - V_{PV(mpp)}$	132.6 – 164.1	V
$I_{FC(nom)} - I_{PV(mpp)}$	15.2 – 16.7	A
L_{FC}, L_{PV}	5	mH
C_{FC}, C_{PV}	2	mF
V_{DC}	400	V
R_{DC}	50	Ohm
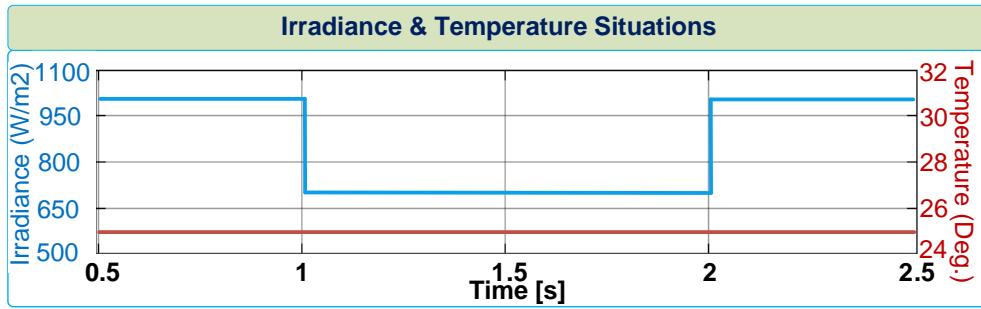
Fig. 3. Irradiance and Temperature characteristics under partial shading condition

The power, voltage and current waveforms of the PV and FC sources and load side are shown in Fig. 4, Fig. 5 and Fig. 6, respectively. It is clear from the figures that a partial shading condition is provided between 1s-2s time intervals. As shown in Fig. 4, the generated power by the PV source reduces while partial shading occurs. The radiation dropped on PV panels is reduced to 700 W/m^2 from 1000 W/m^2 during the partial shading case. The supplied power by PV panels decreases to almost 1 kW from 1.9 kW.
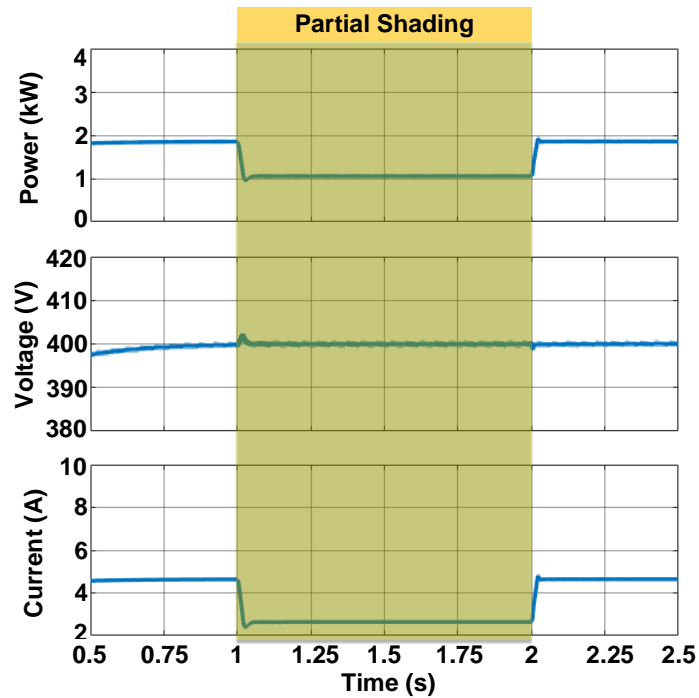
Fig. 4. The power, voltage and current waveforms of PV source under partial shading condition
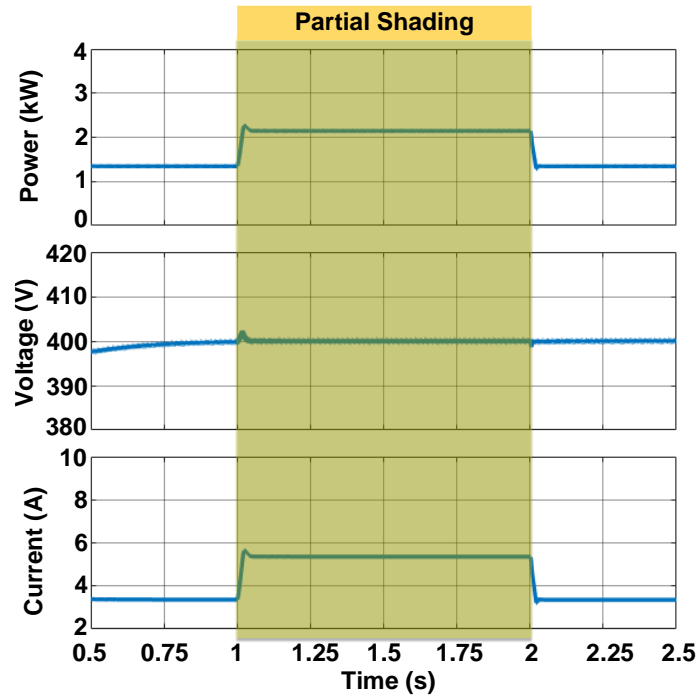
Fig. 5. The power, voltage and current waveforms of PEMFC source
under partial shading condition

At the partial shading time, as illustrated in Fig. 6, the supplied power by the FC source increases in order to compensate for the power lack of the PV source and to meet the consumed power by the load. The injected power by the FC source increases from 2.1 kW to 1.2 kW. Thus, it is obvious from Fig. 6 that the power supplied to the load is kept constant even under a partial shading situation.

Fig. 6. The power, voltage and current waveforms of load side under
partial shading condition

CONCLUSIONS

In this study, a hybrid PV+FC source system is developed for supplying a DC load under the partial shading situation of PV panels. The proposed system is constructed and investigated in a simulation environment. The irradiance on PV panels is changed to analyse the partial shading condition. The irradiance on the PV source is decreased to 700 W/m^2 from 1000 W/m^2 during the partial shading case. The suppli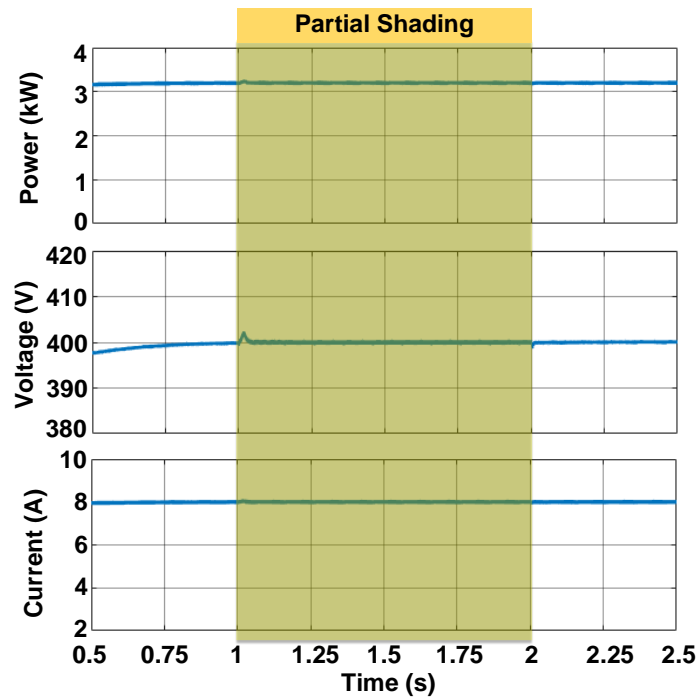ed power by the PV source reduces when the irradiance drops. The PV source power loses almost 900 W power rate under partial shading. The required load power is supported by the FC source under lower irradiance on PV panels. Thus, the FC source rises the generated power by 900 W to support the PV system. As a result, the load energy is sustained even during the power lack of the PV source.

REFERENCES

1. ALTAS, İ.; MENGI,O. A fuzzy logic controller for a hybrid PV/FC green power system. I*nternational Journal of Reasoning-based Intelligent Systems*, 2010. Vol 2, p. 176-183.

2. FERAHTIA, S.; et al., A hybrid power system based on fuel cell, photovoltaic source and supercapacitor. *SN Applied Sciences*, 2020. P. 2.

3. JAVED, S.; ISHAQUE, K. A comprehensive analyses with new findings of different PSO variants for MPPT problem under partial shading. *Ain Shams Engineering Journal,* 2022. Vol. 13(5): p. 101680.

4. BELHAOUAS, N.; et al., A new approach of PV system structure to enhance performance of PV generator under partial shading effect. *Journal of Cleaner Production*, 2021.Vol. 317: p. 128349.

5. FADHEL, S.; et al. Maximum power point analysis for partial shading detection and identification in photovoltaic systems. *Energy Conversion and Management*, 2020. Vol. 224: p. 113374.

6. YANG, B.; et al. PV arrays reconfiguration for partial shading mitigation: Recent advances, challenges and perspectives. *Energy Conversion and Management,* 2021. Vol. 247: p. 114738.

7. CHANDRASEKARAN, K.; SANKAR, S.; BANUMALAR, K. Partial shading detection for PV arrays in a maximum power tracking system using the sine-cosine algorithm. *Energy for Sustainable Development,* 2020. Vol. 55: p. 105-121.

8. ISHAQUE, K.;SALAM, Z. An improved modeling method to determine the model parameters of photovoltaic (PV) modules using differential evolution (DE). *Solar Energy*, 2011. Vol. 85(9): p. 2349-2359.

9. BÜYÜK, M.; AVŞAR, E.; İNCI, M. Overview of smart home concepts through energy management systems, numerical research, and future perspective. *Energy Sources*, Part A: Recovery, Utilization, and Environmental Effects, 2022: p. 1-26.

10. İNCI, M.; et al. Design and analysis of fuel cell vehicle-to-grid (FCV2G) system with high voltage conversion interface for sustainable energy production. *Sustainable Cities and Society*, 2021.Vol. 67: p. 102753.

11. VERMA, P.; KAUR, T. Power control strategy of PV system for active power reserve under partial shading conditions. *International Journal of Electrical Power & Energy Systems*, 2021.Vol. 130: p. 106951.

12. ZHANG, Y.; et al. Performance estimation of photovoltaic module under partial shading based on explicit analytical model. *Solar Energy*, 2021. Vol. 224: p. 327-340.

13. MIRZAEI, A.; et al. Design and construction of a charge controller for stand-alone PV/battery hybrid system by using a new control strategy and power management. *Solar Energy*, 2017. 149: p. 132-144.

14. MAHMOOD, H.; MICHAELSON, D.; JIANG, J. Control strategy for a standalone PV/battery hybrid system. in *IECON 2012 - 38th Annual Conference on IEEE Industrial Electronics Society*. 2012.

15. SHEIKHIPOUR, S.; GHADIMI, A.; MIRZAEI, A. A sensor-less control and optimal energy management algorithm for a stand-alone photovoltaic system considering partial shading condition. *ISA Transactions*, 2021.

16. SAIPRAKASH, C.; et al. Analysis of partial shading effect on energy output of different solar PV array configurations. *Materials Today:* Proceedings, 2021. 39: p. 1905-1909.

17. CHAUDHARY, P.; RIZWAN, M. Hybrid control approach for PV/FC fed voltage source converter tied to grid. *International Journal of Hydrogen Energy,* 2018. Vol. 43(14): p. 6851-6866.

18. KHANH, L.N.; et al., Power-Management Strategies for a Grid-Connected PV-FC Hybrid System. *IEEE Transactions on Power Delivery*, 2010. Vol. 25(3): p. 1874-1882.

EFFECT OF NANOPARTICLE ADDITIVES ON ELECTRICAL AND THERMAL PERFORMANCE FIGURES IN PV/T SYSTEMS; A REVIEW

E. Cuce

Department of Mechanical Engineering, Faculty of Engineering and Architecture, Recep Tayyip Erdogan University, Zihni Derin Campus, 53100 – Rize, Turkey
Low/Zero Carbon Energy Technologies Laboratory, Faculty of Engineering, Recep Tayyip Erdogan University,
Zihni Derin Campus, 53100 – Rize, Turkey

P. M. Cuce

Department of Architecture, Faculty of Engineering and Architecture, Recep Tayyip Erdogan University, Zihni Derin Campus, 53100 – Rize, Turkey
Low/Zero Carbon Energy Technologies Laboratory, Faculty of Engineering, Recep Tayyip Erdogan University,
Zihni Derin Campus, 53100 – Rize, Turkey

S. Guroy

Low/Zero Carbon Energy Technologies Laboratory, Faculty of Engineering, Recep Tayyip Erdogan University,
Zihni Derin Campus, 53100 – Rize, Turkey

ABSTRACT

Electricity and thermal energy are produced by using photovoltaic cells. Scientists have started to use nanoparticles to improve the performance of photovoltaic thermal systems. In this study, the improvements in the basic performance parameters of PV/T systems are investigated when nanoparticles are used as cooling fluid in PV/T systems. The thermal and electrical behaviour of Nano fluids obtained by synthesizing various nanoparticles in different volume ratios with various coolants is investigated. According to the results obtained from the study, it was observed that Al_2O_3 nanoparticle synthesized with ethylene glycol provided 4.11% better thermal results than nanoparticles synthesized with water. In addition, it is observed that the most efficient of the nanoparticles used is Cu, and the Cu/water Nano fluid reaches a thermal efficiency of 79.97%.

Keywords: (PV/T systems, Nano fluids, energy and exergy efficiency, electrical and thermal power)

INTRODUCTION

The depletion of fossil fuels in our world and the increasing energy demand has led people to renewable energy sources. Among the renewable energy sources, solar energy is the most abundant energy available in the world. For the future of positive energy buildings, the building envelope plays and will play a key role in energy generation. Today, thermally or electrically efficient energy generation in the building envelope is currently done via solar thermal collectors and photovoltaic (PV) panels. These systems, of course, need a sufficient surface area oriented towards the sun in order to operate efficiently. However, these surface areas are limited to roofs or facades with suitable orientations. To maximize energy efficiency, every square meter available with an orientation suitable for solar applications should be used in the most efficient way possible [1].

Depending on the cell type, PVs convert 15-22% of incoming solar radiation into electricity, with a larger percentage remaining in the cell as waste heat. Solar radiation increases the temperature of PV modules, causing their electrical efficiency to decrease [2]. The current commercial PV cells convert solar energy into electricity with relatively low efficiency of less than 20% [3]. When the operating temperature of the PV cells increases, the output of the PV cells decreases. Therefore, it is essential to maintain a low operating temperature of PV cells for better performance [4]. The cooling of PV systems and the low heat carrying capacity of PV/T systems are considered major reasons for their low efficiency. Positively, modern research on Nano fluids has made rapid progress in enhancing heat transfer in energy systems [5].

Nanoparticles are defined as dispersions of particles or solid particles with a size in the range of 10-1000 nm. Depending on the preparation method, nanoparticles can be obtained as Nano spheres or Nano capsules [6]. Nano fluid is a suspension of nanoparticles. In the last three decades, Nano fluid has received great attention in nanotechnology, thermal engineering and many other application areas [7]. Nano fluids are one of the new age working fluids with super-improved thermal and rheological properties and act as cooling filters [8]. Thermal conductivity is an important parameter in improving the heat transfer performance of a heat transfer fluid. Many researchers have reported experimental studies on the thermal conductivity of Nano fluids [9]. Javadi et al. [10] have given an overview of the studies on the performance of solar collectors and concluded that the use of Nano fluid instead of conventional fluid improves the thermal properties, efficiency, permeability and extinction coefficient of solar collectors as well as heat transfer [8]. It has been observed that theoretical studies give different results on the effects of particle size on collector efficiency [11,12]. Khanjari et al. [13] have used Alumina/Water and Ag/Water as two different fluids in the PV/T system and examined their thermal and electrical efficiencies with numerical simulation. They have found that the overall efficiency for Alumina/Water ranged from 0.72% to 4.26%, and for Ag/Water, the total yield ranged from 1.33% to 11.54% due to volumetric changes. As a result of the simulations, it has been determined that Ag/Water Nano fluid gives better performance figures than Alumina/Water Nano fluid. Al-Shamani et al. [14] have evaluated the parameters such as electrical, thermal and combined photovoltaic thermal power and efficiency of SiO_2, TiO_2 and SiC Nano fluid-based PVT systems in tropical climate conditions and achieved the highest efficiency from the SiC Nano fluid based system in all respects. It has been found that the electrical efficiency increased to 13.52%, the thermal efficiency to 68.21%, and the combined thermal efficiency to 81.73% for the SiC-based Nano fluid.

Table.1. Maximum enhancement in the thermal, electrical and overall energy efficiency of PV/T systems using Nano fluids as a refrigerant [8].

Investigator	Nano fluid and Concentration	Electrical efficiency increase (%)	Thermal efficiency increase (%)	Overall efficiency increase (%)
Khanjari et al. [13]	Ag/water (10 vol%)	3.9	12.43	11.54
	Al_2O_3/water (10 vol%)	1.83	4.54	4.26
Ghadiri et al. [19]	Fe_3O_4/water (3 wt%)	4.93	46.29	41.80
Al-Shamani et al. [14]	TiO_2/water (1 wt%)	15.73	9.36	11.89
	SiO_2/water (1 wt%)	10.37	3.98	6.43
	SiC/water (1 wt%)	42.97	13.16	18.97
Xu and Kleinstreuer [20]	Al_2O_3/water (4vol%)	1.45	-	-
Xu and Kleinstreuer [21]		9.72	−0.04	1.49
Tang and Zhu [22]	Al_2O_3/water (5 vol%)	−3.73	57.55	29.47
	Al_2O_3/water(0.02wt%)			
Rejeb et al. [23]	Al_2O_3/water (0.4 wt%)	0.15	8.88	–
	Cu/water (0.4 wt%)	0.77	79.97	–
	Al_2O_3/EG (0.4 wt%)	0.16	12.99	–

THERMODYNAMIC ANALYSIS

ENERGY ANALYSIS

By considering the system (PVT or PVT/PCM) as a control volume and assuming a steady state condition, the energy balance for the system can be derived as [15]

$$\sum \dot{E}_{in} = \sum \dot{E}_{out} + \sum \dot{E}_{loss}$$

$$\dot{E}_{sun} + \dot{E}_{mass,in} = \dot{E}_{el} + \dot{E}_{mass,out} + \dot{E}_{loss},$$

(1)

where $\dot{E}_{in}$, $\dot{E}_{out}$ ve $\dot{E}_{loss}$ represent input, output and losses energy, respectively. $\dot{E}_{sun}$ Is the effective solar radiation to the system that can be expressed as and is expressed by the following equation:

$$\dot{E}_{sun} = \dot{G}.A_c.\tau_g.\alpha_{cell} \tag{2}$$

here $\dot{G}$ refers to the rate of the total solar irradiation, A_c the collector area, τ_g the glass cover transmissivity and α_{cell} Is the absorptivity of photovoltaic cells. Eq. (1), the output thermal power of the system can be calculated as:

$$\dot{E}_{mass,out} - \dot{E}_{mass,in} = \dot{E}_{th} = \dot{m}_{nf}.C_{p,nf}.\left(T_{nf,out} - T_{nf,in}\right). \tag{3}$$

The density and specific heat capacity of the Nano fluid are derived using the following equations:

$$\rho_{nf} = \varphi.\rho_n + (1-\varphi).\rho_{bf}; \tag{4}$$

$$C_{p,nf} = \frac{\varphi.(\rho_n C_{p,n}) + (1-\varphi).(\rho_{bf} C_{p,bf})}{\rho_{nf}}. \tag{5}$$

Φ is the volumetric ratio of nanoparticles in the base fluid that can be calculated as;

$$\Phi = \frac{m_n/\rho_n}{m_n/\rho_n + m_{bf}/\rho_{bf}} \tag{6}$$

$\dot{E}_{el}$ is the output electrical power of the system and can be calculated by the following equation

$$\dot{E}_{el} = V_{oc} x I_{sc} x FF. \tag{7}$$

FF is calculated with the following equation:

$$FF = \frac{(VxI)_{max}}{V_{oc}xI_{sc}} \tag{8}$$

The overall energy efficiency of the system is the ratio of the overall output power to the input during a selected time period. Therefore, the overall energy efficiency of the system can be expressed as a function of the thermal and electrical energy efficiencies.[16]

$$\eta_{ov} = \frac{\int_{t1}^{t2}(A_c\dot{E}_{th}'' + A_{pv}\dot{E}_{el}'')dt}{A_c\int_{t1}^{t2}(\dot{E}_{sun}'')dt} = \eta_{th} + r.\eta_{el}. \tag{9}$$

The electrical and thermal efficiency in equation (9) is calculated as follows:

$$\eta_{el} = \frac{\dot{E}_{el}}{\dot{E}_{sun}} = \frac{V_{oc}xI_{sc}xFF}{\dot{G}.A_c.\tau_g.\alpha_{cell}}; \tag{10}$$

$$\eta_{th} = \frac{\dot{E}_{th}}{\dot{E}_{sun}} = \frac{\dot{m}_{nf}.C_{p,nf}.\left(T_{nf,out} - T_{nf,in}\right)}{\dot{G}.A_c.\tau_g.\alpha_{cell}}. \tag{11}$$

EXERGY ANALYSIS AND ENTROPY GENERATION

Similar to the energy analysis, by considering the system (PVT or PVT/PCM) as a control volume and assuming a steady state condition, the exergy balance for the system can be derived as [17]

$$\sum \dot{E}x_{in} = \sum \dot{E}x_{out} + \sum \dot{E}x_{loss};$$

$$\dot{E}x_{sun} + \dot{E}x_{mass,in} = \dot{E}x_{el} + \dot{E}x_{mass,out} + \dot{E}x_{loss}; \qquad (12)$$

$$\dot{E}x_{sun} = \dot{G}\left(1 - \frac{T_{amb}}{T_{sun}}\right). \qquad (13)$$

In Eq.(12), the exergy related to the mass flow rate can be calculated as [18]:
$$\dot{E}x_{mass,out} - \dot{E}x_{mass,in} = \dot{E}x_{th} = \dot{m}_{nf}\left[\left(h_{nf,out} - h_{nf,in}\right) - T_{amb}\left(S_{nf,out} - S_{nf,in}\right)\right]. (14)$$

In which h_{nf} enthalpy of nanofluid S_{nf} and refers to the entropy of the nanofluid. Enthalpy and entropy changes are calculated with the following equations:
$$h_{nf,out} - h_{nf,in} = C_{p,nf}\left(T_{nf,out} - T_{nf,in}\right); \qquad (15)$$

$$S_{nf,out} - S_{nf,in} = C_{p,nf} \ln\left(\frac{T_{nf,out}}{T_{nf,in}}\right) \qquad (16)$$

The output thermal exergy of the system is calculated by the following equation:
$$\dot{E}x_{th} = \dot{m}_{nf} \cdot C_{p,nf} \left[\left(T_{nf,out} - T_{nf,in}\right) - T_{amb} \ln\left(\frac{T_{nf,out}}{T_{nf,in}}\right)\right]. \qquad (17)$$

Since the electrical energy is useful available work, the output electrical exergy of the system is equal to the output electrical power.[16]
$$\dot{E}x_{el} = \dot{E}_{el}. \qquad (18)$$

The exergy loss is calculated by combining equations (13) and (17), and (18):
$$\left(1 - \frac{T_{amb}}{T_{sun}}\right)\dot{G} - \dot{E}_{el} - \dot{m}_{nf} \cdot C_{p,nf} \left[\left(T_{nf,out} - T_{nf,in}\right) - T_{amb} \ln\left(\frac{T_{nf,out}}{T_{nf,in}}\right)\right] = \dot{E}x_{loss}. (19)$$

The entropy generation rate of the system is calculated according to the following equation:
$$\dot{S}_{gen} = \frac{\dot{E}x_{loss}}{T_{amb}}. \qquad (20)$$

Similar to Eq. (9), the overall exergy efficiency of the system can be expressed as a function of the thermal and electrical exergy efficiencies:[16]
$$\varepsilon_{ov} = \frac{\int_{t1}^{t2}\left(A_c \dot{E}x_{th}'' + A_{pv} \dot{E}x_{el}''\right)dt}{A_c \int_{t1}^{t2}\left(\dot{E}x_{sun}''\right)dt} = \varepsilon_{th} + r \cdot \varepsilon_{el} \qquad (21)$$

The electrical and thermal exergy in equation (21) is calculated as follows:
$$\varepsilon_{el} = \frac{\dot{E}x_{el}}{\dot{E}x_{sun}} = \frac{\dot{E}_{el}}{\dot{E}x_{sun}} = \frac{V_{oc} \times I_{sc} \times FF}{\dot{G}\left(1 - \frac{T_{amb}}{T_{sun}}\right)}; \qquad (22)$$

$$\varepsilon_{th} = \frac{\dot{E}x_{th}}{\dot{E}x_{sun}} = \frac{\dot{m}_{nf} \cdot C_{p,nf}\left[\left(T_{nf,out} - T_{nf,in}\right) - T_{amb} \ln\left(\frac{T_{nf,out}}{T_{nf,in}}\right)\right]}{\dot{G}\left(1 - \frac{T_{amb}}{T_{sun}}\right)}. \qquad (23)$$

RESULTS

According to the given equations, Hosseinzadeh et al. [15] have investigated the effects of ZnO/water Nano fluid and PCM usage on the PVT system and found the average surface temperature of NPVT and NPVT/PCM systems to be 47.22 and 42.44 ℃, respectively.

Using the Nano fluid-based PVT and PVT/PCM systems was found to improve the output electrical power by approximately 7.10 and 11.90%, respectively, compared to the conventional PV module. The use of organic paraffin wax as PCM in the Nano fluid-based PVT system improved the output thermal exergy of the system by approximately 79.36% compared to the Nano fluid-based PVT system without PCM. Thus, the use of PCM in the PVT system significantly increased the output thermal exergy of the system. According to the research, the main fluid is also important along with the nanoparticle used. Rajeb et al. [23] obtained a thermal efficiency of 8.88% when the same volume of Al_2O_3 Nano fluid was used together with the water mixture as a cooling liquid, while they obtained a thermal efficiency of 12.99% when ethylene glycol was used instead of water. Khanjari et al. [13] conducted an experimental study at different volume ratios and obtained the highest efficiency using Al and Ag nanoparticles at a 10% volume ratio. They reported that the system using Al/water Nano fluid reached 4.54% thermal efficiency, while the system using Ag/water Nano fluid reached 12.43%.

CONCLUSIONS

Research, experiments, and simulations show that Nano fluid-based PV/T systems work much more efficiently than water-based PV/T systems. Nano fluids consisting of hundreds of different nanoparticles have been used in the literature. The type of Nano fluid used and the type of heat exchangers affect the efficiency of PV/T systems positively or negatively in different parameters such as the mass flow rate of the Nano fluid and the percent volume of the Nano fluid. In the previous literature, traditional PV and Nano fluid-based PVT/PCM systems and ZnO/water Nano fluid PVT systems were compared. In the PV system, ZnO/water Nano fluid with a mass fraction of 0.2%, consisting of a 40-watt monocrystalline silicon PV module and circulated around the PV module with a constant mass flow of 30 kg/h, was used. It has been found that the use of Nano fluids in the system increases the maximum output electrical power up to about 13% compared to the conventional PV system. Furthermore, the use of Nano fluids increased electrical energy efficiency by about 12%. The use of PCM in the system, together with the use of ZnO/water Nano fluid, increased the output thermal power by up to 30%. Due to the use of PCM on the system using ZnO/water Nano fluid, thermal exergy improved by 80%. Furthermore, with the use of PCM in Nano fluid-based PVT, the electrical efficiency of the system increased by 12% compared to the traditional PV system and by 5% compared to the Nano fluid-based PVT system.

Nomenclature		Greeks	
A	Area(m²)	α	Absorptivity
A_c	Collector Area (m²)	η	Energy efficiency (%)
A_{pv}	Photovoltaic Cells Area(m²)	ε	Exergy efficiency (%)
C_p	Specific heat capacity (J kg^{-1} K^{-1})	ρ	Density (kg m^{-3})
$\dot{E}$	Power (W)	τ	Glass cover transmissivity
$\dot{E}x''$	Power per unit area (W m^{-2})		
FF	Fill factor	**Subscripts**	

$\dot{G}$	Solar radiation per unit area (W m^{-2})	amb	Ambient
h	Enthalpy (J kg^{-1})."	c	Collector
I	Electrical Current (A)	cell	Photovoltaic cell
$\dot{m}$	Mass flow rate (kg s^{-1})	eff	Effective
PV	Photovoltaic module	el	Electrical
PVT	Photovoltaic thermal system	g	Glass cover
NPVT	Nano fluid based Photovoltaic thermal system	gen	Generation
r	Packing factor	in	Inlet
s	Entropy (J kg^{-1} K^{-1})	nf	Nano fluid
T	Temperature (K)	oc	Open circuit
V	Electrical voltage (V)	out	Outlet
		ov	Overall
		sc	Short circuit
		th	Thermal

REFERENCES

1. DUPEYRAT, P.; MĚNĚZO, C.; FORTUIN, S. Study of the thermal and electrical performances of PVT solar hot water system. *Energy and Buildings.* 2014 January, Vol. 68, p.751-755.

2. TRIPANAGNOSTOPOULOS, Y. Aspect and improvements of hybrid photovoltaic / thermal solar energy system. *Solar Energy.* 2007 September, Vol 81, p. 1117-1131.

3. HUANG, B.J.; LIN, T.H.; HUNG, W.C.; SUN, F.S. Performance evaluation of solar photovoltaic / thermal systems. *Solar Energy.* 2001, Vol. 70, p 443-448.

4. SKOPLAKI, E.; PALYVOS, J.A. On the temperature dependence of photovoltaic module electrical performance: A review of efficiency/power correlations. *Solar Energy.* 2009 May, Vol. 83, p. 614-624.

5. ABBAS, N.; AWAN B. M.; AMER, M.; AMMAR, M.S.; SAJJAD, U.; ALI, M.H.; ZAHRA, N.; HUSSAIN, M.; BADSHAH, A.M.; JAFRY, T.A. Applications of Nano fluids in photovoltaic thermal systems: A review of recent advances. *Physica A: Mechanics and its Applications.* 2019 December, Vol. 536,122513.

6. MOHANRAJ, VJ.; CHEN, Y. Nanoparticles-a review. *Tropical Journal of Pharmaceutical Research.* 2006 June,5(1),561-573.

7. CHAKRABORTY, S.; PANIGRAHI, K. P. Stability of nanofluid:a review. *Applied Thermal Engineering*, 2020 June, Vol. 174, 115259.

8. YAZDANIFARD, F.; AMERI, M., BAJESTAN, E.E. Performance of Nano fluid-based photovoltaic/thermal systems: A review. *Renewable and Sustainable Energy Reviews.* 2017 September, Vol. 76, p. 323-352.

9. LI, Y.; ZHOU, J.; TUNG, S.; SCHNEIDER, E.; XI, S.; A review on development of Nano fluid preparation and characterization. *Powder Technology,* 2009 December, Vol. 196, p. 89-101.

10. JAVADI, F.S.; SAIDUR, R.; KAMALISARVESTANI, M. Investigating performance improvement of solar collectors by using Nano fluids. *Renewable and Sustainable Energy Reviews.* 2013 December, Vol. 28, p.232-245.

11. TYAGI, H.; PHELAN, P.; PRASHER, R. Predicted efficiency of a low-temperature Nano fluid-based direct absorption solar collector.*Journal of Solar Energy Engineering.* 2009 November, 041004.

12. OTANICAR, P.T.; PHELAN, E.P.; PRASHER, S.R.; ROSENGARTEN, G.; TAYLOR, A. R. Nano fluid-based direct absorption solar collector. *Journal of Renewable and Sustainable Energy 2.* 2010 May, 033102. <https://doi.org/10.1063/1.3429737>.

13. KHANJARI,Y.; POURFAYAZ, F.; KASAEIAN, A.B. Numerical investigation on using of Nano fluid in a water-cooled photovoltaic thermal system. *Energy Conversion and Management.* 2016 August, Vol. 122, p. 263-278.

14. AL-SHAMANI, N.A.; SOPIAN, K.; MAT, S.; HASAN, A.H., ABED, M.A.; RUSLAN, M.H. Experimental studies of rectangular tube absorber photovoltaic thermal collector with various types of Nano fluids under the tropical climate conditions. *Energy Conversion and Management.* 2016 September, Vol. 124, p. 528-542.

15. HOSSAINZADEH, M.; SARDARABADI, M.; PASSANDIDEH-FARD, M. Energy and exergy analysis of Nano fluid based photovoltaic thermal system integrated with phase change material. *Energy.* 2018 March, Vol. 147, p. 636-647.

16. CHOW, T.T.; PEI, G.; FONG, K.F.; LIN, Z.; CHAN, A.L.S.; JI, J. Energy and exergy analysis of photovoltaic –thermal collector with and without glass cover. *Applied Energy.*2009 March, Vol. 86, p.310-316.

17. SARDARABADI, M.; HOSSAINZADEH, M.; KAZEMIAN, A.; PASSANDIDEH-FARD, M. Experimental investigation of the effects of using metal-oxides/water Nano fluids on a photovoltaic thermal system (PVT) from energy and exergy viewpoints. *Energy.*2017 November, Vol. 138, p.682-695.

18. PARK, S.R.; PANDEY, A.K.; TYAGI, V.V.; TYAGI, S. K. Energy and exergy analysis of typical renewable energy systems. *Renewable and Sustainable Energy Reviews.* 2014 February, Vol. 30, p.105-123.

19. GHADIRI, M.; SARDARABADI, M.; PASANDIDEH-FARD, M.; MOGHADAR, J.A. Experimental investigation of a PVT system performance using Nano Ferro fluids. *Energy conversion and Management.* 2015 October, Vol. 103, p. 468-476.

20. XU, Z.; KLEINSTREUER, C. Computational analysis of Nano fluid cooling of high concentration photovoltaic cells. *Journal of Thermal Science and Engineering Applications.* Vol. 6, ISSN-19485085.

21. XU, Z.; KLEINSTREUER, C. Concentration photovoltaic-thermal energy co-generation system using Nano fluids for cooling and heating. *Energy Conversion and Management.* Vol. 87, p. 504-512.

22. TANG, Q. L.; ZHU, Z. Q. Performance study of flowing-over pv/t system with different working fluid. *Applied Mechanics and Materials.* Vol. 488-489, p. 1173-1176.

23. REJEB, O.; SARDARABADI, M.; MENEZO, C.; PASSANDIDEH-FARD, M.; DHAOU, H. M.; JEMNI, A. Numerical and model validation of uncovered Nano fluid sheet and tube type photovoltaic thermal solar system. *Energy Conversion and Management.* Vol. 110, p. 367-377.

PERFORMANCE OF PV SYSTEMS FOR DIFFERENT LOCATIONS IN TURKEY

P. M. CUCE

Department of Architecture, Faculty of Engineering and Architecture, Recep Tayyip Erdogan University, Zihni Derin Campus, 53100 Rize – Turkey
00904642237518-4400
mertcuce@gmail.com

E. CUCE

Department of Mechanical Engineering, Faculty of Engineering and Architecture, Recep Tayyip Erdogan University, Zihni Derin Campus, 53100 Rize – Turkey
00904642237518-1203
erdemcuce@gmail.com

S. OZKAZANC

Department of Mechanical Engineering, Faculty of Engineering and Architecture, Recep Tayyip Erdogan University, Zihni Derin Campus, 53100 Rize – Turkey
sedaozkazanc.94@gmail.com

EXTENDED ABSTRACT

OVERVIEW

The economic growth, rapid population rise, and improving living standards in Turkey have increased the demand for energy notably in recent years. Turkey generally meets its energy demand from fossil fuels, and this is highly dependent on imported energy. The use of clean energy resources is increasing with the developing technologies in the world. On the other hand, the use of fossil resources is decreasing to both reduce environmental pollution and prevent global warming. It is important to reduce the dependency on imported energy and increase the use of clean energy for the increasing energy need in our country. Solar energy, which is one of the renewable energy sources, draws the attention of researchers. In recent years, there have been numerous studies on the performance of PV systems, which is one of the most common applications of solar energy systems. Operational conditions remarkably affect the power output of PV systems. Akbarzadeh and Wadowski [1] found that overheating PV panels due to excessive solar radiation and high temperature notably reduces efficiency. In another study, Rodrigues et al. [2] showed the variation of the output power and output voltage of PV panels depending on the temperature difference. Katkar et al. [3], in their study, stated that the temperature increase in the PV panels notably reduces the voltage produced in the PV cells. The research has experimentally proven that the temperature increase significantly reduces the electrical energy production efficiency in PV cells and modules [4-6]. In order to increase the energy production efficiency in PV systems, the solution proposals in the literature are divided into two groups hardware and software. In software solution proposals, there are most important points such as the determination of

optimization-based solar power plant (SPP) installation points, determination of solar radiation amount, power generation forecasts, and solar tracking systems. In hardware solutions, there are mostly system designs and applications related to cooling the surface of PV panels. Photovoltaic thermal (PV/T) designs have been developed to prevent reductions in power generation efficiencies and to prevent waste of heat in PV panels. For PV/T structures, electrical efficiency and thermal efficiency were considered the efficiency of the system and both efficiencies were taken into account in the designs. In climates with high temperatures, water can be heated while generating electricity. Especially when the ambient temperature rises above 40°C, there is an opportunity where the efficiency of the photovoltaic panels is increased by cooling. In the winter months, when the temperature is low, the sunshine duration of the PV panels is very short, and the temperature can drop to minus degrees. As a result of this situation, the output generation power decreases significantly. Some panels are also made in designs where air or both are used instead of water [7].

In this work, studies in the literature were examined in order to reveal the energy production efficiency of PV panels depending on temperature and radiation in the case of different climatic regions of Turkey. Depending on the studies examined, the output powers of the panels are given in detail, and the performance points are determined.

METHODS

This study covers the months of March 2020 – March 2021 and is limited to 7 provinces in Turkey. Provinces were selected from the eastern, western, northern, southern and central parts of each region. The selected provinces were evaluated on a monocrystalline solar panel with reference to the temperature and radiation values between March 2020 and March 2021. The provinces included in the study; Artvin, Isparta, Istanbul, Izmir, Eskisehir, Malatya and Diyarbakir. Solar cells are photovoltaic devices that convert light energy into electrical energy, and they work as semiconductor diodes. A solar cell generates electricity by the photovoltaic effect. The photovoltaic effect, on the other hand, is the physical phenomenon in which the sun's rays are converted into electricity. Photons are formed when sunlight hits the semiconductor surface, and the electrons inside the atom are released. Photons contain different amounts of energy for each wavelength in the solar radiation spectrum [8]. Generally, six parameters are used to describe the solar cell. These are I_{sc} , I_m , V_{oc} , V_m FF ve η. To reach the maximum power in the solar cell, the following equation is used:

$$P_m = V_m I_m = (FF)V_{oc}I_{sc}. \tag{1}$$

Ideally, the maximum current should equal the short-circuit current $(I_{sc} = I_{max})$. The value of V_{oc} depends on I_0. V_{oc} can be found with the following equation:

$$V_{oc} = \frac{k_B T}{e} ln(1 + \frac{I_L}{I_0}). \tag{2}$$

Another important parameter in solar cells is the filling factor. The fill factor is the parameter that determines the highest efficiency to be obtained from the solar cell. It can be calculated with the following equation:

$$FF = \frac{I_m V_m}{I_{sc}V_{oc}}. \tag{3}$$

The power conversion efficiency of a solar cell is defined as the ratio of the output electrical power to the input optical power. The equation is as follows:

$$\eta = \frac{P_m}{P_{in}} \times 100 = \frac{I_m V_m}{P_{in}} \times 100. \tag{4}$$

The light current produced by the photovoltaic cell, I_{pv}, it also has a linear relationship between the cell and solar radiation and temperature. The luminous flux produced under nominal conditions is given by the equation:

$$I_{PV,cell} = (I_{pv,n} + k_i \Delta t) \frac{G}{G_n}. \tag{5}$$

In order to clearly understand the power change due to temperature change, Azaza and Wallin [9] made experimental measurements in 2015 in Uppsala, Sweden. The power generation output values of the panels are given by the following equation [10]:

$$P_{PV-out} = P_{N-PV} \times \left(\frac{G}{G_{ref}}\right) \times [1 + K_T(T_C - T_{ref})]. \tag{6}$$

The output power (W) in the P_{PV-out} Photovoltaic panel cell, the nominal power (W) of the photovoltaic panel cell in the Pn reference conditions, the G solar radiation (W/m^2), the G$_{ref}$ reference conditions (1000 W/m^2), K$_T$ represents the temperature coefficient of the maximum power, T_C represents the photovoltaic panel cell temperature (°C), T$_{ref}$ represents the photovoltaic panel cell temperature (25°C) in reference conditions. According to this definition, the cell temperature T$_c$ can be calculated using the ambient temperature (T$_{amb}$) as follows:

$$T_C = T_{amb} + (0.0256 \times G). \tag{7}$$

RESULTS

The performance of PV systems depends on the solar radiation intensity. The performance values of 7 provinces selected from 7 different regions of Turkey are compared between March 2020 and March 2021. The power outputs to be obtained from 7 different cities for 13 months are given in Fig. 1.
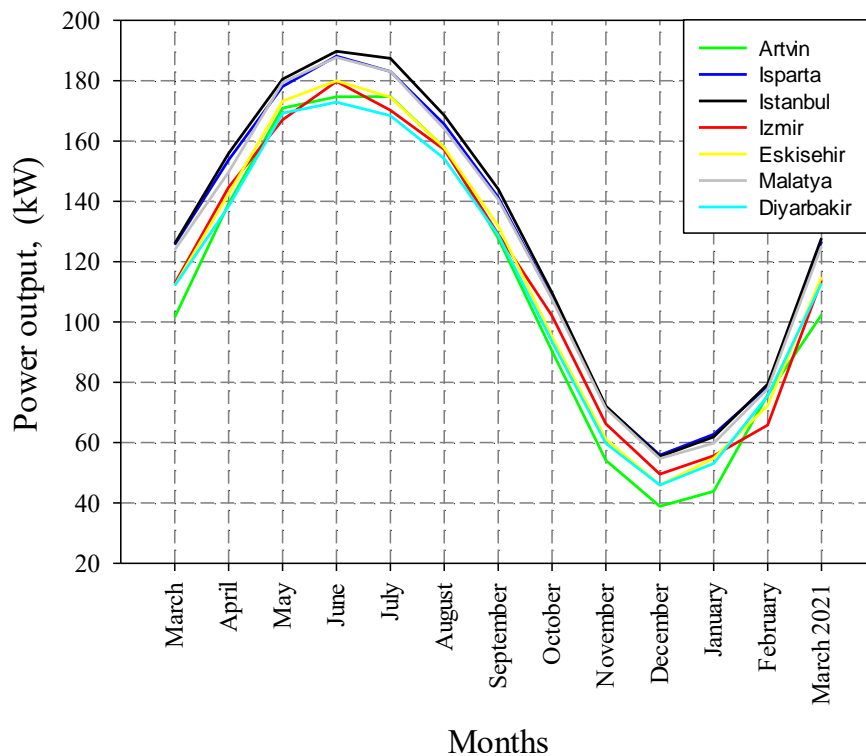
Fig 1. Power output for 7 different locations for 13 months.

CONCLUSIONS

PV systems are attractive systems with their potential. The performance of these systems, which are affected by temperature and solar radiation, is evaluated for 7 different locations in this study. It is seen that the highest power output can be obtained in all provinces during the summer months. In addition, the highest power output can be obtained in the province of Istanbul throughout the year.

Keywords: PV systems, different locations in PV systems

REFERENCES

1. AKBARZADEH, A.; WADOWSKI, T.   Heat Pipe-Based Cooling Systems for Photovoltaic Cells under Concentrated solar Radiation. *Applied Thermal Engineering*, 1996, p. 81-87.

2. RODRIGUES, E. M. G.; MELI´CIO, R.; MENDES, V. Simulation of a solar cell considering single-diode equivalent circuit model. In: International conference on renewable energies and power quality. Spain, 2011.

3. KATKAR, A. A.; SHINDE, N. N.; PATIL, S. P. Performance & Evaluation of Industrial Solar Cell w.r.t. Temperature and Hummidity. IJRMET, 2011, p. 69-73.

4. HASAN, M.A.; SUMATHY, K. Photovoltaic thermal module concepts and their performance analysis: a review. *Renewable and Sustainable Energy Reviews*, 2010, Vol. 14, No. 7, p. 1845-1859.

5. FUDHOLI, A.; SOPIAN, K.; YAZDI, M. H.; RUSLAN, M.H.; IBRAHIM, A.; KAZEM, H.A. Performance analysis of photovoltaic thermal (PVT) water collectors. *Energy Conversion and Management*, 2014, Vol. 78, p. 641-651.

6. BAHAİDARAH, H. M.; BALOCH, A. A.; GANDHİDASAN, P. Uniform cooling of photovoltaic panels: A review. *Renewable and Sustainable Energy Reviews*, 2016, Vol. 57, p. 1520-1544.

7. BIGORAJSKI, J.; CHWIEDUK D. Analysis of a micro photovoltaic/thermal–PV/T system operation in moderate climate. *Renewable Energy*, 2019, Vol. 137, p. 127-136.

8. OZTEKIN, E. K.; CUCE, E. Performance assessment of hybrid photovoltaic thermal (PV/T) collectors and systems: A review. In *International Conference on Advanced Engineering Technologies, ICADET 2017,* Vol. 21, p. 23.

9. AZAZA, M.; WALLIN, F. Multi objective particle swarm optimization of hybrid micro-grid system: A case study in Sweden. *Energy*, 2017, Vol. 123, p. 108-118.

10. DAUD, A.K.; ISMAIL, M.S. Design of isolated hybrid systems minimizing costs and pollutant emissions. *Renewable Energy*, 2012, Vol. 44, p. 215-224.

MODELLING AND DESIGN DC-DC BOOST CONVERTER FOR SOLAR ENERGY

H. G. Erdem, O. Timur
Cukurova University
Electrical Electronics Engineering Department
Sarıçam, 01250 Adana – Turkey
(+09) 542 787 14 30
huruguulerdeem@gmail.com, otimur@cu.edu.tr

ABSTRACT

The decline and inadequacy of fossil fuels have accelerated the exploration and use of renewable energy sources to meet increasing energy demands. In addition, the use of fossil fuels hurts the environment. For this reason, one of the most important renewable energy sources that are coming to the forefront of research is the sun.

Theoretical and general information about solar energy, which is a renewable energy source, such as power generation, storage, main components, power quality of solar energy, and problems with sources, are studied and explained in detail.

A photovoltaic system has been designed, which is widely used in solar energy. The system is formed by increasing the output voltage to the circuit fed by a panel in a certain ratio. In this process, the voltage is raised to the desired voltage level in the case of direct current with the help of the DC-DC Boost Converter.

Keywords: Renewable Energy, Solar Energy, Power Quality, Solar Photovoltaic Panel, DC-DC Boost Converter

INTRODUCTION

In the 21st century, with the development of technology and the rise in living standards, energy consumption has increased traditional practice to meet this requirement. Fossil fuels, which are energy production methods, have a noticeable negative impact on environmental effects [1].

Considering the statistics in the last five years of the last century, almost 90% of the energy production consisted of fossil fuels. During this period, it was observed that fossil fuels, gas, dust, and the like emitted around us during energy production adversely affected the universe we live in. In addition, it has been seen that gases affect the health of living things and cause global warming. Generating energy from fossil fuels' negative effects and exhaustible resources is why the search for alternative energy paved the way for its onset [2-3].

This is clean energy. The biggest advantage of these resources is that they are renewable, that is, inexhaustible, and also, as a result of their use, there are no harmful elements to the environment. This is the most important type of clean energy, photovoltaic energy [5]. On average, the total solar energy reaching our world is productive for a few hours. If it can be used as an energy source, the annual energy need of the world can be satisfied [6].

Photovoltaic energy, being an endless and very powerful source, being reliable, can be directly converted to electrical energy, does not contain moving parts and maintenance future due to its advantages such as almost non-existent costs. It is one of the promising energy sources [7]. Photovoltaic energy technology's aim is comparable to or even more costly than other energy sources. Advantageously, electrical energy can be obtained from the sun.

SOLAR ENERGY

What Is Solar Energy?

Solar can be defined as the energy emitted from the sun. Solar energy photons are the radiation energy released as a result of the conversion of hydrogen atoms in the sun into helium atoms.

The sun is so big that 1 million earth can fit inside it, and the amount of energy it emits is so great that 564 million tons of hydrogen turn into 560 million tons of helium per second. The 4 million tons of energy lost during this transformation is also dispersed into space. This energy emanating from the sun is known as solar energy and ensures the continuation of life on our planet [8].

Solar energy, with its distinctive feature of inexhaustibility, is a great renewable and has potential for sustainable development at present as an environmentally friendly energy source that proposes solutions [9].

METHODS (WHAT IS A PHOTOVOLTAIC SYSTEM?)

Photovoltaic literally means the production of electricity from the photon. This product is provided by Photovoltaic Panels (PV). Photovoltaic systems are the most common method used to generate electricity from the sun. These systems consist of many components.

Although almost everyone thinks of photovoltaic systems as consisting of solar panels, basic components such as batteries, inverters, and charge controllers are also very important for this system [10].

ELECTRICITY GENERATION IN PHOTOVOLTAIC PANEL

The structure of the solar panels used in our time is made of semiconductor materials such as a thyristor, diode, and transistor. Gallium arsenide, cadmium telluride, and the most preferred silicon are used as semiconductor materials in solar panel construction. If we examine in general, it is possible to realize photovoltaic conversion in semiconductors. For this, it is necessary to drop a photon (sunlight) on the joint area.

When a photon is dropped on the region of the semiconductor, an electron-hole pair is formed. The electron-hole pairs are separated from each other by the effect of the magnetic field formed in the environment. In this way, light is converted into electrical energy in semiconductors [11]. In solar cells, the region where this event occurs is divided into three. These are conductive tape, forbidden energy band, and valence band.

The conductive and valence bands are the energy bands. The energy of the incoming photon is the forbidden energy. If it is greater than or equal to the valence band, the photon can lose its energy by removing an electron from the valence band [12]. Thus, it is ensured that the detached electron reaches the conduction band, and the electron-hole pair is formed. This pair is connected by the effect of the electric field in the p-n junction region.

They are separated from each other, like a pump that pushes electrons to the n region and the holes to the p region. Thus, power flow occurs between the ends of the solar cells. This event is the photovoltaic called event.

WHAT ARE THE PHOTOVOLTAIC (PV) SYSTEM TYPES?

Off-Grid Photovoltaic Systems (Storage Systems)

Off-grid photovoltaic systems are systems that are installed separately from the electricity grid, store the electricity produced by solar panels via batteries and convert it into electrical energy that we use at home with inverters. Off-Grid systems consist of four main parts. These are solar panels, battery packs, charge controllers, and inverters.

The system working principle is the electrical energy produced from the solar panel is regulated by the charge controller and stored in the batteries. This stored energy is converted into electrical energy that we use at home with inverters. In a way, this is similar to the principle of charging the car battery of the alternator in vehicles. Battery quality is very important for off-grid photovoltaic systems. Batteries with high charge-discharge efficiency, resistance to high temperatures, and long life should be preferred.

On-Grid Photovoltaic Systems (Grid-Connected Systems)

Photovoltaic On-Grid system consists of four basic elements solar panels, inverter, bidirectional, and data logger.

The system working principle is the electrical energy produced from the solar panels is arranged by coming to the grid-connected inverters and converted into a form that can be transferred to the power line. The electricity produced from the solar panel is used directly

for the load, and the excess is transferred to the grid. When the air is closed, or the production is low, the electricity need is met by transferring electricity from the grid to the load. If there is a problem caused by the mains, the inverter turns itself off. In other words, if there is a power outage in the network, your home will also be cut off [13].

WHAT ARE THE MAIN ELEMENTS OF SOLAR TRIBUNES (PHOTOVOLTAIC (PV) SYSTEM BASIC ELEMENTS)?

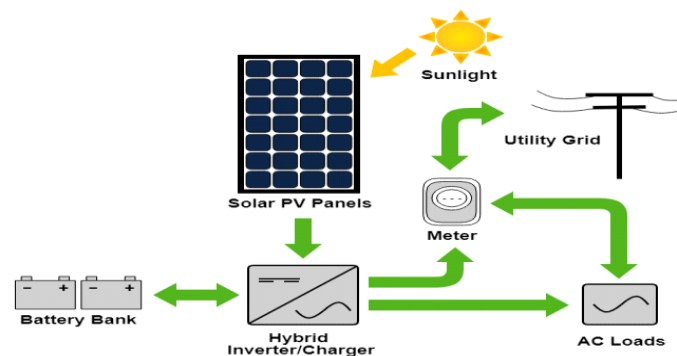The components of solar tribunes are shown in Fig 1. Some of the most important components are described below.

Fig. 1. Photovoltaic Systems

Solar Panel

Solar panels, which are the most basic part of photovoltaic systems, are the part where electricity is produced from the sun. The solar panel converts solar energy into electrical energy using solar cells made of semiconductor silicon material. Solar panels of different capacities are available. These vary according to the area and arrangement of solar cells. Solar panels are widely used in the market. They are solar panels with a capacity of 5W (Watt), 10W, 60W, 100W, 150W, 260W, and 275W.

Charge Controller

The charge controller regulates and stabilizes the dc energy coming from the solar panel and creates stable dc electrical energy for the charging of the batteries. To charge the batteries from a dc source, the charging current and voltage must be regulated and constant. The voltage and current produced by the solar panel are not constant, so a charge controller is needed for efficient charging of the batteries. Charge controllers also prevent reverse current from flowing from the battery to the panels. It protects the battery from overcharging. The charge controller cuts off the electricity from the solar panel when the battery is full. There are two types. These are PWM (Pulse Width Modülation) and MPPT (Maximum Power Point Tracking) charge controllers.

Batteries

Battery quality is very important for off-grid photovoltaic systems with solar storage. The battery should have high charge-discharge efficiency and long life. It should be resistant to temperature and adverse environmental conditions. Batteries commonly used in solar systems are gel batteries and some deep cycle leads acid batteries.

Inverters

Inverters are electronic devices that convert DC electrical energy into AC electrical energy. There are three types of Off-Grid photovoltaic systems square wave, modified sine, and full sine. Modified sine and full sine models are frequently used in solar systems [14].

HOW IS PRODUCED ENERGY STORED?

Excess solar energy can be stored with a Solar Cell. The solar battery is useful in many ways because it helps you take advantage of the electricity your solar system produces when you need it. We use energy to heat and cool our homes during the day, but lights and other electronic devices are mostly used after work and at home in the evening. Unfortunately, this is also when solar panels stop producing energy.

The solar battery helps alleviate this problem by storing the excess electricity produced by your solar panels for your evening consumption. That way, you can continue to use clean energy when you get home from work instead of drawing energy from the power grid, which likely uses coal or some other form of fossil fuel energy.

POWER QUALITY PROBLEMS OF SOLAR PANEL

Power quality problems in solar power plants are as follows can be sorted:
* Transient voltage
* Continuous voltage variations: The general output power voltage level in renewable energy sources may increase or decrease.
* Voltage imbalance: Another important factor affecting power quality is voltage imbalance.
* Wave distortion-Harmonics: The total high-frequency waveform makes up the distorted fundamental waveform.
* Voltage fluctuations and flickers: In a healthy network, the voltage is 50 Hz, and a pure sine wave should be in the form. However, this is not always the case. Network voltage can sometimes oscillate at lower frequencies.
* Power frequency variations: Frequency is one of the most important factors in power quality at the power source, and demand imbalances cause frequency oscillations. For this reason, in grid-connected systems, grid frequency and system frequency are synchronized should be done [15].

DESIGN AND SIMULATION WORKING

DC-DC Converter

The converter is an electronic circuit or electromechanical device that converts a source from one voltage level to another. It is a type of electric power converter. Generally, there are 4 converters. These are AC-AC, AC-DC, DC-AC, and DC-DC.

NOTE: In this project, only DC-DC converters were mentioned. Because "DC-DC Boost Converter Modelling and Design for Solar Energy" will be studied. A DC-DC converter is an electronic circuit or electromechanical device that converts a DC direct current source from one voltage level to another. It is a kind of Electric Power Converter.

Specific to these converters is that the energy flows in both directions of the converter. These converters are commonly used in various applications, and they are connected between two levels of DC voltage, where energy is transferred from one level to another [16]. These converters are; the Boost DC-DC converter, Buck DC-DC converter, Boost-buck non-inverting DC-DC converter, and Boost-buck inverting DC-DC converter.

Which Is The Best Dc-Dc Converter To Use With Solar Pv Panels?

DC-DC Boost Converter is more suitable for PV (photovoltaic) systems connected in series. Since the voltage level of PV is usually low, a boost converter is preferred in most cases. PV cells break down when the pulsed current is consumed. The most typical solution is a boost converter with a constant frequency resonant converter (when you have full resonance and almost no switching losses).

The microprocessor to be used represents the control of the converter. As known, the boost converter is the variable DC voltage of the input, the operating ratio of the switch D (Duty Cycle=D). It is used by changing the PWM (pulse width modulation). It amplifies by switching and passes it to the output. PWM manages the modulation cycle.

Buck, flyback, forward converter, etc., can be used, but to design a good solution, you need to add a current filter that should be taken into account. However, this negatively affects my overall efficiency and power density. The use of the converter depends on the voltage level required for the application. Since the voltage level of the PV is usually low, in most cases, a step-up converter is preferably used. In this project, it will be more useful to use "Boost Converter" as the booster is dc-dc.

Dc-Dc Boost Converter (Topology of Dc-Dc Boost Converter)

The DC voltage applied to increase the converter input gives higher DC to the output. They are circuits that transfer by converting to voltage. Boost converter circuit includes inductance, capacitor, diode, and switching element. When the switch is switched on, the diode is in reverse polarity, it is in the cut. The circuit, coil, and key are completed. This word stores some energy on the coil. The load capacity at the outlet is fed. Here the capacitor current is high is worth. When the switch is switched off, the source voltage and the coil voltage a total tension is seen. The current drawn from the source is continuous. Key in key control, handed over by a control. The state of switching on and off by changing the operating ratio D (Duty Cycle). This toggle can show the status according to the input voltage and, accordingly, the output voltage [17]. Fig.2 shows the design of the DC-DC Boost Converter Topology Circuit.

The microprocessor to be used will show the control of the amplifier converter. As it is known, the amplifying converter, the incoming variable DC voltage of the input, and the switch operating ratio (Duty Cycle=D) by changing D, i.e. PWM (Pulse Width Modulation-Pulse Width Modulation). It raises and transfers it to the output through its switching. Here is microprocessor comes into the circuit, and this PWM (Pulse Width Modulation-Pulse Width). It manages the modulation switching.

CONVERTER CALCULATIONS
Converter coil value;

$$L = \frac{V_{in} \times (V_{out} - V_{in})}{\Delta IL \times fs \times V_{out}}$$

Converter minimum capacity value;

$$C_{min} = \frac{I_{out\,max} \times (V_{out} - V_{in})}{\Delta V_{out} \times fs}$$

Duty Cycle;

$$D = 1 - \frac{V_{in}}{V_{out}}$$

D value varies between 0 <D <1, and the output voltage is higher than the input voltage. Thus, this circuit booster type converter. It is called "Boost Converter". The lowest value of the output voltage D = 0, and the output voltage becomes equal to the input voltage. When the fill ratio is D=1, the output voltage becomes infinite. Therefore, in applications, the D value is selected in the range of 0.1 <D <0.9.

So parameters such as: L (Inductor) =1000uH, C (Capacitor) = 2200uF, R (Resistance) =10Ω and fs (Switching Frequency) = 5MHz.

DC-DC BOOST CONVERTER EXPERIMENTAL WORKING OF SIMULATION DESIGN

Solar energy, wind energy, biomass energy, geothermal energy, hydraulic energy, hydrogen energy, and wave energy are used as renewable energy. The most widely used type of renewable energy is solar energy. Because solar energy is an environmentally friendly energy source with its unique inexhaustible feature and great renewable potential. [5].

Due to certain weather and climatic conditions, the desired output voltage and power of PV panels cannot be obtained. Therefore, efficiency can be increased by using DC-DC boost converters.

Of course, when designing this circuit, attention should be paid to the calculation of circuit elements suitable for the topology, such as PWM, duty cycle, and microprocessor.

If Vin = 20, Vout = 29.85 V, fs = 5 MHz in Equation (3);

$$D = 1 - \frac{V_{in}}{V_{out}} = 1 - \frac{20}{29.85} = 0.33 \Rightarrow \%33$$

If Vin = 20, Vout = 57.4 V, fs = 5 MHz in Equation (3);

$$D = 1 - \frac{V_{in}}{V_{out}} = 1 - \frac{20}{57.4} = 0.65 \Rightarrow \%65$$

Comparing the calculation results, I found that at a high switching frequency (fs = 5 MHz), the output voltage changes (Vout = 29.85 and Vout = 57.4 V), even if I apply a constant input voltage (Vin=20V) and change the duty cycle. This study can benefit from the low cost and high speed of the control circuit. For this reason, it can be recommended to use boost converters for solar energy.

When designing this experiment, the minimum output voltage and current were found at the lowest (D=33%) value of the duty cycle in the 1st experiment. In the second experiment, the maximum output voltage and current were obtained at the highest value of the duty cycle (D=65%).

In section 3.1.2. DC-DC Boost Converter (Topology of DC-DC Boost Converter), dc boost topology is explained. In this direction, the DC-DC Boost converter is obtained in Fig.2. Dc-Dc Boost Converter Circuit in MATLAB, using the Matlab program.
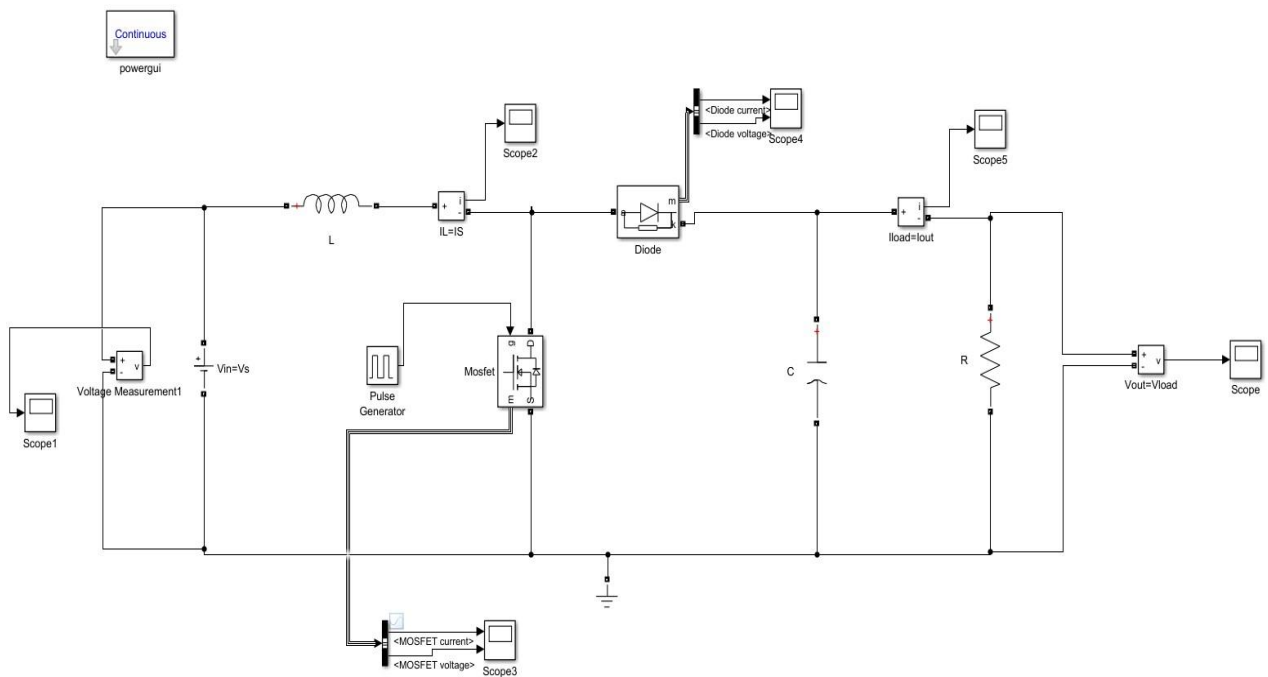

Fig. 2. Dc-Dc Boost Converter Circuit in MATLAB

EXPERIMENT 1: DUTY CYCLE FOR %33

In Fig.3, while the Duty Cycle is 33%, the Minimum Output Voltage value is 29.62 V.

In Fig.4, while the Duty Cycle is 33%, the Output or Load current value is 2.93 A.
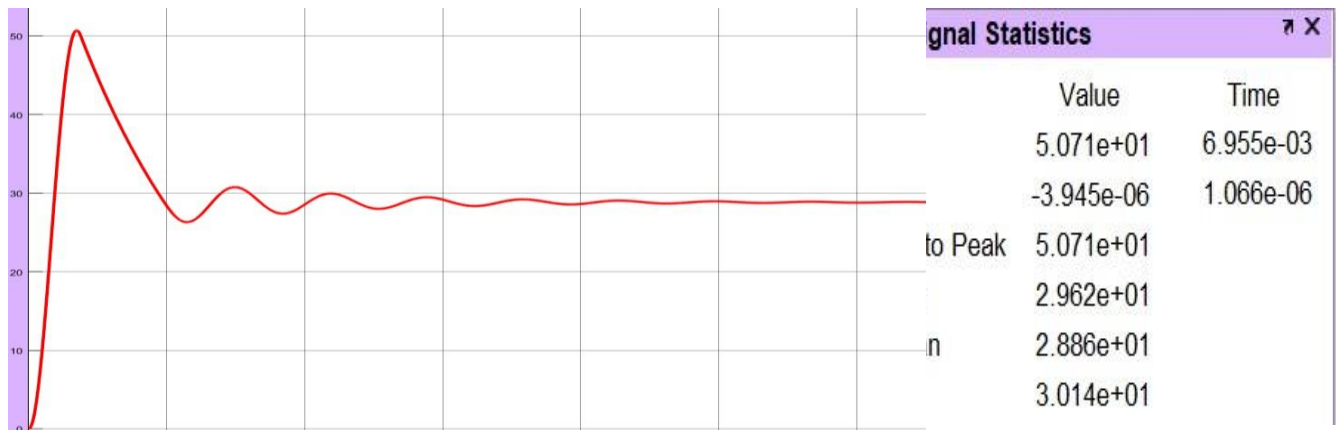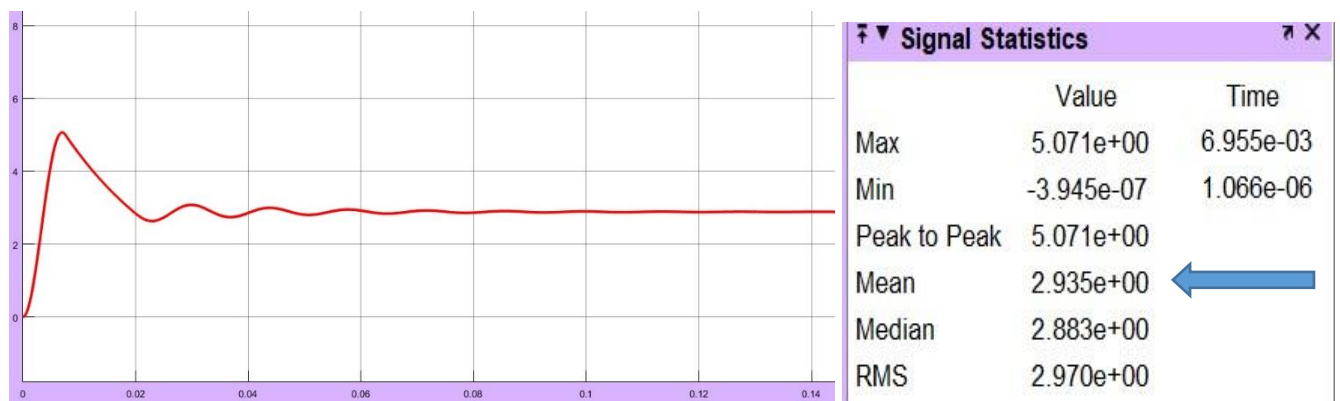
Fig. 3. Vout=Vload=29.62V

Fig. 4. Iload=Iout=2.93A

EXPERIMENT 2: DUTY CYCLE FOR %65

In Fig.5, while the Duty Cycle is 65%, the Maximum Output Voltage value is 53.18V

In Fig.6, while the Duty Cycle is 65%, the Output or Load current value is 5.291 A
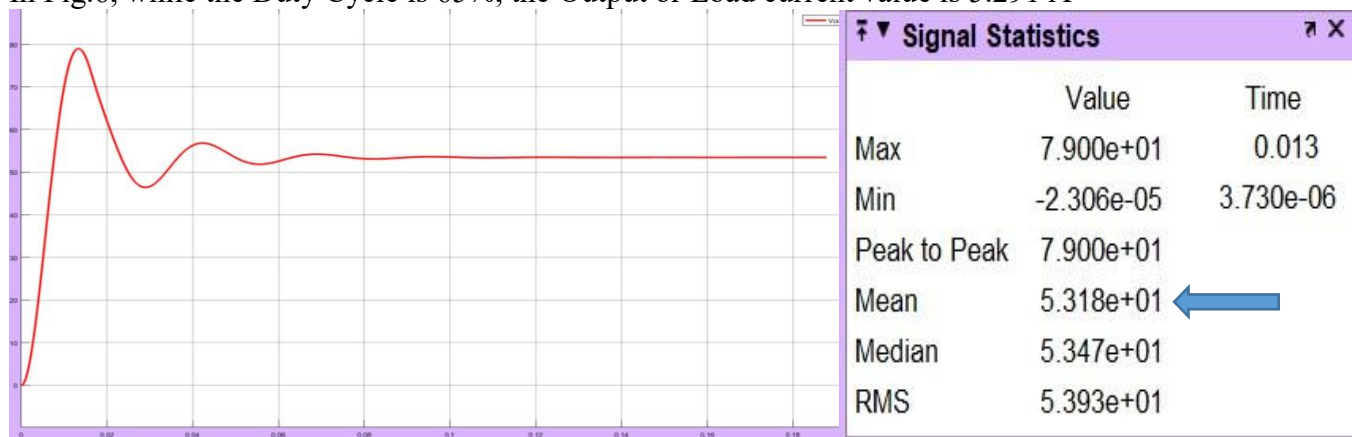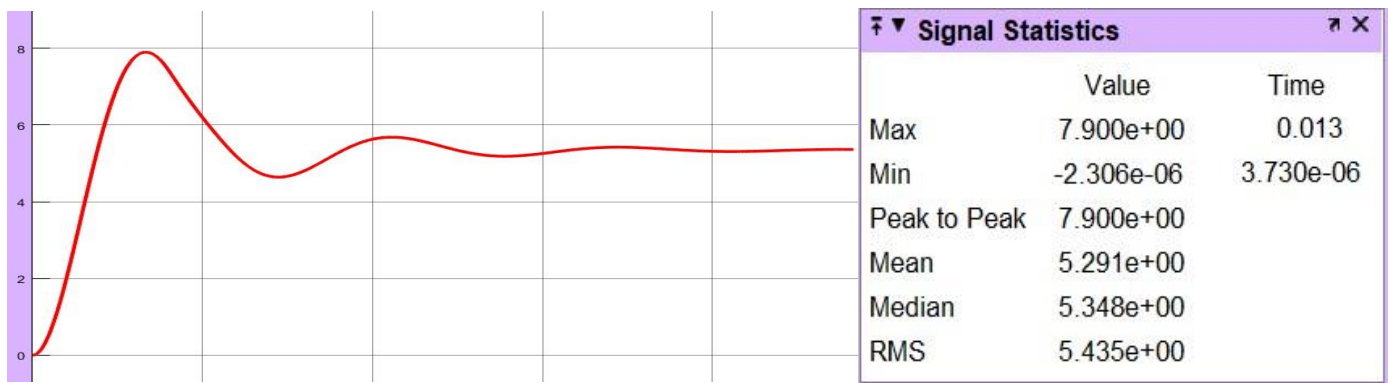

Fig. 5. Vout=Vload=53.18V

Fig. 6. Iload=Iout=5.291A

RESULTS AND DISCUSSION

The most popular renewable energy source application using solar energy is the generation of energy. Photovoltaic panel applications are energy generation with the solar source of the methods. Solar energies have been examined separately, and the types, how it produces electricity, how they store electricity, and the factors that disrupt their power quality have been examined.

In this Project, the output voltage of the solar photovoltaic panel is generally low and should be increased for proper use. So using DC-DC Boost Converter to provide this voltage boost. In this study, a microcontroller-controlled Boost Converter was offered.

As a result of this work, as seen in Fig. 3 and Fig. 4. Show minimum voltage value is Vout=Vload=29.62 V, and the minimum current is Iload=Iout=2.93A. Fig. 5 and Fig. 6 show maximum voltage is Vout=Vload=53.18V, and the maximum current is 5.291 A. So it has been proven that minimum and maximum voltage values can be obtained in different duty cycles.

Necessary studies have been done for the system, and the result may be a circuit. Necessary circuit applications were made according to these simulations and their results. The system can be developed further by carrying out the necessary research and development studies. The system can be made more useful by making studies that will reduce the losses and increase the efficiency even more.

Realized power and control circuit, different duty cycle situations, and it has been operated for different occupancy rates. With this work, the control circuit implemented software and hardware low from the advantages of costly and high speeds. Therefore, it is recommended to be used in Boost Converters. So, the experimental results obtained approximately coincide with the theoretical analysis. It shows the success of the work.

REFERENCES

1. JACOVIDES, C. P.; TYMVIOS, F.S.; ASSIMAKOPULOUS, V. D.; KALTSOUNIDES, N. A. *Comparative Study Of Various Correlations In Estimating Hourly Diffuse Fraction Of Global Solar Radiation*. Renewable Energy, Vol. 31, P. 2492-2504, December 2006.

2. BAYRAM A. *Pomace as a Renewable Energy Source: Production, Properties, Evaluation*. Renewable Energy Sources Symposium, P.106-112, Izmir, 2001.

3. UYAR, T. S. *Energy Sorunu Nedir? Alternatif Enerji Çözüm Müdür?* Neu-Cee 2001 Electrical, Electronic And Computer Engineering Symposium, Pp. 23-26, Lefkoşa Trnc, 2001.

4. ORUÇ, S. Electrical And Electronics Engineering Thesis, Karadeniz Technical University, June 2013.

5. KANGAL, H.; Electrical And Electronics Engineering Master Thesis, Gazi University, Institute Of Science And Technology, January 2008.

6. DEMIRDAĞ, S.; Electrical And Electronics Engineering Master Thesis, Gazi University, Institute Of Science And Technology, October 2007.

7. *Tob Chamber Of Mechanical Engineers, New, And Renewable Energy Resources*, Symposium And Exhibition, Proceedings Book, Mmo Publication No: E / 2003 / 330 October 2003, Kayseri.

8. CLEVELAND, C. *Encyclopedia of Energy, Boston, Elsevier Academic Press*, 2004.

9. ZHANG, X. *Assessment of the effectiveness of investment strategy in solar photovoltaic (PV) energy sector: A case study*. Science Direct Energy Procedia, Vol. 105, P. 2977–2982, 2017.

10. KÖROĞLU, T.; TEKE, A.; BAYINDIR, A.Ç.; TÜMAY, M. Design of Solar Panel Systems. *Journal of Electrical Engineering*, 2010, Vol. 439, P. 98-104.

11. RESTEMLİ, S.; DİNÇADAM, F.; DEMİRBAŞ, M. *Güneş Pileri ile Sıcak Su Elde Etme ve Sokak Aydınlatması*. V. Renewable Energy Resources Symposium, Diyarbakır, 2009,P 42-49.

12. REİSLİ, B.; KALOĞLU, F.; SOLMAZ, S. *Solar Cell and Solar Textiles Technology*, Solar Future Proceedings Book, İstanbul, February 2010, P. 43-49.

13. WEIS, C. Considerations for Off-Grid PV Systems. Retrieved from HomePower:<https://www.homepower.com/articles/solarelectricity/designinstallation/considerations-grid-pv-systems 2013, Januar>.

14. FRANKLIN, E. *Hand Tools Used for Solar Photovoltaic (PV) Systems*, AZ1702. The University of Arizona Cooperative Extension, Tucson, AZ, 2006.

15. PERINÇEK, O. *Fotovoltaik Güç Sistemleri Elektrik Şebekesine Bağlandığında Oluşan Anomaliler*, Electrical and Electronics Engineering Master Thesis, Ege University, 2003.

16. JAKOBSEN, L.T.; ANDERSEN, M.A.E. *Comparison of Two Different High Performance Mixed Signal Controllers for DC/DC Converters*, IEEE Workshops on Computers in Power Electronics, 2006, P. 129 – 135.

17. HASANEEN, B.M.; MOHAMMED, A. A. E. *Design and Simulation of DC/DC Boost Converter*, International Middle-East Power System Conference MEPCON 2008, P. 335 – 340.

OBTAINING ELECTRICAL ENERGY WITH THE AID OF AIR FLOW FORMED IN THE AIR RELEASE CHAMBERS OF THE AIR CONDITIONING SYSTEM IN A TEXTILE FACTORY

O. Karlık
Fırat University, Department of Mechatronics Engineering
Elazığ, 23119 – Turkey
+905310814844
onıurkarlik4441@gmail.com

B. Dandıl
Mustafa Kemal University, Faculty of Engineering
Antakya/Hatay, 31060 – Turkey
+905359777598
besir.dandil@mku.edu.tr

EXTENDED ABSTRACT

OVERVIEW

In recent years, people have tended to use renewable energy sources due to the use of fossil fuels to obtain energy and the damage of fossil fuels to the environment. Wind energy, as a renewable energy source, has been produced in large-scale power plants and has helped to diversify energy.

This study it is aimed to generate energy by placing a horizontal axis wind turbine in the fan chamber while the indoor air, which includes dust and small fibre particles released to the outside by the suction motors thanks to the suction and discharges air conditioning chambers in order to balance the indoor climate in a factory which is producing denim fabric.

With the work to be done, it is aimed to undertake the duty of a source for the air conditioning systems, which have been seen as a consumption element in enterprises until today. It is aimed to create a platform for the use of renewable energy in enterprises, expand the use of renewable energy in industrial factories, and create a production model in which wind turbines can be used indoors, thanks to the wind turbine that will use an uninterrupted air flow when the air speed is continuous, and the fabric weaving business operates.

METHODS

This study was carried out in Çalık Denim Textile company between 2021-2022. In the study, indoor air suction motors, which keep the ambient climate of the weaving mill in balance, transfer the air to the outside environment from a room. During this air transfer, electrical energy was tried to be produced by rotating a wind turbine placed in the room with the help of air reaching a certain speed.

Fig. 1. Indoor Suction Motor in Air Discharge Room

The turbine is positioned on a movable chassis, and as a result of the measurements made with the anemometer, it is positioned in the region where the airflow is fast a 1 kW/h wind turbine was used to generate energy in the air conditioning room. The fan continues to airflow as long as the weaving mill is running. The energy obtained by converting the incoming AC current in the turbine alternator into DC current by the inverter used in the system is stored by 4 12V DC batteries. 220V socket connection is made from the AC output of the inverter, and this energy can be used in appropriate places. The turbine has an off-grid system. An electronic circuit is designed to control and record current, voltage and ambient conditions.

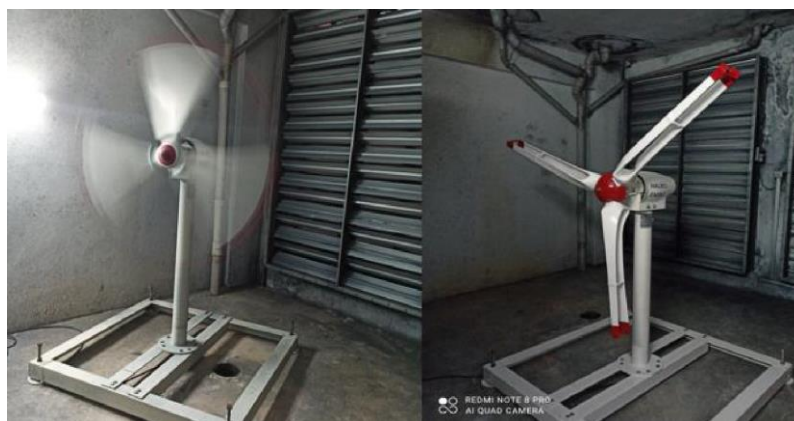Fig. 2. 1 kW/h Wind Turbine in Air Discharge Room

A circuit board is designed to reveal the air profile in the room where the turbine is located and to calculate the power of the turbine. Thanks to the sensors on this circuit board, the voltage and current produced by the turbine will be monitored, the speed of the air discharged by the fan motors will be measured with the anemometer, and the temperature, humidity,

pressure, altitude and air pollution will be determined with the help of the sensors. These detected values are converted into a value by using various algorithms in the microprocessor on the card, and they are instantly displayed on a TFT LCD screen on the card. The obtained data is recorded every 10 minutes and saved to an SD card as a log.
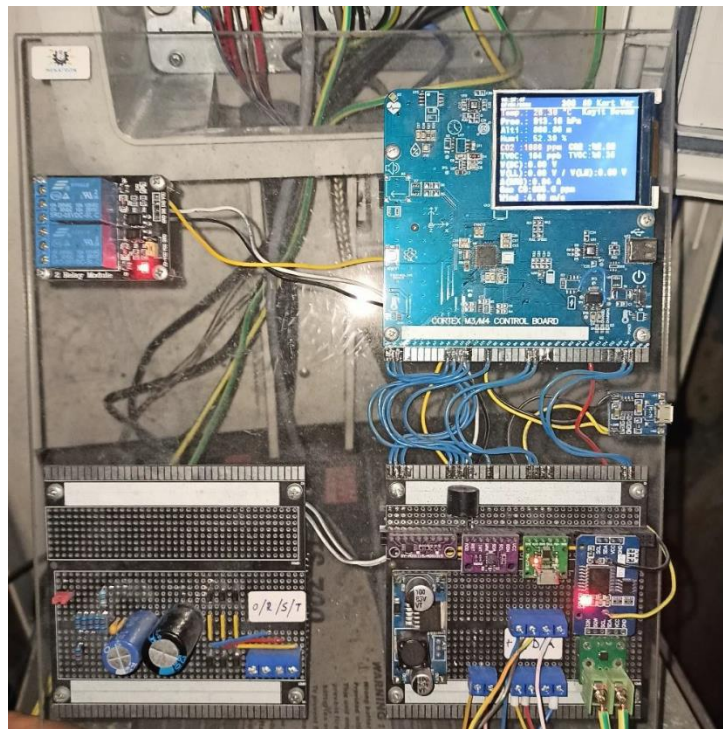

Fig. 3. Sensor Tracker Electronic Circuit

RESULTS

At the end of the measurements taken for about 3 months, the averages of current, voltage, air velocity, ambient humidity, temperature and turbine power were calculated as shown below in Table 1. The turbine voltage is directly proportional to the air speed. Airflow was not interrupted as long as the weaving mill was running. As long as the turbine was running, it did not require maintenance. The energy use of the suction and discharge motors, which energy use has increased or decreased according to the indoor humidity, has been close to the previous months. There has been no significant change in the energy use of air conditioning systems.

Since we can calculate the current and voltage, we calculated the power of the turbine with the formula $P=V.I.\sqrt{3}$. Since the system has a 3-phase supply, the current and voltage are multiplied by $\sqrt{3}$.

Since the efficiency of the turbine is directly dependent on the air speed blown by the fan motor, the climatic conditions of the room were recorded for control purposes only.

In the measurements, it was observed that the air quality of the room was insufficient. TVOC is used to estimate the total Volatile Organic Compounds (VOC) that are present at the same time in the air. Detecting TVOC in the 220 ppb to 660 ppb range indicates poor ventilation efficiency. The average t_{voc} value in the air conditioning room was measured as 304 ppb. The reason for this may be that the turbine takes the air directly on it and directs it to the outdoor air intake motor in the next room after rotation movement.

An average of 141.66 watts of power was obtained from the turbine, and the average air speed was 6.49 m/s.

Table 1. Voltage, current and Air Profile

Date	Time	T(℃)	Pressure (hPa)	Altitude (m)	Humidity (%)	Tvoc (ppb)	Wind (m/s)	V (AC)	I (RMS)	P (Watt)
21.12.2021	13:08:45	27.74	904.78	944.94	52.22	21	4.73	27.58	1.72	82.15
21.12.2021	13:10:55	27.76	904.78	944.95	52.19	9	5.23	30.49	2.39	126.22
21.12.2021	13:20:52	27.43	904.78	944.97	52.94	50	5.64	32.88	2.24	127.57
21.12.2021	13:30:55	27.61	904.84	944.44	50.97	77	5.15	30.02	1.61	83.72
21.12.2021	13:40:55	27.55	904.84	944.45	51.12	263	6.06	35.33	2.59	158.49
21.12.2021	13:50:57	27.63	904.72	945.52	51.47	331	5.48	31.95	2.38	131.7
.	.	.	.	.	.	.	.	.	.	.
.	.	.	.	.	.	.	.	.	.	.
.	.	.	.	.	.	.	.	.	.	.
24.03.2022	14:15:28	32.96	908.05	915.17	36.63	429	7.72	45.01	3.81	297
24.03.2022	00:54:23	33.55	903.94	952.61	34.78	595	7.39	43.08	3.89	290.28
24.03.2022	16:25:39	33.12	908.95	906.98	35.71	567	6.74	39.28	3.98	270.76
24.03.2022	05:44:47	33.23	905.09	942.11	35.42	425	5.48	31.95	4.34	240.15
Avg.		28.61	908.2	913.04	41.86	304	6.49	37.85	2.15	141.66

CONCLUSIONS

In this study, it has been determined that wind turbines producing electricity with wind energy in nature can produce electricity with waste air of factories in closed environments.

A new working model has been created for wind turbines, and the air conditioning systems of industrial factories have served as a source for wind turbines.

It is thought that the installed wind power will increase by using the waste air velocity expelled from the factories located in the regions where the wind speed is low.

Keywords: Renewable energy, air conditioning, wind turbine, waste air

REFERENCES

1. ACAR, E.; DOĞAN A. Evaluation of Turkey's wind and hydroelectric potential and environmental impacts. VII. National Clean Energy Symposium (UTES' 2008)

2. ALBOSTAN, A.; ÇEKİÇ, Y.; EREN, L. Effect of wind energy on Turkey`s energy supply security. *Journal of the Faculty of Engineering and Architecture of Gazi University.* 2009 Vol. 24, No. 4. p. 641–649.

3. ARSLAN, F. M.; TUZCU, H.; GÜNERHAN, H. Theoretical modelling of residential wind turbine blades and comparison of aerodynamic properties affecting power generation, 2017.

4. ATA, R.; ÇETİN, N. S. Construction and energy generation of 3 kW autonomous wind turbine. *Journal of the Faculty of Engineering and Architecture of Gazi University.* Vol. 23, No. 1. p. 41–47, ISSN: 1300-1884 / 1304-4915, 2008.

5. BEKAR, N. Renewable energy resources and energy geopolitics of Turkey. *Türkiye Siyaset Bilimi Dergisi*, 2020 Vol. 3, No. 1. p. 37–54, <https://dergipark.org.tr/tr/pub/tsbder/issue/53350/709200>.

6. ÇOLAK, İ.; DEMİRTAŞ, M. The development of electricity generation from wind energy in Turkey, *TÜBAV Bilim Dergisi*, 2008 p. 55–62. <https://dergipark.org.tr/tr/pub/tubav/issue/21513/230829>.

7. GÜLER, Ö. Wind energy in the world and in Turkey. p. 209–215.

8. İNAN, İ.; AKBULUT, İ.; ASLAN, E. The place and importance of non-renewable and renewable energy sources in solving the energy problem. 2018, Vol.120, No. 237. p. 11–40.

9. YAVUZ, İ.; ÖZBAY, H. Installation and maintenance processes in wind turbines: The case of Bandera. *Journal of Engineering Sciences and Researches*, 2020, Vol. 2, p. 58–68, <https://doi.org/10.46387/bjesr.800527>.

10. AIR QUALITY SHIELD. LINK TO THE INTERNET: <HTTPS://WWW.IBM.COM/DOCS/EN/MWI?TOPIC=SHIELDS-AIR-QUALITY-SHIELD>

THE FEASIBILITY OF USING SRF IN THE CEMENT INDUSTRY

I. Pitak, A. Baltušnikas, G. Denafas
Lithuanian Energy Institute
Breslaujos g. 3, 44403 Kaunas – Lithuania
+37067524856
inna.pitak@lei.lt

EXTENDED ABSTRACT

OVERVIEW

Global warming, increasing waste generation, and depletion of natural energy resources are some of humanity's environmental problems today. All these problems are closely interconnected and entail changes in human life. For example, the depletion of natural resources forces energy-intensive industries to either reduce production capacity or look for alternative ways to solve the current problem. In addition, another critical problem arises for industrial sectors that use solid fuel in coal – increased greenhouse gas emissions. The increase in municipal solid waste (MSW) generation makes people look for ways and methods to process and dispose of non-recyclable fractions. In our opinion, all these three environmental problems can be solved by producing fuel from waste and using it as alternative fuel during clinker firing. What will we get as a result:

1) the amount of non-recyclable waste sent to the landfill will reduce;

2) the consumption of solid fossil fuels will reduce;

3) the greenhouse gas emissions will reduce, such as SRF is 60% composed of biogenic components.

The purpose of this study was to investigate the composition and properties of solid recovery fuel (SRF) and the possibility of using SRF as an alternative fuel in the cement industry. To achieve the aim, it is necessary to perform the following tasks:

– to investigate the main properties of SRF and prove that it is a viable fuel that can be used in clinker firing as an alternative fuel;

– to investigate the properties of the ash obtained after the incineration of SRF to find out does the ash contain clinker forming minerals.

METHODS

According to [1], SRF is a fuel produced from non-hazardous waste following EU standards. Only fuels produced following EN15359 [2] may be called "SRF". SRF is sampled and tested according to EU standards. In the assessment of SRF as an alternative fuel in the cement industry, the following properties were determined:
-   – morphological composition – CEN/TS 15415:2006 [3];

- – chlorine content (Cl) – EN 15408:2011 [4];
- – mercury content (Hg) – EN 16175-1:2016 [5];
- – calorific value (CV) – EN 15400:2011 [6];

– XRD analysis was carried out on BRUKER D8 ADVANCE diffractometer with CuKα radiation at 40 kV in 2Θ (5º÷70º) interval at scanning step 0.02º;

RESULTS

The research area was the production of SRF from refused-derived fuel (RDF) obtained from Lithuania's mechanical-biological treatment (MBT) plants and the study of its properties. At the Kaunas, the MBT plant determined the morphological composition of the material under study (Table 1, Fig. 1).
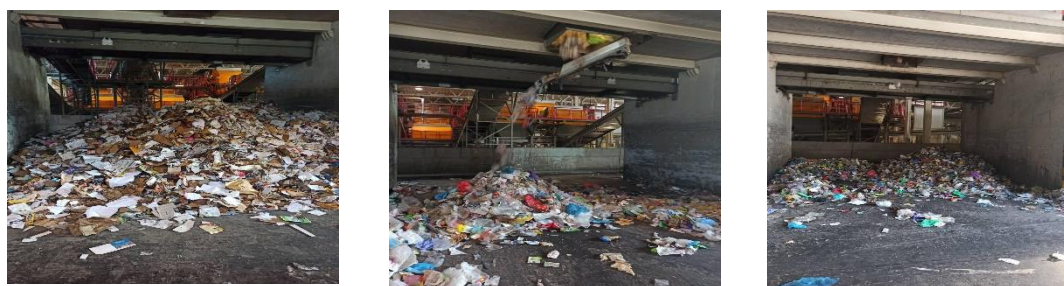
| After the first part of the separation (paper) | After the second part of separation (soft plastic) | After the third part of separation (hard plastic) |

Fig. 1. Morphological composition of RDF

Waste from the Kaunas MBT was taken for the study, with a similar morphological composition as the waste sent for incineration at the cogeneration power plant. From the materials obtained for the study, glass, metals and prohibited materials (chlorine- and mercury-containing) were extracted. In order to use the waste with maximum efficiency, it was proposed to investigate the use of non-recyclable waste fractions as an alternative fuel in the clinker firing. SRF composition was obtained after several technological stages: extraction of prohibited and inert materials, shredding and drying. After that, the prepared SRF was burned in a muffle furnace at a temperature of 950 °C for one hour and ash was obtained for research. The main characteristics of SRF are summarized in Table 1.

Table 1. Characteristics of RDF and SRF

Fraction	Value average, %	
	RDF	SRF
Plastics (PET, PE, HDPE, LDPE, PP, PS)	20.8	19.3
Paper	36.9	31.365
Textile	36.4	30.94
Glass	1.7	
Metal	3.7	
Wood	0.5	0.425
Total	**100**	**82.03**
		Value average, %	Standard values, %
Chlorine content, %	–	0.53	≤ 3 – ≤ 0.2
Mercury content, mg/kg^{-1}	–	0.02	≤ 0.5 – ≤ 0.02
Net calorific value, kcal/kg	–	5294	5971 – 717

Based on the data presented in table 1, it can be said that the prepared SRF belong to the second class in terms of the main classification characteristics [2] and can compete with solid fuel (coal), which cement enterprises currently use.

Table 2 shows the results of the XRD-Rietveld analysis. The Rietveld analysis was used to refine crystal structures ash of SRF. Fig. 2 shows XRD analysis of ash obtained after incineration of SRF.

Table 2. XRD-Rietveld analysis of ash, obtained after incineration of SRF

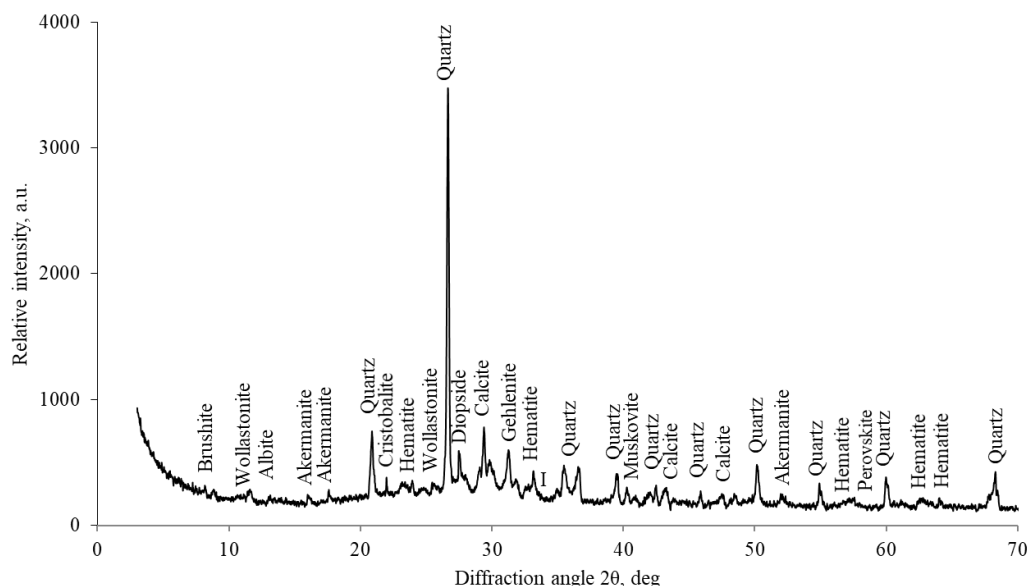| Minerals	Amount, %	Minerals	Amount, %
Quartz (SiO_2)	28.44	Muscovite ($KAl_2(AlSi_3O_{10})$)	3.0
Hematite (Fe_2O_3)	1.42	Albite ($Na(AlSi_3O_8)$)	6.89
Diopside ($CaMg(Si_2O_6)$)	4.87	Brushite ($CaPO_3(OH)2H_2O$)	2.17
Cristobalite (SiO_2)	7.07	Perovskite ($CaTiO_3$)	1.01
Gehlenite ($Ca_2Al(AlSiO_7)$)	2.05	Calcite ($CaCO_3$)	5.78
Akermanite ($Ca_2Mg(Si_2O_7)$)	5.19	Wollastonite ($CaSiO_3$)	5.06

Fig. 2 XRD analysis of ash obtained after incineration of SRF

The XRD-Rietveld analysis shows that the ash of SRF contains crystalline phases. The presence of the crystalline phase is favourable in clinker production since the chemical activity of clinker minerals in relation to water depends on their crystal structure. Therefore, SRF can use as an alternative fuel during the clinker firing because fuel from waste is an alternative to solid fuels, and as a result, we get ready-made clinker, reduce the consumption of natural resources and approach the goals of the circular economy.

CONCLUSIONS

This study investigated the composition and properties of SRF produced from RDF and the possibility of using SRF as an alternative fuel in the cement industry. The characteristics of the SRF have been defined and compared to the European standard. According [2], produced

SRF refers to the second class by classification characteristic: NCV=5294 kcal/kg, Cl=0.53 % and Hg=0.02 mg/kg^{-1}. It has been experimentally proven that the ash obtained after incineration of SRF has crystalline phases and consists of clinker-forming minerals.

Keywords: SRF, RDF, alternative fuel, characteristics, crystalline phases, clinker-forming minerals.

REFERENCES

1. Communication from the commission to the European parliament, the council, the European economic and social committee and the committee of the regions. The role of waste-to-energy in the circular economy. Brussels, 26.1.2017 COM, 34. Link to the internet: <https://eur-lex.europa.eu/legal-content/EN/TXT/PDF/?uri=CELEX:52017DC0034>

2. EN 15359:2011. Solid recovered fuels. Specifications and classes.

3. CEN/TS 15415:2006.Solid recovered fuels. Determination of particle size distribution by screen method.

4. EN 15408:2011. Solid recovered fuels. Methods for the determination of sulphur (S), chlorine (Cl), fluorine (F) and bromine (Br) content

5. EN 16175-1:2016. Solid recovered fuels. Sludge, treated bio-waste and soil - Determination of mercury. Part 1: Cold-vapour atomic absorption spectrometry (CV-AAS)

6. EN 15400:2011. Solid recovered fuels. Determination of calorific value.

ASSESSMENT OF THE THERMAL PROPERTIES FOR SURFACE GEOTHERMAL UTILIZATION OF A PERMEABLE PAVEMENT STRUCTURE FOR PEDESTRIAN AND CYCLE PATHS

C. Rey-Mahía, F.P. Álvarez-Rabanal, L.A. Sañudo-Fontaneda
INDUROT Research Institute, GICONSIME Research Group, Department of Construction and Manufacturing Engineering, University of Oviedo.
Campus of Mieres, Gonzalo Gutierrez Quiros s/n, 33600 Mieres – Spain
UO236881@uniovi.es

EXTENDED ABSTRACT

Global energy demand has increased over the last decades, with cities around the world being the main consumers of energy. In fact, EU cities consume between 60-80% of the total energy produced, which is directly related to the 72.6% of the EU population living in urban areas [1]. This figure is expected to grow in the following years [2]. Thus, this scenario not only contributes towards the energy problem but also in posing other challenges, such as the disruption of the natural water cycle due to the waterproofing of large urban areas [3]. Multifunctional surfaces and structures in urban environments designed in combination with energy techniques have been identified as potential means to alleviate the aforementioned issues whilst minimizing the hydrological impact in urban catchments [4]. Charlesworth et al. [5] gathered numerous studies about the potential thermal use of permeable pavement systems (PPS) in their review study, concluding that the design of Sustainable Drainage Systems (SuDS) together with horizontal geothermal techniques produced promising results, paving the way towards a new line of research. In addition, other studies, such as Rey-Mahía et al. 2019 outlined the need to further investigate heat transmission processes taking place in SuDS, focusing on the materials utilized in the varying layers of their structures [3].

The research presented in this paper aims to continue this line of investigation by assessing the thermal properties associated with several types of materials utilized as sub-base and base layers in PPS. For this purpose, a series of tests were carried out in the laboratory using a climatic chamber and a calibrated hot box, equipment included in the ISO 8990 [6] and the ASTM C1363 [7] standards. These tests can be used to analyse the thermal performance of permeable pavements. Thus, the experiment consisted of subjecting the cross-section of a PPS for pedestrian and cycle paths to a stabilized heat flow. The test began at 20ºC until reaching a temperature higher than 50ºC, maintaining this value until stabilization. The tests were carried out with the PPS under dry, wet and saturated conditions. In saturated conditions, the section is completely filled with water. In wet conditions, the excess is removed, leaving the remains after saturating the section.

Values of temperature and thermal flux were collected in the laboratory tests over the duration of the experiments. As a consequence, it was possible to calculate the value of the thermal transmittance of the studied structure according to standards based on the data collected. Finally, a value of 0.88 W/m^2K was reached under dry conditions, 2.44 W/m^2K for the wet test and 4.45 W/m^2K under the saturated test.

This research presents the thermal performance of materials utilized in the cross-section of PPS under different hydrological scenarios by using a standardized equipment. With the results obtained in the tests, better thermal behaviour in dry conditions has been verified, with heat transfer being three times less than in wet conditions and 6 times less than in saturated conditions. In addition, these experimental data can be used for numerical simulations to optimise the thermal design of the PPS. This will help to improve the thermal performance of surface geothermal systems in combination with PPS, also allowing the study of the inclusion of new materials.

The results obtained help strengthen the knowledge in this new research area, allowing further investigations into the thermal behaviour of PPS and other SuDS in order to optimize their design in combination with heat pump elements. In this way, it will be possible to design PPS with a more efficient cross-section for geothermal use. Thus covering the next research steps set out by other authors [3, 5].

Keywords: Pervious paving systems, Hot-Box test, Ground Source Heat Pumps (GSHP), Sustainable Drainage Systems (SuDS), energy-water nexus, Green Infrastructure (GI), Nature-Based Solutions (NBS).

ACKNOWLEDGEMENTS:

REFERENCES

1. HUNTER, G.; VETTORATO, D.; SAGOE, G. Creating Smart Energy Cities for Sustainability through Project Implementation: A Case Study of Bolzano, Italy. *Sustainability* 2018, Vol. 10, No. 7, P. 2167. https://doi.org/10.3390/su10072167.

2. UNITED NATIONS. *The Millennium Development Goals Report.* United Nation: New York, USA 2015. ISBN 978-92-1-101320-7.

3. REY-MAHÍA, C.; SAÑUDO-FONTANEDA, L.A.; ANDRÉS-VALERI, V.C.; ÁLVAREZ-RABANAL, F.P.; COUPE, S.J.; ROCES-GARCÍA, J. Evaluating the Thermal Performance of Wet Swales Housing Ground Source Heat Pump Elements through Laboratory Modelling. *Sustainability* 2019, Vol. 11, No. 11, P. 3118. <https://doi.org/10.3390/su11113118>.

4. FARAJ-LLOYD, A.; CHARLESWORTH, S.M.; COUPE, S.J. Sustainable Drainage Systems and Energy: Generation and Reduction. *Sustainable Surface Water Management,* 2017; P. 177–192. <https://doi.org/10.1002/9781118897690.ch13>.

5. CHARLESWORTH, S.M.; FARAJ-LLYOD, A.S.; COUPE, S.J. Renewable Energy Combined with Sustainable Drainage: Ground Source Heat and Pervious Paving. *Renewable and Sustainable Energy Reviews,* 2017. Vol. 68, P. 912–919. <https://doi.org/10.1016/j.rser.2016.02.019>.

6. ISO 8990-1994. Thermal insulation. Determination of steady-state thermal transmission properties. Calibrated and guarded hot box.

7. ASTM C1363 - 19. Standard Test Method for Thermal Performance of Building Materials and Envelope Assemblies by Means of a Hot Box Apparatus.

ANALYSIS OF THE EFFECT OF THE ENERGY STORAGE UNIT ON THE PERFORMANCE OF THE SOLAR CHIMNEY POWER PLANT WITH DIVERGENT CHIMNEY DESIGN THROUGH THE MANZANARES PILOT PLANT

E. CUCE

Department of Mechanical Engineering, Faculty of Engineering and Architecture, Recep Tayyip Erdogan University, Zihni Derin Campus, 53100 Rize – Turkey
erdemcuce@gmail.com

P. M. CUCE

Department of Architecture, Faculty of Engineering and Architecture, Recep Tayyip Erdogan University, Zihni Derin Campus, 53100 Rize – Turkey
mertcuce@gmail.com

H. SEN

Department of Mechanical Engineering, Faculty of Engineering and Architecture, Recep Tayyip Erdogan University, Zihni Derin Campus, 53100 Rize – Turkey
harun.sen6169@gmail.com

EXTENDED ABSTRACT

OVERVIEW

The increasing use of fossil fuels for the increasing energy demand in the world in the last century has caused serious environmental pollution. One of the energy sources needed to correct this situation is the sun. It is a renewable energy source that can be an alternative to fossil fuels in terms of solar potential. The sun, which has different uses, has had an important place in human life since ancient times. In recent years, the usage areas of solar energy have been increasing, and researchers have been carrying out intensive studies on this subject. It is seen that researchers use solar energy effectively, except for indoor heating and water heating purposes only with traditional methods. Some of these are solar cookers, fruit dryers and natural ventilation [1-3]. In these methods, it is mainly used in the form of absorption of solar radiation. Unlike these purposes, solar energy can be used to produce electricity directly or indirectly. Electricity generation with direct solar energy is PV systems that have been very popular in recent years. PV systems are solar energy systems that directly convert the solar radiation falling on them into electrical energy with the special materials in their structure [4]. Systems that indirectly convert solar energy into electrical energy are different from PV systems. These systems transfer solar energy to the air in their structures. This increases the kinetic energy of the air in the system. The kinetic energy of the air is converted into electrical energy by means of a turbine [5-6]. Solar chimney power plants are one of the solar energy systems that work in this way. These systems, which consist of 3 structural elements, turbine, collector and chimney, have attracted the attention of researchers in recent years with their simple structures [7]. Solar radiation reaches the ground

through the semi-transparent collector. In the meantime, some of the solar energy is absorbed by the system air. The rest causes an increase in temperature on the ground. The increase in the energy of the system air leads to an increase in its velocity. It is the only outlet of the air with high chimney velocity placed in the collector centre. Therefore, the system air is discharged from the chimney. Meanwhile, the air hitting the turbine, which is at a certain height in the chimney, generates electricity. Although it was first introduced a long time ago, the first application of solar chimney power plants was in the 1980s. The Manzanares facility established in Spain is considered the first application in this field. The system, which has a chimney height of 194.6 m, has a collector in a radius of 122 m [8]. In the first experimental studies on the system, it is seen that it gives a power output of about 50 kW at noon in the summer months [9]. Solar chimney power plants attract great attention after the first application. The reason for this is the pressure difference created by the high chimney in its structure [10]. With this pressure difference, the possibility of generating electricity during the hours when the sun is not present makes the system very attractive. Initial studies after the Manzanares pilot plant mostly focus on power output and efficiency depending on the geometric parameters of the system. However, it is shown by researchers that design changes have significant effects on the system in later periods. It is aimed to increase the performance of the system with the integration of different energy sources and hybrid systems. The geometric and design parameters affecting the performance of the system are given in Table 1.

Table 1. The geometric and design parameters affect the performance of the system.

References	Effects of geometric and climatic parameters	References	Design effects
[11-13]	Since the chimney is the driving force of the system, the increase in the height of the chimney directly increases the performance of the system.	[16-17]	Floor design and slope affect the performance of the system. The rise of the ground towards the chimney for the pilot plant causes a 17% increase in the performance of the system.
[14,6]	Collector size affects the amount of energy entering the system. Therefore, increasing the collector radius improves the performance of the system. However, after a certain point, enlarging the collector does not affect the performance of the system.	[18-19]	The collector slope improves the performance of the system to a certain extent. However, after a certain point, it affects the system negatively.
[7,15]	Environmental temperature and solar radiation intensity have a determining effect on the performance of the system. The solar radiation intensity increases the power output of the system linearly.	[19-21]	The divergent flue design doubles the performance of the system compared to the reference situation (for the Pilot plant). Increasing the chimney inclination angle after a point has a negative effect on the

References	Energy storage	References	Hybrid systems
			performance of the system.
[22-23]	By using different soil and material types on the ground, energy can be stored here during the day, and power output can be obtained even when the sun is not present.	[26-27]	A hybrid system is created with PV modules to be integrated into different parts of the system. In this way, additional power output is obtained from the PV system while the power output is taken from the system. In addition, the PV system works more efficiently with the cooling effect of the air-fluid.
[24-25]	The use of additional water for energy storage on the ground reduces power output during sun hours. However, it provides power output during the hours when there is no sun, thus providing more total power output in the 24-hour period.	[28-30]	Some researchers create a hybrid system to obtain clean water and desalinate seawater. It is stated that while obtaining clean water from the system, an increase in performance is also observed.

By integrating other systems into solar chimney power plants, their performance can be increased. Researchers try to increase the performance of the system by creating hybrid systems with methods such as ground energy storage, using geothermal energy sources, heat exchanger integration, and adding PV. Some examples of energy storage integrated and hybrid systems are given in Table 2.

Table 2. The geometric and design parameters affect the performance of the system.

Although there are many studies on solar chimney power plants, some points are open to improvement. Especially unlike other solar energy systems, the fact that it allows power output during the hours when the sun is not present makes these systems privileged. In this study, this feature is emphasized by using natural materials as an energy storage unit. In addition, a new design is created by using the divergent flue design that improves the power output instead of the standard cylindrical chimney. Performance evaluation of a system with a divergent chimney with an energy storage unit is presented.

METHODS

This study is based on the geometric dimensions of the Manzanares pilot plant. Geometric data of the pilot plant are given in Table 3. The chimney outlet radius is taken as 10.16 m while the work is being carried out. The reason for this is that the maximum power output range in divergent chimney design from previous studies is 3.5-5 AR [21]. The AR expression expresses the ratio of the chimney outlet area to the chimney entrance area. In this study, the AR value is taken as 4. In addition, experimental measurements show that the temperature value remains almost constant throughout the day from 0.5 m below the ground

[9]. For this reason, a floor thickness of 2 m is considered sufficient. The engineering commercial software ANSYS is used for the study. The schema, 3D view and mesh image of the model are given in Figure 1.

Table 3. Geometric data and working dimension details of the Manzanares pilot plant [8].

Geometric parameter	Value
Chimney height	194.6 m
Chimney inlet radius	5.08 m
Chimney outlet radius	10.16 m
Collector radius	122 m
Average collector height	1.85 m
Energy storage unit thickness	2 m

During the analysis, the flow is considered to be continuous and constant. It is assumed that environmental conditions do not change in each analysis. Conservation equations are solved simultaneously, and each equation can be given as:

- Continuity equation

$$\frac{\partial(\rho u)}{\partial x} + \frac{\partial(\rho v)}{\partial y} + \frac{\partial(\partial w)}{\partial z} = 0. \tag{1}$$

- Momentum equation

$$\frac{\partial(\rho uu)}{\partial x} + \frac{\partial(\rho uv)}{\partial y} + \frac{\partial(\rho uw)}{\partial z} = \frac{-\partial p}{\partial x} + \mu\left(\frac{\partial^2 u}{\partial x^2} + \frac{\partial^2 u}{\partial y^2} + \frac{\partial^2 u}{\partial z^2}\right); \tag{2}$$

$$\frac{\partial(\rho vu)}{\partial x} + \frac{\partial(\rho vv)}{\partial y} + \frac{\partial(\rho vw)}{\partial z} = \frac{-\partial p}{\partial y} + \mu\left(\frac{\partial^2 v}{\partial x^2} + \frac{\partial^2 v}{\partial y^2} + \frac{\partial^2 v}{\partial z^2}\right); \tag{3}$$

$$\frac{\partial(\rho wu)}{\partial x} + \frac{\partial(\rho wv)}{\partial y} + \frac{\partial(\rho ww)}{\partial z} = \frac{-\partial p}{\partial z} + \mu\left(\frac{\partial^2 w}{\partial x^2} + \frac{\partial^2 w}{\partial y^2} + \frac{\partial^2 w}{\partial z^2}\right) + \rho g\beta(T - T_a); \tag{4}$$

- Energy equation

$$\frac{\partial(pcuT)}{\partial x} + \frac{\partial(pcvT)}{\partial y} + \frac{\partial(pcwT)}{\partial z} = \lambda\left(\frac{\partial^2 T}{\partial x^2} + \frac{\partial^2 T}{\partial y^2} + \frac{\partial^2 T}{\partial z^2}\right). \tag{5}$$

The boundary conditions of the system are given in Figure 1. The flow regime is considered turbulent [21]. The bossiness approximation is used for density. The convergence criterion is taken as 10^{-6}.
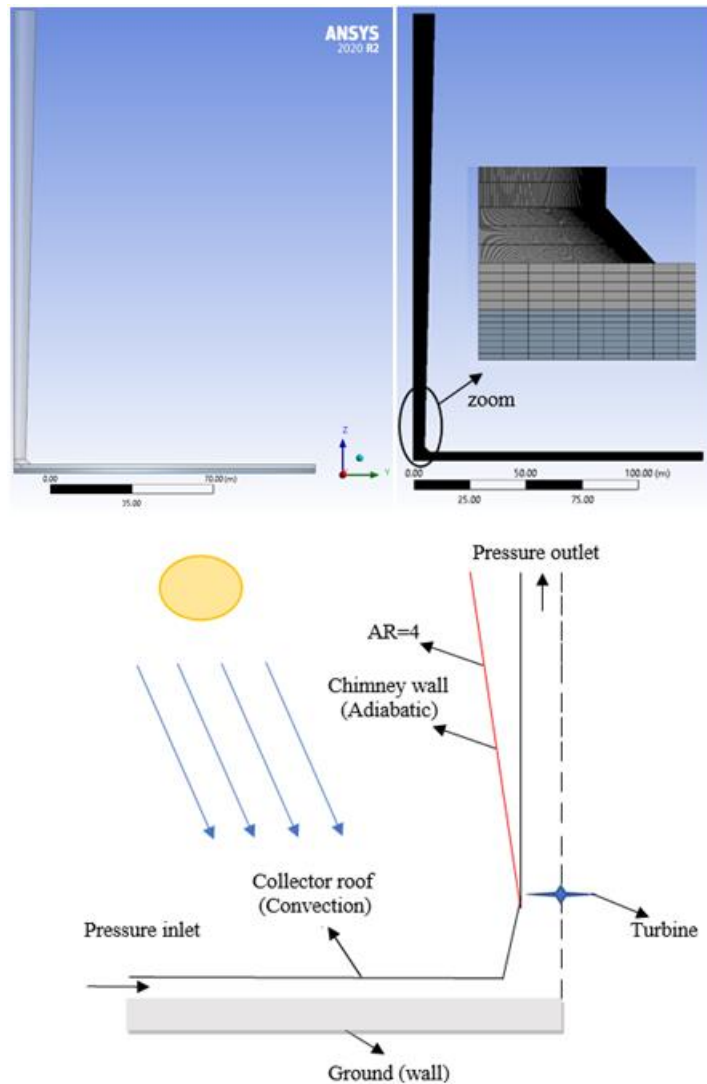
Fig. 1. Solar chimney power plant model and boundary conditions, 3D
visual and mesh view.

RESULTS

Before starting the analysis, a mesh-independent solution is made for the model. For the accuracy of the model, experimental data from the pilot plant is taken as a reference. It has been shown in the previous study that the divergent chimney design gives more power output than the cylindrical chimney [21]. In the study, in addition to the divergent chimney design, the possibility of the system to give power output is interpreted by using an energy storage unit during the hours when there is no sun.

CONCLUSIONS

Solar chimney power plants differ from other solar energy systems in terms of their dependence on the sun. This study highlights the importance of energy storage in the ground, in addition to the fact that the divergent flue design improves the performance of the system.

Keywords: Energy storage, divergent solar chimney power plants.

REFERENCES

1. CUCE, E.; CUCE, P.M. A comprehensive review on solar cookers. *Applied Energy*, 2013, Vol. 102, p. 1399-1421.

2. FERREIRA, A.G.; MAIA, C.B.; CORTEZ, M.F.; VALLE, R.M. Technical feasibility assessment of a solar chimney for food drying. *Solar Energy*, 2008, Vol. 82, No. 3, p. 198-205.

3. KONG, J.; NIU, J.; LEI, C. A CFD based approach for determining the optimum inclination angle of a roof-top solar chimney for building ventilation. *Solar Energy*, 2020, Vol. 198, p. 555-569.

4. CUCE, E.; CUCE, P.M. Optimised performance of a thermally resistive PV glazing technology: An experimental validation. *Energy Reports*, 2019, Vol. 5, p. 1185-1195.

5. CUCE, P.M.; SEN, H.; CUCE, E. Impact of Tower Diameter on Power Output in Solar Chimney Power Plants. *Gazi Mühendislik Bilimleri Dergisi*, 2021, Vol. 7 No.3, p. 253-263.

6. SEN, H.; CUCE, P.M.; CUCE, E. Impacts of Collector Radius and Height on Performance Parameters of Solar Chimney Power Plants: A Case Study for Manzanares, Spain. *Science and Engineering*, 2021, Vol. 2, No. 2, p. 83-104.s

7. CUCE, E.; CUCE, P.M.; SEN, H. A thorough performance assessment of solar chimney power plants: Case study for Manzanares. *Cleaner Engineering and Technology*, 2020, Vol. 1, 100026.

8. SCHLAICH, J.R.; BERGERMANN, R.; SCHIEL, W.; WEINREBE, G. Design of commercial solar updraft tower systems—utilization of solar induced convective flows for power generation. *Journal of Solar Energy Engineering*, 2005, Vol. 127, No. 1, p.117-124.

9. HAAF, W. Solar chimneys: part ii: preliminary test results from the Manzanares pilot plant. *International Journal of Sustainable Energy*, 1984, Vol. 2, No. 2, p. 141-161.

10. SEN, H.; CUCE, E. Dynamic pressure distributions in solar chimney power plants: A numerical research for the pilot plant in Manzanares, Spain. *WSSET Newsletter*, 2020, Vol. 12, No. 1, p. 2-2.

11. ZHOU, X.; YANG, J.; XIAO, B.; HOU, G.; XING, F. Analysis of chimney height for solar chimney power plant. *Applied Thermal Engineering*, 2009, Vol. 29, No.1, p. 178-185.

12. TOGHRAIE, D.; KARAMI, A.; AFRAND, M.; KARIMIPOUR, A. Effects of geometric parameters on the performance of solar chimney power plants. *Energy*, 2018, Vol.162, p. 1052-1061.

13. CUCE, E.; SEN, H.; CUCE, P.M. Numerical performance modelling of solar chimney power plants: Influence of chimney height for a pilot plant in Manzanares, Spain. *Sustainable Energy Technologies and Assessments*, 2020, Vol. 39, 100704.

14. LI, J.Y.; GUO, P.H.; WANG, Y. Effects of collector radius and chimney height on power output of a solar chimney power plant with turbines. *Renewable Energy*, 2012, Vol. 47, p. 21-28.

15. TAYEBI, T.; DJEZZAR, M.; GOUIDMI, H. 3D numerical study of flow in a solar chimney power plant system. Sciences & Technology, 2018, Vol. 3 No. 1, p. 17-20

16. CUCE, E.; CUCE, P.M.; SEN, H.; SUDHAKAR, K.; BERARDI, U.; SERENCAM, U. Impacts of Ground Slope on Main Performance Figures of Solar Chimney Power Plants: A Comprehensive CFD Research with Experimental Validation. *International Journal of Photoenergy*, 2021.

17. CUCE, P.M.; CUCE, E.; SEN, H. Improving electricity production in solar chimney power plants with sloping ground design: an extensive CFD research. *Journal of Solar Energy Research Updates*, 2020, Vol. 7, No. 1, p. 122-131.

18. COTTAM, P.J.; DUFFOUR, P.; LINDSTRAND, P.; FROMME, P. Effect of canopy profile on solar thermal chimney performance. *Solar Energy*, 2016, Vol. 129, p. 286-296.

19. HASSAN, A.; ALI, M.; WAQAS, A. Numerical investigation on performance of solar chimney power plant by varying collector slope and chimney diverging angle. *Energy*, 2018, Vol. 142, p. 411-425.

20. HU, S.; LEUNG, D.Y.; CHEN, M.Z. Effect of divergent chimneys on the performance of a solar chimney power plant. *Energy Procedia*, 2017, Vol. 105, p. 7-13.

21. CUCE, E.; SAXENA, A.; CUCE, P.M.; SEN, H.; GUO, S.; SUDHAKAR, K. Performance assessment of solar chimney power plants with the impacts of divergent and convergent chimney geometry. *International Journal of Low-Carbon Technologies*, 2021.

22. GUO, P.; WANG, Y.; LI, J.; WANG, Y. Thermodynamic analysis of a solar chimney power plant system with soil heat storage. *Applied Thermal Engineering*, 2016, Vol. 100, p. 1076-1084.

23. PRETORIUS, J.P.; KRÖGER, D.G. Critical evaluation of solar chimney power plant performance. *Solar Energy*, 2006, Vol. 80, No. 5, p. 535-544.

24. SEMAI, H.; BOUHDJAR, A.; LARBO, S. Canopy slope effect on the performance of the solar chimney power plant. *International Journal of Green Energy*, 2017, Vol. 14, No. 3, p. 229-238.

25. CHOI, Y.J.; KAM, D.H.; PARK, Y.W.; JEONG, Y.H. Development of analytical model for solar chimney power plant with and without water storage system. *Energy*, 2016, Vol. 112, p. 200-207.

26. SINGH, A.P.; KUMAR, A.; SINGH, O.P. Performance enhancement strategies of a hybrid solar chimney power plant integrated with photovoltaic panel. *Energy Conversion and Management*, 2020, Vol. 218, 113020.

27. RAHBAR, K.; RIASI, A. Performance enhancement and optimization of solar chimney power plant integrated with transparent photovoltaic cells and desalination method. *Sustainable Cities and Society*, 2019 , Vol. 46, 101441.

28. ZHOU, X.; XIAO, B.; LIU, W.; GUO, X.; YANG, J.; FAN, J. Comparison of classical solar chimney power system and combined solar chimney system for power generation and seawater desalination. *Desalination*, 2010, Vol. 250, No. 1, p. 249-256.

29. MING, T.; GONG, T.; de RICHTER, R.K.; CAI, C.; SHERIF, S.A. Numerical analysis of seawater desalination based on a solar chimney power plant. *Applied Energy*, 2017, Vol. 208, p. 1258-1273.

30. MENDEZ, C.; BICER, Y. Integration of solar chimney with desalination for sustainable water production: A thermodynamic assessment. *Case Studies in Thermal Engineering*, 2020, Vol. 21, 100687.

I.2. Bioenergy, Biomass and biofuels

INVESTIGATION OF MUGWORT (*ARTEMISIA DUBIA WALL.*)

A. Bakšinskaitė, V. Tilvikienė
Lithuanian Research Centre for Agriculture and Forestry
Instituto al. 1, LT-58344 Akademija, Kėdainiai distr. – Lithuania
+37061604881
ausra.baksinskaite@lammc.lt

EXTENDED ABSTRACT

OVERVIEW

In 2019, European Commission launched the new Green Deal strategy with the very ambitious goals for the E.U. to become the first climate-neutral continent by 2050. Many sectors have to be changed and adopted by increasing the sustainability of the use of resources. For the agricultural sector, one of the main challenges will be to reduce the use of synthetic fertilizers and pesticides. In this paper, we are focussing on the possibility to change chemical pesticides with natural ones. The pesticides used can help crop plants protect themselves against various diseases or pests, but they are also harmful to the environment.

Plant protection plays a key role in increasing crop production [1]. Crop protection measures aim to maintain and ensure certain standards of yield and quality, which are generally achieved by the control of pests, diseases, and weeds [2]. There are two options: using chemical pesticides, which are very effective or focusing on bio pesticides. Ecological crop protection involves biological methods based on specific microorganisms or natural compounds derived from plants [3]. Biological pesticides are derived from plants belonging to different families. They can be used as plant extracts or essential oils extracted from different parts of the plant (bark, leaves, roots, fruits, seeds, flowers, etc.) The parts of the plant are selected from the active compounds and their abundance in a specific part [4].

One of the ways to reduce pesticide use could be the introduction of allopathic plants, which are not only potential sources of allele chemicals but also renewable biomass to cropping systems. It is expected that one of the potential crops could be *Artemisia dubia.* The genus Artemisia belongs to the Asteraceae family and includes more than 500 species, and they are widespread in various regions of the world [5]. Plants of this genus are mostly used in medicine but are increasingly being immersed in their essential oils, which may have a pesticide effect. One such plant with a strong odour is the perennial mugwort (*Artemisia dubia WALL*). Mugwort has antimicrobial, insecticidal [6], phytochemical and antioxidant properties [5, 7, 8]. Plants of the Asteraceae family are extremely rich in a source of biologically active compounds such as polyphenols, terpenes, and flavonoids. It is expected that allelopathic plants such as mugwort could be widely used in sustainable and organic agriculture because of their potential role not only in controlling weeds and pests but also in promoting crop growth [9], but there is little information about their growth potential, chemical composition and effect on plants and the soil.

The study aimed to analyse mugwort productivity data and evaluate the chemical composition of biomass in different growing conditions.

METHODS

Field and laboratory experiments of Mugwort (*Artemisia dubia WALL*) were performed at the Institute of Agriculture, LAMMC, Kėdainiai distr., Akademija (55 ° 23′50 ″ N, 23 ° 51′40 ″ E), department of Plant nutrition and agroecology and laboratory of Agrobiology.

The field experiment was performed in the already established experiment "Mugwort biomass formation", which was started in 2016. The experiment included 9 different mugwort cultivation technology treatments, the fields were 14 m long and 3 m wide, with IV replicates.

Biomass harvesting of mugwort was performed once, twice, and three times per vegetation season. The amount of biomass was immediately weighed and recorded. After cutting, one sample was weighed and placed in an oven at 105 ° C for 24 hours. A second sample was prepared for chemical composition analysis. Mugwort biomass was determined for carbon and nitrogen content using CHNS-O (ECS 4010 Elemental Combustion System) elemental analyser, dry matter content, and mineral content by analysis with inductively coupled plasma-mass spectrometry (ICP-MS).

RESULTS

After analysing the productivity of mugwort for several years, it can be stated that plants were the most productive in the second growing year (the first year was used for crop establishment, and the yield was not measured). The results show a decrease in yield each year. The highest biomass (18.15 ± 1.78 t ha^{-1}) grown was obtained in plots fertilized with 180 kg ha^{-1} of nitrogen. This yield was obtained in the first harvesting year, while later biomass weight was lowered by 14.27 % every year. Comparing the result with the research by Kryževičienė et al., it can be stated that the yield in our experiments was higher, 22.86 % [7].

According to the results of the research, the total carbon content in biomass ranges from 43.47% to 46.94%. The maximum potency of the total nitrogen content (2.62%) was obtained when performing one harvest during the vegetation and fertilizing at the maximum rate of fertilizer.

A mineral content study was performed to determine which crop biomass is richer in nutrients. Analyses were performed on selected mugwort harvested at different times. The results show that during the October harvest, plants accumulate the most sodium (21.87 mg/kg), potassium (1517.79 mg/kg), and calcium (6031.41 mg kg) compared to other harvests. Compared to other researchers [10], the amount of minerals was lower several times. However, boron (32.47 mg/kg) is accumulated most in July and phosphorus (1470.88 mg/kg) in June.

CONCLUSIONS

The increasing demand for environmentally friendly solutions forces us to look for biological products in crop management systems. One agricultural crop - Mugwort, has the potential as a natural pesticide, but there is a lack of information about it. It is therefore important to evaluate the potential plant used as a bio pesticide. The first results of the

experiments suggest that by harvesting mugwort biomass in the autumn, the highest yield is obtained. However, in the analysis of plant chemical composition, it can be stated that after harvesting in July, the mugwort biomass was richer in nutrition and biologically active substances.

Keywords: Mugwort, biomass, productivity, chemical content

REFERENCES

1. RÖMER, U.; SCHAAK, H.; MUßHOFF, O. The perception of crop protection: Explicit vs. implicit association of the public and in agriculture. *Journal of Environmental Psychology,* 2019, Vol. 66, P. 101-346.

2. ARIAS-ESTÉVEZ, M.; LÓPEZ-PERIAGO, E.; MARTÍNEZ-CARBALLO, E.; SIMAL-GÁNDARA, J.; MEJUTO, J.C.; GARCÍA-RÍO, L. The mobility and degradation of pesticides in soils and the pollution of groundwater resources. *Agriculture, Ecosystems & Environment*. 2008, Vol. 123, P. 247–260.

3. WACHOWSKA, U.; TAŃSKA, M.; KONOPKA, I. Variations in grain lipophilic phytochemicals, proteins and resistance to Fusarium spp. growth during grain storage as affected by biological plant protection with Aureobasidium pullulans (de Bary). *International Journal of Food Microbiology*. 2016, Vol. 227, P. 34–40.

4. LENGAI, G.M.W.; MUTHOMI, J.W.; MBEGA, E.R. Phytochemical activity and role of botanical pesticides in pest management for sustainable agricultural crop production. *Scientific African*, 2020, e00239.

5. POURESMAEIL, M.; NOJADEH, M.S.; MOVAFEGHI, A.; MAGGI, F. Exploring the bio-control efficacy of Artemisia fragrans essential oil on the perennial weed Convolvulus arvensis: Inhibitory effects on the photosynthetic machinery and induction of oxidative stress. *Industrial Crops and Products*. 2020, Vol. 155, 112785.

6. LIANG, J.Y.; G.U.O., S.S.; ZHANG, W.J.; GENG, Z.F.; DENG, Z.W.; D.U., S.S. Fumigant and repellent activities of essential oil extracted from Artemisia dubia and its main compounds against two stored product pests. *Natural Product Research*. [Internet]. 2018, Vol. 34, P. 1234–1238. <https://www.tandfonline.com/doi/full/10.1080/14786419.2017.133127>.

7. KRYŽEVIČIENĖ, A.; ŠARŪNAITĖ, L.; STUKONIS, V.; DABKEVIČIUS, Z.; KADŽIULIENĖ, Ž. Daugiamečių kiečių (Artemisia vulgaris L. ir Artemisia dubia Wall.) potencialo biokuro gamybai įvertinimas. *Žemės ūkio mokslai*. 2010, Vol. 17, P. 32-40.

8. TAHERI MIRGHAED, A.; PAKNEJAD, H.; MIRZARGAR, S.S. Hepatoprotective effects of dietary Artemisia (Artemisia annua) leaf extract on common carp (Cyprinus carpio) exposed to ambient ammonia. *Aquaculture*. 2020.

9. ABRAHAM, A.; PARK, H.; CHOI, O.; SANG, B-I. Anaerobic co-digestion of bioplastics as a sustainable mode of waste management with improved energy production – A review. *Bioresource Technology*. 2021. Available from: <https://linkinghub.elsevier.com/retrieve/pii/S0960852420318113>.

10. ASHRAF, M.; HAYAT, M.Q.; SAMAD MUMTAZ, A. A study on elemental contents of medicinally important species of Artemisia L. (Asteraceae) found in Pakistan. *Journal of Medicinal Plants Research.* [Internet]. 2010, Vol. 4, No. 21, P. 2256–226. Available from: http://www.academicjournals.org/JMPR.

THE ROLE OF BIOMASS AND CARBON CAPTURE IN THE POWER SYSTEM ALIGNED WITH THE EUROPEAN GREEN DEAL

R. Béres, M. van den Broek
University of Groningen
Energy and Sustainability Research Institute Groningen
Nijenborgh 6, 9747 AG Groningen – the Netherlands
+31639424269
r.j.beres@rug.nl

EXTENDED ABSTRACT

OVERVIEW

The E.U. Green New Deal has set a 55% emission reduction target by 2030 (compared to 1990) and carbon neutrality by 2050. Assuming these targets are met in a linear fashion, E.U. energy-related cumulative emissions would reach approximately 53.5 $GtCO_2$ by 2050, using 13% of the global carbon budget (1.5 °C targets with at least 67% likelihood mitigation). This is a significant increase compared to the current 8% E.U. share in global emissions (2020), especially since the European Commission plans to reduce this share [1][2]. Consequently, carbon removal may be required to offset surplus emissions above the carbon budget. This can result in high dependence on carbon removal technologies, such as bioenergy with carbon capture and storage (BECCS), direct air capture (D.A.C.), and afforestation. Energy modelling studies for Europe also show that BECCS and D.A.C. are crucial to reaching net-zero/-negative goals, resulting in 6-13 E.J. biomass demand and 20-170 GW carbon capture and storage (C.C.S.) capacity requirement in the E.U. [3]–[5]. This significant biomass demand can be met without using high sustainability risk biomass [6]. However, upstream emissions or extensive sustainability constraints are not considered, despite the fact that upstream emissions can be 10 - 120 kg CO2eq/G.J. in Europe, and additional sustainability issues emerge when accounting for impacts on soil quality, water use quality/efficiency, biodiversity, competition for land and land use change [7]–[11]. Implementing more comprehensive sustainable biomass standards of the revised Renewable Energy Directive [12] and International Energy Agency [11] reduces availability by 50%-70% and only allows the local use of most biomass types (<500 km radius). Relying on large-scale carbon capture can also be a major risk due to uncertainty and low technology readiness levels [13], [14]. Therefore, it is crucial to tighten sustainability constraints and investigate the role of C.C.S. when modelling the feasibility of large-scale BECCS and D.A.C. implementation since they can have a large effect on the overall power system.

Hence in this study, the effect of various power portfolio options are investigated (including cost-optimized capacity expansion and hourly unit commitment) on the Green Deal and E.U. carbon budget, focusing on 3 critical components of carbon removal:
- Role of bioenergy;
- Sustainable consideration of biomass;
- Role of carbon capture and storage.

The outcomes of this study should reveal the feasibility of E.U. decarbonisation strategies as a function of biomass and C.C.S.

METHODS

This study consists of three main parts: 1. building the E.U. power system model for 2050 generation portfolio optimization; 2. determining carbon removal requirements; 3. constructing biomass availability/sustainability criteria.

MODELLING THE EUROPEAN POWER SYSTEM

The energy model used to optimize the power system, and the role of bioenergy has been constructed in PLEXOS[1]. Within this modelling tool, capacity expansion of technologies as well as hourly unit commitment and economic dispatch (UCED) can be optimized. Spatial resolution is the EU-27, U.K., Switzerland, and Norway grouped into 10 regions in the E.U.: Benelux, Scandinavia, Germany, Iberia, Italy, Central Europe, Baltic, Balkans, France, British Isles as copper plates connected with fixed bidirectional high voltage cross-border transmission lines according to the ENTSOE-E 2027 cross-border expansion strategy [15]. The power system Greenfield capacity expansion for 2050 can choose from a wide range of generators and storage with detailed techno-economic assumptions from PRIMES[2] [16]. Hourly parameters include renewable energy capacity factors (synthesized from ERA-5) and ENSTSO-E power demand for 2050 [15].

CARBON EMISSION CONSTRAINT

The share of EU CO2 emissions compared to global emissions decreases linearly (Fig. 1). Assuming the reduction continues with the same gradient, an average share of 3% is considered for 2020-2050 [2]. Applying this 3% to the global carbon budget of 400 Gt CO2 results in an E.U. carbon budget of 12 $GtCO_2$. The cumulative emissions until 2050 exceed this budget by 42.5 $GtCO_2$. To compensate for these surplus emissions, -0.85 $GtCO_2$ net-negative annual emissions are required from 2050-2100 by the power system.
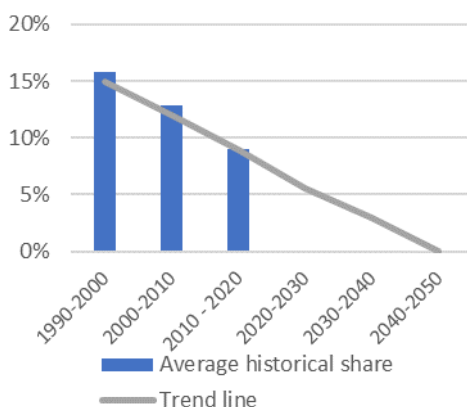

Fig. 1. Share of EU-27 of Global CO_2 emissions

SCENARIOS

---

[1] More information about PLEXOS modeling tool: https://www.energyexemplar.com/plexos
[2] PRIMES is an EU energy system modeling tool by the European Commission: https://e3modelling.com/

The Base scenario includes all generation and storage technologies for 2050 without sustainability considerations for biomass. Additional scenarios exclude biomass or C.C.S. and apply strict RED-II biomass sustainability constraints (Table 1).

Scenarios have free optimization for generators and storage (unless stated otherwise). Fixed properties include transmission network, demand, hydro and geothermal, for the reasons described by van Zuijlen et al. [4]. Solar and wind availability assumptions are adapted from EU-JRC ENSPRESO, with 170 W/m2 average and 3% of the available natural areas for solar, and at least 20% average capacity factor for wind turbine locations [17].

Table 1. Scenarios for 2050 power system (biomass is also used for heat and as feedstock, therefore, only 45% of biomass can be used towards the power system)

Base	Intra-EU trade allowed. Base biomass[1] availability for the power system includes the business as usual E.U. policy and biomass potential[1] for 2050 (3.5 EJ/yr) [17].
No Biomass	Bioenergy capacity is not allowed
No CCS[3]	CCS technologies are not considered, simulating the possibility of C.C.S. stagnating technology readiness level
Strict Biomass	Only strict sustainable biomass used[2] (1.5 EJ/yr) no E.U. trade. Strict biomass availability is in line with E.U. Renewable Energy Directive (RED-II) sustainability criteria, with fossil fuel emission savings of at least 80% after 2026; and with IEA biomass sustainability criteria on land use and competition for land
Strict biomass No CCS[3]	The two above combined

[1]Base biomass potential: Forestry: 2 EJ/yr, Agricultural: 0.4 EJ/yr, Waste: 0.34 EJ/yr, Energy crop: 0.75 EJ/yr
[2]Strict biomass potential: Forestry: 0.8 EJ/yr, Agricultural: 0.16 EJ/yr, Waste: 0.31 EJ/yr, Energy crop: 0.2 EJ/yr
[3]No C.C.S.' excludes all carbon capture technologies if the technology would not reach maturity by 2050. D.A.C.,
 BECCS and C.C.S. for natural gas or coal are excluded

RESULTS

Fig. 2 presents capacity portfolios of the scenarios and the capital costs. A successful decarbonisation strategy of -0.85 Gt CO2 in 2050 fully depends on the availability of C.C.S. Without C.C.S., net-negative cannot be achieved. Therefore, in the 'No C.C.S.' scenarios, a net-zero constraint has been applied. 'No Biomass' scenario has a 35% increase in capital cost requirements due to the increased D.A.C. to meet the emission constraint and increased natural gas capacity to replace the flexibility benefits of BECCS. Strict biomass is not as crucial for the decarbonisation target but has a significant impact on the costs and requires 30% more D.A.C. capacity than 'Base'. Biogas capacity has only been included when C.C.S. is disregarded. It might indicate that carbon capture with natural gas is more cost competitive than zero-emission biogas.
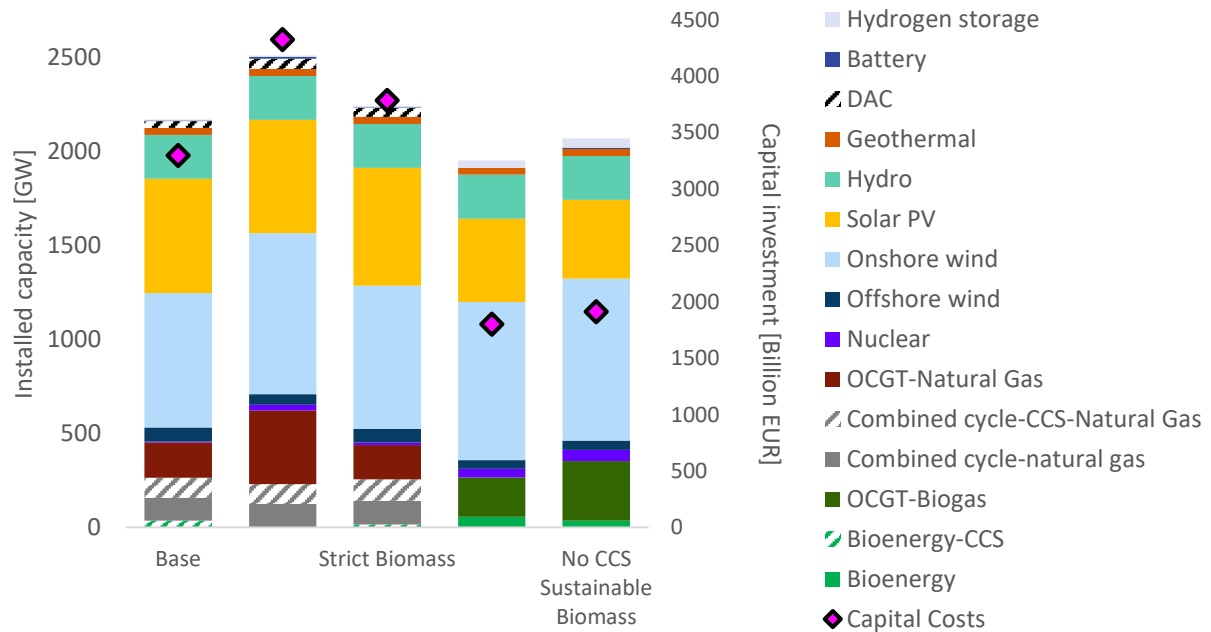
Fig. 2. Preliminary Greenfield capacity expansion results for the E.U., 2050. Bioenergy refers to fluidized bed power plants; OCGT: open cycle gas turbine; capital costs include interest during construction based on an interest of 8% with costs evenly distributed over construction time.

Short-term, hourly resolution simulation results are shown in Table 2. The exclusion of C.C.S. also leads too much more unserved energy (demand that could not be fulfilled) since it then cannot compensate for emissions from flexible power plants. It suggests that flexibility based on biomass is not sufficient to keep the power system reliability as sustainable biomass is limited. Net emissions over the year 2050 exceed the -0.85 $GtCO_2$/year emission limit by 18-51 $GtCO_2$; however, emissions remain net-negative. The exclusion of carbon capture eliminates the possibility of negative emissions. Moreover, zero-emission could not be achieved either without a significant amount of unserved energy: 20% of the demand could not be met. The levelized cost of electricity (Price on Table 2.) has been excluded for 'No C.C.S.' scenarios since the substantial unserved energy increased prices by over 1000 EUR/MWh. Electricity price increases by 37% when biomass is excluded.

Table 2. Short term results

	USE [TWh]	Demand [TWh]	Generation [TWh]	Price [E.U.R./MWh]	Net Emissions [GtCO2]
Base	0.50	4808	4,941	64	-0.34
No Biomass	0.01	4497	4,656	88	-0.67
Strict Biomass	0.47	4,888	5,032	69	-0.54
No CCS	787	3,694	3,845	-	0.00
No C.C.S. Strict Biomass	688	3,794	3,980	-	0.00

USE: Unserved energy (demand that could not be fulfilled), note that 'No C.C.S.' scenarios are set at zero-emission, as negative emission proved to be unfeasible

Keywords: (Bioenergy, C.C.S., D.A.C., linear programming, E.U., Green New Deal, decarbonisation, carbon budget, carbon removal)

REFERENCES

1. *European Comission*, Fit for 55, 2021, [referred on the 23th of August in 2021 y.] Link to the internet: https://ec.europa.eu/clima/citizens/support_en.

2. RITCHIE, H.; ROSER, M. CO₂ and Greenhouse Gas Emissions, *Our World in Data*, [referred on the 24th of August in 2021 y.] Link to the internet: <https://ourworldindata.org/co2-and-other-greenhouse-gas-emissions>.

3. MASSON-DELMOTTE, V.; ZHAI, P.; PÖRTNER, H.O.; ROBERTS, D.; SKEA, J.; SHUKLA, P.R.; PIRANI, A.; MOUFOUMA-OKIA, W.; PÉAN, C.; PIDCOCK, R.; CONNORS, S.; MATTHEWS, J.B.R.; CHEN, Y.; ZHOU, X.; GOMIS, M.I.; LONNOY, E.; MAYCOCK, T.; TIGNOR, M.; WATERFIELD, T. Global warming of 1.5°C An IPCC Special Report on the impacts of global warming of 1.5°C above pre-industrial levels and related global greenhouse gas emission pathways, in the context of strengthening the global response to the threat of climate change, sustainable development, and efforts to eradicate poverty Edited by Science Officer Science Assistant Graphics Officer Working Group I Technical Support Unit. Accessed: the 15th of November, 2020. [Online]. Available :< www.environmentalgraphiti.org>.

4. VAN ZUIJLEN, B.; ZAPPA, W.; TURKENBURG, W.; van der SCHRIER, G.; van den BROEK, M. Cost-optimal reliable power generation in a deep decarbonisation future, *Applied Energy*, 2019, Vol. 253, P. 113587. Doi: 10.1016/j.apenergy.2019.113587.

5. ZAPPA, W.; JUNGINGER, M.; VAN DEN BROEK, M. Is a 100% renewable European power system feasible by 2050?, *Applied Energy*, 2019, Vol. 233–234, P. 1027–1050, Doi: 10.1016/j.apenergy.2018.08.109.

6. ELBERSEN, B.; DALLA LONGA, F.; RUIZ, P.; THIEL, C.; SGOBBI, A.; HENGEVELD, G.; KOBER, T.; NIJS, W.N. The JRC-EU-TIMES model. Bioenergy potentials for E.U. and neighbouring countries, 2015. Doi: 10.2790/39014.

7. CASERINI, S.; LIVIO, S.; GIUGLIANO, M.; GROSSO, M.; RIGAMONTI, L. LCA of domestic and centralized biomass combustion: The case of Lombardy (Italy), *Biomass and Bioenergy*, 2010, Vol. 34, No. 4, P. 474–482. Doi: 10.1016/j.biombioe.2009.12.011.

8. ELBERSEN, B.; FRITSCHE, U.; PETERSEN, J.E.; LESSCHEN, J.P.; BÖTTCHER, H.; OVERMARS, K. Assessing the effect of stricter sustainability criteria on EU biomass crop potential, *Biofuels, Bioprod. Biorefining*, 2013, Vol. 7, No. 2, P. 173–192. Doi: 10.1002/BBB.1396.

9. GONZÁLEZ-GARCÍA, S.; IRIBARREN, D.; SUSMOZAS, A.; DUFOUR, J.; MURPHY, R.J. Life cycle assessment of two alternative bioenergy systems involving Salix spp. biomass: Bioethanol production and power generation, *Applied Energy*, 2012, Vol. 95, P. 111–122. Doi: 10.1016/J.APENERGY.2012.02.022.

10. TONINI, D.; ASTRUP, T. L.C.A. of biomass-based energy systems: A case study for Denmark, *Applied Energy*, 2012, Vol. 99, P. 234–246. Doi: 10.1016/j.apenergy.2012.03.006.

11. *International Energy Agency*. Technology Roadmap: Delivering Sustainable Bioenergy, 2017, Accessed: the 14th of October, 2021. [Online]. Available: <www.iea.org/t&c/>

12. *European Commission*. Directives directive (eu) 2018/2001 of the European Parliament and of the council of the 11th of December 2018 [referred on the 10th of January in 2022 y.] Link to the internet: <https://joint-research-centre.ec.europa.eu/welcome-jec-website/reference-regulatory-framework/renewable-energy-recast-2030-red-ii_en>.

13. *IPCC*. Climate Change 2021 Working Group I contribution to the Sixth Assessment Report of the Intergovernmental Panel on Climate Change Summary for Policymakers, [referred on the 19th of January in 2022 y.] Link to the internet: <https://www.ipcc.ch/report/ar6/wg1/>.

14. KEARNS, D.A.; L.I.U., H.A.; CONSOLI, C.H. Technology readiness and costs of C.C.S. *Global C.C.S. Institute, Brussels*, 2021.

15. *ENTSO-E*. European Power System 2040 - Technical Appendix. [Referred on the 28th of January in 2022 y.] Link to the internet: <https://tyndp.entsoe.eu/tyndp2018/power-system-2040/>.

16. CAPROS, P.; KANNAVOU, M.; EVANGELOPOULOU, S.; PETROPOULOS, A.; SISKOS, P.; TASIOS, T.; ZAZIAS, G.; DEVITA, A. Outlook of the E.U. energy system up to 2050: The case of scenarios prepared for European Commission's "clean energy for all Europeans" package using the PRIMES model, *Energy Strategy. Reviews*, 2018, Vol. 22, P. 255–263. Doi: 10.1016/j.esr.2018.06.009.

17. RUIZ, P.; NIJS, W.; TARVYDAS, D.; SGOBBI, A.; ZUCKER, A.; PILLI, R.; JONSSON, R.; CAMIA, A.; THIEL, C.; HOYER-KLICK, C.; DALLA LONGA, F.; KOBER, T.; BADGER, J.; VOLKER, P.; ELBERSEN, B.S.; BROSOWSKI, A.; THRÄN, D. ENSPRESO - an open, EU-28 wide, transparent and coherent database of wind, solar and biomass energy potentials, *Energy Strategy Reviews*, 2019, Vol. 26, P. 100379. Doi: 10.1016/j.esr.2019.100379.

ORGANIC LOAD RATE INCREASING USING FATTY ORGANIC MATTER IN THE RAW MANURE ANAEROBIC DIGESTION

E. Buivydas, B. Žalys
Lithuanian Energy Institute (LEI)
Breslaujos g. 3, LT-44403 Kaunas – Lithuania
+370 37 351403
Egidijus.Buivydas@lei.lt

K. Navickas, K. Venslauskas, V. Župerka, M. Rubežius
Vytautas Magnus University
K. Donelaičio g. 58, LT-44248 Kaunas – Lithuania

EXTENDED ABSTRACT

OVERVIEW

Since farming manure has been processed in various ways, its harmful effect on the environment is mitigated [1, 2]. However, the food processing industry challenges the food waste utilization problem and searches for an appropriate and environmentally friendly solution every single day. So far, fatty food residue could be used as a renewable fuel [3], but burning that kind of matter does not help to protect the environment from flue gas contaminations. This need for environment-friendly technology drives us to solve the problem of slow biodegradable fatty organic matter, making it recyclable. The latest studies show that manure can also be digested with other organic matter, such as by-products, producing renewable fuel - biogas and the renewable fertilizer - digestate [4]. Our research was dedicated to investigating the possibility of organic load rate increase with fatty organic matter.

METHODS

The entire research was performed at the biogas laboratory of Vytautas Magnus University, Agriculture Academy. Anaerobic digestion opportunities and challenges associated with manure-based substrate and supplements were identified by analysing factors that affect anaerobic digestate composition, digestion process, biogas and methane yield, and methane concentration in biogas. In the first research stage, an inoculum from a wastewater treatment plant and raw manure was used to start the digestion process.

An initial organic load rate of raw manure (mass in kg of volatile solids to one cubic meter of the reactor operating volume per day (kg VS/ (m^3·d)) was selected as a reference organic load rate [5] in our study. The daily feeding input of the digester consisted of raw manure diluted with tap water. The dilution of manure was needed because the dry matter of manure was too high for the appropriate distribution of organic matter. Therefore, the dilution of manure allowed the higher bioreactor's hydraulic load, ensuring better substrate mixing and proper distribution of organic matter [5]. In the further stages, we used fatty organic matter,

which supplemented organic load rate augmentation. The fatty waste added to the raw manure was set to increase the organic load rate in steps by 0, 5 kg VS/ (m^3·d). The entire research was conducted at four organic load rates and lasted 97 days, including a run-up of the digestion process.

RESULTS

Research showed that the organic load rate increased with fatty matter addition raised biogas production, increasing biogas yield, methane concentration and subsequently methane yield. The biogas production steady grew at all organic load rates throughout the entire experiment. Such addition of fatty matter to diluted raw manure significantly increased substrate organic load, justified the substrate mixture as a renewable energy source for biogas production and allowed the utilization of fatty waste using anaerobic digestion technology.
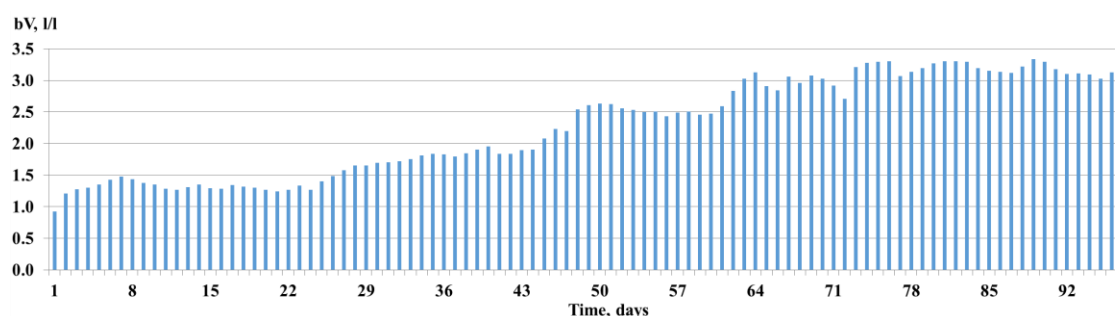

Fig. 1. The biogas production in the entire experiment.

The biogas production b_v (raw biogas volume obtained from the reactor working volume l/l, Fig. 1) continuously raised with some deviation in all our experiments. The highest biogas volume produced 3.36 l/l matched the highest organic load rate, 4.5 kg VS/ (m^3·d).

The nitrogen content of the ammonium ions in digestate was the highest at the highest organic load rate and corresponded to the pH value at the same organic load rate. Low deviations of pH value and ammonium ions concentration in the digestate and continuously increasing biogas production indicated no inhibition of the biogas production process.

The increase in the organic load rate with fatty waste addition was a good measure for supplying more biodegradable organic matter for biogas production. This measure allowed to produce more biogas and utilize fatty waste in the digestion of raw manure. However, some drawbacks were spotted at the end of the experiment: little sludge floatation and scum formation. These drawbacks can be associated with fat usage and need to be investigated in further studies.

CONCLUSION

1. The research results showed that organic load rate increase with fatty matter addition is a possible measure to obtain more biogas.

2. Low deviations of pH values and ammonium ions concentrations in the digestate justified no inhibition of the biogas production process.

Keywords: anaerobic digestion, methane concentration, biogas yield, poultry manure, fat waste, biogas production efficiency.

REFERENCES

1. ESTEVES, E.; HERRERA, A.; ESTEVES, V.; MORGADO, C. Life cycle assessment of manure biogas production: A review. *Journal of Cleaner Production*, 2019. Vol. 219, P. 411–423.

2. BARAL, K.; JÉGO, G.; AMON, B.; B.O.L., R.; CHANTIGNY, M.; OLESEN, J.; PETERSEN, S. Greenhouse gas emissions during storage of manure and digestates: Key role of methane for prediction and mitigation. *Agricultural Systems*, 2018. Vol. 166, P. 26–35.

3. TOLDRÁ-REIG, F.; MORA, L.; TOLDRÁ, F. Trends in Biodiesel Production from Animal Fat Waste. *Applied Sciences,* 2020. Vol. 10, p. 3644.

4. RAHMAN A.; SHAHAZI R.; NOVA S.; UDDIN R.; HOSSAIN S.; YOUSUF A. Biogas production from anaerobic co-digestion using kitchen waste and poultry manure as substrate—part 1: substrate ratio and effect of temperature. *Biomass Conversion and Biorefinery,* 2021. DOI: 10.1007/s13399-021-01604-9.

5. NKUNA R.; ROOPNARAIN A.; RASHAMA C.; ADELEKE R. Insights into organic loading rates of anaerobic digestion for biogas production: a review. *Critical Reviews in Biotechnology,* 2021. DOI: 10.1080/07388551.2021.1942778.

EMISSIONS IMPROVEMENT OF A DIESEL ENGINE FUELLED WITH B20 THROUGH USING OXYGENATED BLENDING COMPONENT

A. ÇAKMAK

Department of Motor Vehicles and Transportation Technologies, Samsun University
Samsun, 55850 – Turkey
+90 362 313 02 20
abdulvahap.cakmak@samsun.edu.tr

EXTENDED ABSTRACT

OVERVIEW

Reducing the exhaust emissions emitted from internal combustion engines is still a challenge for automotive manufacturers. Many techniques and methods have been applied to control harmful exhaust emissions, and also further progress in emissions reduction must be achieved to meet next coming emissions norms. The utilization of oxygenated fuels for controlling exhaust emissions has attracted the interest of researchers in recent decades. The main reasons for this are (i) oxygenated fuels can reduce exhaust emissions without adverse impact on engine performance [1], (ii) oxygenated fuels can be produced from renewable sources, offering to reduce greenhouse gas emissions [2], (iii) the use of oxygenated fuels for reducing exhaust emissions is simpler and more cost-effective way than other emissions control methods [3]. Therefore, the use of oxygenated fuels as an emissions control method is highly advantageous and enough practical to apply in internal combustion engines.

This study aims to improve the exhaust emissions of a direct injection diesel engine fuelled with B20 fuel by using ethyl acetate as an oxygenated biofuel. In the study, ethyl acetate was added to the biodiesel-diesel blend (B20) by 5% and 10% volume to investigate its effect on exhaust emissions. Once measuring fuel properties by following related standards, engine tests were performed on a single-cylinder research diesel engine at various running conditions.

METHODS

Three fuel blends prepared by splash blending were subjected to engine tests. The first is B20 which was used as reference fuel to set baseline data for comparison. The others are EA5, and EA10 were prepared simply by adding 5% and 10% ethyl acetate to the finished diesel-biodiesel blend. Table 1 shows the test fuels' composition. The biofuel fraction of the blends was limited to 20% volume because engine manufacturers approve the use of biofuels up to 20% volume under warranty for their engines. Further, this biofuel blending ratio was preferred to use the test fuels without the need for engine modification. Density, dynamic viscosity, heating value, cold filter plugging point temperature, flash point temperature, and distillation temperature of the test fuel were determined according to related test methods. In order to determine the effects of fuels on exhaust emissions, engine tests were performed for engine loads of 0.9, 1.7, 2.6, and 3.5 kW at a constant engine speed of 1500 rpm.

Table 1. Test fuels' composition (% by volume)

Test Fuel	Diesel	Biodiesel	Ethyl acetate
B20	80	20	0
EA5	80	15	5
EA10	80	10	10

RESULTS

The research showed that the physiochemical fuel properties of the diesel-biodiesel blend were improved by the inclusion of ethyl acetate, and this effect reflected positively on exhaust emissions. It is determined that a great reduction in C.O., NOx, and soot emissions, up to 71%, 50%, and 70%, respectively, were achieved with a slight penalty in fuel consumption when using ethyl acetate. Additional ethyl acetate blended fuels performed improvement in NOx-soot trade-off and NOx-BSFC trade-off without thermal efficiency loss.

CONCLUSIONS

It is concluded that exhaust emissions of a diesel engine fuelled with B20 fuel can be substantially improved by using ethyl acetate without any engine modification. Therefore, ethyl acetate can be recommended as oxygenated fuel for diesel engines. However, investigations regarding transient running conditions of the engine are necessary.

REFERENCES

1. KUMAR, S.; C.H.O., J. H.; PARK, J.; MOON, I. Advances in diesel–alcohol blends and their effects on the performance and emissions of diesel engines. *Renewable & Sustainable Energy Reviews*, 2013, Vol. 22, P. 46–72. doi:10.1016/J.RSER.2013.01.017.

2. DUNN, J. B.; H.A.N., J.; SEABRA, J.; WANG, M. *Biofuel life-cycle analysis*. Handbook of Bioenergy Economics and Policy Vol. II, Springer; 2017, P. 121–61. ISBN: 978-1-4939-6906-7.

3. RAZAK, N. H.; HASHIM, H.; YUNUS, N. A.; KLEMEŠ, J. J. Reducing diesel exhaust emissions by optimization of alcohol oxygenates blend with diesel/biodiesel. *Journal of Cleaner Production,* 2021, Vol. 316:128090. Doi:<https://doi.org/10.1016/j.jclepro.2021.128090>.

HEAVY METAL ADSORPTION USING TORREFIED CORN STALK

Y. Bumin, K. Demircioglu
Istanbul Technical University
Maslak, 34467 – Turkey
+90 534 644 0666, +90 534 730 4820
bumin16@itu.edu.tr demircioglu16@itu.edu.tr

S. Yaman, H. Açma
Istanbul Technical University
Maslak, 34467 – Turkey
+90 532 267 0141
yamans@itu.edu.tr hanzade@itu.edu.tr

EXTENDED ABSTRACT

OVERVIEW

Clean, freshwater resources are getting harder to find every single day. Since life on Earth depends on water, it is crucial for humankind to find easier, faster and cheaper solutions to purify water. Industrial wastewaters should be treated appropriately. Governments are getting more serious about this issue by publishing regulations based on research about the health effects of heavy metal contaminations. Hence, removing contaminants is becoming a bigger priority. In this study, corn stalk (C.S.) is used to produce adsorbent materials to remove heavy metals from wastewater. As heavy metals, Pb^{2+}, Zn^{2+}, Ni^{2+}, Cd^{4+}, Cr^{6+}, Cu^{2+}, Al^{3+} and Mn^{2+} were selected due to their high abundance in the industrial waste waters [1]. Heavy metals have harmful effects on the human body. For example, lead that is exposed to the human body is stored temporarily in bones, blood and tissues [2]. Repeatedly exposure to lead at a high level can cause anaemia, reproductive impacts, kidney failure, and effects on the peripheral and central nervous system that include convulsions, coma, and death [3]. Therefore, according to World Health Organization, the lead concentration in industrial wastewater discharge must be 0.01 mg/L at its maximum [4]. The aim of this project is to find an easy, cheap and quick way of removing selected heavy metals.

METHODS

EFFECT OF TORREFACTION TEMPERATURE ON MASS LOSS

To determine the effect of torrefaction temperature on biomass, the weight of the adsorbents was noted before and after the torrefaction process. The mass loss percentages at different temperatures are determined by the following equation (1):

$$Mass\ Loss\ = \frac{m_i - m_f}{m_i}. \qquad (1)$$

In this equation, m_i and m_f represents the weights of the corn stalk at initial and after torrefaction.

ADSORPTION EFFICIENCY

Corn stalk is chosen as biomass adsorbent. Preparation of the adsorbents from the biomass includes the following procedure. First, the biomass was ground until its grain sizes were smaller than 250 μm. The biomass was torrefied in a tube furnace under a nitrogen atmosphere. In order to find the optimum torrefaction temperature, the corn stalk was torrefied at 150ºC (CS-150), 200ºC (C.S. - 200), 250ºC (CS-250) and 300ºC (CS-300). The solutions were interacted with by the biomass adsorbent for 1 hour. The concentration of the biomass-heavy metal solution was 0.5 g/20 mL. Inductively coupled plasma mass spectrometry (ICP-MS) was used to analyse the solutions for adsorption efficiency. Adsorption efficiencies (q_e) were calculated by the following equation (2):

$$q_e = \frac{(C_i - C_e)V}{m} \qquad (2)$$

In this equation, C_i and C_e represents the concentration of the heavy metal at an initial time and at 1 hour later. V is the volume of the solution, and m represents the mass amount of the adsorbent.

TORREFACTION TEMPERATURE AND PH EFFECT ON ZETA POTENTIAL

The effect of torrefaction temperature on Zeta Potential was investigated by Brookhaven Instruments' PALS Zeta Potential Analyser. Analysis measurements were conducted by 6 runs and 20 cycles at room temperature. Firstly, corn stalks that torrefied at selected temperatures were ground to obtain 50 μm and the smaller particles. Standardized pH solutions were prepared with NaOH and HCl. Then, 1 mg of biomass and 1.7 mL of standardized pH solutions at (1, 2, 3, 4, 5, 7, 9, 11 and 13) were mixed in quartz glass tubes.

ION EFFECT ON ZETA POTENTIAL

At different pH values, the effect of the existence of the least and most adsorbed metal ions was also observed by Zeta Potential Analyser. CST-200 was selected as the best absorber and loaded into the Pb^{2+} and Cr^{6+} solutions at different pH values. Zeta Potential Analysis was conducted after 15 minutes. Results were compared with standardized pH solution results.

RESULTS

When corn stalk is torrefied at 200 ºC and 250 ºC, it is an exceptional absorber for Lead (Pb^{2+}). All the results are shown for corn stalks in Tables 1, 2, 3, 4, 5. And Figures 1, 2, 3, 4, and 5.

Table 1. 150 ⁰C Torrefied Corn Stalk Recovery

150 ⁰C Torrefied Sample	Filtrate I.C.P. (ppm)	Standard solution (ppm)	q_e
C.S.T. (Pb)	65.8	1000	93.42
CST (Zn)	861.8	1000	13.82
CST (Ni)	816.5	1000	18.35
CST (Cd)	690.8	1000	30.92
CST (Cr)	966.7	1000	3.33
CST (Cu)	688.4	1000	31.16
CST (Al)	998	1000	0.20
CST (Mn)	929.9	1000	7.01

Table 2. 200 ⁰C Torrefied Corn Stalk Recovery

200 ⁰C Torrefied Sample	Filtrate I.C.P. (ppm)	Standard solution (ppm)	q_e
C.S.T. (Pb)	44.2	1000	95.58
CST (Zn)	956.3	1000	4.37
CST (Ni)	805.4	1000	19.46
CST (Cd)	594.5	1000	40.55
CST (Cr)	561.3	1000	43.87
CST (Cu)	596.5	1000	40.35
CST (Al)	986	1000	1.40
CST (Mn)	655.1	1000	34.49

Table 3. 250 ⁰C Torrefied Corn Stalk Recovery

250 ⁰C Torrefied Sample	Filtrate I.C.P. (ppm)	Standard solution (ppm)	q_e
C.S.T. (Pb)	3.5	1000	99.65
CST (Zn)	547.7	1000	45.23
CST (Ni)	614.6	1000	38.54
CST (Cd)	374.1	1000	62.59
CST (Cr)	887	1000	11.30
CST (Cu)	359.6	1000	64.04
CST (Al)	842.4	1000	15.76
CST (Mn)	688.6	1000	31.14

Table 4. 300 ⁰C Torrefied Corn Stalk Recovery

300 ⁰C Torrefied Sample	Filtrate I.C.P. (ppm)	Standard solution (ppm)	q_e
C.S.T. (Pb)	100	1000	90.00
CST (Zn)	400	1000	60.00
CST (Ni)	640	1000	36.00
CST (Cd)	420	1000	58.00
CST (Cr)	680	1000	32.00
CST (Cu)	380	1000	62.00
CST (Al)	800	1000	20.00
CST (Mn)	550	1000	45.00

Table 5. Corn Stalk Recovery

Original Sample	Filtrate I.C.P. (ppm)	Standard solution (ppm)	q_e
C.S. (Pb)	90.00	1000	91.00
CS (Zn)	670.00	1000	33.00
CS (Ni)	790	1000	21.00
CS (Cd)	630	1000	37.00
CS (Cr)	800	1000	20.00
CS (Cu)	790	1000	21.00
CS (Al)	780	1000	22.00
CS (Mn)	817.20	1000	18.28

The loss of weight of the corn stalk is shown with respect to torrefaction temperature in Fig 6. It is clear that increasing the torrefaction temperature results in more weight loss.
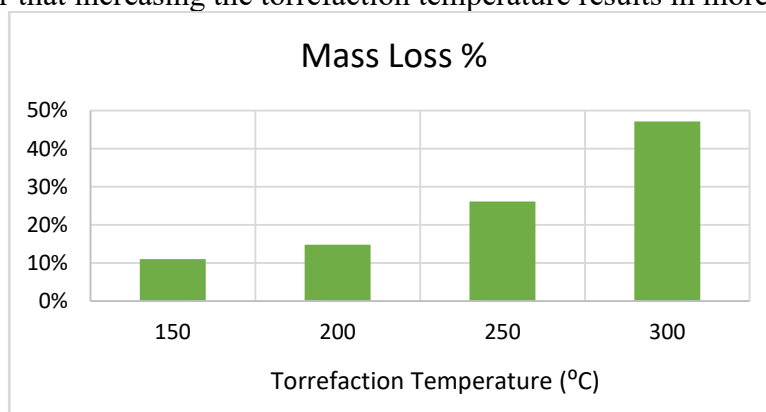
Fig 1. Mass Loss

In Fig 2, adsorption percentages of the heavy metals at different torrefaction temperatures are compared. It can be seen that Pb^{2+} was the heavy metal that was adsorbed the most. Cr^{6+}, on the other hand, was the one that adsorbed poorly.
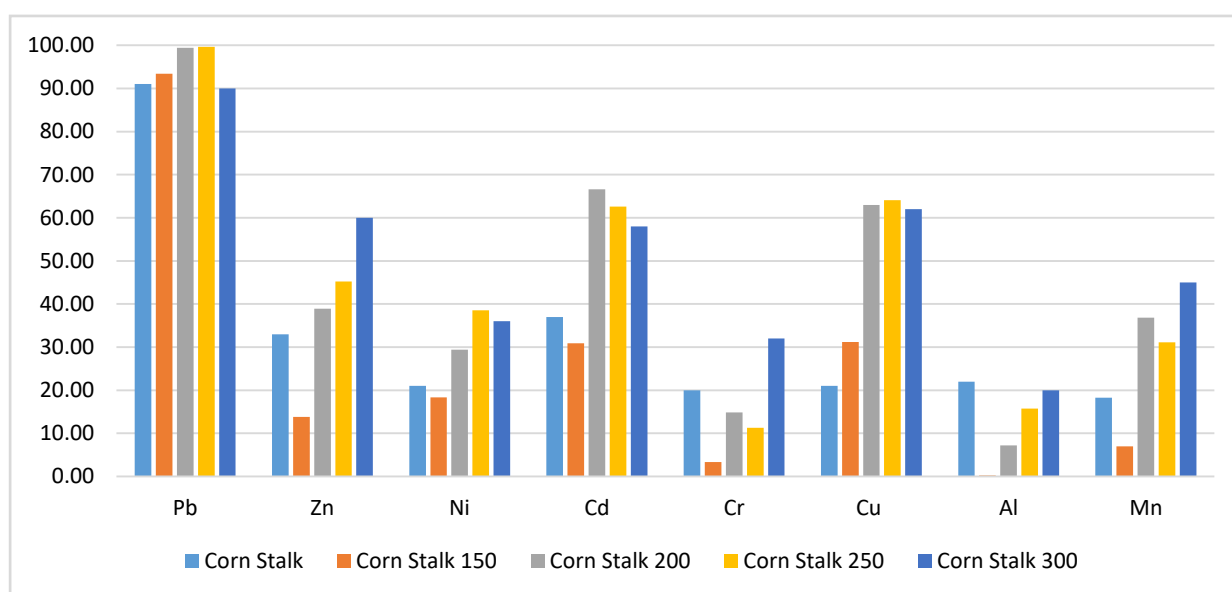
Fig 2. Adsorption Efficiency for Each Heavy Metal Solutions (q_e)

To better understand and explain the effect of torrefaction temperature and pH of the solution, Zeta Potential Analysis was conducted at different values.
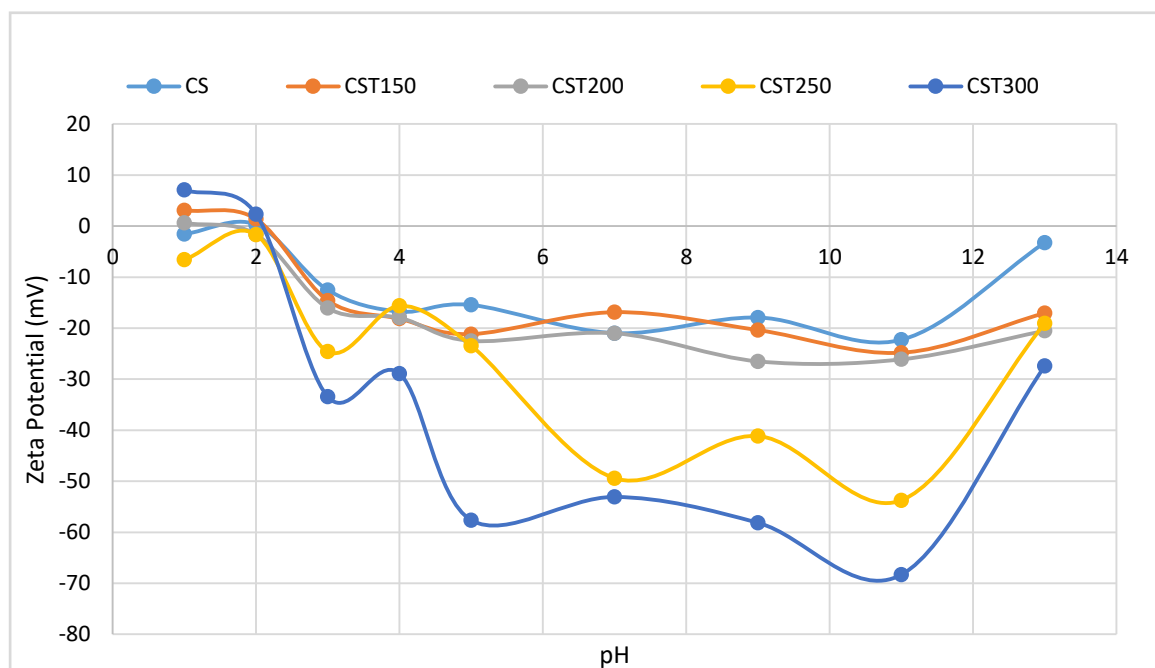

Fig 3. The effect of torrefaction temperature on Zeta Potential

At different pH values, the effect of the existence of the least and the most adsorbed metal ions was also observed by Zeta Potential Analyser.
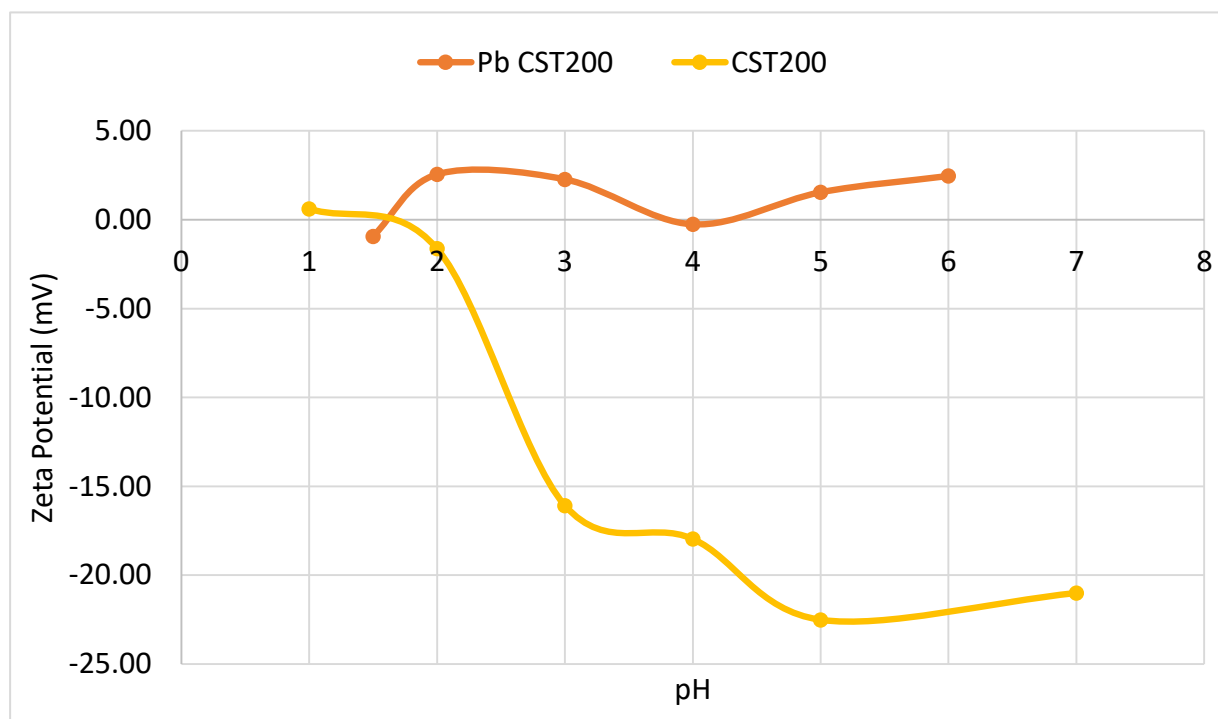

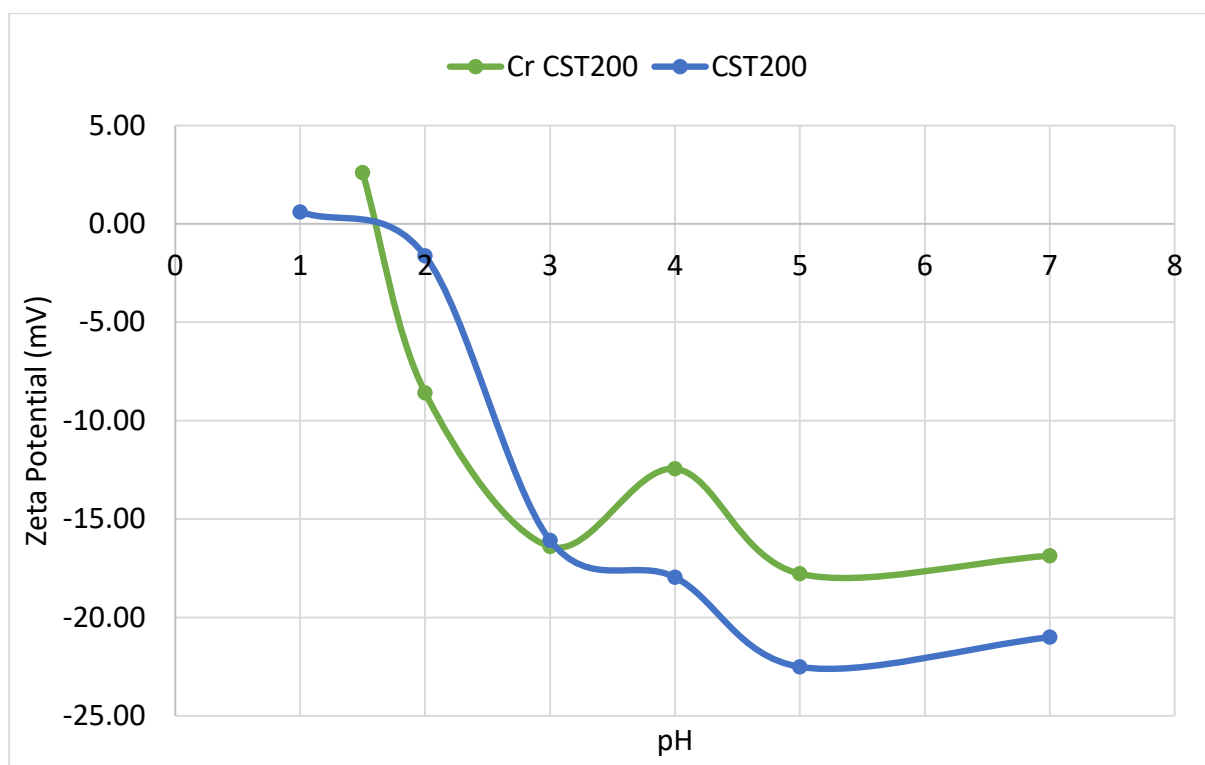Fig 4. The effect of Pb^{2+} Ion on Zeta Potential

Fig 5. The effect of Cr^{6+} Ion on Zeta Potential

CONCLUSIONS

As a result, it was observed that the adsorption efficiency changes due to torrefaction temperature and heavy metal ions. According to the I.C.P. analyses, CST-250 has the best performance on Pb2+ with 99.65% adsorption efficiency (q_e), while Cr6+ was adsorbed poorly with a value of 11.3%. Nonetheless, other analyses were conducted with CST-200 because the adsorption efficiency difference is small enough to be neglected and to make the torrefaction process more energy-friendly.

The torrefaction temperature affects the porosity and functional groups of lignocellulosic biomasses. According to the Zeta Potential Analysis, it was seen that as the torrefaction temperature goes high, the zeta potential increases. This can be explained by the decomposition of the lignin content (a complex phenolic polymer) on the biomass at 160 ⁰C and the higher temperatures. Nevertheless, at high torrefaction temperatures, biomasses become hydrophobic and accumulate on the surface of the solution. This transformation decreases the contingency of the biomass with metal ions. Also, higher pH values provide higher zeta potential differences. However, the pH range of the 1000 ppm heavy metal solutions is between 3-6. Therefore, pulling the solution pH values to the alkali levels causes the formation of metal salts. Zeta potential analysis was conducted at lower pH levels for the Cr6+ and Pb2+ solutions to prevent sedimentation. According to the Zeta Potential results, Pb2+ ions increase the zeta potential to positive levels, while Cr6+ ions affect it less. The big Zeta Potential difference in the Pb2+ solution is probably related to the high adsorption rate. The positive ion load to the surface of the biomass causes the increase of the zeta potential.

Keywords: (Heavy metal removal, lignocellulosic biomass, waste water treatment, torrefaction, adsorption)

REFERENCES

1. WANG, J. Reuse of Heavy Metal from Industrial Effluent Water. *I.O.P. Conference Series: Earth and Environmental Science*, 2018, P. 199.

2. *The National Institute for Occupational Safety and Health (NIOSH)*. Centers for Disease, Control and Prevention, 2021- [referred on the 21st of February in 2022 y.] Link to the internet < https://www.cdc.gov/niosh/topics/lead/health.html >.

3. BOREIKO, C.J. *Encyclopaedia of Electrochemical Power Sources*. Elsevier Science, 2009, P. 233–240. ISBN 978-0-444-52745-5

4. YADAV, M.; GUPTA, R.; SHARMA, R. K. *Advances in Water Purification Techniques: Meeting the Needs of Developed and Developing Countries.* United States: Elsevier, 2019, P. 355–383. ISBN 978-0-12-814790-0

ENERGY CROP OILSEED RAPE (*BRASSICA NAPUS* L.) BIOMASS PRODUCTION DURING PHYTOREMEDIATION PROCESS AT DIFFERENT SOIL WATER CONTENT

I. Kniuipytė[1], M. Praspaliauskas[1], N. Pedišius[1], J. Žaltauskaitė[1, 2], A. Dikšaitytė[2],
[1]Laboratory of Heat Equipment Research and Testing, Lithuanian Energy Institute,
Breslaujos g. 3, LT-44403 Kaunas – Lithuania
+3706 607 50983
inesa.kniuipyte@lei.lt

[2]Department of Environmental Sciences, Vytautas Magnus University,
Universiteto g. 10, LT-53361 Kauno raj. – Lithuania
+3706 877 5711
jurate.zaltauskaite@vdu.lt

EXTENDED ABSTRACT

OVERVIEW

The world economy's super-exponential growth over the last 70 years has resulted in the exploitation of non-renewable resources and an increase in the production of poorly managed waste [1]. Urbanization and the resulting growth of infrastructure and industries have put tremendous pressure on land around the world. To reap the benefits of both clean-up and bioenergy production, energy plants with metal hyper accumulation properties should be used for soil reclamation. Phytoremediation is ideal for the treatment of municipal and industrial waste disposal sites and other polluted areas contaminated with heavy metals (H.M.). The main aspect that hinders the development of this technology is the need to manage the plant biomass material contaminated with H.M. during the entire treatment process [2, 3, and 4]. An integrated, sustainable, phytoremediation approach is in line with the principles of the circular economy and addresses contaminated biomass removal and management and reduces financial costs. It is a purification process that includes the conversion of biomass into energy and the recovery of valuable elements (including H.M.) through phytomining [5]. Various types of woody or energy crops are increasingly used in phytoremediation. Food and forage crops are being phased out to avoid contaminants entering the food chain and posing a serious risk to human health [6]. The suitability of energy plants for phytoremediation is determined by a number of important characteristics. High biomass yields in H.M. contaminated soil are extremely beneficial because it reduces pollutants runoff, soil erosion, and H.M. infiltration into groundwater. [7]. There is a scarcity of research on herbaceous energy plant species in phytoremediation, environmental conditions and changing climatic factors that affect plant growth and performance. Soil water content is one of the most important environmental factors influencing plant physiological processes and biomass production, heavy metal mobility in the soil and bioavailability. Therefore soil water content plays a crucial role in the efficacy of phytoremediation. Both soil water deficit and overwatering can cause a negative impact on plants [8, 9]. Our research aim was to evaluate energy crop oilseed rape (*Brassica napus* L.)

growth and biomass production during the cadmium (Cd) phytoremediation process at different soil water content (S.W.C.). Three different S.W.C.s were simulated: optimal, deficit and elevated. After the phytoremediation process, plant growth, biomass production, and tolerance to metal were analysed. Results showed that S.W.C. has significantly affected plant biomass production in Cd contaminated soil. Although oilseed rape can grow even at high Cd contamination, it has really good tolerance and is suitable for phytoremediation as a hyper accumulator. Optimal soil water content should be maintained for better phytoremediation capability in soil contaminated with high Cd concentrations (>100 mg/kg^{-1}).

METHODS

A phytoremediation mesocosm experiment was performed in the greenhouse of the Vytautas Magnus University (V.M.U.) Open Access Land and Forest Research Centre. Energy crop oilseed rape (*Brassica napus* L) was grown in soil at different Cd concentrations in soil (1, 10, 50, 100, 250 mg/kg^{-1}) and controlled. Plants were sown in vegetation pots filled with a 3 kg soil mixture of field top-soil (taken from V.M.U. Experimental Research Station, Kaunas district), mixed with perlite and fine sand (by volume 5:3:2). Soil water content – S.W.C. (volumetric) was maintained at optimal S.W.C. content which is 30% [10, 11], air temperature averaged 21.1±0.02°C during the day. After 4 weeks of growing, plants were divided into 3 groups by S.W.C. – optimal with S.W.C. of 30%, deficit with S.W.C. of 5-10% and elevated - 40%. Soil water content was measured using a Theta Probe ML2x sensor connected to a hand-held 6 cm long HH$_2$ moisture meter (Delta-T Devices Ltd., Cambridge, UK). Plants were grown for 17 days. After the experiment, plant shoot height, root length and fresh mass were measured. All plants' biomass was dried at 60°C until the constant weight, and then dry weight (D.W.) was measured. Plant biomass production was analysed as the weight of aboveground plant dry matter. Tolerance index (T.I.) was defined as the ratio between the dry matter yields of the plants in contaminated soil in relation to the dry matter yield of the plants from unpolluted (control) soil. T.I. <1 means that plants are under heavy metal contamination stress. If T.I. is equal to 1 – they are not affected by H.M., T.I.>1 means that plants have hyper accumulator tolerance potential. Statistical analysis was made using Statistica 8 software.

RESULTS

Because the heavy metal phytoremediation process strongly depends on plants' growth – dry weight, shoot height and root length were measured, and tolerance to Cd contamination was calculated and analysed (Fig. 1).
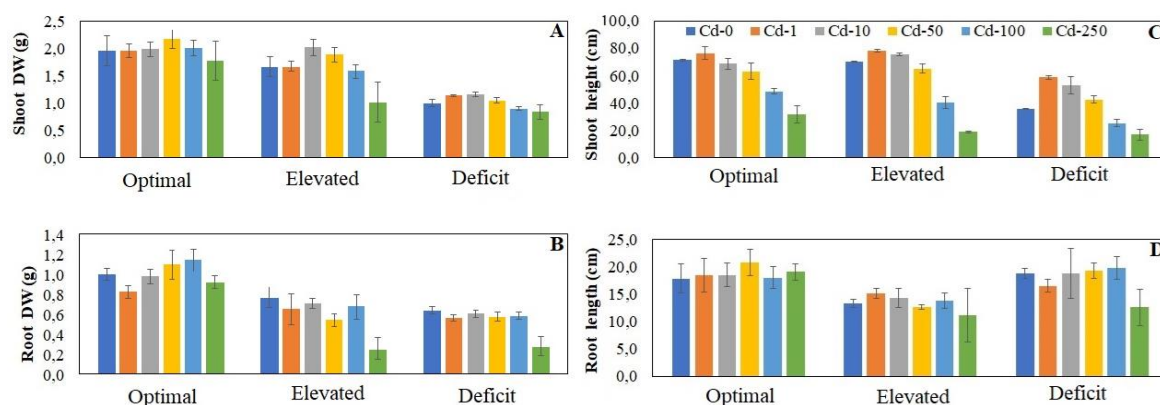
Fig. 1. Oilseed rape (Brassica napus L.) biomass characteristics in Cd contaminated soil under different S.W.C.: shoot D.W. (A), root D.W. (B), shoot height (C), and root length (D).

Factorial analysis of variance (ANOVA) has shown that both Cd concentration in soil and S.W.C. had a significant effect on oilseed rape (*Brassica napus* L.) shoot height (Cd F=155.84 p<0.05; S.W.C. F=115.73, p<0.05; Cd x S.W.C. F=6.27, p<0.05), but only S.W.C. had a significant effect on root length (Cd F=2.11, p>0.05; S.W.C. F=23.32, p<0.05; Cd x S.W.C. F=1.54, p>0.05). Shoot height decreased with Cd concentration in the soil at all investigated S.W.C. However, under the soil moisture deficit, shoots were significantly lower compared to optimal and elevated S.W.C. conditions regardless of Cd concentration in the soil. At the same time, plants grown under S.W.C. deficit had the longest roots meanwhile, at elevated S.W.C., plants formed the highest shoots and shortest roots.

Factorial analysis of variance (ANOVA) has shown that both Cd concentration in soil and SWC had significant effect on B. napus shoot DW (Cd F=7.93, p<0.05; SWC F=47.91, p<0.05; Cd x SWC F=1.27, p>0.05) and root (Cd F=5.17, p<0.05; SWC F=46.20, p<0.05; Cd x SWC F=1.30, p>0.05). The biggest biomass production, i.e., shoots and root D.W. was achieved at optimal S.W.C. At all S.W.C., the biggest decrease in shoot and root D.W. occurred at the highest Cd concentration in soil. The smallest shoot D.W. was recorded for S.W.C. deficit while rooting D.W. at elevated S.W.C.

Factorial analysis of variance (ANOVA) has shown that both Cd concentration in soil and S.W.C. had a significant effect on B. napus tolerance to Cd contamination (Cd F=16.12, p<0.05; S.W.C. F=14.52, p<0.05; Cd x S.W.C. F=2.76, p<0.05) (Fig. 2).
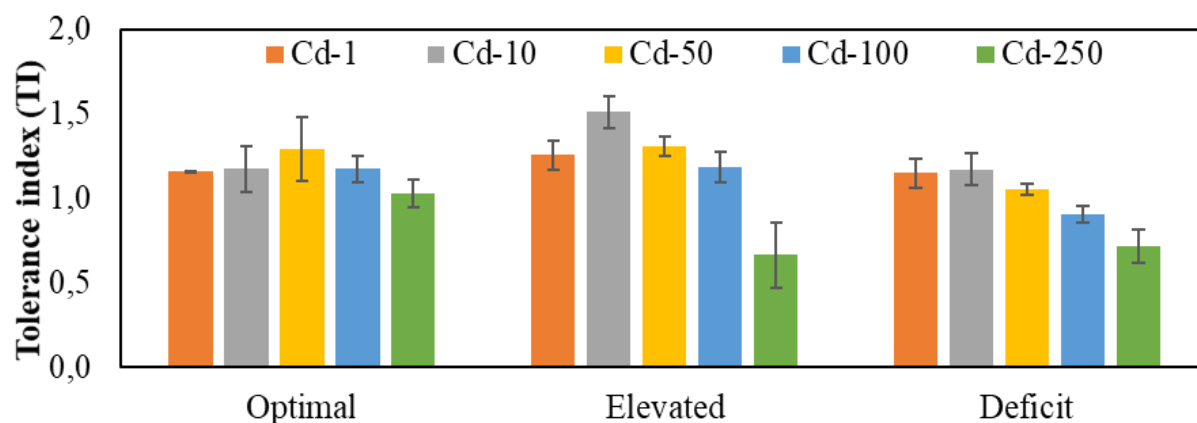
Fig. 2. Oilseed rape (Brassica napus L.) tolerance index (T.I.) in different
Cd concentrations and soil water contents.

Oilseed rape has the possibility to be a good Cd hyper accumulator, but S.W.C. has a significant impact on its tolerance to Cd. At optimal, S.W.C. rape T.I. was bigger than 1, indicating that it has hyper accumulator tolerance potential for soil contamination with Cd. Under elevated SWC, TI >1 was recorded for Cd <100 mg/kg^{-1}. Under S.W.C. deficit, lower T.I. was recorded compared to optimal and elevated S.W.C. at Cd concentration higher than 10 kg/kg^{-1}. While the lowest rape tolerance to soil contamination with Cd was at the highest Cd concentration in soil under elevated S.W.C., it might happen because of the change in heavy metal bioavailability and complex S.W.C. and Cd concentration effect on plants growth. Optimal soil water content should be maintained to achieve better energy crop tolerance to H.M. contamination in the soil during the phytoremediation process at higher Cd soil concentrations because the tolerance index decreases at elevated or deficit S.W.C.

CONCLUSIONS

Our results showed that S.W.C. has a significant effect on oilseed rape (*Brassica napus* L.) growth, biomass production and tolerance to soil contamination with Cd. The biggest total produced biomass and the highest tolerance to Cd soil contamination was achieved at optimal S.W.C. Better biomass production is a relevant economic advantage in the use of energy crops. It should also lead to a bigger content of bio accumulated metal in the plant tissues and possible higher efficiency of the metal removal from the soil. Maintenance of optimal soil water content during the phytoremediation process is crucial in ensuring efficient phytoremediation. It can be stated that oilseed rape (*Brassica napus* L.) has good potential to be used in phytoremediation as a hyper accumulator. It has tolerance to Cd contamination up to 250 mg/kg^{-1} under optimal S.W.C. Further analyses of S.W.C. and different environmental factors impact not only on plant growth and tolerance but also on Cd bioaccumulation, and translocation must be conducted.

Keywords: oilseed rape, biomass, phytoremediation, tolerance index, heavy metal,

REFERENCES

1. STEFFEN, W.; BROADGATE, W.; DEUTSCH, L.; GAFFNEY, O.; LUDWIG, C. The trajectory of the anthropocene: the great acceleration. *Anthropoc. Rev.* , 2015, Vol. 2, P. 81–98.

2. L.I.U., L.; LI, W.; SONG, W.; G.U.O., M. Remediation techniques for heavy metal-contaminated soils: Principles and applicability. *Science of the Total Environment*, 2018, Vol. 633, P. 206–219.

3. LUO, J.; WU, J.; HUO, S.; QI, S.; GU, X.S. A real scale phytoremediation of multi-metal contaminated e-waste recycling site with Eucalyptus globulus assisted by electrical fields. *Chemosphere,* 2018, Vol. 201, P. 262-268.

4. LONE, M.I.; HE, Z.L.; STOFFELLA, P.J.; YANG, X. Phytoremediation of heavy metal polluted soils and water: progresses and perspectives. *Journal of Zhejiang University-SCIENCE B.*, 2008, Vol. 9, P. 210–220.

5. PANDEI, V.C.; BAJPAI, O.; SINGH, N. Energy crops in sustainable phytoremediation. Renewable and Sustainable *Energy Reviews*, 2016, Vol. 54, P. 58–73

6. SHARMA, R.; BHARDWAJ, R.; GAUTAM, V.; BALI, S.; KAUR, R.; KAUR, P.; SHARMA, M.; KUMAR, V.; SHARMA, A.; SONIA, A.K.T.; VIG, A.P.; OHRI, P. Phytoremediation in waste management: hyperaccumulation diversity and techniques. In: Hasanuzzaman, M., Nahar, K., Fujita, M. (Eds.), Plants Under Metal and Metalloid Stress: Responses, *Tolerance and Remediation*. *Springer Singapore*, Singapore, 2018, P. 277–302.

7. HAUPTVOGL, M.; KOTRLA, M.; PRČIK, M.; PAUKOVA, Ž. Phytoremediation Potential of Fast-Growing Energy Plants: Challenges and Perspectives – a Review. *Polish Journal of Environmental Studies*, 2020. Vol. 29, No. 1, P. 505-516.

8. TRINH, T.; WERLE, S.; TRAN. K.; MAGDZIARZ. A.; SOBEK, S.; POGRZEBA, M. Energy crops for sustainable phytoremediation – Thermal decomposition kinetics. *Energy Procedia*, 2019, Vol. 158, P. 873-878.

9. WERLE, S.; TRAN, K.; MAGDZIARZ. A.; SOBEK, S.; POGRZEBA, M. Energy crops for sustainable phytoremediation – Fuel characterization. *Energy Procedia*, 2019, Vol. 158, P. 857-872.

10. DIKŠAITYTĖ, A.; VIRŠILĖ, A.; ŽALTAUSKAITĖ, J.; JANUŠKAITIENĖ, I.; PRASPALIAUSKAS, M; PEDIŠIUS, N. Do plants respond and recover from a combination of drought and heatwave in the same manner under adequate and deprived soil nutrient conditions? *Plant Science*, 2020, Vol. 271.

11. DIKŠAITYTĖ, A.; VIRŠILĖ, A.; ŽALTAUSKAITĖ, J.; JANUŠKAITIENĖ, I.; JUOZAPAITIENĖ, G. Growth and photosynthetic responses in Brassica napus differ during stress and recovery periods when exposed to combined heat, drought and elevated CO2. *Plant Physiology and Biochemistry*, 2019, Vol. 142, P. 59–72.

PROCESSING OF MULTI-CROP PLANTS AND INVESTIGATION OF THE PROPERTIES OF GRANULAR BIOFUELS

R. Petlickaitė, M. Praspaliauskas
Lithuanian Energy Institute
Breslaujos g. 3, LT-44403 Kaunas– Lithuania
+370 685 28646
rita.petlickaite@lei.lt

A. Jasinskas
Vytautas Magnus University Agriculture Academy
Studentų str. 11, LT-53361 Akademija, Kaunas distr. – Lithuania
+370 612 04 002
algirdas.jasinskas@vdu.lt

EXTENDED ABSTRACT

OVERVIEW

It is widely acknowledged that plant biomass is a potential source of renewable energy. Although many studies have been performed to support the suitability of various plants for solid biofuels, the suitability of multi-crop biomass for solid biofuels has not been studied. The cultivation of multifarious plants can help reduce the use of fertilizers and pesticides for several reasons.

In changing climate cultivation of polycultures not only helps to control pests and pathogens but also increases yields. [1, 2–5].

Growing two or more crops in one field increases resource efficiency and results in higher yields per unit area. [1, 6]. Multi-crop improves soil fertility due to biological nitrogen fixation using legumes. The cultivation of multi-crop increases the conservation of the soil by covering the soil and providing better protection against precipitation [1, 7].

The aim of this work is to determine the suitability of multi-crop plants: fibrous hemp, maize and faba bean for the production of granulated biofuel and to investigate the thermal, chemical and physical-mechanical properties of biofuel pellets.

METHODS

The study was conducted in 2020–2021 with biomass of polynomial plants (faba bean, maize and fibrous hemp). These plants were grown at the Experimental Station of Vytautas Magnus University Agriculture Academy. They were sown as a single-crop, a binary and a trinomial crop. The grown plants were harvested, dried, shredded, and ground and biofuel pellets were produced. Seven variants were investigated depending on the biomass composition used: 1) maize (abbreviation M.Z.), 2) hemp (F.H.), 3) faba bean (F.B.), 4) maize and hemp mixture (MIX1), 5) maize and faba bean mixture (MIX2), 6) mixture of fibrous hemp and faba bean,

7) mixture of fibrous hemp, maize and faba bean. After the production of solid biofuel pellets, their physic mechanical, chemical and other basic properties were investigated in order to determine the suitability of the produced pellets for solid biofuel. The research was performed in the laboratories of Vytautas Magnus University Agriculture Academy and Lithuanian Energy Institute in accordance with the following valid E.U. countries' standard methodology.

The experiment will continue for another two years, and then the authors will provide a summary of three years of data.

RESULTS

The results of the investigation show that the three chemical elements (carbon, oxygen and hydrogen) in the biomass pellets account for from 93.1 to 94.9% (Fig. 1).
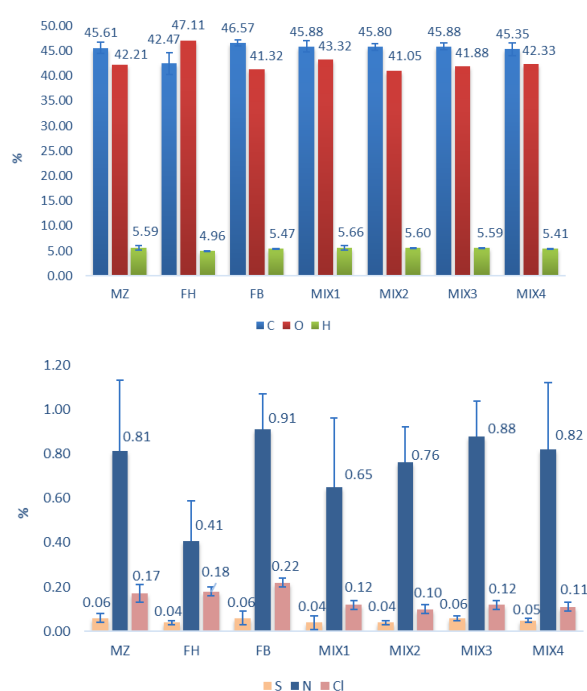

Fig. 1. Chemical elements of biomass pellets

S, N, and Cl quantities were also investigated. N contents did not exceed the maximum permissible levels according to the IWPB standard (≤1.5%) [8]. the value of S did not exceed the maximum permissible value (≤0.04%) of this standard in variants F.H., MIX1 and MIX2. In another three variants, this set value was slightly exceeded. The Cl content in variant MIX2 did not exceed the set limit (<0.1%).

The determined biomass pellet properties are presented in Table 1. These results show that moisture content varied from 3.9 to 8.8%. According to the German DIN 51731 standard, the moisture content of the pellets must not exceed 12% [9]. Ash content in the tested pellets varied from 4.5 to 6.8% and did not exceed the maximum permissible value for non-wood biomass (<7%) [10]. the higher calorific value of investigated pellets varied from 17.96 to 18.29 MJ·kg^{-1}, and the lower calorific value varied from 16.80 to 17.14 MJ·kg^{-1}.

Table 1. Biometric properties of biomass pellets

Type of biofuel	Humidity, %	Ash quantity, %	Higher calorific value, M.J. ·kg⁻¹	Lower calorific value, M.J. ·kg⁻¹
MZ	4.61 ± 0.59	5.78 ± 0.06	18.02 ± 0.86	16.87 ± 0.93
FH	3.86 ± 0.05	5.05 ± 0.04	18.16 ± 0.54	17.14 ± 0.57
FB	6.15 ± 0.28	5.74 ± 0.29	18.23 ± 0.38	17.10 ± 0.41
MIX1	4.44 ± 0.22	4.49 ± 0.05	18.29 ± 0.78	16.99 ± 0.85
MIX2	8.78 ± 0.43	6.78 ± 0.18	17.96 ± 0.32	16.80 ± 0.35
MIX3	8.30 ± 0.15	5.78 ± 0.06	18.17 ± 0.59	17.02 ± 0.63
MIX4	5.63 ± 0.23	6.08 ± 0.05	18.04 ± 0.61	16.92 ± 0.66

The density of the biomass pellets was also investigated. After the investigation of biomass pellets, qualitative properties show that the density of all variants of pellets was very similar and varied from 1106.46 to 1195.75 kg·m⁻³ D.M. (Fig. 2).
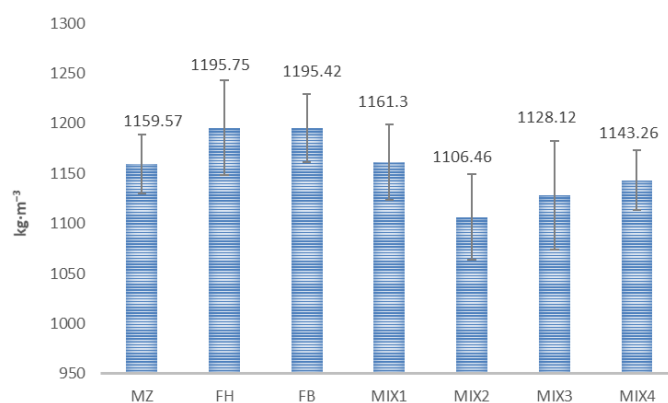

Fig. 2. Pellets density

Melting characteristics of ash are important during the combustion of biofuels, influencing the chemical composition of ash and the slag formation on the surfaces of burning implements.
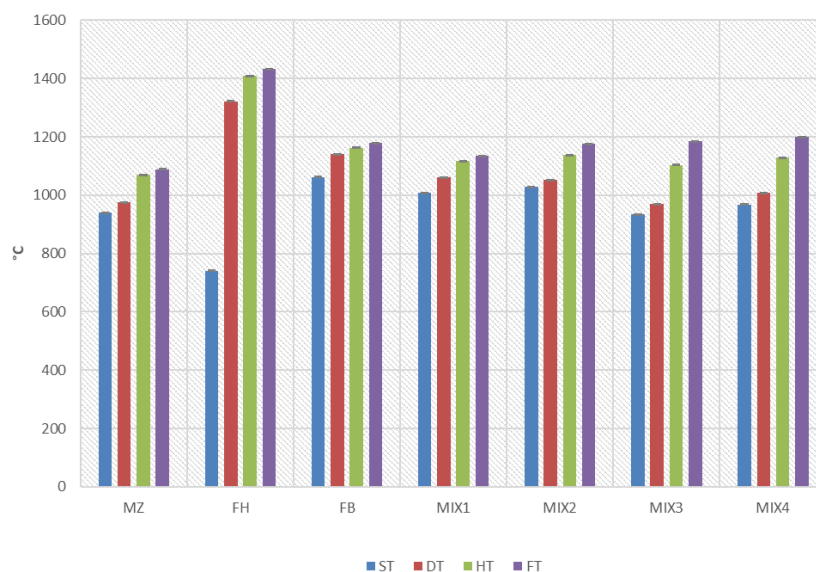
Fig. 3. Ash melting temperatures of biomass pellets

When burning biomass pellets, their melting temperatures were measured. The lowest determined ash softening temperature (S.T.) was that of sample F.H., 741 °C, and the highest one was that of sample F.B., 1062 °C (Fig.3). The initial ash deformation temperature (D.T.) varied from 976 to 1322 °C. The highest one was that of sample F.H., 1322 °C, which indicates that the ash clogging is the lowest on the incinerator's surfaces.

CONCLUSIONS

The pellets from mono and multi-crops had different moisture content. The moisture of maize and faba bean mixture biomass pellets (MIX2) was the highest – 8.78 ± 0.43%, whereas that of fibrous hemp pellets (F.H.) was 2.3 times lower – 3.86 ± 0.05%.

The calorific value of mono and multi-crop plants pellets was sufficiently high and were about 17 M.J. $\cdot kg^{-1}$, and these properties of pellets were close to those of wood biofuels.

Pressed multi-crop plants meet the quality characteristics and standard requirements for solid biofuel pellets.

Keywords: multi-crop; biomass; solid biofuel; pellet properties

REFERENCES

1. PETLICKAITĖ, R.; JASINSKAS, A.; MIELDAŽYS, R.; ROMANECKAS, K.; PRASPALIAUSKAS, M.; BALANDAITĖ, J. Investigation of pressed solid biofuel produced from multi-crop biomass. *Sustainability*, 2022, Vol. 14, No. 799, P. 1-17.

2. BROOKER, R.W.; ALISON, E.; BENNETT, A.E.; et al. Improving intercropping: A synthesis of research in agronomy, plant physiology and ecology. *New Phytologist*, 2015, Vol. 206(1), P. 107–117.

3. SHARMA, G.; SHRESTHA, S.; KUNWAR, S.; TSENG, T.M. Crop Diversification for Improved Weed Management: A Review. *Agriculture*, 2021, Vol. 11, No. 461, P. 1-17.

4. He, H.M.; Liu, L.N.; MUNIR, S.; BASHIR, N.H.; WANG, Y.; YANG, J.; LI, C.Y. Crop diversity and pest management in sustainable agriculture. *Journal of Integrative Agriculture*, 2019, Vol. 1, P. 1945–1952.

5. JENSEN, E.S.; CARLSSON, G.; HAUGGAARD-NIELSEN, H. Intercropping of grain legumes and cereals improves the use of soil N resources and reduces the requirement for synthetic fertilizer N: A global-scale analysis. *Agronomy for Sustainable Development*, 2020, Vol. 40(1), No. 5, P. 1-9.

6. W.U., Y.; HE, D.; WANG, E.; L.I.U. X.; HUTH, N.I.; ZHAO, Z.; GONG, W.; YANG, F.; WANG, X.; YONG, T.; L.I.U., J.; L.I.U., W.; D.U., J.; P.U., T.; L.I.U., C.; YU, L.; WERF, W.; YANG, W. Modelling soybean and maize growth and grain yield in strip intercropping systems with different row configurations. *Field Crops Research.* 2021, Vol. 265, No. 108122, P. 1-13.

7. LITHOURGIDIS, A.S.; DORDAS, C.A.; DAMALAS, C.A.; VLACHOSTERGIOS, D.N. Annual intercrops: An alternative pathway for sustainable agriculture. *Australian Journal of Crop Science*, 2011, Vol. 5(4), P. 396–410.

8. WHITTAKER, C.; SHIELD, I. Factors affecting wood, energy grass and straw pellet durability – A review. *Renewable & Sustainable Energy Reviews,* 2017, Vol. 71, P. 1–11.

9. DIN 51731. Testing of solid fuels, compressed untreated wood. In Requirements and Testing; Deutsches Institut für Normung: Berlin, Germany, 1996.

10. NUNES, L.J.R.; MATIAS, J.C.O.; CATALÃO, J.P.S. Mixed biomass pellets for thermal energy production: A review of combustion models. *Applied Energy*, 2014, Vol. 127, P. 135–140.

THE INFLUENCE OF CO_2 PRETREATMENT OF DAIRY MANURE FOR BIOGAS PRODUCTION

B. Žalys, E. Buivydas
Lithuanian Energy Institute
Breslaujos g. 3, LT-44403 Kaunas – Lithuania
Bronius.Zalys@lei.lt

K. Navickas, K. Venslauskas, M. Rubežius, V. Župerka
Vytautas Magnus University
K. Donelaičio g. 58, LT-44248 Kaunas – Lithuania

EXTENDED ABSTRACT

OVERVIEW

Various technologies for raw materials pre-treatment (thermal, chemical, biological, physical) are used. The impact of enriching with CO_2, the influent to a laboratory scale up-flow anaerobic sludge blanket reactor at CO_2 pressure of $1.01 \cdot 10^5$ Pa was maintained in the influent storage tank, and higher CO_2 dissolution was achieved [1]. It was estimated that 69-86% of the CO_2 dissolved could be utilized in the process. Another research [2] indicated a 25% increase of specific CH_4 yield when continuously injecting CO_2 at a load of 0.49 m^3/d into the first stage of a two-phase anaerobic digestion process, and CO_2 uptake of up to 46% of that injected was ingested. Bajón Fernández et al., 2014 [3] observed an enhancement of CH_4 production in a batch anaerobic digester enriched with CO_2. The production of biomethane from biogas always copes with the formation of CO_2 as a by-product. This by-product CO_2 may be recycled through feedstock which is supplied to the bioreactor as raw material. For this reason, laboratory experiments with CO_2 injection into dairy manure as a pre-treatment method for biogas production were performed.

METHODS

The research methodology consists of two stages. First stage - *dairy manure* (D.M.) pre-treatment with CO_2. Second stage – CO_2 pre-treated D.M. is loaded into a biogas digester.

First stage: D.M. was taken from a litre less dairy farm in southwestern Lithuania. The manure was packaged in an airtight container of 20 litres and stored at 5 °C to be protected from environmental influences throughout the study. D.M. was in a homogenous form, suitable for further pre-treatment. Pre-treatment with the CO_2 injection of dairy manure was performed in a continuously stirred vertical cylindrical gas tight digester with a volume of 3 litres. The digester was custom-made with integrated tubes for the circulation of CO_2 gas. A lower mesophilic temperature was maintained using thermostatic control and an electric heating pad. The substrate was circulated with 100% CO_2 continuously with Schwartzer precision 620 EC-DU-DV pump at the flow rate of 6.5 l/min.

Second stage: Previously untreated and CO_2 pre-treated dairy manure (D.M.) is used for biogas yield and composition research. The second stage is divided into two phases. In the first phase, untreated dairy manure was used for 24 days until a stable biogas yield was reached. In the second phase, the CO_2 pre-treated dairy manure was used for 25 days until stable biogas yield was reached for 10 days.
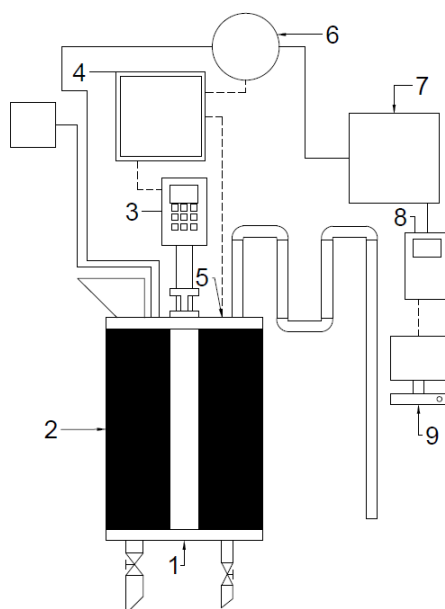

Fig. 1. Scheme of the laboratory biogas digester. 1 - reactor, 2 - heating mat, 3 - mixer controller, 4 - reactor system controller, 5 - temperature sensor, 6 - gas volume meter, 7 - biogas storage tank, 8 - biogas analyser, 9 - data logger

Second-stage experiments were performed in the same laboratory digester (Fig. 1) operated under a mesophilic temperature of 37 ± 1 °C. The daily input to the reactor consisted of 457 g of dairy manure. The water was not used to dilute the dairy manure, as the undiluted volatile solids (VS) content in the D.M. was 7.42%. In this case, a hydraulic bioreactor load of 24 kg/m^3 was maintained, which ensured efficient mixing of the substrate and even distribution of feedstock in the biogas reactor. The volatile solids content of D.M. was determined by samples ignition at 550 ºC. The volumetric organic load of 1.4 kg VS/ (m^{3}d) was used for both experimental research stages. Experimental research was performed in the biogas laboratory of Vytautas Magnus University, Agriculture Academy.

RESULTS

The steady anaerobic digestion process of dairy manure digestion is indicated by the pH of the substrate, which was evenly retained at pH 7.80 ± 0.06 at all 49 days of the continuous experiment with untreated and previously CO_2 pre-treated dairy manure. The pH of untreated D.M. was 7.91 ± 0.09, and the pre-treated pH of D.M. was 7.31 ± 0.08. The pH difference between untreated and pre-treated D.M. was -0.59 ± 0.1.

Results of the first phase of 24 days experiments showed that untreated D.M. itself yielded 114 ± 5 litres biogas from a dry mass kilogram of an anaerobically untreated substrate during laboratory trials at 1.4 kg VS/(m^{3}d) volumetric organic load. Results of the second phase with CO_2 pre-treated substrate for 25 days showed that pre-treated D.M. yielded 135 ± 5 litres

biogas from kg of an anaerobically treated substrate during the same volumetric organic load.

CONCLUSIONS

1. Pre-treatment of dairy manure with CO_2 improved biogas yield from raw material from 114 ± 5 l/kg up to 135 ± 5 l/kg.

2. The anaerobic digestion process of dairy manure was stable, the pH of the substrate remained at pH 7.80 ± 0.06 at all tested organic loads.

3. Further studies are needed to confirm the benefits of CO_2 pre-treatment of dairy manure for the biogas production process. Not only the technical but also the techno-environmental feasibility of the biogas production process must be taken into consideration.

Keywords: biogas, dairy manure, pre-treatment, carbon dioxide injection, feedstock, anaerobic digestion

REFERENCES

1. ALIMAHMOODI, M.; MULLIGAN, C.N. Anaerobic bioconversion of carbon dioxide to biogas in an up-flow anaerobic sludge blanket reactor. 2008. *Journal of the Air & Waste Management Association.* Vol. 58, P. 95–103.

2. SALOMONI, C.; CAPUTO, A.; BONOLI, M.; FRANCIOSO, O.; RODRIGUEZ-ESTRADA, M.T.; PALENZONA, D. Enhanced methane production in a two-phase anaerobic digestion plant, after CO_2 capture and addition to organic wastes. *Bioresource Technol*ogy 2011, Vol. 102, P. 6443–6448.

3. BAJÓN FERNÁNDEZ, Y.; SOARES, A.; VILLA, R.; VALE, P.; CARTMELL, E. Carbon capture and biogas enhancement by carbon dioxide enrichment of anaerobic digesters treating sewage sludge or food waste. *Bioresource Technol*ogy 2014, Vol. 159, P. 1–7.

I.3. Energy efficiency, reliability and security

PASSIVE HOUSE DESIGN IN AMMAN CITY

R. Albadaineh
German Jordanian University
Naji Alhabashneh, 11937 – Jordan
+962797700017
renadaabadayneh@gmail.com

EXTENDED ABSTRACT

OVERVIEW

The residential sector in Jordan accounts for 21% of the net energy consumption and 43% of the total electricity consumption. More than 60 % of the energy consumed in households is used for space heating and cooling. The simulated house has a 186 m² usable floor area which is a typical one-story Jordanian house in Amman city, it was designed to improve its energy performance by implementing retrofitting strategies to reduce heating and cooling loads, achieve minimum energy demand, and obtain high-quality the indoor living environment. Several passive design strategies and techniques were carried out to reach the concept of passive design houses, as illustrated sufficiently in this paper. The impact of each retrofit method was assessed using Design Builder simulation software and Revit software for modelling and the evaluation of the total energy consumption before and after the implementation of passive design methods. The net utilized energy in the simulated building was reduced from 56.57 kWh/m² to 15.25 kWh/m² on an annual basis. The findings of this study indicate that the annual energy saving for heating is about 78% and the indoor air quality and temperature of the house can be improved dramatically compared to their original status.

METHODS

Our case study building specifications and characteristics are listed in Table 1, and our target is to improve the thermal performance of this building and convert it to a passive house design using various strategies that will be mentioned later.

THE BUILDING CHARACTERISTICS

Table 1. Baseline model specifications and characteristics.

The Model specifications	Baseline model
Number of floors	1
Total floor area	186 m²
Number of rooms	9
External walls(U-value)	0.563 W/m². k
Internal walls) U-value)	2.5 W/m². k
Roof(U-value)	0.535 W/m². k
Ground floor(U-value)	1.877 W/m². k

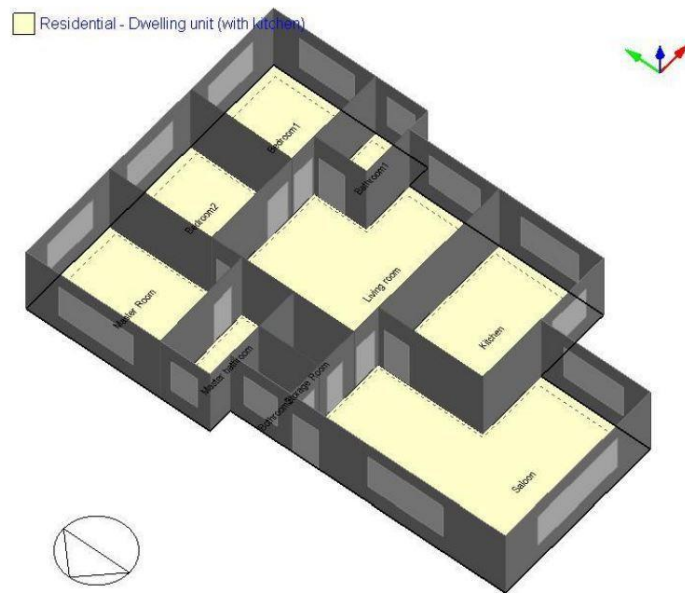| Window frame type	Aluminium frame with polyvinyl chloride (PVC),5.014 W/m². k
Glazing type + U-value	Double glazing with 3.094 W/m². k

Fig. 1. 3D overview of the baseline model

Table 2. Passive design model specifications and characteristics.

The model specifications	Baseline model
Number of floors	1
Total floor area	186 m²
Number of rooms	9
External walls(U-value)	0.158 W/m². k
Internal walls) U-value)	1.048 W/m². k
Roof(U-value)	0.169 W/m². k
Ground floor(U-value)	0.288 W/m². k
Window frame type	Polyurethane (PU) foam with Polyvinylchloride(PVC), 0.799 W/m². k
Glazing type + U-value	Double glazing with argon filled, 1.041 W/m². k

CLIMATE CONDITIONS ANALYSIS OF THE INVESTIGATED AREA

Climate conditions evaluation is an essential guide for energy system design and integration because the energy consumption depends on the outside temperature. Figure 5 shows the minimum and maximum values of the monthly temperature distribution. The annual highest temperature is 32.4 °C in August, and the lowest temperature is 3.6 °C in January. [1] In the simulation of the building, based on the ASHRAE standard, the heating set point was considered 18 °C, and the cooling set point was considered 27 °C.
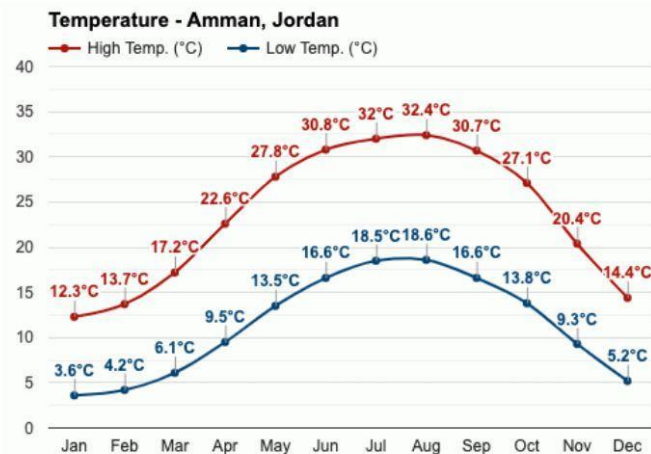
Fig. 2. Monthly average temperature distribution in Amman city.

DESIGN ANALYSIS AND PERFORMANCE OF THE BUILDING THROUGH SIMULATION

"The energy performance of a building becomes efficient only when the occupants of the buildings feel thermal comfort. According to the ASHRAE standard, thermal comfort is defined as "a condition of mind which expresses a satisfaction with the thermal environment" and is rated by the people who occupy the building. So, we can only assume that thermal comfort depends on factors such as air temperature, humidity, and air ventilation, all of these factors depend on the perception of each person. Therefore, to reach thermal comfort in the building, it is necessary to have a balance of energy consumption for heating or cooling in correlation to the indoor temperature, humidity level and ventilation ratio" [2].

Simulation Phases: Building form and aspect ratio for passive house design, Orientation, Zoning and planning, Building envelope components, External walls, Insulation material, Roof, Windows and glazing, Daylight access design factors, Natural ventilation, Landscape strategies, Implementation of shading devices, lighting analysis.

Five Main Requirements to achieve the passive house standards: Specific space heating demand < 15 kWh/m², Specific cooling demand < 15 kWh/m², Specific primary energy demand < 120 kWh/m² including electrical appliances, Air leakage mustn't exceed 0.6 ac/h, Fresh air demand 30 m³/h/person. [3]

Design strategies used to achieve the passive house that was implemented in our proposed design: Super Insulation, highly insulated windows, Passive solar gain, Orientation, zoning and planning, and Natural ventilation strategies.

RESULTS
1. Heating and cooling design
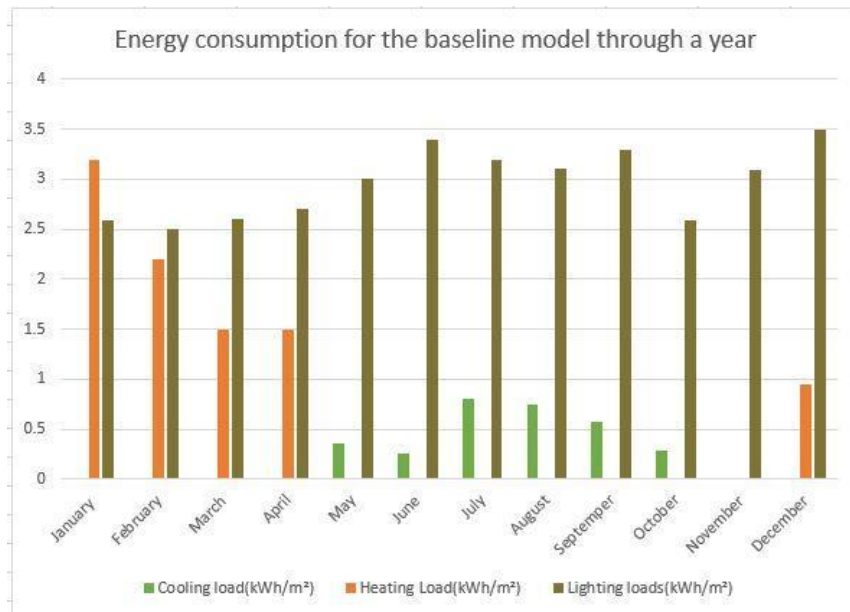
Fig. 3. Energy consumption values before implementing the retrofit strategies.
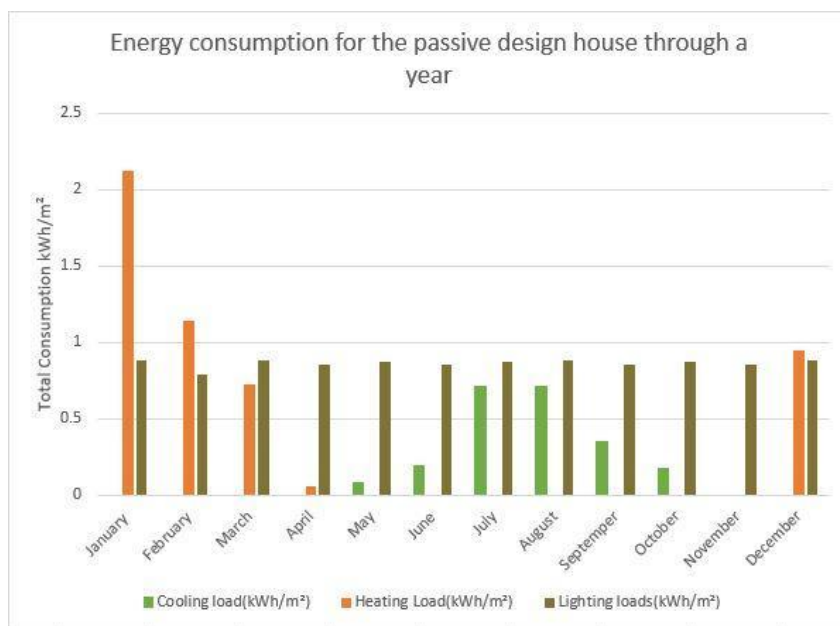
Fig.4. Energy consumption values after implementing the retrofit strategies.

2. Temperature and heat loss analysis
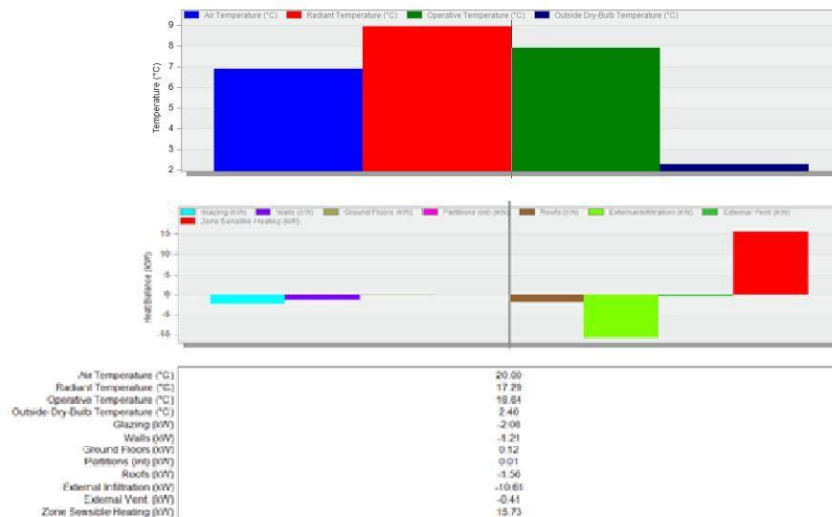
Fig. 5. Temperature and heat loss analysis in the baseline model.
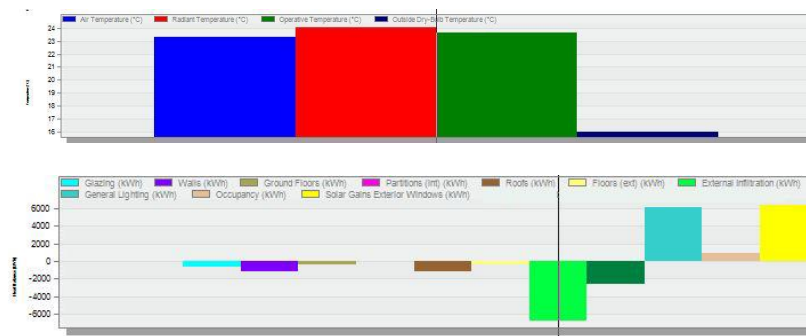
Fig. 6. Temperature and heat loss analysis in the Passive design model.

Table 3. Losses through the building before and after the implementation of the passive design strategies.

Losses types	Baseline model (kW)	Retrofitted model (kW)
Glazing losses	-2.08	-0.079
walls	-1.21	-0.129
Roof	-1.56	-0.13
External infiltration	-10.61	-0.78
Zone sensible heating	15.73	3.83
External ventilation	-0.41	-3.25

3. Solar Gain analysis.
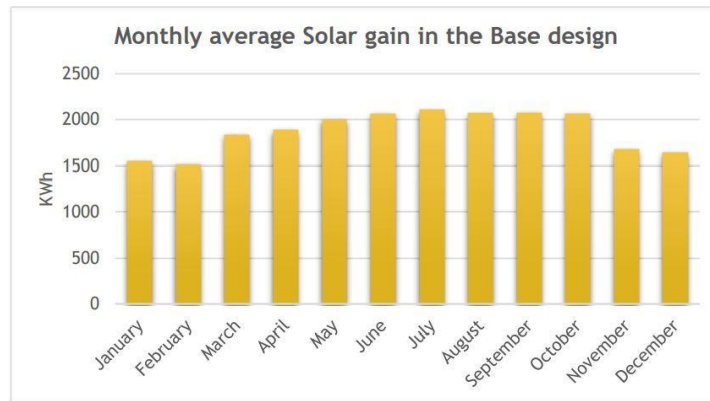
Fig. 7. The monthly average solar gain in the base design.
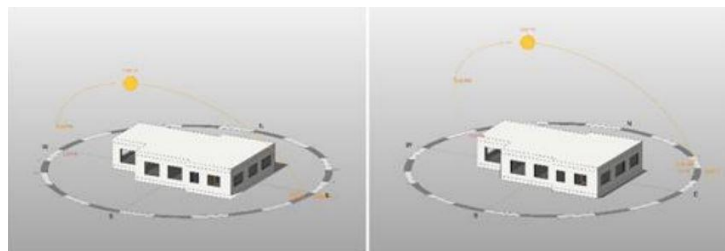
Fig. 8. Solar profile for the base design in winter and summer.
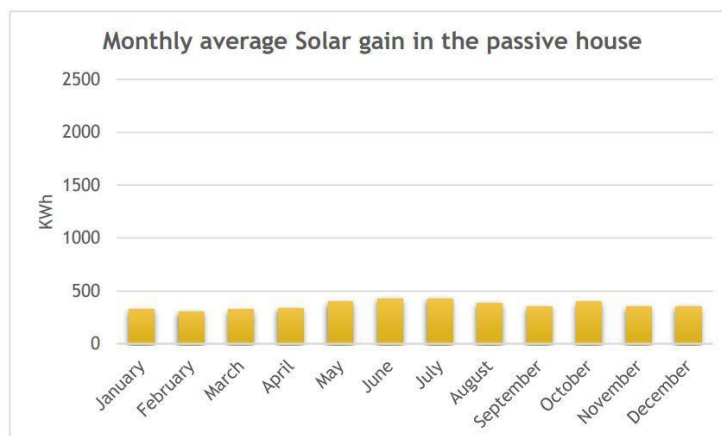
Fig. 9. Monthly Average Solar Gain in the Passive House.
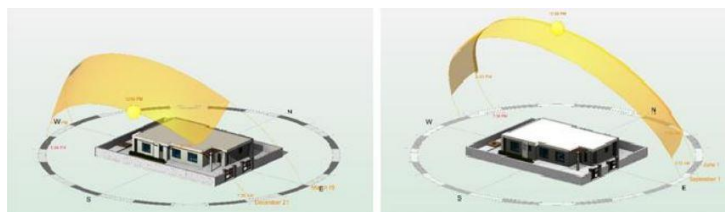
Fig. 10. Solar profile for the passive house in winter and summer.

CONCLUSIONS

A simulation study to improve the energy performance of a house by retrofitting in Amman, Jordan, is presented in this paper. This dwelling was retrofitted using passive energy-saving methods, and it aims to reduce the annual energy consumption. This base house consumed 56.57 kWh/m² of energy for heating, cooling, and lighting, and the house's average

temperature in winter was 9°C. After retrofitting, the actual data shows the energy load was reduced to 15.25 kWh/m². The indoor temperature in the winter reached 18°C, which is much more than the temperature of the base design. And the solar gain was reduced in the passive design due to using a shading device to minimize the indoor temperature during the summer season.

Keywords: (Low carbon buildings, Energy efficiency, Passive house design strategies, Thermal simulation, zero energy buildings, Building energy performance).

REFERENCES

1. Amman, Jordan - Detailed Climate Information and Monthly Weather Forecast. Weather, [referred on the 14th of May in 2021 y.] Link to the internet: <https://www.weather-atlas.com/en/jordan/amman-climate >.

2. JENNIFER, I.A.; HOY, R.; BOHANON, J.; WAYNE THOMANN, R. Ventilation for Acceptable Indoor Quality,©ASHRAE, 2020. 93 p.

3. DICAIRE, D. passivehousecanada, 2022. [referred on the March in 2022 y.] Link to the internet: < https://www.passivehousecanada.com/about-passive-house/>

THE DESCRIPTION OF THE RESULTS MUST BE MADE MORE SPECIFIC IN ANY GENERAL SENTENCESTESTING AND EVALUATING NORMS FOR HOT WATER STORAGE TANKS

M.Sc. T. Bischoff

Bundesanstalt für Materialforschung und -prüfung
Unter den Eichen 87, 12205 Berlin – Germany
+49 30 8104 - 4636
tristan.bischoff@bam.de

EXTENDED ABSTRACT

OVERVIEW

In recent years, domestic space heating has been identified as one of the major fields to improve with regard to the reduction of global CO_2 emissions. Typical heating systems consist of the following main components: A heat source, e. g. gas-boiler, heat pump, pellet-oven etc., heat dissipators, piping and -in many cases- a heat storage tank. This tank is usually well insulated and serves as a buffer tank for space heating and can as well be used to heat domestic hot water for showers and hot water taps. By utilizing hydraulically decoupled heating circuits, it becomes possible for the domestic hot water to be heated the same way as in a water heater, avoiding downtimes and the growth of legionella. In fulfilling all these different functions, the hot water storage tank is an interesting and remarkably complicated component in many regards: it is often connected to several heating circuits as a hydraulic bridge. It does not use fuel on its own. It rather processes the heat fed into it by the heat source(s) of the heating system to their destined uses. This, of course, also depends on the makeup of the system in real property. Therefore, testing hot water storage tanks the proper way has been an ongoing topic in norm- and law-making.

Hot water storage tanks have multiple purposes: Firstly, they serve as a buffer in the space-heating system of a house, providing a kind of compensation for when the heat demand rises abruptly, but the heat source has not generated sufficient heat output yet. Secondly, it is possible to generate domestic hot water within a heat exchanger in the basement of the building as a central source of hot water as opposed to decentralized solutions using electric water heaters, for example. Additionally, connecting many different heat sources with different temperature levels to a hot water tank in a technologically clean fashion (i.e., through the use of stratification-enhancing tank construction and/or control technology) provides the opportunity to save resources by using low-temperature heat sources (solar/underground heat reservoirs tapped by heat pumps) as a source of extra energy. There are several more benefits gained by enhanced space heating designs utilizing heat storage tanks, although economic and ecological concerns need to be considered in conjunction with one another, so a heat storage tank does not always represent the optimal solution to a heat-related issue. Regarding further proliferation of the adoption of heat pumps as a source of renewable heat, storage tanks and their testing norms play a key role in building well-performing heating systems on almost any scale, from small-scale domestic applications to large-scale building complex heating systems as well as industrial applications.

The testing norms currently in existence were examined in our government-funded project (NAPE-project in short). The aim was to evaluate existing technological standards against an intentionally wide variety of test samples in order to reveal presumed weaknesses in either coverage of the field of available devices and weaknesses in the testing procedures themselves. Both of these topics are highly sensitive within the testing institutions, but the overlaying need for improvements in this regard exists.

METHODS

The applied method of evaluating our existing testing norms has been that of the **round-robin trial (RRT)**. In this trial, a single arbitrarily chosen test sample is sent from lab to lab, which all perform the (ideally) same series of actions to determine the efficiency of the device. In the case of our hot water storage tank, the norm EN 12977 or 12897 is applied to determine the standing heat losses of the tank. The norm which is actually chosen depends on the equipment of the laboratory. This alone is the first hint of why hot water storage testing is so special: there are multiple norms currently being used to determine the same physical value: the standing heat losses. These losses, in return, determine the energy class of the storage tank according to the EU energy labels. Adjusting existing regulations to an ever-changing technological market is key to making energy labels as a means of CO_2 reduction work.

RESULTS OF THE RRT
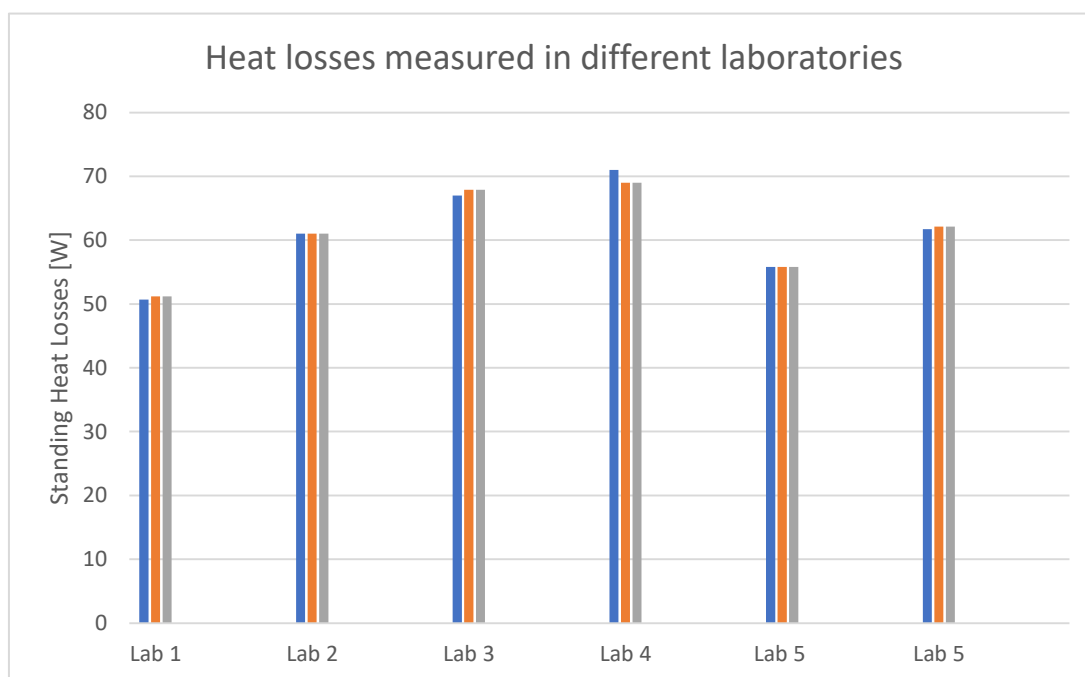
Fig. 1: Testing Results from the RRT with a 200-litre insulated hot water storage tank with a heat exchanger as a test sample

As shown above, in Fig. 1, the Results differ among the various testing labs and beyond that, as is the case with lab 5, between different methods used as prescribed in the appropriate norm. In this special case, each of the testing methods of EN 12897 was repeated a total number of three times. According to our expectations, the deviation between the respective measurement runs with the same method is low. What strikes us as peculiar is the systematic deviation between the two measurement methods: The direct measurement method utilizing

the power consumption of an electrical heating rod has an, on average, 10% lower calculated heat loss than the indirect method, in which the storage tank is loaded and unloaded.

As for the other labs, they were free to choose between methods. The variations in their results, however, cannot solely be explained by the measurement method deviation alone.

OUTLOOK

The results of the RRT will be the subject of further discussion in law-making going forward, providing statistical evidence for the endeavour of changing existing norms and regulations. These concerns topics such as how to handle degradation of the sample over time, as factory new devices tend to have different and often better test results regarding energy efficiency than those with signs of wear. A greater topic regarding norms, in general, is also how specific the instructions given in a norm have to be. This shows an interesting conflict in designing testing norms: On the one hand, nonspecific instructions bear the risk of being misunderstood or interpreted in too big of an interval to provide consistent test results for each of the different testing labs. On the other hand, overly specific requirements for testing run the risk of being outdated quickly or simply being too impractical to be widely adopted as new standards. Balancing these two out is one goal of designing norms.

REFERENCES

1. Commission Delegated Regulation (EU) No 812/2013 of 18 February 2013 supplementing Directive 2010/30/EU of the European Parliament and of the Council with regard to the energy labelling of water heaters, hot water storage tanks and packages of water heater and solar device (Text with EEA relevance) [referred in the 9th of March in 2022 y.]. <http://data.europa.eu/eli/reg_del/2013/812/2018-04-26>.

2. Commission Regulation (EU) No 814/2013 of 2 August 2013 implementing Directive 2009/125/EC of the European Parliament and of the Council with regard to ecodesign requirements for water heaters and hot water storage tanks (Text with EEA relevance) [referred in the 9th of March in 2022 y.]. <http://data.europa.eu/eli/reg/2013/814/2017-01-09>

EXPERIMENTAL INVESTIGATIONS OF THE OPERATION MODE OF A HEAT PUMP APPROPRIATE TO AN AIR HANDLING UNIT

A. Frik, J. Bielskus
Vilnius Gediminas Technical University
Saulėtekio al. 11, LT-10223 Vilnius – Lithuania
anton.frik@vilniustech.lt

EXTENDED ABSTRACT

OVERVIEW

More than a third of the world's final energy consumption is in the buildings sector [1]. In the European Union (EU), the main consumers of energy in buildings are heating, ventilation and air conditioning (HVAC), which account for half of the EU's energy consumption [2]. Among HVAC systems, mechanical ventilation systems play an increasingly important role in the engineering systems of buildings. In modern, well-insulated and airtight buildings, a mechanical ventilation system is a necessity to ensure the highest level of indoor air quality (IEQ) without compromising thermal comfort in buildings in cold climates [3]. Therefore, it is worth looking for technological solutions that increase the energy efficiency of the ventilation system. Appropriate adaptation of a heat pump (HP) to work in a ventilation system is one way to effectively ensure the required but constantly changing heat demand of a system in a cold climate zone [4]. It is important to note that in our case, the heat pump is adapted to the needs of the ventilation system and does not perform the function of the main heating system. The heat pump performs the function of heat recovery/regeneration for the ventilation system, allowing the air supplied by the air handling unit to be heated to the design temperature due to the thermal energy of the exhaust air. This means that the heat pump does not have to compensate for heat losses through external walls or internal heat gains. Thus, in this case, the ventilation system has a certain design supply air temperature, which must be provided over the entire range of outdoor air temperature changes, regardless of internal heat accumulation, the thermal resistance of enclosing structures, or inflow. A change in the temperature of the exhaust air from the room will affect the operation of the heat pump, but the design temperature of the supply air will remain the same. Since there is no heat accumulation in this type of system, the HP for the air handling unit (AHU) must respond immediately to the ever-changing heat demand of ventilation; otherwise, the ventilation system may supply low-temperature air directly to the occupant area, which may cause discomfort or a feeling of the draft, which adversely affects human health. Therefore, ON / OFF or staged operating modes of HP compressors are not suitable for integration into AHUs. In addition, the operation of a variable speed compressor is more efficient compared to staged or ON / OFF operating modes [5–7]. The previous parametric analysis of an AHU [8] revealed the dependencies between the change in the operating cycle of an HP built into the AHU and the change in the outdoor air temperature, which determine its high momentary and seasonal energy efficiency.

The purpose of this work is to determine the correspondence between the operation of an HP with two degrees of control (variable speed compressor and electronic expansion valve) and

the dependences obtained in the analytical model in the presence of an energy demand generated by a variable outdoor temperature. For this purpose, experimental studies were carried out on a specially designed stand.

METHODS

In previous studies [8], a thermodynamic analysis of the characteristic energy conversions of an AHU with an integrated HP has been performed, relating the parameters of air and refrigerant. Figure 1 shows the tendencies of HP condenser, and evaporator isothermal temperature changes obtained in this parametric analysis, which would allow to achieve high efficiency of the HP integrated into the AHU (Fig. 2). These tendencies dictate the concept of optimal HP control, the implementation of which is planned to be experimentally verified in this paper.
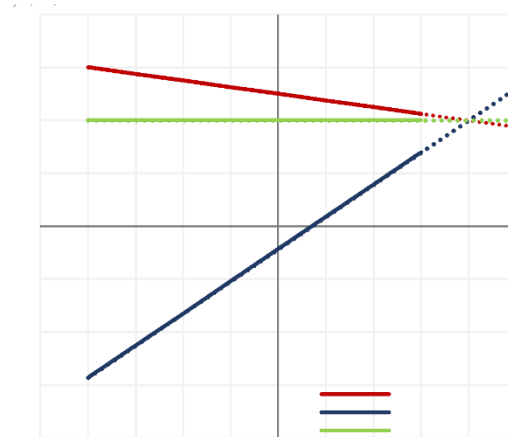
Fig. 1. Refrigerant temperatures T^{CNizot}, T^{EVizot} and room air temperature T^r depending on outdoor air temperature T^l [8]
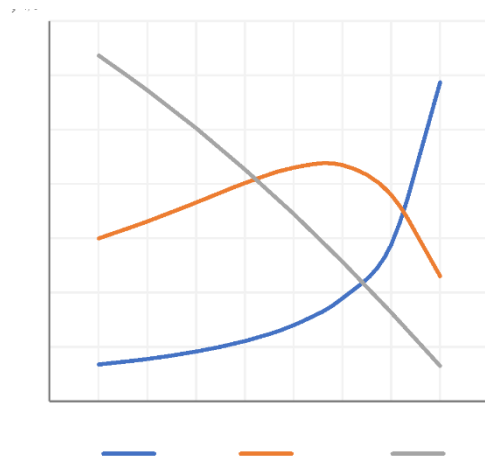
Fig. 2. Coefficient of performance (COP) of HP, AHU and refrigerant flow rate depending on outdoor air temperature T^l [8]

For experimental verification of the dependences obtained in the parametric analysis, an experimental stand of an HP for an AHU was designed and manufactured. At the design stage of the stand, a review and analysis of experimental stands of other researchers of a similar design or purpose were carried out [9]. This experimental study analyses the energy

conversion processes in an AHU, the main energy converters of which are an HP and a heat recovery exchanger (HRE). The scheme of the experimental stand is shown in Figure 3. The HP consists of a condenser (CN), 2 evaporators (EV[1] and EV[2]), a compressor (CM) and electronic expansion valves (EEV[1] and EEV[2]). Together with two fans (supply - F[s] and exhaust - F[e]) and the already mentioned ventilation HRE, we have an experimental stand that simulates the functionality of an AHU. The connection of the air supply, exhaust fans and heat exchanger to the HP heat exchangers is provided via flexible ducts. A photo of the installed stand is shown in Figure 4.
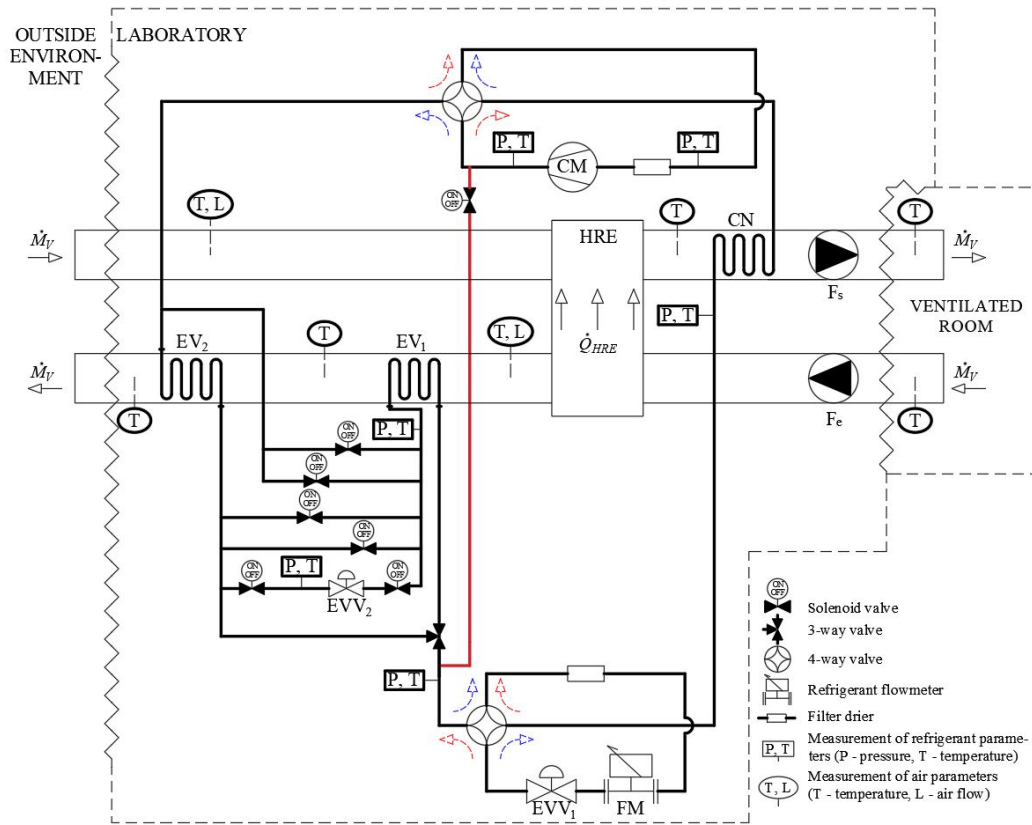
Fig. 3. Scheme of the experimental stand of the HP for the AHU

The stand is also equipped with equipment for measuring air and refrigerant parameters. On the air side, temperature sensors and calibrated diaphragms are installed to measure the air flow. Differential air pressure sensors are installed near the diaphragms to determine the flow rate of air supplied and exhausted by the system. Devices for measuring the pressure and temperature of the refrigerant are provided in the HP circuit after each of the main units (CM, CN, EEV[1,2], and EV1[-2]). A flow meter is provided on the liquid phase side of the refrigerant.

Fig. 4. Experimental stand of an HP for an AHU

RESULTS

Experimental tests were carried out on the operating mode of an HP for an AHU, in which the compressor speed (from 3000 to 8000 rpm) and the throughput of the EEV (from 20 to 80%) were changed. One of the graphs of the obtained results is shown in Fig. 5.
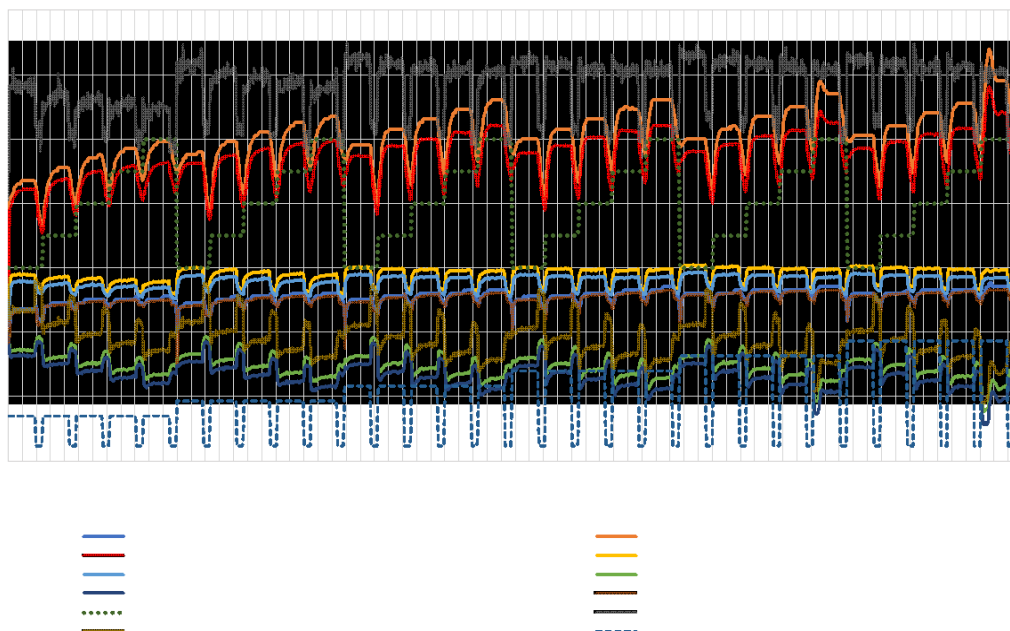
Fig. 5. Summary graph of refrigerant parameters obtained during the experiment

The graph in Figure 5 shows the range of change in the refrigerant parameters. The temperature of the refrigerant after the EEV represents the isothermal temperature of the

evaporator. The isothermal temperature of a condenser is represented by the temperature of the refrigerant after the condenser. Although the changes in the evaporator isotherm in the selected range of outdoor air temperatures (3–8 °C) resemble the optimal trends obtained in the parametric analysis, the course of change in the condenser isotherm is not close to them.

CONCLUSIONS

Preliminary experimental studies show that the change in the operating cycle of the HP in the investigated or extrapolated range of parameters is not close to optimal. It is necessary to look for additional cycle control measures since the traditional ones (VSC and EEV) are not enough to achieve the trends in the operation of the HP obtained in theoretical studies. One such measure could be a compressor with operating characteristics obtained from these studies.

Keywords: air handling unit with integrated heat pump, experimental studies, operating mode, air source heat pump.

REFERENCES

1. Global status report for buildings and construction: towards a zero-emission, efficient and resilient buildings and construction sector. United Nations Environment Programme, 2021 [referred on the 7th of January in 2022 y.]. Link to the internet <https://globalabc.org/resources/publications/2021-global-status-report-buildings-and-construction>.

2. EUROPEAN COMMISSION 2016. An EU strategy on heating and cooling 2016.

3. LST EN 16798-1. Pastatų energinis naudingumas. Pastatų vėdinimas. 1 Dalis. = Energy performance of buildings – Ventilation for buildings. Part 1. Vilnius: Lietuvos standartizacijos departamentas (Lithuanian Standardization Department), 2019.

4. MARTINAITIS, V.; STRECKIENE, G.; BAGDANAVICIUS, A.; BIELSKUS, J. A comparative thermodynamic analysis of air handling units at variable reference temperature. Applied Thermal Engineering, 2018, Vol. 143, P. 385-395.

5. DONGELLINI, M.; MORINI, G.L. On-off cycling losses of reversible air-to-water heat pump systems as a function of the unit power modulation capacity. Energy Conversion and Management, 2019, Vol. 196, P. 966–978. Doi:10.1016/j.enconman.2019.06.022.

6. APREA, C.; MASTRULLO, R.; RENNO, C. Experimental analysis of the scroll compressor performances varying its speed, Applied Thermal Engineering, 2006, Vol. 26, No. 10, P. 983-992.

7. DONGELLINI, M.; ABBENANTE, M.; MORINI, G.L. A strategy for the optimal control logic of heat pump systems: impact on the energy consumptions of a residential building. Proceedings of the 12th IEA Heat Pump Conference, 2017.

8. FRIK, A.; MARTINAITIS, V.; BIELSKUS, J. Energy conversion modes depending on the outdoor temperature for an air handling unit with a heat pump. The 11th International Conference "Environmental Engineering". Vilnius: Vilnius Gediminas Technical University. 2020.

9. FRIK, A.; BIELSKUS, J. Experimental test stand of a heat pump integrated in air handling unit. Mokslas – Lietuvos ateitis / Science – Future of Lithuania, 2020, Vol. 12, P. 1-6

POSSIBILITIES OF THE WASTE HEAT RECOVERY FROM INDUSTRIAL PROCESSES

M. Salem, R. Poškas
Lithuanian Energy Institute
Breslaujos g. 3, LT-44403 Kaunas – Lithuania
+370 62212130
Mohab.Salem@lei.lt

EXTENDED ABSTRACT

OVERVIEW

Energy efficiency is no longer a matter of question nor a luxury. The escalating energy consumption, besides the fossil fuel depletion, made it crystal clear for a foreseen rise in energy prices [1]. In 1970, there was a high surge in industrial fuel prices because of the Middle East oil crisis. Concurrently, many countries had a great influence on redirecting investments to more ecological alternatives and societal-friendly technologies. Since then, more investments have been injected into renewable energy sources, including heat recovery technologies. Nevertheless, this trend faded away thanks to the drop in fuel prices in the mid-1980s. Yet, the energy efficiency procedures had the spotlight again in 2005 because of the increase in fuel prices. Once again, the Kyoto protocol coronated years of endeavours to abate greenhouse gasses (GHGs) and forced energy-intensive industries to cut down emissions [1]. As such, paramount legislation was adopted to mitigate the environmental impact; according to the COP26, the United Nations (UN) raised the bar, the GHG ought to be around 5 billion tonnes lower by 2030 [2].

Around 12 PWh per year is wasted annually as heat energy from the global energy consumption, which comprises 72% [3]. This energy can be classified as follows:
- The low temperature is below 200 °C and seizes about 66%.
- The medium temperature is between 200 and 500°C and makes 25%.
- High temperature, which is above 500°C and makes 9%.

Wasted energy comprises about one-third of the total thermal energy use in the industrial sector. A remarkable amount of this energy can be recovered to increase energy efficiency in industrial processes and reduce greenhouse gases. Food, tobacco, pulp and paper, basic metals, chemical industry and non-metallic minerals are the industries where a considerable amount of waste heat can be exploited [4]. Waste heat recovery technologies can be utilized for many purposes, for instance, providing heating, cooling and electricity. Therefore, these can be classified according to their area of application:
- Recovery as hot air or steam (direct utilizing: heat delivery to district heating or cooling or preheating)
- Conversion to chemical energy as fuel (power utilizing: electricity generation using a generator)
- Thermoelectric power generation (cascade utilization: combining heating, cooling and power) [5].

Although the European waste heat recovery market worth was expected to go beyond €45 billion by 2018, waste heat recovery technologies are still a critical decision for manufacturers and investors [6]. The prime reason is economic efficiency which dwarfs energy efficiency. This is based on the statement that energy efficiency procedures are not always profitable or feasible economically [1]. Consequently, major changes had to be made to the business model to avert any foreseeable impact on the company's profitability [1].

Waste heat recovery in Lithuania may have other aspects, the Baltic States owe an inheritance of extravagant usage of energy resources [7]. As such, Lithuania resorted to restructuring the whole energy sector [8]. In the course of this transformation, Lithuania aims to diversify its energy supply, reduce the reliance on fossil fuels, increase the share of renewable energy and take advantage of wasted heat [9]. The following references explain Lithuanian's intention to utilize waste heat either in industrial processes or district heating, but they did not elaborate any detail on the potential of this policy and the exact outcome and energy savings or its economic efficiency [9], [10] and [11]. Nevertheless, waste energy has been scattered and implemented in many industries in Lithuania, such as textile, chemical, leather, manufacture of metal products and other industries [7].

As mentioned earlier, the implementation of waste heat recovery is a conundrum for investors and experts. The complexity involves the determination of available waste heat energy that can be recovered and the best technology to be used. These technologies aim to reuse the heat recovered via a dirty gas or a dirty liquid medium in the system once again for maximum utilization of the energy input. The recovered head can participate in heat generation and electrical or mechanical power. Waste heat recovery technologies primarily consist of heat exchangers beside other heat recovery systems such as air preheaters, regenerators, recuperators, regenerative burners, heat pipe heat exchangers and direct electric conversion devices [12].

Therefore, in the presentation detailed analysis of the information on the possibility of waste heat recovery in different industrial processes with special emphasis on the Lithuanian case.

Keywords: Waste heat recovery, Industry, Dirty heat sources, Review

REFERENCES

1. WOOLLEY, E.; LUO, Y.; SIMEONE, A. Industrial waste heat recovery: A systematic approach. *Sustainable Energy Technologies and Assessments,* 2018, Vol. 29, P. 50–59. Doi: 10.1016/j.seta.2018.07.001.

2. *COP26-Presidency-Outcomes-The-Climate-Pact.pdf*. Accessed: Jan. 07, 2022. Link to the internet: https://ukcop26.org/wp-content/uploads/2021/11/COP26-Presidency-Outcomes-The-Climate-Pact.pdf

3. GAROFALO, E.; BEVIONE, M.; CECCHINI, L.; MATTIUSSI, F.; CHIOLERIO, A. Waste Heat to Power: Technologies, Current Applications, and Future Potential. *Energy Technology.* 2020, Vol. 8, No. 11, P. 2000413. Doi: 10.1002/ente.202000413.

4. BRÜCKNER, S.; LIU, S.; MIRÓ, L.; RADSPIELER, M.; CABEZA, L.F.; LÄVEMANN, E. Industrial waste heat recovery technologies: An economic analysis of heat transformation technologies. *Applied Energy,* 2015, Vol. 151, P. 157–167. Doi: 10.1016/j.apenergy.2015.01.147.

5. AGATHOKLEOUS, R.; BIANCHI, G.; PANAYIOTOU, G.; ARESTI, L.; ARGYROU, M.C.; GEORGIOU, G.S.; TASSOU, S.A.; JOUHARA, H.; KALOGIROU, S.A.; FLORIDES, G.A.; CHRISTODOULIDES, P. Waste Heat Recovery in the EU industry and proposed new technologies. *Energy Procedia,* 2019, Vol. 161, P. 489–496. Doi: 10.1016/j.egypro.2019.02.064.

6. JOUHARA, H.; OLABI, A.G. Editorial: Industrial waste heat recovery. *Energy*, 2018, Vol. 160, P. 1–2. Doi: 10.1016/j.energy.2018.07.013.

7. KLIOPOVA, I.; STANIŠKIS, J. Application of Waste Energy Utilization Techniques in Lithuanian Industry. *Environmental Research, Engineering and Management*. 2006, P. 32–42.

8. JONYNAS, R.; PUIDA, E.; POŠKAS, R.; PAUKŠTAITIS, L.; JOUHARA, H.; GUDZINSKAS, J.; MILIAUSKAS, G.; LUKOŠEVIČIUS, V. Renewables for district heating: The case of Lithuania. *Energy*, 2020, Vol. 211, P. 119064. Doi: 10.1016/j.energy.2020.119064.

9. *National Energy and Climate Action Plan of the Republic Of Lithuania for 2021-2030.* [Referred on Feb. 22, 2022]. Link to the internet: <https://ec.europa.eu/energy/sites/ener/files/documents/lt_final_necp_main_en.pdf>.

10. *Lithuania - the United Nations. chapter5.pdf.* [referred on the Feb. 22, 2022.]. Link to the internet: <https://www.un.org/esa/sustdev/publications/energy_indicators/chapter5.pdf.>

11. *International Energy Agency*, Lithuania 2021 Energy Policy Review. OECD, 2021. Doi: 10.1787/db346bb1-en.

12. JOUHARA, H.; KHORDEHGAH, N.; ALMAHMOUD, S.; DELPECH, B.; CHAUHAN, A.; TASSOU, S.A. Waste heat recovery technologies and applications, *Thermal Science and Engineering Progress*, Jun. 2018, Vol. 6, P. 268–289. Doi: 10.1016/j.tsep.2018.04.017.

THERMOACOUSTIC-TO-MAGNETOHYDRODYNAMIC ENERGY CONVERTER FOR DEEP SPACE FLIGHTS AND POSSIBILITIES TO IMPROVE IT

A. Brekis

Institute of Physics of the University of Latvia
Miera iela 32, LV-2169 Salaspils – Latvia
arturs.brekis@lu.lv

Riga Technical University
Faculty of Electrical and Environmental Engineering
Azenes iela 12/1, LV-1048 Riga – Latvia

EXTENDED ABSTRACT

OVERVIEW

For Deep Space missions, there is a lack of available solar energy in locations far away from the Sun. So, the traditional technology of energy generation that is used as a power supply for deep Space probes is nuclear fuel. Typically, thermoelectric generators can be an option for decades-long Space flights. However, they have very low efficiency, often less than 2%. So, a novel concept [1] is proposed to convert nuclear heat power into electrical energy that is based on the coupling of a thermo acoustic (TAc) engine and magneto hydrodynamic (MHD) generator (Fig. 1). In this approach, the TAc engine converts 1 kW heat to the mechanical form of energy in the form of sound or pressure oscillations. These vibrations are then converted to 200 W electrical energy by using an MHD generator. An MHD generator is an electric machine where liquid metal (sodium on 100°C) is moving in the magnetic field created by permanent magnets [2]. This movement periodically changes its direction. The movement of electrically conducting media in a magnetic field induces an electromotive force that results in an electric current in Na. Further, the magnetic field created by the Na current induces a voltage in the generator's coil that can finally be connected to the electric load [3]. On the contrary, the thermoacoustic cycle is somehow similar to the Stirling cycle, however, with an almost fully different approach. Here, the temperature difference of 800°C applied on the ends of the specific heat exchanger, called regenerator or stack, creates a spontaneous travelling wave of sound inside the engine's working gas (Argon) on the frequency of 50 Hz. This is obtained when 2 thermoacoustic engines are connected in the loop, so one is working as an amplifier to the other one [4].
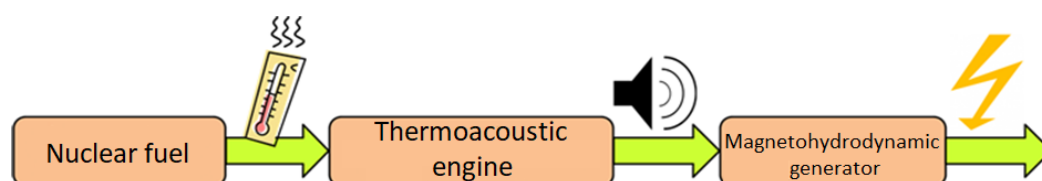

Fig. 1. Concept of thermoacoustic-to-magneto hydrodynamic energy converter "SpaceTRIPS"

The brilliance of this technology is that it doesn't have any moving parts, neither in the TAc engine nor in the MHD generator. The liquid metal is the only moving media. So, it is able to operate without human maintenance for a half-century or even more. In the FP7 project SpaceTRIPS (https://cordis.europa.eu/project/id/312639), the facility was developed, constructed and tested in a sodium laboratory at the Institute of Physics of the University of Latvia (IPUL). A strong team of scientists from France, Italy, Germany, the Netherlands and Latvia were involved. The competence of the team can be justified by the fact that IPUL is the leading institute in the world that has focused exclusively on MHD research for more than 75 years. IPUL have specific stainless steel laboratory equipment for Alkali metal experiments that have no analogues in the world as well as, for example, Dutch company "ASTER" – the worldwide leader in thermoacoustic technologies, that provided sophisticated and unique parts from exotic materials for "SpaceTRIPS" thermoacoustic engine construction. Italy was represented by the company "THALES ALENIA SPACE", which was in charge of proposed technology integration in a Space environment. Finally, France was represented by their leading nuclear company, "AREVA", which was responsible for the "SpaceTRIPS" nuclear fuel concept development. However, an important disadvantage was found for this type of machine. It is the existence of a liquid metal-free surface that can become unstable when it oscillates. Based on the findings of the SpaceTRIPS project, a newly developed MHD generator free surface electromagnetic stabilization method was proposed that in future could increase technology readiness level (TRL) at least by +1.

METHODS

The proposed method of free surface stabilization is based on applying a permanent magnetic field oriented parallel to the direction of the flow (Fig. 2a). In this case, the principle can be explained as follows. When any layer of liquid metal tends to cross the magnetic field lines during the development of the instability, it will immediately induce the electric currents. These currents will interact with the initial magnetic field. It will happen in the way that this field will tend to bring back each deformed liquid metal streamline back to its initial position. Thus, it results in a stabilizing effect on the free surface. To prove this principle experimentally, a test mock-up was created (Fig. 2b) with 2 loudspeakers placed one in front of another, electrically connected in the push-pull regime, connected to a sinusoidal signal generated by a function generator and further connected to an amplifier. The purpose of this is to simulate the work of the TAc engine in a small-scale experiment. On the other hand, the loudspeakers are connected to the 2 transparent cones made from plexiglass and further connected to a U-shaped pipe filled with liquid metal – InGaSn, that will simulate sodium. The Galinstan is chosen due to its low melting temperature of less than 20°C and ease of operation if compared to sodium. On the level of the free surface, the axially magnetized NdFeB permanent magnet is placed as a source of the magnetic field.
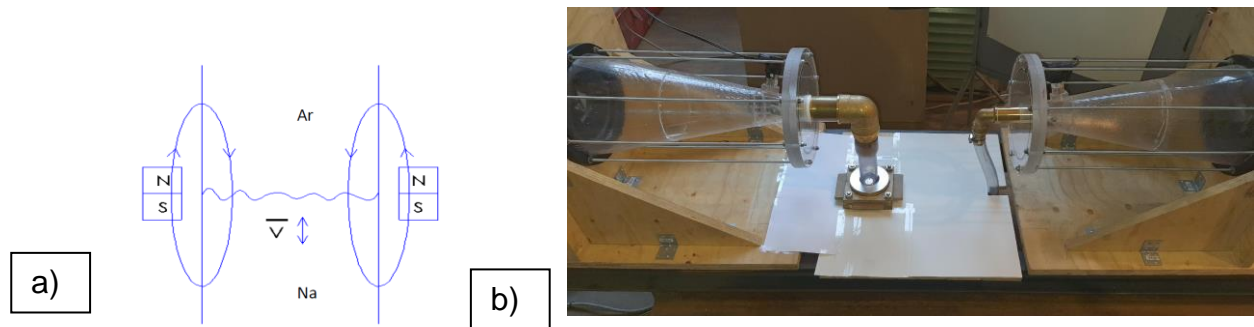
Fig. 2. Liquid metal free surface electromagnetic stabilization method: a) proposed concept; b) built experimental testing stand with loudspeakers

RESULTS

The visual experiment with electromagnetic stabilization was performed on several frequencies, and the stabilization effect was captured on a video camera. The comparison of a case with a magnetic field and without is shown in Fig. 3. It can be seen that a certain stabilization effect is acquired. The magnetic field electromagnetically tends to suppress the liquid metal splashes.

Fig. 3. InGaSn oscillating flow free surface stabilization experiment: a) with the magnetic field created by permanent magnets; b) without magnetic field

CONCLUSIONS

A new concept of liquid metal-free surface electromagnetic stabilization is proposed. Experiments showed that it works, and the stabilization effect can be observed. It can be seen that, in a case with a magnetic field, splashes are jumping at a lower height than in comparison with a case without a magnetic field. So theoretically, it can be implemented in the real "SpaceTRIPS" prototype, thus improving the TRL of the "SpaceTRIPS" facility by at least +1. However, further free surface stabilization experiments should be performed with either a higher magnetic field or in relevant conditions with liquid sodium. This is because sodium electrical conductivity is by an order of magnitude higher than InGaSn. So this would allow having stronger electromagnetic interaction of the liquid metal with a magnetic field. The future scope of this research could involve theoretical or numerical investigation of the described electromagnetic stabilization phenomena.

Keywords: Magneto hydrodynamics, MHD, thermoacoustic, liquid metals, deep Space exploration

REFERENCES

1. BREKIS, A.; FREIBERGS, J.E.; ALEMANY. A. Space thermo acoustic radio-isotopic power system: Space trips, *Magneto hydrodynamics*, 2019, vol. 55, no. 1–2, p. 5–14, doi: 10.22364/mhd.55.1-2.1.

2. GAILITIS, A.; BREKIS, A. Equivalent circuit approach for acoustic mhd generator, *Magneto hydrodynamics*, 2020, Vol. 56, No. 1, P. 3–13. Doi: 10.22364/mhd.56.1.1.

3. BREKIS, A.; ALEMANY, A.; ALEMANY, O.; MONTISCI, A. Space Thermoacoustic Radioisotopic Power System, SpaceTRIPS: The Magnetohydrodynamic Generator, *Sustainability*, 2021, Vol. 13, No. 23, P. 13498.

4. BREKIS, A.; FREIBERGS, J. E.; ALEMANY, A. Initial experimental tests on space trips facility of thermoacoustic-to-mhd energy converter, *Magneto hydrodynamics*, 2020, Vol. 56, No. 2–3, P. 255–267. Doi: 10.22364/mhd.56.2-3.17.

DEVELOPMENT AND INVESTIGATION OF A SYNTHETIC INERTIA ALGORITHM

P. Cicėnas

Laboratory of Smart Grids and Renewable Energy
Lithuanian Energy Institute
Breslaujos g. 3, LT-44403 Kaunas – Lithuania
paulius.cicenas@lei.lt

ABSTRACT

The European Green Deal - a new growth strategy to transform the EU into a fair and prosperous society with a modern, resource-efficient economy in which, by 2050, there will be no greenhouse gas emissions, and economic growth is decoupled from resource use. Energy production and use account for more than 75% of the European Union's (EU) greenhouse gas emissions in all sectors of the economy [1]. The electricity sector must therefore be developed and modernized through the introduction of clean technologies based on renewable energy sources, thus gradually reducing carbon and gas emissions. With each passing year, more and more power sources are being connected to an electricity grid using power electronics [2], [3]. This electricity grid transformation poses new challenges for power system engineers to find new solutions for power-sharing [4], reliable and stable voltage and frequency management [5], and grid stability – from innovative controllers integrated with wind farms [6], [7] to virtual synchronous generator inertia simulation with power frequency drop [8].

The paper presents the methodology to obtain efficient synthetic inertia (SI) algorithm. It allows simulating the inertia response of a traditional generator to an electrical power system. To prove the efficiency of the presented SI algorithm, detailed dynamic calculations were performed in PSSE modelling package using a large real system dynamic model to determine the generator power, angle, voltage, and system frequency change and its angle variation in the presence of a power deficit in the power system. The calculated data were used for comparison between the generated response of the synthetic inertia algorithm at the frequency change of the power system and the conventional generator Fig. 1.
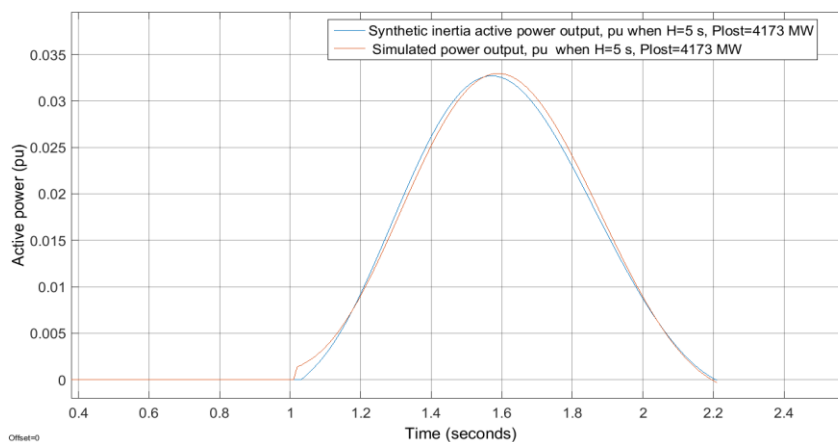
Fig. 1. Comparison of active power outputs of synthetic inertia algorithm and simulated power output, when H=5 seconds and 4173 MW loss of generation

The efficiency of the algorithm was thoroughly investigated using Mean-squared error and Correlation coefficient. The results show that during the active power loss in the power system, the algorithm's active power output is similar to the simulated power output of the generator. Moreover, an obtained algorithm is very convenient to use in the real controller due to its low order transfer function. This algorithm can be easily integrated into controllers of the solar plant, wind farms, and high voltage direct current links to help maintain the power system inertia by injecting synthetic inertia into the power system while the frequency fluctuation exceeds allowable limits.

Keywords: Synthetic inertia, virtual synchronous generator, renewable energy source (RES).

REFERENCES

1. Eur-lex Europa: European Commission, 2019 - [referred on the 5th of March in 2022 y.]. Link to internet <https://eur-lex.europa.eu/legal-content/EN/ALL/?uri=CELEX%3A52019DC0640>.

2. OLIVARES, D.E.; MEHRIZI-SANI, A.; ETEMADI, A.H.; CAÑIZARES, C.A.; IRAVANI, R.; KAZERANI, M.; HAJIMIRAGHA, A.H.; GOMIS-BELLMUNT, O.; SAEEDIFARD, M.; PALMA-BEHNKE, R. Trends in Microgrid Control, IEEE Transactions on Smart Grid, 2014, Vol.5, No. 4, P. 1905-1919.

3. SHRIVASTWA, R.; HABLY, A.; MELIZI, K.; BACHA, S. Understanding Microgrids and Their Future Trends. In Proceedings of the IEEE ICIT. 2019, P. 13-15.

4. BONFIGLIO, A.; BARILLARI, L.; BENDATO, I.; BRACCO, S.; BRIGNONE, M.; DELFINO, F.; PAMPARARO, F.; PROCOPIO, R.; ROBBA, M.; ROSSI, M. Day ahead Microgrid optimization: A comparison among different models. In Proceedings of the OPT-i 2014 - 1st International Conference on Engineering and Applied Sciences Optimization, 2014, p. 1153-1165.

5. FORNARI, F.; PROCOPIO, R.; BOLLEN, M.H.J. SSC compensation capability of unbalanced voltage sags. *EE Transactions on Power Delivery*, 2005, Vol. 20, No. 3, P. 2030-2037.

6. BONFIGLIO, A.; INVERNIZZI, M.; LABELLA, A.; PROCOPIO, R. Design and Implementation of a Variable Synthetic. *IEEE Transactions on Power Systems*, 2019, Vol. 34, No. 1. P. 754-764.

7. GONZALEZ-LONGATT, F.M.; BONFIGLIO, A.; PROCOPIO, R.; VERDUCI, B. Evaluation of inertial response controllers for full-rated power converter wind turbine (Type 4). In Proceedings of the 2016 IEEE Power and Energy Society General Meeting (PESGM), 2016, P. 1-5.

8. D'ARCO, S.; SUUL, J. A.; FOSSO, J. B. A Virtual Synchronous Machine implementation for distributed control of power converters in Smart Grids. *Electric Power Systems Research*, 2015, Vol. 122, P. 180-197.

INVESTIGATION OF WEATHER FORECAST UNCERTAINTY DURING DYNAMIC LINE RATING

E. Csótai, D. Szabó, B. Németh
Department of Electric Power Engineering
Faculty of Electrical Engineering and Informatics
Budapest University of Technology and Economics
Egry József Street 18, 1111 Budapest – Hungary
+36-1-463-5958
csotai.eniko@eszk.org

EXTENDED ABSTRACT

OVERVIEW

From an operational point of view of the electricity system, there is an increasing claim for the higher utilization of transmission capacities. Due to the growing demand for energy, the development of the energy industry, and the integration of renewable energy sources into the power system, some parts of the transmission network can become overloaded. There are several ways to solve this issue, such as building new transmission lines, reconductoring existing lines, and so on. Besides these methodologies, dynamic line rating (DLR) technology offers a more economical solution for the uprating of overhead lines. [1] - [3]

The essence of a DLR system is that with the continuous monitoring of the environmental parameters, a real-time transmission capacity can be determined, which can significantly exceed the currently commonly used static line rating. [4] By planning the generation schedule, it is of paramount importance to take into account the transmission capacity of the power lines. Accordingly, forecasting the transmission capacity of the power lines greatly contributes to efficient trading in the electricity market. However, it requires different weather forecast models. [5]

The aim of this article is to examine the uncertainty of weather forecasts and their effect on line rating prediction. Once the degree of line rating forecast uncertainty has been determined, a safety factor can be established that facilitates a more reliable DLR system.

METHODS

For the forecasting of dynamic line rating, the examination of the uncertainty of different weather forecast models is essential. The inaccuracy of the data provided by weather forecasts should be kept to a minimum or should be corrected in order to avoid potential thermal overloads of the conductors. [6] Accordingly, in the first step of this study, the weather parameters measured by the sensors mounted on transmission line towers are compared with the weather forecasts' output. [7] In the framework of the FARCROSS Horizon 2020 project, weather stations mounted on the towers of four European transmission lines provided the necessary environmental data. For line rating prediction, a weather forecast is provided for each line by an international and an internal weather agency, also,

which are served for the geographical location of the involved transmission lines. Based on the comparison of the weather forecast data and the weather stations' measurements, the influence of the environmental factors on the ampacity (ampere capacity) has been determined. Moreover, the study covers the investigation of weather forecasts' uncertainty. Thus, the obligation for forecast correction is analysed to avoid the thermal overload of the conductors. There are different possible methods distinguished for correcting weather forecast uncertainty. [8]

RESULTS

During the analysis of the weather forecasts in this research, the inaccuracy of each forecast model was determined. By examining the environmental parameters, the influence of each parameter was determined on the line rating calculation [9] [10], and also the correction factors were introduced to eliminate the uncertainty of the forecasts. In the next step, the extra capacity gain is calculated with the weather forecast-based DLR system. A comparison is also presented here to show how the forecast-based system and the transmission capacity calculated on the basis of real-time data relate to each other. Fig. 1 shows that although the forecast-based DLR system is somewhat more conservative, it represents a good tracking of the capacity to meet current environmental conditions.

Fig. 1. Comparison of dynamic line rating calculated based on real-time weather measurements and weather forecast data
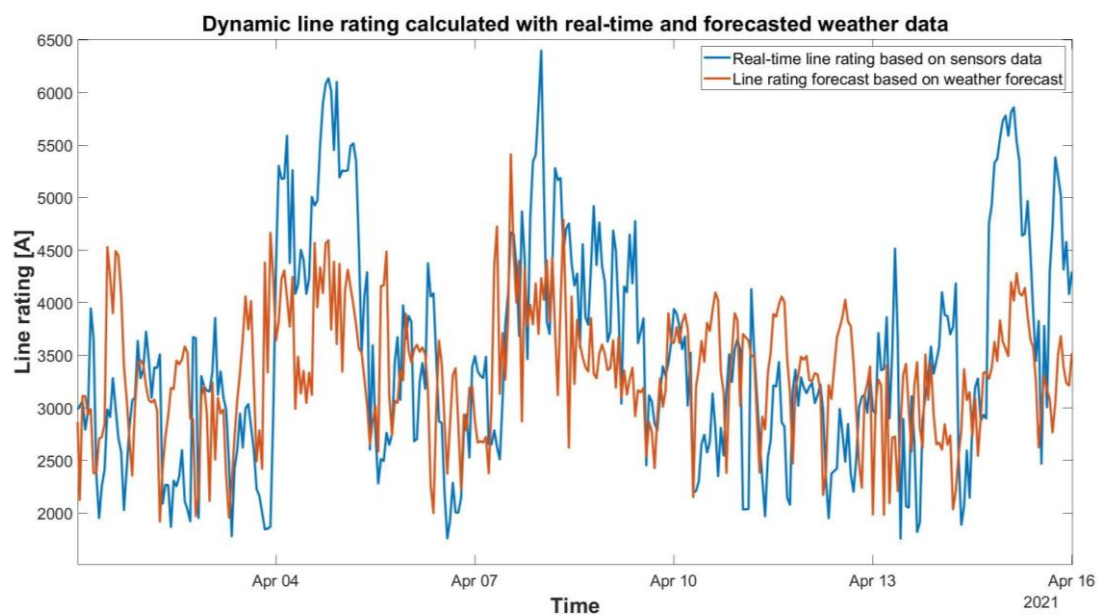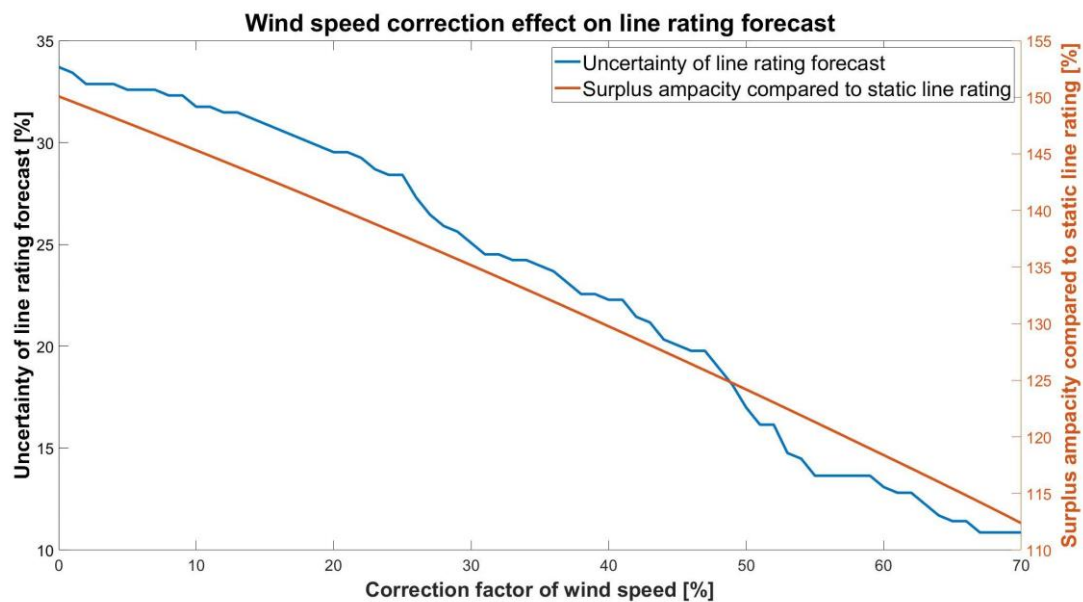
Fig. 2. Correction factor for wind speed and its effect on line rating
forecast

After calculating the line rating, the uncertainty caused by the forecast can be reduced by introducing a correction factor for each environmental parameter, thus, the thermal overloads can be reduced or even avoided. Fig. 2 shows the extent to which the range of the uncertainty can be reduced by correcting the wind speed. However, still remains a considerable extra capacity.

CONCLUSIONS

A DLR system based on the weather forecast can be used as an effective solution for expanding transmission capacity, even in the case of planning generation schedules. By examining the different weather forecasts, it can be concluded that the individual environmental parameters have different influence factors on the calculation of the transmission capacity. However, the uncertainty arising from the forecast must be corrected so that the ampacity determined in this way reduces the risk of thermal overload of the transmission line conductors. The study revealed that the ambient temperature as well as the wind speed and wind direction have the greatest influence on the line rating, so the risk of thermal overloads can be minimized by correcting them. Also, combining the correction of these parameters is also a possible solution, thus increasing the safety factor.

The development of other models also seems to be an appropriate step to reduce the uncertainty arising from the forecasts to close to zero. The research also revealed that night and day forecasts of ambient temperature have different uncertainties, so a thorough examination of this phenomenon is worthwhile, too, as the deviation may be influenced by another parameter (such as solar radiation in this case). For this reason, future goals include the introduction of a time-varying correction of the line rating prediction, where the reduction of uncertainty is continuously based on the comparison of measured and forecasted environmental factors.

Keywords: dynamic line rating, DLR, prediction, weather forecast, a risk factor

ACKNOWLEDGEMENT

chain and demonstrate integrated hardware and software solutions that will facilitate the "unlocking" of the resources for the cross-border electricity flows and regional cooperation.

REFERENCES

1. MARMILLO, J. Simulating the Economic Impact of a Dynamic Line Rating Project in a Regional Transmission Operator (RTO) Environment. *Grid of the Future Symposium,* 2018.

2. MCCALL J. C.; SERVATIUS B. Enhanced Economic and Operational Advantages of Next Generation Dynamic Line Rating Systems. *Grid of the Future Symposium,* 2016.

3. MCCALL, J.; GOODWIN, T. Dynamic Line Rating as a Means to Enhance Transmission Grid Resilience. *Grid of the Future Symposium,* 2015.

4. PHILLIPS, A. Evaluation of Instrumentation and Dynamic Thermal Ratings for Overhead Lines. *Technical Report,* 2013.

5. MCCALL, J.; LINDSEY, K.; SPILLANE, P.; BLISS, R. Real-time reliability-based dynamic line rating system for transmission asset optimization. *GRIDTECH 5th International Exhibition & Conference,* 2015.

6. DUPIN, R.; KARINIOTAKIS, G.; MICHIORRI, A. Overhead lines Dynamic Line rating based on probabilistic day-ahead forecasting and risk assessment. *International Journal of Electrical Power and Energy Systems,* 2019.

7. LOVRENČIĆ, V.; GABROVŠEK, M.; KOVAČ, M.; GUBELJAK, N.; ŠOJAT, Z.; KLOBAS, Z. The Contribution of Conductor Temperature and Sag Monitoring to Increased Ampacities of Overhead Lines (OHLs). *Periodica Polytechnica, Electrical Engineering,* 2015.

8. HAJEFOROSH, S.F.; BOLLEN, M.H.J. Uncertainty analysis of stochastic dynamic line rating. *Electric Power Systems Research,* 2021.

9. HALÁSZ, B.; NEMETH, B.; RÁCZ, L.; SZABÓ, D.; GÖCSEI, G. Monitoring of Actual Thermal Condition of High Voltage Overhead Lines. *Technological Innovation for Resilient Systems. DoCEIS 2018. IFIP Advances in Information and Communication Technology,* 2018, Vol. 521.

10. SZABÓ, D.; GÖCSEI, G.; NEMETH, B. Development of physical DLR calculation method. *7th International Youth Conference on Energy (IYCE),* 2019.

WWW.CYSENI.COM

CHALLENGES AND EXPECTATIONS FOR BATTERY MANAGEMENT SYSTEMS IN ELECTRIC VEHICLES: A REVIEW

A. Farooq, Ö. N. Cora *

Karadeniz Technical University
Department of Mechanical Engineering, Trabzon, 61080 – Turkey
+90 462 377 2945
* oncora@ktu.edu.tr

ABSTRACT

The demand for battery materials and research into battery technologies is steadily rising as the popularity of electric vehicles (EV) grows. The main impediment with electric vehicles is the slow or no development of new battery technologies and the associated battery management systems. High energy density batteries such as Li-ion, Li-S, Solid-State batteries, and others are replacing traditional batteries like lead-acid and Ni-Cd batteries. This study aimed to review the recent developments and one of the challenges faced by electric vehicles: battery management systems.

INTRODUCTION

The first commercial Li-ion battery was produced by Sony in 1991 [1], and it has grown in tremendous popularity since then. Fig. 1 shows the energy density (Wh/kg) of various battery types. It can be clearly seen that the energy density of Li-ion batteries is much higher than any of the currently available alternatives. Fig. 1 shows the dominance of Li-ion batteries in the stationary storage market over the past 10 years.
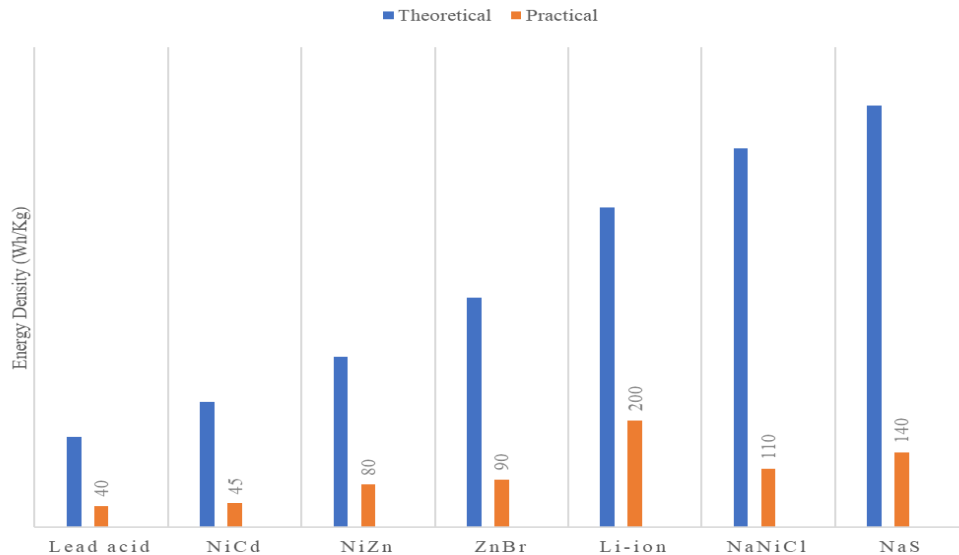
Fig.1. Energy densities (Wh/kg) of different battery systems [2]

The global lithium market was worth USD 2.7 billion in 2020, and it is predicted to increase at a compound annual growth rate (CAGR) of 14.8 percent from 2021 to 2028 [3]. This tremendous growth can be attributed to their high energy (100-270 $Whkg^{-1}$) and power density (250-680 $W kg^{-1}$), long service life (600-3000), higher charging efficiency (80-90%), and low self-discharge rate (3-10 % $month^{-1}$) features [4]. Despite high energy density per kilogram of weight, Li-ion batteries suffer from some serious flaws. They have a small operational window with regards to temperature, current, and voltage. They are flammable due to the presence of organic electrolytes, which raises many security issues like thermal runaways and even explosions [5]. Overcharging or discharging the battery with too many temperature fluctuations will cause the battery to degrade quickly. Additionally, the life-cycle of the batteries is reduced if the depth of discharge (DOD) is higher. Since electric vehicles require a considerable amount of power and voltage, the problem gets worsened when hundreds of Li-ion batteries are connected in series and parallel. As a result, using such a complex battery pack requires special attention. Therefore, a dynamic, robust, and efficient battery management system (BMS) in an EV is of utmost importance.

BATTERY MANAGEMENT SYSTEM (BMS)

The BMS in EVs contains parts like sensors, actuators, controllers with algorithms, and signal wires. It performs the following functions:
- Ensure the batteries run in the safe operational window (proper current, voltage, and temperature).
- Keep the cells and battery pack safe from harm.
- Keep the batteries in a state where they can meet the demands of the vehicles.

BMS executes the following tasks: Battery parameter detection, battery state estimation, safety control, battery balancing, thermal management, communication, logging and data storage, on board diagnosis, and power supply [6]. The process begins with on board current and voltage sensors detecting the current and voltage of each cell. A temperature sensor or a thermocouple measures the temperature of the battery pack at the same time. This information is fed into the battery model, and a suitable estimation method is employed to estimate the battery's individual or joint condition. Finally, this status estimation data is supplied to the charging module, which determines the vehicle's charging requirements. Various battery models (electro-chemical model, thermal model, ageing model, etc.) are used to determine the multi-time scale battery states like the State of Charge (SOC), State of Energy (SOE), State of Health (SOH), State of Power (SOP), State of Temperature (SOT) and State of Safety (SOS) [7] as shown in Fig. 2. Together, these battery state features help maintain both the short and long-term states at their optimum level.
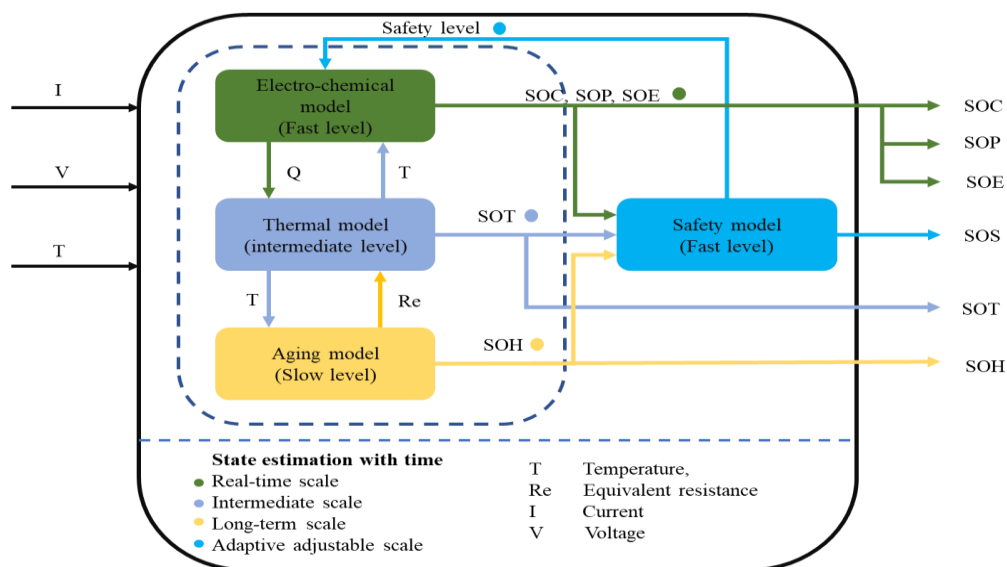
Fig. 2. Timescale of different battery states.

TOPOLOGIES FOR BATTERY MANAGEMENT SYSTEMS

Topology determines how each cell is attached to the BMS. Choosing the right topology is crucial for production cost, maintainability, and dependability. Here, four different topologies are presented and explored briefly. A Centralized topology contains a single printed circuit board (PCB) connected to the cells in series and gives a more compact and cost-efficient solution. Volkswagen e-Up (2014) model used a centralized BMS topology with 17 serially connected modules [8]. In modular topology, the BMS is split into multiple parts due to the presence of a large number of cells in parallel. Tesla Model S and Mitsubishi Motors used this type of topology [9]. The Master-slave topology involves two distinct subgroup configurations. The slave is directly connected to the cells while the master BMS communicates with the slave module. In the distributed BMS topology, small circuits are

connected to cell modules. These cell modules communicate with each other, and the last module is connected to the controller, as shown in Fig. 3 [10].
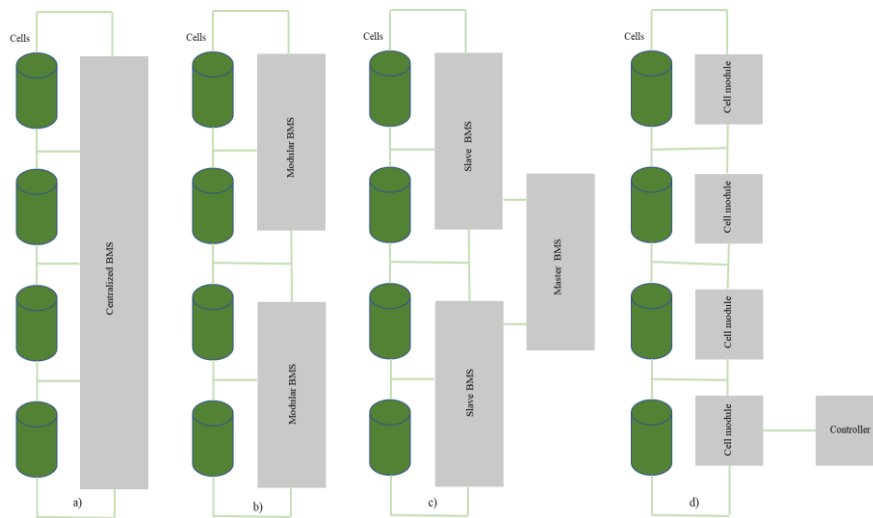
Fig. 3. Different topologies used in BMS a) Centralized, b) Modular, c) Master-Slave, d) Distributed

The traditional wired-BMS topology mentioned above has numerous difficulties, including a large wire harness, scalability issues, a physical wiring failure, and high implementation cost and weight. The Wireless BMS (WBMS) is one of the potential alternatives developed by researchers. WBMS can further be categorized into Bluetooth-based, Wi-Fi-based, Zigbee-based, Internet-of-Things-based, and, Cloud-based WBMS. Until now, Bluetooth and Zigbee-based WBMS have been investigated the most in the last decade. However, research in other areas of WBMS is gaining momentum [11].

CONCLUSION

Lithium-ion batteries are very important for many electronics, powering our laptops, mobile phones, medical devices, drones, cars, as well as rovers on other planets. The wide variety of electrode choices available makes Li-ion battery technology flexible and further enhancement of their performance a possibility. The overall performance parameters of Li-ion batteries, like safety, cycle life, charge/discharge rate, etc., need continuous monitoring by means of an on board battery management system (BMS), which adds to both the complexity and the cost of the battery. Advancements both in battery and its management system technologies will be determinant factors in the widespread adoption of electric vehicles.

Keywords: Lithium-ion battery, Battery management system (BMS), Electric vehicles (EVs).

REFERENCES

1. REDDY, M.V.; MAUGER, A.; JULIEN, C.M.; PAOLELLA, A.; ZAGHIB, K. Brief history of early lithium-battery development. *Materials*, 2020, Vol. 13, No. 8, P. 1884.

2. LAJUNEN, A.; SAINIO, P.; LAURILA, L.; PIPPURI-MÄKELÄINEN, J.; TAMMI, K. Overview of powertrain electrification and future scenarios for non-road mobile machinery. *Energies*, 2018, Vol. 11, No. 5, P. 1184.

3. *Grand View Research*. Rockville (MD): Lithium Market Size, Share & Trends Analysis Report By Product (Carbonate, Hydroxide), By Application (Automotive, Consumer Goods, Grid Storage), By Region, And Segment Forecasts, 2021 – 2028, 202- [referred on the 20th of January in 2022y]. Link to the internet < https://www.marketresearch.com/Grand-View-Research-v4060/Lithium-Size-Share-Trends-Product-30292193/>

4. LIU, K.; LI, K.; PENG, Q.; ZHANG, C. A brief review on key technologies in the battery management system of electric vehicles. *Frontiers of mechanical engineering*, 2019, Vol. 14, No. 1, p. 47-64.

5. ABDIN, Z.; KHALILPOUR, K.R.; *Single and polystorage technologies for renewable-based hybrid energy systems*. Massachusetts: Academic Press, 2018. P. 565. ISBN 978-0-12-813306-4.

6. YILDIZ, M. Battery Management System Architectures for Unmanned Air Vehicles: A Strategic Issue. *Anadolu Strateji Dergisi*, 2021, Vol. 3, No.1, P. 1-12.

7. HU, X.; FENG, F.; LIU, K.; ZHANG, L.; XIE, J.; LIU, B. State estimation for advanced battery management: Key challenges and future trends. *Renewable and Sustainable Energy Reviews*, 2019, Vol. 114, P. 109334.

8. LELIE, M.; BRAUN, T.; KNIPS, M.; NORDMANN, H.; RINGBECK, F.; ZAPPEN, H.; SAUER, D.U. Battery management system hardware concepts: an overview. *Applied Sciences*, 2018, Vol. 8 No. 4, P. 534.

9. UZAIR, M.; ABBAS, G.; HOSAIN, S. Characteristics of Battery Management Systems of Electric Vehicles with Consideration of the Active and Passive Cell Balancing Process. *World Electric Vehicle Journal*, 2021, Vol. 12 No. 3, P. 120.

10. HAUSER, A.; KUHN, R. *High-voltage battery management systems (BMS) for electric vehicles. Advances in battery technologies for electric vehicles*. Massachusetts: Woodhead Publishing, 2015. P. 526. ISBN 978-1-78242-377-5.

11. SAMANTA, A.; WILLIAMSON, S.S. A Survey of Wireless Battery Management System: Topology, Emerging Trends, and Challenges. *Electronics*, 2021 Vol. 10, No. 18, P. 2193.

AN EXPERIMENTAL STUDY ON THE EFFECT OF HEAT EXTRACTING FROM HOT SIDE OF PELTIER WITH NANOFLUIDS ON ELECTRICITY CONSUMPTION IN THERMOELECTRIC REFRIGERATOR APPLICATIONS

T. Guclu

Department of Mechanical Engineering, Faculty of Engineering, University of Bayburt,
Dede Korkut Campus, 69000 - Bayburt, Turkey
Low/Zero Carbon Energy Technologies Laboratory, Faculty of Engineering, Recep Tayyip
Erdogan University,
Zihni Derin Campus, 53100 Rize – Turkey
Corresponding Author tamerguclu@bayburt.edu.tr

P. M. Cuce

Department of Architecture, Faculty of Engineering and Architecture, Recep Tayyip
Erdogan University, Zihni Derin Campus, 53100 - Rize, Turkey
Low/Zero Carbon Energy Technologies Laboratory, Faculty of Engineering, Recep Tayyip
Erdogan University,
Zihni Derin Campus, 53100 Rize – Turkey

E. Cuce

Department of Mechanical Engineering, Faculty of Engineering and Architecture, Recep
Tayyip Erdogan University, Zihni Derin Campus, 53100 - Rize, Turkey
Low/Zero Carbon Energy Technologies Laboratory, Faculty of Engineering, Recep Tayyip
Erdogan University,
Zihni Derin Campus, 53100 Rize – Turkey

ABSTRACT

In this study, the effect of heat extraction on electricity consumption by using a Nano fluid from the hot side of Peltier in thermoelectric refrigerator systems was investigated. In the study, Al_2O_3-Water, TiO_2-Water and SiO_2-Water Nano fluids at a mixture ratio of 0.5% by mass were used as Nano fluids. In addition, in order to compare the data, the tests were repeated with water without the addition of Nano fluids under the same conditions, and these data were determined as the reference state. The tests were carried out for one hour for unloaded condition and for loaded condition (by leaving 1 litre of product to be cooled in the cooling cabinet). According to the results obtained from the experimental study, the use of Nano fluid instead of water as a refrigerant in the system reduces the amount of electricity consumption. In addition, the selection of appropriate Nano fluids is also important in terms of energy consumption. Experimental results showed that Al_2O_3-Water. Nano fluid is more efficient compared to TiO_2-Water and SiO_2-Water Nano fluids in both loaded and unloaded conditions.

INTRODUCTION

Thermoelectric coolers (TECs) are devices that work according to the so-called Peltier effect. The Peltier effect is the principle that when an electrically serial and thermally parallel circuit is created between two semiconductors and current is applied to this circuit, cooling on one surface of the semiconductor materials and heating on the other surface, that is, heat flow from one surface to the other surface [1,2]. In addition to the fact that they do not contain any refrigerants that are harmful to the environment or any moving parts, their most important advantages are their silent and vibration-free operation, the absence of maintenance costs, very precise temperature controls and their compact structure [3]. Thanks to these advantages, they have a wide range of uses, such as mini refrigerator applications, picnic coolers, organ and drug transport boxes, aerospace industry [4]. On the other hand, their coefficient of performance (COP) is low compared to conventional cooling systems. For this reason, studies to increase the efficiency of TECs continue [5]. The most important of the techniques used in studies for this purpose is to keep the hot side temperature of the Peltier at lower values. Liquid-cooled blocks are used on these surfaces to increase the amount of heat dissipated from the hot side of the Peltier [6]. In recent years, the use of Nano fluids as a refrigerant instead of the base liquid has been tried. Thus, the heat transmission coefficients of the cooling liquids are increased, and therefore, the heat interaction is increased [7]. Nano fluid is formed by adding various nanoparticles in various proportions into a fluid such as water, kerosene, or ethylene glycol [8]. In this study, an experimental study was carried out to increase the cooling power of a 36-litre thermoelectric refrigerator. A water-cooled block was added to the hot side of the Peltier system used, and various Nano fluids were circulated from this block at a mixing ratio of 0.5% to increase the efficiency obtained from the cold side. Thus, it is aimed to contribute to the efficient use of energy resources by reaching the desired cooler cabinet temperature in a thermoelectric cabinet earlier.

MATERIAL AND METHODS

First of all, the refrigerator cabinet with a 36-litre internal volume was produced using MDF material, using 60 mm polyurethane foam on the back surface and 60 mm XPS insulation material on the other surfaces.

Then, the Peltier assembly was prepared: a 50 mm thick aluminium ingot was attached to the cold surface of the Peltier, and an aluminium fin was attached to the other surface of this aluminium ingot by means of a thermal paste. The purpose of using aluminium ingots on this surface is that the Peltier assembly does not remain inside the cabinet door. A water-cooled block was attached to the hot surface of the Peltier, again using thermal paste. An aluminium fin is attached to the other surface of the water-cooled block. In addition, small fans are combined on the aluminium fins on both surfaces of the Peltier assembly in order to accelerate the heat dissipation. This prepared Peltier system is placed in the refrigerator cabinet from the middle of the front door.

The refrigerants to be used in the system were prepared: Three different Nano fluids were obtained by mixing 600 ml of water with 0.5% by mass Al_2O_3, TiO_2 and SiO_2 nanoparticles.

In addition, a pump is used in the system to ensure the circulation of the refrigerant, and a heat exchanger is used to effectively remove the heat taken from the hot surface by the refrigerant to the environment.

With the installed system, the refrigerant in the refrigerant reservoir is sent to the water-cooled block with the help of the pump. The refrigerant, which takes the heat from the cooler block, comes to the heat exchanger and returns to the refrigerant reservoir after leaving its heat in the environment. Thus, it completes its cycle.

Experiments were carried out in a laboratory environment. Ambient temperatures of 18, 24 and 30 ^{0}C were created with the help of an air conditioner, and the performance of the system was examined for these conditions. Then, the measurements were repeated by leaving 1 litre of water in the cabinet in order to observe the performance data while there was the product was cooled in the cabinet under the same outdoor conditions. In order to compare the data obtained, reference state data were created by using water as the refrigerant for each case.

Data such as cold and hot fin temperatures, cooling cabinet temperature, cooled product temperature, and refrigerant temperature were measured using K-type thermocouples. The duration of the measurements was determined as 3600 seconds, and the measurements taken every 30 seconds were sent to the computer with the help of a data logger.

RESULTS

It was observed that the temperature of the cooler cabinet decreased to 1.7 °C after 3600 seconds in the tests carried out in the reference condition under no-load conditions at an outdoor temperature of 18 °C. As shown in Figure 1, the specified cooler cabinet temperature is lowered at earlier times using various Nano fluids at a 0.5% mixing ratio. The same temperature value was reached with the fastest Al_2O_3 Nano fluid under the aforementioned conditions.
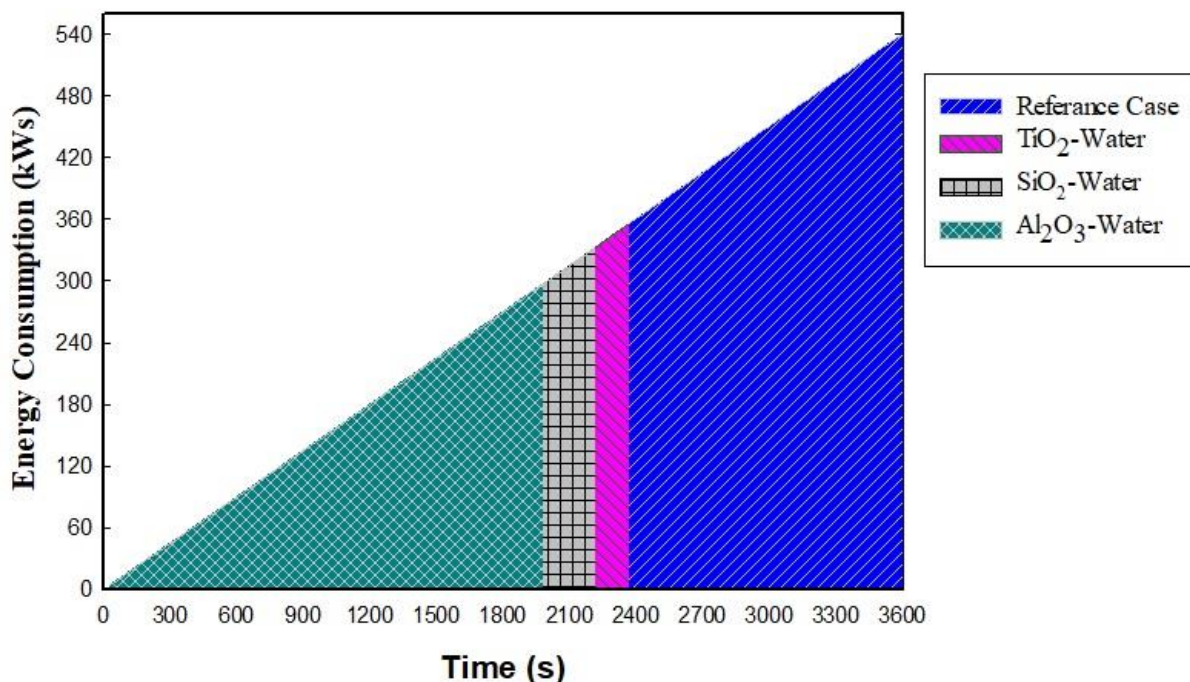

Fig. 1. Comparison of electricity consumption at 18 °C ambient temperature without load conditions

For the reference case, it was observed that the temperature of the cooler cabin decreased to 8.5 °C after 3600 seconds in the loaded condition tests at 24 °C outdoor conditions. In the tests carried out under the same conditions, it was observed that the specified temperature

value was lowered earlier in the cases where Nano fluid was used. As shown in Fig. 2, the temperature value in question was reached with Al_2O_3-Water Nano fluid at the earliest.
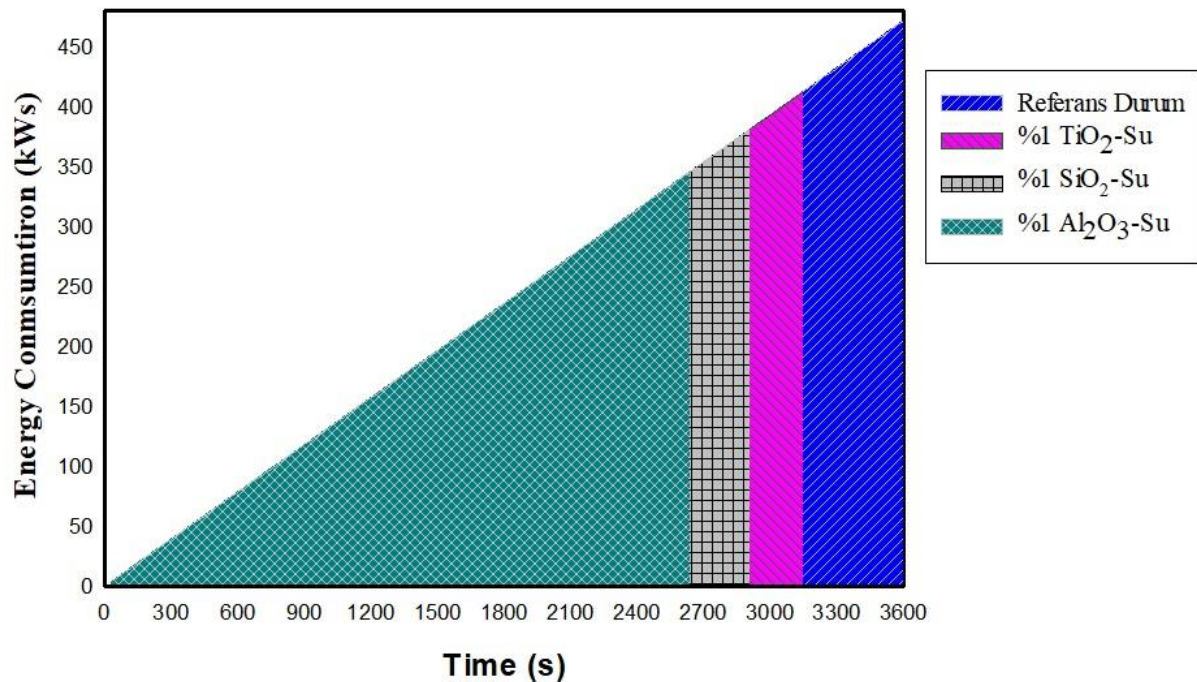
Fig. 2. Comparison of electricity consumption at 24 °C ambient
temperature without load conditions

CONCLUSIONS

In this experimental study, the effect of heat extraction on electricity consumption by using a Nano fluid from the hot side of Peltier in thermoelectric refrigerator systems was investigated. According to the results obtained from the study, the use of Nano fluid instead of water as a refrigerant in the system reduces the amount of electricity consumption. In addition, the selection of appropriate Nano fluids is also important in terms of energy consumption. Experimental results showed that Al_2O_3-Water Nano fluid is more efficient compared to TiO_2-Water and SiO_2-Water Nano fluids in both loaded and unloaded conditions.

Keywords: Thermoelectric cooling, Nano fluids, electricity consumption, space cooling

REFERENCES

1. CUCE, E.; GUCLU, T.; CUCE, P. M. Improving the thermal performance of thermoelectric coolers (TECs) through a Nano fluid driven water to air heat exchanger design: An experimental research, *Energy Conversion and Management*, 2020, Vol. 214, P. 112893, Doi: 10.1016/j.enconman.2020.112893.

2. GUCLU, T.; CUCE, E. Thermoelectric Coolers (TECs): From Theory to Practice, *Journal of Electronic Materials*, 2019, Vol. 48, No. 1, P. 211–230. Doi: 10.1007/s11664-018-6753-0.

3. WANG, X. D.; WANG,Q. H.; XU J. L. Performance analysis of two-stage TECs (thermoelectric coolers) using a three-dimensional heat-electricity coupled model, *Energy*, 2014, Vol. 65, P. 419–429. Doi: 10.1016/j.energy.2013.10.047.

4. Chein, R.; Chen, Y. "Performances of thermoelectric cooler integrated with microchannel heat sinks," *International Journal of Refrigeration, 2005*, Vol. 28, No. 6, P. 828–839. Doi: 10.1016/j.ijrefrig.2005.02.001.

5. YU, J.; WANG, B. Enhancing the maximum coefficient of performance of thermoelectric cooling modules using internally cascaded thermoelectric couples, *International Journal of Refrigeration*, 2009, Vol. 32, No. 1, P. 32–39. Doi: 10.1016/j.ijrefrig.2008.08.006.

6. Gupta, M.; Singh, V.; Kumar, R.; Said, Z. "A review on thermophysical properties of Nano fluids and heat transfer applications," *Renewable and Sustainable Energy Reviews*, 2015, Vol. 74, P. 638–670. Doi: 10.1016/j.rser.2017.02.073.

7. Wiriyasart, S.; Suksusron, P.; Hommalee, C.; Siricharoenpanich, A.; Naphon, P. "Heat transfer enhancement of thermoelectric cooling module with Nano fluid and ferrofluid as base fluids," *Case Studies in Thermal Engineering*, 2021, Vol. 24, P. 100877. Doi: 10.1016/j.csite.2021.100877.

8. CUCE, E.; CUCE, P. M.; GUCLU T.; BESIR A. B.; On the Use of Nano fluids in Solar Energy Applications, *Journal of Thermal Science*, 2020, Vol. 29, No. 3, P. 513–534. Doi: 10.1007/s11630-020-1269-3.

ENERGY CONSUMPTION ANALYSIS IN BUILDINGS

O. Vonžudaitė, R. Urbonas, R. Bakas, L. Martišauskas
Lithuanian Energy Institute
Breslaujos g. 3, LT-44403 Kaunas – Lithuania
Otilija.Vonzudaite@lei.lt

S. Urbonienė
Vytautas Magnus University
Vileikos g. 8, LT-44404 Kaunas – Lithuania
Sigita.Urboniene@vdu.lt

EXTENDED ABSTRACT

OVERVIEW

Currently, 3854 multi-family houses or approximately 10% of the fleet, are renovated in Lithuania. 1300 multi-family houses are in the renovation process [1]. The renovation of the older generation multi-family houses enables to decrease the energy consumption by approximately 30-40% [2]. Thus, a systematic and speedy renovation process affects not only the consumption side but also the heat production and heat supply to the consumers' side. The reliable and comprehensive set of the energy consumption data for each consumer (multi-family or single house) and thorough analysis of the data might provide a tool for the district heating companies to increase the efficiency of heat production and supply to the customers.

METHODS

For the analysis of heat consumption, real data for renovated and un-renovated multi-family houses were taken for the period of 2018-2019 (with colder winter in comparison with 2020). In the analysis, the space heating data were compared to the degree of days as well as to the heated area and even heated volume in order to find possible tendencies. Statistical and graphical analyses were employed to conduct the research on heat consumption tendencies for renovated and unrenovated buildings.

RESULTS

The obtained results, in general, showed the advantages of renovated multi-family houses in terms of energy consumption per area or volume unit. The performed analysis also showed that for the prognosis and further decision-making, reliable and comprehensive data is required. As it is presented in Fig. 1 and Fig. 2 in the time span for October-December of 2019, unexpected differences in heat consumption for renovated and unrenovated multi-family houses are observed. In addition, a very slight lag in energy consumption for the renovated buildings is observed. Thus, the renovated buildings could provide the possibility for the heat supplier to cut the most expensive heat peaks optimising heat prices and prolonging the lifetime of the heat distribution network. Taking into account the current

situation in the energy market and energy security matters, a thorough analysis of possible ways to the development of the heating systems to meet public interest and Green Deal targets should be performed.
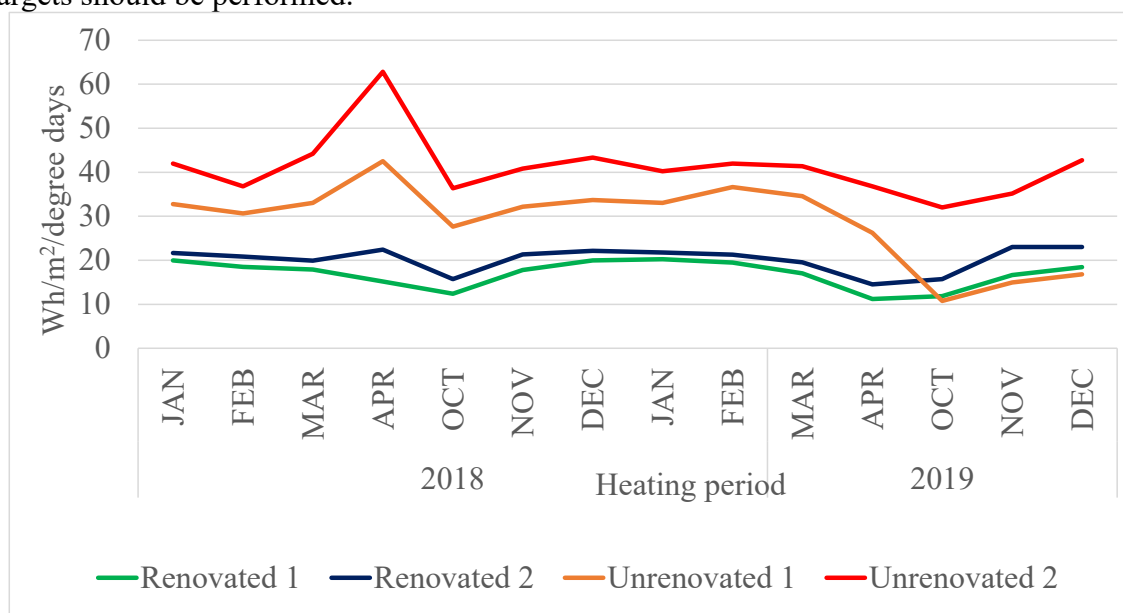
Fig. 1. Sampled comparison of heat consumption in renovated and unrenovated houses taking into account degree of day
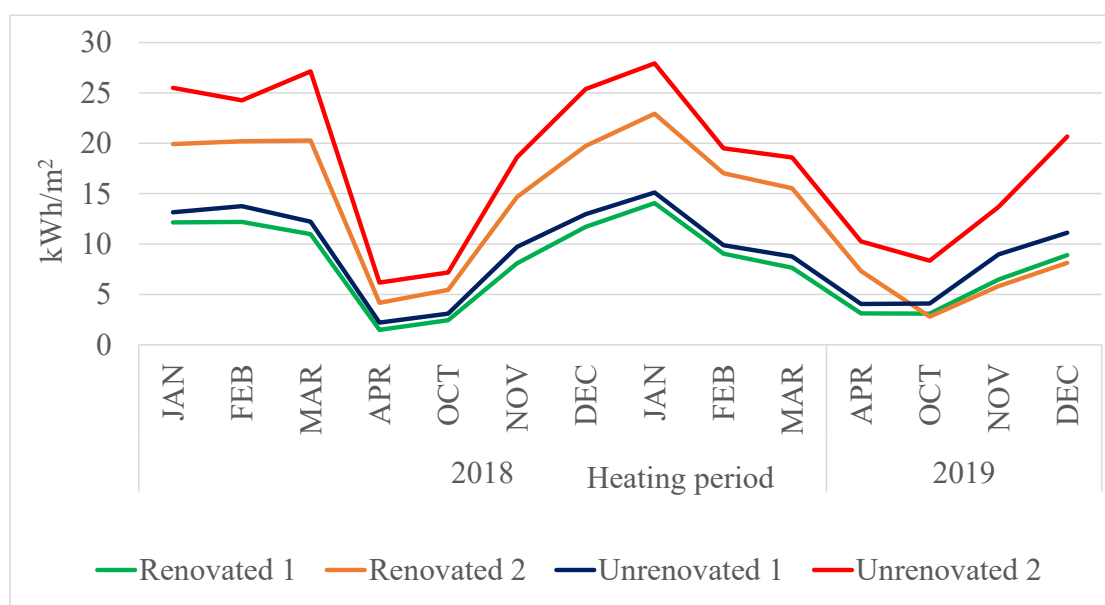
Fig. 2. Sampled comparison of heat consumption in renovated and unrenovated houses

To identify possible energy consumption trends, graphical and statistical data analysis of hourly space heat consumption and outdoor air temperature for different building categories in different cities was performed. The main descriptive statistics of the relative heat consumption data were also calculated. A linear relationship between relative space heat consumption, outdoor air temperature, and other building parameters was determined using correlation analysis. For each analysed building, linear regression models of relative heat consumption and outdoor air temperature were developed, which allow predicting the relative space heat consumption at different outdoor temperatures, interpretations of the

obtained regression equation coefficients, accuracy of each model forecast, and their comparative analysis.
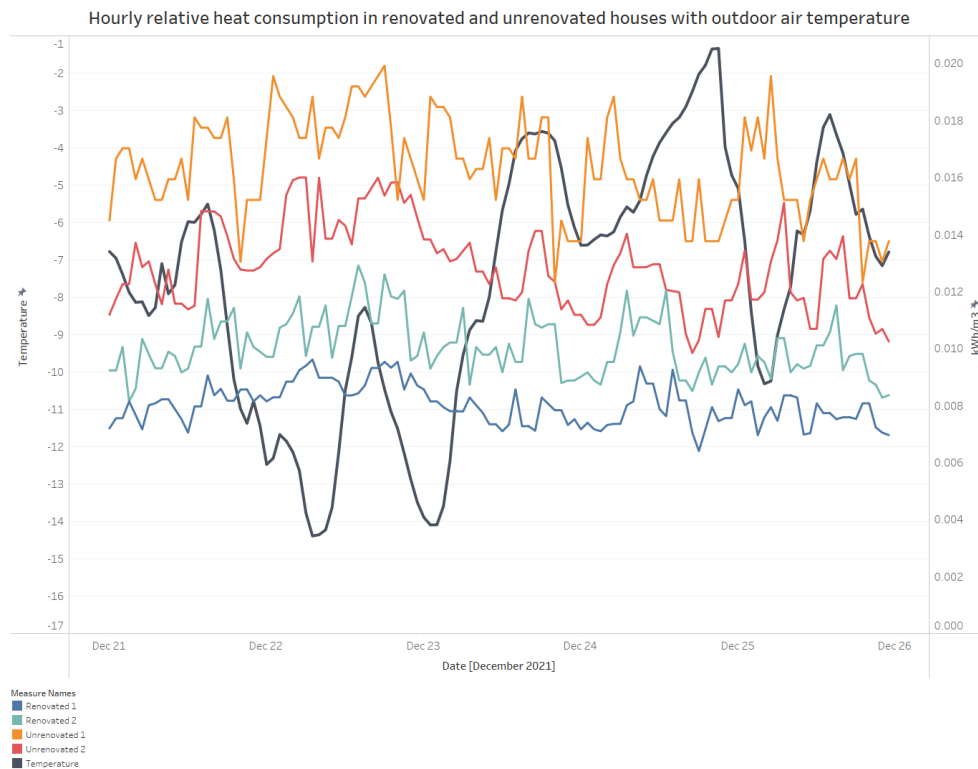
Fig. 3. Hourly relative heat consumption and outdoor air temperature in renovated and non-renovated multi-family buildings

Hourly data on relative space heat consumption and outdoor air temperatures are used to develop regression models. Statistically significant linear regression models of relative space heat consumption and outdoor air temperature were obtained. The coefficient of determination of the first model is 0.76, while of the second model is 0.63, i.e. regression lines explain about 76 % and 63 % dissipation of relative space heat consumption per hour. Statistically significant coefficients of the regression equation and high coefficients of the determination indicate that the models are suitable for predicting relative space heat consumption.
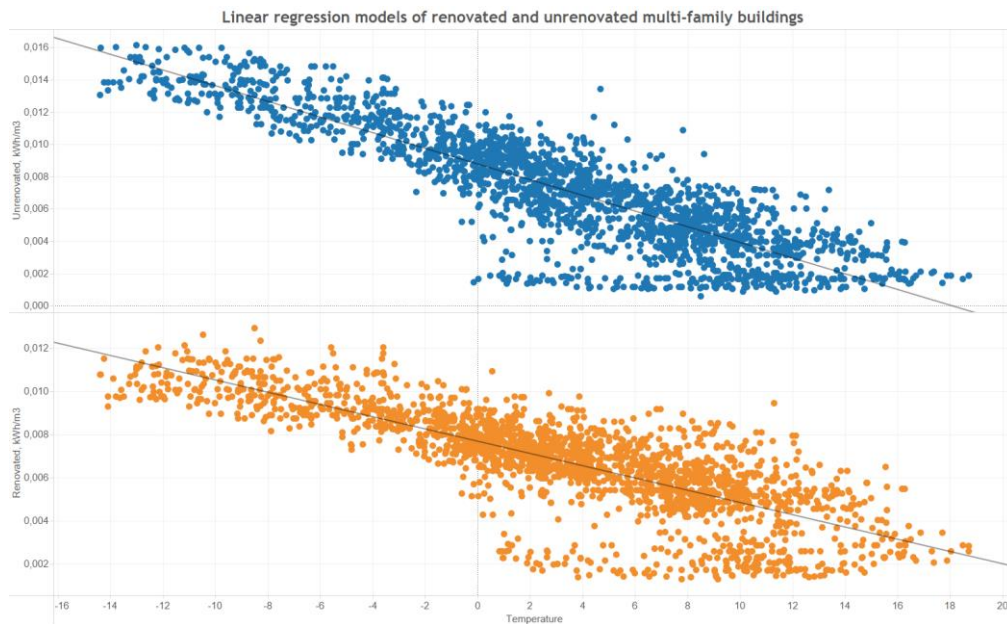
Fig. 4. Linear regression models of renovated and non-renovated multi-family buildings

CONCLUSIONS

1. Reliable and comprehensive data is required for the thorough analysis and decision-making on the renovation process.

2. Society and district heating companies could benefit from the deep analysis of heat consumption behaviour, providing ways to lower the heat process and extending the lifetime of the heat distribution network.

3. Developed regression models are suitable for predicting relative space heat consumption.

Keywords: Energy consumption, renovation, statistical analysis

REFERENCES

1. *Daugiabučių namų atnaujinimo (modernizavimo) programa* – [referred on the 3rd of March in 1852 y.]. Link to the internet <https://map.betalt.lt/> (In Lithuanian)

2. *Šilumos suvartojimas* – [referred on the 30th of March in 1698 y.]. Link to the internet <https://lsta.lt/silumos-ukis/silumos-suvartojimas/ > (In Lithuanian).

NUMERICAL IVESTIGATITION OF THE EFFECT OF METHANE-AIR PARTIALLY PREMIXED COMBUSTION IN RADIANT TUBE HEATERS

S. Özbektaş,
Department of Mechanical Engineering, Ondokuz Mayis University
Turkey
+903623121919
seyda.ozbektas@omu.edu.tr

B. Sungur
Department of Mechanical Engineering, Samsun University
Turkey
+903623130055
bilal.sungur@samsun.edu.tr

ABSTRACT

High-intensity and low-intensity radiant heaters are the most common categorization in heating technology with radiation. Heaters, where combustion occurs in black tubes, are called low-intensity radiant heaters and heaters where the air-gas mixture burns in a burner, and the open, bright flame is seen are called high-intensity heaters. Low-intensity radiant heaters radiated their energy over a wider area than high-intensity heaters because of the larger surface area. Natural gas burners have been widely used in radiant heating technologies because of their advantages in both efficiency and emissions. However, with the promulgation of the more stringent emission regulations, the control of emissions becomes a major issue in combustion systems. This paper aimed to investigate numerically the effect of the partially premixed mixture on a natural gas burner on a radiant heater. The radiant heater placed in the room and the effect of the premixed ratios (from 0% to 40%) on the temperature distribution in the room, efficiency and emissions were analysed. The modelled radiant heater type is a low-intensity U-type radiant tube with 22 kW thermal power. Calculations were made in three-dimensional conditions, and Ansys Fluent package program was used as a Computational Fluid Dynamic program. To model the turbulence Standard k-ε model was used to model the combustion, the eddy dissipation model was used, and to model the radiation, the P1 model was used. Conjugate heat transfer was considered in the radiant tube wall interfaces between the fluid and the solid zones. Results showed that increasing the premixed ratio decreased the flame length in a radiant tube. Also, with the increase of premixed ratios, the exhaust gas temperatures decreased.

Keywords: Combustion, Partially premixed combustion, Radiant heating, Heat transfer, Numerical modelling.

INTRODUCTION

In heating applications, the object which is heated does not directly contact the combustion products or flame. The main advantages of radiant tube heaters are that they can effectively control the atmosphere in the furnace, isolate the workpiece and flue gas in a furnace to reduce combustion loss by oxidation and improve product quality. Therefore, radiant heaters are widely used in refining furnaces in the heat treatment industry. Straight-type radiant tubes were first invented and used in Germany in the 1930s with lower thermal efficiency and higher NO_x emissions. Later, systems such as U-type, W-type, P-type and double P-type were gradually developed and widely used for continuous heat treatment furnaces in the iron and steel industries [1]. In addition, radiant heaters are very effective devices used for heating large, high, semi-open and open environments where traditional heating methods are insufficient. Radiant heating is based on the principle of energy transfer from a hot temperature object to a lower temperature object via electromagnetic wave energy. The more intense the radiant heat, the less the actual air temperature needs to be increased for a comfortable indoor environment. In radiant heating systems, ignition is generally carried out using gaseous fuels, but liquid fuel burners are also available [2].

Radiant heaters are generally divided into two classes. These are high-intensity radiant heaters and low-intensity radiant heaters. In high-intensity radiant heaters, there is mainly visible flame radiation, and surface temperatures are 1000 °C and above. In practice, low-intensity radiant heaters are generally preferred and used. Surface temperatures in low-intensity radiant heaters are around 650 °C at most. The main parts of low-intensity radiant heaters can be listed as burner, radiant tube, reflector, exhaust, and vacuum pump [3].

Computational fluid dynamics (CFD) is widely used today as a useful tool for energy optimization of heating systems. It significantly reduces the need to run costly experiments before making changes to a system and provides information that is difficult to obtain empirically. In many studies by researchers, combustion and heat transfer phenomena in radiant tube heating systems have been investigated both experimentally and numerically. Many of these researches are related to industrial furnace sector applications. Tsioumanis et al. [4] carried out numerical analyses of a flat type recuperative radiant heater without considering the combustion process. They used three different turbulence models in their simulations and compared their results with experimental airflow velocity measurements. They stated that the Standard k-ε model provided partially better results between experimental and computed velocity profiles in the combustion chamber region, among other k-ε turbulence models. They operated the burner to its rated design point of 25 kW thermal input, GCV basis. Air and natural gas were supplied to the pilot and main burner air and fuel inlets accordingly. In another study by the same authors [5], they obtained satisfactory results with experimental data for the temperature profiles and NOx emissions along the walls of the radiant heater, taking into account the combustion phenomenon. Garcia et al. [6] numerically modelled the straight type non-recirculating radiant pipe. They used Eddy Dissipation Concept (EDC) model and the Steady Diffusion Flamelet (SDF) model for comparison. Numerical calculations were performed under two-dimensional axisymmetric conditions. Xu et al. [7] experimentally investigated the performance of a straight tube radiant heater in a horizontal heating furnace. Xu et al. [8] investigated the performance of an M-type and A-type radiant heaters. Comparing the two types of radiant heaters, they stated that the circulation of combustion gases in the double-A radiant heater significantly reduces the maximum temperature in the combustion zone and produces a more homogeneous temperature along the tube.

Maznoy et al. [9] designed a new configuration of a gas-fired infrared heater and experimentally studied the operation with and without preliminary heating of combustion air by recuperating flue gas heat. In their design, the heater is constructed using an annular cylindrical radiant burner mounted inside a stainless steel conical reflector. Scribano et al. [10] experimentally investigated the single-ended self-recuperative radiant tube burner fuelled by natural gas in the non-premixed mode, which is used in the steel industry for surface treatment. They aimed to obtain the best operating conditions in terms of optimum equivalence ratio, thermal power and lower pollutant emissions.

Partially premixed combustion is applied in many combustion systems such as gas turbine engines, internal combustion engines, domestic stoves, furnaces etc. Partially premixed flames occur when a rich mixture of fuel/air mixes with a lean mixture of fuel/air. Several studies are reported on partially premixed flames. Gore and Zhan [11] performed experimental investigations on laminar partially premixed methane-air in an over ventilated co-flow jet flame. They stated that with increasing levels of partial premixing, they observed that the visible flame height decreases and the overall flame colour changes from yellow to blue and the radiative heat loss fraction first decreases and then reaches a constant value. Lyle et al. [12] researched the effect of partially premixing on turbulent jet flames and emission characteristics. They claimed that at sufficiently high levels of partial premixing, a double flame structure consisting of a rich premixed inner flame and an outer diffusion flame is established, similar to laminar flames. Sreenivasan et al. [13] investigate the influence of flow and partial air premixing on liquid petroleum gas (LPG) flames in a lab-scale co-flow burner. Their results showed that in a dual air stream configuration, the partial premixing is optimum at nearly 45% primary air value.

Literature survey showed that there is still a lack in the modelling of radiant heaters with conjugate heat transfer, the effect of fuel-air mixture ratios on heat transfer and the effects of this situation on room temperature distribution. In this paper, the effects of the fuel-air premix ratios in a U-type radiant tube burner placed in the room were investigated. The obtained results were evaluated in terms of temperature distributions of the room, temperature distributions on and inside the radiant heater tube surface, velocity vector distributions around the burner and mass concentration of methane gas.

METHODOLOGY

Within the scope of this paper, the effect of different premix ratios on heat transfer in a U-type radiant heater placed in a 2500 mm x 2050 mm x 2060 mm room was investigated numerically. These room sizes are generally based on the study of Ahanj et al. [14]. In this context, methane was burned with air at premix ratios of 0%, 20% and 40%. The modelled radiant heater had a diameter of 70 mm and a length of 4600 mm. The distance between the radiant tube surface and the reflector is 70 mm, and the reflector is placed 200 mm below the ceiling. The modelled geometry is shown in Fig. 1. The air enters the radiant tube through the entire 70 mm diameter. Then, it proceeds from the primary and secondary air holes in the burner, and the combustion takes place by mixing with the fuel. The burner, where the fuel-air mixture takes place, is placed at a distance of 50 mm from the air inlet and in the centre of the tube. The fuel inlet diameter is 4.5 mm, and methane was chosen as the fuel. In all calculations, the excess air coefficient was 1.5, and the total mass flow rate of the air was calculated according to this situation. The thermal power of the burner was 22 kW, and the mass flow inlet of fuel was set according to this value. Boundary conditions of mass flow inlet at air and fuel inlets, pressure outlet at flue gas outlet are selected. The reflector wall has 95% reflectivity. The wall boundary condition was selected for all room walls, and the

wall temperatures were entered as 300 K. The coupled wall boundary condition is applied at the interfaces where the room and the radiant tube intersect. The eddy dissipation model was used to model the combustion inside the radiant heater tube, and the Standard k-ε model was used to model the turbulence. The P1 model was chosen as the radiation model. The SIMPLE (Semi-Implicit Method for Pressure Linked Equations) scheme was adopted for the pressure-velocity coupling. The convergence criterion was set to 10^{-6} for all equations.
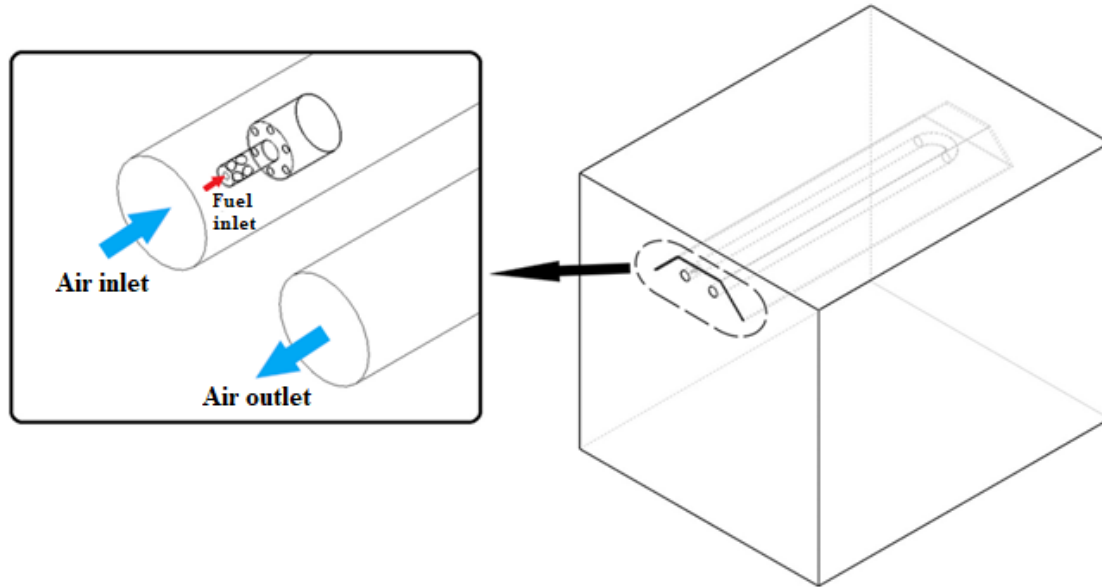
Fig 1. The geometry of the room with a radiant heater

In solving problems with Computational Fluid Dynamics (CFD), geometry should be knitted with a mesh structure. In a good mesh structure, the average element quality and orthogonal quality are expected to be between 0.75-1 values, while the average skewness value is expected to be between 0-0.25 values [15]. The mesh structure properties of the room with a radiant heater are given in Table 1. When Table 1 was examined, it was seen that the necessary conditions for a good mesh structure were met.

Table 1. The mesh structure properties of the room with radiant heater

Average element quality	0.837
Average skewness	0.229
Average orthogonal quality	0.768
Node number	506581
Element number	2944352

The tetrahedral element was used in the meshing process. The interior of the U-type tube, where the combustion takes place, was meshed with a small size and fine mesh structure, while the interior of the room has meshed with a larger and relatively coarser mesh structure. The coarser mesh was chosen because it was good enough to resolve fluid flow in the room. The mesh structure of the room with the radiant heater and the radiant tube is shown in Fig. 2.

a)   b)
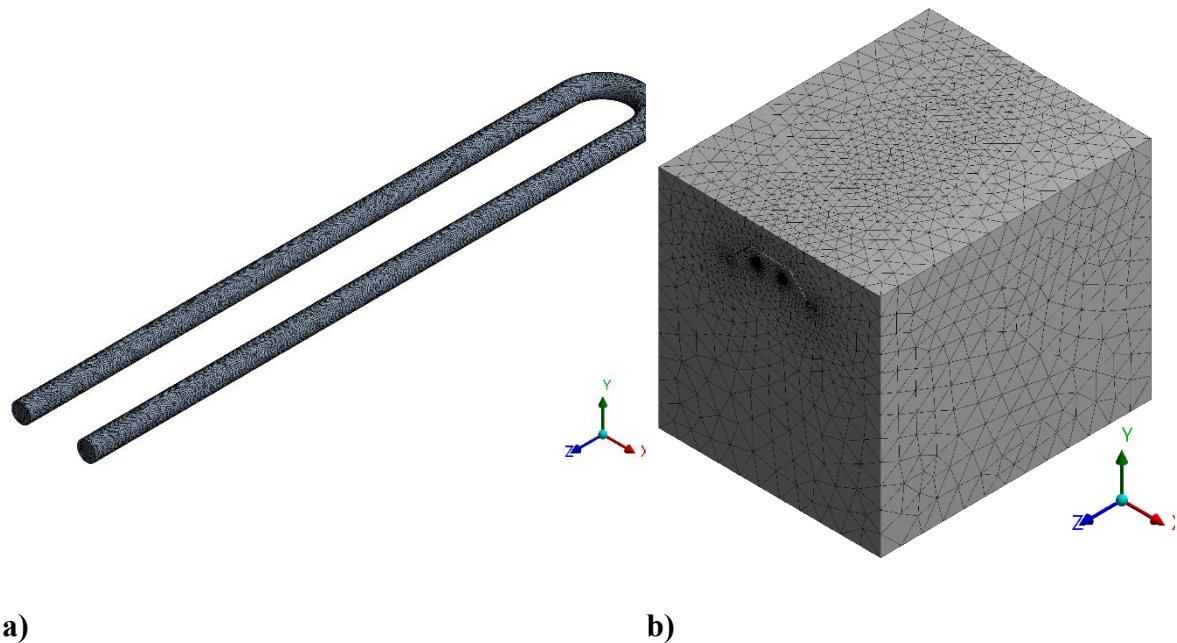
Fig 2. The mesh structure of a) the radiant tube and b) the room with the radiant heater

RESULTS AND DISCUSSIONS

In this paper, the thermal effects occurring in the radiant tube and the room were investigated by changing the fuel-air premix ratios in a U-type radiant heater placed in a closed room. The obtained results were evaluated in terms of temperature distributions occurring in different planes in the room, temperature distributions on the surface and inside of the radiant tube, and mass fraction of methane. In addition, graphs of temperatures in the linear direction from floor to ceiling were drawn at three points in the room, and these values were compared for the three different premix ratios.

The temperature distributions occurring on the surface of the radiant tube were given in Fig. 3. The highest temperatures on the radiant tube surface began to occur at a distance of approximately 600 mm, 540 mm, and 480 mm, respectively, in models with 0%, 20% and 40% premix ratios. Moreover, as the premix ratio increased, the red colour temperature gradient on the radiant tube surface spread over a wider area. With the heat transfer from the combustion gas to the room, the temperatures decreased gradually towards the outlet. In the model with a 40% premix ratio, the temperatures on the radiant tube surface were higher than in other models.
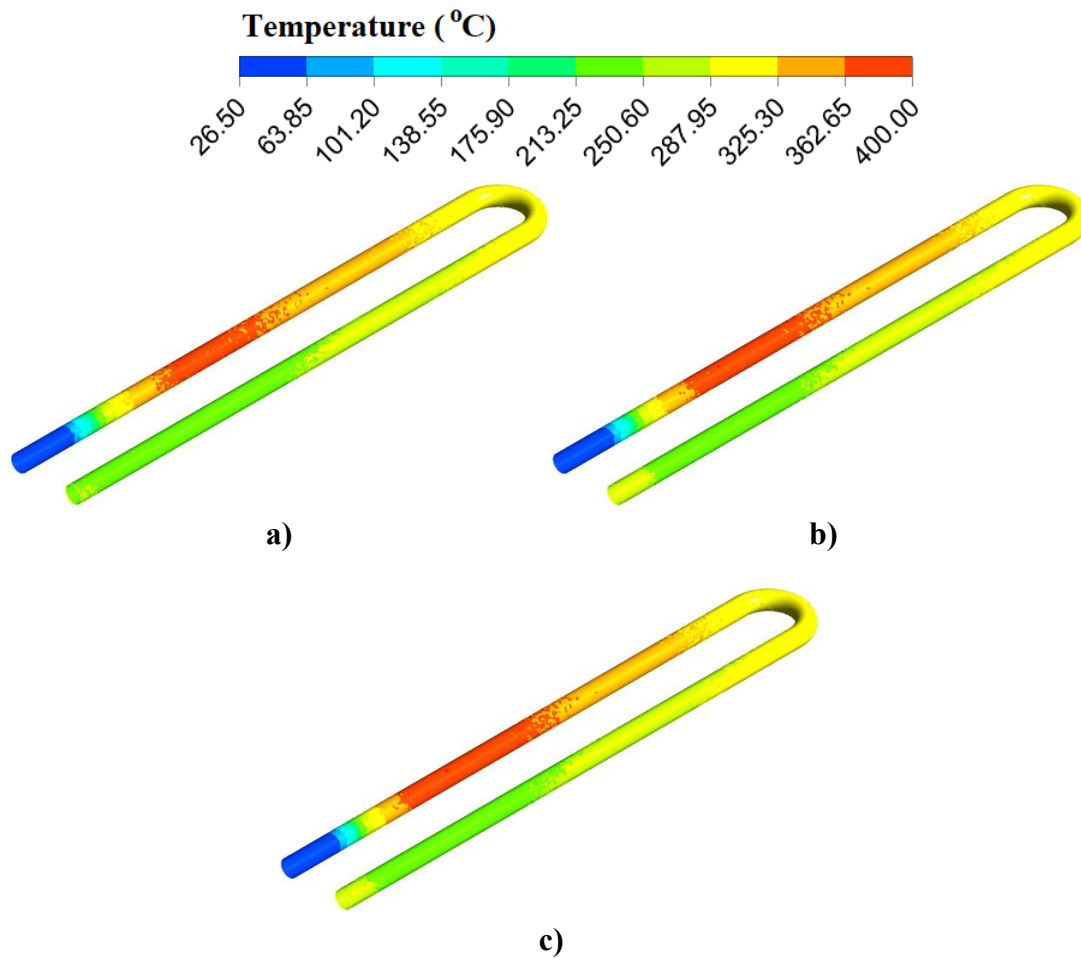
Fig 3. The temperature distributions occur on the surface of the radiant tube. a) 0%, b) 20%, c) 40% premix ratios

The temperature distribution inside the radiant tube is shown in Fig. 4. According to this figure, the flame length decreased as the premix ratio increased. The highest flame temperature was measured at 1875 K in the 0% premixed model, 1880 K in the 20% premixed model and 1894 K in the 40% premixed model.
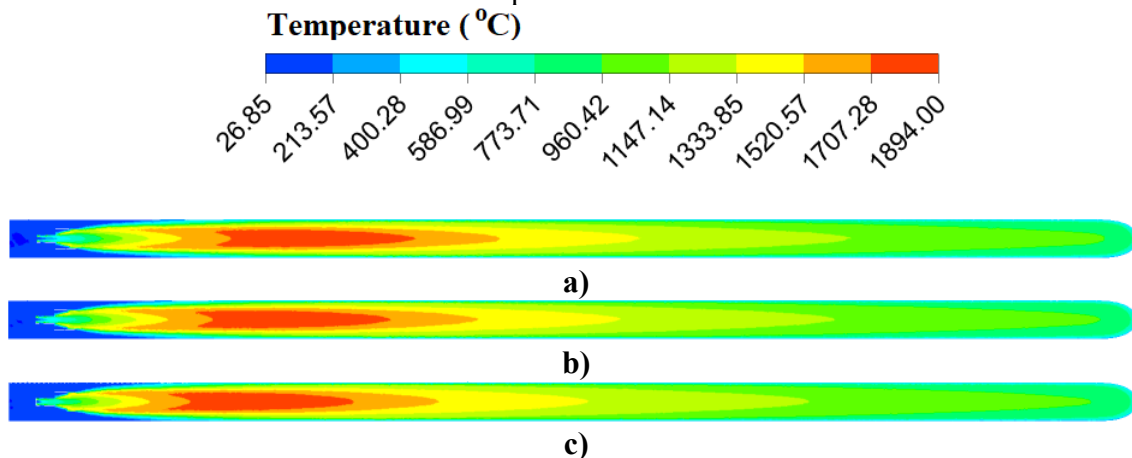
Fig 4. Temperature distribution inside the radiant tube. a) 0%, b) 20%, c) 40% premix ratio

Variation in mass fraction of methane in relation to distance is shown in Fig. 5. According to this figure, the mass fraction of methane decreased rapidly in all models, and as the gas moved, this rate of decrease in mass fraction of methane gradually slowed down. In the 40% premixed model, the methane gas was consumed earlier than in the other models. At a distance of about 600 mm, the methane gas was completely consumed in all models.
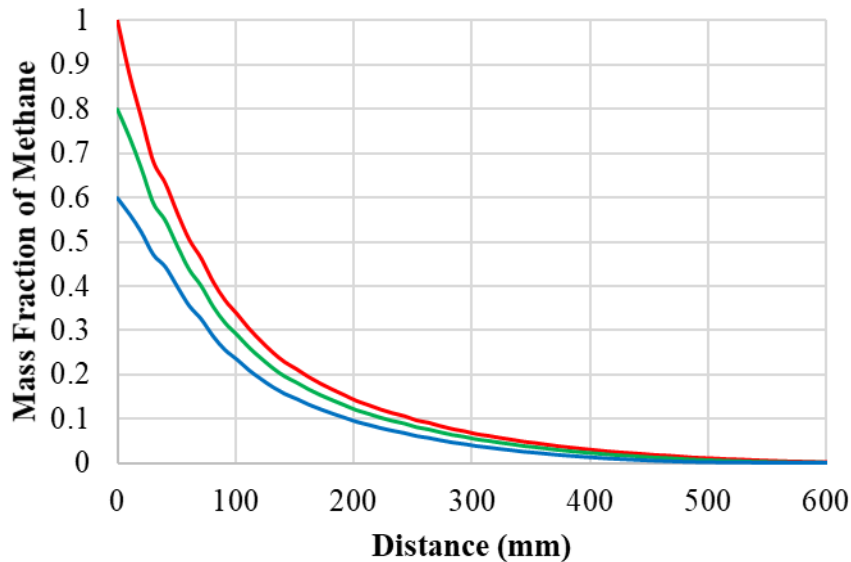
Fig 5. Variation in mass fraction of methane in relation to distance, 0% (red colour), 20% (green colour), 40% (blue colour) premix ratios

Temperature distribution in the XZ plane at 800 mm above the floor was shown in Fig. 6. According to this figure, the highest temperatures occurred in the central regions, and the temperatures decreased towards the edges. When all models were compared, the temperature values in the 40% premixed model were higher than the other models, and the lowest temperatures occurred in the 0% premixed model. In this context, the highest temperature was 35.4°C in the 40% premixed model, 35°C in the 20% premixed model and 33.8°C in the 0% premixed model.
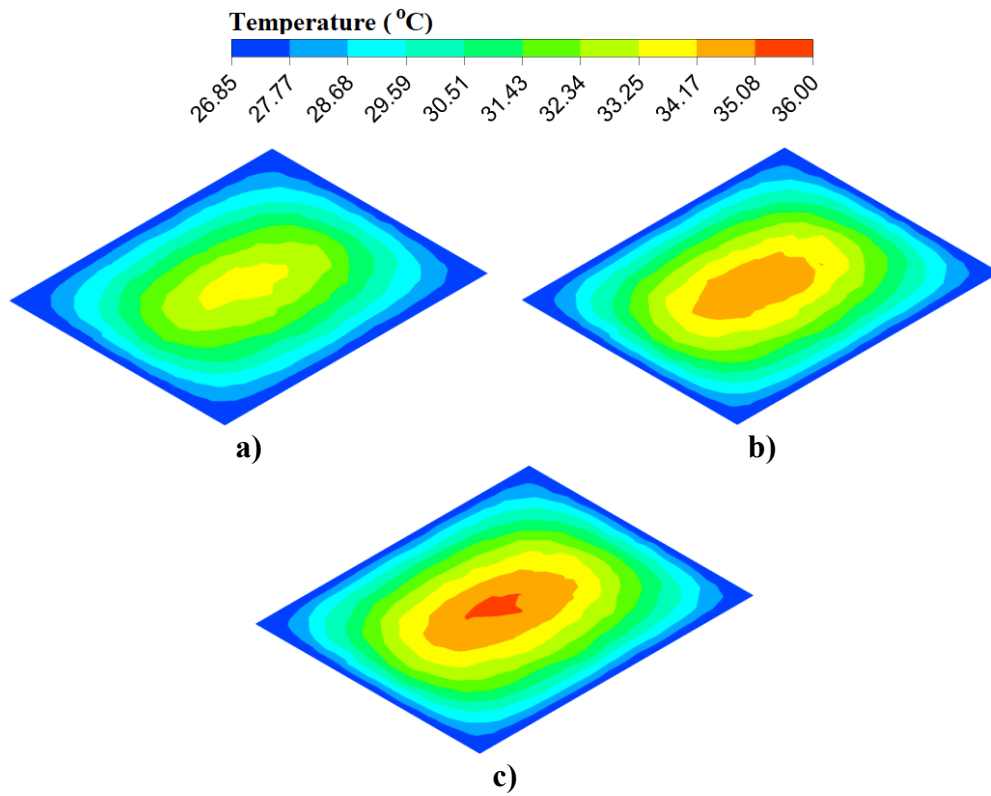
Fig 6. Temperature distribution in the XZ plane at 800 mm above the
floor. a) 0%, b) 20%, c) 40% premix ratios

Fig. 7 shows the temperature distributions in the centre of the room in the YZ plane. When
the temperature distributions in the figure were examined, it was seen that the air was heated
by the effect of the heat transfer occurring on the tube surface. As the premix ratio increased
in the radiant heater, the temperature gradients spread from the radiant tube to the air and
expanded towards the floor.
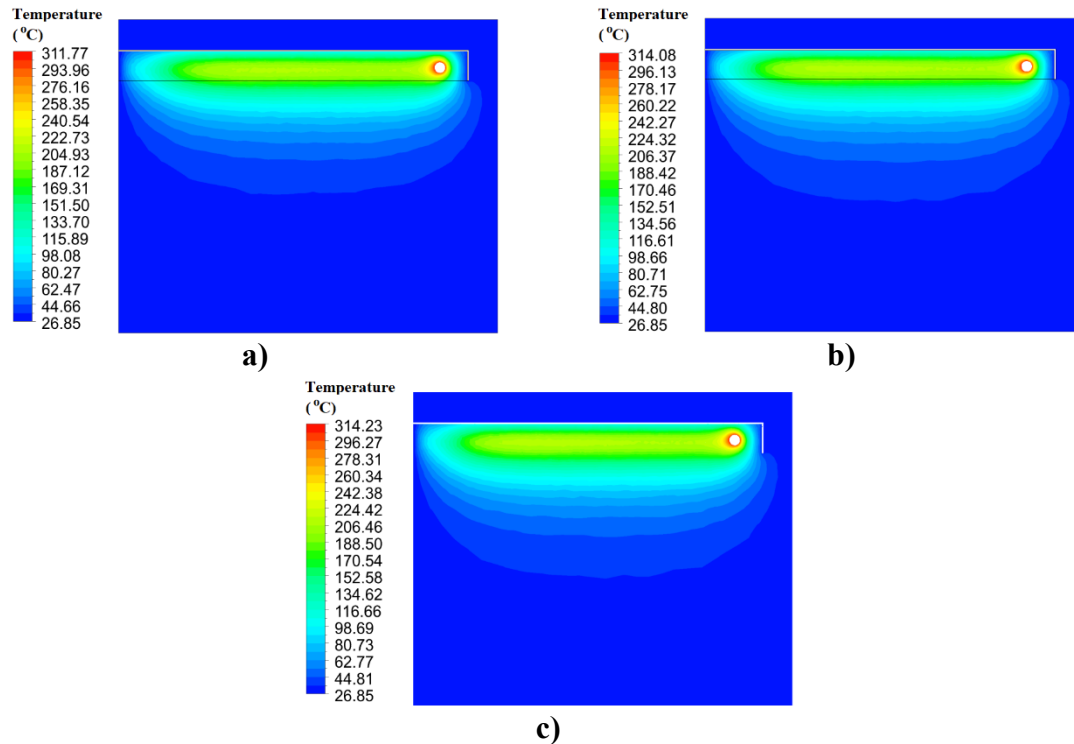
Fig 7. Temperature distributions in the centre of the room in the YZ
plane. a) 0%, b) 20%, c) 40% premix ratios

The three locations determined in the room and the temperature change graphs in the linear direction from the floor to the ceiling at these locations are shown in Fig. 8. Locations A and C were placed to the right and left of the radiant tube, and B was located in its centre. Location A and C are 300 mm from the side walls. Temperature measurements were made from the ground to a height of 1500 mm. When the graphs were examined, temperatures in the B location were much higher than in other locations. As the measurements approached the radiant tube at this location, the temperatures rose in an increasing form and reached approximately 110°C. On the other hand, in locations A and C, temperatures reached approximately 34°C. After a height of approximately 1300 mm in A and C positions, the temperatures began to decrease as the measuring points protruded from the reflection area of the reflector. When all models were compared, the temperatures in the room at 0% premixed conditions were lower than in other models. This situation was especially seen in positions A and C.
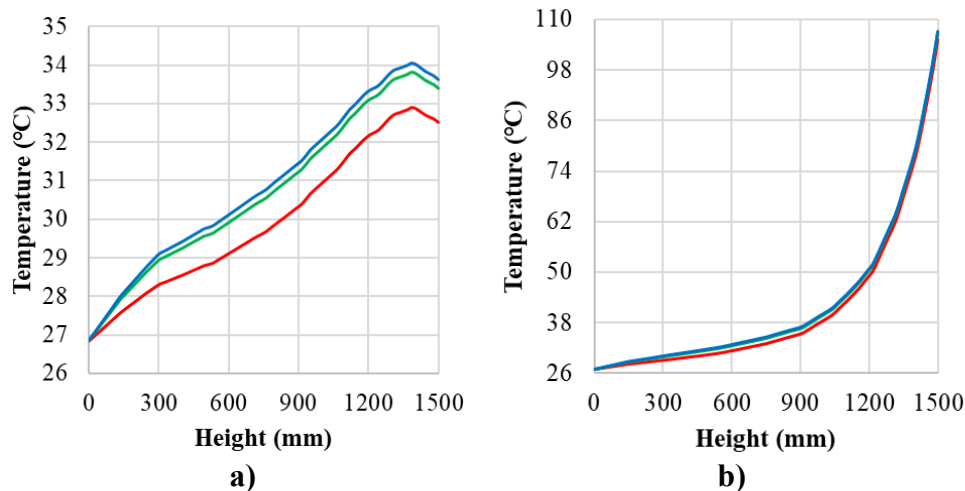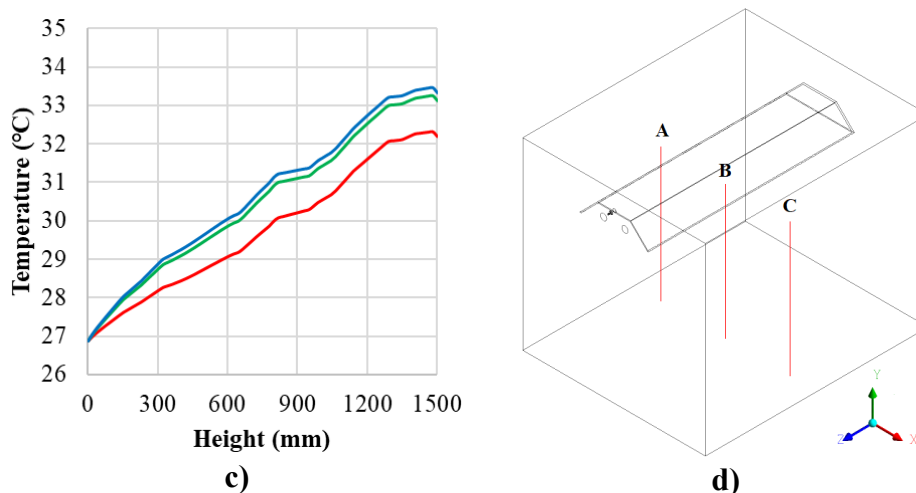
Fig 8. The temperature change graphs in the linear direction from the floor to the ceiling, a) A position, b) B position and c) C position, d) temperature measurement points; in graphs 0% (red colour), 20% (green colour), 40% (blue colour) premix ratios

CONCLUSIONS

In this paper, the effect of the fuel-air premix ratio in a radiant heater with thermal power of 22 kW on the combustion in the radiant tube and the room temperature was investigated numerically. In this context, three different premix ratios, 0%, 20% and 40%, were considered within the scope of the paper. Calculations were carried out for three-dimensional conditions. P1 model was chosen as the radiation model, and Standard k-ε was chosen as the turbulence model. Results were evaluated in terms of temperature distributions occurring in different planes in the room, temperature distributions on the surface and inside of the radiant tube and mass fraction of methane. Besides, graphs of temperatures in the linear direction from floor to ceiling at three locations in the room were drawn, and these values were compared for the three premix ratios.

When the results were evaluated;
- With the effect of the reflector, temperature gradients expanded towards the floor. The temperature gradients in the 40% premixed model more expanded to the room.
- Room temperatures were slightly higher in the 40% premixed model than with 20% or 0% premix.
- Temperatures increased with increasing height from the floor in all models. The highest temperatures occurred in the centre of the room, and the temperatures decreased towards the edges.
- In the model with a 40% premix ratio, the temperatures on the radiant tube surface were higher (by about 3%) than with 0% premix.
- As the premix ratio increased, the flame length decreased (by about 15%), and the flame temperature increased (by about 1%).
- As the premix ratio increased, the methane gas was consumed faster (by about 21%).

Based on these results, it can be said that the increase in premix ratios had a slight improvement in the temperature distribution of the room.

REFERENCES

1. XU, Q.; FENG, J.; DING, C.; CHANG, C.; XIONG, Y.; ZANG, Y. et al. Influence of the operating parameters and nozzle characteristics on flat double-P radiant tube performance. *Applied Thermal Engineering,* 2019, Vol. 155, P. 175–184.

2. CHARLES, E.B. *Industrial Burners Handbook*. 1st Edition. Boca Raton: CRC Press; 2003.

3. HASSAN, S.A. Experimental measurement and numerical simulation to determine characteristics of an infrared tube system. *HVAC&R Research,* 2012, Vol. 18, P. 446–460.

4. TSIOUMANIS, N., BRAMMER, J.G.; HUBERT, J. Flow processes in a radiant tube burner: Isothermal flow. *Fuel*, 2008, Vol. 87, P. 103–111.

5. TSIOUMANIS, N.; BRAMMER, J.G.; HUBERT, J. Flow processes in a radiant tube burner: Combusting flow. *Energy Conversion and Management,* 2011, Vol. 52, P. 2667–2675.

6. GARCÍA, A.M.; RENDON, M.A.; AMELL, A.A. Combustion model evaluation in a CFD simulation of a radiant-tube burner. *Fuel*, 2020, Vol. 276, P. 118013.

7. XU, H.T.; LIAO, X.W.; QU, Z.G.; LI, Y.Z.; CHEN, J. Experimental study of the effect of a radiant tube on the temperature distribution in a horizontal heating furnace. *Applied Thermal Engineering,* 2017, Vol. 113, P. 1–7.

8. XU, Q.; FENG, J.; ZHOU, J.; LIU, L.; ZANG, Y.; FAN, H. Study of a new type of radiant tube based on the traditional M-type structure. *Applied Thermal Engineering,* 2019, Vol. 150, P. 849–857.

9. MAZNOY, A.; KIRDYASHKIN, A.; PICHUGIN, N.; ZAMBALOV, S.; PETROV, D. Development of a new infrared heater based on an annular cylindrical radiant burner for direct heating applications. *Energy*, 2020, Vol. 204, P. 117965.

10. SCRIBANO, G.; SOLERO, G.; COGHE, A. Pollutant emissions reduction and performance optimization of an industrial radiant tube burner. *Experimental Thermal and Fluid Science*, 2006, Vol. 30, P. 605–612.

11. GORE, J.P.; ZHAN, G. NOx emission and major species concentrations in partially premixed laminar methane/air co-flow jet flames. *Combustion and Flame*, 1996, Vol. 105, P. 414-427.

12. LYLE, K.H.; TSENG, K.; GORE, J.P.; LAURENDEAU, N.M. A study of pollutant emission characteristics of partially premixed turbulent jet flames. *Combustion and Flame*, 1999, Vol. 116, P. 627-639.

13. SREENIVASAN, R.; KOLI, S.K.; RAGHAVAN, V. Experimental study of effects of callow air and partial premixing on liquid petroleum gas flames. *International Scholarly Research Network Thermodynamics*, 2012, P. 1-6.

14. AHANJ, M.D.; RAHIMI, M.; ALSAIRAFI, A.A. CFD modelling of a radiant tube heater. *International Communications in Heat and Mass Transfer*, 2012, Vol. 39(3), P. 432–438.

15. Fluent User's Guide, Fluent,Ver. 18, Ansys Fluent Tutorial Guide,Ansys Inc., Canonsburg, PA, 2017.

DETERMINATION OF SEVERE OPERATING CONDITIONS OF A POWER SYSTEM USING A COMPOSITE RANKING APPROACH

A. Trukšinas
Lithuanian Energy Institute
Breslaujos St. 3. LT-44403 Kaunas – Lithuania
+37063001641
arturas.truksinas@lei.lt

EXTENDED ABSTRACT

OVERVIEW

The power system is a complex and incredibly important engineering system. It carries the energy produced by various generating units and transmits it to end users, often over long distances. It supplies electricity to buildings, industrial sites, schools and homes. And it does this every day, all year round. The major function of an electric power system is to improve the system load requirements in the most economical way. A system's ability to provide an adequate supply of electrical energy is usually designated by the term reliability. However, the concept of power system reliability is extremely broad and covers all aspects of the system's ability to satisfy consumer requirements [1]. The concept of reliability has many meanings and cannot be associated with one specific definition. A simple classification of power system reliability is shown in Figure l. It reflects the two main aspects of a power system: system adequacy and system security. These two terms are best described as follows.
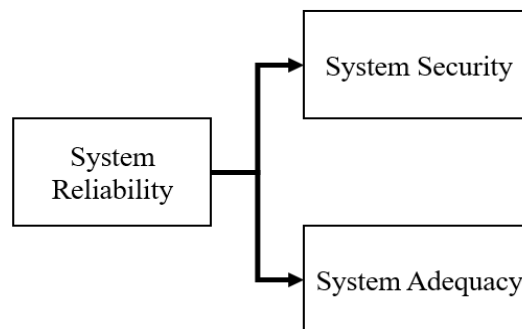
Fig. 1. Subsystem of power system reliability

Adequacy is the ability of the system to provide consumer electricity and required power at any time. This includes facilities needed to produce sufficient energy as well as associated transmission and distribution facilities needed to transport the energy to the actual customer load points. Therefore, adequacy refers to static conditions that do not include system disturbances. System security refers to the ability to respond to disturbances occurring in the system. Therefore, system security means the response to any disturbance that appears in the system. This includes conditions related to local and widespread disturbances and loss of key generation and transmission facilities. Since our proposed technique is related to power system security, it will be discussed in more detail below.

The security of the electrical power system is assessed to determine whether the grid is sufficiently secure against potential contingencies. In general, system security assessment can be divided into two main classes, i.e. static and dynamic security. The former examines the response of the power system to a contingency at a steady state. The static safety study examines the value of overvoltage's and/or under voltages at buses (nodes) and the overload condition of power lines and transformers. If in the event of a contingency, the voltage values of all bus bars are within a predetermined standard range and no line or transformer is overloaded, then the power network is statically safe. Further, analysis of power system safety can be applied through on-line and off-line conditions. The first package is used in the operational phase of the power system, and its results lead to preventive and corrective control policies, while the second package is used in the planning phase of the power system, which includes both - future operating modes and planning of the grid. The above-mentioned categorization is shown in Figure 2 for more detailed information on system security assessment reference [2].
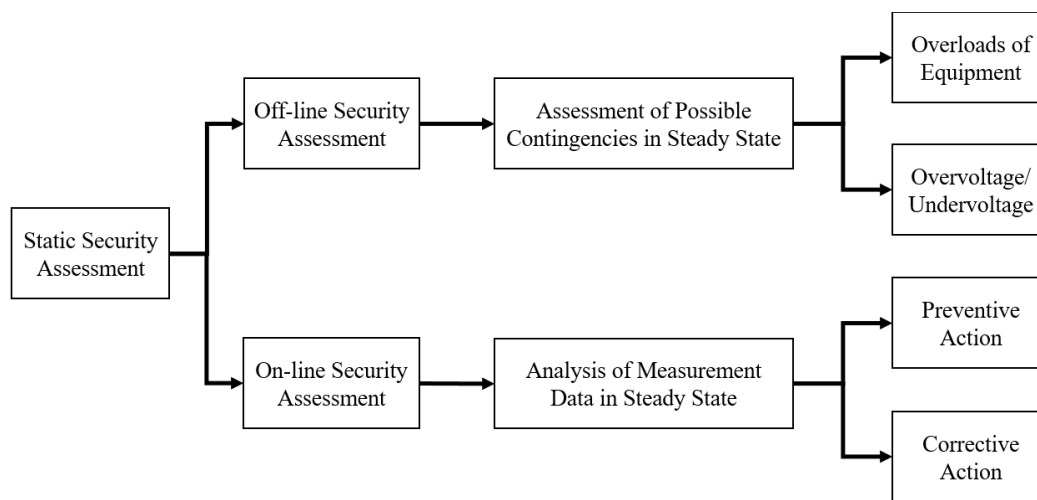
Fig. 2. Categorization of power system security assessment problems [2]

This paper introduces the assessment of the safety of an off-line power system using a combined approach. The objective of the method is to identify the list/set of power system elements whose outage will have the greatest impact on a power system. For a more precise description, a ranking of power lines and buses in normal operation is performed, with the aim of identifying the most affected power system elements. A similar approach is an N-1 method, which disconnects one element of the system and monitors how the voltage of the power system changes at the bus and whether lines and transformers are overloaded. A ranking is performed according to the severity of the fault and using the performance index described in papers [3, 4]. In this case, the N-1 method is used only to verify our proposed method.

The proposed method consists of a deterministic and probabilistic system evaluation. In the deterministic evaluation, the power grid is modelled using the AC power flow method since the chosen method is more accurate (although it is slower compared to DC). In a probabilistic or well-known analytical assessment, the same elements (power lines, transformers or generators) are assessed from a reliability point of view, i.e. the probabilities of their failure rates are calculated. In analytical assessment, reliable initial data is essential. Properly collected and processed data, which is translated into statistics, determine whether the probabilistic assessment of the system is accurate. The issue of data accuracy is presented in reference [5], where the authors from two different institutions (NERC and DOE) compare

data set events and write in a review, "We find evidence that these two datasets may not be accurate and complete. This places in question results of reliability analysis conducted with these data".
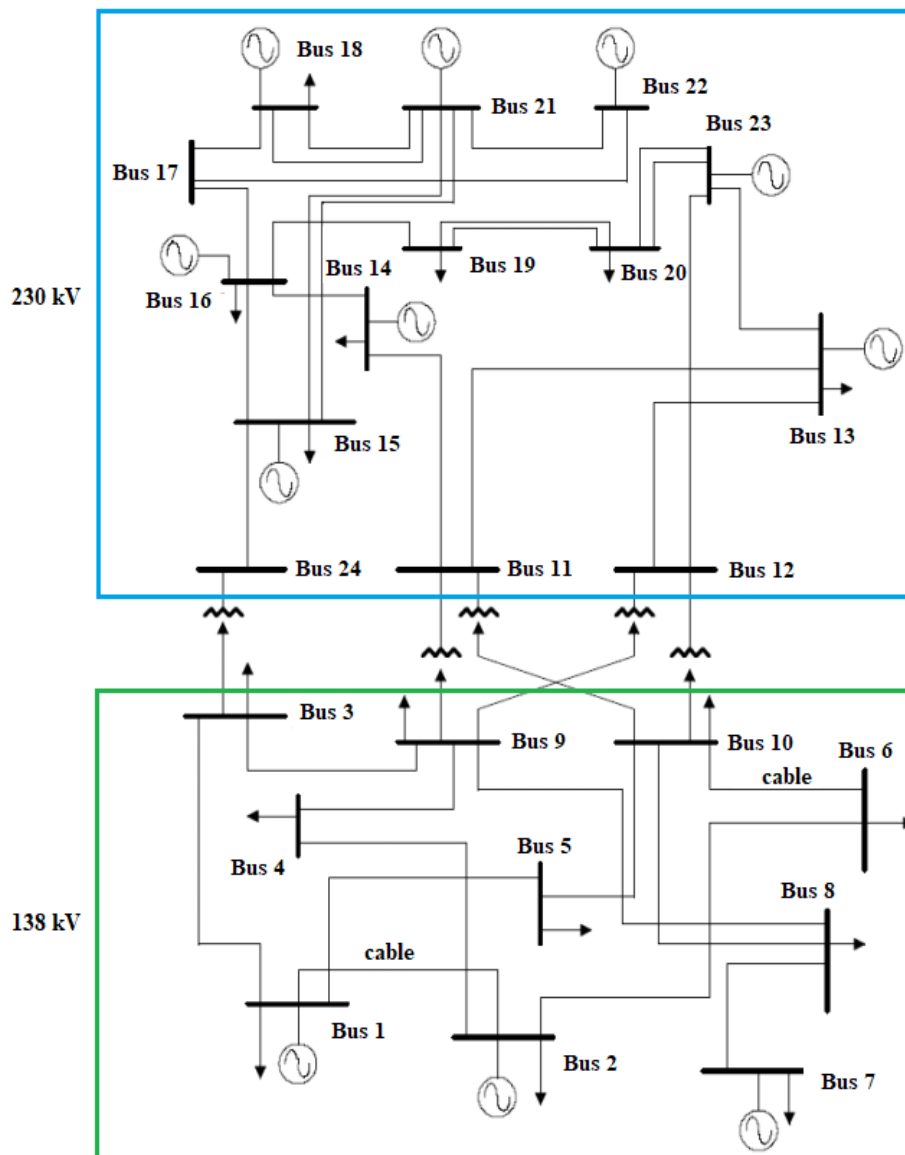
Fig. 3. Network topology of the IEEE RTS-79 system

METHODS

As mentioned above, the proposed approach consists of two parts: deterministic and probabilistic. To validate the proposed method, the frequently used IEEE RTS-79 scheme is chosen, which is shown in Figure 3. This scheme was chosen because it is often found in other scientific papers, and the results of the methods used can be compared. The IEEE RTS-79 scheme consists of 33 power lines, 5 transformers and 24 nodes. The power grid has two voltage levels – 138 kV and 230 kV and 10 buses (with different numbers of units).

Modelling. Input the initial data of the electricity network - load and generation on the buses and the parameters of the power lines (impedance), which depend on the length of the line and voltage level. Ideally, during steady state operation, all 24 nodes of the simulated power

network shall be as close as possible to their nominal values, where the permissible voltage deviation/change is ± 10 % U_N. The conductors shall not be overloaded, i.e. a permissible limit (MVA) is set. Power transformers, unlike power lines, can operate overloaded but for a limited period of time, so a correction factor will be introduced. Thus, the modelling of the static regime aims at ensuring that the permissible limits are not violated. The results obtained for the steady state, voltage at nodes and load on power lines and transformers are used in the proposed rating methodology.

Rating. The power lines and transformers are ranked according to the transmitted power, and a list is compiled from highest to lowest, as shown in Table 1.

Table 1. Ranking of elements by transmit power

Element no.	Power, MVA
n	max
...	…
k	min

The same ranking is done on the basis of the ratio of the transmitted power flow to the permissible power capacity, where a load index is introduced. The element load index is calculated as follows:

$$ELI_i = \frac{EL_i}{EL_{i\,max} \cdot k}, \tag{1}$$

EL_i – Power flow of the i-th element; $EL_{i\,max}$ – the rated power capacity of the i-th element; k – overload factor (used only for transformers).

Table 2. Ranking of elements by ELI index

Element no.	ELI, p.u.
n	max
...	…
k	min

When the static, in this case hourly, operating mode is calculated, it is assumed that the transformer may be overloaded, but this depends on the previous and the current load and ambient temperature. The possible overload level is usually determined by knowing the mentioned parameters and using the curves in Fig. 4.

In the diagram [6]:
K_1 – Initial load as a proportion of rated power,
K_2 – Permitted overload as a proportion of rated power (normally > 1),
t – Duration of K_2 in h,
Θ_a ambient temperature in °C.
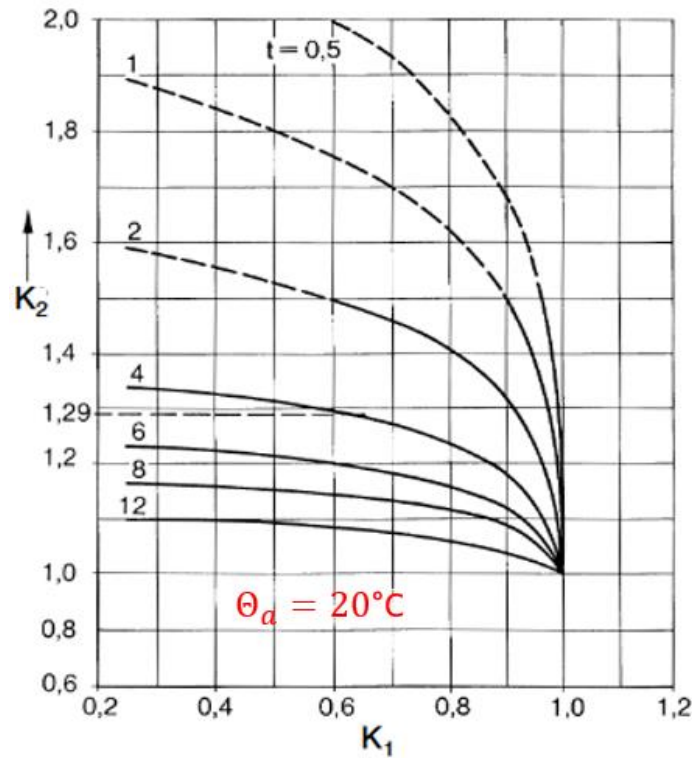
Fig. 4. Air-cooled oil-immersed transformer overload diagram [6]

It is assumed that the transformer can operate at 150% of its rated power for one hour. Node rating is a slightly more complex issue. It requires dedicated software, in this case, PSSE, which calculates the Thevenin impedance based on the grid data, which indicates the strength/weakness of the node with respect to the overall system. Based on the magnitude of the impedance, a ranking is performed as shown in the table. 3. The table also shows the elements connected to the nodes (lines or transformers). Generators are not evaluated in the simplified calculation.

Table 3. Values of the Thevenin impedance

Bus no.	Thevenin Impedance	Element no.	Line no.
n	max	n	...
...	…	...	...
k	min	k	...

From the first and second sets of ranked elements, we select 10% and 30% of the ranked elements from the third set.

RESULTS

Once the initial data (load and generation) are provided, the power flows in the simulated system are calculated. The simulated scheme has 38 elements (33 lines and 5 transformers). We only evaluate the 4 most power transmitting elements, which represent 10% of the ranked elements.

Table 4. Ranking of elements by transmit power

Element no.	Power	Line no.	Element no.	Power	Line no.
16	617.1	110-211	30	149.3	217-218
15	599.2	109-212	3	145.5	101-105
23	475.1	214-216	34	142	219-220
17	447.3	110-212	35	142	219-220
28	343.3	216-217	12	127.3	108-109
22	305.2	213-223	20	117.9	212-213
18	294.9	211-213	5	109.4	102-106
27	289.4	215-224	11	106.8	107-108
7	283.8	103-224	32	76.7	218-221
38	268.9	221-222	33	76.7	218-221
25	248.9	215-221	8	61.1	104-109
26	248.9	215-221	29	61	216-219
21	238.4	212-223	9	59.8	105-110
19	233	211-214	4	46.2	102-104
14	224.5	109-211	2	39.1	101-103
36	219.5	220-223	24	38.3	215-216
37	219.5	220-223	1	37	101-102
31	208.2	217-222	6	29.3	103-109

The following ranking uses the element load index. Also, only 4 items are evaluated.

Table 5. Ranking of elements by *ELI* index

Element no.	Power	Line no.	Element no.	Power	Line no.
16	1.0285	110-211	36	0.4390	220-223
23	0.9502	214-216	37	0.4390	220-223
10	0.9297	106-110	31	0.4164	217-222
15	0.8877	109-212	14	0.3742	109-211
3	0.8314	101-105	8	0.3491	10-109
17	0.7455	110-212	9	0.3417	105-110
12	0.7274	108-109	30	0.2986	217-218
28	0.6866	216-217	34	0.2840	219-220
5	0.6251	102-106	35	0.2840	219-220
22	0.6104	213-223	4	0.2640	102-104
11	0.6103	107-108	20	0.2358	212-213
18	0.5898	211-213	2	0.2234	101-103
27	0.5788	215-224	1	0.2114	101-102
38	0.5378	221-222	6	0.1674	103-109
7	0.5068	103-224	32	0.1534	218-221
25	0.4978	215-221	33	0.1534	218-221
26	0.4978	215-221	29	0.1220	216-219
21	0.4768	212-223	13	0.0989	108-110

Table 5 below shows the list of ranked nodes using Thevenin impedance.

Table 5. Ranking of elements by Thevenin impedance

Bus no.	Thevenin Impedance	Element no.	Line no.
4	0.0700	4, 8	104-102, 104-109
6	0.0601	5, 10	106-102, 106-110
5	0.0568	3, 9	105-101, 105-110
8	0.0516	11, 12, 13	108-107, 108-109, 108-110
3	0.0452	2, 6, 7	103-101, 103-109, 103-224
24	0.0402	7, 27	224-103, 224-215
7	0.0387	11	107-108
22	0.0236	31,38	222-217, 222-221
2	0.0224	1,4,5	102-101, 102-104, 102-106
1	0.0221	...	...
10	0.0218	...	...
9	0.0217	...	...
19	0.0198	...	...
14	0.0198	...	...
12	0.0187	...	...
17	0.0178	...	...
11	0.0173	...	...
20	0.0166	...	...
18	0.0149	...	...
21	0.0146	...	...
15	0.0130	...	...
13	0.0118	...	...
16	0.0116	...	...
23	0.0107	22, 36, 37	223-213, 223-220, 223-220

Using the 3 lists above, 17 (red colour) items have been selected, which, if disconnected, are likely to cause issues with the operation of the electricity system. The N-1 technique is used to verify that these items are correctly identified. Table 6 shows the N-1 results.

Table 6. Results of the simulated system after the N-1 technique

Disconnected element	Overloaded (vulnerable) element
102-106	101-105, 106-110
104-109	106-110
106-110	102-106
211-213	214-216
212-223	214-216
213-223	214-216
215-224	103-109, 106-110, 214-216
103-224	103-109,106-110, 214-216
109-211	214-216

109-212	214-216
110-211	101-105, 108-109

It was found that the ranking of the nodes needs to be refined because, after the N-1 check, it was observed that disconnecting some of the power lines does not cause major problems for the system, even though they are on the ranked list. This is because the calculation of the Thevenin impedance does not take into account the current generation at the node, and therefore additional corrections are likely to be introduced in the future. The target after the corrections is to select 10-20% of the nodes.

CONCLUSIONS

The result of the ranking process shows that the total number of elements screened is 17 out of 38, representing 44.7% of the total number. The N-1 technique is used for verification, where the simulated network operates in a severe mode where one element is disconnected. It shows that in 11 out of 38 modes, the element's bandwidth constraints are violated, and it is overloaded. This mode of operation is therefore undesirable, as it further overloads the system when the relay protection systems are triggered, which can lead to a system collapse. It was found that 7 of the 11 severe operational modes were identified using the item ranking methodology.

REFERENCES

1. BILLINTON, R.; ALLAN, R.N. Power-system reliability in perspective. *ELECTRONICS & POWER*, 1984, Vol. 30, No. 3, P. 231-236

2. GHOLAMI, M.; SANJARI, M.J.; SAFARI, M.; AKBARI, M.; KAMALI, M.R. Static security assessment of power system: A review. *Electrical Energy Systems*, 2020, Vol. 30, No. 9 Link to the internet <https://onlinelibrary.wiley.com/doi/full/10.1002/2050-7038.12432>

3. ÇELO, M.; BUALOTI, R.; VOSHTINA, E. Assessment of the Transmission System Operation Conditions through the Evaluation of Performance Index. *International Journal of Engineering Research and Technology*, 2020, Vol. 13. No. 2, p. 280-286.

4. BULAT, H.; FRANKOVIC, D.; VLAHINIC, S. Contingency Analysis – A Power System Operator Tool. *Energies*, 2021, Vol. 14, No 4.

5. FISHER, E.; ETO, J.H.; LACOMMARE, K.H. Understanding Bulk Power Reliability: The Importance of Good Data and a Critical Review of Existing Sources. 45th Hawaii International Conference on System Sciences. Maui, HI, USA. 2012 January 4-7.

6. BALZER, G.; BOEHLE B.; HANEKE, K.; KAISER, Hans G.; POLHMANN, R.; TETTENBORN, W. *Switchgear Manual*, 9th edition. Berlin: Cornel Sen Girodat, 1993. P. 561. ISBN 3-464-49234-0.

A REVIEW ON ELECTRICAL POWER QUALITY PROBLEMS

B. K. Uzundağ, O. Timur
Cukurova University
Electrical Electronics Engineering Department
Sarıçam, Adana, 01250 – Turkey
05466761228
kaanuzndg@gmail.com, otimur@cu.edu.tr

ABSTRACT

The term electrical power quality refers to the quality of the electricity used. The power quality can be said to be good if the electricity is uninterrupted, does not cause damage to the devices, and does not cause a pause in production. With the development of technology, because of the increased use of non-linear circuit parts and a variety of different sorts of devices, energy power quality issues are becoming more prevalent. As a result of this, today, interest in electrical power quality and solving electrical power quality problems have started to increase. With the motivation from this issue, in order to solve power quality problems, it is necessary to determine what the problems are. When problems are identified and well known, it will be easier to find solutions to these problems. The main purpose of this study is to give information about the electrical power quality issue. In this study, the electrical power quality problems are explained together with the subjects and the DVR system used as a solution to the voltage sag problem is explained. In this study, firstly, the concept of power quality is explained in detail. It has been emphasized why power quality is important and how much damage it causes to the industry per year has been researched. It is explained why power quality deteriorates and which factors deteriorate power quality. The power quality problems in the literature have been researched and classified under various subheadings. The classification was made under seven main titles "transients, short term voltage changes, long term voltage changes, voltage fluctuations–flickers, voltage imbalance, voltage frequency variations and voltage distortions and other sub-titles". All of these sub-headings are explained separately by giving graphical examples. Devices that are widely used in the industry have been researched to correct issues with power quality. The voltage sag problem is explained, and information is given about the reasons for this problem. Then, information is given about the DVR device used as a solution to the voltage sag problem. The features, circuit diagram, internal structure, circuit elements and the DVR system's functioning principles are described. In addition, the advantages and disadvantages of the DVR system are presented.

Keywords: Electrical Power Quality, Power Quality Problems, Sag, Voltage Sag Solution, DVR.

INTRODUCTION

The energy requirement has increased in parallel with the increasing technology. This need has led to increased interest towards renewable energy sources.

Renewable energy has joined today's power system and thus is used for voltage regulation, vibration, harmonic distortion, stability, etc. technical difficulties have arisen. These issues should be limited according to IEC and IEEE standards. [1]

The main purpose of this study is to reclassify the power quality problems in the literature, to give information about the tools that are the solution to the power quality problems and to introduce the DVR device.

ELECTRICAL POWER QUALITY

What Is Electrical Power Quality?

Power quality is that at a determined end of the network, the Voltage maintains the nominal values of amplitude-frequency values, and the voltage waveform maintains the sinusoidal form. A power quality problem arises when voltage, current or frequency variations cause malfunction or poor operation of the consumer's equipment. In other words, the power quality problem can be defined as "variations in operating frequency, voltage, current and that cause user devices to fail or stop working altogether".

"Quality Level" is a term used to describe power quality. The Power Quality Level, depending on the electricity generation and usage, is known as ± 5% fluctuation of voltage in transmission and distribution. [2]

Why Is Power Electrical Quality Important?

Power quality has a significant economic impact that should not be forgotten. In a study conducted in European Union countries, it is estimated that the damage caused by power quality problems in industry and commercial areas is 10 Billion Euros per year. The expenditures made for the elimination of quality problems are approximately 5% of this number. [3]

Why Does Power Quality Deteriorate?

Power quality problems usually occur due to poor connection, leakage in cables, deterioration of electronic circuit elements, lightning strikes to the grid, and faulty grounding.

However, the main causes of power quality problems are when very high current draw loads such as arc furnaces with high harmonic loads are connected to the grid.

TERMS OF ELECTRICAL POWER QUALITY

Transients – Components of The Transitional Regime:

The phenomenon of transient voltage disturbances distorting the sinusoidal waveform of voltages is referred to as transients. Peak amplitude, rising time, and pulse duration are

commonly used to define it. In the old electrical grid, impulsive transients are usually caused by load switching, lightning, and other factors. [4]

Instant Transients

A sudden, non-power frequency changes when voltage, current, or both are constant. [5] The Transients are voltage fluctuations of very short duration (< 0.5 cycles). Switching events, lightning strikes, sudden discharge of induced current, arcs between contacts, etc., create an instantaneous transient. Depending on the magnitude and energy of the violence, they may cause damage to the device. [2] The instantaneous transient waveform is shown in Fig. 1.
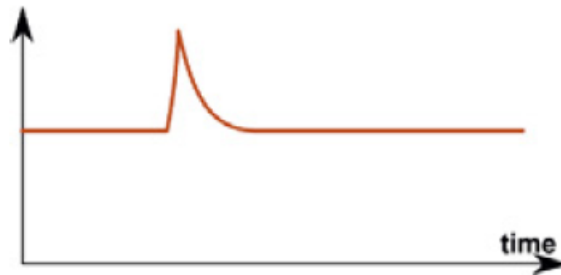
Fig. 1. The instantaneous transient waveform

Oscillating Transients

They are high frequency and short duration fluctuations superimposed on a current or voltage wave. They occur during energizing of transformers, switching events or ferroresonance conditions. [2] The oscillating transient waveform is as in Fig. 2.

Fig. 2. The oscillating transient waveform

Short Term Voltage Changes:

Switching activities, malfunctions, and large power fluctuations in the system create short-term variations, whereas power flow variations cause long-term variations in steady-state. [6]

Three types of short-term voltage changes exist Sag, Swell, and Interruption.

SAG

Voltage sag is defined as a decrease in the rated voltage to a value between 10% and 90% of the effective value for a period of 10ms to 1 minute. [2] A malfunction in the system usually causes a voltage drop in the supply system. They can also be triggered by huge loads being started. [7]

The voltage sag waveform is seen in Fig. 3.
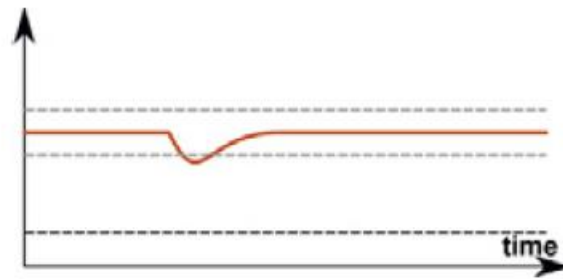
Fig. 3. The voltage sag waveform

SWELL

The opposite of voltage sag is voltage swell. The RMS voltage level is increased from 110 percent to 180 percent of the nominal rate, which is known as voltage swell. The RMS magnitude and also duration level will be used to define it. Normally, voltage swell is linked to system faults. [8] The swell waveform is as in Fig. 4.
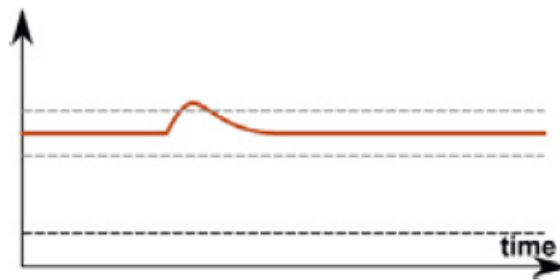
Fig. 4. The swell waveform

INTERRUPTION

Interruptions in the electrical supply can last anywhere from a few milliseconds too many seconds. Insulation failure, lightning, and insulator flashover are the most common causes of these interruptions [7].

LONG-TERM VOLTAGE CHANGES:

These are power outages that last longer than one minute. Problems caused by system faults that are not caused by changes in the load on the system are over voltage and low voltage [9].

PERMANENT INTERRUPTIONS

An interruption is a complete loss of voltage, generally taking from a few cycles to several hours to terminate. A momentary interruption is one that lasts between 0.5 and 150 cycles. Short interruptions are defined as disruptions lasting 3 seconds to 1 minute [10].

LOW VOLTAGE

It is the situation where the voltage in the AC system is less than 90% of its value for more than 1 minute. It occurs in situations such as failure of a capacity bank or overloading of the grid [2].

The Voltage drop waveform is as in Fig. 5.
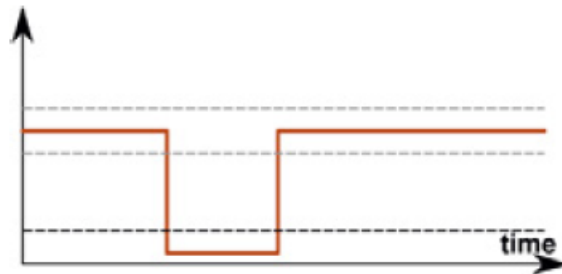
Fig. 5. Voltage drop waveform

OVERVOLTAGE

Voltage surges are sudden increases in voltage that last for a long time. When the RMS value of the voltage is at or above 1.1 p.u., the disturbance is categorized as over voltage. Lightning strikes and circuit switching can create overvoltage. [11-12] Over voltage waveform is as seen in Fig. 6.
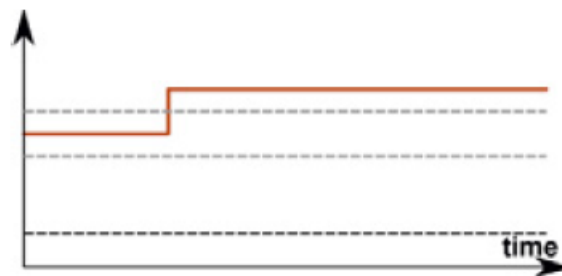
Fig. 6. Over voltage waveform

VOLTAGE FLUCTUATIONS – FLICKERS

Flicker is a visual fluctuation induced by rapid changes in electrical amplitude. Flicker has been linked to non-linear electronic circuits, particularly modern power electronic converters. [13] The voltage fluctuation (Flicker) waveform is as in Fig. 7.
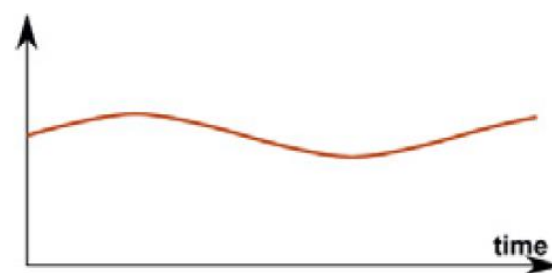
Fig. 7. Voltage fluctuation (Flicker) waveform

VOLTAGE IMBALANCE

The asymmetry of the three-phase load is the primary source of three-phase voltage imbalance in the typical three-phase three-wire distribution network. Too many single-phase load unbalances cause voltage unbalance in Three-phase, four-wire distribution network. [14]

VOLTAGE FREQUENCY VARIATIONS

Electric networks normally operate with 50 or 60 Hz. It is undesirable for the mains voltage to fluctuate. Frequency fluctuations shall not exceed +4%/6% of the nominal frequency, according to "EN 50160," a European Union standard [15].

VOLTAGE DISTORTIONS:

Waveform distortion is the continuous deviation of the wave from an ideal sine waveform. There are five main forms of waveform distortions: DC Offset, Notches, Noise, and Harmonics [2].

DC OFFSET

The presence of a DC current or voltage within an AC power system is defined as DC offset. This may occur due to the effect of half-wave rectifiers. Direct current found in alternating current networks can have a detrimental effect on transformer cores. This causes additional heating and reduced transformer life [3].

NOTCHES

In one full wave of the mains voltage (during 20 ms), the collapses are repeated as the number of rectifier pulses are called notches. It is generally formed by the delay of the switch transfer of the transformer and line inductances feeding the rectifiers [3]. The notch waveform is as in Fig. 8.
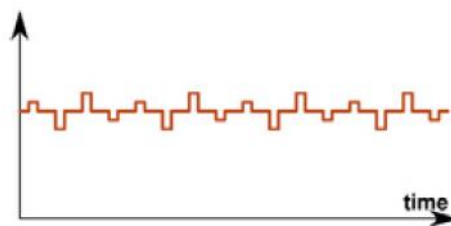
Fig. 8. Notch waveform

NOISE

Noise is defined as undesired electrical signals with a broadband spectral content of less than 200 kHz added to the current or voltage in the phase conductors or present in the neutral conductors. Noise in the power system can be generated by power supplies (switched), circuits used for control, devices used in power electronics and solid state AC-DC converters. Problems with noise become even greater with improper grounding. Noise

creates confusion in programmable controllers and microcircuits. Isolation transformers, noise filters and line regulators can help to mitigate this issue [3]. Noise in a linear signal is shown in Fig. 9 below.
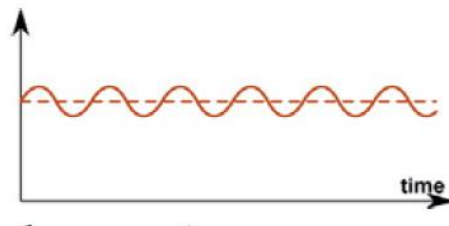
Fig. 9. Noise in a linear signal

HARMONICS

In alternating current power systems, it is desirable that the mains voltage and the current user from the mains be sinusoidal in ideal conditions. However, although the applied voltage is sinusoidal, the current of loads such as power electronics, arc furnaces, and discharge lamps is not sinusoidal. The fact that the current is not sinusoidal can also affect the waveform of the grid voltage. In this case, distortions in the voltage waveform begin [3]. Pure Sine Wave and Harmonic distortion waveforms as in Fig. 10.

Fig. 10. Sine waveform (Left), Sine waveform after harmonic distortion (Right)

SOLUTIONS FOR PROBLEMS WITH POWER QUALITY

When current and voltage waveforms deviate from their intended look, power quality issues exist [16].

To ensure electrical power quality, it is necessary to eliminate issues with power quality. Static VAR Compensator (SVC), Active Power Filters (APF), Unified Power Quality Conditioner (UPQC), Dynamic Voltage Restorer (DVR), Magnetically Controlled Reactor (MCR) and Static Compensator (STATCOM) are all several solutions for quality problems.

SOLUTION TO VOLTAGE SAG PROBLEMS

Special power devices for power electronics have been developed to solve voltage drop problems in electrical distribution systems and end-user loads. One of these devices is the DVR (Dynamic Voltage Restorer).

DYNAMIC VOLTAGE RESTORER (DVR)

Dynamic Voltage Restorers are used for the Voltage Sag problem. They are not effective and cannot be used for other power quality problems. It has low losses, and DVR Injects only the missing part of the supply voltage, it is a cost-effective solution. It is difficult to protect and cannot compensate for interruptions [17].

It can be seen in Figure 11 below that the DVR device is between the mains and the loads and is a series connected with a transformer. The power circuit of the DVR basically consists of a voltage source inverter (VSI) and a direct current (DC) energy source. During voltage drops in the power system, the DVR measures the voltage needed to maintain a steady voltage of the load and generates it using the DC energy source and the inverter. The transformer and inverter voltage is delivered to the electrical power system, and the output voltage is maintained constant. In this way, the load is prevented from being affected by voltage drops. In summary, to decrease the effects of voltage fluctuations in sensitive loads, the DVR sends controlled energy to the grid in series. [16] The parts of the DVR Device are as follows:

a) Injection transformer: It is used in most DVR systems to offer galvanic isolation and to make converter topology and protection devices simpler.

b) Equipment for by-pass: A bypass path is used for the load current when overloads, during faults and during maintenance.

c) Converter: A Voltage Source Converter (VSC) is most commonly used. Pulse width modulation is used in this section to convert DC energy to AC.

d) Equipment for disconnecting: During maintenance and repair, it is utilized to totally separate the DVR device from the mains.

e) Energy storage and DC-link Connection: The VSC produce an AC voltage to the output of the device using a DC-link voltage. Active power injection is required for maintaining supply voltages in most of the voltage dips.

f) Line-filter: To eliminate the switching harmonics caused by the PWM - VSC, a line-filter is added [17].
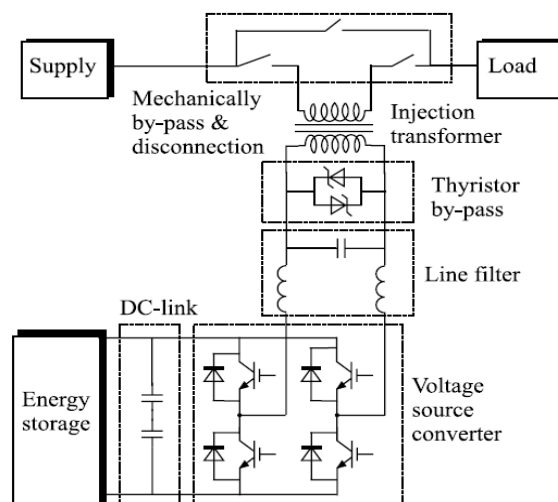
Fig. 11. The conventional DVR structure. DVR's Basic Components: Injection Transformer, Output Filter, Inverter, Energy Storage Unit.

CONCLUSIONS

Humans have always had energy requirements. Electrical energy can't be stored cheaply, and its 'quality' can't be guaranteed while it's being used. The increased demand for electrical energy has revealed a new definition of "more reliable and better quality energy." Electrical energy, like all other industries, places a premium on comprehensive quality. 'Energy

Quality Problems' must be resolved in order to ensure the most efficient use of energy and system capacity. Problems that contribute to low quality should be addressed at the source.

Transients, Short Term Voltage Changes, Long Term Voltage Changes, Voltage Fluctuations–Flickers, Voltage Imbalance, Voltage Frequency Variations and Voltage Distortions are the main Power Quality issues in the literature. Classifying and researching these issues in detail is important for the quality of energy.

As a result, if it is desired to ensure electrical power quality, power quality problems should be learned well, precautions should be taken for problems, and immediate action should be taken when the problem occurs.

REFERENCES

1. KUMARL, V.; PANDEY, A, S.; SINHA, S. *Grid Integration and Power Quality Issues of Wind and Solar Energy System: A Review*, International Conference on Emerging Trends in Electrical, Electronics and Sustainable Energy Systems, ICETEESES–16, IEEE, 2016

2. HEKİM, M. *Investigation of the Effects of Photovoltaic - Wind Turbine Hybrid Power Generation Systems on the National Electricity Grid*. Pamukkale: Pamukkale University - Institute of Science and Technology, 2011.

3. İNCİ, M.; BAYINDIR, K. Ç.; TÜMAY, M. Developing a New Method for Determining Voltage Problems in Dynamic Voltage Restorers. Ankara: *Journal Of The Faculty of Engineering and Architecture of Gazi University*, Çukurova University – Department of Electrical and Electronics Engineering, Yıldırım Beyazıt University – Department of Energy Systems Engineering, 2016.

4. PING, H.; DONGB, L.; XINC, Q. *Influence of Grid-connected Photovoltaic Systems on Power Quality*, 2019 IEEE 2nd International Conference on Automation, Electronics and Electrical Engineering (AUTEEE), 2019.

5. TEKE, A; SARIBULUT, L.; TÜMAY, M. *Power Quality Disturbances and Custom Power Devices*. Adana: Çukurova University, Department of Electrical and Electronics Engineering, June, 2011, Vol.26. No.1.

6. BROECK, G.V.D.; STUYTS, J.; DRIESEN, J. *A* Critical Review of Power Quality Standards and Definitions Applied To DC Microgrids, *Applied Energy*, 2018, Vol. 229, P. 281–288.

7. GAO, M.; Kehinde Awodele, Member IEEE, *Investigation of Power Electronics Solutions to Power Quality Problems in Distribution Networks*, IEEE, 2015.

8. Kavitha, V.; Subramanian, K. *Investigation of Power Quality Issues and Its Solution for Distributed Power System*,2017 International Conference on circuits Power and Computing Technologies [ICCPCT], IEEE,2017.

9. TUR, M. R. *Solution Methods and Recommendations for Power Quality Analysis in Power Systems*. Journal of Engineering and Technology Solution, Batman University, December 2018.

10. EROĞLU, H. I*nvestigation of a Distribution Network in terms of Power Quality and Harmonics*. Konya: Selçuk University – Institute of Science and Technology – Department of Electrical and Electronics Engineering, 2009.

11. ROJIN, R. K. A Review of Power Quality Problems and Solutions in Electrical Power System, *International Journal of Advanced Research in Electrical*, Electronics and Instrumentation Engineering,2013, Vol. 2, No. 11, P. 5605-5614.

12. AGARWAL, S.; KUMAR, S.; ALI, S. *A Research Review of Power Quality Problems in Electrical Power System*, MIT International Journal of Electrical and Instrumentation Engineering, 2012, Vol. 2, No. 2, P. 88-93.

13. MUHAMMAD, A.; SAQIB, A.; ALI, Z. Power Quality Issues and the Need for Active-Power Compensation in the Grid Integration of Wind Power, *Renewable and Sustainable Energy Reviews*, 2015, Vol. 43, P. 51–64.

14. HE, L.; CHAO, L.; YINFAN, Z. Research on New Characteristics of Power Quality in Distribution Network, 2019 IEEE International Conference on Power, Intelligent Computing and Systems (ICPICS), IEEE,2019.

15. DAVID, L.; GÁLVEZ, E.; COLLADO, A. Trends in Power Quality, Harmonic Mitigation and Standards for Light and Heavy Industries: A Review, *Energies* 2020, Vol. 13, P. 5792. Doi: 10.3390/en13215792.

16. İNCİ, M.; BAYINDIR, K. Ç.; TÜMAY, M. Developing a New Method for Determining Voltage Problems in Dynamic Voltage Restorers. Ankara: Journal Of The Faculty of Engineering and Architecture of Gazi University, Çukurova University - Department of Electrical and Electronics Engineering, Yıldırım Beyazıt University - Department of Energy Systems Engineering, 2016.

17. NIELSEN, J. G. *Design and Control of a Dynamic Voltage Restorer*. Denmark: Aalborg Universitet, 2002. ISBN: 87-89179-42-0.

LIFETIME ESTIMATION AND MANAGEMENT SYSTEM OF LITHIUM-ION BATTERIES

G. Vaideliene, J. Razukeviciute, J. Dabulyte-Bagdonaviciene, T. Iesmantas, R. Alzbutas

Kaunas University of Technology, Department of Applied Mathematics
Studentu str. 50, LT-51368, Kaunas – Lithuania
gintare.vaideliene@ktu.lt, justina.razukeviciute@ktu.edu, jurgita.dabulyte@ktu.lt,
tomas.iesmantas@ktu.lt, robertas.alzbutas@ktu.lt

EXTENDED ABSTRACT

OVERVIEW

Lithium-ion batteries (LIBs) have become the standard for electrochemical energy storage in various applications because of their many desirable qualities, including high energy density, high power density, and long cycle life [1].

According to statistics provided by Grand View Research, Inc. [2], the global lithium-ion battery market size was valued at USD 53.6 billion in 2020 and is expected to grow at a compound annual growth rate (CAGR) of 19.0 % from 2020 to 2028. The growth of the market is especially attributed to the growing demand for lithium-ion batteries in electric vehicles.

A Battery Management System (BMS) is essential in LIBs. This device manages a real-time control of each battery cell, communicates with external devices, and calculates the State of Charge (SOC) and State of Health (SOH) using measurements of temperature and voltage, etc. It is the brain of the battery and plays a critical role in its levels of safety, performance, charge rates, and longevity. Key features of the battery management system are shown in Fig. 1.

Fig. 1. Key features of the battery management system

The research aims to develop a model for analysis of battery longevity and reliability data, as well as technology for intelligent diagnostics and prediction of battery status. To achieve this goal, different methods and models need to be considered that could be implemented in a real system in the future. One of such models, for SOH estimation, is introduced in this paper.

METHODS

One of the most important steps for a BMS is battery model selection. BMS, based on the Equivalent Circuit Model (ECM), is very widely used in industry due to the simplicity of the model, the possibility to estimate the complexity of the calculations, and the easy parameterization process [3]. But to achieve more efficient BMS, the more advanced battery diagnostic algorithms and electrochemical models are becoming increasingly popular. In the scientific literature, the most common electrochemical models are P2D, SP, SP+, or SEC. It should be noted that for BMS development based on an electrochemical model, the identification and fitting of parameters under different operating conditions must be performed, as the accuracy of the model output depends on it [3].

Another step for a BMS is to assess the internal state of the battery. The most popular states are SOC and SOH. Various mathematical methods are used to evaluate these parameters. Common estimation approaches include 1) filtering-based methods, for example, Kalman filters or particle filters and their modifications, and 2) data-driven methods, such as various neural networks, genetic algorithms, or support vector machines [4]. It is worth mentioning that data-driven methods exclusively rely on experimental or operational data and often do not require specific knowledge of the battery operation process, require the collection of large amounts of data [5], and are distinguished by a high degree of accuracy [6]. As a good representor of data-driven methods, in this research, a Feedforward Neural Network (FNN) was mainly considered to estimate the SOH of the battery. Some other popular intelligent methods, including FNN, are presented in ref. [7-9].

The determination of SOH and lifetime estimation is critical for several reasons. First, it monitors critical battery failures, which is especially important due to safety issues with LIBs. Second, it allows optimized battery usage and maintenance to maximize efficiency and return on investment. Third, it is necessary to accurately estimate the SOC and degradation process or Remaining Useful Lifetime (RUL). SOH can be expressed as [4]:

$$SOH = \frac{C_a}{C_{rated}} \times 100\%,\qquad(1)$$

where C_a and C_{rated} Are the actual and rated capacity, respectively.

The estimation of battery SOH and RUL depends on many aspects, from the choice of the battery model to the exploitation conditions of a working battery, thus, their estimation and application of BMS are quite challenging. However, they are going to be implemented in one of the Lithuanian companies.

RESULTS

To assess the overall performance of SOH evaluation, a data set consisting of four lithium-ion batteries from the NASA data set [10], with current, voltage, and temperature parameters

were used in this work. A couple of SOH predictions for one selected battery are shown in Fig. 2.
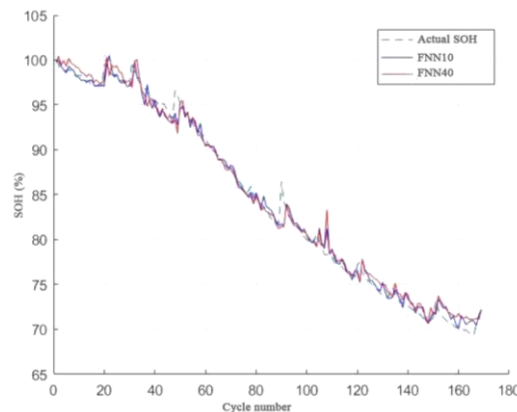
Fig. 2. SOH predictions for the single battery

As it can be observed from Fig. 2, the largest deviation is seen in the 85th cycle when both FNN cases had difficulties predicting such a large jump. Small deviations are also seen in cycles 50 and 105. However, the estimations are quite accurate compared to the actual values.

CONCLUSIONS

The lifetime of batteries depends on many aspects, from the choice of the battery model to the exploitation conditions of a working battery, thus, the estimation and application of BMS are quite challenging, even if it is based on data-driven methods and there is no issue of calculation accuracy.

The performed analysis showed that the evaluation of internal states is one of the essential factors ensuring the effectiveness of BMS. Although the analysis was performed with laboratory data set, this is useful for further research development and for practical and real application of BMS.

ACKNOWLEDGMENT

REFERENCES

1. LYBBERT, M.; GHAEMI, Z.; BALAJI, A.K.; WARREN, R. Integrating life cycle assessment and electrochemical modelling to study the effects of cell design and operating conditions on the environmental impacts of lithium-ion batteries. *Renewable and Sustainable Energy Reviews*, 2021, Vol. 144, P. 111004.

2. Lithium-ion Battery Market Size, Share & Trends Analysis Report by Product (LCO, LFP, NCA, LMO, LTO, Lithium Nickel Manganese Cobalt), By Application, By Region, And Segment Forecasts, 2021 – 2028. Market Analysis Report, 2021. Link to the internet <https://www.grandviewresearch.com/industry-analysis/lithium-ion-battery-market>.

3. LI, W.; CAO D.; JÖST, D.; RINGBECK, D.; KUIPERS, M.; FRIE, F.; SAUER, D.U. Parameter sensitivity analysis of electrochemical model-based battery management systems for lithium-ion batteries. *Applied Energy*, 2020, Vol. 269, P. 115104.

4. WANG, Z.; FENG, G.; ZHEN, D.; GU, F.; BALL, A. A review on online state of charge and state of health estimation for lithium-ion batteries in electric vehicles. *Energy Reports*, 2021, Vol. 7, P. 5141-5161.

5. SHEN, S.; SADOUGHI, M.; CHEN, X.; HONG, M.; HU, C. A deep learning method for online capacity estimation of lithium-ion batteries. *Journal of Energy Storage*, 2019, Vol. 25, P. 100817.

6. NOURA, N.; BOULON, L.; JEMEÏ, S. A review of battery state of health estimation methods: hybrid electric vehicle challenges. *World Electric Vehicle Journal,* 2020, Vol. 11, No. 4, P. 66.

7. CHEN, C.; XIONG, R.; YANG, R.; SHEN, W.; SUN, F. State-of-charge estimation of Lithium-ion battery using an improved neural network model and extended Kalman filter. *Journal of Cleaner Production*, 2019, Vol. 234, P. 1153-1164.

8. CHOI, Y.; RYU, S.; PARK, K.; KIM, H. Machine learning-based lithium-ion battery capacity estimation exploiting multi-channel charging profiles. *IEEE Access*, 2019, Vol. 7, P. 75143-75152.

9. FAN, Y.; CHEN, Z.; WU, J.; WU, H.; HUANG, J. SOH estimation method of lithium-ion battery based on multilayer feedforward neural network. 8th International Conference on Power Electronics Systems and Applications (PESA), 2020.

10. Prognostics Center of Excellence - Data Repository. NASA Ames Progn Res Center. Link to the internet <https://ti.arc.nasa.gov/tech/dash/groups/pcoe/prognostic-data-repository>.

I.4.   Smart energy systems

OVERVIEW OF GRID NODES SELECTION STRATEGIES FOR POWER QUALITY MONITORING

V. Liubčuk
Lithuanian Energy Institute
Breslaujos g. 3, LT-44403 Kaunas – Lithuania
+370 (694) 60 558
vladislav.liubcuk@lei.lt

EXTENDED ABSTRACT

INTRODUCTION

The development of the Smart Grid is inevitable without various monitoring systems. One of them is Power Quality (PQ) monitoring – the newly emerging field which has been attracting more and more attention since the last few years. Low PQ may cause serious damage to both sensitive loads and grid equipment, decrease power supply reliability, and increase outage time which inevitably leads to huge economic losses. Measurements are essential for situation assessment; however, PQ monitors installation is currently associated with high investments and operational costs. Ideally, PQ monitors must be installed at each busbar. Since resources are limited, monitoring of whole power system nodes is hardly implemented. Thus, the grid nodes selection strategy should be determined in order to achieve maximal (desired) observability with a limited number of analysers.

In general, node prioritization strategy depends on the desired aim and can be classified into two large groups regarding focus on either customer or electric power grid. The main aim of the paper is to review world experience in nodes selection strategy for PQ monitoring. Some examples of nodes selection options are given below:
1. Focus on customers – mostly low voltage grid monitoring:
    Industrial customers complaints: point of common coupling (PCC) monitoring or any in-plant grid point monitoring, if required);
    Industrial, commercial and residential customers installed power ratio;
    Type of loads: for example, priority to large electric motors, critical loads (sensitive to voltage sags);
    Random selection of PCC or other points for short-duration measurements with portable PQ monitors;
    Yearly energy consumption;
    Critical (problematic) nodes, which are a priori known by DSO.
2. Focus on electric power grid – mostly high and medium voltage grid monitoring:
    Most critical substations, their technical conditions, for example, availability of communications for remote monitoring;
    Connection points of power plants or PQ mitigation devices (capacitor banks, surge arresters);
    Penetration of distributed generation, renewable energy sources;
    Line length, presence of HVDC lines.

In addition, the type of monitoring must be considered. Firstly, measurements can be made with either fixed or portable PQ monitors or Smart Meters. Each option has its own features, such as registered PQ events, sampling frequency, accuracy and cost. Secondly, monitoring can be either remote or non-remote. In the case of remote monitoring, solving communication issues is required, but many advantages exist, such as diminished resources (time, human, transport) for data gathering, the easier process of data, detect data loss.

LITERATURE REVIEW

Many studies are carried out to investigate how to optimize PQ monitor allocation. In [1] (2005), Belgian DSOs PQ monitoring campaigns, carried out since the 90s, are described: fixed PQ monitors were installed at HV/MV injection substations (starting with the most critical substations). 427 monitors were installed at 218 substations. At the MV level, phase-to-phase voltages were measured, excluding some areas with many overhead lines where phase-to-ground monitoring was performed (for protection systems functioning investigation). In addition, temporary measurements with 64 mobile monitors were performed in order to evaluate the validity of customer complaints, issue advice, or investigate the disturbing effects of some LV load types.

In [2], a PQ monitoring campaign was initiated in 2005 by the Italian Regulatory Authority for Electricity and Gas in order to investigate the present performance of the MV network in terms of PQ: 600 instruments have been installed during 3 years at 400 MV busbars (covered 11 % of MV network) in HV/MV substations. The main selection criteria were: line length and type, number of MV customers, LV customer's density (customers/km^2), and neutral mode. In addition, 200 MV nodes were freely selected by customers (73 installations) and DSOs (127 installations).

In [3], state-of-the-art of PQ monitors allocation before 2013 is briefly summarized. At EHV and HV level, monitoring of all EHV/HV, EHV/MV, and HV/MV substations, connection points of all EHV and HV customers and power stations was considered a good practice. At the MV level, it is recommended to monitor all EHV/MV, HV/MV and selected MV/LV substations and connection points of MV customers. At the LV level, random monitoring of LV PCC with fixed and portable monitors (and possibly with Smart Meters in the future) was considered a good practice.

[4] Presents a novel algorithm for optimal PQ monitor placement in both transmission and distribution systems. In the algorithm, two parameters are used to obtain an optimal solution: topological monitor reach area and coverage control parameter. Monitor reach area determination is based on residual voltage matrix (obtained from the most severe short-circuits simulation) comparison with coverage control parameter (defined threshold). Both the IEEE 34-node distribution system and IEEE 30-node transmission system have been used for algorithm validation; however, any examples of application in practice were not presented. The approach is limited: the most severe short-circuit – three-phase short-circuit – occurs rarely (less than 20 % of all short-circuit events). TSO and DSO are also aiming at single-phase short-circuits (the most frequent event) detection. In addition, the strategy requires a large number of short-circuit simulations (in order to determine monitor coverage), which would be hard to implement in reality in the case of a large power system.

Table 1. Reviewed papers summary

Reference (year)	PQ monitors allocation criterion	Application in practice	Theoretical validation
[1] (2005)	Fixed monitors – at critical HV/MV substations; portable monitors – regarding customer complaints and consultation, and for specific load investigation	Monitoring campaign in Belgian grid since the late 90s	–
[2] (2009)	400 MV busbars in HV/MV substations regarding the total length of lines, line type, neutral mode, the quantity of customers; 200 freely selected MV nodes	Monitoring campaign in Italian grid 2005–2009	–
[3] (2013)	Power stations, all EHV/HV, EHV/MV, HV/MV and selected MV/LV substations, all HV and MV PCC, random LV PCC	No. State-of-the-art review	
[4] (2012)	Most severe short-circuit observability (coverage) is defined by residual voltage threshold	No	IEEE 34-node and IEEE 30-node tests
…	…	…	…

Keywords: Power Quality, monitoring, nodes prioritization, allocation strategy

REFERENCES

1. LAUWERS, P.; PIRENNE, C.; SOMMEREYNS, P.; VANCEOTSEM, W.; JAEGER, E.; WITTE, M. Power Quality Monitoring in Belgian Distribution Networks. *18th CIRED*. Turin, Italy. 2005 June 6–9.

2. CHIUMEO, R.; PORRINO, A.; GARBERO, L.; TENTI, L.; NIGRIS, M. The Italian Power Quality Monitoring System of the MV Network Results of the Measurements of Voltage Dips After 3 Years Campaign. *20th CIRED*. Prague, Czech Republic. 2009 June 8–11.

3. BOLLEN, M.; BAUMANN, P.; BEYER, Y.; CASTEL, R.; ESTEVES, J.; FAIAS, S.; FRIEDL, W.; LARZENI, S.; TRHULI, J.; VILLA, F.; STROM, L. Guidelines for Good Practice on Voltage Quality Monitoring. *22nd CIRED*. Stockholm, Sweden. 2013 June 10–13.

4. IBRAHIM, A.; MOHAMED, A.; SHAREEF, H.; GHOSHAL, P. A New Approach for Optimal Power Quality Monitor Placement in Power System Considering System Topology. *PRZEGLĄD ELEKTROTECHNICZNY* (Electrical Review), 2012, No. 9a, P. 272–276.

DESIGN AND ANALYSIS OF SWITCHED CAPACITOR-BASED QUASI Z-SOURCE DC-DC CONVERTER FOR BATTERY CHARGING APPLICATION

M. M. Savrun

Electrical&Electronics Engineering Department,
Adana Alparslan Türkeş Science and Technology University
Adana – Turkey
+90 506 533 06 53
msavrun@atu.edu.tr

K. Ayten

Electrical&Electronics Engineering Department,
Osmaniye Korkut Ata University
Osmaniye – Turkey
+90 539 461 77 07
kenanayten@osmaniye.edu.tr

ABSTRACT

This study proposes a novel switched capacitor-based quasi Z-source DC-DC converter (SwC_QzC) topology for battery charging applications. Batteries are charged according to a charging protocol, including constant voltage (CV) and constant current (CC) charging algorithms in order to expand the battery lifetime. The charging algorithms operate considering the instantaneous voltage of the battery. On the other hand, battery current ripple is crucial due to its influence on battery life span, and it is desired to be low for as long as possible. In this study, a novel high voltage gain DC-DC converter topology that is equipped with CC/CV charging algorithms has been conducted. The proposed system stands out with reduced current ripple, high voltage gain, and high-efficiency performances. In order to evaluate and test the performance of the proposed system, a 2 kW proof-of-concept model has been conducted in MATLAB/Simulink environment. The system is designed with 48-V input and 132-V output in order to charge the 30-Ah 132-V battery. The performance of the proposed topology has been validated with CC/CV charging operations. In addition, the duty cycle/voltage gain/efficiency and battery current ripple performance of the proposed topology have been investigated. Consequently, the battery charging performance results of the proposed topology shows that the proposed topology and the control scheme operate successfully with high-efficiency values under CC / CV charging modes.

Keywords: Switched capacitor, quasi z-source DC-DC converter, Battery charging, constant current, constant voltage, charging algorithm

INTRODUCTION

In the last decade, the interest in Renewable Energy Sources (RES) has increased with the severe impact of climate change, and a lot of RES has been connected to the grid. However, control of supply-demand balance has become a challenge with increasing RES because of their intermittent nature. Therefore, energy storage systems such as; batteries, supercapacitors and superconducting magnetic energy storage have prevalently started to integrate in order to provide supply-demand balance. Batteries had high energy density step forth with the developing technology inside these energy storage systems. On the other hand, batteries are attracting a growing interest with the widespread use of electric vehicles (EVs) and distributed generations (DGs) [1]. They are performing as a buffer in DG applications in order to mitigate the adverse effect of the intermittent nature of RESs [2]. In addition, they are performing as primary energy units in EV applications to provide propulsion for EVs. For this reason, several studies are carried out on DC-DC converter topologies such as; dual active bridge [3], SEPIC converter [4], high step-up converter [5], non-isolated three-port converter [6], T-type isolated multi-port converter [7] and asymmetrical hybrid multilevel converter [8], used in battery current/voltage regulation [9]. Also, quasi z-source converter topology is commonly used in many applications thanks to simple control, low component and high voltage gain [10]. In the study [11], analysis and equivalent circuits of the quasi-z-source converter have been presented. Also, there is a lot of switched capacitor circuit in the literature. In the study [12], a performance comparison of a quasi-z-source converter with and without switched capacitors has been given. In another study [13], an extended quasi-z-source topology with switched capacitor and inductor was presented. In addition to DC-DC converter topologies, control methods of DC-DC converters are crucial for affecting battery health and lifespan. Batteries are frequently charged with CC/CV charging algorithms to expand the lifetime of battery [14].

The aims of the study are to derive an effective high-gain DC-DC converter topology for battery charging applications and to evaluate the performance under CC/CV charging operations. The proposed topology, which is abbreviated as SwC_QzC, is composed of quasi z-source converter topology, switched capacitor circuit, and an LC filter. The SwC_QzC topology excels with high energy efficiency, high voltage gain, and a simple control structure with a single switch. In order to demonstrate the performance results of the SwC_QzC in terms of battery charging application, a simulation including a 2 kW, 48-V input, 132-V output SwC_QzC model and 30-Ah 132-V battery has been developed in MATLAB/Simulink environment. The performance results of the system show that the SwC_QzC properly performs the charging algorithms under steady-state conditions as well as performs transition between algorithms under transient conditions.

POWER CIRCUIT AND CONTROL SCHEME

In this study, a switched capacitor circuit has been integrated into a quasi-z-source boost converter. The proposed converter topology, which is abbreviated as SwC_QzC, is illustrated in Fig. 1. The SwC_QzC topology has been designed to achieve high voltage gain and low output current ripple with a simple control structure and a high-efficiency value. The proposed converter consists of a quasi-z-source circuit, a switched capacitor, and an output filter, including capacitor (C) and inductor (L).
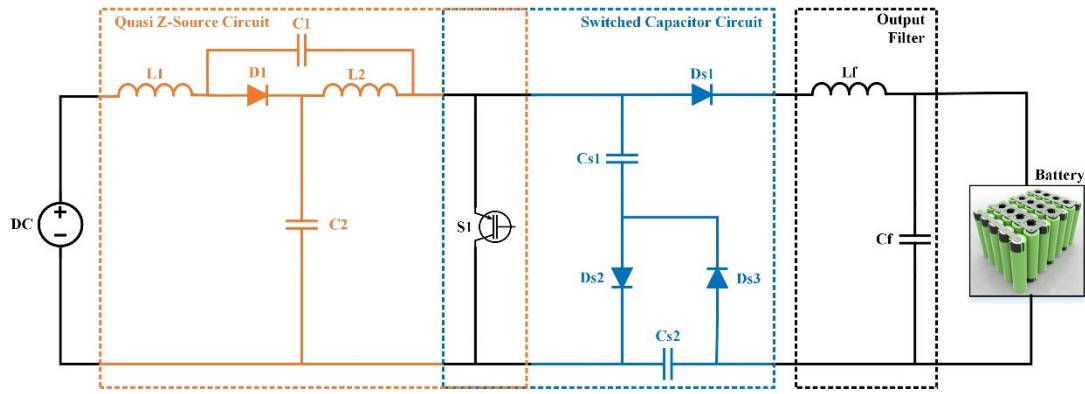
Fig. 1. SwC_QzC Topology

The SwC_QzC integrates the quasi-Z-source and switched capacitor circuits with a common switch which has the capability to regulate the power flow as well as adjust the voltage gain. Since the charging current ripple of the battery is the key issue in regard to extending the battery lifetime, the SwC_QzC topology is equipped with an LC filter to reduce the battery current ripple. In the prosed model, IGBT is used as a switch with a R_{on}=1 mΩ. Parameters of the quasi z-source circuit are L_1=1 mH, L_2=1 mH, C_1=100 μF, C_2=100 μF, and parameters of switched capacitor circuit are C_{S1}=100 μF, C_{S2}=100 μF. All diodes in the model have parameters: R_{on}=1 mΩ and forward voltage V_f=0.8 V. Finally, output filter parameters are determined as L_f=1 mH and C_f=200 μF.
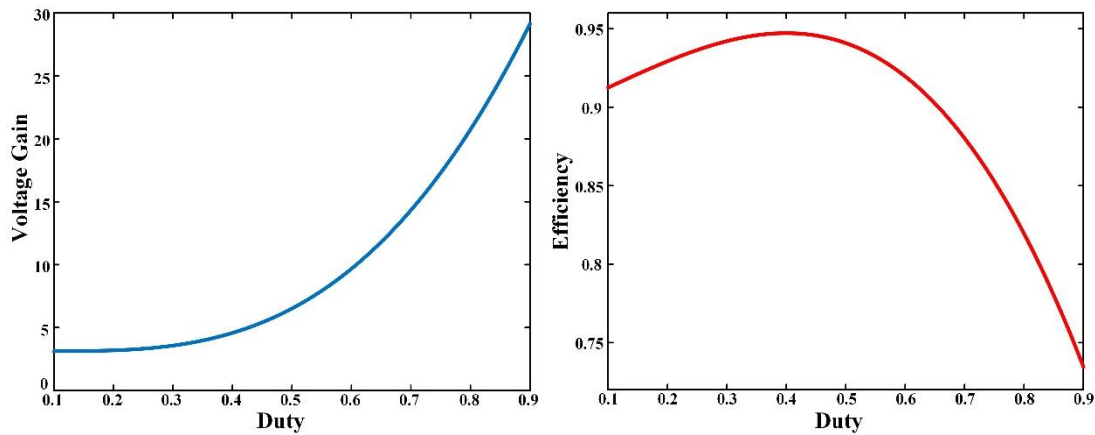
Fig. 2. Voltage Gain and Efficiency Curve of SwC_QzC

The characteristics of SwC_QzC topology are examined, and the voltage gain/efficiency curve according to the duty cycle has been illustrated in Fig. 2. As understood from Fig. 2, the proposed topology provides high voltage gain values up to 30 and high-efficiency values up to 95%. However, the efficiency of SwC_QzC is dramatically decreased in the high duty cycle as expected.
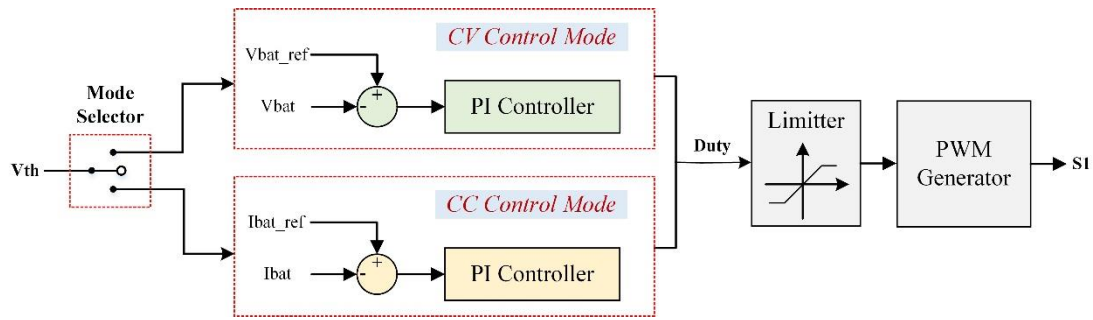
Fig. 3. Control Scheme of Proposed System

The SwC_QzC has been designed as a battery charger that is able to operate in two states: CC and CV. The control of the overall system is carried out using two individual PI controllers, adapted to CC and CV control. The controllers adaptively switch between each other and adjust the duty cycle of the S_1 switch. The control scheme of the proposed system has been illustrated in Fig. 3. As seen from Fig. 3, the charging mode is selected considering the threshold voltage (V_{th}) value determined according to the characteristic voltage value of the battery. Following the determination of charging mode, the measured feedback values (I_{bat} and V_{bat}) and reference values (I_{bat_ref} and V_{bat_ref}) are compared to compute the error values. The computed error values are applied to the PI controllers in order to generate duty cycle values.

PERFORMANCE RESULTS

In order to test and evaluate the performance of the proposed converter, a simulation system including a DC source, the SwC_QzC, and the battery has been modelled in MATLAB/Simulink environment. The parameters of the simulation model are summarized in Table 1. The CC/CV charging performance validation has been conducted under two steady-state and transient conditions, including the switching of CC to CV control.

Table 1. Parameters of the Designed Model

Parameters	Value
Input Voltage	48 V
Nominal Battery Voltage	120 V
Battery Capacity	30 Ah
Switching Frequency	5 kHz
Constant Charging Current Value	15 A
Constant Charging Voltage Value	132 V

The simulation results show the steady-state conditions, in which the time interval of 0.5-1.3 s corresponds to CC charging and the time interval of 1.3-2.3 s corresponds to CV charging, and a transient condition represents the switching of CC to CV charging algorithm. As illustrated in Fig. 4, the battery is charging with a constant 15 and a power rating of 2 kW during the first time interval. The state of charge waveform of the battery validates the charging condition with a gradually increasing curve. The battery is charged with a constant current up to the threshold voltage value. Following reaching the threshold voltage value, the charging algorithm switches to CV from CC at the transient condition. During the second time interval, the battery is charged with a constant voltage value (~132 V). However, the charging current of the battery is in exponentially decaying form (decrease to 15 A from

0.7 A) because the battery voltage approaches the fully charged voltage value. In parallel with the decaying charging current, the charge power decreased to ~100 W from 2 kW. The state of charge waveform of the battery validates the charging condition with a gradually increasing curve with a lower slope in comparison with the first time interval.
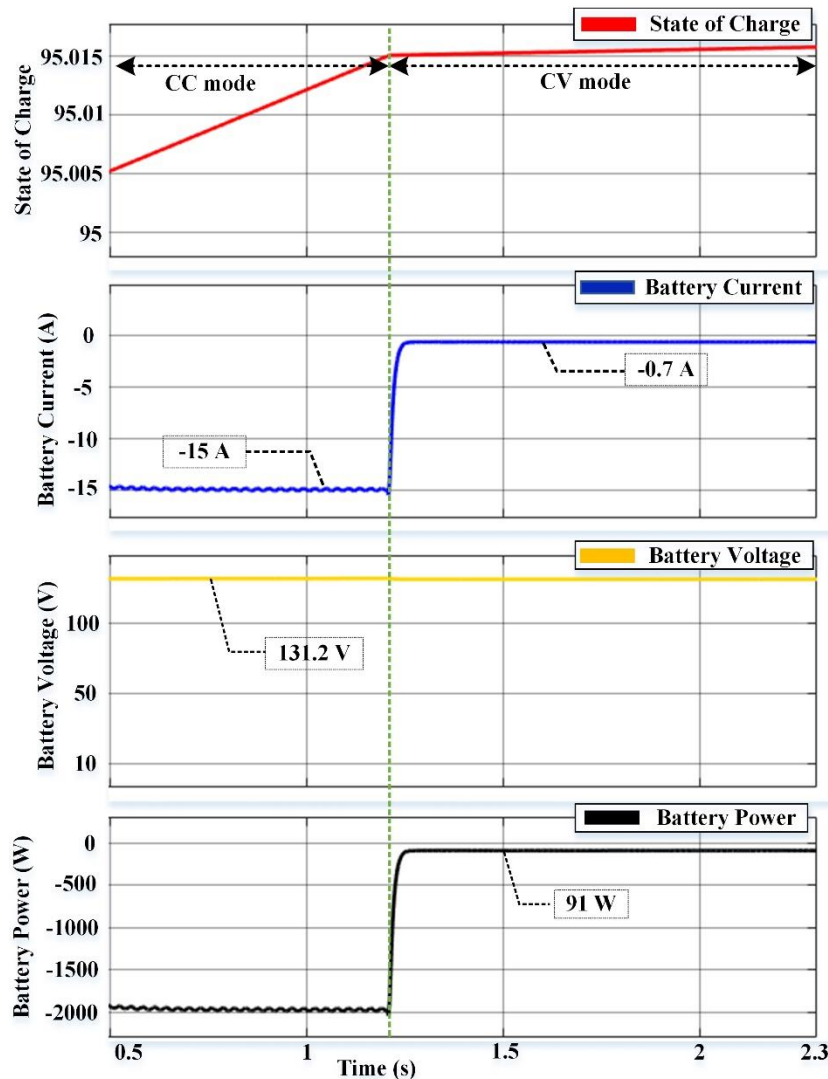
Fig. 4. Performance waveforms of SwC_QzC

CONCLUSIONS

In this paper, switched capacitor-based quasi-z-source converter topology is proposed. SwC_QzC is designed as a battery charger in order to provide the desired feature in battery charging applications. Characteristics features of the proposed topology, such as voltage gain and efficiency, are presented in this study. The outstanding features of the SwC_QzC are; (i) simple control with a single switch, (ii) achieving high voltage gain, (iii) reduced battery current ripple, and (iv) performing battery charging algorithms. The performance validation of the SwC_QzC is evaluated with a MATLAB/Simulink simulation model under CC and CV modes. Performance results illustrate that the proposed converter topology reaches up to 95 % efficiency and 30 gain values as well as performs CC-CV charging functionalities with high efficiency during operations.

REFERENCES

1. HAMIDAN, M. A.; BOROUSAN, F. Optimal planning of distributed generation and battery energy storage systems simultaneously in distribution networks for loss reduction and reliability improvement. *Journal of Energy Storage*, 2022, Vol. 46, No. 103844.

2. WALI, S. B.; HANNAN, MA; REZA, MS; KER, PJ; BEGUM, RA; ABD RAHMAN, MS; MANSOR, M. Battery storage systems integrated renewable energy sources: A biblio metric analysis towards future directions. *Journal of Energy Storage*, 2021, Vol. 35, No. 102296.

3. IYER, V. M.; GULUR, S.; BHATTACHARYA, S. Small-signal stability assessment and active stabilization of a bidirectional battery charger. *IEEE Transaction on Industry Applications*, 2019, Vol. 55, No. 1, P. 563–574.

4. SINGH, B.; KUSHWAHA, R. A PFC Based EV Battery Charger Using a Bridgeless Isolated SEPIC Converter. *IEEE Transaction on Industry Applications*, 2020, Vol. 56, No. 1, P. 477–487.

5. FATHABADI, H. Novel photovoltaic based battery charger including novel high efficiency step-up DC/DC converter and novel high accurate fast maximum power point tracking controller. *Energy Conversion and Management*, 2016, Vol. 110, P. 200–211.

6. AKAR, F. A fuel-cell/battery hybrid DC backup power system via a new high step-up three port converter. *International Journal of Hydrogen Energy*, 2021, Vol. 46, No. 73, P. 36398–36414.

7. SAVRUN, M. M.; İNCI, M.; BÜYÜK, M. Design and analysis of a high energy efficient multi-port dc-dc converter interface for fuel cell/battery electric vehicle-to-home (V2H) system. *Journal of Energy Storage*, 2022, Vol. 45, No. 103755.

8. FOTI, S.; TESTA, A.; SCELBA, G.; DE CARO, S.; TORNELLO, L. D. A V2G Integrated Battery Charger Based on an Open End Winding Multilevel Configuration. *IEEE Open Journal of Industry Applications*, 2020, Vol. 1, P. 216–226.

9. TURKSOY, A.; TEKE, A.; ALKAYA, A. A comprehensive overview of the dc-dc converter-based battery charge balancing methods in electric vehicles. *Renewable and Sustainable Energy Reviews*, 2020, Vol. 133, No. 110274.

10. DING, X.; LI, K.; HAO, Y.; LI, H.; ZHANG, C. Family of the Coupled-Inductor Multiplier Voltage Rectifier Quasi-Z-Source Inverters. *IEEE Transactions on Industrial Electronics*, 2021, Vol. 68, No. 6, P. 4903–4915.

11. WAVEGUIDES, Q.; SUN, W.; BALANIS, C. A. Analysis and Design of Quasi-Z-Source Equivalent DC–DC Boost Converters. *IEEE Transactions on Industry Applications*, 2020, Vol. 56, No. 6, P. 4363–4373.

12. NGUYEN, M. K.; LIM, Y. C.; PARK, S. J. A comparison between single-phase quasi-Z-source and quasi-switched boost inverters. *IEEE Transactions on Industrial Electronics*, 2015, Vol. 62, No. 10, P. 6336–6344.

WWW.CYSENI.COM

13. HO, A.; CHUN, T.; KIM, H. Extended Boost Active-Switched-Capacitor/Switched-Inductor Quasi-Z-Source Inverters. *IEEE Transactions on Power Electronics*, 2015, Vol. No. 10, P. 5681–5690.

14. SHAHJALAL, M.; SHAMS, T.; ISLAM, ME; ALAM, W.; MODAK, M.; HOSSAIN, SB; RAMADESIGAN, V.; AHMED, MR; AHMED, H.; IQBAL, A. A review of thermal management for Li-ion batteries: Prospects, challenges, and issues. *Journal of Energy Storage*, 2021, Vol. 39, No. 102518.

TECHNOLOGY OF INCORPORATING WOOD-BASED TRIBOELECTRİC NANOGENERATORS (TENGS) INTO SMART MANUFACTURING AND INDUSTRY: A REVIEW

E. KOCATÜRK, M. ZOR*, F. ŞEN
Zonguldak Bulent Ecevit University
67900 – Turkey
+90 5383746404
enginkocaturkk96@gmail.com

Z. CANDAN
İstanbul University-Cerrahpaşa
34473 – Turkey
+9 (0212) 3382400
zekic@istanbul.edu.tr

EXTENDED ABSTRACT

Due to the development of technology and the increase in the living population, energy consumption has increased. The increase in energy consumption has led to a decrease in our resources and damage to nature. For these reasons, scientists have tried to turn to less harmful and renewable energy sources and find ways to produce healthier energy. Triboelectric Nano generators are energy generation devices that convert mechanical energy into electricity through a combination of the triboelectric effect and electrostatic induction. Triboelectric Nano generators (TENGs) show superior performance with power density and conversion efficiency. In addition to its advantages, such as flexible design and lightness, it meets the requirements thanks to its various material selectivity. Due to its low density, high power density, wide material variety, efficiency at low frequencies, and cheapness, it is widely used in self-running systems in material selectivity [1-5]. The wood material is a building material that is biodegradable, environmentally friendly, renewable, abundant and preferred due to its affordable cost. Lignocellulosic materials, which are flexible as a result of chemical processes, can be easily converted into micro or nanomaterials. Due to its porous structure and unique feature, it paves the way for the use of materials produced from wood in triboelectric Nano generators. It is predicted that the use of wood material as TENG material will also prevent environmental impact [6-10]. It is seen in some studies that a new generation of wood-based triboelectric Nano generator (W-TENGs) has been designed, and it has been revealed that the Nano generator acts with the effect of friction force in the experiments [11-12]. This study is a summary of current studies of W-TENGs designed with wood and wood-derived materials. This review it is aimed to contribute to the literature knowledge required for the use of TENGs in different fields in the future, in addition to the production, development and design of new TENGs with renewable, environmentally friendly, inexpensive and excellent properties by using wood and wood-derived materials in TENGs. As a result, W-TENG-based self-powered systems will have potential applications in big data analytics, smart home and smart city environments, which will open up new opportunities for wood-based electronics.

Keywords: Smart Materials, Nano generators, Triboelectric, Energy Recovery, Sustainability

REFERENCES

1. WANG, S.; LİN, L.; WANG, L.Z. Triboelectric Nano generators as self-powered active sensors. *Nano Energy*, 2015, Vol. 11, P. 436–462.

2. WANG, LZ; CHEN, J.; LİN, L. Progress in triboelectric Nano generators as a new energy technology and self-powered sensors. *Energy Environmental Science*, 2015, Vol. 8, No. 8, P. 2250–2282.

3. ZHU, G.; PENG, B.; CHEN, J.; JİNG, Q.; WANG, L.Z. Triboelectric Nano generators as a new energy technology: from fundamentals, devices, to applications. *Nano Energy,* 2015, Vol. 14, P. 126–138.

4. DONG K.; PENG X.; WANG, L.Z. Fiber/fabric-based piezoelectric and triboelectric Nano generators for flexible/stretchable and wearable electronics and artificial intelligence. *Advanced Materials*, 2019, Vol. 32, No.5, P. 1902549.

5. MAHAPATRA, B.; PATEL, KK; PATEL, PK A review on recent advancement in materials for piezoelectric/triboelectric Nano generators. *Materials Today: Proceedings*, 2021, Vol. 46, No. 11, P. 5523-5529.

6. ZHAO, C.; FENG, H.; ZHANG, L.; Lİ, Z.; ZOU, Y.; TAN, P.; OUYANG, H.; JİANG, D.; YU, M.; WANG, C.; Lİ, H.; XU, L.; WEİ, W.; Lİ, Z. Highly efficient in vivo cancer therapy by an implantable magnet triboelectric Nano generator. *Advanced Functional Materials*, 2019, Vol. 29, No. 41, P. 1808640.

7. WU, J.; CHANG, C.; CHANG, Y. High-output current density of the triboelectric Nano generator made from recycling rice husks. *Nano Energy*, 2016, Vol. 19, P. 39–47.

8. WANG, H.; WANG, J.; HE, T.; Lİ, Z.; LEE, C. Direct muscle stimulation using diode-amplified triboelectric Nano generators (TENGs). *Nano Energy*, 2019, Vol. 63, P. 103844.

9. WEN, Z.; CHEN, J.; YEH, H.M.; GUO, H.; Lİ, Z.; FAN, X.; ZHANG, T.; ZHU, L.; WANG, L.Z. Blow-driven triboelectric Nano generator as an active alcohol breath analyser. *Nano Energy,* 2015, Vol. 16, P. 38–46.

10. ZHU, G.; CHEN, J.; ZHANG, T.; JİNG, Q.; WANG, Z.L. Radial-arrayed rotary electrification for high performance triboelectric generator. *Nature Communications,* 2014, Vol. 5, No. 3426, P .1-9.

11. WANG, S.; LİN, L.; WANG, ZL Nanoscale triboelectric-effect-enabled energy conversion for sustainably powering portable electronics. *Nano Letters,* 2012, Vol. 12, No. 12, P. 6339–6346.

12. CAİ, C.; MO, J.; LU, Y.; ZHANG, N.; WU, Z.; WANG, S.; NİE, S. Integration of a porous wood-based triboelectric Nano generator and gas sensor for real-time wireless food-quality assessment. *Nano Energy*, 2021, Vol. 83, P. 105833.

I.5. Energy economics and policy

CORPORATE SOCIAL RESPONSIBILITY IN ENERGY SECTOR. WHAT MAIN DIMENTIONS ARE COVERED IN THE GLOBAL SYSTEM INITIATIVES

D. Karaša
Lithuanian Energy Institute
Breslaujos g. 3, LT-44403 Kaunas – Lithuania
+37062020499
darius.karasa@lei.lt

EXTENDED ABSTRACT

OVERVIEW

Corporate social responsibility (CSR) has gained a reputation recently, and energy sector companies started to recognize responsibility for society and the environment, investors and stakeholders. CSR in the energy sector is the main business initiative helping to deal with major risks and challenges [1]. Stakeholders are more frequently demanding information from companies about their economic, environmental and social performance. CSR reports of energy utilities can't provide an assessment of the true impact of energy utilities on the sustainable energy development of the country. Assessment of CSR performance of energy companies requires more deep investigations and application of advanced tools. There is a wide array of rating agencies focusing on CSR, but there is a gap in the context of the energy industry. The aim of this paper is to analyse the main initiatives of the global system in order to categorize the dimensions of corporate social responsibility in the energy sector.

METHODS

A systematic literature review (SLR) assesses the existing knowledge and gaps on specific issues, which will further develop the knowledge base. SLR helps to collect all related publications and documents that fit our pre-defined inclusion criteria to answer a specific research question [2]. The SLR was carried out based on the integration of the Search, Appraisal, and Synthesis and Analysis (SALSA) framework. The SALSA methodology is singled out in the scientific literature as one of the most appropriate tools for identifying, evaluating and systematizing scientific and practical studies [3]. The Preferred Reporting Items for Systematic Reviews and Meta-Analyses (PRISMA) statement guarantees the precision and completeness of the analysis.

RESULTS

CSR indicators could be available from different sources. As an example, international organizations such as the United Nations disclose indicators related to CSR at the country level. CSR analyst organizations quantify firms' CSR efforts [4]. Some authors [5] distinguished four types of organizations that analyse CSR: rating agencies, information providers, rankings and sustainability indices. Rating agencies are the link between stakeholders and companies [6]. They study businesses and make evaluations in social,

environmental and corporate governance terms—using their own research methodologies. The main rating organizations related to CSR rating for the energy sector are provided in Table 1.

Table 1: The main organizations or initiatives for CSR rating

Initiative	Description
U.N. Global Compact	The U.N. Global Compact is a principle-based framework for businesses, stating ten principles in the areas of human rights, labour, the environment and anti-corruption.
Global Reporting Initiative (GRI)	The Global Reporting Initiative (GRI) enables all companies and organizations to report their economic, environmental, social and Governance performance.
World's Most Ethical Companies	This rating is based on a principle-based framework for businesses, stating ten principles in the areas of Governance, Leadership and reputation; Culture of ethics; Ethics and compliance program; Environmental and social impact.
Global 100 Most Sustainable Corporations	The aim of the Global 100 is to reinforce, raise awareness and showcase world leaders in corporate sustainability, including those that have been able to balance environmental performance, social performance and economic performance while delivering superior returns to investors.
OHSAS 18001	Occupational Health and Safety Assessment Series (OHSAS) is an international standard for occupational health and safety management systems.
Social Accountability - SA 8000	Auditable certification standard that encourages organizations to develop, maintain, and apply socially acceptable practices in the workplace. It measures eight areas important to social accountability: child labour, forced labour, health and safety, free association and collective bargaining, discrimination, disciplinary practices, working hours and compensation.
KPMG Survey of Sustainability Reporting	The survey provides a detailed look at global trends in sustainability reporting. Survey reporting on the risks of biodiversity loss, climate-related risk and carbon reduction
GHG Protocol	GHG Protocol supplies the world's most widely used greenhouse gas accounting standards. The standard covers the accounting and reporting of seven greenhouse gases covered by the Kyoto Protocol – carbon dioxide (CO_2), methane (CH_4), nitrous oxide (N_2O) and etc.
Carbon Disclosure Project (CDP)	Carbon Disclosure Project helps companies and cities disclose their environmental impact. It aims to make environmental reporting and risk management a business norm, driving disclosure, insight, and action towards a sustainable economy.
Dow Jones Sustainability Index	The Dow Jones Sustainability Indices (DJSI) evaluates the sustainability performance of companies. The DJSI is based on an analysis of corporate economic, environmental and social performance, assessing issues such as corporate Governance, risk

	management, branching, climate change mitigation, supply chain standards and labour practices.
FTSE4good Index	The FTSE4Good Index is a series of ethical investment stock market indices and rates companies for inclusion-based environmental sustainability, relationships with stakeholders, attitudes to human rights, supply chain labour standards and the countering of bribery.
ECPI Global ESG Alpha Equity Index	The index is a broad benchmark representative of developed market companies that satisfy ECPI ESG criteria. The ECPI ESG Rating Methodology is a rule-based process focusing on a company's Environmental, Social and Governance performance.
MSCI World ESG Index	The MSCI World ESG Leaders Index is a capitalization-weighted index that provides exposure to companies with high Environmental, Social and Governance (ESG) performance relative to their sector peers.

Rating agencies construct their own CSR ratings, which are often used as aggregated multidimensional measures of CSR or CSP [7]. There are no set uniform standards for all applicants for the energy sector. They differ on how to weigh given criteria, but they also differ about what constitutes relevant data for assessing the criteria. Thus, it can be impossible to compare results across rating agencies. However, these ratings may neglect the negative impacts on firms [8] and may have a weak or non-existent theoretical background [7].

CONCLUSIONS

It is crucial for energy sector utilities to overcome health and safety risks, environmental risks as well as reputation risks to provide long-term success. To address this matter, the main initiatives related to CSR were studied. According to the initiatives provided dimensions can be categorized as environmental, social, and economic and Governance impacts to solve the issues the energy sector can cause. Rating agencies construct their own CSR ratings, thus, it is difficult to compare results across rating agencies. Since there is no global system in CRS ratings, further research is needed to develop a comprehensive framework.

Keywords: Corporate social responsibility; energy sector, rating, initiatives

REFERENCES

1. KARAMAN, A.S.; ORAZALIN, N.; UYAR A.; SHAHBAZ, M. CSR achievement, reporting, and assurance in the energy sector: Does economic development matter? *Energy policy*, 2021, Vol. 149, No. 112007

2. MENGIST, W.; SOROMESSA, T.; LEGESE, G. Method for conducting systematic literature review and meta-analysis for environmental science research. *MethodsX*, 2020, Vol. 7, No, 100777.

3. AMO, I.F.; ERKOYUNCU, J.A.; ROY, R.; PALMARINI, R.; ONOUFRIOU, D. A systematic review of Augmented Reality content-related techniques for knowledge transfer in maintenance applications. *Computers in Industry*, 2018, Vol. 103, P. 47-71.

4. PAREDES-GAZQUEZ, J.D.; RODRIGUEZ-FERNANDEZ, J.M.; CUESTA-GONZALEZ, M. Measuring corporate social responsibility using composite indices: Mission impossible? The case of the electricity utility industry. *Revista de Contabilidad,* 2016, Vol. 19, Issue 1, P. 142-153.

5. ESCRIG-OLMEDO, E.; MUÑOZ-TORRES, M.J.; FERNÁNDEZ-IZQUIERDO, M.Á. Lights and shadows on sustainability rating scoring. *Review of Managerial Science,* 2013, Vol. 8, P. 559-574.

6. SCHÄFER, H. International corporate social responsibility rating systems: conceptual outline and empirical results. *Journal of Corporate Citizenship*, 2005, Vol. 20, P. 107–120.

7. WOOD, D.J. Measuring corporate social performance: A review. *International Journal of Management Reviews*, 2010, Vol. 12, P. 50–84.

8. SCALET, S., KELLY, T.F. CSR Rating Agencies: What is Their Global Impact? *Journal of Business Ethics*, 2009, Vol. 94, P. 69-88.

BEHAVIORAL CHANGE INTERVENTIONS FOR SUSTAINABLE ENERGY USE IN HOUSEHOLDS: A SYSTEMATIC LITERATURE REVIEW

G, Stankuniene
Laboratory of Energy Systems Research, Lithuanian Energy Institute
Breslaujos g. 3, LT-44403 Kaunas – Lithuania
+37061422989
gintare.stankuniene@lei.lt

EXTENDED ABSTRACT

OVERVIEW

Greenhouse gases (GHGs) contribute to global warming. Hence European and national policies try to limit them. Household consumption is responsible for 72% of worldwide GHGs emissions. As a result, they are crucial players in achieving the Paris Agreement's 1.5°C goals [1]. The energy sector is crucial to reducing GHGs emissions and resource use in households because household energy usage accounts for over a third of total GHGs emissions from fuel combustion. The growing demand for energy and the failure to meet its savings targets in households has become a major challenge for policymakers and researchers in recent years. [2] This article discusses sustainable energy use in households, as well as barriers and measures that can help to reduce energy demand in the residential sector.

Although many measures are used to achieve sustainable energy usage in households, such as infrastructure and technology development, regulation, financial incentives, and behavioural interventions related to household energy saving methods are still important in order to mitigate the effects of rising energy demand. [3; 4] Policymakers are incorporating non-monetary interventions as measures to reduce household energy consumption. Therefore, researchers to increasingly explore the concept of Nudge, where goals are achieved by reducing cognitive pressures and setting green options as the default option and an alternative for it - the Boost intervention, which seeks to increase the competencies and knowledge of individuals to achieve the desired solutions. [5; 6; 7]

The aim of this article is to review the effectiveness of behavioural interventions in promoting sustainable energy use in households and overcoming the barriers to behaviour that hinder it.

METHODS

A systematic literature review was chosen to consolidate the literature on sustainable energy use in households. A systematic literature search and study was performed using the Stochastic Approach for Link Structure Analysis (SALSA) system, which investigates random walks with graphs derived from the interface structure. [8] The papers obtained during the search were evaluated, and recommendations for the selection of papers were

followed by the "Preferred Reporting Items for Systematic Reviews and Meta-Analysis" (PRISMA) statement, which also guarantees the accuracy and completeness of the analysis. [9]

RESULTS

Researchers recommend three strategies for achieving sustainable energy consumption in households: 1) reduce total energy consumption, 2) shift energy consumption sources to renewables, and 3) improve energy efficiency in residential buildings. For a multitude of reasons, consumers fail to make the best investment or consumption decisions, all of which have one thing in common: people make mistakes and fail to act in their own best interests. [4; 10] Behavioural barriers refer to consumers' difficulties acquiring and comprehending information, as well as psychological biases. This paper identified these behavioural barriers to sustainable energy use in households: 1) Uncertainty on renovation costs/benefits and payback period; 2) Environmental concern / low priority; 3) Lack of trust in governments' policy; 4) Lack of trusted information and experience; 5) Time constraints and the capability to use data; 6) Resistance to change, negative perception of new technologies; 7) Customs, habits, and relevant behavioural aspects; 8) Lack of understanding on saving potentials; 9) Lack of a 'culture of saving. How to achieve energy demand reduction goals through behaviour change interventions can be seen in Fig. 1.
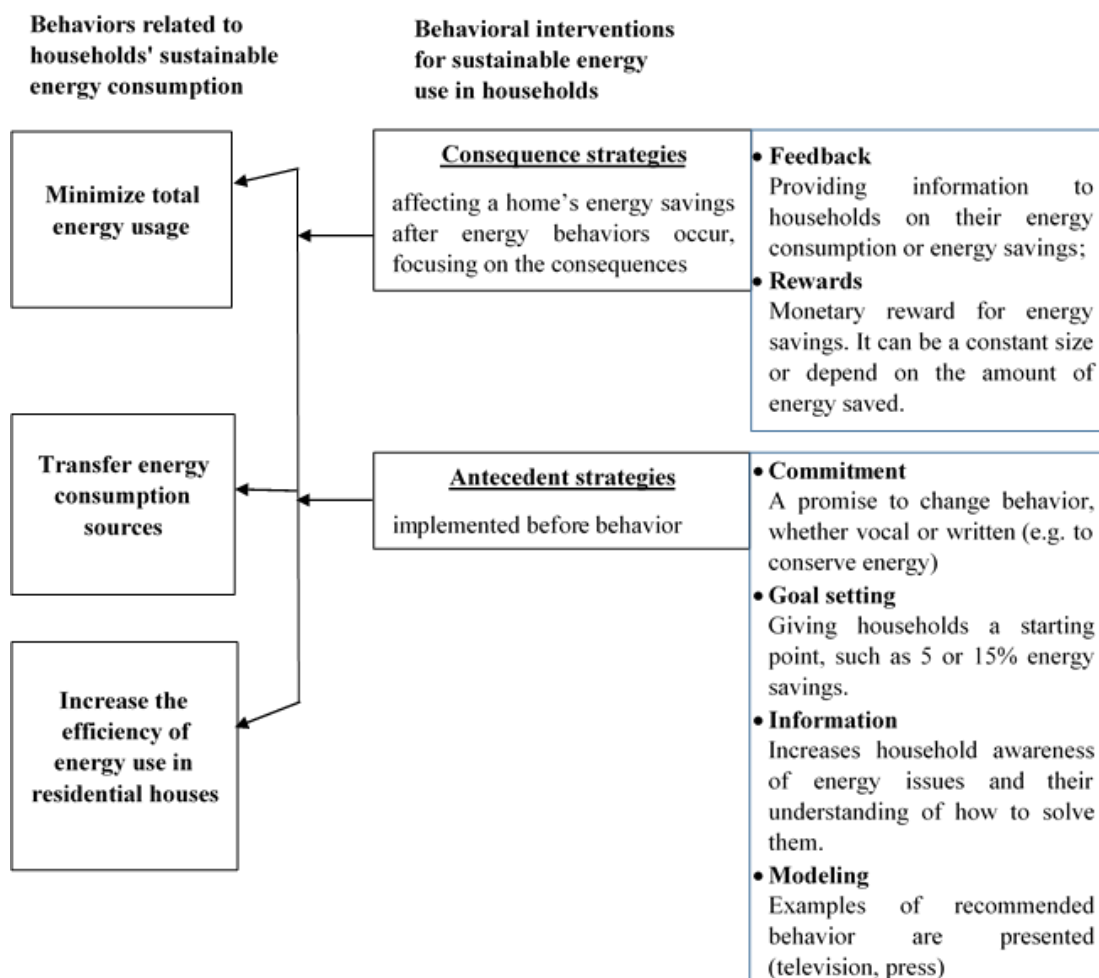

Fig. 1. Behavioural interventions for energy saving in households [4; 11]

CONCLUSIONS

Household energy usage is not always primarily influenced by financial incentives or the rational pursuit of material gain. It's difficult to anticipate household energy usage and conservation based on either fundamental beliefs or pecuniary interests. [12] This systematic literature review has shown that non-monetary behavioural interventions can also help to achieve sustainable energy use in households. According to research, in order to achieve optimal results in reducing GHG emissions in households, multiple nudging techniques should be considered at the same time (e.g. default option, social standards, priming). Other behavioural interventions – boosts, are different from nudges. These are interventions that allow citizens to improve their skills and thus make decisions, and one way to help deepen their competencies is to use the so-called 'rule of thumb'. Coordinating interventions can lead to even more effective results in changing household behaviour towards sustainable energy use.

Keywords: Sustainable energy consumption, households, behaviour change, climate change mitigation.

REFERENCES

1. DUBOIS, G.; SOVACOOL, B.; AALL, C.; NILSSON, M.; BARBIER, C.; HERRMANN, A.; BRUYÈRE, S.; ANDERSSON, C.; SKOLD, B.; NADAUD, F.; DORNER, F.; MOBERG, K.R.; CERON, J.P.; FISCHER, H.; AMELUNG, D.; BALTRUSZEWICZ, M.; FISCHER, J.; BENEVISE, F.; LOUIS, V.R.; SAUERBORN, R. It starts at home? Climate policies targeting household consumption and behavioural decisions are key to low-carbon futures, *Energy Research & Social Science*, 2019, Vol. 52, p. 144-158.

2. KOTSILA, D.; POLYCHRONIDOU, P. Determinants of household electricity consumption in Greece: a statistical analysis, *Journal of Innovation and Entrepreneurship*, 2021, Springer, Vol. 10, P. 1-20.

3. NIELSEN, K.S.; VAN DER LINDEN, S.; STERN, P.C. How Behavioural Interventions Can Reduce the Climate Impact of Energy Use, *Joule*, 2020, Vol. 4, Issue 8, P. 1613-1616.

4. XU, Q.; L.U., Y.; HWANG, B.G.; KUA, H.W. Reducing residential energy consumption through a marketized behavioural intervention: The approach of Household Energy Saving Option (HESO), *Energy and Buildings*, 2021, Vol. 232, Issue 1, 110621.

5. GRÜNE-YANOFF, T.; HERTWIG, R. Nudge Versus Boost: How Coherent are Policy and Theory? *Minds & Machines*, 2016, Vol. 26, P. 149–183.

6. KASPERBAUER, T.J. The permissibility of nudging for sustainable energy consumption, *Energy Policy*, 2017, Vol. 111, P. 52-57.

7. LAZARIC, N.; TOUMI, M. Reducing consumption of electricity: A field experiment in Monaco with boosts and goal setting, *Ecological Economics*, 2022, Vol. 191, 107231.

8. LEMPEL, R.; MORAN, S. SALSA: The Stochastic Approach for LinkStructure Analysis, *ACM Transactions on Information Systems*, 2001, Vol. 19, No. 2, P. 131–160.

9. MOHER, D.; LIBERATI, A.; TETZLAFF, J.; ALTMAN D.G. Preferred reporting items for systematic reviews and meta-analyses: the PRISMA Statement, *Open Medicine*, 2009, No. 3, P. 123-130;

10. ABRARDI, L. Behavioural barriers and the energy efficiency gap: a survey of the literature, *Journal of Industrial and Business Economics*, 2019, Vol. 46, P. 25–43.

11. ABRAHAMSE, W.; STEG, L.; VLEK, C.; ROTHENGATTER, T. A review of intervention studies aimed at household energy conservation, *Journal of Environmental Psychology*, 2005, Vol. 25, Issue 3, P. 273-291.

12. FREDERIKS, E.R.; STENNER, K.; HOBMAN, E.V. Household energy use: Applying behavioural economics to understand consumer decision-making and behaviour, *Renewable and Sustainable Energy Reviews*, 2015, Vol. 41, P. 1385-1394.

ANALYSIS OF THE POTENTIAL SHORT AND LONG-TERM IMPACTS OF THE EU ENERGY POLICY PLANNING ON THE INDUSTRY

K. Rimkunaite
Lithuanian Energy Institute
Breslaujos g. 3, LT-44403 Kaunas – Lithuania
+370 612 10944
krimkunaite@yahoo.com

ABSTRACT

Energy policies and strategies play a key-importance role in any economics, having an especially big effect on its largest energy consumers – energy intensive (further EnI) industries. Even a small change in energy availability and/or market prices has a huge impact on their performance results. Each European Union (EU) member state (MS) has a different industry structure, but all of them are consumers of EnI industries end-production, such as steel, cement or chemicals. Therefore, EU energy transition goals must be achieved in the most efficient and rational ways possible. For a certain period in time, policies set in place were concentrating on the energy sector, in particular, omitting complex pictures and economic activities related. Gradually, there was a move made to laws packages, consisting of several legal acts, having far-reach and complex approaches. The most recent one is the Fit for 55 package, which is still a work in progress. While planning, two different timespans must be taken into account. For EnI, it is easier to adjust to long-term policy changes, but it is almost impossible to do that short term. Decarbonisation is the desired effect, yet any industry needs a certain time to make changes, and it can be calculated in years. Exploring current post-COVID-19 uncertainty and recent changes in globalization trends, it is in EU's best interests to keep its EnI industries competitive and financially capable of making overhauls of production lines and implementing new technologies and innovations needed. The purpose of this paper is to identify and briefly analyse recently adopted and announced EU energy policy changes, concentrating on their potential impacts on the EU industries during the period up to 2030.

Keywords: Energy transition, European Union, Energy policy, industry.

INTRODUCTION

In order to achieve ambitious energy transition goals set for 2030 and 2050, EU has made major changes in its Energy policy planning. They could be projected into the three main areas where technological change will be needed for the industry [15]. The first would be energy efficiency, which is oriented towards savings on the energy demand side. The next area would be more efficient energy production itself. The third one would be the continuous replacement of fossil fuels with renewable energy sources.

Industry plays an important role in energy transition, accounting for approximately one-quarter to one-third of E.U.'s energy consumption and Greenhouse Gases (GHG) emissions [19]. It is obvious that industries are not homogenous and have significant differences across the EU-27. So-called EnI industries have the largest potential to benefit from decarbonisation measures. They include steel, cement, chemicals and nonferrous metals production and rely on standardized production processes, using certain technologies and production lines. Starting with EU's Green Deal, there is a significant policy shift incorporating energy policy into the bigger picture. This allows more efficient long-term planning and inter-sectoral adjustments in case they are/will be needed.

For EnI industries, it means both new opportunities and threats. A political decision was made to set a decarbonisation target for 2030 at 55% less GHG emissions compared to 2005. Any industry always needs time to adjust. It is not a matter of months but more a matter of years. EnI industries investments into material assets are made long-term and used for decades. Sometimes changing technology of production is very costly or even economically non-viable. It is in the industry's best interests to comply with new requirements and implement new technologies, but policymakers on all levels need knowledge of processes in practice.

The aim of this paper is to provide a brief overview of the most recent EU energy policy planning decisions and come up with preliminary insights on their potential impacts on the EnI industries short-term and long-term. To complete this task, there were three objectives set:
- To analyse if the EU energy policy planning process takes into account both short and long-term impacts, paying sufficient attention to both.
- To identify if Energy policy planning, based on actual impact on EnI in practice (especially CO_2 pricing), predicts outcomes and results of policies carried out during recent years precisely enough.
- To formulate potential EU Energy policy planning future impacts on EU EnI industries long-term.

It is worth mentioning that there is still no common ground even among EU MS regarding what is acceptable in energy transition as a part of it. For example, there were long ongoing discussions between Austria and France regarding the classification of nuclear energy as green in the Taxonomy. Poland and other countries also advocated including natural gas as a transitional fuel and considered it green too. This classification is important for financial institutions, and if both fossil fuels were excluded, they would have limited access to funding for new energy projects. Another important aspect is systemic risk occurrences, such as COVID-19 or political insurgencies, that cause fast and radical energy policy shifts at the EU level. The most recent one is EU's goal to reduce reliance on Russian natural gas imports [11] because of its intervention in Ukraine.

So EnI industries make their business decisions under conditions of uncertainty. Some of them will win long-term, and some might take the losses. Natural gas usually is seen as a source of energy, but for the chemical industry, it is a raw material in their production processes, which is still impossible to replace.

This paper consists of three parts.
- The methodology part sets the time and scope limitations for the analysis conducted, explaining principles of EU common policies setting as well.
- The results and discussion part briefly presents findings related to the EnI industry specifics short and long-term.
- The conclusions part summarizes insights made and identifies future research potential.

METHODOLOGY

This paper analyses EU energy policy changes made from 2009 up to the current date and put efforts to identify their potential impact on E.U. industries. That year the major EU energy policy shift was made with the Third energy package introducing current 'rules of the game' for EnI industries and the energy markets structure, unifying it across the entire EU-27. There were efforts made to have a fully-fledged common EU sectoral policy in energy as it was in the common agriculture policy or establishment of the Schengen area cases [26], but EU MS, because of its key importance for the national economics, preferred to keep energy policy on the national level. Energy Union, introduced in 2014 and adopted in 2015, was still very limited because it was based on a step-by-step approach, meaning the introduction of future sectoral strategies, such as EU Liquefied Natural Gas and gas storage strategy and packages, like Winter or Clean energy for all Europeans. Each of these packages bundles certain laws and shifts EU further to the desired common EU energy sector policy. The last document package is Fit for 55 [7]. Analysis in this paper concentrates only on official EU documents, such as strategies and packages. Being affected by all the policy changes most and already being part of the Emission Trade System (further ETS) [25], EnI industries are especially vulnerable to the carbon price changes [1]. Therefore, they are taken into account as well.

There are two different time horizons set. The first one is called short-term and covers a period up to 2 years into the future from the policy change adoption. The second one, called long-term, takes into account the timeframe until 2030 or at least 10 years period after the policy change adoption.

For statistical data, Eurostat [10] and other official publicly available datasets were researched.

RESULTS AND DISCUSSIONS

EU Policies with a Major Impact on Eni Performance

After more or less successful common energy policies implementation, EU noticed that there is a contradiction between different sectoral policies long-term. For example, industrial policies aim to increase competitiveness and attract investors with higher value-added industries, often competing to attract them to certain MS. Environmental policies aim for cleaner and sustainable performance that might incur additional costs. Energy policies aim for energy security and affordable prices – goals that in some cases mean extensive use of fossil fuels or even subsidies for them. So Clean energy for all Europeans package was the

first legislative package which tried to implement a dimensional approach in practice enabling finding contradictions and eliminating them on EU and MS levels.

Table 1 identifies key moments of the new policy introduction. Traditionally the process of adoption takes several years, so theoretically industry is getting time to adjust and incorporate changes into their strategies and business models if it is informed in due time. For example, the clean energy for all Europeans package was introduced for discussions in 2016 but formally was adopted only in 2019. The process was slow because all the 27 MS had to agree, and their interests, in most cases, were different.

Table 1. A brief summary of the main EU policies with the major impact on EnI performance

Document	Year	Remarks
Third energy package	2009	Covers unbundling (electricity and natural gas markets), independent regulators, ACER (Agency for the Cooperation of Energy Regulators), cross-border cooperation and open and fair retail markets [8].
Energy Union	2015	Covers five dimensions: Security, solidarity and trust; A fully integrated internal energy market; Energy efficiency; Climate action, decarbonizing the economy; Research, innovation and competitiveness [4].
Clean energy for all Europeans package (also nicknamed Winter package)	2019	Introduces new laws on Energy performance in buildings, Renewable energy, Energy efficiency, Governance of the energy union (National energy and climate plans), Electricity market design (Regulation (EU) 2019/943, Directive (EU) 2019/944), Risk preparedness and ACER) [3].
Green deal	2020	Covers new policies on Clean energy, Sustainable industry, Building and renovation, Farm to Fork, Eliminating pollution, Sustainable mobility, Biodiversity, and Sustainable finance [2].
Fit for 55 package	Submitted to the European Council in July 2021	Legislative proposals and policy initiatives include the E.U. emissions trading system, Member states' emissions reduction targets, Emissions and removals from land use, land use change and forestry, Renewable energy, Energy efficiency, Alternative fuels infrastructure, CO_2 emission standards for cars and vans, Energy taxation, Carbon border adjustment mechanism, Sustainable aviation fuels, Greener fuels in shipping and Social climate fund [5].

Table 1 shows a radical policy shift within the recent 13 years' time span. The current energy market structure was set in 2009, but only the natural gas of its part is still intact. The third energy package was chosen as a starting point for this paper, though the electricity part of it is already completely overhauled.

Energy Union introduced many common sectoral policies in energy as a result. It might be considered a successful project because now EU MS on a political level are able to discuss potential joint natural gas purchases from the 3rd countries or joint offshore wind parks in

the Baltic, North or Mediterranean seas. For decades, such decisions were discussed only on a national level, and MS kept strong ownership over decisions made, thus limiting cross-border cooperation potential.

SHORT-TERM PERIOD

Risks of Energy Prices Fluctuations and Different Eu-27 Ms Exposure

During the short-term period, there are significant energy price fluctuation effects observed. In energy-intensive industries across the EU, expenses for energy costs can increase 3-4 fold [18]. Any energy prices rise that can be considered insignificant for other industries puts EnI industries business model under high risk of activities discontinuation. Fig. 1 shows EU MS that have the biggest share of energy for industry consumption and EnI industries in their national economics structure.
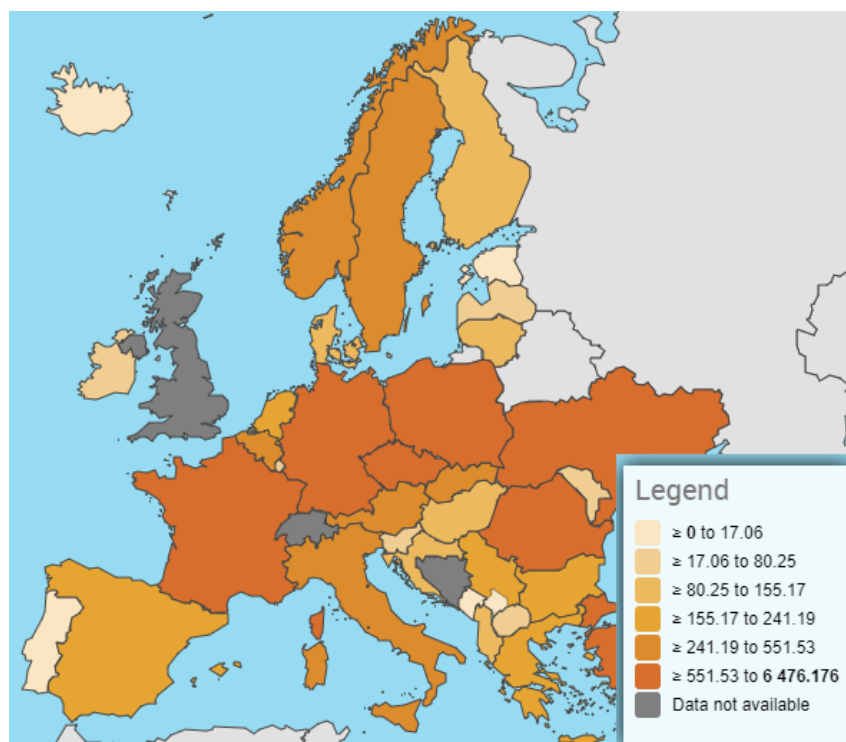
Fig. 1. Final energy consumption in the industry by country in 2020, toe
[Source: Eurostat]

There are industries that can be moved relatively fast from one country to another. For example, such industries are telecommunications or textile. But EnI, industries like steel, cement or fertilizers are bound to a certain location. They depend on reliable raw materials, including energy, supply, standardized production lines that need to be served by qualified personnel, and production logistics that are often made by railways or maritime transport. Also, usually, the production process is 24/7 and its interruption and restarting would mean financial losses, not to mention the fact that restarting would need days or, in some cases, weeks to be done.

Germany leads in energy transition across E.U., and its EnI can be an example of adaptation. Though industrial associations in 2011 claimed that *Energiewende* would make Germany's industry less competitive. Germany, Austria, France, Poland and Romania choose different energy policies, but on the national level, they all have a common goal – to keep industrial

production competitive worldwide. Differences in primary energy sources. For example, Poland aims to replace coal with natural gas, France relies on nuclear power plants, and Germany aims for a balanced renewable and natural gas mix.

ENI Industries Sensitivity to Co2 Price Fluctuation

Despite concerted efforts and analysis made, sometimes E.U. has difficulties identifying and forecasting its energy policy impacts long-term, causing challenges for EnI industries short-term. EnI industries' budgets are planned on an annual basis, so precise forecasting of their potential costs and cash flows, in general, is important for profitability and economic viability.

With current policies during the process of planning, expected potential E.U. energy policy impacts were identified and analysed only long-term, omitting shorter periods. Therefore, potential risks were diminished, and potential benefits disproportionally exaggerated.

For example, carbon dioxide (further CO_2) pricing for ETS participants was expected to have a lesser impact than it had in 2021 and further periods. Annual reductions of free ETS for the industry share in the market and gradually rising CO_2 market price were expected to encourage energy efficiency measures implemented in industrial processes, this way reducing final energy consumption in national EU M.S's energy balances [22]. But the market prices were not expected to rise so fast and sharp within less than one year period, reaching the CO_2 market price that was forecasted for 2045 when policy planning was made in 2019 [6]. Fig. 2 shows the CO_2 price hike that caused some EnI industries to stop or limit their production output in EU MS across Europe.

Fig. 2. CO2 price dynamics in EU ETS, EUR per ton of CO2 [Source: Trading Economics]

In 2020 CO2 price briefly dipped down because of the COVID-19 impact. It caused lockdowns, closures, disrupted logistical chains and lower energy demand in general. This resulted in lower CO_2 emissions [12]. But from the moment when restrictions were lifted, economics recovered much faster than expected, sending CO_2 prices to all-time highs. E.U.'s EnI industries were locked down in sales contracts, so only those which had riskier business

models and operated on a spot basis could adjust their production prices fast enough. The situation becomes even more complicated when clients delay their purchase decision, hoping to get a better price level in the future. In this case, the EnI industry is forced to manufacture 'for the warehouse'.

Changes in Energy Production and Supply – Decentralized Model

The centralized energy supply model provided security of supply to the industries for several decades. The situation is radically changing as energy systems are switching to a decentralized energy supply [20]. It makes industries vulnerable and exposed to energy supply disruptions that are difficult to predict and mitigate [13]. Also, some EnI industries use fossil fuels as raw materials, and it is difficult or impossible to replace them.

Decarbonisation goals lie at the centre of the energy transition currently taking place. Further increase of the renewable energy sources share in the energy mix decreases EUs dependency on external energy sources. It has a positive effect, but transitioning is not smooth and short-term. It creates extra pressure on transmission and distribution grids. Industrial processes require stable energy supply and certain electricity quality because voltage micro-jumps in the grid can damage electronics that are sensitive to them. There is a clear need for successfully commercialized technological energy innovations and increased investment toward Research and Development both in energy production and industrial processes.

The first of the factors driving energy markets short-term is political unpredictability. The most recent manifestation in practice is COVID-19 lockdowns, disrupting industrial activities and energy demand. The second one would be market forces that are working against traditional seasonality patterns. An example could be the low gas storage level in the EUs Underground Gas Storages (further UGS) for the winter season of 2021-2022. In 2021 usual summer drop in prices did not happen, therefore, companies delayed their natural gas purchasing for the future, putting end-users into a financially strained situation when they were forced to pay double or even multiple times higher prices for natural gas, electricity and heating.

War in Ukraine – Additional Uncertainty for Eu Eni Industries

On the 24th of February, 2022, Russian troops invaded Ukrainian territory. Consequently, EU imposed several packages of sanctions, which aim to shift EnI industries from Russia as the primary energy source. EU-27 stopped buying Russian coal; also, there are joint efforts to stop buying Russian oil and natural gas.

Lithuania was the first EU member to cease natural gas imports from Russia completely (both pipeline and liquefied natural gas (LNG)). Other member states negotiated for a transitional period because the infrastructure needed to diversify, especially in land-locked MS, is not in place, and there is the time needed to construct it. Short-term, EU political decisions, such as planned centralized natural gas purchases, might result in energy prices hike. Although later, they will bring EnI industries more advantages because infrastructure projects reconsidered again, such as the Spain-France gas interconnector or LNG import terminals in Germany, will increase competition among energy suppliers.

Transit of Russia's natural gas is an important budget income source for Ukraine, accounting for 2-3 billion EUR revenues annually. Russia's aggression ceased Nord Stream 2 pipeline certification process in Germany, but it also puts EnI industries at risk as end-users. If due

to military activities, there is accidental damage to Ukraine's transmission pipeline system, its effect will be double-sided. Western Europe will not get the physical natural gas flows it needs, and Ukraine might lose part of the potential revenues.

LONG-TERM PERIOD

Risks for Eu Eni Competing Globally

Long-term, the main risk is that if EU policies' effects are difficult to predict, they might cause an exodus of the EnI industries to third countries where restrictions are less tight or do not exist [23]. This might result in a situation when certain products in E.U. cease to exist or be available. If it is not a component or a part of another product, the situation is acceptable, but otherwise, it makes EU more vulnerable and dependable on certain imports from third countries, potentially not matching production standards set within EU. EU aims to prevent such situation introducing Carbon Border Adjustment Mechanism (CBAM). CBAM will create a vis-à-vis level playing field for the products manufactured within and outside EU.

Most recent global events showed that self-reliance in the energy sector is of crucial importance. But if EU abandons one 3rd the country's fossil-fuel suppliers for another, it is still not an acceptable problem solution. Energy transition worldwide was taking a faster pace and gaining momentum, but COVID-19 and the hike in global energy resources prices made coal and other polluting primary energy sources more attractive alternatives.

Countries that chose to use polluting energy sources were able to do so because they do not have formal legislation in place banning such switches even temporarily. It is not the case in EU MS, therefore, their EnI industries face higher risk exposure.

Benefits of New Emerging Technologies

Different analytical scenarios used for forecasting desired outcomes usually depict the future as optimistic or too pessimistic. EU Energy Union's fifth dimension is named research, innovation and competitiveness.

In most of the national EU MS's NECPs, it was the shortest and least clear part of the document. In particular, innovations mean that some new technologies will provide a breakthrough until 2030, but it is very difficult to identify which ones will have the biggest impact. Also, there will be a need to 'normalize' usage of them by solving practical technical issues [14], and it also will take time. Despite that, it is already clear that hydrogen will play a very important role in energy transition even before 2030 [17].

One of the quantitative measures is the number of European patents, but it is a tricky key performance indicator because some of the patents are never commercialized. A potential solution would be advancing the close industry and scientists' cooperation. The industry is always oriented toward gaining a competitive advantage, so there might be cases when some perspective technologies could be locked and accessible to other competitors in the same industry only when the patent period is over. It might be as long as 25 years. Fig. 3 shows patents applications dynamics in 2011-2020.
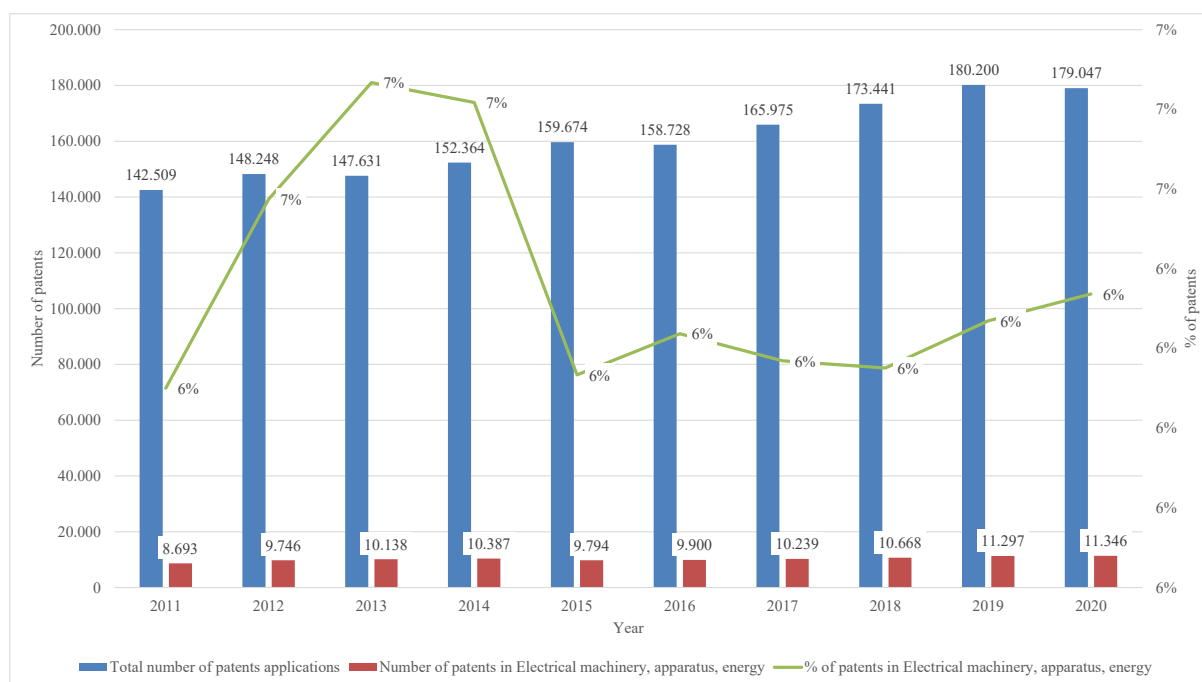
Fig. 3. Dynamics of European patents applications [9] in 2011-2020
[Source: European patents office (EPO) and own authors elaborations]

Energy transition already years ago gave EU's EnI industries a push to implement extensive energy efficiency measures, switch to renewable energy sources when it is possible and change technologies to more efficient ones. It allows to save costs, get ahead in the market and form more positive public opinion.

New Business Models and Eni Potential to Embrace the Change

The most positive effect would be new technologies and business models emerging long-term. Such examples could be commercialized Power-to-gas [21] or Vehicle-to-grid technologies [16]. Also, EU's pioneering in energy transition could give increase the remaining industries' competitiveness worldwide. Of course, if the rest of the world decides to embrace EUs energy transition standards and adjust their EnI industries accordingly.

EnI industries because if their specifics cannot make energy transition within a year or two, but within 5-10 years period, they will be the most important contributors towards the achievement of EU's decarbonisation goals EnI industries cross

In some cases, it will be commercially attractive. In some politically induced changes, for example, the ban of internal combustion engines [24] will radically change logistics and EnI industries costs for its services.

CONCLUSIONS

- EU energy policy planning is oriented long-term, omitting important impacts it causes short-term and affecting all the EUs industries – in particular EnI ones, such as cement, chemicals and metals production.

- There are difficulties in planning the actual outcomes of the new energy policies; because EU expected some changes (for example, CO_2 price) to take place at a much

slower pace than it actually did. Industries have no time to adjust, therefore, they are short-term exposed to unnecessary economical risks that give certain advantages to their competitors in the third countries. Sometimes even effectively putting them out of business.

- Long-term EnI industries will implement a lot of energy-related innovations in practice and switch to new business models that would contribute to EUs decarbonisation goals for 2030 and 2050 significantly. It is very likely that a competitive advantage will be created.

REFERENCES

1. DROEGE, S. Carbon pricing and its future role for energy-intensive industries. Climate Strategies, 2013.

2. European Commission. A European Green Deal [referred on the 27th of February in 2022]. Link to the internet. < https://ec.europa.eu/info/strategy/priorities-2019-2024/european-green-deal_en >.

3. European Commission. Clean energy for all Europeans package [referred on the 27th of February in 2022]. Link to the internet < https://energy.ec.europa.eu/topics/energy-strategy/clean-energy-all-europeans-package_en>.

4. European Commission. Energy Union [referred on the 27th of February in 2022]. Link to the internet: < https://energy.ec.europa.eu/topics/energy-strategy/energy-union_en >

5. European Commission. Fit for 55 – The E.U.'S plan for a green transition [referred on the 27th of February in 2022]. Link to the internet [referred on the 13th of March in 2022]. Link to the internet < https://www.consilium.europa.eu/en/policies/green-deal/eu-plan-for-a-green-transition/>.

6. European Commission, Joint Research Center. Rózsai, M.; Wiesenthal, T.; Mantzos, L.; et al.; the POTEnCIA central scenario: an E.U. energy outlook to 2050, Publications Office, 2019 [referred on the 23rd of January in 2022]. Link to the internet <https://data.europa.eu/doi/10.2760/78212 >

7. European Commission. Legislative Train Schedule: Fit for 55 Package under the European Green Deal. [Referred on the 17th of January in 2022]. Link to the internet <https://www.europarl.europa.eu/legislative-train/theme-a-european-green-deal/package-fit-for-55>

8. European Commission. Third energy package [referred on the 28th of February in 2022]. Link to the internet < https://energy.ec.europa.eu/topics/markets-and-consumers/market-legislation/third-energy-package_en>

9. European Patent Office. Statistics and trends [referred on the 23th of February in 2022]. Link to the internet: < https://www.epo.org/about-us/annual-reports-statistics/statistics.html>

10. Eurostat. Databases. [Referred on the 30th of January in 2022]. Link to the internet <https://ec.europa.eu/eurostat/data/database >

11. International Energy Agency. A 10-Point Plan to Reduce the European Union's Reliance on Russian Natural Gas [referred on the 8th of March in 2022]. Link to the internet <https://www.iea.org/reports/a-10-point-plan-to-reduce-the-european-unions-reliance-on-russian-natural-gas>

12. IQBAL, S.; BILAL, A. R.; NURUNNABI, M.; IQBAL, W.; ALFAKHRI, Y.; & IQBAL, N. It is time to control the worst: testing COVID-19 outbreak, energy consumption and CO_2 emission. *Environmental Science and Pollution Research*, 2021, 28.15: 19008-19020.

13. GERRES, T.; LINARES LLAMAS, P.; BARTEK-LESI, M.; & FELSMANN, B. Which role can carbon contracts for differences play in decarbonizing the European industry? A perspective from E.U. border regions. 2021.

14. GOYAL, N.; HOWLETT, M.; TAEIHAGH, A. Why and how does the regulation of emerging technologies occur? Explaining the adoption of the E.U. General Data Protection Regulation using the multiple streams framework. *Regulation & Governance*, 2021, Vol.15, P. 1020-1034.

15. GUZOVIĆ, Z.; DUIC, N.; PIACENTINO, A.; MARKOVSKA, N.; MATHIESEN, B. V.; LUND, H. Recent advances in methods, policies and technologies at sustainable energy systems development. *Energy*, 2022, No. 123276.

16. KERSCHER, S.; ARBOLEYA, P. The key role of aggregators in the energy transition under the latest European regulatory framework. *International Journal of Electrical Power & Energy Systems*, 2022, Vol. 134, No.107361.

17. KOVAČ, A.; PARANOS, M.; MARCIUŠ, D. Hydrogen in energy transition: A review. *International Journal of Hydrogen Energy*, 2021, Vol. 46, No.16: P. 10016-10035.

18. LUND, P. Impacts of E.U. carbon emission trade directive on energy-intensive industries—Indicative micro-economic analyses. *Ecological Economics*, 2007, Vol. 63, P. 799-806.

19. MAINAR-TOLEDO, M. D.; CASTAN, M. A.; MILLÁN, G.; RODIN, V.; KOLLMANN, A.; PECCIANTI, F.; KUITTINEN, H. Accelerating sustainable and economic development via industrial energy cooperation and shared services–A case study for three European countries. *Renewable and Sustainable Energy Reviews*, 2022, Vol. 153, No.111737.

20. MEUER, J.; LAMARO, F.; VETTERLI, N. Embedding energy optimization in organizations: A case study of a Swiss decentralized renewable energy system. *Energy and Buildings*, 2021, Vol. 235, No.110710.

21. PERPINAN, J.; BAILERA, M.; ROMEO, L. M.; PENA, B.; EVELOY, V. CO_2 recycling in the iron and steel industry via power-to-gas and oxyfuel combustion. *Energies*, 2021, Vol. 14.2, No. 7090.

22. Trading Economics. E.U. Carbon Permits. [Referred on the 23th of January in 2022]. Link to the internet <https://tradingeconomics.com/commodity/carbon>

23. VOGELE, S.; RUBBELKE, D.; GOVORUKHA, K.; GRAJEWSKI, M. Socio-technical scenarios for energy-intensive industries: the future of steel production in Germany. *Climatic Change*, 2020, Vol.162.4, P. 1763-1778.

24. WEISS, D.; SCHERER, P. Mapping the Territorial Adaptation of Technological Innovation Systems—Trajectories of the Internal Combustion Engine. *Sustainability*, 2021, Vol. 14.1, No. 113.

25. ZAKLAN, A.; WACHSMUTH, J.; DUSCHA, V. The EU ETS to 2030 and beyond: adjusting the cap in light of the 1.5° C target and current energy policies. *Climate Policy*, 2021, Vol. 21, P. 778-791.

26. ZIMMERMANN, H.; DÜR, A. Key controversies in European integration. Bloomsbury Publishing, 2021.

INNOVATIVE ENERGY TECHNOLOGIES AND WELL-BEING OF SOCIETY: OVERVIEW OF THEORY

S. Kunskaja
Lithuanian Energy Institute
Breslaujos g. 3, LT-44403 Kaunas – Lithuania
+370 686 88 458
svetlana.kunskaja@lei.lt

EXTENDED ABSTRACT

OVERVIEW

The European Union's international community has set the goal of neutralizing climate impacts by reducing the economy's dependence on fossil fuels and greenhouse gas emissions while at the same time enhancing people's well-being. The energy sector has a key role to play in achieving these goals. Europe's energy future must be based on increasing renewable energies, the flexible integration of different energy sources and the continued efficient use of resources while avoiding pollution and biodiversity loss. Innovative energy technologies have the potential to accelerate fundamental changes in our energy sector with the transition to clean energy. In order to achieve the desired changes, it is important to study and assess the impact on public welfare, taking into account the diversity of the concept of public welfare. Insights from behavioural economics can help understand and shape the direction and scale of energy policy change. The aim of this paper is to examine the main theoretical aspects of energy science, the energy sector, energy resources, innovative energy technologies and public welfare. Methods of the research – systematic scientific literature analysis. Information search for analysis was performed using EBSCO, Scopus, Science Direct, Emerald, and Google Scholar. Basic search parameters were defined as such: search by name, the period from 1985 until 2021, using keywords: energy, energy sector, sustainable energy, energy technologies, innovative energy technologies, sustainable energy technologies, public welfare, and public well-being.

The energy sector. In principle, the same definitions of energy are given by the majority of authors, focusing on the fundamental transformation of the energy sector towards sustainable energy [1, 2, 3, 4, 5, 6, and 7]. *Energy science* examines the challenges that combine the research of energy resources, their rational use and energy development. Energy includes the interconnected energy sectors referred to as *electricity, hydropower, nuclear or nuclear energy, thermal energy, renewable energy, and hydrogen energy*, which involve all companies and installations for the *extraction, production, transformation, transmission, distribution and consumption of various energy sources*. The inherited from the past extensive energy sector focused on high but inefficient consumption of electricity and oil products does not meet current requirements in terms of its essential characteristics (efficiency, management principles, structure, etc.) [8]. Therefore, over the last decade, public policy has focused primarily on the fundamental transformation of the energy sector. The main goals of the National Energy Strategy (Energy Independence) approved by the Government of the Republic of Lithuania in 2010 include energy independence, increasing

competitiveness and sustainable development with environmental protection. The strategy covers all areas related to energy: electricity, heating, gas, and renewable energy. The E.U. has adopted a number of pieces of legislation and strategies for the energy sector at various levels, such as the Third Energy Package, the overall E.U. Energy Sector Strategy Energy 2020, the Energy Roadmap 2050, and others. The Energy Roadmap sets targets for reducing carbon emissions by 2050, ensuring the security of energy supply to consumers, and ensuring competition.

Energy plays a key role in all aspects of *sustainable development* and is one of the *key drivers of social development and economic growth*. The depletion of traditional energy resources, waste hoarding, deforestation, water pollution problems, and soil erosion are just some of the consequences of unbalanced energy development [5]. A new concept is emerging: *sustainable energy*, which is one of the E.U.'s policies priorities.

Sustainable energy is gradually replacing traditional energy, and it can be described as a form of energy that is extracted from inexhaustible resources in order to meet the needs and opportunities of future generations without compromising the energy needs and opportunities of future generations.

The key energy sources. The most important energy sources include 1) non-renewable natural resources and their processed products - oil, coal, natural gas, nuclear energy, peat, combustible shale; 2) renewable natural resources - hydropower, solar energy, wind energy, geothermal energy; 3) the products of human activity classified as renewable resources are wastes from the wood industry and agricultural production, municipal and other combustible wastes, specially grown biofuels and firewood, and biofuels produced from agricultural products. Energy production and use determine the quality of the local, regional and global environment. Therefore, recently in Lithuania, as in many other European countries, increasing attention is being paid to the use of renewable energy sources upon striving to increase the security of energy supply by reducing dependence on fossil fuels, the need for fuel imports and climate change related to greenhouse gas emissions [9,10,11,12]. Renewable energy means aerothermal, geothermal, hydrothermal, ocean energy, hydropower, biomass, biogas, including landfill gas and sewage treatment plant gas, as well as energy from other renewable non-fossil resources that are technologically available now or will be available in the future. These resources accumulate the essential qualities that make them the focus of all research into sustainable energy development.

Innovative energy technologies. Energy technologies are defined as any type of technology that interacts with one or more of the segments in the energy sector [13, 14]. These can be both renewable and non-renewable energy technologies. Innovative energy technologies are technologies that incorporate various forms of renewable energy, innovations that make our energy system more efficient, and products and services that increase consumers' control over energy consumption [13]. Sustainable energy uses innovative energy technologies from renewable energy sources. The main areas of renewable energy technologies are bioenergy (biomass), direct solar energy (solar panels), geothermal energy (geothermal power generation), hydropower (hydroelectric power plants) and wind energy (wind power plants). Thanks to these technologies, renewable energy is produced [15, 16, 17, 18, and 19]. These technologies are divided into 5 groups: solar, wind, hydro, bio and others [13]. Innovative solar technologies are characterized by the development of new elements that use micro-technologies to extract energy from direct or indirect sunlight and have the potential to store energy that can then be transmitted and distributed to the energy grid. *Innovative solar energy technologies* include saltwater solar thermal ponds, multi-node solar cells;

photochemical solar cells; paint-sensitive solar cells; thin film organic photovoltaic cells or polymeric solar cells. Innovative wind technologies are characterized by the development of new wind turbines – an architecture that improves the existing structure of wind plants. Taking advantage of the new architectural type and new possibilities of wind turbines, the most optimal option for obtaining energy from wind power is being sought. *Innovative wind energy technologies* include vertical axis wind turbines; concentrated wind accelerators or diffuser-topped wind turbines or ducted turbines; knife tip energy systems; high-altitude wind turbines and wind turbines; and wind belts. Innovative water technologies focus on new types of hydropower that are able to generate energy from new, hydrokinetic, renewable energy sources – offshore currents, wave battles, space power and thermal energy change. *Innovative hydropower technologies* include micro- and peak-hydropower plants; vortex hydrokinetic hydropower plants; ocean hydrokinetic power plants; osmotic power or salinity gradient power plants; ocean thermal energy changes. Innovative bioenergy technologies focus on the development of biomass biofuels from alternative, renewable energy sources – diesel, gas synthesis, etc. These bio-sources can be used to extract energy instead of not using it at all. *Innovative bioenergy technologies include* synthesis gas, biomass biofuels, and fuels from pyrolysis, biomass biofuels, and biomass microbial fuel cells. *Other innovative energy technologies* include kinetic energy yield, micro natural energy yield; mechanical energy containers; thermal energy tanks; an upgraded energy grid to help store energy.

All elements of the environmental strategy presented by the European Commission are closely linked to sustainable development, where energy technologies, through the dimensions of sustainable development, are inseparable from the environmental dimension. In the concept of sustainable development, one of the key criteria is energy efficiency and effectiveness; energy technologies.

Public welfare. Conceptual models of public welfare and tools for measuring well-being have been developed since the middle of the last century [20, 21, 22, and 23]. The pursuit of public welfare and ensuring the conditions for its creation are also the main goal of the state. Certain areas are clearly regulated and strongly influenced by law (for example, social welfare, health care, and business conditions) [24]. The well-being of society is affected by the economy; social relations between members of society, groups and the community; health; education and care; local environment; personal characteristics of the individual. Traditionally, the size of GDP per capita has been considered an indicator of the well-being of a country's population. However, most modern researchers agree that well-being should be expressed and assessed not only in terms of financial indicators but also in terms of quality of life, expressed in both quantitative and more subjective qualitative terms: economic quality of life, socio-economic quality of life; assessment of the quality of life in the context of sustainable development of society [24]. Measurements of the concept of well-being often compete with indices of health, happiness, and civic power [25]. Sustainable development requires the abandonment of the idea that the growth of well-being is only an economic expression of well-being, so the debate on the necessity of economic growth and its compatibility with the well-being of man and society reflects two opposing worldviews. Economic well-being, health and happiness have positive correlations and causal effects. Studies have confirmed that happiness is a cause of good health and affects the behavioural and immune systems through social relationships, work, and other factors. One of the most popular indices for measuring well-being is the holistic definition of well-being [25]. Various methodologies describe public well-being by indicators, which are often grouped into *economic, social and environmental indicators*, and various aggregate indices are

constructed from these indicators [26, 27, 28, and 29]. For example, the Real Progress Index, as one of the most common indicators of GDP change in measuring the well-being of society, takes into account the market and non-market benefits as well as the social, environmental and economic costs of economic benefits. The Real Progress Index is measured by 26 indicators, which are divided into three groups: economic, environmental and social. Following the Brundtland Report "Our Common Future" (1987), which stated that "humanity must develop in a sustainable way to ensure prosperity in the present without compromising future prosperity" (U.N., 1992), the concept of public welfare has been transformed into the one of a sustainable society upon striving to reconcile economic, social and environmental interests of society [30,31]. Against this background, the well-being of society can be grouped into 3 main sectors of sustainable development: the state of the environment, economic development and social development [30, 31]. *Environmental sector* indicators include air and climate change, water, landscape and biodiversity, and waste management. *Economic sector* indicators include transport, industry, energy, agriculture, housing, and tourism. Indicators of the *social development sector* include employment, poverty and social exclusion, public health, education and science, preservation of cultural identity, and sustainable consumption.

Keywords: sustainable energy, energy technologies, public welfare.

REFERENCES

1. ŠTREIMIKIENĖ, D. Tvari energetikos plėtra. *Aplinkos tyrimai, inžinerija ir vadyba*, 2002, Vol. 1, No. 19, P. 20–29.

2. ŠTREIMIKIENĖ, D. Vietiniai ir globaliniai darnios energetikos plėtros politikos įgyvendinimo Lietuvoje aspektai. *Energetika*, 2002, Vol. 1, P. 53–60.

3. ČIEGIS, R.; ŠTREIMIKIENĖ, D. Integration of sustainable development indicators into sustainable development programmes. *Inžinerinė ekonomika*, 2005, Vol. 2, P. 7–12.

4. KLEVAS, V.; ŠTREIMIKIENĖ, D. Lietuvos energetikos ekonomikos pagrindai. Kaunas: *Lietuvos energetikos institutas*, 2006.

5. ŠIKŠNELYTĖ, I. Elektros energijos rinkos darnumo vertinimas Lietuvoje. *Darnaus vystymosi problemos*, 2015, P. 170–200.

6. PAŽĖRAITĖ, A. Centralizuotos šilumos sektoriaus raida Lietuvoje: strategija ir praktika. *Darnaus vystymosi problemos*, 2015, P. 201–219.

7. ŠTREIMIKIENĖ, D. Energetikos plėtros scenarijų darnumo vertinimas. *Darnaus vystymosi problemos*, 2015, P. 142–169.

8. BAUBLYS, J.; MIŠKINIS, V.; MORKVĖNAS, A. Lietuvos energetikos darna su gamta. *Energetika*, 2011, Vol. 57, No. 2, P. 85–94.

9. MARČIUKAITIS, M.; DZENAJAVIČIENĖ, E.F.; KVESELIS, V.; SAVICKAS, J.; PEREDNIS, E.; LISAUSKAS, A.; MARKEVIČIUS, A.; MARCINAUSKAS, K.; GECEVIČIUS, G.; ERLICKYTĖ-MARČIUKAITIENĖ, R. Atsinaujinančių energijos išteklių naudojimo Lietuvoje patirtis, reikšmė ir siekiai. *Energetika*, 2016, Vol. 62, No. 4, P. 247–267.

10. PAŽĖRAITĖ, A.; KRAKAUSKAS, M.; MIKALAUSKIENĖ, A. Spread of clean technologies in Lithuanian electricity sector. *Transformations in Business & Economics*, 2014, Vol. 13, No. 2, P. 174–187.

11. GECEVIČIUS, G.; DVARIONIENĖ, J. Sustainable energy system development in local communities. *Environmental Research, Engineering and Management*, 2014, Vol. 70, No. 4, P. 46–53.

12. ALIŠAUSKAITĖ-ŠEŠKIENĖ, I. Atsinaujinančius energijos išteklius naudojančių energijos gamybos technologijų namų ūkiuose palyginamasis vertinimas. *PhD Thesis*, Kauno technologijos universitetas, Klaipėdos universitetas, Lietuvos energetikos institutas, 2018.

13. MIKALAUSKAS, I. *Energetikos technologijų visuomeninio priimtinumo vertinimas*. PhD Thesis, Vilniaus universitetas, 2020.

14. MCFARLAND, J.R.; REILLY, J.M.; HERZOG, H.J. Representing energy technologies in top-down economic models using bottom-up information. *Energy Economics*, 2004, Vol. 26, No. 4, P. 685–707.

15. RAGHEB, M. Vertical axis wind turbines. *University of Illinois at Urbana-Champaign*, 2011, Vol. 1, No. 40.

16. KURAVI, S.; TRAHAN, J.; GOSWAMI, D.Y.; RAHMAN, M.M.; STEFANAKOS, E.K. Thermal energy storage technologies and systems for concentrating solar power plants. *Progress in Energy and Combustion Science*, 2013, Vol. 39, No. 4, P. 285–319.

17. BALAGURU, P.; RAJ, B.V.; VIGNESH, B.E. Low cost energy production using wind belt technology. *International Journal of Engineering and Innovative Technology (IJEIT)*, 2013, Vol. 2, No. 9, P. 252–255.

18. BUKALA, J.; DAMAZIAK, K.; KROSZCZYNSKI, K.; KRZESZOWIEC, M.; MALACHOWSKI, J. Investigation of parameters influencing the efficiency of small wind turbines. *Journal of Wind Engineering and Industrial Aerodynamics*, 2015, Vol. 146, P. 29–38.

19. BUKALA, J.; DAMAZIAK, K.; KARIMI, H.R.; KROSZCZYNSKI, K.; KRZESZOWIEC, M.; MALACHOWSKI, J. Modern small wind turbine design solutions comparison in terms of estimated cost to energy output ratio. *Renewable Energy*, 2015, Vol. 83, P. 1166–1173.

20. COLEMAN, J.S. Social theory, social research, and a theory of action. *American Journal of Sociology*, 1986, Vol. 91, No. 6, P. 1309–1335.

21. COLEMAN, J.S. Social capital in the creation of human capital. *American Journal of Sociology*, 1988, Vol. 94, P. S95–S120.

22. MCCALL, S. Quality of life. Oxford: *Oxford University Press*, 2005.

23. AKRANAVIČIŪTĖ, D.; RUŽEVIČIUS, J. Quality of life and its components' measurement. *Engineering Economics*, 2007, Vol. 52, No. 2, P. 44–49.

24. SAMOŠKA, M. Visuomenės gerovės ir verslo sąlygų palankumo vertinimo tyrimų analizė. *Mokslas-Lietuvos ateitis*, 2013, Vol. 5, No. 1, P. 1–6.

25. KVIESKIENĖ, G; KVIESKA, V. Socialinės ekonomikos inovacijų įtaka visuomenės gerovei. *Socialinis ugdymas*, 2012, Vol. 21, P. 5–17.

26. MIZARAS, S; LUKMINĖ, D; DOFTARTĖ, A. Miškų ūkio poveikio visuomenės gerovei vertinimas Lietuvoje. *Žemės ūkio mokslai*, 2019, Vol. 26 No. 3, P. 135–144

27. HÄGERHÄLL, C.M.; ODE, A.; TVEIT, M.S.; VELARDE, M.D.; COLFER, C.J.P.; SARJALA, T. Forests, human health and well-being in light of climate change and urbanisation. *IUFRO (International Union of Forestry Research Organizations) Secretariat*, 2010.

28. STOLL, L.; MICHAELSON, J.; SEAFORD, C. Well-being evidence for policy: A review. *New Economics Foundation*, 2012.

29. TALBERTH, J.; WEISDORF, M. Genuine progress indicator 2.0: pilot accounts for the US, Maryland, and City of Baltimore 2012–2014. *Ecological Economics*, 2017, Vol. 142.

30. JOCIUTĖ, A. Visuomenės darnus vystymasis. Vilnius: *Mykolo Romerio universitetas*, 2013, ISBN 978-9955-19-519-1.

31. SERVETKIENĖ, V. Gyvenimo kokybės daugiadimensis vertinimas, identifikuojant kritines sritis. *PhD Thesis*, Mykolo Romerio universitetas, 2013.

I.6. Hydrogen energy and fuel cell technologies

FUEL CELL SUPPORTED CLAMPING CAPACITOR DC-DC BOOST CONVERTER FOR BATTERY CHARGING APPLICATIONS

M. İnci

İskenderun Technical University, Mechatronics Engineering
Central Campus, 31200, Hatay – Turkey
+90 (326) 613 56 00
mustafa.inci@iste.edu.tr

ABSTRACT

In this study, a novel interface system supplied by a fuel cell (FC) is proposed for battery charging applications. A single-switch high gain dc-dc converter is designed to supply electrical energy from a low voltage FC unit to the battery side in the system structure. The clamping capacitor boost converter (CCBC) is utilised to convert the low FC voltage into a higher voltage at the consumer side in comparison with the conventional boost converter's voltage conversion capability. The converter structure consists of a single switch, an inductor, three capacitors, and three diodes for the voltage conversion process in the proposed system. In the design process, a Horizon H-100 proton exchange membrane FC (PEMFC) is modelled in the rating of 100 W and 12-19 V operation range, and consumer-side voltage is kept at 48 V through the CCBC interface. Besides, the system is operated for different loading conditions: 25%, 50%, 75 %, and 100%. In the performance results, the voltage gain of CCBC is analysed and compared against the conventional boost converter for a wide duty cycle range. Then, the system was tested under different load values, and performance results were observed to show the validity of the proposed system. According to the obtained results, the system achieves to keeps the output voltage at the reference value (48 V) for each loading situation. The case studies show that the electrical power is supplied to consumer-loads effectively and smoothly. The results obtained show that the proposed converter uses a single switch like the classical boost converter, but the voltage conversion is achieved with a higher gain for FC-supported battery charging applications.

Keywords: Clamping capacitor boost converter, Fuel cell, High gain dc-dc converter, loading situations

INTRODUCTION

Technological developments have increased the interest and need for high-gain dc-dc converters used in various electronic applications in recent years. Applications such as electric vehicles, grid integration, robotics, and charging stations are significant application areas of high-gain dc-dc converters [1]. The high-efficient and high-gain step-up converters provide a higher voltage conversion rate in comparison with conventional boost converters [2].

In the literature, several improved dc-dc boost converter topologies are used to obtain higher voltage gain than conventional boost converters [3]. Among these converters, isolated high-gain dc-dc boost converters like a bridge, fly back, and forward are costly structures together with the high dimension and power losses. Some isolated topologies are bridge, fly back, and forward dc-dc converters [4]. But, using a step-up transformer in these topologies induces higher volume and losses together with a high cost [5]. Unlike isolated structures, non-isolated converters like boost [6], interleaved [7], cascaded [8], quadratic [9] and voltage multiplier [10] based are simple and low-cost power electronic topologies to obtain high voltage conversion at the output [11]. Conventional boost converters and interleaved boost converters provide more limited voltage gain compared to advanced boost converters. Interleaved boost converters provide more efficiency and robustness with less current ripples [7]. Cascaded boost converters are the basis for the integration of two or more conventional boost circuits. But, the cascaded topology needs supplementary transistors in addition to excessive switching losses [8]. Quadratic boost converters use a single transistor to obtain high voltage conversion capability [9]. In voltage multiplier-based boost converters, the topologies need extra circuit components to increase higher voltages at the output.

In this study, an alternative high-gain clamping capacitor boost converter (CCBC) supplied by a fuel cell (FC) is proposed for unidirectional charging applications. The method section explains and clarifies the operating principles of FC-supported CCBC utilised for battery charging implementation. The equivalent circuits and operation modes of CCBC are analysed and demonstrated. In the study, a proton exchange membrane FC (PEMFC) is used as an energy provider to supply electrical energy for consumer load. A PI-based controller is implemented to supervise energy transfer from PEMFC to load and to keep the dc-link voltage constant. The main objectives of the proposed PEMFC-supported battery charger system are listed as follows:

- In performance results, the voltage gain analysis of the designed converter is given for different duty cycle ratios to show the voltage conversion in comparison with a conventional boost converter.
- A PEMFC in the rating of 100 W is designed and performed according to the dynamic structure of the Horizon H-100 PEMFC. The electrical characteristics and operating values of PEMFC are explained in detail.
- Different loading situations are created to show the active power flow generated from PEMFC. The system is performed for 25%, 50%, 75%, and 100% loading situations.

THE SYSTEM STRUCTURE

In this section, the sub-components of the system are detailed and explained. The system structure of PEMFC-connected CCBC is presented in Fig. 1.
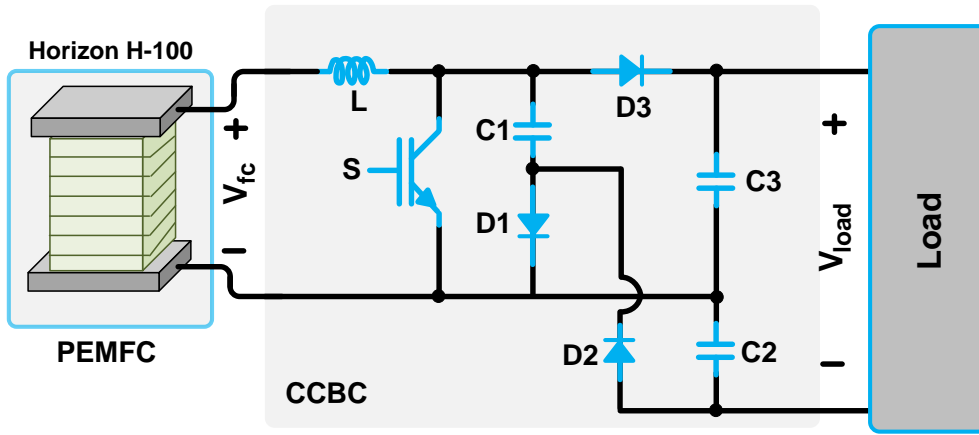
Fig. 1. The structure of the PEMFC-connected CCBC system

PEMFC

In the proposed system, a PEMFC is utilised as an energy generation unit at the input of the dc-dc converter. The dynamic structure of the Horizon H-100 PEMFC is designed and located at the front of the converter. Fig. 2 presents the equivalent circuit and electrical characteristics of Horizon H-100 PEMFC used in the system.
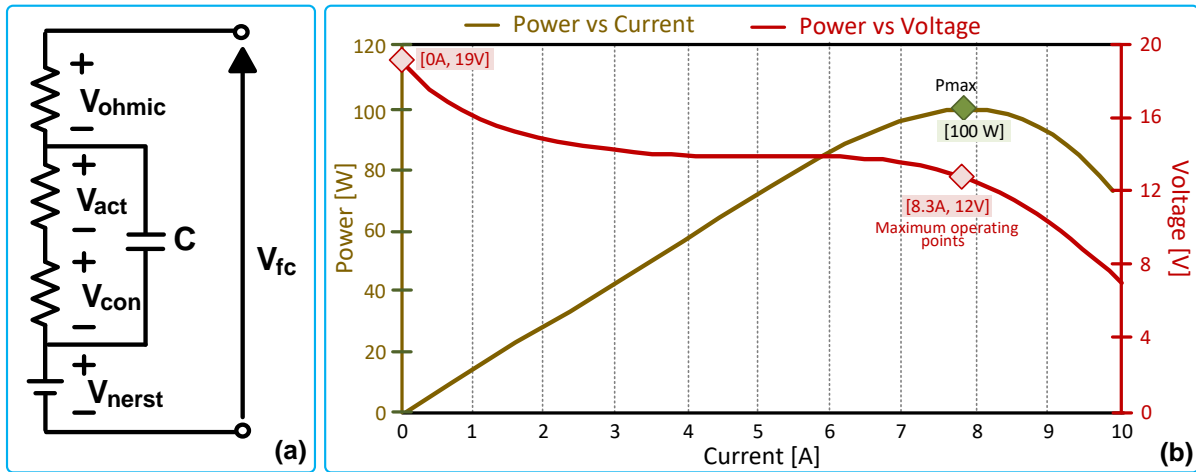
Fig. 2. The equivalent circuit and electrical characteristics of PEMFC

According to the dynamic characteristics of PEMFC, the cell voltage is characterised in terms of Nernst voltage, ohmic voltage, activation overvoltage, and concentration voltage [12].

$$V_{fc} = E_{nernst} - V_{ohm} - V_{act} - V_{con}. \tag{1}$$

In Horizon H-100, the cell number is 20, and stack efficiency is 40% at 12 V. The maximum power of the designed PEMFC is 100 W at maximum operating (12 V, 8.33 A) values. Also, the open-circuit voltage of PEMFC is 19 V when the FC output current is equal to zero [13].

CCBC AND ITS OPERATING PRINCIPLES

The operation modes of PEMFC-connected CCBC are presented in Fig. 3. As shown in the equivalent circuit, the converter consists of a transistor, an inductor, three capacitors, and

three diodes [14]. In operation modes, the elements (blue) are in active operation while the elements (light grey) are in OFF operation.
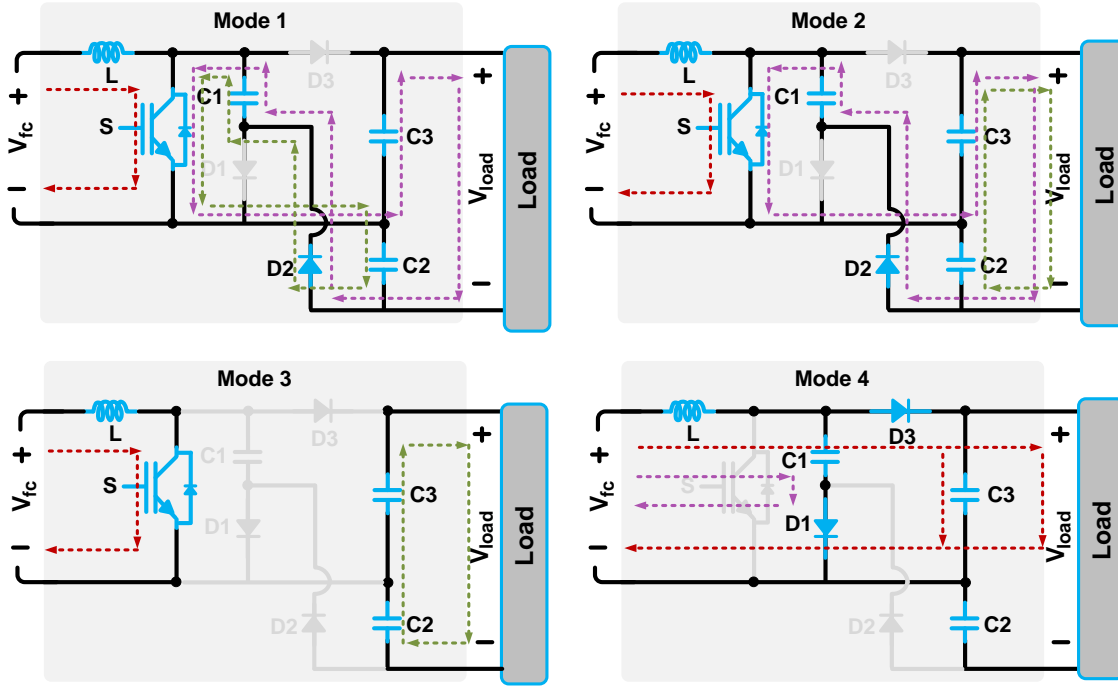
Fig. 3. The operation modes of the CCBC circuit

In mode 1, the switching element (S) is closed, and the inductor (L) is energised. Also, the stored energy in the C1 capacitor is supplied to C2 and C3 capacitors. In mode 2, the current on the C2 capacitor starts to flow in the opposite direction, and all the capacitors ensure power to load. In mode 3, the current and energy on the C1 reach zero. In this mode, C2 and C3 capacitors ensure power to load. In mode 4, the S is open, and D2 is reverse-biased. In this state, the inductor voltage and fuel cell voltage are series-connected with a C2 capacitor to supply power to the load [14].

The load voltage is the sum of C2 voltage and C3 voltage. In this way, the voltage gain (G) between input and output voltages is defined as [14]:

$$G = \frac{V_{load}}{V_{fc}} = \frac{V_{c2} + V_{c3}}{V_{fc}} = \frac{2}{(1-D)} \qquad (2)$$

The inductor is calculated by using Eq. 3.

$$G = \frac{V_{load}}{V_{fc}} = \frac{V_{c2} + V_{c3}}{V_{fc}} = \frac{2}{(1-D)} \qquad (3)$$

The inductor is calculated by using Eq. 3.

$$L = D(1-D)\frac{V_{out}}{2\Delta i_L f_s} \qquad (3)$$

The capacitors are computed by using Eq. 4.

$$C_1 = \frac{I_{load}}{f_s \Delta v_{C1}} \quad C_2 = \frac{(1-D)I_{load}}{f_s \Delta v_{C2}}, \quad C_3 = \frac{(1-D)I_{load}}{f_s \Delta v_{C3}}. \qquad (4)$$

LOADS

In the designed system, resistive components are used as a consumer. The resistance values are selected according to the consumer power rating using constant dc load voltage (48 V). The resistance values are 92 Ω, 46 Ω, 30.2 Ω and, 23.1 Ω for 100%, 75%, 50%, and 25% loading situations, respectively.

RESULTS

This section presents the performance results of the PEMFC-connected CCBC system. The system has been constructed and tested by using the Simulink environment program. The design parameters of the system are given in Table 1.

Table 1. The design parameters of the PEMFC-connected CCBC circuit

Parameter	Symbol	Value
FC voltage	V_{fc}	12V-19V
Load voltage	V_{load}	48 V
Load values	R	92 Ω
		46 Ω
		30.6 Ω
		23 Ω
Switching frequency	f_s	10 kHz
Inductor	L	100 µH
Capacitors	C1	1 mF
	C2	0.5 mF
	C3	0.5 mF
Sample time of simulation	-	2 µs

The voltage gain analysis for CCBC and conventional boost converter is introduced in Fig. 4. It shows that the voltage gain of the CCBC is twice that of the conventional boost converter topology for each different duty cycle value.
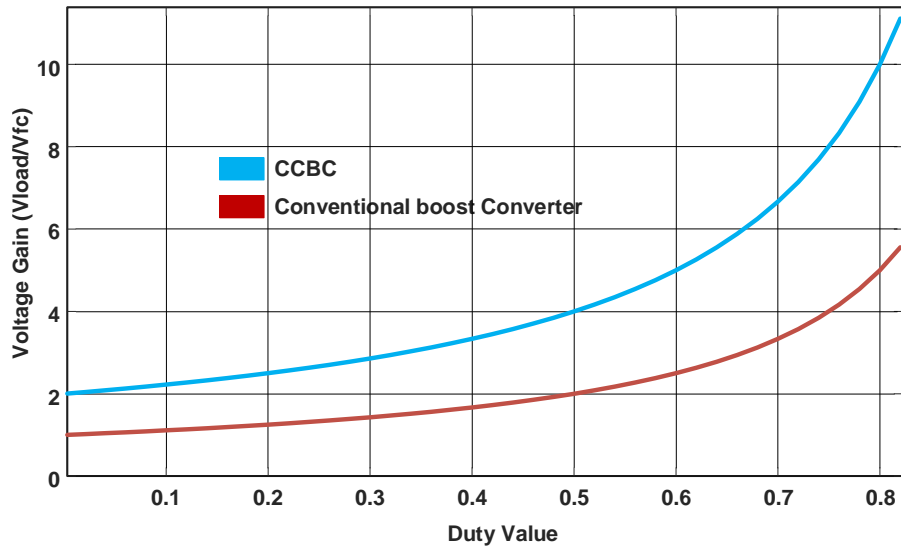
Fig. 4. Voltage gain comparison of CCBC and conventional boost
converter

Fig. 5 shows the performance results for different loading situations: 25%, 50%, 75% and 100%, respectively. In state 1, a load in the rating of 92 Ω is connected to the system, and it consumes 25.05 W at the output. In this state, the FC voltage is 16.13 V while the load voltage is kept at 48.01 V. In state 2, the load value equals 46 Ω, and the consumed power is 50.04 W. In this state, the output voltage is 47.98 V while the FC operates at 15.11 V. In state 3, the FC voltage is 13.76 V, while the load voltage is kept at 47.93 V. The generated power is 75.07 W in this state. Subsequently, the system is performed for the full loading situation. The load value is 23.1 ohm, and the generated power equals 98.96 W when the load voltage is 47.71 V.

Fig. 5. Performance results for different loading situations

The obtained results are given in Table 2. According to the loading situation, the results show consumed power values and FC power values. Also, the efficiency values of the designed system are calculated by using consumed power and FC power for each state.

Table 2. The obtained results for loading situations

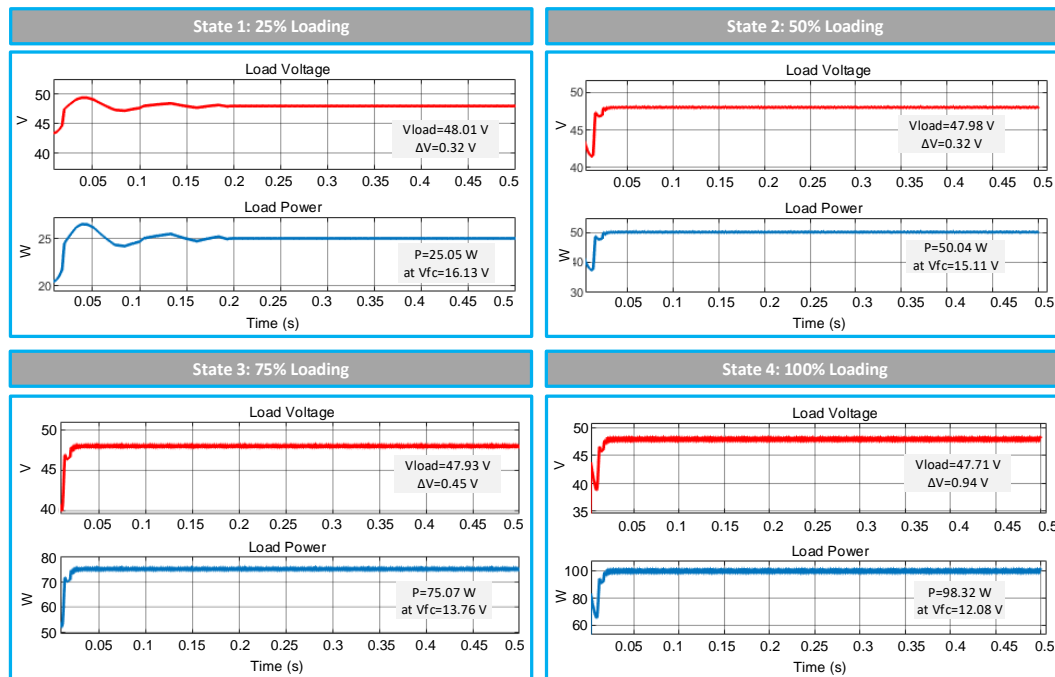|	State 1	State 2	State 3	State 4
Loading (%)	25	50	75	100
Load current (A)	0.52	1.04	1.56	2.06
Consumed power (W)	25.05	50.04	75.07	98.32
FC Power (W)	26.38	51.19	75.43	99.16
Efficiency (%)	94.95	97.75	98.22	99.15

In obtained results, the values show that the output current changes proportionally with the load condition due to the constant output voltage. In addition, it is seen from the results that the system efficiency improves as the load level increases.

CONCLUSIONS

In this study, a high-gain single-switch dc-dc boost converter is fed by a PEMFC for battery charging applications. The operation modes and working principles of CCBC are explained and clarified for different situations. The voltage gain and parameter selection guidelines of the proposed CCBC are given. In the performance section, the system's power rating is designed as 100 W, and the FC voltage range is between 12 V and 19 V. The system has been tested and performed for different loading situations between quarter-loading and full-loading situations. The performance results show that the load voltage is kept at approximately 48 V and FC voltage varies inversely with the generated power. The performance results verify that the system operates at high-efficiency values for different loading situations. The results show that the FC produces more power at lower voltage values in terms of dynamic characteristics. Besides, the voltage ripples values are kept at less than 1 V at the output side of the designed system.

REFERENCES

1. İNCI, M.; BÜYÜK, M.; DEMIR, Mehmet H.; İLBEY, G. A review and research on fuel cell electric vehicles: Topologies, power electronic converters, energy management methods, technical challenges, marketing and future aspects, 2021, *Renewable and Sustainable Energy Reviews*, Vol. 137, P. 110648.

2. İNCI, M.; BÜYÜK, M.; SAVRUN, Murat M.; DEMIR, Mehmet H. Design and analysis of fuel cell vehicle-to-grid (FCV2G) system with high voltage conversion interface for sustainable energy production, 2021, *Sustainable Cities and Society*, Vol. 67, P. 102753.

3. AMIR, A.; AMIR, A.; CHE, Hang S.; ELKHATEB, A.; RAHIM, Nasrudin A. Comparative analysis of high voltage gain DC-DC converter topologies for photovoltaic systems, 2019, *Renewable Energy*, Vol. 136, P. 1147-1163.

4. FARHANI, S.; BARHOUMI, El M.; BACHA, F. Design and hardware investigation of a new configuration of an isolated DC-DC converter for fuel cell vehicle, 2021, *Ain Shams Engineering Journal*, Vol. 12, No. 1, P. 591-598.

5. SRI, Revathi B.; PRABHAKAR, M. Non isolated high gain DC-DC converter topologies for PV applications – A comprehensive review, 2016, *Renewable and Sustainable Energy Reviews*, Vol. 66, P. 920-933.

6. DORJI, S.; WANGCHUK, D.; CHODEN, T.; TSHEWANG, T. Maximum Power Point Tracking of solar photovoltaic cell using Perturb & Observe and fuzzy logic controller algorithm for boost converter and quadratic boost converter, 2020, *Materials Today: Proceedings,* Vol. 27, P. 1224-1229.

7. WU, H. F.; MU, T. T.; GE, H. J.; XING, Y. Full-Range Soft-Switching-Isolated Buck-Boost Converters with Integrated Interleaved Boost Converter and Phase-Shifted Control, *IEEE Transactions on Power Electronics*, 2016, Vol. 31, No. 2, P. 987-999.

8. JIAN, F.; BO, Z.; DONGYUAN, Q.; WENXUN, X. A novel single-switch cascaded DC-DC converter of Boost and Buck-boost converters, 16th European Conference on Power Electronics and Applications, 2014, P. 1-9.

9. SFERLAZZA, A.; ALBEA, C.; GARCIA, G. A Hybrid Control Strategy for Quadratic Boost Converters with Inductor Currents Estimation, 2020, *Control Engineering Practice*, Vol. 103, P. 104602.

10. KOÇ, Y.; BIRBIR, Y.; BODUR, H. Non-isolated high step-up DC/DC converters – An overview, 2022, *Alexandria Engineering Journal*, Vol. 61, No. 2, P. 1091-1132.

11. İNCI, M. Design and Analysis of Quadratic Boost Converter with Inductor-Capacitor-Diode Voltage Multiplier Circuit, 2021, *European Journal of Technique* , Vol. 11, No. 1, P. 23-28.

12. JYOTHEESWARA, Reddy K.; SUDHAKAR, N. A new RBFN based MPPT controller for grid-connected PEMFC system with high step-up three-phase IBC, *International Journal of Hydrogen Energy*, 2018, Vol. 43, No. 37, p. 17835-17848.

13. Horizon, H-100 PEMFC Stack. 2021, Link to the Internet: <http://new.novatorlab.ru/en/katalog/promyshlennost/ toplivnye-elementy/vodorodnyj-toplivnyj-stek-horizon-h-100-pem-fcs-c100>.

14. ZENG, Y.; LI, H.; WANG, W.; ZHANG, B.; ZHENG, Trillion Q. Cost-effective clamping capacitor boost converter with high voltage gain, 2020, *IET Power Electronics*, Vol. 13, No. 9, P. 1775-1786.

STUDY ON THE INFLUENCE OF IONIC MEMBRANE TYPE IN A CO_2 ELECTROLYSER

B. Mitrea, C. Diac, M.T. Iacob, A. Balan, I. Stamatin, E. Lavasani
3Nano-SAE Research Centre, University of Bucharest - Faculty of Physics
Atomistilor 405, PO Box MG-38 – Romania
+ 40214574838
bogdan.mitrea@3nanosae.org

EXTENDED ABSTRACT

OVERVIEW

In fighting global warming, it is essential not only to find new technologies but also to make them affordable and accessible. Acting in this particular way will encourage industries to invest in change and will also help authorities in giving them a base to create regulations knowing that the available solutions are feasible.

One of the innovative ways to recycle CO_2 is the conversion into valuable products, such as reducing the formic acid through electrocatalytic reactions. Each component of an electrolyser can affect the performance, but the membrane is the most significant part of the cell besides the electrocatalysts. The ionic conductivity is the main parameter to get a high conversion yield. High ionic conductivity is desired for an increased reaction rate. Both cationic (mainly Nafion) and anionic membranes were tested in electrolysers for CO_2 conversion. Nafion and other cationic membranes proved to have low yield [1]. The anionic membranes doped with KOH are more appropriate for CO_2 conversion: Polyvinyl alcohol-KOH (PVA-K) and imidazolium functional groups are grafted onto the polymer backbone. The last is a registered trademark as Sustainion [2, 3]. Sustaining outperforms all alkali-doped membranes used in CO_2-electrolysis but is still expensive (800 USD/100 cm² Sustainion) like Nafion. Improving characteristics of PVA-K by engineering molecular weight, backbone length, and crosslinking methods could obtain alkaline-PVA membranes with appropriate Faradaic efficiency to imidazolium salts. The current study aims to increase the Faradaic efficiency by crosslinking different molecular weights PVA with chemical and physical cross linkers.

METHODS

Materials: PVA with 50,000-600,000 MW, chemical crosslinked - glutaraldehyde (1-5% water solutions) – reference, freezer for physical crosslinked freeze (250K)-thaw (RT) repeated cycles.

Solutions of 10-15% PVA are cast in films (1-2mm thickness) on a glass substrate and frozen up to 250K, followed by thawing at RT. Up to five cycles of freeze-thawing are performed. PVA films are treated with a 3% peroxide solution to improve stability in thickness and mechanical properties. Finally, PVA-crosslinked films are boiled in 3M KOH for 1 hour,

washed and kept in 1M KOH before use in CO_2-electrolyser (homemade device). Faradaic efficiency is measured as in ref [2].

RESULTS

Figure 1 shows the basic principle for CO_2-electrolyser, and in table 1, the preliminary results for PVA- 150,000 MW are crosslinked by freeze-thawing and comparison with other membranes.
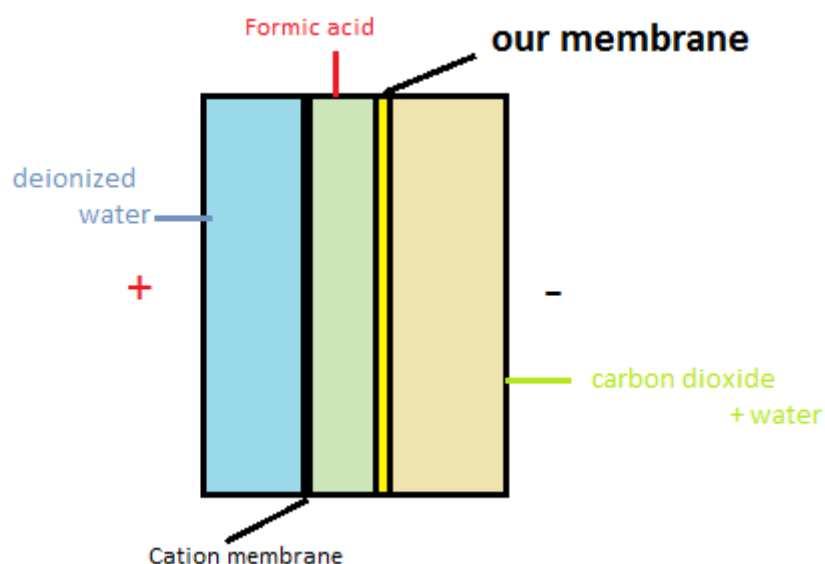
Fig. 1. Simplified schematic of a formic acid cell

Table 1. Membrane area-specific resistance (ASR) and Faradaic efficiency [2, 3].

Membrane	ASR in 1 M KOH, 60 °C (Ω-cm^2)	pH Range	Faradaic efficiency (%)
Sustainion® 37-50	0.045	2-14	>80
Nafion 115	0.52	0-13	N/A
PVA membranes doped 3M KOH [2]	0.5-2 (dependent on crosslinking method)	10-13	40-50
Alkali-doped other polymers	-	>7	<20
PVA- freeze crosslinking, 3M KOH	~ 0.6	>10	~55-60

CONCLUSIONS

PVA-membranes designed by freeze-thawing of the PVA with different MW could be a good perspective to develop new CO_2-electrolysers. Understanding the crosslinking mechanisms related to the PVA tacticity, chain length, MW and insertion of imidazolium functional groups opens a new perspective for CO_2 conversion via electrolysis.

Keywords: CO_2 conversion, CO_2-electrolyser, PVA-membranes

REFERENCES

1. RIDGWAY, P.L.; DELACOURT, C.; KERR, J.K.; NEWMAN, J. Design of an Electrochemical Cell Making Syngas (CO + H2) from CO2 and H2O Reduction at Room Temperature. *Journal of the Electrochemical Society*, 2007, Vol. 155, No. 1, P. B42-B49.

2. KUTZ, R.B.; CHEN, Q.; SAJJAD, S.D.; LIU, Z.; ASEL, I.R. Sustainion Imidazolium-Functionalized Polymers for Carbon Dioxide Electrolysis. *Energy Technology*, 2017, Vol. 5, No. 6, P. 929-936.

3. LIU, Z.; YANG, H.; KUTZ, R.; MASEL, R.I. CO2 Electrolysis to CO and O_2 at High Selectivity, Stability and Efficiency Using Sustainion Membranes. *Journal of the Electrochemical Society*, 2018, Vol. 165, No. 15, P. J3371-J3377.

I.7. Fusion energy, nuclear fission and radiation protection

DEVELOPMENT OF A NUMERICAL MODEL OF QUENCH-20 TEST BASED ON LEI EXPERIENCE ON MODELLING OF QUENCH TESTS

N. Elsalamouny, T. Kaliatka
Lithuanian Energy Institute,
Breslaujos g. 3, LT-44403 Kaunas – Lithuania
+37060445860
Noura.Elsalamouny@lei.lt, Tadas.Kaliatka@lei.lt

EXTENDED ABSTRACT

OVERVIEW

The phenomenon of hydrogen generation can lead to a severe accidents. Hydrogen is considered flammable gas; the rapid increase in hydrogen generation amount could lead to an explosion. Though, it has been investigated in detail by using experimental facilities and modelling tools. QUENCH tests are experiments to investigate the hydrogen source that is generated or produced due to the water or steam injection into the uncovered core of light water reactors (LWR). The QUENCH tests are performed at the QUENCH facility at Karlsruhe Institute of Technology. In the QUENCH facility, the fuel rods are placed with fuel simulators with tungsten heaters surrounded by identical cladding material as light water reactors. The latest test provided in the QUENCH facility is dedicated to BWR assembly (QUENCH-20). QUENCH tests are also used to verify and validate computer codes.

Lithuanian Energy Institute (LEI) has wide experience in modelling different QUENCH tests (QUENCH-03, 06, 10, 18) using different severe accident computer codes (ASTEC and RELAP/SCDAPSIM) [3, 4, 5, 6]. LEI is also provided with the uncertainty and sensitivity analysis for calculation results for some QUENCH tests using statistical tools (SUNSET and SUSA). Recently LEI has been taking part in the International Atomic Energy Agency Coordinated Research Project (IAEA-CRP I I31033), whose main aim is to apply the Best Estimate methodology for the modelling results of severe accident conditions in LWR. In this CRP, LEI is modelling the QUENCH-06 test using RELAP/SCDAPSIM code and providing uncertainty and sensitivity analysis for calculation results using the SUSA tool.

The aim of this work, presented by this paper, is to use LEI's previous experience for the development of a numerical model of the QUENCH-20 test using RELAP/SCDAPSIM code.

METHOD

Looking through the QUENCH test matrix [7], it was found that boundary conditions of the QUENCH-06 test are similar to QUENCH-20 test boundary conditions. Thus, it would be a capability to use the already existing experience of modelling the QUENCH-6 test to develop a numerical model of the QUENCH-20 test.

SIMILARITIES OF QUENCH-6 AND QUENCH-20.

There are similarities between QUENCH-06 and QUENCH-20. Both have similar main operational phases, the bundle cooling boundary conditions, electrical power and quenching water injection (Table 1).

Table 1. The main boundary conditions of the QUENCH-6 and QUENCH-20 tests

Parameter	QUENCH-06	QUENCH-20
Steam flow rate (g/s)	3 g/s	3 g/s
Argon flow rate (g/s)	3 g/s	3 g/s
Water injection (g/s)	40 g/s	50 g/s
Peak Power kW	18.2 kW	18.2 kW
Main phases	(pre-oxidation, transient, Quenching)	(pre-oxidation, transient, Quenching)

DIFFERENCES OF QUENCH-6 AND QUENCH-20

QUENCH -06, and 20 tests have different bundle types. QUENCH-06 test has a PWR bundle type (Figure 1 (a)), which consists of 21 fuel rods simulators, 4 corner rods, a central rod and a shroud. QUENCH-20 test has a BWR bundle type (Figure 1 (b)) that consists of 24 fuel rods simulators, stainless steel control blades with B_4C, a fuel channel box, a water channel box and a corner rod.

(a)

(b)
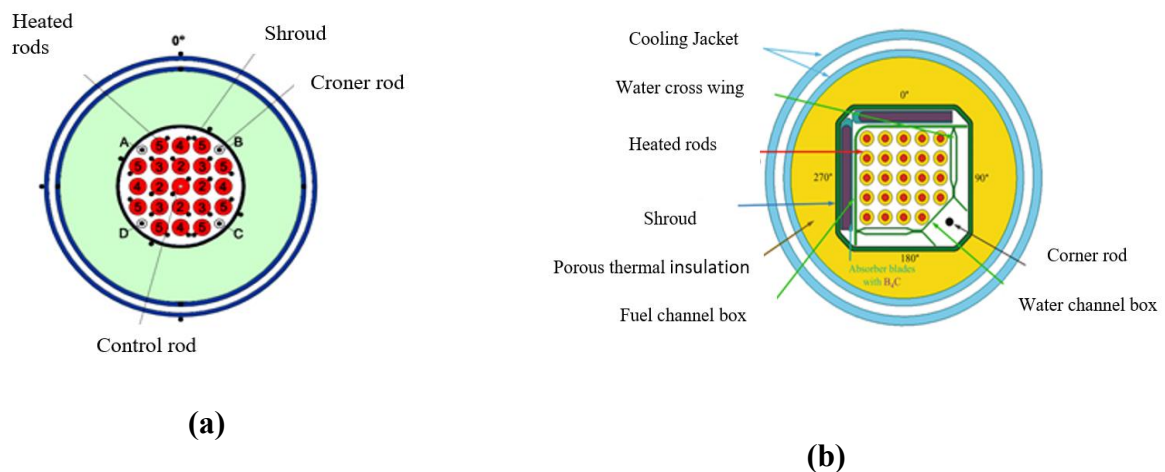
Fig. 1 Bundle type; a) PWR bundle type (QUENCH-06) [1], b) BWR bundle type (QUENCH-20) [2]

RESULTS OF QUENCH-6 AND QUENCH-20

During the QUENCH-06 test, the hydrogen generated when temperature increases, steam interacts with fuel cladding and generates hydrogen. The amount of generated hydrogen at the end of the test is 36 g (32 g before quenching and 4 g during quenching). In the QUENCH-20 test, the hydrogen source term is produced from: the oxidation of Zr claddings (temperature increases, steam oxidises the cladding), and the chemical reactions between B_4C (10g of H_2) and the steam.

The chemical reactions of B4C with steam [2]:

$$B_4C + 7H_2O = 2B_2O_3 + CO + 7H_2 \tag{1}$$

$$B_4C + 8H_2O = 2B_2O_3 + CO_2 + 8H_2 \tag{2}$$

$$B_4C + 6H_2O = 2B_2O_3 + CH_4 + 4H_2 \tag{3}$$
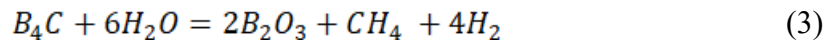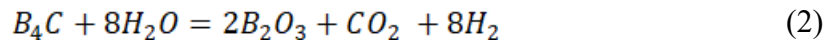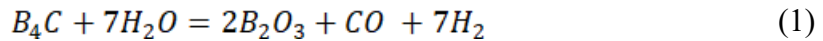
Around 57.4 g (25.4 before quenching, 32 during quenching) of hydrogen was generated at the end of the test. As a result of the bigger amount of hydrogen generated during the QUENCH-20 test. The QUENCH-20 test bundle has more damage, strong degradation, and failure of the shroud than the bundle of QUENCH-06. Because BWR bundle type has more metal, taking into account B_4C reactions and relocations.

As a comparison showed that the boundary conditions of QUENCH-06 are similar to QUENCH-20 test boundary conditions – the same nodalization scheme of the RELAP part could be used for QUENCH-20 test model development.
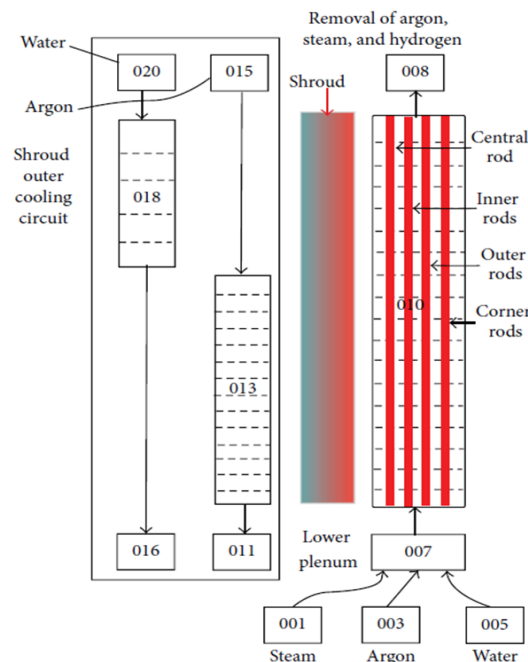
Fig. 3 Nodalization scheme of QUENCH experiment, developed for RELAP/SCDAPSIM [3].

SCDAP part for the QUENCH-20 test model will be changed according to the BWR type bundle and its materials. However, there are some challenges in modelling the BWR bundle. RELAP/SCDAPSIM severe accident code uses a modelling approach based on concentric rings to simulate fuel bundles of LWR. In the QUENCH-20 test is used a quarter of the BWR bundle, which geometry is rectangular. Another challenge is the existence of the absorber blades made from stainless steel and containing B_4C pins inside. To overcome these challenges, some improvements would be made to the code models dedicated to the evaluation of the oxidation phenomena.

CONCLUSIONS

LEI has experience in modelling QUENCH tests which could be used for the new model development. For numerical model development of QUENCH-20, it was used experience

from QUENCH-6 modelling results. A comparison of QUENCH-06 and QUENCH-20 test results showed that both tests have similar boundary conditions and similar test phases. This indicates that the numerical model could be used already developed RELAP part. However, these tests using different bundle types and SCADAP parts in order to model BWR-type fuel assembly should be developed.

A comparison of the QUENCH-06 and QUENCH-20 tests results showed higher hydrogen generation for QUENCH-20 by 40%. Also shroud at the end of QUENCH-20 tests was more significantly damaged. These results are due to B4C oxidation. RELAP/SCDAPSIM code does not have appropriate models to model these phenomena – model improvements or evaluation of additional energy release need to evaluate. These questions will be solved in the future.

Keywords: QUENCH-06, QUENCH-20, RELAP/SCDAPSIM, numerical modelling

REFERENCES

1. SEPOLD, L.; HERING, W.; HOMANN, C.; MIASSOEDOV, A.; SCHANZ, G.; STEGMAIER, U.; STEINBRÜCK, M.; STEINER, H.; STUCKERT, J. Experimental and Computational Results of the QUENCH-06 Test (OECD ISP-45), *Report FZKA-6664, Forschungszentrum Karlsruhe*, 2004.

2. STUCKERT, J; PETERS, U; STEGMAIER, U. Results of metallographic analysis of the QUENCH-20 bundle with B4C absorber 26th International QUENCH Workshop, *KIT*, 2021.DOI: 10.5445/IR/1000141824

3. KALIATKA, T.; KALIATKA, A.; VILEINISKIS, V. Application of Best Estimate Approach for Modelling of QUENCH-03 and QUENCH-06, *Nuclear Engineering and Technology*, 2016 DOI:10.1016/j.net.2015.12.011.

4. KALIATKA, A.; KALIATKA, T.; VILEINIŠKIS, V.; UŠPURAS, E. Best estimate approach for the simulation of reactor core overheating and quenching experiments. Proceeding of *Best Estimate Plus Uncertainty International Conference. Multi-Physics Multi-Scale Simulations with Uncertainty (BEPU 2018)* May 13-18, 2018, Lucca, Italy. 12 p.

5. KALIATKA, T.; UŠPURAS, E.; ALLISON, CH. Modelling of quench 10 experiment on air ingress using RELAP/SCDAPSIM mod 3.5. *Proceedings of the 2017 25th International Conference on Nuclear Engineering ICONE25 July 2-6, 2017, Shanghai, China*. P. 1-7

6. KALIATKA, T. Implementation of QUENCH-10 experiment modelling experience for the modelling of severe accidents in spent fuel pools. *Proceedings 23rd International QUENCH Workshop Karlsruhe Institute of Technology, Germany* (doi:10.5445/IR/1000076201) October 17-19, 2017. p. 366-395.

7. QUENCH Test Matrix. Link to the internet: < https://quench.forschung.kit.edu/24.php>

DEVELOPMENT OF A NEUTRON DIFFUSION CODE OPEN NODE USING THE NODAL EXPANSION METHOD TO SIMULATE THE 3D REACTOR CORE CALCULATION IN CARTESIAN GEOMETRY

H. Satti, O. El Hajjaji, T. El Bardouni, M. Lahdour, A. Nouayti

Abdelmalek Essaadi University
Av. Mfdal Afailal, Street Abi l'Hassan Chadli N: 40, 93040 Tetouan – Morocco
+212653401864
sattihicham@gmail.com

EXTENDED ABSTRACT

OVERVIEW

The finite difference and nodal methods are often used in the neutron community to solve the diffusion equation. A simple way to solve the neutron diffusion equation on a spatial mesh is to evaluate this equation at the mesh points by replacing the partial derivatives with finite differences [1]. The difficulty of generalising the finite difference method to the slow spatial convergence has led engineers to develop new spatial approximation methods, in particular nodal methods [1].

The nodal methods consist in solving the differential equations in three dimensions according to the x, y and z directions, and taking into account the balance equation. This resolution can be done analytically, using the analytical nodal method (ANM) [2], or by assuming a polynomial approximation of the unknowns, nodal expansion method (NEM) [3], [4]. In the case of the polynomial approximation, we introduce an approximation of the transverse leakage, either flat or quadratic. The balance equation allows, finally, to calculate the values of the integrated flux in the meshes $\underline{\phi}$. The unknowns introduced in this formulation are the transverse leakage at the interface of the meshes and the flux in the meshes [5].

The scientific community has developed many open-source tools in order to analyse nuclear reactors. Some of these tools that have been published are VENTURE [6], CITATION [7], ADPRES [8], and OpenNTP [9]. The aim of this work is to present a deterministic calculation code developed by Fortran90 simulating the neutron diffusion in nuclear reactors that are based on nuclear fission. The code's name is OpenNode, it solves the 3D steady state of the multi-group neutron diffusion equation in Cartesian geometries.

The main method integrated into OpenNode is the nodal expansion method (NEM), which discretises the space into a coarse spatial mesh (nodes) as large as a fuel assembly size. The best-known equation that relating flux and current is Fick's law. In order to develop for each node other equations relating nodal flux and partial currents to the faces of the nodes, a polynomial approximation of the flux is considered on the nodes by an expansion in polynomials up to order $N = 4$ [10]. The advantage of NEM over other classical methods such as FDM (Finite Difference Method) is that it doesn't require a very fine mesh to obtain the computational accuracy, thus a reduction in computational cost [11]. The NEM allows

decreasing the number of unknowns by increasing the number of equations [12]. For this purpose, two other approximations have been added for each direction; the first is the weighted residual method to obtain two other balance equations, and the second is the quadratic transverse leakage approximation [13].

The code allows to calculate the effective multiplication factor k_{eff} the neutron flux, the radial and axial power distribution in the nodes. Besides, a graphical user interface was developed by Python with f2py [14] and PyQt5 [15] to simply create the input file, run the source code, plot 2D figures, draw 2D and design 3D geometries using Blender [16].

To test the code, we compatibly compared the results calculated for the IAEA-2D benchmark [17] with those obtained by codes that use FDM as a computational method since they are considered a reference codes such as VENTURE.

METHODS

OpenNode code follows the same background theory of the neutron diffusion used in MOSRA-Light [11]. The basic neutron diffusion equation is (1).

$$\vec{\nabla}\vec{J}_g(\vec{r}) + \Sigma_{r,g}(\vec{r})\phi_g(\vec{r}) = Q_g(\vec{r}). \tag{1}$$

Dividing the space into several k nodes and integrating the neutron balance equation along y and z leads to the following 1-D equation (2):

$$\frac{d}{dx}\underline{J}_{g,x}^k(x) + \Sigma_{r,g}^k\underline{\phi}_{g,x}^k(x) = \underline{Q}_{g,x}^k(x) - \frac{1}{\Delta_y^k}\underline{L}_{g,y}^k(x) - \frac{1}{\Delta_z^k}\underline{L}_{g,z}^k(x). \tag{2}$$

Where $\underline{Q}_{g,x}^k$ and $\underline{L}_{g,y}^k$ are the average nodal source and leakage terms, respectively, in the x direction.

In OpenNode, the 1-D neutron flux is approximated by 4th order polynomial expansion as follows (3):

$$\underline{\phi}_{g,x}^k(x) \simeq \underline{\phi}_{g,0}^k f_0(x) + \sum_{n=1}^4 a_{g,xn}^k f_n(x), with \left(-\frac{\Delta_x}{2} \le x \le \frac{\Delta_x}{2}\right), \tag{3}$$

where:

$f_0(x) = 1$ $f_1(x) = \xi = \frac{x}{\Delta_x^k}$ $f_2(x) = 3\xi^2 - \frac{1}{4}$ $f_3(x) = \xi\left(\xi - \frac{1}{2}\right)\left(\xi + \frac{1}{2}\right)$ $f_4(x) = \left(\xi^2 - \frac{1}{20}\right)\left(\xi - \frac{1}{2}\right)\left(\xi + \frac{1}{2}\right)$.

The outgoing currents are calculated by the incoming currents, the total source, and the transverse leakage terms iteratively using the following response matrix equations (4)

$$\vec{J}_g^{out,k} = \left[A_g^k\right]^{-1}\left[B_g^k\right]\vec{J}_g^{in,k} + \left[A_g^k\right]^{-1}\left[C_g^k\right]\left(\vec{Q}_g^k - \vec{L}_g^k\right) = \left[R_g^k\right]\vec{J}_g^{in,k} + \left[P_g^k\right]\left(\vec{Q}_g^k - \vec{L}_g^k\right) With: \left[R_g^k\right] = \left[A_g^k\right]^{-1}\left[B_g^k\right], \left[P_g^k\right] = \left[A_g^k\right]^{-1}\left[C_g^k\right] \tag{4}$$

Where $\left[P_g^k\right]$ and $\left[R_g^k\right]$ are the nodal coupling matrices that are defined by the node characteristics

The transverse leakage term is approximated quadratically as follows (5):

$$\underline{L}_{g,y}^k(x) \approx \rho_{g,y}^k(x) \equiv \rho_{0g,y,x}^k + \rho_{1g,y,x}^k f_1(x) + \rho_{2g,y,x}^k f_2(x). \tag{5}$$

RESULTS

The techniques and methods developed above are incorporated into OpenNode code. The main window GUI (Graphical User Interface) of OpenNode on all Windows machines is given in Fig.1.
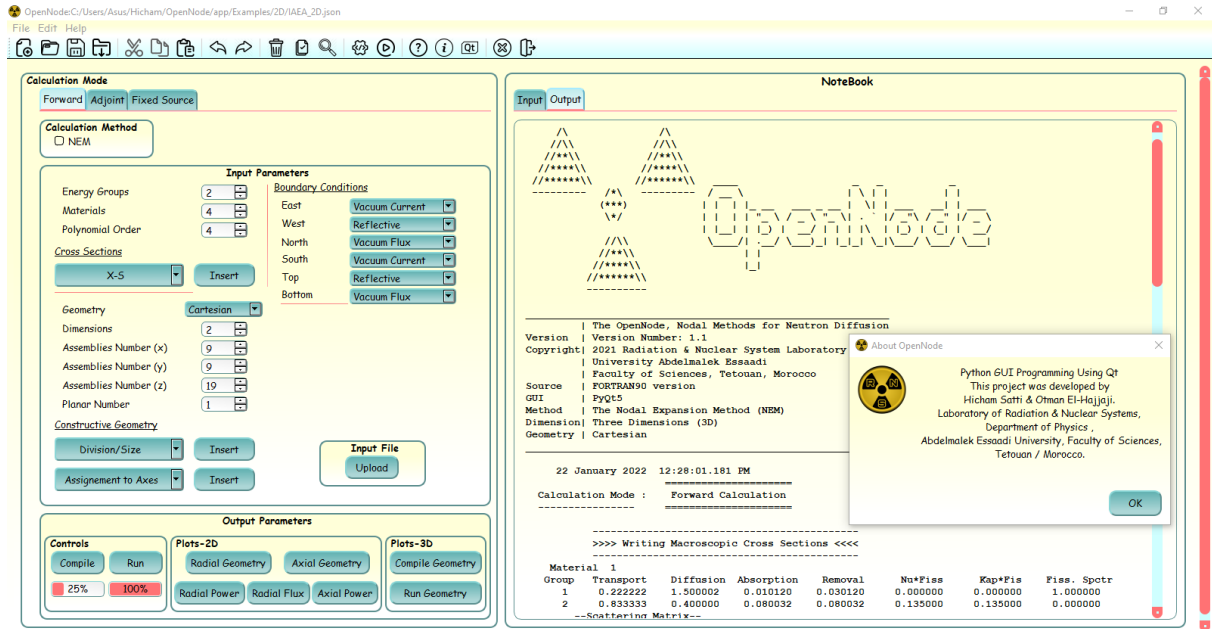
Fig. 1. Main window of OpenNode

The 2D-IAEA benchmark reactor is a 2-group LWR problem consists of 177 fuel assemblies, including 9 rodded fuel assemblies and a zone of water reflector with a vacuum boundary external. The width of each square assembly is 20 cm. The 2D and 3D radial visualisation of IAEA-2D geometry obtained by OpenNode is shown in Fig. 2 and Fig. 3, respectively.

The 2D-IAEA benchmark data, detailed in [18], are defined in Table 1 as follows:

Table 1. Material cross-section of each assembly for the IAEA-2D benchmark

Zone	Material	Group	$D(cm^{-1})$	$\Sigma_a(cm^{-1})$	$\nu\Sigma_f(cm^{-1})$	$\Sigma_{s,1\rightarrow2}(cm^{-1})$	χ
1	**Outer Fuel**	1	1.5	0.01012	0		1
		2	0.4	0.080032	0.135	0.02	0
2	**Inner Fuel**	1	1.5	0.01012	0		1
		2	0.4	0.085032	0.135	0.02	0
3	**Inner Fuel + Control Rod**	1	1.5	0.01012	0		1
		2	0.4	0.130032	0.135	0.02	0
4	**Reflector**	1	2.0	0.00016	0		1
		2	0.3	0.010024	0	0.04	0
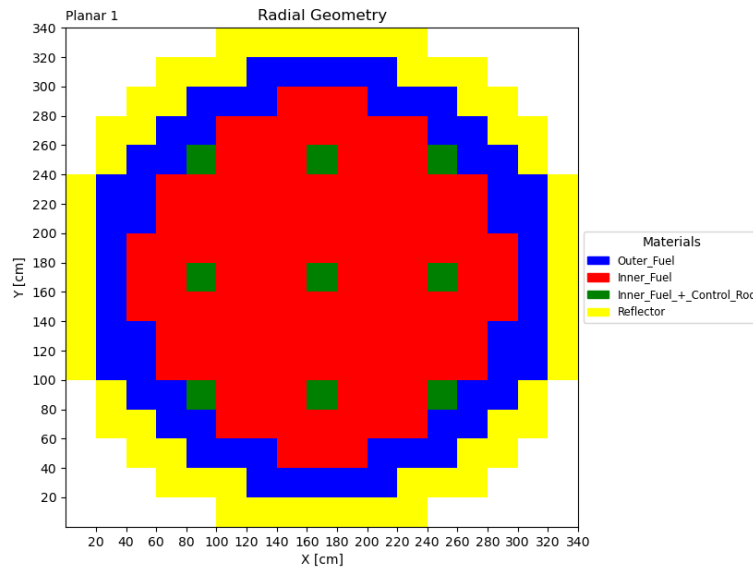
Fig. 2. 2D-Radial Geometry of IAEA
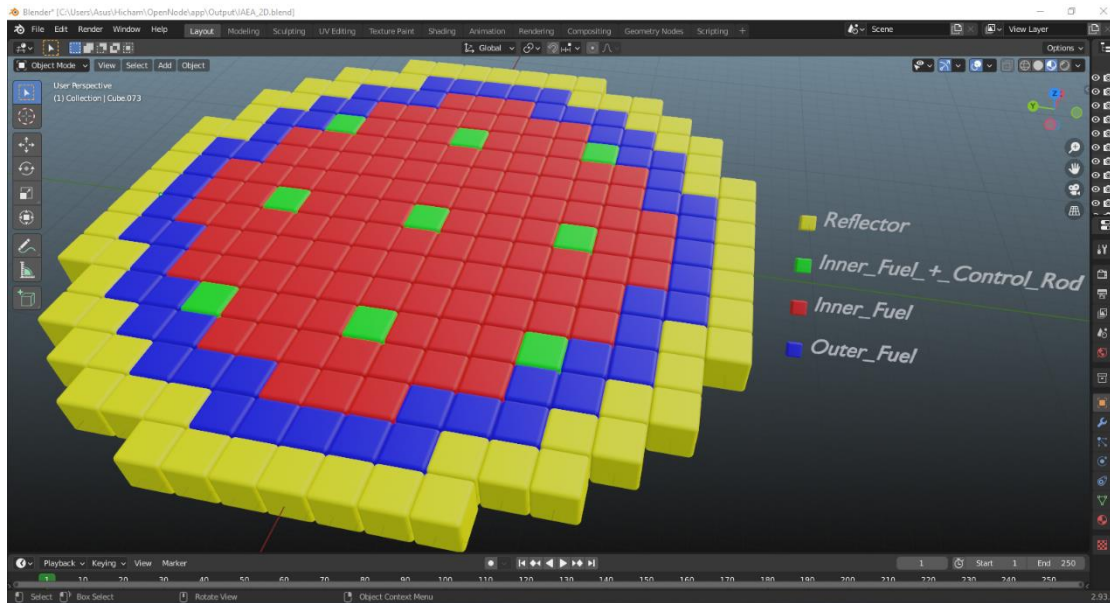
Fig. 3 3D-Radial Geometry of IAEA

The k_{eff} calculated for the three different node sizes and two different polynomial orders is compared to the reference solution given in [17], and they are shown in Table 2. Table 3 shows the distribution of normalised radial power calculated and the reference solution [17] for $5 \times 5 \; cm^2$ mesh size.

In Table 2. the $5 \times 5 \; cm^2$ node size with 964 nodes and 2.7 sec as computational time NEM gives the same reference value of k_{eff} obtained with 147968 nodes and 4800 sec in running time.

In Table 3. The highest error related to the power distribution in the core is 0.43, whereas the lowest value is 0.

The normalised radial scalar fluxes for both thermal and fast energy groups and the normalised radial power were represented in Fig. 4 and Fig. 5, respectively.

Table 2. IAEA-2D effective multiplication factor

Method	Polynomial Order	Node Size (cm)	Divisions	Number of Nodes	$CPU\ Time\ (s)$	k_{eff}	Error
FDM	-	272 x 272	-	147,968	4,800	1.02958	Reference
NEM	2	5 x 5	4 x 4	964	1.98	1.02932	0.02
NEM	4	20 x 20	1 x 1	69	0.04	1.02948	0.009
NEM	4	10 x 10	2 x 2	241	0.25	1.02960	0.001
NEM	4	5 x 5	4 x 4	964	2.71	1.02958	0.0

Table 3. Quarter core distribution of neutron power and k_{eff} the value is given by OpenNode for $5X5\ cm^2$ for 2D-IAEA test benchmark problem compared to those obtained by the FDM method

$k_{eff_{cal}}$	1.02958
$k_{eff_{ref}}$	1.02958
$Error$	0

0.755	0.735	0.692
0.757	0.737	0.695
0.26	0.27	0.43

0.934	0.950	0.975	0.934	0.950
0.935	0.951	0.976	0.935	0.951
0.10	0.10	0.10	0.10	0.10

0.935	1.036	1.070	0.906	0.685	0.935
0.934	1.035	1.070	0.906	0.685	0.934
0.10	0.09	0	0	0	0.10

0.610	1.069	1.179	0.967	0.470	0.610	1.069
0.609	1.068	1.178	0.966	0.471	0.609	1.068
0.16	0.09	0.08	0.10	0.21	0.16	0.09

1.210	1.314	1.345	1.192	0.967	1.210	1.314
1.208	1.312	1.343	1.191	0.966	1.208	1.312
0.16	0.15	0.14	0.08	0.10	0.16	0.15

1.453	1.479	1.469	1.345	1.179	1.453	1.479	1.469
1.450	1.477	1.467	1.343	1.178	1.450	1.477	1.467
0.20	0.13	0.13	0.14	0.08	0.20	0.13	0.13

1.309	1.435	1.479	1.315	1.069	1.309	1.435	1.479
1.308	1.432	1.477	1.313	1.068	1.308	1.432	1.477

0.07	0.20	0.13	0.15	0.09	0.07	0.20	0.13

P_{cal}	0.745	1.309	1.453	1.210	0.610	0.935	0.934	0.755
P_{ref}	0.744	1.306	1.451	1.208	0.610	0.934	0.935	0.757
$Error$	0.13	0.22	0.13	0.16	0	0.10	0.10	0.26

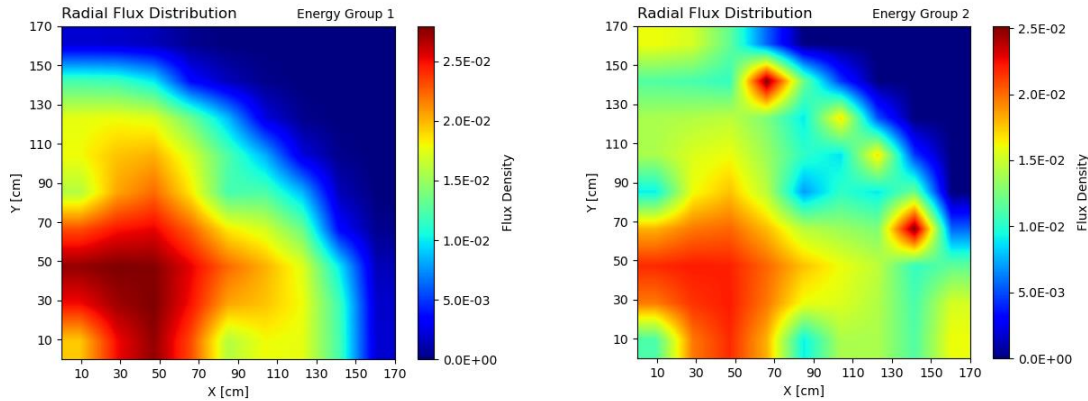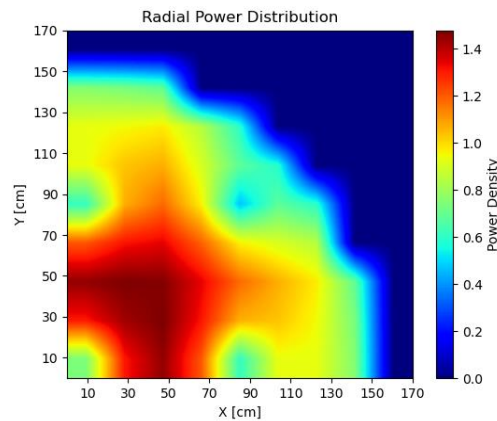Fig. 4. ¼ Radial flux distribution for the thermal and fast energy group

Fig. 5. ¼ Radial power distribution

CONCLUSIONS

The OpenNode nuclear reactor code has been developed to solve the multi-group steady-state neutron diffusion equation in multi-dimensions. OpenNode uses the second and fourth-order nodal expansion methods to expand the flux and second order to expand the transverse leakage. A GUI application has also been developed. A GUI application has also been developed to make the code easier to use for the user.

To test the computational accuracy in OpenNode, the IAEA-2D benchmark was applied as a test problem. The results of the NEM used in OpenNode showed the reasonable accuracy obtained compared to the FDM used in the VENTURE reference code. The good agreement between OpenNode and the reference was achieved when the mesh became fine, and thus the errors related to power and k_{eff} become very close to the reference values, except that

the nodal methods do not require extensive discretisation like the classical methods such as FDM to get close to the exact values

Keywords: Neutron diffusion equation, nuclear fission, nodal methods, flux, current, node, mesh, assembly, GUI.

REFERENCES

1. COSTE-DELCLAUX, M.; DIOP, C.; NICOLAS, A.; BONIN, B. *Neutronique. E-den, Une monographie de la Direction de l'énergie nucléaire*. CEA Saclay; Groupe Moniteur, June 2013

2. SHOBER, R.A.; SIMS, R.N.; HENRY, A.F. Two nodal methods for solving time-dependent group diffusion equations. *Nuclear Science and Engineering,* 1977, Vol. 64, No. 2, P. 582–592.

3. FINNEMANN, H. A consistent Nodal Method for the Analysis of Space-Time Effects in large LWR's. *Tech. rep,* 1975

4. FINNEMANN, H.; BENNEWITZ, F.; WAGNER, M.R. Interface current techniques for multidimensional reactor calculations. *Atomkernenergie,* 1977, Vol. 30, No.2, P. 123–128.

5. LAWERENCE, R.D. Progress in nodal methods for the solution of the neutron diffusion and transport equations. *Progress in Nuclear Energy*, 1986, Vol. 17, No. 3, P. 271–301.

6. VONDY, D.R.; FOWLER T.B.; CUNNINGHAM, G.W. VENTURE: A code block for solving multi-group neutronics problems applying the finite-difference diffusion-theory approximation to neutron transport. *Oak Ridge National Laboratory,* 1977.

7. FOWLER, T.B.; VONDY, D.R. Nuclear reactor core analysis code: CITATION. *Tech. rep*. Oak Ridge National Lab., Tenn, 1969.

8. IMRON, M. Development and verification of open reactor simulator ADPRES. *Annals of Nuclear Energy*, 2019, Vol. 133, P. 580–588.

9. LAHDOUR, M.; EL BARDOUNI, T.; EL HAJJAJI, O.; CHAKIR, E.; ZIANI, H.; AL ZAIN, J.; CHHAM, E.; EL BARBARI, M. OpenNTP: Implementation of the SN method in cartesian 2D geometry and the CP method in cylindrical and spherical 1D geometry. *Computer Physics Communications*, 2021, Vol. 261, P. 107812.

10. GUESSOUS, N. Méthodes nodales de discrétisation des équations de diffusion multigroupe. *These de doctorat, Université libre de Bruxelles,* 1993.

11. OKUMURA, K. MOSRA-Light; high speed three-dimensional nodal diffusion code for vector computers. Japanese. Oct. 1998.

12. OKA, Y. Nuclear reactor design. *Springer,* 2014.

13. SINGH, T.; MAZUMDAR, T.; PANDEY, P. NEMSQR: A 3-D multi group diffusion theory code based on nodal expansion method for square geometry. *Annals of Nuclear Energy,* 2014, Vol. 64, P. 230– 243.

14. PETERSON, P. F2PY: a tool for connecting Fortran and Python programs. *International Journal of Computational Science and Engineering,* 2009, *Vol.* 4, No. 4, P. 296–305

15. DENIS, P.; CUVELIER, T. Créer des applications graphiques en Python avec PyQt5. Editions D-BookeR, 2017.

16. Community, Blender online: Blender - a 3D modelling and rendering package: Blender Foundation. Sticht-ing. Blender Foundation, Amsterdam, 2018- Link to the internet <url:http://www.blender.org>.

17. Center, Argonne Code. Argonne Code Center: Benchmark problem book, report anl-7416 (suppl. 2). *Argonne National Laboratory*, Argonne, IL, June 1977.

18. MÜLLER, E.Z.; WEISS, Z.J. Benchmarking with the multigroup diffusion high-order response matrix method. *Annals of Nuclear Energy,* 1991, Vol. 18, No. 9, P. 535–544.

FULFILLMENT OF LOCAL THERMODYNAMIC EQUILIBRIUM IN ARGON ENVIRONMENT FOR CALIBRATION-FREE LIBS MEASUREMENT OF HYDROGEN ISOTOPES

J. Ristkok, I. Jõgi, P. Paris
Institute of Physics, University of Tartu
W. Ostwaldi 1, 50411 Tartu – Estonia
+372 5466 8219
jasper.ristkok@ut.ee

EXTENDED ABSTRACT

OVERVIEW

To counter the rising energy demand of humanity, a new energy source – fusion – is being researched. So far, for tokamak-type reactors, the record power gain (fusion power relative to input heating power) of 0.67 is held by JET. A new fusion reactor ITER is being built in France, with the first plasma scheduled in 2025. ITER tokamak is unique because it will have a tenfold return of energy, thus being the first fusion reactor to have positive net power. [1]

The fuel to be used in ITER will be a deuterium (D) and tritium (T) mixture. Safety regulations require observations of T retention in plasma-facing components since T is radioactive [2]. Therefore, it is necessary to develop diagnostically methods to measure fuel retention in walls of ITER. One such method suitable for use in ITER is laser-induced breakdown spectroscopy (LIBS).

The exact calibration of LIBS for ITER conditions is very difficult since it requires measuring a large variety of different samples with varying elemental compositions mimicking plasma exposure times and wall materials at different positions on the reactor wall. That is why calibration-free LIBS (CF-LIBS) is considered.

The application of CF-LIBS requires the fulfilment of certain conditions in the laser-induced plasma, and deviation from these conditions might lead to erroneous results. The aim of this work is to estimate the fulfilment of one such necessary condition for CF-LIBS: local thermodynamic equilibrium (LTE).

METHODS

LIBS apparatus (Fig. 1) uses a powerful laser pulse which is focused on a small spot on the investigated material. A small amount of the material is ablated and heated into a plasma plume by the laser beam. The plume emits light characteristics to the investigated material, and the emission spectrum of the plume is then used to determine the elemental composition of the material.

Experiments were carried out in an argon environment at 3, 100 and 760 Torr pressure. The used laser was Nd: YAG laser working on the second harmonic at 532 nm. The laser pulse

of 8 ns duration and 60 mJ energy was directed normally to the target. The pulse was focused onto a spot with a diameter of 0.4 mm. The investigated material was molybdenum (Mo) with hydrogen (H) impurities to simulate ITER-relevant materials with D and T. Spectra were recorded at delay times from 200 ns to 6 µs after the laser pulse and at different distances from the target depending on the plume expansion. The optical fibre collected light
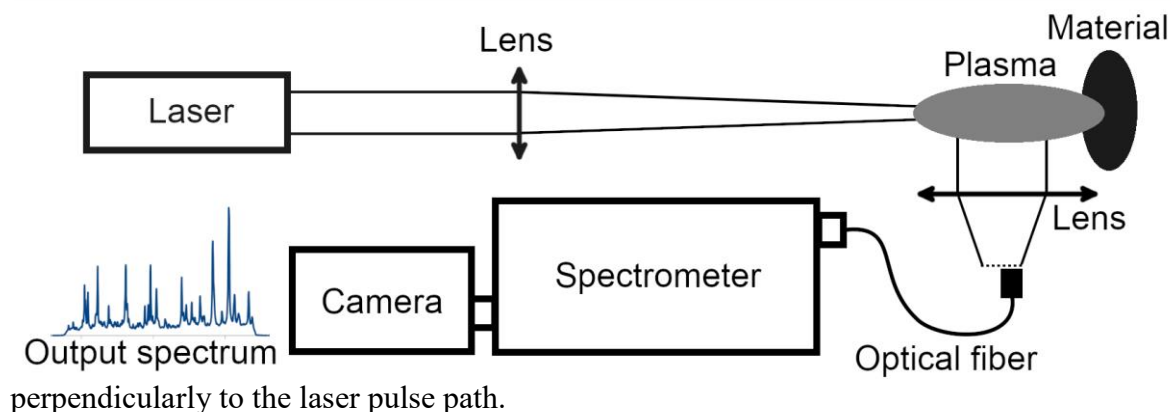

perpendicularly to the laser pulse path.

Fig. 1. The experimental setup of LIBS.

The spectra were recorded in the range of 647-667 nm. There were approximately 40 Mo lines which were fitted with Gaussian contours, and H_α line was fitted with Lorentzian contour. Plasma electron density was calculated from Stark broadening of H_α line and electron temperature with Mo lines from the Saha-Boltzmann plot.

RESULTS

The first criterion for the existence of LTE (Fig. 2) is that electron collisions dominate the energy exchange with the neutrals and ions. The lower limit of electron density for that criterion depends on specific elements and is dictated by the McWhirter criterion [3]. In these experiments, the order of magnitude for necessary electron density was 10^{-16} cm^{-3} for Mo and 10^{-17} cm^{-3} for H. Experiments showed that the McWhirter criterion was better fulfilled at higher gas pressures and smaller delay times and closer to the surface of the investigated material. The criterion wasn't fulfilled for H at any time or distance at 3 Torr and lower pressures.

The second criterion for the existence of LTE is that the relaxation time of plasma (excitation and ionisation equilibria) must be 10 times shorter than the variation time of electron density and temperature [3]. The relaxation time for Mo is in order of 10 ns, but for H, in order of 100 µs. The condition was fulfilled at all investigated conditions for Mo but never for H. Moreover, the relaxation time determines the timespan which is needed for plasma to reach LTE. Therefore, it is impossible to reach LTE at the delay times relevant to LIBS (up to 10 µs). Temperature satisfied this criterion better than electron density.

The third criterion for the existence of LTE is that during the plasma relaxation time, the diffusion lengths of ions and atoms must be 10 times shorter than the various lengths of electron density and temperature [3]. During the previously specified relaxation times, the diffusion length is in order of 1 µm for Mo but 100 µm for H. The order of magnitude of plume dimensions was 1 mm. The criterion was best fulfilled at lower pressures and closer to the investigated material. The variable length of temperature satisfied this condition better than the variable length of electron density. Both variation time and length criteria were fulfilled at qualitatively similar delay times and distances from the target.
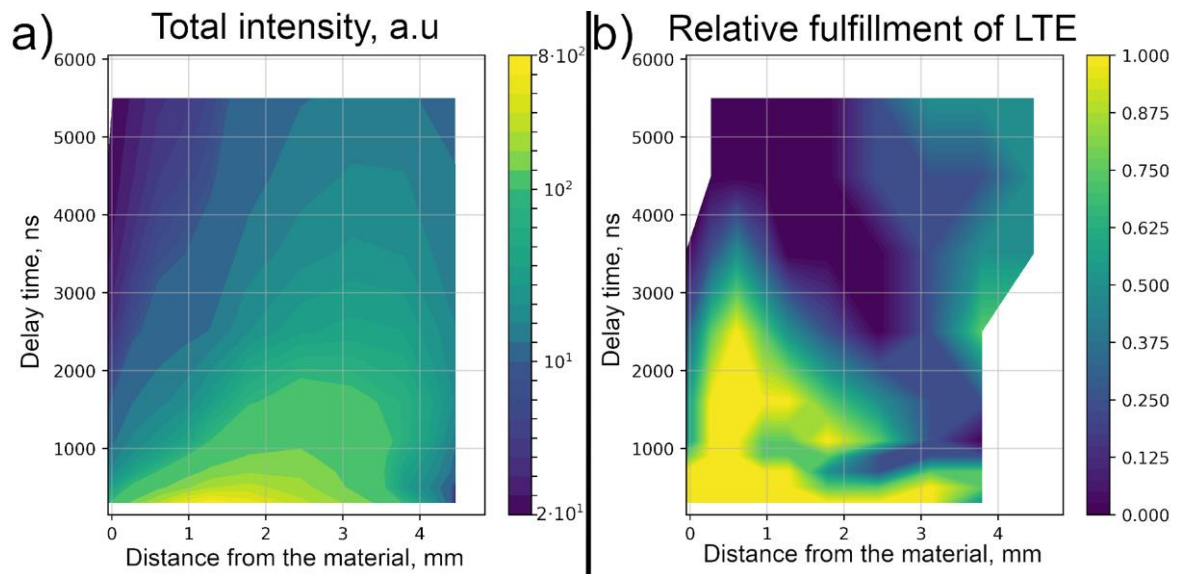
Fig. 2. a) Logarithmic heat map of the total intensity of the plasma plume at 100 Torr gas pressure. This can be used to estimate the location and size of the plasma plume. b) Qualitative heat map for relative fulfilment of 3 necessary conditions for LTE at 100 Torr gas pressure. Value of 1 means best-fulfilled LTE (not necessarily fulfilled LTE), and 0 means least fulfilled LTE.

CONCLUSIONS

Occasionally CF-LIBS might determine erroneous hydrogen isotope concentrations. The results show that one source of such errors is the deviation from LTE. Further research is ongoing to find the optimal experimental setup for CF-LIBS in ITER conditions and to characterise the relation between the accuracy of CF-LIBS and the deviation from LTE.

Keywords: Laser Induced Breakdown Spectroscopy; hydrogen isotope determination; ITER relevant coatings; local thermodynamic equilibrium

REFERENCES

1. *ITER Organization*. What is ITER? [Referred on the 20th of January in 2022 y.]. Link to the internet <https://www.iter.org/proj/inafewlines>.

2. DE TEMMERMAN, G.; BALDWIN, M.J.; ANTHOINE, D.; HEINOLA, K.; JAN, A.; JEPU, I.; LIKONEN, J.; LUNGU, C. P.; POROSNICU, C.; PITTS, R.A. Efficiency of thermal outgassing for tritium retention measurement and removal in ITER. *Nuclear Materials and Energy*, 2017, Vol. 12, P. 267-272.

3. CRISTOFORETTI, G.; DE GIACOMO, A.; DELL'AGLIO, M.; LEGNAIOLI, S.; TOGNONI, E.; PALLESCHI, V.; OMENETTO, N. Local Thermodynamic Equilibrium in Laser-Induced Breakdown Spectroscopy: Beyond the McWhirter criterion, *Spectrochimica Acta Part B: Atomic Spectroscopy*, 2010, Vol. 65, No. 1, P. 86-95.

EXAMINATION OF RESONANCE SELF-SHIELDING PROCESSING FOR RBMK FUEL ASSEMBLY USING SCALE

S. Shirzadi
Lithuanian Energy Institute (LEI)
Breslaujos g. 3, LT-44403 Kaunas– Lithuania
+37062503177
Sahar.Shirzadi@lei.lt

A. Slavickas
Lithuanian Energy Institute (LEI)
Breslaujos g. 3, LT-44403 Kaunas– Lithuania
+37037401810
Andrius.Slavickas@lei.lt

ABSTRACT

Nuclear data libraries are an essential part of the neutron transport calculations as they provide the probabilities for neutron and nuclides interactions. The KENO module of the SCALE code was applied in this study as the tool for neutron transport calculations using both continuous energy and multi-group cross-section data libraries. The presence of resonance self-shielding effect, both energy and spatial, plays an important role in neutron transport calculations. The rigorous treatment of the resonance self-shielding effect requires the calculation at extremely fine mesh points, which is achieved by applying the continuous energy library. The multi-group data library is processed from the point-wise data of the continuous energy library by collapsing cross-sections into 252 group's structure. The approximations and assumptions made using a multi-group data library can cause an inaccurate result in neutron transport calculations for heterogeneous systems such as the RBMK-1500 fuel assembly. Thus, the multi-group library calculation results were compared with the continuous energy library calculation results for benchmarking purposes. Found discrepancies between calculations are demonstrated and explained by comparing separate nuclide reaction rates.

Keywords: Resonance self-shielding, continuous energy, multi-group, RBMK, SCALE

INTRODUCTION

The neutrons distribution in terms of energy, time and space in a nuclear reactor determines the behaviour of a nuclear reactor [1]. The evaluation of a nuclear reactor in terms of neutron spectrum requires solving the neutron transport equation or neutron diffusion equation considering the absorption rate of neutrons in a medium [2]. It is worth mentioning that the more accurate nuclear data results in lower uncertainties of neutron transport calculation.

Continuous energy (CE) and multi-group (MG) energy are two types of neutron cross-section libraries that can be used for deriving information such as neutron spectrum, eigenvalue, and reaction rates [3]. The neutron transport calculation using CE cross-section requires large computer resources for processing the calculations as it considers a large number of energy points [3]. On the other hand, MG cross-sections using average energy upon energy points require lower computer memory while it contains lower accuracy compared with CE cross-sections. Therefore, high-fidelity MG cross-sections are required for neutron transport calculations to do the analysis in a shorter time with a smaller storage space of computers.

The neutron transport calculation using MG cross-section can cause errors compared with CEs cross-section calculation, especially for heterogeneous systems. To explain the origin of these errors, it is worth mentioning that the nuclear reaction rate plays an important role as the basic parameter for neutronic analysis. This parameter provides information about the number of generated and absorbed neutrons in all directions in a unit volume per second. The reaction rates in any medium are directly proportional to the flux in those medium and microscopic cross-sections. However, the determination of neutron flux and these cross-sections for a group of energy points is the main problem of neutron transport calculation. This difficulty comes from the interaction of the neutron with the different types of materials in a fuel assembly.

Different materials absorb neutrons and, in such a way, shield each other from the neutron flux. Even the same material, due to high absorption cross-sections and neutron absorptions in outer layers, can self-shield its inner layers of neutron flux. Such depression of flux is especially dramatic around resonance peaks of microscopic cross-sections. This is the so-called resonance self-shielding effect that is very important for neutron spectrum determination. In the case of CE data library is applied, the resonance self-shield effect is computed directly by applying fine mesh cross-sections with values for each resonance. However, the MG data library contains cross-sections with values averaged over separate resonances. In such a case, the effective cross-sections must be prepared for neutron transport simulations considering the neutron flux depressions (neutron spectrum) due to the resonance self-shielding effect [4]. However, the neutron spectrum itself depends on the effective cross-sections.

CE nuclear data containing a huge number of energy points for each reaction per each nuclide provides the highest fidelity library, which is known as reference nuclear data [5]. In contrast, the use of the MG cross-sections library with fewer energy points requires some approximations and assumptions to simplify the calculations and to solve the neutron transport equation with multi-group energy ranges. The approximations are needed to estimate the neutron spectrum [6]. A uniform distribution of neutrons in the fuel assembly is assumed [6]. The dancoff factor (DF) coefficient is introduced in the simulation to modify the resonance self-shielding effect on neutron transport calculation using MG cross-sections. The user can choose to use either standard DF (DFs) or user-defined (DFu) [6]. DFs are

estimated assuming the simplified fuel pin in the infinite array model. Meanwhile, DFu is estimated using the MCDancoff module of SCALE code considering the real problem geometry. Since the RBMK-1500 fuel assembly is very heterogeneous, the application of DFu in the neutron transport simulation using MG data libraries provides more accurate results compared with DFs [7].

This paper discusses the neutron transport calculations using both CE and MG cross-section data libraries for RBMK-1500 fuel assembly. The discrepancies between calculations are demonstrated and explained by comparing separate nuclide reaction rates.

MODELLING PARAMETERS OF RBMK-1500 FUEL ASSEMBLY

The neutron multiplication factor (k-effective) is a scalar quantity that is obtained from the solution of the neutron diffusion equation. This quantity describes the neutron population in a system with three different values of less, higher than 1 or equal to 1, representing, accordingly, a subcritical, supercritical, or critical system [8]. The k-effective was calculated using SCALE 6.2.3 code (KENO module) using both CE and MG cross-sections libraries for RBMK-1500 fuel assembly assuming normal operating conditions.

The RBMK-1500 fuel assembly contains 18 fuel rods in two rings in which 6 and 12 fuel rods are placed in the first (internal) and second (outer) rings, accordingly (Fig. 1). The fuel pellet has an outer diameter of 1.152 cm. The outer diameter of the cladding and its thicknesses are 1.36 cm and 0.9 cm, respectively. The diameters of the gap and the central holes are 1.17 cm and 1.2 cm, while the inner and outer diameters of the fuel channel are 8 cm and 8.8 cm, accordingly. The fuel assembly is placed in a square block of graphite, which size is 25*25 cm. The distance between the fuel assembly centre and the ring of inner fuel pins is 1.6 cm, while the distance between inner and outer fuel rods is 1.608 cm. The centre-to-centre distance of the fuel rods in the fuel pin rings is 1.59 cm.

The materials of RBMK-1500 fuel assembly (FA) were categorised in 11 mixtures as below [9]:
-   Mixtures 1 and 2 fuel pellets in inner and outer rings.
-   Mixtures 3 and 4, gas material in the gap between fuel pellet and cladding.
-   Mixtures 5 and 6, cladding material.
-   Mixtures 7, gas material inside the central hole.
-   Mixtures 8 and 9, coolant material inside inner and outer rings of fuel pins.
-   Mixture 10, graphite block.
-   Mixture 11, FA structure material.

The resonance self-shielding processing in the case of MG cross-section use is performed considering the triangular pitch configuration of fuel pins (two outer and one inner pin), which has infinite repetition. Thus, the resonance processing is performed only for mixtures 1-6, and 8-9 in such case as the materials of central whole (CH) gas, FA structures and graphite block isn't included in this triangular pitch. The cross-sections for these materials are applied in the neutron transport simulations considering the infinite homogenous conditions.

The considered assumptions for calculation of neutron multiplication factor for RBMK-1500 fuel assembly are as follows [9]:
-   Mixtures 1 and 2: Uranium dioxide, U-234 (0.021%), U-235 (2%), U-236 (0.0018%), U-238 (97.9772%), temperature – 1000 K, density -9.596g/cc.

- Mixtures 3 and 4: He, temperature -1000 K.
- Mixture 5 and 6: Zr (98.9264%), Nb (1%), Hf-178 (0.04%), Fe (0.018%), Ni (0.011%), Al (0.0046%), temperature - 575 K, density- 6.55 g/cc.
- Mixture 7: He, temperature -575 K.
- Mixture 8 and 9: H_2O, temperature – 557 K, density – 0.5 g/cm^3.
- Mixture 10: C- graphite, temperature 750 K, density 1.7051- g/cc.
- Mixture 11: Zr (97.4264%), Nb (2.5%), Hf-178 (0.04%), Fe (0.018%), Ni (0.011%), Al (0.0046%), temperature – 557 K, density – 6.55 g/cc.
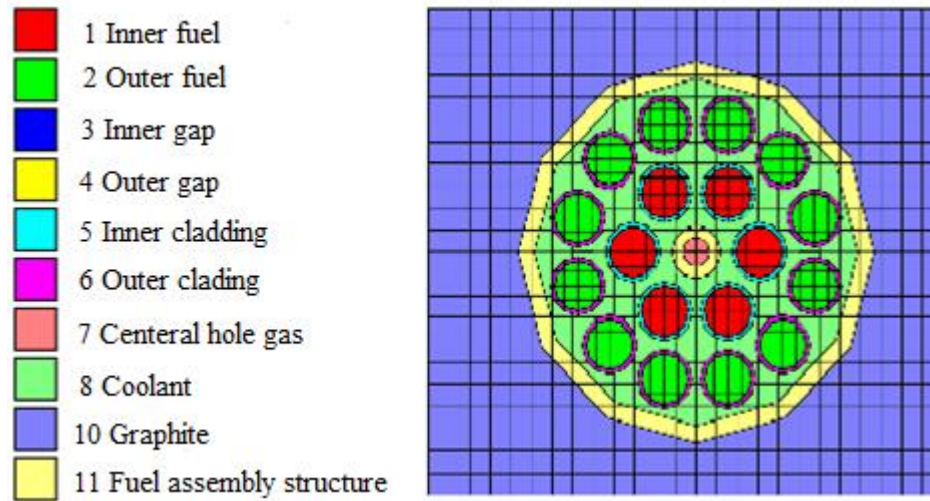

Fig. 1. Schematic illustration of RBMK-1500 fuel assembly.

The neutron multiplication factor and reaction rates for both CE and MG cross sections libraries simulations were estimated considering 10000 generations and 10000 neutrons per generation.

The deviation of reactivity between CE and MG calculations (equation 1) was decomposed to separate reactivity differences for separate geometry regions and separate isotopes using absorption and neutron production reaction rates (equation 2). Equations 1 and 2 are derived from the neutron multiplication factor per generation ($k_{eff} \frac{\sum_i P_i}{\sum_i A_i}$) and reactivity definition ($\rho = 1 - 1/k_{eff}$) as below:

$$\Delta \rho = \rho_{uDF} - \rho_{CE} = \frac{k_{inf.uDF} - k_{inf.CE}}{k_{inf.CE} * k_{inf.uDF}} * 10^5. \tag{1}$$

$$\Delta \rho_i = \sum_i \quad \Delta \rho_i = \Delta \sum_i \quad \left(1 - \frac{1}{k_{inf}}\right) = \sum_i \quad \frac{A_{i.uDF} \sum_i P_{i,CE} - A_{i,CE} \sum_i P_{i,uDF}}{\sum_i P_{i,CE} * \sum_i P_{i,uDF}}. \tag{2}$$

Where k, ρ, Ai, and Pi, are ascribed to neutron multiplication factor, reactivity, neutron absorption and production rate in different geometry regions or for individual nuclides, respectively. The index of i refers to the reaction rate.

RESULTS

Neutron transport simulations can be performed using CE and MG cross-section libraries. However, applying the MG cross-sections library in neutron transport calculations for the RBMK-1500 case represents inaccurate results in comparison with the CE cross-sections library as reference nuclear data. In this section, the origin of the resulted discrepancies in

neutron multiplication factor calculation using both MG and CE cross-section libraries for RBMK-1500 fuel assembly using SCALE code is discussed.

The reactivity is a scalar quantity, which is used to describe the deviation of k-eff in more convenient units. The positive reactivity difference points out the increase of the k-eff value, while the negative – the decrease. In our study, the positive reactivity difference means the overestimation of the k-eff value in the DFu case in comparison with the reference CE case, while the negative difference – is the underestimation of the k-eff value.

The total reactivity difference and differences for separate regions of RBMK-1500 fuel assembly are seen in Fig. 2. The total reactivity difference is 270 pcm in which the fuel assembly structures (both central hole and fuel assembly channel) (156 pcm), and outer fuel (134 pcm) regions have the highest contribution to the total discrepancy.

The interpretation of reactivity differences is more complicated as it is related to deviations of both fractional absorptions and k-eff values. The interpretation of reactivity differences for separate geometry regions is following: if fractional absorption for a geometry region changed relatively more than the k-eff value, then this absorption change is a contributing factor to the change of neutron multiplication factor. The fractional absorption increases show that more neutrons are absorbed in that geometry region, thus it contributes to the negative reactivity difference if the neutron multiplication factor increases or decreases in a relatively lower ratio. And vice versa, the fractional absorption decrease shows that fewer neutrons are absorbed in that geometry region, thus it contributes to the positive reactivity difference if the neutron multiplication factor decreases or increases in a relatively lower ratio.

The fractional absorption for fuel assembly structures decreases by 7.6% from the value of 0.02757 for the CE case to the value of 0.025612 for the uDF case. Fewer neutrons are parasitically absorbed in non-fissile regions of the fuel assembly and can participate in fission reactions. Thus, this change influences the increase of k-eff, and the positive reactivity difference is estimated for this region.

The change of the fractional absorption for outer fuel pins isn't so significant: it increases by 0.06% from the value of 0.615838 for the CE case to the value of 0.616236 for the uDF case. As this increase is still lower than the increase of k-eff, it produces a positive reactivity difference.
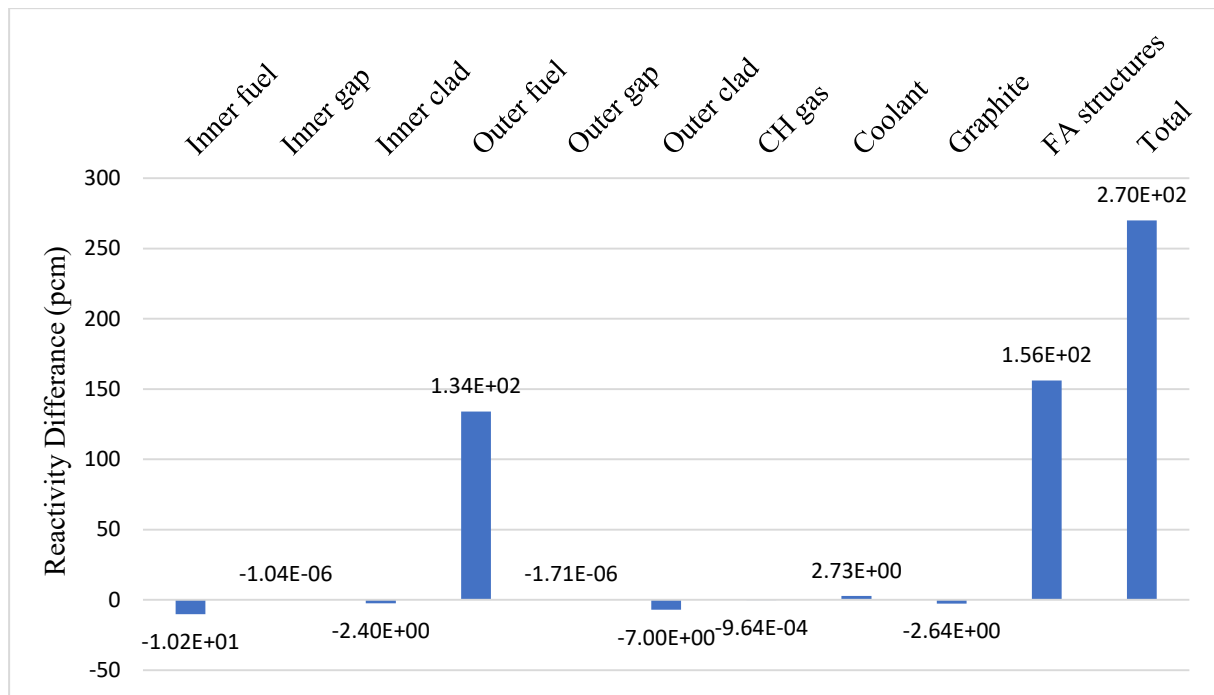
Fig.2. Reactivity differences for FA geometry regions

Fig. 3 shows the reactivity difference in each energy group and the summing of reactivity differences beginning from the lowest energy group and continuing towards the highest energy group. In the epithermal range of neutron spectrum energy, some fluctuations are seen. The first group of fluctuations sums up to zero, while the reactivity differences in the second group of fluctuations sum up to 22 pcm. The sharped increase of reactivity differences appears in the fast energy range of the neutron spectrum.

Fig. 3. The reactivity differences for energy groups

The reactivity differences for outer fuel and fuel assembly structure regions in each group of energy and the summation of it are presented in Fig. 4. The reactivity differences are positive for both regions. The patterns of the change of reactivity difference for the fuel assembly structur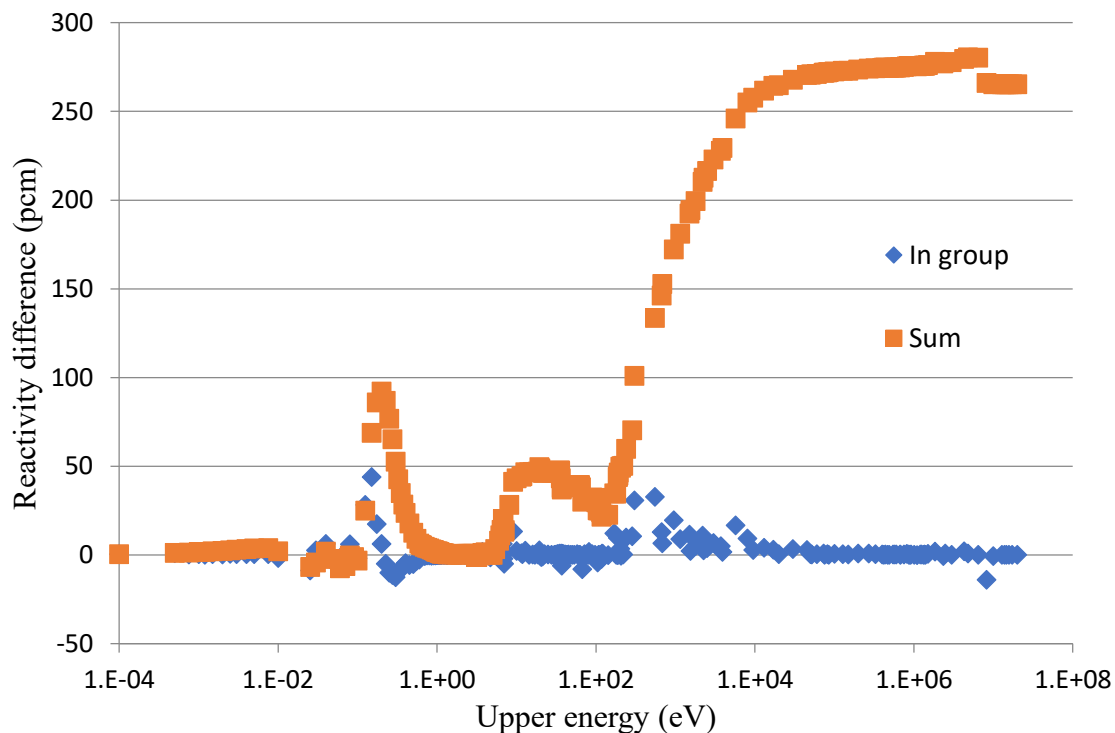e and outer fuel regions are similar to the total reactivity difference (Fig. 4). Three groups of fluctuations are seen in energy ranges of 0.01 eV -1 eV, 5 eV – 143 eV and > 143 eV. The last one is the most important energy region as it contributes a significant part of the total positive reactivity difference.
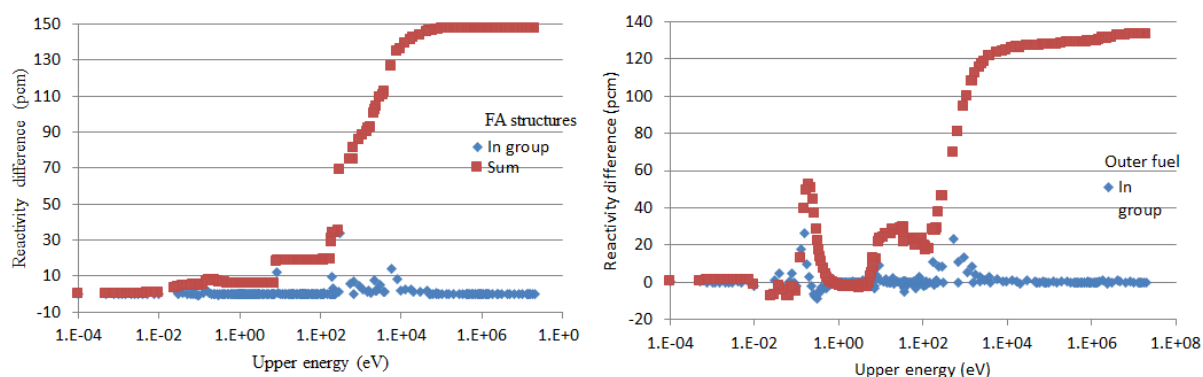
Fig. 4. Reactivity differences over energy for outer fuel region (at the left side) and fuel assembly structure (at the right side)

Fig. 5 illustrates the reactivity differences of fuel assembly structures region that is mainly influenced by the reactivity changes of Zr-91 (70.2 pcm), Nb-93 (22 pcm), Zr-92 (18.5 pcm), Hf-178 (14 pcm), Zr-90 (13 pcm), Zr-96 (10 pcm) and Zr-94 (8 pcm) nuclides. The highest reactivity difference in the fuel assembly structures appears for the isotope of Zirconium (Zr-91) at 70.2 pcm. The reaction rate of Zr-91 is discussed in Fig. 6 to understand the origin of the highest contribution of Zr- 91 in reactivity difference in the fuel assembly structure.

Fig. 5. Reactivity differences for separate nuclides in FA structures regions

According to the given results in Fig. 6, the main contributor to absorption reaction rate change is the change of cross-sections. These changes in cross-sections are mostly seen in the epithermal region (resolved resonance range), where the resonance self-shielding effect

is a remarkable factor in the generation of the discrepancies. It happens because the MG cross-sections of Zr-91 aren't included in the reson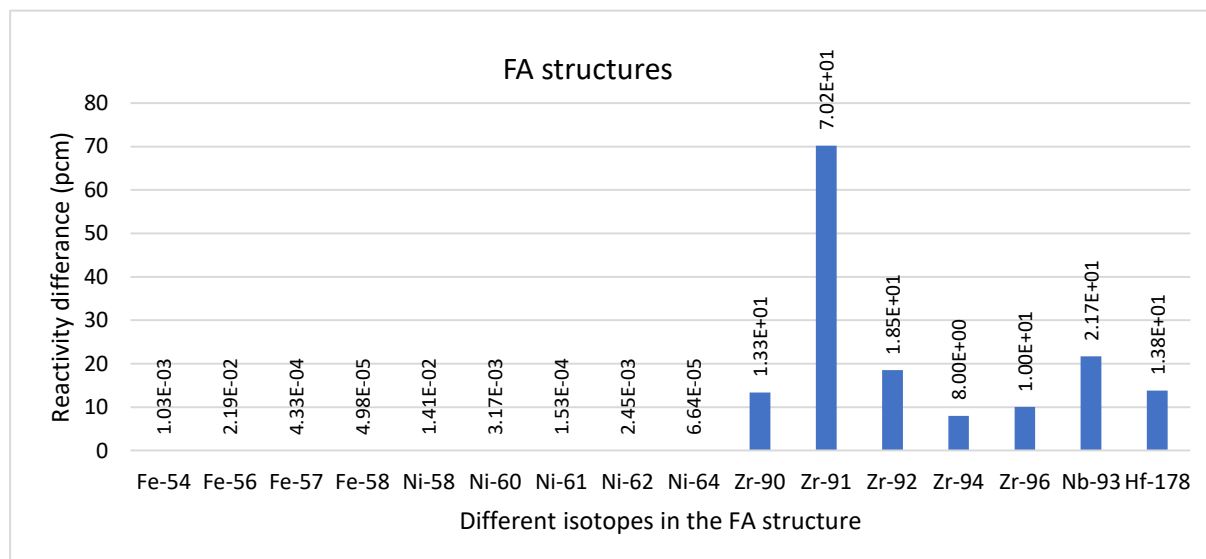ance self-shielding processing as the mixture 10 material is outside the triangular pitch described in the methodology section. The mixture 10 is assumed as an infinite homogenous material with a uniform distribution of neutrons in such a case. Thus, the cross-sections aren't processed and applied directly in simulations. The same explanation is applicable for other nuclides in mixture 10.
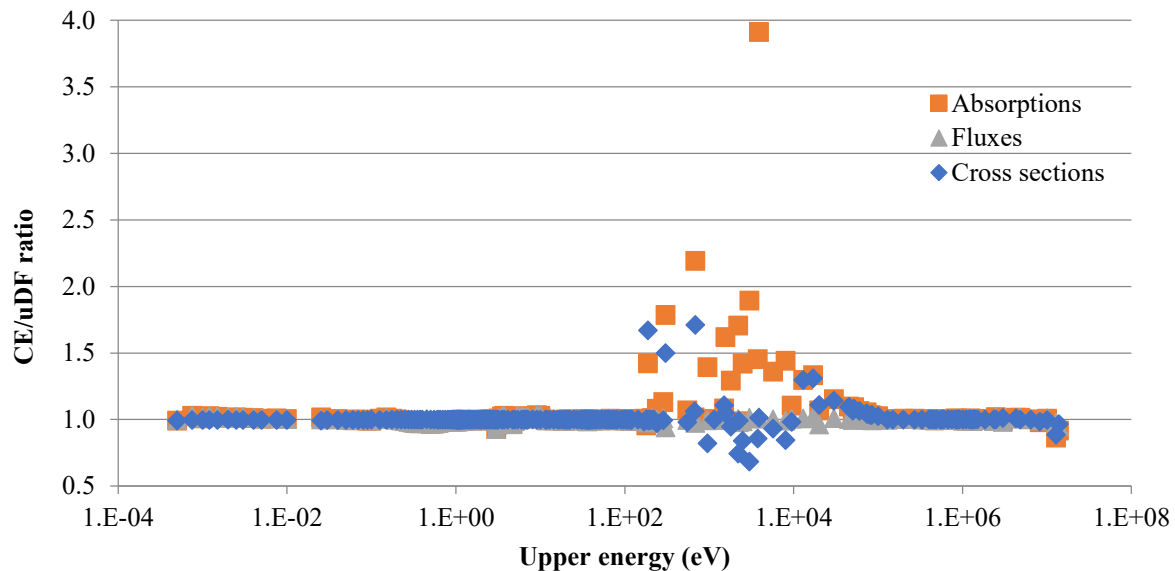
Fig. 6. Zr-91 (FA structures) ratios

CONCLUSION

In this study, the reactivity difference between neutron transport simulation cases with the application of CE and MG cross-sections for RBMK-1500 fuel assembly is discussed. The total estimated reactivity difference resulted at 270 pcm. The regions of the fuel assembly structure and the outer fuel showed the highest contribution of 156 and 134 pcm, respectively. In the region of FA structures, the isotope of Zr-91 showed the highest contribution to the positive reactivity. It is concluded that the reactivity difference for Zr-91 and fuel assembly structures in total appears due to the missed involvement of this mixture in the resonance self-shielding processing.

REFERENCES

1. LAMARSH, John R. Introduction to Nuclear Reactor Theory. 1966, 585 p. ISBN 978-0-89448-040-9.

2. JACQUES, P. Ligou. Elements of Nuclear Engineering. 1986, 525 p. ISBN 3-7186-0363-2.

3. HAMILTONA, S.; EVANSA, T. Continuous-Energy Monte Carlo Neutron Transport on GPUs in the Shift Code. *Annals of Nuclear Energy*, 2019, Vol.128, No. 1492181, P. 236-247.

4. GOLDSTEIN, R.; COHEN, E. Theory of Resonance Absorption of Neutrons. *Nuclear Science and Engineering*, 1962, Vol. 13, No. 2, P. 132-140.

5. KANG SEOG, K.; WILLIAMS, M. L.; WIARDA, D.; CLARNO, K. T. Development of the Multigroup Cross Section Library for the CASL Neutronics Simulator MPACT: Method and Procedure. *Annals of Nuclear Energy*, 2019, Vol. 133, No. 1543238, P. 46-58.

6. SUGIMURA, N.; YAMAMOTO, A. Evaluation of Dancoff Factors in Complicated Geometry Using the Method of Characteristics. *Nuclear Science and Technology*, 2006, Vol. 43, No. 9715547, P. 1182-1187.

7. SLAVICKAS, A.; PABARČIUS, R.; TONKŪNAS, A.S.; RIMKEVIČIUS, S. Neutron Transport Simulations of RBMK Fuel Assembly Using Multigroup and Continuous Energy Data Libraries within the SCALE Code. *Science and Technology of Nuclear Installations*, 2021, Vol. 2021, No. 6673489, p. 1-11.

8. LEWIS, Elmer E. *Fundamentals of Nuclear Reactor Physics*. 2008, P. 287. ISBN: 978-0-12-370631-7.

9. ALMENAS, K.; KALIATKA, A.; USPURAS, E. *Ignalina RBMK-1500*. 1994, P. 132. ISBN: 9986-475-02-3.

NUCLEAR ANALYSIS OF HIGH-POWER LIEBE MOLTEN TARGET AT CERN FOR THE PRODUCTION OF RADIOISOTOPES

B. Togobickij, G. Stankūnas, M. Povilaitis, A. Slavickas
Lithuanian Energy Institute
Breslaujos g. 3, LT-44403 Kaunas – Lithuania
+370 37 401 920
benjaminas.togobickij@lei.lt

EXTENDED ABSTRACT

OVERVIEW

To increase the primary beam intensity in the next generation of ion beam installations, the production of targets capable of dissipating high beam power, especially for molten targets, is a major challenge. In that context, a direct molten loop concept was proposed for short-lived isotopes by EURISOL. To validate this concept, a target prototype was designed and assembled, called LIEBE (Liquid Eutectic lead Bismuth for EURISOL), in the ISOLDE operation environment [1].

LIEBE is a prototype liquid metal target aimed at solving issues of accommodating a high-power ion beam and ensuring adequate extraction of short-lived radioisotopes. LIEBE will use a lead-bismuth eutectic circulating in a 200 °C – 600 °C temperature loop. The eutectic will be driven by an electromagnetic pump to an irradiation chamber, where it will be subjected to the high-power proton beam. Irradiated eutectic will then fall through a grid, which will fragment it into 0.4 mm diameter droplets, into the diffusion chamber [2]. The diffusion chamber is designed to accommodate the fast extraction of radioisotopes from the falling metal droplets. Excess heat deposited by the proton beam will be removed by the water-cooled heat exchanger.

METHODS

The MCNP code was used for the numerical studies required for the nuclear analysis of the LIEBE target. Using the MCNP code, the activity of radioactive sources, the intensity and spatial distribution of the emitted radiation, the activation of irradiated materials, the heat of fission, and other parameters characteristic of the nuclear analysis can be estimated. MCNP allows transport simulations to be performed for all particle types over the entire energy range. One of the many applications of the MCNP code is in the production and destruction of isotopes by accelerators. The usefulness and accuracy of the MCNP code in this area have been already demonstrated [3, 4].

The geometry model of the LIEBE target was available in CAD file format, which is not suitable for direct use as MCNP data input. The CAD geometry model of the LIEBE needed to be converted. The conversion was done using the SALOME software McCAD [5] module, which is a Monte Carlo CAD-based tool used to convert CAD drawings to the MCNP, TRIPOLI, and Geant4 codes geometries. Nevertheless, before the conversion, the CAD

model had to be manually decomposed (see Fig. 1), and since the CAD model of the target was complex and detailed, many elements of the model needed to be manually modified. These modifications were primarily spline and torus surface approximations with cylinders and planes (see Fig. 2).
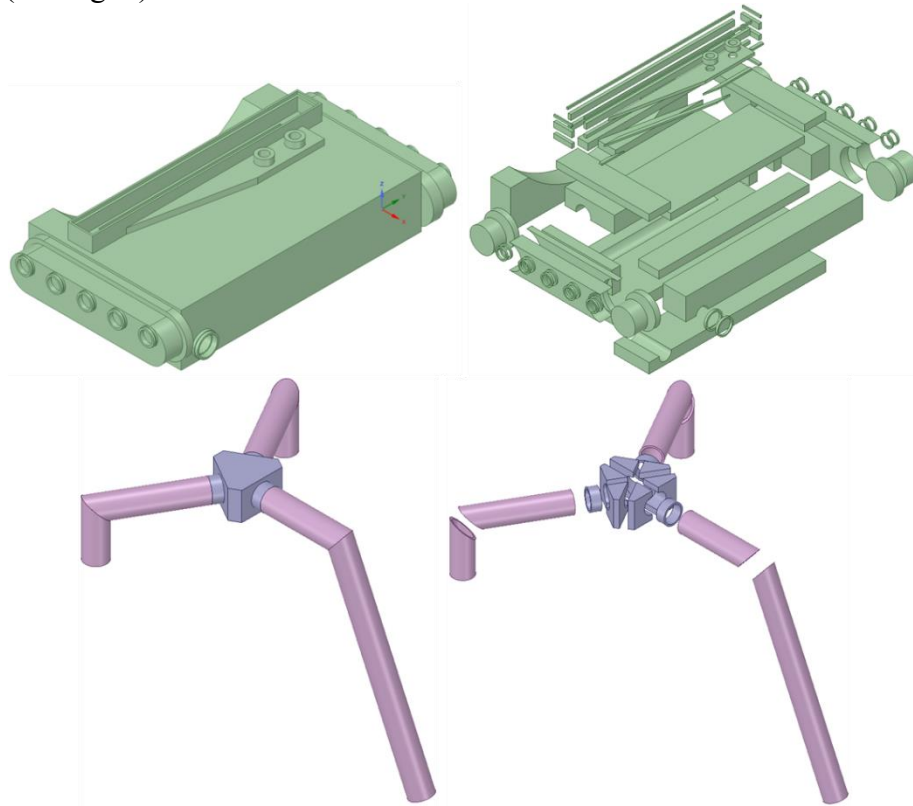
Fig. 1. Examples of component decompositions.
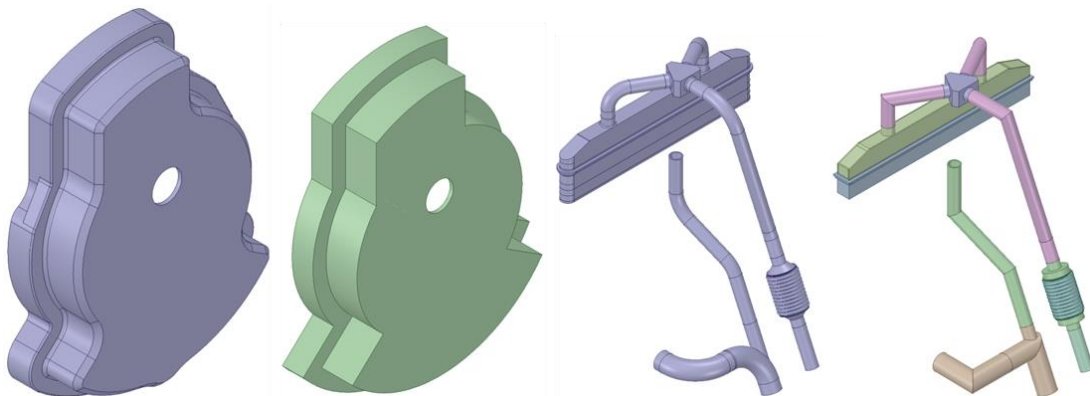
Fig. 2. Examples of component approximations.

RESULTS

To calculate the distribution of neutrons and gamma-rays in and around the target, a proton beam falling on the LIEBE target was modelled using the MCNP code to simulate the proton beam interaction with the target. FENDL-3.1 cross-section data library was used. The proton flux distribution after the impact and resulting nuclear reactions were modelled.

Cross-sections of ^{208}Pb (p, n) and ^{208}Pb (p, g) reactions reach 10 barns, therefore, neutrons and gammas of a wide energy spectrum are generated. To evaluate radiological processes in

the target and surrounding environment, it is necessary to model the resulting distributions of neutron and gamma radiation.

Obtained neutron and gamma distribution in the LIEBE target and its surroundings are presented in Fig. 3 and Fig. 4. The study revealed that, while the most intense neutron and gamma fluxes are localised to the proton beam and target interaction location, most of the device is transparent to them and high fluxes are present in the nearby environment as well, in part due to fraction of proton beam reaching locations under the target (see Fig. 5) in case of considered beamline radius $r = 1.0$ cm. However, to qualitatively estimate resulting doses further, more elaborate simulations are required, which are planned for the nearest future.

Fig. 3. Neutron flux distribution in the LIEBE target, [#/cm^2/s].

Fig. 4. Gamma flux distribution in the LIEBE target, [#/cm^2/s].

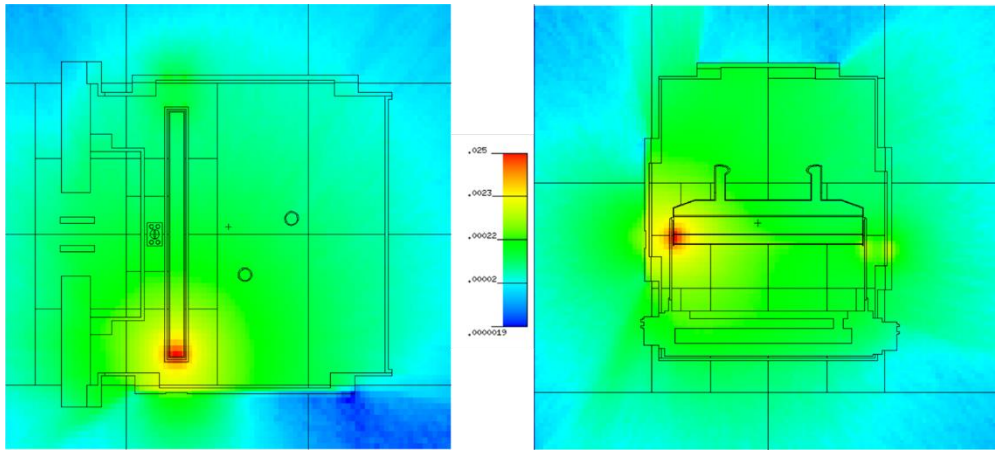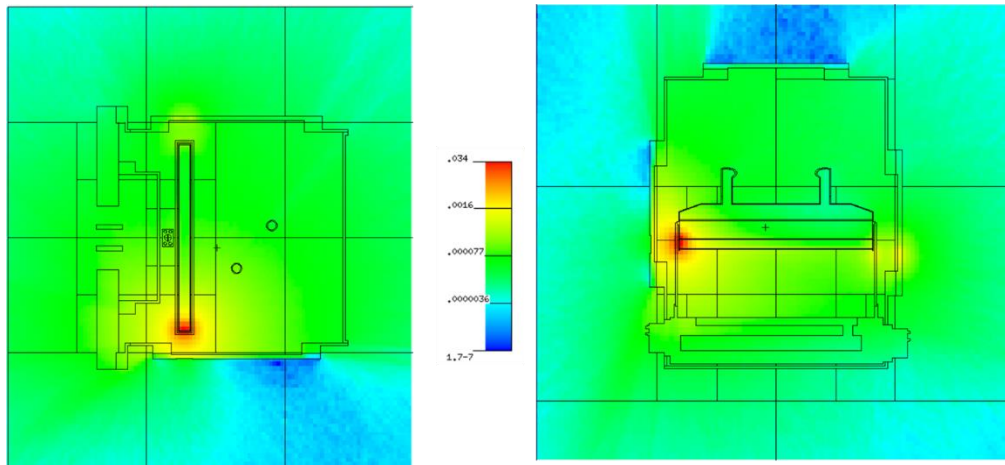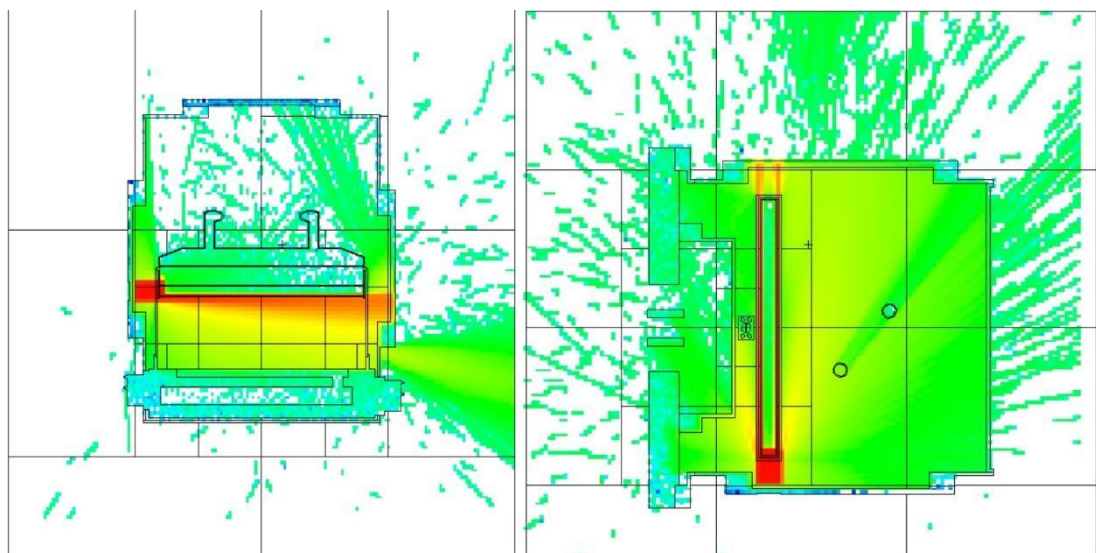Fig. 5. Monoenergetic (70 MeV) proton beam distribution in the LIEBE
target, [#/cm^2/s].

CONCLUSIONS

Preliminary results revealed that the developed model is suitable for further and more detailed simulations, which would enable to quantitatively evaluate possible doses and interactions on the microscopic scale. In addition, from the obtained neutron and gamma flux maps, the proton beam window should be revised since part of the beam penetrates under the LIEBE target construction. This leads to more widely distributed gamma and neutron fluxes. Therefore, from a radiation safety perspective, certain biological safety measures will be evaluated in the future under this study.

Keywords: Monte Carlo, MCNP, LIEBE, proton beam

REFERENCES

1. PAMIES, B.F.; STORA, T.; BARBERO, E.; BAROZIER, V.; BERNARDES, A.P.; CATHERALL, R.; CONDE FERNANDEZ, B.; CREPIEUX, B.; DELONCA, M.; DIERCKX, M.; GOLDSTEINS, L.; GRENARD, J.L.; GRENIER-BOLEY, E.; HOUNGBO, D.; KRAVALIS, K.; LILI, G.; POPESCU, L.; PREVER-LOIRI, L.; RAMOS, J.P.; RIEGERT, J.M.; ROTHE, S.; VEIGA ALMAGRO, C.; VIEITEZ, A. The LIEBE high-power target: Offline commissioning results and prospects for the production of ^{100}Sn ISOL beams at HIE-ISOLDE. *Nuclear Instruments and Methods in Physics Research Section B: Beam Interactions with Materials and Atom*s, 2020, Vol. 463, P. 128-133.

2. HOUNGBO, D.; BERNARDES, A.P.; DAVID, J.C.; DELONCA, M.; KRAVALIS, K.; LAHIRI, S.; LOSITO, R.; MAGLIONI, C.; MARCHIX, A.; MENDONCA, T.M.; POPESCU, L.; SCHUMANN, D.; SCHUURMANS, P.; STORA, T.; VOLLAIRE, J.; VIERENDEELS, J. Development of a liquid Pb-Bi target for high-power ISOL facilities. *Nuclear Instruments and Methods in Physics Research Section B: Beam Interactions with Materials and Atom*s, 2016, Vol. 376, P. 57-59.

3. FASSBENDER, M.; ARZUMANOV, A.; JAMRISKA, D.; LYSSUKHIN, S.N.; TRELLUE, H.; WATERS, L.S. Proton beam simulation with MCNPX: Gallium metal

activation estimates below 30MeV relevant to the bulk production of ^{68}Ge and ^{65}Zn. *Nuclear Instruments and Methods in Physics Research Section B: Beam Interactions with Materials and Atoms*, 2007, Vol. 261, N. 1–2, P. 742-746.

4. SADEGHI, M.; JOKAR, N.; KAKAVAND, T.; GHAFOORI FARD, H.; TENREIRO, C. Prediction of ^{67}Ga production using the Monte Carlo code MCNPX. *Applied Radiation and Isotopes*, 2013, Vol. 77, P. 14-17.

5. LU, L.; FISCHER, U.; PERESLAVTSEV, P. Improved algorithms and advanced features of the CAD to MC conversion tool McCad. *Fusion Engineering and Design*, 2014, Vol. 89, No. 9–10, P. 1885-1888.

I.8.   Cross-cutting energy issues

SETTING AND SOLVING THE TASK OF VIBROACOUSTIC DIAGNOSIS OF A HYDROPOWER UNIT

D. Dzadzamia
Akaki Tsereteli State University
59 Tamar Mepe Street, 4600 Kutaisi – Georgia
+995597572615
Datodzadzamia1@gmail.com

EXTENDED ABSTRACT

OVERVIEW

The technical condition of the hydropower machinery and equipment - is a set of technical parameters characterizing possible deviation from the operating standards of the installation, which in turn may result in possible malfunctions. First vibration increases, and then the noise, temperature, and finally, the smell of smoke and residue seeps out.

In the tasks of technical monitoring and diagnosis, there are two possible approaches to controlling the technical condition of the machinery and equipment.

The first approach is to organize permanent control over changes in the representative parameters of the hydropower machine (trends in these changes). Changes in these parameters characterize changes in the technical condition of the hydropower machinery and equipment during operation in order to indicate the time at which the rate of deterioration of the technical condition becomes critical. The representative parameter refers to, for example, the total levels of vibration or noise, or the levels of their spectral constituents, total vibration energy, temperature, pressure, electrical current, voltage, etc.

The second approach (test check) is based on casual control of the representative parameters of the technical states and their comparison with the limit values, which in turn are established on the basis of a large number of previous diagnostic experiments. The test control method should be used to determine the technical states of the hydropower machinery and equipment, as well as to identify those hydropower machines and parts that are in critical condition [1].

METHODS

Today, a complete vibroacoustic diagnosis is made using the theory of identification.

It is assumed that the technical object exists in the finite set of the technical conditions – S. From this set of technical conditions, there are extracted two subsets: S_1 – a subset of workable technical conditions and S_2 – a subset of unworkable technical conditions.

The vibroacoustic diagnosis procedure is divided into three parts:

The first stage is to address the general problem of acceptability of the present results. With that in mind, the technical condition pertains to the subset S_1 or S_2. Mathematically, this process has the following form:

$$\text{If } \bar{X} \leq \overline{X^{\scriptscriptstyle{\ni}}} \leq \overline{X^{\scriptscriptstyle{\ni}}} + \overline{\delta} \text{ is acceptable} \tag{1}$$

$$\text{If } \bar{X} > \overline{X^{\scriptscriptstyle{\ni}}} > \overline{X^{\scriptscriptstyle{\ni}}} + \overline{\delta} \text{ is unacceptable} \tag{2}$$

Where $\bar{X}$ is a vector of the output measuring parameter, $\overline{X^{\scriptscriptstyle{\ni}}}$ - is a vector corresponding with the reference parameter, and $\overline{\delta}$ - is a permissible deviation from a reference value. If even only one parameter is obtained from a permissible value, the object is considered unworkable and unacceptable, and the objective technical condition moves into the S_2 subset.

The second stage is to address the analysis of the technical conditions. At this stage, a new coefficient of performance is introduced. To do so, by means of $\overline{\delta}$ there is determined the zone, where the existing technical condition is at this moment in time. Coefficient of performance is $\bar{C} = 0 \div 1$. The higher is performance C, the closer it is to 1. Mathematically, this can be expressed in the following form:

$$\bar{C} = 1 - \left| \frac{x - \overline{x^{\scriptscriptstyle{\ni}}}}{\overline{\delta}} \right| \tag{3}$$

Where $\bar{C}$ is a coefficient of performance? If $\bar{C} = 0$, the object is unacceptable, if $\bar{C} = 1$, its state is considered a reference. If $0 \leq \bar{C} \leq 0,25$, the object has a too high a coefficient of performance if $0,25 < \bar{C} \leq 0,5$, we have too low of performance, and if $0,5 < \bar{C} \leq 0,75$ – high coefficient of performance, and if $0,75 < \bar{C} \leq 1$ – too high coefficient performance.

The third stage is to address which class of technical condition the object pertains to in accordance with the existing defects. This is expressed in the following formula:

$$D_{ik} = \sum_{k=1}^{n} [\bar{A}_{ik} - A_k^{\scriptscriptstyle{\ni}}] \tag{4}$$

Where $\bar{A}_{ik}$ are the symptoms, which are obtained as a result of developing signal obtained from measuring $A_k^{\scriptscriptstyle{\ni}}$ - is a reference value, which is placed in the algorithm of diagnosis.

Mathematically, the algorithm of identification has the following form:

$$\text{If } D_{ik} \leq \Delta_{ik}^n \text{ - there is no defect} \tag{5}$$

$$\text{If } D_{ik} > \Delta_{ik}^n \text{ – there is a defect.} \tag{6}$$

Here Δ_{ik}^n is a limiting value, and these values have been obtained statistically and experimentally. If the vibration level is doubled, this already points to the existence of the defect [2].

RESULTS

In Mathcad, there are the "detrend" and "predict" functions for identifying trends in changes and forecasting these changes (Burg's function based on the Autoregression method), which produce good practical results [4]. For illustrative purposes, let us use these functions, for

example, to stop the process at any point in time on the simulated signal below (Fig. 1) and make a prediction of the expected points and find the trend (Fig. 2).

$$x_i := A1 \cdot \cos(2 \cdot \pi f1 \cdot t_i) + \sum_{k=1}^{4}(Ak \cdot \cos(2 \cdot \pi \cdot f_k \cdot t_1))$$
$$x_i := A1 \cdot \cos(2 \cdot \pi f1 \cdot t_i) + \sum_{k=1}^{4}(Ak \cdot \cos(2 \cdot \pi \cdot f_k \cdot t_1)) \tag{7}$$
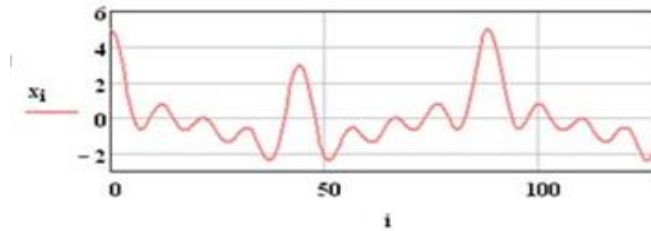
Fig.1 Simulated signal
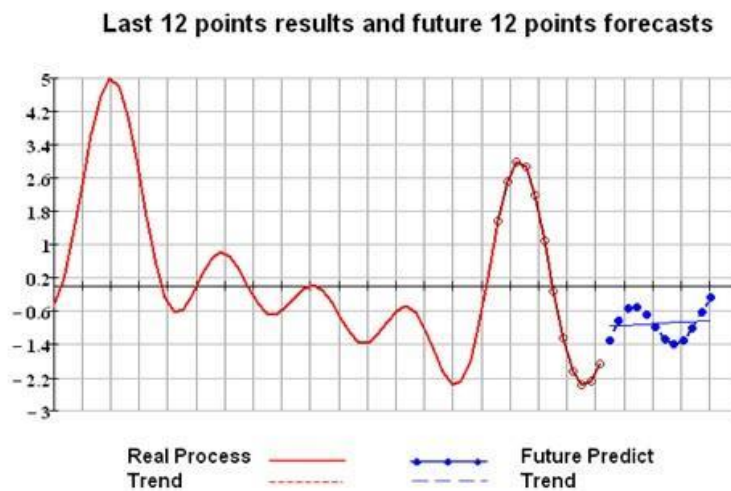
Fig. 2. Predicting and trends of the interrupted signal of the expected points

As we can see, this method predicts very accurate based on the process itself. In real systems, if there is any pattern in the process, the method reveals the pattern and uses it to predict the expected points of the process with high precision. Let us use this method to predict the trends in a change in the total vibration level (dB) of the bearing of the hydropower unit turbine and the expected changes [3].
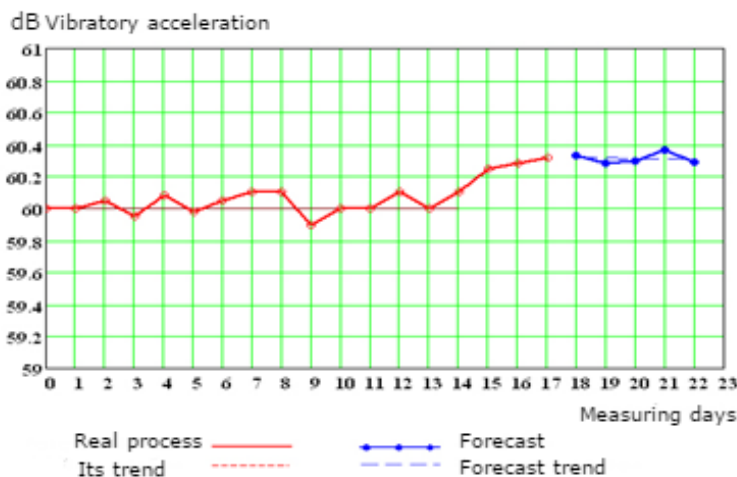
Fig. 3 The example of determining the technical states and predicting the trends

As soon as degradation processes begin in the bearing, the method provides a prediction of the signal coming from the sensor and determines the trend, indicating the operator for the necessary actions. This approach is ideal for process automation, especially since intensive work is currently underway to create automated control systems using vibration signals.

CONCLUSIONS

- The introduction of the vibroacoustic diagnosis and monitoring systems will allow us to control any process in the hydropower units and detect any malfunctions from the very first stage of origin of the fault
- Mathcad can be successfully used not only as an aid but also as a programming environment for building the complete diagnostic systems for the mechanical systems;
- The use of monitoring and diagnosis methods during the operation of the hydropower machinery and equipment allows for reducing the cost of operation through savings in spare parts and petrol, oil and lubricants, as well as to increase the efficiency of the unit in production conditions by excluding unreasonable shutdowns.
- The use of diagnostic methods in automated production allows us to continuously control the accuracy parameters of technological processes, which is a guarantee of high-quality product output.

Keywords: hydropower unit, Vibroacoustic diagnostics, MathCAD software.

REFERENCES

1. NORTON, M.P. Fundamentals of noise and vibration analysis for engineers. Melbourne, Australia: *Cambridge University Press*, 1999, P. 619. ISBN 0-521-34941-9.

2. DIMENTBERG, M.F.; FROLOV, K.V.; MENYAILOV, A.l. Vibroacoustical diagnostics for machine and structures. Taunton, Somerset England: *Research Studies Press*, 1991, P. 630. ISBN 0-863-80116-1.

3. MARINESCU, I.D. Handbook of machine tool analysis. Bosa Roca United States: *CRC Press*, 2002, P. 322. ISBN 0-8247-0704-4.

4. *Mathcad,* version 14.0.0.163. Help. – Parametric Technology Corporation, 2007.

II. PHYSICAL SCIENCES

II.1. Combustion and plasma processes

DETERMINATION OF THE PLASMA-FORMING GAS TYPE INFLUENCE ON ELECTRICAL AND THERMAL CHARACTERISTICS OF THE PLASMA TORCH

M. Aikas, A. Tamošiūnas, D. Gimžauskaitė
Lithuanian Energy Institute
Breslaujos g. 3, LT-44403 Kaunas – Lithuania
Mindaugas.Aikas@lei.lt

EXTENDED ABSTRACT

OVERVIEW

Nowadays, the growth of the population worldwide and, at the same time, intensifying the industrialization process causes higher energy demand and higher waste generation. Such predominant factors lead to environmental challenges, such as pollution of water, air and soil, and climate change in a general way [1, 2]. Waste generation became an integral and custom part of daily activities. But at the same time, waste management remains an issue. Recently, plasma technologies have gained attention as a possible way for waste conversion into valuable products, including syngas, which could contribute to the fulfilment of growing energy demands [3, 4]. However, these technologies are not yet fully developed and require further research at the laboratory scale. Thus, before the plasma technology application for material conversion, it is essential to determine the parametric characteristics of the plasma torch (PT). Such determination helps to guarantee a stable operating mode since each PT has its unique voltage-current characteristics (VCC) under plasma torch geometry, type of working gas used, and flow rate. Accordingly, VCC is the most relevant characteristic of the plasma arc, helping to establish optimal plasma generator parameters [5]. Consequently, the aim of this work is to analyse the impact of two different types of plasma-forming gases (water vapour and air) on the electrical and thermal characteristics of the plasma torch.

METHODS

The electrical and thermal characteristics of the plasma torch were generalized using the theory of similarity. The generalization of the electrical characteristics of the PT was made by applying equation (1):

$$\frac{Ud}{I} = A\left(\frac{I^2}{Gd}\right)^m \left(\frac{G}{d}\right)^n ,$$

(1)

where U – the arc voltage (V), d – the anode diameter (m), I – the arc current (A), G – the total gas flow rate (g/s), A – the coefficient, and m, n – the exponents are constant values depending on the construction and operating regime of the plasma torch [6,7].

The generalization of plasma generator thermal characteristics is similar to the generalization of the electrical characteristics (Eq. 2):

$$\tilde{\eta} = B \left(\frac{I^2}{Gd} \right)^m \left(\frac{G}{d} \right)^n, \qquad (2)$$

where ɳ̃ – the integral coefficient of heat transfer, B – the coefficient established from the dependence of efficiency from the arc current [6, 7].

The operation of the PT was determined at variable ranges of the current and voltage used. The main operational characteristics of the plasma torch are summarized in Table 1:

Table 1. The experimental parameters of the plasma torches

Plasma forming gas	Water vapor	Air
Gas flow rate (g/s)	2.40-4.65	2.23-4.45
Arc current (A)	180-220	160-220
Arc voltage (V)	295-335	194-263
Arc power (kW)	54.0-72.6	32.16-52.58
Plasma torch efficiency, η (%)	52.3-73.2	47.7-63.0

RESULTS

The generalization of the electrical plasma torch characteristics was carried out and is shown in Fig. 1. The general equations of VCC were deduced based on the theory of similarity and are given below.

Plasma-forming gas is water vapor:

$$\frac{Ud}{I} = 0.1 \times 10^2 \left(\frac{I^2}{Gd} \right)^{-0.29} \times \left(\frac{G}{d} \right)^{-0.1}. \qquad (3)$$

Plasma-forming gas is air:

$$\frac{Ud}{I} = 6.3 \times 10^2 \left(\frac{I^2}{Gd} \right)^{-0.51} \times \left(\frac{G}{d} \right)^{-0.15}. \qquad (4)$$
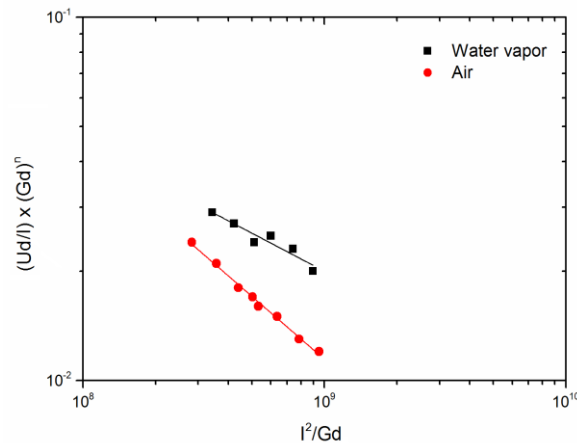
Fig. 1. The generalized water vapor and air plasma torches VCC

These electrical characteristics of the plasma torch help identify and choose the working parameters of the PT, which will guarantee the most stable operation of the system.

The generalized thermal characteristics of the plasma torch operating on water vapor or air are provided in Fig 2. The general equations of the PT thermal efficiency were determined according to the theory of similarity and are expressed below:

$$\frac{Ud}{I} = 0.1 \times 10^2 \left(\frac{I^2}{Gd}\right)^{-0.29} \times \left(\frac{G}{d}\right)^{-0.1}. \tag{5}$$

Plasma-forming gas is water vapor:

$$\tilde{\eta} = 3.89 \times 10^2 \left(\frac{I^2}{Gd}\right)^{-0.32} \times \left(\frac{G}{d}\right)^{-1.17} \tilde{\eta} = 3.89 \times 10^2 \left(\frac{I^2}{Gd}\right)^{-0.32} \times \left(\frac{G}{d}\right)^{-1.17}. \tag{6}$$

Plasma-forming gas is air:

$$\tilde{\eta} = 69.8 \left(\frac{I^2}{Gd}\right)^{-0.22} \times \left(\frac{G}{d}\right)^{-0.95} \tilde{\eta} = 69.8 \left(\frac{I^2}{Gd}\right)^{-0.22} \times \left(\frac{G}{d}\right)^{-0.95};$$

$$\tilde{\eta} = 6.98 \times 10^1 \left(\frac{I^2}{Gd}\right)^{-0.22} \times \left(\frac{G}{d}\right)^{-0.95}. \tag{7}$$
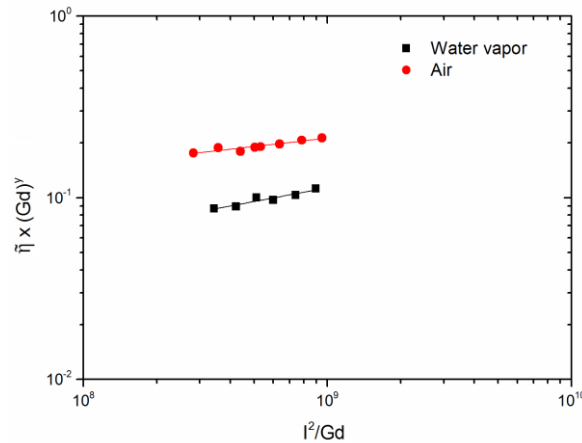
Fig. 2. The generalized thermal characteristics of the water vapor and air plasma torches

These characteristics help optimize the energy losses of the plasma process, taking notice of not only the total energy losses identified by plasma torch voltage-current characteristics.

CONCLUSIONS

The electrical and thermal characteristics of the plasma torch were investigated by applying the principles of similarity theory. The generalized voltage-current characteristics in both cases (water vapor plasma and air plasma) showed a quite equivalent distribution of the measuring points, indicating a stable work of the PT. The plasma torch thermal efficiency varied between 52.3-73.2 % at the current range of 180-220 A when water vapor was used as a plasma forming gas. Meanwhile, 47.7-63 % PT thermal efficiency was received at the current 160-220 A range when the air was used to form a plasma environment. Thus,

obtained results indicated that the water vapor plasma torch showed more efficient operating results.

Keywords: thermal plasma, plasma torch, water vapor, air

REFERENCES

1. RAMOS, A.; ROUBOA, A. Life cycle thinking of plasma gasification as a waste-to-energy tool: Review on environmental, economic and social aspects. *Renewable and Sustainable Energy Reviews*. 2022, Vol. 153, No.111762.

2. CHEN, P.; XIE, Q.; ADDY, M.; ZHOU, W.; LIU, Y.; WANG, Y.; CHENG, Y.; LI, K.; RUAN, R. Utilization of municipal solid and liquid wastes for bioenergy and bioproducts production. *Bioresource Technology*. 2016, Vol. 215, P. 163-172.

3. SIKARWAR, V. S.; HRABOVSKÝ, M.; VAN OOST, G.; POHORELÝ, M.; JEREMIÁŠ, M. Progress in waste utilization via thermal plasma. *Progress in Energy and Combustion Science*. 2020, Vol. 81, No.100873.

4. LI, J.; LIU, K.; YAN, S.; LI, Y.; HAN, D. Application of thermal plasma technology for the treatment of solid wastes in China: An overview. *Waste Management*. 2016, Vol. 58, P. 260-269.

5. PAN, W. X.; MENG, X.; HUANG, H. J.; WU, C. K. Effects of anode temperature on the arc volt-ampere characteristics and ejected plume property of a low-power supersonic plasma. *Plasma Sources Science and Technology*. 2011, Vol. 20, P. 1-8.

6. ZHUKOV, M. F.; ZASYPKIN, I. M. *Thermal plasma torches, Design, Characteristics, Applications.* UK: Cambridge International Science Publishing Ltd, 2007. P. 610. ISBN 13: 978-1-904602-02-6.

7. GRIGAITIENĖ, V.; SNAPKAUSKIENĖ, V.; VALATKEVIČIUS, P.; TAMOŠIŪNAS, A.; VALINČIUS, V. Water vapor plasma technology for biomass conversion to synthetic gas. *Catalysis Today*. 2011, Vol. 167, No. 1, P. 135-140.

ANN LBV MODEL IMPLEMENTATION INTO FLAMEFOAM SOLVER

A. Ambrutis
Lithuanian Energy Institute
Breslaujos g. 3, LT-44403 Kaunas – Lithuania
+370 37 401 920
andrius.ambrutis@lei.lt

EXTENDED ABSTRACT

OVERVIEW

Hydrogen is a valued resource for nowadays industry. As a fuel, it produces large amounts of energy and creates water during the process, unlike most other polluting energy sources. However, the safe use of hydrogen requires reliable tools able to accurately predict combustion. This study presents the implementation of an artificial neural network (ANN) of the laminar burning velocity (LBV) of hydrogen into CFD solver flameFoam. ANN is expected to provide more accurate predictions than currently available correlations. Original ANN was created in previous work [1]. However, while it showed a low prediction error and a high R-squared value of approximately 0.98, it was too large for CFD applications since the calculations took too long. Therefore, based on the original model, a faster but still accurate ANN was developed and implemented into flameFoam. Paper presents the adaptation of the original ANN into a CFD-applicable version and the initial test results of the CFD-ANN simulation.

METHODS

The original ANN consisted of 4 layers with 40, 50, 30, and 10 weights. For the model to be applicable with CFD, the number of weights, and correspondingly required arithmetic operations, had to be reduced. After numerous test models, faster ANN consisted of 4 hidden layers with 7, 10, 7, and 5 weights.

To maintain high accuracy with a lower number of weights, other modifications had to be implemented. The first hidden layer was changed to use the *tanh* activation function (1) while the rest use *ReLU* (2):

$$\tanh(z) = \frac{e^z - e^{-z}}{e^z + e^{-z}} \tag{1}$$

$$ReLU(output) = \begin{cases} output, if\ output > 0; \\ 0, else \end{cases} \tag{2}$$

Moreover, this study increased the number of epochs to 5000. This required multiple re-trains due to a thin line between a well-working and an over fitted, noise-mimicking model.

Since the first hidden layer activation function was changed from *ReLU(2)* to *tanh(1)* and we have reduced the number of weights in hidden layers, ANN could just start to predict values based on *tanh(1),* which would not give a good prediction. Therefore, several checks were made – ANN was tested on a testing set (25% of all data points [1, 2]), LBV curve smoothness was checked, and, finally, a comparison against the experimental results from literature was made (Fig. 1 presents an example for normal conditions). Comparisons showed good agreement of ANN predictions with known values and an R-squared value of approximately 0.997.
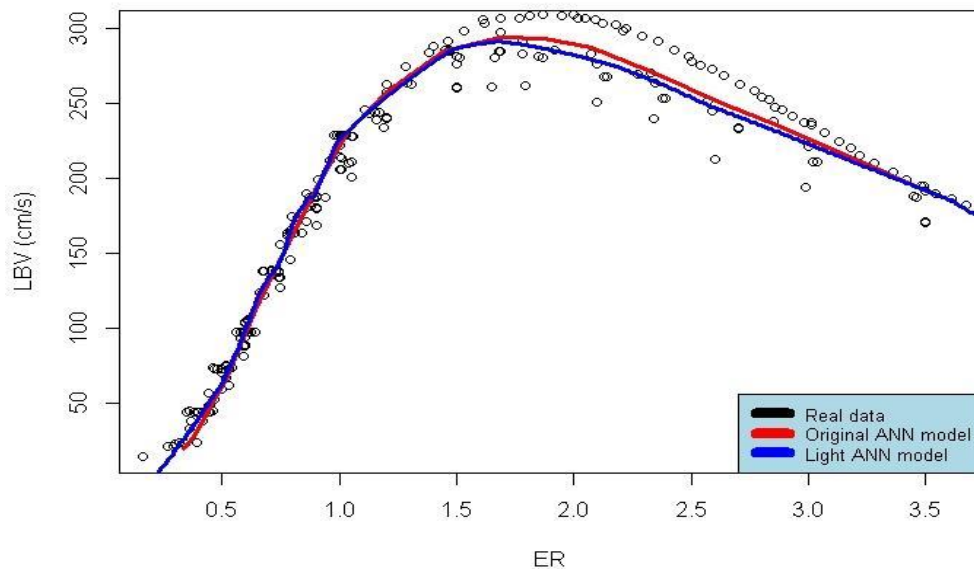
Fig. 1. Comparison of both ANN predictions and experimental data at
normal conditions

To avoid negative predictions, the ReLU (2) function was also applied to the final output function. Another significant modification was switching to a criterion of the average of mean absolute and mean squared errors instead of either of those separately. This should minimize optimal curve points to the average of median and mean, which we believe is most accurate to real predictions due to statistical possibilities.

Obtained ANN was implemented into an open-source combustion solver flameFoam [3].

RESULTS

To test the model artificial test case was simulated. The purpose was to check the results of the CFD-ANN simulation against the results using the established Malet correlation [4]. Conditions of the test were selected to be similar to previously simulated real cases. A shortened vertical acceleration tube was modelled (Fig. 2). It contained nine annular obstacles extending from the wall.

Fig. 2. Vertical cross-section of the case, rotated 90°, bottom on the left.
Light grey – solid walls, blue – fluid region

The case was simulated using a 2-dimensional axisymmetric orthogonal uniform mesh of 1 mm characteristic length with solid and fluid regions. The flame was ignited at the bottom centre. Fluid was initially set at atmospheric pressure and 23° C temperature. Homogenous composition of 11 % H_2 and 89 % dry air was selected. Turbulence was modelled using the k-ε RANS model. Combustion was modelled using progress variable c (0 – fresh mixture, 1 – burnt mixture) and turbulent flame speed closure model with Bradley correlation.

Fig. 3 shows flame evolution and predicted LBV values from the bottom of the facility until the first obstacle. Initially, flame evolutions are similar to both LBV prediction methods. However, it seems that ANN predictions are less sensitive to pressure and temperature variations at this stage, resulting in more uniform predicted LBV values than with Malet correlation. This results in a smoother flame surface with ANN calculation. Another significant difference is that, while at the leading side of the flame, similar LBV values are predicted by both methods, at the trailing, hotter side of the flame, Malet correlation predicts higher LBV values. This leads to slightly faster flame propagation when using Malet correlation.
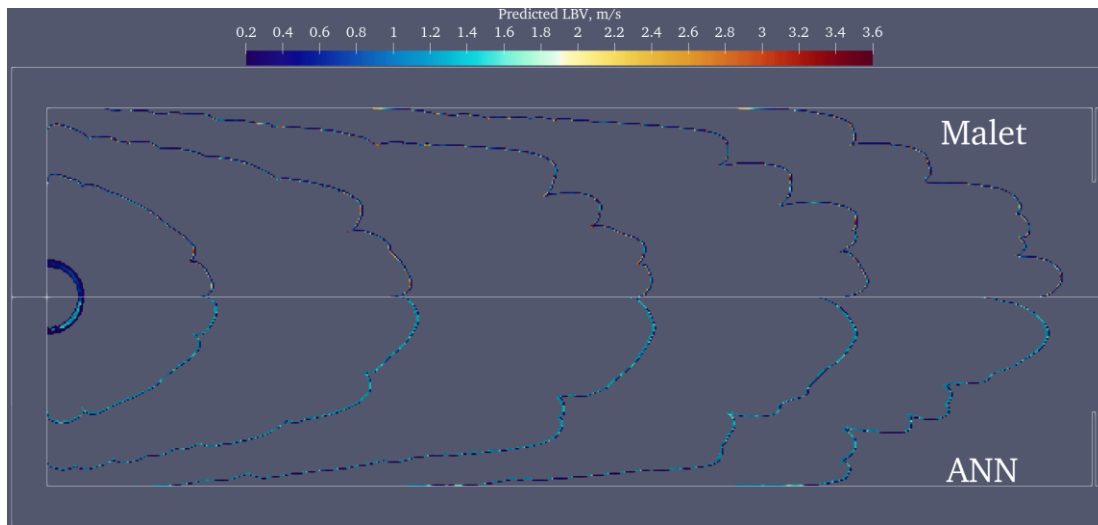
Fig. 3. Flame evolution before the first obstacle and predicted LBV at flame surface (0.05<c<0.95), at times (from left to right) 0.002 s, 0.02 s, 0.04 s, 0.06 s, 0.08 s, 0.1 s.

CONCLUSIONS

A fast ANN able to predict hydrogen LBV in dry air was developed based on a larger ANN. The accuracy of fast ANN was tested against a testing set of data and values from the literature. Additionally, obtained LVB curve smoothness was checked. Predictions of developed ANN showed proper behaviour and an R-squared value of approximately 0.997.

Developed ANN was implemented into combustion solver flameFoam for the prediction of LBV values. Testing CFD-ANN simulations were performed and compared with simulations using established Malet correlation of LBV. The comparison showed similar results with the ANN model predicting more uniform and lower values of LBV. Current ANN is around 25 times faster than the original.

Further planned work is to perform validation of developed CFD-ANN modelling against the experimental data.

Keywords: combustion, artificial neuron network, CFD, laminar burning velocity

REFERENCES

1. AMBRUTIS, A.; POVILAITIS, M. Laminar burning velocity estimation using deep neural network. CYSENI 2021. Proceedings of the annual conference of young scientists on energy issues. [CD]. Kaunas: Lithuanian Energy Institute. 2021 May 24-28, 2021. Link to the internet < https://cyseni.com/wp-content/archives/proceedings/Proceedings_of_CYSENI_2021.pdf >

2. KUZNETSOV, M.; CZERNIAK, M.; GRUNE, J.; JORDAN, T. Effect of Temperature on Laminar Flame Velocity for Hydrogen-Air Mixtures at Reduced Pressures. ISHS 2013. Proceedings of International Conference on Hydrogen Safety. Belgium: Brussel. 2013 September 9-13. Link to the internet <http://www.ichs2013.com/images/papers/231.pdf >

3. POVILAITIS, M.; JASELIŪNAITĖ, J. FlameFoam: An open-source CFD solver for turbulent premixed combustion. *Nuclear Engineering and Design*, 2021, Vol. 383, 111361, ISSN 0029-5493.

4. MALET, F. Etude Expérimentale ET Numérique de La Propagation de Flammes Prémélangées Turbulentes Dans Une Atmosphère Pauvre En Hydrogène et Humide. *Ph.D. thesis*. Université d'Orléans. 2005. Link to the internet <https://inis.iaea.org/collection/NCLCollectionStore/_Public/39/001/39001650.pdf >

PLASMA APPLIED BURNERS FOR COMBUSTING LOW CALORIFIC VALUE GASES

E. Bykov, R. Paulauskas, N. Striūgas
Lithuanian Energy Institute
Breslaujos g. 3, LT-44403 Kaunas – Lithuania
+37063080956
Ernest.Bykov@lei.lt

ABSTRACT

The need for energy resources that do not belong to the group of fossil fuels and the wide availability of various low-calorific gases leads humanity to search for solutions to adapt external sources of force that would allow using of these resources. One of such solutions is the usage of non-thermal plasma applications not only for ignition but also for plasma-assisted combustion (PAC). PAC is a promising technology for improving processes of ignition and flame stabilization, as well as propagating flame speed. This work would be, in general, discussed only non-thermal plasma devices [1]. In addition to the facts mentioned earlier, PAC potentially can improve the efficiency of combustion, the conversion of fuels into other forms [2], the gasification of coal and municipal or industrial solid wastes into syngas (syngas – a mixture of mainly H_2 and CO) [3]. Exist a huge variety of types of plasma, which are shown in Fig. 1, which describes the division of the plasma. The purpose of this paper is to provide a general overview of existing types of systems to the reader, mention the positive and negative sides of each type and provide some possible ways for further investigation.
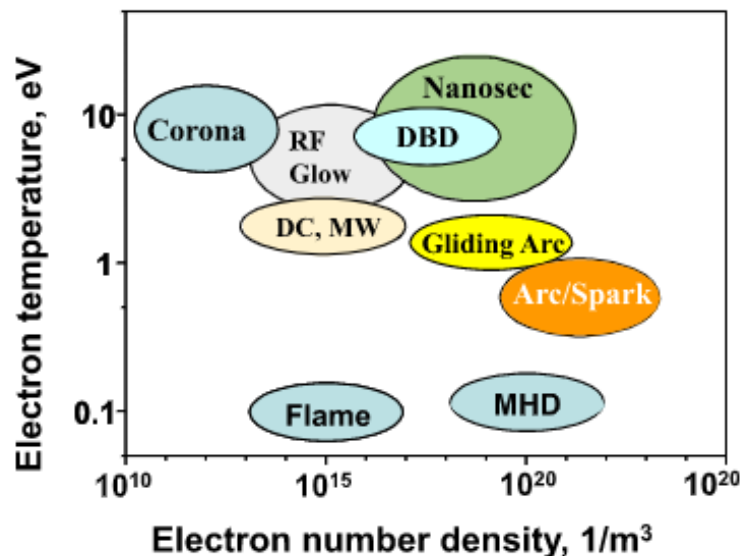
Fig. 1. Schematic of electron temperature and number density for different discharges [4]

TYPES OF PLASMA-ASSISTED BURNERS

Plasma-assisted burners (PAB) could be divided into two major trends – premix and after-mix burners. The premix is a device which consists of the premix chamber, plasma reactor, and burner nozzle. The air and fuel first come to the premix chamber, where they form the fuel-air mixture, after which they move forward to the treatment zone, in which both gases face impact from the plasma source. The other ones, after mix type, usually consist of separate coaxial channels that directly supply different gases (air and fuel) to separate zones. In those types of burners, plasma reacts only with fuel gas, whereupon treated gas mixes with air and combusts. In the first, premix one activates the mechanism of producing additional NOx from air nitrogen, partially decomposing the air into its component parts before reaching the combustion chamber. The second, after mix type, is devoid of such a disadvantage, but, mostly, the construction of after mix burners requires more time and effort to design because such a scheme of the burner is more complicated, and it is hard to reach the same level of efficiency. The second way of dividing the PAB – is by the method of plasma formation.

CORONA DISCHARGE REACTOR

The corona discharge burner is one of the most early-made designs of the PAB. It is known to be a premixed-type burner made from a tube with an inside bore, premix chamber and an extended water-cooled second spiral electrode. The first electrode was formed by cutting out metal to an axial depth, and each of the points was turned inward so that the tips lay on a circle. [5] As an advantage of such construction could be noted the fact that this type of burner is easy to produce, it doesn't require special materials, but on the other hand, it includes all the disadvantages that are characteristic of premixes described earlier. The above-described construction of the corona discharge burner is shown in Fig. 2.
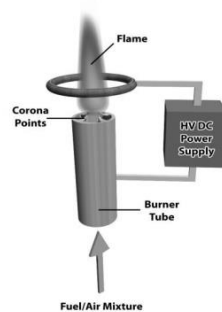
Fig. 2. Corona-influenced burner [5]

MICROHOLLOW CATHODE DISCHARGE

One of the most extensively studied configurations is an array of so-called micro hollow cathode discharges (MHCDs), which have the ability to produce a high-density plasma discharge in a relatively small volume [6-7]. Dielectric barrier discharge PAB ensures a maximum interaction between the plasma discharge and the processed gas. Thereby, the design shown below in Fig. 3 could be counted as one of the most efficient types because the area of the gas treated in one period of time is much higher than at the other types of PAB. At the same time, burners of such design couldn't last long enough to be implemented into some industry processes because the dielectric layer is exposed to high thermal loads, which is not suitable for it.
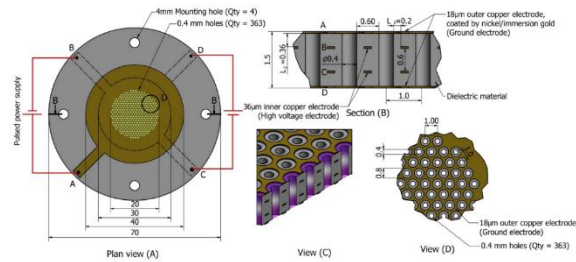
Fig. 3. DBD-type PACB made from layers of dielectric (textolite) and
conductive copper layers [10]

GLIDING ARC IN TORNADO (GAT) AND ADJUSTABLE GLIDING ARC IN TORNADO (AGAT)

The GAT technology is named after the natural tornado, which could have partially the same logic as the gliding arc. Indeed, the phenomenon of reverse vortex flow is its main principle. Fig. 4 shows the scheme of the GAT reactor and its working principle. Two flows enter the cylindrical volume. The first flow is axially injected into the bottom part of the reactor; the second one enters the body tangentially in the nozzles in the upper part. The solid lines represent the tracks of the rotating flow, and the dotted lines show the streamline in the axial plane. That makes the plasma zone well stabilized by the near-wall tangential flow.
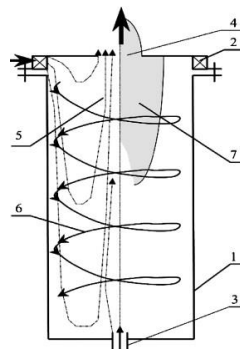
Fig. 4. GAT-type reactor [11]

The AGAT plasma-assisted burners differ in that fact that the electrode configuration could be adjusted to reach the needed parameters of the plasma. Two high voltage electrode geometry has been developed to show different ways one can ignite the discharge (shown in Fig. 5). The first configuration includes a moving annular electrode that can change its position relative to the tip. In the initial position, the cathode ring is 3 mm away from the ground electrode (the gap required for reliable primary ignition of the arc). After ignition, the cathode moves downward, and thus the arc lengthens to the point where it is in non-equilibrium conditions. The second configuration has a helical cathode located coaxially with the tube. The arc discharge is ignited at the top of the spiral electrode and then slides along it until it reaches the smaller diameter ring and thus stabilizes.
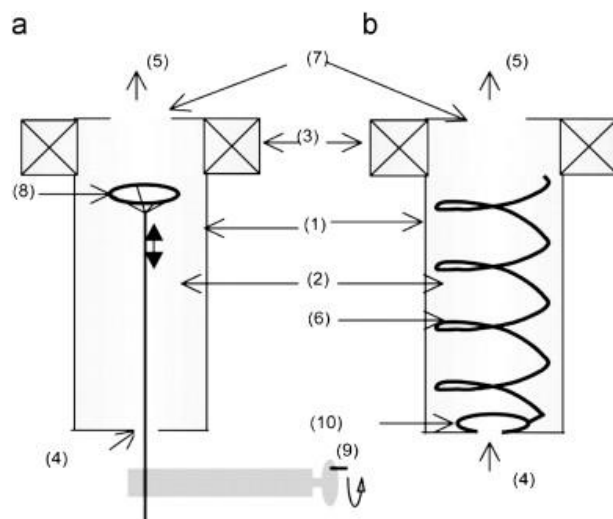
Fig. 5. Reverse GAT-type reactor with moving electrode [11]

MAGNETIC BLOW-OUT GLIDING ARC REACTOR

Reactors and burners with controllable magnetic fields are considered the second generation of plasma-assisted processing installations. A rotating magnetic field is applied to ionized particles thanks to a magnet. Three anodes are installed around one axial cathode, which is made from tungsten. Active particles enter the reactor at a temperature of 500 K along the cathode through a ceramic tube in the upper part of the reactor. A single rotating arc discharge is then created and wound around the cathode. In this case, the transition between non-thermal and thermal regimes could be regulated by the strength of the magnetic field without the use of any external factors or resistive components. The three cascaded discharges are then fed from a three-channel power supply.
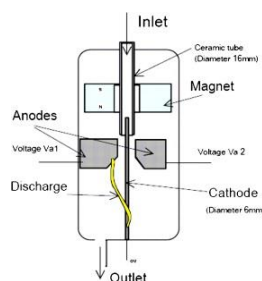
Fig. 6. Magnetic blow-out gliding arc reactor (GREMI, France) [12]

BLADE-ELECTRODE TYPE REACTOR

This type of reactor was designed and first produced by the firm called ECP (Sarl) GlidArc Technologies in France. The benefits of this type of design are that the discharge forms at the closest point on the blade glide along the electrodes, and disappears. Another discharge immediately reforms at the initial spot. That fact makes the spread of corrosion and erosion-corrosion over the element more uniform, which reduces the specific consumption of the blade material per unit time, thereby increasing the service life of the installation. The electrodes do not need to be cooled, so electrical energy is directly and totally transferred to the processed gas. Such a type of system allows to increase the working area by adding additional blades, which could increase the conversion rate of feedstock or allow to change the geometry of some number of blades, which could concentrate specific field strength in higher numbers than on adjacent blades.
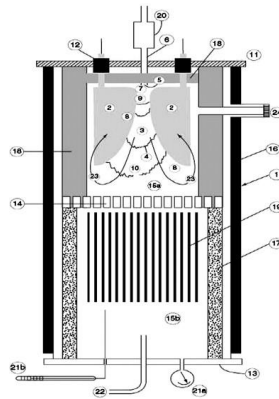
Fig. 7. Scheme of "Glidarc I" reactor (ECP, France) [13]

POSSIBLE DESIGNS OF PAB FOR FURTHER INVESTIGATION

Further development of the DBD plasma reactor designs could be the usage of a "tablet" design with the use of ceramic 3D printing technologies. Thereby, the biggest delay dialer for this type of PAB is the fact that the electrical insulating middle layer faces non-typical thermal stresses and loads, which cause its burnout. To prevent this, the insulating layer could be made from material that is inert to the temperature level which could be reached in those types of equipment. As such, the material could be ceramic, which mankind is already able to print on specialized 3D printers. Fig. 8 shows the prototype model of this type of "tablet" PAB, with the intermediate layer of the dielectric performing the function of the housing.
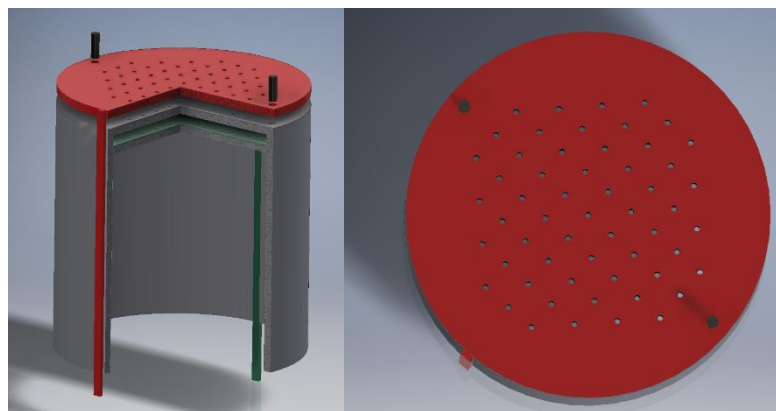
Fig. 8. DBD-type PAB "tablet" design with the intermediate layer of the dielectric performing the function of the housing [from authors archive]

A sliding arc device usually consists of two or more metal electrodes with a divergent gap connected to a DC power source. The treated gas should be fed through the space between the electrodes, as a result of which upward moving electrical discharges process the gas. The application of this type of plasma for the burners was described by Chernichovsky to improve ignition, remove air pollutants, and convert hydrocarbons into synthesis gas [8]. By changing the linear ascending gas flow to a vortex one, it is possible to create discharges similar to a "tornado", as discussed in the book by Friedman and Kennedy [9]. Such a design could be seen in Fig. 9, whereas the rotation movement generator acts as the gas supply unit at the bottom part of the burner. The results of the CFD analysis of such constructions can be seen in Fig. 10.
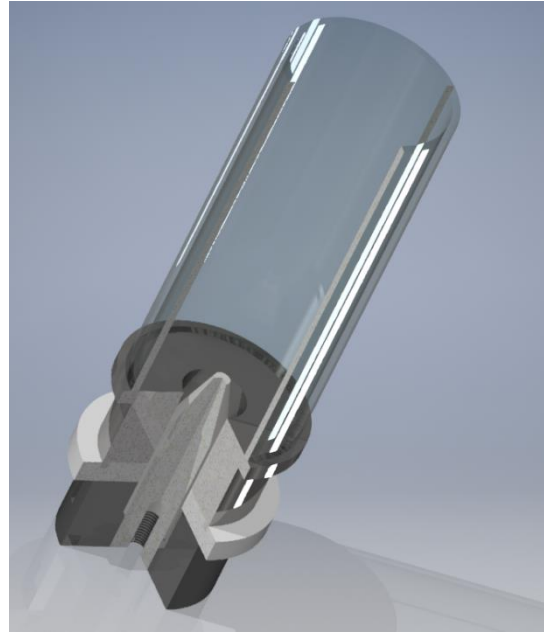
Fig. 9. Vortex-implemented gliding arc type burner [from authors archive]
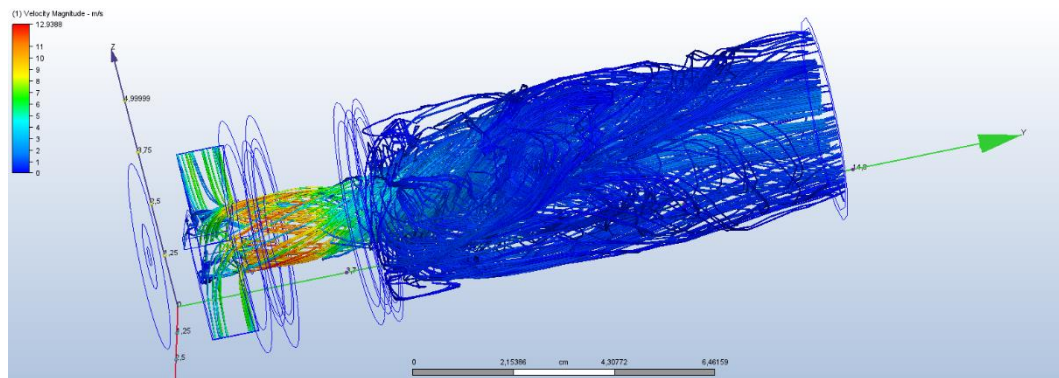
Fig. 10. CFD modelling of the aerodynamic properties of vortex-implemented gliding arc burner [from authors archive]

One of the most promising systems is the system with the after-mix type of layout. Firstly, in such a system is no possibility to face additional NOx generation because of the fact that the air and flammable gas are supplied separately, which could be seen in Fig. 11, where the model of after mix burner with vortex-formatting, air nozzles and needle-type electrodes is shown. This led to the fact that air would not be treated by plasma and would not be decomposed into its constituent parts, one of which (dominant) was nitrogen.
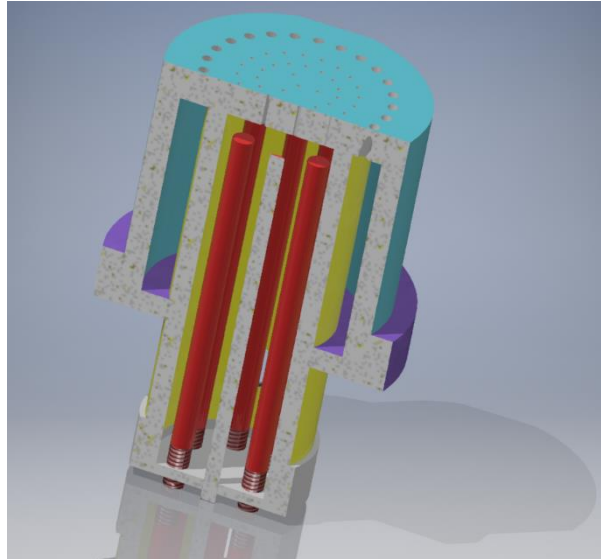
Fig. 11. Model of a prototype of the after mix type burner with vortex-formatting nozzles and needle electrodes in the reaction chamber [from authors archive]

CONCLUSIONS

The review of existing and further designs and techniques of constructing plasma-assisted burners were done in general statements. Were noted in overall positive and negative tips for each type of system, as observed earlier in the texts, and as well as some options were proposed to solve existing problems, improve existing designs and create new ones.

Keywords: (Plasma, Plasma-assisted combustion, Burners)

REFERENCES

1. MATVEEV, I; Plasma Assisted Combustion Gasification and Pollution Control: Volume 1. Methods of Plasma Generation for Pac, Denver, CO, USA: Outskirts, 2013, P. 540. ISBN 9781432786885.

2. MATVEEV, I.; ROMANOVSKY, G. Influence of Plasma Torch on Liquid Fuel Burning in the Combustion Chamber in Proc. 9th *All Soviet Union Conference "Low – Temperature Plasma Generators"*, Frunze, USSR, 1983, P.56-59.

3. MATVEEV, I. Alternative Solutions for MSW-To-Energy Processing, *4th Int. Workshop and Exhibition on Plasma Assisted Combustion*, Falls Church, VA, Sept.16-19 2008, P. 84.

4. YIGUANG, J.; WENTING, S. Plasma assisted combustion: Dynamics and chemistry. *Progress in Energy and Combustion Science,* 2015, Vol. 48, P. 21-83.

5. BRADLEY, D.; NASSER, S. Electrical coronas and burner flame stability, *Combustion and Flame*, 1984, Vol. 55, No. 1, P. 53-58.

6. GOMES, M.; SISMANOGLU B. Characterization of microhollow cathode discharges *Brazilian Journal of Physics*. 2009, Vol. 39, P. 25–30.

7. SCHOENBACH, K. H.; EL-HABACHI, A.; SHI, W.; CIOCCA, M.; High-pressure hollow cathode discharges *Plasma Sources Science and Technology.* 1997, No. 6 468.

8. *CZERNICHOWSKI.* Gliding Arc – applications to engineering and environmental control*, Pure and Applied Chemistry,* 1994, Vol. 66, No. 6, P. 1301-1330*.*

9. FRIDMAN, L.; KENNEDY, A. Plasma Physics and Engineering*,* New York – London: Taylor and Francis, 2004, P. 724. ISBN 9781498772211.

10. ELKHOLY, A. *Development of non-thermal DBD microplasma reactor for combustion applications*. Eindhoven: Technische Universiteit Eindhoven, 2019. P.149.

11. KALRA, C.S.; GUTSO, A.F.L.; FRIDMAN, A.A. Gliding arc discharges as a source of intermediate plasma for methane partial oxidation, *IEEE Transactions on Plasma Science,* 2005, Vol. 55.

12. *CORMIER, J.; RUSU, I.; KHACEF, A.* On the use of a magnetic blow out glidarc reactor for the syngas production by stem reforming. *16th International symposium on plasma chemistry, Taormina, 2003.*

13. *CZERNIKOWSKI,* G. Preparation of the synthesis gas from natural gas and waste hydrocarbons gases *Oil & Gas Science and Technology,* 2001, Vol. 2, P. 181-198

THERMAL CONVERSION OF THE SEAWEED USING PYROLYSIS PROCESS AND AN ANALYSIS OF THE FORMED PRODUCTS

J. Eimontas, N. Striūgas
Lithuanian Energy Institute
Breslaujos g. 3, 44403 Kaunas – Lithuania
+37063454823
Justas.Eimontas@lei.lt

J. Špečkauskienė
Kaunas University of Technology
Studentų st. 50, 51368 Kaunas – Lithuania
+37063950480
Email: joauli@ktu.lt

EXTENDED ABSTRACT

OVERVIEW

In the last few decades world has been facing serious energy sources depletion and environmental deterioration. In order to contribute to the solution of these problems, alternative processes and feedstocks selection could be involved. Biomass energy is a potential substitute for fossil fuel because of its easy storage, transportation, and abundant availability [1]. Moreover, the production and use of biomass for utilization purposes are considered a theoretical "zero carbon" cycle, where the collected biomass is converted into CO_2 and then absorbed by growing plants [2].

An idea of these researches is to utilize seaweed biomass, obtaining an additional energy carriers and contributing to the creation of a cleaner environment. The pyrolysis process could be used for utilization purposes because of the inability to incorporate seaweed wastes into other valuable products industries. This happens because of the high heavy metal contaminations in the feedstock.

Nutrient (N, P) overload in the water causes blooming and oxygen depletion processes. As a consequence, eutrophication processes accelerate, and a high amount of seaweed on the seashores could be obtained.

Collected biomass could be used in alternative thermal treatment processes to obtain additional higher added value energy products. In this experimental research, thermal treatment in micro-and laboratory-scale facilities and formed products analysis of selected utilization systems were analysed.

METHODS

Material

The experiments were performed using the seaweed as a feedstock, which was collected on the Melnrage beach, Klaipeda city, during the wintertime. The most common species of the collected sample was the red algae *Rhodophyta*. Medium salinity Baltic Sea is the perfect place for the growth of this type of algae, which is mainly spread into cold-water pools. The red algae pigmentation varies from reddish-brown to reddish-black; they are described as shiny and dichotomically branched 6-11 times [3]. The collected seaweed samples were washed to avoid sand and other abrasive particles and dried based on ISO 579 standard.

The ultimate and proximate analysis of feedstocks was performed following LST EN 14918 (HHV) by an IKA C5000 calorimeter, LST EN 14774-1 (moisture content), LST EN 14775 (ash content), LST EN 15104 (CHNS content) by a Flash 2000 CHNS analyser, and LST EN 15148 (volatile content). In addition, the minerals and heavy metals content were investigated following LST EN 15411: 2011 and LST EN 15297: 2011 using Induced Plasma Optical Emission Spectrometer (ICP-OES) Optima 8000.Table 1. Ultimate and proximate analysis of the seaweed sample

Table 1. Ultimate and proximate analysis of the seaweed sample

Parameter	Unwashed seaweeds	Washed seaweeds
Ultimate analysis wt.% (d.b.)		
C	34.58	46.93
H	5.16	4.73
O (diff.)	8.74	30.16
N	3.65	4.13
S	3.54	5.13
Cl	0.43	0.05
Proximate analysis wt.%		
Moisture (a.r.)	57.32	62.56
Moisture, *(d.b.)*	2.27	0.60
Volatiles *(d.b.)*	41.82	58.30
Fixed carbon *(d.b.)*	12.01	32.23
Ash *(d.b.)*	43.90	8.87
HHV, MJ/kg	17.21	17.54
LHV MJ/kg	16.43	16.51
Minerals and heavy metals		
As mg/kg	n.d. *	n.d. *
Cd mg/kg	n.d. *	n.d. *
Co mg/kg	n.d. *	n.d. *
Cr mg/kg	2.87	9.11
Cu mg/kg	8.15	8.19
Mn mg/kg	88.19	183.09
Ni mg/kg	7.41	2.49
Pb mg/kg	n.d. *	n.d. *
Sb mg/kg	n.d. *	n.d. *
V mg/kg	n.d. *	n.d. *

Zn mg/kg	40.91	n.d. *
P mg/kg	23373	11952
K mg/kg	12737	10286
Ca mg/kg	10163	6532
Mg mg/kg	1451	1063

THERMAL ANALYSIS

The primary feedstock investigation was performed using the thermal analyser Netzsch Jupiter STA 449 F3 (Germany). Moreover, to evaluate the gaseous products' composition, which was emitted during the pyrolysis experiments, TGA was coupled with Fourier transform infrared spectroscopy analyser (FTIR, Bruker) and gas chromatography with a quadrupole mass spectrometer detector (GC/MS, Agilent 7890A).

The FTIR analyser scan times are 32. The wavelength interval ranges between 650 – 4500 cm^{-1} for all experiments using the LN-MCT (liquid nitrogen) detector with a resolution of 4 cm^{-1}. For the GC/Ms experiments used, a universal HP-5MS column with (5%-Phenyl)-methylpolysiloxane filling. The column's length is 30 m, while the outer and inner diameters are 250 μm and 0.25 μm, respectively. The mass scanning diapason ranges from 13 to 600 m/z.

RESULTS

The primary thermal investigation was performed using the TGA-DTG system. The results are presented in Fig. 1. The results showed that the biomass has two decomposition peaks. The first peak occurred around 300 °C and could be assigned to cellulose and hemicellulose thermal decomposition. Cellulose and hemicellulose tend to start depolymerisation reactions and form monomeric structures around 300 °C [4]. The second peak appeared at 690 °C and belonged to lignin thermal decomposition. The main thermal degradation of lignin could be observed around 700 °C, tending to the formation of aromatic hydrocarbons and heavier structures [5]. After total sample combustion, the investigation showed that the residual mass is around 8.7 wt. % and is a typical result for not high-quality biomass.
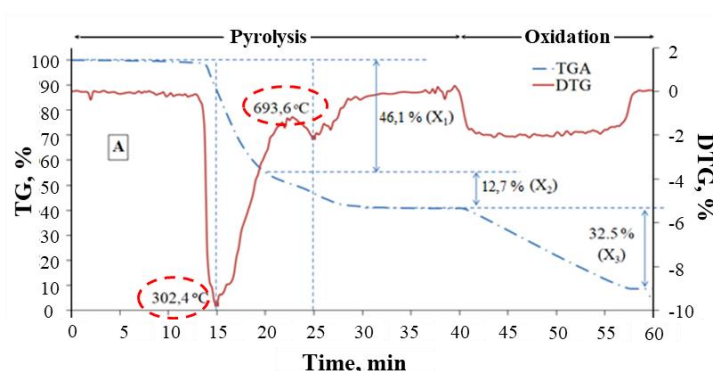
Fig. 1. TGA-DTG results of the seaweed sample

The evolved gasses' functional groups analysis was performed using a combined TGA-FTIR system. The results are presented in Fig. 2. As can be seen from the results, the most abundant functional group around 2300 cm^{-1} is C=O, representing carbon dioxide present. Minor oscillations around 3000 cm^{-1} represent aliphatic hydrocarbons, while vibrations around 1000-1200 cm^{-1} confirm aromatic polycyclic C-H compounds. Two peaks at 1300 cm^{-1} and 1500 cm^{-1} show N-O group oscillations. These functional groups were detected at ~300 °C, while at 700 °C was obtained, only carbon dioxide (O=C=O) vibrations
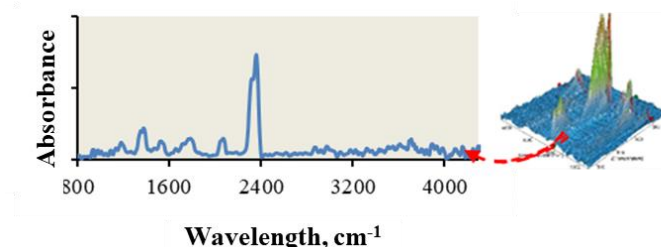
were at 2300 cm^{1}.

Fig. 2. FTIR spectra analysis of the seaweed sample

In order to investigate the exact compounds in the formed gaseous phase, the combined TGA and GC/MS system was used. Moreover, the correlations between FTIR and GC/MS could lead to identifying high molecular mass complex derivatives present. The results are presented in Fig. 3. The main compounds in the volatile seaweed matter are CO_2 (11%), polycyclic aromatic hydrocarbons, acetic acid, alcohol, and methane. Also, around 7% of the total volatile matter composition could be assigned to the furfural compound.
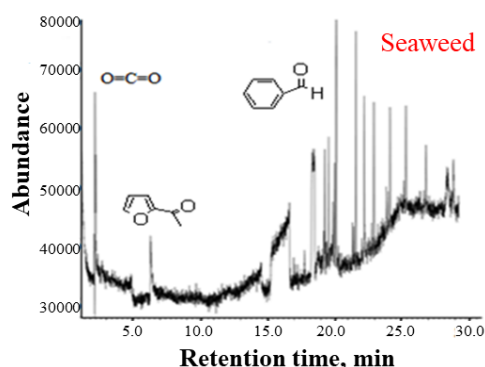
Fig. 3. The results of TGA-GC/MS analysis

CONCLUSIONS

To investigate the thermal treatment for seaweed utilization purposes, TGA-FTIR-GC/MS systems were combined. The results showed that seaweed thermally decomposes at two stages: the first one is around 300 °C and belongs to cellulose and hemicellulose thermal decomposition. In contrast, the second one is around 700 °C and could be assigned to lignin polymeric matrix degradation. The FTIR results correlated with GC/Ms results and showed that the most common functional groups were aliphatic and aromatic C-H, C=O (in CO_2 compound), and nitro (N-O) group. The GC/MS confirmed this analysis and showed the main compounds, which were CO_2, acetic acid, polycyclic aromatic hydrocarbons and some light alcohols. In general, it is clear that the primary investigation of the seaweed sample shows the potential as an alternative feedstock for additional added value energy carriers' generators.

Keywords: Pyrolysis; Biomass; Thermal conversion; Bio-oil;

REFERENCES

1. KIM, JH; JUNG, JM.; CHO, SH.; TSANG, YF.; WANG, CH.; LEE, J.; KWON, E. Upgrading bio-heavy oil via esterification of fatty acids and glycerol. *Journal of Cleaner Production,* 2019, No. 217, P. 633-638.

2. ZHANG, W.; LI, Y.; MA, X.; QIAN, Y.; WANG, Z. Simultaneous NO/CO_2 removal performance of biochar/limestone in calcium looping process. *Fuel*, 2020, No. 262.

3. YEN, H. HU, I.; CHEN, C.; HO, S.; LEE, D.; CHANG, J. Microalgae-based biorefinery - From biofuels to natural products, *Bioresource Technology*, 2013. No. 135, P. 166-174.

4. CHANDEL, A.K.; GARLAPATI, V.K.; SINGH, A.K.; ANTUNES, F.A.F.; SILVA, S.S.D. The path forward for lignocellulose biorefineries: Bottlenecks, solutions, and perspective on commercialization. *Bioresource Technology*, 2018, No. 264, p. 370-381.

5. DHYANI, V.; BHASKAR, T. A comprehensive review on the pyrolysis of lignocellulosic biomass. *Renewable Energy*, 2018, No. 129, P. 695-716.

SYNTHESIS OF ZINC OXIDE NANOPARTICLES BY COMBUSTION METHOD AND INVESTIGATION OF THEIR OPTICAL PROPERTIES

M. Ilickas, R. Mardosaitė, S. Račkauskas

Institute of Materials Science
Kaunas University of Technology
K. Baršausko st., 59, LT-51423 Kaunas – Lithuania
+37064557947
mindaugas.ilickas@ktu.edu

EXTENDED ABSTRACT

OVERVIEW

The exceptional popularity of zinc oxide has several reasons. One of the main is the multifunctionality of the material, which can be applied in various fields. ZnO has a unique combination of optical, piezoelectric, magnetic, and other properties. In addition to the ability to effectively absorb UV radiation, ZnO is a semiconductor with a wide bandgap, the literature indicates that this value is $E = 3.37$ eV [1] and has a relatively high nuclear binding energy (60 MeV), so ZnO is most often chosen for ultraviolet (UV) optoelectronics applications [2]. Zinc oxide tetrapod (ZnO-T) consists of four hexagonal rod structures, also called "legs". Zinc oxide tetrapod (ZnO-T) has a ZnO core from which four "legs" extend to the same extent into the surrounding space, giving them the potential to join "legs" to form a good network with acceptable porosity and mechanical strength [3]. These "legs" are connected to each other through the central core at an angle of 105 ° to 110 ° [4]. The crystal lattice consists of a ZnO core made of zinc blende, and the "legs" are formed from a wurtzite structure. ZnO can be synthesized by vapour transport synthesis and wet chemical methods [3]. In this work, we present an inexpensive, high-yield vapour transport synthesis method for ZnO-T production.

METHODS

The synthesis process is carried out by the rapid oxidation (combustion) method [5], using a synthesis reactor. Depending on the ratio of Zn powder, air mixture, and methane (CH_4) gas in the burner (Fig. 1.), five flame colours can be observed, indicating five different synthesis regimes. When the air supply to the air-gas mixture is off, and the oxygen needed for the combustion reaction is diffusing from the surroundings, a yellow-orange fire is produced, which is called a diffuse flame [6]. When the air supply is on, a blue flame is formed, which may still because incomplete combustion, and a blue flame is called a properly mixed flame [6]. A blue flame is obtained when Zn powder is supplied with a stream of air to produce ZnO. The green flame is obtained by finding the optimal conditions.
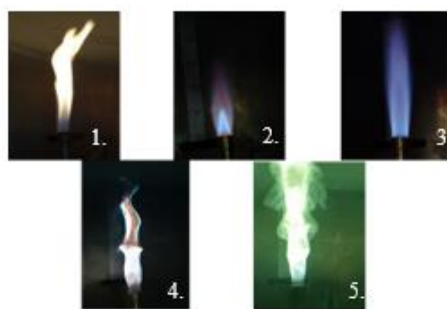
Fig. 1. Flame colours and formation conditions: 1. yellow-orange flame;
2. orange-blue flame; 3. blue flame; 4. Blue-yellow flame; 5. green flame

For centrifugation (Fig. 2.), a 6% (initial ZnO-T particles dissolved in ethanol) suspension was used, which was allowed to settle for 24 h, then placed in an ultrasonic bath for 1 h to give the starting fraction (S_0). The solution of the starting fraction S_0 is centrifuged at 1000 rpm for 15 minutes to obtain fraction I (S_1). The phase of the suspended fraction (F_1) is separated and further centrifuged at 3000 rpm for 15 minutes to obtain fraction III (S_3). This is continued until a precipitated (S_{10}) (fraction X) and suspended (F_{10}) fraction is obtained.
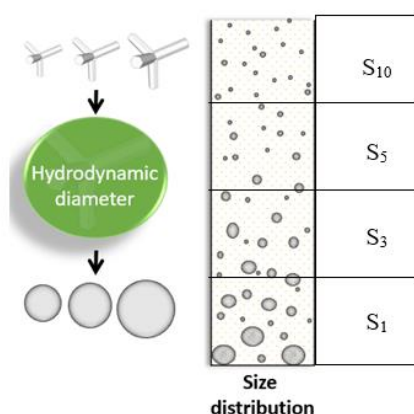
Fig. 2. Schematic of the centrifugation method

Methods of ultraviolet-visible spectrometry (UV-Vis) spectral analysis, scanning electron microscopy (SEM), and X-ray diffraction (XRD) were used for structural studies.

RESULTS

The 300-800 nm wavelength range was chosen for the UV-Vis spectral analysis of the samples (Fig. 3). It was determined how the ZnO nanoparticles in the solution settled on the bottom of the cuvette over time due to gravity. As the test time lengthened, more and more particles were found to settle to the bottom of the cuvette, which corresponds to a decreased intensity peak. The peaks might be blue-shifted quantum confinement effects [9], the 355 nm peak corresponds to the lowest aspect ratio nanostructures – nanoparticles [7], the 370 nm peak can be attributed to nanowires [8], and the 375 nm peak is characteristic to tetrapod [10] also different structures are seen in scanning electron microscopy (SEM) images (tetrapod, unformed tetrapod, different type and size nanowires and nanoparticles).
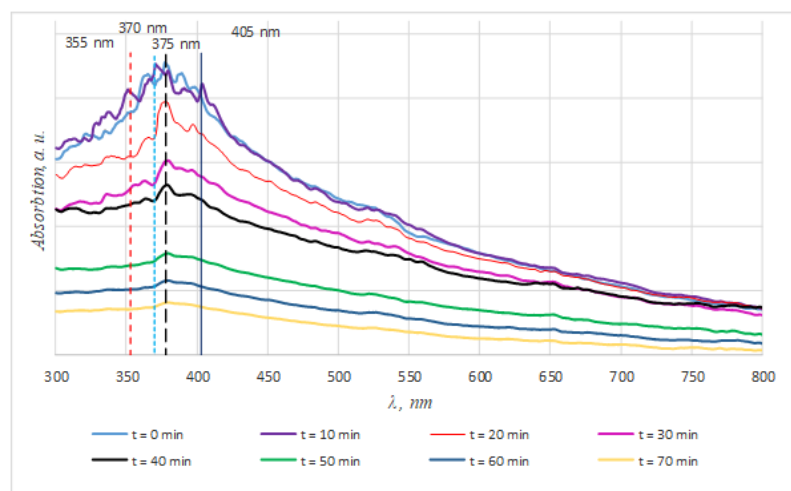
Fig. 3. UV-Vis's absorption spectra of various ZnO structures

Based on UV-Vis spectrometry and SEM, zinc oxide particles of different shapes – tetrapod, nanoparticles, and various 1 D and 3 D nanostructures - are formed during the synthesis, as well as unformed zinc particles (based on X-ray diffraction), also from UV-Vis spectrometry showed a change in particle size (58-64 nm) as the colour of the flame in the burner changed from blue to green and a decrease in particle size with increasing centrifugation speed between 1000 and 10000 rpm (63-52 nm). The size of the particle from the UV-Vis absorbance spectra was estimated using a simplified, effective mass model [11]. The size of the formed ZnO-T crystallites was determined by X-ray diffraction (the largest crystallites formed at the principal plane of formation (1 0 -1) and reached 23 nm), and the smallest number of defects in the sample was found at the principal plane of zinc oxide formation is $1.92 \cdot 10^{-3}$ nm^{-2}.

CONCLUSIONS

Based on UV-Vis and SEM studies, zinc oxide nanoparticles of different forms were formed during the synthesis: tetrapod, nanoparticles, various 1D and 3D nanostructures, and unformed zinc particles were found (based on the XRD study). The XRD method was used to calculate the size of the formed ZnO-T crystallites (the largest crystallites are formed at the principal plane of formation (1 0 -1) and reach 23 nm), and the smallest number of defects in the sample is found at the principal plane of zinc oxide formation. It is $1.92 \cdot 10^{-3}$ nm^{-2}. There is a direct relationship between the colour of the flame and the size of the nanoparticles formed, and it is also observed that the particle size decreases with an increasing centrifugation rate.

Keywords: tetrapod, synthesis, ZnO, nanoparticles

ACKNOWLEDGEMENT

REFERENCES

1. BATTEZ, A. H.; GONZALEZ, R.; VIESCA, L. J.; FERNANDEZ, E. J.; FERNANDEZ, D. J. M.; MACHADO, A.; CHOU, R.; RIBA, J. CuO, ZrO$_2$ and ZnO nanoparticles as antiwear additive in oil lubricants, *Wear*, 2008, Vol. 265, P.422-428 . ISSN 0043-1648.

2. COLEMAN A. Basic Properties and Applications of ZnO. *Zinc Oxide Bulk, Thin Films and Nanostructures*, Elsevier Science, 2006. P. 1–20. ISBN978-0-08-044722-3.

3. YAN, L.; UDDIN, A., WANG, H. ZnO Tetrapods: Synthesis and Applications in Solar Cells. *Nanomaterials and Nanotechnology,* 2015, Vol. 5, No. 1.

4. MISHRA, Y.; ADELUNG, R. ZnO tetrapod materials for functional applications. *Materials Today,* 2018, Vol. 21, No. 6, P. 631–651.

5. NEWTON, C.; WARBURTON, P. A. ZnO tetrapod nanocrystals. *Materials Today*, 2007, Vol. 10, No. 5, P. 50–54.

6. OLŠAUSKAITĖ V. *Analizės cheminiais metodais laboratoriniai darbai: 1 Dalis.* Vilnius: Vilniaus universiteto leidykla, 2015. P. 27. ISBN9786094595035.

7. PARA, A. *E*xtreme, blue-shifted photoluminescence from quantum confinement of core-shell ZnO. *Journal of Materials Science: Materials in Electronics*, 2017, Vol. 28, P. 18842–18848.

8. ALZOUBI, T.; QUTAISH, H.; AL-SHAWWA, E.; HAMZAVY, H. Enhanced UV-light detection based on ZnO nanowires/graphene oxide hybrid using cost-effective low-temperature hydrothermal process. *Optical Materials,* 2017, Vol. 77, P. 226–232.

9. FARHA, K.; FERESHTEK, Z.; LOGHMAN-ESTAKI, M. R.; RAZAVI, R. S. Different morphologies of ZnO nanostructures via polymeric complex sol-gel method: synthesis and characterization. *Journal of Sol-Gel Science and Technology*, 2012, Vol. 64, No. 1, P. 193–199.

10. JACOBS, B.; MAKSOV, A. B.; MUCKLEY, E. S.; COLLINS, L.; MAHJORI-SAMANI, M.; IEVLEV, A.; ROULEAU, C. M.; MOON, J.-W.; GRAHAM, D. E.; SUMPTER, B. G.; IVANOV, I. N. *UV-activated ZnO films on a flexible substrate for room temperature O$_2$ and H$_2$O sensing. Scientific Reports,* 2017, Vol. 7, No. 1, P. 6053.

11. TALAM, S.; KARUMURI, S. R.; NAGARJUNA, G. Synthesis, Characterization, and Spectroscopic Properties of ZnO Nanoparticles. *International Scholarly Research Notices*, 2012, P. 1–6.

IMPLEMENTATION OF LES COMBUSTION MODEL IN FLAMEFOAM SOLVER

J. Jaseliūnaitė, M. Povilaitis
Laboratory of Nuclear Installation Safety
Lithuanian Energy Institute
Breslaujos g. 3, LT-44403 Kaunas – Lithuania
Justina.Jaseliunaite@lei.lt

EXTENDED ABSTRACT

OVERVIEW

Undesired hydrogen combustion can occur during its use as a green fuel, industrial processes, or severe accidents in nuclear power plants [1]. Hydrogen is extremely flammable and has an increased combustion rate, enhanced reaction activity, and combustion limit compared with other mixtures such as methane/air. Consequently, it is important to investigate hydrogen combustion to facilitate risk management for industrial uses or accidental leakages.

Computational fluid dynamics (CFD) simulations have become one of the main tools for numerical investigations. One of the simplest CFD turbulence models is Reynolds averaged Navier-Stokes model (RANS), which is extensively used in engineering applications, whereas a more complex and numerically demanding large eddy simulation (LES) offers the capability to resolve turbulence phenomena in more detail [2]. LES is expected to be beneficial for combustion modelling since most of the integral flame properties are controlled by turbulent mixing, and LES directly simulates large-scale mixing and structures. It also allows explicit identification of fresh and burnt zones with different turbulence characteristics, which enables a more fundamental investigation of flame-turbulence interactions [3].

Therefore, to study flame-turbulence interaction with a custom OpenFOAM solver flameFoam, which up to now only supported RANS [4], the LES model had to be implemented. This paper present implemented model and test simulations of flame propagation in a duct with an obstacle. LES and RANS results are compared; it is shown that while LES qualitatively agrees with RANS, it provides more detailed and resolved transient evolution.

METHODS

Until the reported development, we used RANS and flame progress variable model with turbulent flame closure and selected turbulent burning velocity correlations to simulate combustion in our flameFoam solver, described in detail in a prior paper [4].

To implement the LES model, the source term of the progress variable balance equation was redefined:

$$S_c = \rho_u S_L \Xi_\Delta |\nabla c| S_c = \rho_u S_L \Xi_\Delta |\nabla c|, \tag{1}$$

where ρ_u – fresh mixture density, S_L – laminar flame speed, c – progress variable, and Ξ_Δ – subgrid-scale (sgs) flame wrinkling factor. The literature contains various models of Ξ_Δ, for this work Pitsch and Duchamp de Lageneste's [5] correlation was implemented:

$$\Xi_\Delta = 1 + \frac{u'_\Delta}{S_L} b_3 \left[\frac{\left(\frac{Da_\Delta}{Sc_\Delta}\right)}{\left(1+\frac{b_3^2}{b_1^2 Sc_\Delta} Da_\Delta\right)} \right]^{\frac{1}{2}},$$

(2)

where u'_Δ - sgs velocity fluctuations, Sc_Δ – sgs Schmidt number (assumed $Sc_\Delta = 0.5$), b_1, b_3 – coefficients ($b_1 = 2$, $b_3 = 1$), Da_Δ – sgs Damhohler number:

$$Da_\Delta = Ka^{-2} \left(\frac{u'_\Delta}{S_L}\right)^2,$$

(3)

where Ka – Karlovitz number:

$$Ka^2 = \left(\frac{u'_\Delta}{S_L}\right)^3 \frac{l_F}{\Delta},$$

(4)

where Δ – filter width, l_F – laminar flame thickness.

A 0.552 m long and 0.1 m in diameter duct with one annular obstacle of 0.05 m diameter was chosen as the computational domain (Fig. 1). Mesh with an approximate cell size of 2 mm and a total of 370 175 cells was used. The mixture consisted of 22.65% of H_2 and 77.35% of air. It was ignited in the centre of the base with an ignition radius of 0.005 m. Initial conditions and model constants are given in Table 1. The adiabatic and no-slip boundary conditions were applied to the walls and obstacles. RANS simulation used k-ω SST turbulence model and Bradley correlation, LES – Smagorinsky sgs model. The time step was adjusted to keep the Courant number below 0.35. The pressure and velocity fields were coupled by the PIMPLE method.
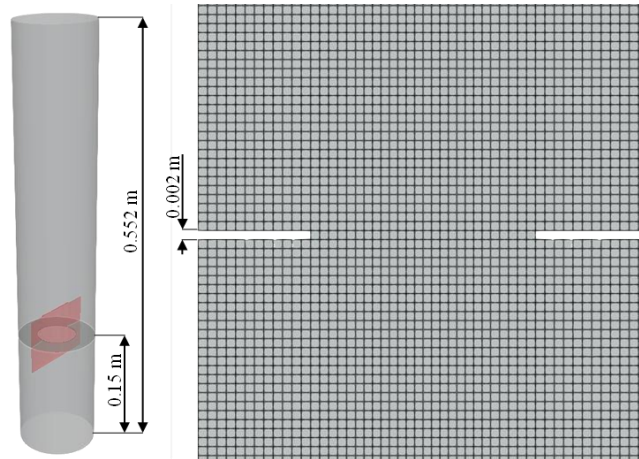
Fig. 1 Computational domain

Table 1 Initial data

Initial conditions		
Pressure	p	100 000 Pa
Temperature	T	293.15 K
The initial hydrogen volume fraction	X^{H_2}	0.2265
Laminar flame speed	S_{L0}	1.25 m/s
Model constants		
Turbulent Schmidt number	Sc_T	0.9
Lewis number	Le	0.5

RESULTS

Fig 2 presents the pressure evolution of both RANS and LES simulations. The pressure was probed at the top of the duct. LES results in higher total pressure, as well as more pronounced pressure peaks than RANS, which corresponds to the reflecting pressure waves.
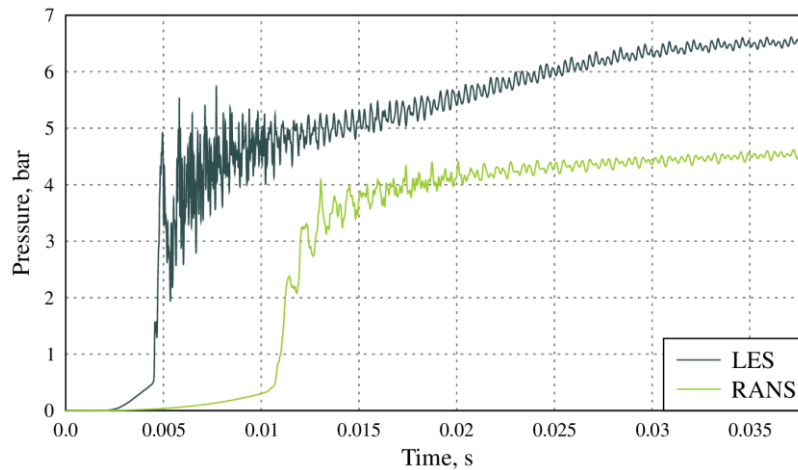
Fig. 2 Pressure evolution

LES and RANS flame front iso-surfaces and velocity fields are compared in Fig. 3. Even at the beginning, there already is a difference between flame fronts, RANS has a smooth hemispherical shape, while LES is distorted and recessed in the middle. Further, the flame is elongated due to obstacles and then stretched in the radial direction. LES results are more complex during the whole flame propagation process. This is also reflected in Fig. 4, showing flow streamlines, corresponding to the last shown moment in Fig. 3. In RANS simulation, flow is settled as a result of averaging, only the largest vortices behind the obstacle are simulated, while LES flow is more chaotic, vortices are interacting with each other thus causing higher speed. More accurate and realistic flame leads to a considerable increase in flame surface area, thus accelerating the combustion process and producing faster and higher pressure rises (Fig. 2).
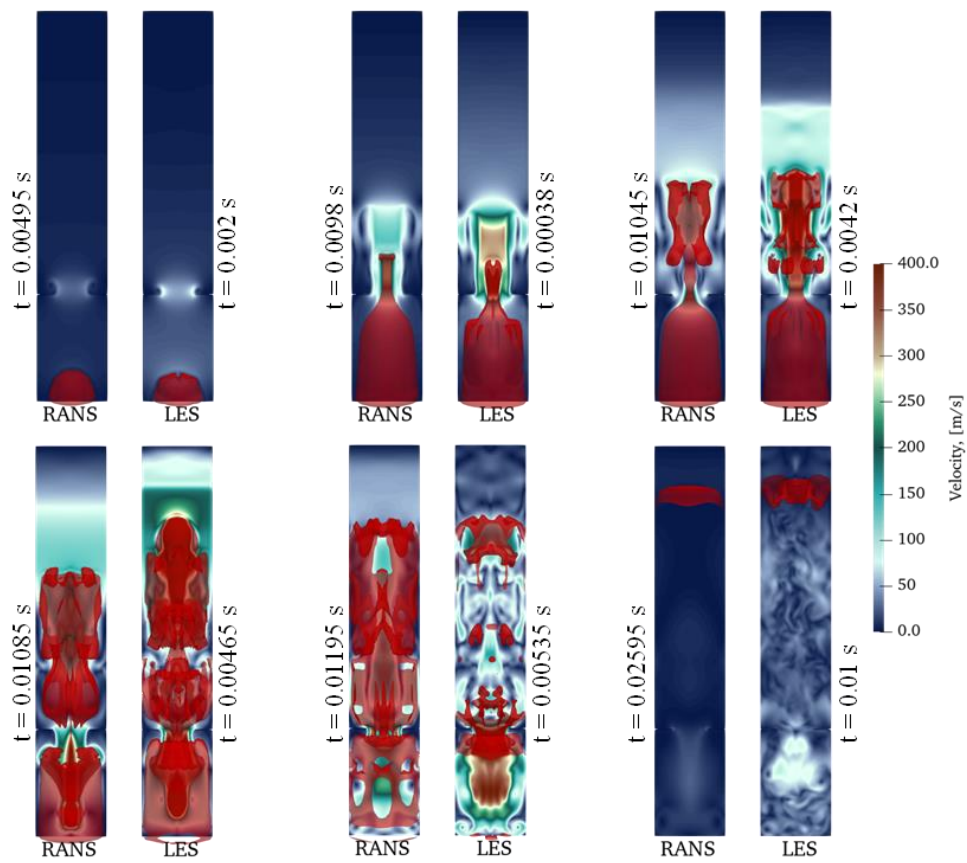
Fig. 3 Snapshots of velocity fields with flame front represented by the red
iso-surface (c = 0.9)
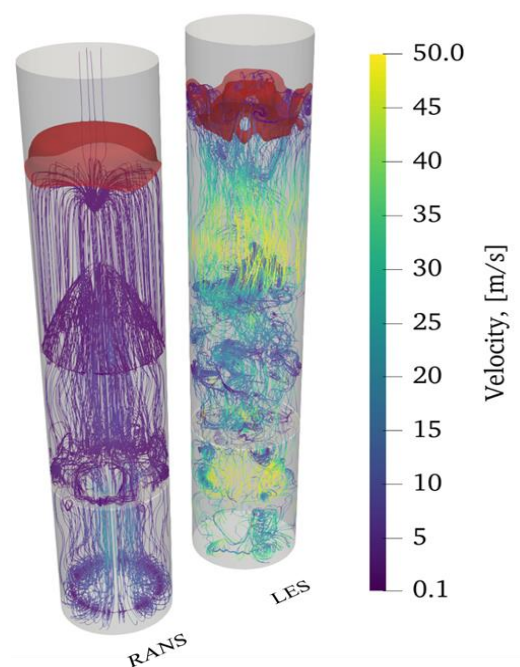
Fig. 4 Velocity streamlines

CONCLUSIONS

This paper presents combustion LES model implementation and simulations with flameFoam solver. Numerical simulation of premixed combustion in duct with one annular obstacle was performed. In LES simulation, fasten and more complex flame propagation and combustion processes were observed, while in RANS, averaging led to a much simpler flame front shape, slower combustion, and weaker pressure. While both simulations agree qualitatively, LES offers significant improvement through greater accuracy and the ability to produce more detailed characterization.

Keywords: Premixed combustion; large eddy simulation (LES); computational fluid dynamics (CFD); turbulent flame propagation

REFERENCES

1. YANG, F.; WANG, T.; DENG, X.; DAND, J.; HUANG, Z.; HU, S.; LI, Y.; OUYANG, M.. Review on hydrogen safety issues: Incident statistics, hydrogen diffusion, and detonation process. *International Journal of Hydrogen Energy*, 2021, Vol. 46, No. 61, P. 31467-31488.

2. LUO, G.; DAI, H.; DAI, L.; QIAN, Y.; SHA, C.; ZHANG, Y.; WU, B. Review on Large Eddy Simulation of Turbulent Premixed Combustion in Tubes. *Journal of Thermal Science*, 2020, Vol. 29, No. 4, P. 853-867.

3. VEYNANTE, D.; VERVISCH, L. Turbulent combustion modelling. *Progress in Energy and Combustion Science*, 2002, Vol. 28, P. 193-266.

4. POVILAITIS, M.; JASELIŪNAITĖ, J. FlameFoam: An open-source CFD solver for turbulent premixed combustion. *Nuclear Engineering and Design*, 2021, Vol. 383, P. 111361.

5. PITSCH, H. D.; LAGENESTE, L. D. Large-eddy simulation of premixed turbulent combustion using a level-set approach. *Proceedings of the Combustion Institute*, 2002, Vol. 29, No. 2, P. 2001-2008.

CATALYTIC PYROLYSIS TG-FTIR INVESTIGATION OF SUNFLOWER SEED SHELLS BIOMASS

I. Kiminaitė
Lithuanian Energy Institute
Breslaujos g. 3, LT-44403 Kaunas – Lithuania
+37037401879
ieva.kiminaite@lei.lt

ABSTRACT

Sunflower seed shells, an abundant lignocellulosic waste generated in the edible oil industry can be converted through pyrolysis to obtain bio-oils. The issue related to such biofuel is a high oxygen content that results in a lower calorific value compared to conventional fuels. A catalyst like ZSM-5 can be employed during the process to resolve the present drawback. For this aim, TG-FTIR research was carried out to investigate different biomass to ZSM-5 catalyst ratios (1:0, 1:1, 1:2, 1:5, 1:10) influence on the composition of volatile products evolved from renewable biomass – sunflower seed shells. Major compounds that were detected included alcohols, aromatic hydrocarbons, aliphatic species, carboxylic acids, CO, CO_2 and H_2O. It was evaluated that ZSM-5 concentration in a sample gives a significant impact on organic oxygen species such as alcohols and carboxylic acid formation with reference to a noticeable decrease in absorbance peaks observed in Py-FTIR spectrums. The greatest results were obtained with a ratio equal to 1:10. Although absorption increase in the range of IR rays that correspond to aromatic hydrocarbons formation was not confirmed. Thus, a supplementary investigation to corroborate the generation of higher-grade bio-oils from catalytic sunflower seed shells pyrolysis is required.

Keywords: Catalytic pyrolysis; biomass; bio-oil; ZSM-5

INTRODUCTION

According to the data of 2019, fossil fuels amounted to approximately 85 % of all fuel sources consumed worldwide [1], which raises concerns related with global warming, human health conditions as well as rapid depletion of the most demanded fuel source globally [2]. The current risk is caused by the particularly slow renewal of petroleum fuel that generally lasts millions of years [3]. Naturally, these issues pose a need for finding an alternative energy source, and renewable biomass is one of the favoured choices [4].

BIOMASS PYROLYSIS

Biomass pyrolysis is a thermochemical conversion technique of the lignocellulosic material to produce valuable chemicals as well as higher energy density liquid or solid fuels compared with the raw biomass as a biofuel itself [5]. Pyrolysis is a process during which stock is heated in the inert atmosphere or when the concentration of an oxidizing agent (e. g. oxygen) is not sufficient for total combustion [6]. Three main products form during biomass pyrolysis include non-condensable gasses, liquid bio-oil and biochar [7]. Distribution by quantity as well as qualitative characteristics of the pyrolysis products highly depends on the process conditions, namely the heating rate, pyrolysis temperature as well as vapor residence time in the pyrolysis zone [8]. Accordingly, lignocellulosic biomass is pyrolyzed, adjusting specific values of the process conditions to obtain adequate yield and composition of the desired product.

When the targeted product is a high energetic value liquid bio-oil – biomass particles of up to 2 mm size are pyrolyzed in a moderate temperature not higher than 650 °C applying an extremely high heating rate – thousands of Celsius degrees per second and a very short vapor residence time, usually less than 2 seconds [7]. Pyrolysis oil generally contains various complex hydrocarbons with high oxygen and water contents (water usually amounts to approximately 20 % of a total bio-oil volume) as well as high acidity that promotes corrosion [8]. These properties of bio-oil impede the utilization of this product as fuel and, therefore, must be upgraded to decrease oxygen content to improve the necessary qualities of bio-oil. A commonly applied method for bio-oil upgrading is catalytic hydro deoxygenation, by which oxygen is removed from bio-oil, followed by water formation [9]. This widely researched approach allows for the production of improved composition bio-oils from a renewable energy source – lignocellulose, and therefore it can be utilized as a petroleum fuel alternative.

CATALYTIC UPGRADING

Biomass pyrolysis bio-oil usually contains a high proportion of oxygenated compounds, oxygen share is over 35 – 40 % in this liquid [10]. To obtain high-grade bio-oils, catalytic pyrolysis can be employed in which zeolite catalyst is mostly applied due to their specific structure that assists in deoxygenation reactions [11]. Previous studies have revealed that among investigated zeolites, Zeolite Socony Mobil–5 (ZSM-5) catalyst with medium-sized pores is one effective option to generate high-grade bio-oils. Intermediate inner size of pores, arrangement of acidic sites (Bronsted and Lewis), as well as a steric hindrance effect determine ZSM-5 selectivity to olefins and aromatic hydrocarbons present in bio-oil [12]. Thus, a major influence on the composition of bio-oil is done during the reaction with the ZSM-5 catalyst resulting in bio-oil deoxygenation also a boost of aromatic species [13]. Y. Hu *et al*. [14] have conducted an investigation on *Enteromorpha clathrate* seaweed and cellulose catalytic co-pyrolysis, and it was estimated that with ZSM-5 catalyst, aromatic

hydrocarbons content in bio-oil increases from 1.7 % to 3.1 % comparing areas of this group chemicals signals in Py – GC/MS chromatograms. Authors have remarked the significant decrease in areas of oxygenated compounds signals as well. The proportion of aldehydes in bio-oil has reduced the most – from 4.8 % to 0.2 %.

The type of catalyst is a major decision to make depending on the product of interest. However, not only the catalyst but the portion of it added during pyrolysis is also an important factor. W. H. Chen *et al*. [15] investigated sawdust waste catalytic pyrolysis, and 4 different biomass to ZSM-5 catalyst weight ratios was chosen equal to 1:0; 1:1; 1:5; 1:10. GC/MS analysis of pyrolysis oils had revealed that the highest concentration of high calorific value aromatic hydrocarbons also as the main product of bio-oil had formed when the ZSM-5 portion by mass was the greatest and took 32.95 %. The lowest formation of oxygenated compounds during catalytic pyrolysis of sawdust was also found with the present ratio of 1:10.

METHODOLOGY

Sample Preparation

Lignocellulosic feedstock chosen for the thermogravimetric (TG) experiments was sunflower seed shells (SSS) biomass in the form of pellets (Ukraine). This shape of the feedstock was also chosen due to some appealing advantages like lower moisture content as well as ease of pulverizing SSS biomass to prepare it for TG analysis. The size of the feedstock particles is a vital factor that influences heat energy transfer as well as the activation energy with essential changes in a decomposition temperature and even evolving products [16]. Thus, SSS biomass pellets (Fig 1. – A) were firstly grinded by means of a rasp to obtain smaller biomass particles (Fig 1. – B), and this mass was sieved through a 250 microns mesh sieve afterwards to obtain an extremely fine fraction of particles in less than 250 μm diameter (Fig 1. – C).

Fig 1. Preparation of sunflower seed shells (SSS) biomass pellets for thermogravimetric analysis

Catalytic pyrolysis of prepared SSS biomass was performed by applying mesoporous ZSM-5 catalyst as described in the research of Chen *et al*. [15]. Five different weight ratios of biomass to catalyst were investigated as follows: 1:0, 1:1, 1:2, 1:5, and 1:10. Prior to a blending of these substances, the catalyst was grinded to a fine powder as well in order to ensure better contact between biomass and ZSM-5. The mixture was then placed in a clean crucible to investigate products by carrying out TG-FTIR and TG-GC/MS analyses.

Thermogravimetric Analysis

Thermogravimetric analysis (TGA) is an analytical technique applied for thermal stability of a material and proportion of volatile compounds estimation when a sample is heated at a persistent heating rate in an atmosphere of specific inertness. These properties of biomass are evaluated from thermogravimetric curves by weight changes upon heating to a defined temperature and experiment time alternatively [17]. The first derivative of such a thermogravimetric curve helps to indicate the main decomposition peaks of a material or even its constituents caused by a temperature elevation.

NETZSCH STA 449 F3 Jupiter instrument with SiC furnace was employed to conduct TGA experiments. Resistant to high temperatures, crucibles were used made of Al_2O_3 with 99.7 % purity. Obtained data were further processed and analysed by means of the NETZSCH Proteus – Thermal Analysis v. 6.0.0 program.

Proximate Analysis

Proximate analysis is an approach that can be implemented by means of TGA. Quantities of moisture, volatile matter, fixed carbon and ash in a material are determined with this technique by applying well-described, standard methods. Experiments were performed following the specification described by Mayoral *et al*. [18] with negligible alterations. The sample was firstly heated from 40 °C to 110 °C temperature in the inert atmosphere of nitrogen with a flowing rate of 60 ml/min and held at this point for 5 min to ensure well moisture evaporation [19]. After this step, the temperature was elevated to 900 °C in the inert atmosphere, and the isothermal step for 7 minutes started afterwards. Then, the temperature was reduced to 800 °C, and the compressed air supply to the oven began at a 25 ml/min flowing rate together with a decreased flow of the protective nitrogen gas at 35 ml/min to estimate the content of inorganic elements in a sample. In all dynamic steps, a constant temperature heating rate of 35 °C/min was used.

Py-FTIR Analysis

During the thermochemical conversion in the inert atmosphere of nitrogen, implemented by the TGA instrument, evolving volatile products were simultaneously analysed by means of two techniques. Fourier transform infrared spectroscopy (FTIR) analysis was carried out employing Bruker Tensor 27 TGA-IR analyser with a heated FTIR gas cell. Evolved gasses were entering FTIR cells through a heated to up to 250 °C transfer line to prevent the condensation of higher molecular weight compounds. Formed gaseous products were identified based on chemical groups by the Mercury-Cadmium-Telluride detector that operates in temperatures near that of liquid nitrogen (-196 °C). Absorption of IR rays was measured in the wavenumber range of 4500 – 650 cm^{-1}. Further processing of obtained spectrums was accomplished by the Opus v7.0 program.

RESULTS AND DISCUSSIONS

Biomass Characterization – Proximate Analysis

Proximate analysis of grinded SSS biomass was performed using thermogravimetric. Obtained TG curve is presented in Fig 2. A and the first derivative of the TG curve is in Fig 2. B. The first weight loss step in the inert atmosphere starting from 40 °C to approximately 190 °C temperature, is related to a moisture release from the sample, and it

makes up 4.71 % of the investigated biomass. The thermal decomposition of SSS biomass started at around 200 °C. Consequently, further temperature elevation caused the emission of volatile compounds taking up to 66.32 % of SSS biomass. The final solid product that develops during the biomass pyrolysis in the atmosphere of N_2 is biochar. To evaluate the fixed carbon content in the sample, formed biochar was incinerated by means of compressed air supply to the furnace that caused oxidation of biochar and accumulated inorganic compounds to form ash with a content of 7.21 % as a residual mass (Res. Mass in Fig 2. A). Fixed carbon content in SSS was evaluated by subtracting moisture, volatile mater and ash percentage from 100 % - fixed carbon amounted to 21.45 % of the SSS biomass weight.
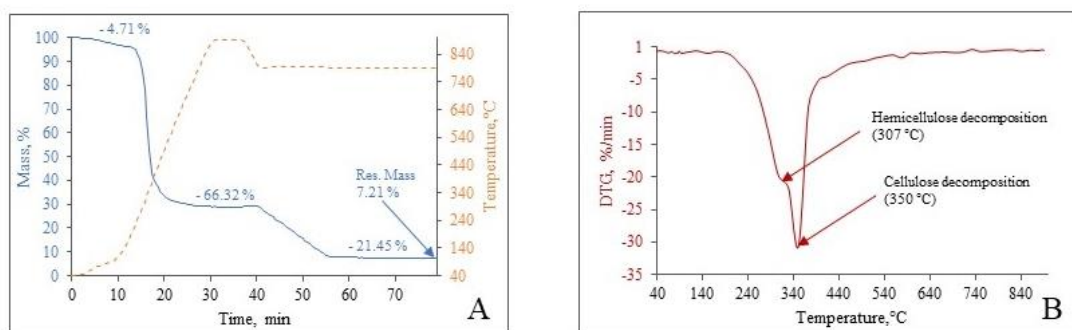
Fig 2. The thermogravimetric curve of SSS biomass proximate analysis
(A) and differential thermogravimetric curve derived from the
thermogravimetric curve in a pyrolysis segment (B)

Two apparent decomposition peaks of a SSS biomass were noticed in a DTG curve during the pyrolysis process. The first peak detects one of the major biomass components – hemicellulose thermal decomposition that occurred at 307 °C temperature with a 19 %/min decomposition rate. Although, the main thermal disintegration took place at 350 °C – cellulose decomposition temperature [20] that decomposed at a 30 %/min rate. The conclusion can be done that the investigated biomass contains higher cellulose content compared with the hemicellulose portion in it. The third biomass component – lignin, degrades in a wide range of temperatures thus, a single peak of decomposition is not always observed [21]. Various volatile products have evolved during the thermal decomposition (pyrolysis) of these main components of SSS biomass that were detected by means of FTIR analysis which results are described below.

PY – FTIR

Fig. 3. Illustrates the FTIR spectrums obtained during the feedstock pyrolysis with different ZSM-5 ratios in a sample at the main thermal decomposition temperature – approximately 350 °C. The main gaseous compounds detected according to the absorbance peaks in the FTIR spectrums are described onwards. Alcohols and aromatic compounds were detected at the lowest wavenumber ranges, respectively, at 1000 to 1300 cm^{-1} and 1367 cm^{-1}. Considerable formation of carboxyl acids was also identified, foremost acetic acid with an absorbance peak at 1766 cm^{-1} [22]. The evolution of CO gasses was detected too and attributed to the doublet at 2100 – 2170 cm^{-1}. A strong absorbance peak at 2350 cm^{-1} wavenumber was related to the development of CO_2 in high yields. Aliphatic compounds also have formed during the catalytic thermal degradation by pyrolysis of SSS biomass that appeared in the FTIR spectrums at the 2803 – 2925 cm^{-1} wavenumber range. Last but not

least, evaporation of H_2O at the main decomposition temperature proceeded as well and was detected at the range of $3573 - 2729$ cm^{-1}.
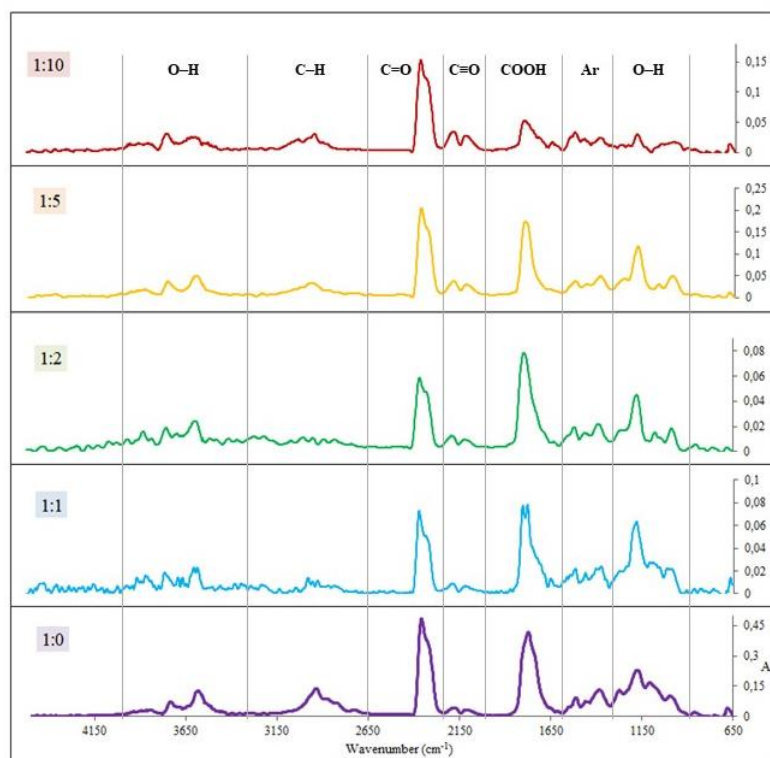
Fig 3. TG-FTIR spectrums of SSS biomass mixed with different ratios of ZSM-5 catalyst obtained at approximately 350 °C decomposition temperature

Intensities of the peaks in the obtained Py – FTIR spectrums were recalculated according to a sample mass since some variations in terms of the weight in different samples occurred. The unified results absorbance values of oxygenated compounds (alcohols and carboxyl acids) had a tendency to decrease with a rise of ZSM-5 share in a sample and were the lowest with the greatest ZSM-5 concentration. However, contrary to expectations, the IR absorbance peaks of aromatic hydrocarbons (Ar in Fig 3.) did not have a tendency to increase with a ZSM-5 share growth in a sample. Although, the increase in IR rays absorbance peak by CO has been identified, which is associated with oxygen transfer from higher molecular weight (condensable) species to gaseous, light mass CO molecules when the ZSM-5 concentration in a sample boosts. Chen *et al*. [15] made an investigation on catalytic level identification of ZSM-5 on a sawdust and sorghum distillery residue biomass and made a conclusion that the highest yields of aromatic hydrocarbons were obtained with biomass to catalyst ratio equal to 1:10, comparing results with the absorbance's obtained with higher ratios. This difference in results obtained may be determined by the variation in the investigated biomass dissimilarity.

CONCLUSIONS

The TG-FTIR approach was employed to evaluate the impact of ZSM-5 catalyst concentration on sunflower seed shells' biomass pyrolysis products. It was estimated that the most suitable ratio of biomass and catalyst was equal to 1:10 due to the considerable reduction of oxygenated species formation. However, absorption peaks of aromatic

hydrocarbons in FTIR spectrums had not elevated under the influence of different ZSM-5 concentrations in a sample. Therefore, the additional investigation in the reactor and actual concentrations of formed compounds is required to make conclusions about the improvement in the quality of sunflower seed shells biomass catalytic pyrolysis bio-oils.

REFERENCES

1. SUNDÉN, B. Hydrogen, batteries and fuel cells. Academic Press, 2019, P. 232. ISBN 978-0-12-816950-6.

2. MARTINS, F.; FELGUEIRAS, C.; SMITKOVA, M.; CAETANO, N. Analysis of fossil fuel energy consumption and environmental impacts in European countries. *Energies*, 2019, Vol. 12, No. 6, P. 964.

3. COYLE, D. E.; SIMMONS, A. R. *Understanding the Global Energy Crisis*. West Lafayette, Indiana: Purdue University Press, 2014, P. 320 p. ISBN 9781557536617.

4. ONG, H.C.; CHEN, W-H.; SINGH, Y.; GAN, YY. CHEN, C-Y.; SHOW, PL. A state-of-the-art review on thermochemical conversion of biomass for biofuel production: A TG-FTIR approach. *Energy Conversion and Management*, 2020, Vol. 209, P. 112634.

5. JAHIRUL, M.; RASUL, M.; CHOWDHURY, A.; ASHWATH, N. Biofuels Production through Biomass Pyrolysis —A Technological Review. *Energies* 2012, Vol. 5, No. 12 P. 4952–5001.

6. DEMIRBAS, A. Pyrolysis mechanisms of biomass materials. Energy Sources, Part A: *Recovery, Utilization and Environmental Effects*, 2009, Vol. 31, No. 13, P.1186-1193.

7. KAN, T.; STREZOV, V.; EVANS, TJ. Lignocellulosic biomass pyrolysis: A review of product properties and effects of pyrolysis parameters. *Renewable and Sustainable Energy Reviews*, 2016, Vol. 57, P. 1126–40.

8. BASU, P. *Biomass Gasification and Pyrolysis: Practical Design and Theory*. Elsevier, 2010. P. 365. ISBN 978-0-12-374988-8.

9. ATTIA, M.; FARAG, S.; CHAOUKI, J. Upgrading of Oils from Biomass and Waste: Catalytic Hydrodeoxygenation. *Catalysts*, 2020, Vol. 10, No. 12, p. 1381.

10. BANKS, S.W.; BRIDGWATER, AV. *Handbook of Biofuels Production*. Woodhead Publishing, 2016. p. 758. ISBN 978-0-08-100455-5.

11. VALLE, B.; PALOS, R.; BILBAO, J.; GAYUBO, AG. Role of zeolite properties in bio-oil deoxygenation and hydrocarbons production by catalytic cracking. *Fuel Processing Technology*, 2022, Vol. 227, P. 107130.

12. NISHU, L. I. U, R.; RAHMAN, M. M.; SARKER, M.; CHAI, M.; Li, C.; *et al*. A review on the catalytic pyrolysis of biomass for the bio-oil production with ZSM-5: Focus on structure. *Fuel Processing Technology*, 2020, Vol. 199. P. 106301.

13. ING, Y.L.; WANG, H.Q.; XIANG, M.; YU, P.; LI, R.Q.; KE, Q.P. The Effect of Ni-ZSM-5 Catalysts on Catalytic Pyrolysis and Hydro-Pyrolysis of Biomass. *Frontiers in Chemistry*, 2020, Vol. 8, P. 790.

14. HU, Y.; WANG, H.; LAKSHMIKANDAN, M.; WANG, S.; WANG, Q.; HE, Z.; *et al.* Catalytic co-pyrolysis of seaweeds and cellulose using mixed ZSM-5 and MCM-41 for enhanced crude bio-oil production. *Journal of Thermal Analysis and Calorimetry,* 2021, Vol. 143, No. 1, P. 827-842.

15. CHEN, W.H.; CHENG, C.L.; LEE, K.T.; LAM, S.S.; ONG, H.C.; OK, Y.S.; *et al.* Catalytic level identification of ZSM-5 on biomass pyrolysis and aromatic hydrocarbon formation. *Chemosphere*, 2021, Vol. 271, P. 129510.

16. AHMED, A.; AFOLABI, EA.; GARBA, MU.; MUSA, U.; ALHASSAN, M.; ISHAQ, K. Effect of particle size on thermal decomposition and devolatilization kinetics of melon seed shell. *Chemical Engineering Communications*, 2019, Vo. 206, P. 1228–1240.

17. RAJISHA, K. R.; DEEPA, B.; POTHAN, L. A.; THOMAS, S. *Interface Engineering of Natural Fibre Composites for Maximum Performance*. Elsevier, 2011. p. 241–74. ISBN 978-1-84569-742-6.

18. MAYORAL, M. C.; IZQUIERDO, M. T.; ANDRÉS, J. M.; RUBIO, B. Different approaches to proximate analysis by thermogravimetry analysis. *Thermochimica Acta*, 2001, Vol. 370, No. 1-2, P. 91–97.

19. ZHANG, W.; HENSCHEL, T.; SÖDERLIND, U.; TRAN, K-Q.; HAN, X. Thermogravimetric and Online Gas Analysis on various Biomass Fuels. *Energy Procedia*, 2017, Vol. 105, P. 162–167.

20. WATERS, C. L.; JANUPALA, R. R.; MALLINSON, R. G.; LOBBAN, L. L. Staged thermal fractionation for segregation of lignin and cellulose pyrolysis products: An experimental study of residence time and temperature effects. *Journal of Analytical and Applied Pyrolysis*, 2017, Vol. 126, P.380–389.

21. CASONI, A. I.; BIDEGAIN, M.; CUBITTO, M. A.; CURVETTO, N.; VOLPE, M. A. Pyrolysis of sunflower seed hulls for obtaining bio-oils. *Bioresource Technology*, 2015, Vol. 177, P. 406–409.

22. LIU, X.; HUA, W.; WU, S. Characterization of Thermo-Chemical Degradation and Pyrolysis Properties for Three Kinds of Biomass Residues. *BioResources*, 2016, Vol. 11, P. 8806–8819.

PLASMA SPECTROSCOPY OF ELECTRIC SPARK DISCHARGE BETWEEN SILVER GRANULES IMMERSED IN WATER

V. V. Ninyovskij, A. M. Veklich, V. F. Boretskij, A. A. Murmantsev
Taras Shevchenko National University of Kyiv
Volodymyrska Str. 64/13, 01601 Kyiv – Ukraine
+380635855647
ninjovskyj0volodymyr@gmail.com

EXTENDED ABSTRACT

OVERVIEW

Today, there is increasing interest in underwater discharge applications (particularly plasma of such discharges). On the one hand, it is due to the need to clarify the physical processes of current flow in such an environment, on the other hand, its practical application in biology, chemistry and electrochemistry. A special place in the variety of its applications is, in fact, the generation of nanoparticles of conducting materials [1]. In particular, for the past few decades, nanoparticles of silver have been gaining much attention and being used in almost every field, including medicine, catalysis, bio sensing, drug delivery, electronics, textile, photonics, optical sensor, nonlinear optical properties, water treatment, pigments, photographic, bactericide, anticancer agent, wound treatment, conductive composites, etc. [2].

It is necessary to investigate directly the process which occurs during nanoparticle formation in order to improve the characteristics and properties of solutions with nanoparticles. Namely, the plasma of discharges, which burns between granules used as a source of metal particles in the obtained solutions, should be studied. Optical emission spectroscopy is the most suitable approach to such investigations. On the one hand, this method enables obtaining with sufficient accuracy the main plasma parameters, such as temperature and electron density, which characterize the processes of nanoparticle formation. On the other hand, the technique does not perturb the plasma parameters and cannot affect the properties of the resulting product.

Therefore, the main aims of this work are the emission spectroscopy investigation of underwater discharge plasma between metal granules, specifically silver, as well as the determination of the main plasma parameters of such discharge – excitation temperature and electron density.

METHODS

A specially developed pulse power source was used to initiate a discharge between metal granules immersed in the deionized water. The voltage applied to electrodes causes a current flow along the chain of closely arranged pairs of granules in the stochastic switching mode. Investigation of the influence of technology process on dispersion and morphology of the

products of metal granules erosion during the formation of local spark discharges was performed by varying electrical parameters of the discharge circuit.

Plasma emission of such discharge was registered by Solar LS SDH-IV spectrometer. The spectral sensitivity of such a device was determined by a tungsten band-lamp and is taken into account during spectroscopy treatment.

The excitation temperature was determined using the method of the intensities ratio of the atomic and ionic Ag spectral lines according to the equation in an assumption of local thermodynamic equilibrium:

$$T^{-\frac{3}{2}}e^{-\frac{E_i-E_a-\chi_i}{kT}} = \frac{I_i}{I_a}N_e\frac{A_ag_a\lambda_i}{A_ig_i\lambda_a}\left(\frac{2\pi mk}{h^2}\right)^{-\frac{3}{2}}, \qquad (1)$$

where I_j, λ_j, A_j, g_j and E_j are emission intensity of the corresponding ionic or atomic spectral line, its wavelength, transition probability, statistic weight and energy of upper level, respectively. k_B is a Boltzmann constant, and T is a temperature.

The electron density of plasma with Argentum vapours in water was determined by the assumption that the Stark effect is a dominant mechanism of spectral lines broadening. In the case of H_α spectral line, the following equation was used [3]:

$$N_e[m^{-3}] = 10^{23} \times \left(\frac{w_s[nm]}{1.098}\right)^{1.47135}, \qquad (2)$$

where w_s is a Stark width of a spectral line.

The Voigt function was used for spectral line approximation to determine both the emission intensity and full width at half maximum FWHM. The necessity of utilization of this approach is caused by the importance of accounting for the instrument function of the used spectrometer.

RESULTS

The emission spectra of underwater discharge between silver granules were registered (see Fig. 1). As one can see, the Balmer H_α spectral line is observed on all spectra. This fact seems naturally for underwater discharge and gives a possibility to determine the electron density in plasma.
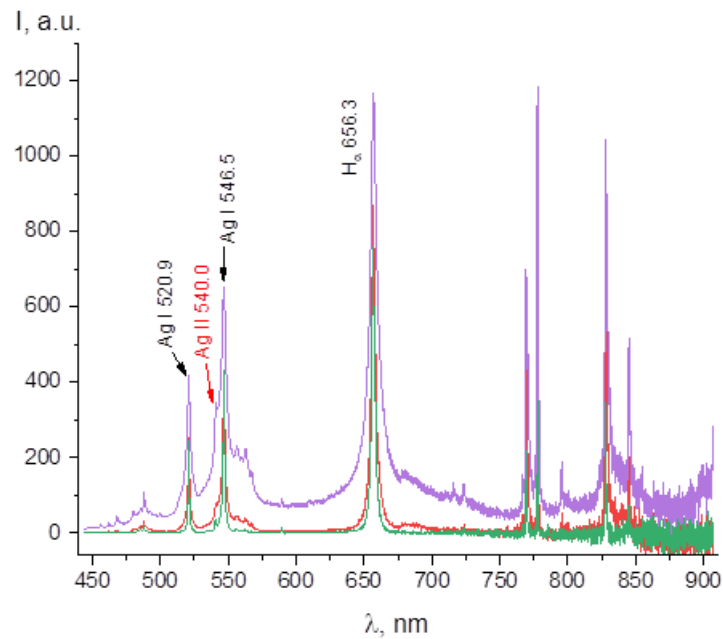
Fig. 1. Typical emission spectra of underwater discharge plasma between silver granules

As mentioned above, the Voigt function was used for spectral line approximation to determine the electron density from the FWHM of H_α spectral line. The typical profile of this line (black dots) and its typical approximation (red curve) are shown in Fig. 2. The instrumental function was taken into account as the Gaussian part of Voigt function ($w_G = 0.26$ *nm*).
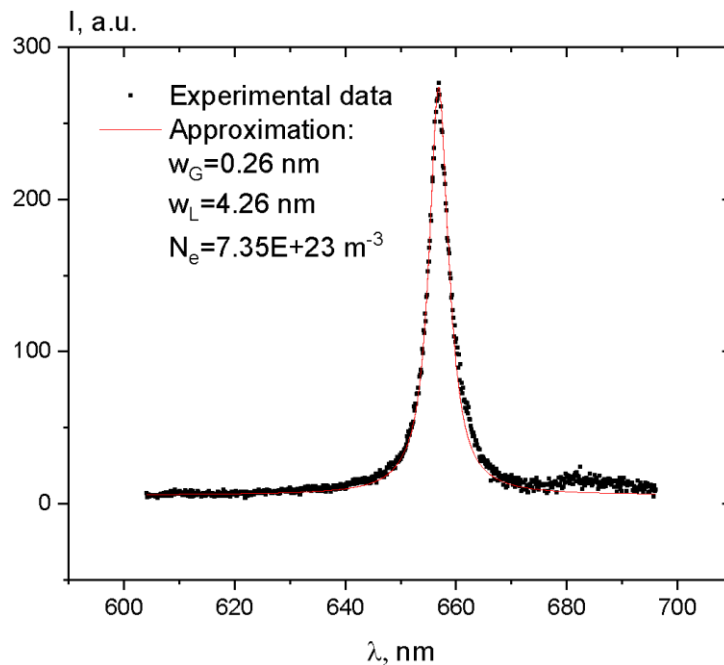
Fig. 2. Typical approximation of contour of Hα spectral line

CONCLUSIONS

The spectra of emission of plasma of underwater electric discharge between silver granules were registered. Such spectra were treated by taking into account of spectral sensitivity of

registering device. Optical emission spectroscopy was used to determine the main plasma parameters: electron density and excitation temperature. The temperature, in this case, was determined using the method of the intensities ratio of the atomic and ionic Ag spectral lines. The electron density was obtained on the assumption that the Stark effect is a dominant mechanism of spectral lines broadening.

Keywords: emission, plasma parameters, underwater discharge, silver granules, Stark effect

REFERENCES

1. VEKLICH, A.; TMENOVA, T.; ZAZIMKO, O.; TRACH, V.; LOPATKO, K.; TITOVA, L.; BORETSKIJ, V.; AFTANDILIANTS, Y.; LOPATKO, S.; ROGOVSKIY, I. Regulation of Biological Processes with Complexions of Metals Produced by Underwater Spark Discharge. *Springer Proceedings in Physics*, 2020, Vol. 247, P. 283-306.

2. SINGARAVELAN, R.; BANGARU SUDARSAN ALWAR, S. Electrochemical synthesis, characterization and phytogenic properties of silver nanoparticles. *Applied Nanoscience*, 2015, Vol. 5, No. 8, P. 983–991.

3. KONJEVIC, N.; IVKOVIC, M.; SAKAN, N. Hydrogen Balmer lines for low electron number density plasma diagnostics. *Spectrochimica Acta Part B*. 2012, Vol. 76, P. 16-22. doi: <10.1016/j.sab.2012.06.026>

PLASMA TORCH POWER INFLUENCE ON THE PROPERTIES OF ALUMINA COATINGS

A. Šuopys, V. Grigaitienė, L. Marcinauskas, R. Kėželis, R. Uscila, M. Aikas

Laboratory of Plasma Processing
Lithuanian Energy Institute
Breslaujos g. 3, LT-44403 Kaunas – Lithuania
+3706930573
airingas.suopys@lei.lt

EXTENDED ABSTRACT

OVERVIEW

Plasma spraying is one of the branches of thermal spraying, and it is widely used to develop various protective coatings. Coatings deposited by atmospheric plasma spray are being used for many applications that require protecting components against corrosion, high temperatures, and wear [1]. The structure of deposited coatings depends on plasma spray parameters, such as plasma flow rate, temperature, or distance between the plasma generator outlet and the substrate [2]. In atmospheric plasma spray, the feedstock powders are injected into the plasma jet, melted, accelerated and launched towards the substrate. Process control and optimization are essential to fulfilling actual application requirements [3-4]. The structure of the coating heavily depends on the melting of ceramic particles in the plasma and their impact velocity. In general, insufficient particle melting and low velocity at impact lead to high porosity levels and poor bonding between coating and the substrate [5]. Mechanical properties of plasma sprayed ceramic coatings highly depend on their microstructure and composition. Alumina is chemically stable and effective even at elevated temperatures, therefore, it is a base for the most popular high-performance ceramic coatings being used in the industry today [6]. Plasma torch power is considered to be one of the most effective ways to control the temperature and velocity of the plasma flow. To evaluate the influence of plasma torch power on the in-flight particles, studies are focusing on the interactions between particles and plasma jet [1], [7-12], but most research in this field is done using argon gas. Therefore the main aims of this research were to deposit Al_2O_3 coatings using air-hydrogen plasma and to investigate the effect of plasma torch power on the microstructure, elemental and phase composition of sprayed coatings.

METHODS

Al_2O_3 and Al_2O_3-13wt.TiO_2 coatings were sprayed on steel (P265GH) substrate at atmospheric pressure using a direct current plasma torch developed at the Lithuanian Energy Institute (Fig. 1) [13]. The steel substrates (dimensions of $40 \times 10 \times 6$ mm) were polished and chemically cleaned before the deposition process to ensure the smoothest possible surface. Air is used as the primary (flow rate of 3.7 g·s^{-1}) and the powder carrier gas (flow rate of 0.75 g·s^{-1}). Additionally, hydrogen is used as a secondary gas (flow rate of 0.06 g·s^{-1}).
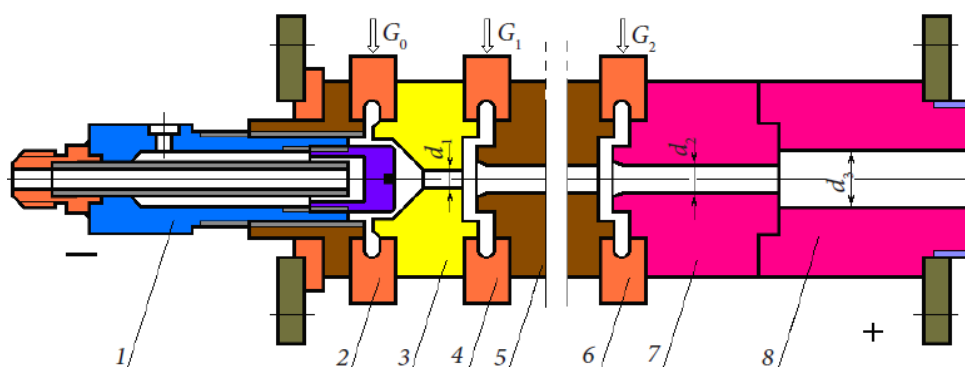
Fig 1. Plasma torch schematic. 1 – Cathode; 2, 4, 6 - insulating rings with plasma-forming gas with tangential injection channels; 3 – intermediate anode; 5, 7 – neutral sections; 8 – anode

The steel substrates were placed on the water-cooled sample holder, and the deposition duration was 60 s. The spraying distance was kept at 70 mm. Conventional 63–140 μm size Al_2O_3 (MOGUL PC15, purity 99.8 %) powders were used as a feedstock material. Coatings were formed using three different power modes: 28 kW, 35 kW and 42 kW, respectively. The elemental composition measurements were performed by energy-dispersive X-ray spectroscopy (EDS) using Bruker Quad 5040 spectrometer. The surface morphology of coatings was analysed by scanning electron microscopy (SEM) using a Hitachi S-3400N. The phase composition was determined using X-ray diffraction (XRD) using CuKα (λ = 0.154059 nm) radiation, and the mean square surface roughness (R_q) was measured using the AMBIOS XP-200 profilometer.

RESULTS

At the initial input power of 28 kW, the mean temperature of the plasma flow was 3100 K (Fig. 2). Increasing the input power to 35 kW, the plasma flow temperature increased to 3300 K. The highest temperature, 3700 K, was observed using 42 kW input power.
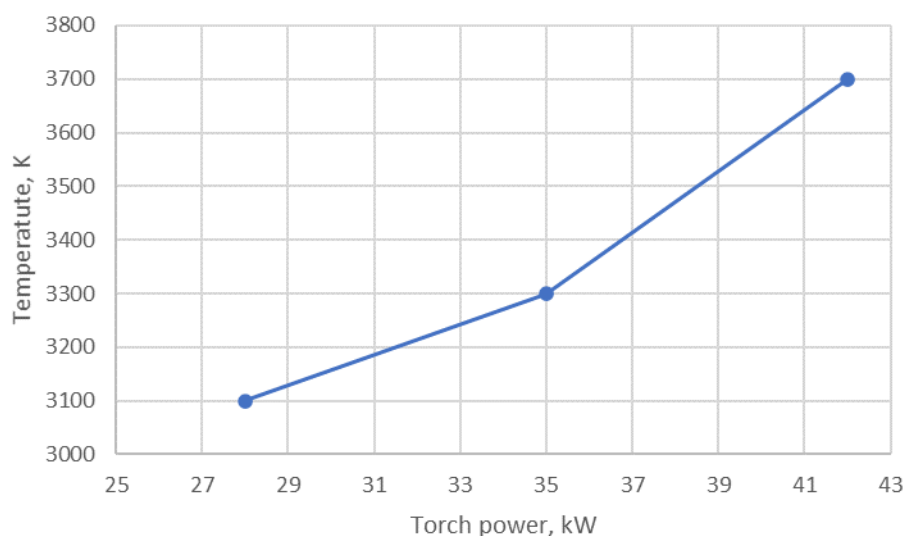
Fig 2. Plasma jet temperature as a function of input power

The same dependency was observed in the plasma flow velocity (Fig. 3). It increased from 970 m/s using 28 kW power to 1160 m/s at 42 kW input power.
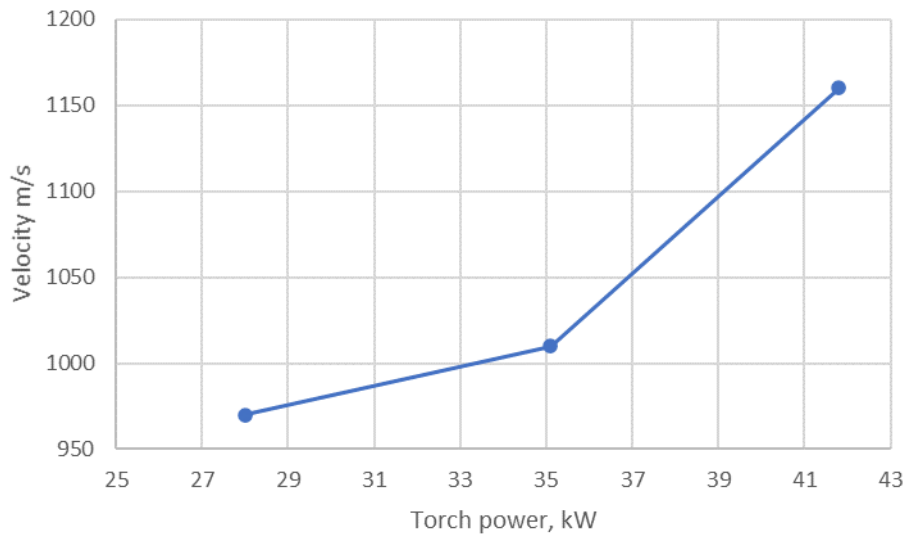
Fig 3. Plasma jet velocity as a function of input power

There are no visible cracks or delamination zones on all three samples. However, there are some more unmolten particles on the surface of alumina coating, using the lowest power (Fig. 4).
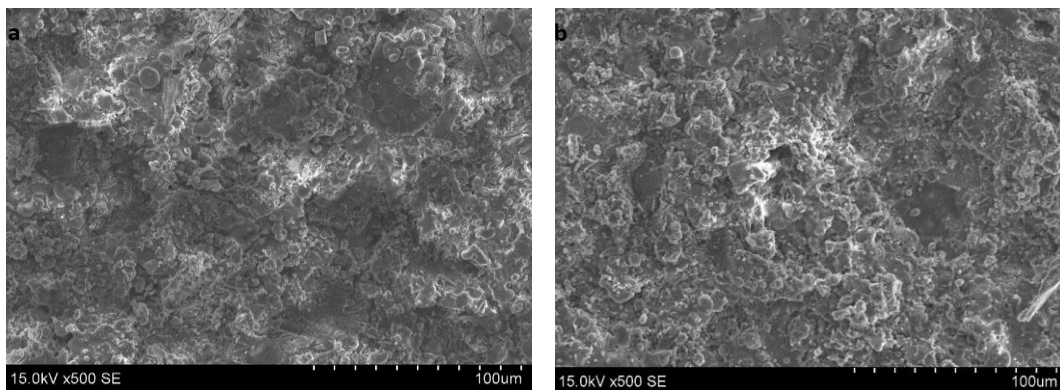
Fig 4. SEM micrographs of coatings surface a)25kW b) 42 kW

By increasing the power, the surface of the coating became smoother. The mean square surface roughness gradually decreased from 7µm (at 28 kW power) to 6, 3 µm (at 35 kW power) and to 5.5 µm (at 42 kW power), respectively.

In all three samples, the dominant phase was α-Al_2O_3. However, the increasing power increased the amount of γ-Al_2O_3 in the coating. This was attributed to the higher melting degree of alumina powders since the gamma phase forms only when the alumina particles are fully melted in the plasma jet. This was also confirmed by S. Yugeswaran et al. [14] and C. J. Li et al. [7]. In their work, the authors also concluded that the formation of the γ-Al_2O_3 phase was only possible from the fully melted alumina particles since the powders consisted of only the α-Al_2O_3 phase.

CONCLUSIONS

Alumina coatings were formed using atmospheric plasma spray at the plasma torch power in the range of 28 kW to 42 kW. The results indicated that the increased plasma torch power did not affect the elemental composition of the coatings. The quantity of aluminium and oxygen were the same, around 39% and 61%, respectively. The increase of the plasma torch input power resulted in a decrease in the α-Al_2O_3 phase and an increase of γ-Al_2O_3, thus contributing to a higher melting degree of alumina powders. This also caused surface roughness R_q to decrease from 7 μm to 5.5 μm

Keywords: (Plasma spraying, plasma torch, Al_2O_3)

REFERENCES

1. LV, M.; ZHANG, G.; GENG, H. Effect of spraying power on the microstructure and thermoelectric performance of plasma sprayed higher manganese silicide's films. *Surface and Coatings Technology*, 2019, Vol. 363, P. 152–160.

2. KAVALIAUSKAS, Ž.; KĖŽELIS, R.; MILIEŠKA, M.; MARCINAUSKAS, L.; VALINČIUS, V.; AIKAS, M.; USCILA, R.; BALTUŠNIKAS, A.; ŽUNDA, A. Influence of different plasma spraying methods on the physical properties of YSZ coatings, *Surfaces and Interfaces*, 2021, Vol. 24, P. 101120.

3. FRIIS, M.; PERSSON, C.; WIGREN, J. Influence of particle in-flight characteristics on the microstructure of atmospheric plasma sprayed yttria stabilized ZrO_2, *Surface and Coatings Technology*, 2001, Vol. 141, No. 2–3, p. 115–127.

4. ZHU, J.; WANG, X.; KOU, L.; ZHENG, L.; ZHANG, H. Prediction of control parameters corresponding to in-flight particles in atmospheric plasma spray employing convolutional neural networks, *Surface and Coatings Technology*, 2020, Vol. 394, P. 125862.

5. VAXEVANIDIS, N. M.; MANOLAKOS, D. E.; PETROPOULOS, G. P. Surface integrity and tribological behaviour of plasma sprayed alumina coatings on steel and aluminium substrates, *Tribology International,* 2004, Vol. 26, No. 1–2, P. 42–47.

6. MISRA, V. C.; CHAKRAVARTHY, Y.; KHARE, N.; SINGH, K.; GHORUI, S. Strongly adherent Al_2O_3 coating on SS 316L: Optimization of plasma spray parameters and investigation of unique wear resistance behaviour under air and nitrogen environment, *Ceramics International,* 2020, Vol. 46, No. 7, P. 8658–8668.

7. LI, C. J.; SUN, B. Effects of spray parameters on the microstructure and property of Al_2O_3 coatings sprayed by a low power plasma torch with a novel hollow cathode, *Thin Solid Films*, 2004, Vol. 450, No. 2, P. 282–289.

8. CALIARI, F. R.; MIRANDA, F. S.; REIS, D. A. P.; FILHO, G. P.; CHARAKHOVSKI, L. I.; ESSIPTCHOUK, A. Plasma torch for supersonic plasma spray at atmospheric pressure, *Journal of Materials Processing Technol*ogy, 2016, Vol. 237, P. 351–360.

9. XIONG, H. B.; ZHENG, L. L.; LI, L.; VAIDYA, A. Melting and oxidation behaviour of in-flight particles in plasma spray process, *International Journal of Heat and Mass Transf*er, 2005, Vol. 48, No. 25–26, P. 5121–5133.

10. ZHANG, D.; ZHENG, L.; HU, X.; ZHANG, H. Numerical studies of arc plasma generation in single cathode and three-cathode plasma torch and its impact on plasma spraying, *International Journal of Heat and Mass Transfer*, 2016, Vol. 98, P. 508–522.

11. GAO, Y., XU, X., YAN, Z., XIN, G. High hardness alumina coatings prepared by low power plasma spraying, *Surface and Coatings Technology*, 2002, Vol. 154, No. 2–3, P. 189–193.

12. MARCINAUSKAS, L. Deposition of alumina coatings from Nano powders by plasma spraying, *Medziagotyra*, 2010, Vol. 16, No. 1, P. 47–51.

13. VALINČIUS, V.; VALATKEVIČIUS, P.; KĖŽELIS, R. Plazminių procesų tyrimas ir technologijų kūrimas Lietuvos energetikos institute, *Energetika*, 2016, Vol. 62, No. 3, P. 124–144.

14. YUGESWARAN, S.; SELVARAJAN, V.; VIJAY, M.; ANANTHAPADMANABHAN, P. V.; SREEKUMAR, K. P. Influence of critical plasma spraying parameter (CPSP) on plasma sprayed Alumina-Titania composite coatings, *Ceramics International*, 2010, Vol. 36, No. 1, P. 141–149.

II.2. Thermal physics, fluid mechanics and metrology

LABORATORY TEST RIG FOR MEASUREMENT OF SEDIMENTATION VELOCITY OF PARTICLES IN MR LIQUIDS

W. Bańkosz

Cracow University of Technology
Faculty of Electrical and Computer Engineering
St. Warszawska 24, 31-155 Krakow – Poland
+48 880 267 939
wojciech.bankosz@doktorant.pk.edu.pl

EXTENDED ABSTRACT

OVERVIEW

In recent years, there has been a continuous increase in interest in intelligent materials. Intelligent materials are structures whose properties can be changed appropriately as a result of an applied external stimulus. Among this type of materials, one can distinguish, inter alia, materials using piezoelectric, electrostrictive and magnetostrictive phenomena as well as shape memory phenomena [1]. Each group of intelligent materials has different characteristic properties that change under the influence of external stimuli. The changing property is a parameter that determines the application potential of material. Magnetorheological fluids (MRF), whose rheological properties change as a result of the applied magnetic field, are of great interest [2, 3]. MR fluids consist of three main components: magnetic particles, carrier fluid and appropriate additives. Ferromagnetic particles of iron (Fe), cobalt (Co), nickel (Ni) or their oxides are very often used as magnetic particles. Particular attention is paid to carbonyl iron, which is characterized by high magnetic properties. Mineral oil, engine oil as well as any low-viscosity synthetic oil are used as the carrier fluid. It is essential that the appropriate carrier fluid does not chemically react with the active particles. As additives, usually surfactants are used, whose task is to reduce agglomeration and sedimentation of magnetic particles. One of the commonly used additives are lithium stearate and ferrous oleate [4 - 6]. MRF respond to changes in the intensity of the external magnetic field. In the absence of forcing, the magnetic molecules are not magnetized, so the total magnetic vector is zero. In such a case, the liquid retains the properties of an ordinary Newtonian fluid, which means that the tangential stresses τ increase proportionally to the liquid deformation velocity [7, 8]. Elementary particles of MRF placed in the area of the magnetic field become magnetized, so they can be considered as microscopic magnets [9]. Due to their unique properties, MRF are used in intelligent drive systems (clutches, brakes), damping systems (shock absorbers, vibration dampers and energy absorbers), as well as in surface treatment - magnetorheological polishing [10]. A significant limitation in the application of MRF is the agglomeration and sedimentation of magnetic particles. In order to select the appropriate additives limiting these processes, it is necessary to measure the MFR particle falling velocity. For this purpose, the most frequently chosen method is visual inspection during sedimentation observation. The determination of the particle falling velocity is based on the determination of the height of the liquid column as a function of time [11]. A visual assessment of sedimentation was presented by Aruna et al. [12], Zhang et al. [13] as well as Zhu [14]. Due to the problems related to the

determination of sedimentation by the visual method (problems include low accuracy and achieving repeatable results), the aim of this work was to design a test rig for measuring the falling rate of MFR particles. The assumption of the work was to automate the process allowing for more precise measurements. In addition, the creation of such a stand will significantly accelerate and facilitate the study of MRF. Thanks to the use of components such as a DC motor, drive shaft and electronic control, data acquisition and the processing of results based on them will improve and accelerate the work of future users of this platform.

METHODS

The concept of the laboratory model is based on the creation of an automated station, which includes the following elements: a PLC (Programmable Logic Controller - control over the entire process of the measurement), a SCADA system (Supervisory Control And Data Acquisition – allowing to visualize the operation of the executive system and displaying the collected data), an RLC meter (its advanced possibilities enable easy data acquisition and sending data to SCADA), measuring sensor (innovative method of measuring MRF sedimentation - induction coil made of winding wire), station platform (supporting structure, where individual parts of the entire model can be embedded).

RESULTS

In the initial phase of the project, a computer model was created using the vector graphics editor - AutoCAD Inventor by AutoDesk, which facilitated the subsequent implementation of the entire structure. After making a sketch of the prototype, the next step was to make the measuring platform from pre-prepared elements. Figure 1 shows the prototype and the actual form of the test rig for measuring the sedimentation of the MRF.
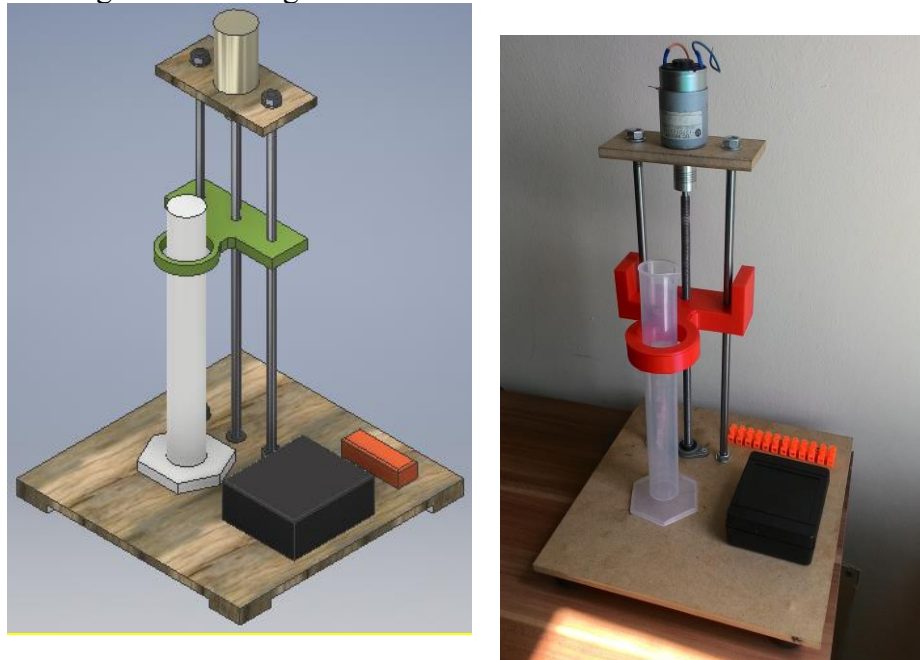
Fig. 1. Computer model versus real platform for liquid sedimentation measurement

CONCLUSIONS

The aim of this project was to create a laboratory test rig for measuring the velocity of falling ferromagnetic molecules. The posted technical documentation, software and collected data

testify to the positive implementation of the project topic. The presented data clearly shows that with the passage time the boundaries of individual sedimentation areas change their location - this proves the correctness used measurement method. The developed solution can be used in the future to test magnetorheological fluids applied in the production of couplings, shock absorbers and vibration dampers. The presented method allows to determine the sedimentation velocity of particles present in the tested liquid. The solution of the work, proposed by the author, in the form of a laboratory test rig is easy to use and can be quickly analysed.

Keywords: magnetorheological fluid, PLC, SCADA, sedimentation, velocity

REFERENCES

1. ASHTIANI, M.; HASHEMABADI, S. H.; GHAFFARI, A. A Review on the Magnetorheological Fluid Preparation and Stabilization. *Journal of Magnetism and Magnetic Materials*, 2015, Vol. 375, P. 716-730.

2. KCIUK, M.; TURCZYN, R. Properties and application of magnetorheological fluids. Journal of *Achievements in Materials and Manufacturing Engineering*, 2006, Vol. 18, No. 1-2, P. 127-130.

3. BICA, I.; LIU, Y. D.; CHOI, H. J. Physical characteristics of magnetorheological suspensions and their applications. *Journal of Industrial and Engineering Chemistry*, 2013, Vol. 19, P. 394–406.

4. KUMAR, J. S.; PAUL, P. S.; RAGHUNATHAN, G.; ALEX, D. G. A review of challenges and solutions in the preparation and use of magnetorheological fluids. *International Journal of Mechanical and Materials Engineering*, 2019, Vol. 14, P. 1-18.

5. COON, A.; YANG, T. H.; KIM, Y. M.; KANG, H.; KOO, J. H. Application of Magneto-Rheological Fluids for Investigating the Effect of Skin Properties on Arterial Tonometry Measurements. *Frontiers in Materials*, 2019, Vol. 6.

6. HAJALILOU, A.; AMRI MAZLAN, S.; LAVVAFI, H.; SHAMELI, K. Magnetorheological Fluid Applications. In: Field Responsive Fluids as Smart Materials. *Engineering Materials*. Springer, 2016. ISBN 978-981-10-2494-8.

7. OLABI, A. G.; GRUNWALD, A. Design and application of magneto-rheological fluid. *Materials and Design*, 2007, Vol. 28, P. 2658–2664.

8. ZAREIE, S.; ZABIHOLLAH, A. The Recent Advances in Magnetorheological Fluids-Based Applications. *Emerging Trends in Mechatronics*, 2020. ISBN 978-1-78984-319-4.

9. BASTOLA, A. K.; HOSSAIN, M. A review on magneto-mechanical characterizations of magnetorheological elastomer. *Composites Part B*, 2020, Vol. 200, P. 108348.

10. GADEKAR, P.; KANTHALE, V. S.; KHAIRE, N. D. Magnetorheological Fluid and its Applications. *International Journal of Current Engineering and Technology*, 2017, P. 932-937.

11. KIKUCHI, T.; KUMAGAE, T.; ABE, I.; INOUE, A. Particle Sedimentation in Magnetorheological Fluid and its effect. *IEEE International Conference on Advanced Intelligent Mechatronics* (AIM), 2017, P. 767-772.

12. ARUNA, M. N.; RAHMAN, M. R.; JOLADARAS, S.; KUMAR, H. Investigation of sedimentation, rheological, and damping force characteristics of carbonyl iron magnetorheological fluid with/without additives. *Journal of the Brazilian Society of Mechanical Sciences and Engineering*, 2020, Vol. 42, P. 228-241.

13. ZHANG, Y.; LI, D.; ZHANG, Z., The study of magnetorheological fluids sedimentation behaviours based on volume fraction of magnetic particles and the mass fraction of surfactants. *Materials Research Express*, 2019, Vol. 6, P. 1-14.

14. ZHU, W.; DONG, X.; HUANG, H.; QI, M. Iron nanoparticles-based magnetorheological fluids: A balance between MR effect and sedimentation stability. *Journal of Magnetism and Magnetic Materials*, 2019, Vol. 491, P. 165556.

15. CHOI, Y.; XIE, L.; WERELEY, N., Testing and analysis of magnetorheological fluid sedimentation in a column using a vertical axis inductance monitoring system. *Smart Materials and Structures*, 2016, Vol. 25, P. 11.

OBSERVING SIZE EFFECTS IN THE THERMAL BEHAVIOUR OF ROCKS

A, Fehér

Department of Energy Engineering, Faculty of Mechanical Engineering,
Budapest University of Technology and Economics
Műegyetem rkp. 3., H-1111 Budapest – Hungary
feher@energia.bme.hu

R. Kovács

Department of Energy Engineering, Faculty of Mechanical Engineering
Budapest University of Technology and Economics
Műegyetem rkp. 3., H-1111 Budapest – Hungary

Department of Theoretical Physics, Wigner Research Centre for Physics, Institute for
Particle and Nuclear Physics, Budapest – Hungary

ABSTRACT

The classical constitutive equation for heat conduction, Fourier's law, plays an essential role in the engineering practise and holds only for homogeneous materials. However, most of the materials consist of certain sort of heterogeneity, such as porosity, cracks, or different materials are in contact.

We used heat pulse measurement method ("flash method"), a standard method in the engineering practise, to measure the thermal diffusivity of various rock samples. During the heat pulse experiment the pulse reaches the front of the sample, and the temperature of the rear is measured with a thermocouple and recorded. We found that the rear side temperature history can deviate from the one predicted by Fourier's law. Therefore, in the evaluation of the experimental data, we used an analytical solution of a non-Fourier model, called Guyer-Krumhansl equation. We present the measurement methodology and data recorded together with the evaluation procedure for two rock samples of types Szaszvar and Szarsomlyo Limestone formations from Hungary. We observed the size dependence of thermal diffusivity for both Fourier and non-Fourier models. Additionally, we also observed the size dependence of the non-Fourier effects, vanishing for thicker samples.

Keywords: heterogeneous materials, non-equilibrium thermodynamics, size effects, Guyer-Krumhansl equation

INTRODUCTION

Engineering practice requires reliable methods to determine the necessary parameters that are sufficient to characterise the behaviour of a material. In the following, we focus on the thermal characterisation of materials, with particular emphasis on heterogeneous materials such as rocks. In previous publications [1, 2], it has been reported that the presence of different heterogeneities can lead to non-Fourier thermal conduction effects due to the simultaneous presence of thermal conduction channels with different characteristic times. Such effects can be observed in the so-called "flash" (heat pulse) experiment, in which the front face of the specimen is excited by a short thermal pulse and the temperature is measured on the rear side [3-5]. This temperature history is used to determine the thermal diffusivity to characterise the transient behaviour of the material.

This non-Fourier effect occurs over a specific time interval, as Figure 1 shows for a typical outcome of the flash experiments; this called over-diffusion. After that interval, the Fourier equation seems to be a suitable choice for modelling, the effect of heterogeneities disappears, furthermore there is no difference between the steady-states described by the Fourier and the non-Fourier heat equation, only the transient evolution of temperature differs in these cases. Our experimental experience suggests that the existence of over-diffusion depends on a number of factors, such as the sample thickness, the typical parallel time scales and the excitation (i.e., boundary conditions) [6].

The evaluation procedure for flash experiments with non-Fourier heat equations is not yet standard. Even numerically, finding solutions to non-Fourier models is not straightforward, some methods may lead to incorrect solutions [7], and commercial built-in algorithms are not efficient for these models.
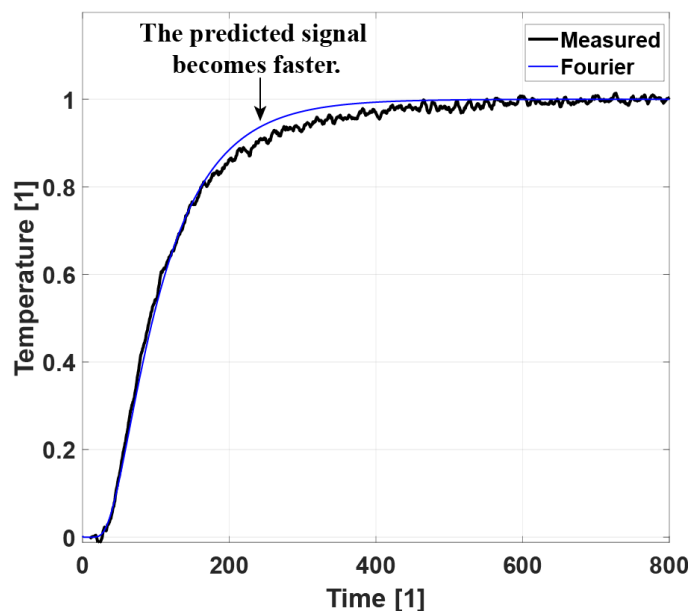
Fig. 1. Measured rear side temperature history for the rock sample and the prediction provided by Fourier's theory, where the dimensionless time is scaled by the heat pulse, which is 0.01 sec [8].

Models for Heat Pulse Experiments

Although there are several generalisations of Fourier's law in the literature [9-14], there is only one of them that has been shown to be reasonable beyond Fourier theory, called the Guyer-Krumhansl (GK) equation [3]. The constitutive equation reads in one spatial dimension

$$\tau_q \, \partial_t q + q + \lambda \, \partial_x T - \kappa^2 \, \partial_{xx} q = 0. \tag{1}$$

In the equation, τ_q is the relaxation time of the heat flux q and κ^2 is a kind of 'dissipation parameter', usually related to the mean free path in kinetic theory. The $\partial_{xx} q$ in the constitutive equation allows to properly characterise the so-called over-diffusive propagation, presented in Figure 1. When the equality $\kappa^2/\tau_q = \alpha$ holds (with $\alpha = \lambda/(\rho c)$), we call it Fourier resonance .condition as that setting recovers the solutions of Fourier equation [2, 16]. Equation (1) is the time evolution equation for the heat flux, and to have a mathematically and physically complete system we need the balance of the internal energy e,

$$\rho c \partial_t T + \partial_x q = 0, \tag{2}$$

in which the equation $e = cT$ is used, where c is the specific heat and ρ is the mass density. All these coefficients are constant, we assume only rigid bodies without a volumetric heat source.

Fig. 2 shows the typical rear side solutions for the Fourier, Maxwell-Cattaneo-Vernotte (MCV) and GK models. It can be seen that while the MCV equation gives sharp wave fronts for the solution, the GK equation provides a significantly better character with the measured data, showing the observed thermal behaviour. Therefore, the GK equation appears to be a necessary extension of the Fourier equation that covers practical needs to determine the thermal properties of heterogeneous materials as accurately as possible.
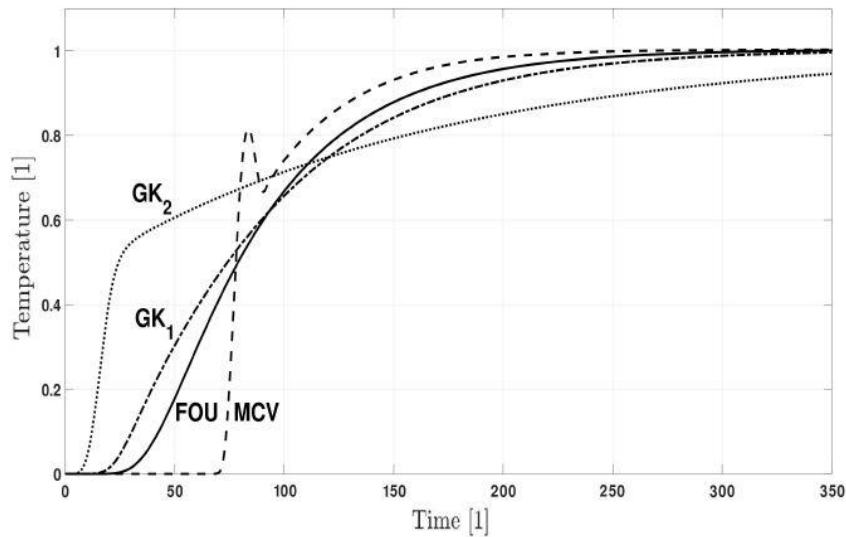
Fig. 2. Typical rear side temperature histories for the Fourier ("FOU"), Maxwell-Cattaneo-Vernotte ("MCV") and Guyer-Krumhansl ("GK1" and "GK2") equations. For the GK model, two different solutions are depicted here: "GK1" is a slightly over-diffusive one showing similar outcome with the experiments, while "GK2" is a strongly over-diffusive solution [8].

In the following, we briefly present the experimental settings together with the applied evaluation procedure for both Fourier and GK heat conduction equations. While for the Fourier equation the evaluation follows a standard, well-known methodology, the utilisation of the GK equation is not straightforward. Therefore, we shortly summarise the developed evaluation method based on [8] in Sec. 3. In Sec. 4., we present our new observations for Szaszvar and Szarsomlyo Limestone Formations in which we found size effects for both the thermal diffusivity and the over-diffusive non-Fourier effect.

HEAT PULSE EXPERIMENT

The heat pulse experiments are used to measure the thermal diffusivity of a material by registering the rear side temperature history. For the specified settings, see Fig. 3 below. The front surface a sample is painted black for absorption, and the rear side is coated with silver in order to achieve good contact with the thermocouple. A flash lamp generates the heat pulse; its length is 0.01 seconds. For further details, we refer to the earlier papers published by our group, [1, 2, 6, 15].
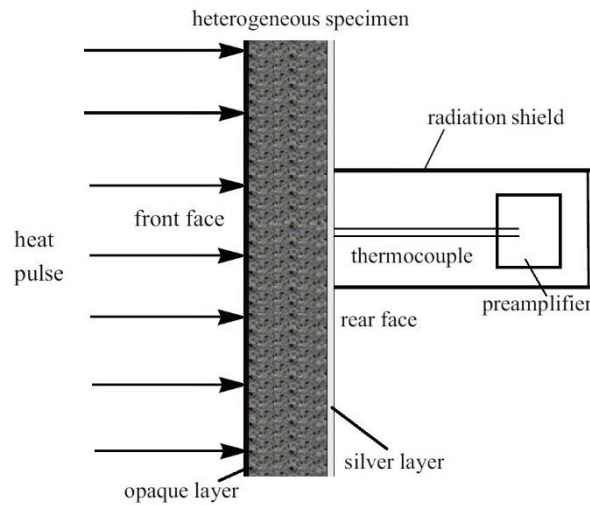
Fig. 3. Arrangement of the heat pulse experiments [15].

EVALUATION METHOD

Evaluation with the Fourier-Theory

The analytical solution of the Fourier equation for the rear side is [15]:
$$T(x = 1, t) = Y_0 \exp(-ht) - Y_1 \exp(x_F), \qquad x_F = -2h - \alpha\pi^2, \qquad t > 30 \qquad (8)$$

Which is analogous with the classical known 'one-term solution'. First, the heat transfer coefficient h is estimated by selecting two temperature values (T_1 and T_2, see Figure 4) at the decreasing part of temperature history and reading the corresponding time instants (t_1 and t_2). In this region $\exp(x_F t) \approx 0$,
$$h = -\frac{\ln\left(\frac{T_2}{T_1}\right)}{t_2 - t_1} \ . \qquad (9)$$

While h can be determined from the rear side temperature history, it should be noted that the sample is small and as long as $h \cdot A_h$ is constant (A_h is the surface area where heat transfer

occurs), it is not necessary to determine a heat transfer coefficient for all surface. In Fourier theory, the thermal diffusivity can be expressed explicitly [8, 15], i.e.

$$\alpha_F = 1{,}38 \cdot \frac{L^2}{\pi^2 t_{1/2}}, \tag{10}$$

and can be determined immediately after reading $t_{1/2}$. The thermal diffusivity is the ratio of the thermal conductivity λ and the specific heat capacity ρc. Then comes the maximum of the temperature history (T_{max}), where the moment of time t_{max} can be read when T_{max} occurs. This gives the heat transfer coefficients, the thermal diffusivity and T_{max}, which are used in the Guyer-Krumhansl theory.
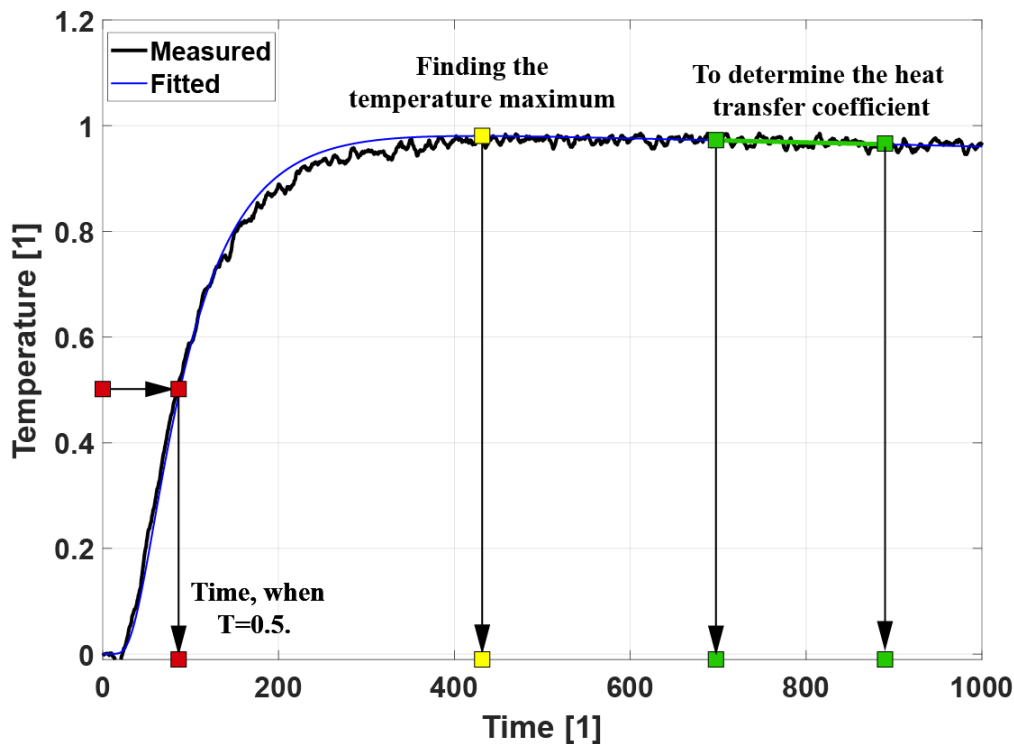
Fig. 4. Schematic representation of the Fourier evaluation method, where the dimensionless time is scaled by the heat pulse, which is 0.01 sec. The green section shows the determination of the heat transfer coefficient, the red squares show the meaning of $\boldsymbol{t_{1/2}}$ and the yellow squares show the location of the maximum temperature [8].

Evaluation with the Guyer-Krumhansl Theory

The situation becomes more difficult in this case, because in contrast to the Fourier theory, it consists of two 'time constants' (x_1 and x_2) instead of one (x_F in Fourier theory). Consequently, it is not easy to find these constants. To check the effect of the simplifications made in the following, a parameter analysis was carried out for all possible τ_q and κ^2 values that may be possible in practice and beyond. However, beyond these, we always had to restrict ourselves to a region $3 > \kappa^2/(\alpha\tau_q) \geq 1$. The lower limit expresses the Fourier case, and all other combinations fall in the over-diffusive region. The highest ratio observed in the experiments so far has been around 2.5, so a value of 3 should be appropriate. For κ^2, the region is $0.02 < \kappa^2 < 1$. We would like to emphasize that the GK theory is not restricted to this region, it also allows the under-diffusive ('wave-like') case, which would be most similar

to the MCV solution (Figure 2). In the GK theory, the rear side temperature history can be expressed as follows [15]

$$T(x = 1, t > 40) = Y_0 \exp(-ht) - Z_1 \exp(x_1 t) - Z_2 \exp(x_2 t), \ x_1, x_2 < 0, \quad (11)$$

Which is also a 'one-term solution'. In the following, we present a step-by-step [8] approach to the determination of the GK parameters, which is illustrated in Figure 5.

Step 1/A. It can be observed (Figure 1) that the temperature predicted by Fourier's theory is close to the measured temperature at the beginning of the process, then rises more rapidly as it approaches the maximum. In other words, the same temperature is reached more quickly in this region with Fourier's theory (usually around 0.7-0.95). Mathematically, this can be expressed by formally writing the equations of Fourier and GK theory as follows where the fraction on the right is close to 1. It would be possible to introduce a correction factor for x in the iteration procedure if we knew more about τ_q and κ^2. After rearrangement, we obtain the following closed formula for x_1:

$$x_1 = x_F \frac{t_{F1} - t_{F2}}{t_{m1} - t_{m2}}. \quad (16)$$

We take 80-90% of T_{max}, and then take the mean of the next 20 subsequent measurement points as x_1. Mathematically, closer data pairs should perform better, but this is not the case due to the uncertainty of the measurement data. In our experience, the mean offers a more consistent value for x_1.
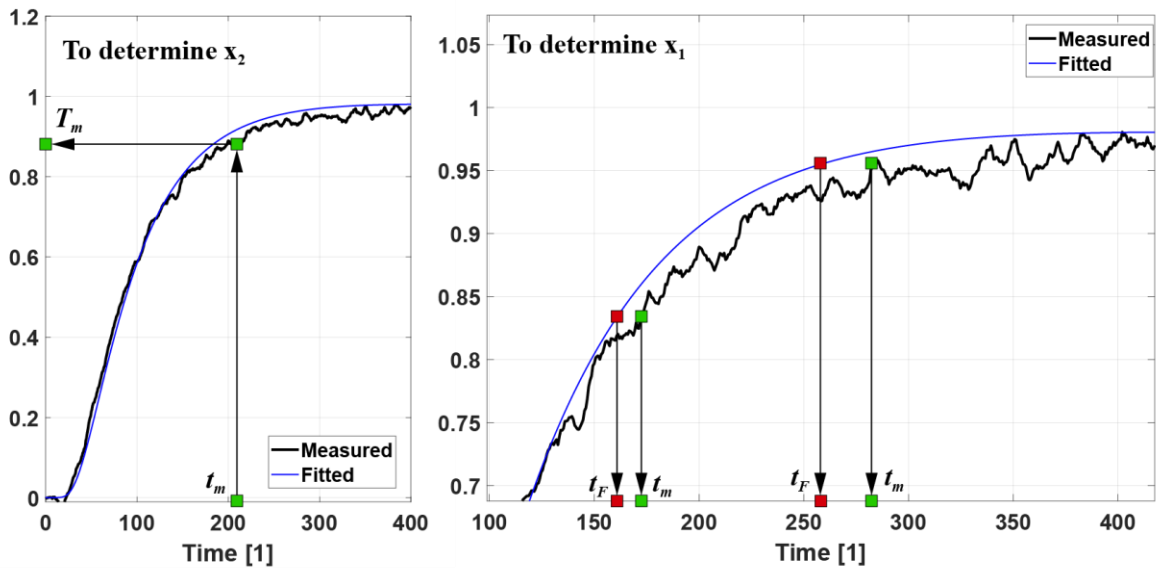
Fig. 5. The schematic representation of the evaluation method using the Guyer-Krumhansl theory. Here, the 'fitted curve' belongs to the Fourier equation [8].

- Step 1/B. In parallel with part A, we can determine the coefficient Z_1 for each t_m and each corresponding $x_{1,m}$,

$$Z_{1,m} = -\exp(-x_{1,m} t_m)(T_m - Y_0 \exp(-ht_m)) \quad (17)$$

where the subscript m represents the value for a measurement point. After 20 subsequent measurement points, the average value of the set $\{Z\}_{1,m}$ is taken.

- Step 2. In this step, to obtain x_2 we rearranged the following equation

$$T = Y_0 \exp(-ht) - Z_1 \exp(x_1 t) - Z_2 \exp(x_2 t), \qquad (18)$$

to x_2 and calculate the average of the values for each t_m giving the average value of the set $\{x_{2,m}\}$. Unfortunately, for noisy data, this approach can result in positive x_2 values. These values must be excluded, otherwise they may lead to instability and meaningless results. Careful filtering of the data can help to solve this problem and in fact we use this to facilitate the calculation.

- Step 3. Now that we have both exponents and coefficients, the analytical expressions can be explicitly rearrange to the GK parameters and the α_{GK}, τ_q and κ^2 values can be calculated [8].

- Step 4. Each parameter of the temperature history can be characterized with R^2, the coefficient of determination [8].

In practice, this evaluation method reduces the number of 'fitted' parameters. Moreover, it is limited to a relatively narrow range, i.e. the evaluation procedure takes only a few seconds instead of running computationally expensive algorithms that take hours.

NON-FOURIER THERMAL BEHAVIOUR

The evaluation procedure described above [8] is used on several rock samples, the results of which are shown below. It is noted that the samples are manufactured by Kőmérő Ltd. as the necessary infrastructure and technology is available there. The thin 1.9 mm thick rock sample is challenging to produce due to, for example, its fragility, so only one of each thickness of rock is available.

Fig.6. Szarsomlyo Limestone Formation sample (left) and Szaszvar Limestone Formation sample (right).

SZARSOMLYO LIMESTONE FORMATION

The results obtained from the evaluation for the Szársomlyó limestone formation are shown in Table 1. The non-Fourier effect is observed for the thinner samples. As the thickness increases, the Fourier theory fits the temperature history well. The evaluations are shown in Figures 7-9. Notably, the difference in thermal diffusivities for both models are significant between cases of 2 mm and 2.15 mm thicknesses. For thicker samples, the Fourier model becomes adequate.

Table 1. Summary of fitted thermal parameters of the Szársomlyó limestone formation.

Szarsomlyo limestone formation	α_F $10^{-6}[m^2/s]$	α_{GK} $10^{-6}[m^2/s]$	τ_q [s]	κ^2 $10^{-7}[m^2]$
2 mm	0.5113	0.5812	0.4180	0.0835
2.15 mm	1.1186	1.0254	0.4010	0.1127
2.85 mm	1.1413	-	-	-
3.85 mm	1.1197	-	-	-
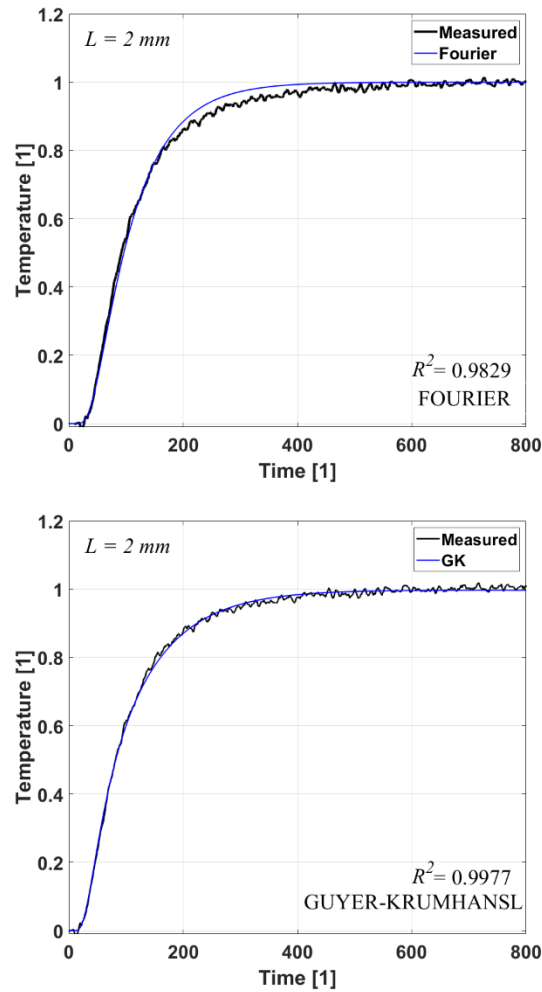
Fig. 7. Rearside temperature history in the L = 2 mm sample of the Szársomlyó limestone formation.
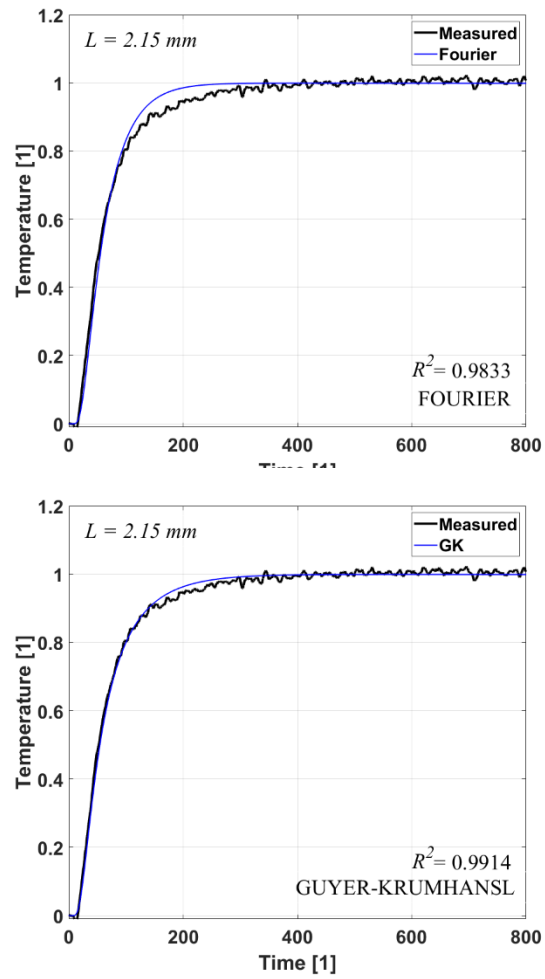
Fig. 8. Rearside temperature history in the L = 2.15 mm sample of the Szársomlyó limestone formation.
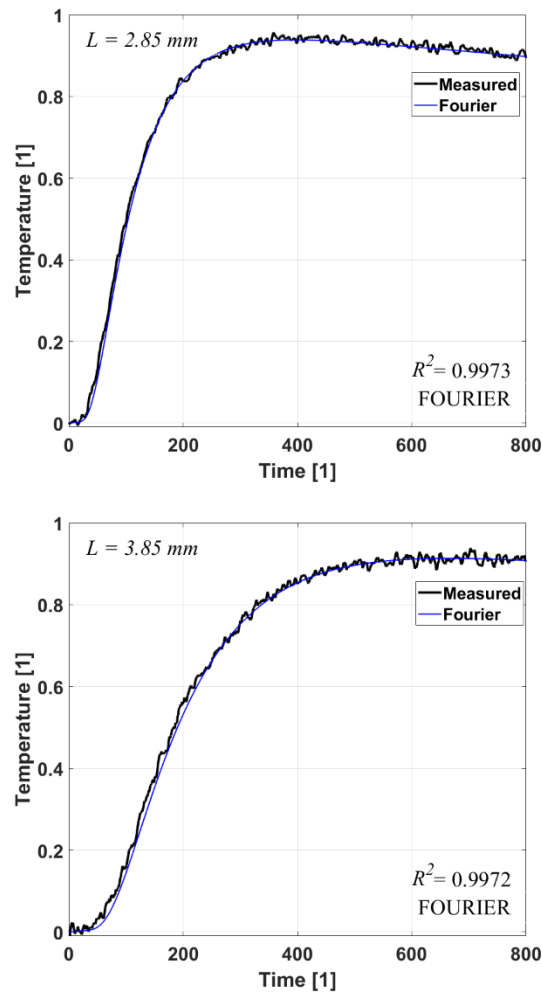
Fig. 9. Rearside temperature history in the L = 2.85 mm and L = 3.85 mm samples of the Szársomlyó limestone formation.

Szászvár Limestone Formation

In the case of the Szászvár Limestone Formation, the results of the evaluation are shown in Table 2.

Table 2. Summary of fitted thermal parameters of the Szászvár limestone formation

Szászvár limestone formation	α_F	α_{GK}	τ_q	κ^2
	$10^{-6}[m^2/s]$	$10^{-6}[m^2/s]$	[s]	$10^{-7}[m^2]$
3.05 mm	1.4048	1.4505	0.4273	0.0815
3.8 mm	0.8598	0.8815	0.5229	0.0409
3.9 mm	1.251	-	-	-

In the case of the rocks, a similar phenomenon can be observed as in the case of the Szársomlyó sample. On thinner samples, a non-Fourier effect is observed, which disappears with increasing sample thickness and the Fourier equation models our rock sample well.

SUMMARY AND DISCUSSION

We have developed an algorithm to efficiently evaluate room temperature heat pulse experiments in which a non-Fourier effect could present. This is called over-diffusive propagation and detunes the thermal diffusivity, even when the deviation is seemingly small or negligible for the rear side temperature history. The presented method is based on the analytical solution of the Guyer-Krumhansl equation, including temperature-dependent convection boundary condition, thus the heat transfer to the environment can be immediately included in the analysis.

We observed the size dependence of the thermal diffusivity for both heat conduction models, therefore it is not unique for the non-Fourier behaviour but also could forecast the presence of over-diffusion. That effect originates in the heterogeneities. Due to the equipment limitations, it is not possible to use samples with representative size, i.e., a size for which the thermal parameters are constant by having the heterogeneous effects averaged. Unfortunately, it is difficult to produce such thin rock samples, therefore it limits the measurements capabilities, however, these results stand as a strong motivation to continue the research and discover these effects more deeply. That dependence is strong for both rock types. Interestingly, the increase could be significant, more than 50 %. Additional size effect can be observed for the over-diffusion phenomenon, too. The modelling capabilities of the Fourier equation are better for thicker samples. Overall, it motivates further research and the need for more samples, providing a better resolution in thickness. Moreover, we also need multiple samples from the same thickness in order to investigate the sudden changes in the size dependence of thermal diffusivity.

We believe that this procedure lays the foundations for more practical engineering applications of non-Fourier models, especially for the best candidate among all of them, the Guyer-Krumhansl equation. It sheds new light on the classical and well-known flash experiments, and we provide the necessary tools to find additional thermal parameters to achieve a better description of heterogeneous materials. It becomes increasingly important with the spreading of composites and foams and helps characterize 3D printed samples with inclusions. With continuing the experiments, our goal is to find a relationship between the non-Fourier coefficients and the material structure. For instance, we aim to analyse multiple foam samples with different inclusion sizes, expectedly connecting production parameters to the non-Fourier effects.

REFERENCES

1. BOTH, S.; CZÉL, B.; FÜLÖP, T.; GRÓF, Gy.; GYENIS, Á.; KOVÁCS, R.; VÁN, P. and VERHÁS J. Deviation from the Fourier law in room-temperature heat pulse experiments. *Journal of Non-Equilibrium Thermodynamics*, 2016, Vol. 41.

2. VÁN, P.; BEREZOVSKY, A.; FÜLÖP, T.; GRÓF, Gy. KOVÁCS, R.; LOVAS, Á. and VERHÁS, J. Guyer-Krumhansl-type heat conduction at room temperature. *EPL*, 2017, Vol. I118, No. 10005.

3. PARKER, W. J.; JENKINS, R. J.; BUTLER, C. P.; and ABBOTT, G. L. Flash method of determining thermal diffusivity, heat capacity, and thermal conductivity. *Journal of Applied Physics*, 1996, Vol. 32, No. 9, P.1679–1684.

4. FEHÉR, A.; MARKOVICS, D.; FODOR, T.; KOVÁCS, R. Size effects and non-Fourier thermal behaviour in rocks. *ISRM International Symposium – EUROCK 2020*, 14-19 June, physical event not held, 2020.

5. JAMES, H. M. Some extensions of the flash method of measuring thermal diffusivity. *Journal of Applied Physics,*1980*, Vol.* 51, No.9, P.4666-4684

6. FÜLÖP, T.; KOVÁCS, R.; LOVAS, Á. RIETH, Á. FODOR, T.; SZÜCS, M.; VÁN, P. and GRÓF, Gy. Emergence of non-Fourier hierarchies. *Entropy, 2018, Vol.* 20, No. 11, P. 832.

7. RIETH, Á. KOVÁCS, R. and FÜLÖP, T. Implicit numerical schemes for generalized heat conduction equations. *International Journal of Heat and Mass Transfer*, 2018, Vol. 126, P. 1177-1182.

8. FEHÉR, A.; KOVÁCS, R. On the evaluation of non-Fourier effects in heat pulse experiments. *International Journal of Engineering Science*, 2021, Vol. 169, 2021, No. 103577, ISSN 0020-7225.

9. VÁN, P. Theories and heat pulse experiments of non-Fourier heat conduction. *Communications in Applied and Industrial Mathematics*, 2016, Vol.7, P. 150-166.

10. MÜLLER, I.; RUGGERI, T. Rational extended Thermodynamics. Springer, 1998.

11. CIMMELI, V. A. Different thermodynamic theories and different heat conduction laws. *Journal of Non-Equilibrium Thermodynamics*, 2009, Vol. 34, P. 299-333.

12. JOSEPH, D. D.; PREZIOSI, L. Heat waves. Reviews of Modern Physics, 1989, Vol. 61.

13. SOBOLEV, S. L. Local non-equilibrium transport models. *Physics-Uspekhi*, 1997, Vol. 40, P. 1043-1053.

14. SOBOLEV, S. L. Nonlocal diffusion models: Application to rapid solidification of binary mixtures. *International Journal of Heat and Mass Transfer*, 2014, Vol, 71, P. 295-302.

15. FEHÉR, A.; LUKÁCS, N.; SOMLAI, L.; FODOR, T.; SZÜCS, M.; FÜLÖP, T.; VÁN, P.; KOVÁCS, R. Size effects and beyond-Fourier heat conduction in room-temperature experiments. *Journal of Non-Equilibrium Thermodynamics*, 2021, Vol. 46, No. 4, P. 403-411.

16. FÜLÖP, T.; KOVÁCS, R.; and VÁN, P. Thermodynamic hierarchies of evolution equations. *Proceedings of the Estonian Academy of Sciences, 2015, Vol.* 64, P. 389-395.

DRAG PERFORMANCE IN THE PRESENCE OF UPSTREAM NOTCHED FLAT PLATE

E. Fırat, F. Fidan
Munzur University, Engineering Faculty, Department of Mechanical Engineering
Aktuluk Campus, 62000 – Turkey
+905555104149
efirat@munzur.edu.tr

ABSTRACT

This study presents a preliminary investigation of drag reductions of a circular cylinder in cross flow through the use of rectangular notched flat plates placed upstream. Four flat plate models with rectangular notches were constructed in order to study the effect on the time-averaged drag, $\langle C_D \rangle$, of both geometric notch parameters (i.e. notch depth, $2a$, and notch length, λ-f) and the ratio of gap between cylinder and plate to cylinder diameter (i.e. dimensionless gap, g/D). The results show that plain flat plate (P00) is the most successful device for reducing $\langle C_D \rangle$ of the entire system in the range of g/D investigated. The maximum drag reduction of 40% at a Reynolds number (Re_D) of 12600 ± 700 occurred for a g/D of 1.75. It is seen that the $\langle C_D \rangle$ for the plain cylinder with P03 (i.e. a notched flat plate) falls to a minimum value of 0.80 at approximately g/D=0.75. At the diameter-based Reynolds number studied (Re_D=12600 ± 700), the reduction in $\langle C_D \rangle$ obtained by a plain flat plate (P00) was only 5% greater than that obtained by a notched flat plate (P03). However, the dimensionless gap required to reach the minimum $\langle C_D \rangle$ is nearly halved when a notched plate placed upstream instead of the plain one.

Keywords: Passive flow control, Drag reduction, Three-dimensional effects, Cylinder, Notched flat plate

INTRODUCTION

Aerodynamic or hydrodynamic flow control is a hotly pursued topic in fluid dynamics and includes methods which bring about a desired change in the simple or complex flow field. Flow control methods can be classified according to energy requirements for their devices; that is, active flow control methods (requiring auxiliary power) and passive flow control methods (requiring no auxiliary power). Dielectric barrier discharge (DBD) plasma actuator [1, 2], synthetic (zero-net-mass-flux) jet actuator [3, 4], steady-suction system [5], and steady-blowing micro jet system [6] are typical examples of active flow control methods. Perforated shell [7], leading-edge tubercles [8, 9], distributed passive jets [10], hexagonal dimples [11], and slits [12] are typical examples of passive flow control methods.

Upstream control body is another passive flow control method. This method utilizes a small bluff control body placed upstream of and parallel to the main bluff body. It is very effective in reducing time-averaged and fluctuating forces acting not only on the main bluff body but also on the entire system consisting of upstream and main bluff bodies; thus, it has attracted the attention of many researchers [13-27]. The effects of various geometrical (i.e. upstream control body shape, upstream control body size, main body shape, gap between upstream control body and main body, angle of incidence/attack, wall proximity, etc.) and physical (i.e. Reynolds number, rotational speed of the upstream control body, etc.) parameters on the aerodynamic, flow, and heat transfer characteristics were tested.

Although many upstream-placed small parts for the reduction of bluff body drag have been proposed in the literature by previous investigators, almost none of these parts enhanced the three-dimensionality within the gap between that part and the bluff body since they have a uniform solid cross-section along their whole span [13-27]. It is well known, for example Tombazis and Bearman [28], Bearman and Owen [29], Nakamura and Igarashi [30], Cai et al. [31], Lam and Lin [32], and Park et al. [33], the fluctuating and time-averaged forces of nominally two-dimensional bluff bodies can be suppressed and/or reduced by introducing some devices which trigger spanwise instabilities to weaken regular and nominally two-dimensional vortex shedding. Furthermore, the devices which trigger spanwise instabilities are generally located at the surface/surfaces of the one main body. In this study, spanwise instabilities will be triggered by the upstream-placed body. This is the major difference between the present experimental investigation and those mentioned above (i.e. [13-33]). In this study, we compared the drag performance of a plain cylinder with upstream notched flat plate to a plain cylinder with upstream plain flat plate.

EXPERIMENTAL SETUP

Experiments were performed in a closed-return, low-speed wind tunnel in the Department of Mechanical Engineering at the Munzur University. The tunnel has a 2.5 m long test section with cross-section 1 m high by 1 m wide. The maximum fee stream turbulence intensity (Tu_x) in the test section is 1%. Tunnel speed was measured with a handheld hot-wire anemometer upstream of the model. To minimize the effects of the floor boundary layer, a ground plane mounted on the tunnel floor in combination with a turntable and force measurement system (Fig. 1). The gap between the bottom wall of the test section and ground plate was 100±0.2 mm. The leading and trailing edges of the ground plane are sharp.

Experiments were conducted at free-stream velocity of U_∞=5.3±0.3 m/s, resulting in a Reynolds number of Re_D=12600±700 based on the diameter of the cylinder (D). The cylinder, upstream plates, and end plates were printed using FDM (Fused Deposition

Modelling) technology on a properly calibrated low-cost 3D printer using PLA+ material (Fig. 2; TEVO 3D Electronic Technology Co., Ltd., Tornado). The cylinder model used in the investigation had a diameter (D) of 40±0.1 mm, a wall thickness of 2±0.1 mm, and a length of 300±0.2 mm. The flat plate models used in the investigation had a wall thickness (t) of 3±0.2 mm, and a length of 300±0.1 mm. Furthermore, they did not bend with the flow. The end plates used in the investigation had a diameter of 220±0.1 mm and a wall thickness of 3±0.2 mm.
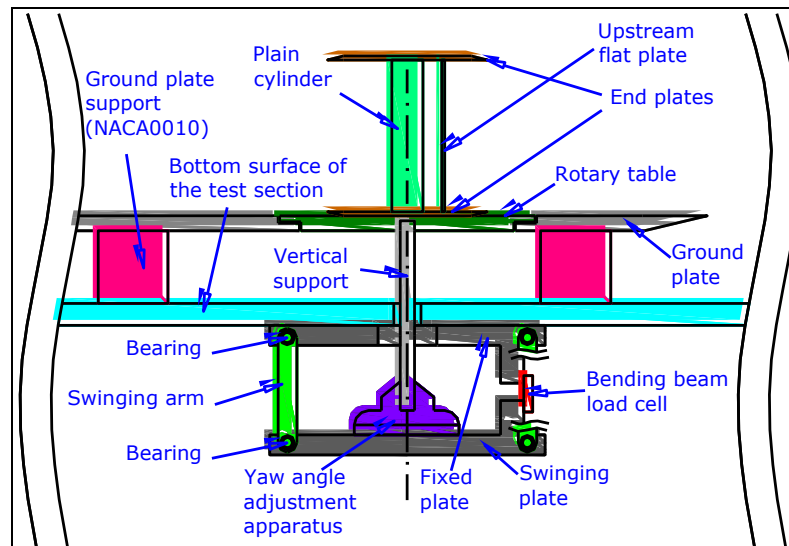
Fig. 1. Schematic of the aerodynamic drag measurement system. Flow is from right to left.
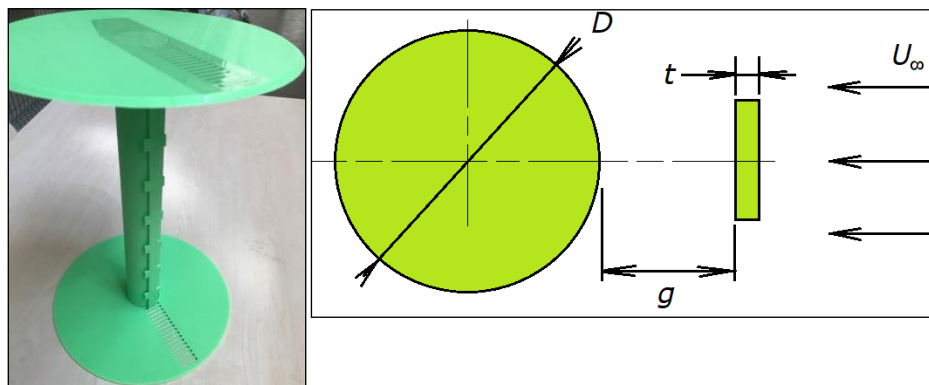
Fig. 2. The picture of entire system (i.e. cylinder with upstream flat plate) fitted with end plates and schematic of the entire system with geometric parameters (in the right side).
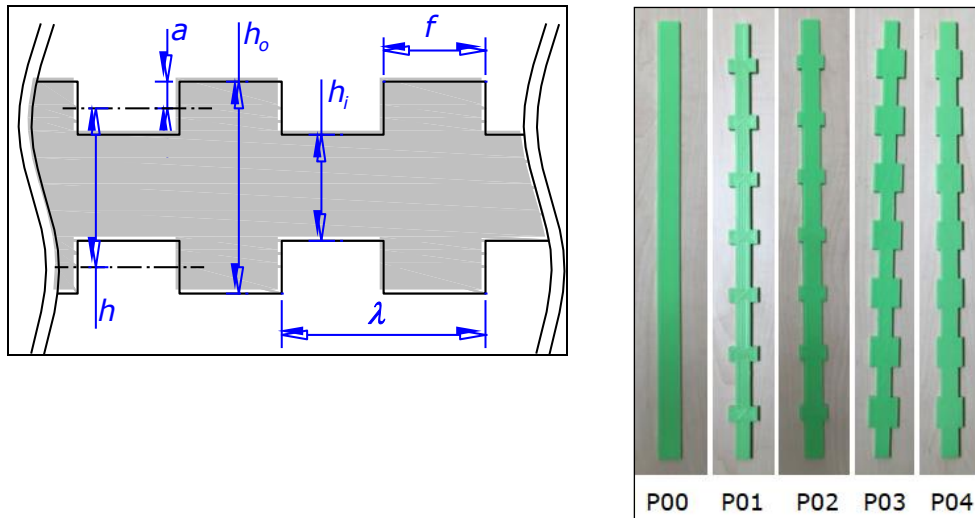
Fig. 3. Geometric parameters of upstream notched flat plate and front views of flat plates with labels (in the right side). Here, $h=h_i+2a$, $h=h_o-2a$, and $\lambda=40\pm0.1$ mm.

Table 1. Terminology regarding upstream plate types

Label	f (mm)	h_i (mm)	h_o (mm)
P00	-	15	15
P01	10	10	20
P02	10	12	18
P03	20	10	20
P04	20	12	18

Figure 2 shows the entire system (i.e. cylinder with upstream flat plate) to be tested with geometric parameters. The entire system was aligned in the vertical direction. The entire system fitted with end plates was fixed to the turntable using a double-sided thin tape. The turntable is concentric with the lower end plate. Flat plates, placed upstream of the cylinder, were moved to different positions by inserting them into the slots on the end plates. End plates were aligned parallel to the flow using a spirit level with a measurement accuracy of 0.06° (STABILA, 11990). Upstream flat plates were aligned perpendicular to the flow using a self-levelling green cross line laser that is accurate to 0.3 mm/m (DeWALT, DW088CG). Fig. 3 shows geometric parameters of notched plate and printed plain/notched flat plates based on the values given in Table 1. Four notched and one plain flat plates were tested.

Aerodynamic drag was recorded by one-component load-cell (ME-Meßsysteme GmbH, KD60-5N), which located under the test section of the tunnel (Fig. 1). The uncorrected time-averaged drag acting on the entire system or single cylinder, $\langle F_{D\text{-}un}\rangle$, was obtained by equation 1.

$$\langle F_{D-un}\rangle = \langle F_{DT-un}\rangle - \langle F_{DS-un}\rangle, \tag{1}$$

where $\langle F_{DT\text{-}un}\rangle$ is the time-averaged drag acting on the components of the drag measurement system inside the test section, end plates, and entire system or single cylinder and $\langle F_{DS\text{-}un}\rangle$ is the time-averaged drag acting on the components of the drag measurement system inside the test section and end plates. The aerodynamic drag was sampled at 200 Hz for 40 s (Marmatek Measurement Technologies, VTA-1704). It was nondimensionalized (drag coefficient) using equation 2.

$$\langle C_{D-un} \rangle = 2 \cdot \langle F_{D-un} \rangle / \left(\rho \cdot U_\infty^2 \cdot A_F \right), \tag{2}$$

where ρ is the air density (kg/m^3) and A_F is the frontal area of the entire system at zero angle of attack (m^2). The frontal area of the entire system and single cylinder is 0.012 m^2. The aspect ratio of upstream plate and single cylinder was 7.5. Although the geometric blockage was small (4%) the correction method due to Allen and Vincenti [34] was applied to all the time-averaged drag data.

$$\langle C_D \rangle = \langle C_{D-un} \rangle - 0.5 \cdot \langle C_{D-un} \rangle^2 \cdot \left(\frac{D}{W} \right) - 2.5 \cdot \langle C_{D-un} \rangle \cdot \left(\frac{D}{W} \right)^2, \tag{3}$$

where $\langle C_D \rangle$ represents the corrected time-averaged drag coefficient of entire system or single cylinder and W represents the width of the test section (m). Throughout the experiments, the angle of attack for the entire system was kept constant at $0 \pm 0.4°$. The uncertainty associated with the drag coefficient measurements is determined to be $\pm 7\%$.

The key parameters investigated in this study are the ratio of gap between cylinder and plate to cylinder diameter (i.e. dimensionless gap, g/D) and the shape of the rectangular notch (i.e. depth, $2a$, and length, λ-f). The dimensionless gaps tested range from 0 to $2 \pm 0.7\%$ in $0.125 \pm 0.7\%$ increments.

RESULTS AND DISCUSSION

Irrespective of the type of plate placed upstream of the plain cylinder, it is evident that the $\langle C_D \rangle$ of the entire system (i.e. cylinder with notched or plain upstream flat plate) is lower than that of the single cylinder (Figs. 4-5). Furthermore, the shape of the entire system resembles that of a single bluff body and the minimum drag reduction is generated when the plain cylinder and upstream flat plate are in contact, at $g/D=0$.

In the case of the plain cylinder with P00, detachment of the plate from the plain cylinder results in a sharp drop in $\langle C_D \rangle$ (Fig. 4 and 5). It is not yet clear why there is a sharp drop in the $\langle C_D \rangle$ as the dimensionless gap is increased from $g/D=0$ to 0.125 but it would seem to be due to the pressure redistribution on the front surface of the cylinder and the rear surface of the plate [16]. From $g/D=0.125$ to 1.75, the drag coefficient of the entire system steadily decreases to a value of $\langle C_D \rangle=0.74$ which is approximately 60% of the drag coefficient for a single cylinder. Further increase in dimensionless gap beyond the point of minimum drag (i.e. for $g/D>1.75$) results in an increase in the $\langle C_D \rangle$ which is consistent with the appearance of the transition regime (generally referred to as bistable regime) where the flow swaps between the current (generally referred to as cavity mode) and next (generally referred to as wake-impingement mode) modes of flow in an intermittent fashion [14-16, 18, 20].
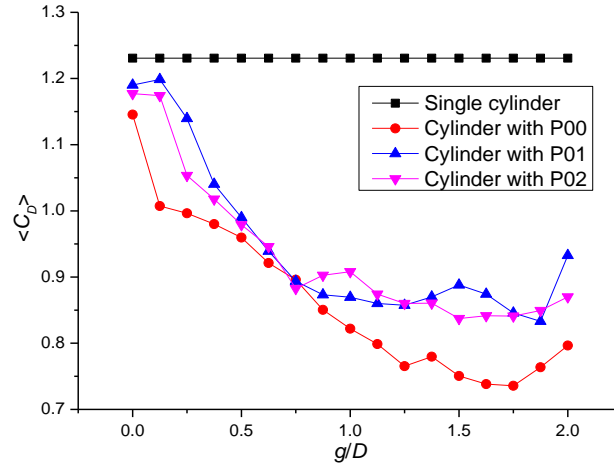
Fig. 4. Variation of corrected drag coefficient, $\langle C_D \rangle$, with dimensionless gap, g/D, for a single cylinder, a cylinder with P00, a cylinder with P01, and a cylinder with P02. Re_D=12600±700.

In the case of the plain cylinder with one of the notched plates (i.e. P01, P02, P03, or P04), a sharp drop in the $\langle C_D \rangle$ was not occurred as the dimensionless gap is increased from g/D=0 to 0.125 but from g/D=0.125 to 0.250. The actual mechanism of this shift is unclear. Compared to the P01 and P02, P00 (plain flat plate) is more successful in reducing $\langle C_D \rangle$ in the range of g/D investigated (Fig. 4).
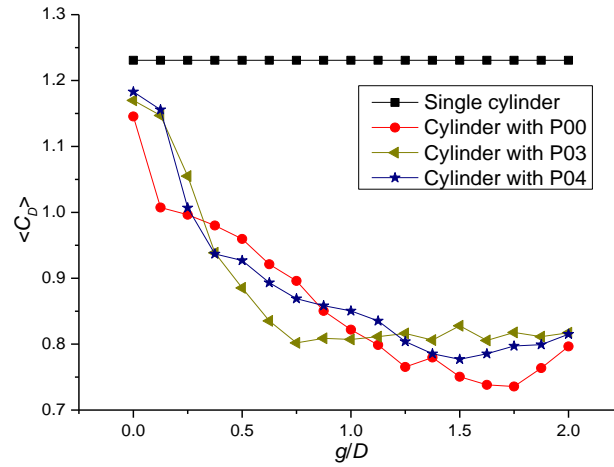
Fig. 5. Variation of corrected drag coefficient, $\langle C_D \rangle$, with dimensionless gap, g/D, for a single cylinder, a cylinder with P00, a cylinder with P03, and a cylinder with P04. Re_D=12600±700.

Figure 5 illustrates that $\langle C_D \rangle$ values of the cylinder with P03 follow a bilinear trend. The time-averaged drag coefficient of a cylinder with P03 undergoes a linear reduction with increasing dimensionless gap, from 1.15 to a minimum value of 0.80 occurring at g/D=0.75. At g/D=0.75, the $\langle C_D \rangle$ for the cylinder with P03 dropped to 0.80 while for the cylinder with P00 data shown in Fig. 5 the $\langle C_D \rangle$ at the same g/D is 0.9, a reduction with the P03 of 11%. The $\langle C_D \rangle$ for the cylinder with P03 remains relatively constant at approximately 0.81 for the remainder of the g/D range investigated (i.e. 0.75<g/D≤2.00).

For the cylinder with P04, trend in the time-averaged drag coefficient have also been plotted in Fig. 5. The $\langle C_D \rangle$ of the cylinder with P04 is following a similar trend with that of the

cylinder with P00. For much of the g/D range investigated, the results for the cylinder with P04 showed only minor differences.

CONCLUSIONS

On the basis of previous investigations, it is clear that upstream control body is an effective means of reducing the drag acting on the main bluff body as well as on the entire system. However, none of these investigations examined the effect of upstream body which does not have a uniform solid cross-section along its whole span. The novelty of this study is the use of a three-dimensional upstream control body (i.e. notched flat plate) which enhances the three-dimensionality within the gap region between the plain cylinder and upstream control body.

This study presents a preliminary investigation of drag reductions of a circular cylinder in cross flow through the use of rectangular notched flat plates placed upstream. Four flat plate models with rectangular notches were constructed in order to study the effect on the time-averaged drag, $\langle C_D \rangle$, of both geometric notch parameters (i.e. notch depth, $2a$, and notch length, λ-f) and the ratio of gap between cylinder and plate to cylinder diameter (i.e. dimensionless gap, g/D).

The results show that plain flat plate (P00) is the most successful device for reducing $\langle C_D \rangle$ of the entire system in the range of g/D investigated. The maximum drag reduction of 40% at a Reynolds number (Re_D) of 12600±700 occurred for a g/D of 1.75. It is seen that the $\langle C_D \rangle$ for the plain cylinder with P03 (i.e. a notched flat plate) falls to a minimum value of 0.80 at approximately g/D=0.75. At the diameter-based Reynolds number studied, the reduction in $\langle C_D \rangle$ obtained by a plain flat plate (P00) was only 5% greater than that obtained by a notched flat plate (P03). However, the dimensionless gap required to reach the minimum $\langle C_D \rangle$ is nearly halved when a notched plate placed upstream instead of the plain one.

REFERENCES

1. AKBIYIK, H.; AKANSU, Y.E.; YAVUZ, H. Active control of flow around a circular cylinder by using intermittent DBD plasma actuators. *Flow Measurement and Instrumentation*, 2017, Vol. 53, P. 215-220. doi: <https://doi.org/10.1016/j.flowmeasinst.2016.12.008>

2. VERNET, J.A.; ÖRLÜ, R.; SÖDERBLOM, D.; ELOFSSON, P.; ALFREDSSON, P.H. Plasma streamwise vortex generators for flow separation control on trucks. *Flow, Turbulence and Combustion*, 2018, Vol. 100, P. 1101-1109. doi: <https://doi.org/10.1007/s10494-018-9891-9>

3. FEERO, M.A.; LAVOIE, P.; SULLIVAN, P.E. Influence of synthetic jet location on active control of an air foil at low Reynolds number. *Experiments in Fluids*, 2017, Vol. 58, No. 99. Doi:< https://doi.org/10.1007/s00348-017-2387-x >

4. QU, Y.; WANG, J.; SUN, M.; FENG, L.; PAN, C.; GAO, Q.; HE, G. Wake vortex evolution of square cylinder with a slot synthetic jet positioned at the rear surface. *Journal of Fluid Mechanics*, 2017, Vol. 812, P. 940-965. doi: <https://doi.org/10.1017/jfm.2016.833>

5. CHEN, G.B.; CHEN, W.L.; YANG, W.H.; GAO, D.L. Suppression of vortex-induced vibration of a box girder using active suction-jet slit. *Journal of Wind Engineering and Industrial Aerodynamics*, 2021, Vol. 216, No. 104713. doi: <https://doi.org/10.1016/j.jweia.2021.104713 >

6. MCNALLY, J.; MAZELLIER, N.; ALVI, F.; KOURTA, A. Control of salient flow features in the wake of a 25° Ahmed model using micro jets. *Experiments in Fluids*, 2019, Vol. 60, No. 7. doi:< https://doi.org/10.1007/s00348-018-2645-6>

7. DURHASAN, T.; AKSOY, M.M.; PINAR, E.; OZKAN, G.M.; AKILLI, H.; SAHİN, B. Vortex street suppression of a circular cylinder using perforated semi-circular fairing in shallow water. *Experimental Thermal and Fluid Science*, 2016, Vol. 79, P. 101-110. doi: <https://doi.org/10.1016/j.expthermflusci.2016.07.001>

8. SEYHAN, M.; SARIOGLU, M.; AKANSU, Y.E. Influence of leading-edge tubercle with amplitude modulation on NACA 0015 air foil. *American Institute of Aeronautics and Astronautics*, 2021, Vol. 59, No. 10, p. 3965-3978. doi: <https://doi.org/10.2514/1.J060180 >

9. HANSEN, K.L.; KELSO, R.M.; DALLY, B.B. Performance variations of leading-edge tubercles for distinct air foil profiles. *American Institute of Aeronautics and Astronautics*, 2011, Vol. 49, No. 1, P. 185-194. Doi: <https://doi.org/10.2514/1.J050631>

10. CLAPPERTON, B.L.; BEARMAN, P.W. Control of circular cylinder flow using distributed passive jets. *Journal of Fluid Mechanics*, 2018, Vol. 848, P. 1157-1178. doi: <https://doi.org/10.1017/jfm.2018.399>

11. BUTT, U.; JEHRING, L.; EGBERS, C. Mechanism of drag reduction for circular cylinders with patterned surface, *International Journal of Heat and Fluid Flow*, 2014, Vol. 45, P. 128-134. Doi: <https://doi.org/10.1016/j.ijheatfluidflow.2013.10.008>

12. KARASU, İ. Flow control over a diamond-shaped cylinder using slits. *Experimental Thermal and Fluid Science*, 2020, Vol. 112, No. 109992. Doi: <https://doi.org/10.1016/j.expthermflusci.2019.109992>

13. IGARASHI, T. Drag reduction of a square prism by flow control using a small rod. *Journal of Wind Engineering and Industrial Aerodynamics*, 1997, Vol. 69, No. 71, P. 141-153. Doi:< https://doi.org/10.1016/S0167-6105(97)00150-5>

14. ZHANG, P.F.; WANG, J.J.; LU, S.F.; MI, J. Aerodynamic characteristics of a square cylinder with a rod in a staggered arrangement, *Experiments in Fluids*, 2005, Vol. 38, P. 494-502. Doi: <https://doi.org/10.1007/s00348-005-0936-1>

15. FIRAT, E.; AKANSU, Y.E.; AKILLI, H. Flow past a square prism with an upstream control rod at incidence to uniform stream. *Ocean Engineering*, 2015, Vol. 108, 504-518. Doi: <http://dx.doi.org/10.1016/j.oceaneng.2015.08.041>

16. PRASAD, A.; WILLIAMSON, C.H.K. A method for the reduction of bluff body drag. *Journal of Wind Engineering and Industrial Aerodynamics*, 1997, Vol. 69, No. 71, P. 155-167. Doi:< https://doi.org/10.1016/S0167-6105(97)00151-7>

17. BOUAK, F.; LEMAY, J. Use of the wake of a small cylinder to control unsteady loads on a circular cylinder. *Journal of Visualization*, 2001, Vol. 4, No. 1, P. 61-72. Doi: <https://doi.org/10.1007/BF03182456 >

18. LEE, S.-J.; LEE, S.-I.; PARK, C.-W. Reducing the drag on a circular cylinder by upstream installation of a small control rod. *Fluid Dynamics Research*, 2004, Vol. 34, P. 233-250. Doi: <https://doi.org/10.1016/j.fluiddyn.2004.01.001>

19. ZHAO, M.; CHENG, L.; TENG, B.; LIANG, D. Numerical simulation of viscous flow past two circular cylinders of different diameters. *Applied Ocean Research*, 2005, Vol. 27, P. 39-55. Doi:< https://doi.org/10.1016/j.apor.2004.10.002>

20. WANG, J.J.; ZHANG, P.F.; LU, S.F.; WU, K. Drag reduction of a circular cylinder using an upstream rod. *Flow, Turbulence and Combustion*, 2006, Vol. 76, P. 83-101. Doi: <https://doi.org/10.1007/s10494-005-9008-0 >

21. IGARASHI, T.; TERACHI, N. Drag reduction of flat plate normal to airstream by flow control using a rod. *Journal of Wind Engineering and Industrial Aerodynamics*, 2002, Vol. 90, P. 359-376. Doi: <https://doi.org/10.1016/S0167-6105(01)00198-2>

22. TRIYOGI, Y.; SUPRAYOGI, D.; SPIRDA, E. Reducing the drag on a circular cylinder by upstream installation of an I-type bluff body as passive control. *Proceedings of the Institution of Mechanical Engineers, Part C: Journal of Mechanical Engineering Science*, 2009, Vol. 223, No. 10, P. 2291–2296. Doi: <https://doi.org/10.1243/09544062JMES1543>

23. ZHOU, L.; CHENG, M.; HUNG, K.C. Suppression of fluid force on a square cylinder by flow control. *Journal of Fluids and Structures*, 2005, Vol. 21, P. 151–167. doi: <https://doi.org/10.1016/j.jfluidstructs.2005.07.002>

24. MALEKZADEH, S.; SOHANKAR, A. Reduction of fluid forces and heat transfer on a square cylinder in a laminar flow regime using a control plate. *International Journal of Heat and Fluid Flow*, 2012, Vol. 34, P. 15-27. Doi: <https://doi.org/10.1016/j.ijheatfluidflow.2011.12.008>

25. MOUSSAOUI, M.A.; JAMI, M.; MEZRHAB, A.; NAJI, H.; BOUZIDI, M. Multiple-relaxation-time lattice Boltzmann computation of channel flow past a square cylinder with an upstream control bi-partition. *International Journal for Numerical Methods in Fluids*, 2010, Vol. 64, P.591-608. Doi:< https://doi.org/10.1002/fld.2159>

26. ROSALES, J.L.; ORTEGA, A.; HUMPHREY, J.A.C. A numerical investigation of the convective heat transfer in unsteady laminar flow past a single and tandem pair of square cylinders in a channel. *Numerical Heat Transfer, Part A: Applications*, 2000, Vol. 38, No. 5, P. 443-465. Doi:< https://doi.org/10.1080/104077800750020388>

27. AYYAPPAN, T.; VENGADESAN, S. Influence of staggering angle of a rotating rod on flow past a circular cylinder. *Journal of Fluids Engineering*, 2008, Vol. 130, No. 031103. Doi: <https://doi.org/10.1115/1.2842224>

28. TOMBAZIS, N.; BEARMAN, P.W. A study of three-dimensional aspects of vortex shedding from a bluff body with a mild geometric disturbance. *Journal of Fluid*

Mechanics, 1997, Vol. 330, P. 85-112. Doi: <https://doi.org/10.1017/S0022112096003631>

29. BEARMAN, P.W.; OWEN, J.C. Reduction of bluff-body drag and suppression of vortex shedding by the introduction of wavy separation lines. *Journal of Fluid Mechanics*, 1998, Vol. 12, P. 123-130. Doi: <https://doi.org/10.1006/jfls.1997.0128>

30. NAKAMURA, H.; IGARASHI, T. Omnidirectional reductions in drag and fluctuating forces for a circular cylinder by attaching rings. *Journal of Wind Engineering and Industrial Aerodynamics*, 2008, Vol. 96, P. 887-899. doi: <https://doi.org/10.1016/j.jweia.2007.06.016 >

31. CAI, J.; CHNG, T.L.; TSAI, H.M. On vortical flows shedding from a bluff body with a wavy trailing edge. *Physics of Fluids*, 2008, Vol. 20, No. 064102. Doi: <https://doi.org/10.1063/1.2931682>

32. LAM, K.; LIN, Y.F. Effects of wavelength and amplitude of a wavy cylinder in cross-flow at low Reynolds numbers. *Journal of Fluid Mechanics*, 2009, Vol. 620, P. 196-220. Doi:< https://doi.org/10.1017/S0022112008004217>

33. PARK, H.; LEE, D.; JEON, W.P.; HAHN, S.; KIM, J.; KIM, J.; CHOI, J.; CHOI, H. Drag reduction in flow over a two-dimensional bluff body with a blunt trailing edge using a new passive device. *Journal of Fluid Mechanics*, 2009, Vol. 620, P. 196-220. Doi: <https://doi.org/10.1017/S0022112006001364 >

34. ALLEN, H.J.; VINCENTI, W.G. Wall interference in a two-dimensional-flow wind tunnel, with consideration of the effect of compressibility. *Annual Report - National Advisory Committee for Aeronautics*, 1944, Vol. 30, Report No: 782, P. 155-184.

WATER VAPOR CONDENSATION ON VERTICAL TUBES FROM BIOFUEL FLUE GAS

L. MINGILAITĖ
Kaunas University of Technology
Studentų g. 56, LT-51424 Kaunas – Lithuania
+370 (62) 818131
laura.mingilaite@ktu.lt

R. POŠKAS
Lithuanian Energy Institute
Breslaujos g. 3, LT-44403 Kaunas – Lithuania
Kaunas University of Technology
Studentų g. 56, LT-51424 Kaunas – Lithuania
+370 (37) 401893
Robertas.Poskas@lei.lt

EXTENDED ABSTRACT

OVERVIEW

Energy demand is increasing considerably in the coming years as the result of population growth and economic development. Due to that, the energy efficiency must be increased by using renewable and alternative fuel sources or improving old energy systems by optimizing them. To increase the efficiency of thermal power and boiler plants, they are equipped with condensing heat exchangers (economizers).

The studies of condensation heat transfer process are mainly focused to the cases of parallel flow in the single vertical tube and horizontal tube bundles in the crossflow. However, there is only limited information on flue gas condensation in a vertical tube bundles [1], especially with small vapor volume fraction in the flue gas. Due to that, there are a lot of gaps in optimizing operation of condensing vertical tubes equipped heat exchangers which are working in the flue gas environment (environment with a mix of non-condensable gases (NCG) and water vapor). Due to that, effect of numerous factors like Reynolds number, condensate formation pattern, etc. has not been investigated in detail.

Shell & tube type condensing economizers are common in Lithuania, where condensation processes investigated in [2]. In this work, preliminary condensation process analysis in a finned tube type condensing heat exchanger was performed.

METHODS

In this experimental investigation of condensation, processes have been performed in the condensing heat exchanger mock-up constructed at the Lithuanian Energy Institute. The experimental setup consists of the heat exchanger (the test section), biofuel boiler, cooling water lines, flue gas line, and data acquisition system.

The test section is finned tube counter-current heat exchanger (internal dimensions 0.302x0.108x1.228 m) with inline arranged vertical tubes (inner diameter 0.014 m) bundles. The test section has three stages and eight parallel rows of tubes, which were installed between holding planes. The tube bundle has a transverse pitch of 0.027 and a longitudinal pitch of 0.13. In the bundle used one-line tubes with a length of 2.85 meters.

The flue gas was produced by burning wood pellets. The boiler's different power level (can be changed from 50-100 percent) was used to produce different flue gases with different amount of NCG by controlling air ratio in fuel combustion process.

During experiments, the flue gas from the boiler went through the gas duct to the inlet of the test section where it flowed around the cooling water tube bundles surface. The condensation process occurred when the flue gas was exposed to cooled surface of tubes. After the condensation process, the remaining flue gas was directly exhausted to the atmosphere through the flue gas pipe (chimney).

During the experiments, thermocouples, flowmeter, micro manometer with a pilot tube were used to measure the flue gas and cooling water temperature, cooling water flow rate, and the flue gas flow rate. The experiment was conducted changing the flue gas (temperature – 414-424 K; velocity – 0.5-2 m/s) and cooling water (flow rate – 2 l/min) parameters and the flue gas composition (water vapor mass fraction – 0.09-0.15).

RESULTS

Fig. 1 shows the temperatures distribution in the test section in case of Re_{in} = 900, when vapor inlet mass fraction is 0.11 and cooling water flow rate is 2 l/min. From the figure, we can see that average flue gas and tube surface temperatures are decreasing along the test section from the inlet position 1 until the outlet position 9 of the test section. Flue gas temperature decreases from 115 ºC to 55 ºC and tube surface temperature increases from 30 ºC to 40 ºC. Cooling water temperature inside tubes increases from its inlet position 9 until the outlet 1 about 10 ºC. The highest difference between flue gas and cooling tube surface temperature is observed in the beginning of the test section. It is known that, when the tube wall temperature from the flue gas flow side is lower than the dew point temperature, water vapor starts to condensate on the wall. Because of that, the temperature difference between the flue gas and the surface of tubes decreases.
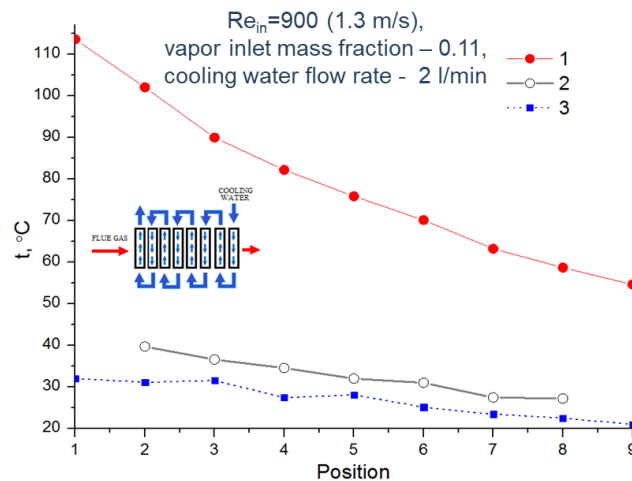
Fig. 1. Typical distribution of temperatures in test section: 1 – average
flue gas flow temperature, 2 – average tube wall surface temperature, 3 –
cooling water temperature in the tube

Condensate was collected in the separate sections of heat exchanger. In order to determine the effects of the flue gas inlet velocity on the condensation capture rate, the experiments are conducted at different flue gas velocities. It is observed that at low flue gas velocity condensate capture rate increases with the increase of water vapor mass fraction. The increases of vapor mass fraction for about 5 percent results in condensate capture increase for about two times – from ~35 percent till approx. 60 percent. In case of higher flue gas velocity on condensate capture rate is similar – increasing. However, at higher flue gas velocity the test section is not capable to condensate such a quantity of vapor as in case with lower flue gas speed.

CONCLUSIONS

- Investigations performed at small flue gas Re number (Re_{in} = 300) showed that condensation efficiency of about 60 percent can be reached.

- Further investigations are intended to investigate the effect of different factors (cooling water flow rate, Re numbers, inlet flue gas temperature, and vapor fraction) on condensation efficiency.

Keywords: condensation, finned tube type condensing heat exchanger, water vapor, non-condensable gases

REFERENCES

1. WANG, E.; LI, K.; HUSNAIN, N.; Li, D.; Mao, J.; Wu, W.; Yang, T. Experimental study on flue gas condensate capture and heat transfer in staggered tube bundle heat exchangers. *Applied Thermal Engineering,* 2018, Vol. 141, P. 819–827.

2. POŠKAS, R.; SIRVYDAS A.; KULKOVAS V.; POŠKAS P. An Experimental Investigation of Water Vapor condensation from Biofuel Flue Gas in a Model of Condenser, (1) Base Case: Local Heat Transfer without Water Injection. *Processes*, 2021, Vol. 9, No.5, P. 844.

CFD STUDY ON PERFORMANCE ANALYSES OF
AN ORGANIC RANKINE CYCLE TURBINE

I. R. Ozdemir *

Department of Mechanical Engineering, Technical University of Denmark
Nils Koppels Allé, 2800, Kgs. Lyngby – Denmark
+45 50 25 91 51
rilteber@gmail.com

Y. Ozturk, B. Ozmadenci

Department of Mechanical Engineering, Bogazici University
Bebek/Istanbul, 34342 – Turkey
yekkta.ozturk@gmail.com , barisozmadenci@gmail.com

ABSTRACT

In this study, using the Computational Fluid Dynamics (CFD) approach, the design and performance analyses of a radial-type inflow turbine was conducted for an organic Rankine cycle. The CFD simulations were carried out at 6 pressure ratios and a rotational speed of 22,728 rpm. The condition with 20 bars inlet and 8 bars outlet pressures seemed to be the optimum operating point, where the turbine delivered 126 kW of power at a mass flow rate of 8.61 kg/s. This corresponded an efficiency of 78.2 %. The results also showed that the streamlines were quite ordered and remained nearly parallel to the walls of the impeller, and the flow Mach number gradually decreased deep inside the cascade. As a result, a subsonic discharge succeeded from the impeller and no tip vortex formation was observed. The analyses of other flow properties inside the turbine proved that all the design criteria set initially were satisfied.

Keywords: Radial inflow turbine design, CFD, organic Rankine cycle.

INTRODUCTION

In the recent years, renewable energy sources have become increasingly important in electricity generation. As the conventional power generation methods do not efficiently convert heat source into electrical power, a significant research has been conducted on how to exploit and integrate low to moderate temperature heat sources into current systems. Organic Rankine cycle (ORC) is one of the thermodynamic cycles that has a profound potential in producing power and, hence, generating electricity, by converting thermal energy that would otherwise be wasted [1].

An organic Rankine cycle is comprised of an evaporator, a condenser, a pump and a turbine. Although the thermodynamic processes involved are similar to that of a steam Rankine cycle, the use of an organic working fluid allows more effective heat recovery from low temperature heat sources. The major advantage of using an organic working fluid is that it mostly requires only one expander stage for the turbine, which lowers both the capital and the maintenance costs [1].

The turbine, where the energy extraction from the working fluid occurs, is one of the most crucial components in a power generating thermodynamic cycle. Therefore, the design of a turbine is critical for the overall efficiency of the cycle. Depending on the inlet and exit conditions and the cycle type, different turbine types are used: Axial flow turbines are most suitable for systems with low pressure ratio and high flow rates, whereas radial flow turbines are generally preferred in high pressure ratio systems with lower flow rates. Since an organic Rankine cycle presents an alternative way of the latter arrangement, a radial inflow turbine (RIT) is found most suitable and preferable choice regarding maximum efficiency and power output [2].

Significant amount of research has been done on the optimization of the RIT design for an ORC. To improve the efficiency of the cycle Dong et al. [3] used the particle swarm optimization algorithm. Loss correlations have been developed to study efficiency of the turbine and its effects on the cycle [4]. Schuster et al. [5] verified the loss correlations present in the literature against experimental results and CFD analyses. Maximizing net power of the cycle is a popular objective function in these studies, where White and Sayma [6] applied two step optimization on an ORC and RIT. On the other hand, maximizing turbine efficiency is the most popular objective function in the literature for the RIT optimisation. The genetic algorithm was also applied on the cycle (Rahbar et al. [7]) to maximize the efficiency of the turbine. Bekiloglu et al. [8] conducted a preliminary design process for an RIT using the multi-objective optimization (NSGA-II) which was based on 28 different working fluids and 3 heat source temperatures $90°C$, $120°C$, and $150°C$: R134a is found to be the optimum working fluid for all of the heat source temperatures analysed. The main geometric parameters of an RIT were optimized for all three heat source temperatures and various working fluids.

Whatever the optimization method is used and the extent of their success, it is still a challenging task to build an ORC/RIT system. Nowadays, the design of real systems has been conducted mainly on ad hoc basis, relying on empirical correlations obtained at some lab-scale models. Hence, a systematic approach is needed, and this requires a better understanding of the fundamental parameters of the turbine system. With the current measurement techniques, it is almost impossible to extract sufficient information on the details of the flow dynamics and the efficiency issues, which precludes the wider use of experimental methods. On the other hand, with the advent of computational methods,

designers rely more and more on numerical techniques in the analyses of complex flow in these devices in order to reduce the iteration loop of the conception-design-test cycle. However, a consistent description of the complex thermo-fluid processes requires well-resolved computations of mass, momentum and energy, which means handling of a large system of stiff partial differential equations. Therefore, it seems necessary to implement numerical models, which are simple but can capture the main features. The present study exploits the working conditions of Bekiloglu et al. [8] to build the detailed 3D design using the CFD tool. The intermediate blade geometry design has been carried out to meet the requirements of the given organic Rankine cycle in terms of power output and with R134a as the working fluid.

DESIGN METHODOLOGY

The results of Bekiloglu et al. [8] for R134a fluid and a turbine inlet temperature of $90°C$ are used to initiate the present 3D design. These parameters, however, were not sufficient per se to fully define a 3D geometry. Thus, while preliminary design results are used to describe some of the geometry variables, additional constraints available in the literature are also considered to finalise the current model [9]. Main geometrical parameters of the cycle shown in Fig. 1, and the design parameters are listed in Table 2.
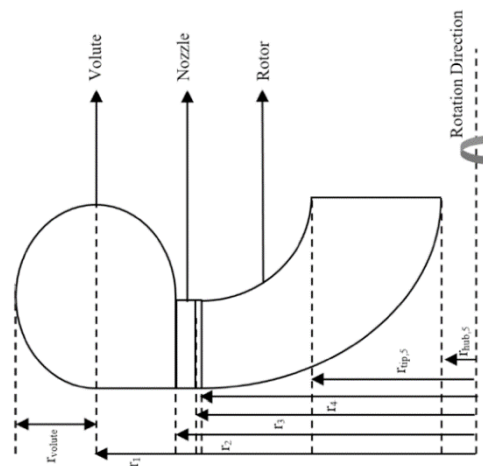
Fig. 1. Main geometrical parameters for an RIT blade **[8]**.
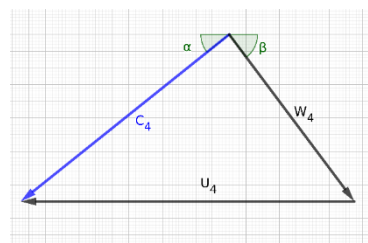
Fig. 2. Velocity triangles at the inlet of the impeller.
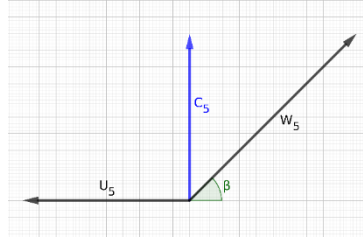
Fig. 3. Velocity triangles at the exit of the impeller.

Table 2. Numerical values of 3D radial inflow turbine design parameters.

Impeller	r_3	52.3 mm	r_4	47.4 mm
	$r_{tip,5}$	33.2 mm	$r_{hub,5}$	13.3 mm
	β_4	56.1°	β_5	60.6°
	Z	14	Ω	2380.1 rad/s
Casing	r_1	89.7 mm	r_2	64.6 mm
	r_3	52.3 mm	r_{volute}	25.1 mm
	r_{sq}	5.00 mm		

GOVERNING EQUATIONS

The flow inside the machine is expected to be compressible and, therefore, the continuity equation in vectorial notation reads

$$\boldsymbol{\nabla} \cdot (\rho\, \mathbf{U}) = \mathbf{0}. \tag{1}$$

Since the period-averaged steady-state performance of the turbine is the focus of this study, steady form of the equations are used. Steady, compressible Navier-Stokes equation is expressed as,

$$\rho(\mathbf{U} \cdot \boldsymbol{\nabla})\mathbf{U} = -\boldsymbol{\nabla}p + \boldsymbol{\nabla} \cdot \boldsymbol{\tau}. \tag{2}$$

R134a is reported to exhibit Newtonian fluid behaviour [10, 11] and, therefore, Equation 2 is used in the following form

$$\rho(\mathbf{U} \cdot \boldsymbol{\nabla})\mathbf{U} = -\boldsymbol{\nabla}p + \mu\boldsymbol{\nabla} \cdot [\boldsymbol{\nabla}\mathbf{U} + (\boldsymbol{\nabla}\mathbf{U})^{\mathrm{T}}], \tag{3}$$

where $\mathbf{U}$, ρ, p, μ denote fluid velocity, density, pressure, and dynamic viscosity, respectively. The Reynold-Averaged Navier-Stokes (RANS) model is used to consider turbulence effects: Realizable k-ϵ turbulence is preferred for the closure as it works better in turbomachinery applications for good accuracy [12, 13, 14]. The transport equations for the turbulence parameters read

$$\rho\boldsymbol{\nabla} \cdot (k\mathbf{U}) = \boldsymbol{\nabla} \cdot \left[\left(\mu + \frac{\mu_t}{\sigma_k}\right)\boldsymbol{\nabla}k\right] + G_k - \rho\epsilon + S_k; \tag{4}$$

$$\rho \nabla \cdot (\epsilon U) = \nabla \cdot \left[\left(\mu + \frac{\mu_t}{\sigma_\epsilon} \right) \nabla \epsilon \right] + \rho C_1 S \epsilon - \rho C_2 \frac{\epsilon^2}{k + \sqrt{\nu \epsilon}} + S_\epsilon, \qquad (5)$$

where G_k is turbulence kinetic energy generation due to the mean velocity gradients; C_1, C_2, σ_k, σ_ϵ are the standard constants [15]; S_i are the source terms.

The temperature of the fluid is solved for using the enthalpy transport equation given as,

$$\nabla \cdot (\rho \, U \, h) + \nabla \cdot (\rho \, U \, K) = \nabla \cdot (\alpha_{\text{eff}} \nabla h), \qquad (6)$$

where the effective thermal diffusivity (α_{eff}) is the sum of laminar and turbulent diffusivities. The ideal gas law is used to calculate density

$$\rho = \frac{p}{RT}. \qquad (7)$$

The R134a fluid is assumed to have constant viscosity and specific heat where its thermophysical properties are given in Table 3.

Table 3. Thermophysical properties of R134a.

M	102.3 kg/kmol	C_p	2437 J/kg K
μ	$7.81 \cdot 10^{-6}$ kg/m s	Pr	3.5

COMPUTATIONAL SETUP

The turbine geometry is shown in Fig. 4. The computational setup has 3 boundaries: inlet, outlet, and casing.
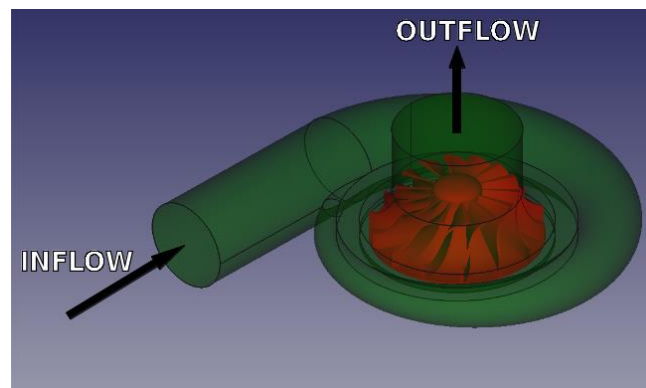
Fig. 4. Computational setup of the problem.

At the inlet, a prescribed value for the pressure is given at each case, and a zero-gradient boundary condition is used for the velocity where the vectors are set to be perpendicular to the surface. Also, a 5% turbulence intensity is given for the inflow with a length scale calculated from the pipe diameter [16]. At the outlet, the pressure is fixed as 8 bar and, for the velocity, a second type (Neumann) boundary condition is imposed as a zero-gradient. All other flow variables are set to have zero gradient at the outlet. The walls are defined as

no-slip, where the rotor has an angular speed of 22,728 rpm. The temperature at the inlet is taken constant at 363 K. The thermal boundary condition at the walls and the outlet is set as adiabatic.

The finite volume method is used for solving the partial differential equations on an open-source platform OpenFOAM [17]. A steady-state compressible solver (rhoSimpleFoam) is used for the turbulent flow inside the machine [18]. It has co-located variable arrangement [19] and uses the SIMPLEC algorithm [12, 15]. Central differencing scheme is used in finite volume discretisation; Gauss linear interpolation schemes are preferred for divergence and Laplacian discretization to preserve second order accuracy [15]. To increase solver speed, geometric-algebraic multi-grid (GAMG) iterative solver is preferred for pressure equations [20]. On the other hand, a preconditioned bi-conjugate gradient (PBiCG) solver is used for velocity, enthalpy, k and epsilon equations. Convergence criteria for pressure and continuity is set to $1.0 \cdot 10^{-3}$, and $1.0 \cdot 10^{-6}$ is used for all of the other variables.

A mesh with 2,003,312 cells is used, which is shown in Fig. 5. In order to ensure smooth transition of the flow variables from the MRF region, the mesh is specifically refined inside the MRF zone and near to its boundary (see Fig. 6). A further refinement is applied near the zones with a steep gradient [12] such as regions close to the walls, inlet-outlet and the rotor blades in order to accurately resolve the turbulence scales in the turbine.
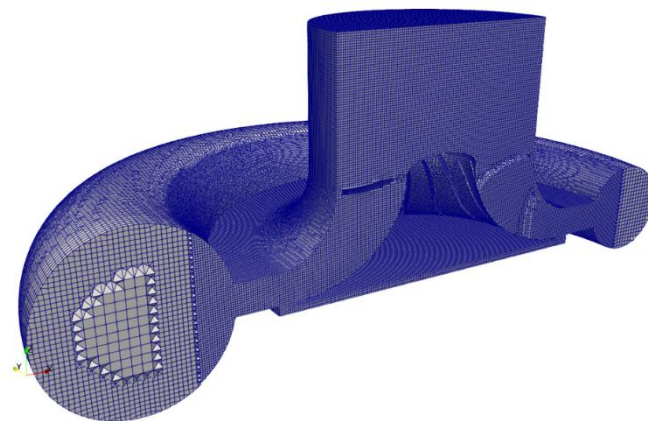
Fig. 5. Mesh of the geometry.
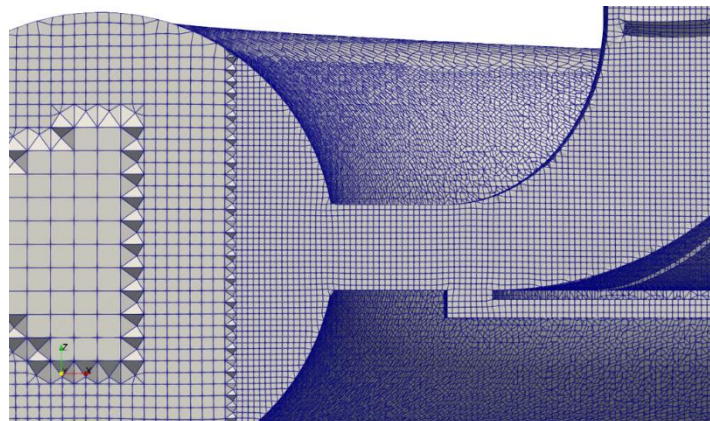
Fig. 6. Mesh refinement inside MRF region.

RESULTS AND DISCUSSION

Characteristic Curves

The CFD simulations are performed for 6 pressure ratios at rotational speed of 22,728 rpm. The pressure and viscous forces on the impeller are recorded and used to calculate the power generated by the turbine. The results of each case are tabulated in Table 4. At the design inlet pressure of 20 bar, the turbine is observed to extract 126 kW of power. Furthermore, the mass flow rate is observed to increase with the inlet pressure (without the turbine being choked) in all the cases considered.

Table 4. CFD results.

p_i [bar]	$\dot{m}$ [kg/s]	$\dot{W}$ [kW]	F_x [N]	F_y [N]	F_z [kN]	M_x [Nm]	M_y [Nm]	M_z [Nm]
10	1.89	7.951	7.050	-45.01	0.501	-0.353	-0.276	-3.34
12	4.34	39.66	91.30	-102.8	1.09	-0.297	-0.299	-16.7
14	5.47	68.35	14.73	-54.61	1.33	1.32	2.07	-28.7
16	6.51	91.21	242.5	-282.8	2.04	0.340	0.781	-38.3
18	7.59	101.6	459.6	-172.2	2.48	2.03	3.95	-42.7
20	8.61	126.5	299.3	-217.8	2.94	1.92	3.41	-53.1

In Fig. 7, the flow coefficient is presented to estimate turbine characteristics where it varies between 0.010 and 0.023 in an amonotonically increasing trend. It reveals that a limit value for the flow coefficient $\dot{m}/T_i p_o$ should exist, which indicates a choked flow. The choked flow occurs when the mass flow rate of the turbine cannot be increased by increasing the pressure ratio [21]. Exploiting the curve representing the data, the mass flow rate for the choked flow can be estimated as 8.91 kg/s. Hence, one can definitely say that the optimum point occurs far away from the limiting point. Furthermore, a marginal increase in the mass flow rate is observed to decrease with increasing the expansion ratio as shown in Fig. 8.
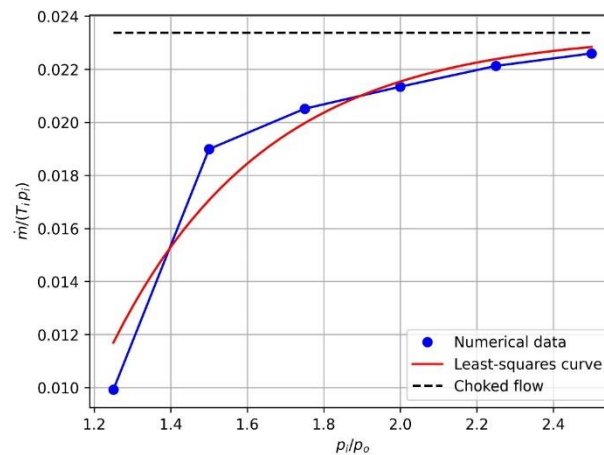
Fig. 7. Turbine characteristics curve.
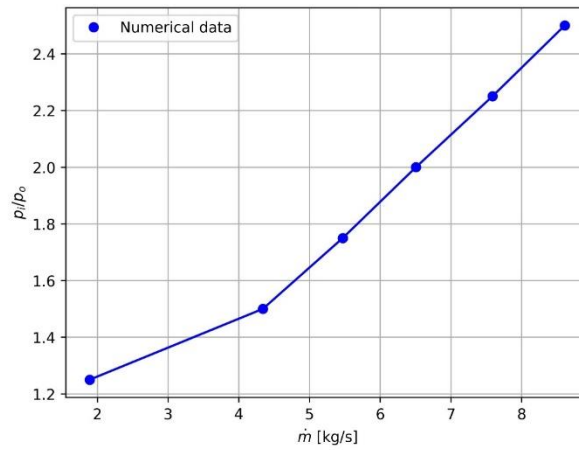
Fig. 8. Expansion ratio vs. mass flowrate.

Efficiency ($\boldsymbol{\eta}$) is an important characteristic of a turbine and it is always desirable to operate at a high efficiency point rather than a high power output situation [22]. The efficiency of the turbine is presented in Fig. 9 and Fig. 10 where both of the plots have an increasing pattern. It is hence deduced that the turbine operates below its maximum efficiency point. Among the simulations conducted, the maximum efficiency is 78.2% and is obtained at 20 bar inlet pressure.
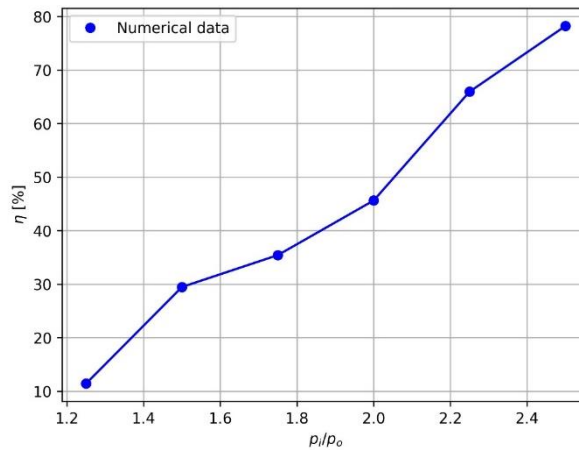
Fig. 9. $\boldsymbol{\eta}$ Vs. expansion ratio.
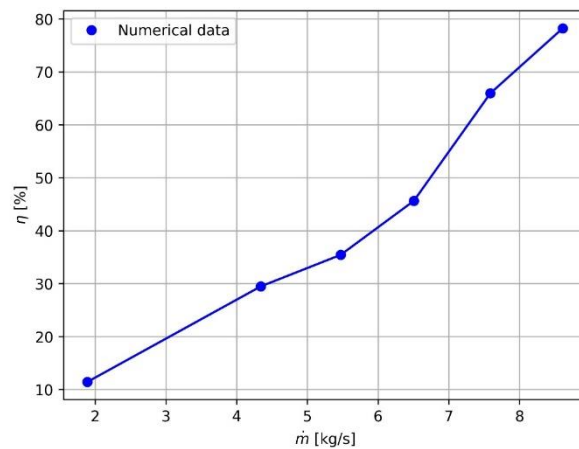
Fig. 10. $\boldsymbol{\eta}$ Vs. mass flowrate.

Flow Field

The flow field is analysed to further study the flow inside the turbine and test the design criteria. We know that the shocks cause sharp discontinuities in the flow field and can exert severe load on the turbine parts, which eventually leads to a catastrophic failure. Hence a shock-free flow field is an important feature. In Fig. 11 and Fig. 12, the pressure and the velocity fields are observed to change smoothly inside the turbine and no shock is observed.
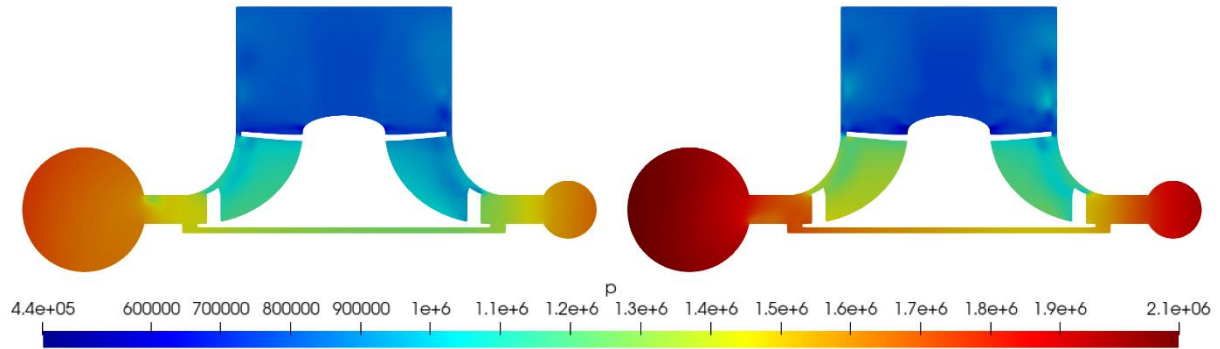
Fig. 11. Pressure field for $p_i = 16$ bar (left) and $p_i = 20$ bar (right),
from yz-section cut.
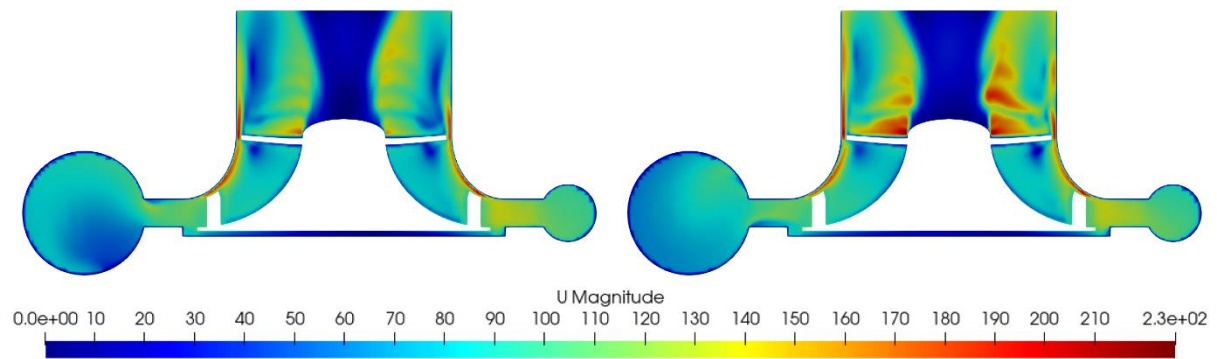
Fig. 12. Velocity field for $p_i = 16$ bar (left) and $p_i = 20$ bar (right),
from yz-section cut.

Another important design criterion is the Mach number inside the turbine, which reveals a subsonic flow at the impeller exit as in Fig. 13: For an expansion ratio of 2.5, the Mach number is observed to decrease along the flow passage and, at the outlet, the Mach number reduces below 0.6, which validates the target outlet Mach number of 0.59 induced at the design stage.
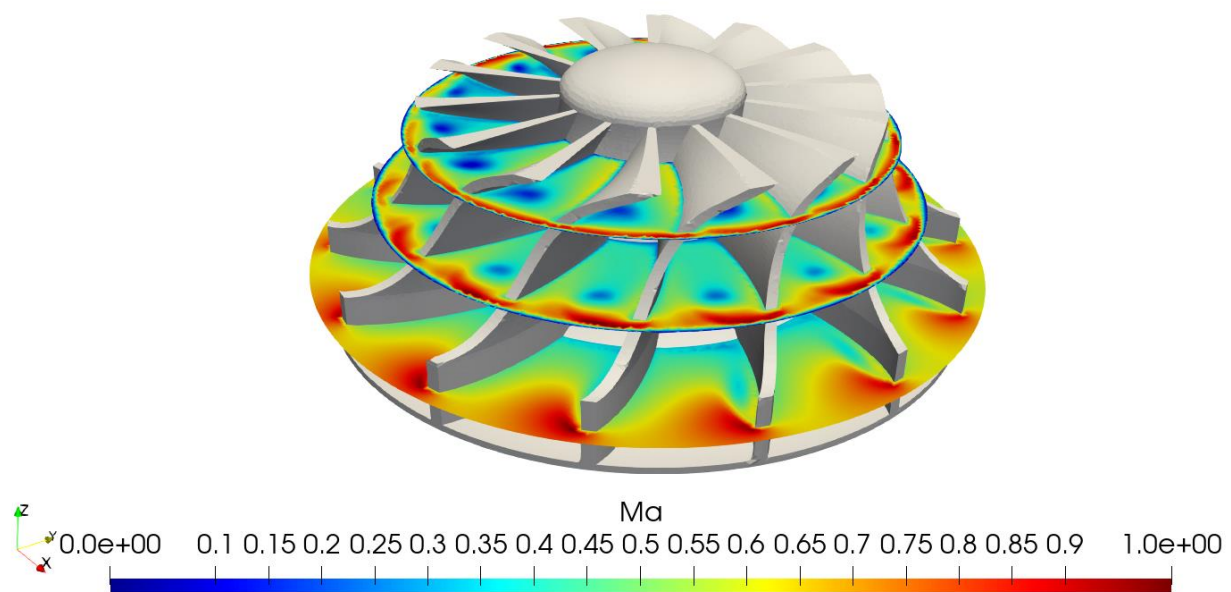
Fig. 13. Mach number distribution around the impeller.

Preventing formation of tip vortices is another vital design goal, as they disrupt the flow inside the cascade and, thus, decrease the efficiency. The streamlines, shown in Fig. 14, prove that the flow smoothly follows the blade boundaries and remains in contact with the edge.
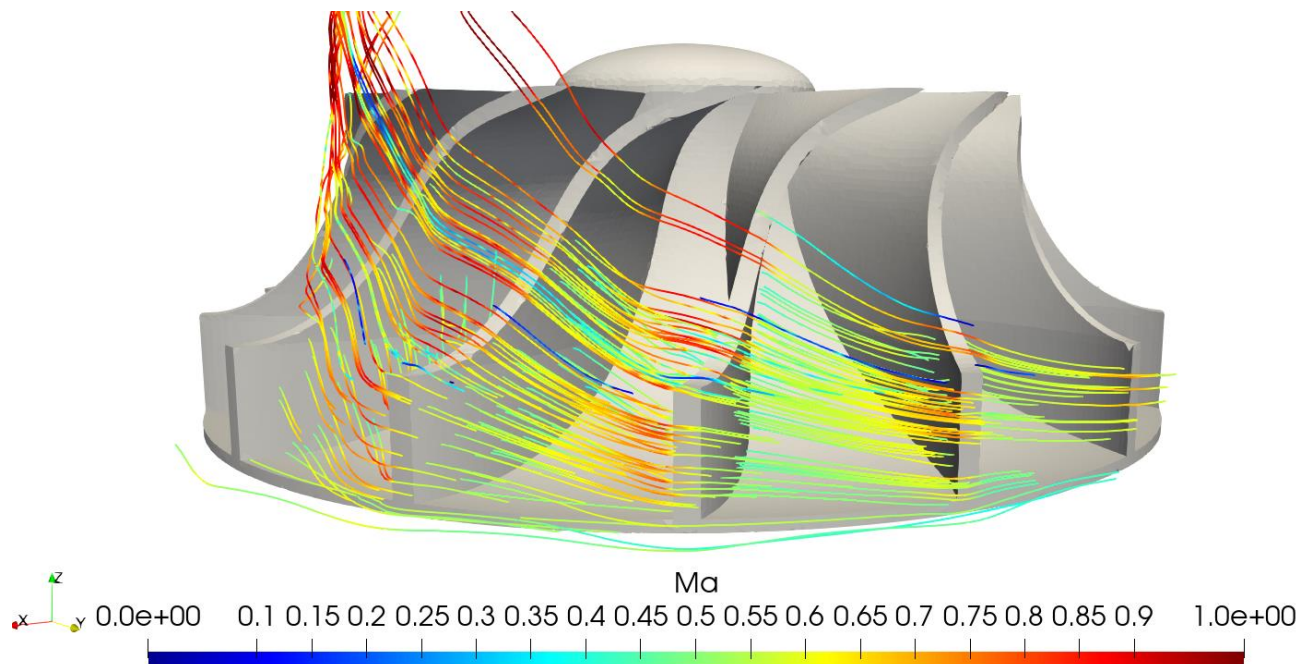
Fig. 14. Streamlines near rotor blades.

CONCLUSIONS

In this study, a 3D design of a radial inflow turbine was conducted for an organic Rankine cycle using R134a as the working fluid. It operated with a pressure ratio of 2.5 and an inlet

temperature of $90°C$. The design was based on the CFD simulations, which were also exploited to test and verify the limits of the turbine. The findings of the design study can be summarized as follows:

- The new design generates 126 kW power at the 22,728 rpm with an expansion ratio of 2.5 and inlet pressure of 20 bars.
- The turbine characteristics curves showed that increasing the pressure ratio reduced the flow coefficient, which indicated the existence of a choked flow. However, the design mass flow rate was 8.61 kg/s, safely away from the choking conditions, which was predicted to occur at a flowrate of 8.91 kg/s.
- Efficiency of the turbine monotonically increased with increasing expansion ratio, up to a maximum of 78.2%.
- The flow smoothly changed inside the turbine and was free of shocks even at the (highest) expansion ratio of 2.5.
- As the flow progressed in the flow passage, the Mach number decreased; the discharge from the impeller occurred as subsonic.
- The streamlines closely followed the impeller blades and no tip vortex formation was observed.

REFERENCES

1. CHEN, H.; GOSWAMI, D.Y.; STEFANAKOS, E.K. A review of thermodynamic cycles and working fluids for the conversion of low-grade heat. *Renewable and Sustainable Energy Reviews*, 2010, Vol. 14, No. 14, P. 3059-3067.

2. SAURET, E.; ROWLANDS, A.S. Candidate radial-inflow turbines and high-density working fluids for geothermal power systems. *Energy*, 2011, Vol. 36, No. 7, P. 4460-4467.

3. Dong, B.; Xu, G.; Li, T.; Luo, X.; Quan, Y. Parametric analysis of organic Rankine cycle based on a radial turbine for low-grade waste heat recovery. *Applied Thermal Engineering*, 2017, Vol. 126, P. 470-479.

4. LIO, L.; MANENTE, G.; LAZZARETTO, A. A mean-line model to predict the design efficiency of radial inflow turbines in organic Rankine cycle (ORC) systems. *Applied Energy*, 2017, Vol. 205, P. 187-209.

5. SCHUSTER, S.; MARKIDES, C.N.; WHITE, A.J. Design and off-design optimisation of an organic Rankine cycle (ORC) system with an integrated radial turbine model. *Applied Thermal Engineering,* 2020, Vol. 174, P. 115-192.

6. WHITE, M.T.; SAYMA, A.I. A generalised assessment of working fluids and radial turbines for non-recuperated subcritical organic Rankine cycles. *Energies,* 2018, Vol. 11, No. 4.

7. RAHBAR, K.; MAHMOUD, S.; AL-DADAH, K., MOAZAMI, N. Parametric analysis and optimization of a small-scale radial turbine for organic Rankine cycle. *Energy,* 2015, Vol. 83, P. 696-711.

8. BEKILOĞLU, H.E.; BEDIR, H.; ANLAŞ, G. Multi-objective optimization of ORC parameters and selection of working fluid using preliminary radial inflow turbine design. *Energy Conversion and Management,* 2019, Vol. 183, P. 833-847.

9. OZDEMIR, I.R.; OZTURK, Y.; OZMADENCI, B. Design and performance analysis of radial inflow turbine for organic Rankine cycles. BSc Thesis. *Bogazici University*, 2021.

10. LAESECKE, A.; BAIR, S. High-pressure viscosity measurements of 1, 1, 1, 2-tetrafluoroethane. *International Journal of Thermophysics,* 2011, Vol. 32, P. 925-914.

11. REHMAN, Z.; SEONG, K.; LEE, S.; SONG, M.H. Experimental study on the rheological behaviour of tetrafluoroethane (R-134a) hydrate slurry. *Chemical Engineering Communications,* 2018, Vol. 205, P. 822-832.

12. VERSTEEG, H.; MALALASEKERA, W. *An Introduction to Computational Fluid Dynamics: The Finite Volume Method*. Pearson Education Limited, 2007, ISBN 9780131274983.

13. HOWARD, J.; PATANKAR, S.; BORDYNUIK, R. Flow prediction in rotating ducts using Coriolis-modified turbulence models. *American Society of Mechanical Engineers*, 1980.

14. JAKIRLIĆ, S.; HANJALIC, K.; TROPEA, C. Modelling rotating and swirling turbulent flows: a perpetual challenge. *Aiaa Journal - AIAA J,* 2002, Vol. 40, P. 1984-1996.

15. FERZIGER, J.; PERIC, M.; STREET, R. *Computational Methods for Fluid Dynamics*. Springer International Publishing, 2019, ISBN 9783319996936.

16. *ANSYS Fluent User's Guide*. ANSYS Inc.: 2013.

17. WELLER, H.; TABOR, G.; JASAK, H.; FUREBY, C. A tensorial approach to computational continuum mechanics using object-oriented techniques. *Computers in Physics*, 1998, Vol. 12.

18. *OpenFOAM: User Guide, Solvers*. OpenCFD Ltd.: 2018- [referred on 07 04 2021] Link to the internet < https://www.openfoam.com/documentation/guides/latest/doc/openfoam-guide-applications-solvers.html>.

19. *Programmer's Guide*. Christopher J. Greenshields: CFD Direct Ltd., 2015.

20. SAAD, Y. *Iterative Methods for Sparse Linear Systems*. Society for Industrial and Applied Mathematics, 2003, ISBN 9780898715347.

21. HENDRICKS, E. Meanline analysis of turbines with choked flow in the object-oriented turbomachinery analysis code. 2016.

22. DIXON, S.; HALL, C. *Fluid Mechanics and Thermodynamics of Turbomachinery*. Elsevier Science, 2013, ISBN 9780124159549.

23. SHAPIRO, A.; SHAPIRO, R. *The Dynamics and Thermodynamics of Compressible Fluid Flow*, *Volume 1,* Wiley, 1953.

THERMODYNAMIC ANALYSIS OF THERMAL DESALINATION SYSTEM WITH HUMIDIFICATION–DEHUMIDIFICATION CYCLE

V.V. Sereda, A.S. Solomakha, N.O. Prytula, <u>N.O. Shvets</u>
National Technical University of Ukraine "Igor Sikorsky Kyiv Polytechnic Institute"
Politehnichna 6, 03056 Kyiv – Ukraine
+380 68 771 53 25
shvets.nazariy@lll.kpi.ua

EXTENDED ABSTRACT

OVERVIEW

The demand for clean drinking water is growing both in Europe and the whole world due to the population growth, the increased rate of urbanization, industrialization, agricultural activity and social and economic development [1]. One of the most promising desalination methods is thermal humidification-dehumidification process [2]. In spite of significant benefits of this technology, it has a key drawback – high thermal energy consumption [3]. In this study, the authors aim to develop a mathematical model for the cycle of air humidification-dehumidification, to carry out a thermodynamic analysis of a thermal desalination system based on salt water heating in an intermediate heater and to determine the system operation conditions to obtain the maximum performance with minimum energy consumption.

METHODS

The diagram of the desalination system based on the working principle of air humidification-dehumidification is shown in fig.1. Air and salt water move in the open circuits. Salt water is pumped to the dehumidifier at the temperature t_{1w}. Then, the salt water circulates through the dehumidifier tubes, being heated up to the temperature t_{2w} removing heat from the saturated air, which is dried by cooling in the tube space of the dehumidifier. Ambient air with the temperature t_{1air} and humidity d_{1air} is supplied to the humidifier by the fan. In the humidifier, the air is heated to the temperature t_{2air} and humidified by direct contact with the salt water heated in a heater up to the temperature t_{3w}. Hot water is sprayed through the nozzles for efficient heat and mass transfer. Some of the water evaporates into the air, while the rest is released as a brine into the lower part of the dehumidifier. At the outlet of the humidifier, the air humidity can reach 100%. Next, the saturated air is supplied to the dehumidifier, where water vapor condenses from the air to produce fresh water. Cooled air with the temperature t_{3air} is removed to the atmosphere.

Fig. 1 – Desalination system working on the air humidification-
dehumidification principle

The desalination system model is a theoretical model developed on the basis of mass and energy balances applied to each of the cycle components, following the laws of thermodynamics [4] with subsequent thermodynamic analysis. The model is calculated with the help of PTC Mathcad engineering software, using CoolProp package to determine the properties of moist air and salt water [5]. The following parameters are then calculated:

1. Gain output ratio (GOR) is the main indicator of the desalination system performance evaluation. It shows how much heat energy is consumed in the desalination process. It numerically equals the ratio of fresh water mass flow rate (G_{fw}), multiplied by the latent heat of vaporization (r), to the thermal energy supplied during the cycle (Q_h):

$$GOR = G_{fw}r/Q_h; \qquad (1)$$

2. Recovery ratio (RR) is the ratio of fresh water mass flow rate obtained in the system to the salt water consumption (G_{sw}):

$$RR = G_{fw}/G_{sw}; \qquad (2)$$

3. Mass flow rate ratio (MR) is the ratio of the salt water mass flow rate to the mass flow rate of the input air (G_{1air}):

$$MR = G_{sw}/G_{1air}. \qquad (3)$$

RESULTS

GOR increases along with increasing salt water temperature at the dehumidifier outlet (see Fig. 2). In addition, for the same t_{2w}, the value of GOR is higher at the lower t_{1w}. Fig. 3 shows that the higher the temperature t_{3w} is, the higher the system efficiency is. In practice, the upper value of the temperature t_{3w} is limited to 50–70 °C in order to prevent scale formation. As the temperature t_{3w} increases, the MR value also increases (see Fig. 4). This means that the higher the temperature of the salt water is at the inlet to the humidifier, the less air needs to be supplied to the humidifier and the fan will consume less electricity. As it is shown in Fig. 5, the

RR coefficient does not actually depend on t1w, and with increasing Δt_{sw} (Δt_{sw} = t2w - t1w), the RR value also increases. This means that the higher the temperature t2w is, the more fresh water can be obtained in the system.

Fig. 2. Dependence of
GOR on t_{1w} and t_{2w}:
$1 - t_{1w} = 10$ °C; $2 - t_{1w} =$
20 °C; $3 - t_{1w} = 30$ °C

Fig. 3. Dependence of GOR on
Δt_{sw} and t_{3w}:
$1 - t_{3w} = 50$ °C; $2 - t_{3w} = 60$ °C; 3
$- t_{3w} = 70$ °C
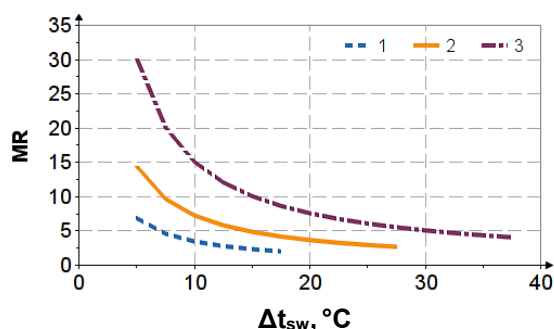
Fig. 4. Dependence of
MR on Δt_{sw} and t_{3w}:
$1 - t_{3w} = 50$ °C; $2 - t_{3w} =$
60 °C; $3 - t_{3w} = 70$ °C
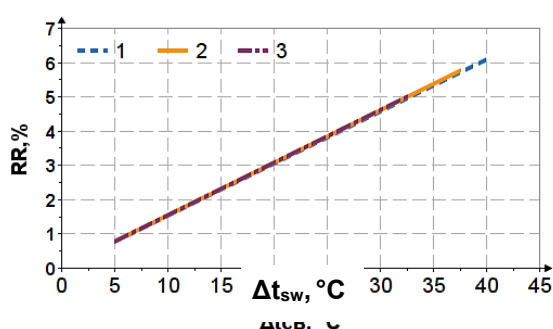
Fig. 5. Dependence of RR on Δt_{sw}
and t_{1w}:
$1 - t_{1w} = 10$ °C; $2 - t_{1w} = 20$ °C; 3
$- t_{1w} = 30$ °C

Heat and mass transfer processes between air and water in dehumidifier and humidifier have low intensity. Due to this, water desalination plants with a humidification-dehumidification cycle provide low (up to 10 l/h) capacity. To obtain considerable fresh water flow rate, it is necessary to significantly increase the area of the heat transfer surface of both the dehumidifier and the humidifier. This solution leads to an increase in metal consumption and cost of the entire plant, which is economically unprofitable in comparison with the membrane desalination technologies.

To obtain 10 L of fresh water during 1 hour of system operation (under optimal conditions GOR = 3.75 and RR = 6%, see fig. 2 and 5), the heater power amounts to 1.73 kW. The use of renewable energy (including solar energy) can significantly reduce the cost of fresh water.

Due to the advantages and disadvantages of desalination with humidification-dehumidification cycle, this technology should be used primarily for small resorts and hotels on the sea coasts of Europe, as well as in private homes in the regions with high intensity of solar radiation.

CONCLUSIONS

The maximum values of GOR and RR for the humidification-dehumidification cycle with additional water heating are 3.75 and 6%, respectively. To obtain such results, the salt water temperature at the inlet to the system (dehumidifier) should be equal to 10 °C, and the salt water temperature at the inlet to the humidifier – 70 °C. At the same time, the air temperature and humidity can have any values.

The main factors limiting further increase in GOR and RR are the limitations of the maximum values of t_{3w} and Δt_{sw}. This necessitates the use of a heater with external heat supply in the cycle.

The most effective way to increase GOR is to use the renewable energy sources (sun, recycled heat, etc.) to heat salt water in the heater. This solution will significantly reduce the cost of thermal energy in the heater and increase the system efficiency (GOR).

Keywords: gain output ratio, humidification-dehumidification, mathematical model, thermal desalination, thermodynamic analysis.

REFERENCES

1. *Nature-based solutions for water*. UNESCO, Paris, France, 2018 [referred on the 20th of January in 2022 y.]. Link to the internet <https://unesdoc.unesco.org/ark:/48223/pf0000261424>.

2. SUBRUMANI, A.; JACANGELO, J.G. Emerging desalination technologies for water treatment: a critical review. *Water Research*, 2015, Vol. 75, P. 164–187.

3. MOHAMED, A.S.A.; AHMED, M.S.; MAGHRABIE, H.M.; SHAHDY A.G. Desalination process using humidification–dehumidification technique: a detailed review. *International Journal of Energy Resources*, 2020, Vol. 45, No. 3, P. 3698–3749.

4. KUDELIA, P.; DUBOVSKYI, S.V. Energy and exergy approaches to problem of rational energy use. *Enerhetyka: ekonomika, tekhnolohii, ekolohiia*, 2020, Vol. 2, P. 7–16.

5. *C++ library of properties for 122 components*, CoolProp.org. [Referred on the 20th of January in 2022 y.]. Link to the internet <*http://www.coolprop.org*>.

ANNULAR SEAL SELF-EXCITED VIBRATION IN LEAKING SPHERICAL VALVES USING COMPRESSIBLE FLOW MODEL

A. Hesham

Arab Academy for Science, Technology and Maritime (AASTMT),
Mechanical Engineering Department.
Abu kir, 1029 – Egypt
+201007038970
hesham.saber@aast.edu

P. Jorge

Universidad de Oviedo, Departemento de Energia.
Wifredo Ricart s/n, Edificio Este (Energia), 33203 – Spain
+34628575742
parrondo@uniovi.es

EXTENDED ABSTRACT

OVERVIEW

Conventional hydropower plants with dams and reservoirs include the following hydraulic components: water intakes, penstocks, turbines, generators, valves, and draft tubes as in the case of the Salime power plant located in Asturias, Spain [1], see Fig 1a.
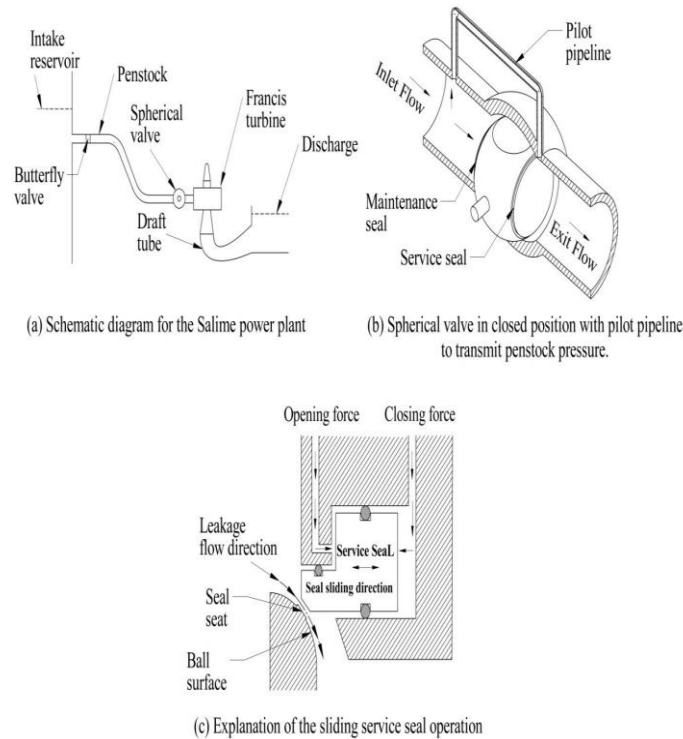
Fig 1. Illustrative diagram for the Salime power plant with section views
for the spherical valve and the sliding service seal.

As seen in Fig 1a, a butterfly valve is usually located close to the water intake and a spherical valve is placed at the downstream end of the penstock, right upstream of the turbine. These valves are not intended for regulation but to close the penstock and shut off the water flowing through the turbine when production stops or in case of long maintenance operations. To achieve water tightness when the spherical valves are closed, they usually incorporate two metallic seal rings that can be tightened onto an annular seat on the valve ball as in Figs (1b and 1c), so that the clearance between the rotating ball and the external casing of the valve becomes blocked. The first seal is the maintenance seal, which is located at the upstream side of the valve, while the other seal is the service seal located at the downstream side. In general, the maintenance seal is applied only during long shutdowns for valve maintenance purposes. Instead, the service seal is always applied after the valve closure whenever the turbine stops. In practice, the maintenance seal always remains fixed and only the service seal can slide to either opened or closed state, as in Fig 1c, where the pilot pipeline transmits the upstream pressure to slide the service seal.

Unfortunately, in practice, the technicians of the plant began to observe events of violent vibrations in the power plant. These vibrations, which happened to take place once the spherical valves were closed and the annular seals tightened, were associated to the successive hitting of the seal against its seat on the ball, and so they would be accompanied by periodic leakage flow through the intermittent gap between ball and seal. Simultaneously with these vibrations, large pressure fluctuations were provoked in the penstock, which risks the safe operation of the power plant.

Kube et al. [2]and Caney and Zulovic [3] attempted to simulate the penstock pressure fluctuations developed at the Gordon plant that were originated by a leaking spherical valve

with retractable seal, similar to the case of the study now presented. However their result, which focused on the prediction of the characteristic frequencies, was preliminary and inconclusive.

The observations of the phenomenon at both Salime and Gordon plants suggest that the vibrations occur when the tightening force reduces, leading to some leakage between the ball and casing of the valve. Nonetheless, the mechanism that excites the vibrations is unclear, as well as what conditions in the system may lead to the development of the vibrations or preclude them. Therefore, the purpose of this study is to construct a simplified theoretical model that considers seal's dynamic characteristics and fluid compressibility, which can:

➢ Explain the mechanism that excites the vibrations observed at the Salime plant.

➢ Simulate the transient behaviour of the Salime plant as a function of the relevant physical and geometrical parameters.

METHODS

Figs (2a and 2b) show the considered spherical valve diagram and hydro-mechanical model representing each group of the Salime power plant. To compute the pressure and flow rate oscillations at the relevant sections of Fig 2b, the water hammer equations [4] are applied at the relevant pipelines with the system boundary conditions and the vibrating seal equation of motion [5]. The transfer matrix method is adopted to compute the system governing equations in the frequency domain since the developed model considers a decayed or diverged sinusoidal pressure and flow rate oscillations, linear friction terms, and linear boundary conditions.

Water hammer equations for pipeline j:

Momentum equation:
$$\frac{\partial H}{\partial x} + \frac{1}{g\,A_j}\frac{\partial Q}{\partial t} + \frac{f_j Q^n}{2g\,d_j A_j^n} = 0 \tag{1}$$

Continuity equation:
$$\frac{g\,A_j}{a_j^2}\frac{\partial H}{\partial t} + \frac{\partial Q}{\partial x} = 0 \tag{2}$$

$$m_{sc}\ddot{y} + c_{sc}\dot{y} + k_{sc}y = F(t)$$

Seal equation of motion:
$$\underbrace{\left(m_{sc} + m_w\right)}_{m_{eq}}\ddot{y} + \underbrace{\left(c_{sc} + c_w\right)}_{c_{eq}}\dot{y} + \underbrace{\left(k_{sc} + k_w\right)}_{k_{eq}}y = 0 \tag{3}$$

m_w, c_w and k_w are the added water mass, damping and stiffness coefficients.
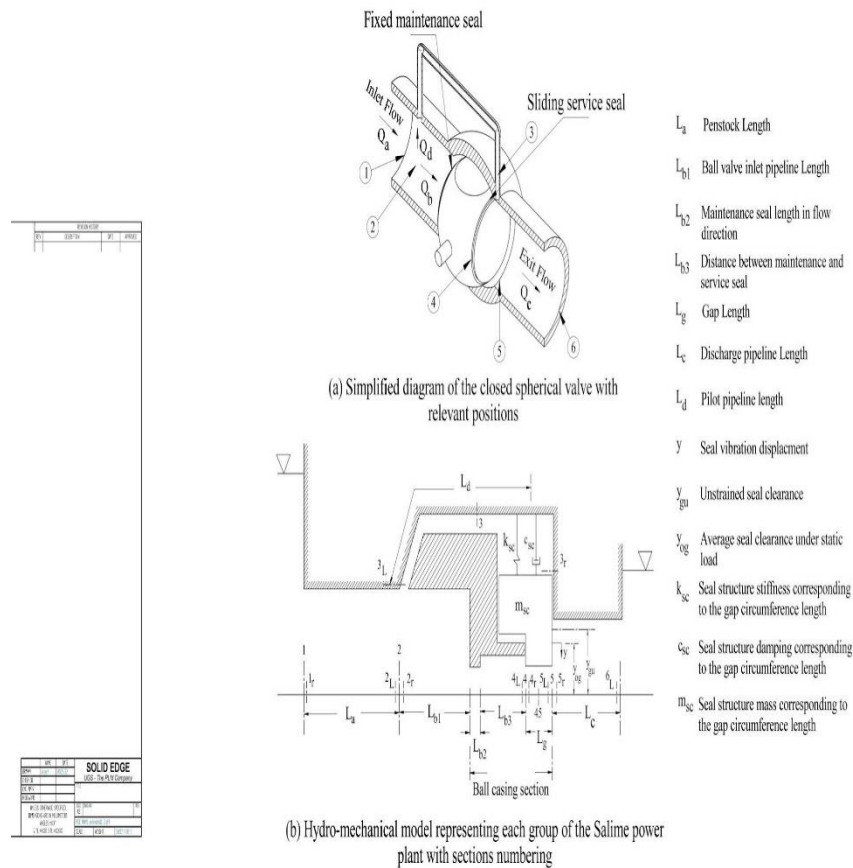
Fig 2. Spherical valve and hydro-mechanical models representing each group of the Salime power plant.

RESULTS

Since fluid compressibility is considered, Fig 3 shows the influence of the input reservoir level H_1 on the vibrating seal dynamic behaviour for the 1st ten oscillation frequencies (harmonics) as they are of practical importance [4]. The dynamic behaviour of the vibrating seal is identified by the seal equivalent damping coefficient c_{eq} and the seal's oscillation frequency f. Fig 3a shows that the instability of the seal's vibration is only established at the 1st harmonic and for values of $H_1>70.3$m where the values of $c_{eq}<0$, as in the case of point C, see Figs (3a and 3g). In contrast, for higher harmonics the system is dynamically stable since the fluid dynamic force damps the seal oscillation as $c_{eq}>0$, see Figs (3a and 3b). In contrast, Figs (3c and 3d) exhibit that H_1 has a negligible influence on the added water stiffness and the seal's equivalent stiffness coefficient at a specific harmonic. Therefore, H_1 has a negligible influence on f as in Figs (3e and 3f).
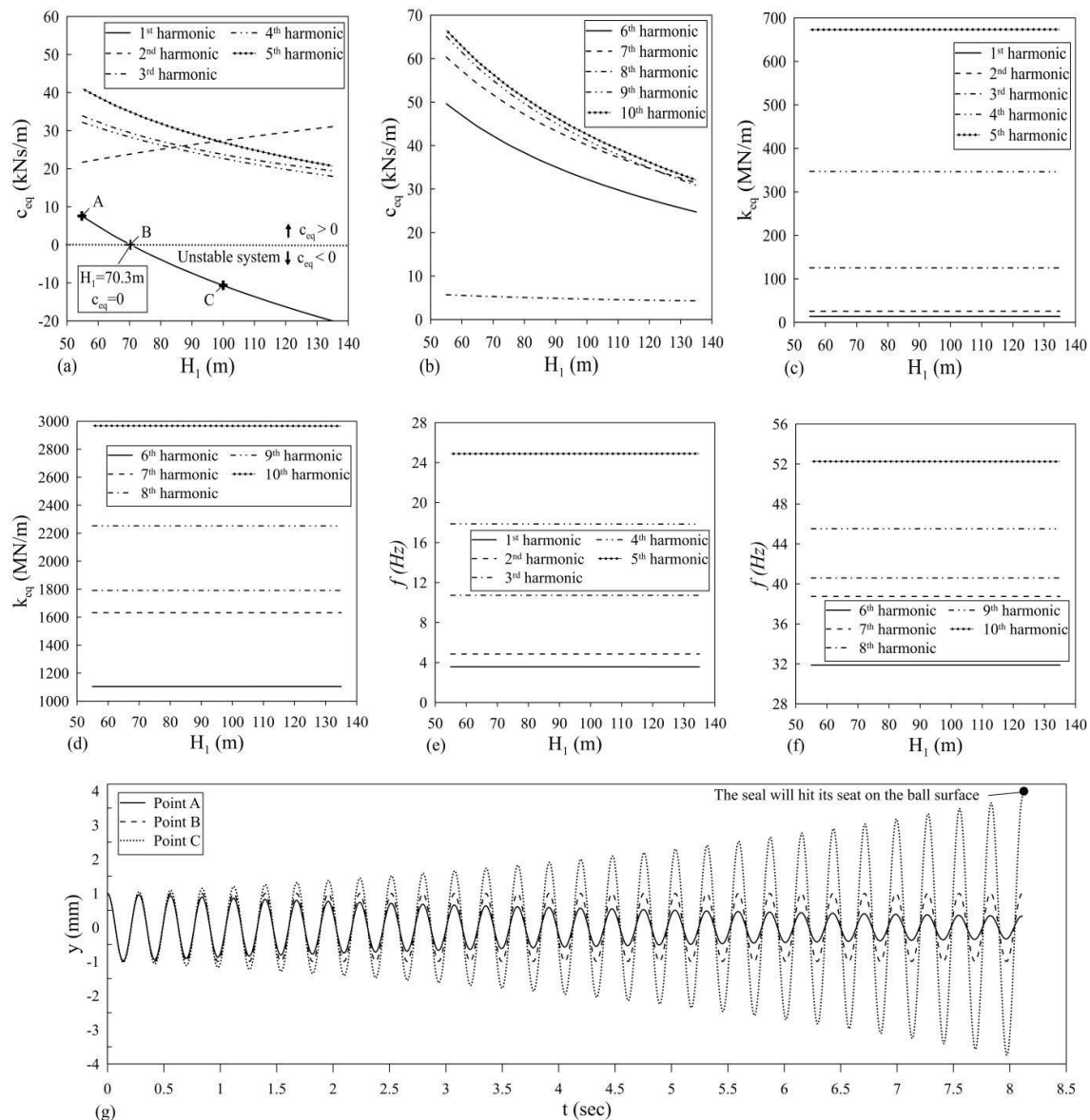
Fig 3. Influence of H_1 on c_{eq}, k_{eq} and f for the 1st ten harmonics.

CONCLUSIONS

The theoretical model developed showed the ability to explain and estimate the periodic seal vibrations depending on the relevant physical and geometrical characteristics of the Salime power plant. The constructed model confirmed that the seal vibrations result from the unstable coupling between the seal vibration motion and the fluid system. So, even if the seal is initially under equilibrium, a slight disturbance can develop pressure and flow oscillations of decaying or incrementing amplitudes depending on the vibrating seal dynamic stability. Also, system analysis showed that the dynamic seal instability is more prone to occur when operating at high input reservoir energy levels for a given gap size. Moreover, the seal vibration instability is more often to be established at the 1st harmonic of the seal periodic vibrations.

Keywords: Spherical valve-water hammer equations- self-excited- vibration.

REFERENCES

1. Gijon: Saltos del Navia C.B., Salto de Salime, [referred on the 23 of January 2022]. <https://www.saltosdelnavia.es/salto-de-salime>.

2. KUBE, S.E.; HENDERSON, A.D.; SARGISON, J.E. Modelling penstock pressure pulsations in hydro-electric power stations. Proceedings of 17th Australasian Fluid Mechanics Conference 2010. Auckland, New Zealand: Auckland University. 2010 December 5-9.

3. CANEY, K.; ZULOVIC, E. Self-excited penstock pressure oscillations at Gordon Power Station in Tasmania and other similar events. Proceedings of Water Power XIV conference. Austin. Texas. 2005 July 21.

4. CHAUDHRY, M.H. *Applied Hydraulic Transients (Third Edition)*. New York: Springer, 2014. 267 p. ISBN 978-1-4939-4401-9.

5. AWAD, H.; PARRONDO, J. Hydrodynamic self-excited vibrations in leaking spherical valves with annular seal. *Alexandria Engineering Journal*, 2020, Vol. 59, No. 3, p. 1515-1524.

NONLINEAR DYNAMIC PERFORMANCE OF THE ANNULAR SEAL IN LEAKING SPHERICAL VALVES IN HYDROELECTRIC POWER PLANTS

A. Hesham
Arab Academy for Science, Technology and Maritime (AASTMT),
Mechanical Engineering Department.
Abu kir, 1029 – Egypt
+201007038970
hesham.saber@aast.edu

P. Jorge
Universidad de Oviedo, Departemento de Energia.
Wifredo Ricart s/n, Edificio Este (Energia), 33203 – Spain
+34628575742
parrondo@uniovi.es

EXTENDED ABSTRACT

OVERVIEW

The Salime power plant is a reservoir power plant that is located in Asturias, Spain [1]. The plant has a nominal power of 160 MW, divided into four power units. Each unit comprises a Francis turbine coupled to an electric generator. Besides, each unit has an individual penstock of 80 m long as well as individual valves and control elements, so that each unit can operate independently, see Fig 1a.

The function of the turbine inlet valve at the Salime power plant is to prevent water flow to the turbine when the turbine is in no-load condition. The turbine inlet valve at the plant is a spherical valve with two metal annular seals, as in Fig 1b. The downstream seal is the sliding service seal responsible to block any leakage between the ball and the valve casing. When the ball valve is in a closed position, the penstock water pressure passes through the pilot pipeline and pushes the seal towards its seat as in Figs (1b and 1c). Therefore in normal conditions, the seal sits on its seat on the ball surface, thus preventing any leakage flow.

Unfortunately, in practice, while the turbine is in no-load condition and the valve is set into a closed orientation, the service seal produces periodic vibrations instead of staying fixed to its seat. These vibrations were noticed as violent internal impacts coincide with high-pressure oscillations in the penstock pipeline. This phenomenon ended, when an alarm sensor located near the turbine inlet valve registered a pressure value exceeding the security limit established at 13.5 bar. In this situation, the alarm sensor caused the closure of the butterfly valve located at the penstock entrance, as in Fig 1a. This operation was effective in stopping the pressure fluctuations and the seal vibrations. However, this solution was undesirable because there was a high water leak and the subsequent operation was complex

and takes a longer time than in usual conditions. Therefore, other correction measures had to be explored to prevent the occurrence of this phenomenon in the plant.

Since there is no external force acting on the seal, thus the seal vibrations are expected to be self-excited due to the presence of an unsteady leaking flow through an oscillating gap. In fact, this problem has been noticed long time ago in several power plants, although the cases mentioned in the literature are very rare. Abbott et al [2] and Wylie and Streeter [3], studied the penstock self-excited vibrations due to the leakage of the penstock valve at the Bersimis No.2 power station (Canada). Also, Kube et al [4] referred to a case of penstock pressure oscillations due to the seal leakage of the turbine inlet valve at the Gordon power station (South-West Tasmania). System analysis concluded that the seal dynamic characteristics must be included to compute the correct values of the penstock pressure fluctuations.

(a) Description of the Salime power plant

(b) Turbine inlet valve (spherical valve)

(c) Explanation of the sliding service seal operation
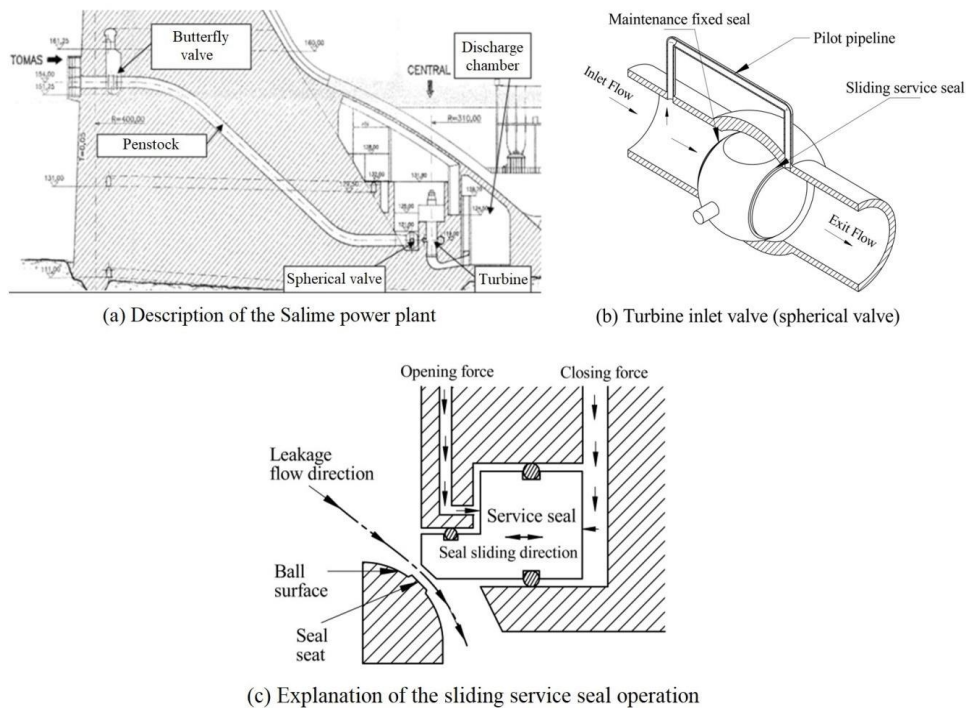
Fig. 1. (a) Description of the Salime power plant and the spherical valve operation mechanism.

According to the mentioned studies, this study aims to present a simplified theoretical model, which can interpret the excitation mechanism of the seal's vibration and simulate the transient behaviour of the plant while considering the seal's dynamic characteristics and the unsteady nonlinear hydraulic losses.

METHODS

(a) Closed spherical valve with relevant sections numbering

(b) Hydro-mechanical model for each group of the Salime power plant

Point 1	Penstock entrance
Point 2	Pilot pressure take off point
Point 3	Annular seal's external face on which the pilot pressure is applied
Point 4	Inlet to seal gap
Point 5	Exit from the seal gap
Point 6	Discharge chamber
L_a	Penstock length up to the valve entrance
L_{b1}	Duct length through the spherical valve to the ball surface
L_{b2}	Fixed maintenance seal length in the flow direction.
L_{b3}	Length between the fixed maintenance seal and the sliding service seal.
L_g	Gap length in flow direction.
L_c	Pipeline length from the ball exit to the discharge chamber
L_d	Length of the Pilot pipeline.
y_{gu}	Unstrained clearance thickness, as the seal is unloaded neither dynamically nor statically
y_{og}	Average clearance thickness after being stressed statically.
y	Vibration displacement of the sliding service seal from the static equilibrium position (i.e. y_{og})
m_{sg}, c_{sg}, k_{sg}	Seal's structure mass, damping and stiffness coefficients corresponding to the seal's gap circumference length

Fig. 2: Closed spherical valve and hydro-mechanical models representing each group of the Salime power plant.

To keep the theoretical model as simple as possible and include the Salime power plant's relevant data, it is determined to consider the spherical valve scheme of Fig 2a and the hydro-mechanical model representing each group of the power plant, as in Fig 2b, where the relevant positions and dimensions are identified in Fig 2. To compute the flow rate and pressure oscillations at the relevant sections of Fig 2b the unsteady energy equation [5] is applied for the relevant pipelines with the vibrating seal equation of motion [6] and system boundary conditions. These equations are solved nonlinearly using the MATLAB SIMULINK where the initial values of the system variables are applied as their steady-state values.

RESULTS

Fig 3 shows the influence of the input reservoir energy level H_1 on the seal vibration displacement y. Fig 3 shows that at the same gap angle $\theta_g=30°$, the instability of the seal vibration is more like to be established at higher values of H_1. By increasing the input reservoir energy level, the fluid dynamic force (acting on the seal) excites more the seal oscillation rather than damping it. In this situation, the fluid system continues to supply energy to the vibrating seal. Therefore, the amplitude of the seal oscillation increases over time leading to a dynamically unstable system as in the case of $H_1=125$ m.

Fig 4 shows the influence of the seal's gap angle θ_g on the seal vibration while operating on the power plant nominal head $H_1=105$ m. Fig 4 exhibits that increasing θ_g increases the severity of the seal vibration since the leakage flow increases and the fluid dynamic force excitation to the seal oscillation increases. Therefore, the probability of the seal dynamic instability increases by increasing θ_g as in the case of $\theta_g=40°$ as in Fig 4.
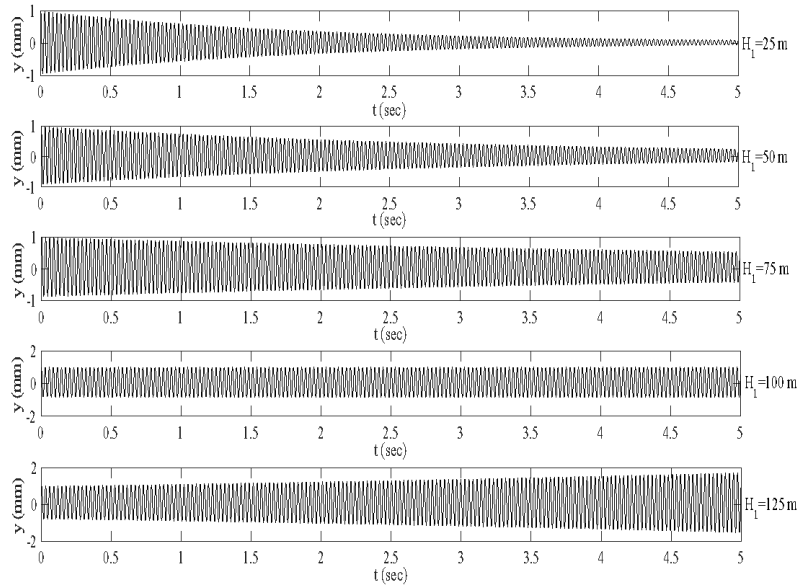
Fig. 3: Relation between y and time t for different values of H_1.
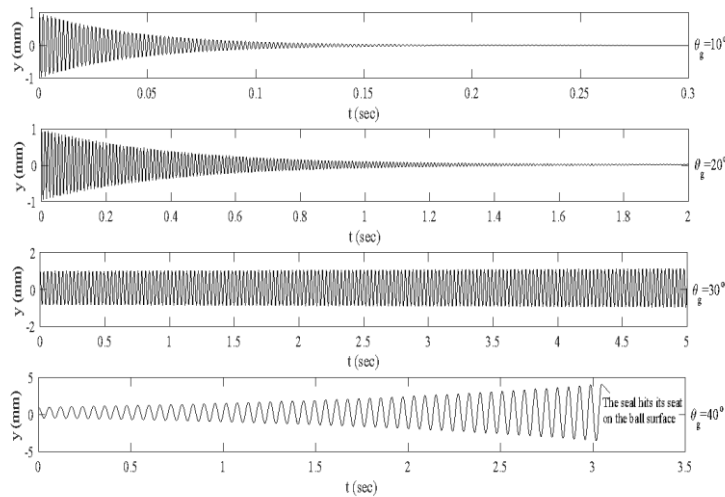
Fig. 4: Relation between y and time t for different values of θ_g.

CONCLUSIONS

The developed hydro-mechanical model showed the ability to estimate the seal periodic vibrations depending on the relevant physical and geometrical characteristics of the power plant. The stability of the seal vibration and the hydro-mechanical system depends significantly on the seal's gap angle and the input reservoir energy level. At a low gap angle and input reservoir energy level, seal vibrations are more likely to be dynamically stable. Also, when seal vibrations are dynamically unstable the seal will hit its seat on the ball surface since the influence of the nonlinear hydraulic losses is minimal.

Keywords: Spherical valves–Self-excited-Vibrations-Turbine inlet valves

REFERENCES

1. Gijon: Saltos del Navia C.B., Salto de Salime, [referred on the 23 of January 2022]. <https://www.saltosdelnavia.es/salto-de-salime>.

2. ABBOTT, H.F.; GIBSON, W.L.; McCAIG, I.W. Measurements of auto-oscillation in a hydroelectric supply tunnel and penstock system. *Journal of Fluids Engineering, Transactions of the ASME*, 1963, Vol. 85, No. 4, P. 625-630.

3. WYLIE, E.B.; STREETER, V.L. Resonance in Bersimis no. 2 piping system. *Journal of Fluids Engineering, Transactions of the ASME*, 1965, Vol. 87, No. 4, P. 925-931.

4. KUBE, S.E.; HENDERSON, A.D.; SARGISON, J.E. Modelling penstock pressure pulsations in hydro-electric power stations. Proceedings of 17th Australasian Fluid Mechanics Conference 2010. Auckland. New Zealand. Auckland University. 2010 December 5-9.

5. MASSEY, B.; WARD-SMITH, J. *Mechanics of Fluids (Eighth edition)*. London and New York: Taylor & Francis Group, 2006. ISBN 0-415-36205-9.

6. AWAD, H.; PARRONDO, J. Hydrodynamic self-excited vibrations in leaking spherical valves with annular seal. *Alexandria Engineering Journal*, 2020, Vol. 59, No. 3, P. 1515-1524.

THE STUDY OF CONVECTIVE INSTABILITY IN A POROUS LAYER WITH THIRD KIND OF BOUNDARY CONDITIONS AND A LACK OF THERMAL EQUILIBRIUM

H. LAGZIRI, H. EL FAKIRI, A. El BOUARDI

Department of Physics, Abdelmalek Essaâdi University
Avenue Palestine B.P. 2117 Tétouan – Morocco
lagziri-hajar7@hotmail.fr

ABSTRACT

The present work analyses the case where both open fluid layers of Horton-Rogers-Lapwood configuration are modelled as third kind of thermal boundary conditions. While the solid one is considered as an adiabatic. The lack of thermal equilibrium regime brings about more than one limiting case. The basic temperature profile for each case is developed analytically via the set of governing equations and boundary conditions. The linear stability analysis is carried out by means of the normal modes method. The eigenvalue problems are solved by a numerical solution with the use of the Runge-Kutta solver and the shooting method.

Keywords: Porous Medium, Shooting Method, Local thermal non-equilibrium, linear stability analysis

INTRODUCTION

When you think of the thermal instability phenomenon, Rayleigh–Bénard cells in a clear Newtonian fluid is the first description that immediately springs to mind. Rayleigh–Bénard convection also emerges in a fluid-saturated porous layer in which the lower surface is heated with uniform temperature. Over the year's convection cells in a porous medium have attracted the attention of many researchers and investigators in different areas. This in turn has led to a large number of studies carried out on what will be later called Darcy–Bénard or Horton-Rogers-Lapwood instability [1-2]. On the other hand, Nield et al. [3-4] described this topic in relevance to other physical features in great detail. The analysis of this configuration has extended the study by involving the variation in the thermal boundaries in the case where both phases have coupled temperature. For example, Barletta et al. [5] had taken into consideration the second kind of thermal boundary conditions by assuming the lower surface as a perfect insulating plate. While Nield et al. [6] carried out the analysis by adopting the first kind of thermal boundary condition. In recent years, the effects of imperfectly conducting boundaries and the lack of thermal equilibrium have become one of the most studied topics. Barletta et al. [7-8] considered both surfaces characterized by external heat transfer in the configuration of vertical cylindrical porous channel and rectangular one. Furthermore, Storesletten et al. [13] suggested the analysis of mixed convection in a porous layer with the impact of viscous dissipation and external heating at the bottom boundary. Effects of two phases with autonomous temperature fields and convective boundary condition on stability analysis was studied by Barletta et al. [12], Lagziri et al. [9-10] and Celli et al. [11] by considering the upper surface with uniform pressure.

Usually, the configuration envisaged in the studies of Horton-Rogers-Lapwood convection is one where the rigid impermeable boundaries are defined as the first kind of thermal boundary condition with the presence of the local thermal equilibrium regime. In the present work, the objective is to analyse the case in which two open parallel boundary layers are subjected to third-kind of thermal boundary conditions rather than perfect conducting temperature walls. The convective thermal boundaries assumed in both surfaces are modelled as Newton cooling law equations. The dimensionless parameters H, γ and Biot numbers appear in the medium by virtue of the difference between the temperature profile of the solid skeleton and the fluid phase. The eigenvalue problems handled from the governing equations by the linear stability analysis and the normal modes method are tackled numerically.

MODELLING OF THE PROBLEM

A horizontal porous layer saturated with a Newtonien fluid and sandwiched between two open parallel boundaries is considered. The solid matrix at the two boundaries is assumed to be as an adiabatic phase while the fluid one is supposed to be heated from below by employing Newton's cooling law at the both surface layers. The linear Oberbeck-Boussinesq approximation together with the lack of thermal equilibrium regime is applicable. The coordinate axes of x* and y* are chosen to be horizontal whereas, the z* axis is considered to be perpendicular to (x*, y*) plan and directed opposite to a gravity force **g**. The relative boundary conditions are defined in Fig (1). The use of these assumptions alongside the curl operator in Darcy law's simplify the governing equations to the following form

$$\nabla^* . \mathbf{u}^* = 0, \qquad\qquad (1a)$$

$$\frac{\mu}{K}\nabla^* \times \mathbf{u}^* - \rho_f \beta g\, \nabla^* \times \left[\left(T_f^* - T_1\right)\mathbf{ez}\right] = 0, \tag{1b}$$

$$(1 - \varphi)\frac{\partial T_s^*}{\partial t^*} = (1 - \varphi)\alpha_s \nabla^{*2}T_s^* + \frac{h}{(\rho C)_s}\left(T_f^* - T_s^*\right), \tag{1c}$$

$$\varphi\frac{\partial T_f^*}{\partial t^*} + \mathbf{u}^*.\nabla^* T_f^* = \varphi\alpha_f \nabla^{*2}T_f^* - \frac{h}{(\rho C)_f}\left(T_f^* - T_s^*\right) \tag{1d}$$

Fig. 1. Porous layer with boundary conditions

Hence, T_0 is the reference temperature [K], g is the modulus of the gravitational acceleration [ms^{-2}], $\mathbf{ez}$ is the unit vector along the z-axis, α is the thermal diffusivity [m^2/s], C is the heat
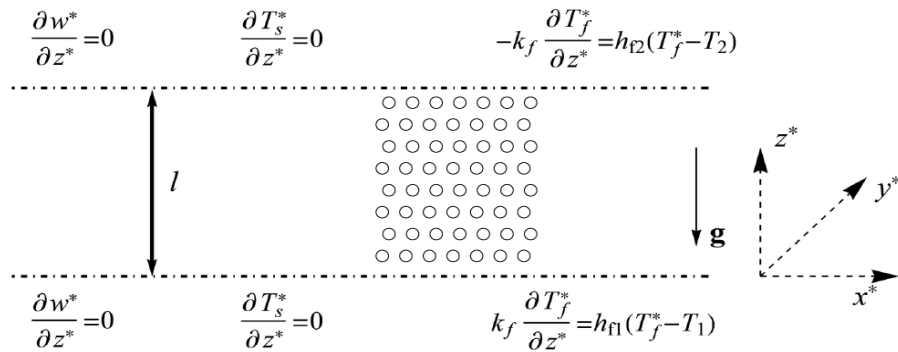
capacity per unit mass [J/(kg K)], β is the thermal expansion coefficient [K^{-1}], h is the inter-phase heat transfer coefficient [W/(m^{3}K)], ρ is the density [kg/m^3], φ is the porosity of the medium, μ is the dynamic viscosity [Pas], k is the thermal conductivity [W/(m K)] and K is the permeability of the medium [m^2]. The subscripts f and s mean the fluid phase and the solid porous medium while the numbers 1 and 2 denote the lower and the upper exterior environment. Otherwise, the dimensionless quantities required to Eqs. (1) And boundary conditions are written as:

$$\nabla^* \to \nabla\frac{1}{l}\,, \quad t^* \to \frac{l^2}{\alpha_f}t, \qquad \mathbf{u}^* \to \mathbf{u}\frac{\varphi\alpha_f}{l}\,, \qquad T_{s,f}^* \to T_2 + T_{s,f}(T_1 - T_2) \tag{2}$$

The extracted dimensionless parameters are:

$$H = \frac{hl^2}{\varphi k_f}, \gamma = \frac{\varphi k_f}{(1 - \varphi)k_s}, R = \frac{\beta\Delta T g K l}{\nu\alpha_m}\,, B_{f1} = \frac{l\,h_{f1}}{k_f}\,, B_{f2} = \frac{l\,h_{f2}}{k_f}, \lambda = \frac{\alpha_f}{\alpha_s}$$

$$k_m = (1 - \varphi)k_s + \varphi k_f, \;\; \alpha_f = \frac{k_f}{(\rho C)_f}, \;\; \alpha_m = \frac{k_m}{(\rho C)_f} \tag{3}$$

The vector $\mathbf{u}$ is the dimensionless velocity field (u, v, w), T is the dimensionless temperature, t is the dimensionless time, l is the thickness of the layer [m] and ν is the kinematic viscosity [m^2/s]. The parameters H, γ, B and R are the dimensionless inter-heat transfer coefficient, the dimensionless thermal conductivity ratio, the Biot number and the Darcy-Rayleigh number. The subscript m means the average.

After substituting Eqs (2) and Eqs (3) into Eqs (1) and boundary conditions we obtain,

$$\nabla^2\psi + \frac{1+\gamma}{\gamma}R\,\frac{\partial T_f}{\partial x} = 0, \tag{4a}$$

$$\lambda\frac{\partial T_s}{\partial t} = \nabla^2 T_s + \gamma H\left(T_f - T_s\right) \tag{4b}$$

$$\frac{\partial T_f}{\partial t} + \frac{\partial \psi}{\partial z}\frac{\partial T_f}{\partial x} - \frac{\partial \psi}{\partial x}\frac{\partial T_f}{\partial z} = \nabla^2 T_f - H(T_f - T_s) \qquad (4c)$$

$$z = 1: \ \frac{\partial \psi}{\partial z} = 0, \quad \frac{\partial T_s}{\partial z} = 0, \quad -\frac{\partial T_f}{\partial z} = B_{f2}T_f \qquad (4d)$$

$$z = 0: \ \frac{\partial \psi}{\partial z} = 0, \quad \frac{\partial T_s}{\partial z} = 0, \quad \frac{\partial T_f}{\partial z} = B_{f1}T_f \qquad (4e)$$

The stream functions employed in Eqs (4) are:
$$u = -\frac{\partial \psi}{\partial x}, \quad w = \frac{\partial \psi}{\partial z} \qquad (5)$$

BASIC STATE

The fluid state is assumed to be motionless inside the solid matrix which means the velocity field can be expressed as
$$\psi_b(z) = 0, \qquad (6)$$

The symbol b describes a basic state.

Local Thermal Equilibrium (LTE)

The LTE can be stemmed from the limiting case of H→∞ only if an infinite amount of heat is transferred between the solid and fluid phases at the interface area, h >>1. In the meantime, the assumption of $k_f \approx O(1)$ has to be valid in order to keep it as finite non-vanishing value. Hence, we can conclude that the two basic temperature fields are identical,
$$T_{sf,b} = \frac{B_{f2}(1 + (1 + B_{f1} - B_{f2}z)\gamma)}{\gamma B_{f2}B_{f1} + B_{f2}(1 + \gamma) + B_{f1}(1 + \gamma)} \qquad (7)$$

Local Thermal Non Equilibrium (LTNE)

When the volumetric heat transfer coefficient is as small as H→0, the thermal coupling between the two phases is harder to be kept because the solid skeleton ceases the exchange of heat with fluid phase. This limit characterizes one of those cases whose basic temperature profiles are not in a local thermal equilibrium condition. Consequently, the two energy balance equations as well as the temperature fields behave autonomously. Thus, each temperature field can be written as,
$$T_{s,b} = \frac{(2 + B_{f1})B_{f2}}{2(B_{f1} + B_{f2} + B_{f1}B_{f2})}, \qquad T_{f,b} = \frac{B_{f1}(1 + (1 + \gamma)B_{f2})}{B_{f1} + B_{f2} + B_{f1}B_{f2}} \qquad (8)$$

STABILITY ANALYSIS

The mathematical procedure considered for a linear stability analysis is the normal mode method. Broadly speaking, the method describes the perturbation solutions in the form of,
$$T_{sf} = T_{sf,b} + \varepsilon \tilde{T}_{sf}(x,z,t), \quad \psi = \psi_b + \varepsilon \tilde{\psi}(x,z,t) \qquad (9)$$

All the nonlinear terms arose by ε^2 are neglected as the amplitude $\varepsilon \ll 1$. Then the perturbation functions $\tilde{T}_{sf}$ and $\tilde{\psi}$ can be written as,

$$\begin{cases} \widetilde{\Psi}(x,z,t) \\ \tilde{T}_s(x,z,t) \\ \tilde{T}_f(x,z,t) \end{cases} = \begin{cases} i\psi(z)e^{i(ax-\omega t)} \\ \theta_s(z)e^{i(ax-\omega t)} \\ \theta_f(z)e^{i(ax-\omega t)} \end{cases} \tag{10}$$

Where a is dimensionless wave number and ω is dimensionless frequency constituted with ωi and ωr as ω=ωi+ωr. In general, substituting Eqs (9) and (10) into Eqs (4) and boundary conditions give rise to,

$$\psi'' - a^2\psi + a\,R\frac{1+\gamma}{\gamma}\theta_f = 0, \tag{11a}$$

$$\theta_s'' - a^2\theta_s + H\gamma(\theta_f - \theta_s) + i\omega\lambda\theta_s = 0, \tag{11b}$$

$$\theta_f'' - a^2\theta_f - H(\theta_f - \theta_s) - a\psi T'_{fb} + i\omega\theta_f = 0, \tag{11c}$$

The linear stability analysis is based on modes whose conditions obey ωi= 0. On the other hand, the principal of exchange of instability for both cases of LTE and LTNE are proved numerically, which means ωr= 0. Therefore, the eigenvalues problem reduces to,

$$\psi'' - a^2\psi + a\,R\frac{1+\gamma}{\gamma}\theta_f = 0, \tag{12a}$$

$$\theta_s'' - a^2\theta_s + H\gamma(\theta_f - \theta_s) = 0, \tag{12b}$$

$$\theta_f'' - a^2\theta_f - H(\theta_f - \theta_s) - a\psi T'_{fb} = 0, \tag{12c}$$

$$\psi'(0) = 0, \qquad \theta_s'(0) = 0, \qquad \theta_f'(0) - \theta_f(0)B_{f1} = 0, \tag{12d}$$

$$\psi'(1) = 0, \qquad \theta_s'(1) = 0, \qquad \theta_f'(1) - \theta_f(1)B_{f2} = 0. \tag{12e}$$

NUMERICAL SOLUTION

The eigenvalue problem relative to the studied configuration is solved numerically via the combined form of the sixth-order Runge-Kutta solver and shooting method. The resulting equations obtained by means of stability analysis and normal modes method are integrated by applying the Runge-Kutta procedure with the initial conditions at target z = 0,

$$\psi'(0) = 1, \quad \theta_f(0) = s_1, \quad \theta_s(0) = s_2 \tag{13}$$

The equation of ψ' (0) =1 serves to fix the normalisation condition. Otherwise, the unknown parameters s_1 and s_2 defined as values of θ_f (0) and θ_s (0) respectively, are determined with the eigenvalue R, by using a shooting method to satisfy the boundary conditions imposed at z = 1,

$$\psi'(1) = 0, \quad \theta_f'(1) - \theta_f(1)B_{f2} = 0, \quad \theta'_s(1) = 0 \tag{14}$$

The numerical procedure performed for this problem is implemented in the Mathematica10 (© Wolfram Research) environment. Furthermore, the Runge–Kutta solver and the shooting method are both of them available through the built-in functions **NDSolve** and **FindRoot**, respectively. These two functions allow us to validate the constraint conditions defined in Eq. (13) in the meantime dealing with the initial value problem presented in Eq. (14). Overall, the input parameters H, γ, a, B_{f1} and B_{f2} have to be prescribed in the numerical set-

up to define the neutral stability curve R(a) as well as the critical values (a$_{cr}$, R$_{cr}$) for the emergence of the convective instability in the medium.

RESULTS AND DISCUSSIONS

The numerical results of the local thermal equilibrium (LTE) case are highlighted in both frames of Fig (1). The right frame describes the marginal stability curves plotted for B$_{f1}$ = B$_{f2}$ = 1, while the left one exhibits the variation curves of R$_C$ with respect to B$_{f2}$ for γ=1. We recall that the stable region usually exists below each neutral stability curve. Overall if we compare the neutral stability curves between them, we will see the region of stability increases as the value of γ decreases even with the presence of the LTE behaviour. This refers to the hidden role played by the thermal conductivity of both phases through the parameter γ on the stability of the medium. On the other hand, the left frame displays the variation of R$_C$ versus B$_{f2}$ for various values of B$_{f1}$ with fixed γ=1. According to this frame, the thresholds values of R attain an infinite value in a case where both Biot numbers of fluid phase simultaneously tend to zero. In other words, the most stable configuration shows up when the ability to exchange heat between both fluid of open surfaces and the external environment becomes too weak. If we look at the curve of B$_{f1}$=10^{-1} we can notice the same behaviour arises even though the fluid of the open lower surface has a huge ability to exchange heat with the environment. Figure (2) describes the threshold values of R versus B$_{f1}$ with different γ for the special case of the local thermal non-equilibrium (LTNE) regime. The uneven effect of Biot numbers for all γ did not exhibit any variation in the behaviour of R$_C$ compared to the previous one of the LTE. Besides, this case supports what have been shown in the right frame of Fig.

Fig. 2. Limiting case of LTE: Plots of R$_c$ versus B$_{f2}$ for γ=1 (l eft frame)

and neutral stability curves Bf1=B$_{f2}$=1 (right frame)
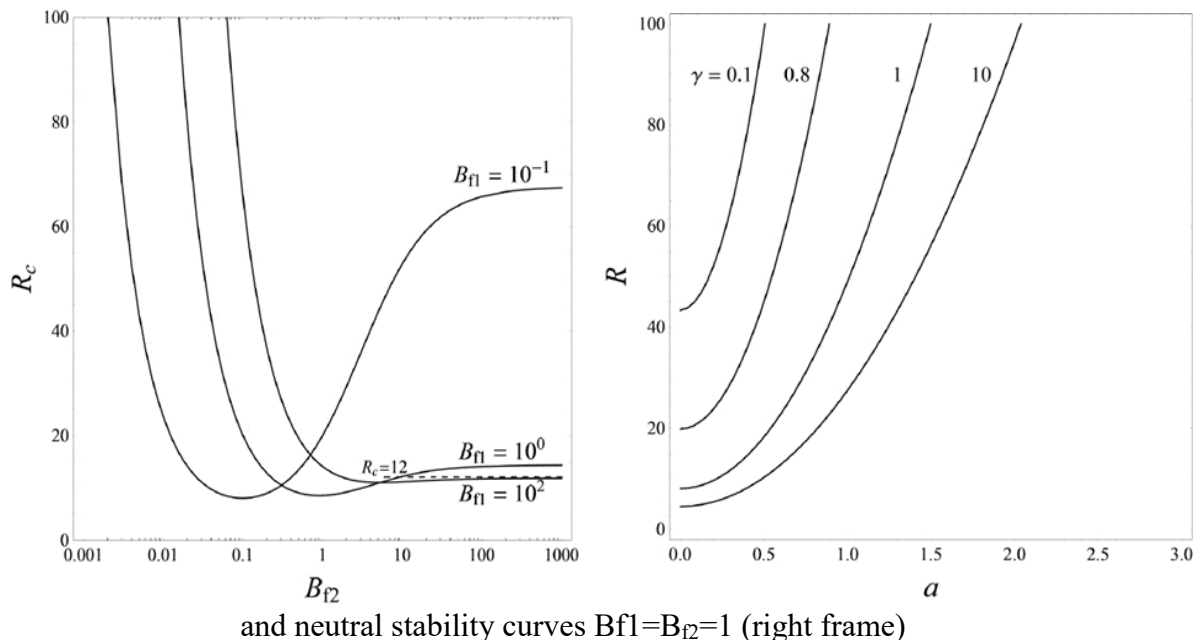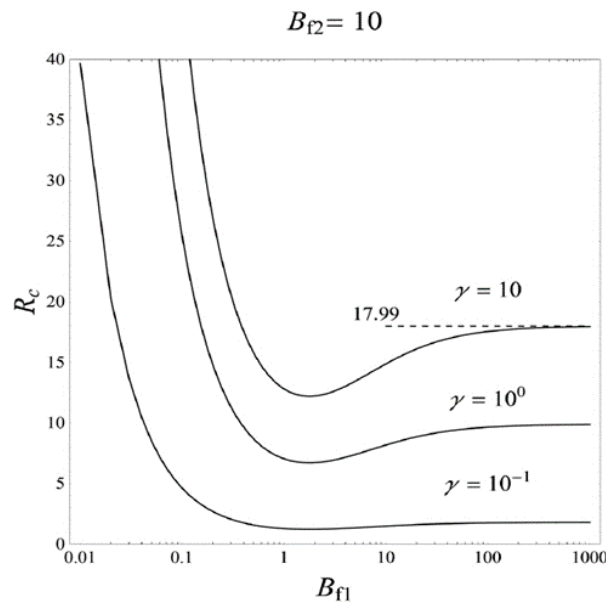
Fig. 3. Limiting case of LTNE: trends of R_C versus B_{f1} for different values of γ

CONCLUSIONS

The study is performed on modelling both free surface layers in the Horton-Rogers-Lapwood configuration with the third kind of thermal boundary conditions using two different temperature phases. The basic flow achieves a stable configuration if both layers have a poor capability of exchanging heat with the external environment. The fluid layer can bring about destabilizing effects if both open surfaces have a higher coefficient of heat transfer with the external medium. Briefly, this behaviour becomes more prominent when a solid phase is much more conductive to a fluid one.

REFERENCES

1. HORTON, C.; ROGERS, F. Convection currents in a porous medium. *Journal of Applied Physics,* 1945, Vol. 16, No. 6, P. 367-370.

2. LAPWOOD, E. Convection of a fluid in a porous medium. Mathematical Proceedings of the Cambridge Philosophical Society, Cambridge University Press. 1948, P.508-521.

3. NIELD, D.A.; BEJAN, A. Convection in Porous Media. New York: Springer, 2013, Vol. 4.

4. NIELD, D.A.; SIMMONS, C.T. A Brief Introduction to Convection in Porous Media. *Transport in Porous Media*, 2018, Vol. 130, No. 1, P. 237-250.

5. BARLETTA, A.; NIELD, D.A. Thermosolutal convective instability and viscous dissipation effect in a fluid-saturated porous medium. *International Journal of Heat and Mass Transfer*, 2011, Vol. 54, No. 7, P. 1641.

6. NIELD, D.A.; KUZNETSOV, A.; XIONG.M. Thermally developing forced convection in a porous medium: parallel plate channel with walls at uniform temperature, with axial conduction and viscous dissipation effects. *International Journal of Heat and Mass Transfer*, 2003, Vol. 46, No. 4, P. 643-651.

7. BARLETTA, A.; STORESLETTEN, L. Onset of convection in a porous rectangular channel with external heat transfer to upper and lower fluid environments. *Transport in Porous Media*, 2012, Vol. 94, No. 3, P. 659-681.

8. BARLETTA, A.; STORESLETTEN, Effect of a finite external heat transfer coefficient on the Darcy-Bénard instability in a vertical porous cylinder. *Physics of Fluids*, 2013, Vol. 25, No. 4.

9. LAGZIRI, H; BEZZAZI, M. Robin Boundary Effects in the Darcy–Rayleigh Problem with Local Thermal Non-Equilibrium Model, *Transport in Porous Media*, 2019, Vol. 129, P. 701-720.

10. LAGZIRI, H; BARLETTA, A; CELLI, M; BEZZAZI, M. The onset of Darcy-Bénard instability in a horizontal porous channel with a free surface using a thermal non equilibrium model, Proceedings of the 4th International Conference on Structural Nonlinear Dynamics and Diagnosis (CSNDD), May 23-25, Marrakech, Morocco, 2016.

11. CELLI, M; LAGZIRI, H; BEZZAZI, M. Local thermal non-equilibrium effects in the Horton-Rogers-Lapwood problem with a free surface, *International Journal of Thermal Sciences*, 2017, Vol. 116, P. 254-2464.

12. BARLETTA, A; CELLI, M; LAGZIRI, H. Instability of a horizontal porous layer with local thermal non-equilibrium: effects of free surface and convective boundary conditions, *International Journal of Heat and Mass Transfer*, 2015, Vol. 89, P. 75-89.

13. STORESLETTEN, L; BARLETTA, A. Linear instability of mixed convection of cold water in a porous layer induced by viscous dissipation, *International Journal of Thermal Sciences*, 2009, Vol. 78, P. 655-664.

MASS TRANSFER AT WATER AND AIR COUNTERCURRENT FLOW IN VERTICAL TUBES

A.S. Solomakha, P.S. Strynada, P.O. Barabash, V.V. Sereda, N.O. Prytula, Y. Liu
National Technical University of Ukraine "Igor Sikorsky Kyiv Polytechnic Institute"
Politehnichna 6, 03056 Kyiv – Ukraine
+38 066 927 73 70
petro.strynada@gmail.com

EXTENDED ABSTRACT

OVERVIEW

Contact heat and mass exchangers are used in many technological processes: cooling of circulating water or flue gases, air humidifying in air conditioning systems, etc. In common devices of this type, vertical tubes can be the main components, in which the liquid film flows under the gravitational force towards the gas flow [1-5]. However, there is no universal dependence for the calculation of such processes. Therefore, the aim of this study was to experimentally investigate the process of mass transfer in the counter-current interaction of the air and water film in a vertical tube.

METHODS

An experimental facility was created, in which the experimental section was a tube with the inner diameter of 34 mm and the length of 1.4 m. At the tube inlet and outlet, air and water flow rates and the dry and wet bulb temperatures were measured. Wetting of the surface was monitored visually through the special glasses in the upper part of the experimental section. The mass transfer coefficient was determined by a specially developed method [6]. The schematic diagram of the facility for the study of mass transfer processes in a vertical film contact apparatus is shown in Fig. 1.
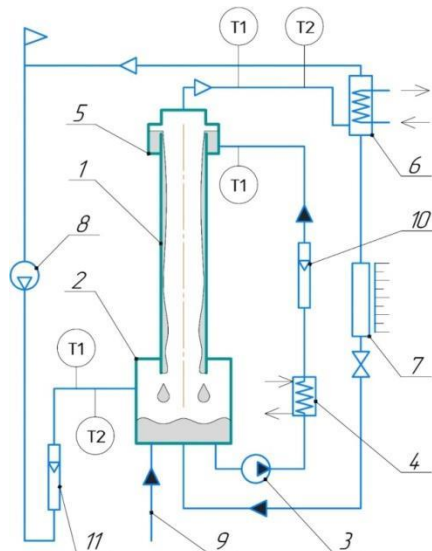
Fig. 1. Schematic diagram of the facility for studying mass transfer in a vertical-tubular film contact apparatus: 1 – heat transfer tube, 2 – collector, 3 – circulation pump, 4 – heater, 5 – sprinkler, 6 – condenser, 7 – meter, 8 – fan, 9 – supply line, 10 – liquid rotameter, 11 – air rotameter

RESULTS

Fig. 2 shows the dependence of the mass transfer coefficient on the air velocity in a vertical tube at a constant water flow rate of 2.4 l/m. An increase in the air velocity above 3.6 m/s causes flooding regime with a subsequent transition to co-current flow of the air and water. The transition to this regime was identified visually and due to a sharp increase in the pressure drop at the experimental setup. We considered this process in more detail in [7-8].
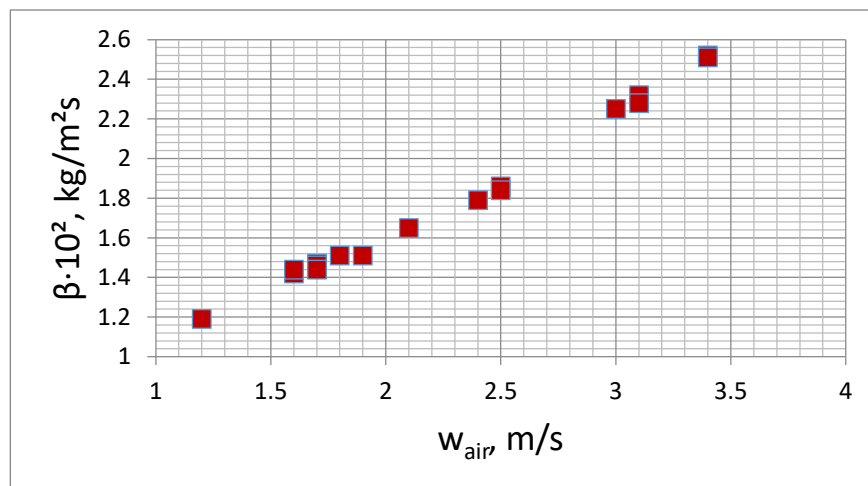
Fig. 2. Dependence of the mass transfer coefficients on the air velocity in a vertical tube

Fig. 3 provides in the dimensionless coordinates the experimental data and results from paper [9]. All the data can be generalized with sufficient accuracy to the equation:

$$Sh = 0.023\,\mathrm{Re}_{air}^{0.83}\,Sc^{0.4}$$

(1)
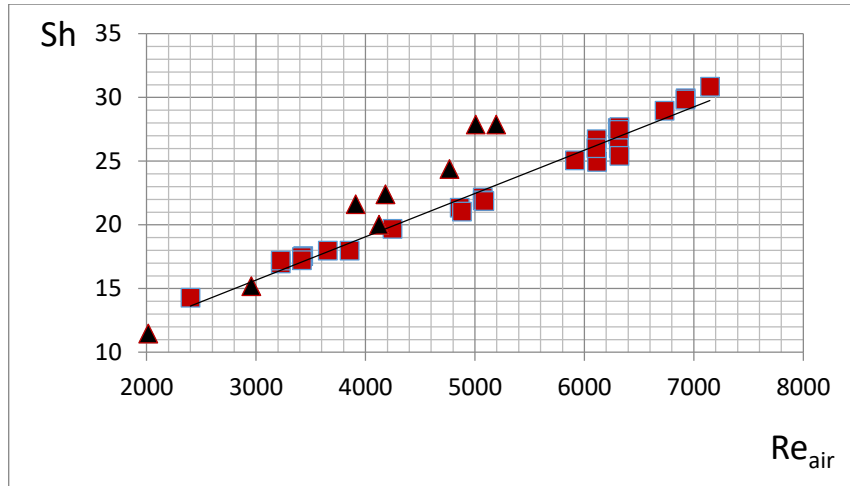
Fig. 3. Dependence of the Sherwood number on the Reynolds number in
a vertical film apparatus:

■ – experiment calculation by equation (1), ▲ – results from [9] with
different water mass flow rate.

In this equation, the Sherwood number:

$$Sh = \frac{K \cdot d}{D} ,$$ (2)

where d is the tube diameter, m; D is the diffusion coefficient, m^2/s; K is the mass transfer coefficient attributed to the difference in concentrations, m/s. The relationship between β and K can be written as

$$K = \frac{\beta \cdot R_{air} \cdot T_{air}}{p_{air}} ,$$ (3)

where R_{air} is the air gas constant, J/ (kg·K); p_{air} is the air pressure, Pa; T_{air} is the average air temperature in the tube, K.

The Reynolds number:

$$Re_{air} = \frac{w \cdot d}{v} = \frac{w \cdot d \cdot \rho}{\mu} ,$$ (4)

where w is the air velocity in the tube, m/s; v is the air kinematic viscosity, m^2/s; μ is the dynamic viscosity, kg/ (m^2/s); ρ is the air density, kg/m^3.

The Schmidt number:

$$Sc = \frac{v}{D} .$$

CONCLUSIONS

An empirical dependence convenient for engineering calculations is suggested. The obtained data and equation correlate with experimental results from paper [9]. The reliability of the experimental technique and processing of its results has been confirmed, which allows using the technique for the experimental research of more complex systems. In the future studies,

it is planned to investigate in more detail the effect of liquid flow on the mass transfer process.

Keywords: mass transfer; contact heat and mass exchangers; counter current flow.

REFERENCES

1. FEDDAOUI, M.; MIR, A.; BELAHMIDI, E. Concurrent turbulent mixed convection heat and mass transfer in falling film of water inside a vertical heated tube. *International Journal of Heat and Mass Transfer,* 2003, Vol. 46, No. 18, P. 3497–3509. Doi: 10.1016/S0017-9310(03)00129-7.

2. GHOSH, S.; PRATIHAR, D.; MAITI, B.; DAS, P. Identification of flow regimes using conductivity probe signals and neural networks for counter-current gas–liquid two-phase flow. *Chemical Engineering Science,* 2012, Vol. 84, P. 417–436. Doi: 10.1016/j.ces.2012.08.042.

3. GHOSH, S.; PRATIHAR, D.; MAIT, I B.; DAS, P. Automatic classification of vertical counter-current two-phase flow by capturing hydrodynamic characteristics through objective descriptions. *International Journal of Multiphase Flow,* 2013, Vol. 52, P. 102–120. Doi: 10.1016/j.ijmultiphaseflow.2012.12.007.

4. WANG, Y.; GUO, Q.; FU, B.; XU, J.; YU, G.; WANG, F. Numerical Analysis of the Flow Characteristics and Heat and Mass Transfer of Falling-Water Films in an Industrial-Scale Dip Tube of a WSCC in an OMB Gasifier. *Industrial & Engineering Chemistry Research,* 2013, Vol. 52, No. 26, P. 9295−9300. Doi: 10.1021/ie2025294.

5. AMI, T.; UMEKAWA, H.; OZAWA, M. Dry out of counter-current two-phase flow in a vertical tube. *International Journal of Multiphase Flow,* 2014, Vol. 67, P. 54–64. Doi: 10.1016/j.ijmultiphaseflow.2014.09.002.

6. SOLOMAKHA, A.; BARABASH, P.; STRYNADA, P.; KUDELYA, P. Mass transfer in counter-current liquid and gas flow in a vertical pipe. *KPI Science News,* 2021, No. 3, P. 7-13. Doi: 10.20535/kpisn.2021.3.239569.

7. BARABASH, P.; SOLOMAKHA, A.; GUROV, A.; PANCHENKO, O. Regimes of motion of water–air flow in a short vertical tube with the underfeed of phases. *Journal of Engineering Physics and Thermophysics,* 2020, Vol. 93, No. 2, P. 443–451. Doi: 10.1007/s10891-020-02139-y.

8. BARABASH, P.; SOLOMAKHA, A.; SEREDA, V. Experimental investigation of heat and mass transfer characteristics in direct contact exchanger. *International Journal of Heat and Mass Transfer,* 2020, Vol. 162, P. 120359. Doi: 10.1016/j.ijheatmasstransfer.2020.120359.

9. WONGWISES, S.; NAPHON, P. Heat- mass transfer and flow characteristics of two-phase counter current annular flow in a vertical pipe. *International Communications in Heat and Mass Transfer*, 1998, Vol. 25, No. 6, P. 819-829. Doi: PII S0735-1933(98)00068-2.

MOLECULAR DYNAMICS STUDY ON BASE ARGON THERMAL CONDUCTIVITY INSIDE NANOCHANNEL

G. Skarbalius, A. Džiugys

Lithuanian Energy Institute
Breslaujos g. 3, LT-44403 Kaunas – Lithuania
+370 37 401993
gediminas.skarbalius@lei.lt

EXTENDED ABSTRACT

OVERVIEW

It has been shown that the suspension of nanoparticles in base fluids even at low concentrations could enhance the thermal properties of the fluid [1]. In turn, this allows to improve the thermal efficiency of systems where cooling/heating plays essential role, e.g., in microelectronics systems. Therefore, Nano fluids and their thermal properties have become a subject of molecular dynamics research [2–4]. However, in molecular dynamics simulations with confined Nano fluids, such as Nano fluid simulations inside nanochannels and nanotubes, it is difficult to control the density of base fluid because the density becomes distorted near the channel walls and nanoparticles due to the liquid-solid interactions.

In this paper, we investigate the dependence of base argon thermal conductivity on argon density inside nanochannel to showcase the influence of changing base fluid density when the nanoparticles are inserted in confined fluid.

METHODS

The argon inside the nanochannel was simulated at 90 K temperature and five different argon densities in the middle of the nanochannel: $\rho = \{1300; 1350; 400; 1450; 1500\}\ kg\ /m^3$. The visual representation of simulated system is given in Fig. 1. The argon atoms interacted via Lennard-Jones (LJ) interaction potential, while the copper interactions within the channel walls were described using EAM interatomic potential for copper [5]. The argon atoms interacted with channel wall atoms also via LJ potential. The equations of motion for argon and channel wall atoms were solved using the velocity-Verlet integration algorithm [6] with a time step value of $2\ fs$. All simulations were performed using LAMMPS molecular dynamics code [7].

In the simulations, the temperature profile in the liquid argon was induced by a constant heat flux $J = 4 \cdot 10^8\ W/m^2$, which was added to the bottom channel wall and subtracted from the top channel wall. Then, the thermal conductivity λ was following equation:

$$\lambda = \frac{J}{\left(\frac{\Delta T}{\Delta z}\right)}, \tag{1}$$

here, $J = 4 \cdot 10^8 \, W/m^2$ is the heat flux, ΔT is difference in temperature across the channel and Δz is the channel width. The average argon temperature was maintained at 90 K with Nosé-Hoover thermostat [8].
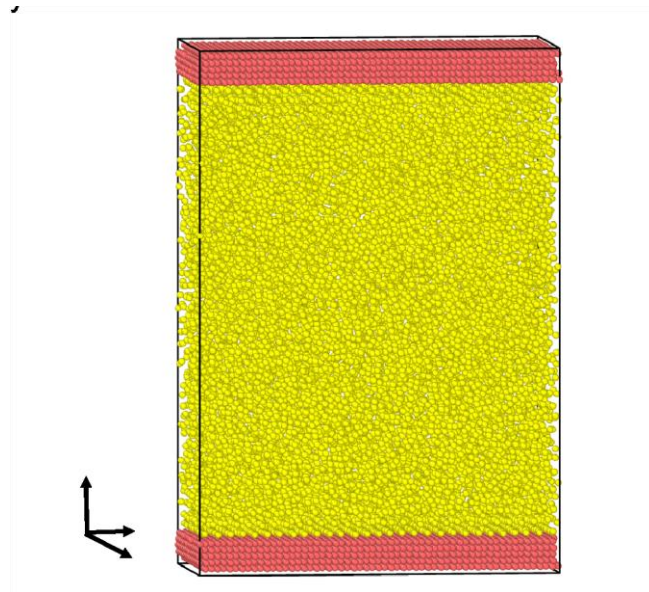
Fig. 1. Visual representation of simulated system. The periodic boundary conditions were applied in x and y while the periodicity was not applied in z axis.

RESULTS

The argon thermal conductivity dependency on argon density inside the nanochannel is given in Fig. 2, which demonstrates that there is no clear dependency of thermal conductivity on the argon density inside the channel apart from the slightly fluctuating thermal conductivity value in different density simulations. Such value fluctuations occur in molecular dynamics simulations due to limited sampling size in finite length simulations. The calculated average value of thermal conductivity in investigated density range was $12.07 \, W/(cmK)$.
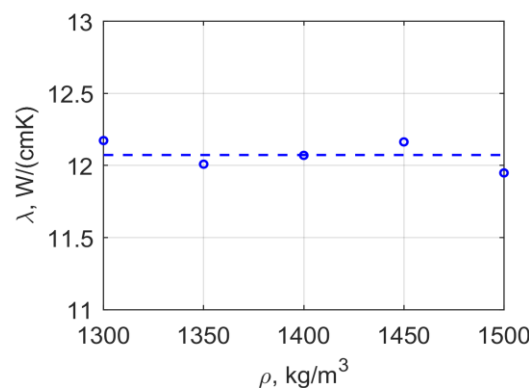
Fig. 2. Base argon thermal conductivity as a function of argon density inside the nanochannel. The circles indicate the thermal conductivity at certain density while the dotted line indicates the average value of thermal conductivity in investigated density range.

CONCLUSIONS

In this paper, we performed a molecular dynamics simulations of heat transfer through argon confined by two parallel coper walls. The simulations were performed at 90 K temperature and five different argon densities in the middle of the nanochannel: $\rho = \{1300; 1350; 400; 1450; 1500\}\ kg\ /m^3$. The results showed that in the investigated density range the thermal conductivity of argon inside the nanochannel does not depend on the argon density. The calculated average value of thermal conductivity in investigated density range was $12.07\ W\ /(cmK)$.

For the further research, we are planning to investigate the contributions of nanoparticle transitional and rotational motion to the enhanced thermal conductivity via means of molecular dynamics simulations.

Keywords: molecular dynamics, Nano fluid, thermal conductivity.

REFERENCES

1. MURSHED, S.M.S.; LEONG, K.C.; YANG, C. Investigations of thermal conductivity and viscosity of Nano fluids. *International Journal of Thermal Sciences*, 2008, Vol. 47, P. 560–568.

2. ABU-HAMDEH, N.H.; ALMATRAFI, E.; HEKMATIFAR, M.; TOGHRAIE, D.; GOLMOHAMMADZADEH, A. Molecular dynamics simulation of the thermal properties of the Cu-water Nano fluid on a roughed Platinum surface: Simulation of phase transition in Nano fluids. *Journal of Molecular Liquids*, 2021, Vol. 327.

3. MOHEBBI, A. Prediction of specific heat and thermal conductivity of Nano fluids by a combined equilibrium and non-equilibrium molecular dynamics simulation. *Journal of Molecular Liquids*, 2012, Vol. 175, P. 51–58.

4. WANG, R.; QIAN, S.; ZHANG, Z. Investigation of the aggregation morphology of nanoparticle on the thermal conductivity of Nano fluid by molecular dynamics simulations. *International Journal of Heat and Mass Transfer*, 2018, Vol. 127, P. 1138–1146.

5. ETESAMI, S.A.; ASADI, E. Molecular dynamics for near melting temperatures simulations of metals using modified embedded-atom method. *Journal of Physics and Chemistry of Solids*, 2018, Vol. 112, P. 61–72.

6. FRENKEL, D.; SMIT, B. *Understanding Molecular Simulation – From Algorithms to Applications*. Academic Press, 2002, ISBN 0-12-267351-4.

7. PLIMPTON, S. Fast Parallel Algorithms for Short – Range Molecular Dynamics. *Journal of Computational Physics*. 1995, Vol. 117, P. 1–42.

8. SAM, A.; KANNAM, S.K.; HARTKAMP, R.; SATHIAN, S.P. Water flow in carbon nanotubes: The effect of tube flexibility and thermostat. *The Journal of Chemical Physics*, 2017, Vol. 146.

NUMERICAL STUDY OF A REACTOR CHAMBER ELEMENT COOLED WITH WATER

R. Uscila
Lithuanian Energy Institute
Breslaujos g. 3, LT-44403 Kaunas – Lithuania
rolandas.uscila@lei.lt

EXTENDED ABSTRACT

OVERVIEW

Combustion processes using solid fuel boilers, melting furnaces, internal combustion engines [1-3] and others are often used in the energy industry. At high temperatures, the working surfaces of the structure must be sufficiently cooled to prevent them from melting. In order to find out the design features, fluid dynamics, the influence of their thermodynamic properties on the cooling system, it is convenient to use the modern CFD software ANSYS FLUINT.

At the Lithuanian Energy Institute in Plasma Technology Laboratory, a volumetric reactor is currently in operation to decompose solid fraction waste [4]. The waste decomposition process requires a high temperature that can be generated by applying a free arc plasma torch. During the decomposition process, the temperature of the molten material reaches 3000-3500 K, so the reactor structure is subjected to high temperatures. Therefore, appropriate cooling of the reactor is essential during the waste decomposition. The determination of proper cooling parameters often is performed applying simulations instead of the expensive experimental methods. Consequently, this paper aims to analyse the influence of the cooling water flow inlet location and water pressure on the temperature of the upper part of the reactor.

METHODS

The upper part of the volumetric reactor is made of a round metal plate (diameter 400mm). In this metal plate, the channel of 4mm for cooling water was milled. This metal plate was boiled on a wider plate with four nipples for incoming and outgoing water. The construction provides four holes (Fig. 1). The first hole is used to supply the raw material to the reactor. The second hole is used for the sampling of the generated gas. The third hole is applied to measure the internal temperature of the reactor using the group of thermocouples. The hole located in the central part of the plate is used to connect the plasma torch to the reactor.
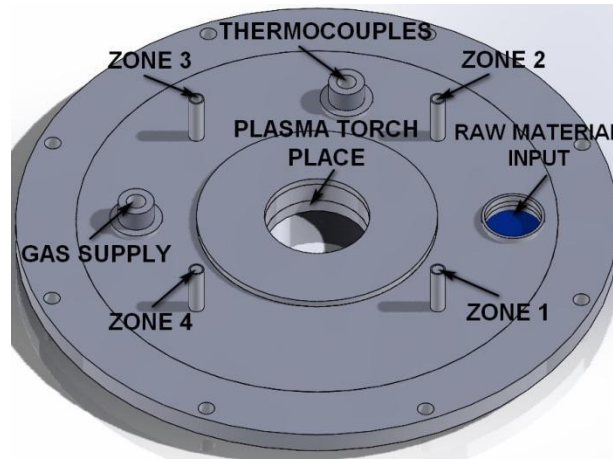
Fig. 1. Cooling water flow inlet, outlet zone location

Numerical Model

The numerical model is created using ANSYS Fluent software. The water inlet boundary conditions are set as flow opening inlets, and outlet boundary conditions are set as pressure opening outlets. The exterior wall is modelled as adiabatic. The simulation is solved to predict the heat transfer and fluid flow characteristics by using the k-e turbulence model. The governing equations for continuity, momentum, energy, k and e in the computational domain are shown as follows [5]:

Continuity:

$$\frac{\partial}{\partial x_i}(\rho u_i) = 0. \tag{1}$$

Momentum:

$$\frac{\partial}{\partial x_i}(\rho u_i u_k) = \frac{\partial}{\partial x_i}\left(\mu \frac{\partial u_k}{\partial x_i}\right) - \frac{\partial P}{\partial x_i}. \tag{2}$$

Energy:

$$\frac{\partial}{\partial x_i}(q u_i t) = \frac{\partial}{\partial x_i}\left(\frac{\partial t}{\partial x_i}\frac{k}{C_p}\right). \tag{3}$$

Turbulent kinetic energy:

$$\frac{\partial}{\partial x_i}(q u_i k) + \frac{\partial p k}{\partial t} = \frac{\partial}{\partial x_i}\left(\left(\mu + \frac{\mu_t}{\sigma_k}\frac{k}{C_p}\right)\frac{\partial k}{\partial x_i}\right) + S_k, \tag{4}$$

where: x_i − coordinate of direction; q − density; u − velocity; P − pressure; C_p − heat capacity; t − time; μ − dynamic viscosity; σ_k − constant; k − turbulent kinetic energy; S_k − source terms.

The model's grid is compacted at the obstructions in the channel. The total number of domains is 57816, of which the solid body is 39651, the fluid is 18165. The boundary conditions are given in Table 1. The simulation of the upper reactor part was performed based on the initial data obtained during the experiments. Accordingly, the initial

temperature of the inlet water was equal to 20.5 °C, while the water pressure ranged from 4 bar to 6 bar. Water debit varied from 0.048 kg/s to 0.063 kg/s. During the simulations, the water inflow and outflow zones, as well as the supply cooling water pressure in the system, were changed. Preliminary data were obtained after the 15 min of simulation. The number of iterations was limited to 5000.

RESULTS

The simulation results of twelve different configurations are provided in Table 1. The obtained results show that water outlet temperature decreases with the increase of water debit and the outlet pressure regardless of the water inlet zone place.

Table 1. Boundary conditions of the simulation of twelve different configurations

Configuration No.	Inlet zone	Outlet zone	Outlet pressure	Inlet temperature	Outlet temperature	Debit kg/s
1	1-2	3-4	4	20.5	39.5	0.048
2	1-2	3-4	5	20.5	36.4	0.055
3	1-2	3-4	6	20.5	33.31	0.063
4	3-4	1-2	4	20.5	41.3	0.048
5	3-4	1-2	5	20.5	38.5	0.055
6	3-4	1-2	6	20.5	35.68	0.063
7	1	3	4	20.5	38.5	0.048
8	1	3	5	20.5	36.12	0.055
9	1	3	6	20.5	32.7	0.063
10	3	1	4	20.5	38.9	0.048
11	3	1	5	20.5	36.27	0.055
12	3	1	6	20.5	34.78	0.063

Accordingly, the lowest water outlet temperature is obtained when the outlet pressure equals 6 bar (configuration No. 3, 6, 9, and 12). Thus, the contours of the cooling water flow trajectories obtained from the third and sixth numerical studies are shown in Fig. 2.
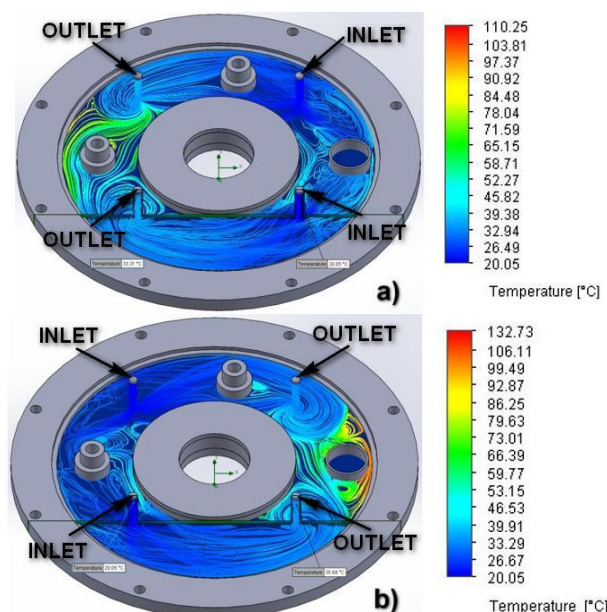
Fig. 2. Comparison of the water flow trajectories a) third configuration,
b) sixth configuration

In the case of configuration No. 6 (Fig 2 b)), more vortices are formed at the point where raw material is fed into the reactor, resulting in areas that can overheat. The measured temperature in the outlet zone amounts to 35.61 ºC, and it is higher ~2 ºC compared to configuration No. 3. The obtained results show that configuration No. 3 is a more efficient option. When only one inlet zone is used, the more favourable results are obtained in configuration No. 9 compared to No 12.

CONCLUSIONS

The numerical study showed that the most efficient cooling occurs when outlet pressure equals 6 bar. Also, it was revealed that it is more efficient to use only one incoming water zone and one outgoing water zone. In the best-case scenario (configuration No. 9), the water heating was 12.7 ºC, and overheating zones were not observed. Thus, configuration No. 9 is most suitable for practical application.

Keywords: CFD, 3D model, water, flow, heat.

REFERENCES

1. BOHNSTEIN, M.; RICHTER, M.; GRAESER, P.; SCHIEMANN, M.; STRÖHLE, J.; EPPLE, B. 3D CFD simulation of a 250 MWel oxy-fuel boiler with evaluation of heat radiation calculation, *Renewable and Sustainable Energy Reviews*, 2021, Vol. 137. ISSN 1364-0321.

2. RAIČ, J.; GABER, C.; WACHTER, P.; DEMUTH, M.; H GERHARDTER, H.; KNOLL, M.; PRIELER, R.; HOCHENAUER, C., Validation of a coupled 3D CFD simulation model for an oxy-fuel cross-fired glass melting furnace with electric boosting, *Applied Thermal Engineering,* 2021, Vol. 195, ISSN 1359-4311.

3. NADERI, A.; QASEMIAN, A.; SHOJAEEFARD, M. H.; SAMIEZADEH, M.; YOUNESI, M.; A. SOHANI, A. HOSEINZADEH. S. A smart load-speed sensitive cooling map to have a high- performance thermal management system in an internal combustion engine. *Energy*, 2021, Vol. 229, ISSN 0360-5442.

4. VALINČIUS, V.; KĖŽELIS, R.; GIMŽAUSKAITĖ, D.; GRIGAITIENĖ, V.; VALATKEVIČIUS, P. The investigation of an electric arc in a plasma chemical reactor for hazardous waste treatment, *Journal of Chemical Technology and Biotechnology*, 2020, Vol. 95, P. 450-456. ISSN 0268-2575, eISSN 1097-4660.

5. AMBEKAR, A.; SIVAKUMAR, R.; ANANTHARAMAN, N.; VIVEKENANDAN, M. CFD simulation study of shell and tube heat exchangers with different baffle segment configurations. *Applied Thermal Engineering,* 2016, Vol. 108, P. 999-1007, ISSN 1359-4311.

II.3. Material sciences and technologies

ATOMIC FORCE MICROSCOPY AS EMERGING TOOL TO INVESTIGATE THE PHYSICO-CHEMICAL PROPERTIES OF LIGNOCELLULOSIC POLYMERS AT THE NANOSCALE

C. Marcuello

Instituto de Nanociencia y Materiales de Aragón (INMA),
CSIC-Universidad de Zaragoza
12, C. de Pedro Cerbuna, 50009 – Spain
cmarcuel@unizar.es

B. Chabbert, V. Aguié -Béguin
FARE Laboratory,
INRAe, Université de Reims Champagne-Ardenne
2, Esplanade Roland Garros, 51100 – France

M. Molinari
CBMN, CNRS UMR 5248, IPB,
Université de Bordeaux
1, All. Geoffroy Saint-Hilaire, 33600 – France

EXTENDED ABSTRACT

OVERVIEW

Governs and policymakers plan to decrease the production of fossil fuels by 6 % per year to limit the global warming according to United Nations (UN) reports. In this context, lignocellulosic polymers can play a crucial role to minimize the use of scarce fossil fuels. Lignocellulose is the main component of the plant cell walls. This biomass produced by photosynthesis is the most promising renewable carbon source for solving current energy and feedstock issues. The global biomass production is estimated to be 146 billion metric tons, comprising mostly wild plant growth and 10 to 50 billion metric tons on a dry basis. Of the main components of lignocellulosic materials, cellulose is one of the most abundant biopolymers in nature and its biosynthesis, chemistry and structure still remain an active field of research. Such is the case that in the last decades, there has been a growing interest in the development of sustainable projects based on green chemistry, which has led to the generation of novel cellulosic and composite materials with cellulose. Due to the high-level of entanglement between the different lignocellulosic polymers which form the plant cell wall more research must be devoted in this field to better understand how they are interacting between each other and their physic-chemical properties. Atomic force microscopy (AFM) is a cutting-edge tool that enables to gather relevant information at the single molecule level [1]. Topography of the studied biopolymers is driven by scanning their surface with sharp AFM tips. The intermolecular interactions between two biomolecules can be deciphered by dynamic force spectroscopy (DFS) attaching covalently one of the biomolecules on the AFM tip and the partner on a solid surface. In addition, Nano indentation with bare AFM tips

measures the mechanical properties of the studied polymers as the Young's modulus and hardness. Finally, the AFM nanoIR combines the capabilities of AFM with infrared spectroscopy. This technique uses the vibrational energy of functional groups and specific atoms to resolve which chemical groups are present in the sample with accurately correlation on the atomic scale. The present work is focused in different methodologies to covalently tether cellulose nanocrystals (CNCs) on AFM levers controlling their coverage. The performance of this functionalized CNCs AFM levers is evaluated by determining the adhesive properties by DFS towards lignocellulosic films based of galactomannan (GM), xylan (XYL), cellulose or lignin in native forms. The impact of relative humidity (RH) on the nanomechanical properties of lignocellulosic films and their adhesion with CNCs functionalized tips was addressed. Finally, the chemistry of native and dignified transversal pine cell wall sections was determined by AFM nanoIR.

METHODS

Cellulose nanocrystals (CNCs) were prepared from bleached ramie fibres (*Boehmeria nivea*), galactomannan (GM) and xylan (XYL) were obtained from konjac galactomannan and wheat arabinoxylan, respectively. CNCs, GM and XYL films were prepared with solutions of 15 mM by casting. Lignin model compounds (LIG) were synthesized by the oxidative polymerisation of coniferyl alcohol (4-hydroxy-3-methoxy-cinnamyl alcohol) and synapyl alcohol (4-hydroxy-3, 5 dimethoxy-cinnamyl alcohol) at 1 g.L^{-1} according to the "Zutropfverban" method. Lignin films were made by spin coating. Raw and dignified pine sections were obtained by cryo-microtrome.

Functionalized CNCs AFM levers were prepared by Langmuir-Blodgett (LB) and chemical procedure by using heterobifunctional p-maleimidophenyl isocyanate linker molecules as detailed elsewhere [2]. Topography, DFS and Nano indentation measurements were carried out with Multimode-8 AFM (Bruker, Santa Barbara, CA, USA) coupled with a humidity generator setup (Wetsys system, Setaram Instrumentation). The chemistry characterization was conducted using NanoIR2 AFM setup (Anasys Instruments). The IR laser source is an OPO laser of 500 mW tunable pulsed with 12 ns long pulsed.

RESULTS

Adhesion force values for CNCs with the studied lignocellulosic films are similar for both functionalization procedures at the same coverage of CNCs. The coverage level of CNCs on AFM tip-less levers positively impacts on the interaction with lignocellulosic films. LB rendered 4.5 greater coverage of CNCs on AFM levers than the chemical procedure (56 % vs 12 %, respectively). Moreover, AFM levers functionalized by LB exhibited more homogeneous CNCs layers compared to chemical procedure due to the lack of non-reacted PMPI spacer molecules. Comparing the different polymer films, the results showed that adhesion forces between CNCs:LIG and CNCs:GM were stronger than CNCs:CNCs and CNCs:XYL (48.0 ± 17.5 nN, 42.6 ± 4.1nN, 14.7 ± 1.5 nN and 11.4 ± 2.5 nN, respectively) at RH of 45 % and coverage of CNCs on the AFM levers of 56 % [2].

RH also promotes higher adhesion properties based on the larger number of hydrogen bonds formed between the lever and the polymer film. The adhesion force increased from 43.6 ± 17.1 nN to 54.0 ± 18.2 nN (CNCs: LIG); from 37.5 ± 4.5 nN to 54.7 ± 4.7 nN (CNCs: GM); from 14.7 ± 1.0 nN to 16.7 ± 2.1 nN (CNCs: CNCs) and from 8.8 ± 1.5 nN to 11.8 ± 2.8 nN (CNCs: XYL) when the RH ranged from 15 % to 95 % with the same coverage of CNCs functionalized AFM levers as aforementioned. In addition, the Young's modulus of the

lignocellulosic films decreased with the moisture from 6.7 ± 0.5 GPa to 5.8 ± 0.6 GPa (LIG); from 9.4 ± 0.6 GPa to 4.3 ± 0.5 GPa (GM); from 10.9 ± 0.8 GPa to 9.2 ± 0.9 GPa (CNCs) and from 7.6 ± 0.3 GPa to 5.1 ± 0.2 GPa (XYL) when the RH varied from 15 % to 95 % [3]. The dramatically decay of Young's modulus observed for GM films is expected due to the considerable hydrophilic nature of this polymer in contrast to XYL and LIG films. The high-degree of crystallinity of CNCs films do not allow the water penetration between the inner CNC rods.

Finally, two transversal plant cell sections were analysed by AFM nanoIR and Nano indentation. Cell corner of raw pine presents more lignin content than S1 and S2 layers (Fig. 1a) exhibiting less stiffness (Fig. 1b). Full IR spectra displayed high peaks at the corresponding lignin peak at 1512 cm^{-1} (Fig. 1c). On the other hand, transversal dignified pine sections underwent the release of lignin (Fig. 1d) showing homogeneous nanomechanical properties of all plant cell regions (Fig. 1e). Full IR spectra demonstrated the decrease of the corresponding lignin peak (Fig. 1f).

CONCLUSIONS

Quantifying and characterization of the chemistry and molecular forces driven at nanoscale is a preliminary step to boost the design of new high-quality green nanocomposites made of lignocellulosic polymers for food active-packaging, papermaking, surface-based on polymer-polymer interaction biosensors, or new binder agents.

Keywords: lignocellulose polymers, adhesion force, relative humidity, stiffness, infrared, atomic force microscopy, nanoscale.
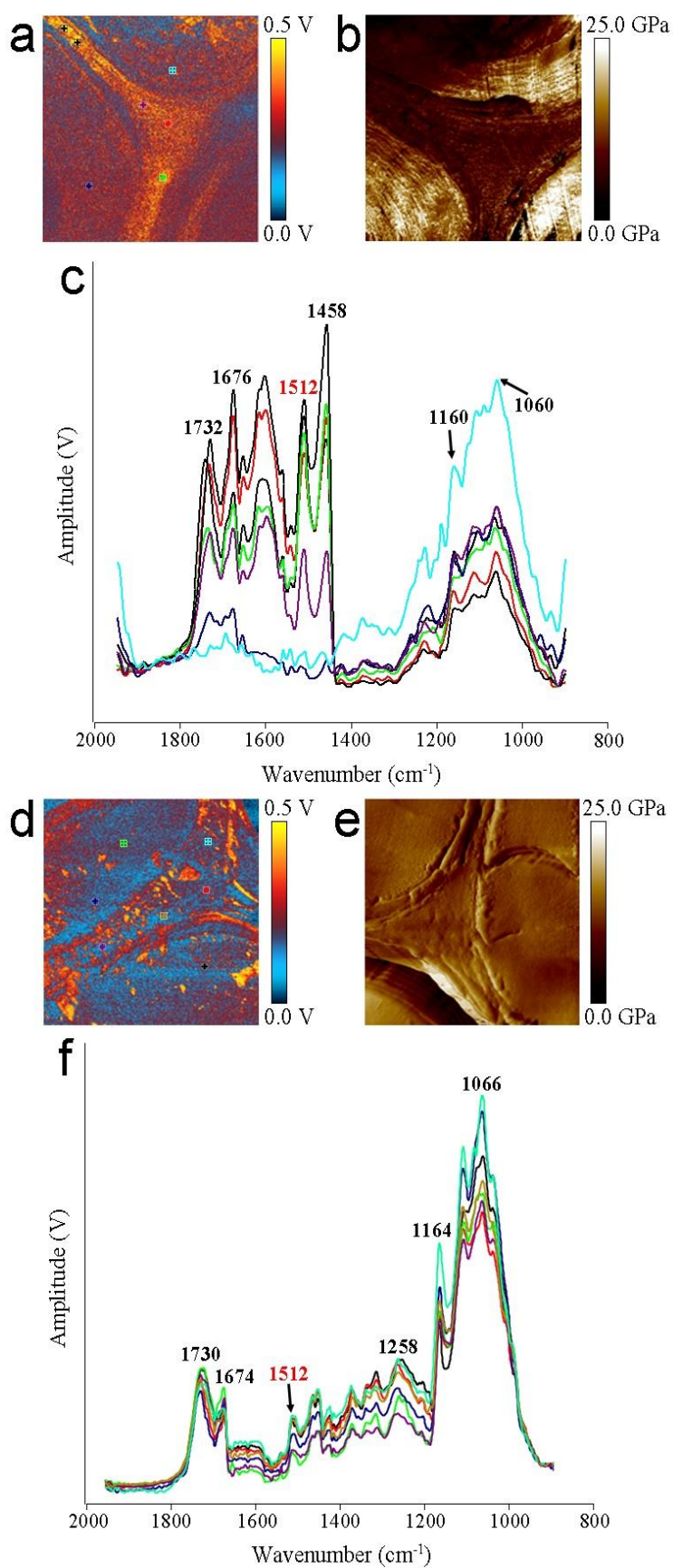
Fig. 1. AFM nano-IR image at 1512 cm^{-1} (a, d), nanomechanical map (b, e) and full nanoIR spectra (c, f) of <u>raw pine</u> and <u>dignified pine</u> transversal sections, respectively.

REFERENCES

1. DUFRÊNE, Y. F.; ANDO, T.; GARCIA, R.; ALSTEENS, D.; MARTÍNEZ-MARTIN, D.; ENGEL, A.; GERBER, C.; MÜLLER, D.J. Imaging modes of atomic force microscopy for application in molecular and cell biology. *Nature Nanotechnology*, 2017, Vol. 12, No. 4, P. 295-307.

2. MARCUELLO, C.; FOULON, L.; CHABBERT, B.; MOLINARI, M.; AGUIÉ-BÉGUIN, V. Langmuir-Blodgett procedure to precisely control the coverage of functionalized AFM cantilevers of SMFS measurements: Application with cellulose nanocrystals. *Langmuir*, 2018, Vol. 34, No. 32, P. 9376-9386.

3. MARCUELLO, C.; FOULON, L.; CHABBERT, B.; AGUIÉ-BÉGUIN, V.; MOLINARI, M. Atomic force microscopy reveals how relative humidity impacts the Young's modulus of lignocellulosic polymers and their adhesion with cellulose nanocrystals at the nanoscale. *International Journal of Biological Macromolecules*, 2020, Vol. 147, P. 1064-1075.

INVESTIGATION OF TiH$_X$O$_Y$ FILMS PRODUCED BY REACTIVE MAGNETRON SPUTTERING TECHNIQUE

M. Urbonavičius, S. Tučkutė, M. Lelis
Lithuanian Energy Institute
Breslaujos g. 3, LT-44403 Kaunas – Lithuania
+370 37 401801
rastine@lei.lt

EXTENDED ABSTRACT

OVERVIEW

Oxyhydrides make up a less known class of multination materials where the oxide and hydride anions are sharing similar sites within the crystal lattice [1]. Most often these materials are oxygen-containing hydrides, but hydrogen-containing oxides were reported as well [2]. Recently, it was realized that in some of these materials H$^-$ and O^{2-} ions might have a possibility to interact via valence charge states of the metal center [1]. This can create uncommon electron energy level structures and can lead to interesting magnetic and optical properties which potentially might have appealing applications in commercial products. In partially oxidized yttrium hydride and several other rare-earth- (Gd, Dy, and Er) hydrides reversible switching of optical transmittance under intense irradiation was observed [3]. Such a feature of yttrium oxyhydride is currently being tested for application in smart windows devices [4]. Titanium is also recognized for its potential to form a corresponding oxyhydride phase [5]. However, the reports on the properties of titanium oxyhydride are still scarce and its practical value is not yet determined. Accordingly, in the current study, we focused on the controllable one-step synthesis and analysis of titanium oxyhydride films as well as the characterization of their structural, optical, and photocatalytic properties.

METHODS

In current study TiH$_x$O$_y$ samples were synthesized using custom modified Kurt J.Lesker PVD-75 physical vapour deposition system, which was equipped with one unbalanced Torrus 3 magnetron. The magnetron had high purity titanium disc target (76 mm diameter, 6 mm thickness, 99.99 % purity) and was powered up by 300 W DC power source. Ar, O$_2$ and H$_2$ gases were supplied by three mass flow controllers which were operated by Nova Fabrica FloTron X multi-channel process control system. In total four types of samples were prepared: sample A was a reference TiO$_2$ film deposited using only Ar and O$_2$ gas mixture, whereas samples B1, B2, and B3 were TiH$_x$O$_y$ films deposited using different Ar: O2:H2 gas flow ratios (going form sample A to sample B3 gas flow ratios were 3.78:1:0, 0.42:1:2.36, 0.67:1:4.78 and 0.75:1:6.25 respectively). Structure and other properties of the deposited films were analysed using XRD (Bruker D8), XPS (PHI 5000 Versaprobe), and SEM (Hitachi S-3400N) techniques. Optical transmission of the films was measured by UV–VIS spectrophotometer (Jasco V-650), whereas their photocatalytic activity was estimated using methylene blue (MB) bleaching test (adopted version of ISO 10678:2010 standard [6]).

RESULTS

Reactive magnetron sputtering under Ar-O_2 atmosphere (sample A) produced colourless transparent film consisting of anatase ant rutile TiO_2 (Fig. 1). When gas mixture was supplemented with hydrogen, the crystallinity of the samples started to weaken, and they started to gain a noticeable tint. At largest hydrogen concentration (sample B3), the effect was especially strong: the sample nearly lost the rutile phase and obtained a dark grey-blue shade. Such result is interesting from several perspectives.
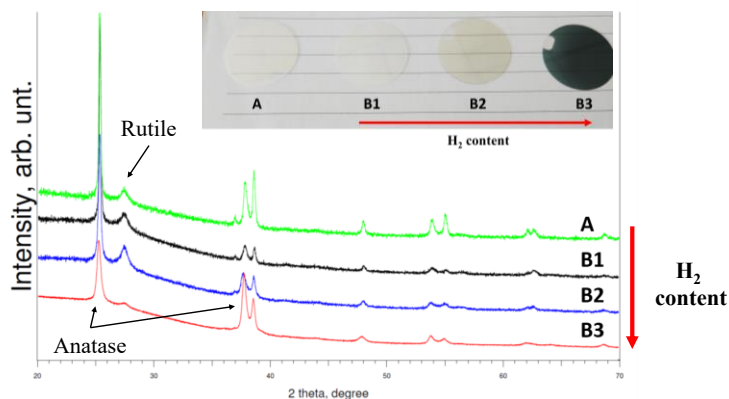
Fig. 1. XRD data of the as-deposited TiH_xO_y films. The inset shows
actual view of the films.

First, it can be noticed that earlier reports of TiH_2 oxidation experiments indicated nearly exclusive formation of rutile phase TiO_2 [5,7,8]. Naturally, the oxidation of TiH_2 and titanium sputtering in reactive Ar-O_2-H_2 atmosphere is not the same. Nevertheless, the decline in the crystallinity of the thermodynamically the most stable TiO_2 phase is not a trivial outcome and is considered as the indication of the alternative route for Ti-O-H system stabilisation.
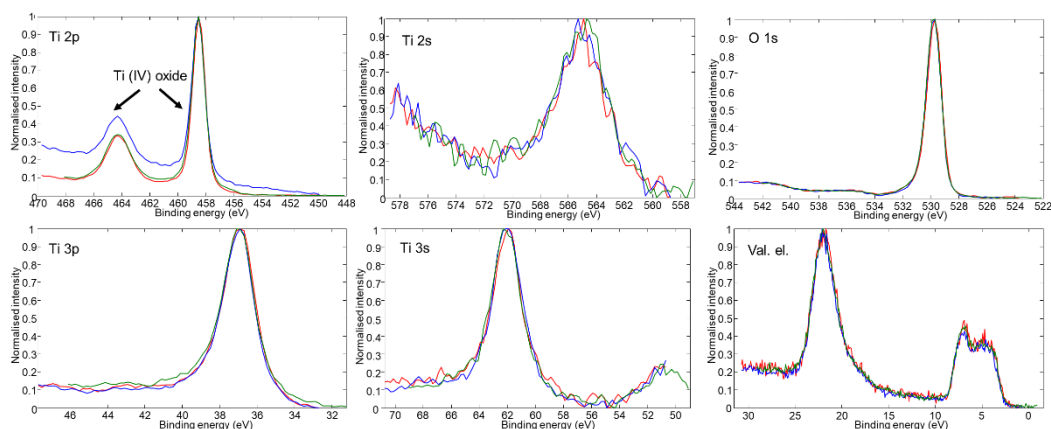
Fig. 2. XPS spectra of the as-deposited TiH_xO_y films: B1 – red, B2 –
blue, B3 - green.

Second, in defected TiO_2 samples (including "black TiO_2" samples produced using hydrogen [9]) the dark colour is commonly attributed to the presence of oxygen vacancies and Ti^{3+} species [10–12]. However, despite significantly different appearance of B1, B2 and B3 samples, their photoelectron spectra of titanium, oxygen and valence band electrons are nearly identical (Fig. 2). Their Ti 2p photoelectron spectra have only to two peaks (at

approximately 458.7 eV and 464.4 eV) which fits with the standard positions Ti $2p_{3/2}$ and Ti $2p_{1/2}$ peaks of Ti(IV) oxide and show no sign of any Ti^{3+} phase (if present such phases should have peaks at approximately 457.3 eV and 462.5 eV). Moreover, in contrast to the traditionally enhanced photocatalytic efficiency of the black TiO_2 powder (enhancement frequently attributed to the presence of Ti (III) oxide), MB bleaching efficiency of the tinted TiH_xO_y films (samples B2 and B3) was weaker in comparison to samples A and B1 which were deposited using lower hydrogen fraction in gas mixture (Fig. 3).
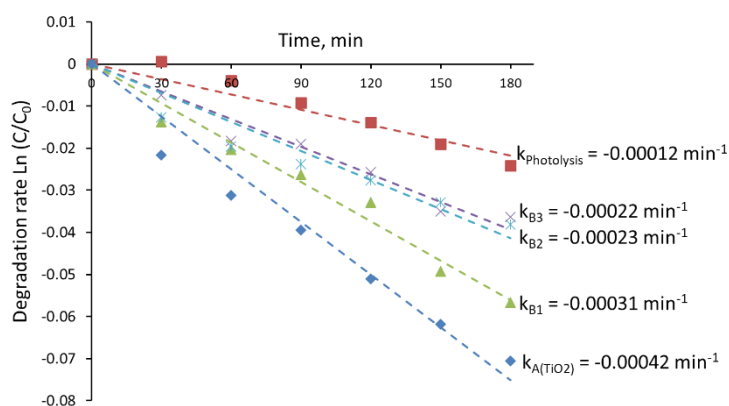
Fig. 3. Estimation of photocatalytic bleaching of MB solution using different TiH_xO_y films.

CONCLUSIONS

Reactive magnetron sputtering of titanium under Ar-O_2-H_2 gas atmosphere can produce corresponding oxyhydride films where different amounts of hydrogen are introduced into crystal structure of anatase and rutile phase TiO_2. By entering into the oxide film structure hydrogen reduces titanium oxide crystallinity, changes colour and promotes the formation of the anatase phase. Photocatalytic bleaching of MB solution using different TiH_xO_y films revealed that bleaching efficiency is becoming smaller when higher hydrogen fraction is used for the film deposition. The estimated band gap values for all TiH_xO_y films remains relatively similar to the standard TiO_2, therefore, the observed changes in photocatalytic efficiency were assumed to be related to the increased charge recombination in TiH_xO_y films.

Keywords: titanium oxyhydride, titanium oxide, reactive magnetron sputtering, optical properties, photocatalysis.

REFERENCES

1. PISHTSHEV, A.; STRUGOVSHCHIKOV, E.; KARAZHANOV, S. Conceptual Design of Yttrium Oxyhydrides: Phase Diagram, Structure, and Properties. *Crystal growth & design,* 2019, Vol. 19, P. 2574–2582, doi:10.1021/acs.cgd.8b01596.

2. KOBAYASHI, Y.; HERNANDEZ, O.; TASSEL, C.; KAGEYAMA, H. New chemistry of transition metal Oxyhydrides. *Science and Technology of Advanced Materials,* 2017, Vol. 18, P. 905–918.

3. BABA, E.M.; MONTERO, J.; MOLDAREV, D.; MORO, M. V; WOLFF, M.; PRIMETZHOFER, D.; SARTORI, S.; ZAYIM, E.; KARAZHANOV, S. Preferential

Orientation of Photochromic Gadolinium Oxyhydride Films. *Molecules,* 2020, Vol. 25, P. 3181.

4. STRUGOVSHCHIKOV, E.; PISHTSHEV, A.; KARAZHANOV, S. Theoretical Design of Effective Multilayer Optical Coatings Using Oxyhydride Thin Films. *Physica status solidi,* 2021, Vol. 258, P. 2100179.

5. FOKIN, V.N.; MALOV, Y.I.; FOKINA, E.E.; TROITSKAYA, S.L.; SHILKIN, S.P. Investigation of interactions in the TiH2-O2 system. *International Journal of Hydrogen Energy,* 1995, Vol. 20, P. 387–389.

6. Fine ceramics (advanced ceramics, advanced technical ceramics) — Determination of photocatalytic activity of surfaces in an aqueous medium by degradation of methylene blue, ISO 10678:2010; 2010.

7. KENNEDY, A.R.; LOPEZ, V.H. The decomposition behaviour of as-received and oxidized TiH2 foaming-agent powder. *Materials Science and Engineering: A,* 2003, Vol. 357, P. 258–263.

8. LAVRENKO, V.A.; SHEMET, V.Z.; PETROV, L.A.; TEPLOV, O.A.; DOLUKHANYAN, S.K. High-temperature oxidation of titanium-hydride powders. *Oxidation of Metals,* 1990, Vol. 33, P. 177–189.

9. GODOY JUNIOR, A.; PEREIRA, A.; GOMES, M.; FRAGA, M.; PESSOA, R.; LEITE, D.; PETRACONI, G.; NOGUEIRA, A.; WENDER, H.; MIYAKAWA, W.; et al. Black TiO2 Thin Films Production Using Hollow Cathode Hydrogen Plasma Treatment: Synthesis, Material Characteristics and Photocatalytic Activity. *Catalysts,* 2020, Vol. 10, P. 282.

10. XIU, Z.; GUO, M.; ZHAO, T.; PAN, K.; XING, Z.; LI, Z.; ZHOU, W. Recent advances in Ti3+ self-doped nanostructured TiO_2 visible light photocatalysis for environmental and energy applications. *Chemical Engineering Journal,* 2020, Vol. 382, P. 123011.

11. DI VALENTIN, C.; PACCHIONI, G.; SELLONI, A. Reduced and n-type doped TiO2: Nature of Ti3+ species. *The Journal of Physical Chemistry C,* 2009, Vol. 113, P. 20543–20552.

12. SARKAR, A.; KHAN, G.G. The formation and detection techniques of oxygen vacancies in titanium oxide-based nanostructures. *Nanoscale,* 2019, Vol. 11, P. 3414–3444.

DEVELOPING THE PROPERTIES OF BORON WASTE WITH SLAG AND TUNCELI PUMICE TO ENSURE USABILITY IN GEOPOLYMER PASTE

M. Şahin Yön
Munzur University, Civil Engineering Department, 62000, Tunceli – Turkey
Fırat University, Civil Engineering Department, 23000, Elazığ – Turkey
mervesahinyon@munzur.edu.tr

M. Karataş
Fırat University, Civil Engineering Department, 23000, Elazığ – Turkey
+90 0424 237 00 00
mkaratas@firat.edu.tr

ABSTRACT

Conventional Portland cement production causes CO_2 emissions to the atmosphere significant degree. For this reason, the production of concrete/mortar without using cement directs scientists to work in this field. The motivation of this study is to produce geo - polymer paste by using waste and natural materials as alternative to cement. Industrial boron waste (BW), granulated blast furnace slag (GBFS) and Tunceli region pumice (TRP) were used for the experimental study. The study was carried out in three stages. In the first stage, samples were prepared by using binary-blended of BW with TRP, the second stage by using binary blended BW with GBFS and the last stage ternary-blended of BW, GBFS and TRP. The most suitable curing temperature, alkali solution ratios ($Na_2SiO_3/NaOH$) and liquid to binder (L/B) ratio for these mixtures were investigated according to their compressive strength. As a result of the experimental study, it was determined that the curing temperature providing the highest compressive strength for binary blended BW with GBFS was 60°C, the L/B ratio was 0.45 and the $Na_2SiO_3/NaOH$ (NS/NH) ratio was 3.0. However, for binary-blended of BW with TRP was 100°C, the L/B ratio was 0.45 and the NS/NH ratio was 3.0 while ternary-blended of BW, GBFS and TRP was 60°C, the L/B ratio was 0.45 and the NS/NH ratio was 1.0.

Keywords: Geopolymer paste, Boron waste, Tunceli region pumice, Granulated blast furnace slag, compressive strength

INTRODUCTION

Conventional Portland cement production causes significant CO_2 emissions to the atmosphere. Amorphous geopolymers produced using alkaline activators offer superior properties such as high strength, low energy consumption, reduction of harmful gas emissions (CO_2, SO_2, etc.) and the use of wastes instead of natural resources. Researchers continue their studies to produce geopolymer mortars using different waste materials (fly ash, silica fume, rice husk, slag, etc.). Koçkal et al. stated that binder type, binder amount and alkali activator (sodium hydroxide) significantly affect the physical and mechanical behaviour of geopolymer samples [1]. Davidovits investigated properties of geopolymer cements and emphasized the advantages of geopolymers [2]. Duxson et al. stated that the geopolymer gel could be the key to the future development of cement materials that are more environmentally friendly, economical, durable and high strength [3]. Aygörmez et al. investigated durability of geopolymer composites. They assessed durability properties of geopolymers starting 365 days after production [4]. Uysal et al. used metakaolin, silica fume, ground granulated blast furnace slag (GBFS), colemanite and polypropylene fibre for their study. The effect on the behaviour of geopolymer composites formed by partially replacing metakaolin with two waste materials was examined in terms of physical properties overall, the results have proven that substitute materials are beneficial [5]. Çelik et al. evaluated high temperature behaviour, some mechanical and microstructural properties of metakaolin based geopolymer mortar composites reinforced with boron wastes reinforced with 4 different fibre types. [6]. Hardjito et al. investigated the geopolymer concrete, silicon and aluminium-rich by-product material such as fly ash with low calcium (ASTM C 618 Class F) activated with high alkaline solution to shape the paste [7]. Haha et al. assessed the two types of slag with different Al_2O_3 content by activating with NaOH and sodium metasilicate. They observed that C-S-H gels found in NaOH activated pastes are more crystalline and contain less water and the formation of calcium silicate hydrate (C-S-H) and sodium-rich C-N-S-H with similar Ca content occurred at longer hydration times [8]. Özodabaş and Yılmaz investigated the durability and strength of alkali-activated blast furnace slag (AAS) mortars with finely ground pumice (P). In their study, instead of cement, 60% and 80% blast furnace slag were used. They said that, the best results were obtained from the samples containing 8% Na_2O [9]. Top and Vapur investigated, fly ash (FA) based geopolymer (GP) concretes by using basaltic pumice (BP) aggregates and fly ash (F Class) mixture for lightweight concrete. [10]. Zhu et al. examined the coarse fly ash substituted 0-40% with granulated blast furnace slag. Geopolymer pastes, and mortars were prepared at a liquid/solid ratio of 0.6-0.8 by mass. They expressed that natural fly ash, liquid/solid ratio and slag substitution play an important role in improving the durability of Alkali Activated Fly Ash concretes [11]. Chi, to activate the granulated blast furnace slag, used the activators with a sodium oxide (Na_2O) concentration of 4%, 5% and 6% by weight of the slag and a liquid sodium silicate modulus (the ratio of SiO_2 to Na_2O) of 0.8. He stated that, the dosage of both Na_2O and H_3PO_4 was added mix is the important factor affecting the properties of fresh AASC blends. [12]. Koçkal et al. due to environmental problems such as high raw material demand, energy consumption and high amount of carbon dioxide emission, investigated the physical and mechanical behaviour of geopolymers with different compositions [13].

In this study, the usability of the waste released after the processing of the boron mine in the geopolymer paste was investigated. In preliminary experimental studies, it has been determined that it is not possible to use boron waste alone in geopolymer paste [14]. In order to increase the workability and compressive strength of BW, TRP which were not used in the literature before, and GBFS were used.

EXPERIMENTAL PROCESS

Materials

For experimental study, Boron Waste (BW), Granulated Blast Furnace Slag (GBFS) and Tunceli Region Pumice (TRP) were used as materials. Turkey has about 70% of world boron reserves. As the country with the majority of boron reserves, the requirement to utilize the waste of the mentioned reserve is of great importance in terms of contributing to the ecology. BW was procured from Eti Mine Enterprises Kırka Boron Operations Directorate as course. To improve paste content GBFS provided from Zonguldak Ereğli Iron and Steel Factory was used. Also, TRP was obtained from the nature of Tunceli- Mazgirt District in Turkey. After this rock was collected, it was washed in the laboratory. The grinded materials for use the as binder in the paste were sieved through a 75 μm sieve. Figure 1 shows the process of grinding of used all materials. Chemical and some physical properties of BW, GBFS and TRP given in the Table 1 were performed by ACME Analitic Laboratory Services Company. NaOH and Na_2SiO_3 were used as alkaline solution. NaOH (NH) is a minimum purity of 98% and is mixed with deionized water to make a 12 M NaOH solution. The Modulus Silica (MS) of the used Na_2SiO_3 (% SiO_2/Na_2O) is 3.13. Liquid sodium silicate consists of 9.2225 Na_2O, 28.875% SiO_2. The specific gravities of NaOH and Na_2SiO_3 are 1.35 and 1.4, separately.
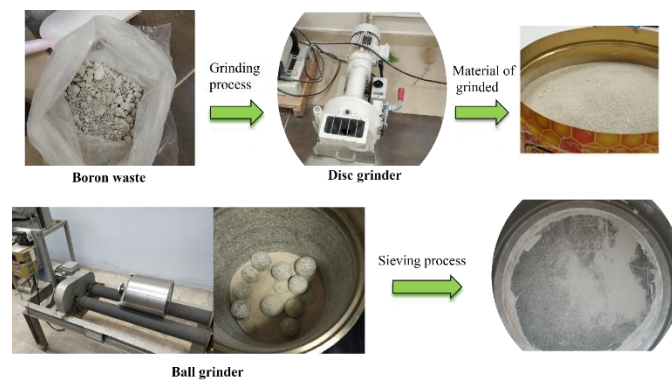
a) Grinding process of BW

b) Grinding process of GBFS

c) Grinding process of TRP

Fig. 1. Grinding process of materials

Table 1. Chemical and some of physical properties of BW, GBFS and TRP

Components %	BW	GBFS	TRP
SiO_2	16.45	39.10	43.62
Al_2O_3	0.96	16.28	16.95
Fe_2O_3	0.28	0.83	13.28
CaO	17.26	35.28	8.13
MgO	17.30	6.45	5.49
Na_2O	5.14	0.44	2.53
K_2O	0.58	0.59	2.02
LOI	34.4	-1	3.4
Specific gravity(g/cm^3)	2.54	2.89	2.98

Firstly, to see the performance of BW in geopolymer paste, trial mixtures produced containing 100% BW. But they did not settle in the mold despite the use of a vibration table. This situation shows that the workability of the samples produced using 100% BW is low. After that samples were exposed to 120 °C and 70 °C temperatures for curing. Fig. 2 illustrates the significant shrinkage and cracks at the samples.

a) After 120 °C cure temperature   b) After 70 °C cure temperature

Fig. 2. States of BW samples after oven cure for various temperature
(adopted from [14])

Table 2 gives compressive strengths of 100% BW mixture and binary mixtures in which BW was replaced with GBFS at levels of 20%, 30% and 50% by weight, for various temperature and L/B. Compressive strength results for 100% BW were found to be very low, especially at 70°C, while the highest strength was found to be approximately 10 MPa at 120°C, with L/b ratio of 0.50.

Table 2. Compressive strengths of preliminary castings for various temperature and L/B

Mixed	BW content (%)	GBFS content (%)	Curing Temperature (ºC)	Solution used (NS/NH) [15]	Liquid/Binder L/b	Compressive strength (MPa)
B100	100	0	120		0.55	5.16
B100	100	0	70		0.55	2.46
B100	100	0	120		0.50	10.57
B100	100	0	70		0.50	1.23
B20+C80	20	80	70	3:1	0.35	48.12
B30+C70	30	70	70		0.35	23.4
B50+C50	50	50	70		0.35	4.62

When the binary mixtures in which BW was replaced with GBFS results were evaluated, it was determined that the slag substitution increased the compressive strength at a high rate. [14]. It was concluded that after the preliminary castings, the BW can be used at a maximum rate of 25%. So, it is aimed to increase the compressive strength of BW with GBFS and TRP. In this experimental study, it is objected to determine the curing temperature and NS/NH ratio that will provide the highest compressive strength by determining the 25% ratio of BW that can be used in geopolymer paste.

Experimental Study

In this part of the study, experimental studies were carried out on samples with maximum BW ratio (25%) to determine the optimum curing temperature, NS/NH ratio and Liquid/Binder (L/B) ratio. Firstly, 25% BW-75% TRP mixture was activated with 12M NaOH and NS. Secondly, 25% BW-75% GBFS mixture was activated with same activators. In the last mixtures, 35% GBFS and 40% TRP were used with 25% boron waste by weight. Since the compressive strength result of %100 BW was low and to save energy, all samples exposed to curing temperatures of 20°C, 60°C and 100 °C instead of 70°C and 120 °C at the preliminary casting. Produced 50x50x50 mm samples are shown in Fig. 3.

a) BW%25-TRP%75   b) BW%25-GBFS%75
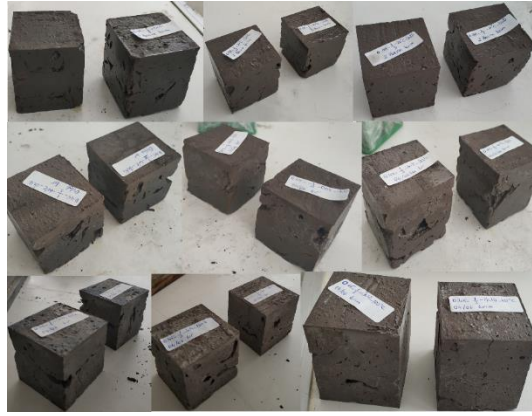
c) BW25% -GBFS35% -TRP40%

Fig.3. All produced samples for various curing temperature, NS/NH ratio and L/B

Samples exposed to curing temperatures of 100 °C and 60°C, consisting of 75% GBFS and 25% BW, are shown in the Fig. 4a. The shrinkage of the samples exposed to 100°C is seen from mould. However, it was seen that there was no shrinkage in the samples cured at 60°C. Fig. 4b represents the shrinkage of the samples which have 75% TRP and 25% BW. In here, it was seen that while crack formation was observed at 60 °C, shrinkage occurred at 100 °C. In the last mixtures, for 60 ºC and 100 ºC, 35% GBFS and 40% TRP were used with 25% BW by weight. As given in the Fig. 4c, it was observed that the samples cured at 100°C shrank, while the samples cured at 60°C did not shrink.

a) 75% GBFS and 25% BW samples   b) 75% TRP and 25% BW samples

c) 35% GBFS, 40% TRP and 25% BW samples

Fig.4. Shrinkage of samples at 100°C

RESULTS AND DISCUSSIONS

The resulting mixtures for BW%25-TRP%75 were subjected to a pressure test and achieved results were given in Figure 5. In this figure L/B shows ratio of Liquid to binder while 1.0, 2.0, 3.0 values represent the NS/NH ratios respectively. When this figure was investigated, maximum compressive strength was obtained from at 100°C for 3.0 NS/NH ratios and L/b=0.45 alkaline solution. Therefore, this L/B ratio was selected for other mixtures. But, shrinkage was observed at these samples at 100 °C. However, it was observed that the lowest strengths occurred at 20°C.

	20°C-1	20°C-2	20°C-3	60°C-1	60°C-2	60°C-3	100°C-1	100°C-2	100°C-3
L/B=0.35	3.76	2.68	2.74	11.52	4.62	3.4	14.48	30.68	16.68
L/B-0.45	4.62	2.76	2.28	9.36	6.8	4.52	17.48	30.5	33.28
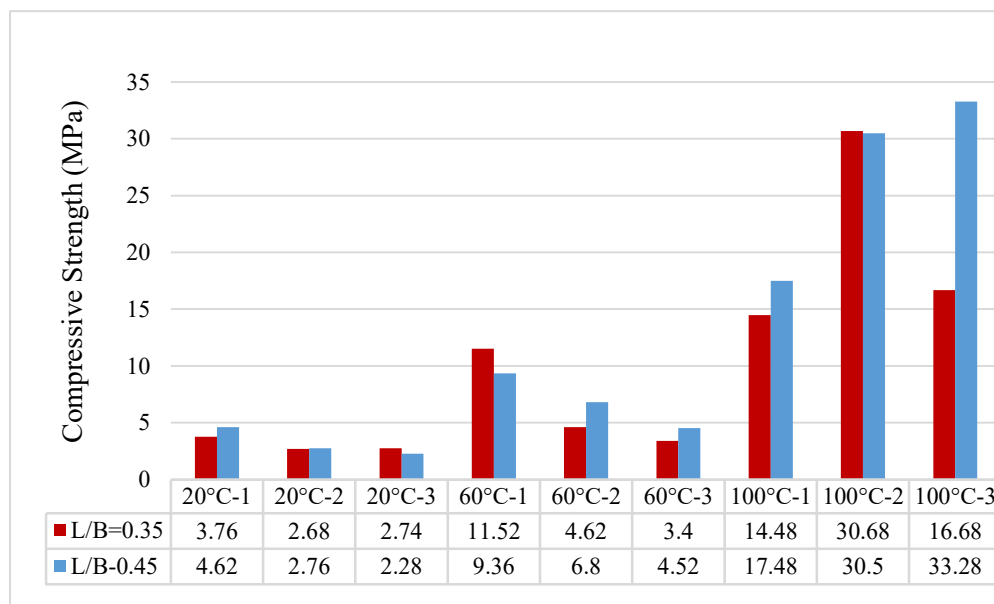
Fig.5. Compressive strengths of 25% BW-75% TRP samples according to various L/B ratios and curing temperatures

Fig. 6 shows compressive strength of 25% BW and 75% GBFS mixtures for 1.0, 2.0 and 3.0 NS/NH ratios and different temperatures. For 3.0 NS/NH ratio and L/b=0.45, the maximum compressive strength was reached the 57.2 MPa at 60°C. When the highest value is compared with other studies, it is seen that it has high strength. For example, Saha and Rajasekaran produced a geopolymer paste mixture using slag and fly ash. They use the GBFS ratio as 50% for the 12 M NaOH solution and found the 28-day compressive strength

of the produced samples to be 48 MPa [16]. Verma and Dev produced geopolymer concrete using 25% fly ash and 75% GBFS. They determined the average compressive strength of the concrete samples as 29 MPa under 13 M NaOH, 1/1 NS/NH and 80 ℃ curing temperature [17].
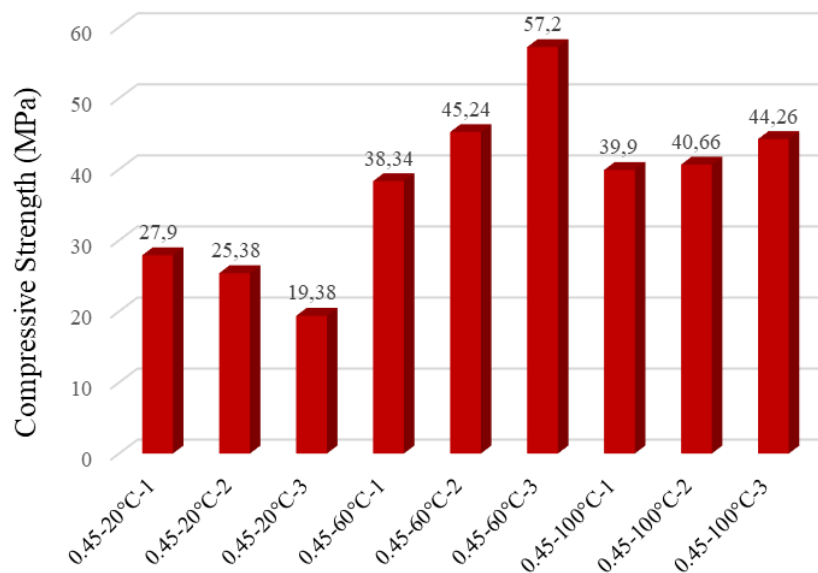
Fig.6. Compressive strengths of 25% BW-75% GBFS samples according
to various NS/NH ratio and temperatures

Compressive strength results of samples consisting of 25% BW, 35% GBFS and 40% TRP was given in Fig. 7. According to this graph, it is seen that the highest compressive strength occurs at 100°C and 1.0 ratio for NS: NH. But shrinkage was observed all samples cured at 100°C. Therefore, in order not to have a significant difference in strength and to gain energy, curing temperature and NS: NH ratio for this triple mix samples was selected as 60°C and 1.0, respectively.
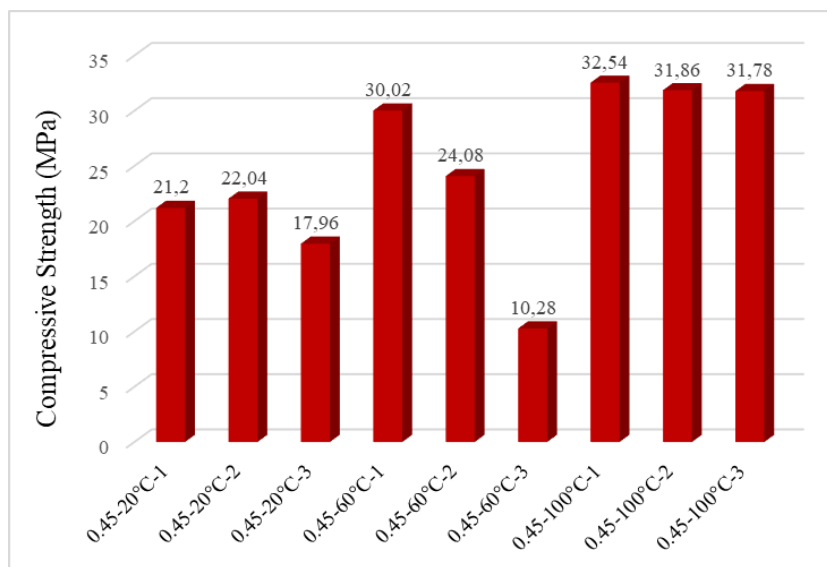
Fig.7. Compressive strengths of 25% BW 35% GBFS and 40% TRP
samples

CONCLUSIONS

In this study, it is aimed to produce geopolymer paste by using industrial wastes and natural stone without using cement.

As a result of the experimental research, the results obtained for the samples produced using 25% BW-75% TRP are given below.
- The compressive strength of TRP and BW mixtures decreases with decreasing temperature.
- In TRP and BW mixtures, it was seen that the samples did not settle in the mold at a ratio of 0.35 L/b.
- The highest compressive strength was achieved in the NS/NH ratio of 3.0 and the Liquid/binder (L/B) ratio of 0.45 in TRP and BW samples. But, shrinkage was observed at these samples.
- As a result of the experimental research, the results obtained for the samples produced using 25% BW-75% GBFS are given below.
- While the lowest strength was occurred at 20°C NS/NH= 3.0, it was determined that the highest strength was obtained in mixtures with 60°C NS/NH=3.0.
- Also, it was seen that the samples cured at 100°C shrank, while at 60°C there was no shrinkage.
- As a result of the experimental research, the results obtained for the samples produced using 25% BW-35% GBFS- 40% TRP are given below.
- While the highest strength was occurred at 100°C NS/NH=1.0, it was determined that the lowest strength was obtained in mixtures with 60°C NS/NH=3.0.
- Although the strength at 100 °C was slightly higher than at 60 °C, it caused serious shrinkage in the samples. In order to prevent this shrinkage and to provide low energy consumption, the optimum temperature was selected as 60 °C and the ratio NS/NH=1.0.
- Consequently, mechanical and durability tests will be done in future studies to investigate the usage of BW in geopolymer mortar and concrete.

REFERENCES

1. KOÇKAL, N. U.; BEYCAN O.; GÜLMEZ N. Effect of binder type and content on physical and mechanical properties of geopolymers. *Sādhanā*, 2018, Vol. 43, No. 4, P. 1–9.

2. J. DAVIDOVITS, "Properties of Geopolymer Cements," First International Conference on Alkaline Cements and Concretes, Scientific Research, 1994, P. 131–141.

3. DUXSON, P.; FERNÁNDEZ-JIMÉNEZ, A.; PROVIS, J. L.; LUKEY, G. C.; PALOMO, A.; VAN DEVENTER, J. S. J. Geopolymer technology: The current state of the art. *Journal of material science*, 2007, Vol. 42, No. 9, P. 2917–2933.

4. AYGÖRMEZ, Y.; CANPOLAT, O.; AL-MASHHADANI, M.M. Assessment of geopolymer composites durability at one year age. *Journal of building engineering*, 2020, Vol. 32, No. 101453.

5. UYSAL, M.; AL-MASHHADANI, M.; AYGÖRMEZ, Y.; CANPOLAT, O. Effect of using colemanite waste and silica fume as partial replacement on the performance of

metakaolin-based geopolymer mortars. *Construction of building and materials*, 2018, Vol. 176, P. 271–282.

6. CELIK, A.; YILMAZ, K.; CANPOLAT, O.; AL-MASHHADANI M.; AYGÖRMEZ, Y., UYSAL, M. High-temperature behaviour and mechanical characteristics of boron waste additive metakaolin based geopolymer composites reinforced with synthetic fibres. *Construction of building and materials*, 2018, Vol. 187, P. 1190-1203.

7. HARDJITO, D.; WALLAH, S. E.; SUMAJOUW, D. M. J.; RANGAN, B. V. On the development of fly ash-based geopolymer concrete. *ACI materials journal*, 2004, Vol. 101, No. 6, P. 467–472.

8. BEN HAHA, M.; LE SAOUT, G.; WINNEFELD, F.; LOTHENBACH, B. Influence of activator type on hydration kinetics, hydrate assemblage and microstructural development of alkali activated blast-furnace slags. *Cement and concrete research*, 2011, Vol. 41, No. 3, P. 301–310.

9. ÖZODABAŞ, A.; YILMAZ, K. Improvement of the performance of alkali activated blast furnace slag mortars with very finely ground pumice. *Construction of building and materials*, 2013, Vol. 48, P. 26–34.

10. TOP, S.; VAPUR, H. Effect of basaltic pumice aggregate addition on the material properties of fly ash based lightweight geopolymer concrete. *Journal of Molecular Structure*, 2018, Vol. 1163, P. 10–17.

11. ZHU, H.; ZHANG, Z.; ZHU, Y.; TIAN, L. Durability of alkali-activated fly ash concrete: Chloride penetration in pastes and mortars. *Construction and building materials*, 2014, Vol. 65, P. 51-59.

12. CHI, M. Effects of dosage of alkali-activated solution and curing conditions on the properties and durability of alkali-activated slag concrete. *Construction and building materials*, 2012, Vol. 35, P. 240–245.

13. KOÇKAL, N. U.; BEYCAN, O.; GÜLMEZ, N. Physical and mechanical properties of silica fume and calcium hydroxide based geopolymers. *ACTA physica polonica a*, 2017, Vol. 131, No. 3, P. 530–533.

14. ŞAHİN YÖN, M.; KARATAŞ, M. Investigation of the usability of boron waste in geopolymer paste. 3rd International Eurasian Conference on Science, Engineering and Technology, 2021, December 15-17.

15. MOHABBI YADOLLAHI, M. DENER, M. Investigation of elevated temperature on compressive strength and microstructure of alkali activated slag based cements. *European Journal of environmental and civil engineering*, 2021, Vol. 25, No.5, P. 924-938.

16. SAHA, S.; RAJASEKARAN, C. Enhancement of the properties of fly ash based geopolymer paste by incorporating ground granulated blast furnace slag. *Construction and building materials*, 2017, Vol. 146, P. 615-620.

VERMA, M.; DEV, N. Effect of ground granulated blast furnace slag and fly ash ratio and the curing conditions on the mechanical properties of geopolymer concrete. *Structural concrete*, 2022, Vol. 23, Iss. 4, P. 2015-2029 (https://doi.org/10.1002/suco.202000536)

PROPERTIES ON YTTRIUM-DOPED/ UNDOPED BARIUM CERATE AND BARIUM ZIRCONATE THIN FILMS FORMED BY E-BEAM VAPOUR DEPOSITION

M. S. C. Covarrubias, M. Sriubas, K. Bockute, A.Poskaite, R. Vazgys, G. Laukaitis
Kaunas University of Technology
Physics Department
Studentu str. 50, LT-51368, Kaunas – Lithuania

M. Gazda
Gdansk University of Technology,
Faculty of Applied Physics and Mathematics
Narutowicza 11/12, 80-233 Gdansk – Poland

EXTENDED ABSTRACT

OVERVIEW

Yttrium-doped/undoped barium cerate ($BaCeO_3$) and barium zirconate ($BaZrO_2$) thin films are used as electrolytes of proton conductive fuel cells (PCFC). $BaCeO_3$ materials at intermediate temperatures present low ion conductivity [1]. However, these materials have shown to be a good diffusion barrier between the metal electrode and the electrolyte to decrease the energy barrier between them [2] and enhance the proton path. Another material is $BaZrO_2$ doped with 20% yttrium which obtained the highest protonic conductivity of 0.11 S/cm^{-1} at 500 ºC (5% H_2, 0.03 Pa (H_2O), Ar) [3] formed by pulsed laser deposition. A type of dopant and different concentrations affect the chemical stability, phase, lattice parameters, grain size, and strains of the materials that influence the proton trapping effect [4] on the Grotthuss mechanism and the resulting protonic conductivity. Yttrium dopant has shown a lower proton trapping effect [4]. Grain boundaries on electrolytes affect ionic conductivity due to the formation of space charge depletion zones [5] formed by positive charges as voids and holes [6] that are surrounded by negative charges. Moreover, low crystallinity adds resistance to the ion conductivity [7]. Therefore, highly dense electrolytes with high crystallinity are required. The proton jump energy is also influenced by lattice parameters which differ for $BaCeO_3$ and $BaZrO_3$, e.g. $a = 8.724$ Å, $b = 6.230$ Å, $c = 6.211$ Å of $BaCeO_3$ [8] and $a = 4.210$ Å [9] of $BaZrO_2$. It is known that the electrolytes may have different microstructure, density, and crystallinity depending on the chosen formation method, therefore, it is important to analyse the formation methods and technological parameters to obtain highly dense and crystalline films. The purpose of this research is to investigate the formation of yttrium-doped/ undoped $BaCeO_3$ and $BaZrO_2$ thin films using e-beam vapor deposition and to analyse the influence of formation parameters and composition on the microstructural properties.

METHODS

The thin films were deposited using e-beam physical vapor deposition system Kurt J. Lesker EB-PVD 75. The initial powders ($BaCeO_3$, 99.9% purity; $BaZrO_2$, 99.9% purity; and $BaZrO_2$ doped with 20% yttrium) were used as a target material to form the thin films. The powders were pressed into pellets and evaporated on substrates. Prior to the deposition substrates were cleaned ultrasonically with isopropanol and acetone. The substrate temperature was changed from 300 ºC to 610 ºC during the deposition. The acceleration voltage of the electron gun was 7.9 kV, and the current was adjusted in the range of 30-100 mA. The initial pressure was 1×10^{-5} Pa and the working pressure range was from 1×10^{-3} Pa to 1×10^{-4} Pa. A profilometer was used to measure the thickness of the formed films which was ~1.4 μm for all deposited samples. The crystalline structure of the thin films was studied by an X-ray diffractometer (XRD). The measurements were performed using Cu Kα ($\lambda = 0.154059$ nm) radiation at a geometry of 2Θ angle in a 20°–70° range and a 0.01° step. The surface topography images and cross-section images were obtained using the scanning electron microscope (SEM). Elemental composition was analysed using an energy-dispersive X-ray spectroscope (EDS).

RESULTS

The thin films of undoped $BaCeO_3$ formed at 500 and 600ºC substrate temperature are highly dense and exhibit a columnar growth (Fig. 1).
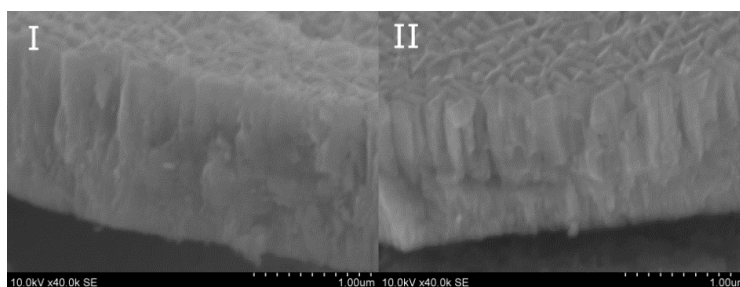
Fig. 1. Cross-section of $BaCeO_3$ formed at 500 ºC (I) and 600ºC (II).

XRD patterns (Fig. 2) confirm the formation of the $BaCeO_3$ orthorhombic phase (ICDD: 04-015-3335) at 500 ºC and 600 ºC substrate temperatures. The crystals are highly oriented towards the (002) plane compared with the random orientation on the pellets. Crystal size was calculated by the Scherrer equation and their values vary from 29.36 to 34.83 nm for 500 ºC and 600 ºC respectively. Crystal sizes are in the low range compared with pellets [10, 11], with values between 30 and 75 nm. Highly orientation is attributed to the orientation of the metal substrate alloys and e-beam formation conditions[12].
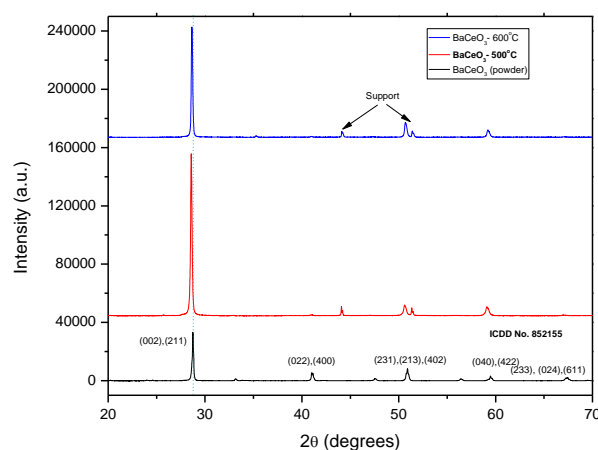
Fig. 2. XRD pattern of $BaCeO_3$ at 500 ºC and 600 ºC substrate temperature.

Compared with barium cerate, barium zirconate doped yttrium 20% (BZY20) formed highly dense films. Oxygen vacancies formed with the presence of dopant also reduce the grain growth activation energy [13].
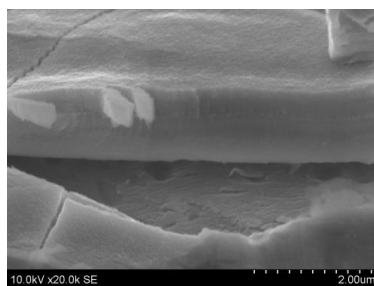
Fig. 3. Cross-section of BZY20.

CONCLUSIONS

Highly oriented (002) $BaCeO_3$ films with high-density columnar growth and highly crystallinity were obtained by e-beam vapor deposition at 500ºC and 600ºC. High dense BZY20 was formed by e-beam vapor deposition.

Keywords: Nanograins, strain, texture

REFERENCES

1. CAMPOS COVARRUBIAS, M. S.; SRIUBAS, M.; BOCKUTE, K.; WINIARZ, P.; MIRUSZEWSKI, T.; SKUBIDA, W.; JAWORSKI, D.; BARTMAŃSKI, M.; SZKODO, M.; GAZDA, M.; LAUKAITIS, G. Properties of Barium Cerate Thin Films Formed Using E-Beam Deposition. *Crystals,* 2020, Vol. 10, No. 12, P.1152.

2. BAE, K.; JANG, D. Y.; JUNG, H. J.; KIM, J. W.; SON, J.-W.; Shim, J. H.. Micro Ceramic Fuel Cells with Multi-layered Yttrium-Doped Barium Cerate and Zirconate Thin Film Electrolytes, *Journal of Power Sources,* 2014, Vol. 248, P.1163–1169.

3. PERGOLESI, D.; FABBRI, E.; D'EPIFANIO, A.; DI BARTOLOMEO, E.; TEBANO, A.; SANNA, S.; LICOCCIA, S.; BALESTRINO, G.; TRAVERSA, E. High Proton

Conduction in Grain-Boundary-Free Yttrium-Doped Barium Zirconate Films Grown by Pulsed Laser Deposition, *Nature Material,* 2010, Vol. 9, No. 10, P. 846–852.

4. YAMAZAKI, Y.; BLANC, F.; OKUYAMA, Y.; BUANNIC, L.; LUCIO-VEGA, J. C.; GREY, C. P.; HAILE, S. M. Proton Trapping in Yttrium-Doped Barium Zirconate, *Nature Materials,* 2013, Vol.12, No.7, P. 647–651.

5. HELGEE, E.; LINDMAN, A.; WAHNSTRÖM, G. Origin of Space Charge in Grain Boundaries of Proton-Conducting BaZrO3, *Fuel Cells*, 2013, Vol. 13, No. 1, P. 19-28.

6. TU, Q.; SHI, T.; CHAKRAVARTHY, S.; CEDER, G. Understanding Metal Propagation in Solid Electrolytes Due to Mixed Ionic-Electronic Conduction, *Matter,* 2021, Vol. 4, No.10, P. 3248–3268.

7. KIM, Y. B.; GÜR, T. M.; JUNG, H.-J.; KANG, S.; SINCLAIR, R.; PRINZ, F. B. Effect of Crystallinity on Proton Conductivity in Yttrium-Doped Barium Zirconate Thin Films, *Solid State Ionics*, 2011, Vol. 198, No.1, P. 39–46.

8. FU, Y. P.; WENG, C. S. Effect of Rare-Earth Ions Doped in BaCeO3 on Chemical Stability, Mechanical Properties, and Conductivity Properties, *Ceramics International, Part B*, 2014, Vol. 40, No.7, P. 10793–10802.

9. GILARDI, E.; FABBRI, E.; BI, L.; RUPP, J. L. M.; LIPPERT, T.; PERGOLESI, D.; TRAVERSA, E. Effect of Dopant–Host Ionic Radii Mismatch on Acceptor-Doped Barium Zirconate Microstructure and Proton Conductivity, *The Journal of Physical Chemistry C* , 2017, Vol. 121, No. 18, P. 9739–9747.

10. SARABUT, J.; CHAROJROCHKUL, S.; SORNCHAMNI, T.; LAOSIRIPOJANA, N.; ASSABUMRUNGRAT, S.; WETWATTANA-HARTELY, U.; KIM-LOHSOONTORN, P. Effect of Strontium and Zirconium Doped Barium Cerate on the Performance of Proton Ceramic Electrolyser Cell for Syngas Production from Carbon Dioxide and Steam. *International Journal of Hydrogen Energy,* 2019, Vol. 44, No. 37, P. 20634–20640.

11. DUBAL, S. U.; BHOSALE, C. H.; JADHAV, L. D. Performance of Spray Deposited Gd-Doped Barium Cerate Thin Films for Proton Conducting SOFCs. *Ceramics International,* 2015, Vol. 41, No. 4, P. 5607–5613.

12. CHOPDEKAR, R. V.; ARENHOLZ, E.; SUZUKI, Y. Orientation and Thickness Dependence of Magnetization at the Interfaces of Highly Spin-Polarized Manganite Thin Films. *Physical Review B*, 2009, Vol. 79, No. 10, P.104417.

13. SHUKLA, S.; SEAL, S.; VIJ, R.; BANDYOPADHYAY, S. Reduced Activation Energy for Grain Growth in Nanocrystalline Yttria-Stabilized Zirconia. *Nano Letters,* 2003, Vol. 3, No. 3, P. 397–401.

NEW FORMALDEHYDE-FREE PARTICLE PANELS MADE FROM AGRICULTURAL WASTES AND CHITOSAN

Y. Khalaf[1, 2], P. El Hage, R. El Hage
[1]*LCPM, EDST-PR2N, Faculty of Sciences II, Lebanese University*
Fanar – Lebanon
yasmina.khalaf@ltu.bg, nina_khalaf@hotmail.com

J. Dimitrova Mihajlova
[2]*Department of Mechanical Wood Technology, Faculty of Forest Industry, University of Forestry, Sofia – Bulgaria*

N. Brosse
University of Lorraine, LERMAB,
54000 Nancy – France

A. Bergeret
Polymers Composites and Hybrids (PCH), IMT Mines Alès,
Alès – France

P. Lacroix
Greenpile, 18 Boulevard Edouard Lachaud,
19100 Brive La Gaillarde –France

EXTENDED ABSTRACT

OVERVIEW

Current environmental problems, deforestation, and tensions over raw materials, are pushing manufacturers to substitute wood in the production of wood-based panels by other alternative lignocellulosic sources. In addition, the replacement of synthetic binders based on non-renewable, petro-sourced, and carcinogenic formaldehyde with other bio based and biodegradable materials is being sought with the aim of pollution reduction and environmentally friendly materials production. Thus, the present work is devoted to the development of new panels using a polysaccharide binder, chitosan, in presence of reinforcements based on miscanthus or spent mushroom substrates combined with olive waste residues.

METHODS

Miscanthus × giganteus (M) from the summer 2018 harvest comes from the EARL Ar Gorzenn Company (Pont Croix, France). The spent mushroom substrate (SMS) is recovered from the "Gourmet mushroom" farm located in Byblos, Lebanon. These resources

underwent grinding followed by automated sieving before use. Olive pomace waste is collected at the "Ghaoui-Ghaoui" olive mill in Darbechtar located in northern Lebanon. This waste has undergone crushing and manual sieving to separate the Olive pomace (OP) from the Olive Stones (OS) waste. Chitosan having a degree of deacetylation greater than 90%, a viscosity of 30 to 100 cps and an average molecular weight of 250,000 g mol^{-1} was purchased from Glentham Life Sciences (Corsham-Wiltshire, United Kingdom).

Four panels were prepared from the different components as shown in Table 1. The binder solution is prepared by dissolving chitosan (4% w/v) in aqueous glacial acetic acid solution (2% v/v) at room temperature using a mechanical stirrer. 24 g of OP or OS are added to the chitosan solution followed by mechanical stirring for 5 minutes. The mixture is then poured onto 36 g of M or SMS particles followed by manual mixing. The mixture is left at room temperature for 30 min to promote reinforcements wetting. Preheating is then applied for 60 min at 105 °C. The partially dried mixture is placed in a Teflon-coated stainless steel mold (180 × 50 × 70 mm^3) and compacted using a backing mold and a hydraulic press to a thickness of 1 cm. Compaction is maintained overnight in an oven at 105 °C. The panels are recovered after cooling and demoulding.

The bulk density, porosity, morphology, water absorption capacity by immersion and mechanical compressive strength before and after immersion are evaluated for the various panels.

RESULTS

Density and Porosity

The average bulk density and the porosity rate are presented in Table 1. Despite the similarity of the total initial weight and the fixed mold dimension, the bulk density of the materials was different depending on the reinforcement type. Thus, the SMS-based panels are much denser than the M-based ones because of significant volume shrinkage of the samples which are probably related to the collapse of the microtubes inside the cells and a reaction of mycelium present in SMS [1].

Table 1. Average bulk density and porosity rate of the panels as a function of the formulations

Sample name	Fibbers (36 g /24 g)	Average $\rho_{apparente}$ (kg/m^3)	Porosity (%)
MOP	Miscanthus / Olive Pomace	665 ±80	16.2
MOS	Miscanthus / Olive Stones	685 ±9	19.4
SMSOP	Spent mushroom substrate / Olive pomace	899 ±47	10.0
SMSOS	Spent mushroom substrate / Olive Stones	806 ±14	15.8

*For all panels: m$_{chitosane}$ = 4.5g; V$_{acetic\ acid\ 2\%}$ = 108 mL; ratio$_{fibres/binder}$ (%/% m/m) = 93/7

The porosity rate decreases with increasing bulk density, and conversely. The most porous panels are MOS and MOP. However, SMSOP has the lowest porosity rate. This phenomenon could be explained by the softening and shrinking of the mycelium [1] after cooking/drying of the panels at 105 °C inducing a decrease in the intrinsic porosity of the SMSs.

Optical Microscopy

Fig. 1 presents the superficial observations of the different panels using a "Ladybird MZ1240 Trinocular" stereomicroscope. The shiny layer on the surface of the fibres corresponds to the presence of the chitosan binder. This can be considered as an indicator of a good wetting of the different particles by the binder. It is visible that the M and SMS are well dispersed and homogeneously oriented parallel to the surface. It appears that OS are dispersed as aggregates. A gap is clearly visible between the particles indicating the presence of pores.
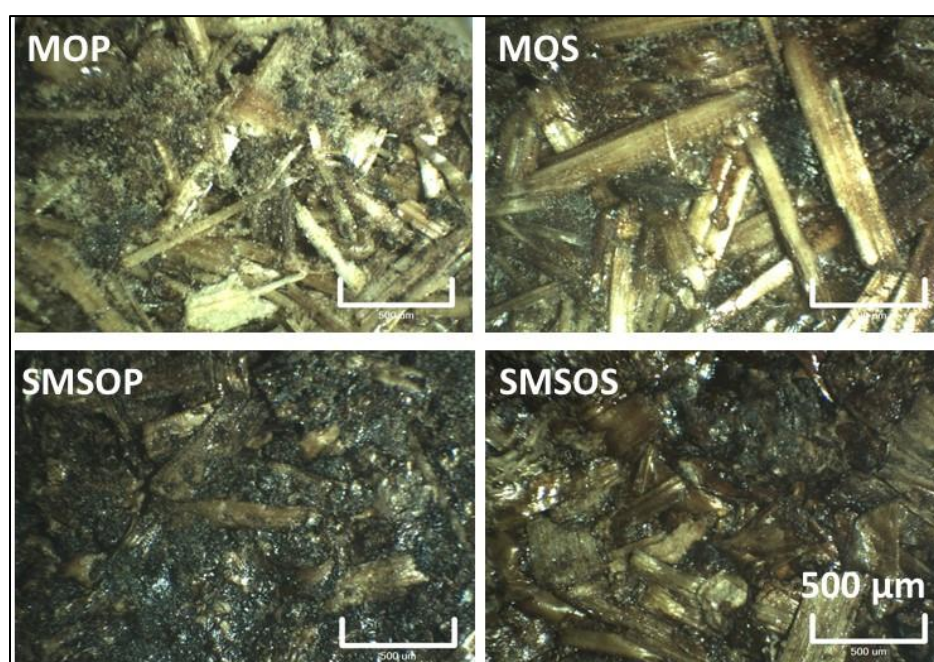
Fig 1. Microscopic observations of the panels surface according to the formulations

Absorption Capacity

The absorption capacity (Δm %) of the panels versus time is presented in Fig. 2. It seems that Δm is independent of the nature of the reinforcements. SMSOS panels have the highest absorption capacity for the first 30 minutes, while for the same duration a low absorption capacity (Δm <10%) is noted for the other panels. After immersion for 5 days, the MOP panels exhibit significant weight gain at saturation, reaching the threshold of 40%. This agrees with the photos of the microscope which show the presence of the large-diameter pores for the MOP panel. The rest of the panels seem to have an intermediate weight gain (32-35%).
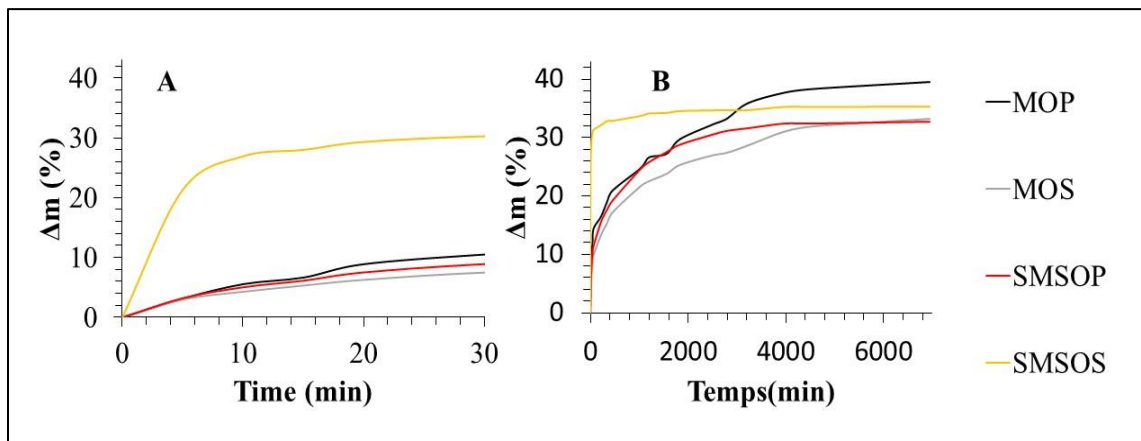
Fig 2. Absorption capacity of the panels versus time (A-for 30 min; B-for 5 days)

Mechanical Behaviour by Compression

Fig. 3 shows the compressive strength (MPa) values of the panels before and after immersion in water. SMSOP panels show the highest strength followed by M panels. This is explained by the presence of minor porosity for SMSOPs and the presence of mycelium. After immersion/drying, the compressive strength appears to be deteriorated for all panels. Only MOP panels seem to have close value to that obtained before immersion.
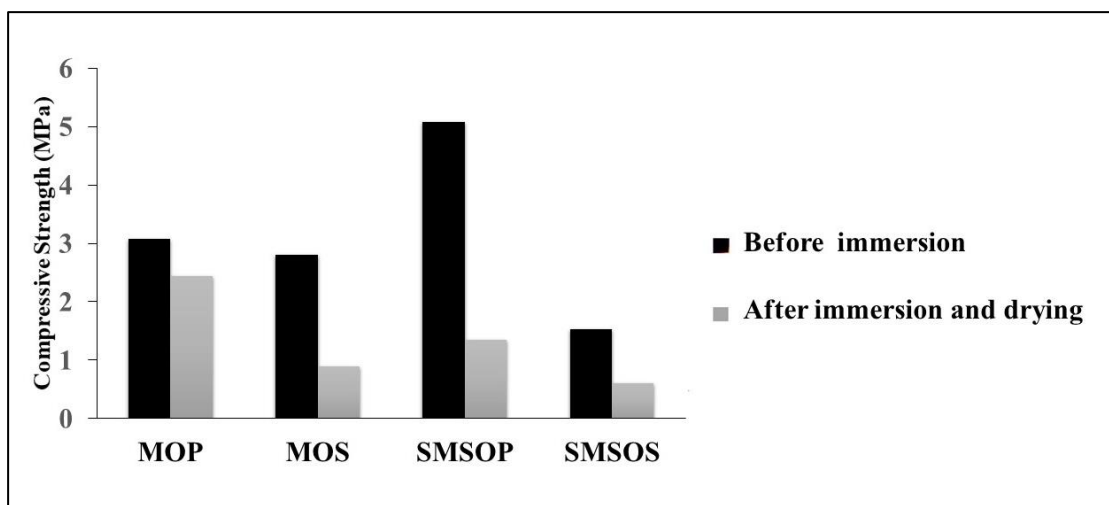
Fig 3. Compressive strength (MPa) of the panels before and after immersion/drying depending on the formulations

CONCLUSIONS

In this study chitosan-based panels using miscanthus and/or spent mushroom substrate with olive pomace waste was produced. Preliminary results show that panels are successfully prepared with an average density between 665 and 899 kg/m^3. The absorption capacity of all panels is less than 40% by weight despite the extended immersion time. To complete this study, additional mechanical bending and internal bonding strength analysis, contact angle analysis and microscopic observations after immersion will be performed. The aim of this study is the production of fully bio-based particleboards using local and/or neglected materials for interior design applications.

Keywords: Particleboards; miscanthus; spent mushroom substrate; olive pomace waste; chitosan

REFERENCES

1. KHOO, S. C.; PENG, W. X.; YANG, Y.; GE, S. B.; SOON, C. F.; MA, N. L.; SONNE, C. Development of formaldehyde-free bio-board produced from mushroom mycelium and substrate waste. *Journal of hazardous materials*, 2020, Vol. 400, No. 123296.

PSEUDOGAP AND FLUCTUATION CONDUCTIVITY IN YBA$_2$CU$_3$O$_{7-\Delta}$ NANOLAYERS

L. V. Omelchenko, A. L. Solovjov, E.V. Petrenko
*B. I.Verkin Institute for Low Temperature Physics and Engineering of National
Academy of Science of Ukraine
47 Nauki ave., 61103 Kharkov – Ukraine
+ (380)-57-340-22-23
omelchenko@ilt.kharkov.ua*

EXTENDED ABSTRACT

OVERVIEW

After thirty years since the high-temperature superconductors (HTSC's or cuprates) discovery the physics behind the pairing mechanism which allows the Cooper pairs formation at T>100K still remains unknown. Importantly, apart from the high Tc's, cuprates possess the so-called pseudogap (PG) which opens below PG temperature T* >> Tc [1-3]. It is believed at present that the proper understanding of the PG phenomenon has to account for the pairing mechanism both in cuprates and new FeAs-based high-Tc superconductors (pnictides), which is important in view of the search for the room-temperature superconductivity. A huge amount of various models has been put forward to explain the PG in HTSC's (see [1-4] and references therein) but the issue as for PG physics also remains rather controversial. We believe the PG to be due to preformed pairs (local pairs (LP's)) formation [2] but the pairing mechanism is very likely of a magnetic type [1, 4]. Thus, the comprehension of the interplay between superconductivity and magnetism is widely considered to be one of the great challenges of condensed-matter physics [1-4].

METHODS

To clarify the issue, we studied the fluctuation conductivity (FLC) and PG in YBa$_2$Cu$_3$O$_{7-\delta}$-PrBa$_2$Cu$_3$O$_{7-\delta}$ (YBCO-PrBCO) superlattices (SL's) and YBCO-PrBCO double-layer films (so-called "sandwiches", SD's) with different layer composition, prepared by pulsed laser deposition [5]. Pr^{+3} atoms are known to have an intrinsic magnetic moment, $\mu_{eff} \approx 3.58\mu_B$ and $\mu_{eff} \approx 2\mu_B$ in the PrBCO compound. Thus, such compounds are considered to be very promising in studying the change of interplay between superconductivity and magnetism in HTSC's which is expected to increase with an increase of the number of PrBCO layers NPR.

Totally three SL's with 4YBCO-1PrBCO (4Y-1Pr), 7Y-7Pr and 7Y-14Pr layer periodicity (samples SL1, SL2, SL3) and two SD's: 400Å PrBCO-500Å YBCO (SD1) and 400Å PrBCO-200Å YBCO (SD2) have been analysed. As expected, SL1 and SD1 demonstrate ρ (T) being typical for unadulterated YBCO films [2] with linear up to ~340 K normal-state resistivity ρ (T) above T*. With increase of NPR ρ (T) is found to demonstrate excessive resistivity being more pronounced in the case of SL3 and SD2. Simultaneously T* shifts towards higher temperatures. But ρ (T) still remains linear above T*.

RESULTS AND CONCLUSIONS

At T≤T* ρ (T) deviates from its normal-state linear dependence resulting in emergence of pronounced excess conductivity:

$$\sigma'(T) = \sigma(T) - \sigma_N(T) = \left[1/\rho(T)\right] - \left[1/\rho_N(T)\right] \tag{1}$$

As a difference between measured ρ (T) and linear normal-state resistivity ρN (T) extrapolated towards the low T region [2]. Near Tc σ′ (T) is always described by the Aslamasov-Larkin and Maki-Thompson fluctuation theories, but the range of the SC fluctuation is at most about 20K above Tc [2]. Equation to describe σ′ (T) in the whole temperature range from T* down to Tc was proposed within the Local Pairs (LP) model in Ref. [2], and finally allowed to get equation for the temperature dependence of pseudogap:

$$\Delta^*(T) = T \ln \frac{e^2 A_4 \left(1 - \frac{T}{T^*}\right)}{\sigma'(T) 16\hbar\xi_c(0)\sqrt{2\varepsilon_{c0}^*}\sinh(2\varepsilon/\varepsilon_{c0}^*)} \tag{2}$$

where A4 is a scaling factor, σ′ (T) is the experimentally measured excess conductivity, ξ_c (0) is a coherence length along the c-axis, ε is a reduced temperature and ε^*_{c0} is the theoretical parameter [2]. Importantly, all these parameters can be determined from experiment within the LP model.
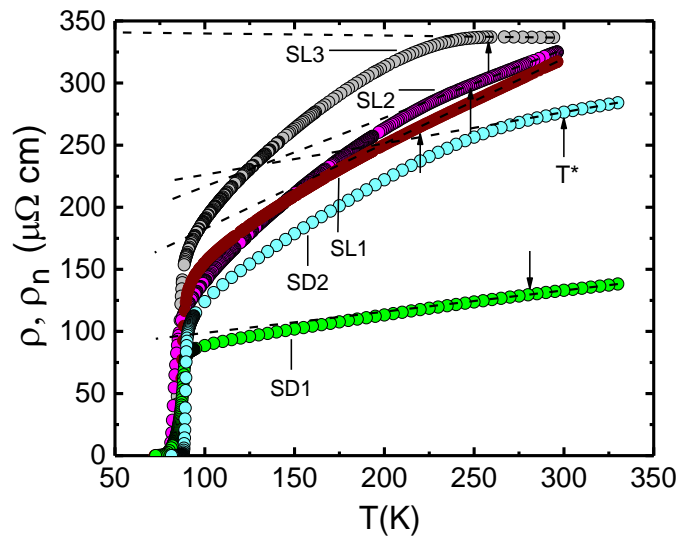
Fig. 1. Temperature dependencies of PG Δ* for all samples studied,
analysed with Eq. (2).

Fig. 1 shows results of the PG analysis obtained for all five samples using Eq. (2) with corresponding set of parameters derived from experiment. As expected, SL1 shows Δ*(T) being typical for unadulterated YBCO films with a wide maximum at T_{max}~130 K and Δ^*_{max} ≈ 250 K. With increase of N_{PR}, Δ^*_{max} decreases but T* increases. Simultaneously pronounced maximum of Δ*(T) appears at high T, which gradually increases along with N_{PR}. The maximum becomes more pronounced for SL3 and SD2 (Fig. 1). For the first time such Δ*(T) with a descending linear region was observed for $SmFeAsO_{0.85}$ between the structural transition temperature T_s=150K and SDW ordering temperature T_{SDW} = 130 K, and is believed to be the more noticeable feature of the magnetic influence in the HTSC's

[2]. To confirm the conclusion, we have compared results obtained for SL3 and SD2 with those found for $SmFeAsO_{0.85}$ and $EuFeAsO_{0.85}F_{0.15}$. Fig. 2 shows that both the range of the descending linear region and its slope are the same for all shown samples. Similarity of the results suggests the presence of the magnetic interaction in YBCO-PrBCO compounds too, which is believed to be responsible for the specific $\Delta^*(T)$ shape at high temperatures (Fig. 2). Thus, one may conclude that the basic mechanism of the interplay between the superconductivity and magnetism is the same in all HTSC's where superconductivity can coexist with magnetism.
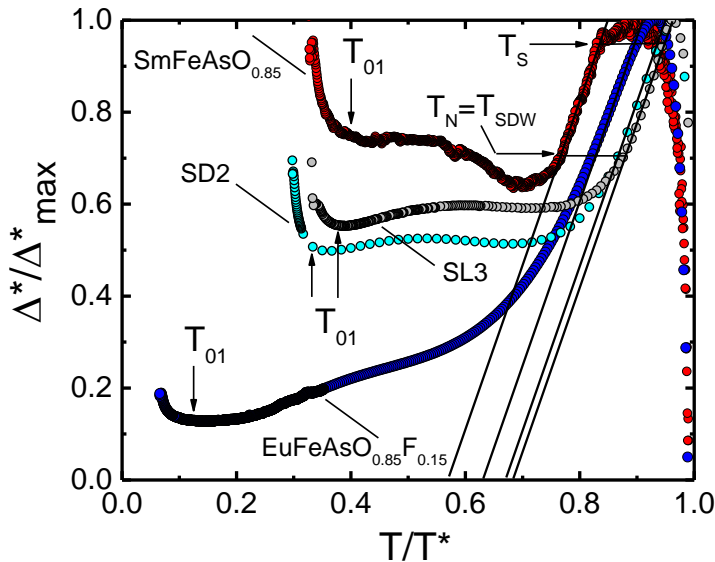
Fig. 2. $\Delta^*(T)/\Delta_{max}$ as a function of T/T* for SL3 and SD2 compared with the Fe-pnictides samples $SmFeAsO_{0.85}$ (Tc =55 K) [2] and $EuFeAsO_{0.85}F_{0.15}$ (Tc=11K) [6]. Equal slope solid lines correspond to the linear $\Delta^*(T)$ region. Horizontal lines designate its length which lasts between T_s and T_{SDW}. Arrows at T_{01} designate the ranges of SC fluctuations.

Keywords: (pseudogap, fluctuation conductivity, superconductivity, superlattice, double-layer films)

REFERENCES

1. KORDYUK, A. A. Pseudogap from ARPES experiment: Three gaps in cuprates and topological superconductivity. *Low Temperature Physics*, 2015, Vol. 41, No. 1, P. 319-343.

2. SOLOVJOV, A. L. Pseudogap and local pairs in high-Tc superconductors, *Superconductors – Materials, Properties and Applications*, Ed. A. M. Gabovich (InTech. Rijeka), 2012, P. 137–170.

3. PETERS, R.; BAUER, J. Local origin of the pseudogap in the attractive Hubbard model. *Physical Review B,* 2015, Vol. 92, No. 1, No. 014511.

4. TAILLEFER, L. Scattering, and Pairing in Cuprate Superconductors, *Annual Review of Condensed Matter Physics*, 2010, Vol. 1, P. 51-70.

5. HABERMEIER, H. U. *Applied Surface Science*, 1993, No. 69, P. 204.

6. SOLOVJOV, A. L.; OMELCHENKO, L.V. Fluctuation conductivity and possible pseudogap state in FeAs based superconductor $EuFeAsO_{0.85}F_{0.15}$ *Materials Research Express*, 2016, Vol. 3, No. 7, P. 1-13.

FLUCTUATION CONDUCTIVITY UNDER THE INFLUENCE OF STRONG MAGNETIC FIELDS IN THIN YBCO FILMS

E. V. Petrenko, L. V. Omelchenko, A. L. Solovjov
B. I. Verkin Institute for Low-Temperature Physics and Engineering
of National Academy of Science of Ukraine
47 Nauky ave., Kharkiv, 61103 – Ukraine
+380502224291
petrenko@ilt.kharkov.ua

D. M. Sergeyev
K. Zhubanov Aktobe Regional State University
34, A.Moldagulova Street, Aktobe, 030000 – Kazakhstan
serdau@rambler.ru

EXTENDED ABSTRACT

OVERVIEW

It is believed that understanding the mechanism of electron pairing in high-temperature superconductors (HTSC) will indicate the direction of synthesis of superconductors with a desired high T_c. For this, it is necessary to study the properties of HTSCs in the normal state, where the pseudogap is opened at the characteristic temperature $T^* >> T_c$. It is known that the low charge carrier density, NF, promotes the formation of paired fermions in cuprates below T^*. That is, the so-called local pairs (LPs) [1, 2], which are considered responsible for the formation of the PG ([2, 3] and references therein). At high temperatures $T \leq T^*$, LPs appear in the form of strongly bound bosons (SBBs), which obey the Bose-Einstein condensation theory (BEC) and can only be formed in systems with small n_F [10]. SBBs are small since $\xi_{ab}(T^*) \sim 10$ Å in YBCO, and very tightly bound pairs, since, according to the theory [4, 5], the binding energy in a pair $\varepsilon_b \sim 1/\xi$. As a result, SBBs are not destroyed by thermal and other fluctuations. However, as the temperature decreases, ξ and, consequently, the size of the pairs grows, and the SBBs are gradually transformed into fluctuating Cooper pairs (FCPs), which already obey the BCS theory near T_c [2, 3, 6]. This is a range of superconducting (SC) fluctuations. Additionally, near T_c, when $\xi_c(T)$ exceeds the size of the YBCO unit cell along the c-axis: $\xi_c(T) > d$, the quasi-two-dimensional state of HTSCs changes to the 3D state [3, 11], since the condensation of FCPs into the SC state is possible only from the 3D state [4, 5].

Applying of an external magnetic field is one of the excellent methods to study SC fluctuations in HTSCs in the vicinity of critical temperature T_c. As an example, consider several attempts to analyse the excess conductivity in YBCO in strong magnetic fields [7-9]. In [7] both $B \parallel ab$ and $B \parallel c$ orientations of external magnetic field were used to study fluctuation conductivity (FLC) in aluminium doped YBCO single crystals with a system of unidirectional twin boundaries (TBs). Obviously, in this case, the results are deeply affected by the aluminium impurities and TBs. Besides, the applied field does not exceed 1.27 T. In

[8], magnetic field B = 12 T was applied to study FLC in YBCO composites, which again were doped with Ag, which deeply affected the results. It is not known whether these were films, single crystals or polycrystals. In addition, the authors did not show the evolution of the FLC with a magnetic field. In fact, only the data at B = 0 and 12 T were shown. In [9], the magnetic susceptibility and FLC were measured in an optimally doped (T_c = 91.1 K) YBCO film in fields up to 9 T perpendicular to the ab plane. But, surprisingly, as in [8], the authors also did not show the evolution of the FLC with a magnetic field. In addition, no attempts were made to use the Aslamasov-Larkin and Maki-Thompson fluctuation theories to describe FLC as a function of B. As a result, the mechanism of the magnetic field influence on the FLC and the vortex motion in YBCO is still unclear.

From the literature, it is known that the orbital motion of the superconducting carriers is strongly suppressed when $H \perp c$ axis is applied. For this reason, only the Zeeman terms contribute to the fluctuation conductivity in this case.

In our work, we focused on the magneto conductivity $\Delta\sigma_H$ analysis when the role of the orbital motion can be neglected on the fluctuation level. We have studied a high quality 100 nm-thick YBCO film with T_c = 88.7 K at $(LaAlO_3)_{0.3}(Sr_2TaAlO_6)_{0.7}$ substrate. The resistive measurements have been performed using Quantum Design PPMS-9 equipment in $H \| ab$ configuration in order to extract the pure Zeeman contributions to $\Delta\sigma_H$.

METHODS

According to Aronov *et al*. [10], the contribution of the Zeeman Effect to the Aslamazov-Larkin (ALZ) and Maki-Thompson (MTZ) terms reads as following:

$$\Delta\sigma_{ALZ} = -0.526 \frac{e^2}{\hbar d \varepsilon^2} \frac{1+\alpha}{(1+2\alpha)^{3/2}} \left[\frac{\omega_s}{4\pi k_B T_c} \right]^2 \tag{4}$$

and

$$\Delta\sigma_{ALZ} = -0.526 \frac{e^2}{\hbar d \varepsilon^2} \frac{1+\alpha}{(1+2\alpha)^{3/2}} \left[\frac{\omega_s}{4\pi k_B T_c} \right]^2 \tag{5}$$

where $\omega_s = g\mu_B H$ is the Zeeman energy, g is the Lande g factor, μ_B is the Bohr magneton, τ_φ is the phase relaxation time, k_B is the Boltzman constant, $\hbar$ is the reduced Planck's constant, d is the length of the unit cell along the c-axis, α and δ are pairing and pair-breaking parameters, respectively, and ε is the reduced temperature.

RESULTS AND CONCLUSIONS

It was shown that the found $\Delta\sigma_H$ is well described within the 3D-ALZ and 2D-MTZ approaches in magnetic fields starting only from 3 T. The clear 3D-2D crossover, observed at 91.7 K, retains up to 6 T, up to which the 2D-MTZ contribution still persists. With further increase of the magnetic field, the magneto-conductivity shows exclusively 3D-ALZ behaviour.

An additional analysis of the upper critical field within the Werthamer–Helfand–Hohenberg (WHH) theory [11] allowed us to determine coherence lengths in the ab-plane (ξ_{ab} = 10.1 Å)

and along the *c*-axis (ξ_c = 3.3 Å), respectively, in a good agreement with the literature data [12].

Keywords: HTSCs, cuprates, high magnetic fields, excess conductivity, fluctuation conductivity, coherence length.

REFERENCES

1. TCHERNYSHYOV, O. Noninteracting Cooper pairs inside a pseudogap. *Physical Review B*, 1997, Vol. 56, No. 6, P. 3372-3400.

2. EMERY, V.J.; KIVELSON, S.A. Importance of phase fluctuations in superconductors with small superfluid density. *Nature*, 1995, Vol. 374, No. 6521, P. 434-437.

3. RANDERIA, M. Pre-pairing for condensation. *Nature Physics*, 2010, Vol. 6, No. 8, P. 561-562.

4. HAUSSMANN, R. Properties of a Fermi liquid at the superfluid transition in the crossover region between BCS superconductivity and Bose-Einstein condensation. *Physical Review B*, 1994, Vol. 49, No. 18, P. 12975-12983.

5. ENGELBRECHT, J. R.; NAZARENKO, A.; RANDERIA, M.; DAGOTTO, E. Pseudogap above T_c in a model with d_{x2-y2} pairing. *Physical Review B*, 1998, Vol. 57, No. 21, P. 13406-13409.

6. SOLOVJOV, A. L.; DMITRIEV, V. M. Fluctuation conductivity and pseudogap in YBCO high-temperature superconductors. (Review), *Low Temperature Physics*, 2009, Vol. 35, No. 3, P. 169-197.

7. VOVK, R. V.; NAZYROV, Z. F.; KHADZHAI, G. Ya.; PINTO SIMOES, V. M.; KRUGLYAK, V. V. Effect of transverse and longitudinal magnetic field on the excess conductivity of $YBa_2Cu_{3-z}Al_zO_{7-\delta}$ single crystals with a given topology of plane defects. *Functional Materials*, 2013, Vol. 20, No. 2, P. 208-216.

8. MALIK, B. A.; RATHER, G. H.; ASOKAN, K.; MALIK, M. A. Study on excess conductivity in YBCO + xAg composites. *Applied Physics A*, 2021, Vol. 127, No. 294.

9. REY, R. I.; CARBALLEIRA, C., DOVAL; J. M., MOSQUEIRA, J.; RAMALLO, M. V.; RAMOS-ÁLVAREZ, A.; SÓÑORA1, D.; VEIRA, J. A.; VERDE, J. C.; VIDAL, F. The conductivity and the magnetization around T_c in optimally doped $YBa_2Cu_3O_{7-\delta}$ revisited: quantitative analysis in terms of fluctuating superconducting pairs. *Superconductor Science and Technology*, 2019, Vol. 32, No. 4, No. 045009.

10. ARONOV, A. G.; HIKAMI, S.; LARKIN, A. I. Zeeman Effect on Magnetoresistance in High-Temperature Superconductors. *Physical Review Letters.* 1989, Vol. 62, No. 8, P. 965-968.

11. WERTHAMER, N. R.; HELFAND, E.; HOHENBERG, P.C. Temperature and Purity Dependence of the Superconducting Critical Field, H_{c2}. III. Electron Spin and Spin-Orbit Effects. *Physical Review,* 1966, Vol. 147, No. 1, P. 295-302.

12. SUGAWARA, J.; IWASAKI, H.; KOBAYASHI, N.; YAMANE, H.; HIRAI, T. Fluctuation conductivity of a c-axis-oriented $YBa_2Cu_3O_y$ film prepared by chemical vapor deposition. *Physical Review B*, 1992, Vol. 46, No. 22, P. 14818-14822.

APPLICATIONS OF AUXETIC MATERIALS

T. Çetin, Ö. N. Cora
Department of Mechanical Engineering, Karadeniz Technical University
Trabzon, 61080 – Turkey
+90 537 604 6839
turan.cetin@outlook.com.tr

EXTENDED ABSTRACT

OVERVIEW

In this study, auxetic materials are examined in terms of production techniques and their applications. Materials contract under uniaxial compression transversely and expand under tension transversely are named as auxetic and featured with a negative Poisson's ratio. These materials exhibit a series of particular characteristics when compared to conventional materials, such as greater indentation resistance, high shear stiffness as well as excellent fracture toughness and unrivalled energy absorption abilities.

INTRODUCTION

The first auxetic foam was fabricated by Lakes et. al. by converting conventional thermoplastic open-cell foam with a thermo-mechanical process in 1987. The foam was compressed tri-axially using a mould to buckle cell ribs. Lakes, then improved the method to fabricate a large specimen using a four-step procedure [1, 3]. Since then, various fabrication processes were developed and/or performed by researchers, including additive manufacturing (e.g. electron-beam melting, selective laser melting, direct laser writing method) to fabricate auxetic structures [3].

The application requirements for cellular auxetic materials can be attained with cell shape and size manipulation. Cellular auxetic materials can be categorized into re-entrant structures, chiral structures, rotational (semi-) rigid structures, crumpled and perforated sheet models, and other complex structures as shown in Figure 1 [1].
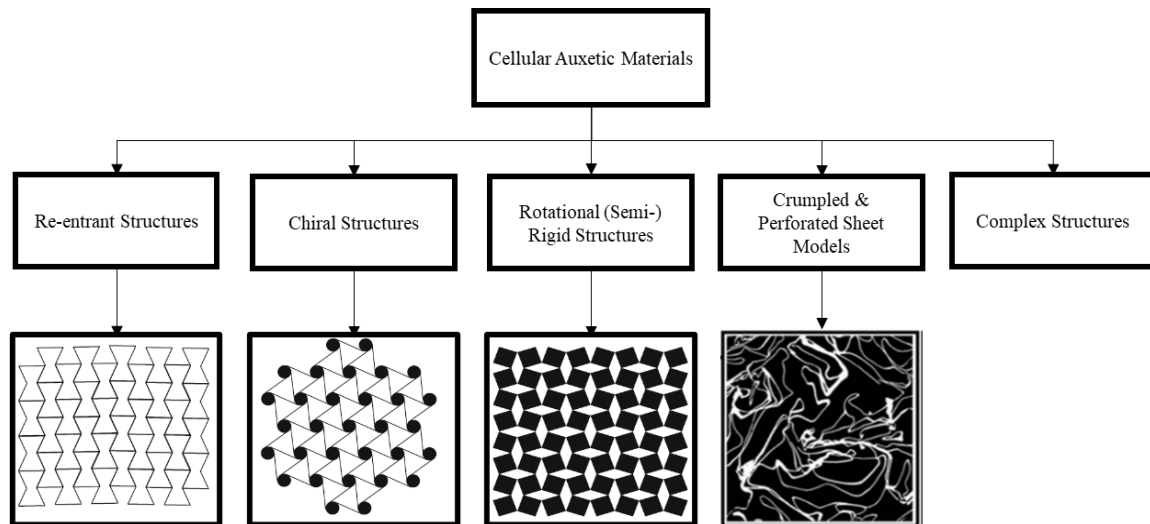
Fig. 1. Classification of cellular auxetic materials. Adapted from [1, 4]

For isotropic materials, the mechanical constants are given in the equations 1, and 2

$$G = \frac{E}{2(1 + v)},\qquad(1)$$

$$K = \frac{E}{3(1 - 2v)},\qquad(2)$$

where G, E, K, and *v* are shear modulus, Young's modulus, bulk modulus, and Poisson's ratio, respectively. Negative Poisson's ratio for auxetic materials results in superior mechanical properties as summarized in Table 1.

Table 1. Mechanical properties of auxetic materials and their benefits. Adapted from [5, 6]

Mechanical Property	Benefits
Synclastic Curvature in Bending	Useful for production of miscellaneous structures.
Variable Permeability	Proper for filtration applications which need controlling of permeability.
High Shear Stiffness	More flexibility for design of auxetics.
Enhanced Indentation Resistance	Increased hardness and strength.
High Fracture Toughness	Higher energy requirement for crack propagation.
Enhanced Energy Absorption	Suitability for various industrial applications.

The plastic Poisson's ratio should be employed to feature the progressive deformation of auxetic materials [3, 7, and 8]. For re-entrant honeycombs under large deformation in the vertical direction, this ratio can be described in the form of incremental strain [3, 6]. When loaded in this direction, the plastic Poisson's ratio increases gradually from negative to positive while the ratio for loading in the horizontal direction is always negative [3].

Re-entrant structures are the materials that provide a good balance between structural rigidity and negative Poisson's ratio, however, in certain applications anisotropy might be a

challenging problem. In spite of re-entrant structures have been studied broadly, rotating rigid and chiral auxetic structures need more investigation [1].

APPLICATIONS OF AUXETIC MATERIALS

Superior properties of auxetic materials result from the negative Poisson's ratio effect making these materials applicable widely in industry. Applications of auxetic materials are summarized in Table 2.

Table 2. Applications of auxetic materials in the industry. Adapted from [1, 9]

Fields	Commercial Applications
Sport	Pads, gloves, helmets, sports shoes.
Textile	Auxetic Fibbers, clothes, functional fabric, colour change straps or fabrics.
Defence	Ultralight wheels, run flat tires, bullet-proof helmets.
Aerospace	Curved body parts, aircraft nose-cones, wing panel.
Medical	Stent, Bandage, wound pressure pad, dental floss, artificial blood vessel, artificial skin, drug release, surgical sutures, muscle/ligament anchors.
Sensors and Actuators	Strain sensors, piezoelectric devices, hygroscopic sensors.

CONCLUSION

- Conventional Poisson's ratio is not applicable to auxetic materials, they need to be characterized by the Plastic Poisson's Ratio.

- Negative Poisson's ratio provides auxetic materials a great potential for many industries, including medical, automotive, textiles, defence, and aerospace applications.

- New methods are under investigation for the cost-effective production of auxetic materials.

- In spite of re-entrant structures which have been studied broadly, rotating rigid and chiral structures need more attention.

Keywords: Auxetics, auxetic structures, Poisson's ratio, plastic Poisson's ratio

REFERENCES

1. KELKAR, P. U.; KIM, H. S.; CHO, K. H.; KWAK, J. Y.; KANG, C. Y.; SONG, H. C. Cellular auxetic structures for mechanical metamaterials: A review, *Sensors*, 2020, Vol. 20, No. 11.

2. CHAN, N.; EVANS, K. E. Fabrication methods for auxetic foams, *Journal of Materials Science*, 1997, Vol. 32, No. 22, P. 5945–5953.

3. ZHANG, J.; LU, G.; YOU, Z. Large deformation and energy absorption of additively manufactured auxetic materials and structures: A review, 2020, *Composites Part B: Engineering*, Vol. 201.

4. LIM, T.C. *Auxetic Materials and Structures*, Singapore: Springer, 2015, P. 591. ISBN 978-981-287-274-6.

5. CHO, H.; SEO, D.; KIM, D. N. *Handbook of Mechanics of Materials*, Taiwan: Springer, 2019, P. 2430. ISBN 978-981-10-6883-6.

6. MAZAEV, V. A.; AJENEZA, O.; SHITIKOVA, M. V. Auxetics materials: Classification, mechanical properties, and applications. TOPME 2019. Proceedings of international conference of young scientists and Students on topical problems of mechanical engineering. Moscow. 2019 Dec 4-6.

7. WANG, D. A.; PAN, J. A non-quadratic yield function for polymeric foams, *International Journal of Plasticity*, 2005, Vol. 22, P. 434-458.

8. DESHPANDE, V. S.; FLECK, N. A. Isotropic constitutive models for metallic foams, *Journal of the Mechanics and Physics of Solids*, 2000, Vol. 48, No. 6, P. 1253–1283.

9. LIU Y.; HU, H. A review on auxetic structures and polymeric materials, *Scientific Research and Essays*, 2010, Vol. 5, No. 10, P. 1052–1063.

THE SENSITIZATION OF TIO$_2$ THIN FILMS BY AG NANOPARTICLES FOR THE IMPROVEMENT OF PHOTOCATALYTIC EFFICIENCY

V. Kavaliūnas, P. Čeplikas, M. Sriubas, G. Laukaitis
Department of Physics, Kaunas University of Technology
Studentų st. 50, LT-51368 Kaunas – Lithuania
+37068174281
vytautas.kavaliunas@ktu.edu

EXTENDED ABSTRACT

OVERVIEW

When light interacts with metallic nanoparticles (mainly Au or Ag [1]), a phenomenon known as localized surface plasmon resonance (*LSPR*) occurs [2]. The material, morphology (size and shape of nanoparticles), optical characteristics of the substrate, as well as the surrounding environment, the distance between the nanoparticles, and distribution, all have a substantial influence on this phenomenon [3–5]. The LSPR effect mainly depends on the refractive index, which directly depends on the distribution and size of nanoparticles on the surface [6]. The study of TiO$_2$ with Ag nanoparticles on the surface shows an increase in photocatalytic efficiency compared to stand-alone TiO$_2$ [7]. Thus, suggesting a viable and alternative modification for TiO$_2$ photocatalytic efficiency enhancement.

METHODS

The preparation of TiO$_2$ thin films:

TiO$_2$ thin films (d = 100 nm) were deposited using a reactive magnetron sputtering technique (PVD-75 Kurt J. Lesker) on glass substrates. A high vacuum (up to $4 \cdot 10^{-3}$ Pa) was reached using dual-stage rotary vane and turbo-molecular pumps before the deposition. Then, the chamber was filled with Ar and O$_2$ gases (99.999% purity) with a ratio of 30% and 70%, respectively, for TiO$_2$ thin films deposition. The working pressure was ~1.87 Pa during TiO$_2$ thin films deposition. Ti target (99.995% purity) with a diameter of 50.8 mm was used for the deposition of TiO$_2$ thin films. A growth rate of 3.7 nm/min using a DC power supply at 250 W sputtering power was achieved.

Formation of Ag nanoparticles on the TiO$_2$ surface:

The Ag thin films (d = 5; 7.5; 10 nm) were deposited by using a magnetron sputtering technique on the surface of TiO$_2$. After creating a high vacuum (up to $4 \cdot 10^{-3}$ Pa) the chamber was filled with a high purity Ar gas until a working pressure of ~2.4 Pa was reached. One Ag target (99.995% purity) with a diameter 50.8 mm was used for the deposition of Ag thin films. A growth rate of 2.5 nm/min for Ag thin films was reached by using a DC power supply at 31 W sputtering power. The solid-state dewetting (SSD) process was used for Ag

nanoparticles (AgNP) formation on the TiO_2 surface. Thus, samples were annealed at a 400 °C temperature for 60 minutes in a vacuum.

Morphological and structural analysis:

The crystal structure of deposited TiO_2 thin films was investigated by an X-ray diffractometer (*XRD*, Brucker D8 Discovery) at 2θ in a range of 20° to 70° (with a 0.01° step) using a Cu Kα ($\lambda = 1.54059$ Å) radiation. The peak analysis was carried out by using a "Match!" crystallographic analysis software. The morphology of TiO_2 thin films and AgNP were analysed by a scanning electron microscope (SEM, Hitachi S-3400N). The optical properties of prepared samples were measured by UV-Vis spectrophotometer (UV-Vis, Ocean Optics USB4000) in a range of 250 to 800 nm (with a 0.2 nm step) wavelength, and the spectra were analysed by "OceanArt" software.

RESULTS

According to the XRD results (Fig. 1), almost all as-deposited TiO_2 thin films with an Ag layer on the surface were amorphous. The SSD process initiated the crystallization of TiO_2 thin films and formation of crystalline Ag nanoparticles. The dominant facets were {101} (at 25.41°) and {004} (at 38.16°) for TiO_2 thin films whereas {111} (at 38.12°) and {200} (at 44.28°) for AgNP.
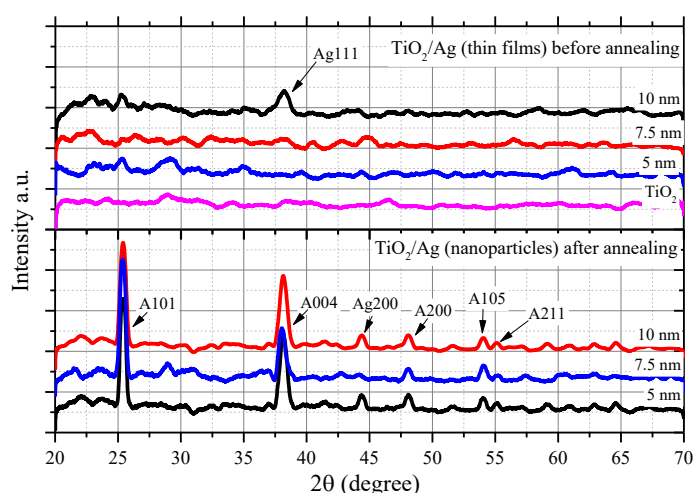
Fig. 1. The XRD spectra of TiO_2/Ag samples before annealing (Ag thin films on TiO_2 surface) and after annealing (Ag nanoparticles on TiO_2 surface).

The SEM images of the TiO_2/AgNP surface (Fig. 2) show the AgNP' size and distribution dependence on the initial Ag thin film thickness. The average AgNP diameter (~26.73 nm to 82.31 nm) increases with increased initial thin film thickness (5 – 10 nm). On the contrary, the density decreases from 396.51 $1/\mu m^2$ to 42.18 $1/\mu m^2$ with increased thickness.
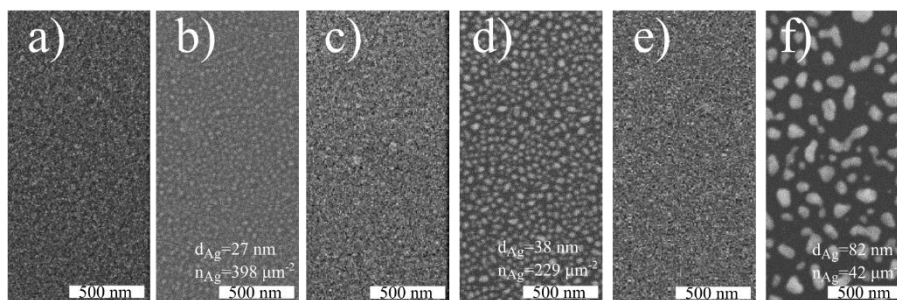
Fig. 2. The SEM images of TiO₂/Ag samples: a) as-deposited and b) annealed (with an initial Ag thickness of 5 nm); c) as-deposited and d) annealed (with an initial Ag thickness of 7.5 nm); e) as-deposited and f) annealed (with an initial Ag thickness of 10 nm).

The LSPR effect can be observed in the transmittance spectra of TiO₂/AgNP (Fig. 3). The transmittance of visible light reached minimum values at the 550 – 650 nm range, respectively to the AgNP size. It can be seen that the LSPR effect increases with an increased size of AgNP on the surface of TiO₂ thin films.
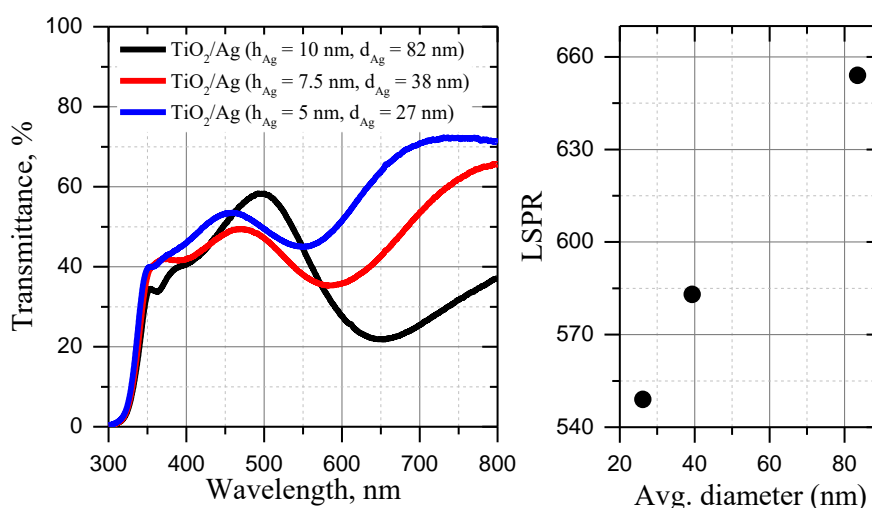
Fig. 3. Transmittance spectra of TiO₂/AgNP and LSPR dependency on the average diameter of AgNP.

CONCLUSIONS

The formation of Ag nanoparticles on TiO₂ thin film's surface was done by a dewetting process to analyse the LSPR effect and how it depends on the properties of nanoparticles. The size of Ag nanoparticles is directly dependant on the initial thickness of Ag thin film on the TiO₂ surface. Finally, the LSPR effect increases with an increased size of Ag nanoparticles. Photocatalytic efficiency depends on formed TiO₂/AgNP properties.

Keywords: TiO₂, silver nanoparticles, photocatalysis, LSPR

REFERENCES

1. ANKER, J. N.; HALL, W. P.; LYANDRES, O.; SHAH, N. C.; ZHAO, J.; VAN, D.; Richard, P. Biosensing with plasmonic nanosensors. *Nature Materials,* 2008. Vol. 7, No. 6, P. 442–453.

2. PETRYAYEVA, E.; KRULL, U. J. Localized surface plasmon resonance: Nanostructures, bioassays and bio sensing—A review. *Analytica Chimica Acta*, 2011. Vol. 706, No. 1, P. 8–24.

3. CHUNG, T.; LEE, Y.; AHN, M. S.; LEE, W.; BAE, S. I.; HWAN, G.; CHARLES, S. H.; JEONG, K. H. Nanoislands as plasmonic materials. *Nanoscale*, 2019. Vol. 11, No. 18, P. 8651–8664.

4. TAN, F.; LI, T.; WANG, N.; LAI, S. K.; TSOI, C. C.; YU, W.; ZHANG, X. Rough gold films as broadband absorbers for plasmonic enhancement of TiO_2 photocurrent over 400-800 nm. *Scientific Reports*, 2016. Vol. 6, P. 1–10.

5. KHAN, M. R.; CHUAN, T. W.; YOUSUF, A.; CHOWDHURY, M. N.K. and CHENG, C. K. Schottky barrier and surface plasmonic resonance phenomena towards the photocatalytic reaction: Study of their mechanisms to enhance photocatalytic activity. *Catalysis Science and Technology*, 2015, Vol. 5, No. 5, P. 2522–2531.

6. SEKHON, J. S.; VERMA, S. S. Refractive Index Sensitivity Analysis of Ag, Au, and Cu Nanoparticles. *Plasmonics*, 2011, Vol. 6, No. 2, P. 311–317.

7. LEMOS DE SOUZA, M.; PEREIRA DOS SANTOS, D.; CORIO, P. Localized surface plasmon resonance enhanced photocatalysis: an experimental and theoretical mechanistic investigation. *RSC Advances*, 2018, Vol. 8, No. 50, P. 28753–28762.

CELLULOSE NANOMATERIALS FOR WATER PURIFICATION IN MEMBRANE TECHNOLOGY: A REVIEW

M. Yildirim, Z. Candan

Department of Forest Industrial Engineering, Istanbul University–Cerrahpasa
34473, Istanbul – Turkey
E-mail: mert.yildirim@ogr.iuc.edu.tr

ABSTRACT

Recent advances in nanoscience and nanotechnology indicate that cellulose nanomaterials, with their unique properties such as high surface area, versatile surface chemistry, excellent mechanical strength, ample hydroxyl content, and biocompatibility, could greatly reduce several current water quality problems. Cellulose nanomaterials are the most abundant, biodegradable, non-toxic, and environmentally friendly biopolymers on the planet. Cellulose nanomaterials are a significant filtration material and are low-cost, sustainable, renewable, inert, and stable across a wide pH/ionic strength range. This review focuses on the most recent developments in nanocellulose-based membranes for water purification.

INTRODUCTION

Rapid population growth, industrialization, and urbanization have all led to considerable water and soil pollution [1]. Water is a scarce resource. Water consumption is expected to increase by 55% by 2050 [2]. One in every five developing countries will face water shortages by 2050. Water scarcity has an impact on the global ecosystem, human health, and food scarcity.

Different techniques are used to remove various contaminants from water [3]. However, high mechanical strength and selectivity without sacrificing water permeability now are required for filters [4].

Nanocellulose is a biodegradable, non-toxic, and environmentally friendly biopolymer with a high surface area, high mechanical strength, and variable surface chemistry making it an attractive candidate for next-generation water filters [5]. Metal ions, dyes, metals, and microorganisms have all been removed via nanocellulose-based membranes [6].

This review focuses on the most recent advances in nanocellulose-based membranes.

MEMBRANE TECHNOLOGY

A membrane is a layer that permits certain components to enter while rejecting others. These selective layers are used in membrane technology for effective separation without the requirement for phase transitions. Nanofiltration (NF), ultrafiltration (UF), and microfiltration (MF) techniques, especially reverse osmosis (RO), are used in water and wastewater treatment as well as in a variety of other applications. Rapid advancements in membrane technology in the last 50 years have made these the preferred technologies in water and wastewater treatment. Many membrane technologies, such as membrane distillation, forward osmosis, electrodialysis, pervaporation, and others, are also quickly evolving and are used in a variety of sectors. Membranes are categorized according to the pore size. Reverse osmosis (0.1–1 nm), nanofiltration (1–2 nm), ultrafiltration (2–100 nm), and microfiltration (100 nm–10 m) are the four types of filtrations [7]. Fig. 1. Shows the characteristics of the different membrane processes.
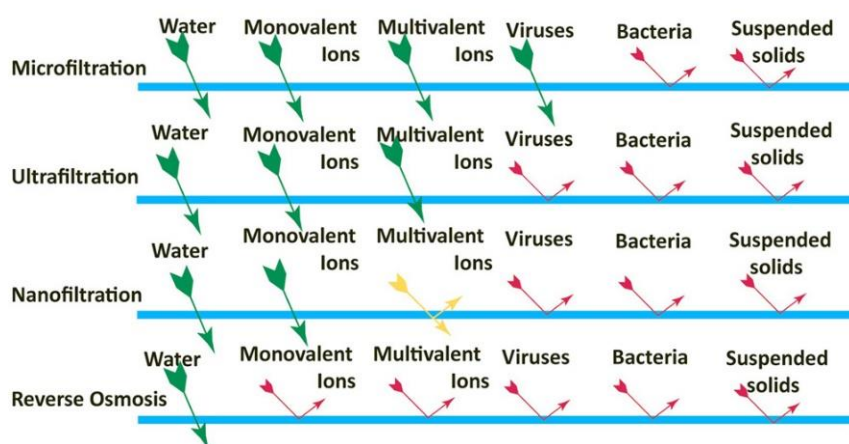
Fig. 1. Different membrane processes and characteristics [8].

LIGNOCELLULOSIC BIONANOMATERIALS

Lignocellulosic biomaterials are three-dimensional biopolymer structures created by linking cellulose, hemicellulose, and lignin along with minor quantities of extractive and inorganic compounds via a network. Nano-sized materials are referred to as lignocellulosic bio nanomaterials and have an external dimension, which means a length interval ranging from 1 nm to 100 nm.

NANOCELLULOSE

Nanocellulose is classified into three types: cellulose-nanofibrils (CNF), cellulose nanocrystals (CNC), and bacterial nanocellulose (BNC). CNF has both crystalline and amorphous regions, whereas CNC is a rod-like particle with mostly crystalline regions. The most generally utilized bacterium species for BNC synthesis is Gluconacetobacter xylinus, which has a high capacity to make gel-like cellulose fibrils that contain 99% pure water in a 3-D Nano network. Fig 2 shows SEM images of various types of nanocellulose.
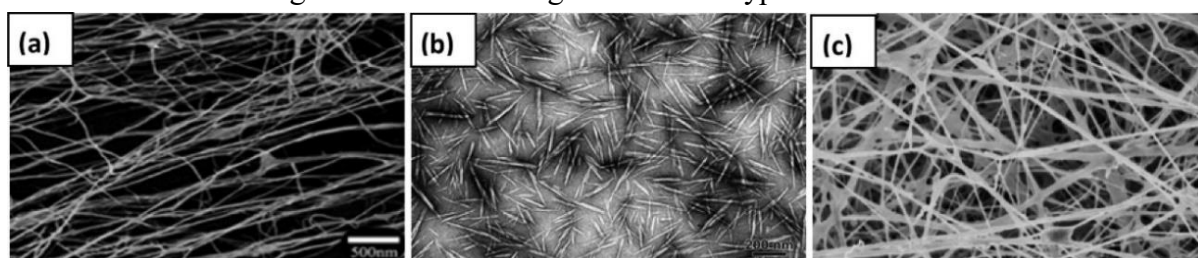
Fig. 2. Different membrane processes and characteristics [9].

APPLICATIONS OF NANOCELLULOSE IN MEMBRANE TECHNOLOGY

The use of nanofiber membranes in water and wastewater treatment is referred to as "new generation." The most important characteristics that differentiate nanofiber membranes from their peers are high porosity and a high surface-to-volume ratio. Although nanofiber membranes are commonly used in commercial air filtration, there have been recent uses in water, wastewater treatment, and desalination. CNFs can provide very porous and strong network components that can be used as filter layers. Cellulose nanomaterials are used as a functional composite material in membrane separation technology.

CONCLUSIONS

Membrane technology has great promise for addressing water and energy scarcity challenges through wastewater treatment, desalination, and clean energy generation. Membrane technology has enormous market potential on a global scale. The development of high-performance nanocellulose-based and nanocomposite membranes and energy-efficient membrane processes is a current trend in membrane science and technology. It has recently become obvious that cellulose nanomaterials could play a key role in many water remediation technologies. The filtration performance of cellulose-based membranes is approaching that of conventional membranes in terms of usability.

REFERENCES

1. ZHANG, D.; CAI, J.; XU, W.; DONG, Q.; Li, Y.W.; LIU, G.; WANG, Z.W. Synthesis, Characterization and Adsorption Property of Cellulose Nanofiber-Based Hydrogels. *Journal of Forestry Engineering,* 2019, Vol. 4, No. 2, P. 92-98.

2. *Organisation for Economic Co-operation and Development*. Link to the internet <https://www.oecd.org/env/indicators-modelling-outlooks/49844953.pdf>.

3. GUPTA, V.K.; ALI, I.; SALEH, T.A.; NAYAK, A.; AGARWAL, S. Chemical treatment technologies for waste-water recycling—an overview. *RSC Advances,* 2012, Vol. 2, No. 16, P. 6380-6388.

4. GOPAKUMAR, D.A.; ARUMUGHAN, V.; PASQUINI, D.; (BEN) LEU, S.Y.; H.P.S., A. K.; THOMAS, S. Nanocellulose-Based Membranes for Water Purification. *Nanoscale Materials in Water Purification,* p. 59–85.

5. CARPENTER, A.W.; DE LANNOY, C.F.; WIESNER, M.R. Cellulose Nanomaterials in Water Treatment Technologies. *Environmental Science & Technology,* 2015, Vol. 49, No. 9, P. 5277–5287.

6. VOISIN, H.; BERGSTRЄOM, L.; LIU, P.; MATHEW, A. Nanocellulose-based materials for water purification, *Nanomaterials,* 2017, Vol. 7, No. 3, P. 57.

7. MAUTNER A. Nanocellulose water treatment membranes and filters: a review. *Polymer international,* 2020, Vol. 69, No. 9, P. 741-751.

8. *Reverse Osmosis & Ozone Water Treatment Specialist*. Link to the internet < http://triotirta.co.id/product-services/hydranautics-ultrafiltration-nanofiltration-reverse-osmosis>.

9. KUMAR, V.; PATHAK, P.; BHARDWAJ, N. K. Wastepaper: An underutilized but promising source for nanocellulose mining. *Waste Management,* Vol. 102, P. 281–303.

III.   ENVIRONMENTAL SCIENCES

III.1. Innovative agriculture, horticulture, and forestry solutions

SWINE MANURE DIGESTATE DERIVED BIOCHAR EFFECT ON SOIL HYDRO-PHYSICAL PROPERTIES, SOIL MICROBIOLOGICAL ENVIRONMENT, AND THEIR INTERACTION

M. Ayaz [*], **D. Feizienė, V. Feiza, V. Tilvikienė**

Institute of Agriculture, Lithuanian Research Center for Agriculture and Forestry, Instituto al. 1, Akademija, LT-58344 Kėdainiai distr. – Lithuania, Tel.: +370 654 22 196.
Muhammad.ayaz@lammc.lt [*], *Dalia.feizie@lammc.lt Virginijus.feiz@lammc.lt*
Vita.tilvikiene@lammc.lt

E. Baltrėnaitė-Gedienė
Vilnius Gediminas Technical University, Vilnius – Lithuania
edita.baltrenaite-gediene@vilniustech.lt

A. U. Khan
School of Forestry, Northeast Forestry University, Harbin – China
khan.aup252@gmail.com

EXTENDED ABSTRACT

OVERVIEW

In recent years, biochar has been used extensively as a soil conditioner to improve soil quality [1]. Soil physical conditions directly influence soil fertility by determining water retention capacity, aeration, and soil permeability, which tends to improve soil productivity [2]. Several studies indicated that good soil structure, porosity, hydraulic conductivity, specific gravity create favourable conditions for essential soil microbial growth, and better water and nutrients use efficiency, in the soil profile [3], [4]. Moreover, biochar addition improved nutrient and water retention and increased root growth substantially than degraded soils with poor physical properties [5]. Biochar amendment improved soil hydraulic conductivity by decreasing soil bulk density and increasing soil porosity [6]. However, some studies have found that biochar has little or even negative effects on soil physical properties. No proof to propose that biochar amendment influenced soil porosity by either direct pore contribution, creation of accommodation pores, or melioration in aggregate stability [7]. The application of biochar lowered macrospores and pore connectivity in the wheat-rice rotation system [8]. Such variations signify that the effects of biochar on soil structure and hydraulic properties are unclear.

METHODOLOGY

Experimental Design

A three-factorial randomized complete block design (RCBD) field experiment was designed with six treatments and three replications each. The combination of the treatments was as follows: B0N0 (No biochar + No Nitrogen fertilizer), B0N1 (No biochar + 160 kg ha-1 Nitrogen fertilizer), B0N2 (No biochar + 120 kg ha-1 Nitrogen fertilizer), B1N1 (25 t ha-1 biochar + 160 kg ha-1 Nitrogen fertilizer), B1N2 (25 t ha-1 biochar + 120 kg ha-1 Nitrogen fertilizer), and B1N0 (25 t ha-1 biochar + No Nitrogen Fertilizer). Ammonium nitrate was used as N fertilizer. The biochar was broadcast and shallow incorporated in to the soil surface during presowing tillage. The main crop was spring barley (Hordeum vulgare L.) which was sown in April 2020 and harvested in August 2020.

RESULTS

Soil Bulk Density and Total Porosity

Due to application of 25 t ha-1 of biochar alone (B1N0) and biochar with 120 kg ha-1 of N fertilizer (B1N2) significantly (>0.05) enhanced soil bulk density (BD) by 10-12 % at 5-10cm depth of soil in the month of May

Whereas, in August, biochar alone and biochar with 160 kg ha-1 of N fertilizer (B1N1) significantly (>0.05) enhanced soil BD by 8-10 % compare to non-biochar treatments.

Volumetric Soil Water Content

In our current study, the volumetric soil water content (VWC) at -4 to -100 hPa suction at 5-10 cm depth was recorded higher (5-7 %) under 25 t ha-1 of biochar with 160 kg ha-1 of N fertilizer application (B1N1) compare to other treatments.

Soil carbon sources

Results suggests that there is big soil carbon sources (SCS) utilization rate and is directly proportional to microbial growth. Carboxylic acid was the leading SCS utilized where amines are the least utilized carbon source.

Soil Microbiological Activity

All the diversity indices (Average Well Colour Development (AWCD), Richness (R), McIntosh Index (U) in the Biology EcoPlate incubated for 96 h, and the higher biodiversity rate was recorded in biochar treated soil.

Correlation between soil physical properties and Carbon Sources

Looking at the trait interrelations between N0, N1 and N2 under B0, separately, BD was found to be significantly positive correlated while total porosity (TP) was significantly negative correlated to amino acids under B0N0 and has no correlation recorded under B0N1 and B0N2.
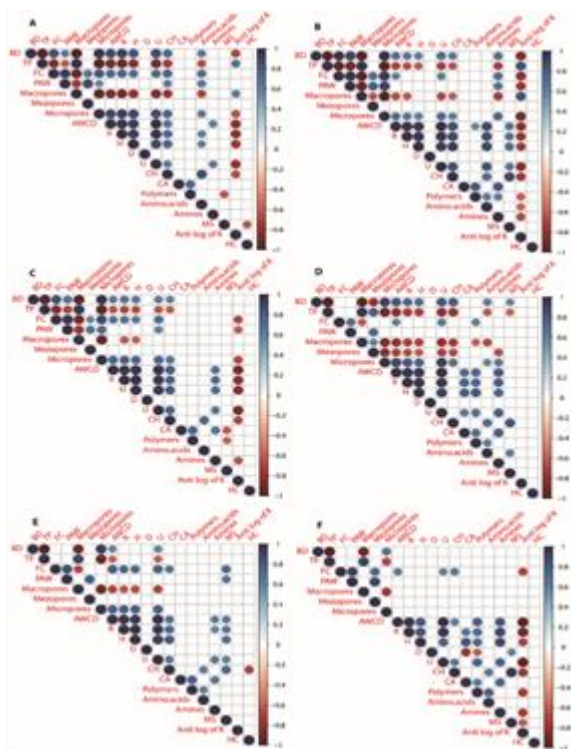
CONCLUSION

The conclusions of this study are as follows:

Biochar alone and with 160kg ha-1 and 120 kg ha-1 of N application significantly reduced soil BD and enhanced TP, as well as substantially enhanced soil macrospores at both the depths during August. Thus, Swine digestate manure derived biochar could be a useful amendment to soil with problem of higher BD and lower TP and in compacted soil with lower soil porosity.

Biochar with 160kg ha-1 of N fertilizer substantially increased VWC at 5-10cm depth at -4 to -100 hPa suction whereas at higher suction (-100hPa to -15500hPa) field capacity and wilting point of soil was recorded higher at both 5-10 and 15-20cm depths even under biochar application, thus could be helpful in drought condition to enhance soil water content

Biochar with and without N fertilizer application has significantly lowered soil hydraulic conductivity by 35-40% at 5-10cm depth only compare to the non-biochar treatments. Thus, Swine digestate manure derived biochar could substantially improve water transmission within the top soil layer.

This study summarized that swine digestate manure derived biochar with and without N fertilizer could be useful amendment depending upon type of soil and environmental factors in improving its hydro-physical properties and microbial abundance.

Keywords: Biochar, Carbon source utilization, Soil indices, Soil hydraulic conductivity, Soil porosity.

REFERENCES

1. ABDULLAH, R. Effects of palm kernel biochar and food waste compost on the growth of palm lily (Cordyline fruticosa), coleus (coleus Sp.), and boat lily (rhoeo discolor), *Applied Ecology and Environmental Research*, 2021, Vol. 19, No. 1, P. 205–218.

2. PAGE, K. L.; DANG, Y. P.; DALAL, R. C. The ability of conservation agriculture to conserve soil organic carbon and the subsequent impact on soil physical, chemical, and biological properties and yield, *Frontiers in Sustainable Food Systems*, 2020, Vol. 4.

3. ROSTAMI, S. Current methods and technologies for degradation of atrazine in contaminated soil and water: A review, *Environmental Technology & Innovation*, 2021, P. 102019.

4. SINGH, Y.; CHOUDHARY, R. L; CHAUDHARY, A; SINGH, N. P. Impact of Conservation Agriculture and Residue Management on Soil Properties under Sugarcane-Based Cropping Systems, in *Conservation Agriculture: A Sustainable Approach for Soil Health and Food Security*, Springer, 2021, P. 239–266.

5. ADEKIYA, A. O.; OLAYANJU, T. M. A.; EJUE, S. W.; ALORI, E. T. Contribution of Biochar in Improving Soil Health, in *Soil Health*, Springer, 2020, P. 99–113.

6. ZHOU, H. Biochar enhances soil hydraulic function but not soil aggregation in a sandy loam, *European Journal of Soil Science*, 2019, Vol. 70, No. 2, P. 291–300.

7. HARDIE, M.; CLOTHIER, B.; BOUND, S.; OLIVEr, G.; CLOSE, D. Does biochar influence soil physical properties and soil water availability? *Plant Soil*, 2014, Vol. 376, No. 1, P. 347–361.

8. FAN, R.; ZHANG, B.; LIANG, A. Straw-derived biochar mitigates CO_2 emission through changes in soil pore structure in a wheat-rice rotation system, *Chemosphere*, 2020, Vol. 243, P. 125325.

TILLAGE AND CROPPING SYSTEMS IMPACT ON SOIL PENETRATION RESISTANCE AND CO₂ EMISSIONS

A. Buivydienė, I. Deveikytė, V. Feiza
Lithuania Research Centre for Agriculture and Forestry
Institute of Agriculture
Instituto al. 1, Akademija, LT-58344, Kėdainiai distr. – Lithuania
+370 642 22292; +370 686 93711; +370 688 87249
agne.buivydiene@lammc.lt, irena.deveikyte@lammc.lt, virginijus.feiza@lammc.lt

EXTENDED ABSTRACT

OVERVIEW

Tillage systems and crop rotation can help maintain soil fertility and increase soil viability while preserving the condition of the soil and its environment [1]. Long-term no-tillage (NT) can be beneficial in improving soil health and yield, especially when NT combined with crop rotation and cover crops [2]. Complex studies, using different tillage and cropping systems, can more objectively evaluate soil properties (physical, chemical, biological) changes under different meteorological conditions. NT has influence on the depth of penetration and on crop roots distribution, which in turn effects the uptake of water and plant nutrients availability [3].

A valuable indicator describing and assessing the physical condition of the soil is soil penetration resistance (PR) [4]. PR is affected by other soil properties, such as size of soil aggregates, soil moisture content and bulk density. The lower soil moisture content, the higher bulk density; higher amounts of small-sized soil aggregates result in higher PR. Frequently, reduced tillage increases the PR compared to conventional tillage (CT) [5].

Different tillage systems can have various effects on soil carbon dioxide (CO_2) emissions [6]. Depth of tillage is closely related to the rate of soil CO_2 emission and physical soil environment [4]. Soil CO_2 emissions are dependent on many factors: soil and atmosphere temperature, soil water content, soil porosity, root volume [7], soil organic carbon content and quality, applied crop rotations with different crop types and tillage systems used [8].

The aim of the research was to determine the impact of tillage practices in combination with different crop rotations on soil penetration resistance and CO_2 emission.

METHODS

Field experiments were performed at the Lithuanian Research Centre for Agriculture and Forestry in the Central part of Lithuania on loamy *Cambisol* (55°23' N, 23°50' E). Topsoil chemical characteristics, on average, were as follows: humus content was 3.1%, P_2O_5 - 200 mg kg^{-1} and K_2O – 150 g kg^{-1}, pH_{KCl} - 6.6. The field experiment was established in 2021 having a split – plot design in four replications. The experiment consists of 2 backgrounds: tillage (conventional tillage (CT); No – tillage (NT)) and crop rotations (Table 1). Catch crop – white mustard (*Sinapis Alba* L.).

Soil penetration resistance was determined with an Eijkelkamp hand-held penetrometer, to 0-40 cm depth, in the spring after sowing.

Soil CO_2 emission was measured in a 0-10 cm and 10-20 cm soil layers with a portable analyser Li-Cor 6400-09 (May – August).

Table 1. Crop rotation treatments

Preceding crop (2020) – 1st element of crop rotation (2021)	
Abbreviation	*Crop rotation*
SW-WW	spring wheat - winter wheat
SW-WW+CC	spring wheat - winter wheat + catch crop
WW+CC-SW	winter wheat + catch crop - spring wheat
WW-SW	winter wheat - spring wheat
P-WW+CC	peas – winter wheat + catch crop

Statistical analysis.

ANOVA analysis of variance was used to evaluate the significant differences between treatments of different backgrounds. The study data were evaluated according to Fisher's (F) criterion, using 95% ($p<0.05$) probability levels. Statistical packages SAS (Statistical Analysis System) were used for statistical data processing.

RESULTS

Using CT and different crop rotations, penetration resistance did not differ significantly within 0-10 cm (1.17-1.40 MPa) and 10-20 cm (1.27-1.41 MPa) soil layers. In spring wheat – winter wheat crop rotation PR was 14-20% lower in the upper layer and by 6-11% in the deeper layer of the soil, than in the other cropping systems investigated. In WW-SW crop rotation the PR was the highest within both soils' layers.

In NT with different crop rotation PR was 19-36% lower in 0-10 cm soil layers as compared to 10-20 cm. In SW-WW crop rotation PR was 2-8% lower in the upper layer of soil than in the soil of other crop rotations. The highest PR in 0-10 cm layer was in P-WW-CC cropping system. PR was the highest in WW+CC-SW crop rotation. PR was 30% lower in CT than in the NT in 0-20 cm soil layers. The results of the other studies were very similar [9].

Many authors have reported higher penetration resistance values under no tillage practices, especially in the upper layers of the soil. Soil penetration resistance has also been shown to vary with depth within the soil profile [4].

Two the most intensive CO_2 emissions were observed in both – conventional (Fig. 1) and no tillage (Fig.2) systems in June and August 2021. Significantly higher CO_2 efflux was registered in early summer in crop rotation: spring wheat – winter wheat + catch crop. It was as twice as higher compared to spring wheat – winter wheat crop rotation under NT and CT tillage system. High emission was registered in August. Emission intensity was also higher in the soil of SW-WW+CC crop rotation under CT tillage, while under NT, intensive emission was from soil of WW+CC-SW crop rotation. Catch cop under both tillage systems was in favour to increase soil viability and increased CO_2 efflux.

Our results demonstrated that average CO_2 efflux was higher (13%) in NT than in CT during plant vegetation. CO_2 efflux means was highest in SW-WW+CC crop rotation during plant vegetation period in both tillage systems.

Meteorological conditions (temperatures and precipitation) had a significant effect on CO_2 efflux. Precipitation increased soil moisture as well as CO_2 emissions. The highest precipitation quantity (average 4.3 mm/day) was fixed in April 29 – June 2 during plant vegetation period. Maximum precipitation (26 mm/day) recorded May's 3 during the entire investigation period. Amount of precipitation was in favour for soil carbon dioxide emission from the soil. In dry conditions, the efflux of CO_2 slows down.
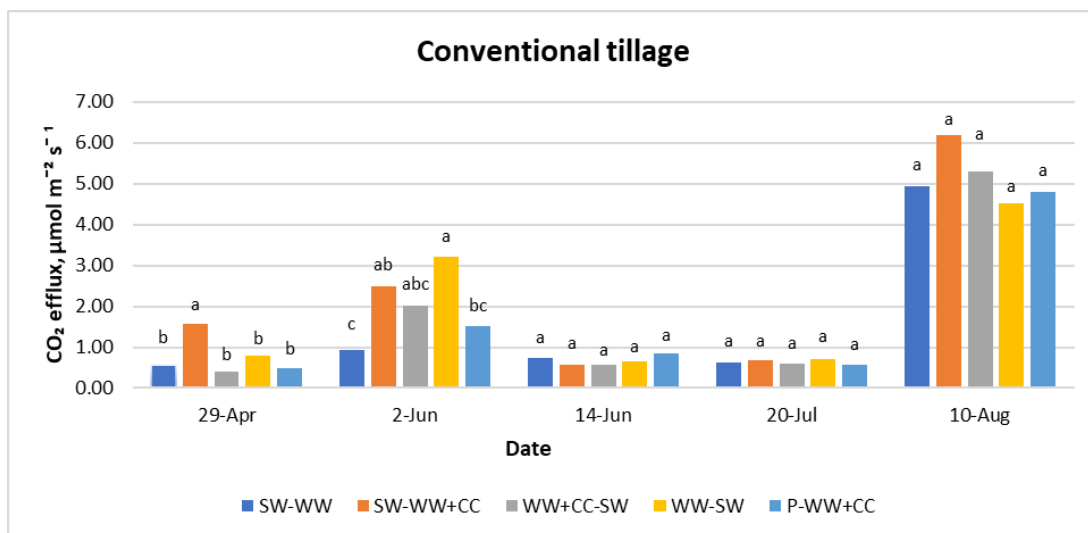
Fig.1 Soil CO_2 efflux during plant vegetation period in 2021. SW-WW - spring wheat - winter wheat, SW-WW+CC - spring wheat - winter wheat catch crop, WW+CC-SW -winter wheat catch crop-spring wheat, WW-SW - winter wheat-spring wheat, P-WW+CC – peas-winter wheat catch crop; different letters indicate significant differences between groups

Dry meteorological conditions (June 14 – July 20) could have led to lower soil CO_2 emissions. Intense heat waves were recorded in both months (July and August). 35°C heat was registered on July 10 according to Dotnuva meteorological station recording. CO_2 effluxes were significantly higher in SW-WW+CC crop rotation (CT, April 29).
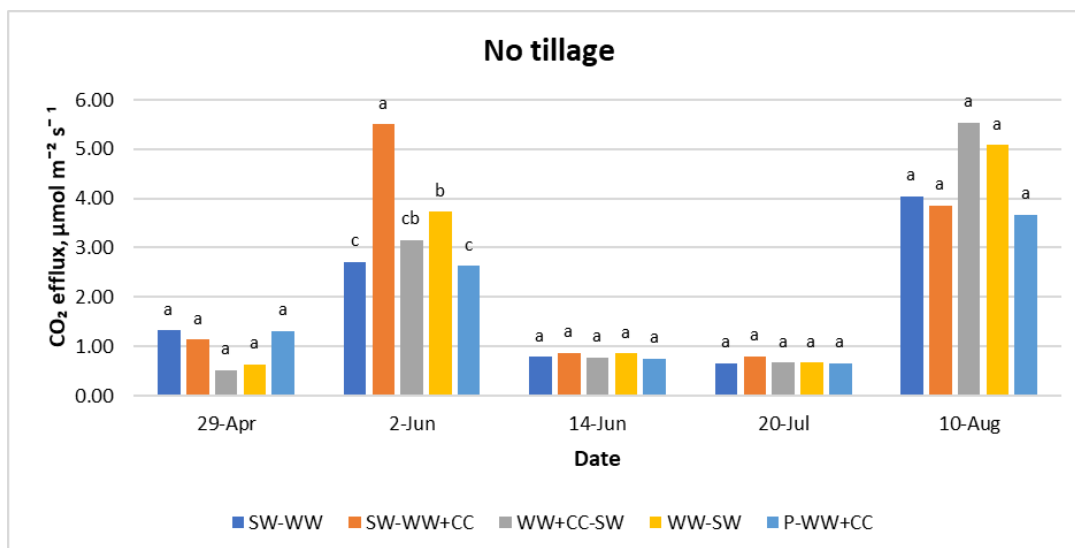
Fig.2. Soil CO_2 efflux during plant vegetation period in 2021. SW-WW - spring wheat - winter wheat, SW-WW+CC - spring wheat - winter wheat catch crop, WW+CC-SW -winter wheat catch crop-spring wheat, WW-SW - winter wheat-spring wheat, P-WW+CC – peas-winter wheat catch crop; different letters indicate significant differences between groups

This may have led to a higher CO_2 efflux in August as well. The higher SR (6.18 μmol m^{-2} s^{-1}) was registered in SW-WW+CC crop rotation (CT, August 10), while by 38% lowest in NT. However, the highest CO_2 efflux (5.53 μmol m^{-2} s^{-1}) was recorded in WW+CC-SW crop rotation using NT, (3.98% lowest in CT) in last studied plant vegetation period.

CONCLUSIONS

Penetration resistance (PR) was found to be the higher in no tillage system than in conventional tillage system. PR was the lowest in SW-WW crop rotation in both tillage systems.

CO_2 efflux was higher in no tillage system than in conventional tillage system during plant vegetation. Emission intensity was highest in SW-WW+CC crop rotation during plant vegetation period in both tillage systems.

Keywords: Tillage, cropping systems, soil penetration, CO_2 emission

REFERENCES

1. SKINULIENĖ, L.; BOGUŽAS, V.; STEPONAVIČIENĖ, V.; SINKEVIČIENĖ, A.; MARCINKEVIČIENĖ, A.; SINKEVIČIUS, A. Ilgalaikės augalų kaitos derinių įtaka dirvožemio CO_2 emisijai ir sliekų kiekiui. *Žemės ūkio mokslai*, 2019, Vol. 26, No. 2, P. 83-93.

2. NUNES, M. R.; MATHIJS VAN ES, H.; SCHINDELBECK, R.; RISTOW, A. J.; RYAN, M. No-till and cropping system diversification improve soil health and crop yield. *Geoderma*, 2018, Vol. 328, P. 30-43.

3. SAHU, G.; MOHANTY, S.; DAS, S. Conservation agriculture - a way to improve soil health. *Journal of Experimental Biology and Agricultural Sciences*, 2020, Vol. 8, No. 4, P. 355-368.

4. AMAMI, R.; IBRAHIMI, K.; LA SCALA JÚNIOR, N.; HMIL, A.; ABROUGUI, K.; CHEHAIBI, S. Soil Physical Properties, Carbon dioxide Emissions and Their Relationships under Different Management Systems in Semi-arid Region of Eastern Tunisia. *Communications in soil science and plant analysis*, 2021, Vol. 52, No. 14, P. 1689-1705.

5. FEIZA, V.; FEIZIENĖ, D.; AUŠKALNIS, A.; KADŽIENĖ, G. Sustainable tillage: results from long-term field experiments on Cambisol. *Zemdirbyste-Agriculture,* 2010, Vol. 97, No. 2, P. 3-14.

6. BURAGIENĖ, S.; ŠARAUSKIS. E. A.; ROMANECKAS, K.; ADAMAVIČIENĖ, A.; KRIAUČIŪNIENĖ, A.; AVIŽIENYTĖ, D.; MAROZAS, V.; NAUJOKIENĖ, V. Relationship between CO_2 emissions and soil properties of differently tilled soils. *Science of the Environment*, 2019, Vol. 662, P. 786-795.

7. KOCHIIERU, M.; FEIZA, V.; FEIZIENĖ, D.; VOLUNGEVIČIUS, J.; DEVEIKYTĖ, I.; SEIBUTIS, V.; PRANAITIENĖ, S. The effect of environmental factors and root system on CO_2 efflux in different types of soil and land uses. *Zemdirbyste-Agriculture,* 2021, Vol. 108, No. 1, P. 3-10.

8. GELYBÓ, G. Y.; BARCZA, M.; DENSCÓ, M.; POTYÓ, I.; KÁSA, I.; HOREL, Á.; POKOVAI, K.; BIRKÁS, N.; KERN, A.; HOLLÓS, R.; TÓTH, E. Effect of tillage and crop type on soil respiration in a long-term field experiment on chernozem soil under temperate climate. *Soil and Tillage Research*, 2022, Vol. 216.

9. STEPONAVIČIENĖ, V.; BOGUŽAS, V.; SINKEVIČIENĖ, A.; SKINULIENĖ, L.; SINKEVIČIUS, A.; KLIMAS, E. Soil physical state as influenced by long-term reduced tillage, no-tillage, and straw management. *Zemdirbyste-Agriculture,* 2020, Vol. 107, No. 3, P. 195-202.

EFFECT OF PEA (*PISUM SATIVUM* L.) VARIETES WITH OAT (*AVENA SATIVA* L.) MIXTURE ON ORGANICALLY GROWN SPRING WHEAT YIELD

G. Čepurna, L. Šarūnaitė,
Lithuania Research Centre for Agriculture and Forestry
Instituto al. 1, Akademija, Kėdainiai distr. – Lithuania
+37066355701
gediminas.cepurna@lammc.lt

EXTENDED ABSTRACT

OVERVIEW

The inclusion of legumes in crop rotation is one of the possible ways to increase the available nitrogen content and does not require investment [1, 2]. Crop production strategies and management practices, such as crop diversification through crop rotation, organic farming are encouraged to increase crop productivity and ecosystem services [3]. Growing cereals after legumes can improve nitrogen availability to other crops, reduce soil erosion, and increase soil organic matter [4]. Diversification of mixed crops with legumes has long been used to improve the sustainable use of nitrogen resources and the resilience of the crop system to various environmental factors [5]. Legume crops have a strong influence on cropping system, as they are directly related to the ability of the soil to react from water to nutrient supply, intensification of agro ecological functions [6, 7]. Mixed plant combinations can make efficient use of all resources, such as sunlight, nutrients, or water, than is usually the case with monoculture, as this significantly reduces the amount of resources available to weeds [8, 9]. Researchers in Germany [10], Sweden [9], Denmark [11], Poland [12], and Ireland [13] are developing binary legume plant and mixed cropping technologies. Technological solutions such as sowing methods and their simplification and combinations, as well as tillage [14], plant variety compatibility and selection, seed rates, etc. The choice of crops for competitiveness to grow in one space is relevant for an effective crop mixing system (crops sowing time, density and arrangement). The present investigation focus was carried out with the objectives to find out the suitable pea cultivar for mixed cropping with oat, their suitable combination of mixed cropping in organic farming system.

METHODS

Experimental sites. The study was carried out at the Lithuanian Research Centre for Agriculture and Forestry, situated at the Central Lithuania's lowland region in three subsequent years 2020-2021, Akademija site (55º24′ N, 23º51′ E). The soil of the experimental site is *Endocalcari–Endohypogleyic Cambisol* (CMg-n-w-can), with a loam texture (19.3% clay, 28.9 % silt, 51.8 sand %). The topsoil (0–25 cm) pH was 7.5, and had available P_2O_5 74-79 mg kg^{-1} soil, and humus contents 2.3 %, and potassium content was 135-140 mg kg^{-1} soil. Total long year rainfall and average temperature were 570.1 mm and 6.5 °C, respectively.

Experimental design. The mixtures design was based on the proportional replacement principle, with mixed pea and oat grain at relative frequencies (50:50, 60:40, 70:30). Oat seed rate was 6.0 and pea 1.0 mln. seeds ha^{-1} for sole crop, as preceding crop of spring wheat – 5.5 mln. seeds ha^{-1}. For the experiment two varieties of semi-leafless field pea (cv. Jura DS and cv. Egle DS) and one oat (cv. Viva DS) were used.

RESULTS

The number of peas was the highest 96 units m^2 when a new variety Egle DS grown as sole crop, while the standard Jura DS was 91 units m^2, we can see it in (figure 1).
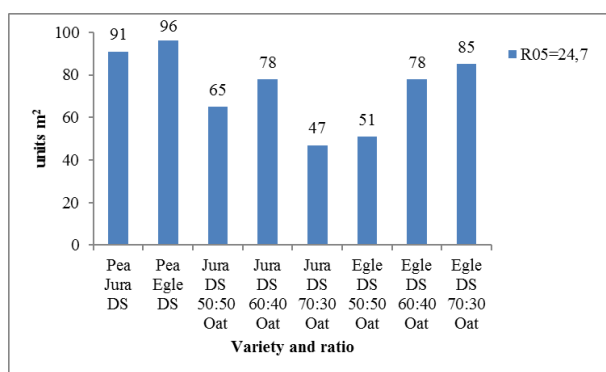
Fig.1 The number of pea depending on the pea sowing rate and different varieties, unit m^2
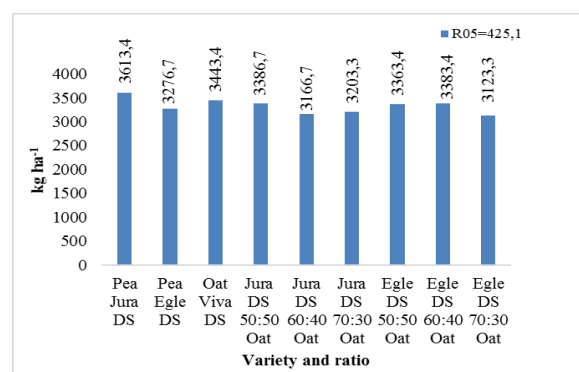
Fig.2 Spring wheat grain yield depending on pre-crops sowing rate and different pea varieties kg ha^{-1}

The number of pea was higher in mixtures with plant ratio 70% pea and 30% oat when the new variety Egle DS was involved, even 77 units m^2, while the same ratio with the standard variety Jura DS produced significantly less 46 units m^2. Increased competitive properties of field pea with oat were observed in new field pea variety and oat mixtures (pea ratio 70% and oat 30%). Oats dominated in all tested mixtures, however, spring wheat grown after peas yielded a higher result. The yield of spring wheat grown after oats were determined without significant difference, but lower by 170 kg ha^{-1} (figure 2) compared to wheat grown after variety pea Jura DS. Spring wheat yield after pre-crop of new variety Egle DS was obtained without significant differences compered to control variety pea Jura DS. Generally, new pea variety Egle DS more positively influenced spring wheat yield when grown as pre-crop in mixtures with oat compared to monocrop.

CONCLUSIONS

The cultivation of intercropping can lead to grain yields when mixed proportions are maintained while maintaining optimal density. The new pea variety, its combinations with oats resulted in the greatest advantage of the mixed harvest, which was mainly influenced by the fixed nitrogen of the peas in the oat grains, the accumulation of higher concentrations of crude protein compared to the monoculture. Studies can optimize the relationship between pea varieties and their mixtures to the effects of cereals to further improve the yield of organic mixed crop systems.

Keywords: mixture, grain legume, yield, organic system.

REFERENCES

1. ARLAUSKIENĖ, A.; JABLONSKYTĖ-RAŠČĖ, D.; ŠLEPETIENĖ, A. Effect of legume and legumefestulolium mixture and their mulches on cereal yield and soil quality in organic farming. *Archives of Agronomy and Soil Science*, 2020, Vol. 66, P. 1058–1073.

2. KASSAM, A.; FRIEDRICH, T.; DERPSCH, R. Global spread of conservation agriculture. *Journal of environmental studies*, 2018, (online) link to the internet: <http://www.tandfonline.com/loi/genv20>.

3. ESPINOZA, S.; OVALLE, C.; ZAGAL, E.; MATUS, I.; DEL POZO, A. Contribution of legumes to the availability of soil nitrogen and its uptake by wheat in Mediterranean environments of central Chile. *Chilean journal of agricultural research,* 2015, Vol. 75, No. 1, P. 111-121.

4. BÜCHI, L.; WENDLING, M.; AMOSSÉ, C.; NECPALOVA, M.; CHARLES, R. Importance of cover crops in alleviating negative effects of reduced soil tillage and promoting soil fertility in a winter wheat cropping system. *Agriculture, Ecosystems & Environment,* 2018, Vol. 256, P. 92-104

5. RANI, K.; SHARMA, P.; KUMAR, S.; WATI, L.; KUMAR, R.; GURJAR, D. S.; KUMAR, D.; KUMAR, R. Legumes for sustainable soil and crop management. *Sustainable Management of Soil and Environment*, 2019, P.193–215.

6. ŠARŪNAITĖ, L.; DEVEIKYTĖ, I.; ARLAUSKIENĖ, A.; KADŽIULIENĖ, Ž. MAIKŠTĖNIENĖ, S. Pea and spring cereal intercropping systems: Advantages and suppression of broad-leaved weeds. *Polish Journal of Environmental Studies*, 2013, P.541–551.

7. GAUDIN, A. C. M.; WESTRA, S.; LOUCKS, C. E. S.; JANOVICEK, K.; MARTIN, R. C.; DEEN, W. Improving resilience of northern field crop systems using inter-seeded red clover: A review. *Agronomy*, 2013, Vol. 3, P. 148–180.

8. BYBEE-FINLEY, K. A.; RYAN, M. R. Advancing intercropping research and practices in industrialized agricultural landscapes. *Agriculture*, 2013, p. 8–80.

9. JENSEN, E.S.; CARLSSON, G.; HAUGGAARD-NIELSEN, H. Intercropping of grain legumes and cereals improves the use of soil N resources and reduces the requirement for synthetic fertilizer N: a global-scale analysis. *Agronomy for Sustainable Development*. 2020, Vol. 40, P. 5.

10. KÖPKE, U.; ATHMANN, M.; HAN, E.; KAUTZ, T. Optimising cropping techniques for nutrient and environmental management in organic agriculture. *Sustainable Agriculture Research*, 2015, Vol. 4, P. 15–25.

11. THORUP-KRISTENSEN K., DRESBØLL D. B., KRISTENSEN H. L. Crop yield, root growth, and nutrient dynamics in a conventional and three organic cropping systems with different levels of external inputs and N re-cycling through fertility building crops. *European Journal of Agronomy*, 2012, Vol. 37, P. 66–82

12. KOŁOTA, E.; ADAMCZEWSKA-SOWIŃSKA, K. Living mulches in vegetable crops production: perspectives and limitations. *Acta Scientiarum Polonorum Hortorum Cultus*, 2013, Vol. 3, P. 127–142.

13. FINNAN, J. M.; BURKE, J. I.; THOMAS, T. M. A comparison between conventional tilled and bicropped winter wheat grown in monoculture over four years. *Sustainable Agriculture Research,* 2015, Vol. 5, P. 24–37.

14. CANALI, S.; DIACONO, M.; CAMPANELLI, G.; MONTEMURRO, F. Organic no-till with rollercrimpers: Agro-ecosystem services and applications in organic mediterranean vegetable productions. *Sustainable Agriculture Research*, 2015, Vol. 4, P. 1–10.

GROUND VEGETATION ASSESSMENT IN THE CLEAR-CUT AND REFOSTESTED SCOTS PINE STANDS

D. Gustienė

¹ Institute of Forestry, Lithuanian Research Centre for Agriculture and Forestry,
² Kaunas Forestry and Environmental Engineering University of Applied Sciences,
Liepų 1, Girionys, LT-53101, Kaunas distr. – Lithuania
+3706548108
dovile.gustiene@lammc.lt

I. Varnagirytė-Kabašinskienė
Institute of Forestry,
Lithuanian Research Centre for Agriculture and Forestry,
Liepų 1, Girionys, LT-53101, Kaunas distr. – Lithuania
iveta.kabasinskiene@lammc.lt

EXTENDED ABSTRACT

OVERVIEW

The functioning of forest ecosystems ensures specific conditions for forest-depending species [1, 2]. Clear-cutting is widely used as a mature stand management regime that causes large changes in the forest ecosystem. Usually, this management system is applied in the light-demanding tree species stands such as Scots pine (*Pinus sylvestris L.*) and is followed by artificial regeneration. Currently, clear-cutting is applied in more than 45% of final felling sites in the mature Scots pine stands in Lithuania [3]. Scots pine is a long-living species (age of its natural maturity is >170 years), therefore, its stands create specific conditions for forest-related species. The changes of the light, humidity, and temperature regime after clear-cutting lead to the alteration of site-specific species (mosses, herbaceous and woody plants) richness, composition, and cover, also chemical soil changes [1,4]. Usually, these differences disappear when site-specific species and soil chemistry reaches the pre-harvest level [1; 4; 5]. This study aimed to assess the changes in the main indices of ground vegetation after clear-cutting and the recovered forest.

METHODS

The study was carried out in the clear-cut and recovered 10 and 30-years old sites, also in the mature 101-years old Scots pine stands. The study was performed in Trakai region, in south-western Lithuania. The ground vegetation species were assessed in three different vertical strata: moss, herb, and shrub layer. A comprehensive description of the methods has been given earlier [6]. Five sample plots of 10×10 m were established systematically in each site. The assessment was performed in five 1×1 m quadrates, a totally 25 m² per site. To assess the cover (percent) of each species visually, a special frame was used. The mean value of each species cover was calculated per site and the Shannon diversity index (H′) was

calculated by the eq. 1. There, n_i is the coverage of the ith species; N is the total coverage of vegetation in the site.

$$H = -\sum \frac{n_i}{N} * ln \frac{n_i}{N}.$$ (6)

RESULTS

The study showed that the mosses were dominant in the understory plant cover, but its species composition depended on stand age. In the fresh clear-cut, four species of the mosses similar to the mature stand were detected: *Pleurozium schreberi* (Brid.) Mitt. *Hylocium splendens* (Hedw.) Schimp. And *Ptilium crista-castrensis* (Hedw.) De Not. Meanwhile, the mean cover of the mosses differed. These species covered 88% in the mature stand and this coverage was 1.6 times higher than in the fresh clear-cut. The biggest number of the mosses (7 species) was detected in the 10-years old Scots pine stand. There, *Pohlia nutans* (Hedw.) Lindb was dominating species, then followed by *Pleurozium schreberi* and *Dicranum polysetum* Sw.

The biggest number (22 species) of vascular plants was found in the clear-cut, the similar number (19 species) in the 10- and 30-years old stands, the smallest number (6 species) was found in the mature forest (Table 1). The specific microclimatic conditions in the clear-cut caused a bigger number of the species more commonly found in the open habitats and this difference from the mature forest was 18 species. The new species was scarcely distributed and observed randomly in the clear-cut, therefore the highest mean species richness was found in the 10- and 30-years stand, 17 and 14 species, respectively.

The highest Shannon species diversity index was obtained in the clear-cut, especially for vascular plants. The stands of *Pinetum vaccinio-myrtillosum* forest type mostly were covered by *Vaccinium myrtillus (L.)* and *V. vitis-idaea* (L.). The species *Pteridium aquilinum* (L.) Kuhn, as one of the dominant species, was obtained only in the clear-cut sites.

Table 1. Mean cover (percent), total and mean species richness (number of species) and Shannon species diversity index (H′) at different sites.

Site type	Vegetation type	Mean cover (percent)	Number of species		Shannon species diversity index (H′)
			Total species richness	Mean species richness	
Clear-cut	Vascular plants	14.8 ± 0.2	22.0	11.0±1.2	1.8±0.2
	Mosses	56.7 ± 4.6	4.0		0.86±0.1
10 years old stand	Vascular plants	39.9 ± 0.7	19.0	17.0±1.9	1.3±0.2
	Mosses	25.1 ± 1.6	7.0		1.3±0.2
30 years old stand	Vascular plants	25.4 ± 0.4	19.0	14.0±1.0	1.3±0.1
	Mosses	93.2 ± 6.6	5.0		1.1±0.1
Mature stand	Vascular plants	16.6± 0.3	6.0	7.0±0.8	0.7±0.1
	Mosses	88.7 ± 6.7	4.0		0.9±0.0

CONCLUSIONS

The study showed that the mosses were dominated species in the *Pinetum vaccinio-myrtillosum* forest type. The vascular plants composed the smaller part in the ground vegetation cover compared to the mosses with the exception of the 10-years old stand. The largest mean cover of vascular plants was obtained in the 10-and 30-years old stands, and it was about 40 and 25 percent, respectively. The lowest mean species richness was obtained in the mature forest, therefore, the total species richness decreased with the stand age.

Keywords: *Pinus sylvestris*, species cover, richness, Shannon species diversity index, mature stand.

REFERENCES

1. ČESONIENĖ, L.; DAUBARAS, R.; TAMUTIS, V.; KAŠKONIENĖ, V.; KAŠKONAS, P.; STAKĖNAS, V.; ZYCH, M. Effect of clear-cutting on the understory vegetation, soil and diversity of litter beetles in Scots pine-dominated forest. *Journal of Sustainable Forestry*, 2019, Vol. 38, No. 8. P. 791-808. Link to the internet <https://doi.org/10.1080/10549811.2019.1607755 >.

2. HEKKALA, A. M.; TARVAINEN O. Dynamics of understory vegetation after restoration of natural characteristics in the boreal forests in Finland. *Forest Ecology and Management*, 2014, Vol. 330, P. 55–66. Link to the internet <https://doi.org/10.1016/j.foreco.2014.07.001>.

3. ME/SFS (Ministry of Environment/State Forest Service). Lithuanian Statistical Yearbook of Forestry 2020 [Lietuvos miškų ūkio statistika 2020]. Butkus A, Dumčiene V, Eigirdas M, Kuliešis A, Vižlenskas D (eds), Lututė, Kaunas, 2021, P. 184.

4. STEFAŃSKA-KRZACZEK, E.; STANIASZEK-KIK, M.; SZCZEPAŃSKA, K.; SZYMURA, TH. Species diversity patterns in managed Scots pine stands in ancient forest sites. PLoS ONE, 2019, Vol. 14, No. e0219620. Link to the internet <https://doi.org/10.1371/journal.pone.0219620>.

5. KARAZIJA, S. Age-related dynamics of pine forest communities in Lithuania. Baltic For, 2003, Vol. 9, P. 50–62.

6. GUSTIENĖ, D.; VARNAGIRYTĖ-KABAŠINSKIENĖ, I.; STAKĖNAS, V. Ground vegetation, forest floor and mineral topsoil in a clear-cutting and reforested Scots pine stands of different ages: a case study. *Journal of Forestry Research*. 2021. Link to the internet < https://doi.org/10.1007/s11676-021-01434-5>.

POPULATION STRUCTURE AND DIVERSITY OF ENDOPHYTIC BACTERIA FROM *ARTEMISIA* SPP. PLANTS AND THEIR POTENTIAL IN SUSTAINABLE AGRICULTURE

S.H. Hadian, S. Supronienė
Lithuanian Research Centre for Agriculture and Forestry
Studentu St. 15A, Akademija, 53362 Kaunas distr. – Lithuania
+370 63831214
shervin.hadian@lammc.lt

EXTENDED ABSTRACT

OVERVIEW

One way to increase crop productivity and sustainability of agricultural practices is to reduce the need and dependency on chemical fertilizers by using efficient, nutrient mobilizing endophytes with crucial roles in plant growth promotion and resistance to pathogen [1]. Most endophytes play crucial roles in plant growth promotion and resistance through their abilities to participate in important processes such as nutrient mobilization, phytohormones production, and pathogen suppression. The genus *Artemisia* L. is one of the largest genera in the Asteraceae family, consisting of more than 500 species that have been used in various treatments since ancient times as folk remedies [2]. *Artemisia* sp. are known for their antimicrobial, insecticidal, parasitical, and phytotoxic properties, which recommend them as possible biological control agents against plant pests and diseases [3]. *Artemisia absinthium* is a strongly aromatic plant that bears numerous oils producing glands on leaves, stems and flowering branches which is used in ethno pharmacology and plant protection [4]. After six years of experimentation *Artemisia dubia* has been selected as one of the most promising energy crops at the Lithuanian Research Centre for Agriculture and Forestry [5]. Study the production of secondary metabolites in *Artemisia dubia* showed high production of biologically important phytochemicals and enhanced pharmacological and insect side activities [6]. Recently *A. dubia* and *A. absinthium* were used as a natural source of bioactive compounds on some plant pests and human pathogens but the role of endophytic bacteria witch associated with *A. dubia* and *A. absinthium* as source of antifungal and antibacterial activity needs to study, so in this study population structure and diversity of endophytic bacteria of *A. dubia* and *A. absinthium* and their activity on inducing plant resistance to plant diseases and plant growth parameters will be investigated. The present study aims to explore bacterial endophytes of ethno medicinal plant *A. dubia* and *A. absinthium* importance as a plant growth promotor and induce resistance against plant diseases.

METHODS

The culturable bacterial endophytic diversity of *A. dubia* plants (collected from field experiment established in Akademija Kėdainiai district) and *A. absinthium* (collected from different districts of Lithuania) will be screened for producing antagonistic compounds following cross-streak and agar well diffusion assay methods against several test fungal pathogen. Population structure and diversity of endophytic bacteria with antagonistic activity

will be analysed with Phylogenetic analysis, morphological, biochemical characterization, and molecular identification by 16S rRNA sequencing. *In vitro* evaluation of other beneficial traits of endophytic bacteria will be done by screening for Plant Beneficial Traits (Indole-3-acetic acid (IAA) production, Phosphate solubilization activity, Nitrogen Fixation Activity and Production of Siderophores). Colonization ability of selected bacterial isolates will be studied on pea plant. *In vivo* screening of selected endophytic bacteria for antagonistic activity against plant pathogens will be done on PDA using the disc diffusion method according to [7]. Greenhouse assays will be done to screening of selected endophytic bacteria for stimulation plant growth and confer resistance to plant diseases by evaluating diseases severity. For statistical analysis, data will be submitted to one-way variance analysis (ANOVA) by using SPSS software.

RESULTS

Although endophytes have emerged in recent years as the novel resources for secondary metabolites of antioxidant, antimicrobial and anticancer activities, the roles of endophytes in plant growth and metabolism have not been fully understood. Literature review clearly demonstrates that *A. absinthium* and *A. dubia* are potential source for the isolation of endophytic bacteria exhibiting pea fungal diseases suppressive and plant growth promoting effect on pea. We expect that this study will present the current development of research into *A. dubia* and *A. absinthium* focuses on the regulatory roles of endophytes. We will report the diversity of cultivable endophytic bacteria from *A. absinthium* and *A. dubia* plants and showing antagonistic activity against plant pathogens by using 16S rRNA gene analysis and their plant beneficial properties. The promoted growth effect of isolated endophytic bacteria will be studied on pea plant through the enhanced ability to produce the Indole-3-acetic acid (IAA) production, Phosphate solubilization activity, Nitrogen Fixation Activity and Production of Siderophores. The antifungal potential of selected endophytic bacteria will be evaluated and measured *in vitro* condition. The colonization ability of endophytic bacteria isolated from *Artemisia* plant will be survived on pea plant and successfully colonizing the peas will be screened for their ability to protect pea from fungal pathogen and enhance plant growth in greenhouse condition. Understanding the endophyte-*Artemisia* plant has the potential to improve agricultural practices for plant growth and plant protection. The aim of our research is to show on the importance role of endophytes in medicinal plant as a plant resistance inducer against plant diseases and plant growth promotor.

CONCLUSIONS

Characterization and identification of microbial endophytes isolated from medicinal plants possessing a vital role to plant protection, improve plant growth and could be used as inoculants to establish a sustainable crop production system.

Keywords: *Artemisia absinthium, Artemisia dubia,* endophytic bacteria, 16S rRNA

REFERENCES

1. GAMEZ, R.; CARDINALE, M.; MONTES, M.; RAMIREZ, S.; SCHNELL, S.; RODRIGUEZ, F. Screening, plant growth promotion and root colonization pattern of two rhizobacteria (*Pseudomonas fluorescens* and *Bacillus amyloliquefaciens*) on banana cv. Williams (Musa acuminata Colla). *Microbiological Research*, 2019, Vol. 220, P. 12 – 20.

2. ABAD, M. J.; BEDOYA, L. M.; APAZA, L.; BERMEJO, P. The *Artemisia* L. genus: a review of bioactive essential oils. *Molecules*. 2012, Vol. 17, No. 3, P. 2542-2566.

3. IVĂNESCU, B.; BURLEC, A.F.; CRIVOI, F.; ROȘU, C.; CORCIOVĂ, A. Secondary Metabolites from Artemisia Genus as Biopesticides and Innovative Nano-Based Application Strategies. *Molecules*, 2021, Vol. 26, No.10, P. 3061.

4. AMORA, D. X.; DE PODESTÁ, G.S.; GRUPIONI, P.H.F.; DAS NASU, É.G.C.; DE FIGUEIREDO, L.D.; FERREIRA, F.C.; DE FREITAS, L.G.; LOPES, E.A.; FERRAZ, S. Effect of essential oils on the root-knot nematode. *Agri-Environmental Sciences,* 2017, Vol. 3, No. 1, P. 15 – 23.

5. ČERNIAUSKIENĖ, Ž.; RAILA, A. J.; ZVICEVIČIUS, E.; KADŽIULIENĖ, Ž.; TILVIKIENĖ, V. Analysis of *Artemisia dubia* Wall. growth, preparation for biofuel and thermal conversion properties, *Renewable Energy*, 2018, Vol. 118, P. 468 - 476.

6. LIANG, J. Y.; GUO, S. S.; ZHANG, W. J.; GENG, Z. F.; DENG, Z. W.; DU, S. S.; ZHANG, J. Fumigant, and repellent activities of essential oil extracted from *Artemisia dubia* and its main compounds against two stored product pests. *Natural Product Research*. 2018, Vol. 32, No.10, P. 1234 - 1238.

7. VETHAVALLI, S.; SUDHA, S. In vitro and in silico studies on biocontrol agent of bacterial strains against *Fusarium oxysporum* f. sp. l*ycopersici*. *Research Journal of Biotechnology*, 2012, Vol. 3, No. 2, P. 22 – 31.

SELECTION OF COMPETITIVE AND EFFICIENT RHIZOBIUM SPP. STRAINS FOR DIFFERENT PISUM SATIVUM GENOTYPES

J. Kaziūnienė, S. Supronienė

Institute of Agriculture, Lithuanian Research Centre for Agriculture and Forestry
Instituto al. 1, Akademija, LT-58344 Kėdainiai distr. – Lithuania
+37062297525;
justina.kaziuniene@lammc.lt

EXTENDED ABSTRACT

OVERVIEW

Biological nitrogen fixation (BNF) process where atmospheric nitrogen is converted to ammonia by microorganisms has a significant role in the global nitrogen cycle and agriculture. It was estimated that the BNF, carried out by prokaryotes, provides Earth's ecosystems with about 200 million tons N per year [1, 2]. Between 150 and 200 million tonnes of mineral nitrogen are required each year by plants in agricultural systems in additional. To meet those requirements, around 100 million tons of nitrogen is produced through the industrial Haber-Bosch process every year [3, 4]. However, irrational fertilization causes many environmental problems, high rates of nitrogen fertilizers change soil pH, encourage nitrates and nitrites accumulation in the soil and plants, leached nitrogen compounds cause water eutrophication and drinking water contamination, gaseous losses of nitrogen contribute to global warming [5, 3].

In 2020 May two different EU strategies "Bringing nature back into our lives" and "The Farm to Fork" were published, where political objectives were indicated. Both these strategies are directed to reduction of pesticides and fertilisers in European agriculture. First aim is to reduce the overall use of synthetic chemical pesticides by 50% and the use of more hazardous pesticides by 50% by 2030. The second is a commitment to reduce nutrient losses by at least 50% while ensuring that there is no deterioration in soil fertility, this commitment will reduce the use of fertilisers by at least 20% by 2030 [6]. These decisions should encourage the use of alternative products in agriculture which are safe for plants and humans. One of alternative is microbial biostimulants, containing diastrophic microorganisms able to fix biological nitrogen from atmosphere. BNF can be improved by optimizing the symbiosis between the rhizobia inoculants and legume plants, leading reduced nitrogen fertilizer [7]. It was determined that BNF could provide over 80% of the nitrogen content in pea crops. In symbiotic associations between plant and rhizobia, 50–465 kg N ha^{-1} y^{-1} biological nitrogen could be fixed [8, 9].

According to statistical data presented in FAOSTAT, pea is a minor field crop in Lithuania. In 2020 only 61.7 thousand hectares were cultivated [10]. However, inclusion of legume plants in rotations can provide a wide range of benefits, improve soil structure, break of pest cycles, and make grass species weed control easier, improve soil microbial biomass growth, increase nitrogen accumulation in soil, reduce nitrogen requirements for nonlegume plants and give much more advantages. Cultivation of legume plants could help to reduce losses of

consistently rising prices of mineral fertilizers and help to implement green revolution strategies [11, 12, and 13]. Thus, the cultivation of legumes and the optimization of biological nitrogen fixation can lead not only productivity of pea cultivation, but to provide other added value which is significant for agriculture [14].

The BNF fixation depends on many environmental factors: soil acidity, alkalinity, temperature, salinity, mineral nutrients, high nitrogen and phosphorus levels and soil type. Rhizobia ability to adapt to these environmental factors and to compete with other soil microorganisms helps to establish an effective symbiosis [15, 16]. To ensure efficient symbiosis, it is important to select appropriate bacterial strains and understand biological nitrogen fixation and symbiosis limiting conditions. In this research we are going to investigate different *Rhizobium* spp. strains competitiveness and symbiosis efficiency with different *Pisum sativum* genotypes.

METHODS

This investigation will be carried out in vegetative pots. *Rhizobium* spp. strains will be isolated from three different soil types by growing five different *Pisum sativum* breeding lines [17, 18]. Then all isolates will be tested for Koch's postulates confirmation, only these isolates which will confirm all Koch's postulates will be selected for identification by 16S rRNA sequencing [19], recA, atpD, and nodC genes sequences will be analysed also [8]. In further investigations selected *Rhizobium* spp. isolates will be tested in sterile and non-sterile (natural-imitating) conditions in vegetative pots experiments with selected *Pisum sativum* genotypes [8, 20]. Pea biometric parameters and nitrogen accumulation in plant will be analysed. In the last stages of experiment, *Rhizobium* spp. strains will be tagged fluorescently and will be determined which strains were the most competitive and provided the highest amount of nitrogen for the plant [21, 22, and 23].

RESULTS

In this investigation:

- Different *Rhizobium* spp. strains will be isolated, tested for Koch's postulates confirmation and analysed by 16S rRNA, recA, atpD, and nodC gene sequencing;

- Phylogenetic trees will be constructed for better isolates phylogenetic diversity analysis;

- Competitive *Rhizobium* spp. strains will be determined in symbiosis studies with *Pisum sativum* genotypes;

- Relationships between competitive *Rhizobium* spp. strains, pea biometric parameters and nitrogen accumulation will be evaluated.

CONCLUSIONS

Nitrogen is one of the most important elements for plants nutrition, so biological nitrogen fixation provides benefits not only for legume plants but and plants which are cultivating in rotations. Higher nitrogen accumulation in plant and in soil could be achieved using *Rhizobium* spp. inoculants for *Pisum sativum* cultivation. To improve biological nitrogen fixation, it is important to select appropriate bacterial strains, which are competitive, efficient, and easy adaptable to environmental conditions.

REFERENCES

1. ADISSIE, S.; ADGO, E.; FEYISA, T. Effect of rhizobia inoculants and micronutrients on yield and yield components of faba bean (Vicia faba L.) on vertisol of Wereillu district, South Wollo, Ethiopia. *Cogent Food Agriculture*, 2020, Vol. 6, No. 1.

2. RASCIO, N.; LA ROCCA, N. Biological Nitrogen Fixation. In: *Encyclopedia of Ecolog*y. EBook, Elsevier Science, 2008, P. 412-179. ISBN 978-0-08-045405-4.

3. UNKOVICH, M.; HERRIDGE, D.; PEOPLES, M. Measuring plant-associated nitrogen fixation in agricultural systems. *Meas plant-associated nitrogen fxation Agric Syst.* Published online 2008 - [referred on the 1th of February in 2022 y.]. Link to the internet <https://www.aciar.gov.au/sites/default/files/legacy/node/10169/MN136%20Part%201.pdf>

4. SHAH, A. Determination of biological nitrogen fixation induced N_2O emission from arable soil by using a closed chamber technique. *Applied and Environmental Soil Science*, 2014.

5. FOLLETT, R.F.; HATFIELD, J.L. "Nitrogen in the Environment: Sources, Problems, and Management", *the Scientific World Journal*, 2001, Vol. 1, P. 920-926.

6. *European Commission*. Communication From The Commission To The European Parliament, The Council, The European Economic And Social Committee, And The Committee Of The Regions Eu Biodiversity Strategy for 2030 Bringing nature back into our lives. Published online 2020 - [referred on the 1th of February in 2022 y.]. Link to the internet <https://eur-lex.europa.eu/legal-content/EN/TXT/?uri=CELEX:52020DC0380>

7. YANG, C.; BUECKERT, R.; SCHOENAU, J.; DIEDERICHSEN, A.; ZAKERI, H.; WARKENTIN, T. Symbiosis of selected Rhizobium leguminosarum bv. viciae strains with diverse pea genotypes: effects on biological nitrogen fixation. *Canadian Journal of Microbiology*, 2017, Vol.63, No.11, P. 909-919.

8. SUPRONIENE, S.; DECOROSI, F.; PINI, F. Selection of Rhizobium strains for inoculation of Lithuanian Pisum sativum breeding lines. *Symbiosis*, 2021, Vol. 83, No. 2, P. 193-208.

9. PANKIEVICZ, V. C. S.; IRVING, T. B.; MAIA, L. G. S.; ANÉ, J. M. Are we there yet? The long walk towards the development of efficient symbiotic associations between nitrogen-fixing bacteria and non-leguminous crops. *BMC Biology*, 2019, Vol. 17, No. 1.

10. CANTON, H. *Food and Agriculture Organization of the United Nations—FAO. In: The Europa Directory of International Organizations 2021*. London: Routledge, 2021. ISBN 978-1-00-317990-0.

11. LUPWAYI, N. Z.; SOON, Y. K. Nitrogen release from field pea residues and soil inorganic N in a pea wheat crop rotation in north western Canada. *Canadian Journal of Plant Science*, 2009, Vol. 89, No. 2, P. 239-246.

12. CHEN C.; NEILL K.; BURGESS M.; BEKKERMAN A. Agronomic benefit and economic potential of introducing fall-seeded pea and lentil into conventional wheat-based crop rotations. *Agronomy Journal*, 2012, Vol. 104, No. 2, P. 215-224.

13. LUPWAYI, N. Z.; LAFOND, G. P.; MAY, W. E.; HOLZAPFEL, C. B.; LEMKE, R. L. Intensification of field pea production: Impact on soil microbiology. *Agronomy Journal*, 2012, Vol. 104, No. 4, P. 1189-1196.

14. YANG, C.; BUECKERT, R.; SCHOENAU, J; DIEDERICHSEN, A.; ZAKERI, H.; WARKENTIN, T. D. Evaluation of growth and nitrogen fixation of pea nodulation mutants in western Canada. *Canadian Journal of Plant Science*, 2017, Vol. 97, No. 6, P. 1121-1128.

15. VANDERLINDE, E. M.; HYNES, M. F.; YOST, C. K. Homoserine catabolism by Rhizobium leguminosarum Bv. viciae 3841 requires a plasmid-borne gene cluster that also affects competitiveness for nodulation. *Environmental Microbiology*, 2014, Vol. 16, No. 1, P. 205-217.

16. ABI-GHANEM, R.; SMITH, J. L.; VANDEMARK, G. J. Diversity of Rhizobium leguminosarum from Pea Fields in Washington State. *International Scholarly Research Notices*, 2013.

17. VINCENT, J. M. *A Manual for the Practical Study of Root-nodule Bacteria*. UK: Blackwell Sci Publ Oxford, 1970, P. 164. ISBN 1-971-070072-6.

18. SAGOLSHEMCHA, R.; DEVI, Y. N.; SINGH, W. R. Plant Growth Promoting Effect and Biocontrol Potential of Rhizobium spp. against Macrophomina phaseolina. *International Journal of Current Microbiology and Applied Sciences*, 2017, Vol. 6, No. 6, P. 2695-2701.

19. LANE, D. J. "16S/23S rRNA Sequencing," *Nucleic Acid Techniques in Bacterial Systematic*, 1991, P. 115-175.

20. HOWIESON, J. G; DILWORTH, M. J. *Working with rhizobia*. Canberra: Bytes 'n Colours, 2016, P. 87. ISBN 978-1-925436-17-4.

21. BELLABARBA, A.; BACCI, G.; DECOROSI, F. Competitiveness for Nodule Colonization in Sinorhizobium meliloti: Combined in Vitro -Tagged Strain Competition and Genome-Wide Association Analysis. *mSystems*, 2021, Vol. 6, No. 4.

22. IRISARRI, P.; CARDOZO, G.; TARTAGLIA, C. Selection of competitive and efficient rhizobia strains for white clover. *Fronters in Microbiology*, 2019, Vol. 10, No. 768.

23. SESSITSCH, A.; HARDARSON, G.; DE VOS, W. M.; WILSON, K. J. Use of marker genes in competition studies of Rhizobium. *Plant Soil*, 1998, Vol. 204, No. 1, P. 34-45.

EMPIRICAL DETERMINATION OF HYDROPONIC SOLUTION BUFFER CAPACITY

G. Kudirka, A. Viršilė
Lithuanian Research Centre for Agriculture and Forestry
Instituto al. 1, LT-58344 Akademija, Kėdainiai distr. – Lithuania
+37066238235
Gediminas.Kudirka@lammc.lt

L. Ragelienė
Vytautas Magnus University
Vileikos g. 8, LT-44404 Kaunas – Lithuania
Lina.Rageliene@vdu.lt

EXTENDED ABSTRACT

OVERVIEW

Hydroponics is soilless crop growing method which uses nutrient solution instead of mineral soil and its popularity has grown over the years due to effective water, nutrients usage for leafy greens cultivation [1]. Nutrient solution (Hoagland's solution) contains all essential micro and macro elements in their respective concentrations [2]. Hoagland's solution used in hydroponics has limited but not quantified buffering capacity [3]. For pH mitigation nutrient solution must contain reasonable amount of protolytic base and acid pair [4]. There are 2 major salts in typical Hoagland's solution which can act as buffering agents in hydroponic solution: NH_4NO_3 and KH_2PO_4. Unfortunately, ammonia useful buffering range is above nutrient solution pH interval used in hydroponics, therefore, $NH4^+/NH3$ buffer will not mitigate pH changes [5]. Mostly nutrient solution buffer capacity comes from second step of phosphate dissociation reaction (1)

$$H_2PO_4^-(aq) \rightleftharpoons HPO_4^{2-} + H^+(aq) \quad pK_{a2}6.86 - 7.2 \quad (1)$$
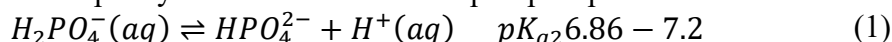
Maximum buffer capacity is reached then desired pH value is equal to buffering agent dissociation constant and buffer effective range is $pK_a \pm 1$[4]. Usually, optimal pH level for hydroponic growth ranges from 5.5 to 6.5 [6] therefore, due to unequal absorption of ions from the nutrient solution during growth phases pH fluctuations accrues [7]. Ion absorption from the nutrient solution changes charge balance between the root inner membrane and the nutrient solution. As cation is absorbed from the nutrient solution H^+ ions are released through the root cells to compensate charge difference; opposite reaction occurs then anion is absorbed – OH^- ion are released for charge compensation [6]. Fluctuations outside optimal pH interval decreases efficiency of mineral nutrition, restricting plant performance, also irreversible changes may occur regarding plant physiology when rhizosphere is in contact with nonoptimal pH levels [8]. Plants grown in nonoptimal pH interval have lower yield: basil (*Ocimum basilicum*) and kale (*Brassica olearacea*), cultivated in hydroponic solution with slightly acidic

pH had higher chlorophyll content and yields compared with leafy greens grown in slight alkaline pH [9]. Root induced changes in the rhizosphere may also affect plant mineral nutrition in various ways [10]. Ion unavailability due to salt precipitation occurs when pH levels is not in optimal range. For instance, at alkali pH iron, calcium, magnesium forms precipitate and becomes unavailable [11]. Hence, hydroponics growth potential can be maximized if hydrogen ion concentration is maintained at optimal interval but practically pH management should not require excessive technological solution and ideally done passively.

Our objective was to empirically determinate nutrient solution buffer capacity using acid/ base titration and according to calculated buffering capacity suggest passive pH management strategy for hydroponic growth.

METHODS

Two stage acid (HCl) and base (NaOH) titration were performed by increasing titrant concentration from 0mM to 2mM in 10 stages, pH was measured at equilibrium point with bench pH/EC meter (HI-5521-02, Hanna, USA) each stage ware replicated 3 times.

RESULTS

Acid/ base titration curve (graphical representation of pH of the solution during titration) of modified Hoagland's solution is shown in Figure 1.
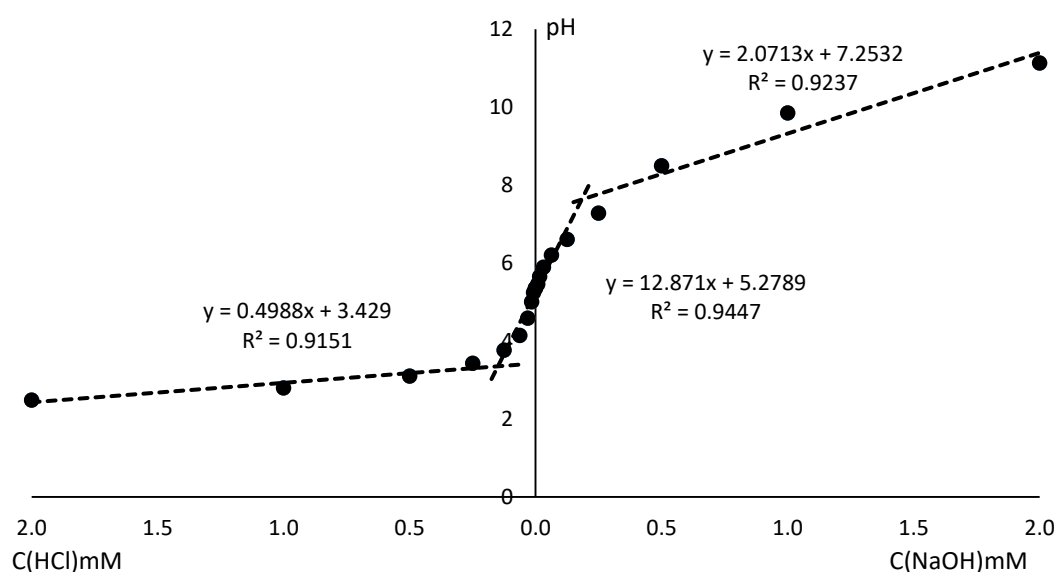
Fig. 15. Titration curve of modified Hoagland's solution, n=3. Titrants: HCl – 0.5 N (normality), NaOH – 0.5 N. Acidic buffer capacity defined as intersection of these straight lines: y=2.0713x + 7.2532 with y=12.871+5.2789. Base buffer capacity defined as intersection of these straight lines: y=0.4988x + 3.429 with y=12.871+5.2789. Combined buffer capacity is the sum of acid and base capacities.

Calculated buffering capacities of modified Hoagland's solution: acid – 0.18 mM, base – 0.15 mM, combined – 0.33 mM. Nutrient solution buffering capacity is broken by ions (H^+/OH^-) released true the root cells due to selective unequal mineral absorption from the nutrient solution. pH changes of nutrient solution can be passively regulated using buffers or ion

exchange resins. pH management is based on ion exchange on a solid surface. Main disadvantage is the removal of cations from nutrient solutions such as magnesium or manganese [12]. Zwitterionic MES (2-(N-morpholino)ethanesulfonic acid) buffer was selected as reasonable candidate for passive pH management in hydroponics due to favourable pK_a value of 6.1 and biological inertness [12]. Theoretically, nutrient solution buffer capacity can be enhanced endlessly. Practically, buffer strength is limited by plant physiology. Plants cannot thrive in buffered nutrient solution with high salinity, ionic strength, or buffer itself can be toxic [13].

CONCLUSIONS

According to calculated combined buffer capacity of modified Hoagland's solution an addition of 3mM MES buffer to the nutrient solution resulted to in increased initial buffer capacity 9-fold.

Keywords: Hydroponics, pH, buffer, buffering capacity, titration curve.

REFERENCES

1. KHAN, S.; PUROHIT, A.; VADSARIA, N., Hydroponics: current and future state of the art in farming, *Journal of Plant Nutrition*,2020 Vol. 44, No. 10, P. 1515–1538.

2. HOAGLAND D. I.; ARNON D. R., Agricultural Experiment Station the Water-Culture Method for Growing Plants Without Soil, *California Agricultural Experiment Station*, 1938, Vol. C347, P. 1–39.

3. SINGH, H.; DUNN, B.; PAYTON, M. Hydroponic pH Modifiers affect Plant Growth and Nutrient Content in Leafy Greens, *Journal of Horticultural Research.*, 2019, Vol. 27, No. 1, p. 31–36.

4. CHIRIAC, V.; BALEA, G. Buffer Index and Buffer Capacity for a Simple Buffer Solution, *Journal of Chemical Education.*, 1997, Vol. 74, No. 8, P. 937.

5. GOYAN, J. E.; SHAIKH, Z. I.; AUTIAN, J. A Kinetic Study of Barbital Degradation in an Ammonia Buffer System**Received December 7, 1959, from the College of Pharmacy, University of Michigan, Ann Arbor., *Journal of the American Pharmacists Association. (Scientific ed.)*, 1960, Vol. 49, No. 10, P. 627–631.

6. SAVVAS, D.; GRUDA, N. Application of soilless culture technologies in the modern greenhouse industry – A review, *European Journal of Horticultural Science.*, 2018, Vol. 83, No. 5, P. 280–293.

7. WANG, L.; CHEN, X.; GUO, W.; LI, Y.; YAN, H.; XUE, X. Yield and Nutritional Quality of Water Spinach (Ipomoea aquatica) as Influenced by Hydroponic Nutrient Solutions with Different pH Adjustments, Inte*rnational Journal of Agriculture And Biology*, 2017, Vol. 19, No. 4, p. 635–642.

8. ANDERSON, T.; MARTINI, M; De Villiers, D.; Timmons, M. Growth and Tissue Elemental Composition Response of Butterhead Lettuce (Lactuca sativa, cv. Flandria) to Hydroponic Conditions at Different pH and Alkalinity, *Horticulturae*, 2017, Vol. 3, No. 3, P. 41.

9. WORTMAN, S. E. Scientia Horticulturae Crop physiological response to nutrient solution electrical conductivity and pH in an ebb-and-flow hydroponic system, *Scientia Horticulturae (Amsterdam)*, 2015, Vol. 194, P. 34–42.

10. TURNER, A. J.; ARZOLA, C. I.; NUNEZ, G. H. High pH stress affects root morphology and nutritional status of hydroponically grown rhododendron (Rhododendron spp.), *Plants*, 2020, Vol. 9, No. 8, P. 1–12.

11. SINGH, H.; DUNN, B.; PAYTON, M. Hydroponic Ph Modifiers Affect Plant Growth And Nutrient Content In Leafy Greens, 2019, Vol. 27, No. 1, P. 31–36.

12. BUGBEE, B. G.; SALISBURY, F. B. An evaluation of MES (2(N-Morpholino)ethanesulfonic acid) and amberlite IRC-50 as pH buffers for nutrient solution studies ∗, *Journal of Plant Nutrition.*, 1985, Vol. 8, No. 7, P. 567–583.

13. THI BICH THAO, H.; YAMAKAWA, T.; SHIBATA, K. Effect of phosphite–phosphate interaction on growth and quality of hydroponic lettuce (Lactuca sativa), *Journal of Plant Nutrition and Soil Science*, 2009, Vol. 172, No. 3, P. 378–384.

COLD PLASMA AND ELECTROMAGNETIC FIELD IMPACT ON ACCUMULATION OF BIOCHEMICAL COMPOUNDS IN NEEDLES OF SCOTS PINE HALF-SIB FAMILIES

Lučinskaitė, V. Sirgedaitė-Šėžienė
Lithuanian Science Centre for Agriculture and Forestry, Institute of Forestry
Liepų st. 1, LT-53101 Girionys – Lithuania
+37064124570
ieva.lucinskaite@lammc.lt

EXTENDED ABSTRACT

OVERVIEW

Scots pine (*Pinus sylvestris* L.) occupies more than 33% of forested area in Lithuania [1]. The species has huge benefits in ecological and social suspects, such as maintenance of sustainable forest ecosystem functioning and ability to increase human health [2]. Unfortunately, pests are the main enemies that strongly affect nature range, growth, and timber quality of Scots pine [3; 4]. Forest trees, for protection against pathogens, accumulate secondary metabolites and antioxidant activity in different tissues [5]. In addition, tree genetic selection is purposeful and important factor in maintaining and enhancing forest biodiversity, since different tree genotypes can synthesize different levels of secondary metabolites [6-8]. One of the tools to increase content of total flavonoids (TFC) and antioxidant activity is by using physical stressors: cold plasma (CP) and electromagnetic field (EMF). These innovative technologies can help to achieve better plants growth, since they can increase resistance to various attacks of pathogens. According to other authors, pre-sowing seeds treatment with CP and EMF is eco-friendly, safe, and they do not cause genetic mutations [9-12].

The aim of the research was to evaluate pre-sowing seeds treatment with CP and EMF influence TFC and antioxidant activity in needles of Scots pine half-sib families. Seeds of 11 different half-sib *P. Sylvestris* families were affected with CP 1 min., CP 2 min. and EMF 1 min. The hypothesis of the research was that TFC and antioxidant activity in *P. Sylvestris* needles strongly depend on half-sib families and on applied biotechnology methods: pre-sowing seeds treatment with CP and EMF. As a result, according to different half-sib tree's response to physical stressors, we could submit recommendation guides for forestry industries that could help to reduce pest's damage for forests in the future.

METHODS

P. Sylvestris seeds were collected from second generation pine seeds orchard in Dubrava regional in Lithuania. The seeds were treated with three different types of stressors: 1) cold plasma 1 minute (CP1); 2) cold plasma 2 minutes (CP2); 3) electromagnetic field 1 minute (EMF1).

Seeds treatment with CP and EMF. **CP**: Seeds were treated using a controlled DBD device that had produced in Kyushu University, Japan [13]. The treatment times were 1 and 2 min. at

a distance of 5 mm between the seeds surface and the electrode plate. **EMF**: Seeds were placed in plastic bags at the centre of the induction coil and exposed to the electromagnetic field 1 min. *Experimental conditions:* induction coil inside diameter 2.5 cm, outside diameter 3 cm.

After treatment (5 days) the seeds were sown in cassettes filled with peat substrate cultivated in blocked randomized cassettes at Laboratory of plantation forestry greenhouse (Girionys, Kaunas) (**Fig. 1**).
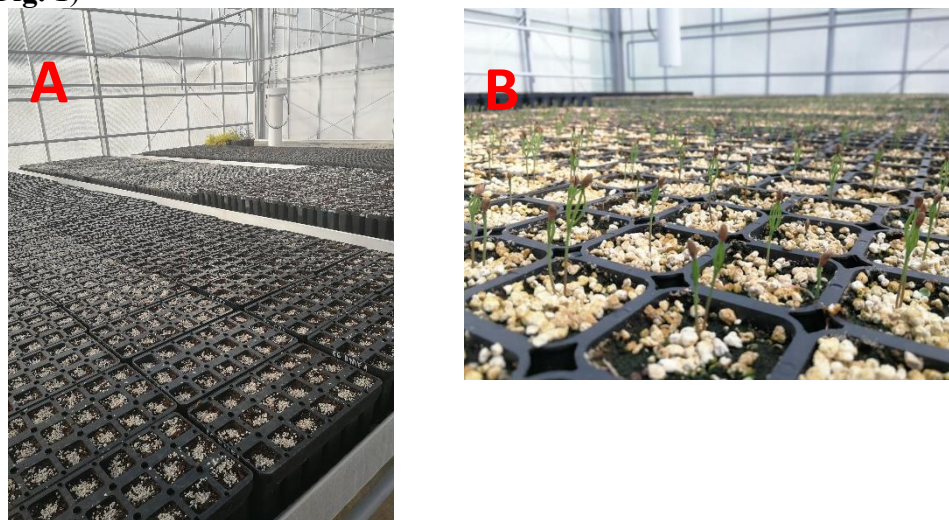
Fig. 1. *P. Sylvestris* seeds in cassettes (A) and the seedlings after 14 days since sowing (B) at Laboratory of plantation forestry greenhouse (Girionys, Kaunas)

Samples of *P. Sylvestris* needles were collected after first its vegetation period in autumn. **Total flavonoid content (TFC) and antioxidant activity:** TFC and antioxidant activity were determined using spectrophotometric method. TFC in needles extracts was determined according to method described in Dróżdż and Pyrzynska (2019) [14]. Antioxidant activity (ABTS assays) was determined according to Lučinskaitė et al. (2021) [15]. Absorbance (470 nm TFC and 734 nm ABTS) was measured with Synergy HT Multi-Mode Microplate reader.

RESULTS

The study showed that the highest concentration of non-affected *P. sylvestris* seeds of TFC was determined in the seedlings of No. 4 (8.92±0.09) and 10J (8.00±0.10) half-sib families (**Table 1.**). In addition, it was established that all applied physical stressors had a positive impact on the TFC in the seedlings of No. 12, 10, and 12J half-sib families. All the applied stressors had the highest positive impact on the TFC in No. 10 Scots pine half-sib family. CP1 increased the TFC in the seedlings of No. 10 family by 3.03 mg g^{-1}, CP2 – 1.38 mg g^{-1}, EMF1 – 0.85 mg g^{-1}, compared to control. Both CP2 and EMF1 stressors had the positive impact on the TFC in No. 12, 10, 12J. CP1 increased the TFC in the seedlings of No. 5J, 12, 10, 12J, 17J, but decreased in No. 9 and 7J half-sib families.

Table 1. TFC in Scots pine half-sib families after first vegetation season.

Scots pine half-sib families	Control (±SE)	Treatment		
		CP1 (±SE)	CP2 (±SE)	EMF1 (±SE)
	Total flavonoid concentration, mg g^{-1}			
5J	6.11±0.02	6.70±0.03***	6.93±0.10***	6.04±0.23
12	6.75±0.08	8.11±0.08***	7.64±0.04***	8.51±0.11***
9	7.64±0.15	6.74±0.14**	7.21±0.18	6.47±0.10***
10	6.98±0.14	10.01±0.02***	8.36±0.40**	7.83±0.07**
4	8.92±0.09	8.57±0.20	7.56±0.08***	9.15±0.25
10J	8.00±0.10	8.35±0.01	7.48±0.19*	6.78±0.20***
2J	7.32±0.10	7.42±0.08	6.30±0.09***	6.77±0.10**
12J	5.33±0.15	6.05±0.06***	5.78±0.12*	5.75±0.11*
17J	7.60±0.17	8.62±0.48*	7.58±0.02	7.24±0.44
1	6.67±0.16	6.63±0.03	6.81±0.18	8.52±0.76*
7J	7.04±0.09	6.09±0.07***	6.01±0.06***	5.85±0.12***

Significant differences between affected and control seeds are shown with * (*$p<0.05$; **$p<0.005$; ***$p<0.001$)

Our results revealed that the highest antioxidative capacity (used by ABTS test) between control seedlings was determined in the seedlings of No. 4 (888.77±39.3 µmol/g) family **(Table 2.).** Statistically significant increase of antioxidant activity was determined in effect of both CP1 and CP2. The results showed that ABTS in the seedlings of No. 12 family after CP1 increased by 110.98 µmol g^{-1}, after CP2 by 103.17 µmol g^{-1}, compared to control.

Table 2. Antioxidant activity in Scots pine half-sib families after first vegetation season.

Scots pine half-sib families	Control (±SE)	Treatment		
		CP1 (±SE)	CP2 (±SE)	EMF1 (±SE)
	ABTS radical scavenging activity, µmol g^{-1}			
5J	477.30±21.4	498.24±12.2	544.91±30.1	513.42±20.0
12	565.37±21.1	676.35±24.1**	668.54±29.2*	607.41±47.5
9	569.23±16.1	696.35±75.8	781.39±91.2*	577.24±34.7
10	746.87±53.9	684.09±28.8	620.38±80.8	570.89±26.7*
4	888.77±39.3	905.03±48.2	734.17±30.6*	821.77±73.5
10J	731.09±24.4	679.27±38.8	758.08±48.0	705.91±25.6
2J	575.58±11.7	538.47±19.4	444.38±25.9***	413.38±25.3***

12J	359.53±16.4	407.81±27.1	443.51±15.5**	403.43±25.5
17J	419.06±21.9	488.43±22.5*	377.36±14.3	461.89±22.0
1	584.12±20.0	597.86±16.6	532.18±13.7*	421.01±16.0***
7J	585.01±37.9	452.85±11.6*	442.31±33.2*	446.19±22.9*

Significant differences between affected and control seeds are shown with * (*$p<0.05$; **$p<0.005$; ***$p<0.001$)

CONCLUSIONS

This study showed that different Scots pine half-sib families accumulate different amount of biological activity compounds and antioxidant activity. Furthermore, results showed that seeds treatment with cold plasma and electromagnetic field had a positive influence on Scots pine resistance mechanisms against pathogens, since the increase of concentration on compounds (total flavonoids content and antioxidant activity) can be indicate the tree's resistance for pests.

Keywords: half-sib families, pathogens, physical stressors, *P. Sylvestris*, flavonoids, antioxidant activity

REFERENCES

1. Lithuanian state forest service. 2019. Forest resource. P.12-25.

2. SIRGEDAITĖ-ŠĖŽIENĖ, V.; MARČIULYNAS, A.; BALIUCKAS, V. Effect of Extracts from Dominant Forest Floor Species of Clear-Cuts on the Regeneration and Initial Growth of Pinus sylvestris L. with Respect to Climate Change. *Plants*, 2021, Vol. 10, issue 5, P. 1-19.

3. MUKRIMIN, M.; KOVALCHUK, A.; GHIMRE, R. P.; KIVIMAENPAA, M.; SUN, H.; HOLOPAINEN, J. K.; ASIEGBU, F. O. Evaluation of potential genetic and chemical markers for Scots pine tolerance against Heterobasidion annosum infection. *Planta*, 2019, Vol. 25, P. 1881-1895.

4. METLA. Forest Finland in Brief, 2013. Link to the internet <http://jukuri.luke.fi/bitst ream/handle/10024/529892/Forest-Finland_2013.pdf?seque nce=1&isAllowed=y.>

5. WITZELL, J.; MARTIN, J. A. Phenolic metabolites in the resistance of northern forest trees to pathogens – past experiences and future prospects. *Canadian Journal of Forest Research*, 2008, Vol. 38, P. 2711–2727

6. BRAGA, R. M.; DOURADO, M. N.; ARAUJO, W. L. Microbial interactions: ecology in a molecular perspective. *Brazilian Journal of Microbiology*, 2016, P. 86-98.

7. PASCALE, A.; PROIETTI, S.; PANTELIDS, L.; STRINGLIS, I. Modulation of the Root Microbiome by Plant Molecules: The Basis for Targeted Disease Suppression and Plant Growth Promotion. *Frontiers in Plant Science*, 2020, Vol. 10.

8. PHENAL, W.; LIU, W.T.; POGLIANO, K.; DORRESTEIN, P. Microbial metabolic exchange-the chemotype-to-phenotype link. *Nature Chemical Biology*, 2011, Vol. 52, P. 26-35.

9. FILATOVA, I.; KALATSKAYA, J.; CHUBRIK, N.; MILDAZIENE, V. Application of plasma and radio wave technologies in agriculture: protection of plants, improvement of plant growth and yield. *Plasma Physics and Plasma Technology*, 2018, Vol. 9, P. 323-327.

10. JIANG, J.; XE, X.; LI, L.; LI, J.; SHAO, H.; XU Q.; YE, R.; DONG, Y. Effect of Cold Plasma Treatment on Seed Germination and Growth of Wheat. *Plasma Science and Technology*, 2014, Vol. 16, No.1. Doi: 10.1088/1009-0630/16/1/12.

11. STARIČ, P.; VOGEL-MIKUŠ, K.; MOZETIČ, M.; JUNKAR, I. Effects of Nonthermal Plasma on Morphology, Genetics and Physiology of Seeds: A Review. *Plants*, 2020. doi: 10.3390/plants9121736.

12. BHARWAJ, J.; ANAND, A.; NAGRAJAN, S. Biochemical and biophysical changes associated with magnetopriming in germinating cucumber seeds. *Plant Physiology and Biochemistry*, 2012, P. 67–73.

13. SARINONT, T.; AMANO T.; ATTRI, P.; KOGA, K.; HAYASHI, N.; SHIRATANI, M. Effects of plasma irradiation using various feeding gases on growth of Raphanus sativus L. *Archives of Biochemistry and Biophysics,* 2016, Vol. 605, P. 129-140.

14. DRODZ, P.; PYRZYNSKA, K. Extracts from pine and oak barks: phenolics, minerals and antioxidant potential. *International Journal of Environmental Analytical Chemistry*, 2019, Vol. 101, P. 464-472.

15. LUČINSKAITĖ, I.; LAUŽIKĖ, K.; ŽIAUKA, J.; BALIUCKAS, V.; ČĖSNA, V.; SIRGEDAITĖ-ŠĖŽIENĖ, V. Assessment of biologically active compounds, organic acids and antioxidant activity in needle extracts of different Norway spruce (Picea abies (L.) H. Karst) half-sib families. *Wood Science and Technology*, 2021, Issue 5, P. 1221–1235.

INFLUENCE OF *USTILAGO MAYDIS* ON THE CHEMICAL COMPOSITION AND AEROBIC STABILITY OF MAIZE SILAGE

l. Merkeviciute - Venslove, E. Venslovas E, A. Slepetiene, J. Ceseviciene, A. Mankeviciene

Lithuanian Research Centre for Agriculture and Forestry,
Instituto al. 1, LT-58344 Kedainiai – Lithuania
+370 63189983
lauksme.merkeviciute-venslove@lammc.lt

EXTENDED ABSTRACT

OVERVIEW

Maize silage is the basic feed used in beef and dairy production [1]. As a result, cattle breeders are interested in the consequences of ensiling plants infected by smut. Maize smut (*Ustilago maydis*) is a fungal disease that occurs in Lithuania and other countries at varying intensities that depends on the weather and agro-technical conditions, the occurrence of other fungal diseases and pests [2, 3]. There are reports that smut can produce toxic substances that reduce value of the silage [4]. The aim of this experiment was to assess the chemical composition and aerobic stability of silage, made from smut-free and smut-infected maize.

METHODS

General

Individual whole corn plants grown in Lithuanian Research Centre for Agriculture and Forestry research fields were harvested by hand. All plants were *Duxxbury* hybrids in kernel dough stage (BBCH 85). Approximately 44% of maize were infected with corn smut in the field. Stalks were cut at around 15 cm above the soil surface. The whole corn plants were divided into two groups: maize, where the ear was visibly and severely infected with *Ustilago maydis* and maize, where the ear was not visibly infected (Picture 1). It was chopped to an average length of 2 cm in a forage chopper. The plants were divided into two treatments: 0% infected and 100% infected. After thorough mixing, the fresh forage (FF) was ensiled in triplicate at approximately 1 kg (fresh weight) in polyethylene bags (28 cm x 40 cm, thickness of 100 and 130 μm, Status Innovations Co., Metlika, Slovenia) and sealed using a vacuum packing machine. After bags were filled with fresh matter, a temperature sensor (Tempmate. ®-S1 Single-Use USB Data Logger, Heilbronn, Germany) was inserted in the middle of each bag. Packed silages were kept in ambient temperature (20 - 22 °C) for 90 days before initial opening.

To start the inflow of oxygen, the bags were opened. The experiment has been conducted with the bags in a horizontal position. Samples were taken on the day of opening and on the 3rd, 7th, 14th and 28th day of aerobic exposure. The sensors were left in the bags during the whole aerobic stage.

Fig. 1. A – smut-free corn cob, B – smut-infected corn cob.

Chemical analysis

Dry matter (DM) content was determined by drying samples at 105 °C for 48 h in a forced-air oven until the weight of the samples was stable. Near infrared spectroscopy calibration equations (ADAS, UK) were used for the prediction of crude protein (CP), starch, neutral detergent fibre (NDF), acid detergent fibre (ADF), fermentation index (FI), metabolic energy (ME), net energy of lactation (NEI), crude fibre (CF), crude fat data, using a NIRS-6500 device with a sample spinning module (Foss-Perstorp, USA), selecting wavelengths between 400 and 2500 nm in reflectance spectra. For NIRS determination, the samples were oven-dried at 65 ± 5 °C temperature to a constant weight and grounded in an ultra-centrifugal mill ZM 200 (Retsch, Germany) to pass a 1 mm screen. Then dried samples were scanned in three replications using cuvettes, and the acquired spectra were processed with equations used in the device (ADAS, UK). Crude ash (CA) content was determined as the mass left after sample incineration at 550 (±10) °C. pH was measured in water extract, by a potentiometric method, using a pH meter (Horiba, UK). Samples that showed inconsistency underwent repeated chemical analysis.

Statistical analysis

Statistical analysis was conducted using packages from the software IBM SPSS Statistics 25 (IBM, USA). Significant differences between the samples were calculated using t-Test: Paired Two Sample for Means. Values with $P \leq 0.05$ were considered statistically significant. Correlation analysis was performed to examine the quantitative relationship between the investigated variables. The significance level was calculated with a regression analysis tool in Excel, data were significant when $P \leq 0.05$.

RESULTS

As shown in the Table 1, smut-free maize characterized with a higher amount of dry matter (329.1 g kg^{-1}), CP (71.3 g kg^{-1}), ADF (255.8 g kg^{-1}), NDF (518.1 g kg^{-1}) and starch (237.2 g kg^{-1}

[1]), than smut-infected maize. However, smut-infected forage had higher amounts of crude fibre (243.0 g kg^{-1}) and crude ash (48.5 g kg^{-1}).

Table 1. Chemical composition of whole corn plants before ensiling.

Item	Smut-free forage	Smut-infected forage
Dry matter, g kg^{-1}	329.1	308.6
g kg [-1] DM		
crude protein	71.3	70.5
crude fibre	216.6	243.0
ADF	255.8	246.1
NDF	518.1	484.6
Starch	237.2	201.3
crude ash	40.8	48.5

Most significant differences between smut-free and smut-infected whole plant corn silages were found in pH and NDF, as it was higher in smut-infected than in smut-free corn silage during the whole period of aerobic exposure; CF with 30.7 g kg^{-1} and 27.6 g kg^{-1} was also higher on the day of the opening and on the 3rd day after it; starch and metabolic energy as it was lower in smut-infected corn silage than smut-free, within the streak of aerobic exposure. Smut-infected maize silage had a significant DM loss during the whole period.

Table 2. Chemical composition of whole corn plant silage after the opening.

Item	Smut-free maize silage			Smut-infected maize silage		
Days after the opening	0	3	7	0	3	7
Dry matter, g kg^{-1}	301.2	335.1	351.0	324.8*	323.0	306.0**
pH	4.1	4.0	4.1	4.3**	4.3**	4.3**
metabolic energy, MJ/kg DM	10.9	10.7	10.7	10.7	10.47*	10.4*
net energy of lactation, MJ/kg DM	6.6	6.5	6.5	6.5	6.3*	6.2**
g kg [-1] DM						
crude protein	93.8	93.7	88.8	85.3*	94.8	91.4
crude ash	54.1	54.4	55.6	54.1	53.0	53.5
NDF	385.8	405.4	405.8	378**	411.6***	448.4***
ADF	210.1	213.8	217.0	201.9	220.3	221.8
crude fibre	188.0	194.0	200.3	200.1	208.0	217.6*
starch	237.3	229.0	223.0	162.0**	156.0***	140.0***
crude fat	24.9	24.4	23.3	30.7***	27.6**	22.3**

NOTE. * - asterisks show if smut-infected corn silage chemical composition indicators differed significantly from smut-free corn silage on the day of initial opening, on the 3rd and on the 7th day after it.

CONCLUSIONS

In conclusion, silage obtained from maize plants not infected with smut (*Ustilago maydis*) showed a lower pH and also had higher amounts of metabolic energy, net energy of lactation and starch within the period of aerobic exposure. Smut-infected maize silage distinguished with

higher amounts of neutral-detergent fibre and crude fibre. Silage made from maize infected with smut does not necessarily differ significantly from that made from smut-free plant material, but it might have a lower aerobic stability, as it showed a loss in dry matter and higher pH. The inclusion of silage additives before ensiling can in part prevent deterioration of silage quality while using smut-infected plants.

Keywords: corn, maize, smut, silage quality.

REFERENCES

1. ABBAS, H.K.; SHI ER,W.T.; PLASENIA, J.; WEAVER, M.A.; BELLALOUI, N.; KOTOWICZ, J. K.; BUTLER, A. M.; ACCINELLI, C.; TORRE-HERNANDEZ, M. E.; ZABLOTOWICZ, R. M. Mycotoxin contamination in corn smut (*Ustilago maydis*) galls in the field and in the commercial food products. *Food control*, 2017, Vol. 71, p. 57-63.

2. POTKANSKI, A.; GRAJEWSKI, J.; TWARUZEK, M.; SELWET, M.; MIKLASEWSKA, B.; BLAJET-KOSICKA, A.; SZUMACHER-STRABEL, M.; CIESLAK, A.; RACZKOWSKA-WERWINSK K. Chemical composition, fungal microflora and mycotoxin content in maize silages infected by smut (Ustilago maydis) and the effect of biological and chemical additives on silage aerobic stability. *Journal of Animal and Feed Sciences*, 2010, Vol. 19, p. 130-142.

3. DU TOIT, J.; POTAKY, J. Effect of silk maturity and pollination on infection of maize ears by Ustilago maydis. *Plant disease*, Vol. 83, No. 7, p. 621-626.

4. DORSZEWSKI, P.; GRABOWICZ, M. The mycological status of green forages and silages from a mixture of legumes with grasses and whole crop maize. *Folia Pomeranae Universitatis Technologiae Stetinensis, Agricultura, Alimentaria, Piscaria et Zootechnica*, 2017, Vol. 338, No. 44/4, p. 33-39.

COMPARISON OF THE FERTILISATION VALUE OF LIQUID ORGANIC FERTILISERS – ANAEROBIC DIGESTATE AND PIG SLURRY

D. Petraitytė, J. Cesevičienė, A. Šlepetienė
*Chemical Research Laboratory, Institute of Agriculture, Lithuanian Research Centre for
Agriculture and Forestry (LAMMC),
Instituto str. 1. LT- 58344 Kedainiai – Lithuania*
danute.petraityte@lammc.lt, jurgita.ceseviciene@lammc.lt

A. Arlauskienė
*Joniskelis Experimental Station, Lithuanian Research Centre for Agriculture and Forestry
Karpiu str. 1, LT – 39301, Joniskelis – Lithuania*
ausra.arlauskiene@lammc.lt

EXTENDED ABSTRACT

OVERVIEW

Organic fertilisers require less resource imports than mineral nitrogen to support soil productivity. Digestate is an alternative source of nutrients that is used in sustainable agriculture as a biological fertiliser and soil improver. Recycling the digestate back to soil valuable nutrients such as nitrogen, potassium, phosphorus and organic carbon for plants is the circular economy concept case [1]. However, it should be noted that in the digestate there are more nutrients than usual NPK and, based on that, its actual economic potential increases [2]. It is known that chemical composition of anaerobic digestate and pig slurry influence soil processes as well as N emission after the field application [3, 4].
The aim of this research was to compare the chemical composition and other characteristics of two liquid organic fertilisers - biogas digestate and pig slurry.

METHODS

The chemical composition of liquid organic fertilisers - pig slurry and anaerobic digestate - was researched in 2019-2021. Pig slurry was obtained from pig farm (55°42′54.8 "N 23°46′33.4″ E, Kauleliskiai, Radviliskis district, Lithuania). Liquid anaerobic digestate – after controlled biological decomposition in biogas plant (56°03′54.6 "N 23°59′13.9″ E, Veselkiai, Pakruojis district, Lithuania) where the main feedstock was pig slurry and industrial crop residues: molasse, mill waste, starch feedstock, pulp, sugar beet pulp. The samples of fertilisers (~2L) were sampled from the storage lagoons in every spring before the main fertilisation that to determine fertiliser basic characteristics.

Analysis of liquid organic fertilisers. The pH was measured by the potentiometric method immediately after the homogenization of the fresh sample. Dry matter (DM) content was measured by drying to a constant weight at 105°C in a forced-air oven. The content of total nitrogen (N_{tot}) was determined by the Kjeldahl method using a spectrophotometric measuring

procedure at 655nm wavelength. Ammonium (N-NH$_4$) and nitrate (N-NO$_3$) nitrogen was analysed spectrophotometrically using HACH Lange LCK 302 and LCK 339 cuvette tests. The total organic carbon (C$_{org}$) content and mobile humic acids (MHA) and mobile humic substances (MHS) were determined after wet combustion by a spectrophotometric measurement at 590nm with glucose as a standard. Complete quantification procedure of mobile humic substances (MHS) and mobile humic acids (MHA) described at Slepetiene et al. [9]. Mobile fulvic acids (MFA) was calculated as difference between MHS and MHA concentrations. The total phosphorus (P) concentrations were quantified spectrophotometrically by a colour reaction with ammonium molybdate vanadate reagent at wavelength 430nm. The total potassium (K) content was determined by the flame atomic absorption. Before determination of N$_{tot}$ and phosphorus the samples were wet digested with sulphuric acid (H$_2$SO$_4$), before determination of potassium - with nitric acid (HNO$_3$) and hydrogen peroxide (H$_2$O$_2$).

Statistical analysis (standard error - SD and data variation - V) of fertiliser characteristics comparing 2 liquid organic fertilisers was calculated using STAT ENG program and basic characteristics analysis was run.

RESULTS

Both liquid organic fertilisers had an alkaline pH; hence, the use of such fertilisers shouldn't have acidifying effect on the soil. The results have revealed that liquid organic fertilisers DM quantity was lower during the dry season (see Table 1). The values N$_{tot}$ varied less, especially in anaerobic digestate (V = 19.1%). By looking at Table 1, one can see that in the majority of cases N$_{tot}$ concentrations were found higher in the pig slurry than in digestate. Mineralized and plant available N (N-NH$_4$ + N-NO$_3$) ranged from 62.3 to 80.6 % in pig slurry (on average 70.2) and from N$_{tot...}$ 60.8 to 83.9 % in anaerobic digestate (on average 71.8 %). Data have shown the predominance of nitrogen dissolved in water in NH$_4$ form. Depending on environmental and soil conditions, when the soil is fertilised with pig slurry or digestate, N-NH$_4$ from these fertilisers is converted to N-NO$_3$. This is due to the influence of soil moisture and temperature [6], as it determines the activity of urease, nitrifying communities as well as nitrification rate in soil [7]. Therefore, slurries and digestates may pose danger to the environment due to the environment due to evaporation of ammonia or nitrate leaching [8].

Table1. Characteristic of liquid organic fertilisers.

Year	pH	DM	N$_{tot.}$	N-NH$_4$	N-NO$_3$	C$_{org.}$	MHS	MHA	MHA: MFA	C:N	P	K
					g kg^{-1}						g kg^{-1}	
Pig slurry												
2019	7.50	14.3	2.32	1.86	0.010	4.53	3.85	0.40	0.12	1.95	0.23	1.44
2020	7.65	31.6	2.36	1.65	0.018	7.41	3.40	1.18	0.53	3.14	0.25	1.66
2021	6.86	40.4	4.74	2.94	0.012	12.87	7.66	1.78	0.30	2.72	0.97	2.05
Mean	**7.34**	**28.8**	**3.14**	**2.19**	**0.014**	**8.27**	**4.97**	**1.12**	**0.32**	**2.60**	**0.48**	**1.72**
SE	*0.24*	*7.66*	*0.80*	*0.41*	*0.003*	*2.45*	*1.35*	*0.40*	*0.12*	*0.35*	*0.24*	*0.18*
V	*5.72*	*46.1*	*44.1*	*32.2*	*34.2*	*51.2*	*47.1*	*61.7*	*65.7*	*23.1*	*87.5*	*18.0*
Anaerobic digestate												
2019	8.20	8.0	1.87	1.56	0.009	1.82	1.57	0.21	0.15	0.97	0.07	1.14
2020	7.72	27.5	2.76	1.66	0.017	10.44	4.18	1.78	0.74	3.78	0.37	1.69
2021	7.77	13.9	2.38	1.79	0.017	4.46	3.12	1.37	0.78	1.87	0.28	0.47
Mean	**7.90**	**16.5**	**2.34**	**1.69**	**0.014**	**5.57**	**2.96**	**1.12**	**0.56**	**2.21**	**0.24**	**1.43**
SE	*0.15*	*5.78*	*0.26*	*0.06*	*0.002*	*2.55*	*0.76*	*0.47*	*0.20*	*0.83*	*0.09*	*0.16*
V	*3.34*	*60.7*	*19.1*	*6.51*	*29.8*	*79.2*	*44.4*	*72.7*	*62.8*	*64.9*	*64.3*	*19.2*

Note: DM - dry matter; Ntot – total nitrogen; N-NH4 - ammonium nitrogen; N-NO3 - nitrate nitrogen; P – total phosphorus; K – total potassium; Corg. – total organic carbon; MHS – mobile humic substances; MHA – mobile humic acids; MFA – mobile fulvic acids; SE – standard error; V - coefficient of variation.

All concentrations of elements and compounds are expressed on natural substance basis.

Anaerobic digestates are classified as more mineralized fertilizers, thus resulting in less $C_{org.}$ And active humus (MHS) as compared to pig slurry. Mobile humic acids (MHA), which are classified as active humus forms and have a low C and increased N content, formed a small part of $C_{org.}$ and did not differ from fertilizer types. However, a significant data of MHA variation was found (V_{PS} = 61.7%, VD = 72.7%). MHA: MFA index showed that most humified substances parts were found in anaerobic digestate, and not in the slurry.

Data have also revealed that narrow carbon to nitrogen (C: N) ratio determines the degradability of organic matter in both fertilizers as well as the availability of N for plants.

The greatest variation in C: N data was observed in anaerobic digestate (V_D = 64.9%). Availability of organic fertilizer N may be reduced by applying agronomic practice. The findings have revealed that pig slurry is richer in P and K than digestates.

The findings have emphasized the potential of digestates not only as a source of nutrients but also as a plant growth stimulator (MHS, MHA) and a soil improver (pH, Corg). Since anaerobic digestate from biogas plants and pig slurry contain useful mineral nutrients (N, P, and K), they are important for crop growth and can be considered as valuable fertilizer.

CONCLUSION

Variations in chemical composition might have been caused by the use of animal feeding stuffs in pig farms and their quality. Nitrogen is one of the main factors shaping both soil fertility and crop productivity. Ntot and NH4 concentrations are lower in anaerobic digestate rather than in pig slurry. Therefore, the use of digestate fertilisers may require more labour force and higher energy costs as a result of a higher fertilisation rate. The forms of digestate Corg. Have shown a high level of humification, which may have a positive impact on soil.

Keywords: liquid anaerobic digestate, pig slurry, nutrients

REFERENCES

1. PROVENZANO, M. R.; CAVALLO, O.; MALERBA, A. D.; FABBRI, C.; ZACCONE, C.; Unravelling (maize silage) digestate features throughout a full-scale plant: A spectroscopic and thermal approach. *Journal of Cleaner Production*. 2018. Vol. 193, P. 372–378.

2. PENG, W.; PIVATO, A. Sustainable Management of Digestate from the Organic Fraction of Municipal Solid Waste and Food Waste Under the Concepts of Back to Earth Alternatives and Circular Economy. *Waste and Biomass Valorization*. 2019. Vol. 10, No. 2, P. 465–481.

3. SLEPETIENE, A.; VOLUNGEVICIUS, J.; JURGUTIS, L.; LIAUDANSKIENE, I.; AMALEVICIUTE, V. K.; SLEPETYS, J.; CESEVICIENE, J. The potential of digestate as a biofertilizer in eroded soils of Lithuania. *Waste Management*. 2020. Vol. 102, P. 441–451.

4. ZILIO, M.; PIGOLI, A.; RIZZI, B.; GEROMEL, G.; MEERS, E.; SCHOUMANS, O.; GIORDANO, A.; ADANI, F. Measuring ammonia and odours emissions during full field digestate use in agriculture. *Science of the Total Environment*. 2021. Vol. 782, P. 146-882.

5. GENG, Y.; WANG, J.; SUN, Z.; JI, C.; HUANG, M.; ZHANG, Y.; XU, P.; LI, S.; PAWLETT, M.; ZOU, J. Soil N-oxide emissions decrease from intensive greenhouse vegetable fields by substituting synthetic N fertilizer with organic and bio-organic fertilizers. *Geoderma*, 2021. Vol. 383, P. 114-730.

6. DROMANTIENÈ, R.; PRANCKIETIENÈ, I.; JODAUGIENÈ, D.; PAULAUSKIENÈ, A. The influence of various forms of nitrogen fertilization and meteorological factors on nitrogen compounds in soil under laboratory conditions. *Agronomy*. 2020. Vol. 10, No. 12.

7. SUTER, H. C.; PENGTHAMKEERATI, P.; WALKER, C.; CHEN, D. Influence of temperature and soil type on inhibition of urea hydrolysis by N-(n-butyl) thiophosphoric triamide in wheat and pasture soils in south-eastern Australia. *Soil Research*. 2011. Vol. 49, No. 4, P. 315–319.

8. MÖLLER, K. Effects of anaerobic digestion on soil carbon and nitrogen turnover, N emissions, and soil biological activity. A review. *Agronomy for Sustainable Development*. 2015. Vol. 35, No. 3, P. 1021–1041.

9. SLEPETIENE, A.; VOLUNGEVICIUS, J.; JURGUTIS, L.; LIAUDANSKIENE, I.; AMALEVICIUTE-VOLUNGE, K.; SLEPETYS, J.; CESEVICIENE, J. The potential of digestate as a biofertilizer in eroded soils of Lithuania. *Waste Management*. 2020, Vol.102, P. 441–451, and Doi: 10.1016/J.WASMAN.2019.11.008.

INFLUENCE OF DIFFERENT FORMS OF SULFUR FERTILIZERS AND APPLICATION TIME ON SULFUR AND NITROGEN CONTENT IN WINTER WHEAT

K. Poškus
Lithuanian Research Centre for Agriculture and Forestry,
Rumokai trial division
Instituto al. 1, Akademija, LT-58344 Kėdainiai distr. – Lithuania
+370 60423133
E-mail: kazimieras.poskus@lammc.lt

Z. Brazienė
Lithuanian Research Centre for Agriculture and Forestry,
Rumokai trial division
Instituto al. 1, Akademija, LT-58344 Kėdainiai distr. – Lithuania
E-mail: zita.braziene@lammc.lt

G. Staugaitis
Lithuanian Research Centre for Agriculture and Forestry,
Kaunas Agrochemical Research Laboratory
Instituto al. 1, Akademija, LT-58344 Kėdainiai distr. – Lithuania
E-mail: gediminas.staugaitis@lammc.lt

EXTENDED ABSTRACT

OVERVIEW

In the absence of sulphur, photosynthesis and protein synthesis are slowed down in plants, and non-protein nitrogen accumulates [1]. Of the crop grown area in Lithuania, sulphur is most needed by rapeseed, but it is also needed by other crops. Sulphur needs for winter wheat are 25-40 kg ha^{-1} [2], but if the leaching of sulphur is estimated, it loses 20-38 kg ha^{-1} during the long growing season of winter wheat [3].

Data from various researchers show unequal performance of sulphur fertilizers for winter wheat. In some experiments, both sulphur fertilizers applied to the soil in the spring or during additional fertilization during the growth increased the yield of winter wheat grain, as well it contained more protein [4; 5], better baking properties [6]. However, the opposite is also obtained when fertilization with sulphur did not increase wheat yield [7] or increased only in some years or in some areas [8].

The sulphur uptake of winter wheat is indicated by the total sulphur concentration in the plants, which must be at least 0.55% for winter wheat during the todllering stage [6]. However, the concentration of total sulphur is not a sufficient indicator for assessing its uptake, as it varies significantly during plant growth, depending on the meteorological conditions of the year, the

size of the plant mass [8]. In this case, the sulphur supply of wheat is better described by the ratio of nitrogen to sulphur (N: S), which in the aboveground part of the plant usually varies in the range of 7–15 during its growth 9]. The optimal range for the N: S ratio is 14-17 [6], 7, 5 in wheat grains [10].

In 2019-2021, at LAMMC Rumokai experimental station studies were carried out to investigate the influence of different forms of sulphur fertilizers and their application time on the sulphur and nitrogen content of winter wheat plants and grains and the relationship between the content of these substances in the leaves during vegetation and grain yield of winter wheat 'Janne' crop.

METHODS

In autumn, before sowing, wheat was fertilised with complex fertilizer NPK 5-21-36 at the rate of $N_{15}P_{63}K_{108}$. In spring, winter wheat was fertilised with nitrogen and sulphur fertilisers according to the research scheme:
1. UAN N_{60} + UAN N_{60} + UAN N_{30}
2. LD $N_{60}S_{15}$ + UAN N_{60} + UAN N_{30}
3. UAN N_{60} + LD $N_{60}S_{15}$ + UAN N_{30}
4. LD $N_{60}S_{15}$ + LD $N_{60}S_{15}$ + UAN N_{30}
5. UAN+Thio-Sul $N_{60}S_{4,9}$ + UAN N_{60} + UAN N_{30}
6. UAN+Thio-Sul $N_{60}S_{4,9}$ + UAN+Thio-Sul $N_{60}S_{4,9}$ + UAN N_{30}

Following fertilizers were used in the study: UAN is a liquid fertilizer with 32 % nitrogen (N) (ammonia N (N-NH$_4$) – 8%, nitrate N (N-NO$_3$) – 8%, amid N (N-NH$_2$) – 16%). LD is named Leader 24-6 liquid fertilizer, which consist of 24% of nitrogen (N) (ammonia N – 5%, nitrate N – 8%, amid N – 11%) and 6% of elemental sulphur (S). Thio-Sul is a liquid fertilizer with 12% nitrogen in the form ammonium (N-NH$_4$) and 26% sulphur in the form thiosulfate ($S_2O_3^{-2}$). The plants were fertilized in the spring after the vegetation resumed on 201-02-04, 2020-03-26, 2021-04-08, the second time 2019-04-26, 2020-04-22, 2021-05-05, the third - 2019-05 -23, 2020-06-03, 2021-06-09.

During wheat vegetation, herbicides, fungicides and insecticides were applied according to the need. The grain yield is given in absolutely pure seed mass at 14% moisture. In them, the crude protein was determined by the Kjeldahl method obtained by multiplying the total nitrogen by a factor of 6.25.

In order to assess the uptake of nitrogen and sulphur by plants, total nitrogen and total sulphur concentrations were determined in the aboveground mass at BBCH stages 30 and 59 during winter wheat growth.

RESULTS

In our study in 2019-2021. The average nitrogen content of winter wheat leaves in BBCH stage 29 ranged from 3.39 to 3.71% (Table 1). The studied fertilization options did not affect the nitrogen content in the leaves. At the BBCH 59 stage, the nitrogen content in the leaves was significantly reduced in the fields fertilized with the Leader 24-6 fertilizer at the BBCH 30 stage. At this stage, Leader 24-6 severely damaged the leaves of the plant. This may have contributed to nitrogen decrease in the leaves.

The sulphur content of the leaves at the stage BBCH 29 was 0.26-0.34%. When UAN-32 fertilizer was applied with Thio-Sul, the sulphur content increased reliably. Fertilization options studied at BBCH stage 59 did not affect the sulphur content in winter wheat leaves.

Table 1. Nitrogen and sulphur contents in winter wheat plants in absolutely dry matter

Variants	Nitrogen content, %		Sulphur content, %	
	BBCH 29	BBCH 59	BBCH 29	BBCH 59
1.UAN N_{60}+UAN N_{60}+UAN N_{30}	3.66	1.67	0.27	0.11
2.LD $N_{60}S_{15}$+UAN N_{60}+UAN N_{30}	3.39	1.6	0.26	0.12
3.UAN N_{60}+LD $N_{60}S_{15}$ UAN N_{30}	3.51	1.47	0.26	0.11
4.LD $N_{60}S_{15}$+LD $N_{60}S_{15}$+UAN N_{30}	3.53	1.36	0.29	0.1
5.UAN+Thio-Sul $N_{60}S_{4,9}$+UAN N_{60} +UAN N_{30}	3.61	1.67	0.34	0.12
6.UAN+Thio-Sul $N_{60}S_{4,9}$ + UAN+Thio-Sul $N_{60}S_{4,9}$ + UAN N_{30}	3.71	1.64	0.28	0.11
LSD_{05}	0.175	0.193	0.056	0.016

The highest grain yield was obtained by fertilizing winter wheat with UAN-32 with Thio-Sul fertilizer (Table 2). Fertilization of wheat with Leader 24-6 resulted in a significantly lower grain yield than fertilization with the same rate of UAN-32 fertilizer. The highest protein content in grains was determined in the fields fertilized with UAN-32 + Thio-Sul. This amount of protein was significantly different from other fertilization options.

Table 2. Yield and quality of winter wheat

Variants	Grain yield t ha^{-1}	Proteins, %
1.UAN N_{60}+UAN N_{60}+UAN N_{30}	6.907	12.02
2.LD $N_{60}S_{15}$+UAN N_{60}+UAN N_{30}	6.615	11.66
3.UAN N_{60}+LD $N_{60}S_{15}$ UAN N_{30}	6.728	11.32
4.LD $N_{60}S_{15}$+LD $N_{60}S_{15}$+UAN N_{30}	6.401	10.81
5.UAN+Thio-Sul $N_{60}S_{4,9}$+UAN N_{60} +UAN N_{30}	7.017	12.41
6.UAN+Thio-Sul $N_{60}S_{4,9}$ + UAN+Thio-Sul $N_{60}S_{4,9}$ + UAN N_{30}	7.072	12.39
LSD_{05}	0.185	0.377

CONCLUSIONS

The highest grain yield and protein content in grain were obtained by fertilizing winter wheat with a mixture of nitrogen fertilizer KAS-32 and sulphur fertilizer Thio-Sul.

Nitrogen and Sulphur Fertilizer Leader 24-6, used in stage BBCH 30, burned wheat leaves little bit, which could reduce nitrogen content in the leaves, grain yield and quality.

A reliable positive correlation was found between the nitrogen content in the leaves at BBCH stage 59 and the grain yield and protein content in the grain (correlation coefficients 0.47 **

and 0.74 **, respectively). The sulphur content in the leaves did not affect the grain yield at this stage but had a positive effect on the protein content in the grain (correlation coefficient 0.50 **).

Keywords: winter wheat, fertilizers, nitrogen and sulphur content in leaves, grain yield, proteins.

REFERENCES

1. SKWIERAWSKI, M.; BENEDYCKA, Z.; JANKOWSKI, K.; SKWIERAWSKI, A. Sulphur as a fertiliser component determining crop yield and quality. *Journal of Elementology*, 2016, Vol. 21, No. 2, P. 609–623

2. Schwefelversorgung von Kulturpflanzen – Bedarfsprognose und Düngung. VDLUFA. Standpunkt, 2000 [referred on the 20th of December in 2000 y.]. Link to the internet <https://www.vdlufa.de/Dokumente/Veroeffentlichungen/Standpunkte/03-schwefel.pdf>

3. ERCOLI, L.; ARDUINI, I.; MARIOTTI, M.; LULLI, L.; MASONI, A. Management of sulphur fertiliser to improve durum wheat production and minimise S leaching. *European Journal of Agronomy*, 2012, Vol. 38, P. 74-82.

4. STAUGAITIENĖ, R.; ŠLEPETIENĖ, A.; ŽIČKIENĖ, L. The effect of sulphur fertilisation on grain yield and quality of spring wheat. *Žemės ūkio mokslai*, 2013, Vol. 20, No 4, P. 266-275.

5. KLIKOCKA, H.; CYBULSKA, M.; BARCZAK, B.; NAROLSKI, B.; SZOSTAK, B.; KOBIAŁKA, A.; NOWAK, A.; WÓJCIK, E. The effect of sulphur and nitrogen fertilization on grain yield and technological quality of spring wheat. *Plant, Soil and Environment,* 2016, Vol. 6, No. 5, P. 230–236.

6. SEDLAR, O.; BALIK, J.; KULHANEK, M.; CERNY, J.; SURAN, P. Sulphur nutrition index in relation to nitrogen uptake and quality of winter wheat grain. *Chilean Journal of Agricultural Research,* 2019, Vol. 79, No. 3. <http://dx.doi.org/10.4067/S0718-58392019000300486>

7. DHILLON, J.; DHITAL, S.; LYNCH, T.; FIGUEIREDO, B.; OMARA, P.; RAUN, W. R. The effect of soil and foliar sulphur application on winter wheat yield and soil properties. *Agrosystems, Geosciences & Envinonment,* 2019, Vol. 3, P. 1-8.

8. KULHÁNEK, M.; BALÍK, J.; ČERNÝ, J.; PEKLOVÁ, L.; SEDLÁŘ, O. Winter wheat fertilizing using nitrogen–sulphur fertilizer. *Archives of Agronomy and Soil Science*, 2014 Vol. 60, No. 1, P. 67–74.

9. KANAL, A.; KAUTZ, T.; ELLMER, F.; RÜHLMANN, J. Effects of long-term organic and mineral fertilization on sulphur and nitrogen supply of spring barley in Berlin-Dahlem (Germany) and Tartu (Estonia). *Archives of Agronomy and Soil Science*, 2003, Vol. 49, P. 543 – 553.

10. JAMAL, A.; MOON, Y. S.; ABDIN, M. Z. Sulphur – a general overview and interaction with nitrogen. *Australian Journal of Crop Science,* 2010, Vol. 4, No. 7, P. 523-529. <Doi/epdf/10.2134/age2018.10.0047>

ENUMERATION AND SCREENING OF CELLULOLYTIC BACTERIA ISOLATED FROM THE SOIL OF CEREAL-BASED CROPPING SYSTEM

A. Shamshitov, S. Supronienė, G. Kadžienė
Lithuanian Research Centre for Agriculture and Forestry,
Institute of Agriculture
Studentu St. 15A, Akademija, LT-53362 Kaunas distr. – Lithuania
arman.shamshitov@lammc.lt, skaidre.suproniene@lammc.lt, grazina.kadziene@lammc.lt

EXTENDED ABSTRACT

OVERVIEW

Crop residues are plant remnants that remain in the field after crop harvest. Straw, roots, shafts, and other tissues of maize, wheat, and rice account for the majority of agricultural residues generated each year, accounting for 40.6 %, 24.2 %, and 15.7 %, respectively [1,2]. Wheat straw is among the most common cereal crop residues with high cellulose, hemicellulose, and lignin content. According to data from the statistics website, grain crop production in Lithuania in 2020 was 6.5 million tonnes [3]. The amount of straw gathered in Lithuania from all sorts of crops differs year to year, but during the previous five years, an average of 3 million tonnes of straw has been collected annually [4, 5]. Crop residues contain approximately 3.0 to 8.2 kg of nitrogen, 0.2 to 0.6 kg of phosphorous, and 7.2 to 23.3 kg of potassium per ton dry matter, in addition to organic carbon [6, 7]. In particular, their biochemical composition and physical structure influence the mineralization process [8].

Fungi are the primary producers of cellulose-degrading enzymes with the highest level of cellulose production [9]. However, in addition to fungi, bacteria are currently considered promising candidates for future strategies because of their broad functional biodiversity and versatility [10]. Certain bacterial strains isolated from agricultural soil showed the ability to degrade cellulose. Most of these bacterial strains belong to genera such as *Cellulomonas* sp, *Cellvibrio* sp, *Clostridium* sp, *Pseudomonas* sp and *Bacillus* sp [11, 12, 13, and 14].

Plant residue decomposition is a key biochemical cycle activity that provides nutritional resources to plant and microbial populations. The role played by the microbial community in regulating complex processes, such as decomposition of crop residues has been inappropriately investigated, but it has been increasingly recognized and demonstrated to be an important factor [15, 16]. Since information about bacterial strains with a cellulolytic activity that decomposes field crop residues, particularly in Lithuania very limited, the present study is conducted to isolate and evaluate potential bacteria.

METHODS

Soil samples were collected in the spring of 2021 from two factorial field experiments that are being conducted in the Institute of Agriculture, Lithuanian Research Centre for Agriculture and Forestry. A factor is different tillage treatments (ploughing – P, harrowing – H, and no-tillage

– NT), and B factor cover crop management (with cover crop – C and without cover crop – W). Cereal cropping sequences consisting of five-member crop rotations (winter wheat - winter rape - spring wheat - spring barley – pea) has a history of more than three complete rotation cycles. In the year of soil sampling, winter wheat was grown. Cover crop white mustard established at pre-harvest of spring barley in 2019. The number of colony-forming units (CFU) of cellulolytic bacteria from different tillage and cover crop management treatments was evaluated on cellulose Congo red agar (CRA) [17]. Bacteria able to use the cellulose on CRA produce the distinct zones around their colonies, which gave a possibility to separate from those that did not produce cellulose. In order to select potential bacterial strains, cellulolytic bacteria were isolated on two selective media: cellulose agar and carboxymethyl cellulose agar (CMC) using the spread plate technique. All different bacterial colonies that appeared on the plates of the two selective media were selected and subjected to the purification process.

All purified isolates were screened for celluloses production on CMC agar plates using Congo red reagent [18] and an iodine solution indicator according to Kasana et al. [19]. The clear zone around the bacterial colony indicated cellulose degradation. The hydrolysis capacity values of primary and secondary screening were calculated as a ratio of clear zone size to colony diameter. Confirmation of cellulose-degrading ability of microbial isolates performed by streaking on the CRA media. Colonies showing a discolouration of Congo red have been taken as positive cellulose-degrading microbial colonies [17]. Selected bacterial isolates were also tested for degradation of other main plant cell polymers such as lignin, and hemicellulose using methylene blue [20] and Congo red [21] respectively. The discolouration of methylene blue has been used as an indicator of lignin peroxidase enzyme activity [22]. The ability of bacteria to degrade xylan, which is a type of hemicellulose, was evaluated by staining xylan agar plates with Congo red reagent. The appearance of the halo zone after staining with Congo red indicates that xylanase is secreted by bacterial culture.

All the results reported are the means of three replicates. Enumeration data of cellulose-degrading bacteria isolated from soil were subjected to two-way analysis of variance (ANOVA) and tested for its significance using LSD (least significant difference) at $P < 0.05$ level.

RESULTS

The influence of different tillage and cover crop management practices on the quantity (count of CFU) of cellulolytic bacteria is shown in Fig. 1. The results showed that there are no significant differences in the number of CFU among compared soil management practises. However, there is a tendency towards an increase in the number of CFU with reduced-tillage (harrowing) and with no-tillage compared to conventional tillage (ploughing).
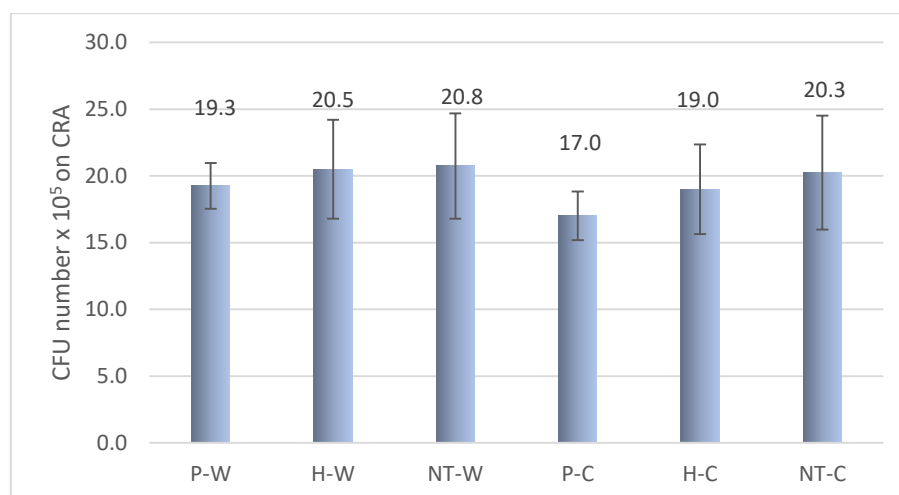
Fig. 1. Enumeration of cellulose-degrading bacteria from different tillage treatments and cover crop management. CFU – colony-forming unit; CRA – cellulose Congo red agar; P – ploughing; H – harrowing; NT no-tillage; C - with cover crop and W - without cover crop. Vertical bars explain the standards deviation of four field replications.

A total of 159 cellulolytic microbial strains were selected based on shape, size, and colony characteristics, and 61 isolates showed cellulolytic activity according to primary screening. Soil sample from H-W treatment showed the highest number of cellulolytic bacteria with 13 isolates (21.31%) followed by P–W - 12 isolates (19.67%), NT–C - 11 isolates (18.03%), NT–W – 10 isolates (16.39%), H–C – 10 isolates (16.39%) and P–C - 5 isolates (8.21%). The primary screening showed that clear zones ranged from 5 to 54 mm, and hydrolysis capacity ranged from 2.1 (H-C.18) to 8.0 (NT-C.25.2). These results are similar to the findings reported by Lu et al. [23], who observed maximum clearing zones ranging between 25 to 64 mm with a maximum hydrolysis capacity value of 4.85-13.11. However, based on the secondary screening, only thirty-eight strains exhibited a cellulolytic zone around the colonies after staining the plates with iodine solution. The hydrolysis capacity values of the cellulolytic bacterial isolates were estimated and varied from 1.5 to 6.7. The cellulolytic bacterium strain HW.18 isolated from soil of harrowing without cover crop had the highest hydrolysis capacity 6.7. Based on the results of this screening greatest number of bacterial isolates that showed halo zone was isolated from soil sample where harrowing without cover crop was used. Confirmation of cellulose-degrading ability of bacterial isolates was performed by streaking on the cellulose Congo red agar. Out of 61 isolates, 47 showed discolouration of Congo red. Changes in the colour of the medium from blue to clear were observed for 5 bacterial strains, which confirms their ability to degrade lignin. The abilities of soil bacterial isolates to break down and assimilate lignin as the primary carbon source aligned with Umashankar et al. [24] findings. Thirteen bacterial isolates were able to degrade hemicellulose. The hydrolysis capacity value ranged from 1.3 (NT-C.32) to 8.0 (P-W.49).

CONCLUSIONS

In our study, it was observed that among sixty-one isolates that showed celluloses activity, twenty-five of them were characterized by the high potent ability to degrade cellulose in all screening assays including Congo red, iodine solution and confirmation test on cellulose Congo red agar. Likewise, the findings indicate that five bacterial isolates have the ligninolytic ability and thirteen isolates xylanolytic.

Keywords: crop residue, cellulose, cellulolytic bacteria

REFERENCES

1. JIANG, D.; ZHUANG, D.; FU, J.; Huang, Y.; WEN, K. Bioenergy potential from crop residues in China: availability and distribution. *Renewable and Sustainable Energy Reviews*, 2012, Vol. 16, No. 3, P. 1377-1382. Doi: 10.1016/J.RSER.

2. SCHNITZER, M.; Monreal, C.M.; Powell, E. E. Wheat straw biomass: a resource for high-value chemicals. *Journal of Environmental Science and Health*, 2014, Vol. 49, No. 1, P. 51-67. Doi:10.1080/03601234.

3. *Official Statistics Portal*. Available online: [accessed on 20 August 2021], <https://osp.stat.gov.lt>.

4. *Official Statistics Portal*. Available online: [accessed on 10 December 2019], <https://osp.stat.gov.lt>.

5. KULOKAS, M.; PRASPALIAUSKAS, M.; PEDIŠIUS, N. Investigation of Buckwheat Hulls as Additives in the Production of Solid Biomass Fuel from Straw. *Energies,* 2021, Vol. 14, No. 2, P. 265. Doi: 10.3390/EN14020265

6. SINGH, B.; RENGEL, Z. The Role of Crop Residues in Improving Soil Fertility. In: Marschner P., Rengel Z. (eds) *Nutrient Cycling in Terrestrial Ecosystems*. *Soil Biology*, 2007, Vol 10. Springer, Berlin, Heidelberg. Doi: 10.1007/978-3-540-68027-7_7

7. GAO, H.; CHEN, X.; WEI, J.; ZHANG, Y.; ZHANG, L.; CHANG, J.; MICHAEL, L.T. Decomposition Dynamics and Changes in Chemical Composition of Wheat Straw Residue under Anaerobic and Aerobic Conditions. *PLoS ONE*, 2016, Vol. 11, No. 7. doi: 10.1371/JOURNAL.PONE.0158172.

8. PRESCOTT, C.E. Litter decomposition: what controls it and how can we alter it to sequester more carbon in forest soils? *Biogeochemistry,* 2010, Vol. 101, No. 1, P. 133–149. Doi: 10.1007/S10533-010-9439-0.

9. BANSAL, N.; TEWARI, R.; SONI, R.; SONI, S.K. Production of celluloses from Aspergillus Niger NS-2 in solid state fermentation on agricultural and kitchen waste residues. *Waste Management*, 2012, Vol. 32, No. 7, P. 1341-1346. doi: 10.1016/J.WASMAN.2012.03.006.

10. OBENG, E.M.; ADAM, S. N. N.; BUDIMAN, C.; ONGKUDON, C. M.; MAAS, R.; JOSE, J. Lignocellulases: a review of emerging and developing enzymes, systems, and practices. *Bioresources and Bioprocessing*, 2017, Vol.4, P. 1-22. Doi: 10.1186/s40643-017-0146-8.

11. SETHI, S.; DATTA, A.; GUPTA, B. L.; GUPTA, S. Optimization of Cellulose Production from Bacteria Isolated from Soil. *International Scholarly Research Notices*, Vol. 2013.

12. BARNALY, S.; SATYAJIT, R.; FOYSAL, H. Isolation and Identification of Cellulolytic Bacteria from Soil Sample and Their Antibiogram. *American Journal of Microbiological Research*, 2019, Vol. 7, No. 3, P.83-90.

13. KIM, Y.K.; LEE, S.C.; CHO, Y.Y.; OH, H. J.; KO, H. Y. Isolation of Cellulolytic Bacillus subtilis Strains from Agricultural Environments., *International Scholarly Research Notices*, Vol. 2012, P. 9.

14. TÓTH, Á.; MÁTÉ, R.; KUTASI, J.; BATA-VIDÁCS, I.; TÓTH, E.; TÁNCSICS, A.; KOVÁCS, G.; NAGY, I.; KUKOLYA, J. Cellvibrio polysaccharolyticus sp. nov., a cellulolytic bacterium isolated from agricultural soil. *International journal of systematic and evolutionary microbiology*, Vol.71, No. 5.

15. WARING, B.G.; AVERILL, C.; HAWKES, C.V. Differences in fungal and bacterial physiology alter soil carbon and nitrogen cycling: insights from meta-analysis and theoretical models. *Ecology Letters*, 2013, Vol. 16, No. 7, pp. 887-894.

16. MELISSA, M.A.; BOBBI, L. H.; REYNALD, L. Microbial crop residue decomposition dynamics in organic and conventionally managed soils. *Applied Soil Ecology,* 2016, Vol. 107, p.347-359.

17. HENDRICKS, C. W.; DOYLE, J. D.; HUGLEY, B. A new solid medium for enumerating cellulose-utilizing bacteria in soil. *Applied and environmental microbiology*, 1995, Vol. 61, No. 5, p. 2016–2019.

18. LISDIYANTI, P.; SUYANTO, E.; GUSMAWATI, N.; RAHAYU, W. Isolation and characterization of cellulose produced by cellulolytic bacteria from peat soil of Ogan Komering Ilir, South Sumatera. *International Journal of Environment and Bioenergy*, 2012, Vol. 3, No. 3, P. 145-153.

19. KASANA, R.C.; SALWAN, R.; DHAR, H.; DUTT, S.; GULATI, A. A rapid and easy method for the detection of microbial celluloses on agar plates using gram's iodine. *Current Microbiology*, 2008, Vol. 57, No. 5, P. 503-507.

20. SASIKUMAR, V.; PRIYA, V. P.; SHANKAR, C. S.; SEKAR, D. S. Isolation and Preliminary Screening of Lignin Degrading Microbes. *Journal of Academia and Industrial Research,* 2014, Vol. 3, No. 6, P.291-294.

21. NAGAR, S.; MITTAL, A.; GUPTA, V. K. A cost-effective method for screening and isolation of Xylan degrading bacteria using agro-waste material. *Asian Journal of Biological Sciences*, 2012, Vol.5, No. 8, P. 384-394.

22. FERREIRA–LEITAO, V.S.; ANDRADE de CARVALHO, M. E.; BON, E. P. S. Lignin peroxidase efficiency for methylene blue decolouration: Comparison to reported methods. *Dyes and Pigments*, 2007, Vol. 4, No. 1, P. 230-236.

23. LU, W. J.; WANG, H. T.; YANG, S. J.; WANG, Z. C.; NIE, Y. F. Isolation and characterization of mesophilic cellulose-degrading bacteria from flower stalks-vegetable waste co-composting system. *Journal of general and applied microbiology*, 2005, Vol. 51, No. 6, P. 353–360.

24. Umashankar, N.; Meghashree, H. M.; Benherlal, P. S.; Mohan, C. Isolation and Screening of Lignin Degrading Bacteria from Different Natural and Organic Sources. *International Journal of Current Microbiology and Applied Sciences*, 2018, Vol. 7, P. 609-617.

THE INFLUENCE OF ORGANIC FERTILIZERS ON ABUNDANCE OF SOIL MICROORGANISMS AND DEHYDROGENASE ACTIVITY IN EAST LITHUANIAN LIGHT SOILS

D. Sivojienė, A. Kačergius
Lithuanian Research Centre for Agriculture and Forestry,
Institute of Agriculture, Vokė Branch
Žalioji Sq. 2, 02232 Vilnius – Lithuania
Diana.Sivojiene@lammc.lt, Audrius.Kacergius@lammc.lt

EXTENDED ABSTRACT

OVERVIEW

Organic fertilizers in their various forms are often used in agriculture. It is important to know the effects of different types of manure on the microorganism's communities in the arable land [1]. Abundance of soil microorganisms is one of the stability and fertility indicators of soil ecosystems. The application of fertilizers to the soil stimulates certain groups of microorganisms those are often involved in phosphorus solubilization, nitrogen mineralization, methane degradation, and degradation of complex organic compounds [2].

Enzymatic activity of the soil is another important indicator [3]. Dehydrogenase enzyme is important in the biological oxidation of organic compounds and often mentioned as the main parameter of the microbiological activity of the soil, which reflects the rate of transformations in the soil [4, 5].

The aim of the research was to investigate how the applied organic fertilizers affect the most active soil microorganisms, which determine the soil fertility and stability and soil dehydrogenase activity.

METHODS

The soil samples were taken from the field of a long-term experiment from a 10–20 cm deep arable layer with four replications. Organic and mineral fertilizers were used in the field experiment differ in concentration. For the investigation were selected organic fertilizers – litter and granulated (poultry and cattle) manure. In the field experiment also were used a non-commercial biological additives *Azotobacter* spp. and *Trichoderma* spp.

For the quantitative analysis of microorganisms, samples were taken in spring, summer, and autumn. The content of microorganisms in colony-forming units (CFU) per 1 g of dry soil was calculated according to the Carter and Gregorich methodology [6].

For the dehydrogenase activity, samples were taken in summer. Analysis was performed according to the Klein and other author's methodology [7]. To each test tube with 1 g soil sample was added 0.2 ml of a 3.0% solution of 2,3,5_triphenyltetrazolium chloride, followed by 0.5 ml of a 1% glucose solution. The tubes were incubated in the dark for 96 hr at 27°C. After incubation 10 ml of methanol was added to each of the tubes followed by mechanically

shaking for 30 sec. Absorbance's were measured on a spectrophotometer at a wavelength of λ=485 nm.

RESULTS

Abundance of fungal and three physiological groups of bacteria were analysed: non-symbiotic diastrophic, organotrophic, and mineral nitrogen assimilating. Second year results were obtained.

The results of investigations showed that the abundance of organotrophic bacteria (except sample with mineral fertilizers MF) was highest in the spring period. An increase in organotrophs was to be expected because the manure was added in the autumn of 2020. According to the studies of other authors fertilization with organic fertilizers initially increases the amount of organotrophic bacteria in beginning of the growing season and the amount of mineral nitrogen-assimilating bacteria n the end of the growing season, as in our case [8]. The abundance of non-symbiotic diastrophic bacteria was highest also in the spring period. Decreased significantly during the summer period. Mineral nitrogen-assimilating bacteria highest abundance was in autumn period. Comparing the data of individual samples with the control, we see that the proportion of mineral nitrogen assimilating bacteria was increased in all samples, except for the samples with *Trichoderma*. The highest abundance of the fungal communities was also determined in autumn.

The activity of dehydrogenases in the soil was in the range 0.8 μg/g/24h to 26.51 μg/g/24h, depending on the fertilization. The lowest dehydrogenase activity was found in the field fertilized peat cattle litter, meanwhile the highest dehydrogenase activity was found in the field fertilized granulated cattle manure with biological substance *Trichoderma* spp.

CONCLUSIONS

Assessing the total abundance of microorganisms, the abundance of organotrophic and diastrophic bacteria was highest during the spring period, while nitrifying bacteria and fungi were highest in the autumn. The first soil dehydrogenase studies showed the lowest activity in the field fertilized peat cattle litter.

Keywords: soil microorganisms, abundance, dehydrogenase activity.

REFERENCES

1. YE, C.; HUANG, S.; SHA, C.; WU, J.; CUI, C.; SU, J.; RUAN, J.; TAN, J.; TANG, H.; XUE, J. Changes of bacterial community in arable soil after short-term application of fresh manures and organic fertilizer. *Environmental Technology*, 2020, Vol. 20, P.1–11.

2. GAUTAM, A.; SEKARAN, U.; GUZMAN, J.; KOVÁCS, P.; HERNANDEZ, J. L. G.; KUMAR, S. Responses of soil microbial community structure and enzymatic activities to long-term application of mineral fertilizer and beef manure. *Environmental and Sustainability Indicators*, 2020, Vol. 8, P. 100073.

3. KACZYNSKA, G.; BOROWIK, A.; WYSZKOWSKA, J. Soil Dehydrogenases as an Indicator of Contamination of the Environment with Petroleum Products. *Water, Air, & Soil Pollution*, 2015, Vol. 226, P. 1-11.

4. MUKHOPADHYAY, S.; MAITI, S. K. Dehydrogenase activity in natural and mine soil – a review. *Indian Journal of Environmental Protection*, 2010, Vol. 30, No. 11, P. 921-933.

5. POURAKBAR, M.; BEHNAMI, A.; MAHDAVIANPOUR, M.; DARIYAN, F. S.; AGHAYANI, E. Developing a method for measurement of dehydrogenase activity in biological wastewater treatment processes applied for toxic compounds degradation. *MethodsX*, 2020, Vol. 7, P. 1-5.

6. CARTER, M. R.; GREGORICH, E. G. Soil Sampling and Methods of Analysis; CRC Press: Boca Raton, FL, USA, 2007, P. 1224.

7. KLEIN, D.A.; LOH, T. C.; GOULDING, R. L. A rapid procedure to evaluate the dehydrogenase activity of soils low in organic matter. *Soil Biology and Biochemistry*, 1971, Vol. 3, P. 385-387.

8. BAKŠIENĖ, E.; RAŽUKAS, A.; REPEČKIENĖ, J.; TITOVA, J. Influence of different farming systems on the stability of low productivity soil in Southeast Lithuania. *Agriculture*. 2014, Vol. 101, P. 115–124.

BIOMASS YIELD AND ITS CHEMICAL COMPOSITION OF DIFFERENTLY MANAGED GRASSLANDS

A. Skersiene, A. Slepetiene
Lithuanian Research Centre for Agriculture and Forestry
Instituto al. 1, 58344 Akademija, Kedainiai distr. – Lithuania
+370 63046188
Aida.Skersiene@lammc.lt

EXTENDED ABSTRACT

OVERVIEW

Grasslands are important ecosystems worldwide for tourism, recreation and wildlife habitat. They provide raw materials for food, biofuels and produce most of the forage for ruminants [1, 2]. One of the ways to improve productivity of grasslands include fertiliser application [3].

The waste product of biogas production is rich in macro- and micronutrients and according to the absorption of elements by plants it resembles mineral fertilizers since nitrogen (N), phosphorus and potassium (K) elements are easily available. These digestate can be applied to the soil after mechanical separation into solid digestate (SD) and liquid digestate (LD). [4–9]. It is known from previous research that the use of digestate in fertilising soils, enables production of large amounts of grass biomass while reducing the use of mineral fertilisers [6, 10–13].

K is a macronutrient and has important roles in plants like osmoregulation, membrane potential regulation, stress adaptation and growth [14]. N is the mineral nutrient required in the greatest amount and its low availability restricts plant growth. Plants assimilate nitrogen as a mineral nutrient mostly from the soil [15–16].

The present study aimed to estimate the changes in grass biomass and its chemical composition as influenced by fertilisation with different rates of solid and liquid digestate.

METHODS

The experiment was established in Surviliskis (55°26′03.07″ N 24°02′12.26″ E), Kedainiai district, in perennial grassland on a *Fluvisol* [17] in 2018. The botanical composition of the grassland was dominated by plants of the *Poaceae* family. There were five fertilisation treatments investigated: without fertilisation, fertilisation with LD at 85 and 170 kg ha^{-1} N and with SD at 85 and 170 kg ha^{-1} N, based on the results of the chemical analysis of the digestate (table 1). A randomised experimental design with three field replicates was used.

Table 1. Chemical composition of the digestate used for fertilisation, 2018, 2019.

		pH	N, g kg⁻¹	K, g kg⁻¹	OM, %
2018	SD	8.2	12.8	7.1	88.3
	LD	8	2.3	1.3	2.3
2019	SD	8.4	17.1	4.8	75.2
	LD	7.4	3.9	1.3	3.5

Fertilisation was performed and samples of grass biomass were taken in 2018 and 2019. The dry matter yield (DMY) of grasses was determined by weighing. The grass samples of 0.5 kg were collected from each plot and dried at a temperature of +105 °C.

K content of the grass biomass was determined using the flame atomic absorption spectrometry measurement on Analyst 200 (PerkinElmer, USA) after the wet digestion process with sulfuric acid [18]; N content by the Kjeldahl method [19].

The data were analysed using the software SAS Enterprice, version 7.1 (SAS Institute Inc., USA). The analysis of variance (ANOVA) was performed, and the data were compared using Fisher's least significant difference (LSD) test at the probability level of $P < 0.05$.

RESULTS

DMY of grasses varied depending on the type and fertilisation rate of the digestate and the year (Fig. 1). In the 1st year of the study, the total DMY of herbage ranged from 3.12 to 5.85 t ha⁻¹, in the 2nd year ranged from 1.88 to 4.98 t ha⁻¹.

Fig. 1. The DMY of grasses (2018, 2019). Notes. I – 1st cut, II – 2nd cut; LD - liquid digestate, SD - solid digestate; error bars are shown as standard error.

The plots fertilised with LD at the rate of 170 kg ha⁻¹ N and 85 kg ha⁻¹ N produced the highest DMY, which were statistically significantly (P>0.05) higher compared to the control. A lower but much larger than the control DMY was observed in the plots fertilised with 170 kg ha⁻¹ N of SD. The results agree with other studies on digestates as fertilisers [6, 9, and 12].

The total DMY yields were lower in 2019, especially in the plots fertilised with 170 kg ha^{-1} N of SD. It may have been caused by a long period of drought in the spring months and in June [20].
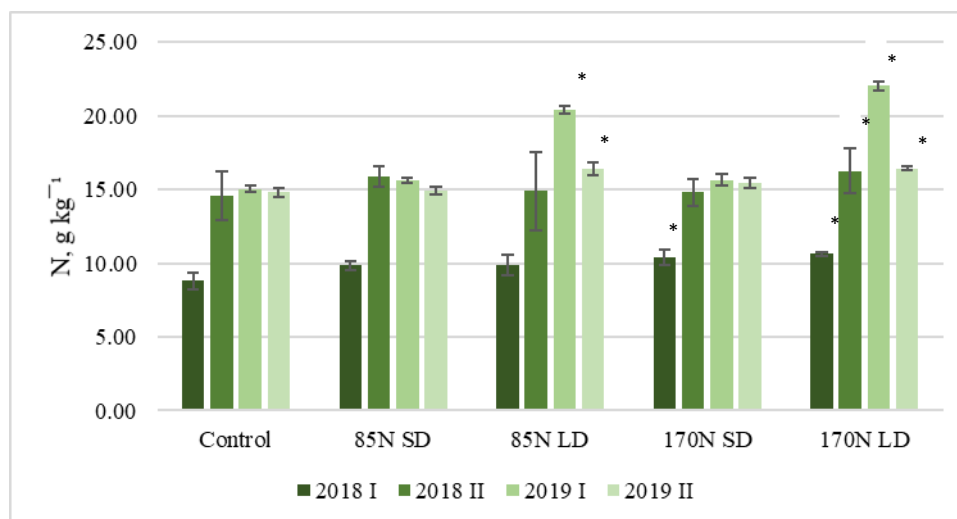
Fig. 2. N content in the DMY of grasses (2018 and 2019).

Notes. I – 1st cut, II – 2nd cut; LD - liquid digestate, SD - solid digestate; error bars are shown as standard error; * – significantly higher at $P < 0.05$ compared with the *control.*

N contents were higher in all digestate-treated plots compared to the control in 2018 and 2019 (fig. 2). The highest N amounts (10.62–22.03 g kg^{-1}) were determined in the grasslands fertilised with liquid digestate rates of 170 kg ha^{-1} N. The amount of K in the biomass did not increase as significantly as N, but a positive trend was observed in all fertilisation treatments (fig. 3). These results confirm data from previous studies that digestates, like other fertilisers, improve the quantity and quality of grass biomass [6, 11–12].
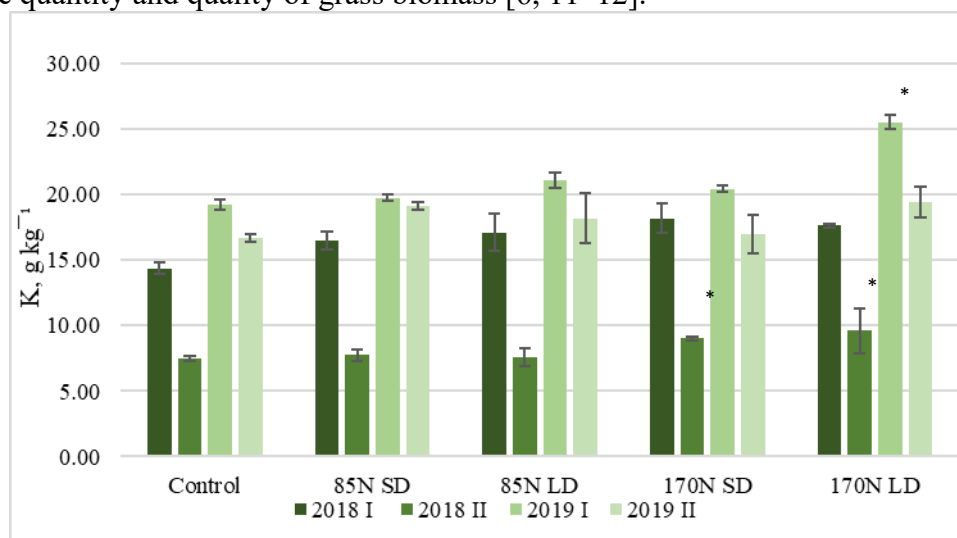
Fig. 3. K content in the dry matter of grasses (2018 and 2019)
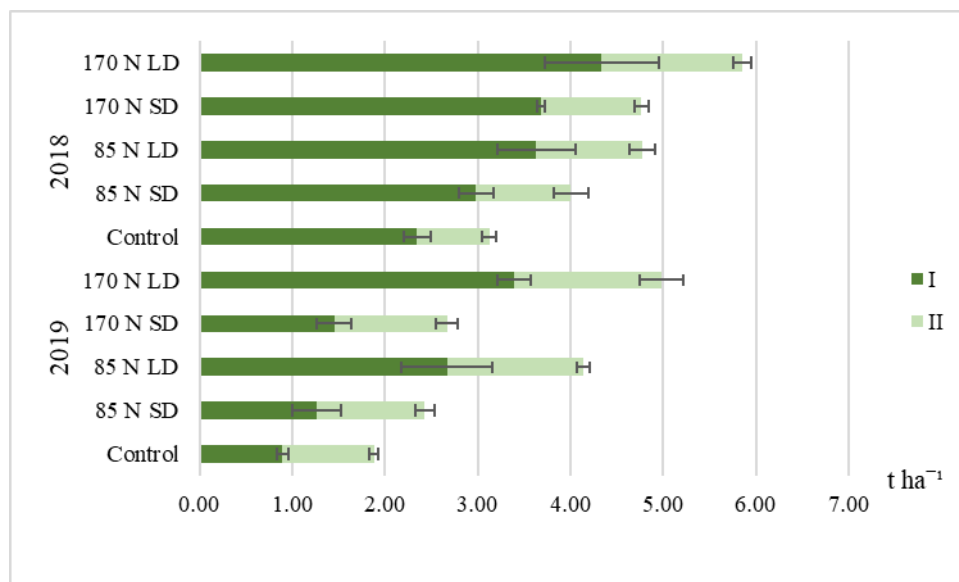
Notes. I – 1st cut, II – 2nd cut; LD - liquid digestate, SD - solid digestate; error bars are shown as standard error; * – significantly higher at $P < 0.05$ compared with the control.

CONCLUSIONS

The highest annual DMY of grasses was produced in the plots fertilised with 170 kg ha^{-1} N of separated LD in 2018 and 2019. The results of the study also showed that digestate can

contribute to the increase of N and K in grass biomass. These nutrients, especially N, are very important for the physiological processes of plants, as well as for the nutritional value of grasses.

Keywords: biofertilisers, grass yield, nitrogen, potassium.

REFERENCES

1. BARNEZE, A. S.; WHITAKER, J.; MCNAMARA, N. P.; OSTLE, N. J. Legumes increase grassland productivity with no effect on nitrous oxide emissions. *Plant Soil,* 2020, No. 446, P. 163–177.

2. GIBSON, David J.; NEWMAN, Jonathan A. (Ed.). Grasslands and climate change. Cambridge University Press, 2019, P. 1-3. ISBN 9781107195264.

3. VARGOVA, V.; KANIANSKA, R.; KIZEKOVA, M.; ŠIŠKA, B.; KOVÁČIKOVÁ, Z.; MICHALEC, M. Changes and interactions between grassland ecosystem soil and plant properties under long-term mineral fertilization. *Agronomy*, 2020, Vol. 10, No. 3, P. 375.

4. KOSZEL, M.; LORENCOWICZ, E. Agricultural use of biogas digestate as a replacement fertilizers. *Agriculture and Agricultural Science Procedia*, 2015, No. 7, P. 119-124.

5. TEGLIA, C.; TREMIER, A.; MARTEL, J. L. Characterization of solid digestates: part 1, review of existing indicators to assess solid digestates agricultural use. *Waste and Biomass Valorization*, 2011, Vol. 2, No. 1, P. 43-58.

6. GŁOWACKA, A.; SZOSTAK, B.; KLEBANIUK, R. Effect of biogas digestate and mineral fertilisation on the soil properties and yield and nutritional value of switchgrass forage. *Agronomy*, 2020, Vol. 10, No. 4, P. 490.

7. MORTOLA, N.; ROMANIUK, R.; COSENTINO, V.; EIZA, M.; CARFAGNO, P.; RIZZO, P.; BRES, P.; RIERA, N.; ROBA, M.; BUTTI, M.; SAINZ, D.; BRUTTI, L. Potential Use of a Poultry Manure Digestate as a Biofertilisers: Evaluation of Soil Properties and Lactuca sativa Growth. *Pedosphere*, 2019, Vol. 29, No. 1, P. 60–69.

8. PASTORELLI, R.; VALBOA, G.; LAGOMARSINO, A.; FABIANI, A.; SIMONCINI, S.; ZAGHI, M.; VIGNOZZI, N. Recycling Biogas Digestate from Energy Crops: Effects on Soil Properties and Crop Productivity. *Applied sciences*, 2021, Vol. 11, No.750, and P. 1-20.

9. EHMANN, A.; THUMM, U.; LEWANDOWSKI, I. Fertilizing potential of separated biogas digestates in annual and perennial biomass production systems. *Frontiers in Sustainable Food Systems*, 2018, Vol. 2, P. 12.

10. KOVÁČIKOVÁ, Z.; VARGOVÁ, V.; JANČOVÁ, L. Effect of digestate application on herbage quality and quantity of permanent grassland. *Agriculture/Pol'nohospodárstvo*, 2013, Vol. 59, No. 2, P. 88-98.

11. WALSH, J. J.; JONES, D. L.; CHADWICK, D. R.; WILLIAMS, A. P. Repeated application of anaerobic digestate, undigested cattle slurry, and inorganic fertilizer N: Impacts on pasture yield and quality. *Grass and Forage Science*, 2018, Vol. 73, No. 3, P. 758-763.

12. TILVIKIENĖ, V.; ŠLEPETIENĖ, A.; KADŽIULIENĖ, Ž. Effects of 5 years of digestate application on biomass production and quality of cocksfoot (Dactylis glomerata L.). *Grass and Forage Science*, 2018, Vol. 73, No.1, P. 206-217.

13. TAMPERE, M.; VIIRALT, R. The efficiency of biogas digestate on grassland compared to mineral fertilizer and cattle slurry. *Research for Rural Development*, 2014, Vol. 1, P. 89-94.

14. JOHNSON, R.; VISHWAKARMA, K.; HOSSEN, M. S.; KUMAR, V.; SHACKIRA, A. M.; PUTHUR, J. T.; HASANUZZAMAN, M. Potassium in plants: Growth regulation, signalling, and environmental stress tolerance. *Plant Physiology and Biochemistry*, 2022, Vol. 172, P. 56-69.

15. KRAISER, T.; GRAS, D. E.; GUTIÉRREZ, A. G.; GONZÁLEZ, B.; GUTIÉRREZ, R. A. A holistic view of nitrogen acquisition in plants. *Journal of experimental botany*, 2011, Vol. 62, No. 4, P. 1455-1466.

16. GARCIA-SERVIN, M.; CONTRERAS-MEDINA, L. M.; TORRES-PACHECO, I.; GUEVARA-GONZÁLEZ, R. G. Nitrate Handbook: Environmental, Agricultural, and Health Effects. CRC Press Routledge, 2022. P. 163-165. ISBN 9780367338220.

17. Group WRB. World Reference Base for Soil Resources 2014, Update 2015; International Soil Classification System for Naming Soils and Creating Legends for Soil Maps; World Soil Resources Reports No. 106; FAO: Rome, Italy, 2015, P. 193.

18. JURGUTIS, L.; ŠLEPETIENĖ, A.; ŠLEPETYS, J.; CESEVIČIENĖ, J. towards a Full Circular Economy in Biogas Plants: Sustainable Management of Digestate for Growing Biomass Feedstocks and Use as Biofertilizer. *Energies*, 2021, Vol.14, No. 14, P. 4272.

19. SAEZ-PLAZA, P.; NAVAS, M. J.; WYBRANIEC, S.; MICHAŁOWSKI, T.; ASUERO, A. G. An overview of the Kjeldahl method of nitrogen determination. Part II. Sample preparation, working scale, instrumental finish, and quality control. *Critical Reviews in Analytical Chemistry*, 2013, Vol. 43, P. 224–272.

20. Lithuanian Hydrometeorological Service under the Ministry of Environment. <http://www.meteo.lt/lt/desimtadieniu-agrometeorologiniu-salygu-archyvas>

THE POTENTIAL OF HEMP FOR BIOCHAR PRODUCTION

U. Stulpinaitė, V. Tilvikienė
Lithuania Research Centre for Agriculture and Forestry
Instituto al. 1, Akademija, Kėdainiai distr. – Lithuania
+37063620394
Urte.stulpinaite@lammc.lt

K. Žiūra
Vytautas Magnus University
Studentų 15A, Akademija, Kaunas distr. – Lithuania
Kestutis.ziura@vdu.lt

EXTENDED ABSTRACT

OVERVIEW

Fibrous hemp is used in many end products derived from cannabinoids, seeds, fibre, and wood core. As a fibrous plant, it is one of the oldest non-food plants in the world [1]. In the 19th century, flax and hemp were the most important fibre crops in Europe. Although hemp cultivation had declined, interest in these crops has recently risen and is expanding rapidly in France, Italy, and the Netherlands [2]. Farmers have been allowed to grow hemp only since 2014 in Lithuania, the declared area under this crop was over 1000 hectares in the same year [3]. After 5 years, the area of hemp was around 9000 hectares. The observed difference in hemp biomass yield (3.4–31.2 t·ha^{-1}) is influenced by environmental conditions, applied fertilization, plant density, and genotypes. The highest biomass yield is set in Italy. Northern Italy - 28.6-31.2 t ha^{-1} dry matter, central Italy - 13.1-26.3 tha^{-1} dry matter, in Latvia - 13.5-21.3 tha^{-1} of dry matter, the least yield is produced in Southwest Germany - 5.2 -12.8 tha^{-1} [9]. These days the most popular cultivars of hemp are "Felina 32", "USO 31", "Epsilon 68", "Finola" [10].

The above-ground parts of fibrous hemp can be used to produce biochar. Biochar is biomass burned at high temperatures in an oxygen-free environment. Interest in biochar has grown in recent years. The use of biochar in agriculture as a fertilizer has also attracted the interest of farmers [4]. Biochar has the potential to reduce carbon emissions, improve water retention and nutrient retention, soil organic matter accumulation, and improve the availability of nutrients such as phosphorus and nitrogen in a variety of soil types. The chemical composition of biochar depends on the chosen raw material in the production process but is constantly enriched with the main nutrients: Ca, Ma, Na, Fe, Mn, Cu, Zn, N, P, and K [4–6]. The use of biochar for soil improvement has also outperformed biomass composting [7]. Biochar improves the quality of the soil, its structure, and its hygroscopic properties, making the soil more resistant to rain, wind, and water erosion. The use of biochar for fertilization also improves the plant uptake of nitrogen fertilizers and reduces nitrogen gas emissions [8,9]. Nitrogen gas has a strong greenhouse effect, so biochar in the soil, thus reducing nitrogen emissions, contributes to tackling climate change [10]. Nevertheless, there is a lack of information about the biochar properties produced from different parts of hemp (stems, leaves, chaff, and fibre). Therefore

the aim of this research was to investigate the biochar production process and biochar potential of different parts of hemp.

METHODS

The field experiment is performed in Akademija, Kėdainiai distr. fields with dimensions of 3x10 m. Sowing time - late May, when the soil warms to 10°C. Hemp Felina 32 seed rate 35 kg·ha^{-1}. Sown at a depth of 3-4 cm, 12.5 cm apart. Biochar production is carried out by slow pyrolysis at 400 ℃, with a heating rate of 6 ℃·h^{-1} and a holding time of 2 h.

RESULTS

The amount of biomass in the whole field reached 28 ta·ha^{-1} dry matter. The amount of biomass without leaves and inflorescence was estimated at 8.08 ta·ha^{-1} dry matter (Fig. 2). The stem part of the hemp is residues accounts for more than half of all biomass. Therefore, if hemp is grown for seeds of leaves, the huge biomass is left and potentially could be used for biochar production.
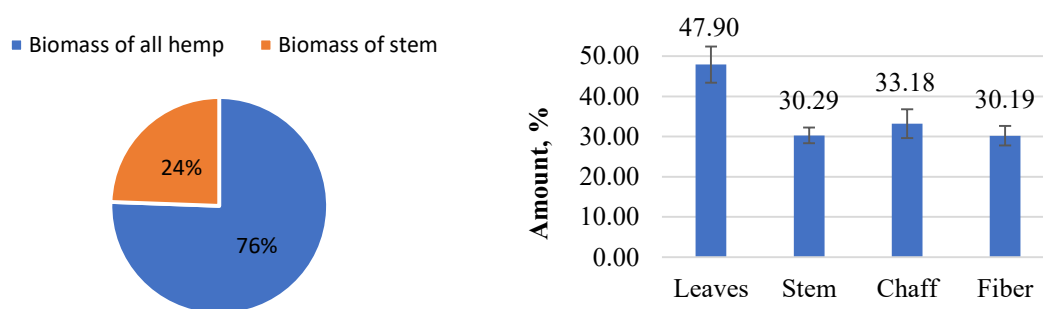
Fig. 2 Biomass yield of all hemp and of the stem (A) and biochar production from different parts of hemp (B)

The biochar production from fibre hemp showed a maximum biochar amount of $47.90 \pm 8.99\%$ of the raw material obtained from the leaves (Fig. 2 B). However, the amount of biochar extracted from other parts of the fibre hemp stem varies between 30.19% and 33.18%.

CONCLUSIONS

1. Fiber hemp has a huge amount of biomass. If hemp is not growing for fibre when stem part is residues, which is the problem of huge biomass content. One of the ways to solve this problem could be the production of biochar.

2. The highest amount of biochar production was obtained from leaves. Less content of the biochar was produced from stem and fibre; however, in some cases, these are the residues, so it's better to use stem for biochar. There are two main benefits of biochar production: improving the soil quality and efficiently utilizing hemp residues.

ACKNOWLEDGEMENTS

WWW.CYSENI.COM

REFERENCES

1. BALDINI, M.; FERFUIA, C.; ZULIANI, F.; DANUSO, F. Industrial Crops & Products Suitability assessment of di ff erent hemp (Cannabis sativa L .) varieties to the cultivation environment, In*dustrial Crops & Produc*ts, 2020, Vol. 143.

2. ZHAO, J.; XU, Y.; WANG, W.; GRI, J.; ROOZEBOOM, K.; WANG, D. Bioconversion of industrial hemp biomass for bioethanol production , 2020, Vol. 281. Doi:10.1016/j.fuel.2020.118725.

3. FERNANDO, A.L. Article in press, 2015. Doi:10.1016/j.indcrop.2015.06.044.

4. LEHMANN, J.; RILLIG, M. C.; THIES, J.; MASIELLO, C. A.; HOCKADAY, W. C.; CROWLEY, D. Soil Biology & Biochemistry Biochar effects on soil biota e A review, S*oil Biology and Biochemistry.* 2011, Vol. 43. Doi:10.1016/j.soilbio.2011.04.022.

5. NANDA, S.; DALAI, A. K.; BERRUTI, F.; KOZINSKI, J. A. Biochar as an Exceptional Bioresource for Energy , Agronomy , Carbon Sequestration , Activated Carbon and Specialty Materials, *Waste and Biomass Valorization*. 2016, Vol. 7. Doi:10.1007/s12649-015-9459-z.

6. WANG, K.; PENG, N.; LU, G.; DANG, Z. Effects of Pyrolysis Temperature and Holding Time on Physicochemical Properties of Swine-Manure-Derived Biochar, *Waste and Biomass Valorization*. 2018. Doi:10.1007/s12649-018-0435-2.

7. LINDHJEM, H.; CORNELISSEN, G.; HALE, S. E.; SØRMO, E.; SPARREVIK, M. Science of the Total Environment Environmental and economic impacts of biochar production and agricultural use in six developing and middle-income countries, 2021, Vol. 755. Doi:10.1016/j.scitotenv.2020.142455.

8. LIAO, X.; NIU, Y.; LIU, D.; CHEN, Z.; HE, T.; LUO, J.; LINDSEY, S.; DING, W. Agriculture , Ecosystems and Environment Four-year continuous residual e ff ects of biochar application to a sandy loam soil on crop yield and N 2 O and NO emissions under maize-wheat rotation, *Agriculture , Ecosystems and Environment*. 2020, Vol. DOI:10.1016/j.agee.2020.107109.

9. ZEESHAN, M.; AHMAD, W.; HUSSAIN, F.; AHAMD, W.; NUMAN, M.; SHAH, M.; AHMAD, I. Phytostabalization of the heavy metals in the soil with biochar applications , the impact on chlorophyll , carotene , soil fertility and tomato crop yield, *Journal of Cleaner Production* , 2020, Vol. 255. Doi:10.1016/j.jclepro.2020.120318.

10. E.P. Notes, Status of Hemp Extracts in Europe, 2019.

11. JASINSKAS, A.; STREIKUS, D.; VON, T. Fibrous hemp (Felina 32 , USO 31 , Finola) and fi brous nettle processing and usage of pressed biofuel for energy purposes, 2020, Vol.149.

12. LI, C.; SUN, Y.; YI, Z.; ZHANG, L.; ZHANG, S.; HU, X. Co-pyrolysis of coke bottle wastes with cellulose , lignin and sawdust : Impacts of the mixed feedstock on char properties, *Renewable Energy*. 2022, Vol. Doi:10.1016/j.renene.2021.09.103.

THE EFFECT OF DEEP SOIL PLOUGHING ON SOIL NITROGEN AND CARBON STATUS

G. Survila, I. Varnagirytė-Kabašinskienė
Lithuanian Research Centre for Agriculture and Forestry,
Liepų 1, Girionys, LT-53101, Kaunas distr. – Lithuania
gediminas.survila@lammc.lt

EXTENDED ABSTRACT

OVERVIEW

Afforestation is facing with two challenges: to grow high productivity forest plantations and to maintain sustainability of forest soils [1–3]. The afforestation typically has benefits associated with carbon sequestration [3, 4]. Different afforestation practices affect the soil organic carbon (SOC) stocks in the topsoil, but their effects on the subsoil SOC are not yet well studied [4]. Deep soil ploughing could be used before afforestation of former agricultural land [5, 6]. Such soil preparation could give additional value for growing trees, and this positively correlates with the higher C sequestration in biomass. The effects of deep soil ploughing are being analysed in literature [7]. Soil ploughing up to 50–60 cm deep before afforestation of former agricultural land can eliminate high-density subsoil or soil compaction induced by harvesting machines [8, 9]. Among other changes in mineral soil properties, the deep placement of nitrogen (N), translocation of SOC from topsoil into subsoil, and, finally, improved long-term soil fertility could be mentioned as the most important [5,10,11]. The aim of this study is to determine the changes of soil N and SOC concentrations and stocks in the soil where deep ploughing was performed before afforestation of former agricultural land.

METHODS

The study was carried out in Širvintos district in November-December 2020. The former cropland was afforested with the mixture of oak, Norway spruce and Scots pine in 2012. Two afforestation practices – non-ploughed soil and deep ploughed soil – were used. The soil was sandy Planosol [12]. Four composite samples of mineral soil (0–10, 10–20, 20–40 and 40–80 cm layers) were sampled for determination of the concentrations of total N, mineral N, and SOC. Total N was determined using the Kjeldahl method, mineral N by the spectrometric method, and SOC concentration using a dry combustion method. Chemical soil analyses were performed by the LAMMC Agrochemical Research Laboratory. The stocks of total N and SOC were calculated according to the methodology given by Vesterdal et al. [13].

RESULTS

The study results showed higher concentrations of SOC and total N in 20–40 cm subsoil layer compared to the 0–20 cm topsoil layers in the sites where deep ploughing was performed before afforestation (Fig. 1). In non-ploughed soil, the concentrations of SOC and total N showed similar trend in the 0–80 cm soil profile: the highest concentrations were obtained in the 0–10 cm topsoil layer and they decreased steadily with a larger depth of the soil profile.

The concentrations of mineral N varied within a range of 1.3–1.6 mg kg^{-1} in 0-80 cm and there were no significant differences between different soil layers in the sites afforested after deep ploughing. In non-ploughed soil, the concentrations of mineral N decreased with greater soil depth from 2.9±0.3 mg kg^{-1} in 0–10 cm soil layer to 0.9±0.0 mg kg^{-1} in 40–80 cm soil layer.
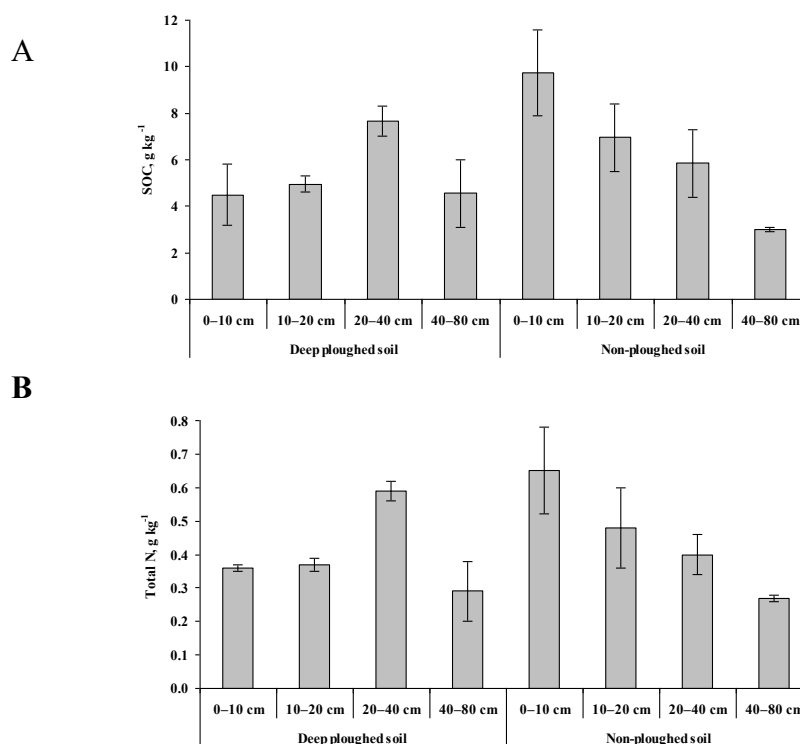
Fig. 1. The concentration of SOC (**A**) and total N (**B**) in deeply ploughed and non-ploughed Planosol, representing the afforested and regenerated site, respectively.

In the sites afforested after deep ploughing, the total N stock in the 0–20 cm topsoil was 3.6 times lower than in the 20–80 cm soil layers. However, in the non-ploughed Planosol, this difference was only 1.6 times. Very similar trend was obtained for SOC stocks: the values were 7.3–5.9 kg ha^{-1} in the 0–20 cm topsoil and 22.8–27.8 kg ha^{-1} in the 20–80 cm soil layer.

CONCLUSIONS

1.   Deep ploughing, performed before afforestation of former agricultural land, increased the concentrations of total N and SOC in the subsoil in comparison with non-ploughed soil. These changes were obtained a decade post-ploughing.

2.   The stocks of total N and SOC were significantly higher in the deeper soil compared with the topsoil layers, while in the non-ploughed sites this difference was less evident.

Keywords: afforestation, deep soil tillage, soil organic carbon, nitrogen

REFERENCES

1. NIJNIK M.; BIZIKOVA L. Responding to the Kyoto Protocol through forestry: a comparison of opportunities for several countries in Europe. *Forest Policy and Economics*, 2008, Vol. 10, No. 4, P. 257–269.

2. EUROPEAN COMMISSION. EU Soil Strategy for 2030. COM (2021) 699 final, Brussels, 2021.

3. FORSTER, E.J.; HEALEY, J.R.; DYMOND, C.; STYLES, D. Commercial afforestation can deliver effective climate change mitigation under multiple decarbonisation pathways. *Nature Communications*, 2021, Vol. 12, No.3831.

4. SHI, S.; ZHANG, W.; ZHANG, P.; YU, Y.; DING. F. A synthesis of change in deep soil organic carbon stores with afforestation of agricultural soils. *Forest Ecology and Management*, 2013, Vol. 296, P. 53–63.

5. HANSEN, K.; VESTERDAL, L.; MUYS, B.; GILLIAMS, S.; ROSENQVIST, L. et al. Guidelines for planning afforestation of former arable land. In: Heil, G.W., Muys, B., Hansen, K. (ed.). Environmental effects of afforestation in North-Western Europe: from field observations to decision support. Springer Science & Business Media, 2007, P. 249–291.

6. SMAL, H.; LIGĘZA, S.; PRANAGA, J.; URBAN, D.; PIETRUCZYK-POPŁAWSKA, D. Changes in the stocks of soil organic carbon, total nitrogen and phosphorus following afforestation of post-arable soils: A chronosequence study. *Forest Ecology and Management*, 2019, Vol. 451, P. 117536.

7. SURVILA, G.; VARNAGIRYTĖ-KABAŠINSKIENĖ, I.; ARMOLAITIS, K. Deep soil ploughing for afforestation: a review of potential impacts on soil and vegetation. *Baltic Forestry*, 2021, Vol. 27, No. 2, No.590.

8. HENINGER, R.; SCOTT, W.; DOBKOWSKI, A.; MILLER, R.; ANDERSON, H.; DUKE, S. Soil disturbance and 10-year growth response of coast Douglas-fir on non-tilled and tilled skid trails in the Oregon Cascades. *Canadian Journal of Forestry Research*, 2002, Vol. 32, P. 233–246.

9. AKINCI, I.; CAKIR, E.; TOPAKCI, M.; CANAKCI, M.; INAN, O. 2004. The effect of subsoiling on soil resistance and cotton yield. *Soil and Tillage Research*, 2004, Vol. 77, P. 203–210.

10. LIU, X.J.; MOSIER, A.R.; HALVORSON, A.D.; ZHANG F.S. The impact of nitrogen placement and tillage on NO, N_2O, CH_4 and CO_2 fluxes from a clay loam soil. *Plant Soil*, 2006, Vol. 280, P. 177–188.

11. ALCÁNTARA, V.; DON, A.; WELL, R.; NIEDER, R. Deep ploughing increases agricultural soil organic matter stocks. *Global Change Biology*, 2016, Vol. 22, P. 2939–2956.

12. IUSS Working Group WRB. World Reference Base for Soil Resources 2014; International Soil Classification System for Naming Soils and Creating Legends for Soil Maps, Update 2015; World Soil Resources Reports No. 106; FAO: Rome, Italy, 2015; P. 192.

13. VESTERDAL, L.; SCHMIDT, I. K.; CALLESEN, I.; NILSSON, L.O.; GUNDERSEN, P. Carbon and nitrogen in forest floor and mineral soil under six common European tree species. *Forest Ecology and Management,* 2008, Vol. 255, P. 35–48.

EFFECT OF EXOGENOUS PHYTOHORMONES ON OILSEED RAPE (*BRASSICA NAPUS* L.) PRODUCTIVITY

M. Urbutis

Lithuanian Research Centre for Agriculture and Forestry
Institute alley 1, 58344 Dotnuva– Lithuania
+37062233320
martynas.urbutis@lammc.lt

EXTENDED ABSTRACT

OVERVIEW

Oilseed rape (*Brassica napus* L.) is an important crop which is widely grown for vegetable oil and is one of the biggest source of oil in the world [1]. Oilseed production depends on biotic and abiotic environmental conditions. Lithuania is north-eastern country of Europe and low temperatures during winter has big impact and are required for rape production [2, 3]. However, despite environment impact exogenous phytohormones affects physiological plant development processes during critical ontogenesis stages: rooting, bud development, flowering or maturity [4]. The goal of experiment was to increase oilseed rape yield by using exogenous phytohormones applications during different organogenesis stages.

METHODS

The research was carried out in field experiment. Oilseed rape (*Brassica napus* L.) were grown in Lithuanian research centre for agriculture and forestry Institute under field conditions during autumn – spring – summer periods. 25 m^2 fields were established and each variant had 3 replications. Experiment will be repeated for 2 years. Mixtures of kinetin (KIN) and indole-3-butyric acid (IBA) at rates of 20 mg l^{-1} KIN + 5 mg l^{-1} IBA (KIN$_{20}$IBA$_5$) and 5 mg l^{-1} KIN + 20 mg l^{-1} IBA(KIN$_5$IBA$_{20}$) were applied as different treatments up to three times during different time of plant development. After 5 days of each application development parameters were analysed (Table 1).

Table 1 Different foliar exogenous phytohormones application time and number of applications per variant.

20 mg l^{-1} KIN + 5 mg l^{-1} IBA			
No	Treatment 1	Treatment 2	Treatment 3
Control	-	-	-
1.1	BBCH 14-16	-	-
1.2	BBCH 14-16	BBCH 31-33	-
1.3	BBCH 14-16	BBCH 31-33	BBCH 57-59
1.4	-	BBCH 31-33	-
1.5	-	BBCH 31-33	BBCH 57-59
1.6	-	-	BBCH 57-59

5 mg l^{-1} KIN + 20 mg l^{-1} IBA			
2.1	BBCH 14-16	-	-
2.2	BBCH 14-16	BBCH 31-33	-
2.3	BBCH 14-16	BBCH 31-33	BBCH 57-59
2.4	-	BBCH 31-33	-
2.5	-	BBCH 31-33	BBCH 57-59
2.6	-	-	BBCH 57-59

Biometric measurements. Ten representative oilseed rape plants were selected from each replication to determine pod number per plant and seed number per pod.

Statistical analysis. MS Excel Version 2010 and XLStat 2020 Data Analysis and Statistical Solution for Microsoft Excel (Addinsoft, France) statistical software were used for data processing. Analysis of variance (ANOVA) was carried out along with Tukey comparison test for statistical analyses, $p \leq 0.05$.

RESULTS

Applying exogenous phytohormones (20 mg l^{-1} KIN + 5 mg l^{-1} IBA; 20 mg l^{-1} IBA + 5 mg l^{-1} KIN) at early development (BBCH 14-16; BBCH 31-33) stages had positive effect on development of pods compared to the other applications (Fig 1).

Fig. 1. Pod number per plant. Treatments: Control – no treatment, Different concentrations of kinetin (KIN) and indole-3-butyric acid (IBA) were applied as follows: 1.1, 2.1 – at BBCH 14-16; 1.2, 2.2 – at BBCH 14-16 and BBCH 31-33; 1.3, 2.3 – at BBCH 14-16, BBCH 31-33 and BBCH 57-59; 1.4, 2.4 – at BBCH 31-33; 1.5, 2.5 – at BBCH 31-33 and BBCH 57-59; 1.6, 2.6 – at BBCH 57-59. Values are mean ± SE of 10 replicates and different letters are differed significantly by Tukey comparison test (P ≤ 0.05).

Furthermore, there was noticed significant seed number per pod reduction with increasing number of pods per plant (Fig. 2).
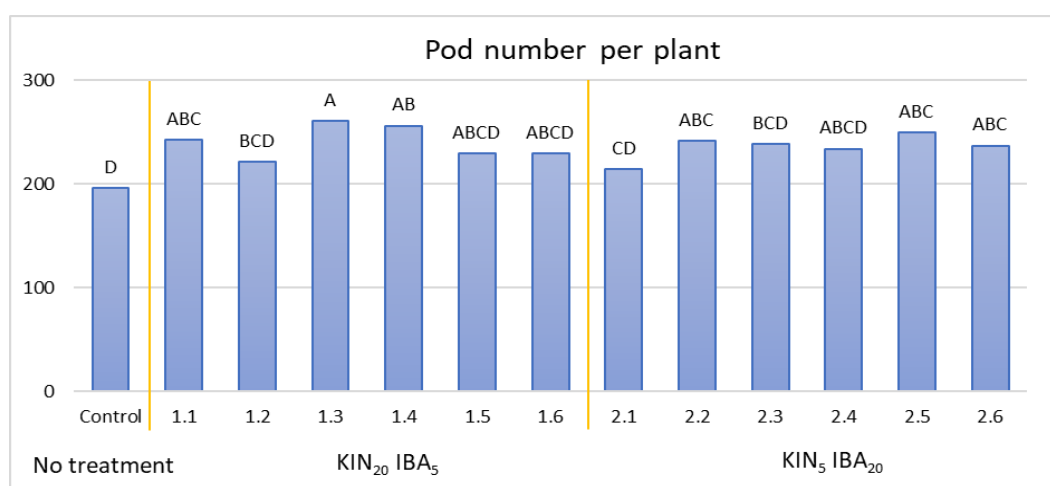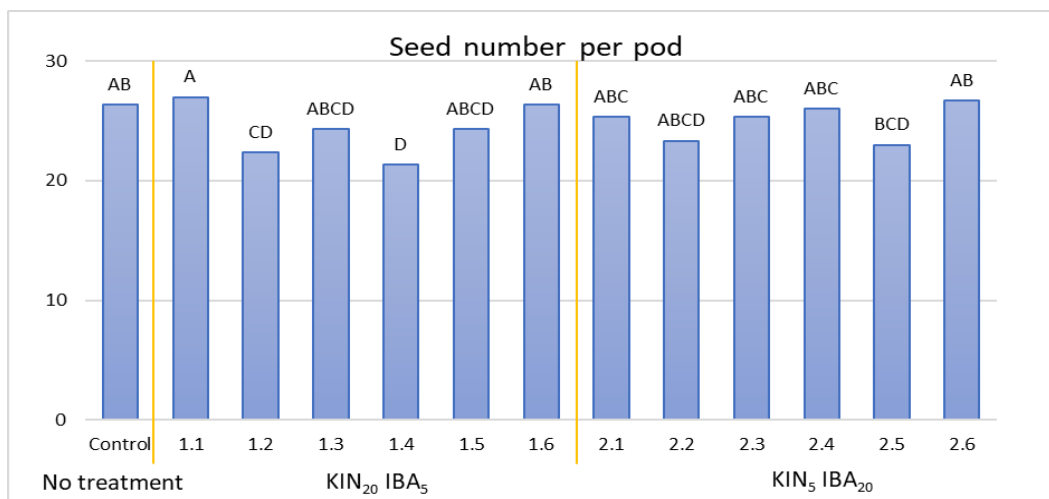
Fig. 2. Seed number per pod. Treatments: Control – no treatment, Different concentrations of kinetin (KIN) and indole-3-butyric acid (IBA) were applied as follows: 1.1, 2.1 – at BBCH 14-16; 1.2, 2.2 – at BBCH 14-16 and BBCH 31-33; 1.3, 2.3 – at BBCH 14-16, BBCH 31-33 and BBCH 57-59; 1.4, 2.4 – at BBCH 31-33; 1.5, 2.5 – at BBCH 31-33 and BBCH 57-59; 1.6, 2.6 – at BBCH 57-59. Values are mean $\pm$ SE of 10 replicates and different letters are differed significantly by Tukey comparison test ($P \leq 0.05$).

CONCLUSIONS

Exogenous phytohormones applications at early stages of development (BBCH 14-16; BBCH 31-33) found to have the greatest significant impact on productivity parameters using 20 mg l^{-1} KIN + 5 mg l^{-1} IBA one or two times throughout plant vegetation.

Keywords: Biostimulants, soil, oilseed rape, stress, fertilizers, biometric parameters, ontogenesis, exogenous phytohormones, cytokines, auxin.

REFERENCES

1. VELIČKA, R.; PUPALIENĖ, R.; BUTKEVIČIENĖ, L. M.; KRIAUČIŪNIENĖ, Z. Peculiarities of overwintering of hybrid and conventional cultivars of winter rapeseed depending on the sowing date. *Acta Scientiarum Polonorum., Agricultura*, 2012, P. 53-66.

2. CAI, T.; MENG, X.; LIU, X.; LIU, T.; WANG, H.; JIA, Z.; YANG, D.; REN, X. Exogenous hormonal application regulates the occurrence of wheat tillers by changing endogenous hormones. *Frontiers in plant science*, 2018, Vol. 9, P. 1886.

3. KRIAUČIŪNIENĖ, Z.; VELIČKA, R.; RAUDONIUS, S. The influence of crop residues type on their decomposition rate in the soil: a litterbag study. *Žemdirbystė Agriculture*, 2012, Vol. 99, P. 227-236.

4. YAKHIN, O. I.; LUBYANOV, A. A.; YAKHIN, I. A.; BROWN, P. H. Biostimulants in plant science: a global perspective. *Frontiers in plant science*, 2017, Vol. 7, No. 2049.

III.2. Toxic free environment

THE TRANSPORT PATHWAYS AND THE POTENTIAL SOURCES OF ^{7}BE IN THE ATHMOSPHER OF GRANADA, SPAIN

I.Berriban, M.Azahraa, E.chhama, A.Nouaytia, H.Ziania,
H.El Yaakoubia
ERSN, Faculty of sciences,
Abdelmalek Essaadi University, Tetouan, Morocco
Street Mhanech2, 93030 – Morocco
+212639094152
imanberriban23@gmail.com

ABSTRACT

Now a days, air pollution becomes progressively more serious. Therefore, an accurate identification of urban air pollution characteristics and associated pollutant transport mechanisms would helps to effectively control and minimize the main sources of the air pollution. This present work devote to specify the transport pathways, and potential sources of ^{7}Be in Granada city (Spain), based on ^{7}Be monitoring data from 2015 to 2017. This analysis has been evaluated using three methods: Clustering analysis by Hybrid Single-Particle Lagrangian Integrated Trajectory (HYSPLIT), the potential source contribution function (PSCF), and the concentration weighted trajectory (CWT), in order to identify the mainly transport pathways affecting air masses during the desired search period at two altitudes 750 m and 3000 m.

According to the obtained results of clustering analysis, five sectors of air masses were identified with different percentage in each altitude. This method showed that there are miltitudes air masses coming to Granada during the sampling period could be classified as: tropical continental air masses coming from the Mediterranean Sea, tropical and polar maritime air masses built over the Atlantic Ocean, and continental air masses produced over Europe and Northern Africa. Furthermore, the results of PSCF (Potential Source Contribution Function) are consistent with those of CWT (Concentration-Weighted Trajectory). Its indicate that the main source areas of ^{7}Be are located in the Atlantic coast of southern Morocco, and Northern Africa.

Keywords: Transport athways, ^{7}Be, potential source, Clustering analysis, PSCF, CWT.

INTRODUCTION

In each place on Earth there are specific geographical, geological, and climatological circumstances that influence the values of environmental radioactivity in the area [1]. Therefore, in order to know the radiation rate of a specific place, it must be adequately characterized radiologically, determining the content of radioactive elements in the various natural ecosystems that form it.

Since several decades ago, a multitude applications of the radionuclides were used, but is still a very powerful tool until now. The atmospheric radionuclides have been used to trace atmospheric transport and exchange processes [2], [3]. There are a three principal sources of atmospheric radioactivity: radon isotopes and their progeny, rayon cosmic produced radionuclides (cosmogenic radionuclides) and anthropogenic radionuclides.

The ^{7}Be is the cosmogenic radionuclide ($t_{1/2}$ = 53.3 days) which it is interest in this study. The ^{7}Be formed by cosmic ray spallation reactions with nuclei of light elements, such as Carbon, Oxygen and Nitrogen in the upper layers of the atmosphere [4], mostly producing in the stratosphere about 66% and in the upper troposphere about 33% [5]. It decays by electron capture with gamma emission (Eγ=477.6).

In this current research, the back-trajectories of air masses and ^{7}Be concentrations data from 2015 to 2017 has been analysed by three methods: Cluster analysis, PSCF, CWT to identify the source regions of the ^{7}Be affecting the air of Granada's city (Spain). These methods has been applied in several studies, such as Cluster Analysis of Back Trajectories coming into the region of Barcelona, Spain, between 1997 and 2002 by [6]. The concentration field method (CWT) of [7] was applied to detect the source areas of ozone. More recently, [8] was applied inverse modeling to investigate source regions of greenhouse gases and halogenated gases in Italian northern Apennines site [9].

MATERIAL AND METHODS

Study Area And Data Sources

The current research has been conducted in Granada city(Spain). Granada is an urban region located in the southeastern part of Andalusia, the region that includes the southen of the Iberian Peninsula. It is mainly encircled with multitude mountains. There are Sierra Gorda in the West, Subbaetic System Sierra de Huétor in the North, Sierra Arana and Sierra Nevada in the East. Granada's climate is continental Mediterranean, with hot and dry summers (Max: 35°C), city is protected from winds by the Sierra due to the fact that the Nevada and cold winters (Min: -4°C) due to the altitude of the municipality in the mountain (738 m).

The ^{7}Be data sets were obtained throughout three consecutive years, starting from January 2015 to December 2017. Specific details, the samples were weekly collected by an air sampler Radeco AVS-60A, as well as the cellulose filters 4.2 cm of effective diameter and 0.8 µm of pore size . The weekly filters collected during each month (4–5 filters) were analysing together. The analysis by Gamma-Spectrometry was performed using a vertical configuration coaxial inverted type germanium detector (HPGe) with a counting time of 90000 s.

The meteorological data developed by the NOAA's Air Resources Laboratory (ARL)[10], has been used as input to generate the back-trajectory and to obtained from GDAS data. Precisely, 96-h daily back-trajectories were calculated and recorded every 6h, namely, at 00:00, 06:00,

12:00 and 18:00 (UTC) in two altitude 750m and 3000m to simulate airflow transport trajectories near the ground surface in Granada during the period of interest, using the Hybrid Single-Particle Lagrangian Integrated Trajectory (HYSPLIT) model.

METHODOLOGY

Trajectory Clustering Analysis

Cluster analysis method is a statistical technique utilized to separate the trajectory data into several classes or clusters. Because this paper aims to define the direction from which the air masses that reach the site have originated. The Euclidean distance clustering method is utilized to cluster the back-trajectories by following equation:

$$d_{ij} = \sqrt{\sum_{n-1}^{p}(x_{in} - x_{jn})^2} ,$$ (1)

where, d_{ij} are the distance between i^{th} and j^{th} endpoints of trajectories , x_{in} is the value of the n_{th} variable of the ith endpoints. x_{jn} is the value of the nth variable of the jth endpoints.

PSCF And CWT Models

The Potential source contribution function (PSCF) model is a simple statistical method. The PSCF combine the residence time of the trajectories (generated by Hysplit) and high concentrations of ^{7}Be (collected and analysed in Granada) besed on conditional probability field (criterion) [11]. It was analyzed to determine the spatial source areas of ^{7}Be. It can be calculated as follows:

$$PSCF = \frac{m_{ij}}{n_{ij}}.$$ (2)

In each cell (i, j) there is the total number of endpoints n_{ij} that pass through it, and m_{ij} the number of endpoints of the same cell link with the trajectories wich have the concentration higher than a chosen criterion (75th). To reduce the uncertainty of some cells have a small value of n_{ij}, we used the weight function W_{ij}, particularly, when the total number of the endpoints in a each cell(i,j) was less than about three times the average value of the end points.

$$WPSCF_{ij} = W_{ij} \times PSCF_{ij}$$ (3)

$$W_{ij} = \begin{cases} 1.00 & n_{ij} > 80 \\ 0.70 & 20 < n_{ij} < 80 \\ 0.42 & 10 < n_{ij} < 20 \\ 0.05 & 10 < n_{ij} < 20 \end{cases}.$$

When the concentrations of the ^{7}Be could be slightly or much higher than the criterion some cells could have similar PSCF value. Therefore, it is hard to notice moderate sources from strong ones. Hence, to avoid the laminations of the PSCF method CWT method was used with the aiming of producing a geographical overview of source areas of ^{7}Be within the study region [14][15]. The CWT can be defined as:

$$CWT_{ij} = \frac{1}{\sum_{l=1}^{M} \tau_{ij}} \sum_{l=1}^{M} c_{ij}\tau_{ijl} ,$$ (4)

- C is the average concentration in the grid cell(i,j).
- L is the indicator of each trajectory.
- M is the total number of trajectories which pass through the cell (i,j).

To eliminate the effect of the small values of n_{ij}, we also applied weighting function described above in CWT analyses.

For two analysis models(PSCF, CWT) , we divided the areas covering all trajectories into 0.5°
× 0.5° cells.

RESULTS

Radioactivity Evolution Of ^{7}be
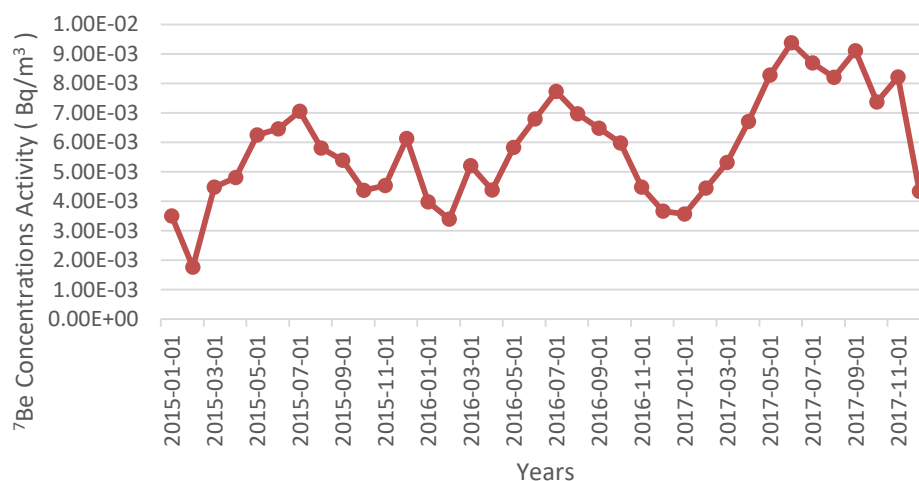
Fig. 1. Time series of ^{7}Be Activities acquired at Granada during the
research period.

Based on time series of ^{7}Be for Granada from 2015 to 2017 (Fig.1), we found that the concentration of ^{7}Be display a regular pattern over annual periods as well as, there is some changes in the activity concentrations of ^{7}Be. This caused by different factors, meteorological conditions (precipitation,humidity, temperature…). The monthly ^{7}Be concentration has an average value of 5.8 mBq m-3. This value is coherent with the average recorded in previous study in Spanish sites located at similar latitudes, such as Ciudad Real (5.36 mBq·m−3), Valencia (4.63 mBq·m−3) and Huelva (5.10 mBq·m−3) in Spain [16],[17].

The highest values of ^{7}Be concentration found during the warm seasons, which reached a maximum value (9.38 mBq·m−3) in June 2017, while the lowest values , was identified during cold seasons which reached a minimum value (1.76 mBq·m−3) in Febrary 2015.

This pattern is well-known and was often observed at mid-latitudes sites [18],[19],[20] and it is due to the vertical convection of the air masses between stratosphere and troposphere in the months concerning the pass from winter to summer [21].

Backward Trajectory Clustering

Actually, the air masses plays a key role in the transport and global distribution of aerosols at the surface Earth's atmosphere. Thus, Air Masses Classification (clustering analysis) method

was used throughout the procedure discussed earlier in Section 2 , in order identify the main origin and pathway of air masses arriving to Granada from January 2015 to December 2017.
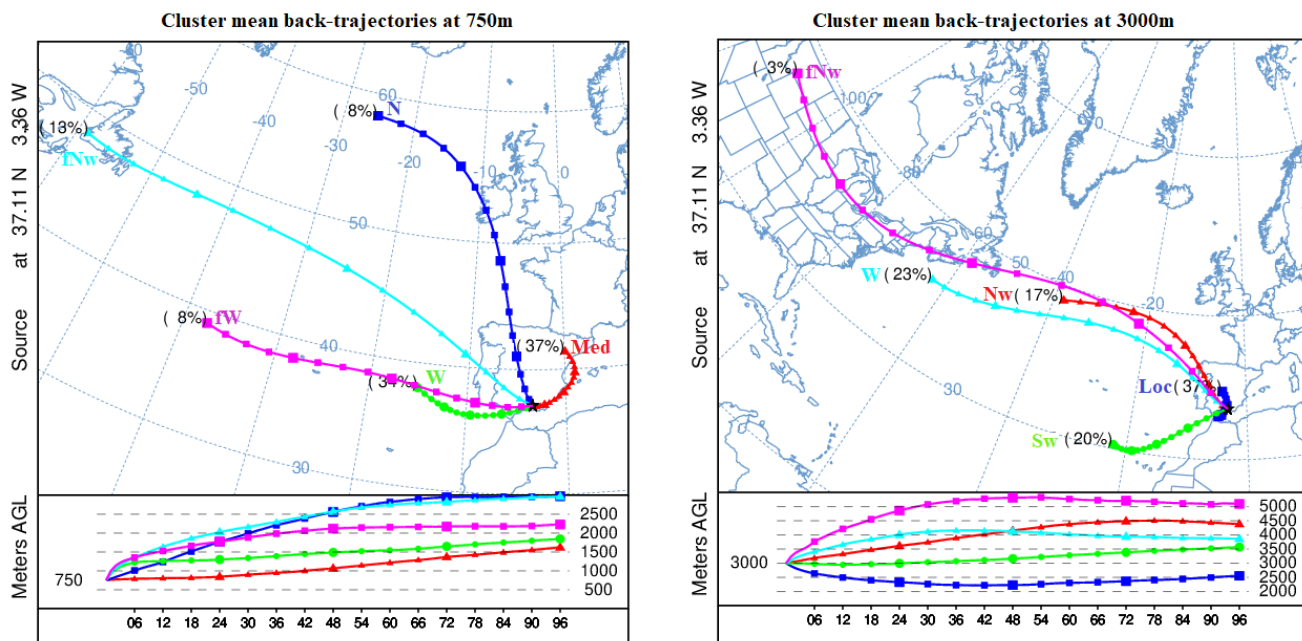
Fig. 2. Cluster mean back trajectories arriving in Granada at two altitude :
750m and 3000m

Fig.2, shows the air masses classification, five clusters were determined for two altitude 750m and 3000m.

As seen in this Figure, and upon the influence of the main air masses over Spain region [22],[23],[24], Five sectors of air masses were identified according to their source regions and described as following:

- North Sector (N, Nw, fNw): This sector includes a continental air masses produced over Europe (N), as well as the polar maritime air masses concentrated as continental over Atlantic Ocean (Nw), and also the most fastest air masses coming from North America (Nwf).

- West Sector (W, fW): This cluster mixes Atlantic tropical and warm polar maritime air masses created over Atlantic Ocean (W). Due to reduce passage time over the Atlantic Ocean, there is a quite fast air masses (fW).

- South West Sector (Sw): This cluster collect continental air masses and tropical maritime crossing the Straits of Gibraltar and the Northern of Africa before coming to Granada. Due to the continental air masses near to Sahel and Sahara dessert, the air masse connected by cluster Sw increase the concentration of n., Amineral dust.

- Local Sector (Loc): This cluster groups continental advection originated close to monitoring station. Thus, they are only detected from height levels (3000 m) with the highest contribution 37%.

- Mediterranean Sector (Med): The Mediterranean cluster composed by warm polar continental air masses formed over Mediterranean Sea, as well as slow tropical

continental air masses arriving from Africa. Therefore, these happening could be connected with the transport of high concentrations of mineral dust and also natural radionuclides (Piñero et al., 2015; Brattch et al., 2015).

PSCF And CWT Models

To investigate the region sources of ^{7}Be in Granada's city , the PSCF and CWT methods have been used. To take into account the different potential sources of ^{7}Be, two altitudes 750m and 3000m were applied. Fig.3 present the result of PSCF and CWT for ^{7}Be in Granada for two altitude 750m ans 3000m from 2015 and 2017. The colors present the contribution levels. For PSCF, the colors show the conditional probability that a cell is a source of ^{7}Be Activity above the 50th percentile value. Wheras, these colors presents the weighted average concentration of
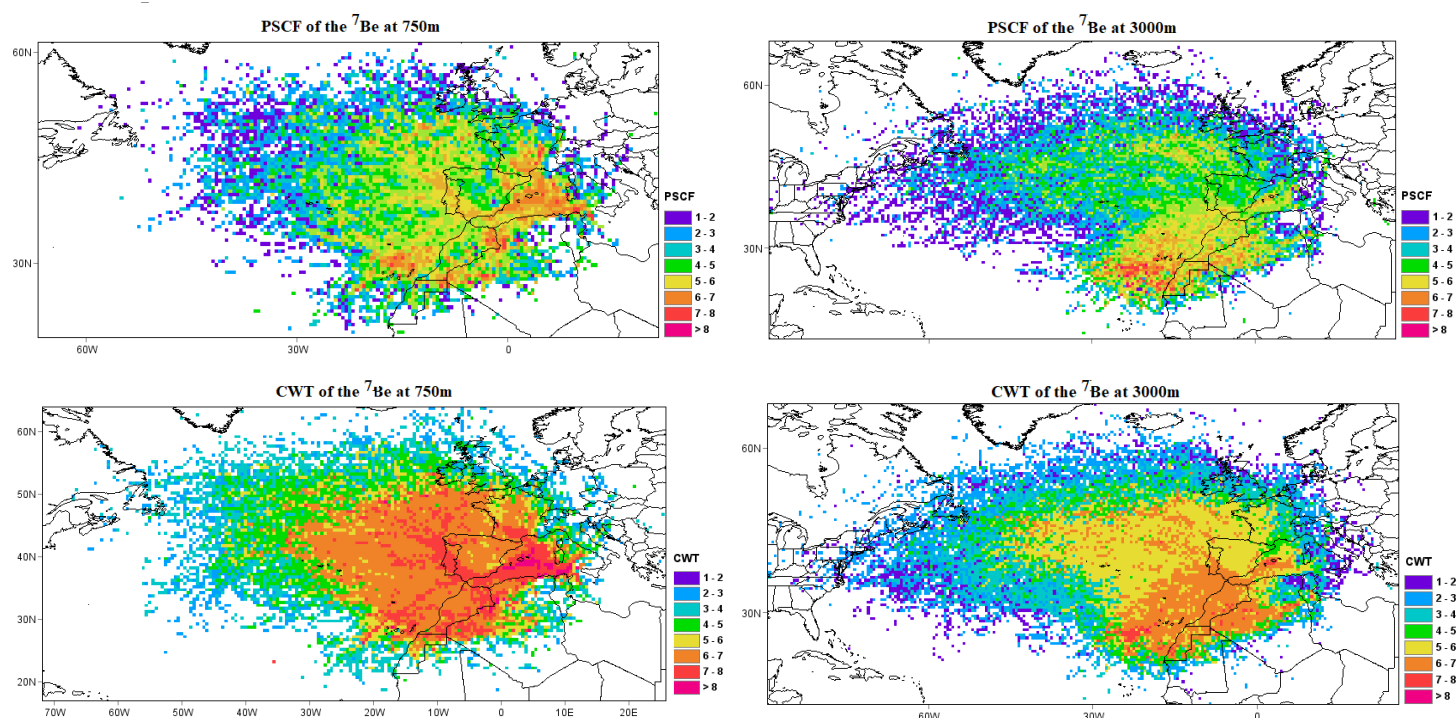
Fig. 3. PSCF values of ^{7}Be in 750 m, and 3000 m during the study period.

According to the results, different regions sources of ^{7}Be identified. At low altitude (750m), strong source regions are mainly found in basin Mediterranean, south eastern France and northwest Africa. On the other hand, in height altitude (3000m), Atlantic ocean of Morocco (Canary Islands) was founded as a source region of ^{7}Be. This caused by tropopause discontinuity in mid-latitude as well as, this region characterizes by cyclone formation and stratosphere-troposphere exchange (STE) promoting mechanisms , therefore, they are rich in ^{7}Be concentration. Fortheremore, The North Africa as source region is explained by African intrusions which increase the vertical transport of air masses, then, increase the concentration of ^{7}Be at the ground surface. Additionally, When CWT results are compared to the WPSCF results, they have basically consistent results for areas contributing to the ^{7}Be concentration in Granada, which demonstrates the credibility and accuracy of the analysis results.

CONCLUSION

Based on ^{7}Be concentrations data and back trajectory analysis from 2015 to 2017, this paper investigate the influence of the origin and the pathway of the air masses, as well as the source

areas related to high concentrations of ^{7}Be in Granada, using different trajectory analysis methods: Cluster analysis, PSCF, CWT. First, we presented an overview of the time series of ^{7}Be activity concentration. The result shows that ^{7}Be display a regular pattern over annual periods due to the origin and atmospheric conditions, the higher values were marked in the warm season and lower values in cold season. Moreover, the result of Clustering analysis provides valuable information about type of air masses arriving to Granada during the sampling period. Finally, PSCF and CWT models indicate that the main source areas of ^{7}Be are located in basin Mediterranean, southeastern France, northwest Africa Atlantic ocean in Morocco (Canary Islands).

REFERENCES

1. FEELY, H, W.; LARSEN, R, J.; SANDERSON, C, G. Factors that cause seasonal variations in Beryllium-7 concentrations in surface air. *Journal of environmental radioactivity*. 1989, Vol. 9, P. 223–249.

2. TUREKIAN, K. K.; GRAUSTEIN, W. C. Natural radionuclides in the atmosphere. *Journal of Treatise on Geochemistry*. 2003, Vol. *4*, P.347.

3. GÄGGELER, H. W.; JOST, D. T.; BALTENSPERGER, U.; SCHWIKOWSKI, M.; SEIBERT, P. Radon and thoron decay product and 210Pb measurements at Jungfraujoch, Switzerland. *Journal of Atmospheric Environment*. 1995, Vol. *29*, P. 607-616.

4. USOSKIN, I. G.; FIELD, C. V.; SCHMIDT, G. A.; LEPPÄNEN, A. P.; ALDAHAN, A.; KOVALTSOV, G. A.;UNGAR, R. K. Short-term production and synoptic influences on atmospheric ^{7}Be concentrations. *Journal of Geophysical Research: Atmospheres*. 2009, Vol. *114, No.*D6.

5. USOSKIN, I. G.; KOVALTSOV, G. A. Production of cosmogenic ^{7}Be isotope in the atmosphere: Full 3-D modeling. *Journal of Geophysical Research: Atmospheres*. 2008, Vol. *113*, No. D12.

6. JORBA, O.; PÉREZ, C.; ROCADENBOSCH, F.; BALDASANO, J. Cluster analysis of 4-day back trajectories arriving in the Barcelona area, Spain, from 1997 to 2002. *Journal of Applied Meteorology*. 2004, Vol. *43, No.* 6, P. 887-901.

7. BONASONI, P.; STOHL, A.; CRISTOFANELLI, P.; CALZOLARI, F.; COLOMBO, T.; EVANGELISTI, F. Background ozone variations at Mt. Cimone station. *Journal of Atmospheric Environment*. 2000, Vol. *34, P.* 5183-5189.

8. CRISTOFANELLI, P.; FIERLI, F.; MARINONI, A.; CALZOLARI, F.; DUCHI, R.; BURKHART, J.; BONASONI, P. Influence of biomass burning and anthropogenic emissions on ozone, carbon monoxide and black carbon at the Mt. Cimone GAW-WMO global station (Italy, 2165 m asl). *Journal of Atmospheric Chemistry and Physics*. 2013, Vol. *13*, P. 15-30.

9. BRATTICH, E.; ORZA, J. A. G.; CRISTOFANELLI, P.; BONASONI, P.; TOSITTI, L. Influence of stratospheric air masses on radiotracers and ozone over the central Mediterranean. *Journal of Geophysical Research: Atmospheres*. 2017, Vol. *122*, P. 7164-7182.

10. DRAXLER R. R.; ROLPH G. D. Hysplit model, NOAA Air Resources Laboratory. [Available at <http://www.arl.noaa.gov/ready/hysplit4. html>.]

11. POLISSAR, A. V.; HOPKE, P. K., PAATERO, P.; KAUFMANN, Y. J.; HALL, D. K.; BODHAINE, B. A.; HARRIS, J. M. The aerosol at Barrow, Alaska: long-term trends and source locations. *Journal of Atmospheric Environment*. 1999, Vol. *33, P.* 2441-2458.

12. POLISSAR, A.; HOPKE, P.; POIROT, R. Atmospheric aerosol over Vermont: Chemical composition and sources. *Journal of Environmental Science and Technology*. 2001, Vol. 35, P. 4604–4621.

13. WANG, L.; LIU, Z.; SUN, Y.; JI, D.; WANG, Y. Long-range transport and regional sources of PM2.5 in Beijing based on long-term observations from 2005 to 2010. *Journal of Atmospheric. Research*. 2015, Vol. 157, P. 37–48.

14. STOHL, A. Computation, accuracy and applications of trajectories—A review and bibliography. *Journal of Atmospheric Environment*. 1998, Vol. *36, P.* 947-966.

15. POLISSAR, A. V.; HOPKE, P. K.; PAATERO, P.; KAUFMANN, Y. J.; HALL, D. K.; BODHAINE, B.; HARRIS, J. M. The aerosol at Barrow, Alaska: long-term trends and source locations. *Journal of Atmospheric Environment*.1999, Vol. *33, P.* 2441-2458.

16. SAN MIGUEL, E. G.; HERNÁNDEZ-CEBALLOS, M. A.; GARCÍA-MOZO, H.; BOLÍVAR, J. P. Evidences of different meteorological patterns governing [7]Be and ^{210}Pb surface levels in the southern Iberian Peninsula. *Journal of environmental radioactivity*. 2019, Vol. *198*, P. 1-10.

17. CHHAM, E.; PIÑERO-GARCÍA, F.; BRATTICH, E.; EL BARDOUNI, T.; FERRO-GARCÍA, M. A. [7]Be spatial and temporal pattern in southwest of Europe (Spain): Evaluation of a predictive model. *Journal of Chemosphere*. 2018, Vol. *205*, P. 194-202.

18. DELRÍO, L.; JIMENEZ, A.; MIRO, C.; PANIAGUA, J.; RUFO, M. Analysis of the temporal evolution of atmospheric [7]Be as a vector of the behavior of other radionuclides in the atmosphere. *Journal of radioanalytical and nuclear chemistry*. 1996, Vol. *207*, P. 331-344.

19. DUEÑAS, C.; FERNÁNDEZ, M. C.; LIGER, E.; CARRETERO, J. Gross alpha, gross beta activities and [7]Be concentrations in surface air: analysis of their variations and prediction model. *Journal of Atmospheric Environment*. 1999, Vol. *33*, P. 3705-3715.

20. DOERING, C.; AKBER, R. Describing the annual cyclic behaviour of [7]Be concentrations in surface air in Oceania. *Journal of environmental radioactivity*. 2008, Vol. *99*, P. 1703-1707.

21. CHHAM, E.; MILENA-PÉREZ, A.; PIÑERO-GARCÍA, F.; HERNÁNDEZ-CEBALLOS, M. A.; ORZA, J. A. G.; BRATTICH, E.; FERRO-GARCÍA, M. A. Sources of the seasonal-trend behaviour and periodicity modulation of [7]Be air concentration in the atmospheric surface layer observed in southeastern Spain. *Journal of Atmospheric environment*. 2019, Vo. *213*, P. 148-158.

22. CAPEL MOLINA , J .J . LOS CLIMAS DE ESPAÑA (The Climates Of Spain). Oikos-Tau, Pp. 429. Carvalho A C, Reis M, Silva. L, Madruga M J. A decade of [7]Be and 210Pb

activity in surface aerosols measured over the Western Iberian Peninsula. *Journal of Atmospheric Environment.* 2013, Vol. 67, P. 193-202.

23. TOLEDANO, C.; CACHORRO, V, E.; DE, FRUTOS, A, M.; TORRES, B.; BERJON, A.; SORRIBAS, M.; STONE, R, S. Analysis of aerosol types at El Arenosillo (Spain). J. Appl. *Journal of Applied Meteorology and Climatology*. 2008, Vol. 48, P. 962-981.

24. CALVO, A, I.; OLMO, F, J.; LYAMANI, H.; ALADOS-ARBOLEDAS, L.; CASTRO, A.; FERNANDEZ-RAGA, M.; FRAILE, R. Chemical composition of wet precipitation at the background EMEP station in Víznar (Granada, Spain) (2002-2006). *Journal of Atmospheric Research*. 2010, Vol. 96, P. 408-420.

REVIEW AND ANALYSIS OF RECENT LITERATURE ON CHEMICAL EXTRACTION OF CHITOSAN FROM SHRIMP WASTES

A. Hosney, K. Barčauskaitė
Lietuvos Agrarinių Ir Miškų Mokslų Centras
Instituto al.1, 58344 Kėdainiai distr. – Lithuania
+37062361165
Ahmed.Hosney@lammc.lt

EXTENDED ABSTRACT

OVERVIEW

During the past decades, the shrimp sustainable industry has gained great importance in the world and showed tangible progress, as well as contributed to increasing aquaculture production. The increasing global interest in sustainable shrimp farming is attributed to the important economic role it plays in supporting the food security strategy, providing a high-value protein source, in addition to the increasing demand for it in the global markets, and its good marketing price. The growth of the green economy and sustainable production are the main factors driving the growth of organic shrimp farming activities [1]. Many shrimp-producing countries are making sincere efforts to comply with the concept of responsible aquaculture due to rapid expansion and growing awareness of the negative impacts of shrimp farming practices on the environment and its own production. Good Aquaculture Practices (GAP) are increasingly being developed and implemented to improve biosecurity, increase cost efficiency, reduce chemical residues, and increase traceability [2]. A substantial portion of the overall fisheries and aquaculture harvest is wasted globally, approximately about 35 percent of the total production [3].

In shrimp aquaculture, the shrimp shells are representing a large portion of the total waste during the moulting process in shrimp production stages or during the processing of harvested shrimps through removing the shells and heads by shrimp producers or by the end-user before cooking. Large quantities of shells wastage generated by the shrimp aquaculture industry are considered one of the most important ecological challenges, through their accumulation in the environment with a slow rate of degradation in the long-term concern which can lead to cause significant environmental impacts [4] and increase the ecological footprint produced by the shrimp aquaculture industry. Dumping and burning of shrimp shells are the most common non-eco-friendly ways of disposal.

The shrimp shells have low economic value by using them as animal feed, however, they are rich in protein, minerals, and chitin. Alternatively, this waste can be used to produce chitin and its derivative chitosan which has a high economic value with low production cost [5]. One of the most economically valuable scenarios is to extract chitosan from shrimp shells, which turns shrimp shells from useless waste into economic wealth represented in chitosan as a commercially important product with a wide range of applications.
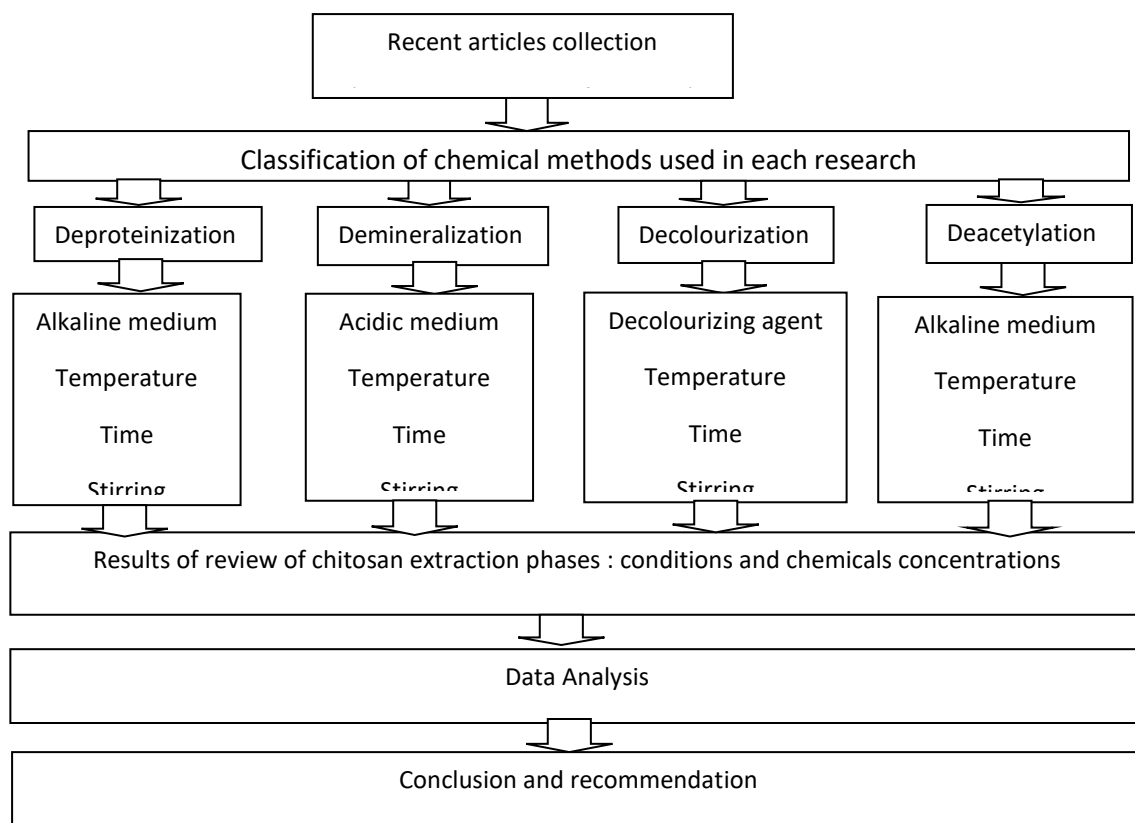
Chitosan is a natural biopolymer with biocompatibility, biodegradability, free toxicity which can enter in different sustainable economic activities such as food, pharmaceuticals, medicine, cosmetics, agriculture, textiles, pulp, and paper, biotechnology, environmental chemistry, and wastewater treatment industries to be a viable environmentally friendly option for shell remediation. In recent years, scientific research on the recovery of chitosan as a valuable material from shrimp shells has been raised to mitigate the ecological footprint caused by the aquaculture industry [6]. Chitin is considered the second most abundant natural polysaccharide after cellulose, present in the exoskeletons of crustaceans, crab, insects, and fungi [7]. Chitosan is a chitin-partially-deacetylated derivative made up of ß-(14)-linked N-acetyl-D-glucosamine homopolymers with three polymorphic conformations (α, β and γ) according to the source of extraction, while chitin is distinguished by its acetyl group. Chitosan has a high molecular weight that resembles cellulose. The main differences between chitosan and cellulose are that chitosan has an amine ($-NH_2$) group in position C-2 rather than the hydroxyl (-OH) group found in cellulose, moreover that chitosan has no plant origin like cellulose [8].

In recent studies chitosan is represented as a highly adaptable and promising active biopolymer. Despite its biodegradability, it can be chemically modified to produce derivatives because it has a free amino group which is the most useful chitin derivative with a variety of biomedical applications. These derivatives are simple to manufacture and commercially available. Chitin and chitosan have numerous applications in the pharmaceutical industry, tissue engineering, water treatment, agriculture, cosmetics, anti-tumour, and anti-microbial agents [9].

The main objective of this paper is to review and to analyse the recent literature on the chemical extraction of chitosan from shrimp wastes. Shrimp shells can be obtained daily through shrimp production from open ponds, indoor farms, or fish markets, then they are washed, dried, grinded to powder and then chemical treatments (Demineralization, Deproteinization, and Decolourization) are conducted to obtain chitin. Then chitosan can be obtained by deacetylation of chitin. Demineralization process whereas the shrimp shells are treated by an acidic solution of HCl, while in deproteinization, the alkaline solution of NaOH is added to the shells under specific temperature at a specific period, then decolourization process is taken place to obtain colourless or white chitin. The final chemical process to convert chitin into chitosan is deacetylation under the effect of an alkaline substance. Detailed procedures of demineralization, deproteinization, decolourization, and deacetylation processes of different articles will be discussed and reviewed in this paper. The data will be obtained from a literature review of chemical extraction chitosan will be analysed to show the variety of chemical extraction techniques and the most usable chemicals of each stage of chitosan extraction from shrimp shells.

METHODS

This paper has been designed to review, report and to study the recent obtained articles and research on the chemical synthesis of chitosan from shrimps' shells by the following methodology:

Recent articles collection

Classification of chemical methods used in each research

| Deproteinization | Demineralization | Decolourization | Deacetylation |

Alkaline medium	Acidic medium	Decolourizing agent	Alkaline medium
Temperature	Temperature	Temperature	Temperature
Time	Time	Time	Time
Stirring	Stirring	Stirring	Stirring

Results of review of chitosan extraction phases : conditions and chemicals concentrations

Data Analysis

Conclusion and recommendation

RESULTS

The results of review and analysis of recently published literature on the chemical synthesis of chitosan from shrimp wastes will show the different recovery methods and stages (Demineralization, Deproteinization, Decolourization, and Deacetylation) of chitosan from shrimp shells. The different concentrations of chemicals and conditions used in different research papers to recover chitosan from shrimp shells will be demonstrated.

CONCLUSIONS

Chitosan is a natural bio-polymer characterized with free toxicity, biocompatibility, and biodegradability, with a variety of medical, agricultural, and industrial applications. This paper reviewed and reported the chemical synthesis of chitosan from shrimp shells due to its importance to convert useless shrimp shells to an economically-valued substance (chitosan) and to mitigate the environmental impacts caused by non-environmentally discharging actions of shrimp wastes. Detailed data of the chemical extraction parameters (Demineralisation, Decolourization, Deproteinisation, Deacetylation phases, stirring, and temperature and time conditions) of chitosan conducted by various scientific researchers have been analysed. This paper will give indications and insights to optimize more eco-friendly methods of extraction of chitosan from shrimp shells in Lithuanian and EU shrimp farms in order to reduce ecological footprint results from this aquaculture sector.

Keywords: (Shrimp shells, Chemical extraction, Chitin, Chitosan).

REFERENCES

1. THE SHRIMP NETWORK. Euroshrimp.net. <https://www.euroshrimp.net/>, 2021.

2. FAO. Fisheries and aquaculture resources, 2006.

3. FAO. The State of World Fisheries and Aquaculture (SOFIA), FAO, 2020.

4. HOSSAIN, S.; KOUSHIC, U. M. Isolation, and extraction of chitosan from shrimp shells. *International Journal of Advanced Research*, 2020, Vol. 8, P. 657–664.

5. RASHMI S. H.; MAHENDRA, B.; Biradar, K. M.; Kittur, A. A. Extraction of chitin from prawn shell and preparation of chitosan. *Research Journal of Chemistry and Environment*, 2016, P. 70-73.

6. HOSSAIN, M. S.; IQBAL, A. Production and characterization of chitosan from shrimp waste. *Journal of the Bangladesh Agricultural University*, 2014, Vol. 12, P.153–160.

7. PANDHARIPANDE, S. L.; PUJARI, N. Review on synthesis, characterisation, and bioactivity of chitosan. *International journal of engineering sciences & research technology*, 2016, P. 334-344.

8. ZARGAR, V.; ASGHARI, M.; Dashti. A. A review on chitin and chitosan polymers: structure, chemistry, solubility, derivatives, and applications, *ChemBioEng Reviews*, 2015, P. 204-226.

9. Islam, A.; Islam, M. S.; Zakaria, M., Paul, S. C.; Mamun, A. A. Extraction and worth evaluation of chitosan from shrimp and prawn co-products. *American Journal of Food Technology,* 2019, Vol. 15, P. 43–48.

TAN SPOT SEVERITY IN SPRING WHEAT AFTER SOWING AT DIFFERENT RATES AND TIMES

A. Lukošiūtė-Stasiukonienė

Lithuanian Research Centre for Agriculture and Forestry
Instituto al. 1, Akademija, LT-58344 Kėdainiai district – Lithuania
+370 622 47703
agne.lukosiute@lammc.lt

EXTENDED ABSTRACT

OVERVIEW

Wheat (Triticum aestivum) is one of the main grain food sources for human consumption and globally is cultivated in regions of diverse climate, soil types, and latitudes [1]. According to the Lithuanian department of statistics [2], spring wheat was the second most popular agricultural cereal crop after winter wheat in 2021. The area sown with spring wheat increased by 11% in 2021 as compared to 2020. This shows the need for this plant.

There are probably no plant species that are not affected by harmful organisms. The most economically important wheat leaf diseases that constitute a major constraint to wheat production globally are tan spot (Pyrenophora tritici-repentis), septoria leaf blotch (Zymoseptoria tritici) [3, 4, 5, 6], and powdery mildew (Blumeria graminis) [4, 5, 7]. Septoria leaf blotch is heavily researched [8], while tan spot has been less intensively studied, and its occurrence and degree of crop losses are less understood [9]. A. F. Justesen [9] with other researchers proposes that farming practices such as tillage methods, spring or winter crops, and adaptation to specific climate are the main drivers determining which of the fungi diseases becomes dominant when mixed infections are evident.

In 2020, the European Commission published a new biodiversity strategy that aims to halt the loss of biodiversity by 2030 [10], setting concrete goals for Europe. For example, the use of chemical and hazardous pesticides and their risks must be decreased by 50%. Hence, reducing the use of chemical and hazardous plant protection products is one of the key objectives of European Union agricultural policy.

Agriculture is increasingly affected by global climate change, which is one of the defining issues of the early 21st century. Sowing methods are one of the management options that also influence the effects of future climate change on plant-pathogen interactions [11]. This study focuses on low-cost and environmentally safe disease control in wheat through the choice of sowing date and seeding rate. This approach is particularly valuable and useful as it informs about future possibilities to reduce the risk of fungal diseases of wheat. How to protect crops from disease without damaging nature is the main problem in crop protection control today. These factors need to be fully analyzed and investigated to reduce crop production's vulnerability to ongoing climate change. This may change future wheat fungal disease risk modeling in cases where pathogens adapt to changed environmental conditions.

This study aimed to compare the susceptibility of spring wheat to fungal disease when sown at different sowing times and rates.

METHODS

A multifactor field experiment was carried out at the experimental field of the Institute of Agriculture of Lithuanian Research Centre for Agriculture and Forestry in 2021. Three seeding rates (400, 500, and 600 viable seeds m^{-2}) and three sowing times (early, optimal and late) were tested. Tan spot (Pyrenophora tritici-repentis) occurred in spring wheat and was the main disease. The severity evaluation of the disease was done in growth stages at BBCH 37–41, 59–65, 75 according to the methods described in the European and Mediterranean Plant Protection Organization (EPPO) standard (PP1/26(4), 2012). The diseased leaf area was visually assessed on all green leaves of 10 randomly selected main tillers per plot. Disease assessments were performed on the background of natural infection. The spring wheat experiments were set up in 4 replications. The replicate blocks were arranged in four blocks in a compact near-square rectangular plot. Full randomization was used in the trials. Duncan's test was used to compare the means of disease severity with a significance level of $p \leq 0.05$.

RESULTS

June and July of 2021 were the hottest months of the year also dangerous rainfall events were recorded in these months, with some areas receiving no rainfall at all and others receiving the heaviest rainfall, creating the most favorable conditions for the spread of the tan spot. Tan spot infection in spring wheat was severe in 2021. The severity of tan spot at the stage of development flag leaf appearance-beginning of booting (BBCH 37–41) on the third leaf was similar at all sowing dates but was higher in the more dense crops (500 and 600 seeds m^{-2}) compared to the fields sown at the lowest sowing rate (400 seeds m^{-2}) on the second and third leaves (Figure 1). At the end of the heading flowering stage (BBCH 59–65), the tan spot infection in the plots at late sowing time was much higher than early and optimal sown plots (Figure 2). In early, optimal and late time sown plots tan spot severity at milk ripening stage (BBCH 75) on the second leaves was similar, but the flag leaves were less affected in the plots sown at the lower seeding rate (400 and 500 seeds m^{-2}) compared with the plots sown at the highest seeding rate (600 seeds m^{-2}) (Figure 3).

The weather conditions are one of the main factors that largely determine the occurrence of fungal diseases. Warmer temperatures favor most fungal species up to their upper-temperature threshold [12]. Conditions considered favorable for infections of tan spot disease include continuous precipitation or high levels of humidity (> 90%) for several hours (> 4 h) [13]. Temperature also plays an important role in tan spot development. The severity of the tan spot was positively correlated with temperature, with an optimum between 18 to 28 °C depending on the variety used [14].

According to Anne-Grete Roer Hjelkrem [15] and other researchers, the dynamic host-pathogen interactions over different phenological stages lead us to hypothesize that different weather variables can affect leaf blotch disease development at different growth stages in the spring wheat development as well.

Fig. 1. The effect of sowing time and seeding rate on tan spot (*Pyrenophora tritici-repentis*) severity in spring wheat at growth stage BBCCH 37–41 in 2021. Columns with the same letters do not differ at p ≤ 0.05
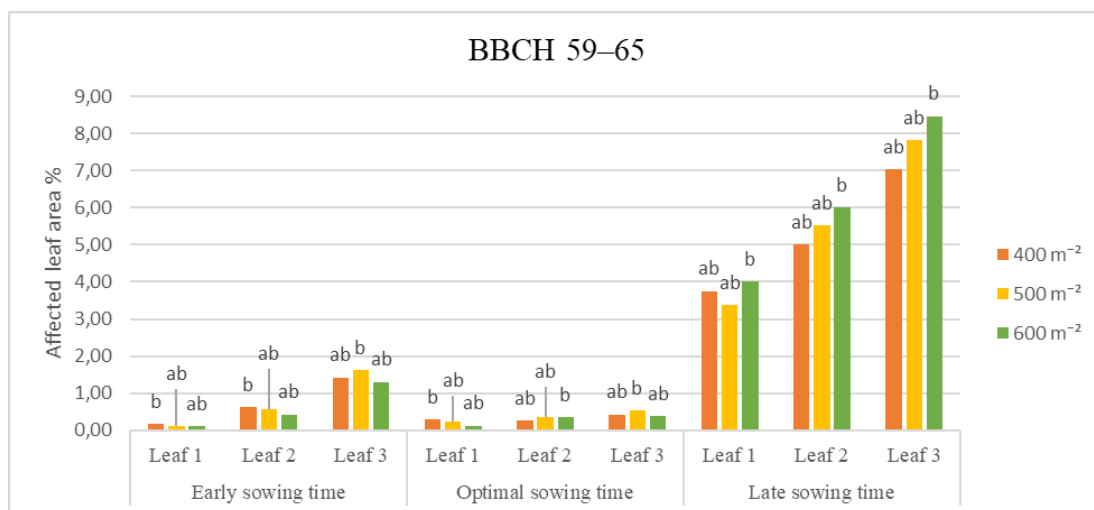
Fig. 2. The effect of sowing time and seeding rate on tan spot (*Pyrenophora tritici-repentis*) severity in spring wheat at growth stage BBCCH 59–65 in 2021. Columns with the same letters do not differ at p ≤ 0.05
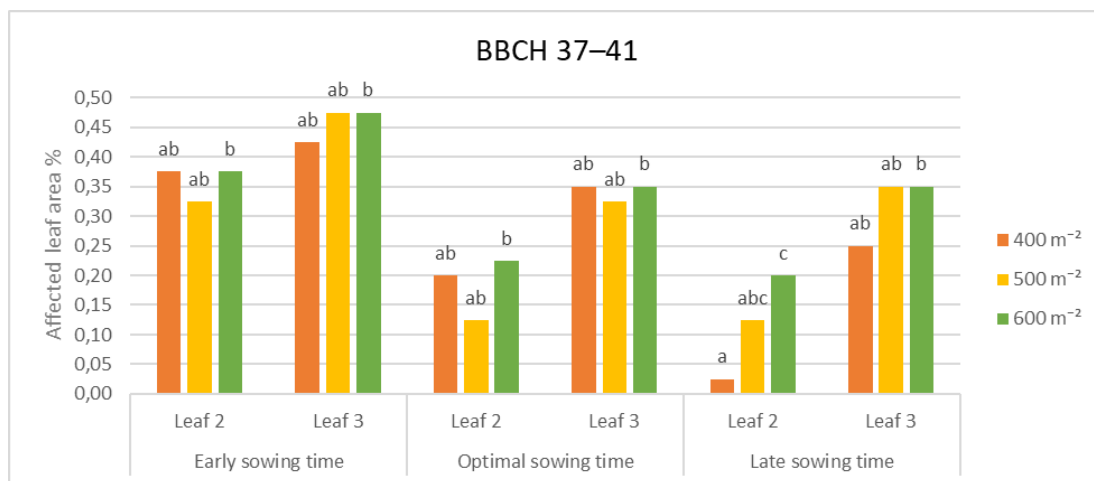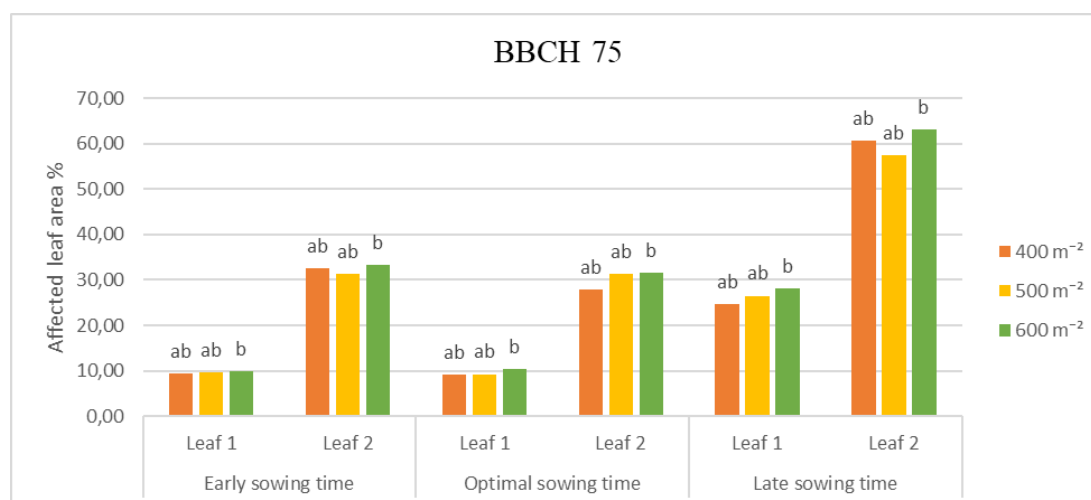
Fig. 3. The effect of sowing time and seeding rate on tan spot (*Pyrenophora tritici-repentis*) severity in spring wheat at growth stage BBCCH 75 in 2021. Columns with the same letters do not differ at

$p \leq 0.05$

CONCLUSIONS

The results of the study suggest that tan spot infection in spring wheat was severe in 2021 and tan spot severity was higher in the late sown crop than in the early and optimum sown crop and there was a tendency for the dense crop to have a slightly higher tan spot severity than the thinner crop.

Keywords: tan spot, spring wheat, sowing time, seeding rate, a fungal disease.

REFERENCES

1. ALIAKBAR, E.; DANIELLE, U.; AMANDA, M; COUNTRYMAN, D. THILMANY, An Overview of Global Wheat Market Fundamentals in an Era of Climate Concerns, *International Journal of Agronomy*, 2017, Vol. 2017, P. 15. DOI: 10.1155/2017/3931897.

2. The Lithuanian Department of Statistics, 2021. Link to the internet <https://osp.stat.gov.lt/statistiniu-rodikliu-analize#/>.

3. RONIS, A.; SEMAŠKIENĖ, R. Relationship of AUDPC values of tan spot and Stagonospora glume blotch with grain infection in winter and spring wheat. *Zemdirbyste=Agriculture*, 2011, Vol. 98, P. 11–18.

4. FERNANDEZ, M. R.; STEVENSON, C. F.; HODGE, K.; DOKKEN-BOUCHARD, F.; PEARSE, P. G.; WAELCHLI, F.; BROWN, A.; PELUOLA, C. Assessing effects of climatic change, region and agronomic practices on leaf spotting of bread and durum wheat in the Western Canadian prairies. *Agronomy Journal*, 2016, Vol. 108, P. 1180–1195. Doi: 10.2134/agronj2015.0451.

5. SINGH, R. P.; SINGH, P. K.; RUTKOSKI, J.; HODSON, D. P.; HE, X.; JØRGENSEN, L. N. Disease impact on wheat yield potential and prospects of genetic control. *Annual Review of Phytopathology*, 2016, Vol. 54, P. 303–322.

6. BANKINA, B.; BIMŠTEINE, G.; ARHIPOVA, I.; KAŅEPS, J.; STANKA, T. Importance of agronomic practice on the control of wheat leaf diseases. *Agriculture*, 2018, Vol. 8. Doi: 10.3390/agriculture8040056.

7. JØRGENSEN, L. N.; HOVMØLLER, M. S.; HANSEN, J. G.; LASSEN, P.; CLARK, B.; BAYLES, R.; RODEMANN, B.; FLATH, K.; JAHN, M.; GORAL, T.; CZEMBOR, J. J.; CHEYRON, P.; MAUMENE, C.; De POPE, C.; BAN, R.; NIELSEN, G. C.; BERG, G. IPM strategies and their dilemmas including an introduction to www.eurowheat.org. *Journal of Integrative Agriculture*, 2014, Vol. 13, No. 2, P. 265–281. Doi: 10.1016/S2095-3119(13)60646-2.

8. FONES, H.; GURR, S. The impact of Septoria tritici blotch disease on wheat: An EU perspective. *Fungal Genetics and Biology*, 2015, Vol.79, P. 3–7.

9. JUSTESEN, A.F.; CORSI, B.; FICKE, A. Hidden in plain sight: a molecular field survey of three wheat leaf blotch fungal diseases in North-Western Europe shows co-infection is widespread. *European Journal of Plant Pathology*, 2021, Vol. 160, P. 949–962. Doi: 10.1007/s10658-021-02298-5.

10. Biodiversity Strategy for 2030, 2020. Link to the internet <https://eur-lex.europa.eu/legal-content/EN/TXT/?qid=1590574123338&uri=CELEX:52020DC0380>.

11. MIEDANER, T.; JUROSZEK, P. Climate change will influence disease resistance breeding in wheat in Northwestern Europe. *Theoretical and Applied Genetics*, 2021, Vol. 134, P. 1771–1785, DOI: 10.1007/s00122-021-03807-0.

12. RACCA, P; KLEINHENZ, B; ZEUNER, T; KEIL, B; TSCHÖPE, B; JUNG, J. Decision support systems in agriculture: administration of weather data, use of geographic information systems (GIS) and validation methods in crop protection warning service, Efficient Decision Support Systems - Practice and Challenges from Current to Future, Chiang Jao, IntechOpen, 2011, P. 331–354. Doi: 10.5772/20809.

13. FRANCL, L. J. Genesis and liberation of conidia of Pyrenophora tritici-repentis. *Canadian Journal of Plant Pathology*, 1998, Vol. 20, No. 4, P. 387–393.

14. DA LUZ, W. C.; BERGSTROM, G. C. Effect of temperature on tan spot development in spring wheat cultivars differing in resistance. *Canadian Journal of Plant Pathology*, 1986, Vol.8, No.4, P. 451–454.

15. HJELKREM, A. G. R.; FICKE, A.; ABRAHAMSEN, U. Prediction of leaf Bloch disease risk in Norwegian spring wheat based on weather factors and host phenology. *European Journal of Plant Pathology volume*, 2021, Vol. 160, P. 199–213. Doi: 10.1007/s10658-021-02235-6.

DETERMINING THE SOURCES OF GROSS ALPHA AND BETA RADIOACTIVITY CONCENTRATIONS IN THE ATMOSPHERE OF CANTABRIA (SPAIN) BY ANALYZING THE BACK-TRAJECTORIES OF AIR MASSES

A. Nouayti, M. Azahra, E. Chham, I. Berriban, T. El Bardouni and H. Ziani
Physics Department (ERSN), Faculty of Sciences,
Abdelmalek Essaadi University
93002 Tetouan – Morocco
Phone number: +212643690194
abdelhamid.nouayti@etu.uae.ac.ma

ABSTRACT

In order to reach a pollution-free environment, firstly, the sources contributing to this pollution must be identified. The present study is part of radiological monitoring in the atmosphere. Therefore, we aimed to investigate the influence of air masses on the activity concentrations of gross alpha and beta in aerosols at the surface level of the Cantabria region, Spain (43°19'12"N,4°3'35.9994"W), in order to identify their source regions. Simultaneous measurements of the gross alpha and beta on airborne have been routinely carried out at the sampling site from 01 January 2014 to 31 December 2015. The air masses back-trajectories were generated by Hybrid Single-Particle Lagrangian Integrated Trajectory (HYSPLIT) and analyzed using Cluster Analysis, trajectory-based source-receptor models: potential source contribution function (PSCF) and concentration weighted trajectory (CWT). The results of the study showed that there is a strong relationship between the air masses coming from the southern cluster (500m and 1500m) which contains slow air masses rich in radioactive aerosols. These air masses come from areas where there is a significant amount of uranium in the ground. Which indicates that the concentrations of gross alpha and beta present in the air of Cantabria due mainly to the presence of radon gas descendants from these areas. Furthermore, the principal geographical source regions of gross alpha and beta were found in the continental region of Spain.

Keywords: Gross alpha and beta, Aerosols, Clustering, Source-receptor models.

INTRODUCTION

Since the birth of the Universe, radioactivity has been present in all matter, everything is naturally radioactive: the soil, the atmosphere and water …Moreover, industrial and human activities using radioactive substances cause the release of radionuclides into the environment. It is important to monitor and study the fate of these radioactive substances in the environment, in order to know their possible impact on human health. A large fraction of the radioactivity present in the aerosol samples is due to the radon gas ^{222}Rn and ^{220}Rn. These gases can escape from soil and rocks, through the disintegration of ^{232}Th and ^{238}U, into the earth's atmosphere, where the subsequent decay products interact with atmospheric gases and aerosols to form radioactive aerosol particles [1]. The radioactivity of aerosol samples depends on the sampling location, i.e., longitude and latitude, height, time of year and meteorological variables: temperature, pressure, wind direction, precipitation, etc [2]. And, several studies show the significant impact of air masses and their trajectories on air quality in a specific region. In this study we will analyze the air masses back-trajectories using cluster analysis and some source-receptor models in order to identify the sources of gross alpha and beta activity concentrations in the atmosphere of Cantabria.

METHODS

Gross alpha and beta activities were measured monthly in the Laboratory of Radiochemistry and Environmental Radiology of the Department of Inorganic Chemistry of Santander-Cantabria (Spain) during 2014-2015. Cantabria is located in northern Spain (43°19'12"N,4°3'35.9994"W), it presents oceanic climate conditions [3], the climate is temperate oceanic, cool and humid on the coast than the rest of the country due to the influence of the Atlantic Ocean. The method used to collect particles emitted into the atmosphere consists of collecting the aerosols through a filter adapted to a vacuum cleaner. Samples were taken weekly, passing air through the filter for 24 hours a day, and the stations operate 7 days a week. This process was repeated all year round, which allows us to perform temporal phenomenological monitoring. Gross alpha and beta activities were measured using the TRI-CARB 1500 liquid scintillator spectrometer. To generate back-trajectories of air masses arriving to Cantabria during the sampling period, we used Hybrid Single-Particle Lagrangian Integrated Trajectory (HYSPLIT) model, which developed by the National Oceanic and Atmospheric Administration (NOAA) Air Resources Lab (ARL). And we used, as input, the Global Data Assimilation System (GDAS1) data with a horizontal resolution of 1°, which corresponds to 100 km×100 km [4]. The back-trajectories of the air masses have calculated 4 times per day (every 6 hours), during the period between 01/01/2014 until 31/12/2015 for three altitudes: 500, 1500, and 3000 m.

In this study. We used clustering analysis, potential source contribution function (PSCF) and concentration weighted trajectory (CWT) models to obtain information on the relationship between origins and trajectories of air masses and the concentrations of alpha and beta in the atmosphere in Cantabria. Clustering is a statistical method which aims to divide the trajectories into homogeneous sub-groups called clusters, and we count on the Euclidean distance to distinguish between trajectories. This analysis was applied using the software Hysplit.[5]

$$d_{mi} = \sqrt{\sum_{k=1}^{n}(lat_{mk} - lat_{ik})^2 + (lon_{mk} - lon_{ik})^2} \qquad (7)$$

$$CSV_m = \sum_{i=1}^{c} d_{mi}; \qquad (2)$$

$$TSV = \sum_{m=1}^{N} CSV_m, \qquad (3)$$

where, d_{mi} is the Euclidean distance between the ith trajectory and the cluster-mean (m), n is the number of endpoints in a trajectory or the length of trajectories, *lon* and *lat* are the longitude and latitude values, respectively, at the endpoints (m,k) and (i,k). CSV_m is the cluster spatial variance for the mth cluster, c is the number of trajectories in the cluster m. TSV is the total spatial variance and N is the number of clusters.

This method of clustering is iterative, initially, the number of clusters equal the number of trajectories. At each iteration, we provisionally merge two clusters and we calculate TSV for this case, and we test that on all the possible combinations, finally, we definitely merge the couple which gives us the minimum value of TSV. So, the number of clusters decreases by one. The iterations continue until the last two clusters are combined, resulting all the trajectories in one cluster. The change in the Total Spatial Variance (TSV) as the trajectories are merged into one cluster will be used to decide the optimum number of clusters for each altitude. [2]

PSCF and CWT models divide the map into small cells. PSCF calculates the conditional probability that a cell is a source of concentration of alpha or beta above a criterion:

$$PSCF = \frac{m_{ij}}{n_{ij}}, \qquad (4)$$

such that m_{ij} is the number of endpoints of trajectories located in the cell(i,j) corespondant to a concentration higher than a value criterion. And nij is the total numbre of endpoits in the same cell [6]. And CWT calculates the average concentration contribution of each cell in the grid:

$$C_{ij} = \frac{1}{\sum_{l=1}^{M} \tau_{ijl}} \sum_{l=1}^{M} C_l \, \tau_{ijl}, \qquad (5)$$

where C_{ij} is the average weighted concentration in a grid cell (i.j), M is the number of endpoints in the the cell (i,j) and C_l is the concentration corresponding to each endpoint.[7]

RESULTS

In this section, we will present and analyse the results obtained in this work. We will study the impact of the air masses, arrived to Santander-Cantabria (Spain), on the concentration of gross alpha and beta activities measured during 2014-2015, and try to identify some areas that are likely to be a source of alpha and beta.

Evolution Of The Concentration Of Gross Alpha And Beta

Gross alpha and beta activities were measured monthly in Cantabria during the sampling period, so that the minimum values of gross alpha and beta concentrations were $2.26.10^{-5} \pm 4.45.10^{-6}$ Bq/m^3 and $15.82.10^{-5} \pm 7.38.10^{-6}$ Bq/m^3 respectively, the both are measured at feb 2014, the maximum values were $12.03.10^{-5} \pm 8.42.10^{-6}$ Bq/m^3 for alpha and $82.125.10^{-5} \pm 1.325.10^{-5}$ Bq/m^3 for beta are measured at Dec 2015. The mean value of concentraion of gross alpha activity is $5.37.10^{-5}$ Bq/m^3 with standard deviation of $2.87.10^{-5}$ Bq/m^3 and for beta, the mean value is $38.04.10^{-5}$ Bq/m^3 and standard deviation equal $17.16.10^{-5}$ Bq/m^3. The figures 1 and 2 present the monthly variation of average concentrations of alpha and beta activities during the sampling period.
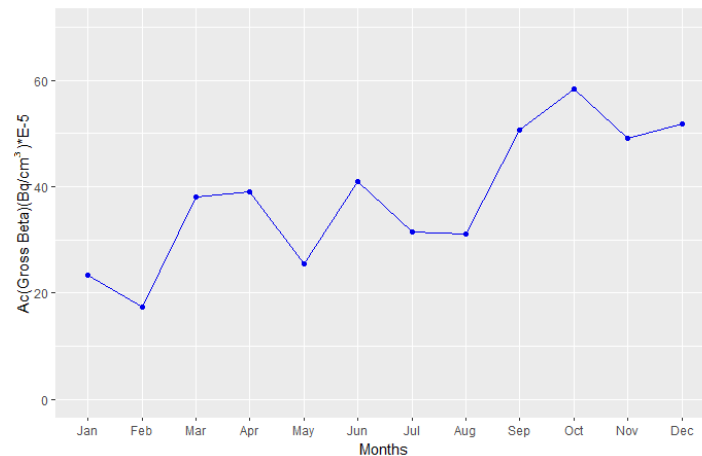
Fig. 1. Monthly variation of average concentration of beta activity
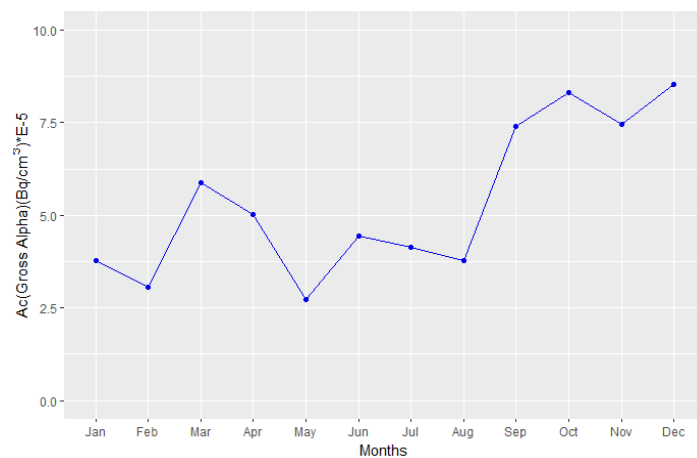
Fig. 2. Monthly variation of average concentration of alpha activity

Clustering Analysis

Using HYSPLIT, we calculated the back-trajectories of the air masses to know their origins and trajectories 72 hours before their arrival in Cantabria, 4 times per day (every 6 hours), during the period between 01/01/2014 until 31/12/2015 for three altitudes: 500, 1500, and 3000 m.

The calculated back-trajectories of air masses for each altitude have divided, by clustering analysis using Hysplit, to sub-groups or clusters. The figure 3 shows the clustering of air masses and the monthly frequencies of clusters at each altitude: 500, 1500, 3000m. As seen in Fig. 3, we have considerate 4 clusters at low altitude (500 m): North (N), fast North-West (fNW), slow South (sS), West (W), 5 clusters at intermediate altitude (1500 m): North-West (NW), fast North-West (fNW), south(S), West (W), North (N), and 5 clusters at high altitude (3000 m): West (W), fast North-West (fNW), North-West (NW), Local (L), South-West (SW). Here is a description of these clusters:

- The northern cluster (N) consists of continental air masses originating in Europe as well as polar marine air masses. These air masses are riche in maritime aerosols and could be identified as marine modified. This cluster is observed at the following altitudes: 28% at 500m and 15% at 1500m.

- The western cluster (W) is formed by tropical maritime air masses generated over the Atlantic Ocean, which have a strong maritime aerosols concentration, its contribution was 21% at high altitude (3000m), 17% at low altitude (500m) and 14% at altitude (1500m).

- Northwest clusters, fNW and NW, contain two kinds of air masses, the first represents some fast air masses generated in North America of continental origin which accounting for 14% at 500 m, 22% at 1500m. The second represent the polar maritime air masses coming from the North Atlantic, this cluster contribute by 18% at 1500m altitude and 20% at 3000m altitude without any contribution at low latitude(500m).

- The Southwest cluster (SW) combines maritime tropical air masses and others continental that cross north Africa and Spain to reach to Cantabria. It has only identified at high altitude (12% at 3000 m).

- The southern clusters S and sS contain short slow continental air masses generated on the Iberian Peninsula. Which will allow them to take the characteristics of the areas they pass through as well as transport the aerosols from these areas to cantabria. S appears at 1500m altitude with a contribution of 30% and sS appears at 500m altitude with a contribution of 41%.
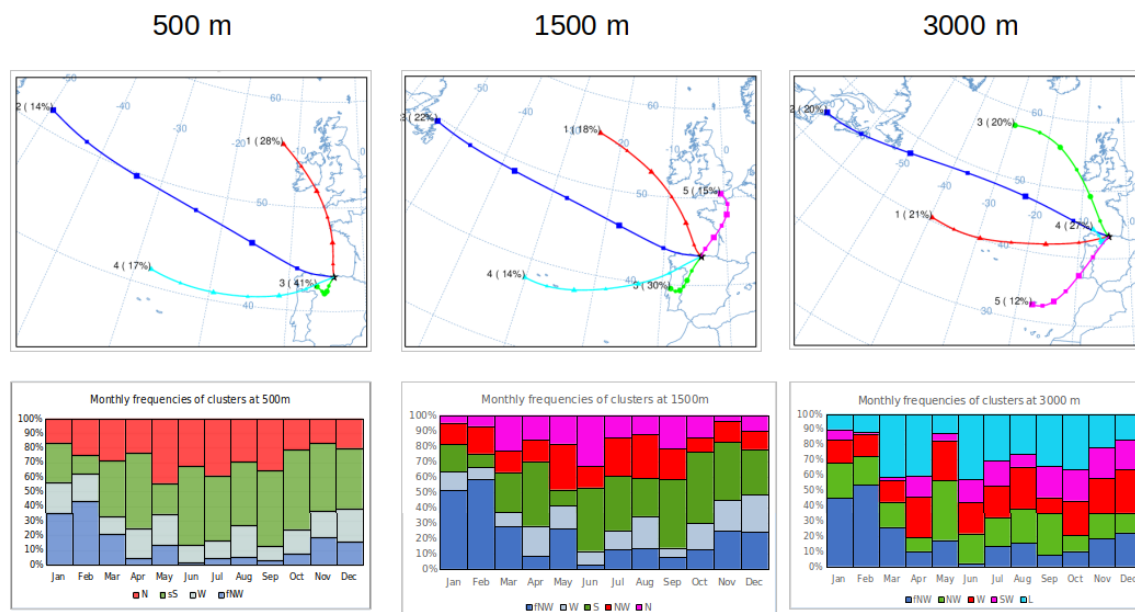
Fig.3. clustering of air masses and the monthly frequencies of clusters at each altitude: 500, 1500, 3000m.

After comparing the monthly frequencies of clusters at each altitude represented in the Fig.3 with the monthly variation curves of the average concentrations of gross alpha and beta (Figs. 1 and 2), we notice that the concentration of alpha and beta variate in the same way with the clusters S and sS. Months, where there is a large proportion of S or sS, show an increase in the concentrations of alpha and beta, and vice versa. Which suggests that there is a strong relationship between the clusters S and sS and the measured concentrations. The Fig. 4 shows the European map of uranium in soil. In this figure we notice that the clusters S and sS comes from regions rich in uranium in the soil. So, the origin of the gross alpha and beta concentrations in the Cantabria region is mainly explained by the presence of the descendants of radon gas

transported from the continental region of Spain rich in uranium to Cantabria by the clusters (S-sS).
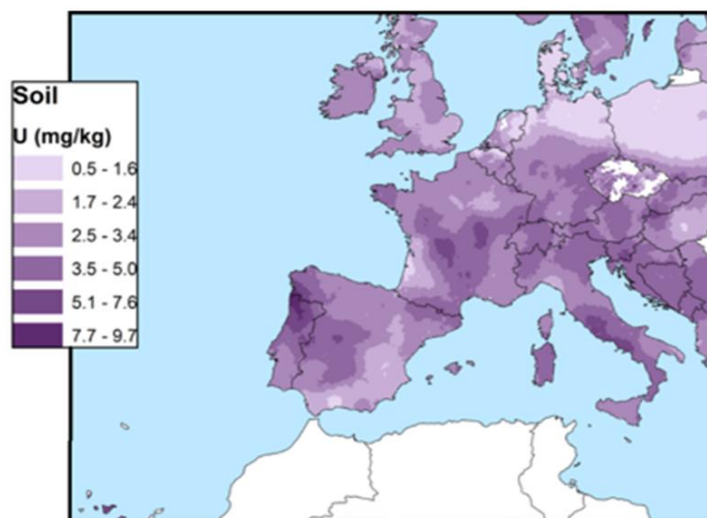
Fig. 4. The European map of uranium in soil [8].

PSCF and CWT analysis have applied to locate geographical areas that can be considered as sources of high concentrations of gross alpha and beta activities, PSCF and CWT analysis results for alpha and beta at: 500, 1500 and 3000 m altitude are shown in the Fig. 5, each color indicates the contribution of the zones to the concentration of alpha and beta activities in Cantabria.

PSCF and CWT highlight the source regions that affect the concentration of gross alpha and beta activities of samples (Cantabria). Also, we note that most of the areas considered as a strong source of gross alpha and beta are located in the continental region of Spain. Most of the region sources highlighted by PSCF and CWT, are granitic areas containing large amounts of uranium as illustrated in the European map of uranium in soil provided by National Competent Authorities and National Laboratories in European countries, as well as literature references (Fig. 4). So, they are rich in the descendants of radon gas attached to aerosols that can be transported to Cantabria. The lowest gross alpha and beta activities concentrations are generally in the Atlantic Ocean, which collects maritime polar air masses. The PSCF and CWT analysis results complete the clustering study results, they are compatible.
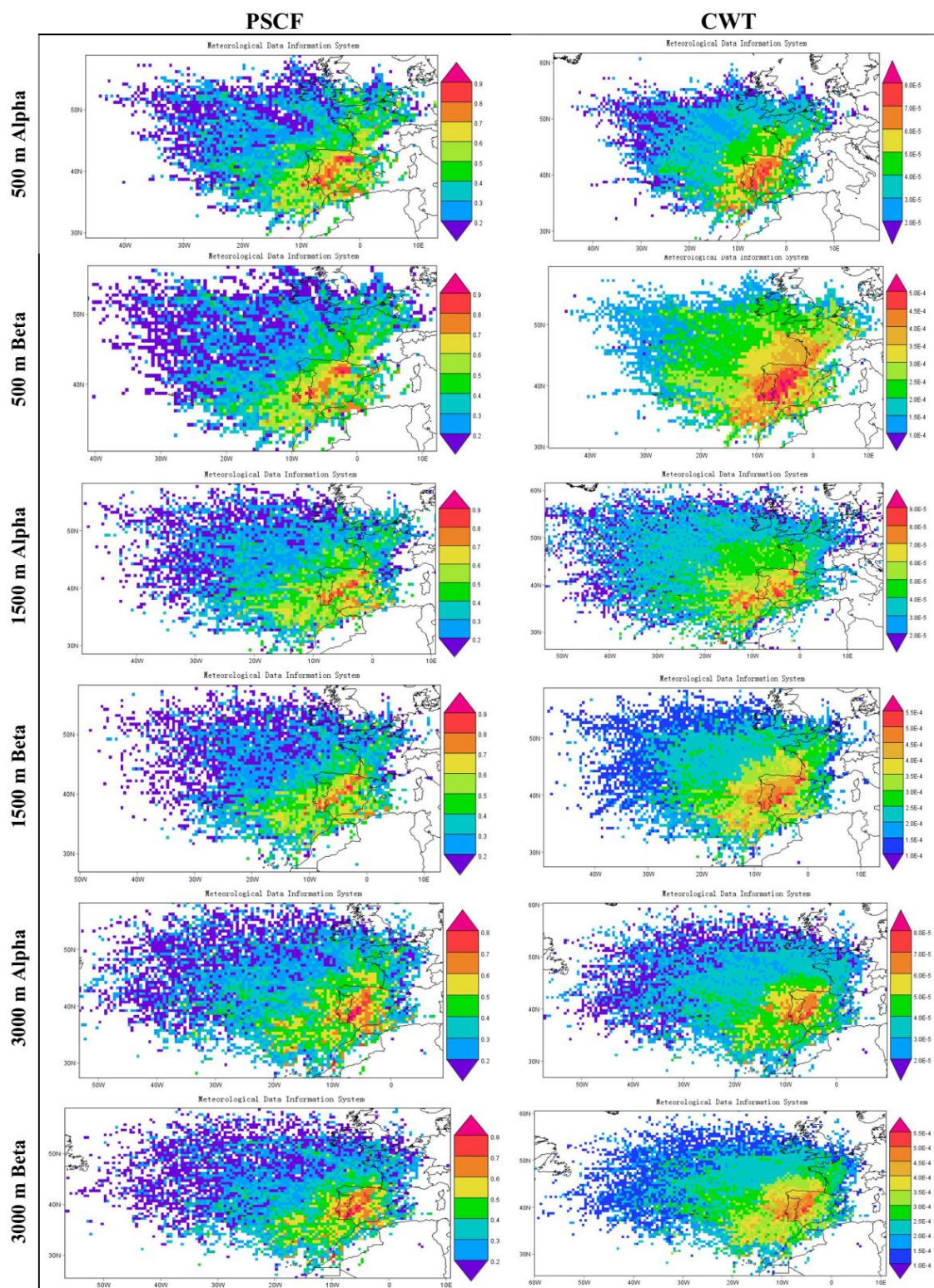
Fig. 5. PSCF and CWT analysis results for alpha and beta at: 500, 1500, 3000 m.

CONCLUSIONS

- The air masses of the southern cluster (S-sS) of continental origin carry different types of radioactive aerosols rich in alpha and beta emitters during their passage from southern Spain to reach Cantabria.

- The results of PSCF and CWT analyzes show that the most intense source regions of gross alpha and beta activity are mainly found in the continental region of Spain, which contains soils rich in uranium.

REFERENCES

1. SCHERY, S. D. Understanding radioactive aerosols and their measurement. Springer Science & Business Media; 2001 Jul 31.

2. PIÑERO-GARCÍA, F.; FERRO-GARCÍA, MA.; CHHAM, E.; COBOS-DÍAZ, M.; GONZÁLEZ-RODELAS, P. A cluster analysis of back trajectories to study the behaviour of radioactive aerosols in the south-east of Spain. *Journal of Environmental Radioactivity*, 2015, Vol. 147, P. 142-52.

3. UZQUIANO, P.; MAB. RUIZ-ZAPATA; MAJ. GIL-GARCIA.; S. FERNÁNDEZ.; AND J. S. CARRIÓN. Late Quaternary developments of Mediterranean oaks in the Atlantic domain of the Iberian Peninsula: The case of the Cantabrian region (N Spain). *Quaternary Science Reviews*, 2016, Vol. 153, P. 63-77.

4. SU, LIN.; ZIBING, YUAN.; JIMMY, CH, FUNG.; AND ALEXIS KH LAU. A comparison of HYSPLIT backward trajectories generated from two GDAS datasets. *Science of the Total Environment ,* 2015 , Vol. 506, P. 527-537.

5. DRAXLER, R.; STUNDER, B.; ROLPH, G.; STEIN, A.; TAYLOR, A. HYSPLIT4 User's Guide Version 4-Last Revision: November 2016. HYSPLIT Air Resources Laboratory: College Park, MD, USA,2016.

6. PEKNEY, J.; DAVIDSON, I.; ZHOU, L.; HOPKE, K. Application of PSCF and CPF to PMF-modeled Sources of PM2. 5 in Pittsburgh. *Aerosol Science and Technology*, 2006, Vol. 40, No. 10, P. 952-961.

7. JEONG, U.; KIM, J.; LEE, H.; JUNG, J.; KIM, Young J.; SONGB, Chul H.; KOO, J. Estimation of the contributions of long range transported aerosol in East Asia to carbonaceous aerosol and PM concentrations in Seoul, Korea using highly time resolved measurements: a PSCF model approach. *Journal of Environmental Monitoring*, 2011, Vol. 13, No.7, P. 1905-1918.

8. The European Atlas of Natural Radiation. The Radioactivity Environmental Monitoring group of the Joint Research Centre (JRC) of the European Commission, [referred on the 4th of March in 2022 y.]. Link to the internet < https://remon.jrc.ec.europa.eu/About/Atlas-of-Natural-Radiation/Digital-Atlas/Uranium-in-soil/Uranium-concentration-in-soil- >.

EMPIRICAL MODELLING AND OPTIMIZATION OF CADMIUM AND HEXAVALENT CHROMIUM BIOSORPTION BY FUNGAL BIOMASS

M. Roşca[1]*, R. M. Hlihor[1]*, P. Cozma[1,2], I. M. Simion[1], C. Filote[1,2]

[1]*"Ion Ionescu de la Brad" Iasi University of Life Sciences, Faculty of Horticulture, Department of Horticultural Technologies,*
3 Mihail Sadoveanu Alley, 700490 Iasi – Romania
mihaelarosca@uaiasi.ro, raluca.hlihor@uaiasi.ro

[2]*"Gheorghe Asachi" Technical University of Iasi, "Cristofor Simionescu" Faculty of Chemical Engineering and Environmental Protection, Department of Environmental Engineering and Management,*
73 Prof. Dr. Docent D. Mangeron Str., 700050 Iasi, Romania

EXTENDED ABSTRACT

OVERVIEW

Various biotic and abiotic factors can influence the performance of heavy metal microbial biosorption and can have not only individual but also cumulative effects on the process [1]. To evaluate the factors effects as well as to optimize the biosorption process, the experimentally obtained data can be empirical modelled and optimized using the design of experiments method (DOE) [1,2]. According to Wass [3] througt the DOE the relationship between the influencing factors and the output of a specific process can be established. The first step in applying the DOE consists in data screening in order to identify the important factors, followed by response surface methodology (RSM) application with the purpose to define the optimal space and finally the model validation [2,3]. Therefore, in this study we used DOE method for empirical modelling and optimization of Cd(II) and Cr(VI) removal from aqueous solutions by *Trichoderma viride* dead biomass.

METHODS

The empirical modelling and optimization of Cd(II) and Cr(VI) biosorption by *Trichoderma viride* was performed with Minitab 17 statistic software package. The magnitude of individual and combined effects of the pH, biosorbent dose, contact time, initial concentration and temperature on process efficiency was established by application of factorial design and the importance by the analysis of variance (ANOVA). Through RSM was generated the mathematical equation that best describes the relationship between the contact time, the initial concentration of ions in solution and the temperature at which the process takes place, which was subsequently used to establish the optimal conditions at which the highest performances are reached. The concordance between experimental data and the statistical models was established based the coefficient of determination values (R^2) and the factors statistically importance based p value (95% confidence interval). The biosorption performance of Cd(II) ions was evaluated in the range of 4-7 for pH, 1-10 g/L for biosorbent dose, 25-500 mg/L for

initial concentration, considering 72 hours maximum contact time and temperature between 25 and 50°C. For Cr(VI) biosorption the pH was varied between 1 and 4, the initial concentration between 25 and 250 mg/L and maximum contact time was 480 hours, considering the same ranges of variation for biosorbent dose and temperature as for Cd(II) biosorption.

RESULTS

The magnitude and importance of the individual and cumulative effects of the factors was highlighted by Pareto chart of the standardized effects (Fig. 1). According to this graph, for example, the variation of pH, biosorbent dose and the initial ion concentration in solution have significant individual effects on Cd(II) biosorption efficiency and the biosorbent dose and temperature on Cr(VI) biosorption. The result of empirical modelling of the experimental data through RSM showed that the relationship between the contact time, the initial concentration of ions in solution, the temperature and Cd(II)/Cr(VI) biosorption efficiency is better described by a second polynomial equation. The coefficient of determination values (R^2) are 84.67% for Cd(II) biosorption, respectively 90.47% for Cr(VI) biosorption, which means that the mathematical equations generated by RSM explain with high accuracy the variability of the response data around its mean.

(a)   (b)
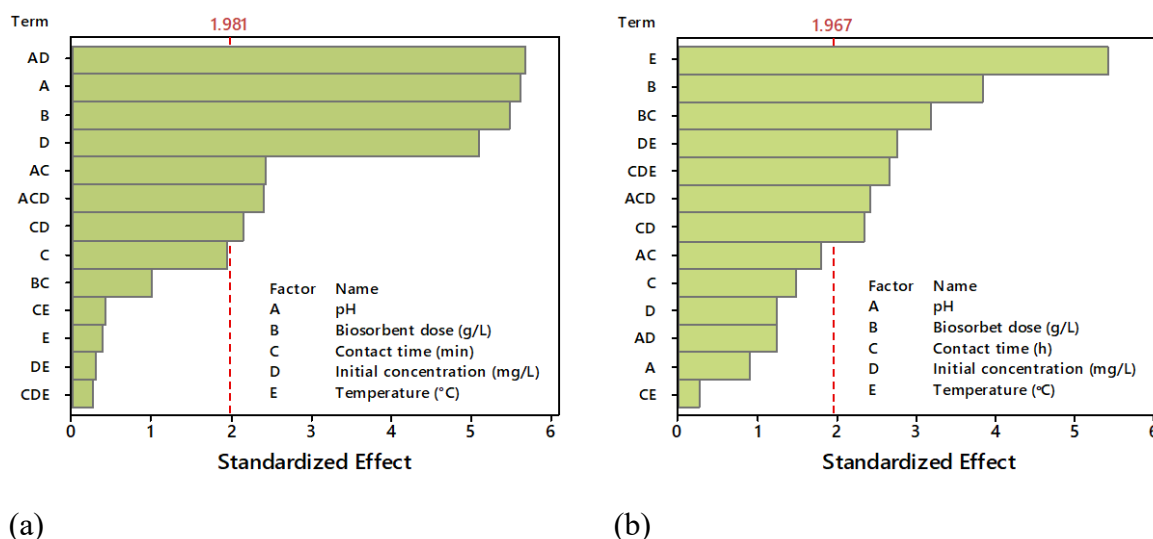
Fig. 1. Pareto chart of the standardized effects of the tested parameters on
(a) Cd(II) and (b) Cr(VI) biosorption by *Trichoderma viride*

CONCLUSIONS

The results of this study have shown that DOE method is useful both in identifying the factors that significantly influence the biosorption efficiency and in optimizing the process. RSM provided a good quality prediction of Cd(II) and Cr(VI) biosorption efficiency for three independent variables (initial concentration, contact time and temperature).

Keywords: biosorption, design of experiments method, process screening, *Trichoderma viride*

ACKNOWLEDGMENTS

REFERENCES

1. ROŞCA, M.; HLIHOR, R.M.; COZMA, P.; SIMION, I.M.; FILOTE, C.; GRECU, C.; STOLERU, V.; GAVRILESCU, M. Scaling-Up Strategies of Heavy Metals Microbial Bioremediation. Proceedings of 2021 International Conference on e-Health and Bioengineering (EHB). Iasi, Romania. 2021 November 18-19.

2. JANKOVIC, A.; CHAUDHARY, G.; GOIA, F. Designing the design of experiments (DOE) – An investigation on the influence of different factorial designs on the characterization of complex systems. *Energy and Buildings*. 2021, Vol. 250, No. 1, P. 111298.

3. WASS, J.A. First Steps in Experimental Design II: More on Screening Experiments. *The Journal of Validation Technology*. 2011, Vol. 17, No. 1, P. 46-53.

HARVEST TIME IMPACT ON MAIZE GRAINS NUTRIENT COMPOSITION AND ZEARALENONE CONCENTRATION

E. Venslovas, A. Mankevičienė, Y. Kochiieru

Lithuanian Research Centre of Agriculture and Forestry
Instituto al. 1, LT-58344 Akademija, Kėdainiai distr. – Lithuania
+37063618505
Eimantas.Venslovas@lammc.lt

EXTENDED ABSTRACT

OVERVIEW

Every year more and more maize are being grown and it is mainly used for farm animal feed and secondarily for human food and biomass [1]. Unfortunately, maize is often infected by *Fusarium* fungi, which can produce mycotoxins [2]. One of the many dangerous mycotoxins is zearalenone (ZEA) [3]. Once ingested, it is immunotoxic, hepatotoxic and hemotoxic, also it causes estrogenic syndrome. For males it results in negative effect on testosterone synthesis and spermatogenesis and for females it results in false heat and abortion [3, 4, 5]. Therefore, Europe Commission Recommendation and Regulation defines the biggest concentration levels for ZEA in maize: in animal feed it is recommended not to exceed 3000 µg/kg, in products intended for human consumption concentration must not exceed 200 µg/kg and in maize snacks and breakfast cereals 50 µg/kg [6, 7]. There is a lack of information about maize grains contamination with ZEA while growing in Lithuania. Therefore, the aim of this study was to investigate whether maize grain harvest time has an impact on ZEA concentration and maize nutrient composition.

METHODS

Two maize hybrids were sown: *Duxxbury* and *Lapriora*. A total of 24 samples were collected in the experimental fields of the Lithuanian Research Centre for Agriculture and Forestry in the autumn of 2021. Samples were taken at three different time points: the first time at physiological maturity (BBCH 87), the second time 10 days and the third time 20 days after the first harvest. All collected samples were stored in a freezer at -18°C until analysis.

The main nutrient components (dry matter (DM), starch, crude protein (CP), crude fat, crude ash (CA), and crude fiber (CF)) were determined in the chemical research laboratory using reference chemical methods: Kjeldahl, gravimetric, polarimetric methods.

ZEA concentrations were determined using an enzyme-linked immunoassay (ELISA) method. Special commercial kits (RIDASCREEN®FAST for ZEA Art. No.: R5502) were used. The lower limit of detection (LOD) for zearalenone is 17 µg/kg.

Means, standard errors, and statistical significancy were calculated using IBM Statistics 25. One-way analysis of variance (ANOVA) was used to detect statistically significant differences. Means were compared using the Duncan's multiple range test ($P<0.05$).

RESULTS

The concentration of ZEA did not change statistically significantly during all harvests in the grains of *Lapriora* hybrid (Fig. 1). ZEA concentration did not differ significantly between the first and the second harvest in the grains of *Duxxbury* hybrid, but it was several times higher in the third harvest. Compared to the first and the second harvests ZEA concentrations were 4 and 15 times higher, respectively. Compared to the third harvest of *Lapriora* hybrid concentration was 7 times higher.

It was determined that DM in *Lapriora* hybrid increased with each harvest from 86.2 % to 88.4 % (Table 1). In the second harvest the content of crude fat increased by 6%, and in the third harvest CP and CA increased by 6 % and 11 % in DM, respectively. The DM content of the *Duxxbury* hybrid increased significantly from 85.2 % to 87.3 % only after the second harvest, but in contrast to the *Lapriora* hybrid, the content of certain substances decreased: CF and CA decreased by 21 % and 25 % in DM, respectively (Table 2). Other nutrient components had no statistically significant changes.
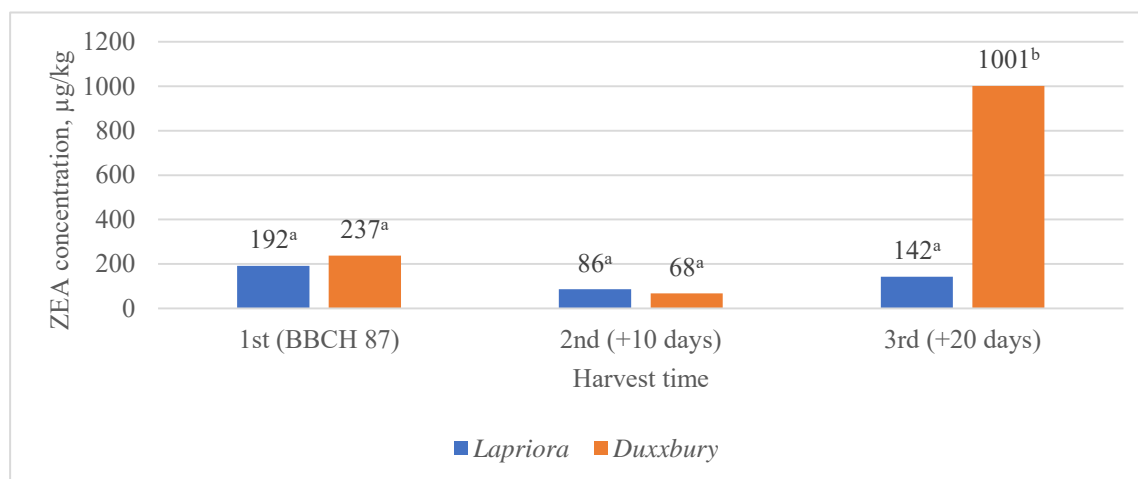
Note. Different letters indicate statistically significant differences between means.

Fig. 1. ZEA concentration changes in hybrid grains at different harvest times.

Table 1. Nutrient composition of *Lapriora* hybrid grains at different harvest times

	DM, %	CP, % in DM	Crude fat, % in DM	CF, % in DM	CA, % in DM	Starch, % in DM
Lapriora 1st harvest	86.2[a]	11.05[a]	4.63[a]	3.08[a]	1.35[a]	73.5[a]
Lapriora 2nd harvest	87.8[b]	11.45[ab]	4.93[b]	3.15[a]	1.34[a]	74.7[a]
Lapriora 3rd harvest	88.4[c]	11.70[b]	4.81[b]	3.53[a]	1.50[b]	73.6[a]

Table 2. Nutrient composition of *Duxxbury* hybrid grains at different harvest times

	DM, %	CP, % in DM	Crude fat, % in DM	CF, % in DM	CA, % in DM	Starch, % in DM
Duxxbury 1st harvest	85.2[a]	10.06[a]	3.04[a]	3.73[b]	1.55[b]	77.4[a]
Duxxbury 2nd harvest	87.3[b]	9.88[a]	2.95[a]	2.93[a]	1.16[a]	77.4[a]
Duxxbury 3rd harvest	87.6[b]	10.05[a]	3.00[a]	2.96[a]	1.17[a]	78.3[a]

Note. Different letters in tables indicate statistically significant differences between the means in the same column.

CONCLUSIONS

ZEA concentration increased several times in the *Duxxbury* hybrid after the third harvest compared to the other hybrid and the rest of the harvests. Delay in harvest showed DM increase in both hybrids. However, while there was an increase in some components in *Lapriora*, it was the opposite for *Duxxbury*.

Keywords: zearalenone, nutrient composition, harvest time

REFERENCES

1. CHOUDHARY, M.; SINGH, A.; GUPTA, M.; RAKSHIT, S. Enabling technologies for utilization of maize as a bioenergy feedstock. *Biofuels, Bioproducts and Biorefining*, 2019, Vol. 14, No. 2, P. 402-416.

2. ALSHANNAQ, A.; YU, J. H. Occurrence, Toxicity, and Analysis of Major Mycotoxins in Food. *International Journal of Environmental Research and Public Health*, 2017, Vol. 14, No. 6, P. 632.

3. GIL-SERNA, J.; VÁZQUEZ, C.; GONZÁLEZ-JAÉN, M.T.; PATIÑO, B. *Encyclopedia of Food Microbiology*. Cambridge: Academic Press, 2014. P. 887-892 .

4. PERAICA, M.; RADIĆ, B.; LUCIĆ, A.; PAVLOVIĆ, M. Toxic effects of mycotoxins in humans. *Bulletin of the World Health Organization*, 1999, Vol. 77, No. 9, P. 754-766.

5. BINDER, S. B.; SCHWARTZ-ZIMMERMANN, H. E.; VARGA, E.; BICHL, G.; MICHLMAYR, H.; ADAM, G.; BERTHILLER, F. Metabolism of Zearalenone and Its Major Modified Forms in Pigs. *Toxins*, 2017, Vol. 9, No. 2, P. 56.

6. Commission Regulation (EC) No. 1881/2006 of 19 December 2006 setting maximum levels for certain contaminants in foodstuffs. *Official Journal of the European Union*, 2006, P. 5-24.

1. Commission Recommendation (2006/576/EC) of 17 August 2006 on the presence of deoxynivalenol, zearalenone, ochratoxin A, T-2 and HT-2 and fumonisins in products intended for animal feeding. *Official Journal of the European Union*, 2006, P. 7.

GENOTOXICITY AND CYTOTOXICITY OF NANOPLASTICS ON SALMONID FISH

A. Bučaitė, M. Stankevičiūtė
Laboratory of Ecotoxicology, Nature Research Centre
Verkių St. 98, 08406 Vilnius – Lithuania
+37065329358
agne.bucaite@gamtc.lt

ABSTRACT

Nanoplastics (NPs) are defined as plastic particles less than 100 nm in diameter. NPs are anthropogenic pollutants whose amounts in aquatic ecosystems have yet to be quantified, raising concerns about their toxicity to living organisms. In this study the effects of polystyrene (PS) NPs on larval stage *Oncorhynchus mykiss* were assessed using erythrocytic nuclear abnormalities and red blood cells morphometry assays. Fish were subjected to 1000 µg/L PS NPs (PS1000) for 32 days. The formation of micronuclei (MN), nuclear buds (NB), nuclear buds on filament (NBf), blebbed nuclei (BL) cells were assessed as genotoxicity endpoints, and 8-shaped, bean-shaped nuclei, fragmented apoptotic (FA) and bi-nucleated (BN) cells as cytotoxicity endpoints. For erythroblast morphometry assay photomicrographs of *O. mykiss* erythroblasts were evaluated using ImageJ 1.52av software. Analyzed morphometric variables were used to measure size and shape associated differences in cellular and nuclear parameters separately. Data analysis was performed using R software (version 4.1.1). Significant increases in genotoxicity (MN + NB + NBf + BL) (PS1000 by 729 %) and cytotoxicity (8-shaped + bean-shaped + FA + BN) (PS1000 by 850 %) were detected when compared to the control. The investigation of potential relationships between measured erythroblast morphometry endpoints using principal component analysis (PCA) yielded two principal components (PCs) which explained 74% of the total variance. Afterwards, PCA was done in control and PS1000 groups separately to explore treatment induced differences. The results of this study show that polystyrene nanoplastics adversely affect fish at the larval stage of development, report genotoxic, cytotoxic effects, and provide information to establish NPs environmental consequences.

Keywords: nanoplastic, ecotoxicology, nuclear abnormalities assay, erythroblast morphometry.

INTRODUCTION

Plastics are an essential yet mostly unseen component of our daily life. Plastic waste is common in nearly all aquatic environments as a result of the high production and single-use nature of many products [1]. Plastic debris present in the environment is classified into two main types: macroplastics and microplastics (MPs) [2]. Moreover, the term "nanoplastic" (NP) is newly introduced as the definition of NP is still being debated. Several studies have established the upper size limit at either 1000 nm or 100 nm [3]. Over the last two decades, there has been a growing awareness of the environmental concerns posed by artificial nanomaterials. It has been observed that they can cause genotoxicity, cytotoxicity in fish [2] as well as other adverse effects in different marine animals [4]. Laboratory studies suggest that smaller NP can enter internal organs (brain, liver, and heart), whereas bigger (>200 nm) NP concentrate mostly in the digestive track, gills, and skin [5]. Thus, the goal of this study was to examine genotoxic, and cytotoxic effects of PS NPs on larval stage rainbow trout (*Oncorhynchus mykiss*, Fig. 1). Researching the effects of pollutants on early life stages is essential because of the developmental stress hypothesis which explains how early life stress affects later-life performance and thus how anthropogenic waste influence the welfare of populations, and eventually ecosystems [6].

METHODOLOGY

Animals And Experimental Design

Eyed stage embryos of rainbow trout (*O. mykiss* Walbaum, 1792) were obtained from hatchery in Trakų Vokė (Lithuania). After acclimatization to laboratory environment under controlled light and temperature (7.5°C), embryos were transferred to the experimental system. The system was filled with fresh, constantly aerated water. Because rainbow trout larvae feed endogenously, they were not fed during the experiment. This species was selected as experimental model because of its ecological and economic importance as well as it had been already used in various studies regarding environmental toxicology [7] [8] [9] [10]. Trout is one of the most widely distributed fish species on the planet and the vast range of its occurrence is due to its excellent acclimation characteristics, which include quick growth [11].

After 32 days of exposure to 1000 µg/L PS NPs (25 nm), blood samples were collected of the treatment (NPs-exposed) group and from the same number of individuals of the control (CTRL) group. Whole-blood samples were taken by heart puncture and smeared on a microscope slide.

Fig. 1. Experimental animal – larval stage rainbow trout (*Oncorhynchus mykiss*).

Erythrocytic Nuclear Abnormalities Assay

For nuclear abnormalities assay air-dried blood smears were fixed in ethanol for 10 min and stained with 10% Giemsa solution in phosphate buffer (pH = 6.8) for 60 min. The stained slides were analysed under bright-field Olympus BX51 microscope (Tokyo, Japan) using an immersion 1000× objective. The formation of micronuclei (MN), nuclear buds (NB), nuclear buds on filament (NBf), blebbed nuclei (BL) cells were assessed as genotoxicity endpoints (Fig. 2), and 8-shaped, bean-shaped nuclei, fragmented apoptotic (FA) and bi-nucleated (BN) cells as cytotoxicity endpoints (Fig. 3). Criteria by Fenech *et al*. [12] were used to identify morphological characteristics of the analyzed nuclear anomalies, and Baršienė *et al*. [7] provided a detailed description. Briefly, the following characteristics were used to categorize MN: (1) non-refractory round and ovoid-shaped particles in the cytoplasm, (2) chromatin-like hue and structure, (3) dimension of 1/3–1/20 of the main nucleus, (4) particles fully detached from the main nucleus (Fig. 2A). NB are extruded nuclear material that resembles a MN and has a nucleoplasmic bridge to the main nucleus that can be narrow or defined (Fig. 2B). Early-stage FA cells had chromatin condensation within the nucleus and intact cytoplasmic and nuclear perimeter, whereas late-stage apoptotic cells had nuclear fragmentation (Fig. 3D-E). A BN cell's two nuclei are relatively similar in size, have intact nuclear membranes, and are located inside the same cytoplasmic boundary (Fig. 3C). Although the two nuclei may come into contact, they should not overlap [12] [13].

Two thousands erythroblasts with intact cellular and nuclear membranes per individual were evaluated. The final results were expressed as the percentage change (% change) compared to the control and were was calculated using equation 1.

$$\% \, Change = \frac{Treatment\, \text{‰} - Control\, \text{‰}}{Control\, \text{‰}} \cdot 100\%. \qquad (1)$$
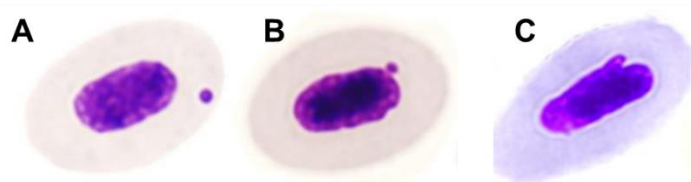
Fig. 2. Photographs of analysed genotoxicity endpoints: A – micronucleus (MN), B – nuclear bud (NB), blebbed nuclei (BL).
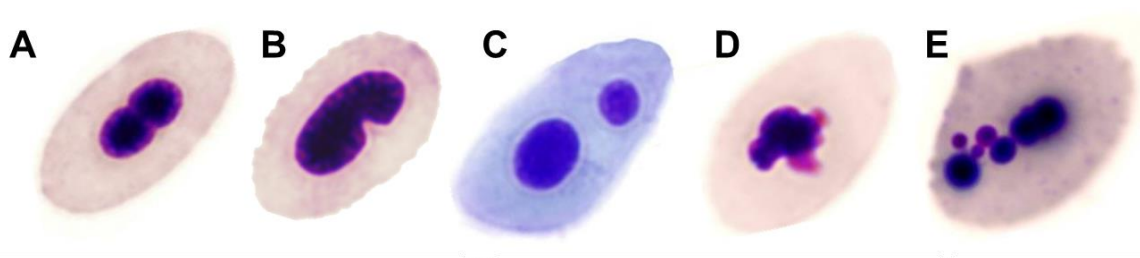
Fig. 3. Photographs of analysed cytotoxicity endpoints: A – 8-shaped nucleus, B – bean-shaped nucleus, C – bi-nucleated (BN) cell, D – fragmented nucleus, E – apoptotic cell.

Erythroblast Morphometry

For this assay the stained slides were analysed using a 40× objective and Olympus DP70 camera system (Tokyo, Japan). Photomicrographs of rainbow trout erythroblasts were evaluated with

the ImageJ 1.52av software [14]. The analysis was carried out according to De Oliveira *et al*. [15] approach, with minor changes made by Guimarães *et al*. [2]. In summary, for each slide/fish, ten random photomicrographs were obtained, totaling 150 photos per experimental group, and ten (10) cells were measured in each analysis field, totaling 1500 erythroblasts per group. Analysed morphometric variables were erythroblast and its nucleus area; erythroblast perimeter and its nucleus perimeter; ratio between nuclear and erythroblast area (nucleus/cell) as well as erythroblast and nucleus circularity, roundness, solidity, and aspect ratio (AR). Later parameters were calculated using equations 2-5. Area and perimeter measure size-associated changes while other parameters indicate changes in cell shape. In several animal groups, including fish [2], reptiles [15] and birds [16], these characteristics have been considered as sensitive cytotoxicity biomarkers.

$$Circularity = 4\pi \times \frac{Area}{Perimeter^2} \qquad (2)$$

$$Roundness = 4 \times \frac{Area}{\pi \times (Major\ axis)^2} \qquad (3)$$

$$Solidity = \frac{Area}{Convex\ area} \qquad (4)$$

$$Aspect\ ratio = \frac{Feret'minimum\ length}{Feret's\ maximum\ length}. \qquad (5)$$

The investigation of potential relationships between measured erythroblast morphometry endpoints was done using principal component analysis (PCA). PCA results for variable contributions were calculated using equations 6-8.

$$Variable\ coordinates = Loadings \cdot The\ component\ SD \qquad (6)$$

$$Variable\ cos^2 = (Variable\ coordinates)^2 \qquad (7)$$

$$Variable\ contribution = \frac{Variable\ cos^2 \cdot 100}{Total\ cos^2\ of\ the\ component}. \qquad (8)$$

Statistical Analysis

The Shapiro-Wilk and Levene tests were used to assess for normality and homoscedasticity in the data. For parametric data, one-way ANOVA was performed (followed by Tukey's HDS *post-hoc* test). To compare the means of non-parametric data, the Kruskal-Wallis test (followed by Dunn's *post-hoc* test) was used. Data analysis was performed using R [17] and R Studio [18] software (versions 4.1.1 and 1.4.1717 respectively).

RESULTS

Nuclear Abnormalities

Significant increases in genotoxicity (MN + NB + NBf + BL) and cytotoxicity (8-shaped + bean-shaped + FA + BN) were detected when compared to the control. Genotoxicity in PS1000 group increased by 729% (Fig. 4B) while cytotoxicity in PS1000 group increased by 850% (Fig. 4A).
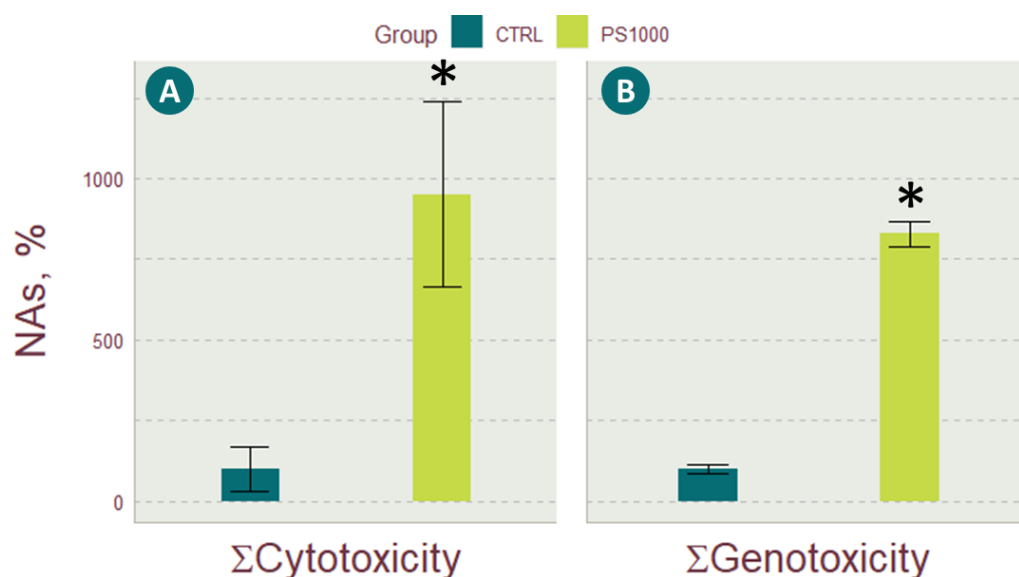
Fig. 4. Percentage change from control of A – total genotoxicity (ΣGentoxicity) and B – total cytotoxicity (ΣCytotoxicity) levels. Asterisks (*) denote significant differences from the control groups, mean ± SEM.

Erythroblast Morphometry

Two principal components (PCs) explained 74% of the total variance (Fig. 5). For PC1 the biggest contributions were associated with nuclear and erythroblast area ratio (11.56%), nuclear circularity (10.69%), nuclear aspect ratio (10.53%), nuclear perimeter (10.44%).

Afterwards, PCA was done in control and PS1000 groups separately to explore treatment induced differences. For PC1 in control group (explained 30.11% of variance) the biggest contributions were associated with nuclear area (19.93%), nuclear perimeter (17.81%), nuclear solidity (13.90%), cellular perimeter (13.53%) and cellular circularity (11.62%). For PC2 (explained 28.67% of variance) the biggest contributions were associated with cellular and nuclear aspect ratio (17.22% and 16.92% respectively), nuclear and cellular roundness (16.85% and 14.22% respectively) and nuclear circularity (12.20%). Highest and lowest variables contributions in CTRL group are shown in Fig. 6A

Meanwhile, for PC1 in PS1000 group (explained 35.18% of variance) the biggest contributions were associated with nuclear circularity (18.71%), nuclear perimeter (16.12%), nuclear and erythroblast area ratio (13.49%), nuclear solidity (11.07%) and nuclear area (10.74%). For PC2 (explained 23.22% of variance) the biggest contributors were cellular area (18.12%), nuclear and cellular roundness (14.03% and 13.36% respectively), cellular and nuclear aspect ratio (13.03% and 11.91% respectively). Highest and lowest variables contributions in PS1000 group are shown in Fig. 6B
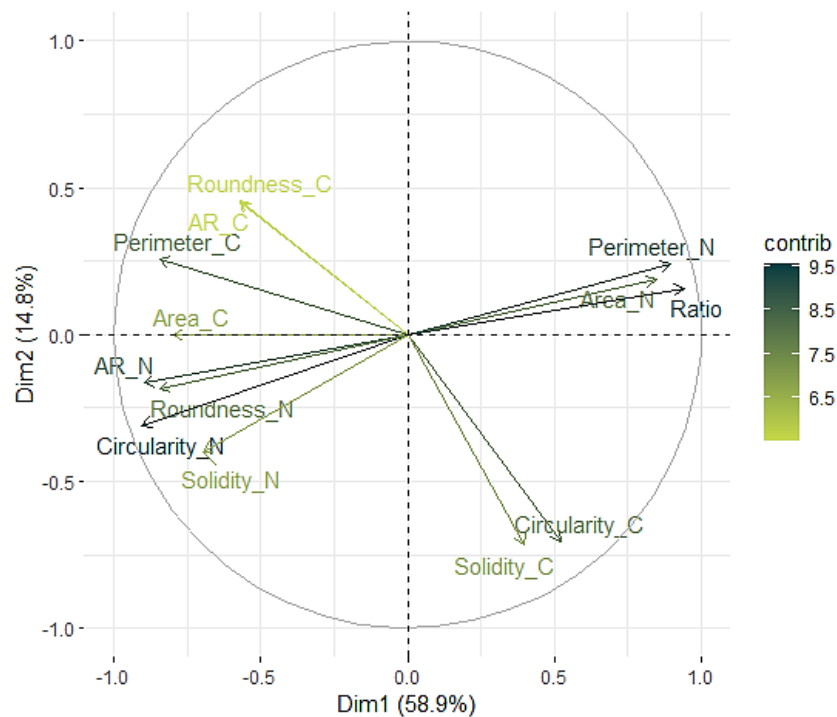
Fig. 5. PCA variables plot for entire dataset. Variable with suffix "_C" means cellular parameter, while suffix "_N" means nuclear parameter. Variables are coloured by contribution. AR – aspect ratio, Ratio – ratio between nuclear and erythroblast area.
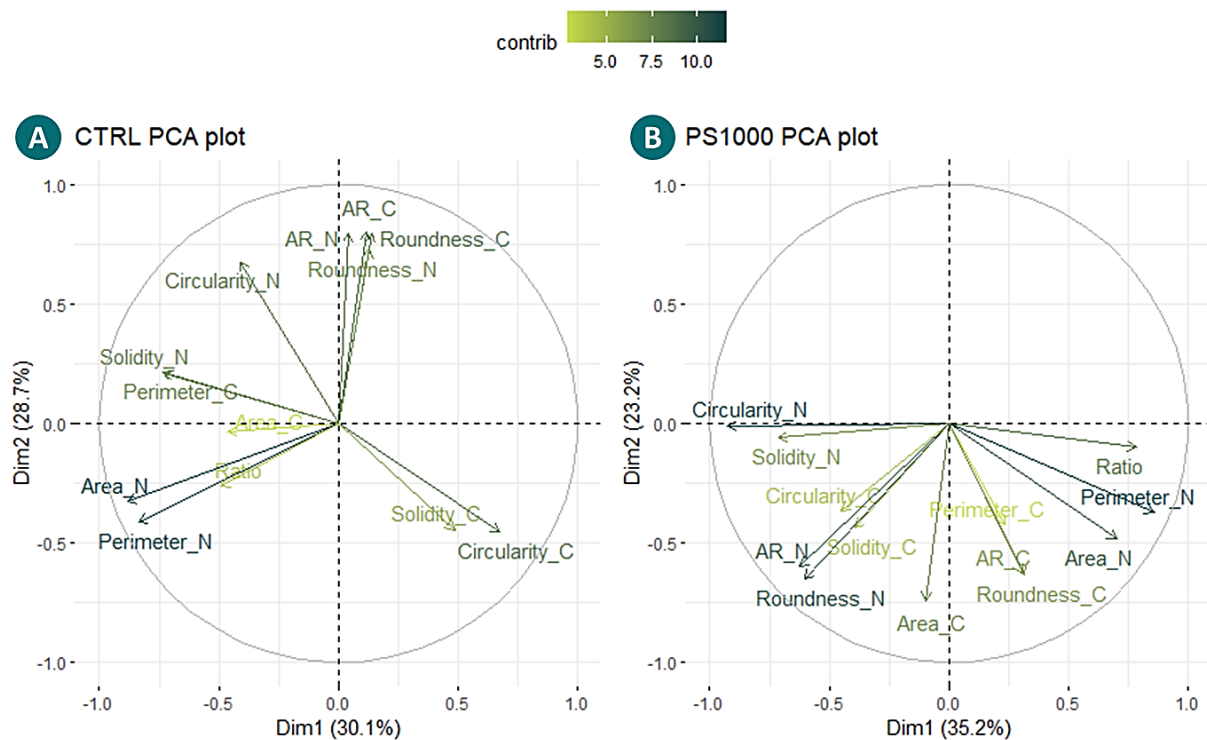
Fig. 6. PCA variables plots for control (CTRL, A) and treatment (PS1000, B) groups separately. Variable with suffix "_C" means cellular parameter, while suffix "_N" means nuclear parameter. Variables are coloured by

contribution. AR – aspect ratio, Ratio – ratio between nuclear and
erythroblast area.

Individuals plot revealed clusters that separated the treatment group from the control group (Fig 7). This separation shows that from avaliable data treated fish differ from control animals. Pearson correlation coefficient values are shown in Fig 8.
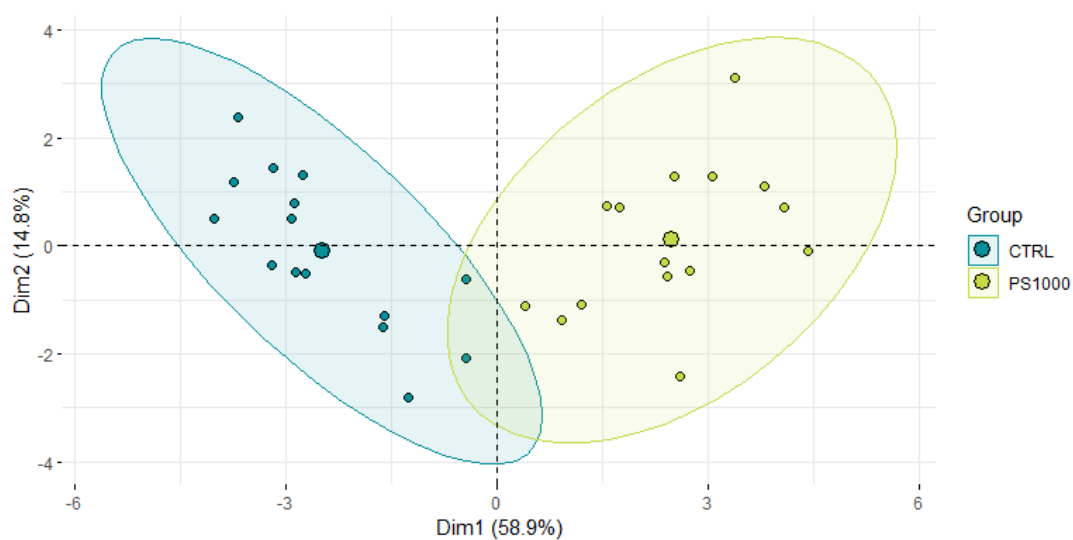
Fig. 7. PCA individuals plot coloured by group. Bigger points denote
centres of ellipses.
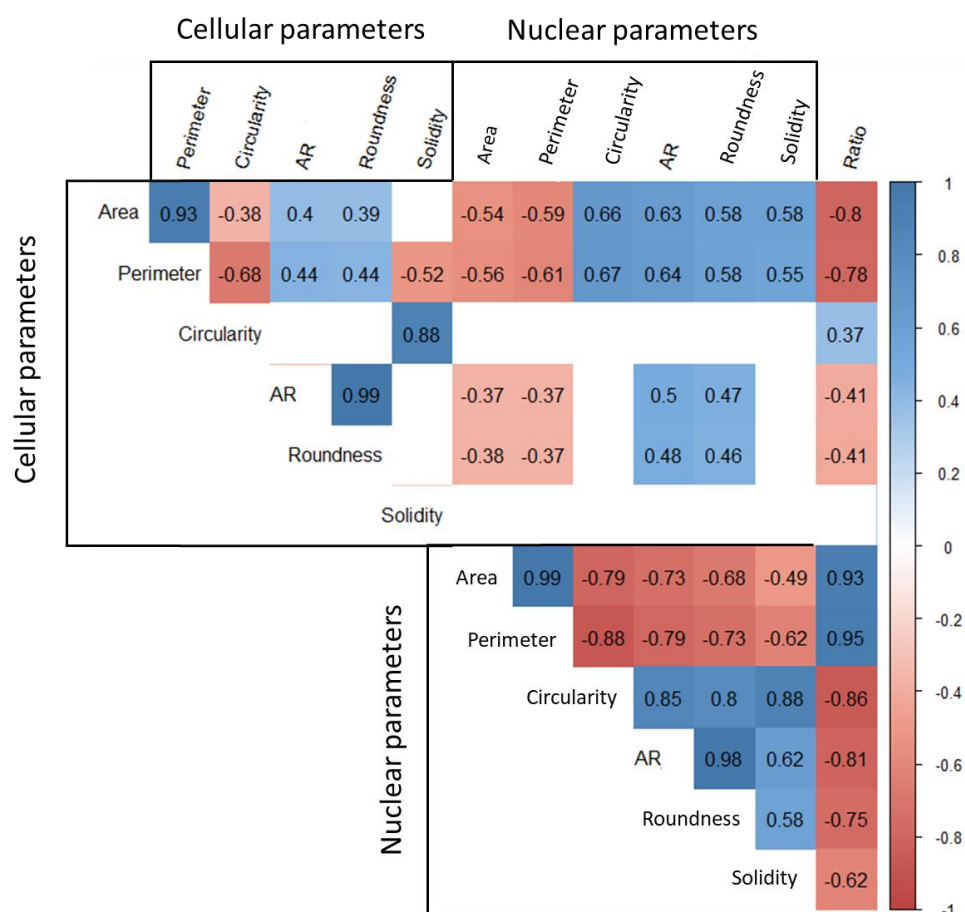
Fig. 8. Correlation coefficients between cellular and nuclear parameters, and correlations not significantly different from 0 are represented by a white box. AR - aspect ratio, Ratio - ratio between nuclear and erythroblast area.

DISCUSSION

This study investigated the biological effects of nanoplastics on *O. mykiss*, namely the genotoxic and cytotoxic responses. Although water pollution is an emerging problem worldwide the impact of many contaminants, such as PS NPs, on aquatic animals are yet unknown. To further our understanding of the toxicity of PS NPs in aquatic biota, the current work demonstrated that these nanomaterials, may cause genotoxic and cytotocix changes in larval stage rainbow trout erythroblasts. These findings are consistent with earlier toxicology research that have exposed fish [2] [19] as well as other aquatic animals [20] to PS NPs.

Significant increase in genotoxic nuclear abnormalities (Fig 4B) has revealed damage to the genetic material of fish larvae. Common theory is that the mechanisms of DNA damage may be associated with oxidative stress as many studies demonstarte that NPs exposure leads to increase in oxidative status biomarkers and antioxidant gene expression [19]. The current study's findings indicate that PS NPs are capable of causing clastogenic effects meanwhile significant increase in total cytotoxic nuclear abnormalieties (Fig. 4A) also suggest aneugenic events and errors in cellular division [21]. The advantage of nuclear abnormalities assay is that it reveals the implications of spindle abnormalities as well as chromosomal breakage [22]. Embryonic stages are perhaps the most vulnerable to DNA damage because the rate of DNA replication is high, cell proliferation is fast, and the cell cycle is considerably shorter than in adult cells. The whole genome of an embryo is replicated at a rate that is 20 to 60 times quicker

than that of a somatic cell [23]. However, a study using sterlet (*Acipenser ruthenus*) demonstrates that mechanisms of DNA damage repair are highly effective in fish embryos [24]. Cytotoxic changes can also be caused by continuous inflammation of damaged tissues and the action of immune system [25].

Erythroblast morphometric variations found in fish exposed to NPs, have shown disruptions in biological processes other than those involved in cell division, which might be regarded as pollutant-induced cytotoxicity biomarkers. Nuclear and erythroblast area ratio having the greatest contribution to varriance (Fig. 5) may imply that NPs cause changes in erythroblast size. Correlation analysis (Fig. 8) demonstrates negative relationship between cellular area and nuclear area ($r = -0.54$) which means in this study increase in nuclear area followed with decrease in cellular area. In birds it has been observed that changes in erythrocytes size have strong positive correlation with genome size (C-value) [26] and poliploidy is knonw to occur in rainbow trout [27] which could explain some size varriations in control group (Fig. 6A). But in treatment group shape associated variables also had high contribution values (Fig. 6B). These findings are consistent, since similar results were published by Guimarães and colleagues [2]. In their study researchers exposed grass carp (*Ctenopharyngodon idella*) juveniles to PS NPs at low concentrations (0.04 ng/L- 34 µg/L), for 20 days. Althought results may be similar the experimental design differences should be taken into consideration: (1) in our study concentration of PS NPs was much higher and the exposure was longer, (2) different fish species were used, (3) we exposed embryos while Guimarães and colleagues used juveniles. Erythroblast morphometric variations may also be connected to oxidative stress, since increase in reactive oxygen species (ROS) contributes to changes in the morphology and viability of erythrocytes [15]. The majority of the nonenzymatic antioxidant capacity of whole blood is found in erythrocytes so they act as mobile free radical collectors that protect other tissues from free radicals. [28].

CONCLUSION

Genetic damage especially in early life stages can cause a variety of health problems known as genotoxic disease syndrome, which includes decreased productive and reproductive capability [29]. Studies like this can help researchers better understand how nanomaterials influence ichthyofauna in contaminated environments.

ACKNOWLEDGEMENT

REFERENCES

1. OLIVEIRA, M.; ALMEIDA, M.; MIGUEL, I. A micro(nano)plastic boomerang tale: A never ending story? *TrAC Trends in Analytical Chemistry*, 2019, Vol. 112, P. 196–200.

2. GUIMARÃES, A.T.B.; ESTRELA, F.N.; PEREIRA, P. S.; DE ANDRADE VIEIRA, J. E.; DE LIMA RODRIGUES, A. S.; SILVA, F. G.; MALAFAIA, G. Toxicity of polystyrene nanoplastics in Ctenopharyngodon idella juveniles: A genotoxic, mutagenic and cytotoxic perspective, *Science of The Total Environment*, 2021, Vol. 752, P. 141937.

3. GIGAULT, J.; HALLE, A.; BAUDRIMONT, M.; PASCAL, P. Y.; GAUFFRE, F.; PHI, T. L.; EL HADRI, H.; GRASSL, B.; REYNAUD, S. Current opinion: What is a nanoplastic? *Environmental Pollution*, 2018, Vol. 235, P. 1030–1034.

4. KIHARA, S.; KÖPER, I.; MATA, J. P.; MCGILLIVRAY, D. J. Reviewing nanoplastic toxicology: It's an interface problem, *Advances in Colloid and Interface Science*, 2021, Vol. 288, P. 102337.

5. TORRES-RUIZ, D. E.; LA VIEJA, M. A.; DE ALBA GONZALEZ, M.; ESTEBAN LOPEZ, M.; CASTAÑO CALVO, A.; CAÑAS PORTILLA, A. I.Toxicity of nanoplastics for zebrafish embryos, what we know and where to go next, *Science of The Total Environment*, 2021, Vol. 797, P. 149125.

6. PETERSON, E. K.; BUCHWALTER, D. B.; KERBY, J. L.; LEFAUVE, M. K.; VARIAN-RAMOS, C. W.; SWADDLE, J. P. Integrative behavioral ecotoxicology: bringing together fields to establish new insight to behavioral ecology, toxicology, and conservation, *Current Zoology*, 2017, Vol. 63, No. 2, P. 185–194.

7. KARBALAEI, S.; HANACHI, P.; RAFIEE, G.; SEIFORI, P.; Walker, T. R. Toxicity of polystyrene microplastics on juvenile Oncorhynchus mykiss (rainbow trout) after individual and combined exposure with chlorpyrifos, *Journal of Hazardous Materials*, 2021, Vol. 403, P. 123980.

8. JAKUBOWSKA, M.; BIAŁOWĄS, M.; STANKEVIČIŪTĖ, M.; CHOMICZEWSKA, A.; JONKO-SOBUŚ, K.; PAŽUSIENĖ, J.; HALLMANN, A.; BUČAITĖ, A.; URBAN-MALINGA, B. Effects of different types of primary microplastics on early life stages of rainbow trout (Oncorhynchus mykiss), *Science of The Total Environment*, 2022, Vol. 808, P. 151909.

9. STANKEVIČIŪTĖ, M.; MAKARAS, T.; PAŽUSIENĖ, J.; ČAPUKOITIENĖ, B.; SAULIUTĖ, G.; JURGELĖNĖ, Ž.; RAUDONYTĖ-SVIRBUTAVIČIENĖ, E.; JOKŠAS, K. Biological effects of multimetal (Ni, Cd, Pb, Cu, Cr, Zn) mixture in rainbow trout Oncorhynchus mykiss: Laboratory exposure and recovery study, *Ecotoxicology and Environmental Safety*, 2021, Vol. 216, P. 112202.

10. HODKOVICOVA, N.; HOLLEROVA, A.; CALOUDOVA, H.; BLAHOVA, J.; FRANC, A.; GARAJOVA, M.; LENZ, J.; TICHY, F.; FALDYNA, M.; KULICH, P.; MARES, J.; MACHAT, R.; ENEVOVA, V.; SVOBODOVA, Z. Do foodborne polyethylene microparticles affect the health of rainbow trout (Oncorhynchus mykiss)? *Science of The Total Environment*, 2021, Vol. 793, P. 148490.

11. JUSZCZAK, M.; SAWICKI SZYMCZAK, T. M.; KAMIŃSKI, P. ICHTHYOLOGY, BREEDING AND ECONOMIC IMPORTANCE OF RAINBOW TROUT IN POLAND, *Folia Pomeranae Universitatis Technologiae Stetinensis Agricultura, Alimentaria, Piscaria et Zootechnica*, 2020, Vol. 351, P. 13–24.

12. FENECH, M.; CHANG, W. P.; KIRSCH-VOLDERS, M.; HOLLAND, N.; BONASSI, S.; ZEIGER, E. HUman MicronNucleus project. HUMN project: detailed description of the scoring criteria for the cytokinesis-block micronucleus assay using isolated human lymphocyte cultures, *Mutation Research*, 2003, Vol. 534, No. 1, P. 65–75.

13. BARŠIENĖ, J.; RYBAKOVAS GARNAGA, A. G.; ANDREIKĖNAITĖ, L. Environmental genotoxicity and cytotoxicity studies in mussels before and after an oil spill at the marine oil terminal in the Baltic Sea, *Environmental Monitoring and Assessment*, 2012, Vol. 184, No. 4, P. 2067–2078.

14. SCHNEIDER, C. A.; RASBAND, W. S.; ELICEIRI, K.W. NIH Image to ImageJ: 25 years of image analysis, *Nature Methods*, 2012, Vol. 9, No. 7.

15. DE OLIVEIRA, J.S.P.; IEIRA, L. G.; CARVALHO, W.F.; DE SOUZA, M. B.; DE LIMA RODRIGUES, A. S.; SIMÕES, K.; DE MELO DE SILVA, D.; DOS SANTOS MENDONÇA, J.; HIRANO, L.Q.L.; SANTOS, A.L.Q.; MALAFAIA, G. Mutagenic, genotoxic and morphotoxic potential of different pesticides in the erythrocytes of Podocnemis expansa neonates, *Science of The Total Environment*, 2020, Vol. 737, P. 140304.

16. EMMANUELA DE ANDR, V.; DE OLIVEIRA FERREIRA, J. R.; MARCEL DOS REIS SAMPAIO, D.; PEREIRA DA COSTA ARAÚJO, A.; MALAFAIA, G. An insight on the mutagenicity and cytotoxicity of zinc oxide nanoparticles in Gallus gallus domesticus (Phasianidae), *Chemosphere*, 2019, Vol. 231, P. 10–19.

17. *R Core Team*: Vienna, Austria: R Foundation for Statistical Computing, R: A language and environment for statistical computing, [referred on the 7th of February in 2022 y.]. Link to the internet <https://www.R-project.org/>

18. *RStudio Team*: PBC, Boston, MA, Integrated Development Environment for R. RStudio. [referred on the 7th of February in 2022 y.]. Link to the internet <http://www.rstudio.com/>

19. ZHANG, Y.T.; CHEN, H.; HE, S.; WANG, F.; LIU, Y.; CHEN, M.; YAO, G.; HUANG, Y.; CHEN, R.; XIE, L.; MU, J. Subchronic toxicity of dietary sulfamethazine and nanoplastics in marine medaka (Oryzias melastigma): Insights from the gut microbiota and intestinal oxidative status, *Ecotoxicology and Environmental Safety*, 2021, Vol. 226, P. 112820.

20. ARINI GIGAULT, A.J.; VENEL, Z.; BERTUCCI, A.; BAUDRIMONT, M. The underestimated toxic effects of nanoplastics coming from marine sources: A demonstration on oysters (Isognomon alatus), *Chemosphere*, 2022, Vol. 295, P. 133824.

21. HEDDLE, J. A.; CIMINO, M.C.; HAYASHI, M.; ROMAGNA, F.; SHELBY, M.D.; TUCKER, J. D.; VANPARYS, Ph.; MACGREGOR, J.T. Micronuclei as an index of cytogenetic damage: Past, present, and future, *Environmental and Molecular Mutagenesis*, 1991, Vol. 18, No. 4, P. 277–291.

22. VAN DER OOST, R.; BEYER, J.; VERMEULEN, N. P. E. Fish bioaccumulation and biomarkers in environmental risk assessment: a review, *Environmental Toxicology and Pharmacology*, 2003, Vol. 13, No. 2, P. 57–149.

23. KERMI, C.; LO FURNO, E.; MAIORANO, D. Regulation of DNA Replication in Early Embryonic Cleavages, *Genes (Basel)*, 2017, Vol. 8, No. 1, P. E42.

24. GAZO, I.; FRANĚK, R.; ŠINDELKA, R.; LEBEDA, I.; SHIVARAMU, S.; PŠENIČKA, M.; STEINBACH, C. Ancient Sturgeons Possess Effective DNA Repair Mechanisms:

Influence of Model Genotoxicants on Embryo Development of Sterlet, Acipenser ruthenus, *International Journal of Molecular Sciences*, 2021, Vol. 22, No. 1.

25. STANKEVIČIŪTĖ, M.; SAULIUTĖ, G.; MAKARAS, T.; ČAPUKOITIENĖ, B.; VANSEVIČIŪTĖ, G, MARKOVSKAJA, S. Biomarker responses in perch (Perca fluviatilis) under multiple stress: Parasite co-infection and multicomponent metal mixture exposure, *Environmental Research*, 2022, Vol. 207, P. 112170.

26. BONATTO, C.C.; MAGALHÃES, B.S.; BRANCO, J.O.; DURIGON, E.L.; SILVA, L. P. Shape and size of red blood cells from the Pygoscelid penguins of Antarctica using atomic force microscopy, *Polar Biology*, 2009, Vol. 32, No. 2, P. 287–293.

27. KIM, H.S.; CHUNG, K.H.; SON, J.H. Comparison of different ploidy detection methods in Oncorhynchus mykiss, the rainbow trout, *Fisheries and Aquatic Sciences*, 2017, Vol. 20, No. 1, P. 29.

28. SIEMS, W.G.; SOMMERBURG, O.; GRUNE, T. Erythrocyte free radical and energy metabolism, *Clinical Nephrology*, 2000, Vol. 53, No. 1, P. S9-17.

29. RAMSDORF, W.A.; VICARI, T.; DE ALMEIDA, M.I.M.; ARTONI, R.F.; CESTARI, M.M. Handling of Astyanax sp. for biomonitoring in Cangüiri Farm within a fountainhead (Iraí River Environment Preservation Area) through the use of genetic biomarkers, *Environmental Monitoring and Assessment*, 2012, Vol. 184, No. 10, P. 5841–5849.

POTENTIAL OF EIGHT SPECIES OF LEGUMES FOR FUEL OIL CONTAMINATED SOIL PHYTOREMEDIATION

R. Meištininkas, N. Pedišius
Lithuanian Energy Institute
Breslaujos g. 3, LT-44403 Kaunas – Lithuania
+37062625693/+37068631623
Rimas.Meistininkas@lei.lt/Nerijus.Pedisius@lei.lt

J. Žaltauskaitė
Vytautas Magnus University / Lithuanian Energy Institute
Vileikos g. 8 LT-44404 Kaunas / Breslaujos g. 3, LT-44403 Kaunas
+37068775711
jurate.zaltauskaite@vdu.lt

EXTENDED ABSTRACT

OVERVIEW

Some of the most common soil contaminants are petroleum products, this type of pollution is widespread, because various petroleum products are very commonly used around the world for various purposes. Contamination of soil with petroleum products can result directly from leaks, accidents and spills in high-traffic areas as well as at facilities involved in the refining, storage and use of petroleum products [1]. It is known, that only in Europe, according to the European Environment Agency, the number of suspected contaminated soil hot spots is around 2.5 million [2]. Meanwhile, in Lithuania, based on the data of the Lithuanian Geological Survey, about 12,000 potential sources of pollution have been identified, most of them are related to soil pollution with oil products. Unlike heavy metals, petroleum products can be broken down into environmentally harmless compounds. A variety of chemical, physical, and biological methods can be used to remediate contaminated soil, but biological ones are the most environmentally friendly [3]. Implementation of leguminous plants for soil phytoremediation is very promising, because they have an ability to fix nitrogen directly from the atmosphere and stimulate the degradation of the oil products in the rhizosphere and their germination rate in petroleum hydrocarbons contaminated soil is better comparing with non-leguminous plant species [4], [5]. Moreover, this type of plant doesn't have to compete with other plants for nitrogen resources, which are often limited in contaminated and degraded soils. During the growing of leguminous plants soil is decontaminated and at the same time the soil fertility and the amount of organic matter may be increased [6]. The efficiency of legumes based phytoremediation depends on the plant species, the composition and concentration of the contaminants, soil type and other environmental factors [7].

The objective of this study was to test eight different legume species and evaluate their potential to remediate fuel oil contaminated soil.

METHODS

Eight species of leguminous plants from the *Fabacea* plant family were grown under laboratory conditions. Two different levels of fuel oil contamination in soil was chosen (2500 mg/kg and 4000 mg/kg). All groups of experiment were carried out in plastic pots, each pot was oval in shape and 25 cm deep. There were a total of 72 pots of tree groups. Each pot was filled approximately 4000 grams of soil. The level of illumination on the surface of the pots reached 22,000 – 24,000 lumens and the duration of lighting was set 12 hours in a 24 – hour interval. The duration of the experiment was 90 days. In order to evaluate the morphometric parameters of the plants, the height of the stems was periodically measured, and the above-ground and underground plant biomass were measured at the end of the experiment. To evaluate the decomposition potential of fuel oil, the residual concentration of fuel oil in the soil was measured by gas chromatography after 45 days and at the end of the experiment (after 90 days).

RESULTS

At the end of the experiment in the group of 2500 mg/kg initial fuel oil contamination all species showed similar results (Fig.1. left side). The largest reduction in fuel oil concentration was recorded in pots with *Pisum sativum* (95.88 %), *Galega orientalis* (95.72 %) and *Lotus corniculatus* (95.60 %). The lowest reduction was recorded in pot with *Lens culinaris* (86.52 %). In the group of 4000 mg/kg initial contamination some legume species were more able to decompose contaminant than others and the levels of degradation differed more than in the first group with lower soil contamination (Fig.1. right side). The best reduction in fuel oil were obtained in pots with *Lotus corniculatus* (95.33 %), *Melilotus albus* (94.68 %) and *Medicago sativa* (94.43 %), while the lowest decomposition potential was obtained in pots with *Onobrychis viicifolia* (81.17 %) and *Lens culinaris* (83.82 %).
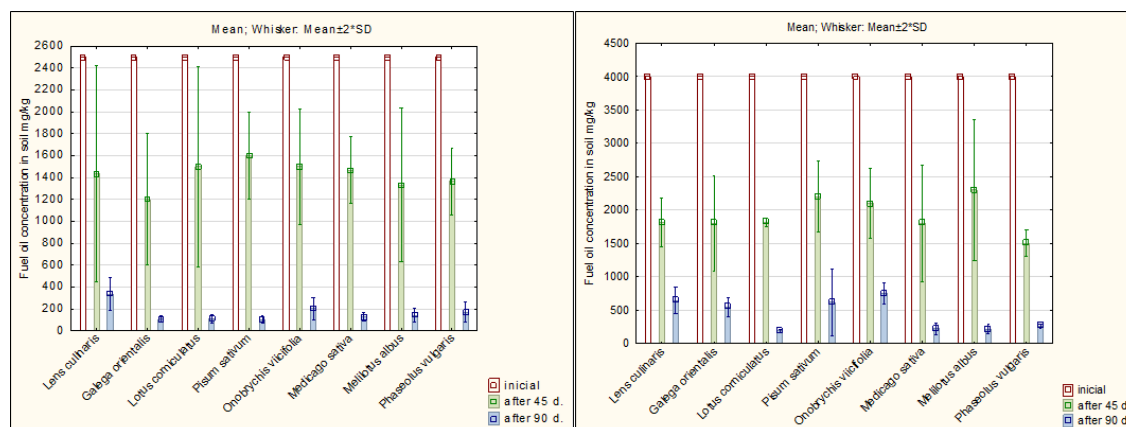
Fig.1. The potential of eight different species of legumes to decompose fuel oil in 2500 mg/kg and 4000 mg/kg soil contamination groups

CONCLUSIONS

Eight species of legumes were tested to evaluate the fuel oil phytoremediation efficiency. The decomposition potential of the oil product depended on the concentration level of the pollutant in the soil. At the concentration of 2500 mg/kg, all tested species of legumes showed similar phytoremediation results. The resistance of plants to contamination as well as the intensity of fuel oil decomposition varied in the group of 4000 mg/kg initial fuel oil contamination. The biggest reduction in fuel oil were obtained in samples with *Lotus corniculatus* (95.33 %),

Melilotus albus (94.68 %) and *Medicago sativa* (94.43 %), while the lowest reduction in samples with *Onobrychis viicifolia* (81.17 %) and *Lens culinaris* (83.82 %).

Keywords: soil bioremediation, fuel oil, petroleum hydrocarbons, legumes

REFERENCES

1. KHAN, M. A. I.; BISWAS, B.; SMITH, E.; NAIDU, R.; MEGHARAJ, M. Toxicity assessment of fresh and weathered petroleum hydrocarbons in contaminated soil-a review. *Chemosphere*, 2018, Vol. 212, P. 755-767.

2. EC. Report from the Commission to the European Parliament, the Council, the European Economic and Social Committee and the Committee of the Regions of the Regions, The implementation of the Soil Thematic Strategy and ongoing activities. COM (2012) 46 final. Link to the internet < https://esdac.jrc.ec.europa.eu/Library/JRC_SOIL/Policy/DGENV/COM(2012)46_EN.pdf >

3. RISKUWA-SHEHU, M. L. Evaluation of the use of legumes for biodegradation of petroleum hydrocarbons in soil. *International Journal of Environmental Science and Technology*, 2017, Vol, 14, P. 2205-2214.

4. CHENG, L.; QIXING, Z.; BINBIN, Y. Responses and roles of roots, microbes, and degrading genes in rhizosphere during phytoremediation of petroleum hydrocarbons contaminated soil. *International journal of phytoremediation,* 2019, P. 1161–1169.

5. POTASHEV, K.; SHARONOVA, N.; BREUS, I. The use of cluster analysis for plant grouping by their tolerance to soil contamination with hydrocarbons at the germination stage. *Science of the Total Environment*, 2014, Vol. 485, P. 71-82.

6. YOUSA, U.; KHAN, A. H. A.; FAROOQ, A.; MUHAMMAD, Y. S.; BARROS, R.; TAMAYO-RAMOS, J. A.; YOUSA, S. Interactive effect of biochar and compost with Poaceae and Fabaceae plants on remediation of total petroleum hydrocarbons in crude oil-contaminated soil. *Chemosphere*, 2022, Vol.286, P. 131-782.

7. OSAM, M. U.; WEGWU, M. O.; AYALOGU, E. O. Soil pH, moisture content and some macro non-metallic elements in crude oil contaminated soils remediated by some wild-type legumes. *International Journal of Engineering Science Invention*, 2013, Vol. 2, P. 54 – 59.

III.3. Sustainable Pest Management

THE OCCURRENCE AND CONTROL OF PEA LEAF WEEVIL (*SITONA LINEATUS* L.) IN BROAD BEAN

M. Almogdad, R. Semaškienė
Lithuanian Research Centre for Agriculture and Forestry
Instituto al. 1, LT-58344 Akademija– Lithuania
+37060753830
mohammad.almogdad@lammc.lt

EXTENDED ABSTRACT

OVERVIEW

A field experiment was carried out in broad bean (*Vicia faba* L.) field to investigate the abundance of the pea leaf weevil (*Sitona lineatus* L.) as influenced by the timing of pest control using insecticides. The study was conducted in broad bean ('Vertigo' var.) during the period of 2019-2020. The study included six spray regimes in addition to untreated control. Yellow water traps were used to monitor the occurrence of pea leaf weevil from the start of germination until the senescence stage. Pea leaf weevil abundance was found in the whole growing season. Two peaks of adult's density were recorded at flowering and when stems begin to darken stages. The foliar insecticides at the local threshold can be recommended as an effective method to protect broad bean from feeding by pea leaf weevils.

METHODS

The research was carried out at Lithuanian Research Centre for Agriculture and Forestry, during the 2019–2020 period. Broad bean 'Vertigo' var. was grown following the recommended agronomic practices. The experiments were laid out in a randomized complete block design (RCBD). Six yellow water traps were distributed to detect the appearance time and the abundance of *S. lineatus*. *S. lineatus* was distinguished from the other Sitona species using morphological descriptors provided in [1]. Also, *S. lineatus* was identified using a published guide, e.g., [2]. Plant growth stages were identified according to Phenological Growth Stage key (BBCH) [3]. Different insecticide regimes using cypermethrin, 500 g l^{-1} were applied as follows: (1) untreated control (UN); (2) at growth stage BBCH 08 (GS08C); (3) when the first pea leaf weevil adult was caught in the yellow water trap (MDC); (4) when the daily air temperature for three days exceeds that of threshold for adult activity (DDC); (5) at the local threshold (5–10 beetles m^{-2}) (THC); (6) at the growth stage BBCH 10–11 (GSC); (7) full control sprays at BBCH 10, 30 and 69 growth stages (FCC). Adults were counted using a 0.25 m^2 frame. Monitoring was taken in the two places of each plot. *S. lineatus* adults were counted at BBCH 16 growth stage. The damage of *S. lineatus* adults on broad bean foliage was assessed at BBCH 18 growth stage. U-shaped notches on leaf margins of 10 plants were counted in each plot. The damage rating was evaluated on each leaf in accordance with a scale (0 to 4). Duncan's multiple range test was used to determine the significance of differences at alpha $\leq$ 0.05 (SAS Institute Inc., USA).

RESULTS

With a few exceptions, the abundance of *S. lineatus* was rather consistent in 2019 and 2020 during practically all broad bean growth stages (Figure 1). The first appearance of *S. lineatus* adults in the traps coincided before plant emerge at BBCH 08 growth stage. In 2019, the dispersing of *S. lineatus* adults to broad bean field coincided with the emergence of seedlings, whereas in 2020, it coincided with the emergence of shoots. The abundance of *S. lineatus* in 2020 was substantially higher than that in 2019. Over the 2019 and 2020 seasons, the density of *S. lineatus* differed across all growth stages.
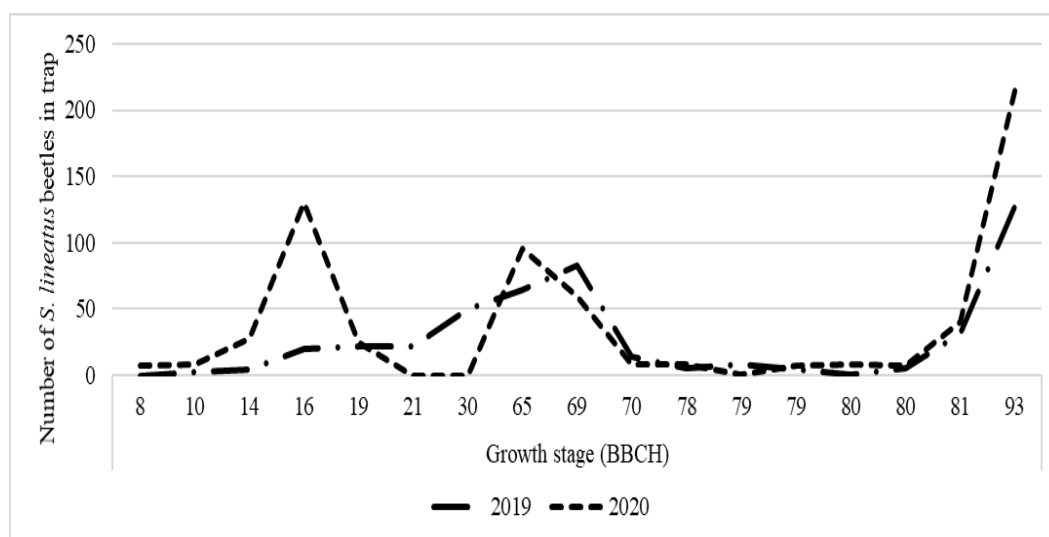
Fig. 1. The abundance of *Sitona lineatus* adults during the growing seasons
(2019–2020)

The damage level (scale out of four levels) in plots treated according to the local threshold was in both study years 1.2 and increased to 2.8 and 2.5 in the untreated control in 2019 and 2020 respectively (Fig. 2). In 2019, insecticide treatments decreased the number of notches per plant. The plants treated by insecticides once according to the local threshold had significantly lower foliar damage compared to the other spray regimes. In 2020, the number of notches per plant was lower in plants treated twice (full control spray) or once according to the local threshold, according to day degree or according to monitoring data spray regime. At the *S. lineatus* adults' density (11.5 beetles m^{-2} in the untreated plots), only the spray regime according to the local threshold had significantly the lowest number of notches on leaves. However, at the high adults' density (17.2 beetles m^{-2} in the untreated plots), the insecticide sprayed twice (full control spray) or once, when the first adult was caught in the traps also reduced the number of notches significantly. Plants treated according to the local threshold had significantly fewer notches than those in the untreated control. In 2020, the plants were attacked by a higher numbers of *S. lineatus* weevils than in 2019 so insecticide application according to the local threshold reduced the foliar damage with no significant differences compared to the other spray regimes.
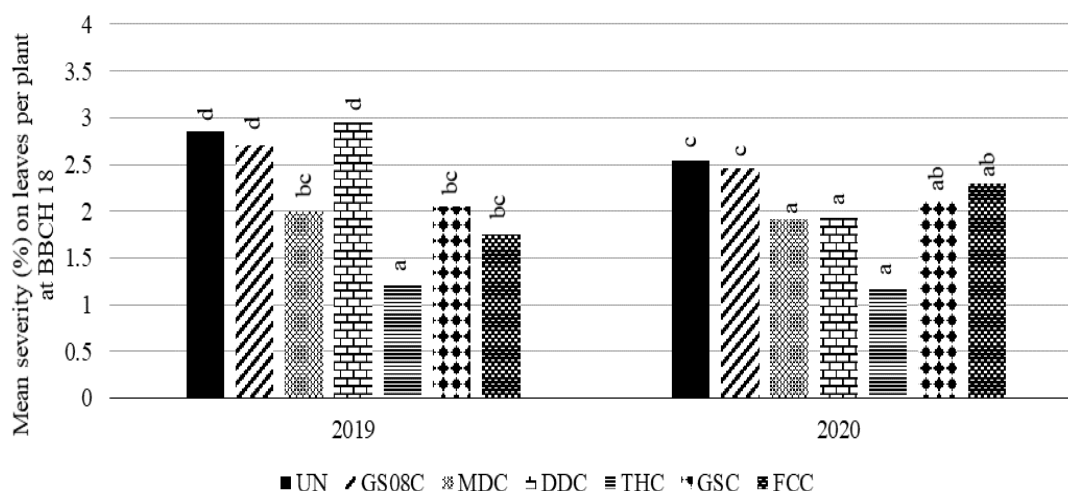
Fig. 2. The effect of spray regime on *Sitona lineatus* feeding notches per
plant on broad bean at BBCH 18 growth stage in 2019–2020

CONCLUSIONS

The peaks of weevil abundance were reached at the stage, when nearly all pods had reached final length (BBCH 79) and at full ripening stage (BBCH 89). Application according to the local threshold gave the significantly lowest number of notches on leaves and significantly decreased the percentage of damaged root nodules compared to the early spray at BBCH 08 growth stage.

Keywords: abundance; broad bean; *Sitona* spp.; spray time; insecticide; notches

REFERENCES

1. BRIGHT, D.; BOUCHARD, P. Coleoptera, Curculionidae, Entiminae. In The Insects and Arachnids of Canada; 2008; Vol. 25, P. 327.

2. PHILLIPS, C.; BARRATT, B. A Guide to Assist Detection of Newly Arrived Sitona Species (Coleoptera: Curculionidae) in New Zealand and Australia; 8th Australasian Conference on Grassland Invertebrate Ecology. Lincoln, Christchurch. 2004.

3. FELLER, C.; BLEIHOLDER, H.; BUHR, L.; HACK, H.; HEß, M.; KLOSE, R.; MEIER, U.; STAUß, R.; BOOM, T.; WEBER, E. Phänologische Entwicklungsstadien von GemüsepflanzenII. Fruchtgemüse und Hülsenfrüchte: Codierung und Beschreibung nach der erweiterten BBCH-Skala - mit Abbildungen. Heft 9, 1995, Vol. 47, P. 217–232.

EFFECTS OF NUN MOTH MASS OUTBREAKS ON NON-TARGET ARTHROPODS IN SCOTS PINE BRANCHES

V. Čėsna, A. Marčiulynas, A. Gedminas, J. Lynikienė, D. Marčiulynienė
Lithuanian Science Centre for Agriculture and Forestry, Institute of Forestry
Liepų st. 1, 53101 Girionys – Lithuania
+37061604924
Vytautas.Cesna@lammc.lt

EXTENDED ABSTRACT

OVERVIEW

Due to possibility to grow under a diverse range of soil and climatic conditions, Scots pine (*Pinus sylvestris* L.) is one of the most economically and ecologically important tree species on hemiboreal forests across Northern Hemisphere [1, 2, 3]. Insect outbreaks constitute the biggest disturbances in forests that cause environmental and economic losses [4, 5, 6]. In *P. sylvestris* forests of Central and North Europe one of the most widespread outbreaks are from the nun moth (*Lymantria monacha* L.) [7, 8, 9]. The last nun moth outbreaks in Lithuania were recorded in 2018-2020 in the area of more than 6,000 ha [10]. For extermination of the outbreaks, there has been used biological insecticide "Foray 76B" that is made by *Bacillus thuringiensis* serovar *kurstaki* (Btk) strain ABTS-351 based formulations [11]. The biological insecticide characterizes toxicity to specific insect species while there has not been founded its direct toxicity to fish, mammals, birds, amphibians, or any non-target organisms [12, 13, 14, 15].

As a consequence of more frequently mass nun moth outbreaks in Europe, a better understanding of the functional changes in Scots pine stands during the outbreaks is needed [16]. In addition, changes in the balance of entomophagous and phytophagous in P. sylvestris stands may have a direct impact on future mass outbreaks [17]. Therefore, a detailed analysis of the changes in non-target insect species during the outbreaks and after the use of the biological insecticide is necessary. The aim of our study was to evaluate outbreaks of L. monacha and "Foray 76B" impact on non-target arthropods in P. sylvestris forests. Hypothesis were: (1) biological insecticide does not trigger abundance of non-target arthropods; (2) L. monacha mass outbreaks induce changes in balance of actively moving arthropods.

METHODS

The study included 12 study sites representing 6 visually healthy (control) and 6 heavily damaged 60-120 years Scots pine stands in Lithuania. The damaged stands were determined by mass outbreaks of *L. monacha* and applied spraying by "Foray 76B" in June 2020. The study sites were distributed into 3 different geographical locations: Kapčiamiestis, Marcinkonys, and Neringa (Fig. 1). Catching of non-target arthropods were conducted from the end of May until the end of October 2021, at monthly (average 28 days interval) collections for 6 months. The arthropods were collected using entomological scoop, performing 50 swings through *P. sylvestris* branches in each study site. Non-target arthropods were collected from stands with similar plant habitat and vegetation. Distance between heavily damaged and control stands was

from 2 to 5 km. Collected entomofauna was sifted and shifted to exterminated pots that were transported on the same day to the laboratory and stored at room temperature. After 20 days of drying, the analysis and identification of insect species were performed.
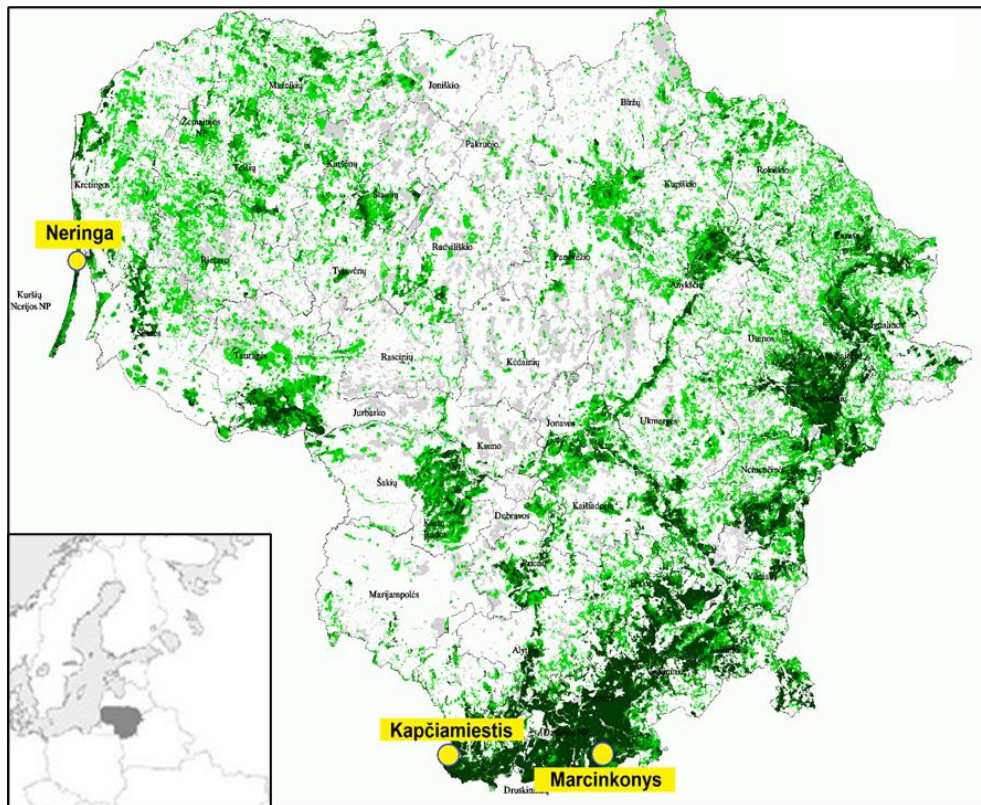
Fig. 1. The study sites in *P. sylvestris* stands in Lithuania. Map by
EUFORGEN 2009, www.euforgen.org [18].

RESULTS

A total of 1170 non-target arthropod individuals were obtained in 6 month period along twelve *P. sylvestris* study sites. Among all a total of 577 arthropods in damaged and 593 in control stands (Fig. 2A). In addition, we found a total of 242 *Chironomus plumosus* individuals that abundance was recorded only on study sites in Neringa. For the significant reasons *C. plumosus* was not included into further data analysis. The highest part of non-target arthropod individuals between 3 different geographical locations were recorded in Kapčiamiestis – 38% (Fig. 2B). Marcinkonys characterized the lowest abundance of non-target arthropods – only 27%. The average number of individuals in damaged stands was 16.0 ± 2.5, while in control stands 16.5 ± 3.2 (statistically insignificant, p > 0.05) (Fig. 3).
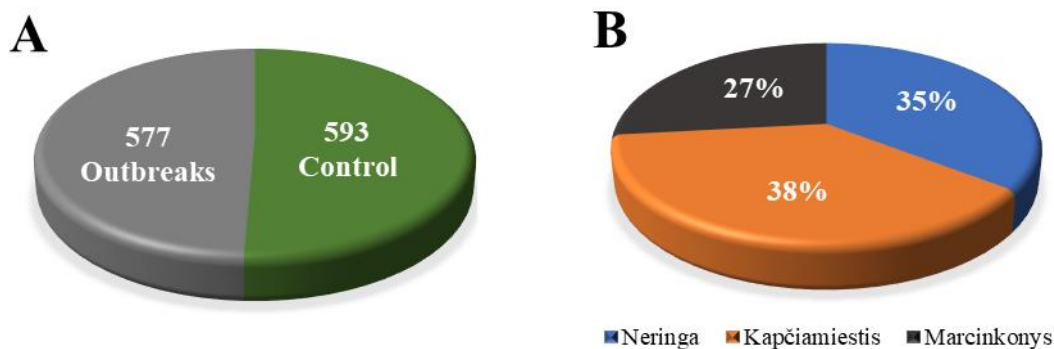
Fig. 2. (A) Abundance of non-target arthropods in damaged and control *P. sylvestris* stands, (B) Relative abundance of non-target arthropods by study site.
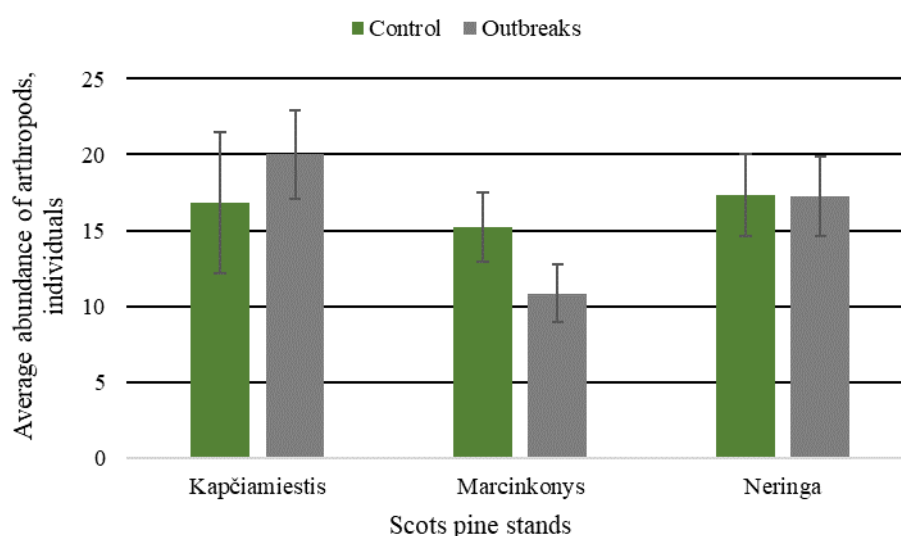
Fig. 3. Average abundance of non-target arthropods in damaged and control stands of P. sylvestris in different study sites.

All the collected non-target arthropod individuals were belonging to 12 orders. The most abundant orders were *Hymenoptera* (30.4%), *Araneae* (28.9%), *Hemiptera* (23.2%), and *Coleoptera* (12.8%). The orders *Diptera*, *Neuroptera*, *Lepidoptera*, *Orthoptera*, *Psocoptera*, *Dictyoptera*, *Opiliones*, and *Odonata* altogether encompassed less than 5% of obtained individuals (Table 1). Significant differences ($p < 0.05$) in insect order abundance were determined between damaged and control stands. Relative abundance of *Araneae* and *Hemiptera* in damaged stands was (1.4 and 1.8 times, respectively) higher than in control study sites. On the contrary, the relative abundance of *Hymenoptera* in damaged stands was 2.6 times lower than in control sites. The relative abundance of *Coleoptera* did not have statistically significant ($p < 0.05$) differences between damaged and control study sites.

Table 1. Relative abundance of arthropod individuals in different *P. sylvestris* stands.

Order	Control, %	Damaged, %	At all, %
Hymenoptera	43.5	17.0	30.4
Araneae	24.1	33.8	28.9
Hemiptera	16.4	30.2	23.2
Coleoptera	12.0	13.7	12.8
Diptera	1.5	1.6	1.5
Neuroptera	1.0	0.9	0.9
Lepidoptera	1.0	0.5	0.8
Orthoptera	0.2	1.4	0.8
Psocoptera	0.3	0.3	0.3
Opiliones	0.0	0.3	0.2
Dictyoptera	0.0	0.2	0.1
Odonata	0.0	0.2	0.1

Based on different distribution of feeding habits of non-target arthropod individuals, we estimated that entomophagous constituted the most part of total individuals both in control (75%) and damaged (58%) study sites (Fig. 4). Phytophagous encompassed 24% in control, and 40% of total individuals in damaged study sites. Other groups constituted only 1% in control, and 2% in damaged *P. sylvestris* stands. The ratio of entomophagous/phytophagous was determined 2.1 times higher in control than in damaged Scots pine stands.
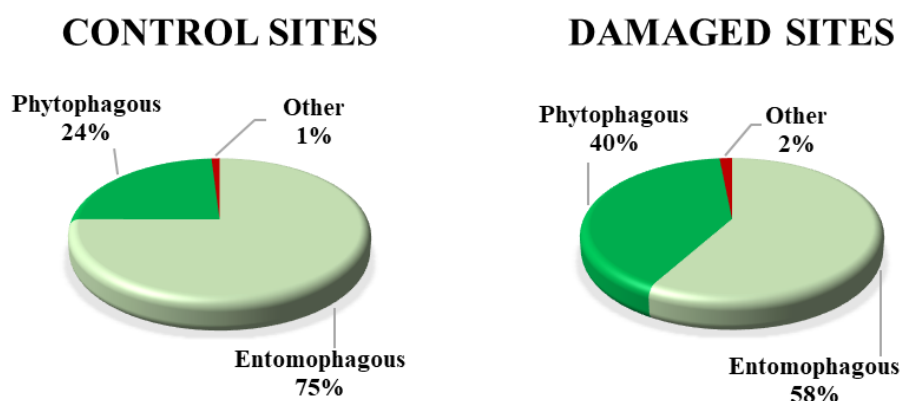
Fig. 4. Abundance of non-target arthropods based on their feeding habits in damaged and control *P. sylvestris* stands.

CONCLUSIONS

The results revealed that although *L. monacha* mass outbreaks did not cause changes in total abundance of non-target arthropods, the outbreaks had a negative impact on the most abundant order – *Hymenoptera*. In summary, the increased total abundance of phytophagous in the damaged pine forests indicates that "Foray 76B" does not affect the abundance of actively moving non-target arthropods.

Keywords: *Lymantria monacha*, Lepidoptera, Foray 76B, *Pinus sylvestris*, insects, entomophagous.

REFERENCES

1. LYNIKIENĖ, J.; MARČIULYNIENĖ, D.; MARČIULYNAS, A.; GEDMINAS, A.; VAIČIUKYNĖ, M.; MENKIS, A. Managed and unmanaged *Pinus sylvestris* Forest stands harbour similar diversity and composition of the phyllosphere and soil fungi. *Microorganisms*, 2020, Vol. 8, P.259.

2. MARČIULYNAS, A.; SIRGEDAITĖ-ŠĖŽIENĖ, V.; ŽEMAITIS, P.; BALIUCKAS, V. The resistance of Scots pine (*Pinus sylvestris* L.) half-sib families to *Heterobasidion annosum*. *Forests*, 2019, Vol. 10 , P. 287.

3. PUHE, J.; ULRICH, B. Global climate change and human impacts on forest ecosystems: Post-glacial development, present situation and future trends in central Europe. *Ecological Studies—Analysis and Synthesis; Springer: Berlin/Heidelberg, Germany*, 2001, Vol. 143.

4. ROBSON, J. R. M.; CONCIATORI, F.; TARDIF, J. C.; KNOWLES, K. Tree-ring response of jack pine and scots pine to budworm defoliation in central Canada. *Forest Ecology and Management*, 2015, Vol. 347, P. 83-95.

5. NETHERER, S.; SCHOPH, A. Potential effects of climate change on insect herbivores in European forests – General aspects and the pine processionary moth as specific example. *Forest Ecology and Management*, 2010, Vol. 259 ,P. 831-838.

6. DE GROOT, M.; OGRIS, N. Short-term forecasting of bark beetle outbreaks on two economical important conifer tree species. *Forest Ecology and Management*, 2019, Vol. 450, P. 117495.

7. NAKLADAL, O.; BRINKEOVA, H. Review of historical outbreaks of the nun moth (*Lymantria monacha*) with respect to host tree species. *Journal of Forest Science*, 2014, Vol. 61, P. 18-26.

8. HOSEK, E. Studie o výskytu kalamit na území ČSR od roku 1900. *Brandýs nad Labem, Lesprojekt*, 1981, Vol.105.

9. GŁOWACKA, B. The nun moth (*Lymantria monacha*) as a pest of coniferous forests in Poland. In: Głowacka B., Malinowski H. (eds): Proceeding of the Integrated management of forest *Lymantriidae*. *Warsaw, Instytut Badawczy Lesnictwa*, 1996, P. 33-40.

10. *Lithuanian Statistical Yearbook of Forestry*; Ministry of Environment, State Forest Service: Kaunas, Lithuania, 2020, p. 14-33.

11. OLIVIERI, M.; MANNU, R.; RUIU, L.; RUIU, P. A.; LENTINI, A. Comparative efficacy trials with two different *Bacillus thuringiensis* Serovar *kurstaki* strains against gypsy moth in Mediterranean cork oak forests. *Forests*, 2021, Vol. 12, P. 602.

12. MEHER, S. M.; BODHANKAR, S. L.; ARUNKUMAR DHULEY, J. N.; KHODAPE, D. J.; NAIK, S. R. Toxicity studies of microbial insecticide *Bacillus thurnigiensis* var. *kenyae* in rats, rabbits, and fish. *International Journal of Toxicology*, 2002, Vol. 21, p. 99-105.

13. BEAVERS, J.; SMITH, G. An avian oral pathogenicity and toxicity study in the mallard: Lab project number: 297-106. *Unpublished study prepared by Wildlife International Ltd*, 1990, P. 19.

14. CHRISTENSEN, K. Dipel technical material (*Bacillus thuringiensis* var. *kurstaki*) – Infectivity and pathogenicity to rainbow trout (*Onchorhyncus mykiss*) during a 32-day state renewal test: Lab project number: 2469.0889.6107.157; 90-2-3219. *Unpublished study prepared by Springborn Laboratories, Inc*., 1990, P. 77.

15. EPA. Reregistration eligibility decision (RED) – *Bacillus thuringiensis*. United States Environmental Protection Agency. EPA 738-R98-004, 1998, P. 157.

16. MELIN, M.; VIIRI, H.; TIKKANEN, O. P.; ELFVING, R.; NEUVONEN, S. From a rare inhabitant into a potential pest – status of the nun moth in Finland based on pheromone trapping. *Silva Fennica*, Vol. 54 .

17. KAISER, L.; ODE, P.; VAN NOUHUYS, S.; CALATAYUD, P. A.; COLAZZA, S.; CORTESERO, A. M.; THIEL, A.; VAN BAAREN, J. Chapter six – the plant as habitat for entomophagous insects. *Advances in botanical research*, 2017, Vol. 81, P. 179-223.

EUFORGEN. 2009. [Referred on the 25th of January in 2022]. Link to the internet <http://www.euforgen.org/species/pinus–sylvestris>.

CLOVE EXTRACT FOR CARROT *ALTERNARIA* SPP. MANAGEMENT

S. Chrapačienė, N. Rasiukevičiūtė, A. Rudinskaitė, A. Valiuškaitė
LAMMC Institute of Horticulture
Kauno str. 30, LT-54333 Babtai, Kaunas distr. – Lithuania
+37037555217
simona.chrapaciene@lammc.lt

EXTENDED ABSTRACT

OVERVIEW

Carrot is one of the most widely cultivated long term survival vegetables worldwide. However, there are significant yield and quality losses during growing and storage due to various diseases. *Alternaria* pathogens are primary to the carrots, as they can cause leaf blight which may affect entire leaf collapse, or black root rot, which spreads quickly in cold storage [1, 2]. For a long time, chemical fungicides were the preventative measure against plant diseases. Nevertheless, chemicals increase environmental pollution, especially soil and water; additionally, microorganisms develop resistance to their exposure [3]. Nowadays, the ambition is to build protection with the least possible damage to nature and human health. The European Union's members are committed to developing alternatives to plant protection products by 2030 [4]. Plant-derived compounds are investigated for disease control; as they have minimal environmental consequences and low toxicity. Studies showed that *Syzygium aromaticum* L., clove, has an antimicrobial impact on opportunistic microorganisms such as *Candida albicans*, *Aspergillus fumigatus, Mucor* spp.*, Salmonella* spp., and others [5, 6]. The study aimed to determine the effect of clove extract on *Alternaria* spp. fungi *in vitro*.

METHODS

In the first part of the experiments, potato dextrose agar medium enriched by different amounts of clove extract to get 0.2, 0.4, 0.6 and 0.8 µL mL^{-1} concentrations were used to evaluate *Alternaria* spp. growth suppression *in vitro*. *Alternaria* spp. isolates obtained from infected carrots. The plant extract was produced from clove buds using extraction with pressurized liquid CO_2. Discs of 7 days old isolates were placed on each Petri dish with an enriched medium, and the diameter of the fungus colony was measured. The control treatment was without investigated extract. Secondly, sterilized carrot pieces were sprayed with 0.8 µL mL^{-1} extract mixed with sterile water and inoculated with *Alternaria* spp. discs. The prevalence of mycelium growth was measured 4 and 7 days after incubation. Petri dishes were incubated at 25±2 °C in the dark for all experiments. Experimental research was carried out at the Laboratory of Plant Protection, LAMMC Institute of Horticulture in Lithuania in 2021.

RESULTS

This study provided new knowledge about the potential of clove extract to suppress *Alternaria* spp. fungi. The assay revealed that the development of fungal mycelium depended on the concentration of the extract in the medium. Our results revelated that clove extract was effective *in vitro* (Fig. 1).
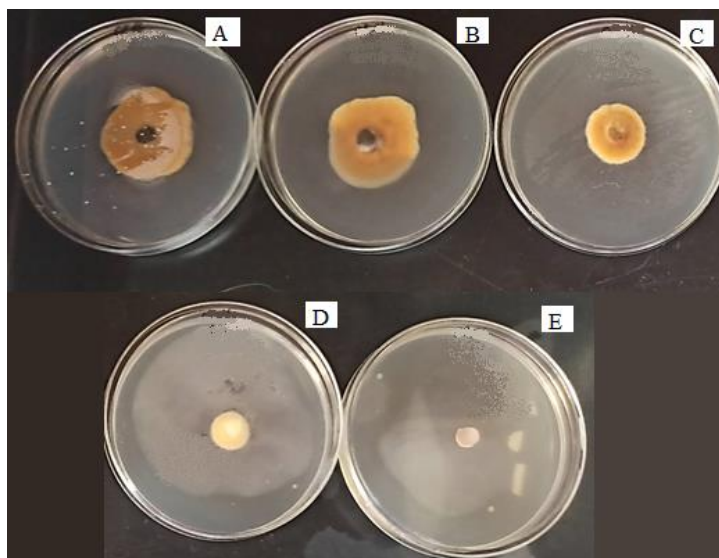
Fig. 1. The comparison of *Alternaria* spp. colony growth on potato dextrose agar after 7 days of incubation. **A**, control (without clove extract), **B**, 0.2 µL mL^{-1}, **C**, 0.4 µL mL^{-1}, **D**, 0.6 µL mL^{-1}, **E**, 0.8 µL mL^{-1} of clove extract.

According to the most sensitive clove extract concentration *in vitro* for *Alternaria* spp. experiments *in vivo* continued. However, *in vivo* experiments did not show significant results.

CONCLUSIONS

To conclude, *S. aromaticum* extract has promising antifungal properties, causing *Alternaria* spp. growth suppression, but further research is needed.

Keywords: *Alternaria* spp., liquid CO_2 extraction, *Syzygium aromaticum* L., *in vitro*

REFERENCES

1. PAWELEC, A.; DUBOURG, C.; BRIARD, M. Evaluation of carrot resistance to Alternaria leaf blight in controlled environments. *Plant pathology*, 2006, Vol. 55, No. 1, P. 68-72.

2. TULEK, S.; DOLAR, F.S. Detection and identification of Alternaria species causing diseases of carrot in Ankara province, Turkey. *Scientific Papers Series B Horticulture*, 2015, Vol. 29, P. 263-264.

3. LIMA, C. B. D.; RENTSCHLER, L. L. A.; BUENO, J. T.; BOAVENTURA, A. C. Plant extracts and essential oils on the control of Alternaria alternata, Alternaria dauci and on the germination and emergence of carrot seeds (Daucus carota L.). *Ciência Rural*, 2016, Vol. 46, P. 764-770.

4. European commission. Communication from the commission to the European parliament, the council, the European economic and social committee and the committee of the regions. 2021- [referred on the 23th of January in 2022 y.]. Link to the internet <https://zur.lt/wp-content/uploads/2021/03/EK_ECO_2021_03_29.pdf>

5. RANA, I. S.; RANA, A. S. Evaluation of antifungal activity in essential oil of the Syzygium aromaticum (L.) by extraction, purification and analysis of its main component eugenol. *Brazilian Journal of Microbiology*, 2011, Vol. 42, No. 4, P. 1269-1277.

6. KAČÁNIOVÁ, M.; GALOVIČOVÁ, L.; BOROTOVÁ, P.; VALKOVÁ, V.; ĎÚRANOVÁ, H.; KOWALCZEWSKI, P. Ł.; VUKOVIC, N. L. Chemical Composition, In Vitro and In Situ Antimicrobial and Antibiofilm Activities of Syzygium aromaticum (Clove) Essential Oil. *Plants*, 2021, Vol. 10, No. 10, P. 2185.

EFFICIENCY OF PLANT EXTRACTS OBTAINED FROM *ARTEMISIA ABSINTHIUM* AGAINST *ACANTHOSCELIDES OBSOLETUS* PESTS

G. M. Daraban[1], M. Bădeanu[2], D. Şuteu[1]*

[1]"Gheorghe Asachi" Technical University of Iasi, "Cristofor Simionescu" Faculty of Chemical Engineering and Environmental Protection, Department of Environmental Engineering and Management,
73 Prof. Dr. Docent D. Mangeron Str., 700050 Iasi – Romania
danasuteu67@yahoo.com

[2]"Ion Ionescu de la Brad" Iasi University of Life Sciences, Faculty of Horticulture, Department of Horticultural Technologies,
3 Mihail Sadoveanu Alley, 700490 Iasi – Romania

EXTENDED ABSTRACT

OVERVIEW

Keeping pests under control in modern agriculture it's a big challenge for practitioners and scientists especially due to crop safety legislation. Moreover, the current technology's detection limits show even traces of contaminants in raw materials, product safety and/or organic products being a desideratum these days [1]. Due to the negative effects of crop and storage pests, pesticides have been developed to neutralize them as effectively as possible. However, this efficiency also comes with a number of shortcomings, such as imbalance of crop-specific ecosystems where pesticides are administered, irreversible effects on pollinators and insects that have irreplaceable roles in the ecosystem, soil contamination, accumulation in crops that provide raw materials for the food industry, negative effects on consumer health, and so on [2]. As a consequence, more and more studies were made by researchers to identify potential substitutes for pesticides with less harmful effects. In this sense, biopesticides coming from plants were considered a sustainable and environmentally-friendly alternative [3]. This paper investigates the effectiveness of biopesticide treatments based on *Artemisia absinthium* collected from spontaneous flora on *Achantoscelides obsoletus* pests. We used several conventional and modern extraction methods of compounds with repellent/insecticide effect to observe the method that presents the highest extraction yield and the confirmation of the proportionality between the degree of extraction and the efficiency on pests.

METHODS

The treatments were obtained by extraction using a series of classical and modern methods such as maceration (M), extraction in the Soxhlet installation (HAE), ultrasonic-assisted extraction (UAE), and a combined approach (UAE + M). The extraction was performed with pure ethanol (96%). The treatments thus obtained were administered to control pests of the species *Achantoscelides obsoletus*. In the case of M method, the contact time between the two phases was 9 days at a temperature of about 20° C, in the case of the HAE method, the time was 2 h and temperature of about 80°C, while for UAE, the established time was 15 min and

temperature 45°C. In the UAE method, the extraction was performed using an ultrasonic bath, SONOREX RK 100 H type (produced by Bandeline Electronic GmbH &Co.KG, Berlin, Germany, bath frequency 35 kHz, power 320 W). The solid/liquid ratio (S/L) was 1/15. The extracts were kept at refrigeration temperature until the time of administration. The administration protocol consisted of the administration of ~ 0.5 mL, after which the monitoring was performed at the following time intervals: 2, 8, 12, 24, 48, 72, 96, 120, 144, and 168h, following the number of pests deaths. *Achantoscelides obsoletus* was monitored under laboratory conditions in growth cages with a 1 L plastic volume provided with ventilation holes and sufficient food. The experiment was performed in duplicate accompanied by two control samples under the same conditions. The mortality was calculated using Eq. 1:

$$\text{Mortality \%} = N_d / N_o * 100, \tag{8}$$

where: N_d represents the number of dead insects, and N_0 represents the initial test insects.

RESULTS

Analysing Fig. 1, it is observed that the most obvious results of the administered treatment are manifested starting with the interval 120 h to 168 h. Also, the extracts using the method UAE + M show a higher level than other extracts in this interval. The efficiency of the treatments on the deposit pest of the species *Achantoscelides obsoletus* follows the order, UAE+M>UAE>HAE>M. The extracts based on M method presented similar results to the control sample.
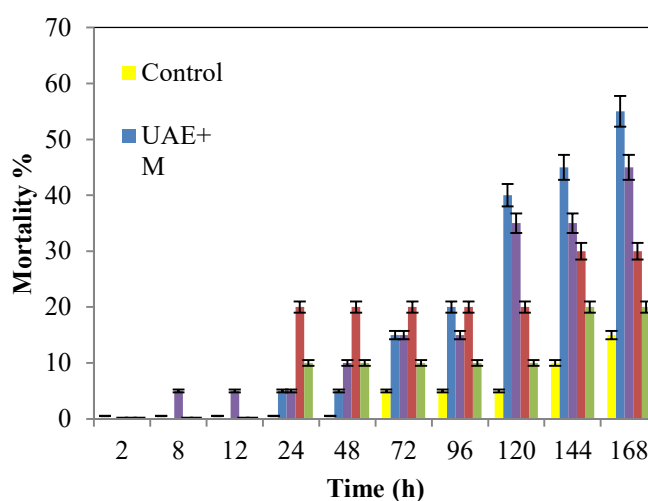
Fig. 1. Mortality (%) of pests of the species *Achantoscelides obsoletus* according to the treatments obtained using different extraction methods based on the species *Artemisia absinthium* at predetermined time intervals

CONCLUSIONS

In conclusion, the use of plants extracts from spontaneous flora can be an alternative to substituting synthetic treatments with side effects on human health and the environment, especially if combined with other non-invasive alternative methods during the storage period.

Keywords: *Artemisia absinthium*, biopesticides, extraction methods, pest control, spontaneous flora

REFERENCES

1. DARABAN, G. M.; HLIHOR, R. M.; APOSTOL, M.; BĂDEANU, M.; ȘUTEU, D. Secondary plant metabolites: sources of principles for use in agriculture, food industry and for human health safety. *2021 International Conference on e-Health and Bioengineering (EHB)*, 2021, P. 1-4, Doi: 10.1109/EHB52898.2021.9657618.

2. ȘUTEU, D.; RUSU, L.; ZAHARIA, C.; BADEANU, M.; DARABAN, G. M. Challenge of utilization vegetal extracts as natural plant protection products. *Applied Sciences*, 2020, Vol. 10, No. 24, P. 8913.

3. AZWANIDA, N. N. A review on the extraction methods uses in medicinal plants, principle, strength, and limitation. *Medicinal & Aromatic Plants*, 2015, Vol. 4, No. 3, P. 3-8.

MOST COMMON FUNGAL DISEASES OF TOMATO IN LATVIA

L. Dučkena, **G. Bimšteine**
Latvia University of Life Sciences and Technologies
2 Liela street, LV-3001 Jelgava – Latvia
+371 29590183
lilija17duckena@gmail.com

EXTENDED ABSTRACT

OVERVIEW

Tomato (*Solanum lycopersicum* L.) is an important vegetable in Latvia. According to data from the Central Statistical Bureau of Latvia, in 2020, tomatoes represented 43.9 % of the total export value of fresh vegetables. The total demand for fresh-market and processing tomatoes is high; therefore, increasing tomato production and improving its quality is of great importance for this country. Fungal diseases are a major limiting factor for tomatoes which cause a serious yield reduction. Economically important diseases in tomatoes are caused by pathogens of different genera – *Alternaria*, *Phytophthora*, *Pythium*, *Rhizoctonia*, *Fusarium*, *Botrytis*, *Septoria*, *Colletotrichum*, *Oidium, Leveillula*, *Fulvia*, and *Verticillum* [1, 2, 3]. There has been fragmented research on tomato diseases in Latvia, and used complexes of agrotechnical techniques for tomatoes have been changing in the last years. In the past, high-pressure sodium lamps were commonly utilized, but nowadays light-emitting diodes (LEDs) are becoming widely adopted in protected horticulture [4]. Also, used cultivars in tomato production are changing. Until now, no wide research on tomato diseases has been carried out in Latvia. The present research aims to diagnose tomato diseases and identify their causal agents in different production systems.

METHODS

Samples of leaves, stems, and fruits with characteristic symptoms of fungal diseases were collected at the beginning and end of the 2021 production season. Samples were collected in six farms that varied in construction (greenhouse structures, high tunnels), size, growing conditions, crop protection (integrated or biological pest management), and cultivar ('Beorange' F1, 'Fontana' F1; 'Cristal' F1, 'Tamaris' F1, 'Organza' F1, 'Aurea' F1, 'Gourmandia' F1, 'Juliet' F1, 'Gloriette' F1, 'Tasty' F1, 'Bolzano' F1, 'Fuji Pink' F1, 'Belfast' F1, 'Berner Rose', 'Sonnenherz', 'Orange Queen', 'Ananas', 'Green Zebra', 'Black Prince'). At the beginning of intensive tomato production, a total of 125 samples with characteristic disease symptoms were collected and 202 isolates were obtained and identified to genera level. Identification of diseases was performed at the LLU Plant Pathology Scientific Laboratory of the Institute of Soil and Plant Science. Late blight (caused by *Phytophthora* spp.), leaf mold (caused by *Fulvia* spp.), and powdery mildew (caused by *Oidium* spp.) were identified visually if conidia were seen; in other cases, isolation of fungi was conducted. Pure cultures (isolates) of *Alternaria*, *Stemphilium*, *Botrytis*, *Fusarium*, *Colletotrichum* were obtained by pathogen isolation on potato dextrose agar. Morphological characteristics of the isolates were used to

identify the fungi: colour and texture of the mycelium, staining of the medium, and characteristics of spore and sclerotia formation.

RESULTS

Determined fungi varied depending on the growing conditions. In 2021, at the beginning of intensive tomato production, the two most common fungi isolated from infected tomatoes were *Alternaria* spp. and *Botrytis* spp. (29% and 25% of isolates, respectively). Diseases of tomato leaves were caused by *Alternaria* spp., *Botrytis* spp., and *Fulvia* spp. Tomato fruits were infected by pathogens of different genera – *Alternaria, Botrytis, Fusarium*, and *Colletotrichum.* At the end of intensive tomato production, a wider spectrum of diseases was observed. The dominant diseases were different leaf spots caused by the genera *Botrytis*, *Alternaria*, *Oidium*, *Fulvia*, and *Phytophthora*. Diseases of tomato fruits were caused by *Alternaria* spp., *Botrytis* spp., and *Phytophthora* spp. Also, at the end of intensive tomato production, complex infection of *Alternaria/Stemphilium* was observed on tomato leaves and fruits (Fig. 1).
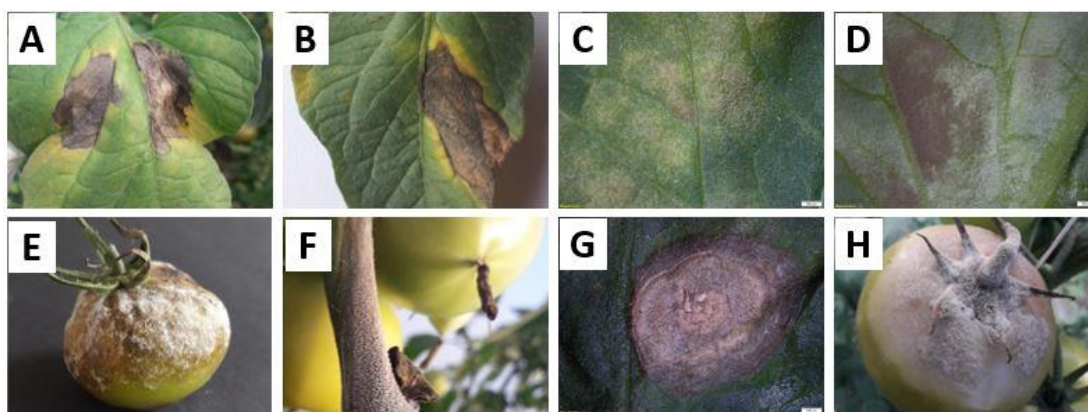
Fig. 1. Symptoms of diseases caused by different pathogens – *Alternaria/ Stemphylium* spp. (A), *Alternaria* spp. (B), *Fulvia* spp. (C, D), *Phytophthora* spp. (E), and *Botrytis* spp. (F-H) – on tomato leaves, stems, and fruits.

In high tunnels and small greenhouses with a polyethene film or polycarbonate cover, the microclimate is partially controlled, therefore, a wider spectrum of diseases was observed there. In such conditions, grey mold (caused by *Botrytis* spp.) was commonly found because of the high relative humidity and optimal temperature in those constructions. This disease was especially severe in biological farms, where a lot of vegetables are grown together, such as lettuce, pepper, and others that also host plants of grey mold. Gray mold mostly affects leaves, stems, and fruits, and symptoms are observed at any stage of tomato plant development. *Alternaria* spp., which causes early blight, was also often observed. At the end of intensive tomato production, fungal pathogen *Stemphylium* spp., which causes grey leaf spot disease, was observed. During the investigation, mostly both *Alternaria* spp. and *Stemphylium* spp. were isolated from the same tomato plants and the same blotches, indicating a complex disease. Also, in greenhouses and high tunnels, leaf mold (caused by *Fulvia* spp.) and late blight (caused by *Phytophthora* spp.) were identified. In large industrial glasshouses, many resources are invested in sanitation to prevent disease outbreaks and the climate control system is fully automatic, therefore, the spectrum of diseases was not so wide there. One of the most severe diseases in the large glasshouses was grey mold (caused by *Botrytis* spp.). Another occasionally severe disease there was powdery mildew (caused by *Oidium* spp.). Symptoms of powdery mildew are

visible mainly on leaves, and the severity of the disease may vary depending on cultivars because the causal agent is a highly specialized obligate parasite [5].

CONCLUSIONS

The most important diseases affecting tomatoes in Latvia are an early blight, caused by *Alternaria* spp., grey mold, caused by *Botrytis* spp., late blight, caused by *Phytophthora* spp., powdery mildew, caused by *Oidium* spp., and leaf mold, caused by *Fulvia* spp. Further research is required to identify the species of pathogens.

Keywords: Solanum lycopersicum L., Alternaria, Botrytis, Phytophthora, Oidium, Fulvia

REFERENCES

1. SANOUBAR, R.; BARBANTI, L. Fungal diseases on tomato plant under greenhouse condition. *European Journal of Biological Research*, 2017, Vol. 7, No. 4, P. 299-308.

2. KUMAR, S. P.; SRINIVASULU, A.; BABU, K. R. Symptomology of major fungal diseases on tomato and its management. *Journal of Pharmacognosy and Phytochemistry*, 2018, Vol. 7, No. 6, P. 1817-1821.

3. HUA, L.; YONG, C.; ZHANQUAN, Z.; BOQIANG, L.; GUOZHENG, Q.; SHIPING, T. Pathogenic mechanisms and control strategies of *Botrytis cinerea* causing post-harvest decay in fruits and vegetables. *Food Quality and Safety*, 2018, Vol. 2, No. 3, P.111-119.

4. PAUCEK, I.; PENNISI, G.; PISTILLO, A.; APPOLLONI, E.; CREPALDI, A.; CALEGARI, B.; SPINELLI, F.; CELLINI, A.; GABARRELL, X.; ORSINI, F.; GIANQUINTO, G. Supplementary LED interlighting improves yield and precocity of greenhouse tomatoes in the Mediterranean. *Agronomy*, 2020, Vol. 10, No. 7, P. 1002.

5. HÜCKELHOVEN, R.; PANSTRUGA, R. Cell biology of the plant–powdery mildew interaction. *Current opinion in plant biology*, 2011, Vol. 14, No. 6, P. 738-746.

DIVERSITY OF FUNGI ON *CHAENOMELES JAPONICA* IN LATVIA

I. Jakobija, A. Kluga
Latvia University of Life Sciences and Technologies
Institute for Plant Protection Research "Agrihorts"
Paula Lejina st. 2, LV-3004 Riga – Latvia
+371 29434992
inta.jakobija@llu.lv

B. Bankina
Latvia University of Life Sciences and Technologies
Liela st. 2, LV-3001 Riga – Latvia
+371 26391893
biruta.bankina@llu.lv

EXTENDED ABSTRACT

OVERVIEW

The area of Japanese quince plantations for fruit production in Latvia has increased in recent years. With it, there is also a potential for an increase in disease occurrence. It has been established that fruit rot in some growing seasons reached agronomically significant development [1] and leaf spots appeared as a problem [2] in Japanese quince plantations in Latvia. There is a lack of overall information in the literature about the diversity of fungi on *Chaenomeles japonica*. Several disease symptoms have been described by Norin and Rumpunen [3]. According to their findings, fungi were found on *C. japonica* fruits, shoots, leaves, and inflorescences in Sweden and in Romania, Australia and Canada [3]. Information is also available about the occurrence of fungi of *C. japonica* in the Botanical garden of Vilnius University [4]. The presence of pathogenic fungi causing disease symptoms on *C. japonica* has been reported in Russia [5]; however, that information is fragmented and insufficient. The aim of the present study is to determine the diversity of fungal genera associated with *C. japonica* in Latvia.

METHODS

In the monitoring of eight Japanese quince plantations in Latvia, samples of leaves, shoots, inflorescences and fruits with visible disease damages were collected in three vegetation seasons of 2017–2019. The fungi obtained from damages on different parts of Japanese quince were cultivated on potato dextrose agar (PDA) at the temperature of $+20^{\circ}$C in the dark. In addition to PDA, damaged areas of the leaves, associated with fungal diseases, were cultivated on both PDA and V8 juice. Fungal isolates were identified using the results obtained from ITS region sequencing. Sequencing results were analyzed using FinchTV chromatogram – an open access desktop application – and were identified using NCBI BLAST® database. Relative density of fungal genera was determined as the proportion of the particular genera of fungi in relation to all fungal isolates obtained.

RESULTS

A total of 36 genera of fungi were identified among 538 fungal isolates obtained from the damaged leaves, fruits, flowers and shoots of *C. japonica*. Representatives of identified genera were well-known pathogens of *C. japonica*, other *Chaenomeles* species, and plants from the family Rosacea. Also, pathogens of other plants, fungi causing secondary infection, and different saprotrophs and endophytes were identified. *Fusarium* spp., *Alternaria* spp., *Botrytis* spp., and *Sarocladium* spp. prevailed with the relative density of 21%, 15%, 13%, and 9% respectively. The values of the relative density of the genera *Clonostachis, Cladosporium, Epicoccum, Trichoderma, Monilinia,* and *Boeremia* were within the range of 3% to 6%, but the relative densities of the other 26 fungal genera were less than 2%. *Alternaria, Fusarium, Sarocladium, Epicoccum, Botrytis, Cladosporium, Boeremia, Clonostachis, Arthrinium,* and *Akanthomyces* were isolated from the leaf spots on C. *japonica* plants. Various damages, such as different types of spots and rot, on *C. japonica* fruits, as well as overwintered mummified fruits were observed in the investigation. *Botrytis, Fusarium, Alternaria, Allantophomopsis, Coniophora, Penicillium* and *Trichothecium* spp. were found in the mummified fruits. Whereas *Botrytis, Fusarium, Alternaria, Neofabraea, Diaporthe, Arthrinium, Allantophomopsis, Boeremia,* and *Stagonosporopsis* spp. were associated with fruit spots. The genera *Botrytis, Fusarium, Alternaria*, *Monilinia*, *Penicillium,* and *Crustomyces* spp. were most frequently isolated from the fruits in all stages of their development. Various shoot damages on the shoots of Japanese quince were observed. Most frequently the *Fusarium, Botrytis, Alternaria, Diaporthe, Didymella, Trichoderma, Monilinia, Clonostachis, Cladosporium, Allantophomopsis,* and *Arthrinium* species were obtained from the damaged *C. japonica* woody parts. *Fusarium, Alternaria, Clonostachis,* and *Coniophora* spp. were found on the dead or wilted flowers of *C. japonica.*

CONCLUSIONS

A high diversity of fungi on *C. japonica* were found during the investigation. They belonged to 36 genera. Among all fungal genera identified on *C. japonica,* prevailing fungi were from the genera of *Fusarium*, *Alternaria, Botrytis,* and *Sarocladium.* The high diversity of determined fungi revealed that the current situation is complex and it is not possible to identify the pathogens under field conditions. Further research is required to clarify the degree of the pathogenicity of different fungi and their interactions.

Keywords: Japanese quince, *Botrytis, Alternaria, Monilinia*

ACKNOWLEDGEMENTS

REFERENCES

1. JAKOBIJA, I.; BANKINA, B. Incidence of fruit rot on Japanese quince (*Chaenomeles japonica*) in Latvia. *Research for rural development 2018*. Vol.2, P. 83-89.

2. JAKOBIJA, I.; KLUGA, A.; BANKINA, B. Leaf spot diseases as an emerging problem in *Chaenomeles japonica* plantations. AGROECO 2020. Agroecosystem sustainability: Links between carbon sequestration in soils, food security and climate change: 3rd international scientific virtual conference AgroEco 2020 programme and abstracts, Lithuania, Kaunas, 2-3 Dec. 2020 / Vytautas Magnus University, Agriculture Academy Kaunas, 2020. P. 27.

3. NORIN, I.; RUMPUNEN, K. Pathogens on Japanese quince (*Chaenomeles japonica*) plants. *Japanese quince – Potential fruit crop for Northern Europe.* Department of Crop Science, Swedish University of Agricultural Sciences, 2003, P. 37–54. ISBN 91-631-3765-8.

4. GRIGALIŪNAITĖ, B.; ŽILINSKAITĖ, S.; RADAITIENĖ, D. Japoninio svarainio *(Chaenomeles japonica)* fitosanitarinė būklė Vilniaus universiteto botanikos sode. *Optimization of Ornamental and Garden Plant Assortment, Technologies and Environment: Scientific Articles*, 2012. Vol. 3, No. 8, P. 25–29.

5. FEDULOVA, Y.; KUKLINA, A.; SOROKOPUDOV, V.; SOROKOPUDOVA, O.; SHLAPAKOVA, S.; LUKASHOV, Y. Screening of phytopathogens and phytopathoges on *Chaenomeles* (*Chaenomeles* Lindl.) cultivars. *BIO Web of Conferences*, 2020, Vol. 17, P. 1-4.

POTENTIAL BACTERIAL ANTAGONISTS FOR THE CONTROL OF *MONILINIA* SPP. PATHOGENS

A. Kolytaitė, B. Frercks
Institute of Horticulture,
Lithuanian Research Centre for Agriculture and Forestry,
Kauno Street 30, LT-54333 Babtai, Kaunas distr. – Lithuania
augustina.kolytaite@lammc.lt, birute.frercks@lammc.lt

B. Kabalinaitė
Faculty of Natural Sciences,
Vytautas Magnus University,
Vileikos Street 8, LT-44248 Kaunas – Lithuania

EXTENDED ABSTRACT

OVERVIEW

Brown rot is one of the main diseases in all stone fruit growing areas and is caused by several *Monilinia* spp. [1, 2, 3]. These pathogens infect blooms, twigs and fruits in the field with a variety of symptoms, including blossoms blight, cankers on woody tissues and fruit rot [4, 5].

Chemical management is not sufficient to control brown rot in orchards. Moreover, consumers prefer buying pesticide-free production. This leads to the need to introduce alternative methods, such as physical or biological control [5]. So far, several antagonistic microorganism species have been found, including *Bacillus* and *Pseudomonas spp.* [6, 7, 8]. Few *Bacillus* species inhibited *M. laxa* in apricots and peaches [6]. *P. synxantha* strain DLS65 has been succesfully tested *in vitro* and *in vivo* against *M. fructicola* and *M. fructigena* [7]. To the date, there is a commercial product against pathogenic fungi ('Serenade® ASO', Bayer AG), but it is not specific for *Monilinia* spp. and is not accessible to small orchard growers.

The strategy for biological control is to isolate microorganisms from the local host of a particular disease and test their inhibitional activities to ensure the efectiveness of a natural killer against the pathogen without harming the plant [9, 10, 11, 12]. However, the specific stone fruit antagonists against *Monilinia* species are still lacking for orchards in the Baltic sea region.

The aim of this study is to evaluate the antagonistic properties of endofitic bacteria naturally distributed in plum orchards against *M. fructigena*.

METHODS

Isolates of the pathogenic fungi *M. fructigena* were collected from decaying plum fruits at the Lithuanian Research Centre for Agriculture and Forestry Institute of Horticulture, in the selective stone fruit orchard in autumn, 2021. The pathogens were visually identified, subcultivated and used in *in vitro* experiments. Endophytic bacteria samples were isolated from

plum tree buds of annual shoots. The annual shoots (approximately 30 cm in length) were randomly selected by going diagonally across the orchard. Leaves were discarded immediately in the field and shoots were kept at 4 °C until further analysis.

Six various methods for bud sterilisation with minor modifications were chosen (Table 1). All buds from shoots were collected to form a pool and 30 plum buds were randomly selected for each sterilisation method. The sterilisation scheme is shown in Table 1.

Table 1. Scheme of bud sterilisation methods

Method \ Step		Hydrogen peroxide [13, 14, 15]	Sodium hypochlorite [15]	Ethanol [14]	Mercuric chloride [13, 17]	Bleach [18]	Combined method [19]
1.	Main sterilization agent	H_2O_2, 3% 10 min	NaClO, 5% 5 min	C_2H_5OH, 70% 3 min	$HgCl_2$, 0,1% 10 min	ACE 5 min	C_2H_5OH, 70% 5 min, H_2O_2, 3% 20 min, C_2H_5OH, 70% 1 min
2.	Wash with sterile-distilled water	4 times, 2 min	Once, 10 min	4 times, 1 min	7 times, 1 min	4 times, 1 min	5 times, 1 min
3.	Macerate buds in 5 ml of sterile-distilled water for 30 min [14]						
4.	Filtrate the suspension, centrifugate 5 min x 4000 rpm, discard the supernatant						
5.	Add 5 ml of sterile-distilled water and resuspend [14]						
6.	Cultivate 20 µl of final suspension on LB agar media [14]						
7.	Incubate plates at 28 °C for 7 days [19]						

Plates with restreaked single colonies were incubated for another 48 hours [19]. The bacterial and fungal stock cultures were stored at 4 °C on Petri dishes containing Luria-Bertani (LB, peptone, 10 g; yeast extract, 5 g; NaCl, 10 g; agar, 10 g per litre, pH 7,2 - 7,3) and Potato Dextrose Agar (PDA, Sharlab, S. L., Barcelona, Spain), respectively [5].

The evaluation of the antagonistic activity of the isolated bacterial strains was performed according to the following protocols with some modifications [5, 20]. The mycelium disc (5 mm diameter) was placed in the centre of a Petri dish with PDA medium. Approximately 1 cm away from the mycelium disc bilaterally a loopful of each strain was streaked (3-4 cm), in three replicates. Dual culture plates were incubated at 28 ºC in a dark chamber. The plate with a fungus only was used as a control. Radial growth inhibition was calculated as follows:

$$\%I = \left(\frac{C-T}{C}\right) \cdot 100. \qquad (5)$$

Measurements were taken at 8 and 14 days.

RESULTS

The average number of successfully isolated endophytic bacteria by different six sterilisation approaches are shown in Fig. 1. The data show that there were no significant differences between applied sterilisation approaches. However, the lowest number of bacteria was obtained using mercuric chloride or combined sterilisation method. The reason could be the intensive penetration of sterilising agent into deeper bud tissues, which affects viability of microorganisms [21]. The highest number of isolated bacteria was obtained by using bleach or sodium hypochlorite, although there were no significant differences among them.
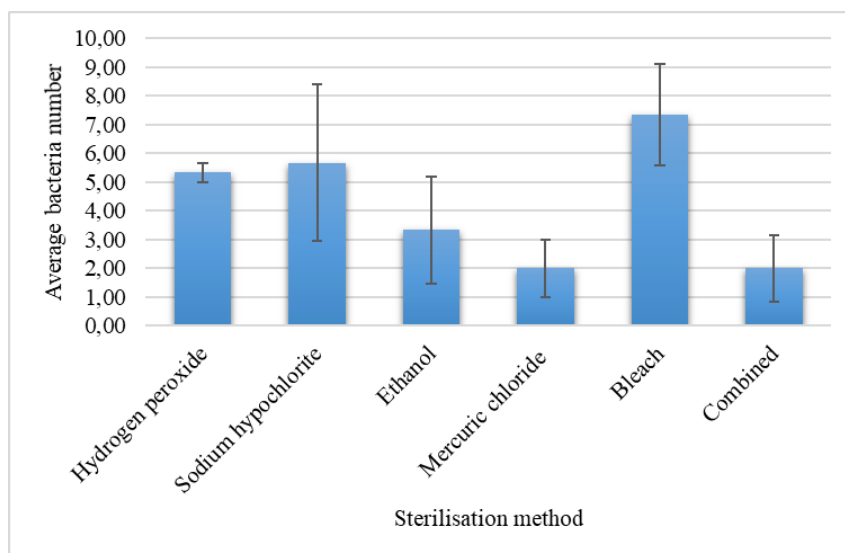
Fig. 1 Number of endophytes using different sterilisation method

The average number of potential antagonists by each sterilisation method is given in Fig. 2. In total 77 endophytes were obtained, of which 16 microorganisms can be potential antagonists. The highest number of antagonists was reached using bleach as the main sterilisation agent.
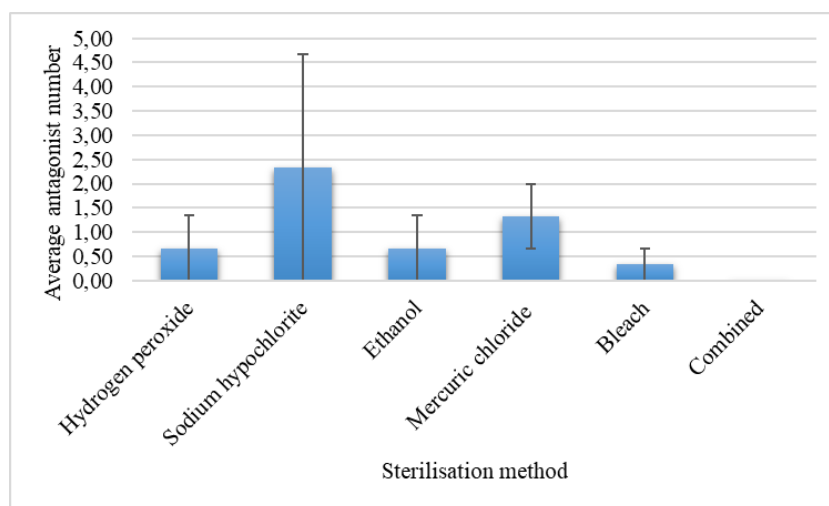
Fig. 2. Number of antagonists using different sterilisation method

The antagonistic activity of bacteria against *M. fructigena* ranged from 2,21 % to 73,55 % (average 42,27±11,71 %) after 8 days of incubation. In total 16 antagonists had inhibition of 30 % and 8 of them had reached inhibition of 50 % or higher. After 14 days inhibition of 30 %

was still observed in 13 isolates, of which 6 had inhibition rate of 50 % or higher. Examples of potential antagonists are shown in Fig. 2.
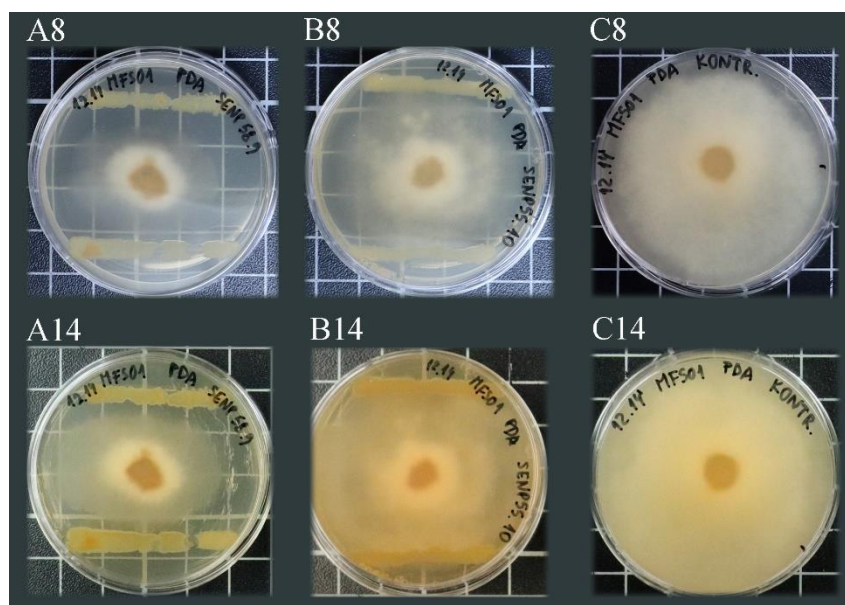
Fig. 2. Inhibition of *M. fructigena* growth by bacterial antagonists. A8, B8 and A14, B14 – dual culture plates after 8 and 14 days, respectively. C8 and C14 – control plates.

CONCLUSIONS

Sterilisation with mercuric chloride or combined sterilisation method is the least favourable for effective endophyte isolation.

In total 13 naturally distributed bacterial endophytes are potential antagonists against *M. fructigena*.

Keywords: antagonists, endophytes, bacteria, *Monilinia*, brown rot, inhibition.

REFERENCES

1. MEYER, M. D.; ZHANG, G. R.; PEDERSEN, D. K.; BRADLEY, C. A. First report of Phomopsis stem canker of sunflower in Illinois caused by *Phomopsis helianthi*. *Plant Disease*, 2009, Vol. 93, No. 7.

2. CAL, A.; GELL, I.; USALL, J.; VINAS, I.; MELGAREJO, P. 2009. First report of brown rot caused by *Monilinia fructicola* in peach orchards in Ebro Valley, Spain. *Plant Disease*, 2009, Vol. 93, No. 7.

3. CAL, A.; MELGAREJO, P. Effects of long-wave UV light on *Monilinia* growth and identification of species. *Plant Disease*, 1999, Vol. 83, No. 1, P. 62-65.

4. MARTINI, C.; MARI, M. *Monilinia fructicola, Monilinia laxa (Monilinia Rot, Brown Rot)*. Academic Press, 2014. P. 233-265. ISBN 9780124115521.

5.   GRZEGORCZYK, M.; ŻAROWSKA, B.; RESTUCCIA, C.; CIRVILLERI, G. Postharvest biocontrol ability of killer yeasts against *Monilinia fructigena* and *Monilinia fructicola* on stone fruit. *Food Microbiology*, 2017, Vol. 61, P. 93-101.

6.   RUNGJINDAMAI, N.; JEFFRIES, P.; XU, X. Epidemiology and management of brown rot on stone fruit caused by *Monilinia laxa*. *European Journal of Plant Pathology*, 2014, Vol. 140, No. 1, P. 1-17.

7.   AIELLO, D.; RESTUCCIA, C.; STEFANI, E.; VITALE, A.; CIRVILLERI, G. Postharvest biocontrol ability of *Pseudomonas synxantha* against *Monilinia fructicola* and *Monilinia fructigena* on stone fruit. *Postharvest Biology and Technology*, 2019, Vol. 149, P. 83-89.

8.   JANAKIEV, T.; DIMKIĆ, I.; UNKOVIĆ, N.; LJALJEVIĆ, G. M.; OPSENICA, D.; GAŠIĆ, U.; STANKOVIĆ, S.; BERIĆ, T. Phyllosphere fungal communities of plum and antifungal activity of indigenous phenazine-producing *Pseudomonas synxantha* against *Monilinia laxa*. *Frontiers in Microbiology*, 2019, Vol. 10.

9.   BELLOWS, Thomas S.; FISHER, T. W. *Handbook of Biological Control*. Academic Press, 1999, P. 710. ISBN 9780122573057.

10. HAJEK, A.; EILENBERG, J. *Microbial Antagonists Combating Plant Pathogens and Plant Parasitic Nematodes. In Natural Enemies: An Introduction to Biological Control*. Cambridge University Press, 2018, P. 308-324.

11. THAMBUGALA, K. M.; DARANAGAMA, D. A.; PHILLIPS, A. J. L.; KANNANGARA S. D.; PROMPUTTHA I. Fungi vs. fungi in biocontrol: an overview of fungal antagonists applied against fungal plant pathogens. *Frontiers Cellular Infection Microbiology*, 2020, Vol. 10.

12. SANTOYO, G. (in press). How plants recruit their microbiome? New insights into beneficial interactions. *Journal of Advanced Research*, 2021.

13. BAJAJ, Y. P. S. *High-Tech and Micropropagation I. Biotechnology in Agriculture and Forestry*. Springer, Berlin, Heidelberg, 1991. 48 p. ISBN 978-3-642-76415-8.

14. DAVOUDPOUR, Y.; SCHMIDT M.; CALABRESE F.; RICHNOW H. H.; MUSAT N. High resolution microscopy to evaluate the efficiency of surface sterilization of *Zea mays* seeds. *Plos One*, 2020, Vol. 15, No. 11.

15. KÖSE Merve, S. H.; DOGAN, M.; SADI, G. Surface sterilization of *Staurogyne repens* (Nees) Kuntze with hydrogen peroxide. *Bulletin of Biotechnology*, 2020, Vol. 1, No. 2, P. 39-42.

16. ETMINANI, F.; HARIGHI, B. Isolation and identification of endophytic bacteria with plant growth promoting activity and biocontrol potential from wild pistachio trees. *Plant Pathology Journal*, 2018, Vol. 34, No. 3, p. 208-217.

17. Merck. Explant Sterilization – Plant Tissue Culture Protocol. Merck. 2022. [referred on the 25th of January in 2022 y.]. Link to the internet <https://www.sigmaaldrich.com/LT/en/technical-documents/protocol/cell-culture-and-cell-culture-analysis/plant-tissue-culture/explant-sterilization>.

18. TOMASZEWSKA-SOWA, M.; FIGAS, A.; KEUTGEN, N.; KEUTGEN, A. Establishing an efficient explant superficial sterilization protocol for *in vitro* micropropagation of bear's garlic (*Allium ursinum* L.). *Herba Polonica*, 2016, Vol. 61, No. 4, P. 66-77.

19. MILIŪTĖ, I. Obelų ir pušų endofitinės kilmės bakterijų savybės, susijusios su augalų augimo skatinimu bei patogenų biokontrole. Master Thesis, Faculty of Natural Sciences, Department of Biology, Vytautas Magnus University, 2013. 88 p.

20. RATANAPROM, S.; NAKKANONG, K.; NUALSRI, C.; JIWANIT, P.; RONGSAWAT, T.; WORAATHAKORN, N. Overcoming encouragement of dragon fruit plant (*Hylocereus undatus*) against stem brown spot disease caused by *Neoscytalidium dimidiatum* using *Bacillus subtilis* combined with sodium bicarbonate. *The Plant Pathology Journal*, 2021, Vol. 37, No. 3, P. 205–214.

21. AFZAL, I.; SHINWARI Zabta, K.; SIKANDAR, S.; SHAHZAD, S. Plant beneficial endophytic bacteria: mechanisms, diversity, host range and genetic determinants. *Microbiological Research*, 2019, Vol. 221, P. 36-49.

INHIBITION OF *FUSARIUM* SPP. GROWTH BY *SALVIA OFFICINALIS* ESSENTIAL OIL *IN VITRO*

G. Laurinaitytė, L. Dėnė
LAMMC Institute of Horticulture
Kauno st. 30, LT-54333, Babtai, Kaunas distr. – Lithuania
+37037555217
greta.laurinaityte@ktu.edu

EXTENDED ABSTRACT

OVERVIEW

One of the most common group of microorganisms that causes yield-reducing diseases is fungi. The infection with fungal pathogens of the genus *Fusarium* usually results in harvest decay and vast reduction of the quality of various vegetables and fruits [1]. Diseases, caused by *Fusarium avenaceum* and *Fusarium poae*, is common in strawberry fields all over the world, and various parts of the plant can be infected, including fruit, leaves, blossoms, and roots [2]. However, the significant crop loss from these contagious pathogens can be prevented or reduced by various plant protection systems [3]. Despite advances in many technological areas [4], plant protection means mostly contain synthetic chemicals that can be dangerous to animals and humans, as well as damage ground water and soil with unsafe contaminants, thus their usage must be ecologically benign and long-term [5]. Instead of using chemicals, new plant protection products of biological origin are being developed. Speaking about the variety of biological plant protection means, extracts of various plants are receiving a lot of attention these days. The previous studies have pointed out the antimicrobial, antioxidant, and antifungal properties of many aromatic plants' compounds [6]. Due to their environmental and renewable qualities, a variety of essential oils have been discovered to have strong antifungal activity and are gaining favour in the agricultural industry [7]. Essential oils obtained from plants are nonphytotoxic chemicals that might be used as natural pesticides to protect crops [8]. *Salvia officinalis*, also known as sage, is a widespread aromatic plant of *Lamiaceae* family [6]. The biological characteristics of *S. officinalis* essential oil are mostly due to α- and β-thujone, camphor and 1,8-cineole [9]. Therefore, this research aimed to evaluate the inhibition of *Fusarium avenaceum* and *Fusarium poae* growth by sage (*Salvia officinalis* L.) essential oil.

METHODS

F. avenaceum and F. poae pathogens were isolated from infected strawberry plants. Single-spore isolate colonies grown on PDA for seven days, were used for the experiments. Dried sage leaves were used for the extraction of essential oil (EO) using Clevenger apparatus. Potato dextrose agar medium was mixed with essential oil making 800-1400 µL L^{-1} concentrations. Medium with extract was poured in Petri dishes and 7 mm diameter disc of pathogens' colony was placed in the centre. After 2, 4 and 7 days, radial colony growth (cm) of the pathogens was measured. Results were compared with radial colony growth in control Petri dishes, where no essential oil was added.

RESULTS

The results revealed contrasting inhibition of the fungi depending on the amount of oil. The high inhibition using tested EO was observed on *F. avenaceum*, however, *F. poae* was significantly resistant to all examined concentrations of EO. According to the results, after two and four days of inoculation inhibition of *F. avenaceum* growth was not statistically significant compared to control, however, on the 7th day essential oils successfully reduced pathogen growth. Treatment with 1200 µL L^{-1} concentration essential oil had the highest inhibitory effect against *F. avenaceum* since radial colony growth was 0.91 cm lower than in control treatment after 7 days of inoculation. The results of the 7th day measurements are presented in the Figure 1.
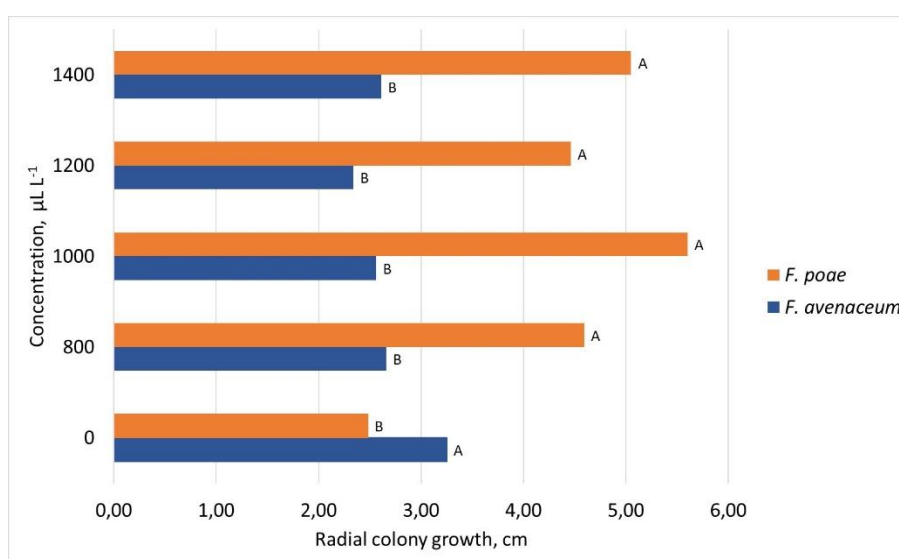
Fig. 16. Radial colony growth of *F. poae* and *F. avenaceum* on the 7th day after inoculation after treatment with *S. officinalis* essential oil under different concentrations

CONCLUSIONS

To conclude, although none of the tested concentrations supressed the growth of *F. poae*, significant antifungal activity against *F. avenaceum* was discovered. The highest inhibition of pathogen growth was achieved with 1200 µL L^{-1} concentration of essential oil, as it reduced the growth of the fungus compared with control treatment the most. Based on the results of this study, application of sage essential oil could be an alternative technique for control of *F. avenaceum*. To determine *S. officinalis* essential oil's efficiency on different fungi, more experiments should be conducted in the future.

Keywords: biocontrol, fungal pathogens, *Fusarium avenaceum*, *Fusarium poae*, sage essential oil.

REFERENCES

1. YANG, J.; HSIANG, T.; BHADAURIA, V.; CHEN, X. L.; LI, G. Plant fungal pathogenesis. *BioMed Research International,* 2017, Vol. 2017.

2. PASTRANA, A. M.; BASALLOTE-UREBA, M. J.; AGUADO, A.; CAPOTE, N. Potential inoculum sources and incidence of strawberry soilborne pathogens in Spain. *Plant Disease,* 2017, Vol. 101, No. 5, P. 751-760.

3. OERKE, E. Crop losses to pests. *The Journal of Agricultural Science,* 2006, Vol. 144, No. 1, P. 31-43.

4. VURRO, M.; MIGUEL-ROJAS, C.; PÉREZ-DE-LUQUE, A. Safe nanotechnologies for increasing the effectiveness of environmentally friendly natural agrochemicals. *Pest Management Science*, 2019, Vol. 75, P. 2403-2412.

5. POGACEAN, M.; GAVRILESCU, M. Plant protection products and their sustainable and environmentally friendly use. *Environmental Engineering and Management Journal*, 2009, Vol. 8, P. 607-627.

6. ALEXA, E.; SUMALAN, R. M.; DANCIU, C.; OBISTIOIU, D.; NEGREA, M.; POIANA, M. A.; RUS, C.; RADULOV, I.; POP, G.; DEHELEAN, C. Synergistic antifungal, allelopatic and anti-proliferative potential of *Salvia officinalis* L., and *Thymus vulgaris* L. essential oils. *Molecules*, 2018, Vol. 23, No. 1, P. 185.

7. ABBEY, J. A.; PERCIVAL, D.; ABBEY, L.; ASIEDU, S. K. PRITHIVIRAJ, B., SCHILDER, A. Biofungicides as alternative to synthetic fungicide control of grey mould (*Botrytis cinerea*) – prospects and challenges. *Biocontrol Science and Technology*, 2018, Vol. 29, P. 207-228.

8. ANTUNES, M. D. C.; CAVACO, A. M. The use of essential oils for postharvest decay control. A review. *Flavour and Fragrance Journal*, 2010, Vol. 25, P. 351-366.

9. RAAL, A.; ORAV, A.; ARAK, E. Composition of the essential oil of *Salvia officinalis* L. from various European countries. *Natural Product Research*, 2007, Vol 21, P. 406-411.

WEED GERMINATION DYNAMICS IN WINTER WHEAT AND WINTER OILSEED RAPE UNDER DIFFERENT TILLAGE

L. Meškauskienė, G. Kadžienė, B. Jomantaitė
Lithuanian Research Centre for Agriculture and Forestry
Institute of Agriculture
Instituto al. 1, Akademija, LT-58344 Kėdainiai distr. – Lithuania
+370 614 25433; +370 686 49431; +370 654 56955
loreta.meskauskiene@lammc.lt, grazina.kadziene@lammc.lt, birute.jomantaite@lammc.lt

EXTENDED ABSTRACT

OVERVIEW

The control of weeds in agriculture has been a significant concern since the beginning of agriculture. Plants compete for the resources they share (light, water, nutrients). However, usually, research only accounts for the competitive effect of the crop up on weeds and rarely for competition between weed species in the field. [1]. Developments in weed management have strongly focused on monitoring of weed germination dynamic. Assumptions about and simplifications of weed biology are necessary for any model of weed population dynamics. That lets us know better about the population of the weeds, which are common in different fields and increasing the efficiency of herbicides or substituting herbicides with other single tactics such as mechanical control [2]. Weed control is essential to reduce crop yield losses. Prevent the spread of weed seeds by reducing their stocks in the soil. Most of the weed seeds entering the soil are matured seeds of annual weeds before crop harvest [3;4]. Extensive research on weed biodiversity, germination dynamics, and seed bank changes using different intensities of tillage, catch crops would allow us to assess the potential for integrated weed control, not only in traditional but also in sustainable tillage practices. Regarding changes in the composition of the weed community using one or the other conservation agriculture principle, the results vary depending on the system. However, there is a strong tendency to filter perennials (the organs of perennial weeds are not damaged) [5].

Integrated weed control has been poorly implemented, with little evidence of a concomitant reduction in herbicides. Others research on this topic has focused on how crop yields and weeds are affected by different factors such as tillage, herbicide application times and rates, catch crops, and sowing patterns [6].

Traditional weed control measures must move from a single tactic and growing season to integrated weed management. It will make farming systems more sustainable in practice. Consider more than one harvest season and focus on managing weed communities instead of individual species control. The effects on weed abundance seemed different for each of these two principles: reducing tillage tends to increase weed abundance while crop diversification tends to decrease it [7;8]. Soil tillage is widely known as the main factor explaining the community's high percentage of annual species [9]. By frequently disturbing the soil surface, soil tillage filters mainly plant able to survive unfavourable perturbations in the form of seeds or, to a lesser extent, underground organs capable of vegetative propagation (e.g., rhizomes)

[10]. Weed seeds buried by soil tillage remain dormant before being brought back to the soil surface by the following soil tillage [11;12]. Due to the absence of soil disturbance when adopting conservation agriculture, seeds remain concentrated on the soil surface, and annual species are partly replaced by perennials [9].

Should the ongoing controversy regarding the effects of glyphosate on human health and the environment lead to a ban on glyphosate, the options available to farmers for control of perennial weeds will be severely restricted [13]. If the European Commission bans glyphosate, the chemical farms will have to reorient and use more sustainable agricultural methods (growing cover crops, applying crop rotation), reducing weeds, and improving degraded soil quality. The main target of our study is to adapt growing technologies without broad-spectrum herbicides, such as glyphosates.

METHODS

The field experiment was started in the Institute of Agriculture, Akademija, Kėdainiai district in 2021. The research aim is to evaluate proper integrated weed management in sustainable tillage for winter wheat (W) and winter oilseed rape (R) growing technologies. The previous crop for W was field pea (P) and for R – spring barley (B). The experiment was established at split-plot design in 4 replications.

Table 1. Experimental design

Factor A – tillage	
C	Conventional ploughing (20-22 cm).
H	Harrowing (8-10 cm).
N	No tillage – direct drilling.
Factor B: weed control technologies	
T	Traditional (intensive herbicides usage, including glyphosate application before or after drilling, before emergence of crop).
WTP	winter **W**heat, **T**raditional weed control (including glyphosate application before drilling), after field **P**ea.
RTM	winter oilseed **R**ape, **T**raditional weed control (including glyphosate application after drilling before emergence of crop), after spring **B**arley.
I	Integrated (cover crops, herbicides usage on-demand, excluding glyphosate).
WIP	winter **W**heat, **I**ntegrated weed control (white mustard was drilled after field pea harvest), after field **P**ea
RIB	winter oilseed **R**ape, **I**ntegrated weed control (field beans drilled between the rows in oilseed rape), after spring **B**arley.

In traditional weed control technology, glyphosate was applied after oilseed rape drilling before germination and before winter wheat drilling. Subsequently, when the barley volunteers germinated, graminicides were sprayed in all treatments. No other herbicides were applied on oilseed rape in the autumn. The herbicide the broad-leaved weed control will be selected according to weed spectrum and used in spring of 2022.

Assessment of weed and crop germination were carried out five times: first counting was done after germination and weekly after that. Determination of the species composition of weeds and crop: density (number), growth stages of development in winter wheat and winter oilseed rape.

The assessments were performed at four fixed quadrates in each plot using 50 x 50 cm (0.25 m^2) metal frames. Averages were calculated for each plot and used in the calculation of mean and the standard error.

RESULTS

Winter wheat and winter oilseed rape are the most common in the farmers' fields. For that reason, it is essential to find the best way to adapt integrated weed management into farms and get more benefits. Observations of weed germination dynamics have shown that annual broadleaves weeds predominate in the crop.

During the monitoring and calculation of weed germination in winter wheat after pea, it was observed that in the first year of the integrated technology, the number of weeds was higher than with the traditional cultivation technology (Fig.1). There was lower weed density in no-till compared with conventional tillage. Higher weed density in conventional tillage might occur due to better tilth and exposure of weed seeds to the upper soil layers.

Observing the germination of weeds weekly, showed that the number of weeds increased in all plots until the moment when the oilseed rape started to overgrow them, thus creating interspecies competition (Fig.2).
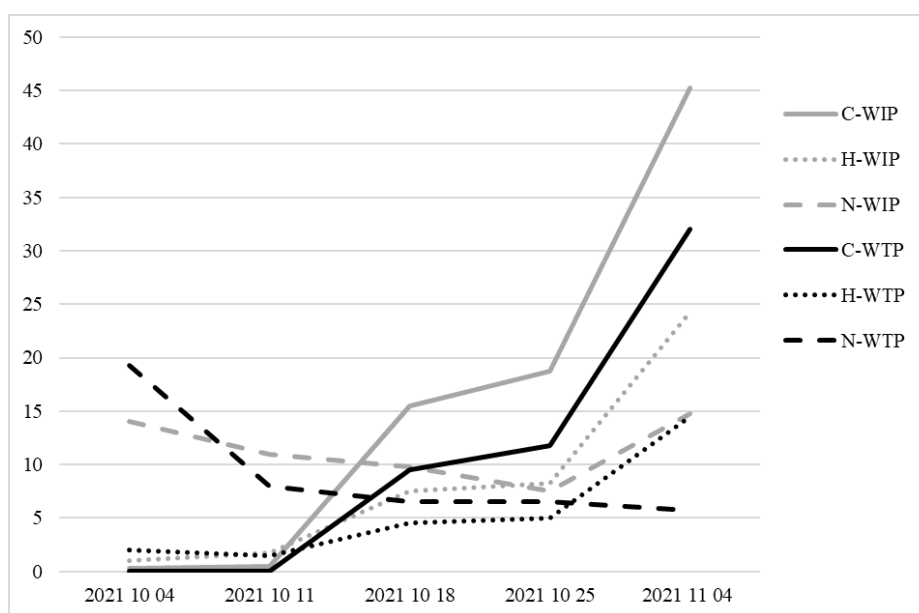
Fig. 1. Weed germination dynamics in winter wheat after peas

(C- Conventional ploughing; H – Harrowing; N – No-tillage. WIP – winter wheat, integrated, after peas; WTP – winter wheat, traditional, after peas)
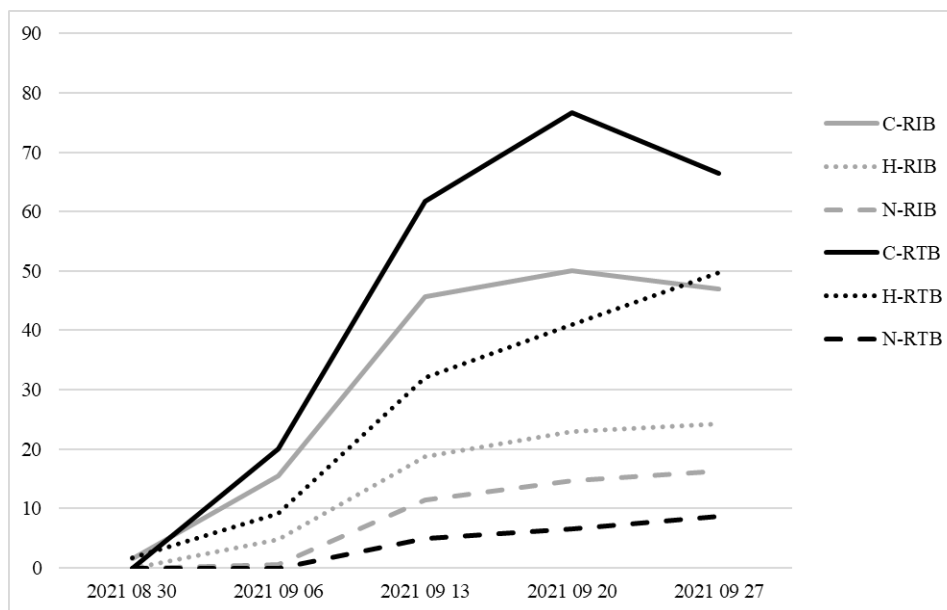
Fig. 2. Weed germination dynamics in winter oilseed rape after spring
barley

(C- Conventional ploughing; H – Harrowing; N – No-tillage. RIB – winter oilseed rape, integrated, after spring
barley. RTB – winter oilseed rape, traditional, after spring barley)

CONCLUSIONS

Weed germination depended on the chosen soil tillage; growing was more intense in
conventional than in sustainable or no tillage.

Monitoring the weed growth dynamics is expected to help select the right time to apply
herbicides, select the right products, and justify the principles of integrated weed control.

Keywords: (Weed dynamics, sustainable tillage, integrated weed management)

REFERENCES

1. HOLST, N.; RASMUSSEN, I. A.; BASTIAANS L. Field weed population dynamics: a
    review of model approaches and applications. *Weed research*, 2007, Vol. 47, Issue 1, P. 1-
    14.

2. RIEMENS, M.; SØNDERSKOV, M.; MOONEN, A.C.; STORKEY, J.; KUDSK, P. An
    Integrated Weed Management framework: A pan-European perspective. *European Journal
    of Agronomy*, 2022, Vol. 133, P.126-443.

3. KADŽYS, A. AUŠKALNIENĖ, O.; AUŠKALNIS, A. The influence of weed control on
    weed seed rain in spring barley and spring wheat crops. *Zemdirbyste-Agriculture*, 2008,
    Vol. 95, No.3, P. 94–102.

4. PILIPAVIČIUS, V. Weed seed rain dynamics and ecological control ability in
    agrophytocenosis. *Herbicides – advances in research*, 2013, P. 51–83.

5. SCHUSTERA Mauricio, Z.; GASTALB, F.; DOISYC, D.; CHARRIERB X.; MORAESA,
    A.; MÉDIÈNEC, S.; BARBUC Corentin, M. Weed regulation by crop and grassland

competition: critical biomass level and persistence rate. *European Journal of Agronomy*, 2022, Vol. 133, P. 125-963.

6. SCHÜTTE, G.; ECKERSTORFER, M.; RASTELLI, V.; REICHENBECHER, W.; RESTREPO-VASSALLI, S.; RUOHONEN-LEHTO, M.; WUEST, S. A. G.; MERTENS, M. Herbicide resistance, and biodiversity: agronomic and environmental aspects of genetically modified herbicide-resistant plants. *Environmental Sciences Europe*, 2017, Vol. 29, No. 5.

7. ARLAUSKIENĖ, A.; JABLONSKYTĖ-RAŠČĖ, D.; ŠARŪNAITĖ, L.; TOLEIKIENĖ, M.; MASILIONYTĖ, L.; GECAITĖ, V.; KADŽIULIENĖ, Ž. Perennial forage legume cultivation and their above-ground mass management methods for weed suppression in arable organic cropping systems. *Chemical and Biological Technologies in Agriculture*, 2021, Vol. 8, P. 34.

8. KADZIENE, G.; SUPRONIENE, S.; AUSKALNIENE, O.; PRANAITIENE, S.; SVEGZDA, P.; VERSULIENE, A.; CESEVICIENE, J.; JANUSAUSKAITE, D.; FEIZA, V. Tillage and cover crop influence on weed pressure and *Fusarium* infection in spring cereals. *Crop protection,* 2020 Vol. 127.

9. DERROUCH, D.; DESSAINT, F.; FRIED, G.; CHAUVEL, B. Weed community diversity in conservation agriculture: post-adoption changes. *Agriculture, Ecosystems & Environment*, 2021 Vol. 312, P. 107-351.

10. BAJW, A.; Ahsan, A. Sustainable weed management in conservation agriculture. *Crop Protection*, 2014 Vol. 65, P. 105-113

11. AUŠKALNIENĖ, O.; KADŽIENĖ, G.; JANUŠAUSKAITĖ, D.; SUPRONIENĖ, S. Changes in seed bank and weed flora as affected by different soil tillage systems. *Zemdirbyste-Agriculture*, 2018, Vol. 105, No.3, P. 221–226.

12. FARMER, J. A.; BRADLEY, K. W.; YOUNG, B. G.; STECKEL, L. E.; JOHNSON, W. G.; NORSWORTHY, J. K.; DAVIS, V. M.; LOUX, M. M. Influence of tillage method on management of *Amaranthus* Species in Soybean. *Weed Technology*, 2017. Vol. 31, P. 10–20.

13. KUDSK, P.; MATHIASSEN, S. K. Pesticide regulation in the European Union and the glyphosate controversy. *Weed Science*, 2020, Vol. 68, P. 214 - 222

ENVIRONMENTAL RISKS CAUSED BY LONG-TERM FUNGICIDE USE IN APPLE ORCHARDS

R. Rancāne, A. Valiuškaitė
Lithuanian Agriculture and Forestry Sciences Center, Institute of Horticulture
Kauno st. 30, LT-54333 Babtai – Lithuania
+371 26361918
regina.rancane@lammc.lt

V. Zagorska
Institute for Plant Protection Research "Agrihorts"
Paula Lejina st. 2, LV-3004 Jelgava – Latvia
+371 29740492
viktorija.zagorska@llu.lv

EXTENDED ABSTRACT

OVERVIEW

In apple orchards, the use of pesticides is relatively high for numerous pests and diseases control [5]. The highest consumption of pesticides is required to control apple scab, caused by *Venturia inaequalis* (Cooke) G. Winter 1875, which is the most important apple disease, causing economic losses in many apple production areas, including the Baltic region [6, 7]. Fungicides are sprayed most intensively during the primary infection period from the start of bud break (BBCH 53), which is usually set in April until the end of June, when most of the overwintered leaves are decomposed. Apple scab is one of the diseases that need to be controlled preventively, and fungicides are used to protect healthy leaves from becoming infected. For detection of infection risks, the decision support system RIMpro (RIMpro B.V., Zoelmond, Netherlands) has been used in Latvia since 2003 [4]. According to RIMpro, protective fungicide applications are recommended to control apple scab. In integrated pest management (IPM) 6–12 fungicide sprays are commonly applied against apple scab each season. Up to 85% of applications are done by protective fungicides, mainly using products containing active substances dithianon, captan, mancozeb, and copper (II) hydroxide. Higher doses than curative fungicides usually characterize protective products. Considering that public concern about the possible side effects of pesticides on health and the environment has been increasing over the past decade, there is a need to evaluate the risks of using different substances. One way to reduce the number of protective sprays would be using systemic fungicides when there is an increased infection risk [3]. However, its outdated and no longer recommended due to resistance developed by the pathogen to individual single-site fungicide groups. The most commonly used groups are anilinopyrimidines (cyprodinil) and demethylation inhibitors (difenoconazole). Relatively less commonly used are guanidines (dodine), and quinone outside inhibitors (kresoxim-methy). Recent observations show a reduction of fungicide efficacy therefore it was suspected that in some orchards *V. inaequalis* had developed fungicide resistance. Our study aimed: (i) to assess which substances have been used more intensively so far and to determine pesticide risk indicators, and (ii) to analyse the use of curative fungicides

causing resistance risk. Collection and analysis of fungicide use data is a valuable tool to the farmer that could support IPM implementation, avoiding the use of more harmful substances and avoiding resistance risk.

METHODS

The 10-year spray data were collected from six orchards to assess potential risks from fungicide use. For environmental risk assessment, a pesticide risk indicator was used, the pesticide load (PL), which was recently introduced in Denmark [2]. The PL consists of three sub-indicators for human health (PL_{HH}), ecotoxicology (PL_{ECO}), and environmental fate (PL_{FATE}), respectively. A pesticide load (PL) was calculated and expressed as the PL per unit of the active substance (kg or L) for each sub-indicator. In addition, 12 samples of apple scab were collected in 2020 and 2021 to determine whether fungicide resistance had developed against difenoconazole and cyprodinil in the apple orchards and the sensitivity of the fungus was evaluated on the population level.

RESULTS

Fungicide use data reported by the farmers from 10 growing seasons showed a marked variation between farms and years, but it is visible that protective fungicides are the most important group overall, followed by systemic fungicides. More widely used protective substances in the analyzed period were mancozeb, copper (II) hydroxide, and captan. These three active substances also formed the highest total pesticide load. The highest load by environmental fate sub-indicator was for the copper (II) hydroxide, and the highest load by the human health was for the captan. However, the evaluation methodology must be revised considering that mancozeb has been identified as an endocrine disruptor without adding the hazard statement [1]. Reducing the number of registered active substances will increase the consumption of the remaining active substances. Resistance tests showed reduced sensitivity of the pathogen to difenoconazole and cyprodinil. Sensitivity of the apple scab population to cyprodinil was reduced and showed a strong correlation with the intensity of use of anilinopyrimidines.

CONCLUSIONS

Protective substances form the highest total pesticide load. Reducing the range of protective products available to farmers, the use of curative products may increase thus increasing incidence of fungicide resistance. The solution would be to use more plant protection products, which are allowed in organic growing, but also safety of them should be further assessed.

Keywords: *Venturia inaequalis*, pesticide load, pesticide risk indicator, resistance risk, RIMpro

REFERENCES

1. COMMISSION IMPLEMENTING REGULATION (EU) 2020/2087 of 14 December 2020, [referred on the 24th of January in 2022 y.]. Link to the internet <https://eur-lex.europa.eu/legal-content/EN/TXT/?uri=CELEX:32020R2087>.

2. KUDSK, P.; JØRGENSEN, L. N.; ØRUM, J. E. Pesticide Load—A new Danish pesticide risk indicator with multiple applications. *Land Use Policy*, 2018, Vol. 70, P. 384–393.

3. KUNZ, S.; HINZE, M.; MÖGEL, G.; VOLK, F. Control of apple scab by curative applications of biocontrol agents. 13th International Conference on Cultivation Technique

and Phytopathological Problems in Organic Fruit-Growing. Proceedings of the Conference. Germany: Ecofruit, 2008.

4. RANCANE, R.; EIHE, M.; JANKOVSKA, L. Adaption of simulation model RIMpro for primary apple scab control in Latvia. *Acta Horticulturae*, 2008. Vol. 803, p. 214-218.

5. SIMON, S.; BRUN, L.; GUINAUDEAU, J.; SAUPHANOR, B. Pesticide use in current and innovative apple orchard systems. *Agronomy for Sustainable Development*, 2011. Vol. 31, No. 3, P. 541-555.

6. TIIRMAA, K.; UNIVER, T.; UNIVER, N. The evaluation of scab resistant apple cultivars in Estonia. *Agronomy Research*, 2006. Vol. 4, P. 413-416.

7. VALIUŠKAITĖ, A.; USELIS, N.; KVIKLYS, D.; LANAUSKAS, J.; RASIUKEVIČIŪTĖ, N. The effect of sustainable plant protection and apple tree management on fruit quality and yield. *Zemdirbyste-Agriculture*, 2017. Vol. 104, No. 4, P. 353-358.

THE SOWING TIME AND CULTIVAR EFFECT ON OCCURRENCE OF DISEASES AND OVERWINTERING IN WINTER WHEAT

A. Sabeckis, R. Semaškienė
Lithuanian Research Centre for Agriculture and Forestry
Instituto al. 1, LT-58344 Akademija, Kedainiai distr. – Lithuania
+370 6 5864657
aurimas.sabeckis@lammc.lt

EXTENDED ABSTRACT

OVERVIEW

Winter wheat is one of the most important and widely grown cereal crop in Lithuania. According to official data, last year winter wheat area accounted for more than a half of all grown cereals nationally. As climate changes in our region, warm autumn not only prolongs winter wheat vegetation but also induces opportunities for crop pests and pathogens to thrive. Rise in the annual mean of temperature by approximately 2 °C was recorded in northern Lithuania throughout 1961-2015 period with a distinguishable mid-winter warming. Furthermore, projected future scenarios suggests that temperature of September and November will increase, thus delaying the dormancy start of winter wheat [1].

Fusarium spp. and other seed-borne pathogens can negatively affect seed germination and considerably reduce plant viability in early growth stages [2]. According to Jonavičiene's research (2017) root damages in winter wheat is caused by *Fusarium* species *graminearum* and *avenaceum Microdochium* spp. *nivale* and *majus* pathogens [3]. *Microdochium* pathogens proliferate in tissues of winter cereals and in favourable conditions cause snow mould.

Bankina et al. [4] observed strong connection between early sowing and snow mould incidence. More developed cereal crops are more susceptible to this disease [5] and it results in winter damage, that can significantly affect yield variability [6]. The possible solutions to avoid winter damage would be late sowing, the usage of pathogen-resistant cultivars and fungicide treatments [7]. Aim of this study was to evaluate sowing time and cultivar influence on winter wheat overwintering in the context of weather conditions from autumn until early spring.

METHODS

Winter wheat field experiment were carried out in Lithuania in 2020–2021. Untreated seeds of four cultivars: 'Ada', 'KWS Emil', 'Etana' and 'Skagen' were sown at optimal sowing time (18th of September) and late sowing time (8th of October). Field germination at the end of emergence was evaluated by counting number of seedlings on five marked 2 m length rows diagonally across each 15 m^2 plot. Second count of surviving plants in same rows was carried out in spring. Infection levels of seedling blight (scale 0–3) and foliar diseases (% of damaged area) assessed in late autumn and early spring by 30 randomly picked seedlings from each plot.

RESULTS

Snow cover formed on unfrozen ground and temperatures fluctuated around 0 °C for more than a month during winter 2020-2021. Such conditions were ideal for high occurrence of snow mould. Snow mould severity percentage ranged from 12.4 to 55.1% and from 8.4 to 17.0% in optimal and late sowing timings respectively. At optimal time sown cv. 'Etana' was significantly more damaged compared to other cultivars while all late sown cultivars showed similar susceptibility to snow mould. At high infection level cv. 'Skagen' showed lower susceptibility to diseases in this trial.

The amount of surviving plants numbers at the end of wheat wintering implies that for the most of grown cultivars (except 'Skagen') late sowing time had positive effect on wheat wintering. Overall overwintering percentage ranged from 88.5 to 73.7 (optimal sowing time) and from 91.6 to 59.9 in late seeding. Data suggested that cv. 'Ada' had the highest percentage of survived plants in both optimal and late sown plots. 'KWS Emil' had slightly lower surviving plant numbers compared to other cultivars of optimal sowing time. Most plants were lost in late sown plots of cv. 'Skagen'. Probably that high infestation of seedling blight in this variety affected surviving of crop during winter.

The damage of root rot on plants varied from 7.8 to 20.8 percent in plots of optimal sowing time and from 9.2 to 19.2 % in late sown plots. The data suggested that sowing time did not have influence on root rot severity for each cultivar, but differences between cultivars recorded. Seedlings of cv. 'Skagen' were significantly more damaged by seedling blight at both sowing times compared to other cultivars.

CONCLUSIONS

In summary, one-year results showed that later sown winter wheat is less susceptible to snow mould thus increasing percentage of overwintered plants. No sowing time influence of severity of seedling blight was established. Cv. 'Skagen' was significantly more damaged by seedling blight and late sown plots had the most plant lost during winter.

Keywords: Overwintering, snow mould, winter wheat.

REFERENCES

1. JUKNYS, R.; VELIČKA, R.; KANAPICKAS, A.; KRIAUCIUNIENE, Z.; MASILIONYTĖ, L.; VAGUSEVIČIENĖ, I.; PUPALIENĖ, R.; KLEPECKAS, M.; SUJETOVIENE, G. Projecting the impact of climate change on phenology of winter wheat in northern Lithuania. *International Journal of Biometeorology,* 2017, Vol. 61, P. 1-11.

2. SHAHIDUL, I., S.; SARKER, N., I.; ALI, A. Effect of seed-borne fungi on germinating wheat seed and their treatment with chemicals. *International Journal of Natural and Social Sciences.* 2015. Vol. *2,* P. 28-32.

3. JONAVIČIENĖ, A. Daigų pašaknio puvinių (Fusarium spp., Microdochium spp.) ir pavasarinio pelėsio (Microdochium spp.) sukelėjai, išplitimas ir žala migliniuose javuose. *Daktaro disertacija,* 2017, P. 69-81.

4. BANKINA, B.; RUZA, A.; KATAMADZE, M.; KREITA, D.; PAURA, L. Snow Mould Development under Conditions of Central Part of Latvia. *Rural Sustainability Research,* 2012, Vol.27, No.1, P. 1-5.

5. PONOMAREVA, M., L.; GORSHKOV, V. L.; PONOMAREV, S., N.; KORZUN, V.; MIEDANER, T. Snow mold of winter cereals: a complex disease and a challenge for resistance breeding. *Theoretical and Applied Genetics,* 2021, Vol. 134, P. 419-433.

6. PELTONEN-SAINIO, P.; HAKALA, K.; JAUHIAINEN, L. Climate-induced overwintering challenges for wheat and rye in northern agriculture. *Acta Agriculturae Scandinavica, Section B, Soil and Plant Sciences*, 2011, Vol. 61, P.75-83.

7. SERENIUS, M.; HUUSELA-VEISTOLA, E.; AVIKAINEN, H.; PAHKALA, K.; LAINE, A. Effects of sowing time on pink snow mold, leaf rust and winter damage in winter rye varieties in Finland. *Agricultural and Food Science*, 2005, Vol. 14, P. 362-376.

EVALUATION OF *ZYMOSEPTORIA TRITICI* POPULATION AGGRESSIVENESS IN LITHUANIA

K. Verikaitė
Lithuanian Research Centre for Agriculture and Forestry
Instituto al. 1, LT-58344 Akademija, Kedainiai distr. – Lithuania
+370 6 4771662
karolina.verikaite@lammc.lt

EXTENDED ABSTRACT

OVERVIEW

Plant pathogenic fungi *Zymoseptoria tritici* is one of the most common wheat pathogens in Lithuania which causes the disease Septoria tritici blotch (STB) on wheat leaves. Pathogenicity is pathogen's ability to infect plant tissue and not only cause damage to the host but also spread the disease further. Virulence and aggressiveness are considered components of pathogenicity. Virulence is defined as the pathogen's ability to infect the host and aggressiveness – as the amount of damage the pathogen causes to the host [1]. There are several components of aggressiveness. Suffert et. al. [2] distinguished these in particular: incubation and latent periods, disease intensity and sporulation. It is known that disease intensity may fluctuate not only due to climatic situation over years but also due to differences in *Z. tritici* populations locally [3]. Therefore, *Z. tritici* was tested to determine possible differences between aggressiveness components of this pathogen populations in Lithuania.

METHODS

Leaf samples with STB lesions originating from different locations of Lithuania were collected in 2019 and 2020. Each year twenty isolates representing different locations were isolated from leaves. Two winter wheat cultivars ('Arkadia' as more susceptible and 'Kena DS' as less susceptible) were used for inoculation in a greenhouse each year. Inoculation was performed on a labelled area (2 cm) of the second leaf of 21-day-old seedlings. To determine pathogen virulence these parameters were assessed: incubation and latent periods, STB infection intensity, sporulation [2]. To evaluate the incubation period, the interval between inoculation and occurrence of first symptoms was assessed, latent period – interval between inoculation and occurrence of pycnidia. To evaluate disease intensity inoculated leaves were assessed visually 24 days post inoculation (dpi). To assess sporulation all pycnidia were counted on labelled leaf area (2cm).

RESULTS

The incubation period of different isolates varied between 10-18 dpi and 6-10 dpi in 2019 and 2020 respectively. In 2019 the incubation period for the majority of isolates in both cultivars was 14 days and in 2020 it was 8 days. Although the incubation period differed greatly between the years, the latent period was similar — 16-24 dpi in 2019 and 14-24 dpi in 2020. Cultivars did not influence incubation and latent periods length despite their different susceptibility to the pathogen.

Disease intensity 24 days post inoculation in 2019 ranged from 10.3 to 100% on cv. 'Arkadia' and from 4 to 100 % on cv. 'Kena DS'. The isolate from Pasvalys district had the lowest intensity on both cultivars. The disease intensity of isolates from Kėdainiai, Raseiniai and Pakruojis districts(central and north Lithuania) reached 100 % on both cultivars. In 2020 disease intensity 24 dpi varied between 25-100 and 31.3-100 % on cv. 'Arkadia' and 'Kena DS' respectively. The lowest disease intensity was recorded with an isolate from Trakai district(southeast Lithuania) on both cultivars. Whereas the highest intensity was from isolates coming from Radviliškis and Kelmė districts on cv. 'Kena DS' and Radviliškis, Kėdainiai and Šiauliai districts(central and north Lithuania) on cv. 'Arkadia'.

All field isolates produced pycnidia on both cultivars. The count of pycnidia ranged from 3 to 292 and from 11 to 257 in 2019 and 2020, respectively. In both years, lower sporulation was observed on the cultivar 'Kena DS'. The mean count of pycnidia on this cultivar was 40.1 in 2019 and 47.7 in 2020. Meanwhile, on the cultivar 'Arkadia', the sporulation was more than two times higher - the mean count of pycnidia was 132.8 in 2019 and 115.6 in 2020. Although the tendencies of total pycnidia count of isolates were similar on both cultivars, in 2019, two isolates had contradictory values on different cultivars. While on cv. 'Arkadia' isolate from Pasvalys(north Lithuania) district had high pycnidia count (140), on cv. 'Kena DS' was low (3). And the opposite outcome was of the isolate coming from Vilnius district(southeast Lithuania) on cv. 'Kena DS' the count of pycnidia was 143 whilst on cv. 'Arkadia' was 24. Morais et al. [4] established that isolates of Z. tritici are more adapted to induce disease on the cultivar from which they were isolated. Although the original cultivars of our isolates are unknown, our gathered data might coincide with findings of other researchers.

Taken trait by trait, the isolates from 2019 had different aggressiveness depending on cultivars. While on cultivar 'Kena DS' isolate from Pasvalys district(north Lithuania) had low disease intensity and sporulation, on cultivar 'Arkadia' had moderate sporulation. Meanwhile, in 2020 the isolate from Trakai district(southeast Lithuania) could be considered as the least aggressive amongst all isolates. This isolate on both cultivars had a long latent period (24 dpi), low disease intensity and lowest count of pycnidia. From correlation analysis, it was found that sporulation is affected both by incubation and latent periods' length. Correlations between sporulation and incubation or latent periods showed a negative relationship between these indicators.

CONCLUSIONS

In summary, the two-year research showed a tendency of isolates coming from central and north regions of Lithuania to induce higher disease intensity and sporulation. Results of this study showed that the longer incubation and latent periods, the lower sporulation.

Keywords: *Zymoseptori tritici*, aggressiveness, winter wheat

REFERENCES

1. PARIAUD, B.; RAVIGNÉ, V.; HALKETT, F.; GOYEAU, H.; CARLIER, J.; LANNOU, C. Aggressiveness and its role in the adaptation of fungal plant pathogens. *Plant Pathology*, 2009, Vol. 58, P. 409-424.

2. SUFFERT, F.; SACHE, I.; LANNOU, C. Assessment of quantitative traits of aggressiveness in *Mycosphaerella graminicola* on adult wheat plants. *Plant Pathology*, 2013, Vol. 62, P. 1330–1341.

3. VAGNDORF, N.; JUSTESEN, A.; ANDERSEN, J.; JAHOOR, A.; SINDBERG, S.; JØRGENSEN, L. Resistance stability to Septoria tritici blotch and comparison of screening methods for ranking STB disease. *Journal of Plant Diseases and Protection*, 2019, Vol. 126, P. 191–201.

4. MORAIS, D.; LAVAL, V.; SACHE, I.; SUFFERT, F. Inferring the origin of primary inoculum of *Zymoseptoria tritici* from differential adaptation of resident and immigrant populations to wheat cultivars. *European Journal of Plant Pathology*, 2016, Vol. 145, P. 393–404.

PUCCINIA STRIIFORMIS F.SP. *TRITICI* RACES DETECTED AMONG LATVIAN ISOLATES COLLECTED IN 2020–2021

L. Zemeca
Latvia University of Life Sciences and Technologies
Institute of Plant Protection Research "Agrihorts"
Paula Lejina 2, LV-3004 Jelgava – Latvia
Faculty of Agriculture
Liela iela 2, LV-3001 Jelgava – Latvia
+371 25920888
liga.zemeca@llu.lv

B. Bankina
Latvia University of Life Sciences and Technologies
Faculty of Agriculture
Liela iela 2, LV-3001 Jelgava – Latvia
+371 26391893
biruta.bankina@llu.lv

I. Morocko-Bicevska
Latvia University of Life Sciences and Technologies
Institute of Plant Protection Research "Agrihorts"
Paula Lejina 2, LV-3004 Jelgava – Latvia
Institute of Horticulture
Graudu iela 1, LV-3701, Cerini, Dobeles novads – Latvia
+371 29866256
inga.morocko@llu.lv

EXTENDED ABSTRACT

OVERVIEW

Yellow rust (caused by *Puccinia striiformis* f.sp. *tritici*) has been considered as one of the main wheat diseases in cereal growing regions [1]. In susceptible varieties, yield losses can reach 100% [2] if fungicides are not applied. In recent years new, aggressive races of *P. striiformis* f.sp. *tritici* have been identified in Europe [3]. In total, eleven isolates of *P. striiformis* f.sp. *tritici* were collected in Latvia and multiplied. The race identification was made based on an isolate infection type assessed at seedling stage on wheat differential set with diverse known resistance genes. According to assessment data, two isolates were identified as genetic lineage PstS7 (race Warrior), five as PstS10 (race Warrior ⁻), while four isolates caused symptoms that did not correspond to any prevalent genetic lineages of the pathogen in Europe.

METHODS

Eleven samples of uredospores of *P. striiformis* f.sp. *tritici* were collected in the North-Western part of Latvia during two vegetation seasons. Spore multiplying, wheat inoculation, and disease assessments were made according to [4]. Multiplication of uredospores was performed in a greenhouse of Plant Protection Research Centre "Agrihorts" of the Latvia University of Life Sciences and Technologies. A differential set of twenty wheat genotypes ('Ambition', 'Avocet Yr6', 'Avocet Yr8', 'Avocet Yr9', 'Avocet Yr17', 'Avocet S', 'Avocet YrSp', 'Carstens V', 'Cartago', 'Chinese 166', 'Cortez', 'Heines Kolben', 'Hybrid 46', 'Kalyansona', 'Lee', 'Moro', 'Opata', 'TP 981', 'Vilmorin 23' and 'VPM1') was used for phenotyping. At the two-leaf stage, plants were inoculated with uredospores of *P. striiformis* f.sp. *tritici* and placed in a growth chamber in the dark, at 10 ºC with a high humidity level (> 70%), for sixteen hours. On the next day, plants were moved to the greenhouse with the following growth conditions: humidity 70%, and a sixteen-hour daylight period with 17 ºC and 12 ºC during the night period. After three weeks, assessments were done following the internationally used disease scoring scale [4]: 0 - the incompatible reaction with no symptoms; 1-2 - chlorotic and necrotic flecks; 3-4 - chlorosis and necrosis with limited sporulation; 5-6 - chlorosis and necrosis with moderate sporulation; 7 - abundant sporulation with chlorosis; 8-9 - abundant sporulation with dense chlorosis and necrosis (score 7-9 was considered as compatible reaction).

RESULTS

Compatible or incompatible reactions between *P. striiformis* f.sp. *tritici* isolates and wheat differentials were analysed, and virulence phenotyping was performed. Observed infection type and information about resistance genes of each wheat genotype and known virulence genes of most common races in Europe allowed defining the race for most of the studied isolates.

One isolate in 2020 and one in 2021, was identified as Warrior race belonging to PstS7 genetic lineage. Three isolates in 2020 and two isolates in 2021 corresponded to Warrior(–) race (PstS10 genetic lineage) (Table 1). Both genetic lineages have been common in Europe since 2011 [5]. Two isolates in 2020 and two isolates in 2021 showed virulence phenotype on wheat seedlings different from those known of main genetic lineages in Europe. Detailed research on race typing, including these isolates, are necessary.

Table 1. Genetic lineages of *P. striiformis* f.sp. *tritici* identified in Latvia in 2020-2021.

Place of collection	Genetic lineage	Race	Virulence phenotype	Number of isolates	
				2020	2021
Talsu novads, Latvia; Dizstende, Latvia	PstS7	Warrior	1,2,3,4,-,6,7,-,9,-,-,17,-,25,-,32,Sp,AvS,Amb	1	1
Dizstende, Latvia	PstS10	Warrior(–)	1,2,3,4,-,6,7,-,9,-,-,17,-,25,-,32,Sp,AvS	3	2

CONCLUSIONS

Aggressive races of *P. striiformis* belonging to the PstS7 and PstS10 genetic lineages were found in Latvia in 2020-2021. Identified races are destructive and able to cause epidemics on wheat fields. Considering genetic variability, identification of the races of *P. striiformis* f.sp. *tritici* should be done every year and research should be continued.

Keywords: *P. striiformis*, genetic lineages, phenotyping

REFERENCES

1. CHEN, X.; KANG, Z. *Stripe rust.* The Netherlands: Springer Nature, 2017, P. 719. ISBN 978-94-024-1109-6.

2. HOVMØLLER, M.S.; WALTER, S.; BAYLES, R.A.; HUBBARD, A.; FLATH, K.; SOMMERFELDT, N.; DE VALLAVIEILLE-POPE, C. Replacement of the European wheat yellow rust population by new races from the centre of diversity in the near-Himalayan region. *Plant Pathology*, 2016, Vol. 65, No. 3, P. 402-411.

3. HOVMØLLER, M.S.; SØRENSEN, C.K.; WALTER, S.; JUSTESEN, A.F. Diversity of *Puccinia striiformis* on cereals and grasses. *Annual Review of Phytopathology*, 2011, Vol. 49, No. 1, P. 197–217.

4. HOVMØLLER, M.S.; RODRIGUEZ-ALGABA, J.; THACH, T.; SØRENSEN, C. K. Race typing of *Puccinia striiformis* on wheat. *Wheat Rust Diseases*, 2017, Vol. 1659, P. 29–40.

5. RODRIGUEZ-ALGABA, S.; THACH, J.; SØRENSEN, T.; HANSEN, C. K.; LASSEN, J. G.; HOVMØLLER, M.S. Yellow rust epidemics worldwide were caused by pathogen races from divergent genetic lineages. *Frontiers in Plant Science.*, 2017, Vol. 8, P. 1557.

III.4. Food sciences and technologies

ELECTRICAL CONDUCTIVITY PROPERTIES DURING HEATING OF OAT MILK WITH OHMIC HEATING SYSTEM

A. Goksu
Munzur University
Aktuluk, 62000, Tunceli – Turkey
+905078903502
aligoksu58@hotmail.com

E. Karakavuk
Munzur University
Aktuluk, 62000, Tunceli – Turkey
+905542906996
ekarakavuk@hotmail.com

S. Sabanci
Munzur University
Aktuluk, 62000, Tunceli – Turkey
+905448844321
serdalsabanci@hotmail.com

ABSTRACT

Depending on the developing technological situations, the tendency of people to use alternative products of plant-based milk is increasing. In the present study, it was aimed to heat oat milk from 10 to 90 °C in 5 different voltage gradients and to examine the change of electrical conductivity value during the process. It has been found that the heating time with the ohmic system varies between 78 and 336 s. In addition, it has been determined that the time to reach the target temperature shortens as the voltage gradient increases in the heating process with this system. When the electrical conductivity value was examined, the electrical conductivity value increased due to the molecular mobility in the product as the temperature increased. Also, it was determined that the relationship between temperature and electrical conductivity was linearIt has been determined that oat milk can be heated using the ohmic heating system. It is expected that the use of current methods in such products will make a serious contribution to the literature.

INTRODUCTION

Ohmic heating, which is called by different names such as joule heating and electrical resistance heating, is based on the principle of heating the product between two electrodes. The alternating current passing through the product creates heat generation in the product and heats the product [1]. In addition, ohmic heating process is defined as homogeneous, fast, and efficient heating. Ohmic heating process is studied by researchers in areas such as heating [2], evaporation [3], extraction [4], thawing [5] and cooking [6]. One of the most important parameters of the ohmic heating process is the electrical conductivity values [7]. The importance of electrical conductivity is expressed by the studies for the fast and homogeneous heating of products [8,9].

Plant-based milk is preferred as an alternative to animal-derived milk due to the nutritional preference and health problems of people [10,11]. Almond, soy, coconut, hazelnut, and oat milk are the leading alternative plant-based milks [12]. Studies on the use and production of oat milk, especially in terms of its functional properties, have been increasing recently.

The milk needs to be heated in order to be used in subsequent processes. In particular, if it is used in yogurt or pastry products, it must be pasteurized. Electrical heating is preferred in the industry because the temperature control of it is easy and operating costs are lower. One of the most important parameters of ohmic (electrical) heating is electrical conductivity (EC). Because EC describes the relationship between current, voltage and physical properties of the system. Energy generation and heating rate vary depending on the applied voltage gradient and the electrical conductivity value of the food. Due to the sudden rise to the desired temperatures, the heating time in ohmic systems is very short and this affects the quality of the product positively [13-15].

If you were to walk into a grocery store today, there would be countless options for an oat drink. The number of options has increased significantly compared to the options available ten years ago. Possible reasons for the diversification of the dairy market include the impending global warming crisis and a growing movement for ethical treatment of animals. The estimated global market value of oat milk is approximately US$ 4,000,000,000 and is expected to grow at a rate of 9.8% per year [16]. The aim of the present study was heating the oat milk, whose production has become increasingly important, from 10±1 °C to 90±1 °C at different voltage gradients by ohmic heating process and to examine EC change during the process. In this way, it is aimed to provide data for commercial productions by using alternative techniques.

METHODS

Old fashioned rolled oats were purchased from a local grocery store. After adding 100 g of the oats and 1000 ml of distilled water (ice cold) into the blender, the blender (Waring, HGB2WTS3, USA) was run for 20 seconds. Then, the obtained mixture was filtered into a clean container with a high quality tightly woven nut milk bag. The sediment-free milk was taken into a glass bottle and stored in the refrigerator at +4 °C until the time of use.

60 ml of the oat milk sample was taken and heated in 5 different (20, 25, 30, 35 and 40V/cm) voltage gradients from approximately 10 °C to 90 °C in the ohmic heating cell. Ohmic heating system consists of a computer, power supply, electrodes (stainless steel, 1×40×150 mm), test cell (40×60×100 mm) and T-type thermocouple (Cole Parmer, UK). Temperature, current and voltage values were recorded every second with a custom-made microprocessor. Electrical conductivity values were calculated with Equation 1 using the data received from the system.

In addition, Equation 2 was used to express the relationship between temperature and electrical conductivity.

$$EC = \frac{I}{V} \times \frac{L}{A}$$ (1)

$$EC = axT + b$$ (2)

Here, I, V, L and A donate current (ampere), voltage (volts), distance between two electrodes (m) and electrode contact area (m^2), respectively. Also, T denotes temperature while a and b are equation constants. SPSS 25 (IBM, USA) program was used for the statistical evaluation of the study and the confidence interval was accepted as 95%. All experiments were repeated 3 times.

RESULTS

Time dependent temperature change during heating of the milk from 10±1 °C to 90±1 °C using ohmic heating is given in Figure 1. As a result of the heating process, the time for the oat milk to reach the desired temperature was determined as 336, 220, 142, 100 and 78 seconds for the voltage gradients of 20 V/cm, 25 V/cm, 30 V/cm, 35 V/cm and 40 V/cm, respectively ($p<0.05$). As can be seen from the data here, the increase of voltage gradients shortens the heating time. Similarly, the processing time was shortened as the voltage gradient increased during the heating of the products using the ohmic heating process. It has been reported that the processing times are shortened due to the increasing voltage gradient in the thawing [17], evaporation [18], cooking [19], distillation [20] and extraction [4] processes, which are among the food engineering applications. Electrical conductivity is one of the most important parameters in the ohmic heating process. It was determined that the electrical conductivity value increased with temperature. The main reason for this is that the molecular mobility in the product increases with the increasing temperature value and accordingly the electrical conductivity increases [21].
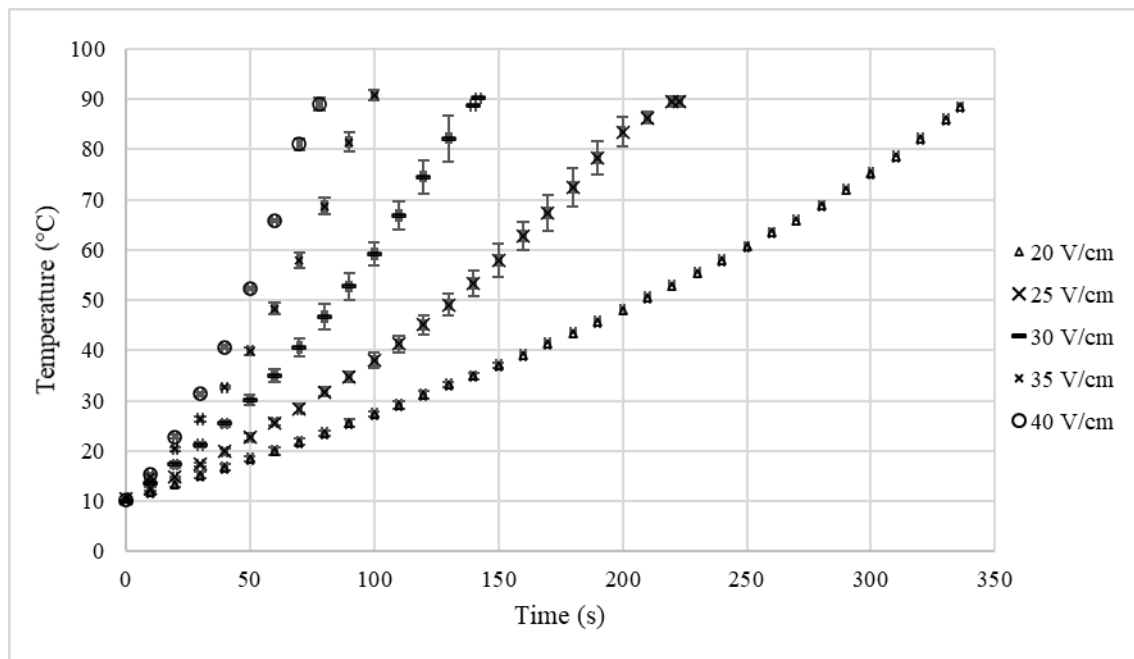
Fig. 4. Time dependent temperature change of oat milk at different voltage gradients, While the longest operating time was obtained at 20V/cm, the standard deviations of the mean values were higher at 25 and 30V/cm voltage gradients.

The change of the electrical conductivity value depending on the temperature during heating of the milk in 5 different voltage gradients is given in Figure 2. It has been found that the electrical conductivity value of the milk varies between 0.13-0.51 S/m. Also, the electrical conductivity value increases as the temperature value increases during the heating process. EC value can be obtained at different temperature and voltage gradients for different products. Because the electrical conductivity value changes depending on the system properties and the components in the product. Therefore, having more data for such products contributes more to system development.
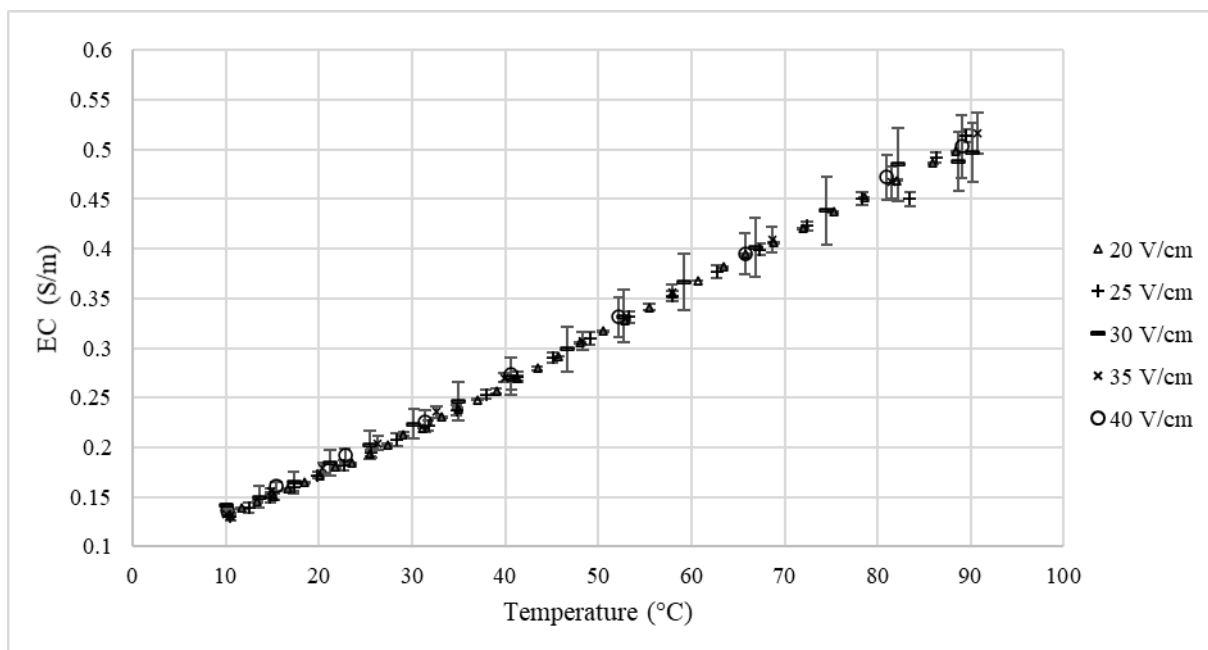
Fig. 5. The change of the electrical conductivity value depending on the temperature at different voltage gradients during heating of oat milk, Although the voltage gradients were different, the electrical conductivity was similar and the standard deviations of the mean values were higher in the 30V/cm voltage gradient.

During the heating of milk with ohmic system, there was a positive relationship between temperature and electrical conductivity value and this relationship was found to be linear. The temperature-EC equations of the linear relationship are given in the table for the different voltage gradients. When the overall ohmic heating studies are examined, it has been reported in different studies that the electrical conductivity value increases as the temperature increases and there is a linear relationship between temperature and EC [22, 23]. However, it has been reported that while EC-temperature is linear during the heating period, especially in evaporation studies where molecular mobility is restricted, the EC-temperature relationship is negatively affected after boiling starts [24]. In fact, as the total soluble solid content increases, it has been determined that the EC values are negatively affected due to the decreasing current values. Cevik (2021), in his study with ohmic heating at 13, 15, 17 and 19 V/cm voltage gradients, reported that the electrical conductivity values of verjuice samples increased linearly depending on the increase in temperature [25]. In a different study, it was reported that the electrical conductivity values of grape juice samples, which were subjected to ohmic heating at 4 different voltage gradients, increased linearly with temperature [26]. In addition, the researchers found that the highest electrical conductivity values were obtained at 85 °C and a voltage gradient of 30 V/cm.

Table 5. The temperature-EC equations

Voltage Gradient V/cm	Equation S/cm	R^2
20	0.4826xT+ 7.3765	0.9954
25	0.4814xT + 7.4045	0.9992
30	0.4771xT + 8.1953	0.9979
35	0.4746xT + 8.2475	0.9991
40	0.4781xT + 8.2423	0.999

CONCLUSIONS

The milk samples were heated up to 90±1 °C with ohmic heating process in 5 different voltage gradients, the processing time is shortened with the increasing voltage gradient, and serious foaming has occurred at the higher voltage. It has been determined that the electrical conductivity value varies between 0.13-0.51 S/m. It has been determined that the electrical conductivity value increases as the temperature value increases and there is a linear relationship between temperature and EC.

Keywords: Ohmic heating, Oat milk, Electrical Conductivity, Temperature

REFERENCES

1. ICIER, F. Ohmic heating of fluid foods. In novel thermal and non-thermal technologies for fluid foods, *Academic Press*, 2012, Vol. 1, p. 305-367.

2. SABANCI, S.; ÇEVIK, M.; GÖKSU, A. Investigation of time effect on pectin production from citrus wastes with ohmic heating assisted extraction process, *Journal of Food Process Engineering*, 2021, Vol. 44, No. e13689.

3. COKGEZME, O.F.; SABANCI, S.; CEVIK, M.; YILDIZ, H.; ICIER, F. Performance analyses for evaporation of pomegranate juice in ohmic heating assisted vacuum system, *Journal of Food Engineering,* 2017, Vol. 207, P. 1-9.

4. ÇILINGIR, S.; GOKSU, A.; SABANCI, S. Production of Pectin from Lemon Peel Powder Using Ohmic Heating-Assisted Extraction Process, *Food and Bioprocess Technology*, 2021, Vol. 23, P. 1-12.

5. CEVIK, M.; ICIER, F. Effects of voltage gradient and fat content on changes of electrical conductivity of frozen minced beef meat during ohmic thawing, *Journal of Food Process Engineering,* 2018, Vol. 41, No. e12675.

6. SENGUN, I. Y.; TURP, G.Y.; ICIER, F.; KENDIRCI, P.; KOR, G. Effects of ohmic heating for pre-cooking of meatballs on some quality and safety attributes, *LWT-Food Science and Technology*, 2014, Vol.55, P. 232-239.

7. KAUR, N.; SINGH, A. K. Ohmic heating: concept and applications—a review, *Critical reviews in food science and nutrition,* 2016, Vol.56, P. 2338-2351.

8. ARIÇ SÜRME, S.; SABANCI, S. The usage of Ohmic heating in milk evaporation and evaluation of electrical conductivity and performance analysis, *Journal of Food Processing and Preservation,* 2021, Vol. 45, No. e15522.

9. BOZKURT, H.; ICIER, F. Ohmic thawing of frozen beef cuts, *Journal of Food Process Engineering,* 2012, Vol. 35, P. 16-36.

10. DESWAL, A.; DEORA, N.S.; MISHRA, H.N. Effect of concentration and temperature on the rheological properties of oat milk, *Food and bioprocess technology*, 2014, Vol. 7, P. 2451-2459.

11. DESWAL, A.; DEORA, N.S.; MISHRA, H.N. Optimization of enzymatic production process of oat milk using response surface methodology, *Food and Bioprocess Technology,* 2014, Vol. 7, P. 610-618.

12. AYDAR, E.F.; TUTUNCU, S.; OZCELIK, B. Plant-based milk substitutes: Bioactive compounds, conventional and novel processes, bioavailability studies, and health effects, *Journal of Functional Foods*, 2020, Vol. 70, P. 103975.

13. SASTRY, S. K.; SALENGKE, S. Ohmic heating of solid-liquid mixtures: a comparison of mathematical models under worst-case heating conditions, *Journal of Food Process Engineering*, 1998 Dec, Vol:21, p.441-58.

14. ICIER, F.; YILDIZ, H.; SABANCI, S.; CEVIK, M.; COKGEZME, O.F. Ohmic heating assisted vacuum evaporation of pomegranate juice: Electrical conductivity changes. *Innovative food science & emerging technologies*, 2017 Feb, Vol:39, p.241-246.

15. DARVISHI, H.; HOSAINPOUR, A.; NARGESI, F.; KHOSHTAGHAZA, M.H.; TORANG, H. Ohmic processing: temperature dependent electrical conductivities of lemon juice, *Modern Applied Science,* 2011 , Vol. 5, p.209.

16. SETHI, S.; TYAGI, S.K.; ANURAG, R.K. Plant-based milk alternatives an emerging segment of functional beverages: a review, *Journal of food science and technology,* 2016 Sep, Vol:53(9), p.3408-3423.

17. CEVIK, M.; ICIER, F. Effects of voltage gradient and fat content on changes of electrical conductivity of frozen minced beef meat during ohmic thawing, *Journal of Food Process Engineering*, 2018, Vol. 41, p.e12675.

18. SABANCI, S.; ICIER, F. Applicability of ohmic heating assisted vacuum evaporation for concentration of sour cherry juice, *Journal of Food Engineering,* 2017, Vol.212, P. 262-270.

19. BOZKURT, H.; ICIER, F. Ohmic cooking of ground beef: Effects on quality, *Journal of food engineering,* 2010, Vol.96, p.481-90.

20. GAVAHIAN, M.; FARAHNAKY, A.; SASTRY, S. Ohmic-assisted hydrodistillation: A novel method for ethanol distillation, *Food and Bioproducts Processing*, 2016, Vol. 98, p.44-9.

21. IÇIER, F.; BAYSAL, T. Dielectrical properties of food materials-1: Factors affecting and industrial uses, *Critical reviews in food science and nutrition*, 2004 Nov, Vol:44, P. 465-471.

22. DARVISHI, H.; HOSAINPOUR, A.; NARGESI, F.; KHOSHTAGHAZA, M.H.; TORANG, H. Ohmic processing: temperature dependent electrical conductivities of lemon juice. *Modern Applied Science*, 2011, Vol.5, P. 209.

23. ICIER, F.; ILICALI, C. Electrical conductivity of apple and sourcherry juice concentrates during ohmic heating, *Journal of Food Process Engineering*, 2004, Vol.27, P. 159-80.

24. ICIER, F.; YILDIZ, H.; SABANCI, S.; CEVIK, M.; COKGEZME, O.F. Ohmic heating assisted vacuum evaporation of pomegranate juice: Electrical conductivity changes, *Innovative food science & emerging technologies*, 2017, Vol.39, P. 241.

25. CEVIK, M. Electrical conductivity and performance evaluation of verjuice concentration process using ohmic heating method, *Journal of Food Process Engineering*, 2021, Vol. 44, No.e13672.

26. KUMAR, T.; SMITH, D.D.; KUMAR, S.; VIMLA, B. Effect of voltage gradient and temperature on electrical conduc-tivity of grape (Vitis vinifera L.) juice during ohmic heating. *International Journal Current Microbiology Applied Science*, 2018, Vol.7, P. 1914-1921.

BIOCHEMICAL COMPOSITION OF DIFFERENT MORPHOLOGICAL PARTS OF THE RASPBERRY

A.Ispiryan, D. Urbonavičienė, P.Viškelis J.Viškelis
Lithuanian Research Centre for Agriculture and Forestry
Instituto al. 1, Akademija, LT-58344 Kėdainiai distr. – Lithuania
+370 347 37 271
audrone.ispiryan@lammc.lt

EXTENDED ABSTRACT

OVERVIEW

Optimization of innovation and food technological processes not only increases the profits of companies, but also allows to achieve the set goals of the green course. The aim of this research was to collect data on biochemical composition of different parts of the raspberry different morphological parts and to present potential of usage in various fields of food industry.

METHODS

Chemical composition was determined of freeze-dried samples powder. Total phenolic content was determined by the Folin-Ciocalteu's spectrophotometric method [1] using gallic acid as the standard. Ascorbic acid content was measured by official titrimetric method [2].

RESULTS

The biochemical composition of berries (ripe and unripe), leaves, stems, leaves, inflorescence, seeds and roots total phenolic compounds, ascorbic acid (vitamin C) and micronutrients was determined. The amount of total phenolic content ranged from 1700 to 6500 mg/100 g gallic acid equivalent (GAE) per gram of dry weight (mg GAE/100g DW). The highest value was detected in berries, which is 26% higher than it was detected in the lowest value in the seeds. The amount of ascorbic acid content ranged from 60 to 140 mg/100 g of dry weight. The highest value was detected also in berries.

The chemical composition of micronutrients of different morphological parts of raspberry is presented in Table 1.

The data provided by the study confirm the need to properly optimize the processing of raspberries by exploiting all parts of the plant according to its biochemical compounds, to strengthen the marketing of the products sold as labelling, consumer information and presentation of the actual composition of the product.

Table 1. Micronutrient content of different raspberry morphological parts

Research parameter	Sample name and test results						
In natural matter	Ripe berries	Unripe berries	Leaves	Stems	Inflorescence	Seeds	Roots
Calcium content (Ca)%	0,13	0,59	**1,15**	0,65	0,72	0,13	0,83
Magnesium content (Mg)%	0,14	0,31	**0,47**	0,15	0,37	0,11	0,16
Boron (B) mg/kg	17,5	29,5	**41,8**	22,0	31,3	7,23	17,6
Zinc content (Zn) mg/kg	20,7	26,1	18,0	17,5	**38,6**	18,0	18,9
Copper content (Cu) mg/kg	6,90	**10,2**	4,98	3,20	6,05	2,93	6,05
Iron content (Fe) mg/kg	37,2	57,1	83,4	46,0	59,1	35,6	**1551**
Manganese content (Mn) mg/kg	57,8	179,2	164,4	119,3	**248,7**	40,4	76,2

CONCLUSIONS

In conclusion, this research shows that different morphological parts of raspberry plant represent a potential source of natural food ingredients. The first study comparing the chemical composition of individual parts of the different morphological parts of raspberry is particularly significant in the development of waste-free technologies, increasing the economic value of raspberry farms.

Keywords: raspberry, different morphological parts, total phenolic compounds, C vitamin, micronutrients.

REFERENCES

1. SINGLETON, V.L.; ORTHOFER, R.; LAMUELA-RAVENTÓS, R.M. Analysis of total phenols and other oxidation substrates and antioxidants by means of Folin-Ciocalteu reagent. Meth Enzymol 1999, Vol. 299, p. 152-178.

2. HELRICH, K.E. the Association of Official Analytical Chemists. In AOAC Official Methods of Analysis; AOAC: Arlington, VA, USA, 1990.

BIOECONOMY BASED BIOREFINING SOLUTIONS FOR VALORISATION OF FOOD WASTES TO OBTAIN BIOACTIVE AND FUNCTIONAL INGREDIENTS

L. Klavins
The Natural Resource Research Centre of the University of Latvia
Jelgavas street 1, LV-1004, Riga – Latvia
+371 26688942
Linards.Klavins@lu.lv

EXTENDED ABSTRACT

OVERVIEW

Food loss and food waste are some of the major issues being recognized as a part of modern society. Approximately one-third of all the food is lost along the production and supply chain, leading to losses of valuable resources as well as creating environmental problems. The current food processing, production, consumption, and waste management approaches are not corresponding to the principles and aims of sustainability. The food waste and organic waste management problem becomes yet more urgent considering the aims set by a variety of environmental initiatives to abandon fossil material-based production and promote bio-based economy – bioeconomy, thus achieving climate neutrality and development of resource-saving practices [1]. Despite the efforts put in place by the EU achieving the set aims and the transition to bioeconomy much more knowledge and innovation is needed also in respect to properties of biomaterials, production and waste processing.

Juice production is an industry that produces fruit or berry press residues (pomace) as a by-product, which is often discarded in landfills or composted. Although these solutions are within the framework of the goals set by the different environmental initiatives, this type of waste lacks recognition, despite being rich in bioactive ingredients that could be retrieved. The research aims to study the composition of *Vaccinium genus* berries, common for NE Europe, as well as biorefining possibilities of their pomaces to support the development of extract applications in bioeconomy. The investigated berry press residues contain a variety of ingredients, polyphenols and lipids are the groups of interest due to their application potential in various products, where these compounds could be used as functional ingredients. Anthocyanins are the main polyphenols of berries – they are plant pigments that provide the vibrant colour of the berries while lipids are plant metabolites that are part of cell membranes and have a regulating function within the plant. Exploring the potential of berries and their industry by-products have the potential to reduce food loss and at the same time provide new, innovative, natural and healthy products with functionality for human consumption (Fig 1).

METHODS

Biomass used in this research has been obtained from local juice producing companies. The obtained press residues have been freeze-dried or dried in an airflow oven at 40˚C. Samples were homogenized using a blade mill with a 1 mm mesh size. A variety of extraction methods

have been used. Polyphenols have been extracted using mostly polar solvents by ultrasound-assisted extraction, solvent-solvent extraction, Soxhlet, while the lipids have been extracted using non-polar solvents in Soxhlet extraction unit, ultrasound-assisted extraction or supercritical CO_2 extraction. Obtained extracts depending on the compounds of interest have been analysed using UPLC-MS/MS, UPLC-FT-ICR-HRMS or GC-MS to identify individual substances. Group parameters have been estimated using spectrophotometric methods in microwell plates, for example, Folin-Ciocalteu for total polyphenolics, a pH differential method for estimation of total anthocyanins, DMAC assay for total flavanol contents, DPPH, ABTS, FRAP, ORAC, CUPRAC for determination of free radical scavenging activity. Application potential has been assessed using microbial assays, SPF (Sun Protection Factor) assay, as well as cell viability tests.

RESULTS

The obtained results indicate that all five of the investigated *Vaccinium* species berries bog cranberries *(Vaccinium oxycoccos L.),* American cranberries *(Vaccinium macrocarpon L.),* blueberries *(Vaccinium corymbosum L.),* bilberries *(Vaccinium myrtillus L.),* lingonberries *(Vaccinium vitis-idaea L.)* and bog bilberries *(Vaccinium uliginosum L* and their press residues are a valuable source of polyphenolics. These compounds can be extracted using ultrasound-assisted extraction and slightly acidic ethanol – the optimal extraction conditions have been optimised using RSM approach [2]. Moreover, the extraction process has been optimised to extract procyanidins (especially procyanidin A2) from American cranberry press residues – in total 61 different procyanidins have been identified using UPLC-FT-ICR-HRMS ranging from dimers up to decamers. Antioxidant activity of the extracted polyphenlics has been attributed to the procyanidins as well as other phenolic compounds present in the berry press residues. Additionally, since press residues also contain the seeds and skins (which contain plant wax) the lipid profiles of all 5 of the berries were investigated. Free fatty acids, sterols, triterpenoids, and aliphatic hydrocarbons were identified. Berry press residues were rich in unsaturated omega fatty acids, beta-sitosterol, amyrins, oleanolic and ursolic acid, to name a few [3].
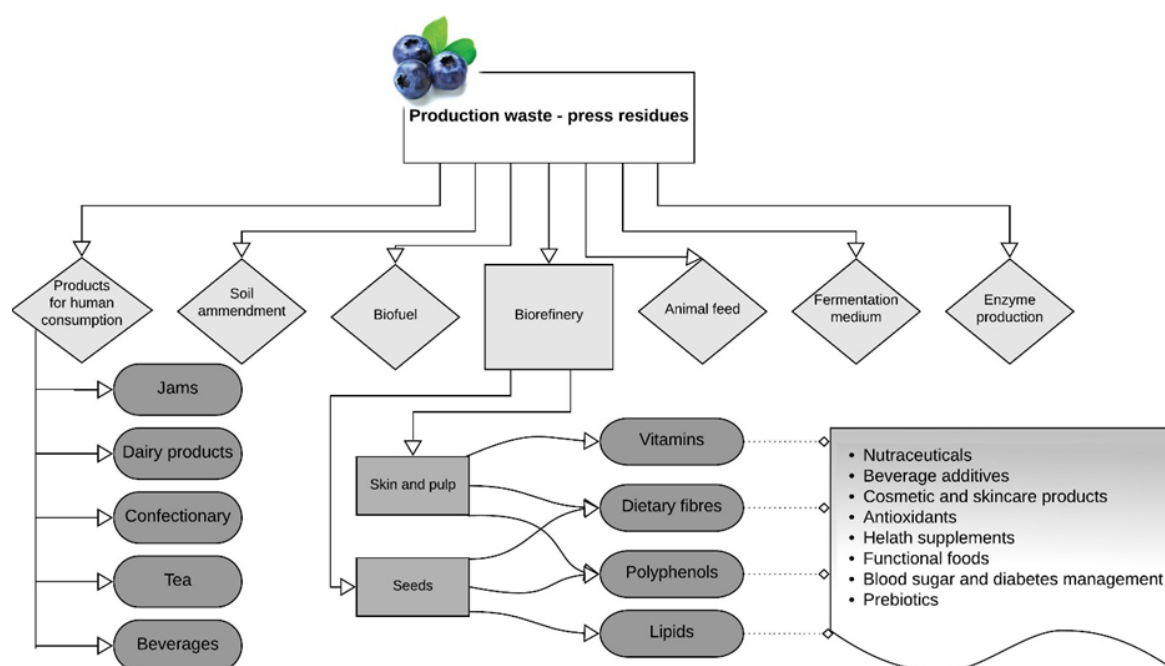
Fig. 1. Proposed biorefinery approach for the valorisation of berry press residues.

CONCLUSIONS

Berries are a natural source of a variety of biologically active compounds that have different effects on human health. The obtained ingredients show potential to be used in innovative products as functional ingredients, however, the effect of these compounds as well as the possibilities to obtain them must be further investigated to increase the viability of the processes used, thus justifying the inputs.

Keywords: Berries, press residues, pomace, lipids, polyphenolics, biorefinery, bioeconomics

REFERENCES

1. *European Green Deal*. [referred on the 20th of February, 2022]. Link to the internet <https://ec.europa.eu/info/strategy/priorities-2019-2024/european-green-deal_en>

2. KLAVINS, L.; KVIESIS, J.; NAKURTE, I.; KLAVINS, M. Berry press residues as a valuable source of polyphenolics: Extraction optimisation and analysis. *LWT*, 2018, Vol. 93, P. 583-591.

3. TRIVEDI, P.; KARPPINEN, K.; KLAVINS, L.; KVIESIS, J.; SUNDQVIST, P.; NGUYEN, N.; HÄGGMAN, H. Compositional and morphological analyses of wax in northern wild berry species. *Food chemistry*, 2019, Vol. 295, P. 441-448.

PROSPECTS OF USING INFARED SPECTROSCOPY FOR THE ANALYSIS OF BEE PRODUCTS

S. I. Litvynchuk, V. A. Kuzinska, V. V. Vyshniak, V. E. Nosenko, I. V. Hutsalo
National University of Food Technologies
68 Volodymyrska Str., 01601 Kyiv – Ukraine
+38 (044) 287-92-78
litvynchuk@nuft.edu.ua

EXTENDED ABSTRACT

OVERVIEW

Bee products have unique healing and nutritional properties. They include honey, propolis, bee pollen, royal jelly, beeswax, bee bread, bee venom. Bee products are widely used in the food, cosmetics and medicine industries. In addition, such products are the best immunostimulants in the fight against COVID-19 [1].

However, there is a problem of considerable food falsification in the world. It is also applying to valuable bee products. Unfortunately, falsified and contaminated with impurities (paraffin, ceresin, antibiotics, pesticides, etc.) bee products lead to economic and moral losses for real producers, processors and consumers of bee products. Due to the available economic benefits and the lack of official analytical methods that can detect counterfeits, we are surrounded by unscrupulous producers, which illegally practice the production of low-quality substitutes of bee products. At the same time, the image of the industry in the international arena is worsening, there is a decline of beekeeping farms and people's health is at risk due to the consumption of low-quality products.

Therefore, a particularly important task today is to develop cheap, publicly available express methods for diagnosing the quality and safety of bee products. Since the method of near infrared spectroscopy (NIR) is a powerful modern method for analysing the quality of various foods, it can be used to assess the quality of honey [2]. The authors of the research [3] have analysed the freshness of honey and check its quality for authenticity using the method of Fourier transform infrared spectroscopy (FTIR). Infrared reflection spectroscopy in combination with multidimensional modelling can be an effective tool for simultaneous quantification of different groups of compounds and many physicochemical parameters of bee pollen [4].

METHODS

In this work, the method of near infrared diffuse reflectance spectroscopy was used. Analysis of the reflection spectra was performed on a spectrometer "Infrapid-61" (company «LaborMIM», Hungary). The wavelength ranges at which the samples were analysed was 1.33 – 2.37 μm. Spectral analysis of each sample was performed for 2 minutes. At the same time, the repeatability of the results was quite high (the reliability of approximation R^2 was at least 98%).

RESULTS

As a result of experimental studies, dry multicomponent mixtures of powdered food products were analysed, the main component of which was white sugar or powdered sugar. These were industrial designs manufactured by Ukrainian manufacturer. They had impurities of ginger, cinnamon, cardamom, bodian, cloves, as well as bee pollen. Separately, spectral analysis of white sugar, powdered sugar and bee pollen was carried out.

All samples were examined without prior sample preparation. For analysis, the sample was loaded into a ditch compartment and the spectrum of diffuse reflection was measured.

The obtained results have showed the corresponding correlation between the reflection spectra and food powders of different compound with the content of bee pollen, which in the future may find wide practical application in the food industry.

Infrared reflection spectra of natural beeswax and its counterfeits (containing paraffin, ceresin and their mixtures of different concentrations) were also analysed. All reflection spectra were analysed from different surfaces of the samples, namely the smooth surface formed after melting and hardening of the sample, and from the crushed samples.

As a result of the research conducted by method infrared spectroscopy of reflection, it was found that:

- the obtained reflection spectra from the smooth surfaces of the samples (beeswax, paraffin, ceresin and their mixtures) have a similar structure with two clearly expressed maxima of different intensities;

- infrared spectra of diffuse reflection of crushed samples undergo certain changes compared to the spectra obtained from the smooth surface of the samples;

- the most intense maxima do not change their position but there is a redistribution of spectral lines in intensity;

- infrared spectrum of natural beeswax has a number of features that distinguish it from other spectra of the studied samples.

That is to say, the proposed method of near infrared spectroscopy can be used to analyse wax raw materials and used to identify natural and adulterated (with the presence of impurities of different concentrations) beeswax successfully.

CONCLUSIONS

The analysis of the obtained experimental data allows us to conclude that infrared spectroscopy of reflection can be a promising rapid method for the analysis of bee products and solve a number of problems related to the control of their quality and safety.

Keywords: infrared spectroscopy, bee products, analysis.

REFERENCES

1. STANGACIU, S. Beekeeping products are the best allies of the immune system in the fight against the disease COVID-19. Overview of the online conference. Presentation II. *Phitotherapy. Chasopys*, 2020, No. 4, p. 61-71.

2. WĘGLIŃSKA, M.; SZOSTAK, R.; KITA, A.; NEMŚ, A.; MAZUREK, S. Determination of nutritional parameters of bee pollen by Raman and infrared spectroscopy. *Talanta*, 2020, Vol. 212, No. 120790.

3. PAULIUC, D.; CIURSĂ, P.; ROPCIUC, S.; DRANCA, F.; OROIAN, M. Physicochemical parameters prediction and authentication of different monofloral honeys based on FTIR spectra. *Journal of Food Composition and Analysis*, 2021, Vol. 102, No. 104021.

4. PUŚCION-JAKUBIK, A.; BORAWSKA, M. H.; Socha, K. Modern methods for assessing the quality of bee honey and botanical origin identification. *Foods*, 2020, Vol. 9, No. 8, P. 1028.

BERRIES WITH HIGH ANTHOCYANIN ACCUMULATION FOR ANTHOCYANIN EXTRACTION: A SHORT OVERVIEW

A. Petruškevičius, D. Urbonavičienė, P. Viškelis
Institute of Horticulture,
Lithuanian Research Centre for Agriculture and Forestry
Instituto al. 1, Akademija, LT-58344 Kėdainiai distr. – Lithuania
+370 684 04218
aistis.petruskevicius@lammc.lt

EXTENDED ABSTRACT

OVERVIEW

In the developed countries there's a noticeable increase of metabolic and cardiovascular disorders that are linked with improper, unbalanced diet and constant mental stress paired with sedentary lifestyle [1]. Ischemic heart diseases and cognitive decline disorders like dementia and Alzheimer's disease are predicted to become an increasingly prevalent problem, especially in the aging societies [2], [3] and according to United Nations statistics, population of people aged 65 or older is currently the fastest growing age group worldwide [4]. Research studies published in the last decade show that phenolic compounds like anthocyanins and diet enrichment with them can have a positive effect on health. It was found that polyphenols can have anti-inflammatory properties, reduce the risk of oncological disorders, oxidative stress and illnesses that are caused by it – like cognitive decline, cardiovascular diseases [5]. Phenolic compounds are divided into two main groups – flavonoids and non-flavonoids. Anthocyanins are a part of the flavonoid group. Anthocyanins are water soluble pigments and accumulate in plant fruits, flowers, and vegetative organs in the cell vacuoles [6].

Anthocyanins are widely used in the food industry as a food colouring additive. Because of its non-toxicity, abundance, fast biodegradability, and positive impact on health, it is getting an increasing attention not only as a natural food colorant, but also as a functional ingredient [7]. With the ever-increasing market demand for healthier, sustainably produced food options these features are easily marketable. Cyanidin, delphinidin, malvidin, petunidin, peonidin and pelargonidin are among the most common anthocyanins. Their colour ranges from red/orange (pelargonidin), magenta (cyanidin) to blue (delphinidin) [8]. In the acidic environment anthocyanins usually gain a red hue, in alkaline – typically blue/violet. Anthocyanins are highly unstable are sensitive to temperature, acidity, and are easily oxidised, gaining a brown colour [8], [9], [10]. This instability of natural anthocyanins causes some difficulties in cost-efficient industrial application of anthocyanin-based food colouring [10].

Anthocyanin-rich flowers and fruits are a common ingredient in traditional cuisines worldwide, where they have been used for both enrichment of food with their vibrant colours and as spice, as well as in the traditional medicine for many illnesses ranging from treatment of bladder stones, spasms, mild pain relief, indigestion, fever [8], [11]. For finding the cause of these apparent benefits of anthocyanin rich plants healing capabilities numerous studies have been conducted. The results linked these positive health effects with specific anthocyanins and other

polyphenols found in various fruits and berries – in the *in vitro* studies it was found that anthocyanins reduced oxidative damage [12], increased mitochondrial respiration [13] and insulin secretion [14], while *in vivo studies* have found that chokeberry anthocyanins reduced male rat body weight gain [15], while anthocyanins found in blueberries reduced the risk of cardiac injury [16].

Anthocyanin research for the food industry use shows a lot of possible benefits and could improve the quality of food products by replacing current unnecessary ingredients with functional ones, while anthocyanin application in the pharmaceutical supplement or medicine production could help establish new methods to either treat or prevent illnesses that are likely to become increasingly prevalent in the upcoming decades. The review aims, to identify the richest in anthocyanin berries that could be used for the anthocyanin extraction.

METHODS

In the reviewed research papers, published from 2004 to 2017, the main method of total anthocyanin estimation was pH differential method, with the absorption at 510 and 700 nm. High-performance liquid chromatography (HPLC) was used to identify and separate individual anthocyanins by their polarity. [17, 18, 19, 20, 22, 23].

RESULTS

Preliminary findings show the highest anthocyanin contents in *Sambucus nigra and vaccinium myrtillus* species with total anthocyanin contents up to 8.1 and 4.5 mg/g fresh weight respectably (Table). Slightly lesser anthocyanin content was found in *Ribes nigrum* berry with anthocyanin contents ranging from 1.5 to 3.8 mg/g FW. The least anthocyanin was found in species *Vaccinium vitis-idaea* with anthocyanin contents going up to 0.5 mg/g FW.

Table. 1. Total anthocyanin contents of various berries in mg/g fresh weight

Family	Genus	Species	Total anthocyanin content, mg/g FW
Ericaceae	*Vaccinium*	*Vaccinium myrtillus*	2.4 – 4.5 [17], [18], [19]
		Vaccinium vitis-idaea	0.3 – 0.5 [19], [20]
Grossulariaceae	*Ribes*	*Ribes nigrum*	1.5 – 3.8 [21], [20]
Adoxaceae	*Sambucus*	*Sambucus nigra*	6.7 – 8.1 [17], [21]

CONCLUSIONS

With the broadening range of use cases for anthocyanins in both pharmaceutical and food industries, the demand for weight-efficient anthocyanin sources is likely to increase and as such it is useful to identify which berries are the most suitable for this purpose. While preliminary findings show that *Sambucus nigra and Vaccinium myrtillus* are among the most attractive choices as a berry of choice for anthocyanin extraction because of their high total anthocyanin content, further literature analysis is required to make this conclusion more reliable.

Keywords: berries; anthocyanins; human health; HPLC

REFERENCES

1. SLOOP, G. D.; WEIDMAN, J. J.; ST CYR, J. A. Perspective: interesterified triglycerides, the recent increase in deaths from heart disease, and elevated blood viscosity. *Therapeutic Advances in Cardiovascular Disease*, 2018, Vol. 12, No. 1, P. 23–28.

2. KHAN, M. A.; HASHIM, M. J.; MUSTAFA, H.; BANIYAS, M. Y.; AL SUWAIDI, S. K. B. M.; ALKATHEERI, R.; LOOTAH, S. N. A. H. Global Epidemiology of Ischemic Heart Disease: Results from the Global Burden of Disease Study. *Cureus*, 2020, Vol. 12, P. 7.

3. BACIGALUPO, I.; MAYER, F.; LACORTE, E.; DI PUCCHIO, A.; MARZOLINI, F.; CANEVELLI, M.; VANACORE, N. A Systematic Review and Meta-Analysis on the Prevalence of Dementia in Europe: Estimates from the Highest-Quality Studies Adopting the DSM IV Diagnostic Criteria. *Journal of Alzheimer's Disease*, 2018, Vol. 66. No. 4, P. 1471–1481. DOI:10.3233/JAD-180416

4. *UN*. World population prospects 2019: highlights. 2019. [referred on the 15th of January in 2022 y.]. Link to the internet <https://population.un.org/wpp/Publications/Files/WPP2019_10KeyFindings.pdf >.

5. MATTIOLI, R.; FRANCIOSO, A.; MOSCA, L.; SILVA, P. Anthocyanins: A Comprehensive Review of Their Chemical Properties and Health Effects on Cardiovascular and Neurodegenerative Diseases. *Molecules,* 2020, Vol. 25, No.17.

6. CELLI, G. B.; GHANEM, A.; BROOKS, M. S. L. Optimization of ultrasound-assisted extraction of anthocyanins from haskap berries *(Lonicera caerulea L.)* using Response Surface Methodology. *Ultrasonics Sonochemistry*, 2015, Vol. 27, P. 449–455.

7. CAI, D., LI, X.; CHEN, J.; JIANG, X.; MA, X.; SUN, J.; BAI, W. A comprehensive review on innovative and advanced stabilization approaches of anthocyanin by modifying structure and controlling environmental factors. *Food Chemistry*, 2022, Vol. 366.

8. KHOO, H. E.; AZLAN, A.; TANG, S. T.; LIM, S. M. Anthocyanidins and anthocyanins: Colored pigments as food, pharmaceutical ingredients, and the potential health benefits. *Food and Nutrition Research*, 2017, Vol. 61.

9. RAWDKUEN, S.; FASEHA, A.; BENJAKUL, S.; KAEWPRACHU, P. Application of anthocyanin as a color indicator in gelatin films. *Food Bioscience*, 2020, Vol. 36.

10. YANG, P.; YUAN, C.; WANG, H.; HAN, F.; LIU, Y.; WANG, L.; Yang, L. Stability of Anthocyanins and Their Degradation Products from Cabernet Sauvignon Red Wine under Gastrointestinal pH and Temperature Conditions. *Molecules,* 2018, Vol. 23, P. 354–373.

11. RIAZ, G.; CHOPRA, R. A review on phytochemistry and therapeutic uses of Hibiscus sabdariffa L. *Biomedicine and Pharmacotherapy*, 2018, Vol. 102, P. 575–586.

12. SAMADDER, A.; ABRAHAM, S. K.; KHUDA-BUKHSH, A. R. Nanopharmaceutical approach using pelargonidin towards enhancement of efficacy for prevention of alloxan-induced DNA damage in L6 cells via activation of PARP and p53. *Environmental Toxicology and Pharmacology*, 2016, Vol. 43, P. 27–37.

13. SKATES, E.; OVERALL, J.; DEZEGO, K.; WILSON, M.; ESPOSITO, D.; LILA, M. A. Berries containing anthocyanins with enhanced methylation profiles are more effective at ameliorating high fat diet-induced metabolic damage. *Food and Chemical Toxicology*, 2017, Vol. 111, P. 445–453.

14. LEE, J. S.; KIM, Y. R.; PARK, J. M.; KIM, Y. E.; BAEK, N. I.; HONG, E. K. Cyanidin-3-glucoside isolated from mulberry fruits protects pancreatic b-cells against glucotoxicity-induced apoptosis. *Molecular Medicine Reports*, 2015, Vol. 11, P. 2723–2728.

15. QIN, Y.; XIA, M.; MA, J.; HAO, Y.; LIU, J.; MOU, H. Anthocyanin supplementation improves serum LDL-and HDL-cholesterol concentrations associated with the inhibition of cholesteryl ester transfer protein in dyslipidemic subjects. *The American Journal of Clinical Nutrition*, 2009, Vol. 90, P. 485–492.

16. LIU, Y.; TAN, D.; SHI, L.; LIU, X.; ZHANG, Y.; TONG, C. Blueberry anthocyanins-enriched extracts attenuate cyclophosphamide-induced cardiac injury. *PLoS ONE*, 2015.

17. RIMPAPA, Z.; TOROMANOVIĆ, J.; TAHIROVIĆ, I.; SAPCANIN, A.; SOFIĆ, E. Total content of phenols and anthocyanins in edible fruits from Bosnia. *Bosnian Journal of Basic Medical Sciences / Udruženje Basičnih Mediciniskih Znanosti*, 2007, Vol. 7, P. 117–120.

18. AABY, K.; GRIMMER, S.; HOLTUNG, L. Extraction of phenolic compounds from bilberry (Vaccinium myrtillus L.) press residue: Effects on phenolic composition and cell proliferation. *LWT - Food Science and Technology,* 2013, Vol. 54, No. 1, P. 257–264.

19. DRÓŻDŻ, P.; ŠĖŽIENĖ, V.; PYRZYNSKA, K. Phytochemical Properties and Antioxidant Activities of Extracts from Wild Blueberries and Lingonberries. *Plant Foods for Human Nutrition*, 2017, Vol. 72, P. 360–364.

20. LEE, J.; FINN, C. E. Lingonberry (Vaccinium vitis-idaea L.) grown in the Pacific Northwest of North America: Anthocyanin and free amino acid composition. *Journal of Functional Foods*, 2012, Vol. 4, No. 1, P. 213–218.

21. BENVENUTI, S.; PELLATI, F.; MELEGARI, M.; BERTELLI, D. Polyphenols, Anthocyanins, Ascorbic Acid, and Radical Scavenging Activity of Rubus, Ribes, and Aronia. *Journal of Food Science*, 2004, Vol. 69, No. 3, P.164–169.

22. BOBINAITĖ, R.; VIŠKELIS, P.; VENSKUTONIS, P. R. Variation of total phenolics, anthocyanins, ellagic acid and radical scavenging capacity in various raspberry (Rubus spp.) cultivars. *Food chemistry*, 2012, Vol. 132, No. 3, P. 1495-1501.

23. PATARO, G.; BOBINAITĖ, R.; BOBINAS, Č.; ŠATKAUSKAS, S.; RAUDONIS, R.; VISOCKIS, M.; VIŠKELIS, P. Improving the extraction of juice and anthocyanins from blueberry fruits and their by-products by application of pulsed electric fields. *Food and Bioprocess Technology*, 2017, Vol. 10, No. 9, P. 1595-1605.

ESSENTIAL OILS COMPOSITION, TOTAL PHENOLIC CONTENT AND ANTIOXIDANT ACTIVITY OF *ARALIA CORDATA* THUNB. LEAVES AND BERRY

V. Puzerytė, P. Viškelis, A. Balčiūnaitienė, D. Urbonavičienė
Lithuanian Research Centre for Agriculture and Forestry
Institute of Horticulture
Kauno st. 30, LT-54333 Babtai, Kaunas distr. – Lithuania
+370 643 35 003
viktorija.puzeryte@lammc.lt

EXTENDED ABSTRACT

OVERVIEW

Medical plants are increasingly being used for medicinal and therapeutic purposes to treat various diseases and ailments, as well as for health improvement [1, 2]. Many plants contain large amounts of antioxidants such as polyphenols, which can significantly absorb and neutralise harmful free radicals, quenching singlet and triplet oxygen, or decomposing peroxides [3]. Furthermore, it is reported that phenolic compounds with antioxidant properties have anticancer, antibacterial, and anti-inflammatory properties [4]. The most common *in vitro* methods used to evaluate the antioxidant activity are $ABTS^{\bullet+}$ (2,2'-azinobis(3-ethylbenzothiazoline-6-sulfonic acid), $DPPH^{\bullet}$ (2,2-diphenyl-1-picrylhydrazyl) and FRAP (ferric reducing antioxidant power) [5]. Essential oil is frequently found in various parts of plants, including roots, stems, leaves, flowers, and fruits. Plant essential oils have good biological activity, including antibacterial, antifungal, antiviral and antioxidant activity, aroma and flavour [6]. *Aralia cordata* Thunb *(A. cordata)* is a medicinal plant belonging to the Aralaceae family, grown mainly in China, Japan, and Korea, used in culinary and folk medicine, acknowledged as a medical herb with anti-nociceptive, antidiabetic, antioxidant, and anti-inflammatory activities [7, 8, 9]. This plant is also grown in Lithuania but is not yet known and used. It is produced only by some Lithuanian herbalists and folk medicine specialists. This research aimed to determine the bioactive compounds and antioxidant activity of *A. cordata* leaves and berries and investigate the essential oil composition obtained from plant material by hydrodistillation was studied by gas chromatography-mass spectrometry (GC-MS).

METHODS

The study was carried out at the Institute of Horticulture, Lithuanian Research Centre for Agriculture and Forestry. Antioxidant activity and total phenolic concentrations were examined in a freeze-dried *A. cordata* ethanol/water mixture (70/30, v/v %) [10]. The total antioxidant activity was tested using the $DPPH^{\bullet}$ scavenging capacity, $ABTS^{\bullet+}$ radical cation assay, and ferric reducing antioxidant power (FRAP) [10, 11, 12]. Essential oils were extracted using the hydrodistillation method, and the chemical composition of essential oils was analysed by the GC-MS.

RESULTS

The total phenolic content obtained in *A. cordata* berry was 918 mg GAE/100 g and in leaves 2328 mg GAE/100 g DW. To properly estimate the antioxidant activity of the ethanol extracts of berry and leaves, different antioxidant capacity assays (ABTS$^{\bullet+}$, DPPH$^{\bullet}$ and FRAP) were used. The results showed that the leaves extract obtained the highest value in all radical scavenging assays. In addition, the yield of essential oils was detected in the fresh leaves (0.15 ml/100 g) and berries (0.09 ml/100 g). Twelve compounds were identified in fresh *A. cordata* leaves, the most significant amount of β-pinene (75.59%), β-ocimene (15.25%) and α-limonene (7.24%) were obtained. Seven compounds were identified in fresh berries, and the highest amount of β-pinene (61.49%), α-ocimene (30.10%), and limonene (5.41%) were established.

CONCLUSIONS

The result demonstrated that *A. cordata* leaves had significantly high antioxidant activity potential, and it is a good source of bioactive compounds. Furthermore, by comparing the amount of essential oils in *A. cordata* leaves and berries, it was determined that the leaves accumulate a larger amount of essential oils. Besides, the most significant amount of compounds was identified in leaves compared to berries. Also, these results will form the basis for the selection of the *A. cordata* plant for further investigation of their novel bioactive components and their application in the food and pharmaceutical industry.

Keywords: *Aralia cordata*; antioxidant activity; phenolic compounds, essential oil

REFERENCES

1. SHAKYA, A.K. Medicinal Plants: future source of new drugs. *International Journal of Herbal Medicine*, 2016, Vol. 4, No. 4, P. 59-64.

2. HAMBURGER, M.; HOSTETTMANN, K. Bioactivity in plants: the link between phytochemistry and medicine. *Phytochemistry*, 1991, Vol. 30, No. 12, P. 3864-3874.

3. OLAS, B.; ŽUCHOWSKI, J.; LIS, B.; SKALSKI, B.; KONTEK, B.; GRABARCZYK, Ł.; STOCHMAL, A. Comparative chemical composition, antioxidant and anticoagulant properties of phenolic fraction (a rich in non-acylated and acylated flavonoids and non-polar compounds) and non-polar fraction from *Elaeagnus Rhamnoides* (L.) A. Nelson fruits. *Food Chemistry*, 2018, Vol. 247, No. 1, P. 39-45.

4. TAPIERO, H.; TEW, K.; BA, G.N.; MATHE, G. Polyphenols: Do they play a role in the prevention of human pathologies? *Biomedicine & Pharmacotherapy*, 2002, Vol. 56, No. 4, P. 200-207.

5. CHAVES, N.; SANTIAGO, A. ALÍAS, J.C. Quantification of the antioxidant activity of plant extracts: analysis of sensitivity and hierarchization based on the method used. *Antioxidants*, 2020, Vol. 9, No. 1, P. 76.

6. ALI, B.; AL-WABEL, N.A.; SHAMS, S.; AHAMAD, A.; KHAN, S.A.; ANWAR, F. Essential oils used in aromatherapy: a systemic review. *Asian Pacific Journal of Tropical Biomedicine*, 2015, Vol. 5, No. 8, P. 601-611.

7. WEN, J. Generic delimitation of *Aralia* (Araliaceae). *Brittonia*, 1993, Vol. 45, No. 1. P. 47-55.

8. KIM, J. G.; LEE, J. W.; LE, T. L. P.; HAN, J. S.; KWON, H.; LEE, D.; HONG, J. T.; KIM, Y; LEE, M. K.; KWANG, B.Y. Diterpenoids and diacetylenes from the roots of *Aralia Cordata* with inhibitory effects on nitric oxide production. *Journal of Natural Products*, 2021, Vol. 84, No. 2, P. 230-238.

9. JANG, J.Y.; SEONG, Y.H. Anti-Nociceptive and anti-inflammatory effect of an ethanol extract of the leaf and stem of *Aralia Cordata. Natural Product Sciences*, 2014, Vol. 20, No. 4 P. 301-305.

10. BOBINAITĖ, R.; PATARO, G.; LAMANAUSKAS, N.; SATKAUSKAS, S.; VISKELIS, P.; FERRARI, G. Application of pulsed electric field in the production of juice and extraction of bioactive compounds from blueberry fruits and their by-products. *Journal of Food Science and Technology*, 2015, Vol. 52, No. 9, P. 5898-5905.

11. URBONAVIČIENĖ, D.; BOBINAS, Č.; BOBINAITĖ, R.; RAUDONĖ, L.; TRUMBECKAITĖ, S.; VIŠKELIS, J.; VIŠKELIS, P. Composition and antioxidant activity, supercritical carbon dioxide extraction extracts, and residue after extraction of biologically active compounds from freeze-dried tomato matrix. *Processes*, 2021, Vol. 9, No. 3, P. 467.

12. BOBINAITĖ, R.; VIŠKELIS, P.; VENSKUTONIS, P. R. Variation of total phenolics, anthocyanins, ellagic acid and radical scavenging capacity in various raspberry (*Rubus Spp.*) cultivars. *Food Chemistry*, 2012, Vol. 132, No. 3, P. 1495-1501.

ENZYMATICALLY HYDROLISED OATS (*AVENA SATIVA* L.) BIOCHEMICAL COMPOSITION AND SUGARS PROFILE

P. Štreimikytė, P. Viškelis, J. Viškelis
Lithuanian Research Centre for Agriculture and Forestry
Institute of Horticulture
Kauno st. 30, LT-54333 Babtai – Lithuania
+370 643 18 479
paulina.streimikyte@lammc.lt

EXTENDED ABSTRACT

OVERVIEW

Enzymatically hydrolysed oats (*Avena sativa*) are a source of sugars and dietary fibers [1]. In particular, dietary fibers are, known as carbohydrates, consist of three or more monomeric sugars units [2]. However, different plant materials and enzymes release different amounts and lengths of sugars to aqueous media [3]. Continuously, these extracts may be used for beneficial strains growth, for green nanoparticles synthesis, and used as prebiotics potently [4,5]. The research aims to determine the alteration of biochemical composition in oats after enzyme-assisted water extraction. Variation of amylases (AL), glucoamylase (GA), and non-starch polysaccharides (NSP) enzymes were used for enzymatic hydrolysis. Because the plant material is complex, with varied compositions and matrices, enzymes are used in mixtures or cocktails.

METHODS

Two different batches were performed for analysis. Milled oat cereals (> 0.5 mm) were homogenized with distilled water in a ratio of 1:5. Continuously, for the first batch 0.15% of AL and 0.15% NSP, and for the second batch 0.45% AL+AG, 0.15% NSP was incorporated. After 2,5 hours at 68ºC enzymatic extraction, liquid and solid fractions of oats were collected. Further on, the analysis of neutral detergent (NDF) and acid detergent fiber (ADF) with an ANKOM fiber analyser was implemented to evaluate hemicellulose, cellulose, and lignin content. Moreover, maltotriose, raffinose, maltose, glucose, galactose, fructose, xylose, arabinose, and ribose identification using HPLC analysis of extracts and after Minekus et al. [6] INFOGEST *in vitro* stimulated digestion was performed.

RESULTS

Table 1. shows hemicellulose, cellulose, and lignin content after ADF and NDF analysis. Results indicated that hemicellulose, cellulose and lignin content in hydrolyzed fractions were approximately 15,41 - 12,27% lower than control samples, which implements the non-starch polysaccharides enzymes hydrolytic properties. As results showed, 22,40% of *A. sativa* control consists of hemicellulose. Its content with AL, NSP and AL, GL, and NSP were 12,62% and 6,67%, respectively. It indicates that glucoamylases cleave the released hemicellulose components into smaller monomers.

Table 1. Fiber content of *A. Sativa* control and after enzymatic extraction

Sample name	Hemicellulose, cellulose, and lignin, %	Cellulose and lignin, %
A. Sativa control	40,76 ± 1,97	18,36 ± 0,51
A. Sativa I batch	28,49 ± 0,85	15,87 ± 1,83
A. Sativa II batch	25,38 ± 2,45	18,91 ± 3,45

For the profile of the sugar, glucose quantity was 94,5 ± 0,9 %, while the composition of other sugars differed 0,2 - 2,0 % in enzyme-assisted extracts. Similar tendencies were observed in samples after simulated *in vitro* digestion where dominated glucose monomeric units with 92.5 ± 1,45% and other saccharides varied in a range of 0,3 – 5,1%. In general, compared with control extracts prepared without enzymes, sugars content increased after hydrolysis for the first and second batches by 1,19 ± 0,04 and 1,43 ± 0, 09 times, respectively.

Table 2. Sugars and organic acids content after INFOGEST *in vitro* digestion of enzymatically hydrolysed samples

Sugar name	Sample name		
	A. Sativa control	*A. Sativa* I batch	*A. Sativa* II batch
DP3* %	0,5	0,6	0,5
Rafinose, %	1	0,4	0,5
Maltose, %	0,7	0,4	0,4
Glucose,%	90,1	93,1	92,1
Galactose, fructose, xylose, %	6,8	4,4	5,1
Arabinose, %	0,5	0,9	0,9
Ribose,%	0,4	0,3	3
Sugars, %	100	100	100
Sugars, g/kg	484,56 ± 0,80	695,99 ± 1,11	576,4 ± 1,83
Sugars and organic acids content g/kg	532,90 ± 12,74	762,54 ± 6,42	625,23 ± 1,83

*DP3 – degree of polymerization (DP), which identify trisaccharides with three monomeric units.

Results also indicate that the organic acid content in extracts hydrolysed with the AL and NSP enzymes cocktail increases the organic acid content by 18,21 g/kg compared to control. It correlates with Chen et al. [7] evaluation on α-amylase and A. *sativa* flours. Results showed

increased total phenolic content, especially avenanthramide 2c, ferulic and gallic acids compared after α-amylase treatment of 60min at 60 ºC.

CONCLUSIONS

Results indicate the significant role of enzymes incorporation in extraction methods. Fibers and starches were disturbed by releasing various lengths of saccharides and organic acids in an aqueous extract with cellulolytic and amylolytic enzymes. Additionally, extraction with mild extraction conditions and safe solvent were evaluated. Differentiation of monomeric sugars units indicates the structure of dietary fibers and sugars content of *A.sativa*, which includes xyloglucans, arabinoxylans, and mostly glucans and starches. Grain modification using enzymes-assisted extraction creates novel approaches for developing higher added-value products and comprehensive applications for green synthesis development.

Keywords: *Avena sativa*, enzymes-assisted extraction, fibers, sugars, *in vitro* digestion

REFERENCES

1. MORALES-POLANCO, E.; CAMPOS-VEGA, R.; GAYTÁN-MARTÍNEZ, M.; ENRIQUEZ, L.G.; LOARCA-PIÑA, G. Functional and Textural Properties of a Dehulled Oat (Avena Sativa L) and Pea (Pisum Sativum) Protein Isolate Cracker. *LWT - Food Science and Technology,* 2017, 86, P. 418–423.

2. ZHANG, Z.; YANG, P.; ZHAO, J. Ferulic Acid Mediates Prebiotic Responses of Cereal-Derived Arabinoxylans on Host Health. *Animal Nutrition,* 2021.

3. MIGKOS, T.; IOANNIDOU, G.; KARAPATSIA, A.; FLEVARIS, K.; CHATZIDOUKAS, C. Enzymatic Hydrolysis for the Systematic Production of Second-Generation Glucose from the Dual Polysaccharide Reserves of an Anti-Pollutant Plant. *Bioresource Technology,* 2021, Vol. 340, 125711,

4. CRUZ-CASAS, D. E.; AGUILAR, C. N.; ASCACIO-VALDÉS, J. A.; RODRÍGUEZ-HERRERA, R.; CHÁVEZ-GONZÁLEZ, M. L.; FLORES-GALLEGOS, A. C. Enzymatic Hydrolysis and Microbial Fermentation: The Most Favorable Biotechnological Methods for the Release of Bioactive Peptides. *Food Chemistry: Molecular Sciences,* 2021, Vol. 3, 100047.

5. BALCIUNAITIENE, A.; VISKELIS, P.; VISKELIS, J.; STREIMIKYTE, P.; LIAUDANSKAS, M.; BARTKIENE, E.; ZAVISTANAVICIUTE, P.; ZOKAITYTE, E.; STARKUTE, V.; RUZAUSKAS, M.; LELE V. Green Synthesis of Silver Nanoparticles Using Extract of Artemisia Absinthium L., Humulus Lupulus L. and Thymus Vulgaris L., Physico-Chemical Characterization, Antimicrobial and Antioxidant Activity. *Process*, 2021, Vol. 9, 1304.

6. MINEKUS, M.; ALMINGER, M.; ALVITO P.; BALANCE, S.; BOHN, T.; BOURLIEU, C.; CARRIÈRE, F.; BOUTROU, R.; CORREDIG, M.; DUPONT, D.; DUFOUR, C.; EGGER, L.; GOLDING, M.; KARAKAYA, S.; KIRKHUS, B.; LE FEUNTEUN, S.; LESMES, U.; MACIERZANKA, A.; MACKIE, A.; MARZE, S.; MCCLEMENTS, D.J.; MÉNARD, O.; RECIO, I.; SANTOS, C. N.; SINGH, R. P.; VEGARUD, G. E.; WICKHAM, M. S.; WEITSCHIES, W.; BRODKORB, A. A standardised static in vitro digestion method suitable for food - an international consensus. *Food Funct.,* 2014, Vol. 5, No. 6, P. 1113-1124.

7. CHEN, D.; SHI, J.; HU, H.; DU, S. Alpha-amylase treatment increases extractable phenolics and antioxidant capacity of oat (*Avena Nuda* L.) flours. *Journal of Cereal Science*, 2015, Vol. 65, P. 60-66

BIOREFINING OF CHERRY POMACE INTO VALUABLE NUTRIENTS BY USING SUPERCRITICAL FLUID AND PRESSURIZED LIQUID EXTRACTIONS

L. Tamkutė*, V. Morkūnienė, A. Pukalskas, M. Pukalskienė, P. R. Venskutonis
Kaunas University of Technology
Radvilėnų pl. 19, Kaunas – Lithuania
laura.tamkute@gmail.com

EXTENDED ABSTRACT

OVERVIEW

Two *Prunus* species avium and cerasus are globally traded, which is called sweet (*Prunus avium*) and sour (*Prunus cerasus*) cherries. Cherries are from the *Prunus* genus (*Eucerasus* Section) and the *Amygdyloideae* subfamily of *Rosaceae* [1]. In recent years, sour cherry has been a very popular fruit in the world. It is characterized by a sour taste, juiciness, colour, which is changing from light to dark red, and a specific aroma. The health benefits of cherries are known for ages. Consumption of cherries has a positive effect on prevention of cardiovascular, Alzheimer's and inflammatory diseases, improve appetite and lower blood pressure. All these beneficial advantages of sour cherries are due to high content of bioactives. These fruits are rich in various phytochemicals such as anthocyanins (cyanidin 3-glucosylrutinoside, cyanidin 3-rutinoside, cyanidin 3-sophoroside, cyanidin 3-glucoside etc.), polyphenols (3-caffeoylquinic, 5-caffeoylquinic and p-coumaric acids; catechin and epicatechin derivatives; glycosides of quercetin and kaempferol), carotenoids, some lipophilic compounds etc [2]. Today, cherries are consumed as fresh fruits or used for production of wine, juice, jam, they can be dried or processed into other products. Pressing cherry juice generates large amounts of pomace, most of which currently are discarded as a waste. Therefore, there is an urgent need of cherry pomace valorisation studies for their conversion into higher added value ingredients. The aim of this work was to develop separation technology for producing various nutrients (products rich in bioactive components) from cherry pomace using biorefining and green extraction concepts, as well as characterization of obtained extracts.

METHODS

Dried cherry pomace was fractionated by different sieves into 6 different fractions, ground in a centrifugal high-speed mill using a 0.5 mm sieve and stored in the hermetically closed glass jars in dark, dry and cool room (<18 °C). The chemical composition of ground cherry pomace fractions was analysed according to the methods established by the Association of Official Analytical Chemists. Pomace first of all was defatted by supercritical fluid extraction with carbon dioxide (SFE-CO_2) using 45 MPa pressure and 53°C temperature [3]. The lipophilic extracts were analysed by different methods. Triacylglycerols (TAGs), sterols and tocopherols content were analysed by ultra performance liquid chromatography (UPLC), while fatty acids composition was determined by gas chromatography (GC). Total carotenoids content was measured by spectrophotometric method. Defatted pomace was further extracted by pressurized liquid extraction (PLE) with mixture of ethanol and water (70:30). Antioxidant activity of

different fractions polar extracts was evaluated by using different *in vitro* antioxidant capacity assays: the ABTS assay, which measures the relative ability of antioxidants to scavenge the ABTS, as compared with a Trolox standard; the Oxygen Radical Absorbance Capacity (ORAC) assay, which measures a fluorescent signal from a probe that is quenched in the presence of Reactive Oxygen Species (ROS) and added antioxidant absorbs the generated ROS. Total phenol content (TPC) was measured by *Folin-Ciocalteu* method. The anthocyanins composition of polar extracts was analysed by ultra performance liquid chromatography (UPLC). Proanthocyanidins content in extracts was measured by spectrophotometric method.

RESULTS

Proximate analysis of cherry pomace was performed before the application of supercritical fluid extraction with carbon dioxide (SFE-CO_2) and highly depends on the primary composition of every fraction. The crude protein content varied from 9.71% to 16.41%. The highest protein content was found in 5F (16.41%), while the lowest in 3F (9.71%). The fat content of all the samples ranged between 5.04% (3F) and 12.16% (5F). Lipids were isolated by supercritical fluid extraction with carbon dioxide (SFE-CO_2). Thus, the highest extract yield (8.69%) was obtained from 5F. In other fractions except the 2F, the extract yield was similar from 3.38% to 3.94%. Linoleic, oleic and palmitic acids were major compounds in extracted triacylglycerols. The concentration of carotenoids was higher in CO_2 than in Soxhlet extracts, 1.22-2.56 and 0.56-1.93 mg β-carotene/g, respectively. Consequently, SFE-CO_2, as a green extraction method, may be recommended for the recovery of lipophilic compounds from cherry pomace. PLE-EtOH/H_2O parameters were optimized by response surface methodology for obtaining the highest extract yields and for recovery of proanthocyanidins from pomace residues after SFE-CO_2. The highest yield (29.64%) and recovery of proanthocyanidins (170.2 mg/g dw) was achieved at 120 °C, using 3 extraction cycles, 10 min each. UPLC-MS/MS results indicated that among 4 quantified anthocyanins, cyanidin-3-O-glucosyl-rutinoside was the major constituent, followed by cyanidin-3-O-rutinoside (16.3 and 15.9 mg CGE/100 g dw, respectively). The extracts obtained by different extraction methods were characterized by their antioxidant potential. Thus all measured values for lipophilic fractions were rather low, while PLE-EtOH/H_2O recovered the majority of polar polyphenolic antioxidants. PLE-EtOH/H_2O extracts demonstrated higher TPC, ORAC and ABTS•+-scavenging than CO_2 extracts.

CONCLUSIONS

In conclusion, the proposed biorefining scheme of cherry pomace utilizing green and modern extraction techniques may serve as a platform for producing various functional ingredients for foods and nutraceuticals.

Keywords: cherry pomace, supercritical fluid extraction, pressurized liquid extraction

REFERENCES

1. HUMMER, K.E.; JANICK, J. *Rosaceae: Taxonomy, economic importance, genomics.* FOLTA, K.M., GARDINER, S.E. (Eds.), *Genetics and Genomics of Rosaceae, plant genetics and genomics*: Crops and models 6, Springer-Verlag, New York, 2009, P. 1-17, ISBN 978-0-387-77490-9.

2. DAMARA, I.; EKSI, A. Antioxidant capacity and anthocyanin profile of sour cherry (*Prunus cerasus* L.) juice. *Food Chemistry,* 2012, Vol. 135, Issue 4, P. 2910-2914.

3. TAMKUTĖ, L.; LIEPUONIŪTĖ, R.; PUKALSKIENĖ, M.; VENSKUTONIS, R. Recovery of valuable lipophilic and polyphenolic fractions from cranberry pomace by consecutive supercritical CO_2 and pressurized liquid extraction. *Journal of Supercritical Fluids*. 2020, Vol. 159.

INVESTIGATION OF THE EFFECT OF OHMIC HEATING ASSISTED EVAPORATION ON COLOR IN APPLE JUICE PRODUCTION

A. Goksu
Munzur University
Aktuluk, 62000 – Turkey
+905078903502
aligoksu58@hotmail.com

E. Karakavuk
Munzur University
Aktuluk, 62000 – Turkey
+905542906996
ekarakavuk@hotmail.com

S. Sabanci
Munzur University
Aktuluk, 62000 – Turkey
+905448844321
serdalsabanci@hotmail.com

ABSTRACT

In this study, color changes of apple juice concentrates obtained by ohmic heating assisted evaporation and traditional method at 13, 15 and 17 V cm^{-1} voltage gradients were investigated. Under atmospheric conditions, apple juices were concentrated from 15% to 50% total soluable solid content values. The L* value was determined as 22.41 before the process and the brightness decreased significantly under all extraction conditions. The a* value was determined as -1.43 in clear apple juice, 1.9 in apple concentrate obtained by the traditional method, and 0.43, 0.75, and 0.71 in the ohmic system for voltage gradients of 17, 15 and 13 V cm^{-1}, respectively.

When the b* values analyzed, a decrease occurred with the concentration process and the highest decrease was detected in traditional concentration process ($p<0,05$). The ΔE value is a value that shows the total color changes of the product, and it is known that the color change is more as the value increases. In the study, it was determined that the ohmic assisted evaporation affected the product color less than the traditional method.

Keyword: Apple juice, Ohmic Concentration, Color Properties

OVERVIEW

The concentration process is preferred in the food industry in order to consume fruit products or produce alternative fruit products throughout the year. The process is achieved by evaporating the water from the product. In this way, while the volume of the product is reduced, the storage cost is decreased and a microbially safer product is obtained. However, undesirable

component formation and quality losses occur in thermal concentration processes. Therefore, the researchers focused on alternative heating applications instead of the traditional evaporation process.

Ohmic heating process (joule or electrical resistance heating) is one of the alternative heating methods. This method is based on the principle of heating by passing an alternating current through the product between the two electrodes [1]. In this way, the product is heated quickly and homogeneously, and the ohmic system is also a highly efficient technique. In the literature, Ohmic heating process has been used in studies such as extraction [2], distillation [1,3], thawing [4], cooking [5], pasteurization [6], etc.

The aim of the study presented in the paper is to concentrate freshly squeezed apple juice which had 15% water total soluble solid content (TSSC) at 3 different voltage gradients (V cm-1) up to 50±1.0% TSSC and compare its color properties with apple juice obtained by the traditional method.

METHODS

The apple used in the study was purchased from a local market and subjected to sorting, washing, squeezing, and clarification processes, respectively. Apple juices were obtained by squeezing the apples through these processes with a whole fruit juicer (Philips, HR1861). Clarification was carried out according to the method specified in Tulek 2006 [7]. This process was done as follows: depectinization with 1 ml/L pectinase (Tito, Turkey) and 1 ml L^{-1} α-amylase (Tito, Turkey) after filtration and clarification were carried out with 1 gL^{-1} gelatin (Merck, Germany) – 2.5 g L^{-1} bentonite (Sigma Aldrich, Germany). Samples were then stored in 500 ml containers at -24 °C until analysis moment. Ohmic heating assisted evaporation process consists of a computer, test cell (Dimensions: 90×100×60 mm), custom designed microprocessor, T-type thermo-couple, adjustable power supply and electrodes (Dimensions: 1×60×150 mm). The ohmic and traditional system used in the concentration of apple juice is given in Fig. 1. Evaporation was carried out at 3 different voltage gradients (13, 15 and 17 V cm-1) and the juice samples were concentrated from 15% to 50±1.0% TSSC content. The temperature, voltage and current values measured in the system were recorded by the processor at 1 second intervals.
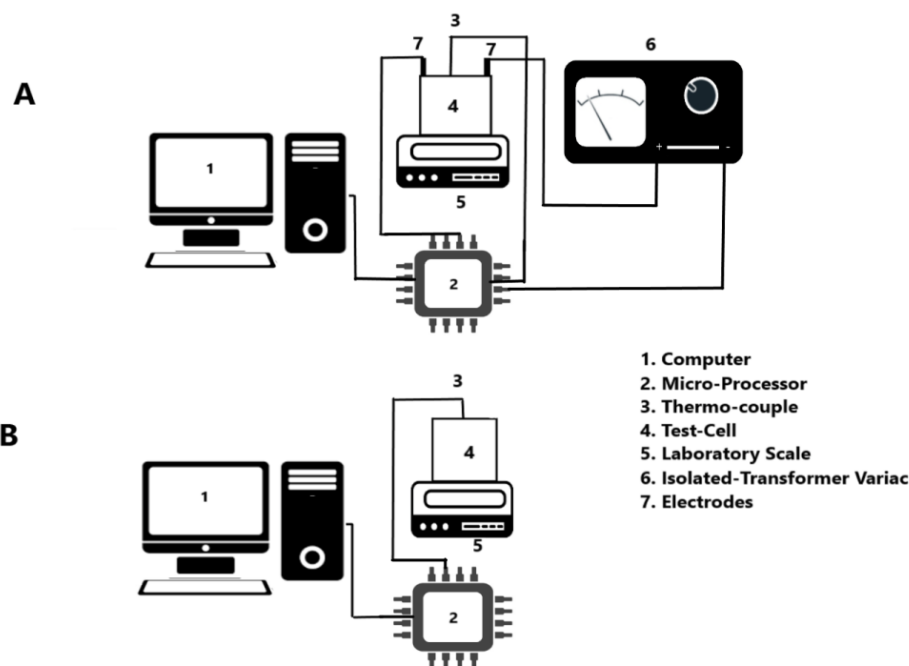
Fig. 6. The schematic representation of the evaporation system; A: Ohmic
Heating, B: Traditional Heating System

The TSSC values and the colour measurement of the clear apple juice were measured with a Temperature Compensation featured digital refractometer (HI96801, Hanna, Romania), and a digital colour measuring device (Cr-400, Konica Minolta, Japan), respectively. For Colour Evaluation, L*, a* and b* values were measured, and the total colour difference was determined by ΔE (equation 1).

$$\Delta E = \sqrt{(L_0 - L_i)^2 + (a_0 - a_i)^2 + (b_0 - b_i)^2},$$

(9)

here, L* values indicate the degree of lightness from black to white (range: 0–100). b* values represent the yellowness or blueness (range: -127 to +127); a* values represent the redness or greenness (range: -127 to +127).

In order to determine the effect of voltage gradients, one-way analysis of variance Duncan test was applied in SPSS 25 program. The confidence interval was chosen as 95% and all procedures were repeated 3 times.

RESULTS

The colour values of fresh, clear and evaporated apple juices are given in Table 1. L*, a*, and b* values for clear apple juice were measured as 22.4±0.0, -0.41±0.1, and 5.7±0.0, respectively. As a result of the evaporation process, L* and b* values decreased, but a* values increased ($p<0.05$). The most colour change was observed in the fruit juice obtained by the traditional method, and the total colour difference values varied between 5.13 and 2.53 ($p<0.05$). As a result, when the colour values of the concentrated samples obtained with the ohmic heating system were examined, this method was an effective method for preserving the colours.

Table 6 The changes in the color properties during evaporation for different methods and their process conditions

Name of standards/ Conditions	17 (V cm^{-1})	15 (V cm^{-1})	13 (V cm^{-1})	Traditional	Clear Juice
L*	21.52±1.01[b]	21.19±0.45[b]	21.17±0.18[b]	19,34±0.34[c]	22.41±0.02[a]
a*	0.43±0.23[b]	0.75±0.46[b]	0.71±0.43[b]	1.9±0.07[a]	-0.41±0.12[c]
b*	5.21±0.01[b]	5.05±0.37[d]	5,24±0.11[cd]	5.05±0.04[a]	5,70±0.03[bc]
ΔE	1,83±0,02[a]	1,50±0,16[b]	1,83±0,25[b]	3,90±0,25[a]	

Different letters ([a] to [d]) within rows are significantly different ($p < 0.05$).

The L* value indicates the brightness of the product and as the value increases, the brightness of the product increases. Burdurlu and Karadeniz (2003) stated that the L* value decreased when the TSSC value and the storage time increased in the concentration process at 50 ˚C [8]. Sabancı et al. (2019) concentrated the pomegranate juice under vacuum with a conventional and ohmic evaporator and obtained the highest L* value at 10 V cm-1 ohmic evaporation. The a* value indicates the redness and greenness of the product, and as +a* increases, the redness increases, and as -a* increases, the greenness value increases [9]. Bozkır and Baysal (2017), in their study with apple juice, determined a* values to be 5.12 for unprocessed apple juice, and 4.89, 3.79 and 5.03 for concentrates in rotary, rising film and vacuum microwave evaporator, respectively [10]. Tunç et al (2021) produced molasses with a vacuum ohmic assisted evaporator and stated that the a* value increased with the application of the process that statement is similar to the data obtained in this study [11]. b* indicates yellowness and blueness; As +b* values increase, yellowness increases, whereas as -b* increases, blueness increases. Bozkır and Baysal (2017) determined the b* value in unprocessed apple juice before the process as 8.01, after the applied process processes, they were measured as 7.2, 6.31 and 7.35 in the rotary, rising film, and vacuum microwave evaporator, respectively, and they found that it decreased compared to the value before the process [10]. Tunç et al (2021) produced molasses in a vacuum ohmic assisted evaporator and similarly stated that the b* value decreased compared to the unprocessed product [11]. ΔE indicates the color difference of the product. Tunç et al (2021) determined that the ΔE value of the product obtained in traditional vacuum evaporation was higher than the ΔE value of the products obtained in ohmic vacuum evaporation [11].

ACKNOWLEDGES

CONCLIUSIONS

As a result, apple juice was successfully concentrated using ohmic heating assisted evaporation process. It has been determined that the colour values of apple juice samples obtained by ohmic heating assisted evaporation process are better preserved than the traditional method. It is thought that the ohmic heating assisted evaporation process can be used in industry as an alternative method.

REFERENCES

1. ÇILINGIR, S.; GOKSU, A.; SABANCI S. Production of pectin from lemon peel powder using ohmic heating-assisted extraction process, *Food and bioprocess technology,* 2021, Vol.14, P. 1-12.

2. SABANC, I .S.; ÇEVIK, M.; GÖKSU, A. Investigation of time effect on pectin production from citrus wastes with ohmic heating assisted extraction process. *Journal of food process engineering.* 2021, Vol. 44, No. e13689.

3. GAVAHIAN, M.; FARAHNAKY, A.; SASTRY, S. Ohmic-assisted hydrodistillation: a novel method for ethanol distillation, *Food and bioproducts processing.* 2016, Vol. 98, P. 44-49.

4. CEVIK, M.; ICIER, F. Characterization of viscoelastic properties of minced beef meat thawed by ohmic and conventional methods, *Food science and technology international*, 2020, Vol. 26, P. 277-290.

5. BOZKURT, H.; ICIER, F. Ohmic cooking of ground beef: effects on quality, *Journal of food engineering,* 2010, Vol. 96, P. 481-490.

6. ACHIR, N.; DHUIQUE-MAYER, C.; HADJAL, T.; MADANI, K.; PAIN, JP.; DORNIER, M. Pasteurization of citrus juices with ohmic heating to preserve the carotenoid profile, *Innovative food science & emerging technologies,* 2016, Vol. 33, P. 397-404.

7. TULEK, Y.; YILMAZ, S. Use of clarifying agents and ultra filter to decrease fumaric acid, hmf and increase clarity of apple juice, *Journal of food quality,* 2006, Vol. 29(3), P. 216-228.

8. BURDURLU, H.S.; KARADENIZ, F. Effect of storage on nonenzymatic browning of apple juice concentrates, *Food chemistry*, 2003, Vol. 80, P. 91-7.

9. SABANCI, S.; CEVIK, M.; COKGEZME, O.F.; YILDIZ, H.; ICIER, F. Quality characteristics of pomegranate juice concentrates produced by ohmic heating assisted vacuum evaporation, *Journal of the Science of Food and Agriculture,* 2019, Vol. 99, P. 2589-95.

10. BOZKIR, H.; BAYSAL, T. Concentration of apple juice using a vacuum microwave evaporator as a novel technique: Determination of quality characteristics, *Journal of Food Process Engineering*, 2017, Vol. 40, p. e12535.

11. TUNÇ, M.T.; AKDOĞAN, A.; BATACI, C.; KAYA, Z.; ODABAŞ, H. İ. Production of grape pekmez by Ohmic heating-assisted vacuum evaporation, *Food science and technology international*, 2022, Vol. 28, P. 72-84.

III.5. Plant biology and physiology

EFFECT OF ANTIBIOTIC TIMENTIN ON CHANGES IN PROTEOME AND ROS ACCUMULATION IN *NICOTIANA TABACUM* L. SHOOTS *IN VITRO*

E. Andriūnaitė, I. Tamošiūnė, P. Haimi, D. Baniulis
Institute of Horticulture, Lithuanian Research Centre for Agriculture and Forestry
Kaunas str. 30, 54333 Babtai, Kaunas distr. – Lithuania
+370 37 55 52 53
elena.andriunaite@lammc.lt

EXTENDED ABSTRACT

OVERVIEW

In vitro plant culture is a biotechnological tool that is commonly used for plant micropropagation, for genetic resources conservation, or for genetic manipulation. Antibiotics are commonly used to inhibit/prevent *in vitro* micro-organism contamination or during *Agrobacterium*-mediated DNA transfer to act as a control agent for bacterial growth [1]. However, long-term use of antibiotics can become phytotoxic, especially using higher antibiotic concentrations that are required to effectively control contamination [2]. The low phytotoxic effect of Timentin on tobacco tissues *in vitro* has been described [3]. However, the impact of long-term use of antibiotic is not well understood and, in particular, changes in the patterns of protein expression in plant explants have not been considered. Therefore, the aim of this study was to assess the long-term effect of Timentin on cultivated *in vitro* tobacco (*Nicotiana tabacum* L.) shoots. As plant response to a stressor is a complex process that usually involves a variety of physiological, cellular, and molecular changes. The analysis of the accumulation of reactive oxygen species (ROS), such as superoxide anion ($O_2^{\bullet-}$) and hydrogen peroxide (H_2O_2) in tobacco shoot tissues, were assessed. Moreover, proteomic analysis was used to establish the molecular basis of the antibiotic-induced decline of the adaptive capacity of the tobacco shoots.

METHODS

Cultivated tobacco (*Nicotiana tabacum* L.) shoots *in vitro* were grown as described by Andriūnaitė et al. [4]. The shoots of the second experimental group of post-antibiotic treatment were maintained on a nutritional medium supplemented with Timentin (ticarcillin/clavulanate) at 250 mg/L concentration (at least for 6 months). Following the antibiotic treatment, the shoots were transferred to the nutritional medium without antibiotics under the same conditions as control shoots and maintained for at least one culture passage. For analysis, samples were collected 7 days after shoot transfer to fresh medium. The accumulation of $O_2^{\bullet-}$ was investigated using Nitro blue tetrazolium (NBT) and H_2O_2 production was detected using a 3,3′ - Diaminobenzidine (DAB) staining [5]. Proteins were prepared using phenol extraction and ammonium acetate precipitation and analyzed according Tamošiūnė et al. [5]. Statistically significant differences in protein abundance between the experimental groups using four biological repeats. A threshold value of at least a 1.5-fold difference in protein abundance was used, peptides were analyzed by liquid chromatography-tandem mass spectrometry fingerprinting and gene ontology (GO) terms were assigned.

RESULTS

The superoxide $O_2^{\bullet-}$ and hydrogen peroxide H_2O_2 accumulation was detected in tobacco shoots *in vitro* by NBT and DAB staining, respectively. The NBT staining revealed that $O_2^{\bullet-}$ accumulates in leaves and mechanically damaged tissues of control and antibiotic-treated tobacco shoots. Timentin treatment had resulted in a 1.3-fold increase in $O_2^{\bullet-}$ accumulative concentration in shoot tissues. Meanwhile, no significant differences in H_2O_2 accumulation were detected in tobacco shoots grown with or without antibiotic. To assess protein expression differences associated with the enduring effect of Timentin, the proteome of the post-antibiotic treatment experimental group was compared to control shoots at 7 days after transfer to a fresh medium where the largest difference in MDA accumulation was detected between the two experimental groups.

Protein abundances hierarchical cluster analysis revealed 10 differentially expressed proteoforms in tobacco shoots, 4 proteoforms were significantly upregulated, and 6 were downregulated (from 1.5 to 2.3-fold). Peptide fingerprinting of trypsin digested proteins using liquid chromatography-tandem mass spectrometry (LC-MS/MS) fingerprinting identified 6 unique proteins and were associated with 18 GO terms that were summarized as 12 distinct biological processes based on semantic similarity. The GO analysis revealed that identified proteins are linked to photosynthesis, metabolism and stress response. Several assigned GO terms were related to cell activity involved in photosynthesis. This included 3 GO terms, photosystem II assembly (GO:0010207) and stabilization (GO:0042549), as well as photorespiration (GO:0009853) proteins. In addition, a considerable part of assigned GO terms was related to cell metabolism. This includes phosphorylation (GO:0016310), thiamine (GO:0006772) and carbohydrate (GO:0005975) metabolic process as well as oxazole or thiazole (GO:0018131) biosynthetic process proteins that have been shown to take part in plant response to stress. Another group of GO terms was connected to a stress response function, such as defence response (GO:0006952) GO term. Indirect involvement in the defence response was seen in by changes in response to cadmium ion (GO:0046686), cellular copper ion homeostasis (GO:0006878) and copper ion transport (GO:0006825) protein expression.

CONCLUSIONS

Our study found that tobacco shoots grown in the nutritional medium supplemented with Timentin had increased detectable $O_2^{\bullet-}$ levels compared to the control group. The increased accumulation of the $O_2^{\bullet-}$ or derived ROS could lead to an increase in cell membrane injury after prolonged exposure to the antibiotic which could eventually lead to altered gene expression or cell death. Proteome analysis revealed numerous differences in protein abundance, mostly stimulating the expression of proteins involved in photosynthetic processes. The results of ROS accumulation and protein expression analysis provide an original insight into the molecular basis of plant response upon the long-term effect of antibiotic. These findings pave the way for further studies about the effect on plant culture *in vitro* in response to antibiotic-induced stress.

Keywords: antibiotic, *Nicotiana tabacum*, stress, proteome, ROS.

REFERENCES

1. MORENO-VÁZQUEZ, S.; LARRAÑAGA, N.; UBERHUAGA, E.C.; BRAGA, E.J.B.; PÉREZ-RUÍZ, C. Bacterial contamination of in vitro plant cultures: confounding effects on somaclonal variation and detection of contamination in plant tissues. *Plant Cell, Tissue and Organ Culture (PCTOC)* 2014, *119*, 533-541, doi:10.1007/s11240-014-0553-x.

2. TANG, H.; REN, Z.; KRCZAL, G. An evaluation of antibiotics for the elimination of Agrobacterium tumefaciens from walnut somatic embryos and for the effects on the proliferation of somatic embryos and regeneration of transgenic plants. *Plant Cell Reports* 2000, *19*, 881-887, doi:10.1007/s002990000201.

3. CHENG, Z.M.; SCHNURR, J.A.; KAPAUN, J.A. Timentin as an alternative antibiotic for suppression of *Agrobacterium tumefaciens* in genetic transformation. *Plant Cell Reports* 1998, *17*, 646-649, doi:10.1007/s002990050458.

4. ANDRIŪNAITĖ, E.; TAMOŠIŪNĖ, I.; ALEKSANDRAVIČIŪTĖ, M.; GELVONAUSKIENĖ, D.; VINSKIENĖ, J.; RUGIENIUS, R.; BANIULIS, D. Stimulation of *Nicotiana tabacum* L. *in vitro* shoot growth by endophytic *Bacillus cereus* group bacteria. *Microorganisms* 2021, *9*, 1893, doi:10.3390/microorganisms9091893.

5. TAMOSIUNE, I.; STANIENE, G.; HAIMI, P.; STANYS, V.; RUGIENIUS, R.; BANIULIS, D. Endophytic *Bacillus* and *Pseudomonas* spp. modulate apple shoot growth, cellular redox balance, and protein expression under *in vitro* conditions. *Frontiers in Plant Science* 2018, *9*, 889, doi:10.3389/fpls.2018.00889.

PHYTOTOXIC STRESS OF LEAD TO THREE MEDICINAL PLANTS GERMINATION AND SEEDLINGS DEVELOPMENT

M. Apostol[*], R. M. Hlihor[*], L. Hagiu Zaleschi, I. M. Simion
"Ion Ionescu de la Brad" Iasi University of Life Sciences, Faculty of Horticulture,
Department of Horticultural Technologies,
3 Mihail Sadoveanu Alley,
700490 Iasi – Romania
mariabrinza2007@yahoo.com; raluca.hlihor@uaiasi.ro

EXTENDED ABSTRACT

OVERVIEW

Heavy metals have become a global problem as soil contamination is the cause of both the loss of agricultural production and several dangerous health effects as they are known to enter the food chain. Lead, the most common pollutant of the heavy metals in the environment [1], ranks second among all hazardous heavy metals [2] and is considered to be a very toxic metal for plants and other living organisms, including humans [3]. Plants absorb lead and accumulate metal in the roots, stems, leaves, and sometimes even in seeds affecting the growth and productivity of plants; the extent of the effects depends on the plant species. Some herbs with medicinal properties exhibit good abilities to absorb heavy metals and thus they are considered to be a good choice for phytoremediation when these species are grown for by-products (e.g. essential oils). These aspects provide us the context to compare the phytosociological effects of Pb(II) on medicinal plants represented by the species basil (*Ocimum basilicum* L.), lavender (*Lavandula angustifolia* L.), and oregano (*Origanum vulgare* L.).

METHODS

The studies carried out in this paper include investigations in laboratory conditions within the Horticultural Research Center from "Ion Ionescu de la Brad" Iasi University of Life Sciences, Romania, regarding the process of germination and growth of some species of medicinal plants under the stress generated by lead. The purpose of this research focuses on a comparative study on the phytotoxicity generated by Pb(II) on three selected species, basil (cultivar 'Aromat de Buzau') obtained from Vegetable Research Development Station, Buzau, Romania, lavender (cultivar 'Hidcote Blue') and oregano (cultivar 'Aureus'), both obtained from 'Agrosem Impex' Targu Mures, Romania. Eleven concentrations of Pb(II) (5, 10, 20, 30, 50, 70, 100, 150, 200, 250 and 500 mg/L solution) were applied to selected medicinal plants seeds. In parallel, control samples were prepared with sterile distilled water. Ten seeds previously selected and sterilized were placed in Petri plates lined with filter paper and wetted with 3 mL of Pb(II) sterile solutions prepared from 1000 mg/L stock solution. At every 3 days, the seeds were wetted with sterile deionized water. All tests were performed in a plant growth chamber, at a temperature of $20 \pm 1\,°C$ for 8 hours (darkness) and $22 \pm 1\,°C$ for 16 hours (light). The seeds began to germinate after 48-72 hours, the minimum radicle length emergence at 2 mm being considered as the germination count. After the required days for the germination process (14 days for basil and 21 days for lavender and oregano), we determined the germination degree, the relative

germination index, the vigour index of the seeds/seedlings, toxicity index, tolerance index, length of radicle, hypocotyl and leaves. The results obtained were compared with the control sample for each specie used in the study. The average of the 3 replicates for each specie used was determined and the data are presented as ± standard error of the mean, the error being less than 5%.

RESULTS

Regarding seeds germination, Pb (II) presence shows very similar effects in the case of basil and lavender, varying between 50% and 90% germination degree. The highest inhibition on seeds germination was observed for oregano, the germination varying between 40% and 83%. However, under stress conditions caused by the presence of Pb (II) at concentrations between 5 mg/L and 30 mg/L, the lavender seeds showed the highest degree of germination (90%-100%) as indicated in Fig. 1. In all species, the development and growth of the seedlings decrease with the increase of the contamination levels of Pb (II), consequently, germs no longer develop and predict a decrease in the length of the plants (Fig. 2). We observed that at concentrations exceeding 100 mg/L Pb (II) for all three species, the seedlings either no longer develop or develop abnormally (data not shown).
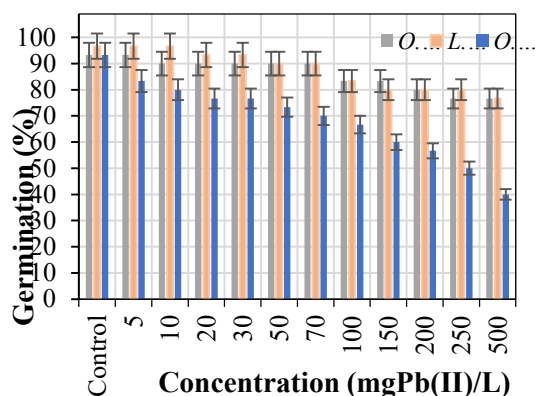
Fig. 1. Influence of lead stress conditions on seeds germination
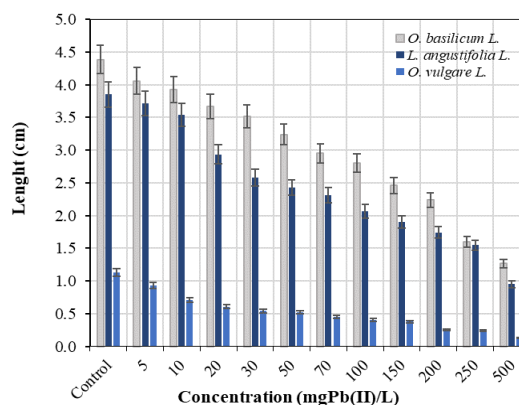
Fig. 2. Influence of lead stress conditions on seedlings growth

CONCLUSIONS

For all the tested medicinal plants species, the seeds germination percentage was affected by increasing Pb (II) concentration from 5 mg/L to 500 mg/L. The lowest percentage of germination within the studied concentrations ranges was obtained for oregano 'Aureus' (40%) and the highest percentage of germination for the lavender 'Hidcote Blue' cultivar (90%). A decrease in seedlings size was also observed along with increasing lead concentrations, affecting in a higher degree the oregano 'Aureus' seedlings. The toxicity index values increase with the increase of metal concentration in solution for the studied species in the following order, oregano > lavender > basil, and looking in particular at plant components, radicle > leaves > hypocotyl.

Keywords: Heavy metals, lead, medicinal plants, seed germination, seedling development

REFERENCES

1. LAMHAMDI, M.; BAKRIM, A.; AARAB, A.; LAFONT, R.; SAYAH, F. Lead phytotoxicity on wheat (*Triticum aestivum* L.) seed germination and seedlings growth. *Comptes Rendus Biologies*, 2011, Vol. 334, No. 2, P. 118-126.

2. KUMAR, A.; PRASAD, M.; SYTAR, O. Lead toxicity, defense strategies and associated indicative biomarkers in *Talinum triangulare* grown hydroponically. *Chemosphere*, 2012, Vol. 89, No. 9, P. 1056-1065.

3. KAYA, A. R. Effects of lead phytotoxicity on different peanut varieties germination and seedling growth. *Applied Ecology and Environmental Research*, 2020, Vol. 18. No. 5, P. 6725-6738.

A COMPARISON OF THE TOXICITY EFFECTS CAUSED BY HEAVY METALS TO LAVENDER GERMINATION AND SEEDLINGS DEVELOPMENT

L. Hagiu Zaleschi[1*], R. M. Hlihor[1*], I. M. Simion[1], M. Apostol[1], D. M. Asiminicesei[1,2]
[1]" Ion Ionescu de la Brad" Iasi University of Life Sciences, Faculty of Horticulture,
Department of Horticultural Technologies,
3 Mihail Sadoveanu Alley,
700490 Iasi – Romania
laurazaleschi@uaiasi.ro; raluca.hlihor@uaiasi.ro

[2]"Gheorghe Asachi" Technical University of Iasi, "Cristofor Simionescu" Faculty of
Chemical Engineering and Environmental Protection, Department of Environmental
Engineering and Management,
73 Prof. Dr. Docent D. Mangeron Str., 700050 Iasi – Romania

EXTENDED ABSTRACT

OVERVIEW

Inorganic pollutants, such as heavy metals, are a category of pollutants of wide interest for risk studies because of the impacts they can have on the ecological receptors and on human health [1]. Environmental pollution through anthropogenic activities and the atmospheric deposition of heavy metals inevitably causes plant contamination [2]. Lavander is the most cultivated species for ornamental, medicinal and cosmetic purposes. It is widely used in French cuisine for its aroma and in alternative medicine for antioxidant, antimicrobial, antibacterial, anticonvulsant, antidepressant, sedative and calming properties [3]. The aim of the present study was to investigate and compare the effects posed by Pb(II), Cd(II) and Ni(II) treatments applied in single solutions, to the early growth of *Lavandula angustifolia* L. "Hidcote Blue" (lavender). The results are the basis of further investigations of heavy metals stress on lavender in soil.

METHODS

Our study is based on the assessment of plant stress indicators such as germination degree, tolerance, toxicity and vigour indexes for lavender seeds achieved by observing the seedlings development under 7 treatments with Pb(II) (PbCl$_2$), Cd(II) (CdCl$_2$) and Ni(II) (NiCl$_2$) with concentrations ranging from 5 mg/L to 100 mg/L. In parallel, control samples were prepared with sterile distilled water. Prior to the germination test, the seeds were surface-sterilized in 20% NaClO solution for 60 seconds and then rinsed with distilled sterile water for 4 times. Subsequently, a solution of 96% ethyl alcohol was applied for 60 seconds and then, the seeds were washed with distilled sterile water for 7 times. Ten sterilized seeds were placed in Petri plates lined with filter paper wetted with 3 mL of heavy metals sterile solutions previous prepared from stock solutions of 1000 mg/L. At every 3 days, the seeds were wetted with sterile deionized water. All tests were performed in an MRC PGI-550RH plant growth chamber, at a

temperature of 20 ± 1 ° C for 8 hours (darkness), 22 ± 1 ° C for 16 hours (light), a relative air humidity of about 80% and a luminous intensity of 8,000 lux. The lavender seeds began to germinate 48-72 hours after the start of the experiment. The germination process consists of opening the seeds and radicle sprouting of at least 2 mm. After the 21 days required for the germination process, the number of germinated seeds was assessed together with radicle, hypocotyl and leaves measurements. All the tests were made in triplicate. The average of the 3 replicates for each pollutant treatment was determined and the data are presented as ± standard error of the mean (±SEM).

RESULTS

The assessment of lavender seeds stress caused by heavy metals has shown that the germination degree is mostly affected by the presence of Ni(II) at a concentration of 100 mg/L. As the concentration of Pb(II), Cd(II) and Ni(II) increased, the germination degree of the tested seeds decreased up to 83.33%, 53.33% and 33.33%, respectively. (Fig. 1). The length of the seedlings also decreased with increasing metal concentration in solution up to 100 mg/L, following the order Pb (II)>Cd(II)>Ni(II). As resulted from our tests, in terms of seedlings elongation, the most toxic metal was Ni (II), the average length of lavender seedlings decreasing by 90.22% compared to the control sample. Small differences were recorded when Cd (II) was used, while Pb (II) showed the lowest degree of inhibition in the development of lavender seedlings (Fig. 2). Toxicity index, tolerance index and vigour index were also assessed (data not shown). The results showed that lavender seeds tolerate in a higher degree lead toxicity, compared with cadmium and nickel toxicity. We observed that lavender seedlings were more affected by Ni (II) presence in solution, decreasing the vigour index and tolerance index along with increasing nickel concentration up to 100 mg/L (data not shown).
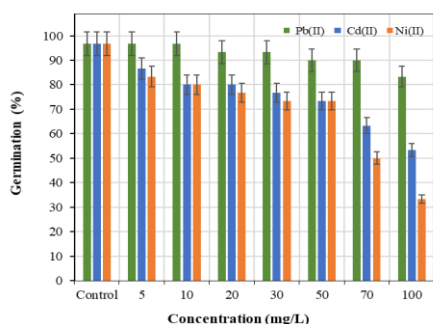
Fig. 1. Influence of heavy metal stress conditions on lavender seeds germination
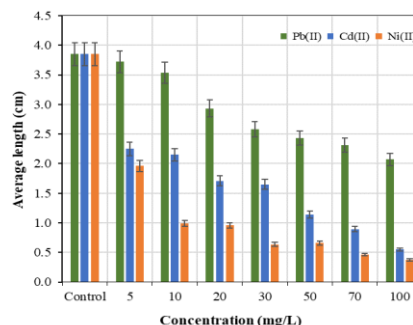
Fig. 2. Influence of heavy metal stress conditions on lavender seedlings growth

CONCLUSIONS

Our study shows that seeds germination and seedlings growth of *Lavandula angustifolia* "Hidcote Blue" were affected especially by the presence of Ni (II), their inhibition is represented mainly by the damage of the radicle system after a concentration of 10 mg/L. By increasing metals concentrations, all investigated parameters were highly affected, following the metal toxicity order Ni(II)>Cd(II)>Pb(II). We can summarize that the inhibition effects of *Lavandula angustifolia* "Hidcote Blue" seeds and seedlings depend on both metal type and applied treatment.

Keywords: contamination, heavy metals, medicinal plants, *Lavandula angustifolia* "Hidcote Blue", toxicity

REFERENCES

1. BRIFFA, J.; SINAGRA, E.; BLUNDELL, R. Heavy metal pollution in the environment and their toxicological effects on humans. *Heliyon*, 2020, Vol. 6, No. 9, P. e04691.

2. MASINDI, V.; and MUEDI, L. K. *Environmental Contamination by Heavy Metals*, Heavy Metals, 2018. Hosam El-Din M. Saleh and Refaat F. Aglan, IntechOpen, DOI: 10.5772/intechopen.76082. <https://www.intechopen.com/chapters/60680>.

3. MUNTEAN, L. S. Treatise of cultivated and spontaneous medicinal plants (in Romanian). Risoprint Publishing, 2007, Vol.1. ISBN 978-973-751-463-9.

ECOTOXICOLOGICAL RESPONSES OF BASIL (*OCIMUM BASILICUM* L.) TO SINGLE AND BINARY MIXTURE OF EAD AND CADMIUM

R. M. Hlihor[1*], L. Hagiu Zaleschi[1], M. Apostol[1], I. M. Simion[1], D. M. Asiminicesei[1,2]
[1]*"Ion Ionescu de la Brad" Iasi University of Life Sciences, Faculty of Horticulture,*
Department of Horticultural Technologies,
3 Mihail Sadoveanu Alley, 700490 Iasi – Romania
raluca.hlihor@uaiasi.ro

[2]*"Gheorghe Asachi" Technical University of Iasi, "Cristofor Simionescu" Faculty of*
Chemical Engineering and Environmental Protection, Department of Environmental
Engineering and Management,
73 Prof. Dr. Docent D. Mangeron Str., 700050 Iasi – Romania

EXTENDED ABSTRACT

OVERVIEW

Heavy metals are among the contaminants causing the most serious stress for plants and other living organisms. The toxicity of heavy metals in mixtures on plants has complex mutual interactions. The information provided by researches comprising of single metal contamination does not reflect the toxicity and stress levels caused to plants when multiple metals are present together in environmental compartments [1]. The cultivation of less stress-tolerant aromatic crops such as basil (*Ocimum basilicum* L.) in contaminated soils could be considered as a sustainable strategy for site remediation [2]. Given these aspects, this paper focuses on our preliminary findings related to the ecotoxicological effects of Pb (II) and Cd (II) in single and binary mixtures to basil. Based on the stress caused to seed germination, radicle, hypocotyl and leaves elongation, tolerance, toxicity and vigour indexes values, ecotoxicological indicators were determined. The results obtained suggested that basil seedlings have a higher tolerance to Pb (II) compared to Cd (II), while the binary mixture stimulates the growth of the radicle.

METHODS

Heavy metal treatments consisted of $PbCl_2$ and $CdCl_2$, in single and binary systems. Selected basil (*Ocimum basilicum* L. cultivar 'Aromat de Buzau') seeds were put into contact with heavy metals solutions to assess different parameters (radicle, hypocotyl and leaves length, germination, tolerance and toxicity indexes (%) and vigour index). The investigation was performed under laboratory conditions within the Horticultural Research Center from "Ion Ionescu de la Brad" Iasi University of Life Sciences, Romania. The cultivar was obtained from Vegetable Research Development Station, Buzau, Romania. The methodology was used in line with the OECD guidelines for testing of chemicals [3]. Prior to the germination test, selected basil seeds were surface-sterilized in 20% NaClO solution for 60 seconds and then rinsed with distilled sterile water 4 times. Subsequently, a solution of 96% ethyl alcohol was applied for 60 seconds and then, the seeds were washed with distilled sterile water for 7 times. 10 seeds of

basil were put in Petri plates and contaminated in the single system in 8 treatments with heavy metals from 5 mg/L to 100 mg/L and 1 treatment in the binary system (50 mg/L Pb(II) and 2.5 mg/L Cd(II)). Control sample was also used in both systems for comparison. To avoid water loss and seed fungal contamination, Petri plates were sealed with parafilm, then placed in a growth chamber at 22 ± °C, under a photoperiod of 16 h light/8 h dark. The number of germinated seeds was counted every day over a period of 14 days. The minimum radicle length emergence at 2 mm was considered as the germination count. All the experiments were carried out in triplicate and the data were expressed as ± standard error of the mean.

RESULTS

As can be seen in Fig. 1, in the case of stress caused by Pb(II) and Cd(II) in the single system, the most affected plant component is the radicle, its length decreasing with the increase of concentration of the pollutant from 5 mg/L to 100 mg/L, from 2.9 cm to 1.7 cm for Pb(II) (Fig. 1a) and, from 1.18 cm to 0.09 cm for Cd(II) (Fig. 1b), respectively. Compared to the control sample, where the radicle length is 3.03 cm, at the concentration of 5 mg/L its length decreases for Pb(II) by 4.29% and for Cd(II) by 61.05%. The same pattern could be observed in the case of 100 mg/L metal concentration, where the decrease in length is more visible, thus, the radicle length decreases in the case of Pb(II) by 43.89% and in the case of Cd(II) by 97.02%.

(a)   (b)
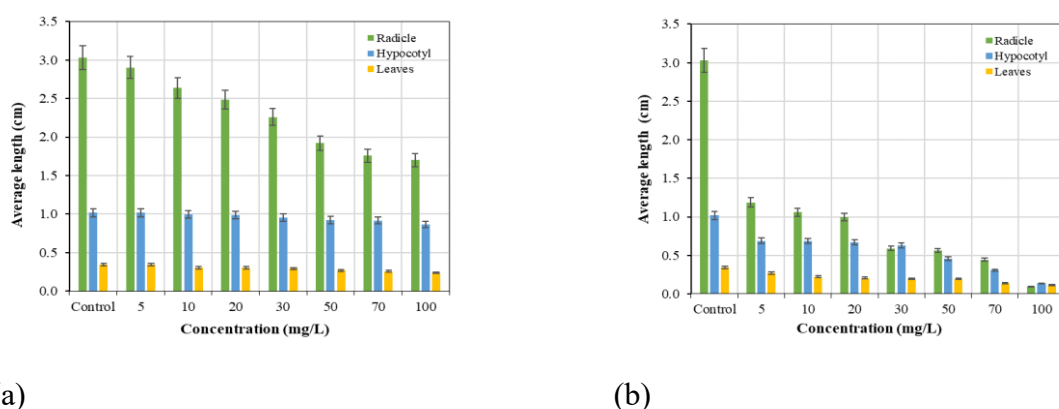
Fig. 1. Influence of Pb(II) (a) and Cd(II) (b) on the growth and early stage development of radicle, hypocotyl and leaves of basil seedlings

Results showed that Pb(II) and Cd(II) stress was mainly present in the radicle and hypocotyl and the seedlings of basil were visibly affected by the increase of metal concentration. In the binary mixture consisting of 50 mg/L Pb(II) and 2.5 mg/L Cd(II), we could observe that the toxicity index reached -1.65% for radicle, 30.49% for hypocotyl, and 39.22% for leaves. According to our data, the binary mixture shows an increase in the radicle system, slightly stimulating its growth.

CONCLUSIONS

Our findings show that under laboratory conditions basil leaves have increased tolerance to the toxicity of Pb(II) and Cd(II) applied in single treatments, compared to the radicle and hypocotyl. On the other side, when applied in binary mixture, the combined effect showed stress only to the hypocotyl and leaves, stimulating the growth of the radicle.

Keywords: ecotoxicological indicators, heavy metals, inhibition, *Ocimum basilicum* L., stress

REFERENCES

1. SHEN, X.; LI, R.; CHAI, M.; CHENG, S.; NIU, Z.; QIU, G. Y. Interactive effects of single, binary and trinary trace metals (lead, zinc and copper) on the physiological responses of Kandelia obovata seedlings. Environmental Geochemistry and Health, 2019, Vol. 41, No. 1, P. 135-148.

2. PANDEY, V. C.; RAI, A.; KORSTAD, J. Aromatic Crops in Phytoremediation: From Contaminated to Waste Dumpsites. In: Phytomanagement of Polluted Sites: Market Opportunities in Sustainable Phytoremediation, 2018, p. 255-275, ISBN 978-0-12-813912-7.

3. OECD/OCDE, OECD/OCDE 208: OECD GUIDELINES FOR THE TESTING OF CHEMICALS, Terrestrial Plant Test: Seedling Emergence and Seedling Growth Test, 2006.

COLD PLASMA-INDUCED CHANGES IN STEVIA REBAUDIANA SEED GERMINATION AND PHYTOHORMONE CONCENTRATION

A, Judickaitė,
Department of Biochemistry, Faculty of Natural Sciences
Vytautas Magnus University,
LT-44404 Kaunas – Lithuania
+37067404169
augustejud@gmail.com

K. Koga[1, 2], M. Shiratani[2]
[1]Department of Electronics,
Faculty of Information Science and Electrical Engineering Kyushu University
819-0395 Fukuoka – Japan
[2]Plasma-Bio Research Division,
Center for Novel Science Initiatives, National Institutes of Natural Sciences
105-0001, Tokyo – Japan

R. Žūkienė
Department of Biochemistry
Faculty of Natural Sciences
Vytautas Magnus University,
LT-44404 Kaunas – Lithuania

EXTENDED ABSTRACT

LITERATURE

Stevia rebaudiana is known as a plant on increased consumer demand and considered as natural source of sweeteners steviol glycosides (SGs) [1]; however, its sexual propagation is limited due to poor germination of seeds.

Cold plasma (CP) methods have been intensively explored in last decades and studies concluded that CP improves seed germination and yield of various crops [5]; and cultural seeds production [2-5]. Recently we have demonstrated for the first time [6] that pre-sowing treatment of stevia seeds with CP stimulates seed germination and SGs biosynthesis in plant. We have previously confirmed in various plants that CP stimulates germination by inducing complex changes in the molecular processes within the seed by increasing the ratio of gibberellins (GA, stimulating phytohormones) with abscisic acid (ABA, inhibiting phytohormone) [7]. In this study we are aiming to determine, how physical stressors, such as low pressure capacitively-coupled cold-plasma (CP), atmospheric pressure dielectric barrier discharge cold plasma (DBD) and vacuum affect germination of *Stevia rebaudiana* seeds and the concentrations of acting phytohormones.

METHODS

SEED TREATMENT WITH COLD PLASMA (CP):

CP discharge is generated between a 3.5 cm diameter spiral copper electrode built on top of airtight stainless steel (app. 0.001 m^3) chamber and the chamber's frame by radiofrequency generator (430 MHz) at specific power density of 45W.

200 seeds were evenly distributed in a single layer on uncovered sterile glass Petri dish ($\varnothing$ 4 cm) placed in chamber on ceramic stand (5 cm to the electrode). Prior to seed treatment with CP, partial vacuum (100±1 Pa) was created. Duration of treatment was 2, 5 and, 7 min (referred to as CP2, CP5 and CP7).

Untreated seeds were used as control, and as additional control vacuum-treated seeds (for 5 min.) were used (referred to as V5).

SEED TREATMENT WITH DIELECTRIC BARRIER DISCHARGE PLASMA (DBD):

Seeds were treated using DBD device [9,10] at atmospheric pressure with exposure area of plasma $4\times4.38 \text{ cm}^2$ (at room temperature with 45-55% humidity). The discharges, generated by wire electrodes (separated by ceramic filler) were produced in the air between gap of electrodes by applying pulsed voltage (7.0kV). Current, and power density were 0.2A and 3.1W/cm^2, respectively. For treatment seeds were placed under electrode on glass plate in distance of 8 mm (from seeds surface). To prevent electrode from heating up and surface temperature from exceeding 35°C, 2 minutes breaks after each treatment were made. After – treatment with DBD was continued until the intended duration of exposure was reached. Seed groups treated for 2, 5 and 7 min. referred to as DBD2, DBD5 and DBD7.

DETERMINATION OF PHYTOHORMONES

Extracts were prepared from control, vacuum, CP5 and DBD5 samples. 200 seeds per group (app. 0.04 g) were homogenized with 85% (v:v) methanol (1:40 w:v). Samples were left on a rotary shaker for 24 h. at 150 rpm at 4°C for extraction. After shaking extracts were centrifuged at 13,000x g for 5 min. at 4°C. Supernatant was collected and stored at -20°C until further phytohormone analysis with high performance liquid chromatography (HPLC).

HPLC system Agilent 1200 (Agilent Technologies Inc. Germany) with diode detector was used for quantitative analysis of phytohormones. Separation was performed by modified method [6]; using Symmetry C18 column (30×100 mm, particle size 3.5 µm) (Waters Corporation, USA). The column temperature was 20°C, sample volume - 10 µl, mobile phase flow rate - 0.3 ml/min. Gradient elution was applied (Table 1) using the eluents: A - 50% methanol, B - 50% methanol with 1.2% acetic acid, C - water and D – 100% methanol.

Table 1. Composition of HPLC gradient.

Time, min	Part of eliuent, %		
	B	C	D
0	25	60	0
10	50	25	25
20	50	25	25
25	40	0	60
30	25	60	0

Gibberellic acid (GA3), gibberellin A7 (GA7), and abscisic acid (ABA) were detected at 254 nm. Phytohormones were identified by retention time and peak spiking with standards. Standard phytohormone solutions of GA3, GA7 (TransMIT, Germany), and ABA (Sigma Aldrich, Germany) were used for phytohormones analysis.

GERMINATION TEST

Seeds were sown 6 days after treatment with CP, DBD, and vacuum in 8x8x8 cm container filled with universal peat substrate (UAB Durpeta, pH 5.5–6.5) consisting of highland peat (79.6%) with shredded wood fiber (19.8%). Seeds were arranged on the surface of watered substrate, three replications of 66 seeds were prepared for each group. Germination conditions were; temperature – 25°C, relative humidity - 55–65%, photoperiod – 16 h. Germinated seeds were counted daily.

RESULTS

The results of germination show the tendency of CP and DBD to increase the percentage of germinated seeds and germination rate (Table 2), but only CP5 and CP7 significantly increased final germination percentage compared to control group.

Table 2 Indices of germination kinetics of seeds calculated from Richards plots.

	Control	V5	CP2	CP5	CP7	DBD2	DBD5	DBD7
Vi	14.14±0.44	19.19±3.64	16.67±4.87	19.70±3.15*	21.21±3.03*	17.17±3.64	13.13±1.01	15.15±1.52
Me	3.35±0.41	4.93±0.84	4.19±0.14	4.52±0.60	3.87±0.60	2.58±1.26	2.68±0.66	3.97±0.43
Qu	0.69±0.16	1.46±0.08	1.23±0.27	1.21±0.16	0.96±0.16	1.12±0.27	0.44±0.27	1.20±0.52

Vi, the final germination percentage; Me, the median germination time; Qu, the quartile deviation;
Mean values ± standard error of means are presented (n = 3); * - significantly different from the control group (p ≤ 0.05).

Effects of CP, DBD and vacuum treatment on concentrations of phytohormones

Treatments with vacuum substantially increased GA3 concentration, DBD5 – GA7, and CP5 and DBD5 – ABA concentration compared to control (Fig. 1).
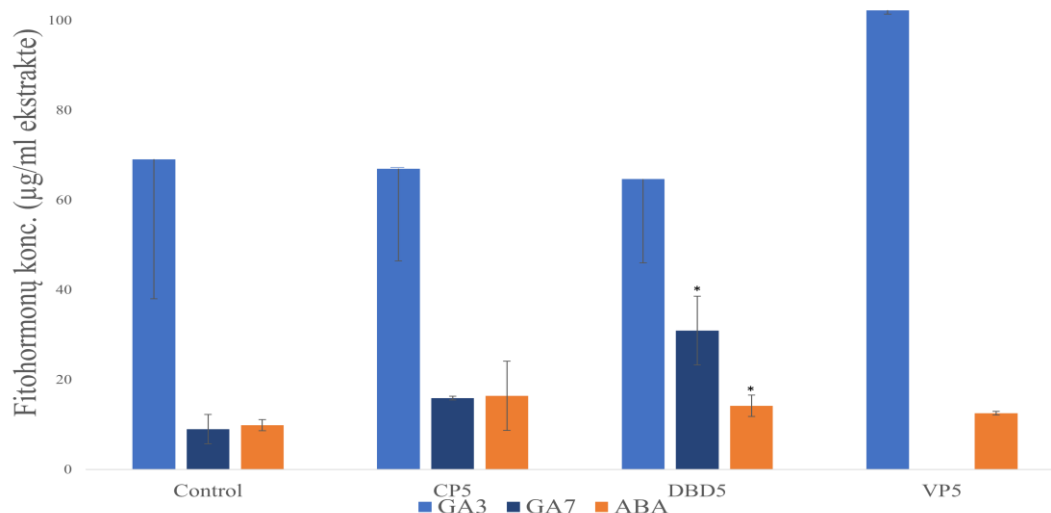
Fig. 1. Amount of phytohormones in dry seeds of stevia. ABA—abscisic acid, GA3—gibberellin 3, GA7—gibberellin A7. The means ± standard errors are presented (n = 2). * - statistically significant difference in comparison to control ($p \leqslant 0.05$).

However, the ratio between ABA and GAs (Table 2) does not correlate with the results of germination. CP5 increased the germination percentage, but only ABA/GA7 is showing a decrease, not ABA/(GA3+GA7), this ratio is increased.

Table 7 Ratio of phytohormones in stevia seed extracts.

Ratio	Control	CP5	DBD5	VP5
ABA/GA7	1.10	1.03	0.45	N/A
ABA/(GA3+GA7)	0.12	0.19	0.14	0.12

CONCLUSIONS

Stevia seed treatments with cold plasma, for 5 and 7 min has positive effect on germination, however this stimulation is not induced by the changed ratio of phytohormone concentrations. Further research of treatment conditions and wider spectrum of other phytohormones is needed to determine the mechanism of cold plasma effects in seeds of stevia.

Keywords: *Stevia rebaudiana*, cold plasma, germination, phytohormones.

EFERENCES

1. DUFOUR, T.; GUTIERREZ, Q.; BAILLY, C. Sustainable improvement of seeds vigor using dry atmospheric plasma priming: Evidence through coating wettability, water uptake, and plasma reactive chemistry. *Journal of Applied Physics*, 2021, Vol. 129. DOI: 10.1063/5.0037247

2. IVANKOV, A.; NAUCIENE, Z.; ZUKIENE, R.; DEGUTYTE-FOMINS, L.; MALAKAUSKIENE, A.; KRAUJALIS, P.; MILDAZIENE, V. Changes in Growth and Production of Non-Psychotropic Cannabinoids Induced by Pre-Sowing Treatment of Hemp

Seeds with Cold Plasma, Vacuum and Electromagnetic Field. *Applied Sciences,* 2020, Vol. 10. DOI:10.3390/app10238519 .

3. SARAPIROMA, S.; YU, L. D. Low-pressure and atmospheric plasma treatments of sunflower seeds. *Surface and Coatings Technology*, 2021, Vol. 406.

4. VOLKOV, A. G.; HAIRSTON, J. S.; PATEL, D.; GOTT, R. P.; XU, K. G. Cold plasma poration and corrugation of pumpkin seed coats. *Bioelectrochemistry*, 2019, Vol. 128, P. 175-185. DOI: 10.1016/j.bioelechem.

5. GANTAIT, S.; DAS, A.; BANERJEE, J. Geographical Distribution, Botanical Description and Self-Incompatibility Mechanism of Genus Stevia. *Sugar Tech* 2018, No. 20, P. 1–10. DIO: 10.1007/s12355-017-0563-1.

6. JUDICKAITE, A.; LYUSHKEVICH, V.; FILATOVA, I.; MILDAŽIENE, V.; ŽUKIENE, R. The Potential of Cold Plasma and Electromagnetic Field as Stimulators of Natural Sweeteners Biosynthesis in Stevia rebaudiana Bertoni. *Plants,* 2022, 11, Vol. 611.

7. ŽŪKIENĖ, R.; NAUČIENĖ, Z.; JANUŠKAITIENĖ, I.; PAUŽAITĖ, G.; MILDAŽIENĖ, V.; KOGA, K.; SHIRATANI, M. Dielectric barrier discharge plasma treatment-induced changes in sunflower seed germination, phytohormone balance, and seedling growth. *Applied physics express*, 2019, Vol. No. 12, p. 126003 Bristol: IOP Publishing Ltd, 2019, Vol. 12, No. 12.

8. SARINONT, T.; AMANO, T.; KITAZAKI, S.; KOGA, K.; UCHIDA, G.; SHIRATANI, M.; HAYASHI, N. Growth enhancement effects of radish sprouts: Atmospheric pressure plasma irradiation vs. heat shock. *Journal of Physics: Conference Series*. 2014, Vol. 518, No. 1, P. 012017.

9. KITAZAKI, S.; KOGA, K.; SHIRATANI, M.; HAYASHI, N. Growth control of dry yeast using scalable atmospheric-pressure dielectric barrier discharge plasma irradiation. *Japanese Journal of Applied Physics*. 2012, *Japanese Journal of Applied Physics*, 2012, Vol. 51 No. 11S, P. 11PJ02.

10. KITAZAKI, S.; SARINONT, T.; KOGA, K.; HAYASHI, N.; SHIRATANI, M. Plasma induced long-term growth enhancement of Raphanus sativus L. using combinatorial atmospheric air dielectric barrier discharge plasmas. *Current Applied Physics*. 2014, Vol. 14, No. S149 p.S153. DOI: 10.1016/j.cap.2013.11.056.

EFFECT OF LIGHT INTENSITY ON THE GROWTH AND ANTIOXIDANT RESPONSE OF SWEET BASIL 'OPAL' AND LETTUCE 'NIKOLAJ'

L. Kristina*, R. Sutulienė, S. Giedrė

Lithuanian Research Centre for Agriculture and Forestry, I
nstitute of Horticulture
Kauno Str. 30, LT-54333 Babtai, Kaunas dist. – Lithuania
kristina.lauzike@lammc.lt

T. Pūkas

Elektros taupymo sprendimai, UAB
Molėtų g. 13, PC MOLĖTŲ LINK, 14260 Didžioji Riešė / Liepu g. 15, 53290 Linksmakalnis,
Kaunas distr. - Lithuania

EXTENDED ABSTRACT

OVERVIEW

Considering environmental factors in agriculture, light and nutrients are one of the most important elements for productive plant growth. Due to low penetration of light in greenhouses, additional light sources such as high-pressure sodium lamps, light-emitting diodes (LEDs) are used for supplemental lighting [1]. One of the goals of Europe's green deal is to reduce energy consumption, the goal in greenhouse is to grow high-value products with less energy [2]. LED lamps are superior to sodium lamps in their low power consumption and ability to easy control light intensity [1,3,4]. Light intensity affects plant development, metabolism, the activity of the antioxidant system and other. The leave area, the amount of accumulated dry mass, the total amount of phenols and the abundance of other plant parameters vary significantly depending from the light intensity [4-7]. To fulfil the requirements for growth and development of a plant light alone is not enough, nutrients are needed as well. Nitrogen deficiency inhibits plant growth and development, reduces photosynthesis and leaf area, phosphorus deficiency also inhibits growth and photosynthesis. Restriction of other essential nutrients also has a negative effect on the physiological parameters of the plant [8-11]. Lack of nutrients also reduces the accumulation of phenolic compounds and increases antioxidant activity [12,13]. The aim of this study was to evaluate the effect of fertilization at different light intensities on the growth of lettuce and basil and the response of the antioxidant system.

METHODS

Sweet basil (*Ocimum basilicum*, 'Opal') and lettuce (*Lactuca sativa*, 'Nikolaj') were grown in a greenhouse under three different lighting intensity conditions (in May, Lithuania: 55°60′ N, 23°48′ E): the photosynthetic photon lux density (PPFD) of natural lighting beside leaves of basil and lettuce was 80 µmol m^{-2} s^{-1}), with supplemental light-emitting diodes (LEDs) lighting the total PPFD of 150 and 250 µmol m^{-2} s^{-1} was maintained. Day/night temperatures of 20±3/16±3°C with a 16-h photoperiod were maintained. Half of the plants were grown without

additional fertilization; the other half were fertilized twice a week with complex of fertilizers (NPK 3-1-3, Plagron, Netherlands).

Biometric measurements. Five representative basil and lettuce plants were selected for leaf area (cm^2) evaluation with a leaf area meter (AT Delta – T Device, UK). Stem diameter and plant height were additionally measured for basil(mm). The dry mass of plants was determined by drying them in +70ºC for 48 h. (Venti cell 222, Medcenter Einrichtungen, Gräfeling, Germany) to constant weight.

Antioxidant activity. Extracts were prepared by grinding 0,5 g of plant leaves with liquid nitrogen and diluting with 5 mL of 80% methanol. Each of three biological replicates consisted of at least three conjugated plants and were repeated in three analytical replicates. Antioxidant properties of basil and lettuce leaves were evaluated as the 2-diphenyl-1-picrylhydrazyl (DPPH) [14], 2,2′-azino-bis (3-ethylbenzothiazoline-6-sulfonic acid) (ABTS) [15] radical scavenging activities, and Fe^{2+} reducing antioxidant power assay (FRAP) [16]. The methods were adapted to be performed with a microplate reader "SPECTROstar Nano" (BMG LABTECH, Germany).

Statistical analysis. MS Excel Version 2010 and XLStat 2020 Data Analysis and Statistical Solution for Microsoft Excel (Addinsoft, France) statistical software were used for data processing. Analysis of variance (ANOVA) was carried out along with Tukey multiple comparisons test for statistical analyses, $p \leq 0.05$, three biological replicates, conjugated sample (from five plants leaves) for biochemical analysis - three analytical replicates.

RESULTS

Photosynthetic photon lux density had a significant positive effect on both basil and lettuce vegetative growth, regardless of fertilization (table 1). For both plants, basil and lettuce, an average leaf area decreased, less leaves were formed in lower light conditions.

Table 1 Light intensity and fertilization effect on basil and lettuce biometric measurements. Values are mean ± SE of 5 replicates and different letters are differed significantly by Tukey multiple comparisons test (P ≤ 0.05).

The photosynthetic photon lux density (PPFD)	Fertilization	Total leaf area cm^2		Number of leaves		Average leaf area cm^2	
		Basil	Lettuce	Basil	Lettuce	Basil	Lettuce
80 µmol m^{-2} s^{-1}	-	68.2±5.35a	128.3±20.95a	6±0.0a	3.8±0.4a	11.4±0.89a	33.8±2.26a
	+	113.4±12.98b	154.3±36.85a	6±0.0a	4.2±0.4a	18.9±2.16b	36.7±5.45a
150 µmol m^{-2} s^{-1}	-	273.2±50.58c	363.5±57.74b	8±0.0b	5.2±0.4b	34.2±6.32c	69.9±7.94b
	+	214.8±22.94c	450.8±30.47bc	9.2±0.4c	6.2±0.4c	23.3±1.34b	72.7±1.77b
250 µmol m^{-2} s^{-1}	-	409.1±42.78d	477.4±41.50c	10±0.0d	7±0.0d	40.9±4.28d	68.2±5.93b
	+	393.1±28.32d	516.9±55.08c	10±0.0d	7±0.0d	39.3±2.83d	73.8±7.87b

Significantly higher DPPH, ABTS and FRAP activity was found in under PPFD 150 μmol m^{-2} s^{-1} and under 250 μmol m^{-2} s^{-1} grown unfertilized basil and lower in under PPFD 150 μmol m^{-2} s^{-1} and under 250 μmol m^{-2} s^{-1} grown fertilized basil (Fig. 1). Meanwhile lower DPPH, ABTS and FRAP activity was found in under natural light grown lettuce.
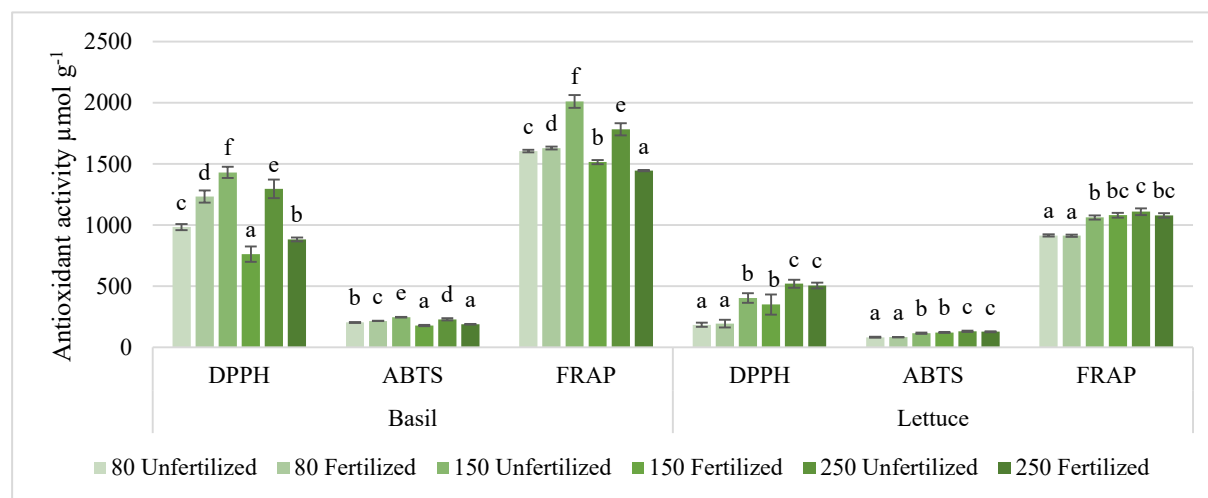
Fig. 1 Light intensity and fertilization effect on basil and lettuce antioxidant system response. Values are mean ± SE of 10 replicates and different letters are differed significantly by Tukey multiple comparisons test (P ≤ 0.05).

CONCLUSIONS

Light intensity was found to have the greatest significant effect on both lettuce and basil biometric parameters and the response of the antioxidant system. Meanwhile, the intensity of fertilization had a significant effect on the development of both plants (more leaves were formed as a result of more intensive fertilization) and the accumulation of phenolic compounds.

Keywords: Lactuca sativa; Ocimum basilicum; LED;

REFERENCES

1. BIAN, Z. H.; YANG, Q. C.; LIU, W. K. Effects of light quality on the accumulation of phytochemicals in vegetables produced in controlled environments: a review. *Journal of the Science of Food and Agriculture*, 2015, Vol.95, P. 869-877.

2. WOLF, S.; TEITGE, J.; MIELKE, J.; SCHÜTZE, F.; JAEGER, C. The European Green Deal—more than climate neutrality. *Intereconomics*, 2021, Vol. 2, P. 99-107.

3. KATZIN, D.; MARCELIS, L.; VAN MOURIK, S. Energy savings in greenhouses by transition from high-pressure sodium to LED lighting. *Applied Energy*, 2021.

4. HASAN, M.; BASHIR, T.; GHOSH, R.; LEE, S. K.; BAEH. An overview of LEDs' effects on the production of bioactive compounds and crop quality. *Molecules* 017, P.22-1420.

5. EBISAWA, M.; SHOIJI, K.; KATO, M.; SHIMOMURA, K.; GOTO, F.; YOSHIHARA, T. Supplementary ultraviolet radiation B together with blue light at night increased quercetin content and flavonol synthase gene expression in leaf lettuce (Lactuca sativaL.). *Environmental. Control in Biology*. 2008, P.1-11.

6. LIU, Y.; QIAN, C.; DING, S.; SHANG, X.; YANG, W.; FANG, S. Effect of light regime and provenance on leaf characteristics, growth,and flavonoid accumulation in Cyclocarya paliurus(Batal) Iljinskaja coppices. Bot.Stud. 2016, P. 28-58.

7. FLORES, M.; URRESTARAZU, M.; AMORÓS, A.; ESCALONA, V. High intensity and red enriched LED lights increased growth of lettuce and endive. *Italian Journal of Agronomy*, 2021.

8. MU, X.; CHEN, Y. The physiological response of photosynthesis to nitrogen deficiency. *Plant Physiology and Biochemistry*, 2021, P. 76-82.

9. MENG, X.; CHEN, W. W.; WANG, Y. Y.; HUANG, Z. R.; YE, X.; CHEN, L. S.; YANG, L. T. Effects of phosphorus deficiency on the absorption of mineral nutrients, photosynthetic system performance and antioxidant metabolism in Citrus grandis. *Plos one*, 2021, Vol.2.

10. YONEYAMA, K.; XIE, X.; KIM, H.I.; KISUGI, T.; NOMURA, T.; SEKIMOTO, H.; YOKOTA, T.; YONEYAMA, K. How do nitrogen and phosphorus deficiencies affect strigolactone production and exudation? *Planta,* 2012, *P.* 1197–1207.

11. TABAGLIO, V.; BOSELLI, R.; FIORINI, A.; GANIMEDE, C.; BECCARI, P.; SANTELLI, S.; NERVO, G. Reducing nitrate accumulation and fertilizer use in lettuce with modified intermittent Nutrient Film Technique (NFT) system. *Agronomy,* 2020, Vol.10, P. 1208.

12. JUSZCZUK, I. M.; WIKTOROWSKA, A.; MALUSÁ, E.; RYCHTER, A.M. Changes in the concentration of phenolic compounds and exudation induced by phosphate deficiency in bean plants (*Phaseolus vulgaris* L.). *Plant Soil* 2004, p. 41–49.

13. SAKAMOTO, M.; KOMATSU, Y.; SUZUKI, T. Nutrient Deficiency Affects the Growth and Nitrate Concentration of Hydroponic Radish. *Horticulturae*, 2021, Vol. 7, P. 12- 525.

14. SHARMA, O. P.; BHAT, T. K. DPPH Antioxidant Assay Revisited. Food Chemistry 2009, P. 1202–1205.

15. RE, R.; PELLEGRINI, N.; PROTEGGENTE, A.; PANNALA, A.; YANG, M.; RICE-EVANS, C. Antioxidant Activity Applying an Improved ABTS Radical Cation Decolorization Assay. Free Radical Biology and Medicine 1999, Vol. 26, P. 1231–1237.

16. BENZIE, I. F. F.; STRAIN, J. J. The Ferric Reducing Ability of Plasma (FRAP) as a Measure of "Antioxidant Power": The FRAP Assay. Analytical Biochemistry 1996, P. 70–76.

IMPACT OF FOLIAR SELENATE AND ZINC OXIDE APPLICATION ON THE ACCUMULATION OF MINERALS, CHLOROPHYLL A AND PROTEIN IN TWO PEA (*PISUM SATIVUM* L.) SEED VARIETIES

M. Malka, G. D. Laing
Ghent University, Faculty of Bioscience Engineering,
Department of Green Chemistry and Technology,
Coupure links 653, B-9000 Gent – Belgium
+48721849466
maksymilian.malka@ugent.be

T. Bohn
Luxembourg Institute of Health, Department of Population Health,
Nutrition and Health Research Group,
1 A-B, Rue Thomas Edison, L-1445 Strassen – Luxembourg
+352621216637
Torsten.Bohn@lih.lu

EXTENDED ABSTRACT

OVERVIEW

Pea (*Pisum sativum* L.) is an important legume and staple crop grown globally and employed for human and animal nutrition (1). Selenium (Se) and zinc (Zn) are important cofactors for several antioxidant enzymes in plamts (2, 3). Foliar Se/Zn application is a highly efficient strategy of plant biofortification (4; 5). However, the effect of such treatments on concentrations of macrominerals, macronutrients and bioactive compounds in pea has been poorly investigated. A two-year pot experiment was performed to study the effect of foliar-applied sodium selenate (0/50/100g Se/ha) and zinc oxide (0/375/750g Zn/ha) at flowering stage on concentrations of Mg, chlorophyll a and protein in seeds of two pea varieties (Ambassador, Premium).

METHODS

A two-year (2014/15) outdoor pot experiment was conducted in Nitra, Slovakia (48.305 N, 18.096 E). The experiment was arranged with four replicates per treatment, two pea varieties (Ambassador, Premium) and five different treatments, including one unamended control and 2 levels of foliar-applied Se as sodium selenate (50 and 100g Se/ha) and Zn as zinc oxide (375 and 750g Zn/ha).

Methods included: 1) protein concentration: via the Dumas method with the TruSpec CHNS analyzer (LECO, Saint Joseph, MI) 2) Mg concentration: via ICP-OES (Varian Vista MPX, Palo Alto, CA, USA) 3) chlorophyll a: via spectrophotometric method (6, 7) 4) statistical analysis: SPSS version 19.0 (IBM, Chicago, IL, USA).

RESULTS

Our previous study highlighted that foliar-applied sodium selenate improved seed Se accumulation in both varieties dose-dependently. Premium accumulated greater amounts of Se in seeds than Ambassador. Highest Se accumulation was found in seeds of Premium treated with 100 g Se/ha (7.84 mg/kg vs. control (0.16 mg/kg), DW). Contrarily, seed Zn concentration was not significantly affected by foliar-applied zinc oxide (unpublished results). Concentration of Mg, chlorophyll a and protein were positively affected in part by Se and Zn treatments. Mg concentration significantly increased (vs. control) in Ambassador treated with Se1 in 2015 (Table 1). Chlorophyll a concentration significantly increased (vs. control) in Premium upon Zn1 treatment in 2015 (Table 1). All Se and Zn treatments significantly increased protein concentration (vs. control) in Premium in 2014, while Zn1 treatment significantly increased protein concentration (vs. control) in Premium in 2015 (Table 2).

Table 1. Effect of foliar Se and Zn treatments on the concentration of Mg and chlorophyll a in seed of two pea varieties (Ambassador and Premium) in 2014/15 growing season. Note: Control (without Se and Zn), Se1 - 50 g Se/ha, Se2 - 100 g Se/ha, Zn1 - 375 g Zn/ha, Zn2 - 750 g Zn/ha; mean $\pm$ SD; n = 4.

Year	Treatment	Mg (mg/kg DW)		Chlorophyll a (mg/100g DW)	
		Ambassador	Premium	Ambassador	Premium
2014	Control	1247 ± 39.4	1152 ± 37.3	32.7 ± 6.28	26.4 ± 4.31
	Se1	1249 ± 72.4	1135 ± 72.6	29.2 ± 2.15	34.5 ± 3.81
	Se2	1247 ± 52.7	1149 ± 108	30.4 ± 3.72	30.6 ± 5.90
	Zn1	1257 ± 14.3	1151 ± 152	31.3 ± 2.22	26.6 ± 4.13
	Zn2	1234 ± 20.0	1143 ± 97.1	33.0 ± 2.24	27.9 ± 1.65
	p-value	0.970	0.999	0.574	0.076
2015	Control	1382 ± 32.8^A	1441 ± 25.5^C	30.2 ± 1.76	10.7 ± 4.04^A
	Se1	1455 ± 7.02^B	1341 ± 10.0^{AB}	27.2 ± 6.60	12.5 ± 4.37^{AB}
	Se2	1418 ± 24.2^{AB}	1380 ± 29.2^B	27.7 ± 9.17	14.2 ± 3.61^{AB}
	Zn1	1411 ± 45.8^{AB}	1333 ± 19.6^A	21.3 ± 3.80	21.5 ± 6.13^B
	Zn2	1386 ± 11.2^A	1314 ± 16.7^A	27.3 ± 4.34	16.9 ± 2.33^{AB}
	p-value	0.015	<0.001	0.308	0.023

Means within a column not sharing the same superscript letters are significantly different. P-values in the same row mean the effect of Se/Zn dose.

Table 2. Effect of foliar Se and Zn treatments on the protein concentration in seed of two pea varieties (Ambassador and Premium) in 2014/15 growing season. Note: Control (without Se and Zn), Se1 - 50 g Se/ha, Se2 - 100 g Se/ha, Zn1 - 375 g Zn/ha, Zn2 - 750 g Zn/ha; mean ± SD; n = 4.

Year	Treatment	Protein (% DW)	
		Ambassador	Premium
2014	Control	22.2 ± 0.58	21.5 ± 0.25^A
	Se1	21.9 ± 0.42	22.1 ± 0.15^B
	Se2	22.2 ± 0.40	22.3 ± 0.23^B
	Zn1	21.0 ± 0.75	22.5 ± 0.28^B
	Zn2	21.5 ± 0.77	22.5 ± 0.13^B
	p-value	0.064	<0.001
2015	Control	24.7 ± 0.18^E	26.6 ± 0.42^C
	Se1	24.2 ± 0.10^D	25.3 ± 0.12^A
	Se2	23.5 ± 0.13^C	26.0 ± 0.18^B
	Zn1	20.0 ± 0.15^A	27.6 ± 0.22^D
	Zn2	23.1 ± 0.13^B	25.7 ± 0.24^{AB}
	p-value	<0.001	<0.001

Means within a column not sharing the same superscript letters are significantly different. P-values in the same row mean the effect of Se/Zn dose.

CONCLUSIONS

This study provides new nutritional data on Se/Zn biofortified pea. The results are important for improving agronomic biofortification of pea with Se/Zn.

Keywords: oxidative stress, macrominerals, macronutrients, selenate, zinc oxide, bioactive compounds, foliar application.

REFERENCES

1. POWERS, S. E.; THAVARAJAH, D. Checking Agriculture's Pulse: Field Pea (Pisum Sativum L.), Sustainability, and Phosphorus Use Efficiency. *Frontiers in Plant Science*, 2019, Vol. *10, p. 1489.* https://doi.org/10.3389/fpls.2019.01489

2. HASANUZZAMAN, M.; BHUYAN, M. B.; RAZA, A.; HAWRYLAK-NOWAK, B.; MATRASZEK-GAWRON, R.; Al MAHMUD, J.; NAHAR, K.; FUJITA, M. Selenium in plants: Boon or bane? *Environmental and Experimental Botany*, 2020, Vol *178,* https://doi.org/10.1016/j.envexpbot.2020.104170

3. RAJPUT, V. D.; HARISH, SINGH, R. K.; VERMA, K. K.; SHARMA, L.; QUIROZ-FIGUEROA, F. R., MEENA, M.; GOUR, V. S.; MINKINA, T.; SUSHKOVA, S.;

MANDZHIEVA, S. Recent developments in enzymatic antioxidant defence mechanism in plants with special reference to abiotic stress. *Biology*, 2021, Vol *10*. https://doi.org/10.3390/biology10040267

4. DELAQUA, D.; CARNIER, R.; BERTON, R. S.; CORBI, F. C. A.; COSCIONE, A. R. Increase of selenium concentration in wheat grains through foliar application of sodium selenate. *Journal of Food Composition and Analysis*, 2020, Vol *99,* https://doi.org/10.1016/j.jfca.2021.103886

5. SATTAR, A.; WANG, X.; Ul-ALLAH, S.; SHER, A.; IJAZ, M.; IRFAN, M.; ABBAS, T.; HUSSAIN, S.; NAWAZ, F.; Al-HASHIMI, A.; Al MUNQEDHI, B. M.; SKALICKY, M. Foliar application of zinc improves morpho-physiological and antioxidant defense mechanisms, and agronomic grain biofortification of wheat (Triticum aestivum L.) under water stress. *Saudi Journal of Biological Sciences*. 2021 https://doi.org/10.1016/j.sjbs.2021.10.061

6. KAULMANN, A.; JONVILLE, M. C.; SCHNEIDER, Y. J.; HOFFMANN, L.; BOHN, T. Carotenoids, polyphenols and micronutrient profiles of Brassica oleraceae and plum varieties and their contribution to measures of total antioxidant capacity. *Food Chemistry*, 2014, Vol *155*, p. 240–250, https://doi.org/10.1016/j.foodchem.2014.01.070

7. LICHTENTHALER, H. K.; BUSCHMANN, C. Chlorophylls and Carotenoids: Measurement and Characterization by UV-VIS Spectroscopy. *Current Protocols in Food Analytical Chemistry*, 2001 ,Vol. *1*. https://doi.org/10.1002/0471142913.faf0403s01

SOIL CONTAMINATION WITH PLANT SEEDS IN A PRE–EROSION CEREAL-GRASS CROP ROTATION

V. Matyžiūtė, R. Skuodienė

Lithuanian Research Centre for Agriculture and Forestry
Vezaiciai Branch, Gargzdu str. 29, Klaipeda district – Lithuania
+370-640-23683, +370-678-48664
vilija.matyziute@lammc.lt

ABSTRACT

The experiment was carried out at the Vezaiciai Branch of the Lithuanian Research Centre for Agriculture and Forestry on the hilly topography of Zemaiciai Highland (latitude 55°577′ N, longitude 22°482′ E, 185.0 m above sea level). The southern exposition slope's soil was slightly eroded Eutric Retisol (loamic) (RT-eu.lo) the steepness of the slope was 9-11º. The aim of the study - to study the impact of a hilly relief to the changes of seeds in a soil of pre-erosion cereal-grass crop rotation. Hypothesis – it is predicted that the seedbank of hilly relief is reliant on plant sequence in crop rotation and nutrients and moisture differentiation in the soil. The study included different parts of the hill (summit, midslope and footslope). According to the average data, considering the hilly relief conditions, the number of seeds in the soil seedbank during autumn was 20% higher than at the spring. The highest number of seeds at the autumn was determined on the summit (40625 seeds m-2). Due to variations in humidity and temperature, as well as the impact of soil biota during the autumn-winter-spring period at the spring, the seed bank was 2.1 times lower at the summit of the hill compared to the autumn. The highest count during the spring was determined on the midslope of the hill (36451 seeds m-2). The soil in 0-5 cm depth in the pre-erosion cereal-grass crop rotation was the most polluted with plant seeds (61%). In the soil seed bank of the midslope of the hill, the number of seeds was by 12,0% and 49,8% higher compared to the summit and footslope parts.

Keywords: hilly relief, soil seed bank, pre-erosion cereal-grass crop rotation

INTRODUCTION

The weed seedbank is the reserve of viable weed seeds present on the soil surface and scattered in the soil profile. It consists of both new weed seeds recently shed and older seeds that have persisted in the soil for several years [7]. Due to uneven soil erosion in selective parts of the hill, different conditions in the hilly topography become present for the plant development, including differences in soil humidity, acidity, richness in nutrients, humus, and others [9]. The alterations of weed communities and the pollution of soil with weed seeds appears because of differences in soil pH, pedological aspects and crop management [11]. The weed incidence is largely based on the pollution of soil with weed seeds, on the biological properties of the cultivated plant, and its overshadowing abilities [6][13]. Soil tillage has a significant influence on the dynamics of weed seeds [8][12]. The highest number of weed seed species was found in the treatments with reduced and no-tillage treatments in a soil layer of 0–5 cm. In deeper soil layers (5–10, 10–20 cm), no differences in weed seed species number were found [1]. Tillage systems cause changes in the density and composition of soil weed seedbank [5], especially in weed seed composition in the upper 0–15 cm soil layer [2].

The aim of the study - to study the impact of a hilly relief to the changes of seeds in a soil of pre-erosion cereal-grass crop rotation. Hypothesis – it is predicted that the seedbank of hilly relief is reliant on plant sequence in crop rotation and nutrients and moisture differentiation in the soil.

METHODS

The experiment was carried out at the Vėžaičiai Branch of the Lithuanian Research Centre for Agriculture and Forestry, on the midslope soil of Žemaičiai Highland covered by different anti-erosion agrophytocenoses [3] in Kaltinėnai (lat. 55°577′ N, long. 22°482′ E, 185.0 m a. s. l.). The steepness of the slope was 9–11°. The soil of the southern exposition slope was slightly eroded Eutric Retisol (loamic) according to WRB (2015) with a texture of sandy loam. Agrochemical and physical properties of the soil are presented in Table 1.

Table 1. Agrochemical and physical properties of the arable (0–15 cm) soil layer (2020)

| Soil properties | Part of the hill | | | | | |
| | summit | | midslope | | footslope | |
	0–5 cm	5–15 cm	0–5 cm	5–15 cm	0–5 cm	5–15 cm
Soil acidity (pH$_{KCl}$)	5.6	5.4	5.3	5.1	5.1	5.1
Mobile P$_2$O$_5$ mg kg^{-1}	192	201	165	168	149	148
Mobile K$_2$O mg kg^{-1}	209	112	198	98	223	107
N$_{total}$ %	0.078	0.077	0.097	0.096	0.106	0.101
C$_{org}$ %	10.9	0.8	1.1	1.0	1.1	1.0
Soil texture	sandy loam	sandy loam	sandy loam	sandy loam	sandy loam	sandy loam
Sand %	79.2	77.4	75.6	75.9	73.0	69.7
Silt %	15.5	17.8	19.0	18.8	19.0	22.5
Clay %	5.3	4.8	5.4	5.3	8.0	7.8

A pre-erosion cereal-grass crop rotation, which had a previous crop rotation of spring barley as a second plant in 2020, was used in the research. During winter, stubble was left on the slope to secure its soil from erosion, while minimal soil cultivation was applied in spring. Spring barley "Luokė" was sowed across the slope, the rate being 220 kg ha^{-1}. NPK 9-14-27+7S 250 kg

ha^{-1} was used after sowing as a mineral fertiliser. Spring barley was sprayed with BBCH 32 MCPA (a.i. MCPA 750 g/l) 30 ml and Arrat (a.i. dicamba-sodio + tritosulfuron) 10 ml. The next year, 2021, the third crop rotation plant - spring barley "Taifun" - was cultivated with a density of 250 kg ha^{-1}. Mineral fertilisation - NPK 15-15-15 600 kg ha^{-1} before sowing.

The research slope was 65 metres in length. The research strip was 3.2 metres wide.

The study included different parts of the hill (summit, midslope and footslope). To assess the impact of the hill slope on soil contamination by seeds, the seed bank was investigated at the depths of 0–5 and 5–15 cm. The seed bank was estimated from soil samples taken in spring and autumn of 2020 and 2021. In each model plot, 2 kg of soil from 20 positions were collected using an agrochemical drill. The soil was dried out. In total, five 100 g samples were taken out of 2 kg soil sample and weighed. Later, the soil samples were wet-sieved through a 0.25 mm sieve until all contents of the soil were washed out. The remaining mineral part of the soil was separated from the organic part and weed seeds using the saturated salt solution. Weed seeds were identified using binoculars with 8.75× magnification. The number of weed seeds (A) was recalculated to thousands of unit per m^2:

$$A = n \times h \times p \times 100,$$

where A is number of seeds, seeds, m^2; n – the counted number of seeds in the soil sample; h – the depth of plough layer, cm; p – soil bulk density, g cm^3.

The crop weed analysis was carried out in stationary 0.25 m^{-2} lots in six different parts of the field. The weediness was evaluated in 2020 in spring barley during BBCH 58 and BBCH 86 stages. In 2021 the weediness was evaluated in the spring barley crop during the stages of BBCH 32 and BBCH 87. During both evaluations the weed type composition was determined. The number of weeds were recounted by the unit of m^{-2}.

Chemical analyses were carried out at the Chemical Research Laboratory of the Institute of Agriculture, Lithuanian Research Centre for Agriculture and Forestry. Before establishing the experiment, soil agrochemical characteristics were determined from the samples taken from the depths of 0–5 and 5–15 cm. Soil acidity (pH) was measured by the potentiometric method in the extraction of 1 M KCl (pHKCl) according to standard ISO 10390:2005 (Soil quality – Determination of pH). In the soil, mobile P_2O_5 and K_2O were determined using the Egner-Riehm-Domingo (AL) method (LVP D-07:2016), total nitrogen (Ntot) content by the Kjeldahl method, and organic carbon (Corg) by the Dumas dry combustion method. Soil bulk density was determined with a 100 cm^3 cylindrical drill by the Kachinsky method. Soil texture was determined by the Fere triangle (FAO recommended method) according to the percentage of sand, silt, and clay fractions in the graphical diagram.

Significance of the differences between the means was determined according to the Fisher's protected least significant difference (LSD) at 0.05 probability level. The experimental data were subjected to the analysis of variance (ANOVA). The actual data of the seed bank were transformed (Sqr(x + 1)).

RESULTS

The composition of the soil seed bank depends on the plant communities appearing in a particular area both at the present moment and also in the past, as well as on the biological properties of plants. Changes in land-use and management practices influence the distribution

of seeds in the soil and the established vegetation [10]. Since the appearance of the plants to germinate, grow and develop on the hilly topography, they had different conditions [4], because, as other authors state, while the amount of physical clay and mud increase on the lower parts of the slope, the humidity reserves increase, as well as the amount of humus and nutrients, and the acidity decreases (Table 1). The average data for 2020–2021 show that at the soil depth of 0–15 cm of the pre-erosion cereal-grass crop rotation, the number of seeds reached 71742, 83487, and 40906, respectively, in the summit, the midslope, and the footslope parts of the hill. Considering the hilly relief conditions, the number of seeds in the soil seedbank during autumn was 20% higher than at the spring. The highest number of seeds at the autumn was determined on the summit (40625 seeds m^{-2}).

Due to variations in humidity as well as the impact of soil biota during the autumn-winter-spring period at the spring, the seed bank was 2.1 times lower at the summit of the hill compared to the autumn. The highest count during the spring was determined on the midslope of the hill (36451 seeds m^{-2}) compared to the hill's slope. This could have been caused by seed transportation due to precipitation. The soil in 0-5 cm depth in the pre-erosion cereal-grass crop rotation was the most polluted with plant seeds (61%) (Fig. 1).
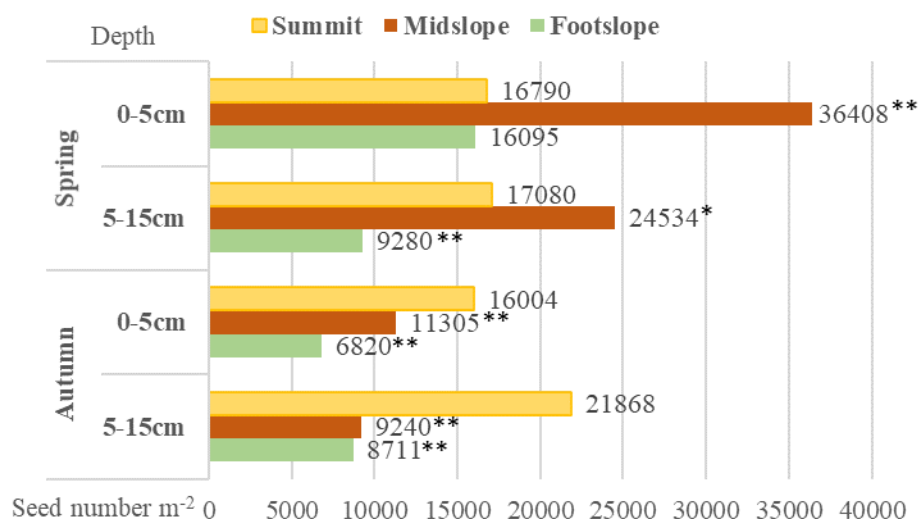
Fig. 1. Plant seed number in a pre-erosion crop-rotation soil, Kaltinenai, 2020-2021. * and ** – significant at 0.05 and 0.01 probability levels

The weed seed bank in spring consisted of, the seeds represented 24 species including 3 meadow species, 20 segetal, and one tree (Table 5). The species composition of the soil seed bank in nearby parts of the hill varied slightly (Cs = 0.64–0.82). The most similar species composition of the soil seed bank was in the summit and midslope parts of the hill (Cs = 0.82), while it was the greatest in the summit and footslope parts of the hill (Cs = 0.64).

The weed seed bank in autumn consisted of, the seeds represented 18 species including 17 segetal, and one tree. The species composition of the soil seed bank in nearby parts of the hill varied slightly (Cs = 0.86–0.92).

The seed bank in the soil consisted of 24 species of seeds in spring and 20 species of weed were determined in the crop. When the spring seed bank species composition was determined with crop I acounting number of weed type composition, it was determined that there were 11 common plant species. *Viola arvensis* Murr. (17,6% in the seed bank; 24% on the top of the

soil), *Setaria viridis* P. B. (18,5% in the seed bank; 21,9% in the crop) and *Spergula arvensis* L. (4,1% in the seedbank; 10,3% in the crop) accounted for the biggest part of the plant species (Fig 2).
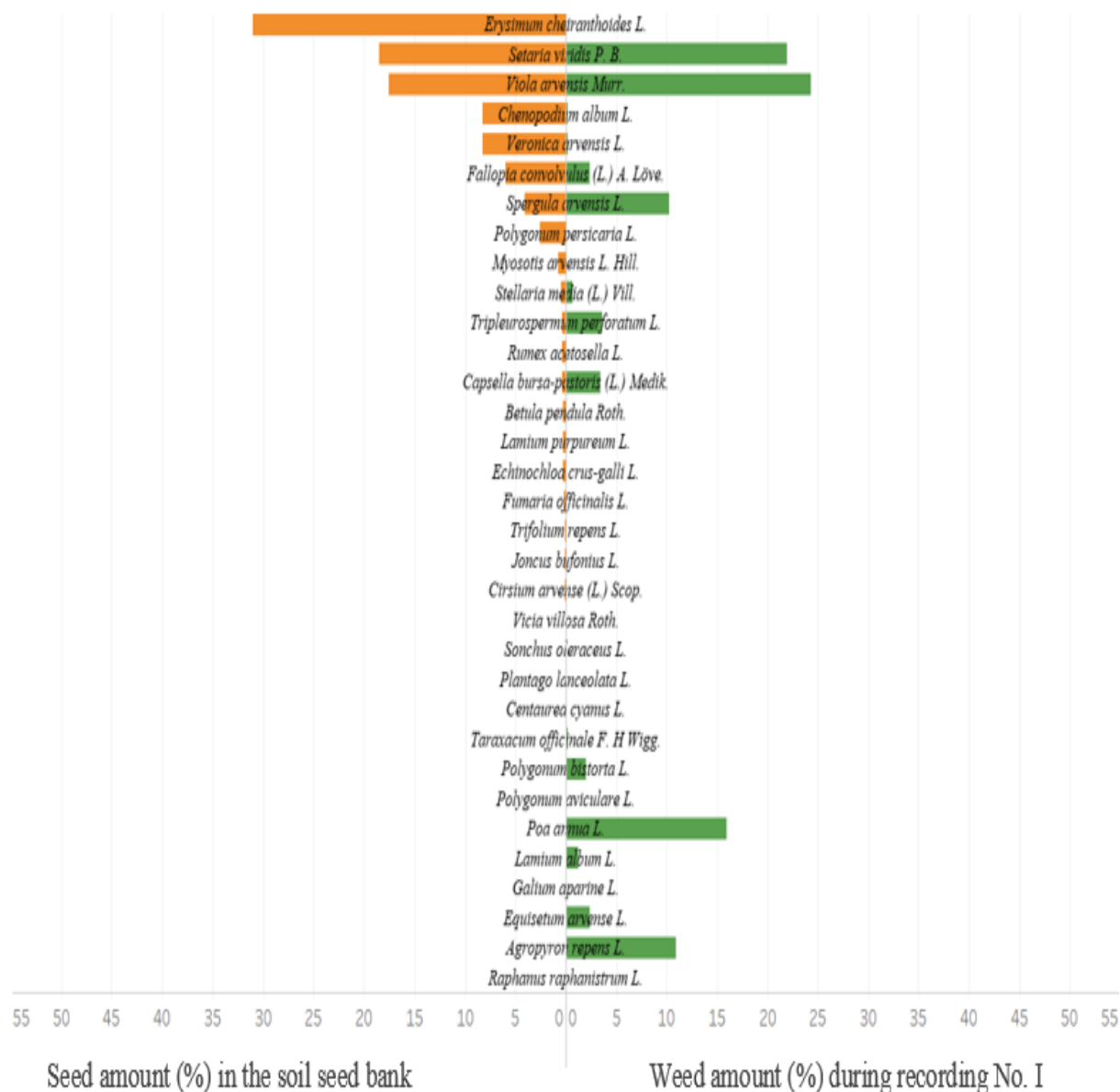
Fig. 2. The interaction of soil seed bank and weeds in the pre-erosion cereal-grass crop rotation in spring, average data. Kaltinenai, 2020-2021.

The seed bank in the soil consisted of 19 species of seeds and 21 species of weed were found in the crop in autumn. When the autumn seed bank species composition was compared to the crop II count's weed species composition, 8 common plant species were determined. *Viola arvensis* Murr. (15,2% in the seed bank; 4,1% in the crop), *Setaria viridis* P. B. (26,5% in the weed bank; 54,1% in the crop) were the most common (Fig 3). *Setaria viridis* P. B. (54,1%) and *Poa annua* L. (34,1%) overshadowed the crop in autumn the most. *Setaria viridis* P. B. (26,5%), *Viola arvensis* Murr. (15.2%) and *Echinochloa crus-galli* L. (13,2%) comprised a big part of the soil seed bank.
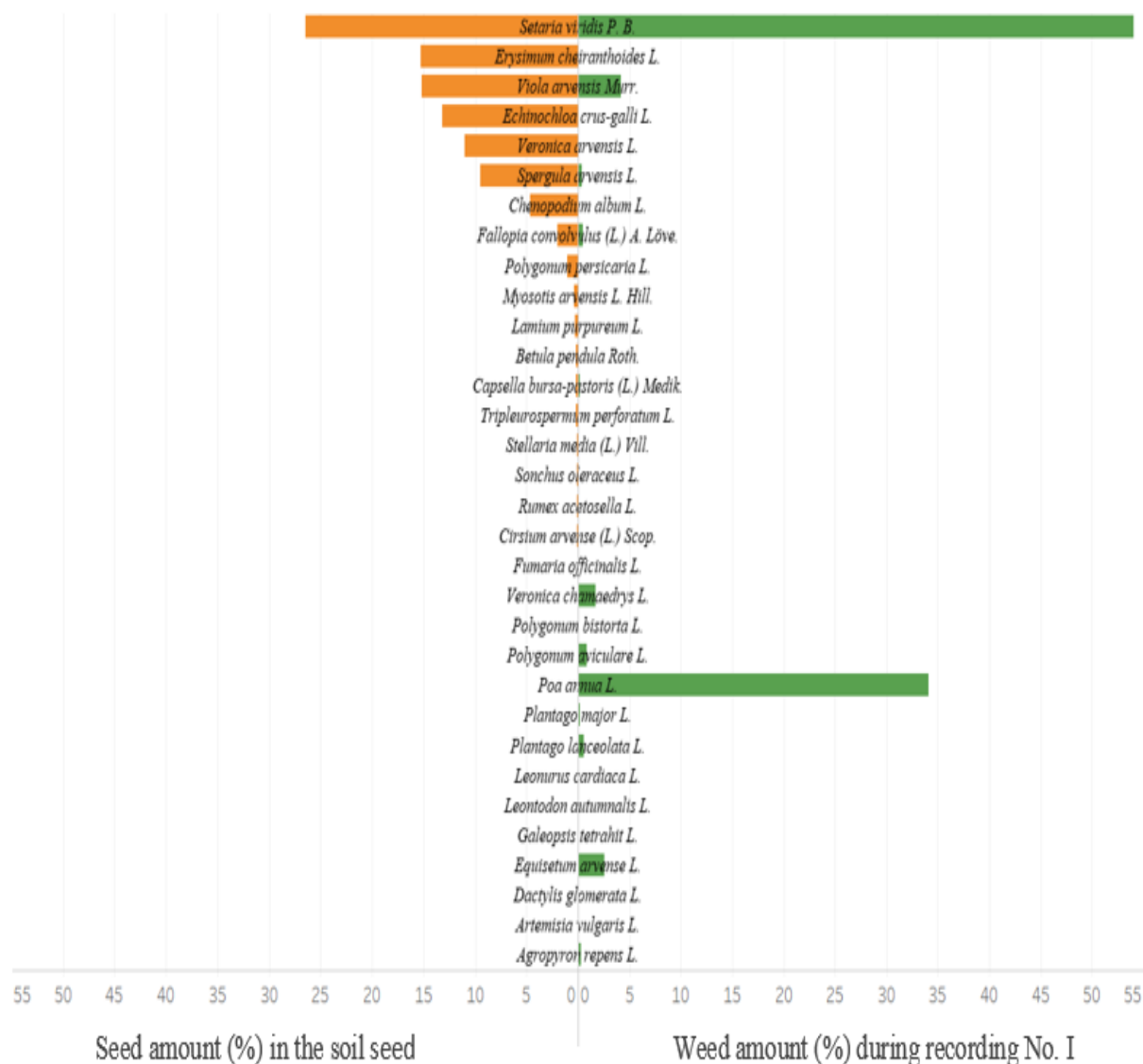
Fig. 3. The interaction of soil seed bank and weeds in the pre-erosion
cereal-grass crop rotation in autumn, average data. Kaltinenai, 2020-2021.

CONCLUSIONS

In the soil seed bank of the midslope of the hill, the number of seeds was by 12,0% and 49,8% higher compared to the summit and footslope parts. The number of seeds at the soil depth of 0–5 and 5–15 cm soil changed depending on the relief. At the depth of 0–5 cm, the number of seeds increased in the downslope direction, 60,9%, 64,0%, and 64,3%, respectively, in the summit, midslope, and footslope parts of the hill.

REFERENCES

1. AUŠKALNIENĖ, O.; AUŠKALNIS, A. The influence of tillage system on diversities of soil weed seed bank. *Agronomy Research*, 2009, Vol. 7, P.156–161.

2. BARBERI, P.; LO CASCIO, B. Long-term tillage and crop rotation effects on weed seed bank size and composition. *Weed Research*, 2001, Vol. 41, P. 325–340.

3. JANKAUSKAS, B.; JANKAUSKIENĖ, G. Long-term soil erosion studies on the Žemaičiai Upland: 2. Intensity of water erosion. *Zemdirbyste-Agriculture*, 2003, Vol.82,P. 20–34.

4. JARAŠIŪNAS, G.; KINDERIENĖ, I. Impact of agro-environmental systems on soil erosion processes and soil properties on hilly landscape in Western Lithuania. *The Journal of Environmental Engineering and Landscape Management*, 2016, Vol. 24, P. 60–69.

5. JOSE-MARIA, L.; SANS, F.X. Weed seedbanks in arable fields: effects of management practices and surrounding landscape. *Weed Research*, 2011, Vol. 51, P. 631–640.

6. MAIKŠTĖNIENĖ, S.; VELYKIS, A.; ARLAUSKIENĖ, A.; SATKUS, A. Javų stelbiamosios gebos įtaka sunkiuose priemoliuose plintančioms piktžolėms [Investigations of weed-suppressing ability of cereals on clay loam soils (summary)]. Vagos. 2006, Vol. 72, No. 25, p. 25–32.

7. MENALLED, F. Weed seedbank dynamics & integrated management of agricultural weeds. *Agriculture and Natural Resources*. 2008, P. 200-1008.

8. MOONEN, A. C.; BARBERI, P. Size and composition of the weed seedbank after 7 years of diferent cover-crop-maize management systems. *Weed Research*. 2004, Vol. 44, P. 163–177.

9. MONSTVILAITĖ, J.; KINDERIENĖ, I.; Reljefo įtaka agrofitocenozėms. Augalininkystė kalvoto reljefo sąlygomis. Mokslinė konferencija. 2000, P. 64-72.

10. REINE, R..; CHOCARRO, C.; FILLAT, F. Soil seed bank and management regimes of semi-natural mountain meadow communities. *Agriculture, Ecosystems and Environment*, 2004, Vol.104: P. 567–575.

11. SKUODIENĖ, R.; REPŠIENĖ, R.; KARČAUSKIENĖ, D.; ŠIAUDINIS, G. Assessment of the weed incidence and weed seed bank of crops under different pedological traits. *Applied ecology and environmental research*, 2018, Vol. 16, P. 1131-1142.

12. SKUODIENE, R.; KARČAUSKIENE, D.; ČIUBERKIS, S.; REPŠIENE, R.; AMBRAZAITIENĖ D. The influence of primary soil tillage on soil weed seed bank and weed incidence in a cereal-grass crop rotation. *Zemdirbyste-Agriculture*. 2013, Vol.100, P. 25-32.

13. STARKUTĖ, R.; BUNDINIENĖ, O.; ZALATORIUS, V. Tręšimo įtaka piktžolių paplitimui ir įvairovei pupų pasėlyje. Lietuvos agrarinių ir miškų mokslų centro filialo sodininkystės ir daržininkystės instituto ir Aleksandro Stulginskio universiteto mokslo darbai. Sodininkystė ir daržininkystė, 2018, Vol. 37, P. 3–4.

EVALUATION OF HEAVY METALS IN *PEGANUM HARMALA* SEEDS

T.A. Nasibova, **E.A. Garaev, G.R. Zeynalova, D.S. Gafarova, S.A. Pashayeva, N.S. Huseynova**
Azerbaijan Medical University
Anvar Gasimzade 14, AZ1022 Baku– Azerbaijan
tnesibova@amu.edu.az

EXTENDED ABSTRACT

OVERVIEW

Nowadays increasing of heavy metal content in the environment is one of the most important problems. This increase especially in the water, and soil, which is the source of our food, indicates potential future problems. Abundance of heavy metals in these resources also affects plants used for various purposes like food, traditional medicine, etc. This can lead to intoxication and diseases caused by heavy metals. Some plants are widely used for traditional medicinal purposes. *Peganum harmala* is a such plant with its use in African and Arabian countries, Iran, Uzbekistan, Greece, Spain, Italy, China, India, Mexico and America. Its seeds are used as herbal tea, or by directly eating for sedative, abortifacient, antiemetic, blood sugar lowering, anti-constipation, etc. [1]. Such wide geographic and pharmacological use increases the likelihood of chemical compounds such as heavy metals accumulating in the body and damaging it. This plant is not cultivated, and usually grows wild near human settlements; that is, its heavy metal content is also not controlled. These properties also increase the likelihood of intoxication and accumulation caused by heavy metals.

METHODS

For qualitative and quantitative determination of heavy metals in the *P. harmala* seeds, collected at 25.5°C in September 2019 from the sandy-soil area of Khaldan, Azerbaijan. In order to determine the natural amount of heavy metals in the plant, care was taken to ensure that there were no contaminants in the environment (plant, etc.). Dried and powdered seeds was treated at 90 °C with "king's water" (nitric acid: hydrochloric acid, molar ratio 1:3). After this process solution was cooled off, diluted with water, and filtered. 1 ml from the final solution diluted 100 times, added to the vial [2], transferred to the ICP-MS 7700 (Agilent Technologies, United States) for qualitative and quantitative analysis [3].

RESULTS

As a result, the most abundant heavy metal in *P. harmala* seeds is manganese (Mn) with 71.8 mg/kg. It is an extremely critical heavy metal for plant and animal growth. Manganese plays a role in bone growth and cholesterol production. Perosis (deformities of the foot and leg bones), eggshell formation, and reproductive abnormalities in chickens [4], skeletal anomalies, and ataxia in mammals may arise from its insufficient intake. Poor reproductive performance in elderly mammals is characterized by depressive or irregular estrus, low pregnancy rate,

abortion, stillbirths, and small birth weights [5]. High Mn concentrations have been shown to affect human lungs and brains [2]. Mn has a maximum authorized WHO limit of 200 mg/kg in medicinal plants, although its usual oral intake is 11 mg/day [6]. The level of manganese in *P. harmala* satisfies the required guidelines, according to the findings.

After manganese, iron (Fe) is the second most prevalent heavy metal in *P. harmala* seeds, with 58.5 mg/kg. It is the most widely distributed as a key element in all plants and animals [7]. Iron is required for hemoglobin production, and iron requirement is high in milk-fed, pregnant mammalians, and mammalians during ovulation [4]. It is unlikely to be deficient in grazing ruminants unless there are diseases that induce chronic blood loss or parasite infestations [5,8]. At high concentrations, on the other hand, it damages tissues and causes a variety of health problems in humans. It's also linked to anemia and neurological diseases in humans [7]. The WHO recommends a threshold of 20 mg/kg of iron in medicinal plants, while food intake is between 10 and 28 mg per day [6]. This demonstrates that, the amount of this element must be monitored for medical purposes.

Mercury (Hg) and arsenic (As), at 0.016 mg/kg and 0.03 mg/kg, respectively, are the least common. The element As can alternatively be classified as a metalloid [8]. These two elements are also among the most hazardous heavy metals. In little levels, causes negative consequences in humans and animals [9]. However, the presence of less than the needed amount of mercury and arsenic in the plant demonstrates that the plant was not poisoned by these elements.

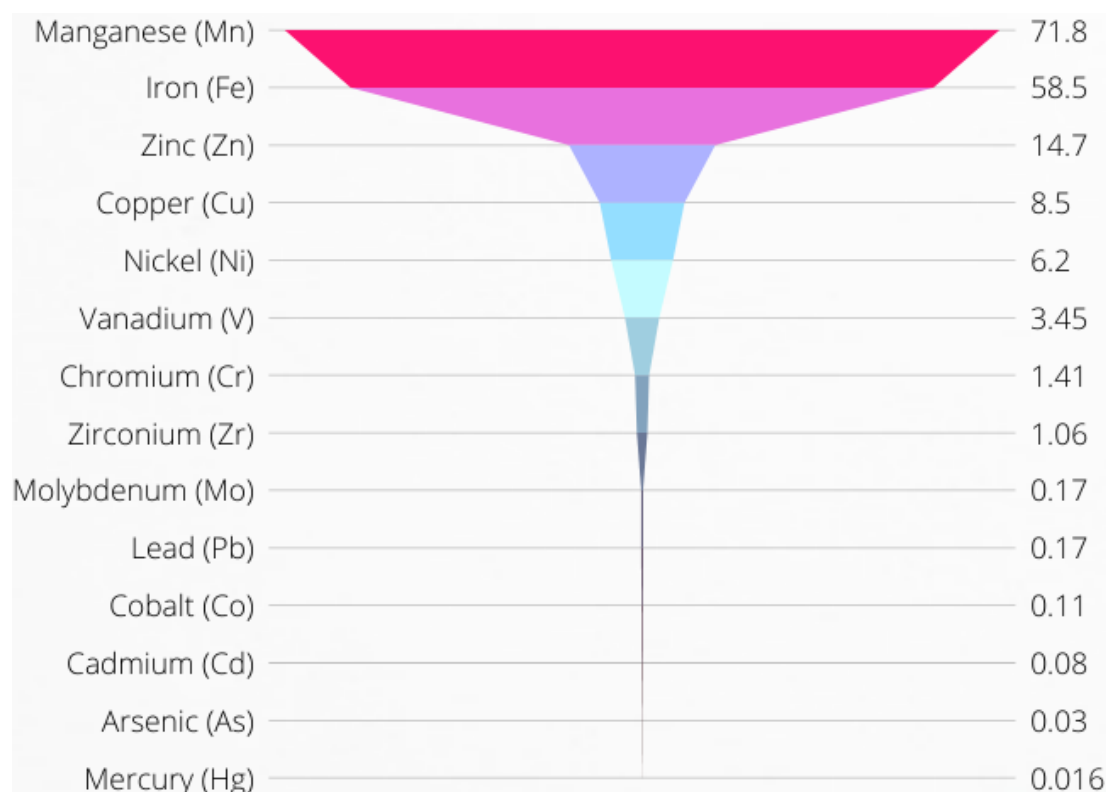| Element	mg/kg
Manganese (Mn)	71.8
Iron (Fe)	58.5
Zinc (Zn)	14.7
Copper (Cu)	8.5
Nickel (Ni)	6.2
Vanadium (V)	3.45
Chromium (Cr)	1.41
Zirconium (Zr)	1.06
Molybdenum (Mo)	0.17
Lead (Pb)	0.17
Cobalt (Co)	0.11
Cadmium (Cd)	0.08
Arsenic (As)	0.03
Mercury (Hg)	0.016

Fig. 1. Heavy metal content of *Peganum harmala* seeds (in mg/kg)

CONCLUSIONS

Based on the results, the heavy metals in the *Peganum harmala* seeds are at normal levels in the conditions of natural growth away from the risk of environmental pollution.

Keywords: *Peganum harmala*, heavy metal, manganese, iron, mercury, arsenic

REFERENCES

1. PRATAMA, M. R. F.; NASIBOVA, T.; PRATIWI, D.; KUMAR, P.; GARAEV, E. *Peganum harmala* and its alkaloids as dopamine receptor antagonists: in silico study. *Biointerface Research in Applied Chemistry*, 2021, Vol. 11, No. 3, p. 10301-10316. DOI: 10.33263/BRIAC113.1030110316

2. JOHN, S. A.; SENTHIL, T. K.; MUTHURAMAN, G.; MAJEED, A.; MAJEED, M. Mineral elements, and their ICP-MS validation in Crepidium acuminatum (D.Don) Szlach.- An Ashtavarga plant. *Asian Journal of Biochemical and Pharmaceutical Research,* 2017, Vol. 7, No. 4, P. 38-46. DOI: 10.24214/AJBPR/7/4/3845

3. RÓDENAS DE LA ROCHA, S.; SÁNCHEZ-MUNIZ, F. J.; GÓMEZ-JUARISTI, M.; MARIN, M. T. L. Trace elements determination in edible seaweeds by an optimized and validated ICP-MS method. *Journal of Food Composition and Analysis,* 2009, Vol. 22, No. 4, P. 330–336. DOI: 10.1016/j.jfca.

4. GURSOY, E.; MACIT, M. Determination of mineral contents of some legume and cereal forages grown as naturally in pastures of Erzurum province. *Alinteri Journal of Agriculture Science*, 2017, No. 32, P. 1-9.

5. SPEARS, J. W. *Minerals in Forages*. In: GC Fahey (Ed), Forage Quality, Evaluation, and Utilization, 2015.

6. *World Health Organization.* Quality Control Methods for Medicinal Plant Materials. Geneva: Switzerland, 1998.

7. FUORTES, L.; SCHENCK, D. Marked elevation of urinary zinc levels and pleural-friction rub in metal fume fever. *Veterinary and Human Toxicology*, 2000, Vol. 42, No. 3. P. 164–165.

8. VERNON, R. E. Which Elements Are Metalloids? *Journal of Chemical Education*, 2013, No. 90, P. 1703–1707.

9. JAISHANKAR, M.; TSETEN, T.; ANBALAGAN, N.; MATHEW B. B.; BEEREGOWDA, K. N. Toxicity, mechanism and health effects of some heavy metals. *Interdisciplinary Toxicology*, 2014, Vol. 7, No. 2. P. 60–72.

EFFECTS OF DIFFERENT SIZES OF ZINC OXIDE AND COPPER OXIDE NANOPARTICLES ON GROWTH PARAMETERS AND ANTIOXIDATIVE ACTIVITY *OF LACTUCA SATIVA*

K. Stašytė, R. Sutulienė, J. Miliauskienė, A. Brazaitytė
Lithuanian Research Centre for Agriculture and Forestry,
Institute of Horticulture, Department of Plant Physiology
Kauno St. 30, Babtai, LT-54333, Kaunas distr. – Lithuania
+37063360636
kamile.stasyte@vdu.lt, ruta.sutuliene@lammc.lt; jurga.miliauskiene@lammc.lt;
ausra.brazaityte@lammc.lt

EXTENDED ABSTRACT

OVERVIEW

The use of nanoparticles (NPs) in agriculture is a new and promising area for agricultural improvement by reducing the negative impact of chemicals on the environment, improving the nutritional value of food and production by controlling pests and nutrients in plants [1]. Studies on the effects of metal-based nanoparticles on leafy greens will enrich knowledge about the benefits or risks of NPs to plants.

Minerals like copper (Cu) and zinc (Zn) plays an important role in human nutrition. Copper is an important element in the formation of red blood cells and is particularly important for the functioning of the immune system [2]. Previous studies indicated that the effects of CuO and ZnO NPs generally depend on the plant species and the concentration of the nanoparticle solution, but there is still a lack of information on the effects of nanoparticle sizes on plants. According to the literature, CuO NPs may have different effects on plants, e.g. phytotoxicity of CuO nanoparticles was determined for soybeans (*Glycine max* cv. Kowsar) grown in soil and used CuO 25, 50, and 250 nm NPs, which was solidified in a viscose gel and buried in the ground [3]. It was also found that the non-enzymatic antioxidant activity was improved when lettuce (*Lactuca sativa*) was sprayed with a 20 mg/l concentration of CuO NPs and works better than the application through the soil [4]. Spraying with 50 nm ZnO NPs at a concentration of 25 and 100 mg/l concentration improved morphological properties, reduced oxidative stress damage, and an intensified antioxidant system in cucumbers [5]. Besides, Coriander (*Coriandrum sativum*) has more intense photosynthesis, synthesis of antioxidative enzymes, and better nutritional value after the soil was supplemented with 100, 200, and 400 mg/kg ZnO NPs [6]. The aim of the study is to investigate the effect of different sizes of CuO and ZnO nanoparticles suspensions on lettuce growth and antioxidant system.

METHODS

The research was carried out in closed, controlled environment chambers (4 × 6 m) in a phytotron complex at the Lithuania Research Centre for Agriculture and Forestry, Institute of Horticulture, from November 7 to December 10. At first stone wool germination cubes (2 × 2 × 3,5 cm) were soaked in distilled water, then the lettuce (*Lactuca sativa,* cv. Little Gem) was

sown. On the fifth day after sowing, plants were irrigated with hydroponic solution pH – 5.5 and the electrical conductivity (EC) was 1,36 mS/cm. Two weeks after sowing, lettuce was transferred to large hydroponic systems with Ph 5,5 and EC – 1,38 mS/cm. The plants were sprayed with solutions of different sizes CuO (10, 20, 80 nm; 20 mg/l) and ZnO (18, 35-45, 80-200 nm; 200mg/l) after 10 days of lettuce growing in hydroponic systems. A week later, the fresh and dry mass of the leaves and roots of the plants, as well as the leaf area, electrolyte leakage were measured.

Antioxidant activity of lettuce leaves was evaluated by ABTS (2,2'-azino-bis-3-ethylbenzothiazoline-6-Sulfonic Acid) [7], DPPH (2,2-diphenyl-1-picrylhydrazyl) [8], and FRAP – total phenolic compound activity [9] analysis. Extracts were prepared by weighing 0.1 g of the lyophilized sample and adding 5 ml of 80% methanol. 2 hours samples were rotating in the caroused. After 24 h. Of storage at 4 °C and centrifuge at 3000 rpm. The supernatant was used for further analysis. All biochemical analysis was performed in 3 biological and 3 analytical replications.

RESULTS

The effects of CuO (10, 40, 80 nm; 20 mg / l) and ZnO (18, 35-45, 80-200 nm; 200 mg / l) NPs were evaluated on lettuce growth parameters (Table 1.). The strongest effect on lettuce growth rates was spraying them with CuO 80 nm NPs. The smallest roots had lettuce sprayed with ZnO 18 nm in size NPs. The lowest dry and green leaf masses were in lettuce sprayed with ZnO 18 nm and CuO 40 nm NPs, and the smallest leaf area was in lettuce sprayed with CuO 10 nm NPs.

Table 1. Effect of CuO (CuO1 – 10nm; CuO2 – 40 nm; CuO3 – 80 nm) and ZnO (ZnO1 – 18 nm; ZnO2 – 35-45 nm; ZnO3 – 80-200 nm) nanoparticle suspensions on lettuce growth rates, averages followed by letters indicating differences between control and other variants at $p < 0.05$ (n = 10) by Tukey's (HSD) test. FW – fresh weight, DW – dry weight, EL – electrolyte leakage.

	Leaf FW, g	Leaf DW, g	Roots GW, g	Roots DW, g	EL, %	Leaf area, cm^2
Control	48.294 c	3.044 c	9.612 ab	0.297 a	75.325 b	829.157 a
CuO 1	57.030 a	3.369 b	6.720 c	0.240 b	58.509 c	522.477 e
CuO 2	39.416 e	2.417 e	6.815 c	0.194 c	52.905 c	648.180 d
CuO 3	57.393 a	3.598 a	10.408 a	0.300 a	89.363 a	857.365 a
ZnO 1	38.605 e	2.754 d	4.702 d	0.148 d	70.449 b	681.495 c
ZnO 2	45.295 d	2.880 cd	6.225 c	0.175 cd	79.092 b	712.037 c

ZnO 3						766.015
53.034 b	2.951 c	8.894 b	0.236 b	52.564 c		b

The effects of CuO (10, 40, 80 nm; 20 mg / l) and ZnO (18, 35-45, 80-200 nm; 200 mg / l) NPs were evaluated on lettuce antioxidant activity (Fig. 1). Antioxidant activity was strongest after spraying lettuce with ZnO 35-45 nm (DPPH – 2147,471 mM TE/g dry weight; ABTS – 3465,28 mM TE/g green weight; FRAP – 3113,877 µmol/g) and CuO 40 nm (DPPH – 2220,869 mM TE/g dry weight; ABTS – 3311,051 mM TE/g green weight; FRAP – 2907,381 µmol/g) NPs. The lowest antioxidant activity was found in lettuce sprayed with CuO 10 nm (DPPH – 1977,562 mM TE/g dry weight; ABTS – 2989,248 mM TE/g green weight; FRAP – 2572,554 µmol/g) and ZnO 80-200 nm (DPPH – 1985,287 mM TE/g dry weight; ABTS – 2947,463 mM TE/g green weight; FRAP – 2662,381 µmol/g) NPs suspensions.
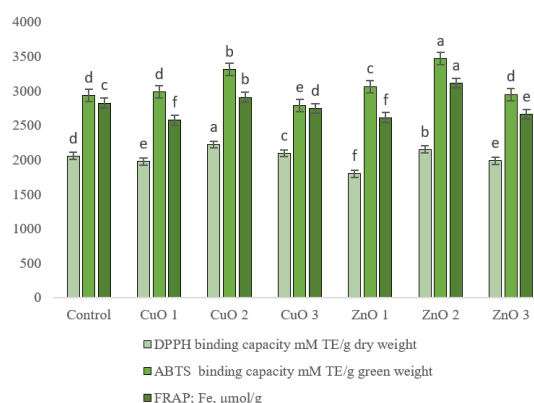
Fig. 1. Effect of CuO (CuO1 – 10nm; CuO2 – 40 nm; CuO3 – 80 nm) and ZnO (ZnO1 – 18 nm; ZnO2 – 35-45 nm; ZnO3 – 80-200 nm) nanoparticle suspensions on antioxidant activity (DPPH, ABTS, FRAP) in lettuce. Averages ± standard deviation are given, with letters indicating differences between control and other variants when $p < 0.05$ (n = 10) according to Tukey's (HSD) test.

CONCLUSIONS

CuO 80-200 nm NPs have a positive effect on lettuce's fresh and dry mass of leaf and roots, electrolyte leakage, and leaf area. The highest antioxidant activity has lettuce sprayed with ZnO 35-45 nm and CuO 40 nm NPs.

Keywords: (CuO nanoparticles; ZnO nanoparticles; Lettuce; Antioxidant activity; ABTS; DPPH; FRAP)

REFERENCES

1. PRASAD, R.; BHATTACHARYYA, A.; NGUYEN, Q. D. Nanotechnology in Sustainable Agriculture: Recent Developments, Challenges, and Perspectives. *Frontier in microbiology*, 2017, Vol. 8.

2. WARE, M. Health benefits and risks of copper. *Medical News Today, 2017*- [referred on the 10th of December in 2021 y.]. Link to the internet <https://www.medicalnewstoday.com/articles/288165>.

3. YUSEFI-TANHA, E.; FALLAH, S.; ROSTAMNEJADI, A.; POKHREL, L. R. Particle size and concentration dependent toxicity of copper oxide nanoparticles (CuO NPs) on seed yield and antioxidant defence system in soil grown soybean (*Glycine max* cv. Kowsar). *Science of The Total Environment*, 2020, Vol. 715, No. 136994.

4. KOHATSU, M. Y.; LANGE, C. N.; PELEGRINO, M. T.; PIERETTI, J. C.; TORTELLA, G.; RUBILAR, O. Foliar spraying of biogenic CuO nanoparticles protects the defence system and photosynthetic pigments of lettuce (Lactuca sativa). *Journal of Cleaner Production*, 2021, Vol. 324, No. 129264.

5. GHANI, M. I.; SALEEM, S.; RATHER, S. A.; REHMANI, M. S.; ALAMRI, S.; RAJPUT, V. D. et al. Foliar application of zinc oxide nanoparticles: An effective strategy to mitigate drought stress in cucumber seedling by modulating antioxidant defense system and osmolytes accumulation. *Chemosphere*, 2022, Vol. 289, No. 133202.

6. PULLAGURALA, V. L.; ADISA, I. O.; RAWAT, S.; KALAGARA, S.; HERNANDEZ-VIEZCAS, J. A.; PERALTA-VIDEA, J. R. et al. ZnO nanoparticles increase photosynthetic pigments and decrease lipid peroxidation in soil grown cilantro (*Coriandrum sativum*). *Plant Physiology and Biochemistry*, 2018, Vol. 132, P. 120-127.

7. RE, R. PELLEGRINI, N.; PROTEGGENTE, A.; PANNALA, A.; YANG, M., and RICE-EVANS, C., Antioxidant activity applying an improved ABTS radical cation decolorization assay, *Free Radical Biology and Medicine*, 1999, Vol. 26, P. 1231-1237.

8. SHARMA, O. P.; BHAT, T. K. DPPH Antioxidant Assay Revisited. *Food Chemistry*, 2009, Vol. 113, P. 1202–1205.

9. BENZIE, I. F. F.; STRAIN, J. J. The Ferric Reducing Ability of Plasma (FRAP) as a Measure of "Antioxidant Power": The FRAP Assay. *Analytical Biochemistry*, 1996, Vol. 239, P. 70–76.

EFFECTS OF COPPER OXIDE NANOPARTICLES ON THE ANTIOXIDANT PROPERTIES OF DROUGHT-AFFECTED *PISUM SATIVUM* L.

R. Sutulienė, J. Miliauskienė

Lithuanian Research Centre for Agriculture and Forestry,
Institute of Horticulture, Department of Plant Physiology
Kauno g. 30, LT-54333 Babtai – Lithuania
+37065398181
ruta.sutuliene@lammc.lt; jurga.miliauskiene@lammc.lt

L. Ragelienė
Vytautas Magnus University, Faculty of Natural Science, Department of Biochemistry
Vileikos g. 8, LT-44404 Kaunas – Lithuania
+370 37 327 902
lina.rageliene@vdu.lt

EXTENDED ABSTRACT

OVERVIEW

Abiotic stresses such as drought have a detrimental impact on plant productivity and yields of all major crops, thereby causing significant losses [1]. Peas, like other legumes, are more sensitive to water stress. Peas are extremely useful for the soil, in crop rotation and as a source of protein in the diet, so it is particularly important to discover new agronomic practices and maintain plant resilience [2]. This could be the use of certain nanoparticles (NPs) due to unique physicochemical properties: shape, size, crystal structure, chemical composition, physiochemical stability, and surface area [3].

Copper (Cu) is an essential trace element required for plant growth and development [4] and is included in proteins and metal enzymes required to perform various metabolic functions in plant cells. It is also actively involved in vital cellular processes such as mitochondrial respiration, electron transfer from photosynthesis, cell wall metabolism, hormone signalling, protein trafficking, and iron mobilization [5, 9]. In previous studies, researchers found that using higher concentrations of CuO NPs (from 100 mg / L to 1000 mg / L) suspensions had negative effects on lettuce [6], wheat [7] and mung bean [8] root length, fresh mass, and shoot length. Other researchers have found that using smaller CuO NPs (25 nm) at a concentration of 50 mg/kg decreased the production of oxidative stress biomarkers and at a concentration of 500 mg/kg increased enzymatic antioxidants in soybean plants [9]. However, there is still a lack of knowledge about how CuO NPs affect the antioxidant system of pea plants. The aim of this study was to determine the influence of different concentrations and application of CuO NPs on the antioxidant system of drought-affected peas.

METHODS

Copper oxide NPs (particle size: 25-55nm; purity: 99.95+%) were used for this experiment (US Research Nanomaterials, Inc, Houston, TX USA). The concentrations of 50, 25, 12.5 ppm NPs were suspended in deionized water and dispersed using ultrasonicator for 60 min. The research was carried out in a greenhouse (3 × 6 m, h = 2 m) at the Lithuanian Research Centre for Agriculture and Forestry, Institute of Horticulture, Babtai, from May 6 to June 22. Before sowing, green pea (*Pisum sativum* L. cv. Respect, Maribo Seed International ApS, Denmark) seeds were sterilized in 5% sodium hypochlorite solution. Pea seedlings were thinned to 7 plants per pot 5 days after sowing. The granulometric composition of the soil was heavy loam, pH 7.4 $\pm$ 0.1; concentration of humus – 3.6$\pm$0.1%; P_2O_5 - 243$\pm$8 mg kg^{-1}; K_2O - 348$\pm$37 mg kg^{-1}; NH_4 – 4 $\pm$0.6 mg kg^{-1}; NO_3 – 22$\pm$0.9 mg kg^{-1}; SiO_2 – 39$\pm$0.8 mg kg^{-1}. Depending on the composition of the soil, peas were supplementally fertilized with nitrate. Then, the peas were irrigated with a cylinder every other day with 100 ml of tap water in each vegetative container to maintain 80% substrate moisture (SM). Peas were sprayed or irrigated with a 12.5, 25, 50 ppm concentration of CuO NP suspension when they reached stage 40 on the BBCH scale [10]. After spraying or irrigating, part of the vegetation pots was maintained with normal substrate moisture (80%), while in others were initiated drought by maintaining low substrate moisture (30%). Samples were collected after 10 days of drought exposure.

Antioxidant properties of pea leaves were evaluated as the DPPH (2-diphenyl-1-picrylhydrazyl) [11], ABTS (2,20-azino-bis (3-ethylbenzothiazoline-6-sulphonic acid) [12] radical scavenging activities, and Fe^{2+} reducing antioxidant power assay (FRAP) [13], also total contents of phenolic compounds [14] were determined. Extracts were prepared by grinding 0,3 g of plant leaves with liquid nitrogen and diluting with 5 mL of 80% methanol. After 24 h, the samples were centrifuged for 10 min at 3000 rpm (Hermle Z300K, Germany), extracts were filtered through cellulose filters and the supernatant was used for further analyses. All biochemical analysis was performed in 3 biological replications. Each of three biological replicates consisted of at least three conjugated plants and were repeated in three analytical replicates.

RESULTS

As can be seen in the graphs (Fig. 1), all concentrations of CuO NPs suspension influenced the antioxidant system of peas. The effect of drought (SM 30%) reduced the activity of the antioxidant system of pea plants from 17 to 96% compared to the control plants (SM 80%). However, peas sprayed or irrigated with CuO NPs suspensions showed a positive effect on the efficiency of the antioxidant system. We can distinguish Fe^{2+} reducing antioxidant power (Fig. 1 d) as it increased from 33 to 67% compared to control plants. In addition, we can observe that a concentration of 50 ppm of CuO NPs had increased the activity of the antioxidant system in DPPH (Fig. 1 b) and the total amount of phenolic compounds (Fig. 1 c) by 40 and 18%, respectively, compared to the control plants. Antioxidant activity was stronger when plants were irrigated with CuO NPs suspension than when sprayed with respect to ABTS radical scavenging efficiency (Fig. 1 a).

(a)

(b)

(c)

(d)
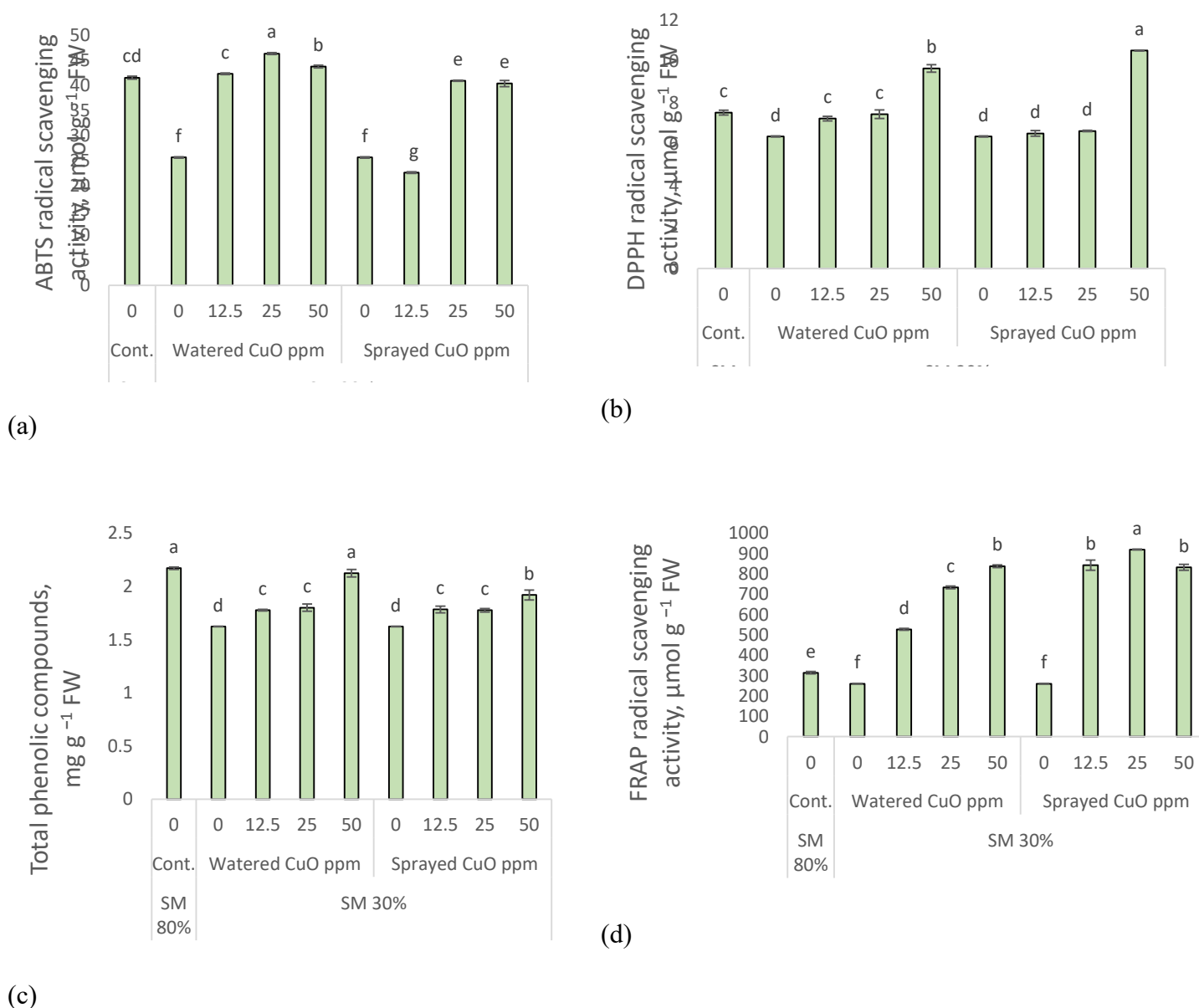
Fig. 1. Influence of drought stress and CuO NPs (0; 12,5; 25; 50 ppm) on ABTS (a) and DPPH (b) radical scavenging activity; total phenolic compounds (c); FRAP, Fe^{2+} reducing antioxidant power (d) in *P. sativum* L. Cont. – control plants, substrate moisture (SM) 80%; drought stress – SM 30%. Values are mean ± SE of three replicates and different letters are differed significantly by Tukey HSD Test (P < 0.001).

CONCLUSIONS

CuO nanoparticles have a positive effect on the antioxidant system of drought-affected pea plants, depending on the concentration. Therefore, the use of CuO NPs in the environment needs to be thoroughly investigated and criteria for sustainable use need to be defined.

Keywords: (CuO nanoparticles; Drought; Antioxidant activity; Pea; DPPH; ABTS; FRAP; TPC)

REFERENCES

1. GILLIHAM, M.; ABLE, J.A.; ROY, S.J. Translating Knowledge about Abiotic Stress Tolerance to Breeding Programmes. *Plant Journal*, 2017, Vol. 90, P. 898–917.

2. PRASAD, R.; BHATTACHARYYA, A.; NGUYEN, Q. D. Nanotechnology in Sustainable Agriculture: Recent Developments, Challenges, and Perspectives, *Frontiers in Microbiology*, 2017.

3. MA, X.; GEISER-LEE, J.; DENG, Y.; KOLMAKOV, A. Interactions between engineered nanoparticles (ENPs) and plants: Phytotoxicity, uptake and accumulation, *Science of The Total Environment*, 2010, Vol. 408, P. 3053-3061.

4. SHAW, A.K.; HOSSAIN, Z. Impact of Nano-CuO Stress on Rice (Oryza Sativa L.) Seedlings. *Chemosphere* 2013, Vol. 93, P. 906–915,

5. CHANDRA, S.; KUMAR, A.; TOMAR, P.K. Synthesis and Characterization of Copper Nanoparticles by Reducing Agent. *Journal of Saudi Chemical Society* 2014, Vol. 18, P. 149–153.

6. HONG, J.; RICO, C.M.; ZHAO, L.; ADELEYE, A.S.; KELLER, A.A.; PERALTA-VIDEA, J.R.; GARDEA-TORRESDEY, J.L. Toxic Effects of Copper-Based Nanoparticles or Compounds to Lettuce (*Lactuca Sativa*) and Alfalfa (*Medicago Sativa*). *Environmental Science: Processes & Impacts*, 2015, Vol. 17, P. 177–185.

7. DIMKPA, C. O.; MCLEAN, J. E.; LATTA, D. E.; MANANGÓN, E.; BRITT, D. W.; JOHNSON, W. P. CuO and ZnO nanoparticles: phytotoxicity, metal speciation, and induction of oxidative stress in sand-grown wheat. *Journal of Nanoparticle Research*, 2012, Vol. 14.

8. NAIR, P. M. G.; CHUNG, M. Copper oxide nanoparticle toxicity in mungbean (*Vigna radiata* L.) seedlings: physiological and molecular level responses of in vitro grown plants. *Acta Physiologiae Plantarum*, 2014, Vol. 36, P. 2947–2958.

9. YUSEFI-TANHA, E.; FALLAH, S.; ROSTAMNEJADI, A.; POKHREL, L.R. Particle Size and Concentration Dependent Toxicity of Copper Oxide Nanoparticles (CuONPs) on Seed Yield and Antioxidant Defense System in Soil Grown Soybean (*Glycine Max* Cv. Kowsar). *Science of The Total Environment*, 2020, Vol. 715.

10. MEIER, U. Growth Stages of Mono- and Dicotyledonous Plants: BBCH-Monograph Entwicklungsstadien Mono- Und Dikotyler Pflanzen; Biologische Bundesanstalt für Land- und Forstwirtschaft in Berlin und Braunschweig, Eds.; Blackwell-Wiss, Verl: Berlin Wien, 1997; ISBN 9783826331527.

11. SHARMA, O.P.; BHAT, T.K. DPPH Antioxidant Assay Revisited. *Food Chemistry* 2009, 113, 1202–1205.

12. RE, R.; PELLEGRINI, N.; PROTEGGENTE, A.; PANNALA, A.; YANG, M.; RICE-EVANS, C. Antioxidant activity applying an improved ABTS radical cation decolorization assay, *Free Radical Biology and Medicine*, 1999, Vol. 26, P. 1231-1237.

13. BENZIE, I. F. F.; STRAIN, J. J. The Ferric Reducing Ability of Plasma (FRAP) as a Measure of "Antioxidant Power": The FRAP Assay. *Analytical Biochemistry*, 1996, Vol. 239, p. 70–76.

14. AINSWORTH, E.; GILLESPIE, K. Estimation of total phenolic content and other oxidation substrates in plant tissues using Folin–Ciocalteu reagent, *Nature Protocols*, 2007, Vol. 2, P. 875–877.

PLANT GROWTH-PROMOTING *PAENIBACILLUS* SP. AFFECTS HYBRID POPLAR'S (*POPULUS TREMULA* X *P. ALBA*) PHENOLICS, ANTIOXIDANT ACTIVITY, AND PTHOTOSYNTHESIS PIGMENTS

D. Vaitiekūnaitė, G. Striganavičiūtė, V. Mishcherikova, V. Sirgedaitė-Šėžienė
Lithuanian Research Centre for Agriculture and Forestry, Institute of Forestry
Liepu st. 1, LT-53101 Girionys – Lithuania
+37037547221
doroteja.vaitiekunaite@lammc.lt

EXTENDED ABSTRACT

OVERVIEW

Globally agriculture, horticulture and agroforestry sectors rely on chemical fertilization to achieve necessary yields for the expanding human population. However, chemical fertilizers have been linked to deleterious effects on the ecosystems, biodiversity, and human health. Bacterial biofertilizers can be an eco-friendly alternative to chemical fertilizers, at the very least limiting their use [1]. However, before their implementation in field trials, in-depth studies need to be done. Compared to biofertilizer studies regarding food crops, research concerning trees is still scarce, likely due to difficulties in study realization. However, research on both woody and herbaceous plants point towards possibilities in using bacteria as inoculants to improve plant growth, health and adaptability [1]–[3]. While some studies highlight just one aspect of the inoculant, it's quite common that the same species affects their host plant in a variety of ways simultaneously [2], [4]. In our study poplar microshoots *in vitro* were inoculated with *Paenibacillus* sp., that was reported to be an effective biofertilizer *in vitro*, enhancing poplar root growth [4]. The aim of this study was to figure out whether growth-promoting *Paenibacillus* sp. bacteria affects *Populus* sp. microshoot free radical scavenging capacity, secondary metabolite, and photosynthesis pigment content in hopes of figuring out the holistic impact in may have.

METHODS

The experiment was done with a hybrid poplar *Populus tremula* x *P. alba in vitro* clone culture. *Paenibacillus* sp. was used for microshoot inoculation. Growth conditions and inoculation procedure was previously described [4]. Sample measurements were taken after 4, 6 and 8 weeks. Amounts of chlorophyll a (CHLA) and b (CHLB), carotenoid (CAR), total phenol (TPC), total flavonoid contents (TFC) [2], antioxidant activity via DPPH (2,2-diphenyl-1-picryl-hydrazyl-hydrate) and ABTS (2,2'-azino-bis(3-ethylbenzothiazoline-6-sulfonic acid)) assays were studied [5]. Pooled data from three independent experiments was used in statistical analysis (R software [6]). ANOVA, Kruskall-Wallis and Tukey's pairwise comparison tests as well as correlation analysis were carried out.

RESULTS

Data on tested *Populus* sp. biochemical parameters is shown in Fig. 1 (ANOVA). No significant results were obtained after 4-week incubation. However, after 6 weeks the amount of CHLA was the only insignificant metric; all the results after 8 weeks were statistically significant. CAR, ABTS and DPPH, TPC and TFC were lower in the experimental group post 6th week of incubation, while CHLB amount has increased compared to their respective control groups.
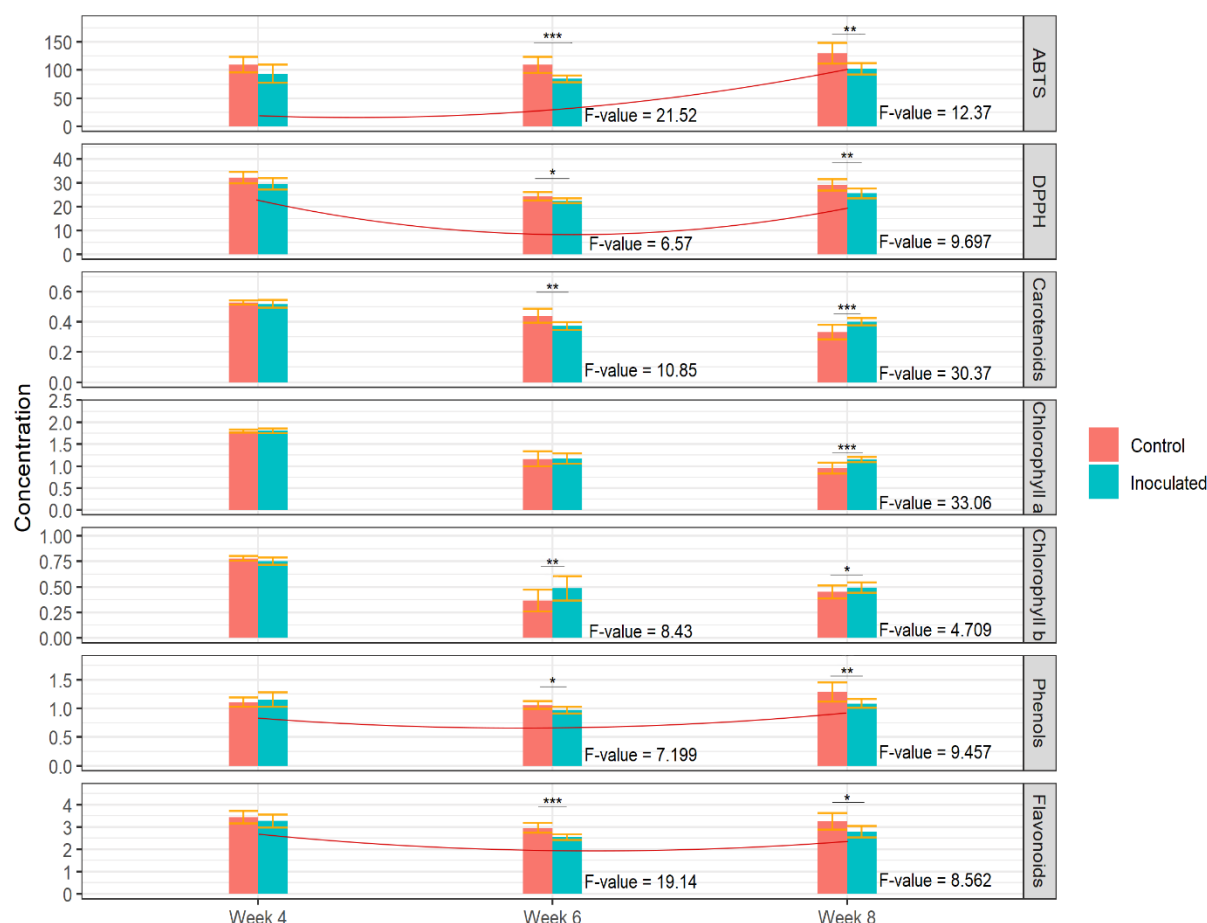
Fig. 1. The amounts (mg/g - phenolics and pigments, mM/g - antioxidant activity) of tested bioactive compounds in the inoculated and control groups during the experimental period. *p-values: *** - ≤0.001, ** - ≤0.01, * - ≤0.05* (post hoc Tukey Honest Significant Differences test (HSD) was performed for multiple pairwise-comparison between the means of groups). Red lines denote the same upward trajectory observed in several of the tested parameters.

Comparatively, ABTS and DPPH, TPC and TFC had decreased after 8th week of incubation and amounts of photosynthesis pigments has increased in regard to their respective control groups. An obvious upward trend in the amounts of plant antioxidant capacity and phenolics over the experimental period in both control and experimental groups can be seen. However, photosynthesis pigment contents did not exhibit an analogue trend. After the 6th week the amounts of CHLA and CAR were lower in the inoculated plants relative to the control, while the amount of CHLB increased. After the 8th week, all the photosynthesis pigment contents had increased in the experimental group.

The correlation between the amount of bioactive compounds in the experimental and control groups can be seen in Fig. 2. In both the control and experimental groups, amounts of TPC-TFC, DPPH-CHLB, CHLA-CHLB, CHLA-CAR, CHLB-CAR, TPC-ABTS displayed strong to moderate positive correlations. At the same time, a moderately negative correlation between TPC-CAR, ABTS-CAR and a moderately positive correlation between TFC-ABTS were noted in the control group, and moderately positive correlations in TFC-CHLA, DPPH-CHLA, TFC-CHKB, TFC-CAR, DPPH-CAR were observed in the experimental group. This demonstrates that the inoculation with *Paenibacillus* sp. changed how photosynthesis pigments relate to other tested metrics between the control and experimental groups. Most notably, inoculation seemingly affected TFC's relationship to all the pigments.
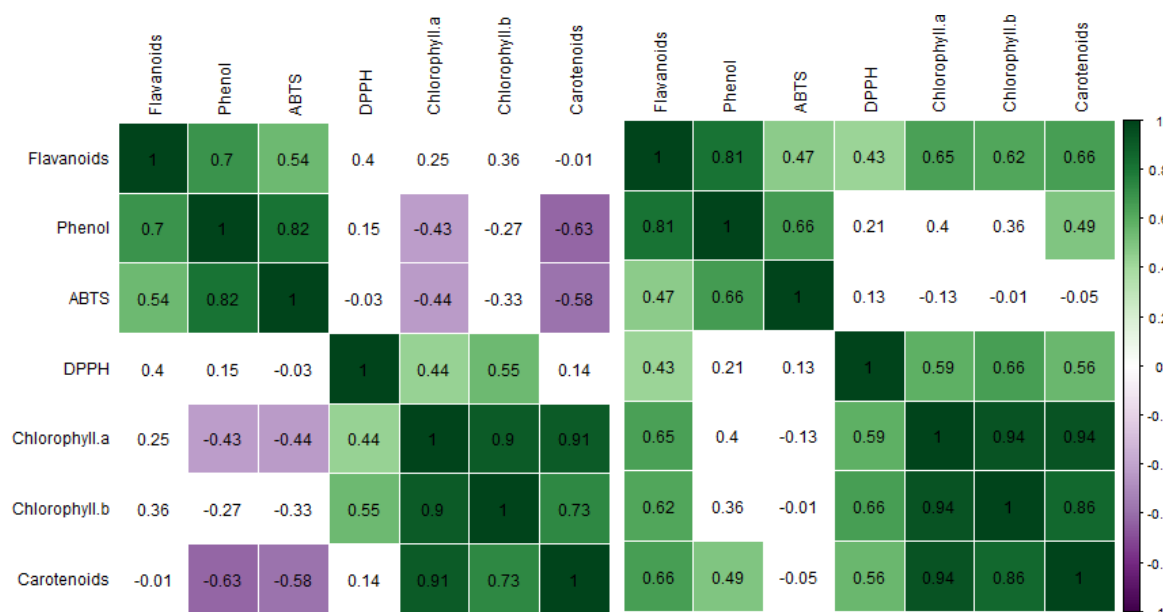
Fig. 2. Correlation between the concentration of tested bioactive compounds in control (left) and experimental (right) groups (week 8) (Pearson correlation coefficient). Coloured squares represent statistically significant data (*p<0.05*).

CONCLUSIONS

Overall, the effects on *Populus* sp. antioxidant activity, phenolics and photosynthesis pigments could potentially be understood as promising and that *Paenibacillus* sp. may have a positive effect on their *Populus* sp. hosts without secondary repercussions to the plant's biochemistry and health, hence at least partially confirming our hypothesis. Still, auxiliary information needs to be collected to understand more about the *Paenibacillus* sp.-poplar interaction prior to open ecosystem trials.

Keywords: bacteria, *Populus*, *Paenibacillus*, phenols, flavonoids, DPPH, ABTS, chlorophyll, carotenoids.

REFERENCES

1. KOUR, D. Microbial biofertilizers: Bioresources and eco-friendly technologies for agricultural and environmental sustainability. *Biocatalysis and Agricultural Biotechnology*., 2020, Vol. 23.

2. STRIGANAVIČIŪTĖ, G.; ŽIAUKA, J.; SIRGEDAITĖ-ŠĖŽIENĖ, V.; VAITIEKŪNAITĖ, D. Priming of resistance-related phenolics: a study of plant-associated bacteria and *Hymenoscyphus fraxineus*. *Microorganisms*, 2021, Vol. 9, No. 12.

3. RABIEY, M. Endophytes vs tree pathogens and pests: can they be used as biological control agents to improve tree health? *European Journal of Plant Pathology*., 2019, Vol. 155, No. 3, p. 711–729.

4. VAITIEKŪNAITĖ, D.; KUUSIENĖ, S.; BENIUŠYTĖ, E.; Oak (*Quercus robur*) associated endophytic *Paenibacillus* sp. promotes poplar (*Populus* spp.) root growth in vitro. *Microorganisms*, 2021, Vol. 9, No. 6. p. 1151.

5. CHANDRASEKARAN, M.; CHUN, S. C.; OH, J. W.; PARAMASIVAN, M.; SAINI, R. K.; SAHAYARAYAN, J. J. *Bacillus subtilis* CBR05 for tomato (*Solanum lycopersicum*) fruits in South Korea as a novel plant probiotic bacterium (PPB): implications from total phenolics, flavonoids, and carotenoids content for fruit quality. *Agronomy*, 2019, Vol. 9, No. 12.

6. R Foundation for Statistical Computing, "R: A language and environment for statistical computing." Vienna, Austria, 2013. <https://www.r-project.org/>

THE EFFECT OF DIFFERENT LOW TEMPERATURES DURING COLD ACCLIMATION ON SHOOT BIOMASS GROWTH AND METABOLITE ACCUMULATION IN WINTER WHEAT

G. Vaitkevičiūtė, R. Armonienė
Lithuanian Research Centre for Agriculture and Forestry
Instituto al. 1, Akademija, LT-58344, Kėdainiai distr. – Lithuania
+370 630 78 833
gabija.vaitkeviciute@lammc.lt

Y. Gibon
INRAE Bordeaux-Aquitaine Bât. IBVM
71, av. Edouard Bourlaux, 33882, Villenave d'Ornon – France
+33(0)5 57 12 26 51
yves.gibon@inrae.fr

EXTENDED ABSTRACT

OVERVIEW

Common wheat (*Triticum aestivum* L.) is one of the staple crops, producing a fifth of the proteins and calories consumed by the human population worldwide [1]. Winter wheat varieties are sown in autumn and the subsequent prolonged exposure to low positive temperatures induces cold acclimation (CA), which ultimately results in freezing tolerance (FT) and allows them to survive low negative temperatures in winter. CA promotes numerous molecular mechanisms, affecting the patterns of gene expression and metabolic processes, as well as the efficacy of photosynthesis [2]. During CA, winter wheat remains in the vegetative phase and is able to carry out photosynthesis efficiently, whereas under identical environmental conditions spring wheat experiences temperature-induced inhibition of photosynthesis [3]. This ability, combined with the prolonged vegetation period, results in winter wheat providing yields that are up to 36% larger than those of spring wheat [4,5]. However, the longer and warmer autumns, caused by climate change, may negatively impact the process of CA, thus, leading to insufficient FT of plants and a higher risk of winterkill [6]. Therefore, more research is required to understand how prolonged warm temperature during autumn affects the mechanism of CA. The aim of this work was to assess the effect of different low temperatures on winter wheat shoot biomass growth and metabolite accumulation during 7 weeks of CA.

METHODS

Two winter wheat varieties 'KWS Ferrum' and 'Lakaja DS' of lower and higher FT, respectively (unpublished data) were sown in peat moss substrate in 125 cm^3 well trays in a randomized pattern in 2 CA treatment groups and 3 biological replications for each sampling point. Each biological replication is comprised of 3 plant leaves pooled together. Wheat was grown in a greenhouse at 18 °C temperature and 12 h photoperiod. Once the three-leaf stage was reached, plants were transferred to a PlantMaster (CLF Plant Climatics GmbH, Germany)

phytotron and kept in 12 h photoperiod, 200 μmol m^2/s light intensity and 4·45 g/m^3 total humidity. Group I was subjected to consistent CA at 2 °C; group II was exposed to prolonged warmer CA at 10 °C for 4 weeks and 2 °C for 3 weeks. Leaf tissue samples were collected once per week in 8 sampling points (1 sampling point before CA and 7 points during), instantly submerged in liquid N$_2$, ground using the Mixer Mill MM 400 (Retsch, Germany), weighed out into 50 mg fresh weight (FW) aliquots and stored at -80 °C.

To assess shoot biomass growth, 'KWS Ferrum' and 'Lakaja DS' were planted in 3 biological replications in 1.5 dm^3 pots with peat moss substrate in 2 groups and exposed to the same conditions as described previously. For the duration of the experiment, once per week, starting from time point 0, images of winter wheat plants were taken with the EOS 2000D RGB sensor (Canon, Taiwan). ImageJ [7] was used to process these images and measure green leaf area (GLA).

Ethanolic fractionations of winter wheat leaf samples were carried out using a Microlab STAR automated liquid handling platform (Hamilton Robotics, Switzerland) at the HiTMe facility at Bordeaux-Metabolome [8]. Supernatants were used to measure chlorophyll a and b [9], glucose, fructose, and sucrose content [8] using the MP96 microplate reader (Safas, Monaco). Amino acid content measurement was performed using the Xenius microplate fluorescence reader (Safas, Monaco) [10]. Protein [11] and starch [12] contents were measured in the pellets with the MP96 microplate reader (Safas, Monaco). Finally, pellets were washed twice with 0.5M NaOH using a Microlab STARlet automated liquid handling platform and lyophilised with a BenchTop Pro freeze dryer (SP Industries, USA). Remaining pellet weight - CWC - was determined with a 1702 analytical balance (Sartorius AG, Germany). Statistical analyses were conducted using RStudio v. 1.4.1717 [13] and MetaboAnalyst v. 5.0 [14]. Unpaired t-tests were carried out between varieties and treatment groups at week 7 of CA to assess the differences in chlorophyll a and b, CWC, glucose, fructose, sucrose, starch, amino acid, and protein contents in leaf samples.

RESULTS

Prolonged warm temperature during CA had a significant effect on winter wheat shoot biomass growth. In these conditions, both 'KWS Ferrum' and 'Lakaja DS' grew significantly more shoot biomass throughout 7 weeks ($p < 0.05$) compared to the same varieties, exposed to consistently low CA temperature. Furthermore, both varieties, subjected to 10 °C for 4 weeks, had continued to grow in shoot biomass even after the temperature was lowered to 2 °C for 3 weeks. 'Lakaja DS' had significantly less GLA ($p < 0.05$) compared with 'KWS Ferrum' in lower CA temperature treatment (see fig. 1).
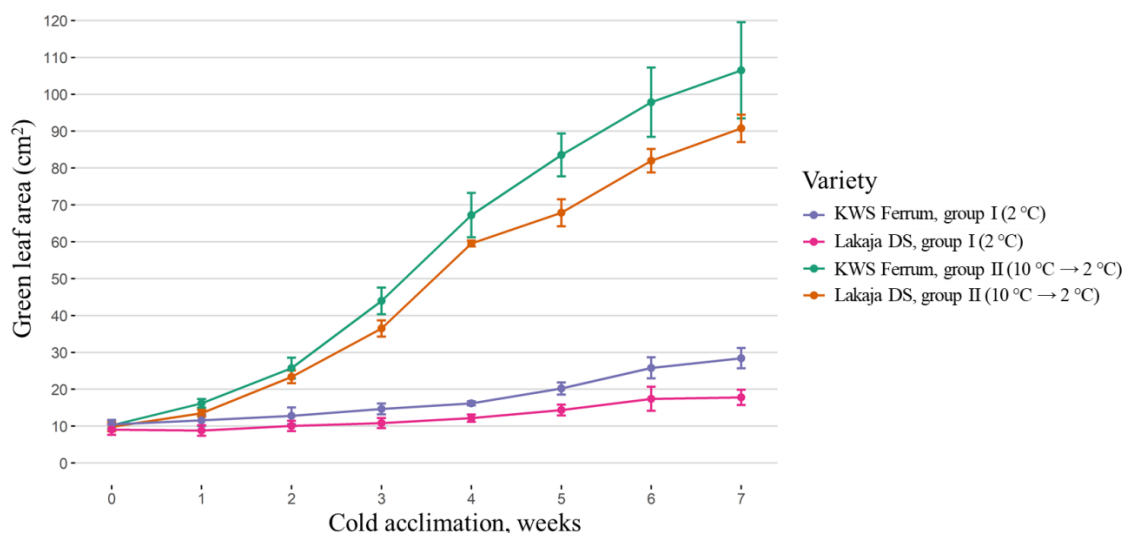
Fig. 1. Dynamics of shoot biomass growth (measured as GLA) during the course of 7 weeks of CA. The vertical error bars indicate ±SD.

Significant differences were found for CWC, chlorophyll b, starch, amino acid and protein contents ($p < 0.05$) (see fig. 2). At higher CA temperature, both varieties grew significantly more shoot biomass, gained more CWC and less amino acid content, compared to lower CA temperature ($p < 0.05$). No significant differences were found within or between treatment groups and varieties for chlorophyll a, glucose, fructose or sucrose content ($p < 0.05$). The more freezing-tolerant variety 'Lakaja DS' was shown to contain more chlorophyll b and less starch compared to the less freezing-tolerant 'KWS Ferrum' in prolonged warmer CA temperature conditions, as well as to accumulate more protein at lower CA temperature conditions. Strikingly, these results suggest that during CA the 'KWS Ferrum' variety, which grew more shoot biomass, had a higher metabolic carbon/nitrogen (C/N) ratio than the 'Lakaja DS' variety. Indeed, the former had lower protein content and higher starch levels. It has been suggested that the increase in protein content compensates for the temperature-dependent decrease in catalytic activity, thus increasing tolerance to low temperature [15]. Besides, antifreeze proteins including dehydrins, which provide protection against abiotic stress, have previously been shown to accumulate in winter wheat during CA, thus, increasing their FT [16]. Furthermore, the relatively strong increase in amino acids observed at 2 °C in 'Lakaja DS' probably contributes to increased FT by decreasing the freezing point, which is not the case with starch. However, when subjected to prolonged warmer temperature during CA, 'Lakaja DS' contained less amino acids and proteins, compared to the same variety kept at lower CA temperature, thus, indicating that higher temperature may lead to insufficient CA and FT [6].
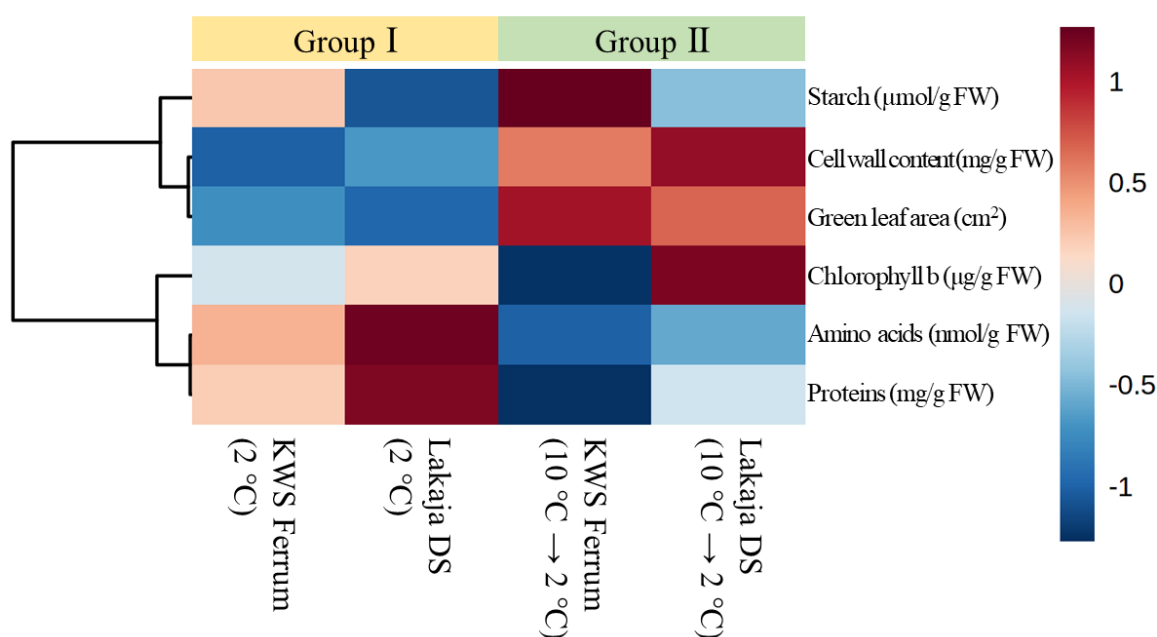
Fig. 2. Heatmap, representing the differences in values of 6 statistically significant (p < 0.05) metabolites and features among the 2 winter wheat varieties and 2 treatment groups at week 7 of CA. Data were scaled from -1 to 1 and the heatmap was drawn using Pearson distance method and Ward clustering method. CWC and GLA were clustered in one closely related group, whereas amino acid and protein contents composed another closely related group.

CONCLUSIONS

The prolonged warm temperature during CA significantly affected winter wheat shoot biomass growth and metabolite accumulation. Both varieties, kept at 10 °C for 4 weeks and 2 °C for 3 weeks of CA, grew significantly more shoot biomass compared to plants subjected to 2 °C during CA (p < 0.05). Furthermore, at higher CA temperature, both varieties accumulated more CWC and less amino acid content compared to plants exposed to consistently lower CA temperature at week 7 (p < 0.05). The more freezing-tolerant variety 'Lakaja DS', which contained more chlorophyll b and less starch compared to 'KWS Ferrum', grew less and gained more protein content when subjected to a prolonged lower temperature during CA (p < 0.05). The present study indicates that maintaining a relatively low C/N ratio may play an important role in the acquisition of FT.

Keywords: abiotic stress, climate change, *Triticum aestivum* L.

ACKNOWLEDGEMENTS

REFERENCES

1. ZHU, T.; WANG, L.; RIMBERT, H.; RODRIGUEZ, J.C.; DEAL, K.R.; DE OLIVEIRA, R.; CHOULET, F., KEEBLE-GAGNÈRE, G.; TIBBITS, J.; ROGERS, J.; EVERSOLE, K.;

APPELS, R.; GU, Y.Q.; MASCHER, M.; DVORAK, J.; LUO, M. C. Optical maps refine the bread wheat *Triticum aestivum* cv. Chinese Spring genome assembly, *The Plant Journal*, 2021, Vol. 107, No. 1, P. 303–314.

2. HÜNER, N.P.A.; DAHAL, K.; BODE, R.; KUREPIN, L.V.; IVANOV, A.G. Photosynthetic acclimation, vernalization, crop productivity and 'the grand design of photosynthesis', *Journal of Plant Physiology*, 2016, Vol. 203, P. 29–43.

3. DAHAL, K.; KANE, K.; SARHAN, F.; GRODZINSKI, B.; HÜNER, N.P.A. Cold acclimation inhibits CO2-dependent stimulation of photosynthesis in spring wheat and spring rye, *Botany*, 2012, Vol. 90, No. 6, P. 433–444.

4. ENTZ, M.H.; FOWLER, D.B. Agronomic performance of winter versus spring wheat, *Agronomy Journal*, 1991, Vol. 83, P. 527–532.

5. FOWLER, D.B. Wheat production in the high winter stress climate of the great plains of North America—an experiment in crop adaptation, *Crop Science*, 2012, Vol. 52, No. 1, P. 11–20.

6. RAPACZ, M.; JURCZYK, B.; SASAL, M. Deacclimation may be crucial for winter survival of cereals under warming climate, *Plant Science*, 2017, Vol. 256, P. 5-15.

7. ImageJ, [referred on the 17th of January in 2022]. Link to the internet <https://imagej.nih.gov/ij/>.

8. GEIGENBERGER, P.; LERCHI, J.; STITT, M.; SONNEWALD, U. Phloem-specific expression of pyrophosphatase inhibits long distance transport of carbohydrates and amino acids in tobacco plants, *Plant Cell & Environment*, 1996, Vol. 19, No. 1, P. 43–55.

9. ARSOVSKI, A.A.; ZEMKE, J.E.; HAAGEN, B.D.; KIM, S.; NEMHAUSER, J.L. Phytochrome B regulates resource allocation in *Brassica rapa*, *Journal of Experimental Botany*, 2018, Vol. 69, No. 11, P. 2837–2846.

10. BANTAN-POLAK, T.; KASSAI, M.; GRANT, K.B. A comparison of fluorescamine and naphthalene-2,3-dicarboxaldehyde fluorogenic reagents for microplate-based detection of amino acids, *Analytical Biochemistry*, 2001, Vol. 297, No. 2, P. 128–136.

11. BRADFORD, M.M. A rapid and sensitive method for the quantitation of microgram quantities of protein utilizing the principle of protein-dye binding, *Analytical Biochemistry*, 1976, Vol. 72, P. 248–254.

12. HENDRIKS, J.H.; KOLBE, A.; GIBON, Y.; STITT, M.; GEIGENBERGER, P. ADP-Glucose Pyrophosphorylase is activated by posttranslational redox-modification in response to light and to sugars in leaves of *Arabidopsis* and other plant species, *Plant Physiology*, 2003, Vol. 133, No. 2, P. 838–849.

13. RStudio, [referred on the 17th of January in 2022]. Link to the internet <https://www.rstudio.com/>.

14. MetaboAnalyst, [referred on the 17th of January in 2022]. Link to the internet < https://www.metaboanalyst.ca/home.xhtml>.

15. STRAND, Å.; HURRY, V.; HENKES, S.; HUNER, N.; GUSTAFSSON, P.; GARDESTRÖM, P.; STITT, M. Acclimation of Arabidopsis Leaves Developing at Low Temperatures. Increasing Cytoplasmic Volume Accompanies Increased Activities of Enzymes in the Calvin Cycle and in the Sucrose-Biosynthesis Pathway, *Plant Physiology*. 1999, Vol. 119, No 4, P. 1387-1398.

16. VÍTÁMVÁS, P.; PRÁŠIL, I.T.; VÍTÁMVÁS, J.; KLÍMA, M. Relationship between WCS120 protein family accumulation and frost tolerance in wheat cultivars grown under different temperature treatments, *Plants*, 2021; Vol. 10, No. 6, P. 1114.

PATHOGENICITY OF ASYMPTOMATICALLY RESIDING *FUSARIUM* SPECIES IN NON-GRAMINEOUS PLANTS TO SPRING WHEAT

Zavtrikovienė E.[1], **Supronienė S.**[1], **Gorash A.**[1], **Gustaitytė J.**[2], **Stonytė G.**[2]

[1] *Institute of Agriculture, Lithuanian Research Centre for Agriculture and Forestry*
Instituto 1, Akademija, LT 58344 Kėdainiai distr. – Lithuania
[2] *Faculty of Chemical Technology, Kaunas University of Technology*
Radvilėnų pl. 19, LT – 50254 Kaunas – Lithuania
+37065851220
evelina.zavtrikoviene@lammc.lt

EXTENDED ABSTRACT

OVERVIEW

Despite significant efforts in recent decades to combat Fusarium head blight (FHB), a disease remains one of the most important and widely studied diseases of wheat and other cereal plants [1]. FHB is mainly associated with *Fusarium* species, the majority of which are potential trichothecene producers. Mycotoxins produced by *Fusarium* fungi are harmful to humans and animals. This disease is also a major global concern because it can reduce grain yields by up to 60% [2]. In recent decades*, Fusarium* species have become more prevalent in Northern Europe [3]. The primary source of FHB infection is host plant residues that remain in the soil. Wheat (*Triticum* L.), barley (*Hordeum vulgare* L.), rice (*Oryza sativa* L.), oats (*Avena sativa* L.), rye (*Secale cereale* L.), triticale (×*Triticosecale* Wittmack), and maize (*Zea mays* L.) are the main primary host plants of pathogenic *Fusarium* spp. To date, studies have focused on small grain cereal as a host plant for these pathogens, but it has recently been discovered that several non-gramineous plant species can serve as asymptomatic alternative hostplants and the harbour with FHB associated *Fusarium* fungi [4, 5]. Although there are several studies demonstrating the ability of *Fusarium graminearum* to reside in non-gramineous plants internal tissues and cause FHB associated symptoms, however other *Fusarium* spp. and its role in the epidemiology of the FHB remain unclear [5, 6]. It is therefore, necessary to investigate the ability of asymptomatically existing *Fusarium* species to cause FHB symptoms in cereals. The aim of this study was to evaluate the pathogenicity *of Fusarium avenaceum*, *F. culmorum,* *F. graminearum,* and *F. sporotrichioides* derived from three non-gramineous plant species grown in cereal cropping system – *Brassica napus* L., *Pisum sativum,* and *Beta vulgaris* to spring wheat under greenhouse conditions.

METHODS

The pathogenicity of *Fusarium* strains isolated from non-gramineous hostplants to spring wheat was determined according to Purahong et al. [7]. A total of 45 *Fusarium* isolates, including 35 from non-gramineous plants and 11 from spring wheat, were maintained from the collection of Microbiology Laboratory, Lithuanian Research Centre for Agriculture and Forestry and were used for floret inoculation. Pots (LxWxH: 13.0x8.8x11.5 cm) were filled with a commercial, pH-adjusted (5.5 - 6.5) substrate, and four spring wheat seeds were planted per pot. FHB-

susceptible spring wheat breeding line "DS-1403-3-DH" was used for pathogenicity tests. The greenhouse maintained ± 25 ºC during the day and ±19 ºC at night with 14-hour light and 10-hour dark mode. Wheat plants with mineral fertilizer complex (NPK, 11-11-21) were fertilized one week after planting (3 g of fertilizer per pot) watered 2 times a week. The spikes were inoculated during anthesis. Twenty microliters (10µl / floret) of each *Fusarium* isolate suspension and sterile water for negative control were injected into two adjacent florets at the centre of the spike (without wounding). The inoculated spikes were covered with polyethylene bags for 72 hours to ensure the required moisture. The suspension of each isolate was used for inoculations of 15 spikes (3 spikes x 5 replicates). FHB incidence and severity (%) of inoculated spikes were evaluated at 7th (BBCH 69-71), 14th (BBCH 73) and 21st (BBCH 73-75) days post-inoculation (DPI) based on Engle et al. [8]. Grain weight per spike was evaluated at the full ripening stage (BBCH 89). Collected data were transformed as log (x + 0.5) and were processed for ANOVA with Tukey's Means Separation Test (p=0.05**).**

Fig. 1. A) Inoculation of spring wheat florets with *Fusarium* isolate suspension without wounding the spike. B) Incubation of inoculated spikes for 72 h. C) Spring wheat spike infected with FHB after 21 days post-inoculation (DPI).

RESULTS

After 21 DPI in *Fusarium* inoculated spikes FHB severity ranged from 9.3% to 69.6% and were significantly higher (p <0.01) compared to water control (4.4%). In *F. avenaceum* inoculated spikes FHB severity values varied from 9.3% to 19.0% (on average 12.6%). Isolate 19p from *Brassica napus* showed the highest FHB severity (19%), isolate from *Beta vulgaris* 33.3s and from *Pisum sativum* 10ž were least pathogenic (7.8 % and 8.0%) and did not differ from water control. In *F. culmorum* infected spikes FHB severity values ranged from 9.5% to 45.7% (on average 31.8%), highest value (45.7%) observed in isolate 15.1 1 from *Beta vulgaris*. In *F. graminearum* inoculated spikes FHB severity values varied from 11.7% to 69.6% (on average 26.8%). Isolate 5z3p3-1 from *Pisum sativum* showed the highest FHB severity value (69.6%). In *F. sporotrichioides* inoculated spikes FHB severity values ranged from 9.7% to 16.7% (on average 11.9%). The highest FHB severity (16.7%) showed isolate 1.7 from spring wheat. Isolate 37 s from *Pisum sativum* was least pathogenic (8.2%) compared to other *F. sporotrichioides* isolates and did not differ from water control. At full ripening stage (BBCH 89), *F. graminearum* isolate 5z3p3-1from *Pisum sativum*, *F. sporotrichioides* isolate 8VK5V19 from spring wheat, and *F. culmorum* isolate 26š from *Brassica napus*, showed significant (p <0.05) reduction of grain weight per spike (41.4%, 43.1%, and 55,4% respectively) compared to water control. Based on the overall results, it can be concluded that FHB severity varied among the *Fusarium* species but not among the host plants. At the greenhouse conditions, *F. avenaceum*, *F. culmorum*, *F. graminearum,* and *F. sporotrichioides* isolates from

symptomless Brassica napus, *Pisum sativum,* and *Beta vulgaris* were able to cause FHB symptoms and reduce grain weight.

CONCLUSIONS

The information presented in this study might be useful in better understanding the pathogenicity of *Fusarium* fungi derived from non-gramineous plant species of cereal cropping systems. Based on results obtained in this study, it can be concluded that asymptomatic non-gramineous plants such as *Brassica napus*, *Pisum sativum, Beta vulgaris* can harbour pathogenic *F. avenaceum*. *F. culmorum*, *F. graminearum,* and *F. sporotrichioides*. *Fusarium* fungi derived from mentioned plants can cause FHB and reduce grain yield.

Keywords: greenhouse, *Fusarium*, non-gramineous, pathogenicity, spring wheat.

REFERENCES

1. SAVARY, S.; WILLOCQUET, L.; PETHYBRIDGE, S. J.; ESKER, P.; MCROBERTS, N.; NELSON, A. The global burden of pathogens and pests on major food crops. *Nature Ecology & Evolution*, 2019, Vol. 3, No 3, P. 430–439.

2. MATNY, O. N. Fusarium Head Blight and Crown Rot On Wheat & Barley: Losses And Health Risks. *Advances In Plants & Agriculture Research*, 2015, Vol. 2, P. 39-45.

3. SUPRONIENĖ, S.; SAKALAUSKAS, S.; MANKEVIČIENĖ, A.; BARČAUSKAITĖ, K.; JONAVIČIENĖ A. Distribution of B type trichothecene producing *Fusarium* species in wheat grain and relation to mycotoxins DON and NIV concentrations. *Zemdirbyste-Agriculture*, 2016, Vol. 103, P. 281–288.

4. RASIUKEVICIUTE, N.; SUPRONIENE, S.; KELPSIENE, J.; SVEGZDA, P.; KADZIENE, G.; SNEIDERIS, D., IVANAUSKAS A., TREIKALE O. Susceptibility of Non-Cereal Crops to *Fusarium Graminearum* Complex and Their Role Within Cereal Crop Rotation As A Source Of Inoculum For Fusarium Head Blight. *Spanish Journal of Agricultural Research*, 2018, Vol. 16, No. 4.

5. SUPRONIENĖ, S.; KADZIENE, G.; IRZYKOWSKI, W.; SNEIDERIS, D.; IVANAUSKAS, A.; SAKALAUSKAS, S.; SERBIAK, P.; SVEGZDA, P.; AUSKALNIENE, O.; JEDRYCZKA, M. Weed species within cereal crop rotations can serve as alternative hosts for *Fusarium graminearum* causing Fusarium head blight of wheat. *Fungal ecology*, 2019, Vol. 37, P. 30-37.

6. SUPRONIENĖ, S.; KADZIENE, G.; IRZYKOWSKI, W.; SNEIDERIS, D.; IVANAUSKAS, A.; SAKALAUSKAS, S.; SERBIAK, P.; SVEGZDA, P.; KELPSIENE, J.; PRANAITIENE, S.; JEDRYCZKA, M. Asymptomatic weeds are frequently colonized by pathogenic species of *Fusarium* in cereal-based crop rotations. *Weed research*, 2019, Vol. 59, P. 312-323.

7. PURAHONG, W.; NIPOTI, P.; PISI, A.; LEMMENS, M.; PRODI, A. Aggressiveness of different *Fusarium graminearum* chemotypes within a population from Northern-Central Italy. *Mycoscience*, 2014, Vol. 55, P. 63-69.

8. ENGLE, J.S.; LIPPS, P.E.; MILLS, D. Fusarium head blight severity scale for winter wheat. Bulletin, 2003, AC-48-03, Extension Factsheet, Ohio State University.

BIOLOGICALLY ACTIVE SUBSTANCES OF CHIKORY (*CICHORIUM INTYBUS*) AND PLANTAIN (*PLANTAGO LANCEOLATA*)

M. Budvytis, Ž. Kadžiulienė
Lithuanian Research Centre for Agriculture and Forestry
Instituto al. 1 Akademija,. LT-58344 Kėdainiai distr. – Lithuania
+370 674 38989
mindaugas.budvytis@lammc.lt

R. Stankevičius
Lithuanian University of Health Sciences
Tilžės g. 18, 47181 Kaunas – Lithuania
+370 610 07416
rolandas.stankevicius@lsmuni.lt

EXTENDED ABSTRACT

OVERVIEW

The world faces challenges, such as excessive use of antibiotics for ruminant inflammations treatment. Researchers made across the globe suggest that various phytoactive substances have positive effect to the animal health, productivity or disease prevention (1;2). Some studies are made with green tea extracts and curcuma on influence of those substances on milking cow health, reducing inflammatory processes. The data of this study indicate that cows were supplemented with a plant product, consisting of green tea and curcuma extract in the most sensitive time of cow's lactation - from week 3 prepartum to week 9 of lactation. As results show, product had some positive effect on inflammation as well as concentration of stress hormone. Hepatic lipid concentrations were also reduced in the cows, supplied with this preparation. This data suggests that feeding the plant product attenuated metabolic stress in the liver. Finally, as a side effect, it was observed that supplementation of the phytoactive product increased the amount of energy-corrected milk yield during early lactation (2). To ensure cows get more plant active products from regular feeds, available locally, it's important to find a nutritive grasses, that characterize in antioxidant as well as nutritive qualities. Many plants (grasses) contain phytochemicals, which fed to ruminants can be useful for animal health as well as contain high nutritive value and green mass gain as a feed stuff (3; 4). Identification of new herbs and new forage mixtures is an important step to get a well balanced swards which generates good yields in local conditions as well as have high nutritive value and antioxidant properties. The objective of preliminary study was focused on perennial herb species as common chicory (*Cichorium intybus*) and plantain (*Plantago lanceolata*) to determine antioxidant properties which were identified using total phenolic content and antiradical activity.

METHODS

Two grasses were analysed: chicory (*Cichorium intybus*) and plantain (*Plantago lanceolata*) – growing as a monoculture and in mixture with each other, perennial ryegrass, meadow fescue white clover and red clover. For analyses were used herbage of first sward age year of the swards. Herbs for making tests were milled. UV–visible light spectrophotography Folin–Ciocâlteu method was used for determining ammount of phenolic compounds. Antiradical activity was measured by using spectrophotometric – DPPH method.

Herbage were taken from the first year swords.Statistical analysis. To analyse the effects of the treatment, an analysis of variance (ANOVA) was conducted. Significant differences between the experimental treatments were determined using Duncan's multiple range test at the 5% probability level ($p < 0.05$).

RESULTS

The phenolic compounds were evaluated in the herbage of first two cuts of swards. The amount of the phenolic compounds differed depending on sward mixture and cuts. In the first cut significantly the highest amount of the phenolic compounds was obtained in chicory grown in mixture with the perennial ryegrass and chicory alone. The lowest amount accurred for chicory grown with meadow fescue (Table 1). In the second cut the highest amount of the phenolic compounds were found in chicory herbage which grown in mixture with perrenial ryegrass as in the first cut. Reliable antiradical activity was significantly higher in chicory herbage grown alone, meanwhile in second cut in chicory from mixture with perennial ryegrass.

Analysing phenolic compounds in the plantain herbage, we find, that in the both cuts the most reliable phenolic compound had plantain herbage obtained from swards with perrenial reygrass (Table 2). Meanwhile antiradical activity in the first cut was highest in plantain herbage which grown with meadow fescue and similar activity obtained in plantain monoculture. In the second cut the antiradical activity significantly higher was observed in plantain grown in the mixture with meadow fescue.

Assessing phenolic compaunds on average in both types of forbs, one can see a tendency for higher amounts of phenols to accumulate in plantain herbage regardless of the composition of the swards. However, for a more comprehensive assessment, it is necessary to take into account the fertility of the swards and the ratio of these forbs in the swards.

Table 1. Amount of phenolic compounds and antiradical activity in herbage of the chicory (*Cichorium intybus*) grown in different swards.

Forbs	Amount of phenolic compounds, mg GRE/g DW		Antiradical activity, µmol TE/g DW	
	I cut	II cut	I cut	II cut
Chicory	32,0 bc	23,9 bc	1699 e	1003 bcd
Chicory (chicory x plantain)	27,3 abc	24,5 c	1024c	835 b
Chicory (chicory x p. ryegrass)	34,7 c	33,2 d	630a	1070d
Chicory(chicory x meadow fescue)	22,3 a	22,0 bc	1463d	936 bcd
Chicory (chicory x white clover)	22,8 a	19,7 b	798 b	552a
Chicory (Chicory x red clover)	24,2 a	14,1 a	769 b	568 a

Note: Different letters indicate significant differences between the treatments (p < 0.05).

Table 2. Amount of phenolic compounds and antiradical activity in herbage plantain (*Plantago lanceolata)* grown in different swards.

Forbs	Amount of phenolic compounds, mg GRE/g DW		Antiradical activity, µmol TE/g DW	
	I cut	II cut	I cut	II cut
Plantain	40,7 b	31,1 b	1539 b	1117 bc
Plantain (Plantain x chicory).	26,5 a	37,8 d	879 a	1303 cde
Plantain (Plantain x p. reygrass)	46,8 d	40,9 d	1957 c	1473 e
Plantain (fescue x plantain)	37,6 b	32,4 b	1562b	1328 cde
Plantain (Plantain x white clover)	33,3 c	21,0 a	1039 a	770 a
Gyslotis (Plantain x red clover)	37,6 b	25,8 e	1352 b	948 ab

Note: Different letters indicate significant differences between the treatments (p < 0.05).

CONCLUSIONS

The preliminary research results showed that both of those forbs had high antiradical activity as well as common   phenolic compounds count. Concentrations of bioactive compounds in the plant biomass may vary during the growing season and age of the swards. Further research on forbs of different sward age is needed. It can be expected that the incorporation of these forbs into grassland mixtures can improve the quality of herbage used as forage.

Keywords: Forbs; Fitoactive substances; Antiradical activity; Phenolic compounds

REFERENCES

1. LOMBARDI, D.; VASSEUR, E.; BERTHIAUME, R.; DEVRIEST. J.; BERGERON, R. Feeding preferences and voluntary feed intake of dairy cows: Effect of conservation and harvest time of birdsfoot trefoil and chicory, *Journal of Dairy Science*, 2015, 98: P. 7238–7247.

2. WINKLER, A.; GESSNER, K.; KOCH, C.; ROMBERG, F.; DUSEL, G.; HERZOG, E. Effects of a plant product consisting of green tea and curcuma extract on milk production and the expression of hepatic genes involved in endoplasmic stress response and inflammation in dairy cows, *Archives of Animal Nutrition*, 2015, Vol. 69, No. 6, P. 425–441

3. NAVARRETE, S.; KEMP, P.D.; PAIN, S.J.; BACK, P. J. Bioactive compounds, aucubin and acteoside, in plantain (Plantago lanceolata L.) and their effect on in vitro rumen fermentation, *Animal Feed Science and Technology*, 2016, Vol. 222, P. 158–167

4. OLAGARAY, K.E.; BRADFORD, B. J. Plant flavonoids to improve productivity of ruminants – A review, *Animal Feed Science and Technology*, 2019, Vol. 251, P. 21–36

III.6. Plant genetics and breeding

DEVELOPMENT OF NEW SSR MARKERS FOR *MONILINIA* SPP. SPECIFICITY

R. Antanynienė, B. Frercks

Institute of Horticulture, Lithuanian Research Centre for Agriculture and Forestry,
Kauno Street 30, LT-54333 Babtai, Kaunas dist. – Lithuania
+37067052099
Raminta.Antanyniene@lammc.lt, Birute.Frercks@lammc.lt

EXTENDED ABSTRACT

OVERVIEW

Brown rot is the most prevalent and economically important pre- and postharvest disease of stone and pome fruits in *Rosaceae* family and is caused by *Monilinia* spp. [1]. These pathogens cause a wide range of diseases including brown rot, twig canker, and blossom blight. The genus *Monilinia* includes three of the most important phytopathogenic species – *M. fructigena*, *M. laxa* and *M. fruciticola* [2]. *Monilinia fructicola* (Winter) Honey pathogen is the most dangerous pathogen of the genus in the whole world if prevention is not done properly [3]. *M. fructicola* is a quarantine pathogen in Europe and is listed in the European and Mediterranean Plat Protection Organisation (EPPPO) database in category A2 [4]. This pathogen is already found in thirteen European countries (EPPO2019) and is spreading to new areas due to the strong spore dispersal [5]. In 2018, a transcriptome analysis of *M. fructigena*, *M. laxa*, and *M. fructicola* was performed, which is important for further molecular and genetic studies on population biology, plant-pathogen interactions, and physiology of *Monilinia* species [6]. Knowledge of the genetic structures of pathogen populations can be useful for tracking and distinguishing genotypes. Microsatellites (SSR) are widely used to analyse genetic diversity between and within species and provide insight into changes in population genetics [7]. Conventional methods for constructing primer pairs require *a priori* information about DNA sequences and are time-consuming and expensive [8]. Since the genomes of *Monilinia* pathogens are available in the National Centre for Biotechnology Information database, SSR primers can be generated more easily [9,10,11]. Using bioinformatics tools, it is possible to create microsatellite primers more effectively. The Genome-wide Microsatellite Analysing Tool Package (GMATA) is a platform for identifying SSRs and generating primers [12]. However, in order to use the generated primers for a broader range of reserches, their specificity should be validated under laboratory conditions. The aim of the study was to develop SSR primers and analyse their specificity for three *Monilinia* species: *M. fructigena*, *M. fruicticola* and *M. laxa*.

METHODS

This research was performed in apple and plum orchids at the institute of Lithuanian Centre for Agriculture and Forestry, in the summer of 2020. In total 48 isolates were collected from plum (21) and apple (27) fruits with visible *Monilinia* spp. pathogens mycelium.

Mycelium of *Monilinia* spp. was collected according to the method of Amiri *et al*. [13] and grown on potato dextrose agar (PDA) (Scharlab, Spain) for 10 days at 22 °C in 16/8-h day/night mode.

Monilinia spp. genomic DNA was extracted using the Genomic DNA Purification Kit (Thermo Scientific™, USA) according to the manufacturer's instructions. The concentration and quality of the extracted DNA were assessed using the NanoPhotometer™ (Implen, Germany).

For the identification of *Monilinia* spp. multiplex PCR was used according to the method of Côté *at al*. (2004), using MO368-8R primers specific for *M. fructigena* (402 bp) and *M. polystroma* (425 bp), MO368-10R for *M. fructicola* (535 bp), Laxa-R2 for *M. laxa* (351), and MO368-5 - common reverse primer for all *Monilinia* spp. (535 bp). The following thermocycling conditions were used for the PCR reaction: initial denaturation at 94°C for 10 min; 7 cycles at 94°C for 30 s, 59 to 65°C for 45 s, and 72°C for 60 s; followed by 25 cycles at 94°C for 30 s, 58°C for 45 s, and 72°C for 60 s, the elongation process at 72°C for 10 min. The results were observed in 1.3% agarose gel under UV light 'E.A.S.Y Win 32' (Herolab, Germany).

SSR markers and primers for *M. laxa, M. fructigena*, and *M. fructicola* were created and evaluated under *in silico* conditions previously [14] using electronic PCR module within GMATA software [12]. In this study, 8 primer pairs (Table 2) were selected according to their association with pathogenesis-related genomic regions [6] to evaluate their specificity under laboratory conditions. PCR and electrophoresis conditions were the same as described above.

RESULTS

After multiplex polymerase chain reaction (m-PCR) *M. fructigena*-specific fragment was detected as dominant (97%) and the *M. laxa*-specific fragment was detected in only 3% of all samples.

The specificity of the designed primers for the *Monilinia* species is shown in Fig.1. Fragments for primers ML104 (358 bp), MFg90 (292 bp), and MFg39 (346 bp) were observed under laboratory conditions for the pathogens of *M. laxa* and *M. fructigena*. The results were controversial to those observed under in silico conditions [14].

ML2 (348 bp) and ML86 (336 bp) SSR primers were specific for the *M. laxa* pathogen. The ML2 (348 bp) primer did not amplify any fragments in the *M. fructigena* samples. However, the ML86 SSR primer amplified smaller fragments (250 bp) in *M. fructigena*. This indicates that the ML86 primer amplifies fragments of different sizes in both species, allowing species differentiation.

Three primers ML159 (313 bp) - specific for the pathogen of *M. laxa*, MFg27 (239 bp) and MFg2 (260 bp) - specific for *M. fructigena* under *in silico* conditions, were amplified in both species but the luminosity of the fragments was different. This might be related to a polymorphism that is different in *M. laxa* and *M. fructigena*.
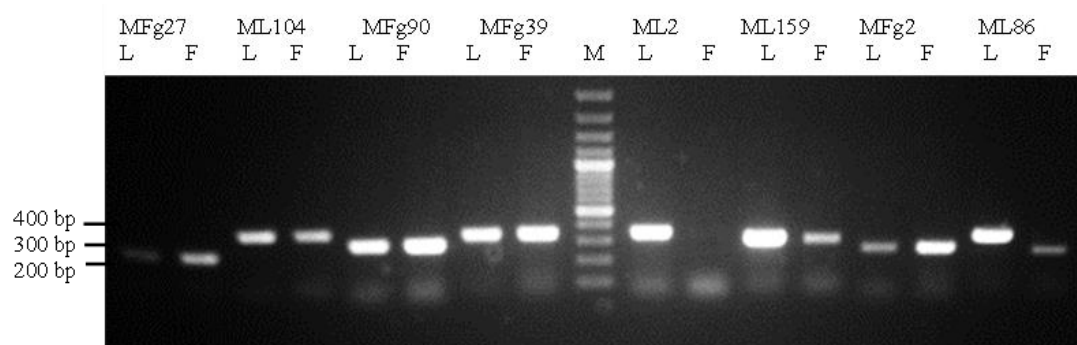
Fig. 1. The specificity of the primer in *Monilinia* spp. In picture – Primer names; L – positive *M. Laxa* control; F – positive *M. fructigena* control; M – 100 bp marker.

The specificity of the species-specific primer ML2 was evaluated for all samples in laboratory conditions. The results confirmed that this primer is specific for *M. laxa* pathogen (Fig.2).

Fig. 2 The specificity of ML2 primer for isolates. In picture - L- *M. Laxa* sample; F – *M. fructigena* sample; M – 100 bp marker, K- - negative control.

All primers associated with pathogenesis were specific for *M. fructigana* or *M. laxa* species under *in silico* conditions. In this study, analysis of the specificity of 8 primers under laboratory conditions using an m-PCR method showed that only 5 primers could be used for further analysis of *Monilinia* spp. (Table 1).

1 Table. Pathogenesis related SSR primer specificity for *Monilinia* spp.

SSR primer *	Fragment size (bp)	*In silico* specificity	Specificity under laboratory conditions
MFg27	239 bp	*M. fructigena*	*M. fructigena*
MFg39	346 bp	*M. fructigena*	-
MFg90	292 bp	*M. fructigena*	-
ML2	348 bp	*M. laxa*	*M. laxa*
ML86	336 bp	*M. laxa*	*M. laxa*
ML104	358 bp	*M. laxa*	-
ML159	313 bp	*M. laxa*	*M. laxa*
MFg2	260 bp	*M. fructigena*	*M. fructigena*

*SSR primers created under *in silico* conditions [14]

CONCLUSIONS

Five SSR primer pairs can be used for species-specific analysis of *Monilinia* spp.: ML2, ML86, and ML 159 primers for the pathogen *M. laxa* and MFg2, MFg27 for *M. fructigena*. Results obtained *in silico* do not always agree with laboratory results. Laboratory analyses should be performed to confirm the specificity of the primers generated.

Keywords: Brown rot, *Monilinia* spp., SSR, Microsatellites, primer specificity.

REFERENCES

1. VASIĆ, M.; VICO, I.; JURICK, W. M.; DUDUK, N. Distribution and Characterization of *Monilinia* spp. Causing Apple Fruit Decay in Serbia. *Plant Disease*, 2017, Vol. 102, No. 2, P. 359–369.

2. BELLAMY, S.; XU, X.; SHAW, M. Biocontrol agents to manage brown rot disease on cherry. *European Journal of Plant Pathology*, 2021, Vol., 161, P. 493–502.

3. DINI, M.; RASEIRA, M. C. B.; UENO, B. Blossom blight resistance in peach: heritability and segregation in progenies from reciprocal crosses. *Plant breeding applied to agriculture*, 2021, Vol. 68, No. 6, P. 555-563.

4. EUROPEAN AND MEDITERRANEAN PLANT PROTECTION ORGANIZATION. *Monilinia fructicola*. EPPO Bulletin, 2009, Vol. 39, No. 3, P. 337–343.

5. JÄNSCH, M.; FREY, J.; HILBER-BODMER, M.; BROGGINI, G.; WEGER, J.; SCHNABEL, G.; PATOCCHI, A. SSR marker analysis of *Monilinia fructicola* from Swiss apricots suggests introduction of the pathogen from neighbouring countries and the United States. *Plant Pathology*, 2012, Vol. 61, No. 2, P. 247–254.

6. DE MICCOLIS ANGELINI, R.; ABATE, D.; ROTOLO, C.; GERIN, D.; POLLASTRO, S.; FARETRA, F. *De novo* assembly and comparative transcriptome analysis of *Monilinia fructicola*, *Monilinia laxa* and *Monilinia fructigena*, the causal agents of brown rot on stone fruits. *BMC Genomics*, 2018, Vol. 19, No. 436.

7. GUVEN, H.; EVERHART, S. E.; DE MICCOLIS ANGELINI, R. M.; Ozkilinc, H. Genetic diversity assessments of brown rot pathogen *Monilinia fructicola* based on the six simple sequence repeat loci. *Journal of Plant Diseases and Protection*, 2021, Vol. 128, P. 1459–1465.

8. DUHAN, N.; MESHRAM, M.; LOAIZA, C. D.; KAUNDAL, R. CitSATdb: Genome-Wide Simple Sequence Repeat (SSR) Marker Database of *Citrus* Species for Germplasm Characterization and Crop Improvement. *Genes*, 2020, Vol. 11, No. 12:1486.

9. LANDI, L.; DE MICCOLIS ANGELINI, R. M.; POLLASTRO, S.; ABATE, D.; FARETRA, F.; ROMANAZZI, G. Genome sequence of the brown rot fungal pathogen *Monilinia fructigena*. *BMC Research Notes*, 2018, Vol. 11, No. 1, P. 10–12.

10. RIVERA, Y.; ZELLER, K.; SRIVASTAVA, S.; SUTHERLAND, J.; GALVEZ, M.; NAKHLA, M.; PONIATOWSKA, A.; SCHNABEL, G.; SUNDIN, G.; ABAD, Z. G. Draft genome resources for the phytopathogenic fungi *Monilinia fructicola*, *M. fructigena*, *M.*

polystroma, and *M. laxa*, the causal agents of brown rot. *Phytopathology*, 2018, Vol. 108, No. 10, P. 1141–1142.

11. DE MICCOLIS ANGELINI, R. M.; ROMANAZZI, G.; POLLASTRO, S.; ROTOLO, C.; FARETRA, F.; LANDI, L. New High-Quality Draft Genome of the Brown Rot Fungal Pathogen *Monilinia fructicola*. *Genome Biology and Evolution*, 2019, Vol. 11, No. 10, P. 2850–2855.

12. WANG, X.; WANG, L. GMATA: An Integrated Software Package for Genome-Scale SSR Mining, Marker Development and Viewing. *Frontiers in Plant Science,* 2016, Vol. 7, No. 1350.

13. AMIRI, A.; HOLB, I. J.; SCHNABEL, G. A new selective medium for the recovery and enumeration of *Monilinia fructicola*, *M. fructigena*, and *M. laxa* from stone fruits. *Phytopathology*, 2009, Vol. 99, No. 10, P. 1199-1208.

14. ŽUKAUSKAITĖ, R.; KABALINAITĖ, B.; FRERCKS, B. *Monilinia* spp. SSR markers distributed genomic-wide. CYSENI 2021. Proceedings of the 17th international conference of young scientists on energy issues. Kaunas: Lithuanian Energy Institute. 2021 May 24-28.

EXPRESSION OF *PR1*, *PR6* AND *COI1* GENES IN RESPONSE TO BLACKCURRANT REVERSION VIRUS INFECTION

A. D. Juškytė, I. Mažeikienė, V. Stanys
Lithuanian Research Centre for Agriculture and Forestry,
Institute of Horticulture
Kaunas str. 30, Babtai, LT-54333 Kaunas distr. – Lithuania
ana.dovile.juskyte@lammc.lt

EXTENDED ABSTRACT

OVERVIEW

The blackcurrant reversion virus (BRV) is one of the most damaging pathogen in *Ribes* plantations. BRV attacks leaves, flowers and berries, blackcurrants stop harvesting and die within 3 – 4 years. Several genes and molecular markers are known to confer resistance to BRV [1-4]. Defence response genes' *Pathogenesis related* (*PR*) and *Coronatine insensitive 1* (*COI1*) homolog emphasizing the *R. nigrum* genome have been already found and specific primers identifying these genes in blackcurrants have been designed [5]. *PR*s are induced through the action of the salicylic (SA) or jasmonic (JA) acids signaling compounds and often used as markers of the enhanced defensive state conferred by pathogen induced systemic acquired resistance (SAR) [6]. Meanwhile, *COI1* is considered as a marker for defense responses mediated by the JA and thus, induced systemic resistance (ISR) [7]. However, defense pathways related to BRV resistance in *Ribes* genus are still unknown. The aim of this study is to perform *PRs* and *COI1* expression and determine which signalling pathway is responsible for resistance to BRV in blackcurrants 1×10^5.

METHODS

Three weeks old *in vitro* propagated microplants of BRV resistant cultivar Aldoniai and susceptible – Ben Tirran were mechanically inoculated with BRV through roots. This method ensures greater inoculum-plant contact and more efficient virus transport through the plant. BRV concentration in 1 µl of inoculate was approximately 3.325×10^9 copies, according qRT-PCR data by relative quantification strategy. Infected plants were maintained 2 – 8 days in a growth chamber at 4 °C temperature. Total RNA was isolated using GeneJET Plant RNA Purification Mini Kit, cDNA was synthetised using Maxima H Minus First Strand cDNA Synthesis Kit (Thermo Scientific). BRV detection in microshoots was investigated by PCR using the specific primer pair P1/P2 (210 bp) [8] and visualized in 1.3% agarose gel. *PRs* and *COI1* expression was analyzed by qRT-PCR using specific primers in 3 biological replicates [5]. Relative expression was assessed by 2(-Delta Delta C (T)) method [9], where mock inoculated microplants were used as a control, *Actin* – as reference gene.

RESULTS

After mechanical inoculation under *in vitro* conditions, two cultivars for presence of BRV infection after 2, 4, 6, 8 days post inoculation (dpi) were screened. It was determined, that in

resistant genotype Aldoniai the specific fragment of virus RNA2 was amplified up to 6 dpi (Fig. 1A), meanwhile in susceptible cultivar Ben Tirran – on all days after inoculation (Fig. 1B).
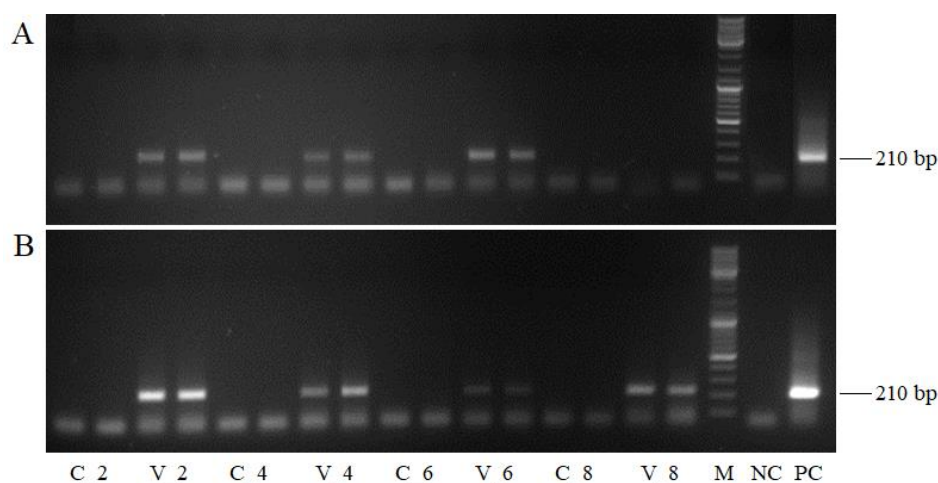

Fig. 1. Detection of BRV specific fragment in cv. Aldoniai (A) and cv. Ben Tirran (B). C_2, C_4, C_6 and C_8 – mock inoculated plants on 2, 4, 6 and 8 dpi, V_2, V_4, V_6 and V_8 – BRV inoculated plants on 2, 4, 6 and 8 dpi; M – size standard SM0333 (Thermo Scientific), NC – negative control, PC – positive control.

The expression profiles of *PR1*, *PR6* and *COI1* homologs in *R. nigrum* during biotic stress were compared by qRT-PCR (Fig. 2). It was observed that resistant to BRV cv. Aldoniai showed an augmented expression of *PR1* comparing to mock inoculated plants (Fig. 2A). *PR1* had the maximum expression value 17.83 with significant difference on 2 dpi in resistant genotype. Later, the expression of this gene began to decline to 1.17 on 8 dpi. The expression levels of *COI1* and *PR6* during entire period of the experiment varied from 0.84 to 1.44 and from 0.24 to 1.37 respectively, and significant differences were observed.
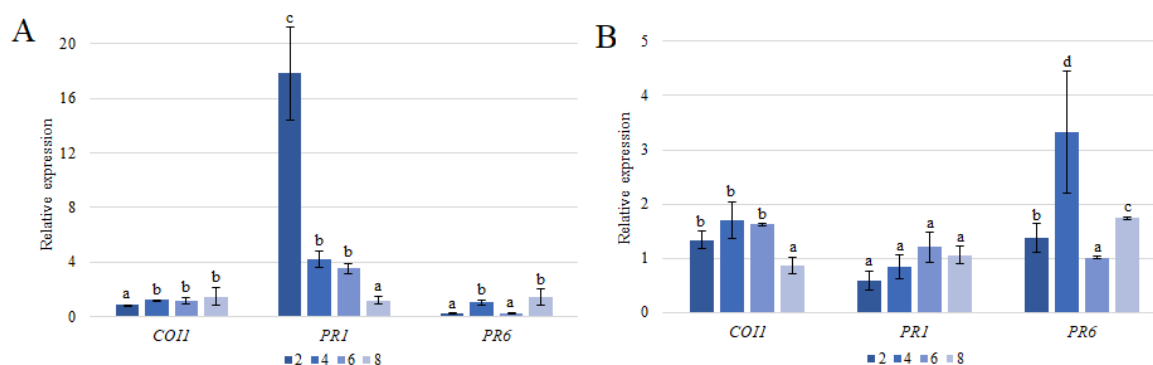

Fig. 2. Relative expression of *COI1*, *PR1* and *PR6* in resistant cv. Aldoniai (A) and susceptible cv. Ben Tirran (B) in response to BRV. Data presented as mean and SEM. Letters indicate statistically significant differences (P ≤ 0.05) between means of individual gene data.

In susceptible genotype Ben Tirran, the expression levels of *PR6* were fluctuating and transcripts of this gene had the highest expression value 3.33 with significant difference on the 4 dpi (Fig. 2B). During the entire period of the experiment, the expression of *COI1* tended to decrease, meanwhile *PR1* – to increase, but no significant differences were obtained in many cases.

CONCLUSIONS

Genes associated with the response to biotic stress confirmed BRV infection in blackcurrant microplants but expressed differentlly. BRV resistant *R. nigrum* cv. Aldoniai on 2 day activates the defense response of the SA signalling pathway, which is confirmed by the intense expression of the *PR1*. In susceptible *R. nigrum* cv. Ben Tirran, relatively high expression of the JA-depended *PR6* was detected on 4 dpi. Thus, the blackcurrant's immune system activates *PR* genes involved in systemic acquired resistance in response to BRV infection *in vitro*. Similar expression levels of the *COI1* was observed in both genotypes.

Keywords: Blackcurrant reversion virus, defence response, gene expression

REFERENCES

1. ANDERSON, M. M. Resistance to gall mite (*Phytoptus ribis* Nal.) in the *Eucoreosma* section of *Ribes*. *Euphytica*, 1971, Vol. 20, P. 422-426.

2. KNIGHT, R. L.; KEEP, E.; BRIGGS, J. B.; PARKER, J. H. Transference of resistance to black currant gall mite *Cecidophyopsis ribis*, from goosebery to black currant. *Annals of Applied Biology*, 1974, Vol. 76, P. 123-130.

3. BRENNAN, R.; JORGENSEN, L.; GORDON, S.; LOADES, K.; HACKETT, C.; RUSSELL, J. The development of a PCR-based marker linked to resistance to the blackcurrant gall mite (*Cecidophyopsis ribis* Acari: *Eriophyidae*). *Theoretical and applied genetics*, 2009, Vol. 118, No. 2, P. 205-211.

4. MAZEIKIENE, I.; BENDOKAS, V.; STANYS, V.; SIKSNIANAS, T. Molecular markers linked to resistance to gall mite in blackcurrant. *Plant Breeding*, 2012, Vol. 131, P. 762-766.

5. JUŠKYTĖ, A. D.; MAŽEIKIENĖ, I.; STANYS, V. Putative genes of *Pathogenesis related proteins* and *Coronatine insensitive protein* 1 in *Ribes* spp. *Plants*, 2022, Vol. 11, No. 3, P. 355.

6. VAN LOON, L. C.; REP, M.; PIETERSE, C. M. J. Significance of inducible defense-related proteins in infected plants. *Annual Review of Phytopathology*, 2006, Vol. 44, P. 135-162

7. KAZAN, K.; MANNERS, J. M. Jasmonate signaling: toward an integrated view. *Plant Physiology*, 2008, Vol. 146, No. 4, P. 1459-1468

8. LEMMETTY, A.; LATVALA-KILBY, S.; LEHTO, K. Comparison of different isolates of Black currant reversion virus. *Acta Horticulturae*, 2001, Vol. 551, P. 45-49.

9. LIVAK, K.; SCHMITTGEN, T. Analysis of relative gene expression data using real-time quantitative PCR and the 2(-Delta Delta C (T)) Method. *Methods*, 2001, Vol. 25, No. 4, P. 402-408.

DIPLOID AND TETRAPLOID DAYLILY (*HEMEROCALLIS* L.) REGENERATION *IN VITRO* USING THIDIAZURON (TDZ)

E. Misiukevičius
Lithuanian Research Centre for Agriculture and Forestry
Department of Orchard Plant Genetics and Biotechnology
Kauno g. 30, Babtai, LT-54334 Kauno distr. – Lithuania
+370 639 43 982
*Edvinas.Misiukevicius@lammc.lt*

EXTENDED ABSTRACT

OVERVIEW

Daylilies (*Hemerocallis* L.) is one of the popular ornamental flowering plants with over 95 000 varieties worldwide. Most *Hemerocallis* species are diploid (2n), with only known triploid *H. fulva* var. *kwanso* [1]. Tetraploid (4n) daylilies were induced with colchicine more than 70 years ago. Both diploid and tetraploid daylilies have high interest and commercial value. It is essential to propagate individual forms. However natural plant multiplication coefficient is low. There were various approaches to improve *in vitro* multiplication to meet market demand better. However, daylilies are conspicuously challenging to propagate using tissue culture [2]. Progress reached with growth regulator thidiazuron (TDZ). It has been shown to promote shoot regeneration more expeditiously than other cytokinins as well it is attained at much lower concentrations [2, 3]. This experiment aims to evaluate diploid and tetraploid daylily varieties' regeneration in different thidiazuron concentrations.

METHODS

In this experiment, for induction of micropropagation, young scapes 14 diploid (2n) and 14 tetraploid (4n) varieties were used. Scapes were washed under running water for 1 hour. Then sterilized with 70% ethyl alcohol, washed with aseptic water, sterilized with mercuric chloride for 7 minutes, and washed three times with aseptic water. Twenty-four pieces of scapes (6 pieces per vessel with four multiplication) were used per variant of each variety. Murashige and Skoog (MS) [4] media with pH 5,9 and 10,3g/l phyto agar were selected for daylily multiplication. Prepared media were sterilized at 121°C for 30 minutes. The assigned quantity of TDZ (0; 1; 5; 10; 15 mg/l) was added to the autoclaved medium in an aseptic environment. After four weeks, callus induction frequency (%) and mortality rate (%) were observed. After 12 weeks of callus induction frequency (%), the number of regenerated shoots and shoots height (cm) were observed. The experimental data were processed by the analysis of variance (ANOVA). The mean value of results corresponding standard deviation (SD) for every treatment. The least significant difference (LSD) was carried out with a significance level of $p < 0.05$.

RESULTS

Callus induction and mortality. The control culture medium without TDZ did not form a callus, and most of the explants died during the first four weeks of cultivation. TZD's presence in cultivation media increases the chances to regenerate daylilies from scape pieces (Fig. 1.). Even the smallest concentration of TDZ resulted in callus induction. As well as decreasing shoot mortality rate by half (Fig. 1. B). Concentration 5-15 mg/l explants of tetraploid plants induced callus 1.5-1.6 times more frequently than diploid plants (Fig. 1. A). Tetraploids tend to have significantly lower mortality at 5-15 mg/l and higher concentrations.
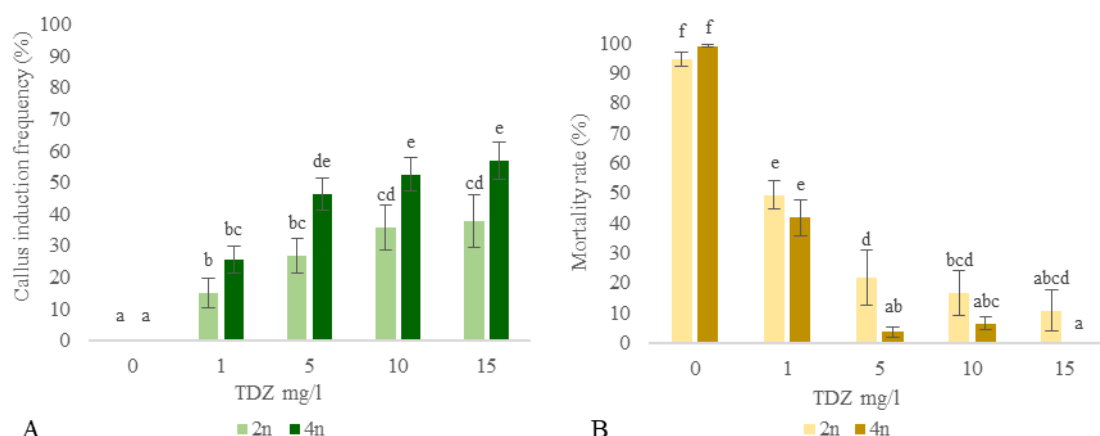
Note. Means (x̄ ±SD) followed by the same letters (a, b,..) are not significantly different (A – LSD 14,71; B – LSD 14,33).

Fig. 1. Callus induction frequency (A) and mortality rate (B) after four weeks in diploid (2n) and tetraploid (4n) daylily varieties using different TDZ concentrations.

After 12 weeks since the start of the experiment frequency of callus induction appeared more similar. Explants of tetraploid plants form more callus than diploid only by 1.07 times (2n – 37.28%; 4n – 39.81%). Diploid and tetraploid varieties showed more consistent results (Fig. 2). Different concentrations of TDZ in the tetraploid group showed an increase of callus induction, while diploids had minimal differentiation. The maximum callus induction rate was at the highest concentration of 15 mg/l – 48% (2n) and 62% (4n).
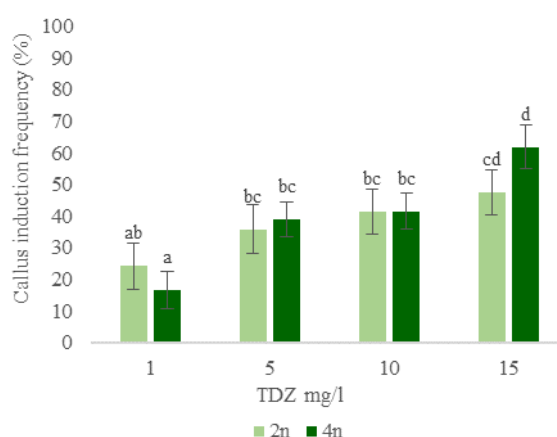
Note. Means (x̄ ±SD) followed by the same letters (a, b,..) are not significantly different (LSD 18,77).

Fig. 2. Callus induction frequency after 12 weeks in diploid (2n) and tetraploid (4n) daylily varieties using different TDZ concentrations.

**The adventitious shoot formation**. The highest number of regenerating shoots in diploids was observed in the highest concentration of 15 mg/l TDZ resulting average of 4 nodes per explant (Fig. 3. A). Diploids, on average, tend to form 2.56 shoots which are 1.14 times more than tetraploids (2.25). TDZ concentration increase regenerating shoot number more evenly in tetraploids than diploids. Tetraploids did not appear significantly different from concentrations 5 to 15 mg/l. Shoot height decreases with higher concentrations of TDZ (Fig. 3. B). The highest shoots were formed in 1 mg/l of TDZ. The height of nodes in diploid and tetraploid varieties mostly depends on the growth regulator related to the number of shoots.
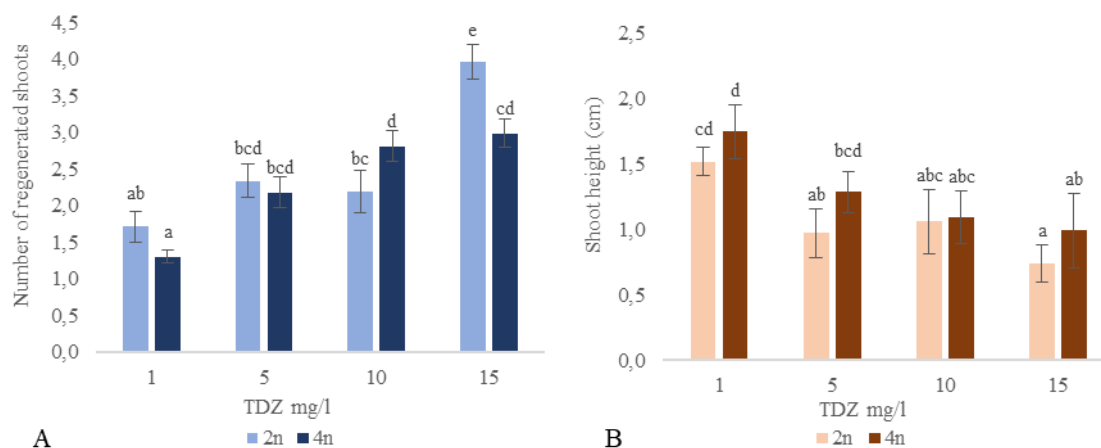
Note. Means (x̄ ±SD) followed by the same letters (a, b,..) are not significantly different (A – LSD 0,65; B – LSD 0,47).

Fig. 3. Regenerated shoot number (A) and height of shoots (B) in diploid
(2n) and tetraploid (4n) daylily varieties using different TDZ concentrations.

CONCLUSIONS

The degree of regenerating daylilies *in vitro* relies on ploidy level and the concentration of growth hormone. TDZ is vital in growing media as none of the control survived. Compared to diploids, tetraploids have higher callus induction frequency, lower mortality rate, and slightly higher regenerated shoots. Diploids tend to regenerate more adventitious shoots than tetraploids.

Keywords: plant ploidy, growth-regulating thidiazuron, *in vitro* daylily regeneration, plant micropropagation, daylily ploidy.

REFERENCES

1. SAITO, H.; MIZUNASHI, K.; TANAKA, S.; ADACHI, Y.; NAKANO, M. Ploidy estimation in Hemerocallis species and cultivars by flow cytometry. *Scientia Horticulurae*, 2002, Vol. 97, P. 185–192.

2. MATAND, K.; SHOEMAKE, M.; LI, C. High frequency in vitro regeneration of adventitious shoots in daylilies (Hemerocallis sp.) stem tissue using thidiazuron. *BMC Plant Biology*, 2002, Vol. 20, 31. DOI:10.1186/s12870-020-2243-7.

3. GOVINDARAJ, S. *A Potent Phytohormone for in vitro regeneration*. In Ahmad N., Faisal M. (eds) *Thidiazuron: From Urea Derivative to Plant Growth Regulator*. Singapore: Springer, 2018. P. 393-418. DOI:10.1007/978-981-10-8004-3_22.

4. MURASHIGE, T.; SKOOG, F. A revised suitable medium for rapid growth and bioassays with tobacco tissue culture. *Physiologia Plantarum*, 1962, Vol. 15, P. 473-497.

MICROSATELLITE ANALYSIS OF SCOTS PINE CLONES WITH DIFFERENT LENGTHS OF TRACHEID CELLS

A.V. Padutau, V. Baliuckas

Institute of Forestry, Lithuanian Research Centre for Agriculture and Forestry
Instituto al. 1, LT-58344 Akademija, Kėdainiai distr. – Lithuania
Aliaksandr.Padutau@lammc.lt

EXTENDED ABSTRACT

OVERVIEW

Cellulose is the most important raw material for the production of paper, textiles, artificial fibers and films [1]. The main source of cellulose fibers is the wood of coniferous (pine, spruce) and hardwood (birch, aspen) species, which are widely distributed in Europe. The size and shape of polymer fibers have a significant impact on the properties of the cellulose pulp and derivatives. So, the length of the fiber is one of the significant factors that determine the strength of cellulose materials. Cellulose, with a longer fiber length, is used to produce higher quality materials such as viscose. Like any biological trait, the length of the cellulose fiber is controlled by the genetic apparatus of the plant cell [2]. Based on all of the above, the study of the heritability of the cellulose fiber length trait is relevant. This allows the selection of trees with certain hereditary properties to create specialized forest plantations. The goal of present work is SSR-assay of Scots pine clones with different lengths of tracheid cells (and, accordingly, the length of cellulose fibers) to identify molecular markers associated with this trait.

METHODS

In the present study, both microscopic analysis of wood and molecular genetic analysis were used. Wood samples were collected from Scotch pine trees (clones) growing on the 2nd generation forest seed orchard of Gomel forest enterprise and clone archive of the Korenevka forest research enterprise. The total number of studied trees (clones) was 138 pcs. Wood samples were taken using a Pressler drill (Haglof) with 5 mm collection tube diameter. Maceration of tissues was carried out in 10% HNO_3 and 10% $K_2Cr_2O_7$ (1:1) mix. The study protocol is detailed in the article [3]. Tracheid length was measured using a Leica Galen III microscope with a 10x4 ocular micrometer. The measurements were carried out using a Goryaev container. The measurement was carried out separately for early and latewood (from 10 to 30 tracheids) and averaged.

DNA was extracted from wood samples according to the CTAB-protocol [4]. PCR amplification ot 10 SSR markers (Pttx 4001, Pttx 4011, Pttx 3116, Psyl 2, Psyl 16, Psyl 17, Psyl 18, Psyl 36, Psyl 42, Psyl 44) was performed according to the standard protocol [5]. Electrophoretic assay was performed using Applied Biosystems 3500 Genetic Analyzer.

RESULTS

Tracheid cell length varied between clones in the range 2.5-4.2 mm. There are three groups were identified: <3.0 mm (I), 3.0-3.7 mm (II, numerous) and >3.7 mm (III). Only samples from

the first and third groups were analyzed by SSR-assay. An analysis of the frequencies of occurrence of allelic variants showed the absence of pronounced associations with the cell length parameter for most markers. The exception was for PtTx 4011, where the frequency of the allele 261 was 0.75 in the first group, and only 0.39 in the third group (Fig. 1). The level of observed heterozygosity for most loci was also similar between the groups.
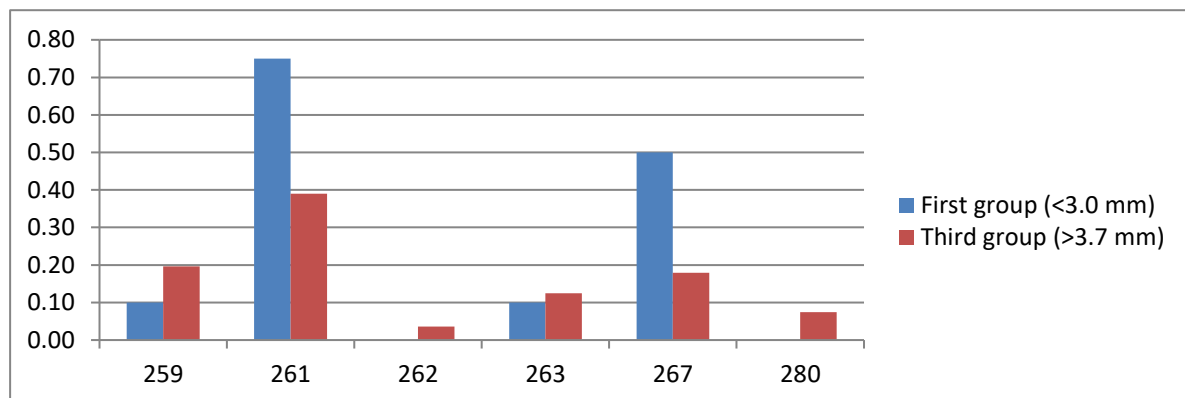

Fig. 1. Allelic frequencies in groups of Scotch pine trees differing in cellulose fiber length (SSR-marker PtTx 4011)

At the same time, for the Psyl 42 marker, the Ho value in the first group was 0.60, in the third group - 0.48, for the Psyl 36 marker - 0.10 and 0.37, respectively. The correlation coefficient for the trait pair "individual heterozygosity of trees - length of tracheid cells" in the first group was 84%, in the third group - 36%.

CONCLUSIONS

SSR-assay showed that among the analyzed groups of trees, features of the genetic structure were revealed. Further research of the valuable traits diagnosis we are going to continued using an additional set of genetic markers.

Keywords: Scots pine clones, SSR markers, length of the tracheid cells.

REFERENCES

1. Manufacture of paper and paperboard, Part 1: Technology for the production and processing of paper and paperboard, St. Petersburg, 2005, Vol. 2, P.423.

2. IVANOV, S. N. Paper technology, Moscow: School papers, 2006, No. 3, P.696.

3. TERENTYEVA, E. P.; UDOVENKO, N. K.; PAVLOVA, E.A. Chemistry of wood, cellulose and synthetic polymers. St. Petersburg, 2015, P.83.

4. DEMEKE, T.; JENKINS, G. R. Influence of DNA extraction methods, PCR inhibitors and quantification methods on real-time PCR assay of biotechnology-derived traits. Analytical and Bioanalytical Chemistry, 2010, Vol. 396, P. 1977–1990.

5. MUKHINA ZH, M.; DUBINA, E. V. Molecular markers and their use in selection and genetic studies. Polythematic network scientific journal of the Kuban State Agrarian University, 2011. P. 14.

III.7. Global change and environmental footprint

DETECTING SINKING CITIES THROUGH THE COMBINATION OF RADAR TECHNIQUES

A. Alonso-Díaz, M. Solla, A. Elseicy

CINTECX, GeoTECH Research Group, Universidade de Vigo
Vigo, 36310 – Spain
Emails: alex.alonso@uvigo.es, merchisolla@uvigo.es,
ahmedmossadibrahim.elseicy@uvigo.es

EXTENDED ABSTRACT

OVERVIEW

Climate change is increasing the level of the oceans on average about 2.6 mm per year. However, this increase reaches between 7.8 – 9.9 mm per year in coastal cities [1]. This is because two factors coexist in coastal cities: (1) the rise in sea level and flooding, and (2) the subsidence of cities motivated mainly by human factors, such as the extraction of water, fuel, or underground gas; the construction of barriers against river flood; mining activities and the overweight of cities due to buildings transmitting loads not supported by the terrain [2].

Fig. 1 shows the average sea level rise from 1993 to 2015, while Fig. 2 presents the population density around the world nowadays. Observing these Figures, it can be demonstrated that most of the population lives in coastal areas and the effects of rise sea level is therefore more noticeable in that areas.
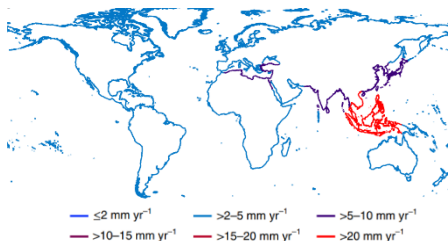
Fig. 1. World rise sea level per year from 1993 to 2015 (obtained from [2])

Fig. 2. World's density population in 2022 (Obtained from Wikimedia commons)

According to the Flanders Institute, the 60 per cent of the World's population already lives in coastal areas. Moreover, the 70 per cent of the coastal population lives south, south-east and east of Asia. As it is illustrated in Figure 1, the sinking cities problem affects the most populated areas. For this reason, it is vital to mitigate and anticipate this effect. As informed by other authors [1], if the effect is reduced to 5 mm per year, about 20-35 million people will not be exposed to this danger by 2050.

It is becoming clear that the challenge of assessing sinking cities hazards will become more common in the future. New technological developments are therefore needed aiming the early detection of sinking phenomena, thus providing valuable information to plan preventive

maintenance. Within this context, this work proposes the combination of two complementary Non-Destructive Testing (NDT) techniques: Interferometric Synthetic Aperture Radar (InSAR) and Ground Penetrating Radar (GPR).

METHODS

The InSAR method uses microwaves emitted from satellites or Unmanned Aerial Vehicles (UAVs) to obtain images. After applying specific interferometric processing, Digital Elevation Models (DEMS) are obtained. Recent advances in the capabilities of this technique have been motivated many new applications (e.g., to obtain tendencies in urban areas [3]).

To demonstrate the evolution of InSAR, and its usefulness in detecting subsidence in cities, Fig. 3 shows the annual evolution of scientific articles dealing with the analysis of urban areas from InSAR, while Figure 4 illustrates the World interest rate on InSAR technology in the last 5 years.
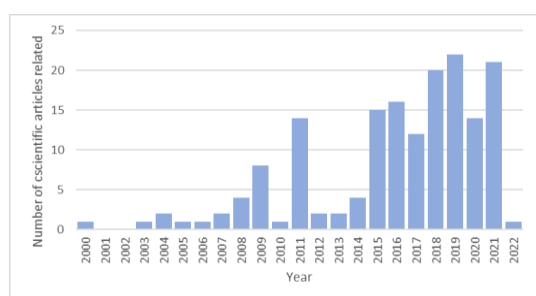
Fig. 3. Number of scientific articles relatives to InSAR in Urban Areas per year. Source: Scopus and Web of Science)
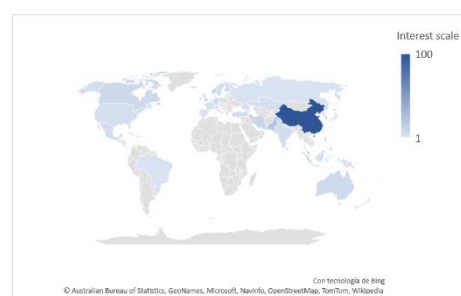
Fig. 4. Comparative of interest in technology   InSAR around the World in the last 5 years (obtained from Groogle trends)

The GPR method is a geophysical technique which uses electromagnetic waves to evaluate subsurface defects, such as subsidence in roads [6].

Furthermore, the combination of both radar techniques is gaining strength in recent years, as demonstrated in Fig. 5, showing the number of scientific papers dealing with the combination of both InSAR and GPR methods.
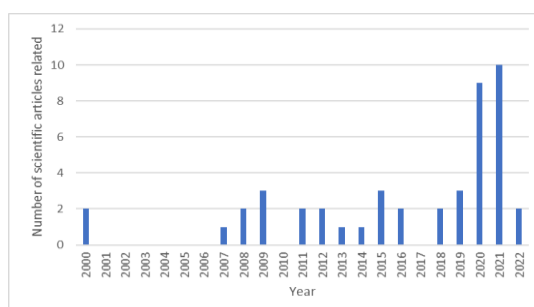
Fig. 5. Annual evolution in number of articles published combining InSAR and GPR

Some results showing the combination of both techniques will be included in the paper.

CONCLUSIONS

This article highlights the danger posed by the effect of the coastal sinking cities. Likewise, a possible solution is proposed to detect early sinking phenomena, thus alerting the need for action and proving valuable information for decision-making and risk assessment. First, InSAR is proposed to identify critical areas at network scale. Next, GPR gives information about the condition state of the subsoil through on-site measurements.

Keywords: NDT, InSAR, GPR, subsidence, climate change, sinking cities

REFERENCES

1. MIMURA, N. Rising seas, and subsiding cities. *Nature Climate Change*, 2021. 11, P. 296-297.

2. NICHOLLS, R. J.; LINCKE, D.; HINKEL, J., BROWN, S.; VAFEIDIS, A. T.; MEYSSIGNAC, B.; HANSON, S. E.; MERKENS, J. L.; FANG, J. A global analysis of subsidence, relative sea-level change and coastal flood exposure. *Nature Climate Change*, 2021. 11, P. 338-342.

3. PEPE, A.; CALÒ, F. A Review of Interferometric Synthetic Aperture RADAR (InSAR) Multi-Track Approaches for the Retrieval of Earth's Surface Displacements. *Applied Sciences*. 2017. 7, P. 12-64.

4. WAI-LOK LAI, W.; DÉROBERT, X.; ANNAN, P. A review of Ground Penetrating Radar application in civil engineering: A 30-year journey from Locating and Testing to Imaging and Diagnosis. NDT & E INTERNATIONAL 2018. 96, P. 58–78.

5. TOSTI, F.; GAGLIARDI, V.; D'AMICO, F.; ALANI, A. M. Transport infrastructure monitoring by data fusion of GPR and SAR imagery information. *Transportation Research Procedia*. 2020. 45, P. 771-778.

6. BIANCHINI CIAMPOLI, L.; GAGLIARDI, V.; CLEMENTINI, C.; LATINI, D.; DEL FRATE, F.; BENEDETTO, A. Transport Infrastructure Monitoring by InSAR and GPR Data Fusion. *Surveys in Geophysics*. 2020. 41, P. 371-394.

A COMPARISON OF THE ENVIRONMENTAL IMPACTS CAUSED BY HEAVY METALS REMOVAL FROM AQUEOUS SOLUTION BY MICROBIAL BIOMASS

I. M. Simion[1*], R. M. Hlihor[1*], C. Filote[1,2], M. Roşca[1]

[1]*"Ion Ionescu de la Brad" Iasi University of Life Sciences, Faculty of Horticulture,
Department of Horticultural Technologies,
3 Mihail Sadoveanu Alley,
700490 Iasi – Romania*
simion.i@uaiasi.ro; raluca.hlihor@uaiasi.ro

[2]*"Gheorghe Asachi" Technical University of Iasi, "Cristofor Simionescu" Faculty of
Chemical Engineering and Environmental Protection, Department of Environmental
Engineering and Management,
73 Prof. D. Mangeron Bd.,
700050 Iasi – Romania*

EXTENDED ABSTRACT

OVERVIEW

Living standards, development of industries and inefficient management of wastes, have led to an increase of environmental pollutants, especially heavy metals in wastewaters. Some heavy metals, even at low concentration can accumulate in human tissues after repeated exposure, e.g. arsenic, cadmium and lead [2,3]. The removal of heavy metals can be made in two ways, either by conventional methods or non-conventional methods. Bonton et al. [1] made a comparative Life Cycle Analysis of these ways and concluded that the conventional way could generate more environmental impact than the non-conventional one. A non-conventional way for heavy metals removal from wastewaters could be the use of microorganism. This method is considered less harmful for the environment and low cost [4].

METHODS

Our study is based on the assessment of the environmental impacts associated with the biosorption of Cr (VI) and Cd (II) from aqueous solution at a concentration of 25 mg/L at laboratory scale by *Trichoderma viride (T. viride)* fungal biomass. The fungal biomass represented by *T. viride* was isolated from a forest soil from Iaşi, Romania, from a depth of 8-10 cm. The Life Cycle Assessment system boundary consists in microorganism isolation, preparation of dead biomass and the biosorption of Cr (VI) and Cd (II) from aqueous solution followed by the treated wastewater and waste landfilling. The assessment of Cr (VI) and Cd (II) biosorption by *T. viride*, after following the four steps of Life Cycle Assessment (LCA) methodology: (i) goal definition and scope; (ii) inventory analysis; (iii) impact assessment with four sub-phases: classification, characterization, normalization, weighting; (iv) improvement assessment, gives us the ability to identify the impacts, in terms of energy, fuels, and emissions generated by each stage of the process. By identifying the environmental impacts within the

stages of the process we can improve it were necessary, for assuring the sustainability of the process in terms of environmental protection. The evaluation was assisted by a dedicated software, GaBi software, based on LCA methodology as indicated in the international standard ISO 14040.

RESULTS

The results of the assessment on the application of *T. viride* species for heavy metals removal from aqueous solution, indicate a negative environmental impact for the biosorption process of Cr (VI) ions from aqueous solutions, for all impact categories specific to the ReciPe16 method. The most significant value of the environmental impact determined by the use of non-viable fungal species, both in the case of removal of Cr (VI) and Cd (II) ions was obtained for the impact category *ionizing radiation* (IR) followed by *climate change terrestrial ecosystems* (CCTE) and *climate change human health* (CCHh) as shown in Fig. 1.
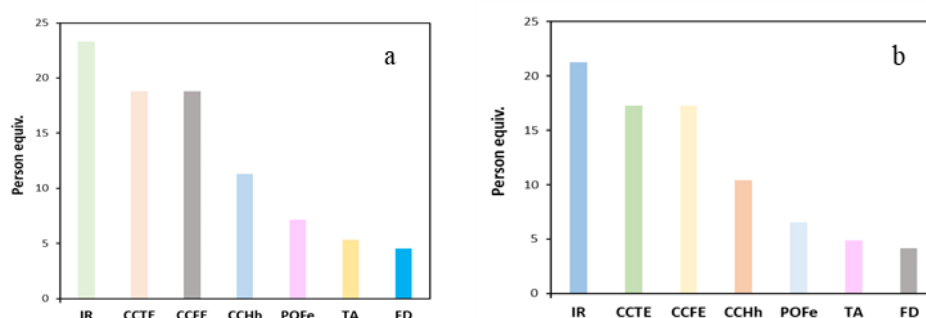
Fig. 1. Environmental impact of biosorption of Cr (VI) (a) and Cd (II) (b) from aqueous solution inbatch system using fungal biomass of *T. viride* considering ReCiPe 2016 method

CONCLUSIONS

The LCA methodology can be successfully applied in biosorption studies to assess material flows and to identify options for minimizing waste and reducing pressure on natural resources. The application of the Life Cycle Assessment methodology allows us to identify the stages that generate a negative impact on the environment and thus we can implement measures to reduce them. As we observed in our study, the biosorption process itself puts pressure to the environment in terms of energy consumption for the most part, and less to the substances used in the process.

Keywords: biosorption, heavy metals, impact categories, Life Cycle assessment

ACKNOWLEDGMENT

REFERENCES

1. BONTON, A.; BOUCHARD, C.; BARBEAU, B.; JEDRZEJAK, S. Comparative life cycle assessment of water treatment plants. *Desalination*, 2012, 284, 42e54. https://doi.org/10.1016/j.desal.2011.08.035.

2. HLIHOR, R. M.; APOSTOL, L.C.; SMARANDA, C.; SIMION, I. M.; FORTUNA, M. E.; DIACONU, M.; BULGARIU, L.; GAVRILESCU, M. Target compounds and pollutants, biosorbents and bioaccumulators, in Biosorption and Bioaccumulation: Principles and Applications in Environmental Bioremediation, Iasi, Romania: Politehnium Publishing House, 2016.

3. HU, G.; RANA, A.; MIAN. H. R.; SALEEM, S.; MOHSENI, M.; JASIM, S.; HEWAGE, K.; SADIQ, R. Human health risk-based life cycle assessment of drinking water treatment for heavy metal(loids) removal. *Journal of Cleaner Production*, 2020, 267, 121980.

4. FILOTE, C.; ROȘCA, M.; HLIHOR, R. M.; COZMA, P.; SIMION, I. M.; APOSTOL, M. GAVRILESCU, M. Sustainable Application of Biosorption and Bioaccumulation of Persistent Pollutants in Wastewater Treatment: Current Practice. *Processes*, 2019, P. 1–39.

AIR QUALITY ASSESSMENT IN RELATION WITH INCREASING DIESEL CONSUMPTION

A. Minderytė, J. Pauraite, S. Byčenkienė
Center for Physical Sciences and Technology
Savanorių ave. 231, LT-02300 Vilnius – Lithuania
+3705264 9211
office@ftmc.lt

EXTENDED ABSTRACT

OVERVIEW

Since the 1990s, European governments have been encouraging drivers to buy diesel vehicles rather than gasoline-powered ones. The reason for this was higher fuel efficiency and lower CO_2 emissions, yet it emits higher levels of particulates including black carbon (BC) [1]. According to IPCC, black carbon (BC) is the only component of aerosol particles that has a positive effect on atmospheric radiative balance [2]. However, BC has an impact not only on atmospheric radiative balance, it also raises a threat to air quality and, thus human health. Due to the formation during combustion processes, BC aerosol particles are small (around 200 nm) with porous surface and exhibit strong absorbative characteristics. Even small amounts of absorbed volatile organic compounds (VOCs), polycyclic aromatic compounds (PACs) or heavy metals can impose a severe health risk such as pneumonia, DNA damage, oxidative stress [3]. Therefore, BC may not be the main hazardous constituent of aerosol particles but act as a potential carrier for other combustion-derived toxic materials. Currently there are no regulatory terms which control the levels of BC mass concentration in EU; however, it is crucial to identify the specific sources and develop mitigation strategies in order to improve air quality and minimize personal exposure to hazardous atmospheric pollutants.

In our study BC source apportionment was performed using Aethalometer model which separates the sources into fossil fuel combustion and biomass burning. This model uses source-specific absorption Angstrom exponent (AAE) values, however AAE depends on various site-specific parameters, such as: common sources of pollution, fuels used. Thus, the determination of individual values of the AAE for the urban environment is important in order to perform a qualitative source apportionment and to assess the contribution of pollution sources.

METHODS

The measurements were deployed in Vilnius (urban background site) using an Aerosol Chemical Speciation Monitor (ACSM) (Aerodyne Research Inc., USA) and a 7-wavelength Aethalometer (Model AE31 Spectrum, manufactured by Optotek, Slovenia). In order to determine the quantitative contribution of fossil fuel combustion (BC_{tr}) and biomass burning (BC_{wb}), Aethalometer model was used and a combination of the most suitable Ångström absorption exponent (AAE) values was established. BC source apportionment is based on examining the differences in particle optical absorption of different wavelengths of light. This

source specific characteristic is defined by AAE which describes the wavelength variation in aerosol absorption. The aerosol absorption coefficient b_{abs} is defined as:

$$b_{abs}(\lambda) = b_0 \lambda^{-AAE}, \tag{10}$$

where λ, b_{abs}, b_0 indicate wavelength, aerosol absorption coefficient and wavelength independent constant, respectively. Source apportioned BC mass concentration was calculated as follows using method presented by Sandradewi *et al.* [4]:

$$b_{absBCtr} = \frac{b_{abs}(\lambda_1) - b_{abs}(\lambda_2) \cdot \left(\frac{\lambda_1}{\lambda_2}\right)^{-AAE_{wb}}}{\left(\frac{\lambda_1}{\lambda_2}\right)^{-AAE_{tr}} - \left(\frac{\lambda_1}{\lambda_2}\right)^{-AAE_{wb}}}; \tag{11}$$

$$b_{abs\,total}(\lambda) = b_{abs,BCtr}(\lambda) + b_{absBCwb}(\lambda), \tag{12}$$

where $b_{abstotal}$ is the total BC absorption at wavelength λ_1. In this work λ_1 was selected to be 470 nm, while λ_2 - 880 nm [5].

RESULTS

BC source apportionment results showed increasing BC_{tr} contribution over the period 2014 – 2020 (51% in 2014, 61% in 2017, and 65% in 2020). To investigate the impact on the environment of transport related pollution, a quantitative characteristic – BC absorption coefficient was evaluated (Fig. 1). Over the course of the examined years a large increase was observed (3.6 times) in traffic related BC_{tr} optical absorption.
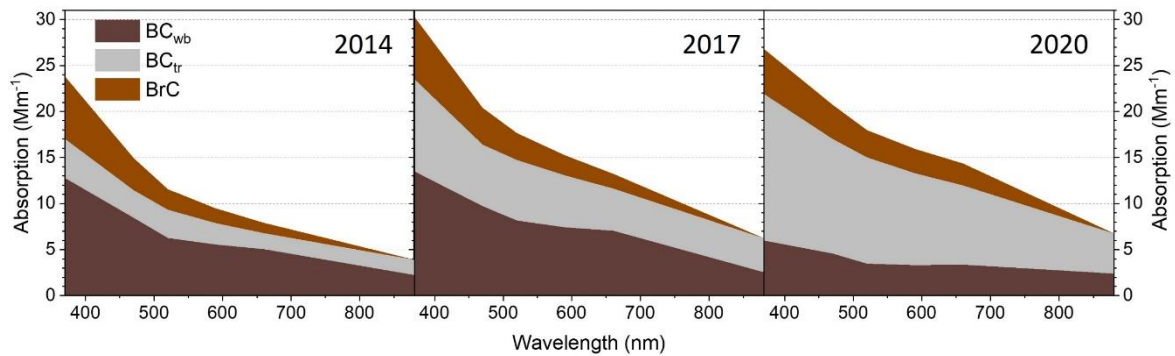
Fig. 1. Absorption coefficients of BC_{tr}, BC_{wb}, BrC as a function of wavelength for 2014, 2017 and 2020.

This rises a great concern about atmospheric radiative balance as the energy absorbed by BC aerosol particles is kept in the atmosphere in the form of heat. For further statistical analysis, transport statistics were examined (Table 1). It was observed that over the period 2014-2020 PC diesel category increased by 83.9%. From earlier studies it has been established that diesel vehicle exhaust emission contain more BC compared to petrol [6]. Thus, the transport related pollution increase can be attributed to the sharp increase in the number of diesel vehicles.

Table 1. Increase in the number of vehicles of different types in 2014, 2017, and 2020. PC – personal cars, LD – light duty vehicles, HD – heavy duty vehicles.

	Category	Change 2014/17, %	Change 2017/20, %	Change 2014/20, %
Passenger Cars	PC all	22.3	15.4	41.1
	PC petrol	-18.1	13.4	-7.2
	PC diesel	57.1	17.0	83.9
	PC LPG	-18.2	-5.2	-22.5
Light Duty Vehicles	LD all	28.4	19.8	53.9
	LD petrol	-19.1	-15.8	-31.9
	LD diesel	32.6	21.7	61.4
Heavy Duty Vehicles	HD all	15.8	25.9	45.8
	HD petrol	-16.5	0.2	-16.3
	HD diesel	17.3	26.8	48.7
	Buses	-8.7	6.1	-3.2
L-category	Motorcycles	27.3	44.8	84.3
ALL		22.1	16.8	42.6

CONCLUSIONS

The study provides a quantitative assessment of pollution associated with diesel vehicles and points out that from 2014 to 2020 with an increase in the number of diesel vehicles of as much as 83.9%, a 3.6-fold increase in BC_{tr} optical absorption and changes in aerosol composition were observed. This significant increase in diesel vehicles-related pollution and light absorption raises a concern for local air quality. Regarding the negative impacts of BC on human health and the atmospheric radiative balance, the results of this study address air quality issues and seek possible measures to combat air pollution.

REFERENCES

1. ANENBERG, C.; SCHWARTZ, J.; SHINDELL, D.; AMANN, M.; FALUVEGI, G.; KLIMONT, Z; JANSSENS-MAENHOUT, G.; POZZOLI, L.; Van DINGENEN, R.; VIGNATI, E.; EMBERSON, L.; MULLER, Z.; WEST, J.; WILLIAMS, M.; DEMKINE, V.; HICKS, K.; KUYLENSTIERNA, J.; RAES, F.; RAMANATHAN, V. Global Air Quality and Health Co-benefits of Mitigating Near-Term Climate Change through Methane and Black Carbon Emission Controls. *Environmental Health Perspectives,* 2012, Vol. 120, No. 6, P. 831–839.

2. *Global Warming of 1.5 °C. An IPCC special report on the impacts of global warming of 1.5 °C above pre-industrial levels and related global greenhouse gas emission pathways, in the context of strengthening the global response to the threat of climate change.* Intergovernmental Panel on Climate Change, 2018. [referred on the 1st of March in 2022 y.]. Link to the internet < https://www.ipcc.ch/sr15/>

3. ROVELLI, S.; CATTANEO, A.; NISCHKAUER, W.; BORGHI, F.; SPINAZZE, A.; KELLER, M.; CAMPAGNOLO, D.; LIMBECK, A.; CAVALLO, M.; Toxic trace metals in size-segregated fine particulate matter: Mass concentration, respiratory deposition, and risk assessment. *Environmental Pollution*, 2020, Vol 266, P. 115242.

4. SANDRADEWI, J.; PRÉVÔT, H.; WEINGARTNER, E.; SCHMIDHAUSER, R.; GYSEL, M.; BALTENSPERGER, U. A study of wood burning and traffic aerosols in an Alpine valley using a multi-wavelength Aethalometer. *Atmospheric Environment* 2008, Vol. 42, No. 1, P. 101–112.

5. ZOTTER, P.; HERICH, H.; GYSEL, M.; EL-HADDAD, I.; ZHANG, Y.; MOČNIK, G.; HÜGLIN, Ch.; BALTENSPERGER, U.; SZIDAT, S.; PRÉVÔT, H. Evaluation of the absorption Ångström exponents for traffic and wood burning in the Aethalometer-based source apportionment using radiocarbon measurements of ambient aerosol. *Atmospheric Chemistry and Physics*, 2017, Vol. 17, No. 6, P. 4229-4249.

6. IARC: Diesel Engine Exhaust Carcinogenic. WHO, 2012. [referred on the 1st of March in 2022 y.]. Link to the internet https://www.iarc.who.int/news-events/iarc-diesel-engine-exhaust-carcinogenic/

COMPARISON OF THE ANTHROPOGENIC BLACK CARBON EMISSIONS FROM DIFFERENT TYPES OF FUEL USED FOR RESIDENTIAL HEATING IN THE VILNIUS

D.Pashneva, I. Uogintė, J. Pauraitė, A. Minderytė,
L. Davulienė, K. Plauškaitė, M. Skapas, V. Dudoitis,
J. Andriejauskiene, V. Ulevicius, D. Jasinevičienė, S. Byčenkienė
Center for Physical Sciences and Technology
Saulėtekio ave. 3, LT-10257 Vilnius – Lithuania
+37060455746
daria.pashneva@ftmc.lt

V. Araminienė, V. Gudynaitė-Franckevičienė, I. Varnagirytė-Kabašinskienė
Lithuanian Research Centre for Agriculture and Forestry
Instituto av. 1, Akademija, Kėdainiai distr. – Lithuania

E. F. Dzenajavičienė, N. Pedišius, E. Lemanas, T. Vonžodas
Lithuanian Energy Institute,
Breslaujos str. 3, LT-44403 Kaunas – Lithuania

P. Sicard
ARGANS, 260 route du Pin Montard, Biot – France

EXTENDED ABSTRACT

OVERVIEW

Traffic and heating are the main sources of black carbon (BC) in urban areas [1]. In recent years renewable energy trend may lead to a redistribution of BC sources between fossil fuel and biomass burning by increasing contribution from biomass burning [2]. Determination of fuel properties and composition as well as combustion conditions is the essential prerequisite for reducing emissions from combustion and have impact on regional and global climate change, air quality, public health and ecosystems [3]. The increase in BC by 1 µg m^{-3} is at least eight times larger than the estimated effect of a 1 µg m^{-3} increase in particle matter (PM). WHO report from 2012 concluded that "reduction in exposure to PM$_{2.5}$ containing BC and other combustion-related PM material for which BC is an indirect indicator should lead to a reduction in the health effects associated with PM"[4]. Lacking reliable information about technology and fuels used in household sector, inventories on BC emissions are subject to large uncertainty [5]. Thus, this work aims to evaluate BC emission levels for the most common biomass fuels (mixed wood pellets, oak, ash, birch and spruce firewood) and two types of agro-biomass (triticale and rape straw pellets) burned in modern and old heating systems.

METHODS

Measurements were performed during July-October 2020 at an urban background station in Vilnius. Aerosol mass concentration measurements of individual biomass boilers were performed in the laboratory test facility. Gravimetric particle matter analysis method according to standard EN 13284 was used for assessment of BC mass concentration from individual boilers, burning solid biomass fuel. In this method, the PM collected in the filters are heated to various temperatures. As the heating temperature rises, volatiles are first removed from the collected sample, and at 550 C BC burns leaving only minerals. Changes in the mass of the sample during heating are evaluated by weighing to determine the concentration of BC in the combustion products. The biomass fuel was burned in three modes: (1) with increased excess air, (2) with air supply as defined in the heating system specifications, and (3) with increased air deficiency. The aethalometer (A Magee Scientific Company Aethalometer model AE31) provided continuous real-time measurements of BC mass concentration.

RESULTS

Analysis of BC source apportionment during the 4-month period showed that the contribution of BC_{FF} to total BC concentration was higher compared to BC_{BB}, reaching 54% ($\pm$50%) and 46% ($\pm$40%), respectively. The mean BC mass concentration determined was 0.69 ($\pm$0.64) μg m^{-3}, which is comparable to the warm season in Lithuania. The studies on the combustion of solid biomass fuels in modern and old heating systems showed that BC emissions are significantly higher in old systems. Comparison of the fuels showed that BC emissions were highest when woody fuels were burned, and a certain, albeit weak, dependence on wood type was evident. The amounts of BC emissions per 1 kg of fuel burned measured during the research and the highest emissions to birch firewood (about 5.00 mg kg^{-1} fuel), which is double or even higher compared to other firewood species Fig 1.
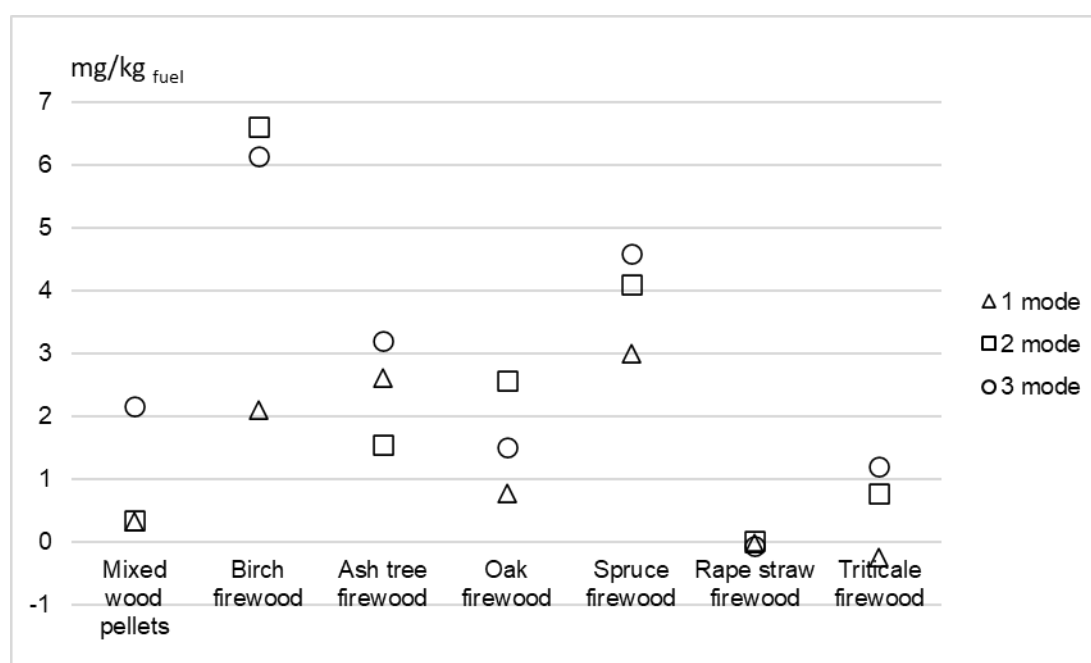
Fig. 1. BC emissions per volume of fuel. The biomass fuel was burned in three modes: (1) with increased excess air, (2) with air supply as defined in the heating system specifications, and (3) with increased air deficiency.

CONCLUSIONS

This study showed a significant contribution of transport (54%) and combustion of firewood and agro biomass to BC emissions during the warm season in the urban background environment from July to October 2020 and confirmed the need to improve the efficiency of reducing BC emissions from combustion of solid biomass. Replacing old boilers with modern ones and using fuels with lower black carbon emissions can help improve air quality by removing BC from the air.

This work was carried out in the framework of the project "Investigation of aerosol black carbon emissions from biomass incineration units and deposition on tree foliage" (RTO Lithuania).

Keywords: Black carbon, biomass fuels, agro-biomass, residential heating

REFERENCES

1. HELIN, A. Characteristics and source apportionment of black carbon in the Helsinki metropolitan area, Finland, *Atmospheric Environment*, 2018, vol. 190, No. January, P. 87–98.

2. SAARIKOSKI, S.; NIEMI, J.; AURELA, M.; PIRJOLA, L.; KOUSA, A. Sources of black carbon at residential and traffic environments, *Atmospheric Chemistry and Physics*, 2021 , P. 1–27.

3. HRONCOVÁ, E.; LADOMERSKÝ, J.; ANDRÁŠ, P.; TURISOVÁ, I. Thermal treatment of wood for mitigating of climate change, *Key Engineering Materials*, 2016, Vol. 688, P. 195–203.

4. RECHE, C. Real-time indoor and outdoor measurements of black carbon at primary schools, *Atmospheric Environment*, 2015, Vol. 120, P. 417–426.

5. ZHANG, Y. Evidence of major secondary organic aerosol contribution to lensing effect black carbon absorption enhancement, *npj Climate and Atmospheric Science*, 2018, Vol. 1, No. 1, P. 155–162.

ASSESSMENT OF THE SUITABILITY OF *BETULACEAE* AND *SALICACEAE* FAMILY TREES FOR THE ENVIRONMENTAL PROTECTION AGAINST PERSISTENT ORGANIC POLLUTANTS

G. Striganavičiūtė, V. Sirgedaitė-Šėžienė

Lithuanian Science Centre for Agriculture and Forestry, Institute of Forestry
Liepų st. 1, 53101 Girionys - Lithuania
+37064639238
greta.striganaviciute@lammc.lt

EXTENDED ABSTRACT

OVERVIEW

Anthropogenic pollution of regional, rural, and urban ecosystems is a constant issue in recent decades [1]. Based on newest research, persistent organic pollutants (POPs) are resistant to biological, chemical, and photolytic degradation. Because of this, they remain in the contaminated medium or travel long distances due to their semi-volatile properties [2]. They have toxic effects on both humans and various animal species [3]. Many POPs were widely used from the 1930s to the 1980s, when long-term toxicity was not well-studied. In response to growing global concerns, in 2001 a global treaty, The Stockholm Convention on Persistent Organic Pollutants [4], based on the United National Environmental Programme, was ratified by the international community, with the aim of eliminating or restricting the production and use of 12 of the most damaging POPs [5].

There can be many different forms of POPs, both natural and anthropogenic. POPs that are characterized by their persistence and bioaccumulation properties include many of the formerly used organochlorine-based insecticides such as dieldrin, dichloro-diphenyl-trichloroethane (DDT), toxaphene and chlordane and several industrial chemical products or by-products, including polychlorinated biphenyls (PCBs), dibenzo-p-dioxins (dioxins) and dibenzo-p-furans (furans). Many POPs are currently or have been used as pesticides, solvents, pharmaceuticals, and industrial chemicals [6]. Although some POPs occur naturally (e.g., from volcanoes), most are man-made [7]. POPs are a matter of concern because of their toxicity and tendency to accumulate in food chains [8].

Vegetation has been shown to be a globally important part in the removal and storage of the atmospheric POPs and their transfer to soil from falling litter. Vegetation is therefore an important reservoir for POPs [9]. Plants can absorb, transfer, and accumulate POPs in their tissues. The use of plants to restore contaminated soil and water has long been recognized as a cost-effective method. Plants usually act as pumping and filtering systems in the phytoremediation process as they absorb POPs in the rhizosphere [10]. The process varies depending on the physical and chemical properties of POPs and vegetation species as well as plant's growth stage [11]. Specific POPs can also be separated from the atmosphere by deposition on the leaves or uptake through the stomata [10]. However, there are no fixed enzymes in the plants that can degrade or detoxify POPs [12].

Bacteria found in plant species, but not obviously damaging their plant hosts are called endophytic. These endophytic bacteria can increase plant tolerance to pollutant stress and utilize contaminants e.g., POPs. Among the technologies being developed for this purpose, bioaugmentation, in which POP-degrading bacteria enter the contaminated site from an external site, is expected to be a safe and inexpensive in situ strategy. However, POP-degrading bacteria are rare in nature and have been extremely difficult to isolate and enrich [13].

Phytoremediation is a promising way to clean soil and water contaminated with organic and inorganic contaminants [14-16]. However, the presence of organic pollutants, including POPs, in soil and water reduces plant growth and phytoremediation efficiency [17-19]. The combined use of plants and bacteria has recently been proposed to increase the efficiency of remediation of soil contaminated with POPs [20-22]. Plants provide space and nutrients to the bacteria. In exchange, rhizosphere, epiphytic and endophytic bacteria improve bioavailability and allow mineralization of organic pollutants.

Tree species suitable for phytoremediation are selected based on their resistance to environmental stress, which is related to the overall viability of trees (photosynthetic and growth parameters, nitrogen balance index, antioxidant levels) and their ability to synthesize and mobilize secondary metabolites [23].

Hence, profiling plant's growth patterns, secondary metabolism, photosynthesis, and antioxidant systems, may shine some light on the direct effect POPs can have on them. Furthermore, introducing potentially beneficial bacteria would then likely allow to ascertain the impact they can have on this POP-plant interaction, with hopefully advantageous results. There is not much research done on how POPs affect the secondary metabolism of plants, especially trees.

Tree species representing the *Betulaceae* (birch, alder) and *Salicaceae* (poplar, willow) families were selected for this research because they can be used for the remediation of contaminated sites and substrates [24,25]. To ensure their effective application it is important to conduct studies not only to select POP-resistant tree genotypes, but also to assess POP interactions with tree's growth and biochemical parameters. The possibility of beneficial symbiosis between tree genotypes selected for phytoremediation and POP-degrading microorganisms can potentially significantly increase the efficiency of environmental clean-up.

The main objective of the study is to evaluate the suitability of trees belonging to the *Betulaceae* and *Salicaceae* families for the reduction of persistent organic pollutants in the environment using innovative biotechnological measures. It is important to discover tree genotypes that, with the help of bacteria, will be able to reduce the concentration of POPs in the environment.

Keywords: Persistent organic pollutants, phytoremediation, *Betullaceae, Silicaceae*, bacteria, secondary metabolites.

REFERENCES

1. MANZETTI, S.; van der SPOEL, E. R.; van der SPOEL, D. Chemical Properties, Environmental Fate, and Degradation of Seven Classes of Pollutants. *Chemical Research in Toxicology*, 2014, Vol. 27, No. 5, P. 713–737.

2. HANEDAR, A.; GÜNEŞ, E.; KAYKIOĞLU, G.; ÇELIK, S.Ö.; CABI, E. Presence and distributions of POPS in soil, atmospheric deposition, and bioindicator samples in an

industrial-agricultural area in Turkey. *Environmental Monitoring and Assessment*, 2019, Vol. 191, No. 1, P. 42.

3. HOLT, E.; KOČAN, A, KLÁNOVÁ, J.; ASSEFA, A.; WIBERG, K.. Spatiotemporal patterns and potential sources of polychlorinated biphenyl (PCB) contamination in Scots pine (*Pinus sylvestris*) needles from Europe. *Environmental Science and Pollution Research*, 2016, Vol. 23, P. 19602-19612.

4. The Stockholm Convention on Persistent Organic Pollutants, opened for signature May 23, 2001, UN Doc. UNEP/POPS/CONF/4, App. II (2001), reprinted in 40 ILM 532 (2001) [hereinafter Stockholm Convention]. The text of the convention and additional information about POPs is available online at the United Nations Environment Programme's (UNEP's) POPs Web site, <http://irptc.unep.ch/pops/>.

5. RYLOTT, E.L.; JOHNSTON, E.J.; BRUCE N.C. Harnessing microbial gene pools to remediate persistent organic pollutants using genetically modified plants-a viable technology, *Journal of Experimental Botany*, 2015, Vol. 66, No. 21, P. 6519-33.

6. RITTER, L.; SOLOMON, K.R.; FORGET, J.; STEMEROFF. M. O'LEARY, C. Persistent organic pollutants. United Nations Environment Programme. Archived from the original (PDF) on 2007-09-26. Retrieved 2007-09-16.

7. EL-SHAHAWI, M.S.; HAMZA, A.; BASHAMMAKHB, A.S.; AL-SAGGAF, W.T. An overview on the accumulation, distribution, transformations, toxicity and analytical methods for the monitoring of persistent organic pollutants. *Talanta*, 2010, Vol. 80, No. 5, P. 1587–1597.

8. MASON, F.; BARAK, N. A catchment survey for heavy metals using the eel (*Anguilla anguilla*). *Chemosphere*, 1990, Vol. 21, P. 659

9. DUMANOGLU, Y.; FALAY, E.; TUNA, G.; ALTIOK, H.; KARA, M.; BAYRAM, A.; TOLUNAY, D.; ELBIR, T.; ODABASI, M. Biomonitoring the spatial variations of PCBs and PBDEs in an industrial region. *Organohalogen Compounds*, 2014, Vol. 76, P. 1008-1011.

10. ZHU, X.; NI, X.; LIU, J.; GAO, Y. Application of Endophytic Bacteria to Reduce Persistent Organic Pollutants Contamination in Plants. *CLEAN - Soil, Air, Water*, 2014, Vol. 42, No. 3, P. 306–310.

11. WHITE, J. C.; MATTINA, M. I.; EITZER, B. D.; IANNUCCI-BERGER, W. Tracking Chlordane Compositional and Chiral Profiles in Soil and Vegetation. *Chemosphere,* 2002, Vol. 47, P. 639.

12. MALIK, B.; PIRZADAH, T.B.; HAKEEM, K. R. *Phytoremediation of persistent organic pollutants (POPs)*, Academic press, Phytoremediation, 2022, P. 415-436, ISBN 9780323898744.

13. KAZUHIRO, T. Study on the biodegradation of persistent organic pollutants (POPs). *Journal of Pesticide Science*, 2020, Vol. 45, No. 2, P. 119–123.

14. KHAN, M.U.; SESSITSCH, A.; HARRIS, M.; FATIMA, K.; IMRAN, A.; ARSLAN, M.; SHABIR, G.; KHAN, Q.M.; AFZAL, M. Cr-resistant rhizo-and endophytic bacteria

associated with *Prosopis juliflora* and their potential as phytoremediation enhancing agents in metal-degraded soils. *Front Plant Sci,* 2014, Vol. 5, P. 755.

15. McCUTCHEON, S.; SCHNOOR, J. Phytoremediation: transformation and control of contaminants. *Environmental Science and Pollution Research*, 2004, Vol. 11, No. 40, P. 40.

16. SCHWITZGUÉBEL, J.P.; SCHRÖDER, P. Phytotechnologies to promote sustainable land use and improve food safety: Outcomes and outlook from the European COST Action 859. *Environmental Science and Pollution Research,* 2009, Vol. 16, P. 743–744.

17. GERHARDT, K.E.; HUANG, X-D.; GLICK, B.R.; GREENBERG, B.M. Phytoremediation and rhizoremediation of organic soil contaminants: potential and challenges. *Plant Science,* 2009, Vol. 176, P. 20–30.

18. IBÁÑEZ, S.; ALDERETE, L.S.; MEDINA, M.; AGOSTINI, E. Phytoremediation of phenol using *Vicia sativa* L. plants and its antioxidative response. *Environmental Science and Pollution Research*, 2012, Vol. 19, P. 1555–1562.

19. MENCH, M.; SCHWITZGUÉBEL, J.P.; SCHROEDER, P.; BERT, V.; GAWRONSKI, S.; GUPTA, S. Assessment of successful experiments and limitations of phytotechnologies: contaminant uptake, detoxification and sequestration, and consequences for food safety. *Environmental Science and Pollution Research,* 2009, Vol. 16, P. 876–900.

20. BECERRA-CASTRO, C.; PRIETO-FERNÁNDEZ, Á.; KIDD, P.S.; WEYENS, N.; RODRÍGUEZ GARRIDO, B.; TOUCEDA-GONZÁLEZ, M.; ACEA, M.J.; VANGRONSVELD, J. Improving performance of *Cytisus striatus* on substrates contaminated with hexachlorocyclohexane (HCH) isomers using bacterial inoculants: Developing a phytoremediation strategy. *Plant Soil*, 2013, Vol. 362, P. 247–260.

21. GLICK, B.R. Using soil bacteria to facilitate phytoremediation. *Biotechnology Advances,* 2010, Vol. 28, P. 367–374.

22. HASLMAYR, H.P.; MEIßNER, S.; LANGELLA, F.; BAUMGARTEN, A.; GELETNEKY, J. Establishing best practice for microbially aided phytoremediation. *Environmental Science and Pollution Research*, 2014, Vol. 21, P. 6765–6774.

23. WITZELL, J.; MARTÍN JUAN, A. Phenolic metabolites in the resistance of northern forest trees to pathogens — past experiences and future prospects. *Canadian Journal of Forest Research*, 2008, Vol. 38, No. 11, P. 2711–2727.

24. LEWIS, J.; QVARFORT, U.; SJÖSTRÖM, J. *Betula pendula*: A Promising Candidate for Phytoremediation of TCE in Northern Climates. *International Journal of Phytoremediation*, 2015, Vol. 17, No. 1, P. 9–15.

25. MARMIROLI, M.; PIETRINI, F.; MAESTRI, E.; ZACCHINI, M.; MARMIROLI, N.; MASSACCI, A. Growth, physiological and molecular traits in *Salicaceae* trees investigated for phytoremediation of heavy metals and organics. *Tree Physiology*, 2011, Vol. 31, No. 12, P. 1319–1334.

OVERVIEW: NEW APPROACH TO USE MODIFIED UREA FERTILIZERS

S. S. F. Swify, R. Mažeika

Lithuanian Research Centre for Agriculture and Forestry.
Instituto al. 1, Akademija, LT-58344 Kėdainiai distr. – Lithuania
Phone +370 6071494
Samar.Swify@lammc.lt

EXTENDED ABSTRACT

OVERVIEW

The high demand for nitrogen fertilizers is due to their having the element Nitrogen (N) which is most important for crops productivity. In addition, to meet the increasing food demand, the agricultural sector is bound to use even larger quantities of fertilizers [1]. Urea is the most commonly used N source due to its high concentration and relatively inexpensive. However, Urea is easily soluble in water and evaporates into the air so urea fertilizer is a low fertilizer efficiency [2]. Conventional methods also impair nitrogen use efficiency (NUE) by plants, limiting crop yields. Moreover, its contribution to environmental pollution in terms of hazardous gaseous emissions and water eutrophication [2]. Therefore, many technological interventions, especially those geared towards the use of different compounds based on ecological raw materials, to improve urea use efficiency as a main fertilizer of nitrogen and reduce the emissions to the environment [3]. One of the most common attempts to reduce nitrogen fertilizer losses by making it in a controlled or slow-release form which several methods and materials have been reported [3,4]. Thus, the release of nitrogen is controlled so that the amount of excess nitrogen in the form of nitrate that enters the water is reduced, thereby reducing water pollution [3-5]. To this end, it's important to understand the difference between modified urea nitrogen fertilizers types and the benefits of using them. The two most common types are called "slow release nitrogen" (SRN) and "controlled release nitrogen" (CRN) [6]. These terms are frequently used interchangeably, but they should not be; they do not mean the same thing. While both release nitrogen at a slower rate than straight urea, the mechanism by which they do so is vastly different. At the most basic level, SRN and CRN sources are distinguished by a single defining characteristic: coated or uncoated. SRN does not use any type of coating to provide extended release nitrogen, whereas CRN is completely reliant on coatings to delay nitrogen release. These coatings are at the heart of the primary distinction between the two types of nitrogen. Many studies have shown that slow release or controlled release fertilizer (CRF or SRF) can improve nutrient use efficiency and reduce crop and environmental damage because it is Eco-friendly and pollutes the environment minimally [7-11].

Slow Release Nitrogen (SRN)

Slow release nitrogen has been identified as a result of interactions with mineral or organic materials [6]. Initially, Sulphur was used in SRF production [12], but it was discontinued due to its burst effect, inconsistent results, and high cost due to the additional requirements of sealants, plasticizers, and binders [3,13]. Recently, eco-friendly biopolymers such as starch,

lignin, and cellulose were used as alternative materials for SRF implementation instead of synthetic polymers [14–16]. Hydroxypropyl methylcellulose (HPMC) is a white to slightly off-white fibrous or granular free flowing powder with no odor or taste. It is made by modifying alkali cellulose from purified wood pulp by reacting it with methyl chloride and propylene oxide to obtain the methyl and hydroxyl ether groups, and it is widely used in food, drug, and dietary supplement industries [17]. It is an excellent polymer for fertilizer film coating [18]. Polyvinyl alcohol (PVA) has also been studied for use in fertilizer and since at high content, it can control the process release. These polymers slowed down the release of diltiazem HCl from the matrices and could potentially be used for the controlled delivery process of the nutrients [19].

Controlled Release Nitrogen (CRN)

Controlled release nitrogen differs fundamentally from SRN in both technology and mode of nitrogen release. CRN particles are completely encapsulated in organic resin or polymer coatings. These coatings are the secret to delaying the release of nitrogen in a CRN type. The use of controlled-release urea (CRU), for which several methods and materials have been reported, is an approach that improves Nitrogen use efficiency (NUE) and reduces environmental pollution [3,4]. One such technique for producing controlled release coated urea (CRCU) is the physical introduction of urea granules into an appropriate coating material [4]. The development of CRCU is an eco-friendly technology that not only reduces nitrogen loss due to volatilization and leaching but also changes the kinetics of nitrogen release, keeping the balance between the requirements of the plants and the nutrients stock at a rate that is more compatible with their metabolic needs [4,5,8]. The CRFs have been classified diversely according to the literature [20-23] as shown in Fig. 1.
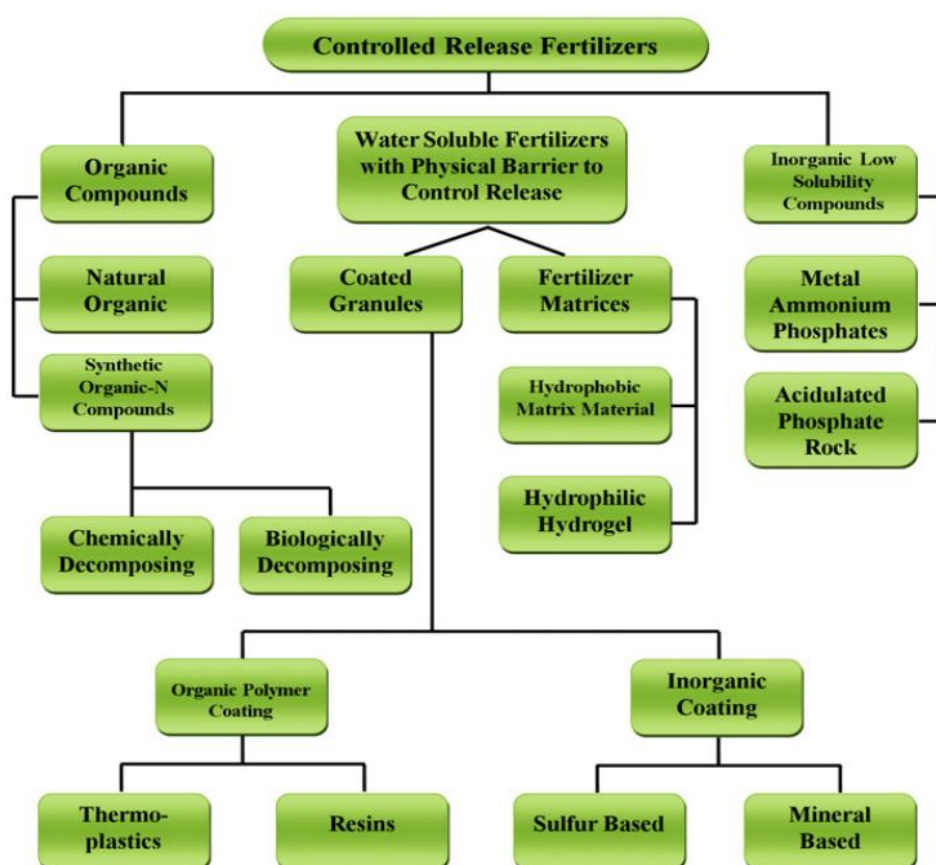

Fig. 1. Classification of controlled release fertilizers [4].

Stabilized Nitrogen

Stabilized nitrogen products, sometimes called "inhibitors," are used to extend the time that nitrogen remains in the form of urea or ammonium in the soil, but they're not the same as slow or controlled-release fertilizers [24]. After urea fertilizer application to soil, it must first be converted through two processes, the first of which is known as hydrolysis. The urease enzyme plays an important role in the breakdown of urea into ammonium, causing increases in the soil pH in the surrounding area of the granules and resulting in NH3 losses via volatilization that average 16% of N applied worldwide and can reach 40% or more in hot and humid conditions [25,26]. Stabilized nitrogen prevents this urease enzyme from working for several days [26]. Many such compounds act as urease inhibitors, but only N-(n-butyl) thiophosphoric triamide (NBPT) has been used globally, and it has been the most successful in a market that has grown at a rate of 16 percent per year over the last ten years. When compared to urea, NBPT-treated urea reduces NH3 loss by approximately 53%. Yield gain from NBPT application is in the order of 6.0 percent and ranges from 0.8 to 10.2 percent depending on crop species. Nitrification inhibitors typically increase NH3 volatilization and combining them with urease inhibitors partially negates the latter's benefits in reducing NH3 loss [26].

CONCLUSIONS

Recently, urea modified fertilizers play a vital role in mineral nitrogen availability in the soil and decrease the nitrogen release rate to increase the use efficiency of fertilizer by crops. As well, a large number of studies have reported the positive effects of urea-slow or controlled release compounds on different crops yield. Moreover, still there are many studies to enhance understanding of the impact of these compounds to improve formulations and integrate them with agronomic practices capable of reducing losses and increasing NUE.

Keywords: Modified Urea, Nitrogen Losses, Eco-friendly, Coating, Uncoating, Inhibitors

REFERENCES

1. MATEO-SAGASTA, J.; ZADEH, S.M.; TURRAL, H. *More People, More Food, Worse Water? A Global Review of Water Pollution from Agriculture*; Food and Agriculture Organization of the United Nations (FAO): Rome, Italy, 2018.

2. TERMAN, G. L., Volatilization losses of nitrogen as ammonia from surface-applied fertilizers, organic amendments, and crop residues. *Advances in Agronomy*,1979, Vol. 31, P. 189–223.

3. AZEEM, B.; KUSHAARI, K.; MAN, Z.B. Effect of coating thickness on release characteristics of controlled release urea produced in fluidized bed using waterborne starch biopolymer as coating material. *Procedia Engineering*, 2016, Vol. 148, P. 282–289. <https://doi.org/10.1016/j.proeng.2016.06.615>

4. AZEEM, B.; KUSHAARI, K.; MAN, Z.B.; BASIT, A.; THANH, T.H. Review on materials & methods to produce controlled release coated urea fertilizer. *Journal of Controlled Release*, 2014, Vol. 181, P. 11–21.< https://doi.org/10.1016/j.jconrel.2014.02.020>

5. BARČAUSKAITĖ, K.; BRAZIENĖ, Z.; AVIŽIENYTĖ, D.; SILVA, M.; DRAPANAUSKAITE, D.; HONER, K.; GVILDIENĖ, K.; SLINKSIENE, R.; JANCAITIENE, K.; MAZEIKA, R.; STAUGAITIS, G.; DAMBRAUSKAS, T.; BALTAKYS, K.; BALTRUSAITIS, J. Mechanochemically synthesized gypsum and

gypsum drywall waste cocrystals with urea for enhanced environmental sustainability fertilizers. *Journal of Environmental Chemical Engineering*, 2020, Vol. 8 No. 4, P. 103965. <https://doiorg/101016/jjece2020103965>

6. KAREEM, S.A.; DERE, I.; GUNGULA, D.T.; ANDERW, F.P.; SADDIQ, A.M.; ADEBAYO, E.F.; TAME, V.T.; KEFAS, H.M.; JOSEPH, J.; PATRICK, D.O. Synthesis and Characterization of Slow-Release Fertilizer Hydrogel Based on Hydroxy Propyl Methyl Cellulose, Polyvinyl Alcohol, Glycerol and Blended Paper. *Gels* 2021, Vol. 7, P. 262. <https://doi.org/10.3390/gels7040262>.

7. ROSHANRAVAN, B.; SOLTANI, S.M.; RASHID, S.A.; MAHDAVI, F.; YUSOP, M.K. Enhancement of nitrogen release properties of urea– kaolinite fertilizer with chitosan binder. Chem. Special. *Bioavailability*. 2015, Vol. 27, P. 44–51. <http://doi.org/10.1080/09542299.2015.1023090>

8. GHORMADE, V.; DESHPANDE, M.V.; PAKNIKAR, K.M. Perspectives for nano-biotechnology enabled protection and nutrition of plants. *Biotechnology Advances* 2011, Vol. 29, P. 792–803. <http://doi.org/10.1016/j.biotechadv.2011.06.007>

9. TIAN, C.; ZHOU, X.; DING, Z.; LIU, Q.; XIE, G.; PENG, J.; EISSA, M.A. Controlled-release N fertilizer to mitigate ammonia volatilization from double-cropping rice. *Nutrient Cycling in Agroecosystems*. 2021, Vol. 119, P. 123–137. <http://doi.org/10.1007/s10705-020-10108-3>

10. SHOJI, S. Innovative use of controlled availability fertilizers with high performance for intensive agriculture and environmental conservation. *Science China Life Sciences*. 2005, Vol. 48, P. 912–920.

11. CHEN, J.; WEI, X. *Controlled-release fertilizers as a means to reduce nitrogen leaching and runoff in container-grown plant production.* In Nitrogen in Agriculture-Updates; Khan, A., Fahad, S., Eds.; Books on Demand: Norderstedt, Germany, 2018; P. 33–52.

12. AYUB, G.S.E.; ROCHA, S.C.S.; PERRUCCI, A.L.I. Analysis of the surface quality of sulphur-coated urea particles in a two-dimensional spouted bed. *Brazilian Journal of Chemical Engineering,* 2001, Vol. 18, P. 13–22. <http://doi.org/10.1590/S0104-66322001000100002>

13. GONZÁLEZ, M.E.; CEA, M.; MEDINA, J.; GONZÁLEZ, A.; DIEZ, M.C.; CARTES, P.; NAVIA, R. Evaluation of biodegradable polymers as encapsulating agents for the development of a urea controlled-release fertilizer using biochar as support material. *Science of The Total Environment*. 2015, Vol. 505, P. 446–453. <https://doi.org/10.1016/j.scitotenv.2014.10.014>

14. MULDER, W.J.; GOSSELINK, R.J.A.; VINGERHOEDS, M.H.; HARMSEN, P.F.H.; EASTHAM, D. Lignin based controlled release coatings. *Industrial Crops and Products*, 2011, Vol. 34, P. 915–920. <https://doi.org/10.1016/j.indcrop.2011.02.011>

15. LUM, Y.H.; SHAABAN, A.; MOHAMAD, N.; DIMIN, F.; YATIM, N.M. Boric acid modified starch polyvinyl alcohol matrix for slow-release fertilizer. *e-Polymers* 2016, Vol. 16, P. 151–158. < https://doi.org/10.1515/epoly-2015-0259>

16. ÖZEN, ˙I.; OKYAY, G.; ULA¸S, A. Coating of nonwovens with potassium nitrate containing carboxymethyl cellulose for efficient water and fertilizer management. *Cellulose* 2018, Vol. 25, P. 1527–1538. <http://doi.org/10.1007/s10570-018-1655-0>

17. GHOSAL, K.; CHAKRABARTY, S.; NANDA, A. Hydroxypropyl methylcellulose in drug delivery. *Der Pharmacia Sinica*, 2021, Vol. 2, P. 152–168.

18. BIANCHI, S.E.; ANGELI, V.W.; SOUZA, K.C.B.D.; MIRON, D.D.S.; CARVALHO, G.D.A.; SANTOS, V.D.; BRANDALISE, R.N. Evaluation of the solubility of the HPMC: PVA blends in biological fluids in vitro. *Journal of Materials Research*. 2011, Vol. 14, P. 166–171.< http://doi.org/10.1590/S1516-14392011005000033>

19. GAAZ, T.S.; SULONG, A.B.; AKHTAR, M.N.; KADHUM, A.A.H.; MOHAMAD, A.B.; AL-AMIERY, A.A. Properties and applications of polyvinyl alcohol, halloysite nanotubes and their nanocomposites. *Molecules*, 2015, Vol. 20, p. 22833–22847.<Phttp://doi.org/10.3390/molecules201219884>

20. SHAVIV, A. Controlled release fertilizers, IFA International Workshop on Enhanced-Efficiency Fertilizers, Frankfurt, International Fertilizer Industry Association, Paris, France, 2005.<https://doi.org/10.1021/jf60177a039>

21. TRENKEL, M.E. Slow-and controlled-release and stabilized fertilizers: an option for enhancing nutrient use efficiency in agriculture, IFA, International fertilizer industry association, 2010.

22. LIU, L. A review: controlled release systems for agricultural and food applications, in: N. Parris, L.S. Liu, et al., (Eds.), New Delivery Systems for Controlled Drug Release from Naturally Occurring Materials, ACS Symposium series, 2008, Vol. 992, P. 265–281. <http://doi: 10.1021/bk-2008-0992.ch014>

23. ROSE, R. *Slow release fertilizers* 101, in: R.K. Dumroese, L.E. Riley, T.D. Landis (Eds.), 2002,Technical.

24. JIAO, X. G.; LIANG, W.; CHEN, L.; ZHANG, H. J.; WANG, P.; WEN, D. Effect of slow-release urea fertilizers on urease activity, microbial biomass, and nematode communities in an aquic brown soil. *Science China Life Sciences*. 2005, Vol. 48, No. 1, P. 26-32.

25. ZHOU, L.; CHEN, L.; LI, R.; WU, Z. *Behavior of soil urea N and its regulation through incorporating with inhibitors hydroquinone and dicyandiamide*. In L. Ji, G. X. Chen, E. Schnug, C. Hera, & S. Hanklaus Eds., Fertilization in the third millennium fertilizer, food security and environmental protection, proceedings, 2003, Vol. 2, P. 1175–1192.

26. CANTARELLA, H; OTTO, R.; SOARES, J. R.; SILVA, A. G. B. Agronomic efficiency of NBPT as a urease inhibitor: A review, *Journal of Advanced Research*, 2018, Vol. 13, P. 19-27.

ENVIRONMENTAL WELLBEING IN THE CONTEXT OF SUSTAINABLE DEVELOPMENT: EVIDENCE FROM THE POST-COMMUNIST ECONOMIES

S.-R. Ulman, C. Cautisanu

CERNESIM Environmental Research Center, Institute of Interdisciplinary Research,
"Alexandru Ioan Cuza" University of Iasi
Carol I Street, 700506 Iasi – Romania
simona.ulman@uaic.ro, cristina.cautisanu@uaic.ro

EXTENDED ABSTRACT

OVERVIEW

Sustainability calls for increased levels of economic, social, and environmental wellbeing. Considering the national contexts, there are certainly differences in regard to their capacity of attaining sustainable development and its three main dimensions (for example, [1-5]). The first major aim of this paper was to compare the national levels of the two sub-dimensions of environmental wellbeing, i.e. Natural Resources and Climate & Energy, and their components between 2006 and 2020 in the post-communist economies. Secondly, putting Climate & Energy, with their major components, i.e., energy use, energy savings, greenhouse gases and renewable energy, in the centre of the analysis, as the major weaknesses of environmental wellbeing within the analysed group of countries, we observed the nature of the influence of human and economic wellbeing upon each of them.

METHODS

Our analysis was focused on sustainable development across the 19 post-communist economies (Bosnia-Herzegovina, Bulgaria, Croatia, Czech Republic, Estonia, Georgia, Germany, Hungary, Latvia, Lithuania, Macedonia, Moldavia, Montenegro, Poland, Romania, Slovenia, Serbia, Slovakia, and Ukraine), using data collected between 2006 and 2020 from the official website of the Sustainable Society Index. Table 1 details the components of economic, human and environmental wellbeing.

Table 1. Economic, human, and environmental wellbeing's components (SSI)

Economic Wellbeing Components	Human Wellbeing Components	Environmental Wellbeing Components
	Sufficient food (HW_SF)	Biodiversity (EnvW_BD)
Organic farming (EcW_OF)	Sufficient to drink (HW_SD)	
	Safe sanitation (HW_SS)	Renewable water resources (EnvW_RWR)
	Education (HW_ED)	
	Healthy life (HW_HL)	Consumption (EnvW_CS)
Genuine savings (EcW_GS)		Energy use (EnvW_EU)
	Gender equality (HW_GE)	Energy savings (EnvW_ES)
Gross domestic product (EcW_GDP)	Income distribution (HW_ID)	Greenhouse gases (EnvW_GG)
Employment (EcW_EMP)	Population growth (HW_PG)	Renewable energy (EnvW_RE)
Public debt (EcW_PD)		
	Good governance (HW_GG)	

We structured our analysis in two parts. Firstly, we compared the average levels of Natural Resources and Climate & Energy components of Environmental Wellbeing in 2006-2020 period. Secondly, starting from the main results obtained in this comparison analysis, we identified the most stringent environmental problems. In order to understand the influence of the human and economic components on the major weaknesses of the environmental dimension in this group of countries over the entire period, panel data-specific methods were applied (pooled, fixed and random effects).

RESULTS

The general results showed that (1) the components of the Environmental Wellbeing registered a different evolution among the Post-communist economies across the 2006–2020 period (Fig. 1); (2) there is still sufficient room for improvement in terms of environmental sustainability in the Post-communist economies, especially in the case of Climate & Energy components (Fig. 1); (3) these environmental components were closely linked to both components of economic and social dimensions (Table 2), and (4) the determinants of energy use, energy savings, greenhouse gases and renewable energy were found to be different in the Post-communist economies (Table 2 and Fig. 2).
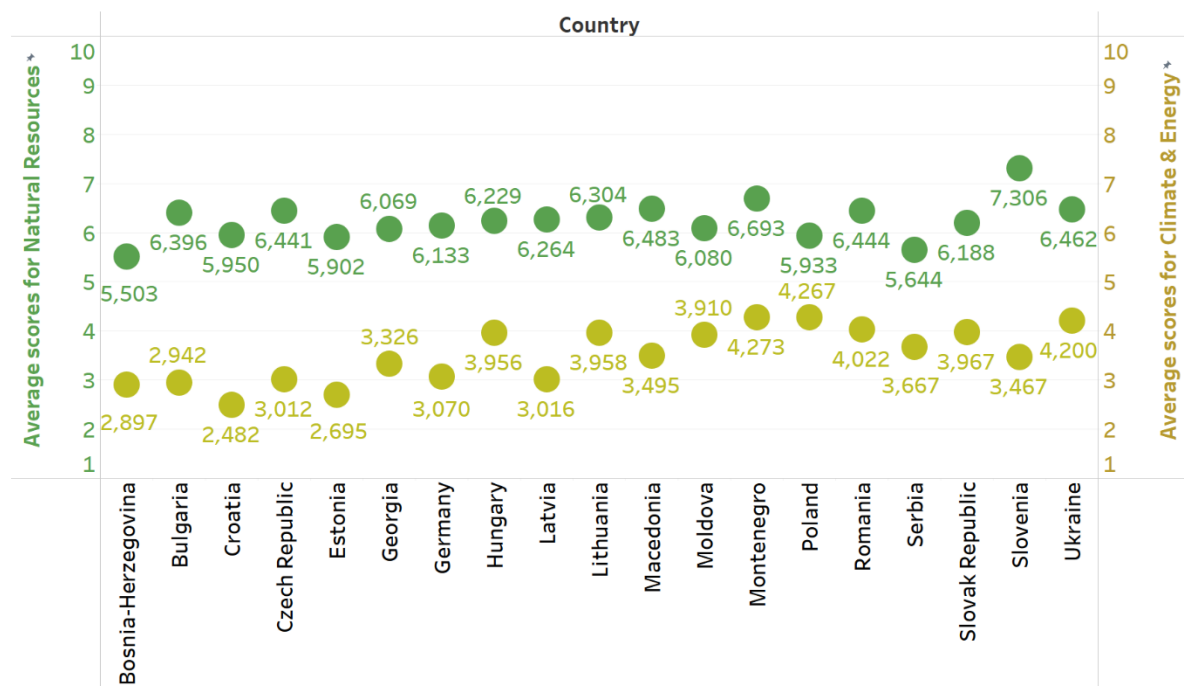
Fig 1. Comparative analysis between average levels of Natural Resources and Climate & Energy components of Environmental Wellbeing in 2006-2020 period

Table 2. Relation between components of Climate & Energy from Environmental Wellbeing and components of Economic and Human Wellbeing

			Dependent variable			
			Energy use	Energy Savings	Greenhouse Gases	Renewable Energy
Human wellbeing	**Basic Needs**	HW_SF	-1.149 [a] (0.854)	-1.433 (1.482)	-4.329*** (0.778)	-2.502*** (0.413)
		HW_SD	-2.163** (0.783)	-1.668** (0.834)	-3.087*** (0.786)	-0.124 (0.184)
		HW_SS	-0.183*** (0.053)	0.346** (0.167)	-0.276*** (0.058)	-0.047 (0.050)
	Personal Development & Health	HW_ED	-0.103 (0.144)	-0.097 (0.200)	-0.415*** (0.183)	0.203*** (0.071)
		HW_HL	2.114*** (0.224)	-1.162* (0.697)	-0.234 (0.262)	0.172 (0.124)
		HW_GE	-0.487 (0.379)	1.044 (0.672)	-0.091 (0.420)	0.621*** (0.176)
	Well-balanced Society	HW_ID	-0.184*** (0.071)	0.008 (0.111)	-0.186*** (0.084)	0.049 (0.032)
		HW_PG	0.533*** (0.130)	-0.385 (0.314)	0.548*** (0.172)	0.120 (0.082)
		HW_GG	-0.645** (0.243)	-1.980*** (0.548)	-1.354*** (0.289)	-0.216 (0.146)
Eonomic wellbeing	**Transition**	EcW_OF	-0.023 (0.047)	0.255*** (0.084)	0.177*** (0.072)	0.085*** (0.041)
		EcW_GS	-0.053 (0.084)	0.067 (0.128)	-0.004 (0.075)	-0.091*** (0.032)

Economy	EcW_GDP	-0.183 (0.250)	1.147*** (0.427)	0.519*** (0.217)	0.010 (0.083)
	EcW_EMP	-0.183*** (0.066)	-0.102 (0.160)	-0.184*** (0.080)	-0.207*** (0.033)
	EcW_PD	-0.044 (0.052)	-0.411*** (0.071)	-0.217*** (0.062)	0.018 (0.016)
	(Constant)	30.693*** (13.027)	42.785*** (19.073)	88.584*** (13.923)	21.341*** (6.039)
	R^2	0.703	0.440	0.686	0.522

Notes: [a] denotes the standard error specific to each coefficient from the PCSE regression models. ***, **, * denote the statistical significance at 1%, 5% and 10% level. Source: SSI database, computed in STATA v.13

Fig. 2. Snapshot of panel analysis results

Although different components of human and economic dimensions of sustainability seemed to still exercise a negative influence on the most vulnerable sectors of environmental wellbeing, the Greenhouse Gases seemed to be the most affected, with determinants like sufficiency in food and drinkable water, safe sanitation, education, good governance, employment, and public debt (Fig. 2).

CONCLUSIONS

This study draws attention to the fact that the patterns of development applied in the group of the Post-communist economies seem to strengthen the sustainable goals, but not sufficient for exceeding the traditional growth-oriented model. Accordingly, focusing on the environment and its main weaknesses as being observed in this study, it was shown that Climate & Energy sub-dimension and its components still registered low levels compared to the Natural Resources ones among the Post-communist economies, as well as that the economic and social components still negatively influenced environmental wellbeing in the analysed context.

Keywords: environmental performance; natural resources; climate & energy; human and economic wellbeing; Post-communist economies; panel data models

ACKNOWLEDGEMENTS:

WWW.CYSENI.COM

REFERENCES

1. VAN DE KERG, G.; MANUEL, A.R. A comprehensive index for a sustainable society: The SSI — the Sustainable Society Index. *Journal of Ecological Economics*, 2008, Vol. 66, No. 2-3, P. 228-242.

2. *Sustainable Society Index—Your Compass to Sustainability.* Kowalski, S.; Veit, W. [reffered on the 5 March 2021 y.]. Link to the internet: <https://ssi.wi.th-koeln.de/index.html>.

3. ULMAN, S.R.; MIHAI, C.; CAUTISANU, C. Peculiarities of the Relation between Human and Environmental Wellbeing in Different Stages of National Development. *Sustainability,* 2020, Vol. 12, 8106.

4. ULMAN, S.R.; MIHAI, C.; CAUTISANU, C. Inconsistencies in the Dynamics of Sustainable Development Dimensions in Central and Eastern European Countries. *Polish Journal of Environmental Studies*, 2021, Vol. 30, P. 2779–2798.

5. ULMAN, S.R., MIHAI, C., CAUTISANU, C., BRUMĂ, I.S., COCA, O., STEFAN, G. Environmental Performance in EU Countries from the Perspective of Its Relation to Human and Economic Wellbeing. *International Journal of Environmental Research and Public Health*, 2021, Vol. 18, No. 23, 12733.

THE EFFECT OF UNDERGROUND STRUCTURES ON THE GROUNDWATER FLOW INTRODUCED AT A RIVERSIDE PILOT AREA IN BUDAPEST

F. Wagner

Budapest University of Technology and Economics,
Department of Hydraulic and Water Resources Engineering
Műegyetem rkp. 3., 1111 Budapest – Hungary
+36309449699
wagner.flora@emk.bme.hu

ABSTRACT

In riverside municipal areas, the main cause of change in groundwater flow is the growing number of buildings, with underground structures reaching the aquifer. A good example for this is the Lágymányos pilot area in Budapest, Hungary, where the groundwater levels are also highly influenced by the river Danube. Over the area a series of piezometer wells are set to observe groundwater levels measured monthly manually. The aim of this research is to examine the effects of new buildings on the well levels with determining linear regression equations for the last 18 years. The research shows that using homogeneous data series is essential, when predictions are made from data series. Linear regression and its correlation factor proved to be a good indicator to show the change in the relations, as their difference means how strong or weak the connection between the independent variables is. A huge difference between the groundwater level calculated with the river and the groundwater level calculated with a chosen further well means that the examined intervention weakened the relation of the chosen well and the river. Using inhomogeneous data series are not suitable for predicting the groundwater levels. The research also shows examples when the construction has less impact on a relation if there are already other obstructive buildings

Keywords: groundwater levels, linear regression, municipal area, underground structures

INTRODUCTION

Groundwater plays a significant role in our whole life – in industry, in agriculture and within domestic settings. When interfering with aquifers, the quantity and quality of groundwater can change. Our job is to assist the decision-making processes, as well as to estimate the effects of these decisions as accurately as possible. Modelling the groundwater flow is a great way to identify effects of pollution transport too [1]. In riverside municipal areas, the main cause of change in groundwater flow is the growing number of buildings, with underground structures reaching the aquifer.

Modelling the groundwater regime is a specialised task when surface water is nearby. Researchers work on providing a comprehensive and logical approach for identifying, understanding, and evaluating the key factors and the processes controlling groundwater-surface water interactions and understanding their relationship with environmental problems [2]. The unknown effects of this relationship can also be dangerous to humans – such as groundwater-related threats that occur during floods, as these may include concentrated leakage of groundwater behind levees, heave, or even potential uplift of the topsoil layer at the protected areas [3].

With growing demands on water resources and increasing uncertainties in water supply associated with climate changes, the awareness, that groundwater and surface water need to be managed together as a single resource greatly increased. Characterizing, quantifying and modelling groundwater–surface water interactions, as well as outlining new methods and models to improve our understanding of processes and dynamics at the groundwater–surface water interface are new scientific challenges [4] [5].

A good example for an urban area where groundwater is heavily impacted by a river is the Lágymányos pilot area in Budapest, Hungary. A series of piezometer wells are set to observe groundwater levels in the area. At present, two of them are equipped with continuous recorder, while others are measured occasionally manually. Their daily data series are reconstructed with using multiple correlation [6].

The aim of this research is to examine the effects of new buildings on the well levels using linear regression equations set for the last 18 years.

Pilot Area

The pilot area is partly formed on the filled-up riverbed [7] [8]. The filling of this area is a mixed material, with the main component being slag from a nearby power station [9].

Fig. 1. Wells in the pilot area

This slag contains some heavy metal in such quantities that could exceed health limit. To control the washout of these dangerous materials, the environmental authority ordered the setting up and operation of several monitoring wells for a certain period. Thus, seven wells were set up in the area as shown on Fig. 1. Since then, the well TVF was abandoned, but the other six are still in operation. Though they are originally for water quality control, the levels were also recorded from 2004 [10]. The water quality observations stopped after the period required by authority, but the groundwater level measurements continued and have been ongoing for more than 20 years [11].

METHODOLOGY

The two piezometer wells equipped with continuous recorders are situated within different surroundings. One of the wells (ELTE-1) is located between a set of buildings from an earlier time. The other well (GWM-31) is a bit further away, with recently constructed buildings nearby. The other wells are measured occasionally with the use of a manual water level meter. The daily data series of these wells are reconstructed with using multiple correlation [12] involving the levels of the river, and the levels measured by one of the continuously recorded piezometers [13].

Specific time periods of the years examined were selected based on significant interventions, such as new constructions and floods [14]. These data sets are considered homogeneous. The specific time periods were divided into shorter, equal subperiods, as the duration of the originally selected specific time periods were not equal. The creation of these equal subperiods made uniformed calculations possible. The results for all the subperiods were averaged within a time period, and then were compared.

During the calculations for each time period, the linear regression equations and the correlation factors were computed between the wells and the Danube, then between the wells and the GWM-31, and lastly between the wells and the ELTE-1. The root-mean-square errors (RMSE) [15] were also computed for each time period, between the groundwater levels calculated from the linear regressions with the wells and the Danube, GWM-31 and ELTE-1.

To further analyse the relationships within each period, we carried out a series of estimations – the groundwater levels were estimated for the year 2021, using all the linear regression equations. It is a common problem when working with groundwater data, that data is only available from an earlier and older time period, and that we need to take current circumstances

into consideration. Our series of estimations demonstrated this, showing the differences, similarities and gradual changes occurring in the results of these equations, using data with different characteristics from these time periods.

Time Periods

Regular groundwater measurements began in February 2004 and have continued to date. Numerous large-scale interventions took place during these past 18 years. Time periods were determined by new constructions and 3rd flood warning level (the highest floods in Hungary) [14]. Foundation levels were provided by the XI. district local authority. Data sets were considered homogeneous within each period. Seven time periods were created, which are as follows:

- 1 period: Initial condition, up until the flood in 2006. (Fig.2.).The IBM building, the north and south blocks of Eötvös Loránd University, the I block of BME, and the I, B, G, C, D buildings of Infopark have already been built.
- 2 period: Following the flood in 2006 and before further construction began. No major constructions or investments took place during this period.
- 3 period: Start of further constructions, up until the flood in 2010. (Fig.3.)

Major development began in 2007 with the starting of the construction of Infopark E building. The building includes a three-storey underground garage, with foundation level of 86,50 MASL. This was followed by the constructions of BME Q and MTA TTK Q2 buildings. Both buildings have two underground levels, and their foundation level is set at 90 MASL.

Fig.2. Pilot area in October 2005, with the initially built buildings

Fig.3. Pilot area in September 2009 (Orange buildings were built in the 3. period)

- 4 period: After the flood in 2010 until the flood in 2013. No major constructions or investments took place during this period.
- 5 period: After the flood in 2013 until the start of new riverside construction. No major constructions or investments took place during this period.
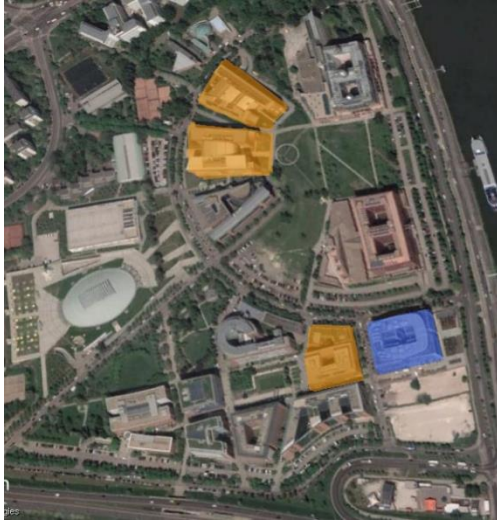
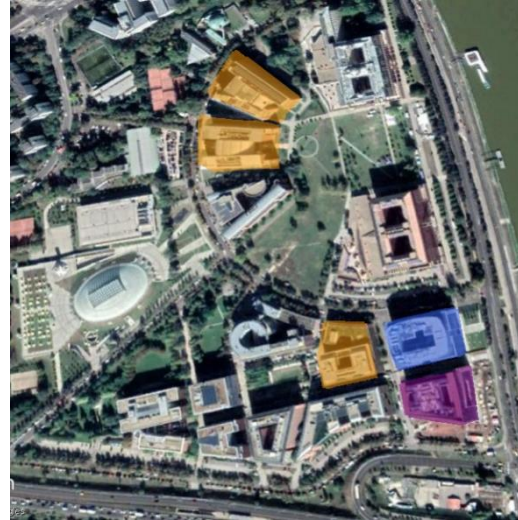| Fig.4. Pilot area in April 2018 (Blue building is Ericson headquarters built in the 6. period) | Fig.5. Pilot area in October 2020 (Purple building is Evosoft headquarters built in the 7. period) |

- 6 period: Construction of the Ericson headquarters (Fig.4.)

Construction begun on the Ericson headquarters. This has a four-storey underground garage, and at its deepest point it is 21 meters below the ground. Its foundation level is estimated at 83,70 MASL.

- 7 period: Construction of the Evosoft headquarters until 2021. (Fig. 5.)

The newest building is located south to the Ericson headquarters. It also has a four-storey underground garage. Its foundation level is set at 83,70 MASL.

The amount of data for these above seven time periods were different due to the different duration lengths of the time periods. The approximate monthly data series were divided into shorter, equal subperiods, each containing 8-10 data, and the calculations were performed uniformly. The results of the subperiods were averaged within a time period, and then compared.

Shading Effect

As the number of buildings had grown in time, the amount of groundwater flow directions without any obstacles decreased. This process is shown on Fig. 6-9.[16]

Fig.6. Shading effect at well
GWM-21

Fig.7. Shading effect at well
ELTE-1

Legend:

- ● Monitoring well
- ▮ Shading effect of buildings from the 1. period
- ▮ Shading effect of buildings from the 3. period
- ▮ Shading effect of Ericson from the 6. period
- ▮ Shading effect of Evosoft from the 7. period

Fig.8. Shading effect at well
GWM-11

Fig.9. Shading effect at well
GWM-21

According to these figures, the impact of a new building on an existing relationship can be limited, if other obstacles already influence the relationship.

RESULTS

Correlation Factors

The correlation factors with the GWM-31 are high for the three wells farthest from the river (shown in Fig 10.), but these decrease for the two riverside wells. These factors were between 0.70-0.80 during the first five periods, but after the effect of the two additional riverside constructions, they reached a lower value. Fitting a linear trend line to the correlation factors makes the declining relation between the two riverside wells, and the GWM-31 as well as the rest of the inside area, more visible. The rest of the wells in the inward area react very similarly to the events.
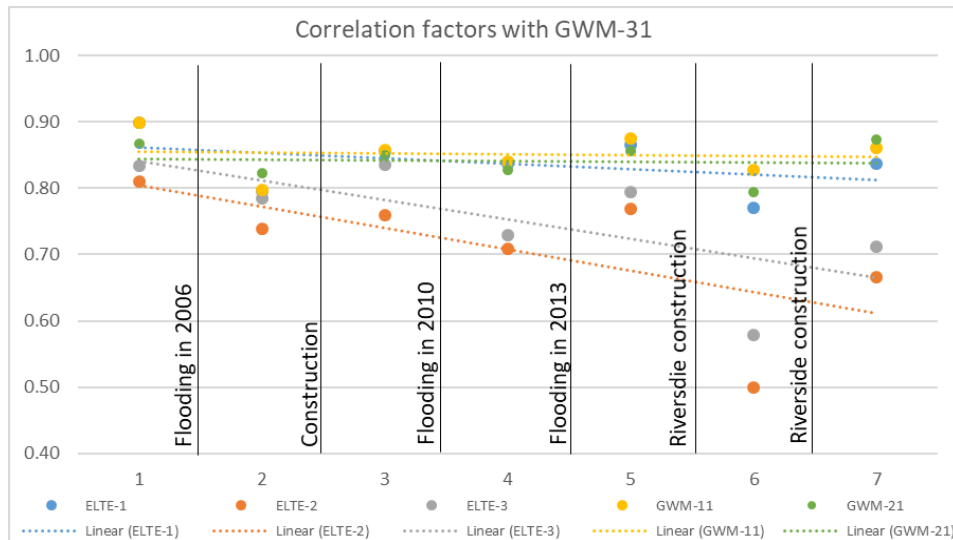
Fig. 10. Correlation factors with GWM-31

Fig. 11. shows that the relation between the Danube and the riverside wells are strong and constant, but the correlation factors for the other wells decrease rapidly, showing the strong effect of the new buildings.

Fig. 11. Correlation factors with the Danube

ELTE-1 has similar correlation factors (Fig. 12.) as GWM-31, but the values are higher for the riverside wells, as ELTE-1 still has a stronger relation with the river, in contrast to GWM-31.
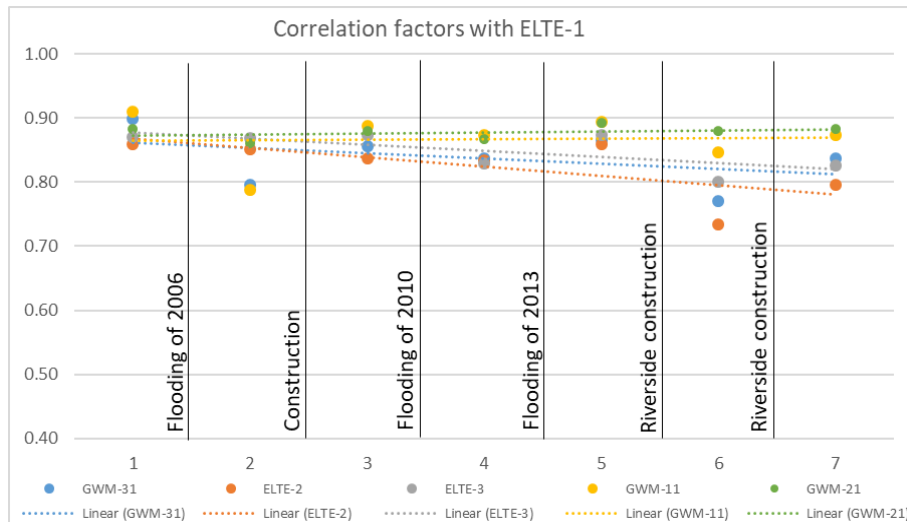
Fig. 12. Correlation factors with ELTE-1

Difference Between The Linear Correlations

The RMSE errors between the groundwater computed with ELTE-1, GWM-31, and with the Danube are shown in Fig. 13.

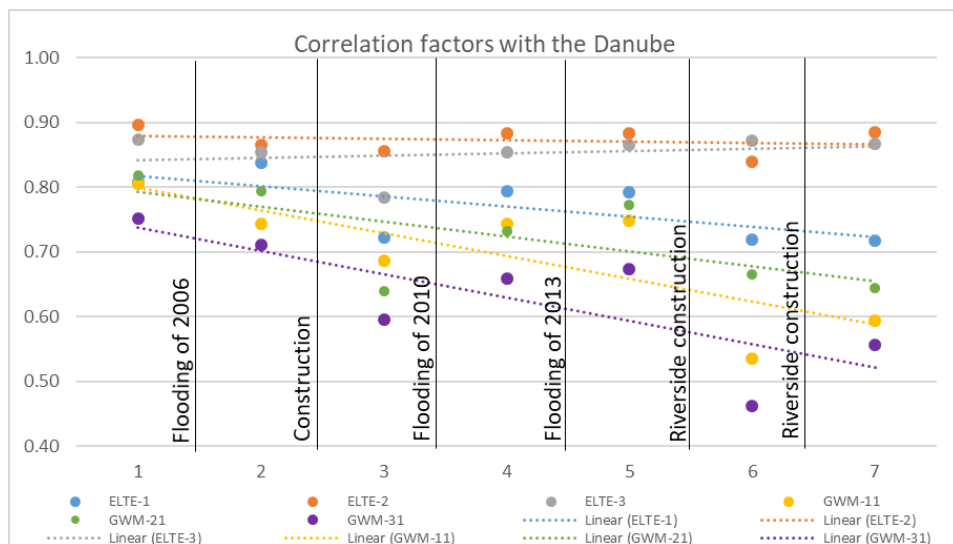The calculated groundwater levels differ when the linear regressions use other independent variables. Their difference shows how strong or weak the connection between the independent variables is. A great difference between the groundwater level calculated with the river and the groundwater level calculated with a chosen further well means, that the examined intervention weakened the relation of the chosen well and the river. [11]

The largest error shows at the riverside wells. The outstanding value in the 7. period is affected by the record lowest water level and by a new riverside building, which greatly weakened the relation of the inward and riverbank areas. It explains that computations are more inaccurate for ELTE-2 and ELTE-3 with ELTE-1 and GWM-31.

Fig. 13. RMSE errors [m] between the groundwater levels computed from different linear regressions for each well

Change In Estimation

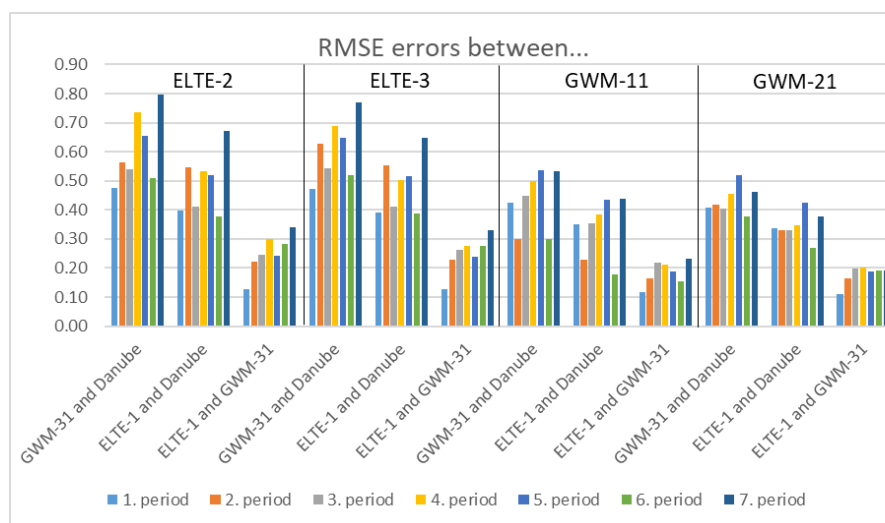The next step to analyse the change in the relationships was testing it on new data. We made several estimation series using each linear regression equation obtained from the data of their own time period and made computations with data from 2021. This way, we made estimations for the present day from previously valid relationships. The difference between measured data and estimations shows quantitatively the impact of underground structures. The riverside wells were not included in this analysis, as the Danube has significantly more effect on them as anything else.

When analysing the change in RMSE-values at the well GWM-11 (Fig.14), it shows that the relationship obtained after the flood of 2006 (2. period), and after the construction of the Ericson headquarters (6. period) is the least valid for the present day. When comparing with the others (Fig.16-17), the equation from the 2. period estimates higher water levels than the other ones, showing that the groundwater would be higher there, if the constructions after 2006 would have stopped, as three new building had been built near GWM-11 since then. This effect is most significant when the water level is low, smaller than 97,50 MASL. The effect of the Evosoft headquarters is more prominent when the water level is higher than 97,50 MASL. It predicts lower water levels, meaning that the construction had great impact on this area, possibly because of groundwater pumping. If the pumping would have continued, the groundwater would be even lower than the present level. During the construction of the Evosoft headquarters, the groundwater had changed its direction of flow because of the previous building, so its effect was more subtle.

At the well GWM-21, the change in RMSE-values is smaller (Fig.15), the only bigger difference is with the equation from the 7. period with ELTE-1. This well was already in between buildings, but the new obstacle in the groundwater flow had an impact on this well, as well as on the well ELTE-1. It should be noted that the change of RMSE values shows relation to the interventions for both wells. When comparing to the other estimations (Fig. 18-19), this difference is negligible. This comparison shows, that this well, which is in between buildings, has only a little change in its behaviour when the further away circumstances change. The reason for this is that its relation to the environment is already enormously affected by the existing buildings.
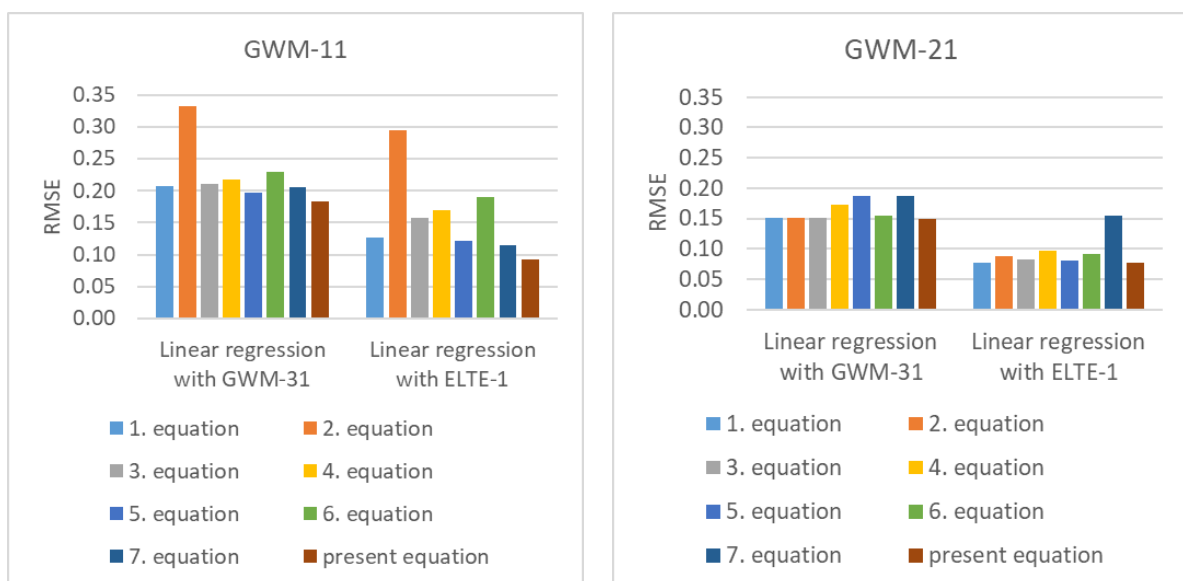
Fig. 14. RMSE values of each equation for 2021 at well GWM-11

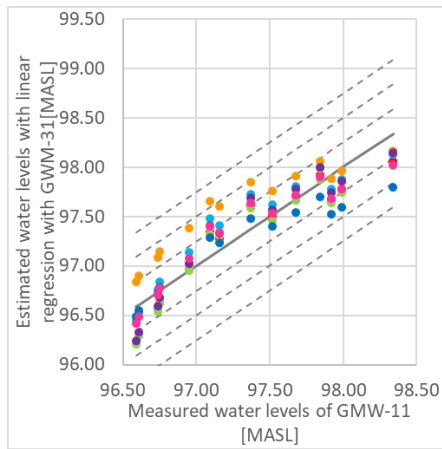Fig. 15. RMSE values of each equation for 2021 at well GWM-21

Legend:
- 1. equation
- 2. equation
- 3. equation
- 4. equation
- 5. equation
- 6. equation
- 7. equation
- present
- measured

Fig.16. Estimated water levels of GWM-11 with GWM-31
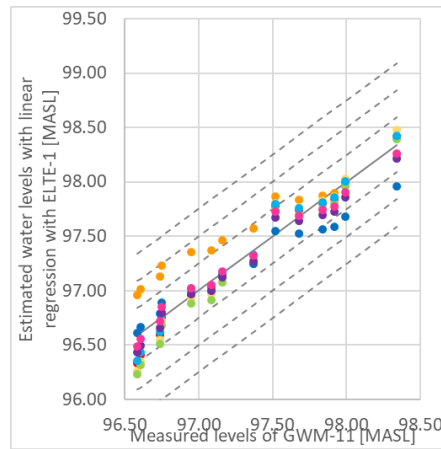
Fig.17. Estimated water levels of GWM-11 with ELTE-1
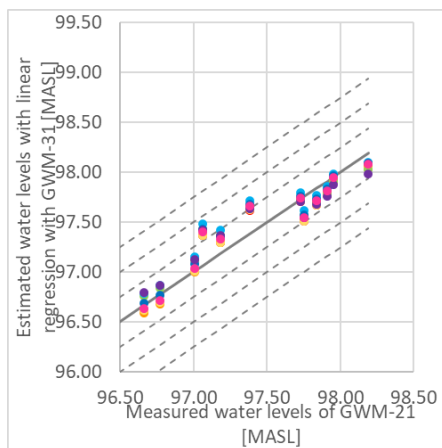
Fig.18. Estimated water levels of GWM-21 with GWM-31
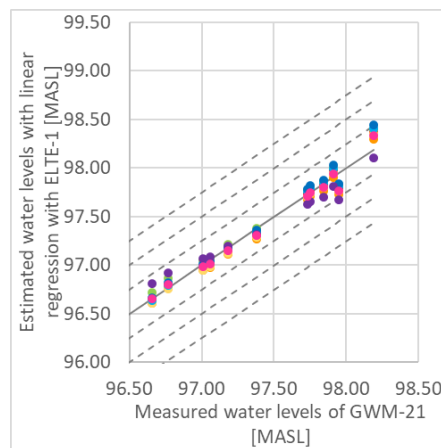
Fig.19. Estimated water levels of GWM-21 with ELTE-1

CONCLUSIONS

As this research shows, when discussing and comparing long data series, it is essential that the calculations are used on homogeneous data series. This is attainable with defining shorter time periods based on interventions (constructions or high flood). Using linear regression is a good method to show the change in the relations affected by these events. The calculated groundwater levels differ when the linear regressions use other independent variables. Their difference shows how strong or weak the connection between the independent variables is. An extensive difference between the groundwater level calculated with the river, and the groundwater level calculated with a chosen further well means, that the examined intervention weakened the relation of the chosen well and the river. Using linear regression equations on the present data showed the importance of using homogeneous data series, because it was not suitable for predicting the measured groundwater levels. The construction has less impact on this relation if there are other obstructive buildings already influencing this relationship.

REFERENCES

1. BEAR, J.; VERRUIJT, A.. Modeling Groundwater Flow and Pollution, D.Reidel Publishing Company, 1992, P. 414.

2. CONANT, B.; ROBINSON, C. E.; HINTON, M. J., RUSSELL, H. A. J. A framework for conceptualizing groundwater-surface water interactions and identifying potential impacts on water quality, water quantity, and ecosystems. *Journal of Hydrology*, 2019, Vol. 574, P. 609–627. <https://doi.org/10.1016/j.jhydrol.2019.04.050.>

3. JULÍNEK, T.; DUCHAN, D.; ŘÍHA, J. Mapping of uplift hazard due to rising groundwater level during floods. *Journal of Flood Risk Management*, 2020, Vol. 13, No. 4, P. 162-174. <https://doi.org/10.1111/jfr3.12601.>

4. FLECKENSTEIN, J. H.; KRAUSE, S.; HANNAH, D. M.; BOANO F. Groundwater-surface water interactions: New methods and models to improve understanding of processes and dynamics. *Journal of Advances in Water Resources*, 2010, Vol. 33, P. 1291– 1295. <https://doi.org/10.1016/j.advwatres.2010.09.011>

5. ŠOLTÉSZ, A.; BAROKOVÁ, D.; ČERVENANSKÁ, M.; JANÍK, A. Hydrodynamic analysis of interaction between river flow and ground water. *International Multidisciplinary Scientific GeoConference Surveying Geology and Mining Ecology Management*, SGEM 1, 2016, P. 823-830.

6. WAGNER, F. The reconstruction possibilities of groundwater data series with gaps introduced at a pilot area in Budapest. CYSENI 2021. Proceedings of annual conference of young scientists on energy issues. [CD]. Kaunas: Lithuanian Energy Institute.

7. IHRIG, D. A magyar vízszabályozás története (The history of the water regulation in Hungary)., VIZDOK, Budapest, 1973.

8. TŐRY, K. A Duna és szabályozása (The Danube and its regulation). Akadémiai Kiadó, Budapest, 1952.

9. CSOMA, R.; GÁLOS, M. River–groundwater interaction over the region of Infopark-Budapest, Periodica Polytechnica Vol. 56/2., 2012.

10. SZÍVÓS, B.; CSOMA, R.; GÁLOS, M. A Darcy-féle áteresztőképességi együttható eloszlásának vizsgálata a Lágymányosi-öblözet területén (The distribution of Darcy coefficient of Seepage at the Lágymányos region). Mérnökgeológia – Kőzetmechanika 2013 (Engineering geology – Rock mechanics 2013), Hantken Kiadó, Budapest, 2013.

11. LÜKŐ, G.; MEGYESI, T. B.; WAGNER, F. Talajvízjárás folyóparti területen kisvizes időszakban (Groundwater regime at a riverside area in low water period), Student Research Society, Budapest University of Technology and Economics, 2015.

12. KRZYWINSKI, M.; ALTMAN, N. Multiple linear regression. *Nature Methods*, 2015, Vol. 12 (12), P. 1103–1104.

13. SAHOO, S.; JHA, M.K. Groundwater-level prediction using multiple linear regression and artificial neural network techniques: a comparative assessment. *Hydrogeology Journal*, 2013, Vol. 21, P.1865–1887.

14. KUKUCSKA, P.; GÁLOS, M.; CSOMA, R. Tározódás talajban dunai árhullámok esetén (Storage in soil in case of the Danube's floods). Mérnökgeológia-Kőzetmechanika 2015 (Engineering geology – Rock mechanics 2015), Hantken Kiadó, Budapest, 2015.

15. DAWSON, C.W.; ABRAHART, R. J.; SEE, L.M. HydroTest: a web-based toolbox of evaluation metrics for the standardised assessment of hydrological forecasts, *Environmental Modelling & Software*, 2007, Vol. 22 , P.1034-1052.

16. WAGNER, F.; CSOMA, R. Beépítés hatása a talajvíz áramlási viszonyaira a Lágymányosi-mintaterületen (The effect of buildings on groundwater flow at the Lágymányos region). *Hungarian Hydrological Society 2021 XXXVIII*. National assembly.

BIOMONITORING OF AIR POLLUTION IN THE CONTEXT OF CLIMATE CHANGE

V. Černiauskas

Lithuanian Research Centre for Agriculture and Forestry, Institute of Forestry
Liepų st. 1, LT-53101 Girionys – Lithuania
+37060876929
valentinas.cerniauskas@lammc.lt

EXTENDED ABSTRACT

OVERVIEW

Air pollution is one of the most serious problems in Europe [1]. According to the United Nations, more than 55% of the world's population lives in urban areas, and by 2050 expected to increase to 68% [2]. Urban air pollution is a major environmental problem as it affects the health of ecosystems, crops, climate change, human health, and well-being [3; 4]. Urban air pollution can be divided into two component groups: gaseous components and particulate matter. Gaseous compounds include nitrogen dioxide (NO_2), carbon monoxide (CO), ground-level (tropospheric) ozone (O_3), and volatile organic compounds (VOCs). Particulate matter is divided into those with an aerodynamic diameter less than 10 μm (PM_{10}) and 2.5 μm ($PM_{2.5}$) [3; 5]. These air pollutants may cause the incidence of respiratory, cardiovascular disease, also increase the risk of premature mortality [6; 7].

Biomonitoring refers to the observation and assessment of the condition and ongoing changes in ecosystems, biodiversity, and the landscape, including natural habitats, populations, and species [8]. Tropospheric O_3 is a strong oxidant that, at elevated concentrations, can negatively affect physiological functions, phenology, carbon allocation and growth of plants. Tropospheric O_3 formation occurs when carbon monoxide (CO), volatile organic compounds (VOCs) and nitrogen oxides (NOx) react in presence of sunlight in the atmosphere [9]. Tropospheric O_3, one of the main air pollutants, which causes visible damages to the leaves of vascular plants, and this is related even to relatively low concentrations of O_3 [10].

The growth and development of urban trees and green spaces have an impact on the stability of ecosystems [11]. Urban forests, trees and green infrastructure remove particulate matter (PM) and pollutants from the air and subsidize to improving human well-being and health [12]. For this reason, it is important not only to identify air pollution but also to contribute to the potential reduction of air pollution. Scientists aim to improve air pollution absorption by selecting the most suitable tree species and trying to adapt alternatives as green roofs and green walls in areas with a small amount of green spaces [13; 14]. The mentioned solutions are an additional opportunity to increase urban air pollution abatement rates due to the lower efficiencies compared to new trees planted, but still, it remains a less efficient alternative [14].

To reduce air pollution in urban areas, city planners need a suitable selection of plant species. The aim of this study is to overview the possibilities of biomonitoring of air pollution in urban areas in the context of climate change. More specifically, the selection of woody plants-

bioindicators, as the most suitable for the determination of the air pollutants ($PM_{2.5}$, PM_{10}, NO_2, O_3, and SO_2) in urban areas will be analyzed. Tree species that can effectively decrease air pollutants in urban areas to reduce air pollution will be overviewed.

In order to classify urban trees according to their effectiveness in improving urban air quality, a species-specific air quality index (S-AQI) was calculated [15]. This index evaluates the deposition of pollutants on the foliage of woody plants (PM, NO_2, O_3), plant pollutant emissions (as an allergen) and the concentration of volatile organic compounds (VOCs) in the plant (diseases, pests, drought, ground-level ozone-induced foliage damage). The species-specific assessment of the air quality index on a 10-point scale. If score from 1 to 4 points is not recommended to plant this species plants, 8-10 points indicate that the species is recommended for urban landscaping programs.

It is important to identify and map the dominant tree species in urban areas to quantify the associated environmental benefits to assist city planners in ensuring that green spaces are used properly. The most common woody plant species in Kaunas, Lithuania was identified and evaluated their S-AQI (indices rounded): Norway maple (*Acer platanoides* L.) – 9 points; common hawthorn (*Crataegus monogyna* Jacq.) – 9 points; European larch (*Larix decidua* Mill.) – 8-9 points; European ash (*Fraxinus excelsior* L.) – 7 points; lime tree (*Tilia sp.* L.) – 7 points; pine (*Pinus sp. L.*) – 6 points; european white birch (*Betula pendula* Roth.) – 5 points; horse chestnut (*Aesculus hippocastanum* L.) – 5 points; oak (*Quercus sp.* L.) – 4 points; poplar tree (*Populus sp.* L.) – 4 points; black locust (*Robinia pseudoacacia* L.) – 4 points; willow (*Salix sp.* L.) – 3 points and spruce (*Picea sp.* Dietr.) – S-AQI has not been assessed, but according to previous studies, this species is not highly valued in urban greenery. One reason is that deciduous trees are able to remove more pollutants from the air due to the ability of larger leaf suction tips.

Summarizing the distribution of S-AQI index points among the currently most popular tree species in Kaunas, Lithuania we see that the best for the city's greenery are three tree species – *Acer platanoides*, *Crataegus monogyna* and *Larix decidua*. This study can help urban landscaping planners select the most effective tree species that reduce air pollution.

Keywords: ozone pollution, tree species, bioindicators, urban areas

REFERENCES

1. GUZMÁN, P.; TARÍN-CARRASCO, P.; MORALES-SUÁREZ-VARELA, M.; JIMÉNEZ-GUERRERO, P. Effects of air pollution on dementia over Europe for present and future climate change scenarios. *Environmental Research*, 2022, Vol. 204. No.112012.

2. *2018 revision of world urbanization prospects*. New York: UN DESA, 2018 [referred on the 17th of January in 2022 y.]. Link to the internet <https://www.un.org/development/desa/en/news/population/2018-revision-of-world-urbanization-prospects.html>.

3. NOWAK, D. J.; HIRABAYASHI, S.; DOYLE, M.; MCGOVERN, M.; PASHER, J. Air pollution removal by urban forests in Canada and its effect on air quality and human health. *Urban Forestry and Urban Greening*, 2018, Vol. 29, P. 40–48.

4. ESCOBEDO, F. J.; NOWAK, D. J. Spatial heterogeneity and air pollution removal by an urban forest. *Landscape and Urban Planning*, 2009, Vol. 90, No. 3–4, P. 102–110.

5. GLENCROSS, D. A.; HO, T. R.; CAMIÑA, N.; HAWRYLOWICZ, C. M.; PFEFFER, P. E. Air pollution and its effects on the immune system. *Free Radical Biology and Medicine*, 2020, Vol. 151, P. 56–68.

6. KAMPA, M.; CASTANAS, E. Human health effects of air pollution. *Environmental Pollution*, 2008, Vol. 151, No. 2, P. 362–367.

7. LEE, B. J.; KIM, B.; LEE, K. Air pollution exposure and cardiovascular disease. *Toxicological Research*, 2014, Vol. 30, No. 2, P. 71–75.

8. BONDARUK, J.; JANSON, E.; WYSOCKA, M.; CHAŁUPNIK, S. Identification of hazards for water environment in the Upper Silesian Coal Basin caused by the discharge of salt mine water containing particularly harmful substances and radionuclides. *Journal of Sustainable Mining*, 2015, Vol. 14, No. 4, P. 179–187.

9. SICARD, P.; PAOLETTI, E.; AGATHOKLEOUS, E.; ARAMINIENĖ, V.; PROIETTI, C.; COULIBALY, F.; DE MARCO, A. Ozone weekend effect in cities: Deep insights for urban air pollution control. *Environmental Research*, 2020, Vol. 191, No. 110193.

10. AGATHOKLEOUS, E.; SAITANIS, C. J.; FENG, Z.; DE MARCO, A.; ARAMINIENE, V.; DOMINGOS, M.; SICARD, P.; PAOLETTI, E. Ozone biomonitoring: A versatile tool for science, education and regulation. *Current Opinion in Environmental Science and Health*, 2020, Vol. 18, P. 7–13.

11. TAKAHASHI, M.; FENG, Z.; MIKHAILOVA, T. A.; KALUGINA, O. V.; SHERGINA, O. V.; AFANASIEVA, L. V.; HENG, R. K. J.; MAJID, N. M. A.; SASE, H. Air pollution monitoring and tree and forest decline in East Asia: A review. *Science of the Total Environment*, 2020, Vol. 742, No. 140288.

12. WEBER, C.; LOTFI, M. Ecosystem Services Provided by Urban Vegetation: A Literature Review. *Fresenius Environmental Bulletin*, 2013, Vol. 22, No. 12 C.

13. YANG, J.; YU, Q.; GONG, P. Quantifying air pollution removal by green roofs in Chicago. *Atmospheric Environment*, 2008, Vol. 42, No. 31, P. 7266–7273.

14. JAYASOORIYA, V. M.; NG, A. W. M.; MUTHUKUMARAN, S.; PERERA, B. J. C. Green infrastructure practices for improvement of urban air quality. *Urban Forestry and Urban Greening*, 2017, Vol. 21, P. 34–47.

15. SICARD, P.; AGATHOKLEOUS, E.; ARAMINIENĖ, V.; CARRARI, E.; HOSHIKA, Y.; DE MARCO, A.; PROIETTI, C. Should we see urban trees as effective solutions to reduce increasing ozone levels in cities? *Environmental Pollution*, 2018, Vol. 243, P. 163–176.

REDUCING CLIMATE CHANGE THROUGH THE USE OF WOOD AND ITS PRODUCTS AND PROMOTING THE BIOECONOMY IN LITHUANIA

S. Kadziauskas

Lithuanian Research Centre for Agriculture and Forestry
Instituto al. 1, Akademija, LT-58344 Kėdainiai distr. – Lithuania
+370 62904292
skirmantas.kadziauskas@lammc.lt

EXTENDED ABSTRACT

OVERVIEW

Climate change is having a negative impact on ecosystems and threatening humanity. To mitigate this effect, many countries in the world have the United Nations Framework Convention on Climate Change In the process of implementing the Convention, they are committed to reducing greenhouse gases emissions and/or increase absorption. In implementing the Paris Agreement on Climate Change, each party to the agreement chooses national climate change mitigation measure in individual sectors. The forestry sector, including timber products, makes a significant contribution to climate change mitigation. Forests absorb carbon dioxide from the atmosphere and store it carbon in biomass, soil, and some deforestation can be conserved after deforestation in wood products. Increasing carbon stocks in wood products is United Nations recognized tool for climate change mitigation. The Intergovernmental Panel on Climate Change is developing guidelines that set out the differences carbon accounting methods for wood products. Depending on the available data on wood products, Member States may choose the method. Wood flow analysis is consistent the highest carbon accounting method, where annual carbon receipts are accounted for, using country-specific data. The main purpose of this work is to analyze the industrial wood flows in Lithuania and to determine carbon stocks and their quantitative changes in wood products. The results of this work can be used not only for carbon accounting of wood products. Wood flow analysis can be useful in analyzing wood processing sector in Lithuania and in making decisions on the use of wood. It is recommended that such analyzes in Lithuania would be performed periodically. From the collected primary data, we can see that a significant part of wood in Lithuania is used as sawn timber, which allows coal to be locked for up to 35 years. However, at this point, we can significantly increase the consumption of sawn logs in the construction sector by replacing iron and concrete structures, thus locking up even more carbon in wood.

METHODS

1. Tasks under which the methodology is developed.

1.1. To identify the main buyers of raw wood and to find out the quantities of wood purchased, exported and imported in Lithuania, as well as the assortment structure in 2017 period.

To implement this task, data was collected on the buyers of raw timber sold and the quantities purchased by them from the State Forest Enterprise and the BALTPOOL timber exchange in 2017-2020. After receiving the data on the buyers, they were be surveyed - how many and what assortment structure of raw wood or wood products semi-finished products were used in the production process. In total, more than 100 companies was surveyed. An analysis of the data obtained will be performed later.

1.2. To To perform the analysis of wood flow, determining the use of raw wood for the production of primary HWP and to analyze the changes in individual primary HWP, their sales in Lithuania and exports

To implement this task, a survey was prepared and sent to Lithuanian wood product producers / processors and exporters to find out the use of wood in primary production processes and their sale in the local market, as well as exports. Manufacturers of wood products will also be asked to indicate the shelf life of their products, taking into account the technical characteristics of the products.

RESULTS

Analysis Of Exported Wood

Preliminary analysis of exported timber revealed that in 2017. 1899 thousand tons were exported from Lithuania m^3 of raw wood. Most of the pulpwood were exported – 912 thousandS m^3, 684 thousand tons of sawn logs were exported. m^3, plywood – 167 thousand. m^3 and firewood – 136 thousand. m^3. Most of the raw wood was exported to Latvia, Poland and Sweden (Table 7).

Table 1. Quantities of exported timber by ranges and importing countries.

Assortment / Importing country	Latvia	Poland	Sweden	Germany	Finland	China	Other*
Saw logs	439	87	59	67	-	18	14
Pulpwood	260	232	293	-	115	-	12
Panel wood	117	50	-	-	-	-	-
Firewood	82	54	-	-	-	-	-
Total	898	423	352	67	115	18	26

* Insignificant quantities of timber exported to other countries are classified as "Other".

CONCLUSIONS

The results of this work can be used not only for carbon accounting in wood products. Wood flow analysis can be useful in analyzing the wood processing sector in Lithuania and in making decisions on wood use.

It is recommended that such analyzes be performed periodically in Lithuania, as this would enable the analysis of wood use trends and carbon accounting in wood products, applying the top-tier method.

Evaluating the essential and other results of the research, it can be concluded that:

The analysis of wood flow in Lithuania revealed the flows of industrial wood use for the production of primary wood products. This analysis is in line with the tier three carbon accounting approach set out in the IPCC guidelines, where annual carbon revenues are accounted for using country-specific data.

Keywords: harvesting wood product, climate change, forest, carbon absorbing, carbon cycle, bioeconomy

REFERENCES

1. KAIRIŪKŠTIS L.; DARAŠKEVIČIUS V.; P. JAKAS et al. Miškininkystė. – V.:Mokslas, 1979. -312 p.

2. CHEN, J.; COLOMBO, S. J.; TER-MIKAELIAN, M. T.; & HEATH, L. S. 2010. Carbon budget of ontario's managed forests and harvested wood products, 2001–2100. *Forest Ecology and Management,* 259(8), P. 1385-1398. DOI:<https://doi.org/10.1016/j.foreco.2010.01.007.>

3. UNITED NATIONS 2015. United Nations Framework Convention on Climate Change. 2015. Conference of the Parties, Twenty-first session, Paris, 2015.

4. PILLI, R.; GRASSI, G.; KURZ ,W.A.; FIORESE G.; AND CESCATTI, A. 2017. The European forest sector: past and future carbon budget and fluxes under different management scenarios. *Biogeosciences*, 2017, Vol. 14, P. 2387–2405. DOI:10.5194/bg-14-2387-2017.

CHANGES IN THE FUNGAL COMMUNITY OF SCOTS PINE (PINUS SYLVESTRIS) ACROSS A LATITUDINAL GRADIENT, STRETCHING FROM SLOVENIA TO NORTHERN FINLAND

V. Mishcherikova, D. Marčiulynienė, A. Marčiulynas, J. Lynikienė, A. Gedminas,
Institute of Forestry, Lithuanian Research Centre for Agriculture and Forestry
Liepų str. 1, Girionys, LT-53101 Kaunas district – Lithuania
+370 682 67 866
lammc@lammc.lt

A. Menkis
Department of Forest Mycology and Plant Pathology, Uppsala BioCenter, Swedish
University of Agricultural Sciences,
P.O. Box 7026, SE-75007 Uppsala – Sweden
+46 18-673209
audrius.menkis@slu.se

O. Prylutskyi
Department of Mycology and Plant Resistance, V.N. Karazin Kharkiv National University
4 Svobody Sq., 61022 Kharkiv – Ukraine
prylutskyi@karazin.ua

EXTENDED ABSTRACT

OVERVIEW

In Europe, Scots pine (*Pinus sylvestris* L.) is one of the most important tree species, with forests covering more than 28 million hectares, representing more than 20 percent of the productive forest area [1]. According to a report by the Intergovernmental Panel on Climate Change (IPCC), extreme droughts caused by climate change are expected to have a severe impact on *P. sylvestris* stands, reducing their viability and increasing their susceptibility to pests [2–6].

It is well known that beneficial plant-associated microorganisms may stimulate plant growth and enhance resistance to disease and abiotic stresses [7]. This now makes it possible to test whether some general patterns occur and whether different groups of plant-associated microorganisms respond differently or in the same way to climate change [8].

Fungi are important parts of the plant microbiome [12], the formation of which is highly dependent on climatic factors [9–12]. Climate change–associated disturbances can significantly alter microbial communities and functional profiles [13]. To investigate the possible effects of climate change on changes in fungal communities, a gradient of latitude diversity is suggested as it reflects the corresponding climate change as well as changes in temperature and precipitation along the gradient [14].

The overall objective of the study was to determine: i) which of the factors studied have the greatest influence on fungal communities associated with Scots pine tissue and rhizosphere soil ii) how the diversity of fungal communities associated with Scots pine varies with the climate gradient; iii) what impact climate change may have on the diversity of the Scots pine fungi community in the future. We hypothesized that the fungal community associated with *P. sylvestris* will qualitatively and quantitatively respond to changes in latitude, and therefore be differently affected by climate change.

METHODS

Sampling of needles, shoots, roots, and soil was carried out during April – August 2019, in 12 forests research plots growing in the different environmental conditions in Slovakia, Poland, Lithuania, Latvia, Estonia and Finland (Table 1). In each research plot the health status, the damage category, the nature of the damage, visual assessment of tree crown defoliation, dechromation and dry branch content in the crown of 30 trees per plot were determined. The chemical composition of the soil was also determined, and meteorological data were collected from the nearest meteorological stations (Table 2).

DNA was isolated individually from each type of sample, a DNA fragment of the ITS2 rRNA gene region of each sample was amplified and subjected to high-throughput sequencing [15]. All climatic data were obtained from WorldClim database (version 2.0, http://worldclim.org/version2). For data analysis Bioclimatic variable set, with resolution 10 minutes was used. To predict the movement of communities, the future climate data used downscaled on COUPLED MODEL INTERCOMPARISON PROJECT PHASE 6 (CMIP6) climate projections. using Beijing Climate Center climate system model version 2 (BCC-CSM2-MR) global climate models (GCM) with the Shared Socio-economic Pathways 1-2.6 for the 2021-2040, 2041-2060, 2061- 2080 and 2081-2100 time period with the same bioclimatic variables. All statistical analyses were performed in R version 4.1.2 [16].

Table 1. Qualitative and quantitative indicators of fungal diversity in the studied areas

Plot code	Country	latitude	longitude	No.of fungal Sequences	No. of Fungal Taxa	Shannon Diversity Index
1	Slovakia	49.12828	21.52911	7810	275	4.19
2	Poland	51.14677	22.51708	10309	275	3.65
3	Poland	52.76811	23.07772	8207	307	3.65
4	Lithuania	54.42106	24.95953	5788	192	4.15
5	Lithuania	56.05342	23.67956	13017	264	4.39
6	Latvia	57.57453	24.43836	5462	245	4.38
7	Estonia	59.12831	24.38680	7202	293	3.84

8	Finland	60.86994	25.53239	7516	178	2.27
9	Finland	62.88581	25.82095	5623	297	4.30
10	Finland	64.71347	25.58140	7037	297	4.34
11	Finland	66.37568	26.21304	8389	229	3.78
12	Finland	67.80227	26.78214	10426	242	4.03

FUNGuild v1.0 was used to identify the functional groups (guilds) of fungal communities. All OTUs that do not match the FUNGuild taxon database have been classified as "unassigned" [17].

Table 2. Health stands parameters and chemical soil conditions in Scots Pine research plots

Plot code	MTA[1]	Df [2]	Dch [3]	DB [4]	CDT [5]	pH1 mol/1 KCl	P_2O_5 mg/kg	K_2O mg/kg	Ca mg/kg	Mg mg/kg	Cl mg/kg	NaCl ms/cm
1	80	20.50	7.00	16.17	1.57	3.9	10	221	1118	244	5.3	4.65
2	70	21.17	6.67	17.67	1.70	3.6	13	72	553	98	3.6	2.73
3	50	28.67	8.17	16.83	2.30	4.1	95	26	93	39	3.6	2.2
4	65	16.17	6.17	16.00	1.63	3.9	10	51	208	41	3.6	3.02
5	70	43.67	30.33	36.17	2.83	4.3	38	48	323	66	3.6	3.88
6	90	20.00	5.00	19.00	1.57	3.6	47	41	402	96	5.3	2.3
7	70	17.67	2.17	15.17	1.70	4.9	13	70	971	134	3.6	3.38
8	60	40.83	9.00	28.17	2.30	3.8	19	54	154	41	5.3	2.87
9	70	43.50	9.67	25.50	2.47	4.1	134	28	219	53	3.6	2.76
10	60	15.83	16.00	15.00	1.77	3.5	13	32	168	39	5.3	1.99
11	80	18.00	2.00	13.67	1.63	3.9	25	28	171	43	3.6	2.17
12	60	29.67	8.67	27.67	2.00	3.5	36	79	258	64	3.6	2.84

[1] – Mean tree age;[2] – Defoliation; [3] – Dechromation;[4] – Dry Branches;[5] – Category of tree damage

RESULTS

The comprehensiveness of sampling was represented by the Good's coverage estimator (>99%), and more of the rarefaction curves that tend to reach the saturation indicating most of the fungal diversity in the tissues and soil samples. A total of 1749 fungal OUT's (operational taxonomic unit) clusters at 97% similarity were observed in all research plots for *Pinus sylvestris* (Table 2).

Biodiversity indicators for pine do not change in the latitudinal gradient. on the Redundancy analysis (RDA), show that from all factor main connection to changing of fungi diversity and composition were: phosphorus and calcium concentration in the soil, Mean Diurnal Range (max. temperature per month – min. temperature per month)), Mean Temperature of Wettest

Quarter and Precipitation of Driest Month. Based on this we predicted how fungi population related to *P. sylvestris* potentially will react according to CMIC6 climate projection (Fig. 1). We can see that absolute communities are likely to shift to cooler and wetter regions.
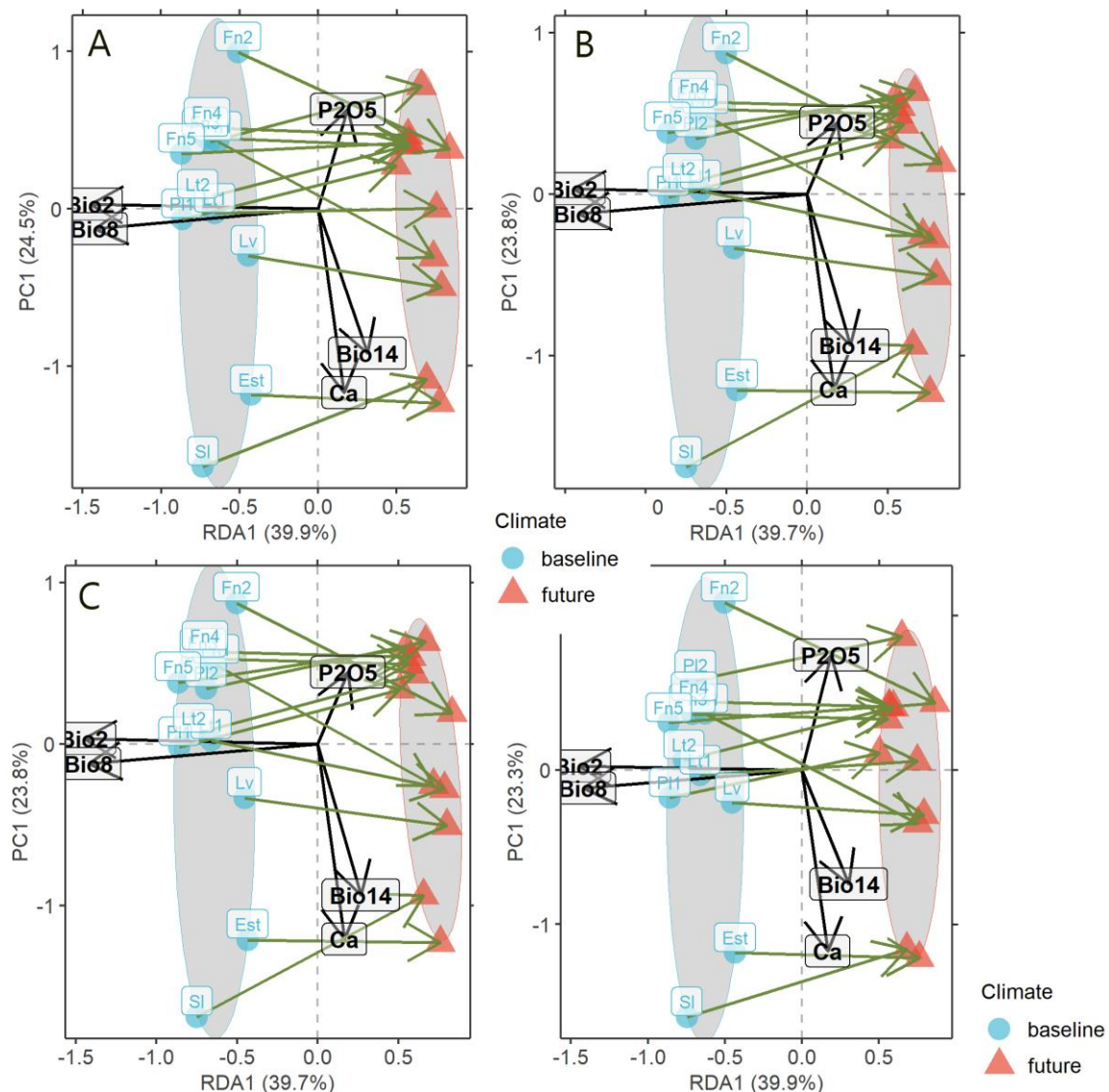

Fig. 1 Based on the main parameters of the regulating communities of Scots pine predicted shift of communities under the CMIP6 climate projections: A – 2019 – 2040 years; B – 2019 – 2060 years; C – 2019 – 2080 years; 2019 – 2100 years. Main parameters: P2O5 - phosphorus concentration in soil; Bio2 – Mean Diurnal Range; Bio8 - Mean Temperature of Wettest Quarter; Bio14- Precipitation of Driest Month (with constant soil parameters)

The guiding factors ($p < 0.05$) of the compositions and structure of the fungus communities of needles are the Mean Diurnal Range and Temperature Annual Range. For shoots, the key factors ($p < 0.05$) were the same Mean Diurnal Range and Temperature Annual Range, as well as Min Temperature of Coldest Month. The composition and structure of the rhizosphere grouping is influenced by the largest number of factors, among which are ($p < 0.05$): Annual Mean Temperature, Mean Diurnal Range, Isothermality, Temperature Seasonality, Temperature Annual Range, Precipitation of Wettest Month, Precipitation Seasonality, Precipitation of Warmest Quarter, concentration of Ca and P2O5 in soil and salinity. For soil

the key drivers of community change were daily average range setting a particular direction for the community, annual rainfall, wettest month rainfall, wettest quarter rainfall, driest quarter rainfall, coldest quarter participation, acidity.

FUNGuild analysis defined 54% from all OTUs in 7 trophic guilds, 46% of OTUs was unidentified. Of them 20% of species belonged to the pathotrophic group, 6% to the pathotrophic-saprotroph group, 4% to Pathotroph-Saprotroph-Symbiotroph group, 4% to the pathotropho-symbiotroph group, 39% occupied the saprotroph niche, 5% were saprotroph-symbiotrophs, and 22 % symbiotrophs. The largest number of pathotrophs was found in the needles, the smallest in the organic soil layer. Saprotrophs dominated in needles, symbiotrophs – in needles and roots (Fig.2).
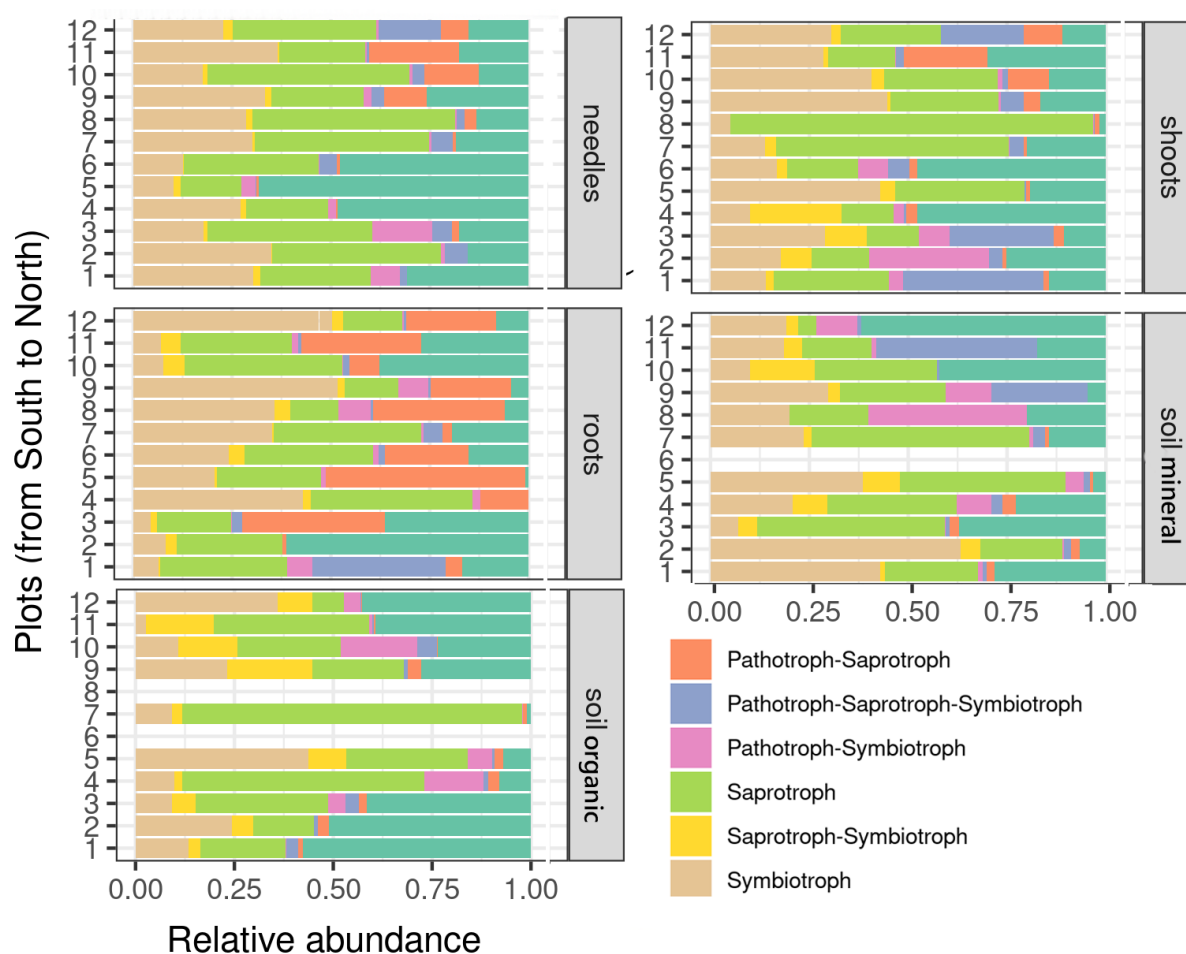

Fig. 2 Relative abundance of trophic guilds in different pine tissues based on FUNGuild analysis. Unidentified species was removed.

CONCLUSIONS

The chemical parameters of the soil studied by us did not show dependence on latitude, despite this, they significantly influenced the biodiversity of fungal communities. Diversity indicators (richness and Shannon index) for pine practically do not change in the latitudinal gradient. Communities of pine generally reacted to changes in climatic parameters, to a lesser extent to the chemical parameters of the soil. Fungal communities were affecting mostly by continentality, as well as in the amount of annual precipitation. Under the pressure of climate

change, tree populations are expected to shift along the gradients indicated above. The various fungus guilds did not show a uniform latitude distribution.

Keywords: Scott pine, mycobiont, functional diversity

REFERENCES

1. RIDO, D.; SAN-MIGUEL-AYNAZ, J.; CAUDULLO, G.; DURRANT, T.H.; MAURI, A. editors. European atlas of forest tree species. Luxembourg: Publications Office of the European Union; 2016.

2. BĀDERS, E.; JANSONS, Ā.; MATISONS, R.; ELFERTS, D.; DESAINE, I. Landscape Diversity for Reduced Risk of Insect Damage: A Case Study of Spruce Bud Scale in Latvia. Forests. Multidisciplinary Digital Publishing Institute; 2018, Vol. 9, P. 545.

3. NETHERER, S.; MATTHEWS, B.; KATZENSTEINER, K.; BLACKWELL, E.; HENSCHKE, P.; HIETZ, P.; et al. Do water-limiting conditions predispose Norway spruce to bark beetle attack? New Phytologist. 2015, Vol. 205, P. 128–41.

4. MÄKINEN, H.; NÖJD, P.; MIELIKÄINEN, K. Climatic signal in annual growth variation in damaged and healthy stands of Norway spruce [Picea abies (L.) Karst.] in southern Finland. Trees. 2001, Vol. 15, P. 177–85.

5. TREML, V.; MAŠEK, J.; TUMAJER, J.; RYDVAL, M.; ČADA, V,.;LEDVINKA, O.; et al. Trends in climatically driven extreme growth reductions of Picea abies and Pinus sylvestris in Central Europe. Global Change Biology. 2021, Vol. 28, P. 557-570.

6. MASSON-DELMOTTE, V. P.; RANI, S.L. IPCC, 2021: Climate Change 2021: The Physical Science Basis. Contribution of Working Group I to the Sixth Assessment Report of the Intergovernmental Panel on Climate Change. 2021;

7. BERG, G.; RYBAKOVA, D.; FISCHER, D.; CERNAVA, T.; VERGÈS, M.C.C.; CHARLES, T. Microbiome definition re-visited: old concepts and new challenges. *Microbiome*. 2020, Vol. 8, P. 103.

8. COMPANT, S.; VAN DER HEIJDEN, M.; SESSITSC, A. Climate change effects on beneficial plant–microorganism interactions | FEMS Microbiology Ecology | Oxford Academic, 2010, Vol. 73, P. 197 - 214

9. SURYANARAYANAN, T. S.; SHAANKER, R. U. Can fungal endophytes fast-track plant adaptations to climate change? *Fungal Ecology*. 2021, Vol. 50, NO. 101039.

10. U'REN, J.M.; LUTZONI, F.; MIADLIKOWSKA, J.; ZIMMERMAN, N.B.; CARBONE, I.; MAY, G.; et al. Host availability drives distributions of fungal endophytes in the imperilled boreal realm. *Nature Ecology & Evolution*. 2019, Vol. 3, No.1430.

11. OITA, S.; IBÁÑEZ, A.; LUTZONI, F.; MIADLIKOWSKA, J.; GEML, J.; LEWIS, L.A.; et al. Climate and seasonality drive the richness and composition of tropical fungal endophytes at a landscape scale. *Communications Biology*, 2021, Vol. 4, P. 1–11.

12. NGUYEN, D.; BOBERG, J.; IHRMARK, K.; STENSTRÖM, E.; STENLID, J. Do foliar fungal communities of Norway spruce shift along a tree species diversity gradient in mature European forests? *Fungal Ecology*, 2016, Vol. 23, P. 97–108.

13. NAYLOR, D.; SADLER, N.; BHATTACHARJEE, A.; GRAHAM, E.B.; ANDERTON, C.R.; MCCLURE, R.; et al. Soil Microbiomes Under Climate Change and Implications for Carbon Cycling. *Annual Review of Environment and Resources*. 2020, Vol. 45, P. 29–59.

14. KINLOCK, N. L.; PROWANT, L.; HERSTOFF, E.M.; FOLEY, C.M.; AKIN-FAJIYE, M.; BENDER, N.; et al. Explaining global variation in the latitudinal diversity gradient: Meta-analysis confirms known patterns and uncovers new ones. *Global Ecology and Biogeography,* 2018, Vol. 27,P. 125–41.

15. MARČIULYNIENĖ, D.; MARČIULYNAS, A.; LYNIKIENĖ, J.; VAIČIUKYNĖ, M.; GEDMINAS, A.; MENKIS, A. DNA-Metabarcoding of Belowground Fungal Communities in Bare-Root Forest Nurseries: Focus on Different Tree Species. Microorganisms. Multidisciplinary Digital Publishing Institute; 2021, Vol. 9, No. 150.

16. R Core Team. R: A language and environment for statistical computing [Internet]. Vienna, Austria: R Foundation for Statistical Computing; 2021. Available from: <https://www.R-project.org/>.

17. NGUYEN, N. H.; SONG, Z.; BATES, S.T.; BRANCO, S.; TEDERSOO, L.; MENKE, J.;et al. FUNGuild: An open annotation tool for parsing fungal community datasets by ecological guild. *Fungal Ecology*, 2016, Vol. 20, No. 241.